ASNR23 ABSTRACT PROCEEDINGS

SCIENTIFIC PODIUM PRESENTATIONS

Monday, May 1, 2023
9:30-10:30 AM
ASPNR Programming: Essentially Emergent Pediatric Neuroimaging (Essentials Track)

645

Fetal Brain Parenchymal Hemorrhage: Etiology, Imaging Findings, and Outcomes

E George[1], R Vassar[2], A Mogga[3], Y LI[2], M Norton[4], D Gano[4], O GLENN[4]
[1]University of California San Francisco, San Francisco, CA, [2]UCSF, San Francisco, CA, [3]Albany Medical College, Albany, NY, [4]University of California, San Francisco, San Francisco, CA

Purpose
To determine the etiology, MRI findings, and outcomes in fetal brain intraparenchymal hemorrhage (IPH).
Materials and Methods
We searched reports of all fetal brain MRIs performed at our institution from 1998 to March 2022 to identify cases of IPH. Cases with germinal matrix hemorrhage (GMH) or extra-axial/intraventricular hemorrhage (IVH) in the absence of IPH were excluded. Images were re-reviewed to identify distribution of hemorrhage and other CNS and placental abnormalities, and electronic medical records were reviewed to identify etiology and postnatal outcomes.
Results
The study cohort consisted of 48 fetuses with IPH. Median GA at the time of MRI was 23.5 weeks (IQR: 21.97-27.57 weeks) and the majority were singleton gestation (73%, 35/48). Twin-twin transfusion syndrome (TTTS) affected 92% (12/13) of the twin gestations; 7/12 (58%) were the recipient twin, and 8/12 (67%) underwent placental laser ablation. IPH was commonly supratentorial (73%, 35/48, Figure), occurred in deep gray nuclei in 42% (20/48), in the cortex in 31% (15/48), with evidence of schizencephaly in 15% (7/48) and polymicrogyria in 13% (6/48). There was superimposed diffuse injury in 44% (21/48), porencephaly in 13% (6/48), and small brainstem in 23% (11/48). Associated findings included ventriculomegaly (65%, 31/48), GMH 73% (35/48), IVH (46%, 22/48). The placenta was abnormally heterogenous in 15% (7/48). The most common etiology of IPH was TTTS (12/48, 25%). Among singletons, genetic causes were most frequent (10/35, 29%, Figure), and the cause was unknown in 34% (12/35). Half of the study cohort was liveborn (24/48, median GA: 38 weeks; IQR: 34.93-39.14 weeks) while 33% (16/48) underwent voluntary termination. The remainder underwent spontaneous intrauterine demise (n=3), reduction by radiofrequency ablation (n=3), and the outcome was unknown in 2 cases. Three infants died in the NICU or within 1 year of life, 6 were lost to follow-up and 3 were <1 year old at the time of last follow-up. Of the 24 liveborn (46%), 11 had clinical follow-up for >1 year; among them, 91% (10/11) had cerebral palsy, 36% (4/11) had epilepsy, 55% (6/11) had language/cognitive impairment, and 45% (5/11) had hearing/vision impairment.
Conclusions
Fetal IPH is associated with high prevalence of superimposed diffuse brain injury. Twin pregnancy-related complications and genetic causes were the most common etiologies of IPH in our cohort. Fetal IPH is associated with high rates of cerebral palsy among children who survive beyond one year.

MRI Finding	N (%)
Location	
Supratentorial	35/48 (72.9)
Infratentorial	5/48 (10.4)
Supra- and Infratentorial	4/48 (8.3)
Diffuse IPH	4/48 (8.3)
Focal IPH	23/48 (47.9)
Diffuse Injury+ Focal IPH	21/48 (43.8)
Unifocal IPH	25/44 (56.8)
Multifocal IPH	19/44 (43.2)

Etiology of IPH	N (%)
TTTS	12/48 (25)
COL4A1/2 variants	7/48 (14.6)
Other genetic cause	3/48 (6.3)
Fetal comorbidity	4/48 (8.3)
Maternal comorbidity	2/48 (4.2)
Unknown	12/48 (25)
Multiple Factors	3/48 (6.3)
Intrauterine transfusion	3/48 (6.3)
Other	2/48 (4.2)

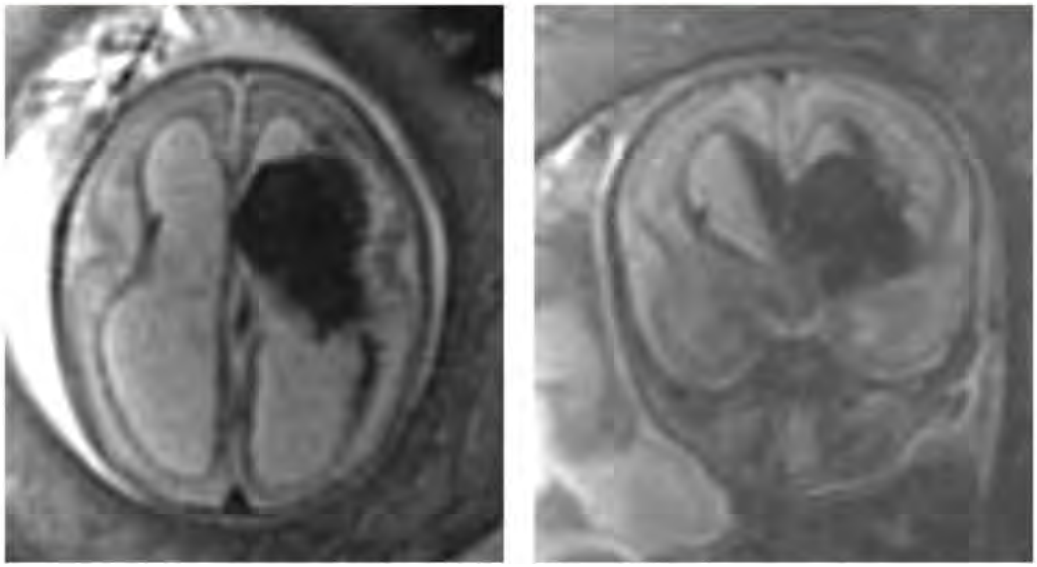

(Filename: TCT_645_Picture1.jpg)

Monday, May 1, 2023

9:30-10:30 AM

Scientific Abstract Session: Tumors 1

429

Adult-type Diffuse Glioma Segregation by 1H-MRS. Impact of Molecular Criteria Implemented in the WHO 2021 Classification of CNS Tumors.

C Majos[1], A Pons-Escoda[1], P Naval-Baudin[1], C Rubio[1], J Castell[1], N Vidal[1], G Plans[1], J Bruna[1], M Cos[1]

[1]Hospital de Bellvitge, L'Hospitalet de Llobregat, Spain

Purpose

The 2021 updated WHO classification of brain tumors has evolved the implementation of molecular criteria and classifies diffuse-glioma subgroups as astrocytoma, IDH-mutant; oligodendroglioma, IDH-mutant and 1p/19q codeleted; and glioblastoma, IDH-wildtype. On the contrary, in the 2007 classification they were classified by histology as oligodendroglioma, low grade astrocytoma, anaplastic astrocytoma and glioblastoma. Our aim is to assess the impact of the new criteria in the performance of 1H-MRS to classify adult-type diffuse gliomas by comparing the results to segregate 2007-defined to 2021-defined subgroups in the same set of patients.

Materials and Methods

Retrospective study with inclusion criteria: 1)Surgically resected untreated brain tumor, 2)Adult-type diffuse glioma on histology, 3)Known IDH mutation and 1p/19q codeletion status, 4)Pathology report providing diagnosis according to both 2007 and 2021

criteria, 5)TE, 30ms 1H-MRS available on the pre-surgical MR exam. Patients were classified according to 2021 criteria as IDH-mutant and 1p/19q codeleted (n=32), IDH-mutant and 1p/19q non-codeleted (n=55), and IDH-wildtype (n=230), and according to 2007 criteria as oligodendroglial (n=58), low grade astrocytoma (n=25), and high-grade astrocytoma (n=234). Differences between groups were assessed with the Mann-Whitney U-test, ROC curves were constructed with the resonances showing the highest differences, and two-step decision-trees based on the points with higher AUC-ROCs were elaborated to segregate tumor types.
Results
The main differences were found on Lipids at 0.9 ppm (Lip 0.9) and 1.3 ppm (Lip 1.3). The first step of the two decision-trees, one for 2007 and the other for 2021 classification criteria, was based on the Lip 1.3 and allowed the discrimination of high-grade and low-grade gliomas (WHO 2007 criteria, AUC=0.89) and IDH-mutant and IDH-wildtype gliomas (WHO 2021; AUC=0.87). Lip 0.9 was used in the second step to discriminate between oligodendroglial and low-grade astrocytoma (WHO 2007; AUC=0.70) and between 1p/19q codeleted and 1p/19q non-codeleted tumors (WHO 2021; AUC=0.78). The classifier performed better when tumor groups were defined with 2021 criteria (WHO 2007, 218/317 satisfactory classifications, 69%; WHO 2021, 239/317 satisfactory classifications, 75%).
Conclusions
The molecular criteria adopted in the 2021 WHO classification of CNS tumors provide better metabolomic characterization of adult-type diffuse gliomas, demonstrated by better tumor-group segregation by 1H-MRS.

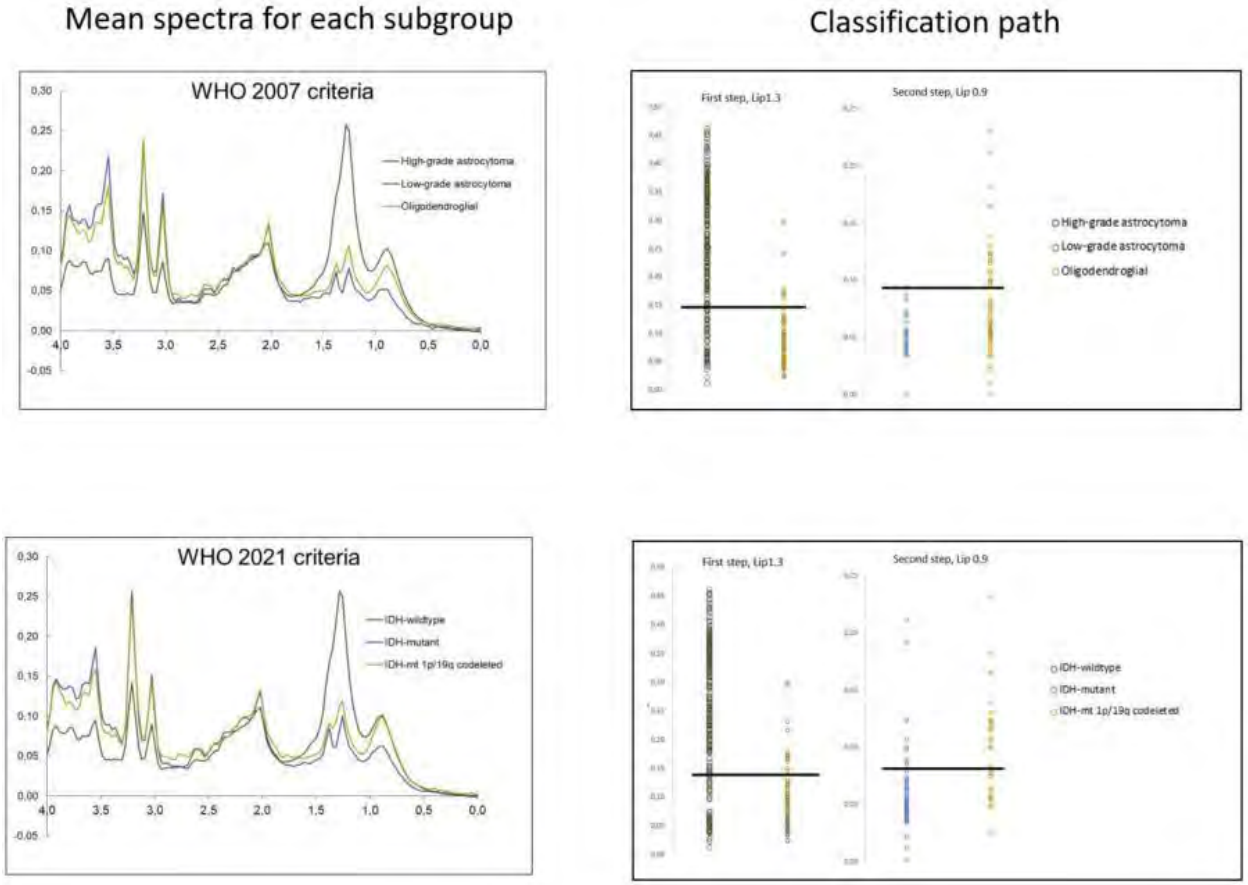

(Filename: TCT_429_Figure_3.JPG)

1297

Association between MR spectroscopic imaging findings and radio-pathomic maps of cellularity in a 53-year-old female diagnosed with a glioblastoma

S Bobholz[1], J Lupo[2], A Lowman[1], S Duenweg[1], A Winiarz[1], F Kyereme[1], J Connelly[1], D Coss[1], M Krucoff[3], M Agarwal[1], A Banerjee[1], P LaViolette[1]
[1]Medical College of Wisconsin, Milwaukee, WI, [2]UCSF, San Francisco, CA, [3]Medical College of Wisconsin`, Milwaukee, WI

Purpose
Previously published radio-pathomic models have used autopsy tissue samples as ground truth to non-invasively predict areas of hypercellular tumor beyond the contrast enhancement (1,2). This study compared pre-surgical findings from radio-pathomic maps of cell density to MR spectroscopic imaging (MRSI) acquired in a 53-year-old female diagnosed with a glioblastoma to identify the association between cell density and metabolic activity.
Materials and Methods
Pre-surgical imaging data from a 53-year-old female diagnosed with a surgically confirmed glioblastoma (IDH1-wildtype, EGFR amplified, p53 positive) acquired at UCSF was included in this study. T1-weighted images pre- and post-contrast administration, T2-

weighted FLAIR images, and apparent diffusion coefficient (ADC) images calculated from diffusion weighted imaging were used to generate radio-pathomic maps of cellularity using a previously trained model. MRSI was collected to measure the choline to N-acetyl aspartate (Cho/NAA) index for 10 mm isotropic voxels across the brain. Tumor-related membrane synthesis and turnover results in an increased choline signal and neuronal displacement and loss results in reduced NAA signal, leading to a higher Cho/NAA index in metabolically active tumor. The full resolution cell density map was then resampled to the dimensions of the spectroscopic imaging, and both images were masked using the FLAIR hyperintense region. A Pearson's correlation was then used to examine the association between voxel-wise cellularity values and Cho/NAA index.

Results

A positive association was observed between Cho/NAA index and predicted cell density values ($r = 0.386$, $p = 0.032$, Figure 1a). Visual inspection of the data revealed similar patterns of suspected tumor and edema occurring on both the spectroscopic imaging and the cell density maps (Figure 1b).

Conclusions

These results suggest that predicted cell density values from autopsy-based radio-pathomic models may associate with metabolically active tumor. Larger studies are essential for understanding the generalizability of this finding, as well as understanding the pathological basis for areas of discordance between the two modalities (i.e. hypercellular, metabolically inactive tumor and hypocellular, metabolically active tumor).

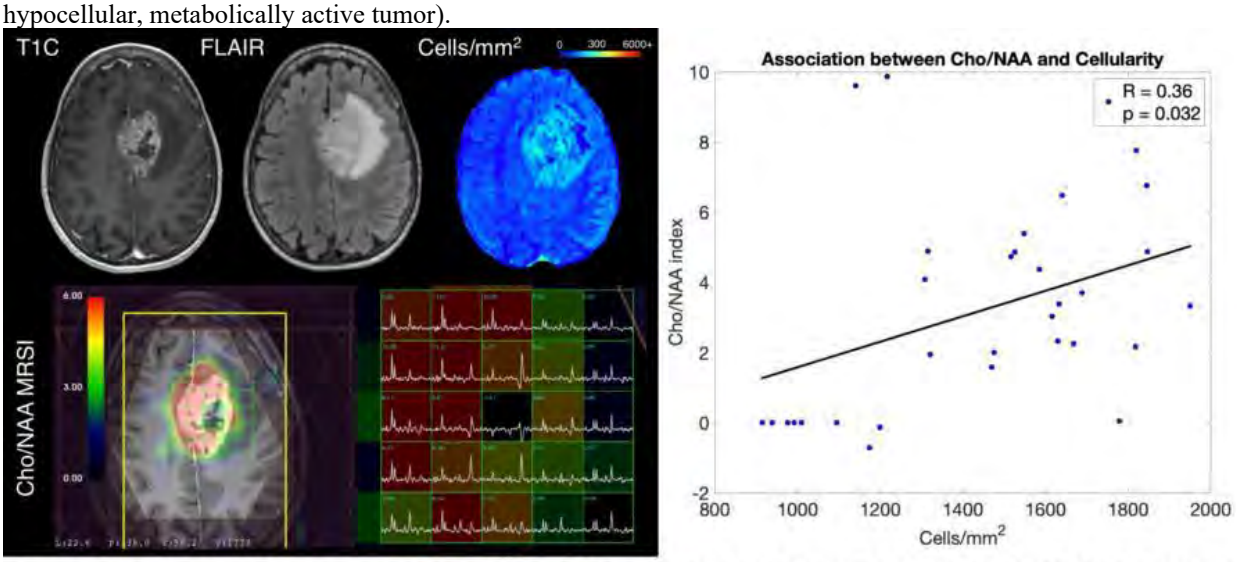

Figure 1: (left) Example imaging slice from T1C, FLAIR, cellularity and Chol/NAA MRSI, demonstrating simimilar patterns of deliniation between tumor and non-tumor portions of the FLAIR hyperintense region. (right) Scatterplot showing the association between cellularity and Cho/NAA index across the FLAIR hyperintense region, indicating a positve correlation.

(Filename: TCT_1297_SB_ASNR23_AB2_Fig.jpg)

508

CEST Imaging of the APT and ssMT Predict the Overall Survival of Patients with Glioma at the First Follow-Up after Completion of Radiotherapy at 3T

N von Knebel Doeberitz[1], F Kroh[2], J Breitling[2], S Graß[2], P Bachert[3], M Ladd[3], H Schlemmer[4], A Korzowski[3], D Paech[4]

[1]German Cancer Research Center, Heidelberg, Germany, [2]German Cancer Research Center, Heidelberg, Outside U.S., [3]German Cancer Research Center, Heidelberg, BW, [4]German Cancer Research Center, Heidelberg, Baden-Württemberg

Purpose

Chemical exchange saturation transfer (CEST) imaging of the amide proton transfer (APT) and semisolid magnetization transfer (ssMT) have been demonstrated to be associated with therapy response assessment and progression-free survival (PFS) of patients with glioma in the first follow-up after completion of radiotherapy at 3 and 7T(1). However, therapy response and PFS are based on response assessment in neuro-oncology (RANO) criteria, which represents a possible source of error due to overlapping features of radiation-induced changes and viable tumor tissue(2). Therefore, the Purpose of this prospective study was to compare the clinical potential of asymmetry-based (APTwasym), Lorentzian-fit-based (PeakAreaAPT and MTconst) and relaxation-compensated (MTRRexAPT and MTRRexMT) CEST contrasts of the APT, rNOE and ssMT for the prognostication of the overall survival (OS) of patients with glioma in the first follow-up after completion of radiotherapy at 3T.

Materials and Methods

In this prospective clinical study, 54 study participants with diffuse glioma underwent CEST MRI at 3T between July 2018 and December 2021 4 to 6 weeks after the completion of radiotherapy according to (3-5). Glioma-associated contrast enhancement (CE) and whole tumor (WT) tissue were segmented on T2w-TIRM and contrast-enhanced T1w images. Kaplan-Meier analysis and logrank-test were used for statistical analyses.

Results

72 study participants (mean age 59±16 years; 43 men) were enrolled. The prognostic values of the APTw, MTRRexAPT and MTconst

were influenced by glioma location. The APTw demonstrated a strong association with OS (HR=4.66, p<0.001) before and after stratification for glioma location. The MTconst (HR=2.54, p=0.044) was associated with the overall survival of participants with non-midline gliomas, whilst the MTRRexAPT (HR=2.44, p=0.056) showed a trend.

Conclusions

The APTw exceeds Lorentzian-fit-based and relaxation-compensated CEST imaging of the APT and ssMT in predicting the overall survival of patients with glioma in the first follow-up after completion of radiotherapy at 3T.

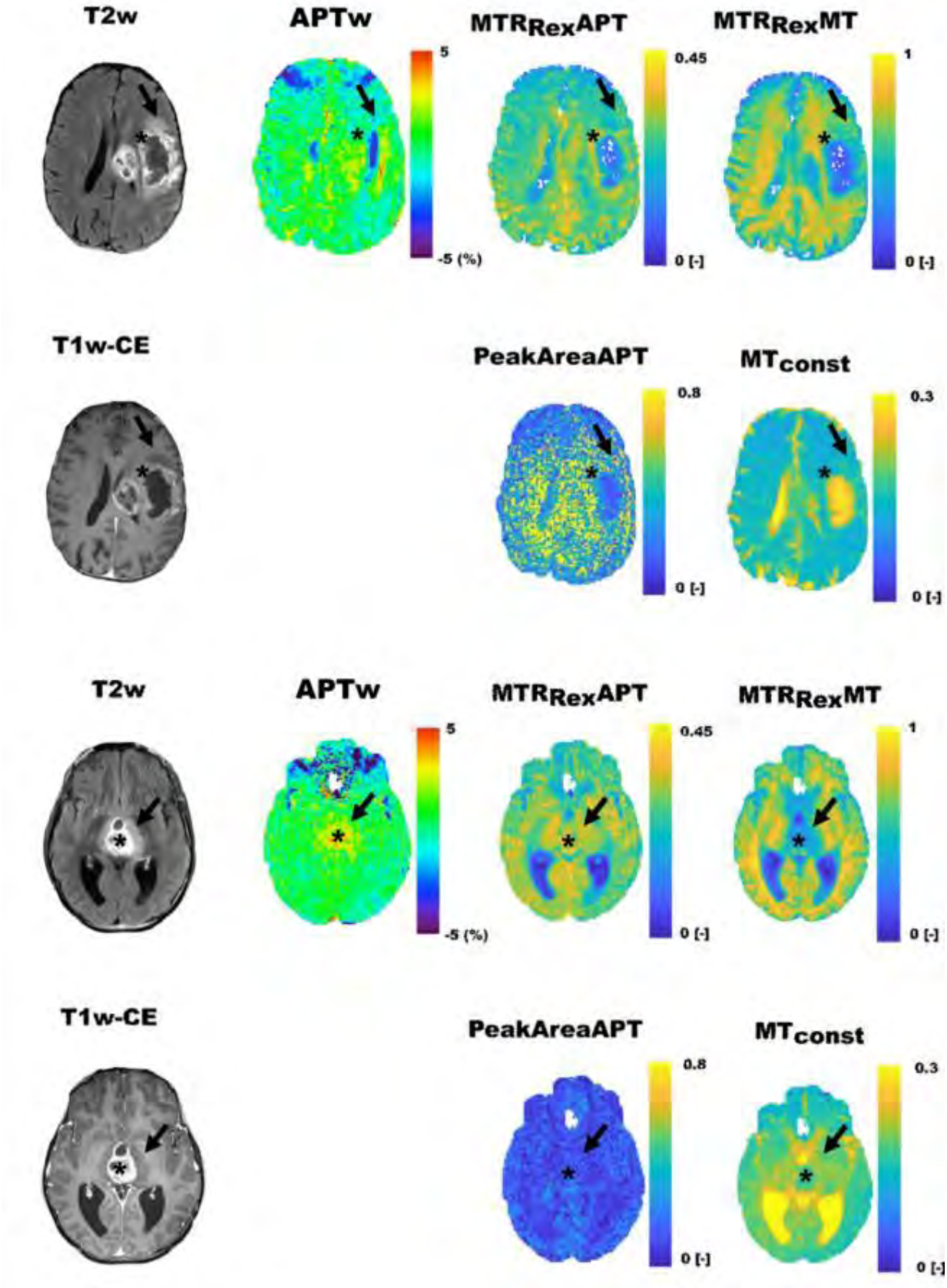

(Filename: TCT_508_Figure1_y.jpg)

502

Delayed Contrast and Multiparametric MRI for Treatment Response Assessment in Brain Metastases Following Stereotactic Radiosurgery

M Patel[1], J Jen[1], S Meade[1], H Benghiat[1], A Hartley[1], C Watts[2], P Sanghera[1], V Sawlani[1]

[1]Queen Elizabeth Hospital, Birmingham, West Midlands, [2]University of Birmingham, Birmingham, West Midlands

Purpose

Following stereotactic radiosurgery (SRS), brain metastases increase in size in up to a third of cases (1). Conventional MRI is limited for distinguishing between tumour recurrence and SRS-induced changes. Delayed contrast MRI treatment response assessment maps (TRAM) assess contrast clearance (CC), with tumour vascularity showing a rapid rise and rapid clearance of contrast over time. We assess the ability of delayed contrast MRI and functional multiparametric MRI techniques of diffusion, perfusion and spectroscopy to distinguish between radiation-related effects and tumour tissue.

Materials and Methods

A retrospective review was performed on 23 patients who had TRAM and multiparametric MRI between October 2018 to April 2020. Studies were restricted to cases with brain metastases enlarging post-SRS with uncertainty at the MDT meeting, impacting management. MRI was performed at 3T including DWI, PWI, MRS, and 3D T1 MPRAGE at 3-5, 20-30 and 70-90 minutes after administration of IV contrast. Contrast clearance, ADC, rCBV, and Cho/Cr ratio were calculated from an ROI in the enhancing lesion. Outcome was established from MRI follow-up at 6 months.

Results

Primary tumours were breast (n=8), lung (n=6), melanoma (n=4), neuroendocrine (n=2) and renal cell carcinoma (n=2), mean age 56 years, 50% female. 59% (n=13) were classified as having radiation-related changes on follow-up. Contrast clearance between the 3-5 and 70-90 minute imaging was significantly higher in tumour recurrence (23.6% vs. 2.5% decrease, $p<0.05$), as were rCBV and Cho/Cr ratio (rCBV 3.1 vs. 1.5, Cho/Cr 2.3 vs. 1.4, $p<0.05$). For tumour recurrence, the accuracy/sensitivity/specificity of using TRAM alone (CC>0%) was 63%/100%/38%, rCBV alone (>2.0) was 77%/75%/79% and for both Cho/Cr alone (>1.8) and combined with TRAM, it was 90%/88%/92%. Neuroradiologist assessment of all techniques was 95%/100%/92%.

Conclusions

This study shows the effectiveness of TRAM and multiparametric MRI for treatment response assessment in patients with brain metastases treated by SRS in clinical practice. Although a delayed contrast MRI study is a very sensitive tool for detecting tumour progression, it lacks specificity. The accuracy of differentiating between tumour and treatment-related effects increases when delayed contrast MRI is used in combination with other advanced techniques such as MRS. By combining all these techniques, neuroradiologists had the highest accuracy, sensitivity and specificity for detecting progression in post-SRS brain metastases.

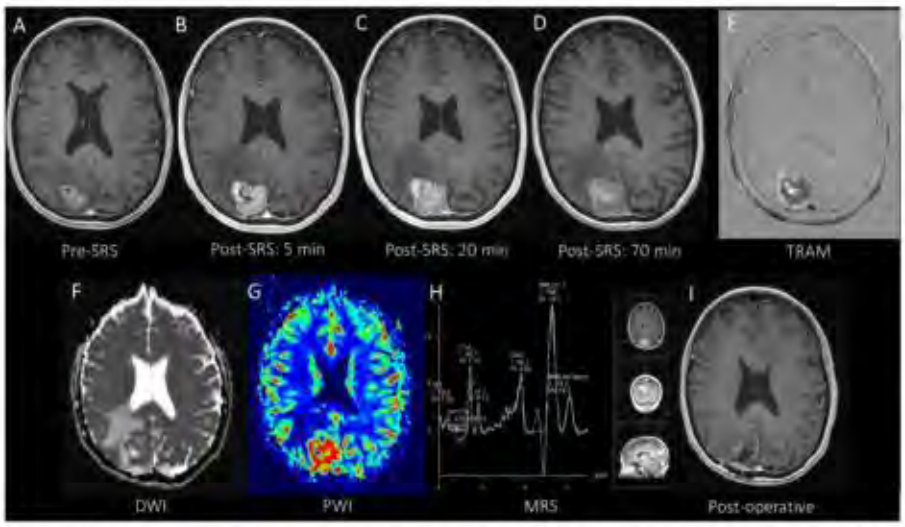

Figure 1. Tumour recurrence. (A) Pre-SRS imaging shows a right occipital metastatic lesion. (B) Post-SRS there is an increase in the size of the enhancing lesion. (C,D) Delayed contrast MRI performed at 20 and 70 minutes. (E) TRAM subtraction map between the 5 and 70 minutes imaging shows predominant contrast washout within the lesion. (F) Reduced diffusivity on the ADC map. (G) Raised rCBV throughout the lesion on perfusion imaging. (H) Raised choline/creatine ratio on spectroscopy. TRAM and multiparametric MRI are consistent with tumour recurrence. (I) The patient had resection of the lesion confirming recurrent disease.

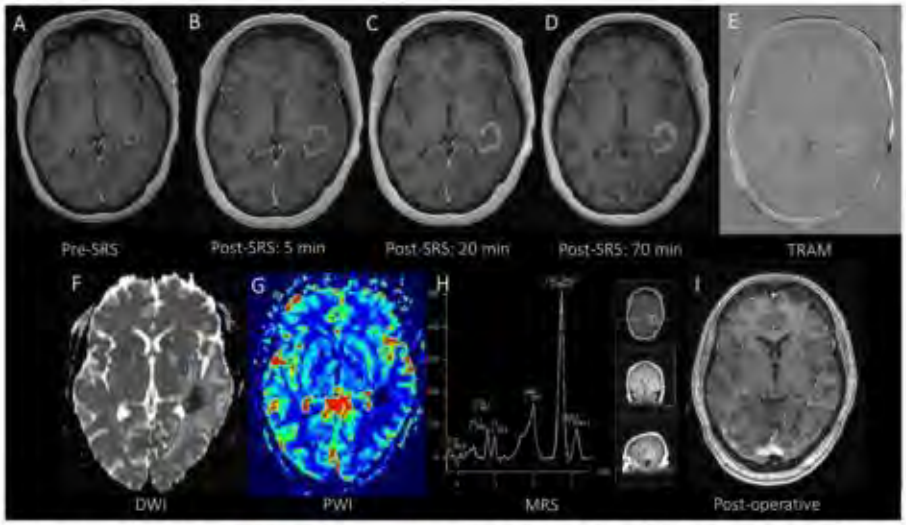

Figure 2. SRS-induced changes. (A) Pre-SRS imaging shows a left peri-trigonal metastatic lesion. (B) Post-SRS there is an increase in the size of the enhancing lesion. (C,D) Delayed contrast MRI performed at 20 and 70 minutes. (E) TRAM subtraction map between the 5 and 70 minutes imaging shows predominant contrast pooling. (F) Elevated diffusivity within the contrast-enhancing area, and reduced diffusivity within the core of the lesion on the ADC map. (G) Low rCBV throughout the lesion on perfusion imaging. (H) No elevation of choline/creatine ratio on spectroscopy. TRAM and multiparametric MRI are consistent with radiation change, (I) confirmed on the 12 month follow up imaging showing regression of the lesion.

Single parameters	DWI (ADC <1.000)	77	67	64
	PWI (rCBV <1)	77	75	79
	MRS (Cho/Cr ratio >1.3)	91	89	91
	TRAM (5-70 min change <0%)	64	100	38
Combined parameters	MRS + TRAM	80	95	66
	MRS + TRAM + PWI	82	58	100
Neuroradiologist assessment	All parameters	95	100	92

Table 1. Summary table of results showing the accuracies, sensitivities and specificities of each of the single parameters based on cut-off values, combined parameters and neuroradiologist assessment of all parameters.

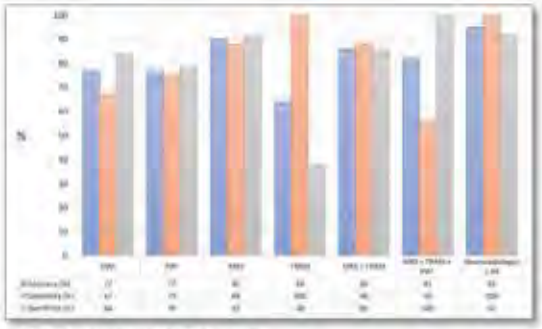

Chart 1. Summary chart of results.

(Filename: TCT_502_Figures.jpg)

706

Delta Radiomic Correlates of Apoptosis and Oxidative Stress in a First-in-Human Phase 0/1 Trial of 5-Aminolevulinic Acid Sonodynamic Therapy in Recurrent Glioblastoma

L Alhilali[1], A Tovmasyan[2], A Tien[2], T Margaryan[2], J Harmon[2], A Hong[2], W Yoo[3], S Fakhran[4], A Svec[5], S Mehta[2]

[1]Barrow Neurological Institute, Phoenix, AZ, [2]Ivy Brain Tumor Center, Phoenix, AZ, [3]Ivy Brain Tumor Center, Phoenix , AZ, [4]Banner Health System, Mesa, AZ, [5]Creighton University - Arizona, Phoenix, AZ

Purpose

5-aminoleveulinic acid sonodynamic therapy (5-ALA SDT) is a drug-device strategy that exploits the metabolic liabilities of cancer. Following systemic administration of 5-ALA, incomplete tumor metabolism leads to accumulation of a photosensitive intermediary, protoporphyrin-IX (PpIX). Activation of PpIX by non-invasive, non-ablative magnetic resonance-guided focused ultrasound (MRgFUS) induces cytotoxic reactive oxygen species and tumor cell death. The purpose of this study was to determine whether MR radiomics features may detect changes of apoptosis and oxidative stress after 5-ALA SDT.

Materials and Methods

Ascending energy doses of MRgFUS (200J, 400J, 800J) for 5-ALA SDT were tested in adult patients with recurrent glioblastoma (GBM) undergoing planned re-resection. Volumetric post-contrast MR was performed 48hr prior and 48 hr after 5-ALA SDT. Pyradiomics software was used to extract 105 quantitative features from segment enhancing tumor volumes on pre- and post-treatment MR. Percent change in each radiomic feature between the pre- and post- MRI was then correlated with percent change in molecular markers of apotosis (cleaved caspase-3, ClCas-3) and oxidative stress (4-hydroxynonenal, 4HNE; reduced to oxidize GSH ratio, 2GSH-GSSG; redox couple cysteine/cysteine, 2Cys/CySS). Recursive feature elimination with cross-validation with multivariate ridge regression was used to prevent overfitting and account for multicollinearity.

Results

A total of 8 patients (mean age 62.3, range 46-80, 50% male) were included. Average tumor volume was 45.9 cc (range 18.5 cc-195.7 cc). Mean increases were seen in ClCas-3 (1.3 fold), 4HNE (127 fold), 2GSH-GSSG (1.1 fold), and 2Cys/CySS (1.3 fold) after 5-ALA SDT. Change in only one radiomic feature was significantly associated with increased ClCas-3 after ridge regression elimination, Small Area Low Gray Level Emphasis (SALGLE), p=0.04. SALGLE is the proportion of the joint distribution of smaller size zones with lower gray-level values, and is correlated with tumor heterogeneity. Univariate regression demonstrated a strong effect size (R=-0.649, 1.84). No radiomic changes were associated with oxidative stress markers.

Conclusions

Changes in radiomic features can be detected after 5-ALA SDT, potentially offering a mechanism to non-invasively monitor treatment effects in this novel drug-device strategy.

1315

Differentiation of IDH-Wildtype Glioblastomas and Grade 4 IDH-Mutant Astrocytomas Using MRI Features and Tumor Volumetrics

D Serrano[1], D Timaran[2], L Nunez[3], A Rodriguez[3], R Riascos[3]

[1]UT Houston, Sugar Land, TX, [2]University of Texas Health Science Center Houston, Houston, TX, [3]The University of Texas Health Science Center at Houston, Houston, TX

Purpose

According to the 2021 update of the WHOs Classification of Tumors of the Central Nervous System, there are two subtypes of grade 4 glial neoplasms; IDH-wildtype glioblastomas (GBMs) and grade 4 IDH-mutant astrocytomas. This distinction is important as IDH mutations confer different biological properties that alter tumor aggressiveness, with the presence of an IDH mutation having a more favorable prognosis. The purpose of this study is to identify if MRI phenotypes can differentiate between IDH-wildtype and IDH-mutant WHO grade 4 gliomas on preoperative MRI exams.

Materials and Methods

A retrospective review of 271 patients WHO grade 4 gliomas was performed. Preoperative brain MRI examinations were evaluated and assigned values based on Visually AcceSAble Rembrandt Images (VASARI) MRI feature set. In addition, volumetric measurements of tumor enhancement, FLAIR hyperintensity, and necrosis were calculated based on semiautomatic segmentation. Associations between MRI features, volumetric measurements, and tumor type was assessed by univariate analysis performed using X2/Fisher's exact test with Monte Carlo simulation for categorical variables and non-parametric analysis with Mann-Whitney U test for continuous variables. Multivariate analysis was performed using the logistic regression analysis test.

Results

239 IDH-wildtype GBMs and 32 grade 4 IDH-mutant astrocytomas were reviewed. 5 volumetric measurements and 7 MRI features demonstrated statistical significance in differentiating between the two tumor on univariate analysis. IDH-wildtype GBMs demonstrated greater enhancing tumor volume, necrosis volume, percentage of enhancing tumor, and percentage of tumor necrosis. MRI features including enhancement quality, enhancement thickness, definition of enhancing margin, diffusion characteristics, cortical involvement, presence of non-enhancing tumor crossing the midline, and the presence of satellite lesions, were also statistically significant discriminators between the two tumors on univariate analysis. On multivariate analysis, enhancement quality, thickness of enhancement, presence of satellite lesions, and presence of non-enhancing tumor crossing the midline demonstrated statistical significance.

Conclusions
Enhancement quality, thickness of enhancement, presence of satellite lesions, and presence of non-enhancing tumor crossing the midline demonstrated statistical significance and may serve as discriminating biomarkers for differentiating between IDH mutations in grade 4 gliomas

Table 2. Association between MRI features and tumor type

MRI Features	IDH-Wildtype Glioblastoma (N=239)	Grade 4 IDH-Mutant Astrocytoma (N=32)	P-value
Tumor location			0.10
• Frontal	78 (32.4%)	19 (59.4%)	
• Temporal	91 (37.8%)	7 (21.9%)	
• Insular	8 (3.3%)	1 (3.1%)	
• Parietal	49 (20.3%)	4 (12.5%)	
• Occipital	9 (3.7%)	1 (3.1%)	
• Brain stem	0 (0.0%)	0 (0.0%)	
• Corpus callosum	6 (2.5%)	0 (0.0%)	
Enhancement quality			<0.01
• None	5 (2.1%)	4 (12.5%)	
• Minimal/mild	21 (8.7%)	14 (43.8%)	
• Marked/avid	215 (89.2%)	14 (43.8%)	
Multifocal/multicentric			0.13
• None	196 (81.3%)	29 (90.6%)	
• Multifocal	29 (12.0%)	1 (3.1%)	
• Multicentric	11 (4.6%)	0 (0.0%)	
• Gliomatosis	5 (2.1%)	7 (6.3%)	
Enhancement thickness			<0.01
• None	6 (2.5%)	5 (15.6%)	
• Thin	37 (15.4%)	6 (18.8%)	
• Thick/nodular	184 (76.4%)	12 (37.5%)	
• Solid	14 (5.8%)	9 (28.1%)	
Definition of enhancing margin			<0.01
• None	3 (1.2%)	4 (12.5%)	
• Well defined	95 (76.4%)	15 (25.0%)	
• Poorly defined	146 (22.4%)	17 (62.5%)	
Hemorrhage (Yes)	106 (44.0%)	17 (58.6%)	0.17
Diffusion characteristics			<0.01
• Facilitated	66 (27.4%)	18 (58.1%)	
• Restricted	90 (37.3%)	4 (12.9%)	
• Mixed	85 (35.3%)	9 (29.0%)	
Ependymal extension (Yes)	185 (76.8%)	20 (62.5%)	0.09
Cortical involvement (Yes)	203 (84.2%)	32 (100%)	0.01
Deep white matter invasion			0.09
• None	138 (57.3%)	13 (40.6%)	
• Internal Capsule	38 (15.8%)	4 (12.5%)	
• Brain Stem	6 (2.5%)	0 (0.0%)	
• Corpus callosum	59 (24.5%)	15 (46.9%)	
Non-enhancing tumor crosses midline (Yes)	198 (82.2%)	20 (62.5%)	0.02
Satellites (Yes)	83 (34.4%)	2 (6.5%)	<0.01
Calvarial remodeling (Yes)	7 (2.9%)	0 (0%)	1.00

(Filename: TCT_1315_IDHWTvsMut.JPG)

750

Imaging Spectrum of the Developing IDHwt GBM WHO Grade 4: A Retrospective Longitudinal Observation Study

S Currie[1], K Fatania[1], R Gilliver[1], J Start[1], M Lee[1], R Frood[1], L Murray[1], A Chakrabarty[1], R Mathew[1], S Short[1], A Scarsbrook[1]
[1]*Leeds Teaching Hospitals NHS Trust, Leeds, West Yorkshire*

Purpose
Glioblastoma (GBM), the most common malignant adult brain tumour, has the typical radiological appearance (TRA) of a centrally necrotic, peripherally enhancing tumour with surrounding oedema. Knowledge of imaging appearances prior to TRA GBM may aid early detection and improve overall survival (OS). Purpose: Determine whether developing GBM display a spectrum of imaging changes that are detectable on routine clinical imaging.

Materials and Methods
Retrospective longitudinal observational study. Patients with pre-operative imaging diagnosed with isocitrate dehydrogenase wildtype (IDHwt) GBM (01/01/2014–31/03/2022) were identified from a neuroscience centre. Imaging was reviewed by an experienced neuroradiologist. Imaging patterns preceding TRA GBM were analysed.
Results
76/555 (14%) patients had imaging preceding TRA GBM; 57 had solitary and 19 had multiple lesions (total=84 lesions). Of these 76, at the time of tissue sampling, 20 lesions never had imaging showing TRA GBM; classed as 'non-TRA GBM'. At the time of initial imaging 83% had a cortical or cortical/subcortical lesion. Earliest imaging feature for 84 lesions: T2 hyperintensity/CT low density (n=18), CT hyperdensity (n=51), T2 iso-intensity (n=15). When CT and MRI were available all CT hyperdense lesions showed T2 iso-intensity, reduced diffusivity, and the following enhancement patterns: none 26%, nodular 35%, solid 29%, patchy peripheral 10%. Mean time to develop TRA GBM from T2 hyperintensity=140/179 days and from CT hyperdensity=69/95 days for patients not receiving/receiving treatment respectively. All 20 non-TRA GBM showed CT hyperdensity and/or T2 iso-intensity. Compared to TRA GBM, non-TRA GBM were smaller, had less oedema and better OS (17 vs. 10 months).
Conclusions
Developing GBM show a spectrum of imaging features, progressing through T2 hyperintensity to CT hyperdensity, T2 iso-intensity, reduced diffusivity, and variable enhancement to TRA GBM. Red flags for non-TRA GBM lesions are cortical/subcortical hyperdense/T2 iso-intense/low ADC. Future research correlating this imaging spectrum with pathophysiology may provide further insight into GBM growth and contribute to potential screening.

Monday, May 1, 2023
9:30-10:30 AM
Scientific Abstract Session: White Matter Diseases

1239
Comparison of Lesion Evolution in Pediatric Demyelinating Diseases Using Myelin and Axonal-sensitive MRI
N Saadat[1], F Yu[2]
[1]University of Texas Southwestern, Dallas, TX, [2]UT Southwestern, Dallas, TX

Purpose
Pediatric demyelinating disorders include multiple sclerosis (MS), neuromyelitis optica spectrum disorder (NMOSD), anti-myelin oligodendrocyte glycoprotein (MOG) associated disorders (MOGAD), clinically isolated syndrome (CIS), and acute disseminated encephalomyelitis (ADEM). MRI plays a crucial role in the diagnosis and management of these diseases but lacks specificity for the underlying pathophysiology. Novel imaging biomarkers tailored to imaging myelin and axonal integrity should enhance our understanding and ability to characterize evolution of these diseases. In this study, we sought to compare the evolution of focal demyelinating lesions in pediatric MS and other demyelinating diseases using advanced MR imaging.
Materials and Methods
This prospective study was approved by the Institutional Review Board committee and complies with the Health Insurance Portability and Accountability Act Guidelines. Fourteen subjects with pediatric CNS demyelinating disorders (eight MS and five non- MS cases) and two healthy controls were included in this study. All subjects underwent MR imaging on the same 3T scanner (Siemens Prisma) at two consecutive time points (one year apart). Myelin volume fraction (MVF), and neurite density index (NDI) were derived from multi-echo GRE and multi-shell diffusion imaging data, respectively. MVF and NDI were then coupled to estimate the myelin g-ratio.
Results
When comparing lesion evolution among MS patients' first scan with follow-up scan, there was a significant decrease in calculated mean MVF (0.164 ± 0.026 vs. 0.131 ± 0.022, p-value 0.016) and NDI (0.414 ± 0.059 vs. 0.331 ± 0.050, p-value 0.009) without notable change in g-ratio (0.812 ± 0.030 vs. 0.821 ± 0.045, p-value 0.635). In non-MS patients, no significant change was observed between mean MVF (0.188 ± 0.064 vs. 0.173 ± 0.072, p-value 0.722), NDI (0.346 ± 0.111 vs. 0.378 ± 0.109, p-value 0.658), and g-ratio (0.750 ± 0.020 vs. 0.784 ± 0.061, p-value 0.289).
Conclusions
Our findings suggest pediatric MS demonstrates greater loss of tissue microstructure within lesions compared to non-MS over the same time period. Using myelin and axonal-sensitive MRI to assess these diseases could enhance our understanding of disease pathophysiology, and lead to enhanced diagnosis and management.

1503

High gradient diffusion MRI reveals reduced axon density and increased axon diameter in white matter lesions associated with migraine

L Eskandarian[1], K Gaudet[2], M Li[3], S Huang[4], K Eikermann-Haerter[5]

[1]Massachusetts General Hospital, Harvard Medical School, Boston, MA, [2]Massachusetts General Hospital, Boston, MA, [3]New York University Grossman School of Medicine, New York, NY, [4]Massachusetts General Hospital, Harvard Medical, Boston, MA, [5]New York University, New York, NY

Purpose

Migraine is among the most prevalent neurological diseases, marked by unilateral headaches lasting between 4-72 hours. White matter lesions (WML) have been shown in neuroimaging studies to occur two to four times more often in migraine patients, especially in patients with aura [1-4]. Advanced diffusion MRI methods have been used to expand our knowledge of the microstructural basis of WMLs in migraineurs [2]. Here, we used high-gradient strength diffusion MRI on the Connectome scanner to explore microstructural differences in axon diameter and density in migraine patients compared to healthy controls (HC).

Materials and Methods

This IRB-approved study included 16 migraine patients with aura and 16 age- and sex-matched HC. Demographic and clinical features are shown in Table 1. MR imaging was performed on a 3T Connectome scanner (MAGNETOM Connectom, Siemens Healthcare, Erlangen, Germany) equipped with maximum gradient strength of 300 mT/m. Structural T1W 3D MPRAGE, T2 SPACE FLAIR and multi-shell diffusion MRI with b-values ranging from 50 to 6,000 s/mm2 (TE/TR = 3600/77 msec, 2×2×2 mm3 voxels, r = 2) were obtained using up to 64 directions per shell. Diffusion MRI data were fitted to the TractCaliber model [5] to obtain estimates of axon diameter index, hindered diffusivity, CSF volume fraction, and restricted volume fraction in the normal-appearing white matter (NAWM) and lesions of migraine and HC, as shown in Figure 1. A two-sample t-test and Pearson's correlation coefficient were used. P-values < 0.05 were considered significant.

Results

In migraine patients, restricted volume fraction (fr) was significantly reduced in NAWM compared to HC ($p = 0.0003$), consistent with reduced axon density (Fig. 2). Axon diameter (a), hindered diffusivity (Dh) and CSF volume fraction (fcsf) of white matter lesions were significantly higher compared to HC and NAWM of the same subjects ($p < 0.0001$). In migraine patients, fr of white matter lesions was significantly reduced compared to HC ($p < 0.0001$).

Conclusions

Our study showed microstructural alterations in the white matter of migraine patients, including reduced axonal density in NAWM compared to HC as well as reduced axon density and increased axon diameter within lesions compared to NAWM. Our results are in line with histopathological studies suggesting that white matter hyperintensities may be driven by silent infarct-like episodes and merit further validation in a larger clinical cohort as well as correlation with radiologic-pathologic studies.

Subject	Healthy Controls	Migraine Patients	P-value
Cortical GM			
Sex M/F	2/14	2/14	1
Age, years Mean (SD)	34.9 (11.1)	35.6 (10.4)	0.87
Race, Ethnicity	1 Asian 3 Black 1 Caucasian, Hispanic 8 Caucasian, Non-Hispanic 3 Unreported	1 Black 1 Caucasian, Hispanic 13 Caucasian, Non-Hispanic 1 Persian	
Migraine Disease Characteristics			
Disease Duration Mean (SD)	19.7 (10.7), range 7-42		
Laterality	7 bilateral, 9 unilateral: 5 on left, 4 on right, 2 inconsistently unilateral		
Aura Type	11 visual, 1 non-visual, 4 mixed		
Attack Frequency*	7 frequent, 9 less frequent		
Currently Taking Prescription Antimigraine Medication	11 yes, 5 no		
Change in Memory	8 general change in memory, 8 no change		
History of Head Trauma**	13 no history, 3 history of concussions		

Table 1. Demographic and clinical features of study participants
* Frequent attacks defined as a minimum of 10 per month
** No recent head trauma nor coinciding with initial migraine onset

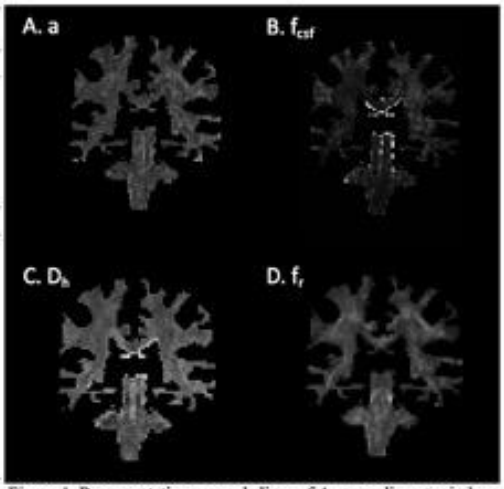

Figure 1. Representative coronal slices of A. axon diameter index, B. CSF volume fraction, C. hindered diffusion coefficient, and D. restricted volume fraction

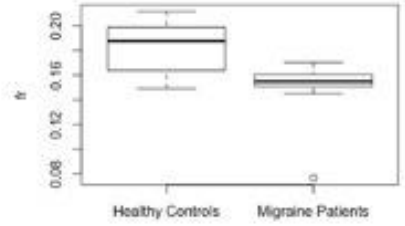

Figure 2. Migraine patients and healthy controls restricted volume fraction mean values

Subject	Healthy Controls (n=16) Mean (SD)	Migraine Patients (n=16) Mean (SD)	P-value
NAWM			
a	3.04 (0.2)	3.78 (0.3)	0.62
D_h	0.00068 (0.00008)	0.00047 (0.000075)	0.82
f_{csf}	0.1 (0.01)	0.12 (0.02)	0.77
f_r	0.18 (0.02)	0.15 (0.02)	0.0003

Table 2. Migraine patients and healthy controls Tract Caliber metrics values
a = axon diameter index; D_h = hindered diffusion coefficient; f_{csf} = CSF volume fraction; f_r = restricted volume fraction; NAWM = normal-appearing white matter.

(Filename: TCT_1503_TractCal.jpg)

676

Histogram Analysis of Mean Diffusivity Maps for Differentiating Tumefactive Demyelinating Lesions from Brain Metastases

M White[1], Y Zhang[1], M Aizenberg[1], R Zabad[1], F Yu[1], M Schissel[1]
[1]*University of Nebraska Medical Center, Omaha, NE*

Purpose

Tumefactive demyelinating lesion (TDL) refers to a large (≥2cm) tumor-like abnormality. The imaging features, such as mass effect, vasogenic edema, central necrosis, and ring enhancement, may make TDL not easily distinguishable from ring-like cystic/necrotic metastasis on conventional MRI. It has also been reported that DWI can be less helpful in differential diagnosis, as metastases may display elevated diffusion similar to TDLs. Histogram study, a method to analyze lesions voxel by voxel, can establish the intensity distribution and provide quantitative information about lesion heterogeneity. We therefore conducted a retrospective study to determine whether histograms of mean diffusivity (MD) calculated from DTI could be used to differentiate TDLs from metastases. We hypothesized that the distribution of MD reflects the difference in lesions' heterogeneity between TDLs and metastases.

Materials and Methods

31 TDLs in 22 cases and 27 metastases in 21 cases were included. All lesions are ≥2cm and show ring/peripheral contrast enhancement. Areas evaluated were designated as whole lesion and peripheral enhanced component. The parameters derived from the histogram analysis of MD maps included: MDmax, MDmean, MDmin, MDmedian, MDrange, MD10th/25th/75th/90th percentile, Skewness, Kurtosis, and Entropy. All measured MD values were normalized with MD measurements from CSF of lateral ventricle. Histograms were constructed using a bin size of 0.1. Shapiro-Wilk test was performed to assess the normal distribution. The two sample t-tests or non-parametric Wilcoxon rank sum tests were performed to compare the MD ratio between TDLs and metastases. ROC analysis was conducted by fitting a logistic regression model to each individual predictor.

Results

For enhanced components, TDLs had significantly higher MDmean, min, median, and MD at all percentiles than metastases. For whole lesions, TDLs showed significantly higher MDmin and 10th percentile but significantly lower MDmax, mean, median, and 75th/90th percentile than metastases. Metastases showed significantly higher Kurtosis, Entropy, and MDrange than TDLs. MD10th showed the best differentiating performance for enhanced components (0.941 AUC, 88.89% Sen, 93.55% Spe). Entropy showed the greatest differentiating ability for whole lesions (0.922 AUC, 77.78% Sen, 93.55% Spe).

Conclusions

Metastases have a greater variation of MDs than TDLs. Histogram analysis of MDs may effectively demonstrate the lesions' heterogeneity and help to distinguish TDL from metastases.

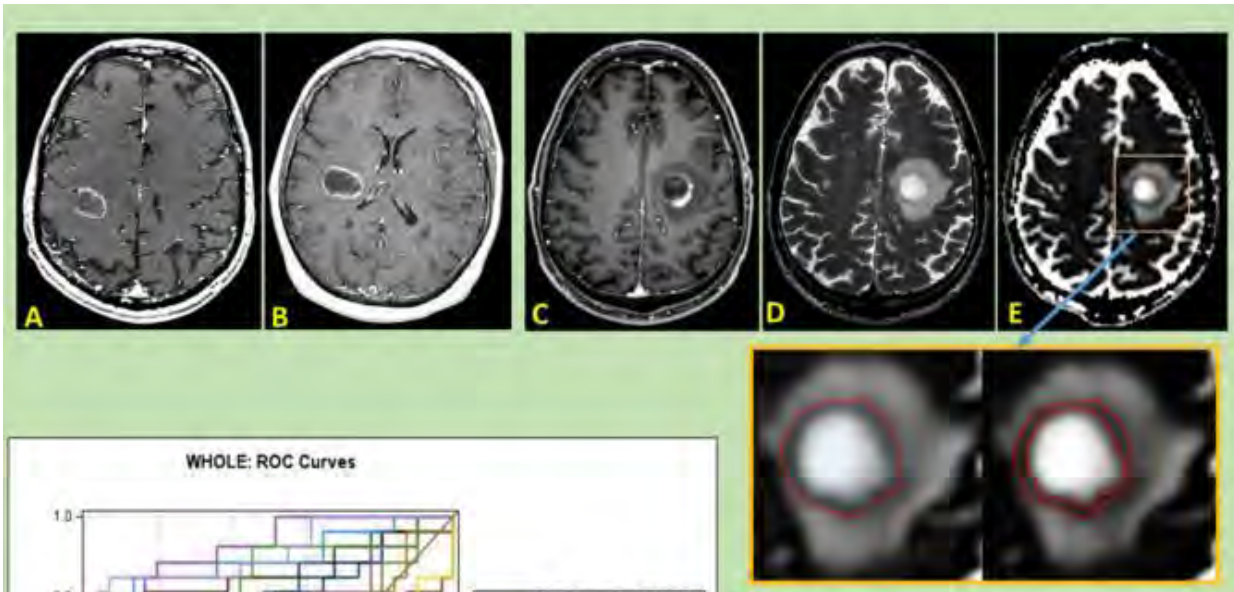

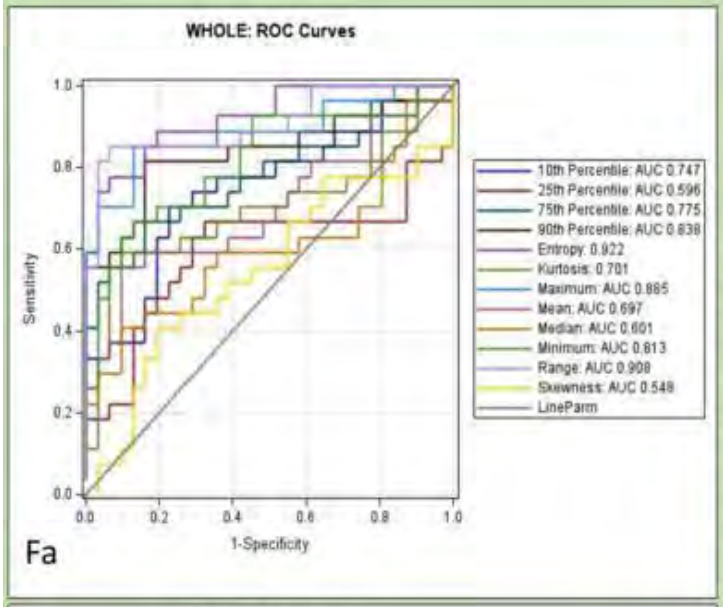

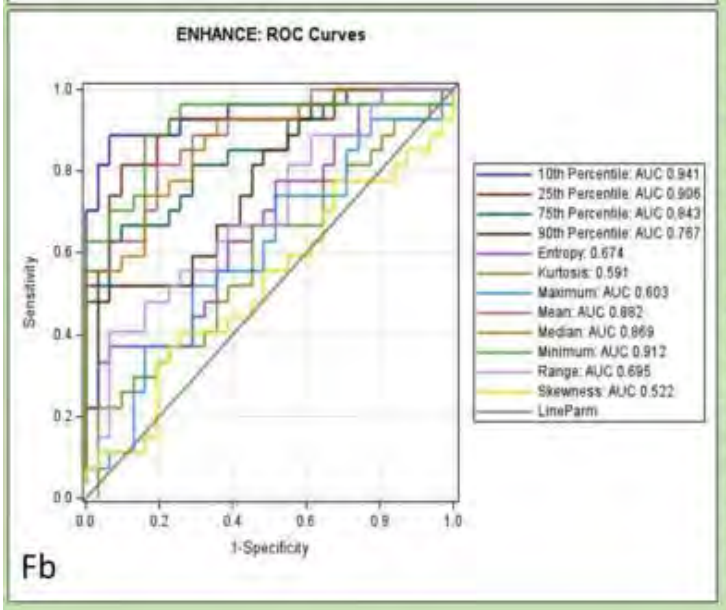

Figure

[A & B] is to show similarity in image features, peripheral/ring enhancement, of metastatic lesion (A) and tumefactive demyelinating lesion (TDL) (B).

[C, D, & E] is about the setting of ROI and shows left front lobe TDL with ring-enhanced (C) &T2 hypointense rim (D) and perilesional edema. Restricted diffusion of ring-enhancing rim is depicted on mean diffusivity map (E). Orange Box on (E) marks the site where the ROIs are set for measuring the MD of whole lesion and peripheral enhanced rim (images with red rim).
This TDL has a certain degree of elevated perfusion (not shown), and the possibility of metastatic lesion could not be completely ruled out.

[F] Receiver operating curve of mean diffusivity histogram for differentiating TDL from metastasis.
For whole lesion (Fa), Entropy showed the greatest ability to differentiate between the two groups (0.922 AUC, 77.78% sensitivity, 93.55% specificity).
For enhanced component (Fb), MD10th had the greatest ability to differentiate between the two groups (0.941 AUC, 88.89% sensitivity, 93.55% specificity).

(Filename: TCT_676_Figure.jpg)

604

Imaging Natural History and Phenotype Variability in TUBBA-related leukodystrophy and H-ABC

C ALVES[1], M Stellingwerff[2], R D'Aiello[3], F Gavazzi[4], B Charsar[4], A Vossough[5], M van der Knaap[6], A Vanderver[4]

[1]Children's Hospital of Philadelphia, Philadelphia, PA, [2]VU University Medical Center, Amsterdam, Amsterdam, [3]Childrens Hospital of Philadelphia, Philadelphia, PA, [4]Children Hospital of Philadelphia, Philadelphia, PA, [5]CHOP-UPENN, Philadelphia, PA, [6]Amsterdam University Medical Centers, Amsterdam, Netherlands

Purpose

Hypomyelination with atrophy of the basal ganglia and cerebellum (HABC), a subset of TUBBA- related leukodystrophy has a toddler onset, characteristic imaging features, and has been associated with a recurrent mutation(p.Asp249Asn). We sought to determine longitudinal imaging disease progression and imaging phenotype variability between the recurrent p.Asp249Asn versus other variants in TUBB4A-related leukodystrophy.

Materials and Methods

We retrospectively reviewed brain MRI studies (baseline and follow-ups) of 92 subjects with leukodystrophy from VU University Medical Center- Amsterdam, NL and Children's Hospital of Philadelphia, USA with proven TUBB4A pathogenic variants. MRIs were reviewed independently by 2 pediatric neuroradiologists with final agreement in searching for signal and structural abnormalities. The data was analyzed at the level of the full cohort and among key sub-cohorts including by variant and age at symptom onset.

Results

Hypomyelination was a constant and early feature, present in 95% at baseline-MRI. Cerebellar atrophy was noted in 45% of baseline studies progressing from superior vermis to diffuse involvement. The posterior aspect of the putamen was the most frequent area affected in the basal ganglia presenting with atrophy and T2 hyperintensity, although normal at baseline in 65% of the overall cohort. A statistically significant difference by genotype in putamen involvement was noted, mostly affecting patients with the recurrent p.Asp249Asn variant(71% vs 21%, p <0.001). Additional imaging findings included caudate head atrophy(20%), deformity of the septum pellucidum and fornix(28%), with or without basal ganglia atrophy, and mineralization in the basal ganglia(27%). Hypomyelination + cerebellar atrophy + striatal involvement was seen in 71% of p.Asp249Asn variants vs 18% of non-p.Asp249Asn variants.

Conclusions

This study represents the largest cohort of neuroradiological review of individuals with confirmed pathogenic TUBB4A variants. Longitudinal imaging changes across the spectrum of TUBB4A -related leukodystrophy include myelin disease (hypomyelination), and progressive atrophy of the cerebellum and striatum. This constellation of findings is most often seen in association with the recurrent p.Asp249Asn variant, confirming the association of this variant with the imaging features of H-ABC. This offers a better understanding of the natural history of the disease and improves understanding of the variability of the imaging patterns in TUBB4A-related leukodystrophy.

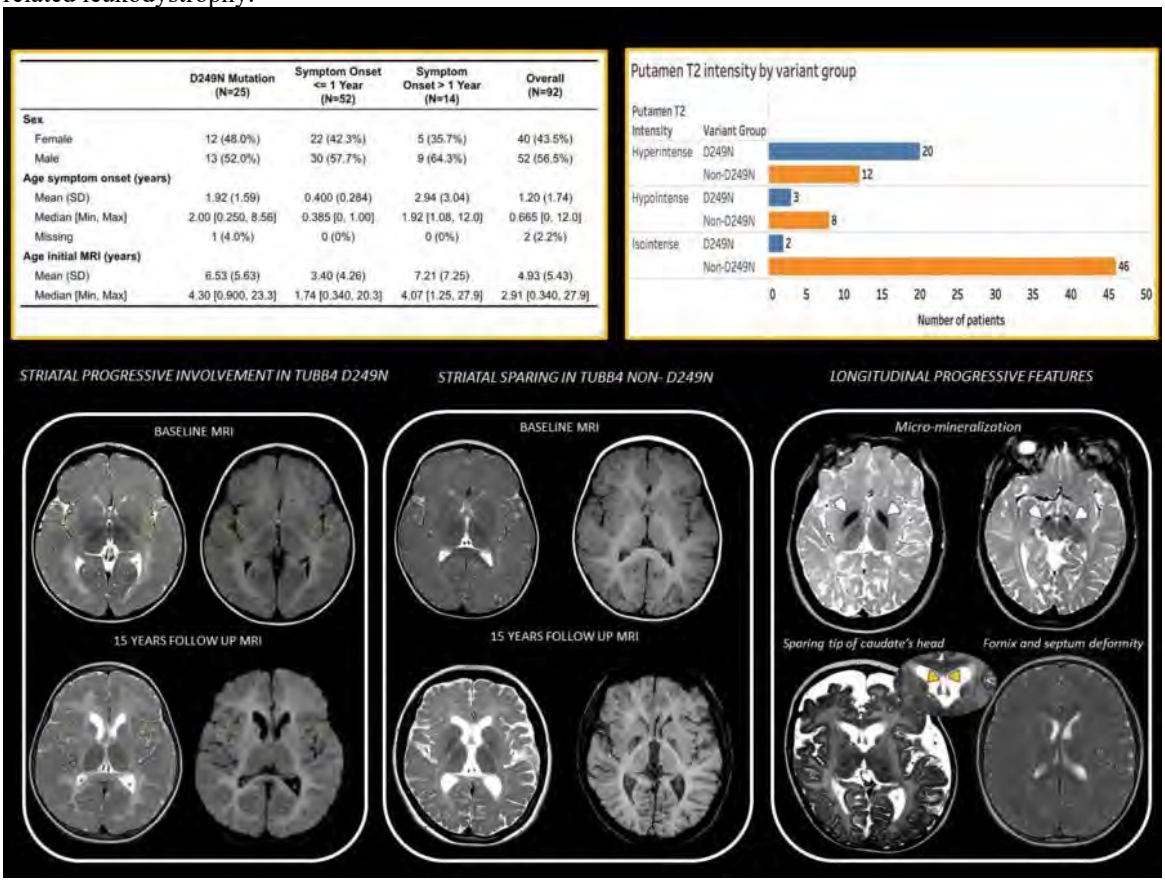

(Filename: TCT_604_Figure1300.jpg)

1487

Leptomeningeal enhancement, a specific marker for myelin oligodendrocyte glycoprotein antibody-associated disorder (MOGAD) in pediatric demyelinating syndromes

A Goldman-Yassen[1], A Lee[2], G Gombolay[1]

[1]Emory University School of Medicine and Children's Healthcare of Atlanta, Atlanta, GA, [2]Emory University School of Medicine, Atlanta , GA

Purpose

Leptomeningeal enhancement can be the initial presentation of a neuroinflammatory syndrome associated with antibodies against myelin oligodendrocyte glycoprotein (MOG-abs). In the appropriate clinical context, MOG-abs can identify MOG-associated disorder (MOGAD), an acquired demyelinating syndrome that includes features of neuromyelitis optica, multiple sclerosis-like, optic neuritis, and acute disseminated encephalomyelitis. However, no previous studies in have compared the rate of leptomeningeal enhancement in MOGAD to other demyelinating syndromes. Here, we evaluate MRI scans of children who presented with MOGAD, multiple sclerosis (MS), and aquaporin-4 antibody positive neuromyelitis optica spectrum disorders (AQP4-NMOSD) to determine the prevalence of leptomeningeal enhancement and determine the specificity of leptomeningeal enhancement as a marker of MOG-AD.

Materials and Methods

We performed a retrospective review of pediatric patients who presented to our institution with a demyelinating syndrome between 4/2013 and 12/2020 was performed. Clinical and laboratory data were extracted from the medical record. Neuroimaging was reviewed by a board certified neuroradiologist for the presence of leptomeningeal enhancement. Fisher exact test was used to compare the rates of leptomeningeal enhancement between patient groups.

Results

Forty-eight subjects were included in the analysis (median age 12 [IQR9-15], 75% female sex): 20 subjects with MS, 7 with AQP4-NMOSD, and 21 with MOGAD. These subjects underwent a total of 169 scans, median of 3 (IQR 1-5). Contrast was administered in 165 scans. Leptomeningeal enhancement was seen on 19/57 scans in MOG-AD and on no scans in MS (59) or AQP4-NMO (49) ($p<0.001$). Cranial nerve enhancement was noted in one MS patient on multiple follow-up scans.

Conclusions

Leptomeningeal enhancement is a specific marker for MOGAD in pediatric demyelinating syndromes. Further work is needed to correlate imaging findings with clinical prognosis.

1279

Linking disability and white matter integrity in multiple sclerosis

V Stepanov[1], S Coelho[2], B Ades-aron[3], M Lan[1], D Novikov[4], E Fieremans[5]

[1]New York University Grossman School of Medicine, New York, NY, [2]NYU School of Medicine, Center for Advanced Imaging and Research, New York, NY, [3]N/A, N/A, [4]New York University School of Medicine, New York, NY, [5]NYU Grossman School of Medicine, New York, NY

Purpose

Multiple sclerosis (MS) is a chronic autoimmune disease characterized by inflammatory and neurodegenerative processes leading to irreversible neurological impairment[1]. Here, we use advanced diffusion MRI (dMRI) (including DTI, DKI and biophysical Standard Model (SM)[2] to identify the cellular pathology underlying disease progression and compare against volumetry as an established outcome measure in MS[3].

Materials and Methods

We studied 46 MS patients (47±12 years, 32 female) that were characterized clinically with Expanded Disability Status Scale (EDSS) of 3 (median) ± 2.3(standard deviation), oral Symbol Digit Modalities Test (SDMT) of 48±13 and with Nine-Hole-Peg test (9HPT) for dominant hand of 23.9±8.5s. The patients underwent brain MRI on a 3T Siemens Prisma, including T1 MPRAGE with 1mm isotropic voxel, and multi-shell dMRI (tacq=27') with voxel size 2mm isotropic, consisting of conventional linear encoding (ranging from b=0 to 6000 s/mm2) and varying B-tensor shapes[4] and echo-times[4] (60-130ms). The dMRI data was preprocessed using DESIGNER[5] and parametric maps extracted of DTI fractional anisotropy [FA], mean/axial/radial diffusivities [MD/AD/RD]), DKI (mean/axial/radial kurtosis [MK/AK/RK]), and SM[2,4] (axonal water fraction [f], free water fraction [fw], intra-axonal diffusivity Da, extra-axonal axial/radial diffusivities [De∥/De⊥], fODF anisotropy [p2]), (Fig. 1A). Regional values for 3 white matter regions-of-interest (ROIs) were extracted, and volumes were calculated using Freesurfer.

Results

Widespread correlations are observed between dMRI and SM-parameters and clinical measures (Fig1B), where increased fw, T2e and decreased De∥with more disability and cognitive impairment indicate increased inflammation and gliosis, while increased De⊥ and decreased Da are suggestive of demyelination and neuronal injury, such as beading. Interestingly, DTI/DKI and volumetric data demonstrated correlations with SDMT only. Overall strongest correlations are observed for dMRI-derived SM parameters.

Conclusions

Diffusion MRI is more sensitive to tracking MS disease progression of disability and cognitive decline as compared to brain morphometry. The specific directional changes highlight the specificity of SM-parameters to understand how different underlying pathological processes contribute to disease progression and suggest the potential of advanced diffusion and the SM to provide quantitative prognostic markers of disability in MS.

Fig. 1

A

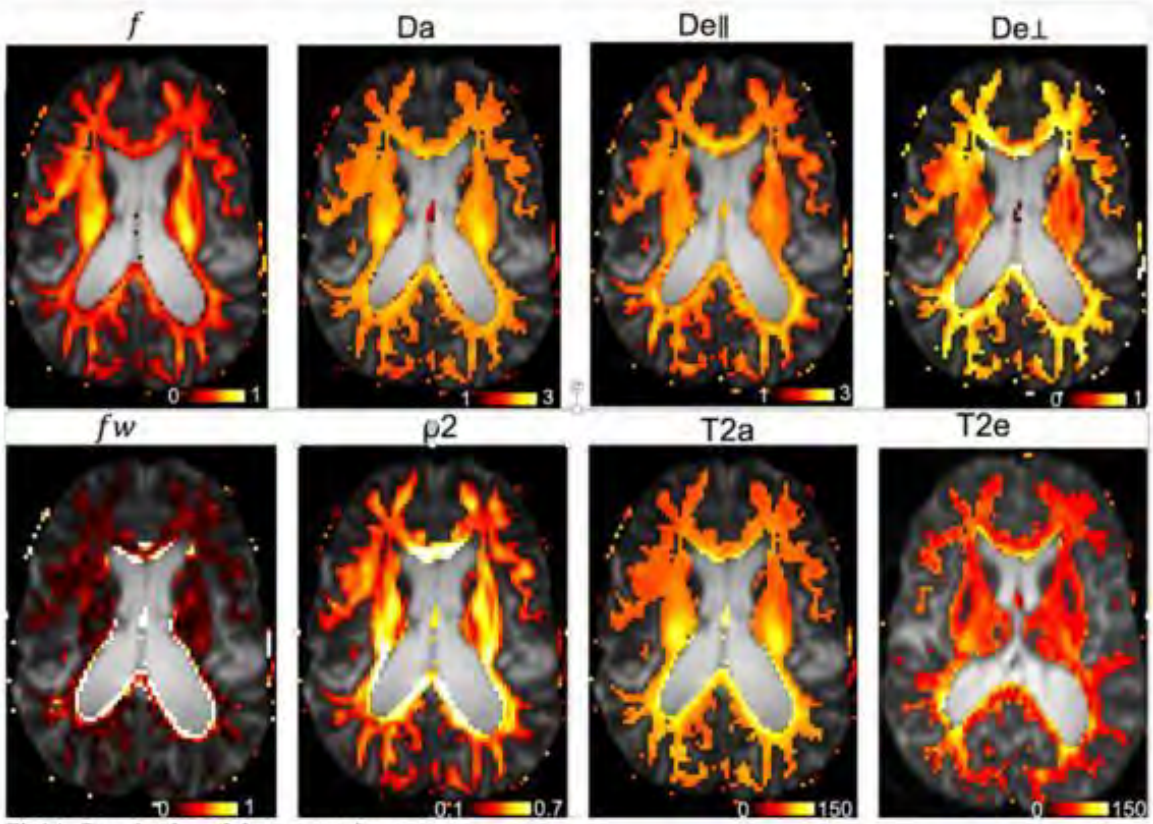

Fig1A. Standard model parametric maps.
f - Axonal water fraction (AWF)/neurite density (decrease is suggestive for demyelination, degeneration and axonal loss), $\mathbf{D_a}$ - Axonal diffusivity along axons (decrease is suggestive for axonal injury, beading), **De||**– extra-axonal axial diffusion (decrease – inflammation and gliosis), $\mathbf{D_e^{\perp}}$ – extra-axonal radial diffusion(increase caused by demyelination), **p2** – fiber orientation distribution function (decrease is caused by gliosis and microglial activation), $\mathbf{f_w}$ - free water fraction (increase with inflammation). **T2a** and **T2e** – intra- and extra-axonal relaxation times. While their roles have yet to be established, 1/T2a can be a potential marker for mitochondria density, which increases with demyelination in MS, whereas 1/T2e can serve as a marker for surface area density of myelin and myelin debris in the EAS.

B

ρ EDSS	RD	FA	rk	Da	De⊥	De‖	f	fw	ρ2	T2a	T2e
genu of corpus callosum	0.17	-0.20	-0.13	**-0.31**	-0.08	**-0.37**	-0.08	**0.46**	-0.02	-0.06	0.26
splenium of corpus callosum	0.07	-0.06	-0.03	**-0.34**	**-0.37**	**-0.41**	0.00	**0.30**	0.11	-0.16	**0.32**
superior corona radiata	0.20	-0.22	-0.25	-0.17	0.01	**-0.43**	-0.14	**0.54**	0.01	-0.09	**0.31**
superior longitudinal fasciculus	0.19	-0.13	-0.18	-0.19	-0.02	**-0.30**	-0.14	**0.38**	0.04	-0.03	0.28

ρ 9-Hole-Peg Test	RD	FA	rk	Da	De⊥	De‖	f	fw	ρ2	T2a	T2e
genu of corpus callosum	0.14	-0.18	-0.17	**-0.34**	0.11	**-0.36**	-0.19	**0.32**	0.00	0.00	0.14
splenium of corpus callosum	0.13	-0.20	-0.07	-0.22	-0.07	**-0.44**	-0.06	**0.24**	-0.05	-0.05	0.21
superior corona radiata	0.22	-0.23	-0.27	-0.24	**0.31**	**-0.33**	-0.27	**0.34**	0.09	-0.12	0.25
superior longitudinal fasciculus	0.22	-0.12	-0.13	-0.21	0.10	-0.20	-0.17	**0.37**	0.24	-0.08	**0.32**

ρ SDMT	RD	FA	rk	Da	De⊥	De‖	f	fw	ρ2	T2a	T2e
genu of corpus callosum	**-0.36**	**0.42**	0.24	**0.31**	-0.03	**0.35**	0.28	**-0.46**	0.27	**-0.31**	-0.24
splenium of corpus callosum	-0.22	0.26	0.23	0.16	0.03	**0.45**	0.19	**-0.41**	0.19	-0.04	**-0.42**
superior corona radiata	**-0.39**	0.30	**0.37**	0.19	**-0.33**	**0.35**	0.24	**-0.55**	0.00	-0.12	**-0.44**
superior longitudinal fasciculus	**-0.39**	**0.39**	**0.34**	0.27	-0.08	**0.50**	0.25	**-0.48**	0.09	-0.15	**-0.39**

Clinic_metrics	Ventricles	Cortex	WM	GM
EDSS	0.10	0.13	-0.10	0.15
SDMT	-0.11	0.07	**0.34**	0.02
HolePegTest	0.13	-0.03	-0.02	-0.04

Fig1B. Correlation of diffusion parameters measured in four different regions of interest and clinical metrics.
Significant correlations ($p<0.05$) are bolded (explanation is in the text).

(Filename: TCT_1279_ASNR_preliminary.jpg)

1298

Prediction of Active Multiple Sclerosis Algorithmic-Derived Lesions Through Use of Logistic Regression Classifier and First-Order Features

V Nguyen[1], A Hasse[2], E Tao[3], J Jang[4], A Javed[2], T Carroll[2], K Kawaji[1]

[1]Illinois Institute of Technology, University of Chicago, Chicago, IL, [2]University of Chicago, Chicago, IL, [3]Illinois Institute of Technology, Chicago, IL, [4]Philips Healthcare, Gainesville, FL

Purpose

Contrast-enhanced MRI is the current standard for diagnosis and tracking of Multiple Sclerosis (MS) via detection of active lesions[1]. In this study, we examined the feasibility of using automated lesion segmentation and logistic regression classification on first-order features of segmented T1w pre-contrast lesions to predict lesion enhancement status.

Materials and Methods

An analysis of 3T (Philips; Best, The Netherlands) MRI exams of 40 patients with clinically diagnosed MS was performed. T1w images were registered to the FLAIR and lesions were segmented from all FLAIR images using SPM12_LST's lesion prediction[2]. Lesions with volume between 30 and 3000 mm3 were applied to the registered T1w images as a mask to derive nine first-order features that were statistical measures of signal intensity (SI): mean, median, standard deviation, variance, maximum, minimum, range, skewness, and kurtosis. Contrast-enhancing (CE) lesions were determined by thresholding based on mean and standard deviation of T1w post-contrast lesion SI and T1w post-contrast normal white matter SI. CE lesions were verified against an experienced neurologist's assessment. Logistic regression was performed on the nine features extracted from the T1w pre-contrast images with 80% of the data used for training, 20% used for testing, and 5-fold validation for both. A receiver operator characteristic (ROC) analysis, area under the curve (AUC), overall accuracy, and True Positive Rate (TPR) were used to assess model performance.

Results

A total number of 332 lesions were identified, with 32 CE. Using all nine features yielded a training data AUC of 0.90, accuracy of 88.3%, and TPR of 94.0% for training data. For test data, an AUC of 0.87, accuracy of 86.6%, and TPR of 93.0% were obtained. The best model used a subset of features and improved TPR to 94.7% for training data.

Conclusions

This initial work demonstrates the feasibility of predicting active lesions in MS patients using clinical scans already acquired in routine clinical practice. The lesion detection algorithmic used allows automation of MRI examination with a high degree of precision and accuracy, thus improving efficiency of clinical workflow in busy clinical practices. We will demonstrate unique lesion textural characteristics embedded in T1w pre-contrast images which would be used to classify and predict enhancement in the post-contrast images. This is critically essential for reducing risks of contrast agents in certain patient populations and reducing costs.

Figure 1: Flowchart depicting the analysis pipeline, beginning with segmentation from the FLAIR image **(red)** then application of the lesion segmentation map to the T1w pre- and post-contrast images. Normal white mater signal intensity measured outside of lesions **(blue)**. Classification of active lesions is established by comparison of T1w post-contrast signal intensity values of lesions to T1w post-contrast signal intensity of normal white matter values. First-order features are derived from T1w pre-contrast lesions and used in logistic regression classification.

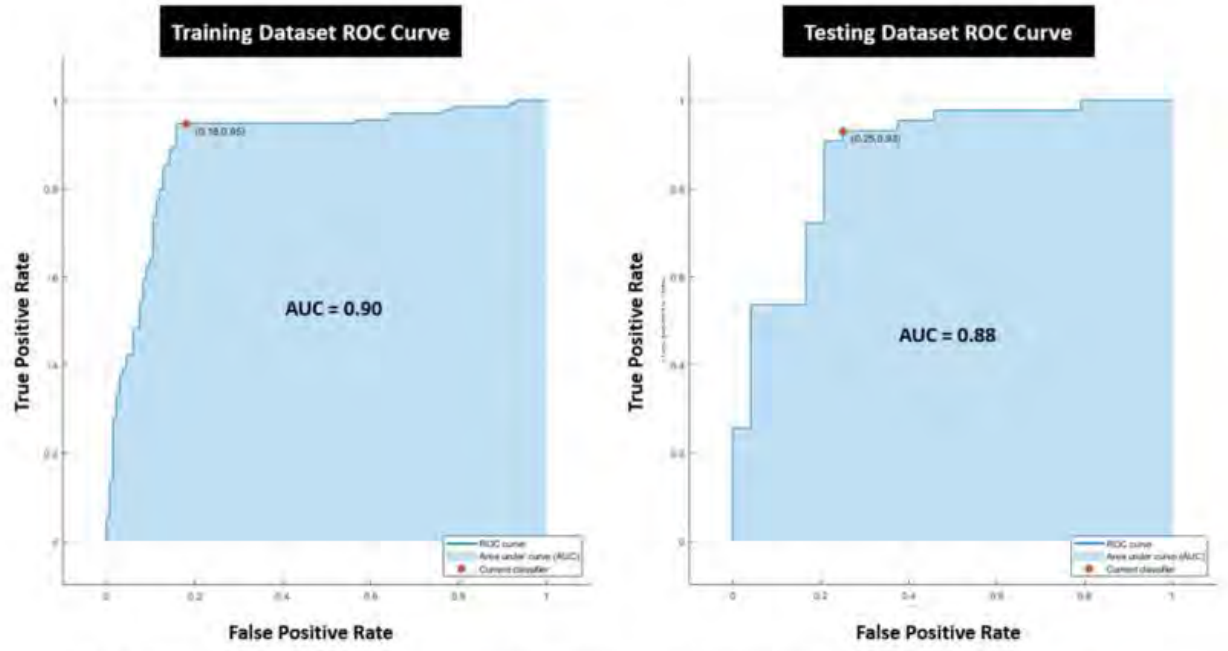

Figure 2: ROC curve for logistic regression fit of features extracted from T1w pre-contrast lesion data. Features used are: mean, maximum, minimum, skewness, kurtosis, and variance.

(Filename: TCT_1298_ASNR_fullfigure.jpg)

Monday, May 1, 2023

10:45-11:45 AM

Scientific Abstract Session: Stroke 1

910

Can Second Acquisition of Contrast Enhanced MRA Neck Provide Additional Information in the Acute Stroke Setting?

P Shah[1], H Kale[1], M Shrivastava[1], D Sanghvi[1], M Munshi[1]

[1]*Kokilaben Dhirubhai Ambani Hospital, Department of Radiology, Mumbai, Maharashtra*

Purpose

Double-concentration MRI contrast agents (such as Gadobutrol) are frequently used in contrast- enhanced MR angiography (CE-MRA) of the head and neck. The higher concentration at lower volumes (to maintain contrast dosage) provides a high peak

concentration of the contrast agent at the time of sampling the center of k-space (which provides most of the image contrast), albeit for a shorter period of time. In order to avoid mis-timing the peak concentration of intraluminal contrast (due to shorter duration of peak), a 2nd acquisition is sometimes performed. We aim to evaluate additional information obtained on careful evaluation of the second acquisition on CE-MRA in patients with acute stroke with ICA/MCA stem occlusion.

Materials and Methods

A retrospective study was conducted.Inclusion criteria : Patients with CE-MRA brain and neck showing ICA and/or MCA stem occlusion and subsequent DSA. Evaluation of CE-MRA and DSA was performed by experienced neuroradiologists (3) and a neurointerventionist respectively.The radiologists were blinded to the DSA findings. The site of ICA occlusion was evaluated on the 1st and 2nd phase of the MRA. Collateral scoring was also performed. In case of disagreement as to the level of occlusion and/or collateral scoring, consensus was used. In many cases MR perfusion with post-processing (including hypoperfusion index ratio, HIR) was available. These findings of CE-MRA were subsequently compared with DSA findings.

Results

There was an 85.7% (31 out of 36) concordance of the level of ICA occlusion between the 3 observers on the 1st and 2nd phase of the CE-MRA neck. In 7 patients there was a significant difference in the perceived level of ICA occlusion between the 1st and 2nd phases of the examination for all readers which approximated the level of occlusion seen on DSA.Scoring for collaterals was done using both the initial and 2nd phase of MRA. The scoring for collaterals was correlated with HIR (as a surrogate marker for collateral supply). A trend towards higher HIR with poorer collateral score was seen.

Conclusions

Evaluation of second phase CE-MRA may help in: Identification of exact site of occlusion and collateral circulation assessment especially when MR perfusion or software is unavailable. To the best of our knowledge no studies related to MR evaluation of delayed phase of CE-MRA neck are available.

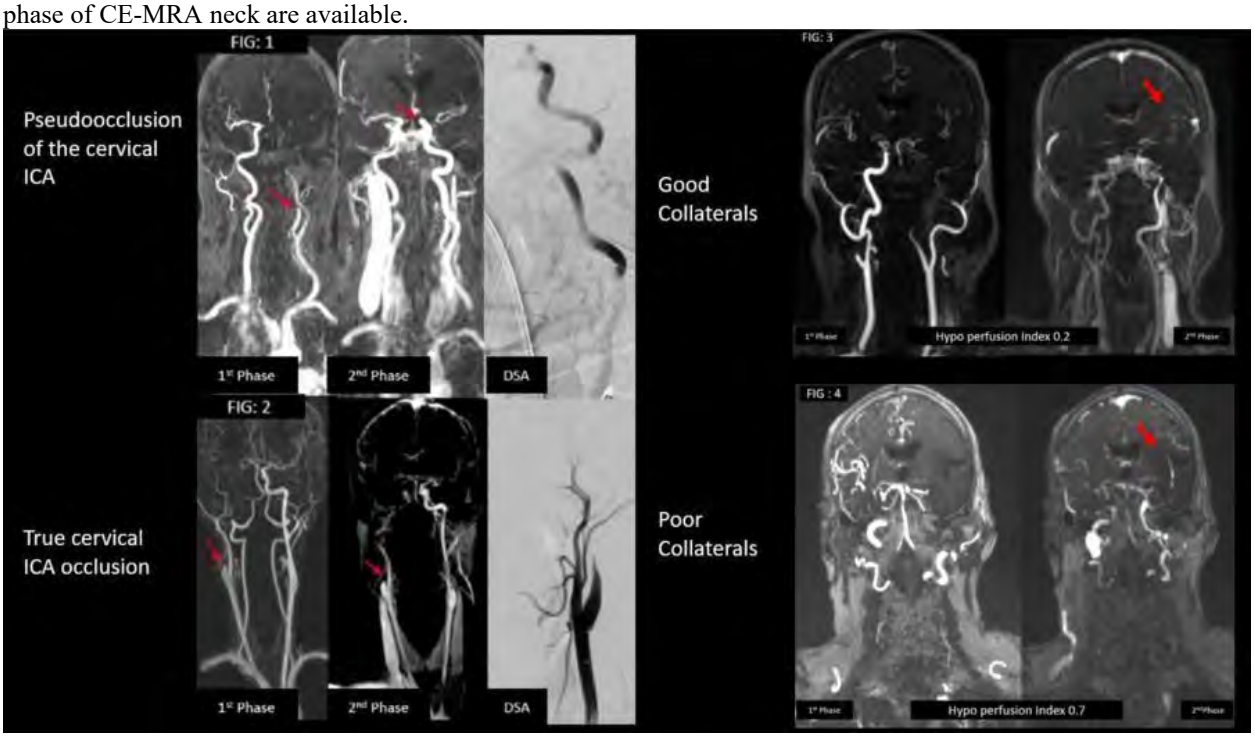

(Filename: TCT_910_asnr2023.JPG)

1421

Contrast-enhanced FLAIR and the Relationship to Hemorrhagic Transformation in Patients with Large Vessel Occlusion Treated with Mechanical Thrombectomy

S Rogers[1], C Reynolds[1], A Frazzitta[1], B Renshaw[1], A Bhandari[1], S Vedantham[1]
[1]*University of Arizona, Tucson, AZ*

Purpose

Hemorrhagic transformation (HT) after reperfusion therapy in acute ischemic stroke (AIS) is associated with poor outcomes. Blood-brain barrier breakdown (BBBD) by perfusion imaging has been associated with HT, as have other imaging markers of BBBD including early parenchymal enhancement on T1 weighted imaging and hyperintense acute reperfusion marker (HARM) on FLAIR. However, no studies have addressed the implication of enhancement on FLAIR or hyperacute HARM in AIS and their correlation with HT.

Materials and Methods

IRB approval was obtained. We retrospectively reviewed consecutive patients with LVO treated with mechanical thrombectomy (MT) in our institution from January 2020 – August 2022. We included patients who had MRIs with both unenhanced FLAIR (U-FLAIR) and contrast-enhanced FLAIR (CE-FLAIR), either before or after MT. We found the region of maximum signal intensity on CE-

FLAIR by manual windowing and recorded a standardized ROI in this region and measured another ROI at the same location on U-FLAIR. A standardized ROI in the contralateral, normal-appearing white matter was also measured on both CE-FLAIR and U-FLAIR. We recorded the presence of hyperacute HARM, defined as sulcal enhancement seen only on CE-FLAIR. The degree of HT based on post-thrombectomy MRI or CT was evaluated according to Heidelberg rating (iHT), as was symptomatic HT (sHT) according to joint commission guidelines of hemorrhage on imaging and worsening NIHSS. Detailed clinical information was recorded.
Results
156 patients underwent thrombectomy; preliminary analysis of 33 patients with post-thrombectomy MRI showed infarct maximum signal intensity ratio ROI of CE-FLAIR/U-FLAIR was a significant predictor (p=0.006) of dichotomized iHT (≤1 vs. ≥2) with AUC of 0.783 (CI: 0.611–0.954) and correlated with antiplatelet therapies (p=0.048), but not sHT (p=0.927). The max ROI ratio of CE-FLAIR to the normal contralateral white matter ROI was also a significant predictor (P=0.028) of dichotomized Heidelberg rating, AUC 0.724 (CI: 0.55 – 0.898). Hyperacute HARM was seen in 26% of cases. It was not correlated with iHT or sHT but was less likely in cryptogenic stroke (p=0.006).
Conclusions
Increasing enhancement and max ROI values on CE-FLAIR after thrombectomy correlates with higher imaging grades of HT, but a correlation with clinically significant HT could not be found on preliminary analysis. Hyperacute HARM was frequently seen, and although not found to correlate with HT it may provide insight into stroke etiology.

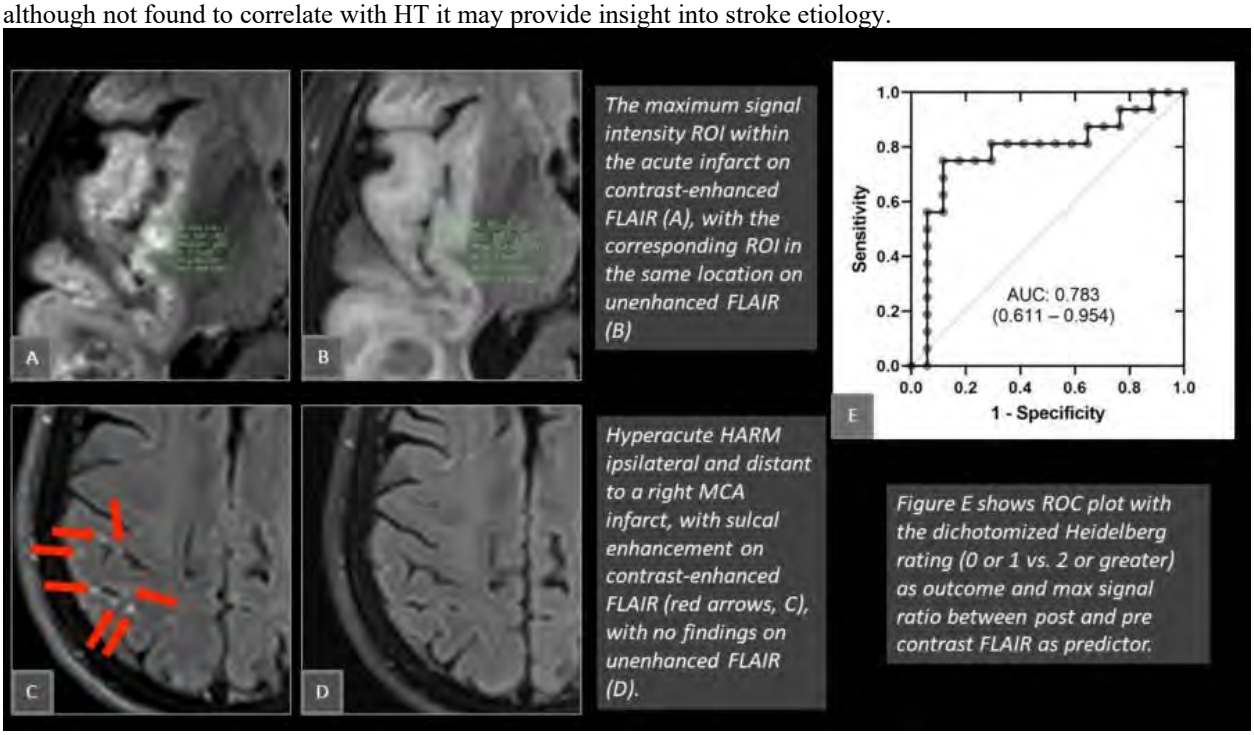

(Filename: TCT_1421_FLAIRthrombectomyfigure1.jpg)

689

Good Clinical Outcome Decreases with more than two Retrieval Attempts in Patients with Extensive Baseline Infarct

L Winkelmeier[1], T Faizy[1], L Meyer[1], C Heitkamp[1], M Schell[1], G BROOCKS[1], H KNIEP[1], J Fiehler[1], F Flottmann[1]
[1]University Medical Center Hamburg-Eppendorf, Hamburg, Germany

Purpose
Purpose: The RESCUE-Japan LIMIT trial [1] provided first high-level evidence that patients with acute ischemic stroke and extensive baseline infarct benefit from endovascular treatment (EVT). To achieve endovascular reperfusion, more than one retrieval attempt is often required. We hypothesized that the benefit of endovascular reperfusion in extensive baseline infarct is influenced by the number of retrieval attempts.
Materials and Methods
Materials and Methods: Retrospective multicenter study of patients from the German Stroke Registry recruited from 2015 to 2019. We included patients who underwent EVT for acute large vessel occlusion in the anterior circulation with extensive baseline infarct defined as Alberta Stroke Program Early CT Score (ASPECTS) 3-5. Successful reperfusion was specified as Thrombolysis in Cerebral Infarction (TICI) score of 2b-3. The study cohort was divided into patients with failed reperfusion (TICI 0-2a) and successful reperfusion at 1st, 2nd or ≥3rd retrieval attempt, respectively. The primary outcome was good clinical outcome (GCO) defined as 90-day modified Rankin Scale score 0-3.
Results
Results: 182 patients with extensive baseline infarct met the inclusion criteria. Successful endovascular reperfusion was obtained in 80.7% (Figure A). The median number of retrieval attempts was 2 [IQR, 1-3]. GCO was achieved in 32.4% of patients. The likelihood

of GCO decreased with the number of retrieval attempts required for successful reperfusion (Figure B). Successful reperfusion at 1st attempt showed the highest odds of GCO (adjusted odds ratio, 7.48 [95% CI, 1.70-39.64]), followed by success at 2nd attempt (adjusted odds ratio, 5.44 [95% CI, 1.14-30.74]). Success at ≥3rd attempt was no longer associated with GCO compared with failed reperfusion (adjusted odds ratio, 2.11 [95% CI, 0.50-10.35])(Figure C-D).

Conclusions

Conclusion: In patients with extensive baseline infarct, successful reperfusion within the first 2 retrieval attempts is linked to improved clinical outcome compared with patients with failed reperfusion. In EVT for strokes with large ischemic region, at least 2 retrieval attempts should be performed in cases of persistent occlusion.

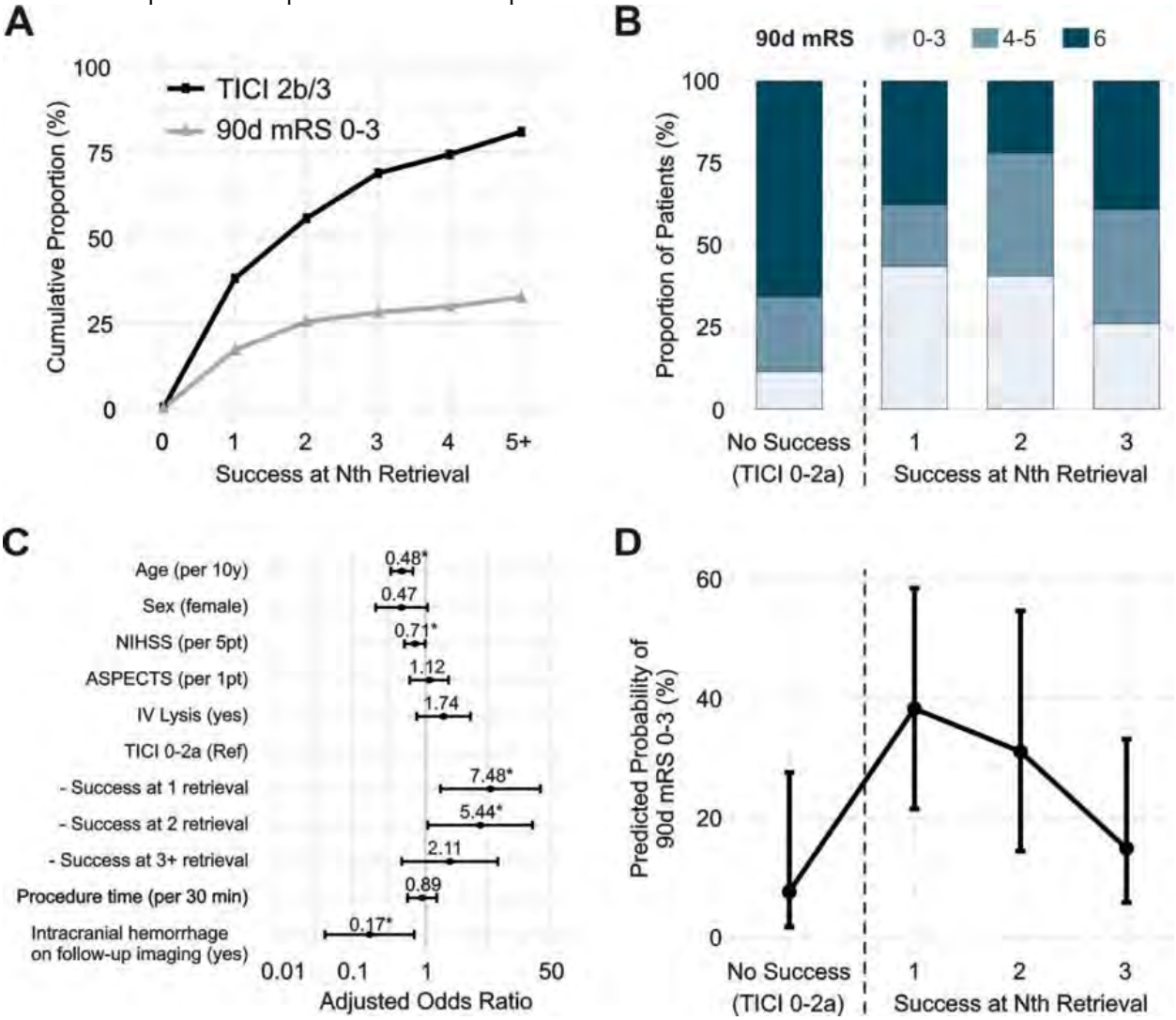

(Filename: TCT_689_corel_retrievals.jpg)

905

National Utilization Trends in CT Brain Perfusion Imaging and Intracranial Mechanical Thrombectomy Following Expansion of Acute Stroke Therapeutic Eligibility

C Berkheimer[1], S Ryan[2], R Gallagher[3], A Ajam[4], M Luttrull[5], X Nguyen[4]

[1]Lake Erie College of Osteopathic Medicine, Erie, PA, [2]Ohio State University, Columbus, OH, [3]The Ohio State University, Columbus, OH, [4]Ohio State University Wexner Medical Center, Columbus, OH, [5]OSU Wexner Medical Center, Dublin, OH

Purpose

Landmark clinical trials over the past decade have led to widening of the therapeutic window for acute stroke. In 2017 and 2018, the DAWN and DEFUSE-3 trials extended eligibility for MT to a maximum of 24 hours, influencing guideline updates in support of CT perfusion (CTP) to identify potential MT candidates (1-3). The goal of this study is to analyze recent trends in CTP and MT usage to assess the impact of updated stroke management guidelines on clinical practice.

Materials and Methods

The Cosmos platform (Epic Systems, Verona, WI), a multi-institutional data aggregation tool containing health records data from billions of encounters across the U.S., was used to retrospectively identify millions of patients with medical encounters during the study period (2015-2021). For each calendar quarter, all individuals who had at least one encounter of any type in the given quarter were identified. Quarterly volumes of MT and brain CTP performed were obtained using queries for each procedure's billing code and

reported as a proportion of each quarter's active patient population. Data for MT volumes were only available beginning in 2016 with the introduction of its billing code.

Results

The number of billed CTP procedures in early 2015 was 4.3 per 100K active patients, which increased to 10.2 per 100K by late 2017 when the DAWN trial was published online and 13.4 per 100K in early-2018 following the online publication of the DEFUSE-3 trial. Since then, quarterly CTP volumes have rapidly increased, reaching 46.6 per 100K active patients by the end of 2021. The number of MT procedures in early 2016 was 1.4 per 100K active patients, gradually increasing to 5.8 per 100K by late 2021. Over the study period, CTP utilization increased by over 900%, while MT utilization increased by over 300%.

Conclusions

On a per-population basis, CT perfusion utilization increased, particularly over the past 4 years following DAWN and DEFUSE-3. Although causation cannot be proven in this study, the observed increases in CTP utilization likely reflect recent evidence-based adjustments to stroke guidelines. The continuing linear rise in CTP volume suggests that the number of stroke patients being evaluated for MT eligibility continues to increase, as corroborated by the concurrent increases in MT procedures performed over the study period. Additional studies analyzing population-based outcomes are needed to quantify the impact of these practice changes on population health.

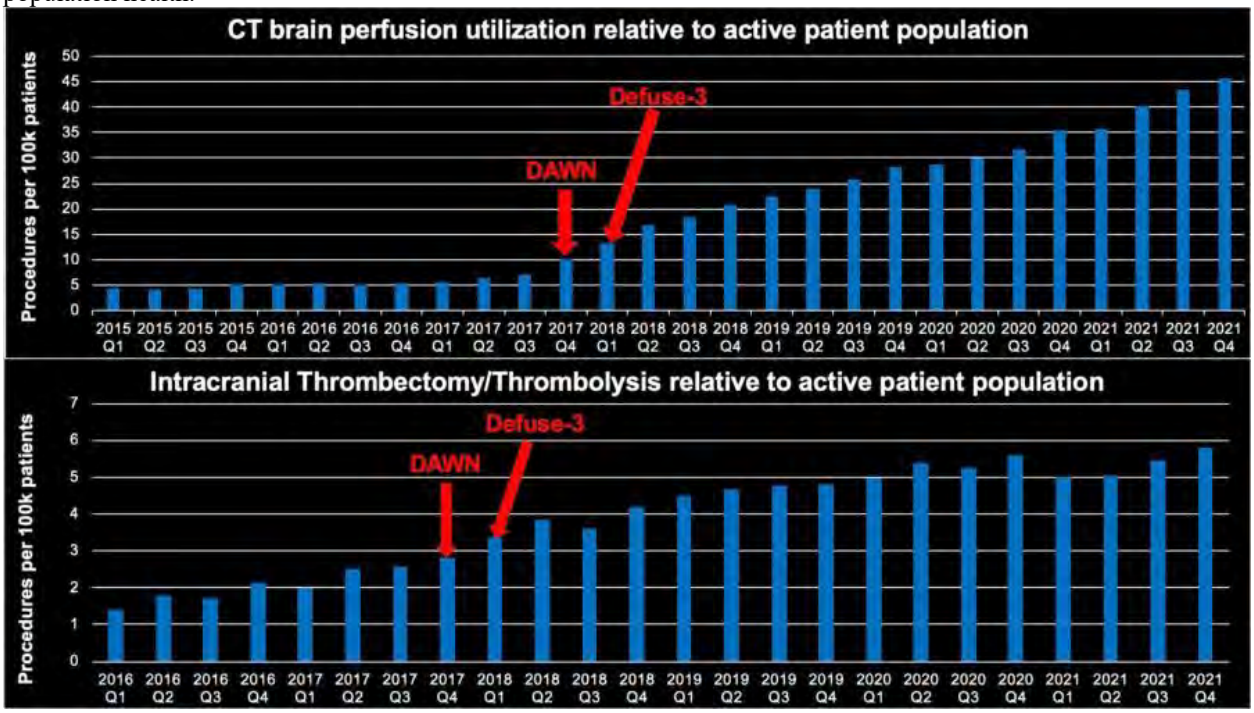

(Filename: TCT_905_ScreenShot2022-11-14at45531PM.jpg)

909

Prognostic Value of Arterial Spin-Labeling Perfusion in Anoxic Brain Injury

D Weinert[1], B Beutler[2], A Lerner[3], M Shiroishi[4], P Nguyen[1], M Ulanja[5], D Antwi-Amoabeng[5], R Assadsangabi[6]

[1]Keck School of Medicine, University of Southern California, Los Angeles, CA, [2]LAC + USC Medical Center, Los Angeles, CA, [3]USC Keck School of Medicine, Los Angeles, CA, [4]KECK SCHOOL OF MEDICINE, USC, Los Angeles, CA, [5]Christus Ochsner Lake Area Hospital, Lake Charles, LA, [6]University of Southern California, Los Angeles, CA

Purpose

Anoxic brain injury is a potentially lethal clinical entity with generally poor prognosis resulting from prolonged hypoxia. However, there are limited tools to predict outcomes and likelihood of recovery among patients presenting with anoxic brain injury. Arterial spin-labeling (ASL) perfusion MRI has been used to detect global and focal cerebral ischemic changes (1) and may have a role in the assessment of anoxic brain injury. We aimed to investigate the relationship between ASL perfusion findings and prognosis in patients with suspected anoxic brain injury secondary to cardiac arrest.

Materials and Methods

We performed a retrospective review of MRI reports at our institution using keywords and relevant Boolean operators to identify participants with clinical suspicion for anoxic brain injury who underwent at least one MRI study within 15 days of cardiac arrest. ASL perfusion signal intensity was measured in 12 brain regions (bilateral cerebral lobes, basal ganglia, and thalami) and scored on a 0-12 scale using cerebellar signal intensity as the reference value. We analyzed receiver operator characteristics (ROC) of ASL perfusion scores to assess its performance for predicting the following clinical features: (1) myoclonus status epilepticus (MSE) within the first day of arrest; (2) absent extensor or motor reflexes at day 3 post-arrest (EMR); and (3) absent brainstem reflexes (BSR) at any point during the first 15 days following cardiac arrest. The optimal cutoff point was selected based on sensitivity and specificity

analyses. Univariate logistic regression was used to assess the odds of the selected clinical parameters for scores above the optimal cutoff point.
Results
A total of 28 cases were included. ROC analysis showed that ASL scores ≥7 were associated with high odds of absent BSR (OR 2.14 p = 0.53 95% CI: 0.19 - 23.7) with a specificity of 100% and a negative predictive value of 85.7%. An ASL score ≥7 was also associated with high odds of MSE (OR 1.19 p = 0.82 95% CI: 0.26 - 5.50) with a sensitivity of 100% and a positive predictive value of 57.1%. The area under the ROC curve was 0.5156 for the performance of ASL perfusion in predicting absent BSR and 0.5234 for predicting MSE.
Conclusions
Preliminary results support ASL scores ≥7 as a highly specific cutoff for predicting clinical anoxic brain injury. Full results will include analyses for additional clinical findings, including duration of resuscitation, Glasgow Coma Scores (GCS), EEG findings, and discharge dispositions.

1361

The effect and interaction of bridging intravenous thrombolysis and extended time from onset on functional outcome: A Subanalysis of the German Stroke Registry

L Meyer[1], M Bechstein[1], U HANNING[2], H KNIEP[1], J Fiehler[3], G BROOCKS[4]
[1]University Medical Center Hamburg-Eppendorf, Hamburg, Hamburg, [2]UNIVERSITY MEDICAL CENTER HAMBURG-EPPENDORF, HAMBURG, Germany, [3]University Hospital Hamburg-Eppendorf, Hamburg, AS, [4]University Hamburg, Hamburg, NA

Purpose
Clinical evidence for bridging intravenous thrombolysis (IVT) in the subgroup of ischemic stroke patients treated with thrombectomy in the extended time window outside of randomized trials remains limited. This study aims to compare effects of IVT and time from onset to admission for improving treatment decision-making in daily clinical practice.
Materials and Methods
All currently available data of patients enrolled in the German Stroke Registry-Endovascular Treatment (GSR-ET) treated with thrombectomy for anterior circulation stroke were included. Baseline characteristics, procedural (modified Thrombolysis in Cerebral Infarction Scale, mTICI) and clinical outcome (National Institutes of Health Stroke Scale, NIHSS; modified Rankin Scale, mRS) parameter as well as complications were analyzed for all patients with regard to extended time windows, defined as the time from symptom onset of 6 to 24 hours. Favorable functional outcome was defined a modified Rankin Scale score of mRS 0-2 at 90-days.
Results
Out of 13 082 patients currently enrolled in the GSR-ET, 757 patients presented in the extended time window (>6 hours) at the hospital of which 353 patients were mothership patients and 46 patients received bridging IVT (13%). The median age was 76 (IQR, 65-83) and 50.3 % were women. In multivariable logistic regression analysis including all patients, IVT (adjusted OR 1.74; 95CI 1.5-2.03; p<0.001) was significantly associated with mRS 0-2 at 90-days and showed a significant interaction (adjusted OR 0.9; 95CI 0.98-0.99; p=0.027) with time from onset to admission (figure 1) showing an inflection point at approximately 10 hours. In all mothership patients, the rate of successful recanalization (TICI ≥2b) was 76% and favorable functional outcome (mRS≤2) was observed in 41.5% at 90-days treated in the extended time window (>6 Hours). Mortality was 18% at 90-days.
Conclusions
This study suggests a significant interaction between the effect of bridging intravenous thrombolysis and extended time from onset to admission on long-term functional outcome in daily clinical practice indicating a treatment benefit of IVT up to 10 hours from onset. Further studies are warranted to investigating these effects to improve treatment decision making in this subgroup.

Figure 1: Predictive margins of intravenous thrombolysis for favorable functional outcome (modified Rankin scale (mRS) 0-2) at 90-days adjusted for pre-stroke mRS, admission NIHSS (national institute of health stroke scale), admission Alberta stroke programme early CT score (ASPECTS) score, mothership patients, final recanalization grade (modified thrombolysis in cerebral infarction scale)

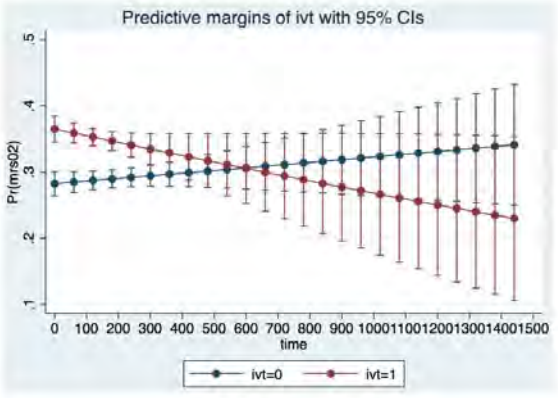

(Filename: TCT_1361_asnr-ex.jpg)

356

The relationship between CT perfusion and post-endovascular therapy contrast extravasation on dual energy CT in acute ischemic stroke patients

M Robbe[1], F Pinckaers[1], R van Oostenbrugge[2], W van Zwam[1], A Postma[1]

[1]Department of Radiology, Maastricht University Medical Centre+, Maastricht, Limburg, The Netherlands, [2]Department of Neurology, Maastricht University Medical Centre+, Maastricht, Limburg, The Netherlands

Purpose

Background: In acute ischemic stroke patients, CT perfusion (CTP) is used for the estimation of ischemia (as core) and hypoxia (as penumbra). Both could possibly lead to blood brain barrier disruption (BBBD), which could result in contrast extravasation (CE) during endovascular stroke therapy (EVT). As such, CE might be a surrogate marker for BBBD. Objective: To investigate the relationship between CTP derived parameters and CE on dual-energy CT (DECT) immediately after EVT.

Materials and Methods

All patients treated with EVT in our center from 2010 up and including 2019 were screened. Included patients had an anterior large vessel occlusion and received both CTP at baseline and DECT within 3 hours post-EVT. The CTP core and penumbra thresholds were set at rCBF<20% and Tmax>6s, respectively. The Alberta stroke programme early CT score (ASPECTS) was used to score penumbra and core on CTP (forming a CTP-ASPECTScore and CTP-ASPECTScore+penumbra), and to score CE on iodine maps of DECT (forming a CE-ASPECTS). The relationship between CTP-ASPECTScore and CTP-ASPECTScore+penumbra, and CE-ASPECTS was assessed using Spearman's rank correlation. A delta ASPECTScore-CE (CTP-ASPECTScore minus CE-ASPECTS) was calculated.

Results

Out of a total of 654 EVT records, 109 patients were included. The median CTP-ASPECTScore+penumbra, CTP-ASPECTScore and CE-ASPECTS were 2 (IQR 1-4), 7 (IQR 4-10), and 6 (IQR 3-8) respectively. The correlation between CTP-ASPECTScore+penumbra and CE was .15 (P=.13), and the correlation between CTP-ASPECTScore and CE was .23 (P=.02).The median ASPECTScore-CE was 0 (IQR -2-2) indicating that the amount of CTP-ASPECTScore is not structurally lower or higher than the amount of CE-ASPECTS.

Conclusions

We found a weak but significant correlation between CTP-ASPECTScore and CE-ASPECTS, indicating core tissue might not result in CE, and CE might not always be caused by core.

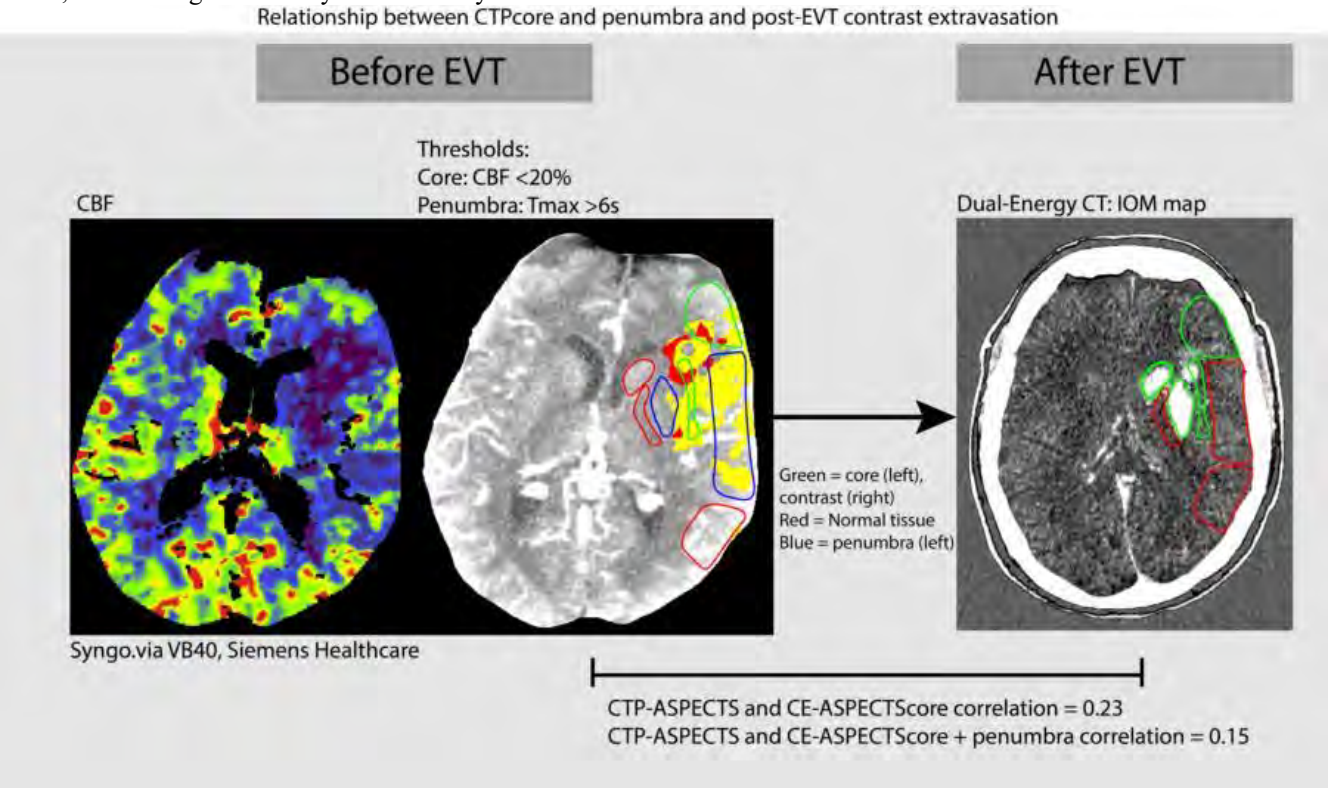

(Filename: TCT_356_AbstractR5316.jpg)

Monday, May 1, 2023
10:45-11:45 AM
Scientific Abstract Session: Tumors 2

1271

A comparison of radio-pathomic maps of cell density to rCBV for detecting infiltrative tumor outside contrast enhancement in de-novo glioblastoma

S Bobholz[1], A Lowman[1], S Duenweg[1], A Winiarz[1], F Kyereme[1], J Connelly[1], D Coss[1], M Krucoff[2], M Agarwal[1], A Banerjee[1], P LaViolette[1]

[1]Medical College of Wisconsin, Milwaukee, WI, [2]Medical College of Wisconsin`, Milwaukee, WI

Purpose

Radio-pathomic maps of tumor cell density have recently demonstrated the ability to detect glioblastoma tumor invasion outside of T1+Gd contrast enhancement. Relative cerebral blood volume (rCBV) maps derived from dynamic susceptibility contrast perfusion imaging have been used in glioblastoma imaging to identify areas of increased blood volume related to advanced tumor growth. This study used rCBV maps and radiologic annotations from the publicly available PENN-GBM dataset to determine the within-contrast and outside-contrast association between rCBV values and autopsy-based radio-pathomic maps of cellularity validated outside of the traditionally defined tumor region.

Materials and Methods

This study included imaging data from 456 pre-surgical glioblastoma cases from the PENN-GBM dataset. A previously published algorithm using T1, T1+Gd, FLAIR, and ADC as inputs to predict segmented cellularity from autopsy tissue samples was used to generate whole-brain cellularity masks for each included patient (1,2). Per-subject mean cellularity values and rCBV estimates were then calculated for the automated radiological segmentations included with the PENN-GBM dataset, including ROIs for the necrotic core (NC), contrast-enhancing region (CE), and FLAIR-hyperintense area of mixed tumor plus edema (FH) (3). Pearson's R correlations were then computed for the mean cellularity and rCBV values within the CE and FH regions to compare the strength of association between perfusion values and hypercellularity in the presence and absence of contrast enhancement.

Results

A positive correlation was observed between rCBV and predicted cell density estimates within the contrast-enhancing region ($r = 0.280$, $p < 0.001$, Figure 1b). No correlation was observed between rCBV and predicted cell density within the non-enhancing FLAIR hyperintense region ($r = 0.0162$, $p = 0.731$, Figure 1c).

Conclusions

The results from this study support the hypothesis that increased rCBV derived from perfusion may not reflect hypercellular tumor presence beyond the contrast-enhancing region. Future research into the pathological and genetic properties of occult tumor invasion pre-angiogenesis is warranted to better understand the distinction between hypercellular and hyperperfused areas of tumor.

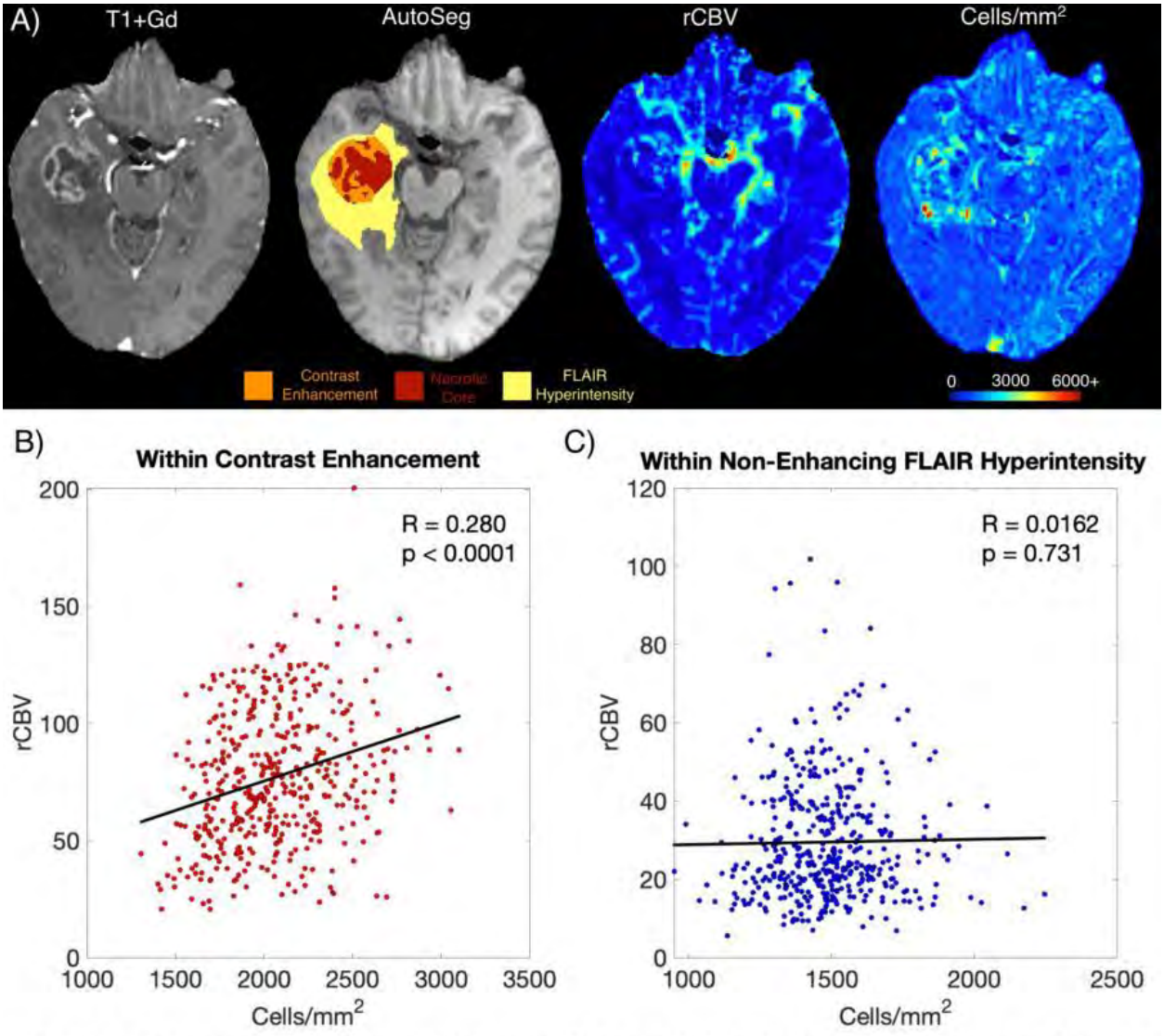

Figure 1: A) Example images included in this analysis. B) Scatterplot showing the association between rCBV and cellularity within contrast enhancement. C) Scatterplot showing the association between rCBV and cellularity in non-CE FLAIR hyperintense regions

(Filename: TCT_1271_SB_ASNR23_AB1_Fig.jpg)

136

Automated Segmentation of Diffusion Abnormalities on Post-operative MR Imaging in Patients Undergoing Resection for High Grade Glioma

D Barboriak[1], J Barboriak[1], A Friedman[1], H Friedman[1], K Peters[1], A Desjardins[1]
[1]*Duke University Medical Center, Durham, NC*

Purpose

The clinical significance of hyperintensities on diffusion-weighted images (DWI) in patients after resection of high grade glioma (HGG) is unclear (1). These abnormalities frequently manifest as regions of enhancement on follow-up MRI, and if not recognized can be misdiagnosed as recurrent tumor. We studied automated software methods to measure these abnormalities to improve comparability of results across centers and to facilitate their use in future multicenter trials.

Materials and Methods

MRI scans obtained within 60 days before resection (pre-op), within 14 days after resection (post-op), and follow-up studies (81± 29 [mean±SD] days post-op), were retrospectively studied in 58 patients with HGG (age 51.7±13.3 years, 43% female, diagnosis 78% GBM, 14% Grade 3 astrocytoma, 3% Grade 3 oligodendroglioma, 4% other). Acute-stroke Detection Segmentation software (2) was used to segment DWI abnormalities, resseg algorithm (3) to segment operative sites and a majority vote of the mic-dkfz, scan and xfeng algorithms to segment enhancing tumor (4). Post-op DWI abnormalities were included in the analysis if they were new from pre-op study, within the brain parenchyma, and had any intersection with a 2cm zone around the operative site.

Results

Using these automated methods, 57 of 58 cases had measurable abnormalities on post-op DWI. In two cases, the abnormalities followed a clear vascular territory. The volume of these abnormalities (DWIvol) correlated with the growth of enhancement on the

follow up study (r=.34, p<.01). Median DWIvol decreased from post-op to follow-up study (7.8 vs. 0.9 cc, p<.0001). DWIvol was strongly correlated pre-operative tumor enhancement volume (r=.49, p<.005). There was a trend toward correlation of DWIvol and extent of resection (r=.24, p=.1).

Conclusions

DWIvol on post-op MRI in patients after resection of HGG correlates with enhancement growth on follow-up MRI, while DWIvol decreases on follow-up, supporting face validation of this automated image processing approach. Post-op DWI abnormalities are ubiquitous and strongly correlate with pre-op tumor enhancement volume. This correlation may be a confounding factor when studying the clinical relevance of these findings.

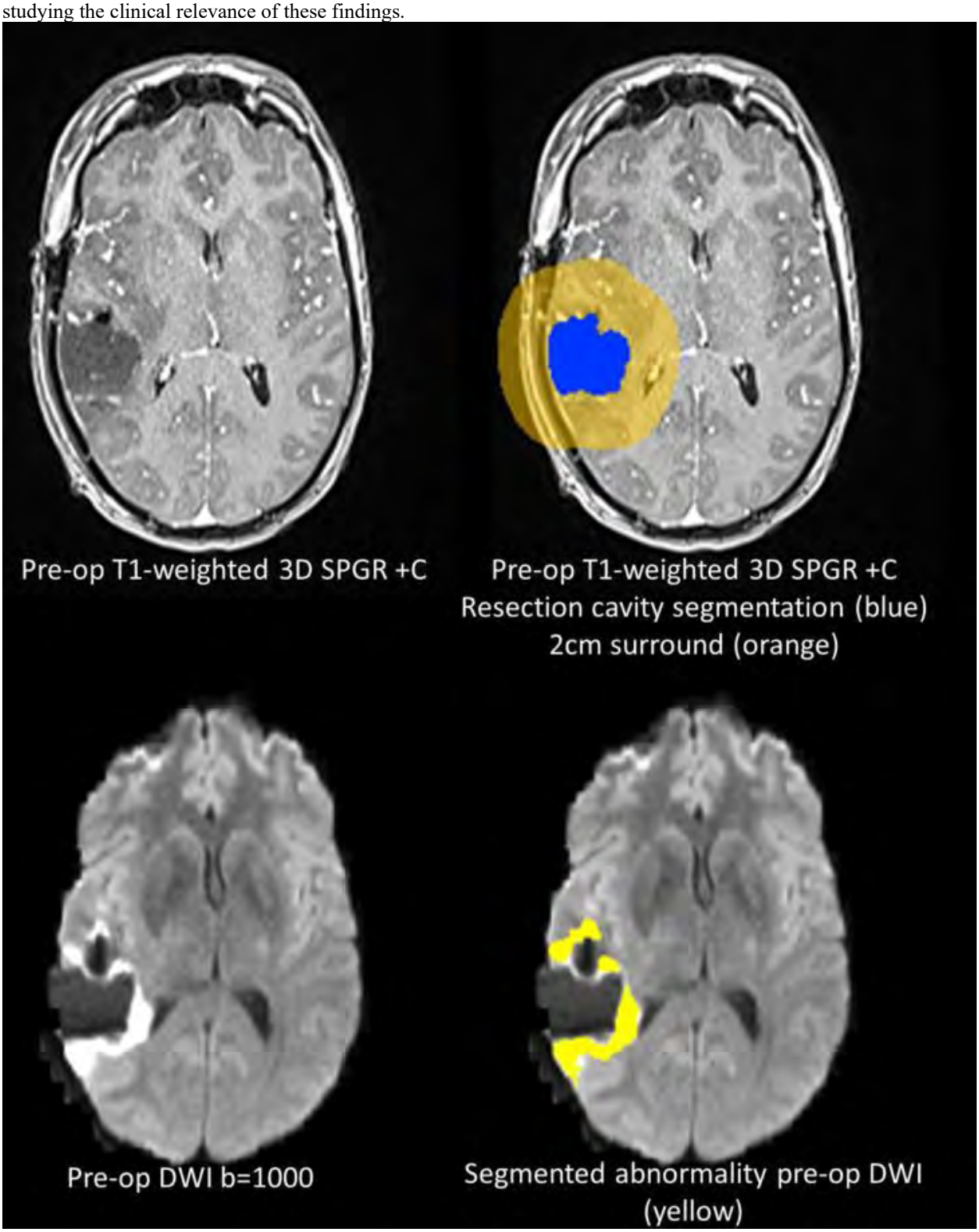

(Filename: TCT_136_Abstract_graphic_20221106_cropped.jpg)

497

Change in tumor growth rate as a predictor of overall survival in recurrent glioblastoma treated with chemotherapy

S Oshima[1], A Hagiwara[1], C Raymond[1], N Cho[1], J Lu[1], B Eldred[1], A Lai[2], P Nghiemphu[1], N Salamon[1], T Cloughesy[1], B Ellingson[1]
[1]University of California, Los Angeles, Los Angeles, CA, [2]University of California Los Angeles, Los Angeles, CA

Purpose

Progression-free survival at 6 months from start of treatment (PFS6) based on response assessment in neuro-oncology (RANO) criteria [1] has been proposed as an endpoint in recurrent glioblastoma (GBM), but it relies on only post-treatment changes in tumor size and a slow growing, non-responding tumor could reach PFS6 by chance. Previous studies have suggested an association between post-treatment tumor growth rates (TGR) with overall survival (OS) in GBM [2]. Here, we propose a new endpoint using a combination of PFS6 and TGR change before and after treatment start to achieve more reliable determination of the therapeutic effect [3]. The aims of this study are to 1) study the usefulness of PFS6 and newly proposed endpoint and 2) assess the impacts of change in TGR on OS in recurrent GBM.

Materials and Methods

We retrospectively studied 66 cases of 1st or 2nd recurrent GBM treated with chemotherapy (CCNU, TMZ or Carboplatin). Contrast-enhancing (CE) tumor volumes were quantified by using subtraction maps of CE T1-weighted MR images [4]. TGR was computed using pre-treatment scans (3 scans prior to treatment start) and post-treatment scans. We determined the new response category as follows: patients were categorized as "Responders" if they reached PFS6 and TGR had slowed after treatment start and "Non-Responders" if they do not reach PFS6 or TGR had not slowed. We compared OS between PFS6 positive and negative and between "Responders" and "Non-Responders" using a log-rank test. The association of TGR change with OS was studied using univariate and multivariate Cox regression.

Results

Stratification by PFS6 (Log-rank P=.04 for analysis of all 66 cases and P=.009 for 48 cases without radiation therapy) and "Responders" vs "Non-Responders" for the new endpoint (P=.02 for all cases; P=.008 for 48 cases without radiation therapy) resulted in significant differences in OS. Cox regression revealed that a decrease of TGR (μL/day; P=.001), smaller baseline tumor volume (μL; P=.005), smaller number of recurrences (P=.007) and MGMT promoter methylation (P=.02) were significantly associated with longer OS after controlling for age, sex and concomitant radiation therapy.

Conclusions

The newly proposed endpoint of treatment response, as well as PFS6, can be useful in prediction of OS. Results of Cox regression analysis indicate that both baseline tumor size and change in TGR are important imaging biomarkers for evaluating prognosis and treatment effect in recurrent GBM.

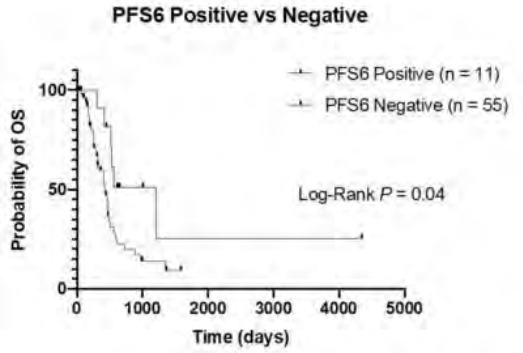

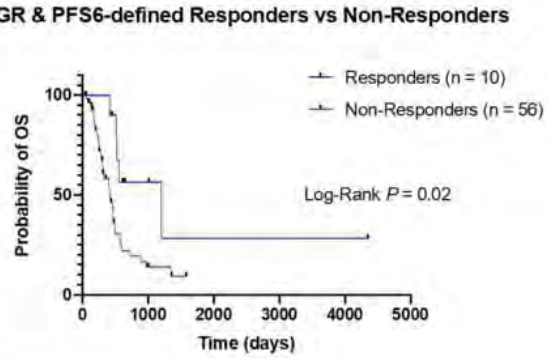

Multivariate Cox proportional hazards model for OS

	Hazard Ratio (95% CI)	*P* value
Change in tumor growth rate (per 1-μL/day increase)	16.27 (3.28–80.56)	0.001
Baseline tumor volume (per 1-μL increase)	1.1 (1.03–1.17)	0.005
Number of recurrences (1st vs 2nd)	0.26 (0.10–0.70)	0.007
MGMT promoter methylation (methylated vs unmethylated)	0.39 (0.17–0.88)	0.02
Radiation therapy (with vs without)	0.51 (0.20–1.30)	0.16
Age (per 1-year increase)	1.03 (0.98–1.08)	0.26
Sex (male vs female)	0.73 (0.29–1.80)	0.49

(Filename: TCT_497_ASNR_figure.jpg)

739

Intra-Subject Heterogeneity of Lesion SUV and SUVR on [68Ga]DOTATATE PET/MRI in Patients with Multiple Meningiomas – Implications for Tumor Biology and Clinical Management

S Chang[1], A Haghdel[1], S Kim[1], M Roytman[1], R Ramakrishna[1], S Pannullo[2], T Schwartz[3], J Osborne[2], R Magge[3], E Lin[1], J Knisely[1], J Ivanidze[4]

[1]Weill Cornell Medicine, New York, NY, [2]New York-Presbyterian Hospital/Weill Cornell Medicine, New York, NY, [3]Weill Cornell Medicine/NewYork-Presbyterian Hospital, New York, NY, [4]Weill Cornell Medicine Radiology, Larchmont, NY

Purpose

Patients with meningiomas commonly present with multiple lesions and have significant recurrence rates. Contrast-enhanced MRI has substantial limitations in differentiating recurrence from treatment related change. Somatostatin receptor 2 (SSTR2)-targeted PET imaging of meningiomas using [68Ga]-DOTATATE PET/MRI and PET/CT has demonstrated substantial clinical benefit [1-4]. While diagnostic thresholds have been established , there is substantial heterogeneity in avidity across subjects, and SUV does not appear to correlate with WHO grade [1, 5]. However, the degree of intra-subject heterogeneity of meningioma SSTR2 expression, and thereby DOTATATE PET standardized uptake value (SUV), is unknown. Our purpose was to assess intra-subject heterogeneity of lesion PET SUV and SUV ratio (SUVR) in patients with ≥ 3 meningiomas and evaluate for association with WHO Grade.

Materials and Methods

Patients were enrolled prospectively on our observational clinical trial (NCT04081701). Inclusion criteria were ≥ 3 lesions radiographically compatible with meningioma, at least one of which was pathologically proven. Maximum SUV and SUVR (relative to superior sagittal sinus SUV) were obtained. Clinical and demographic subject characteristics were collected via chart review. Histogram analyses were used to characterize Intra-subject heterogeneity of lesion SUV and SUVR. The effect of WHO Grade on intra-subject heterogeneity was assessed via one-way ANOVA. Analyses were repeated following exclusion of 13 patients who had previously received radiotherapy.

Results

39 patients met inclusion criteria. Clinical and demographic characteristics are shown in Figure 1a. Intra-subject heterogeneity is visualized via histogram analysis in Figures 1b-d. There were no significant differences in intra-subject SUV and SUVR standard deviations when stratifying by WHO grade (p=0.56, 0.49, 0.27, 0.27).

Conclusions

A wide range of intra-subject lesion SUV and SUVR variability can be seen in our cohort. Intra-subject lesion SUV and SUVR variability did not differ significantly when stratifying by WHO Grade. Our results suggest that new lesions in a patient should be evaluated individually based on published diagnostic thresholds; the range of SUV of pre-existing lesions does determine SUV of new meningiomas a patient may develop subsequently. This work has the potential to advance clinical translation of DOTATATE PET/MR and PET/CT in patients in meningioma, thereby improving clinical outcomes.

A)

N Patients	39
Age	60.8 (27-86)
Sex	66.67% F (26/39)
N meningiomas per patient	Median: 4, Range: 3-14 (48.8% with 3, 25.6% with 4-5, 25.6 with >5)
WHO grade	10.3% (4/39) WHO grade unknown
	28.2% (11/39) WHO grade 1
	38.5% (15/39) WHO grade 2
	23.1% (9/39) WHO grade 3
Radiation history	33.3% (13/39)

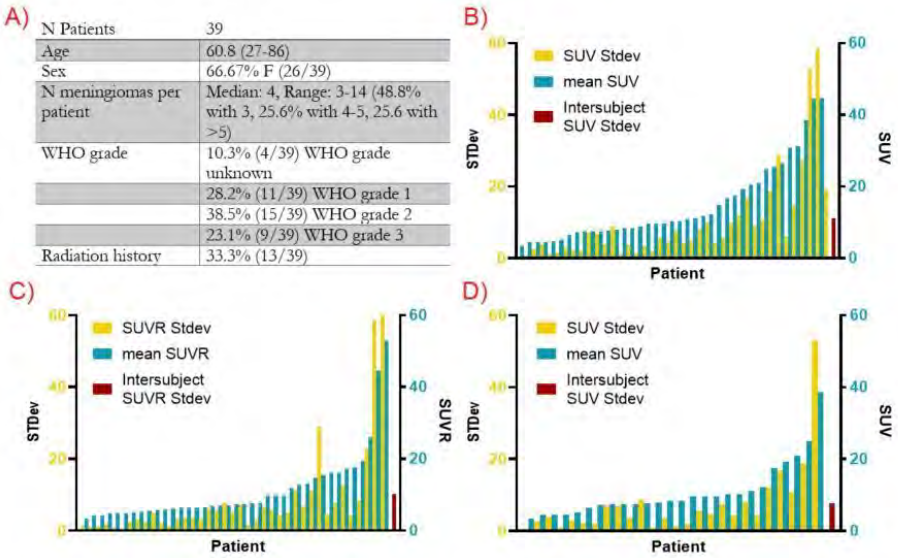

Figure 1. **A)** Clinical and demographic characteristics of the study population. **B)** Histogram analysis of intra-subject lesion SUV standard deviations plotted against mean SUV. **C)** Histogram analysis of intra-subject lesion SUVR standard deviations plotted against mean SUVR. **D)** Histogram analysis of intra-subject lesion SUV standard deviations plotted against mean SUV in patients without a radiation history. Of note, the mean standard deviations of the respective SUV or SUVR values of the described cohort is also included in red in each figure.

(Filename: TCT_739_SeJungChrisChang-ASNR2023FINAL.jpg)

687

Longitudinal dynamic contrast-enhanced GRASP MRI to differentiate brain metastasis progression from radiation necrosis after stereotactic radiosurgery

M Lee[1], A Berger[1], E Lotan[1], D Kondziolka[1], G Fatterpekar[1]
[1]NYU Grossman School of Medicine, New York, NY

Purpose

Differentiating brain metastasis progression from radiation necrosis (RN) remains challenging but important for clinicians, as each implies a different therapeutic approach [1]. Golden-angle radial sparse parallel (GRASP) dynamic contrast-enhanced MRI provides high spatial and temporal resolution to analyze tissue enhancement, which may differ between tumor progression (TP) and RN. This study investigated the utility of longitudinal GRASP MRI in distinguishing TP from RN following gamma-knife stereotactic radiosurgery (SRS).

Materials and Methods

Brain metastasis patients managed with SRS at our institution from 2013-2020 who had GRASP MRI before and at least once after SRS (n=48) were retrospectively analyzed. TP (n=16) was pathologically confirmed. RN (n=16) was diagnosed on either resected tissue without evidence of tumor or on lesion resolution on follow-up imaging. As a reference, a separate group of non-small lung cancer patients that showed favorable response with tumor control and without RN on subsequent imaging were included (n=16). GRASP imaging was obtained using MRI systems with field strength of 1.5T or 3T. Mean contrast wash-in and wash-out slopes normalized to the superior sagittal sinus were compared between groups. Receiver-operating characteristic analysis was performed to determine diagnostic performance.

Results

TP showed a significantly steeper post-SRS wash-in slope than RN on all 3 follow-ups (scan 1: 0.29±0.16 vs. 0.18±0.08, p=.021; scan 2: 0.35±0.19 vs. 0.18±0.09, p=.004; scan 3: 0.32±0.12 vs. 0.17±0.07, p=.002; Fig 1). No significant differences were found in post-SRS wash-out. Post-SRS wash-in slope differentiated TP and RN with AUC 0.74, sensitivity 75%, specificity 69% on scan 1; AUC 0.85, sensitivity 92%, specificity 69% on scan 2; and AUC 0.87, sensitivity 63%, specificity 100% on scan 3 (Fig 2). Fig 3 shows an example of TP at baseline (A), which mildly decreases in size on the 1st follow-up (B) but grows on the 2nd and 3rd scans (C and D). Mean normalized wash-in was 0.38 at baseline (E), 0.31 at follow-up 1 (F), 0.33 at follow-up 2 (G), and 0.40 at follow-up 3 (H). Fig 4 shows examples of RN baseline (A), which decrease in size on the 1st follow-up (B), are larger on the 2nd follow-up (C), and are nearly resolved with no measurable enhancement on the 3rd follow-up (D). Mean normalized wash-in was 0.16 on baseline (E), 0.13 on follow-up 1 (F), and 0.15 on follow-up 2 (G).

Conclusions

Longitudinal GRASP MRI may help to differentiate metastasis progression from RN.

Fig 1

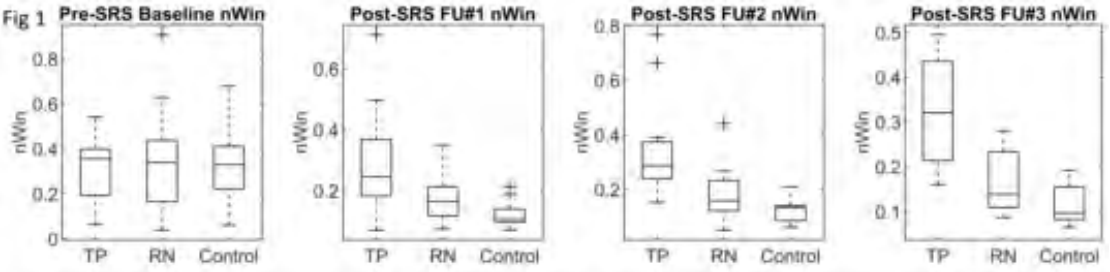

Fig 2

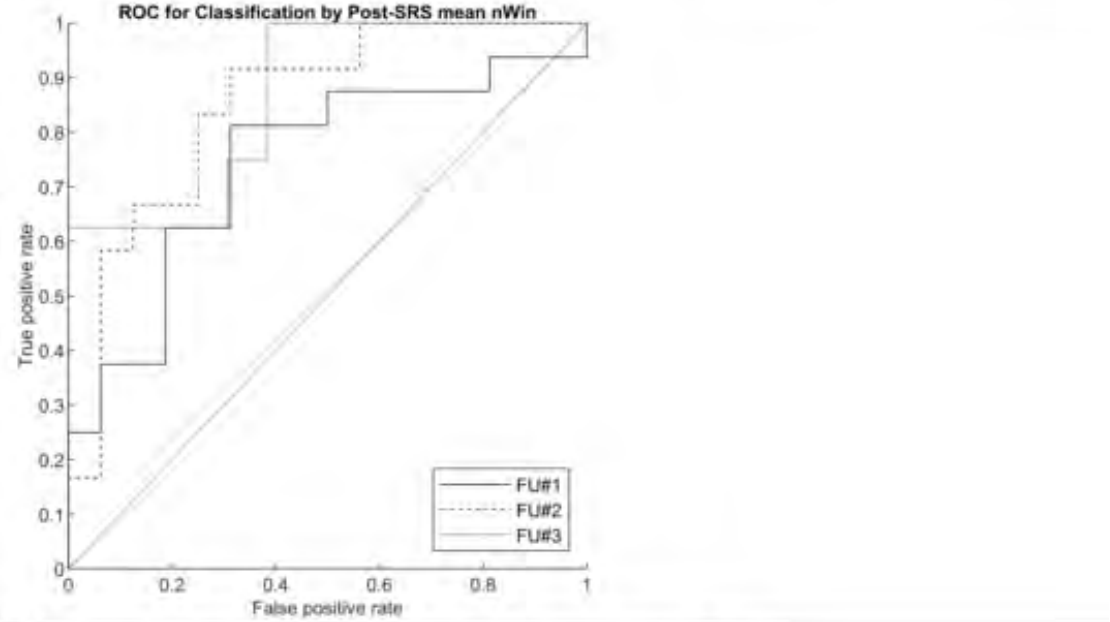

Fig 3

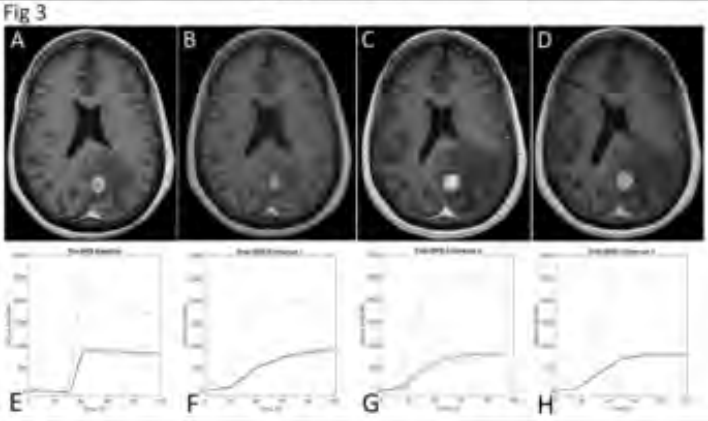

Fig 4

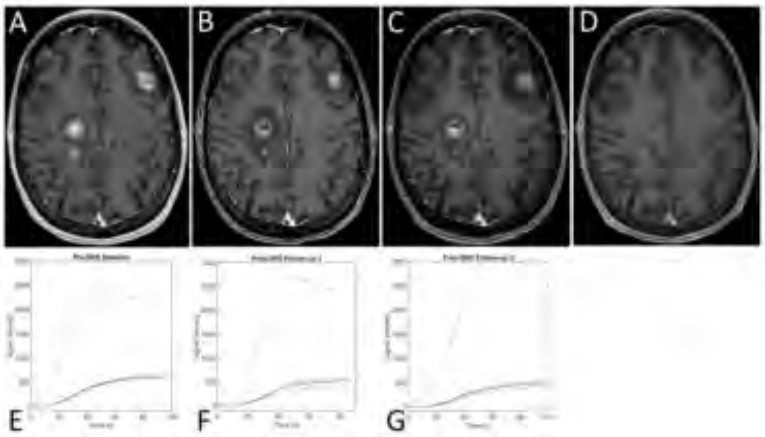

(Filename: TCT_687_ASNRfig.gif)

620

Multiparametric MRI for Identifying Radioimmunomic Signatures in Pediatric Low-grade Glioma

N Khalili[1], A Fathi Kazerooni[2], A Kraya[2], M Kim[1], R Jin[3], A Familiar[2], S Bagheri[1], A Vossough[4], P Storm[2], C Davatzikos[5], A Nabavizadeh[6]

[1]Children's Hospital of Philadelphia, philadelphia, PA, [2]Children's Hospital of Philadelphia, Philadelphia, PA, [3]University of Pennsylvania, philadelphia, PA, [4]CHOP-UPENN, Philadelphia, PA, [5]University of Pennsylvania, Philadelphia, PA, [6]University of Pennsylvania, Wynnewood, PA

Purpose

Increasing evidence suggests that the tumor immune microenvironment (TIME) substantially impacts tumor behavior and complicates response to anti-tumor therapies, in particular, immunomodulatory agents. With the recent promising results of immunotherapy in pediatric low-grade glioma (pLGG), understanding the TIME has gained increasing attention. Detailed characterization of the TIME could aid in patient stratification for novel immunotherapies as well as for monitoring treatment response and detecting mechanisms of resistance. As surgical resection is not feasible for many pLGG tumors, non-invasive tools that provide dynamic and global characterization of the TIME are highly needed.

Materials and Methods

Transcriptomic data for a cohort of 197 subjects was retrospectively collected from the Open Pediatric Brain Tumor Atlas (OpenPBTA). Using consensus clustering algorithm, patients were categorized into three groups (Group1-3) based on their immunological profiles. Then, radiomic signatures of these immune profiles (radioimmunomics) were extracted through machine learning (ML) analysis of readily available conventional MRI scans.

Results

Our analysis revealed greater immune cell infiltration in non-BRAF mutated pLGGs. Group1 showed more enrichment in M1 macrophages and a higher immune score as compared with Group2 and Group3. Tumor inflammation score (TIS), which is a predictor of clinical response to anti-PD-1 blockade, was significantly elevated in Group1 compared with Group2 ($p= 1.4e-7$) and Group3 ($p= 0.0054$). Radiomic features, including volumetric, morphologic, histogram, and texture descriptors, were extracted from the segmented tumor regions on readily available multiparametric MRI (mpMRI) scans of 71/197 patients. Multivariate ML models that were trained to predict the three immunological groups based on radiomic features (using cross-validated random forest classifier along with recursive feature elimination) yielded an AUC of 0.72 for this multi-class classification problem.

Conclusions

Through this study, we showed the presence of distinct immunological subgroups in pLGG that may display variable responses to immunotherapies. Furthermore, using pre-operative conventional mpMRI, we developed radioimmunomic signatures that could aid in stratifying patients based on their TIME. These initial promising results have encouraged us to explore additional features that could potentially increase the accuracy of our radioimmunomics model.

761

Reproducibility of Pseudocontinuous Arterial Spin Labeling Measured Perfusion in Healthy Volunteers and Glioblastoma Patients

L Zhou[1], D Udayakumar[1], Y Wang[2], M Pinho[1], M Youssef[1], J Maldjian[1], A Madhuranthakam[1]

[1]UT Southwestern Medical Center, Dallas, TX, [2]Philips Healthcare, Shanghai, China

Purpose

The purpose of this study was to evaluate the intra-session repeatability and inter-session reproducibility of brain and tumor perfusion measured using 3D pseudo-continuous arterial spin labeled (pCASL) MRI with TSE based Cartesian acquisition with spiral profile reordering (CASPR) (1) in comparison to 3D pCASL with GRASE in 20 healthy volunteers and 20 glioblastoma (GBM) patients at 3T.

Materials and Methods

With IRB approval, 20 healthy volunteers and 20 newly diagnosed GBM patients were recruited. Each healthy volunteer was scanned twice (Fig. 1A) using the imaging protocol (Fig. 1B), while the 20 GBM patients were imaged as shown in Fig. 1C. All scans were performed on a 3T MR scanner (Ingenia, Philips Healthcare) with a 32-channel head coil. ASL scans followed the consensus paper (2) with two different readouts: TSE-CASPR and GRASE. Processing pipeline for healthy volunteer is shown in Fig. 2A. For GBM patients, tumor ROIs and normal appearing brain ROIs were extracted. Linear regression, Bland–Altman, intraclass correlation coefficient (ICC), and within-subject coefficients of variation (wsCV) analyses were performed.

Results

Averaged ASL cerebral blood flow (CBF) maps from volunteers are shown in Fig. 2B among three conditions. For GBM patients, only intra-session repeatability was evaluated since brain perfusion changes are anticipated at different time points due to treatment. Linear regression and Bland-Altman analyses of mean CBF values among normal appearing ROIs and tumor regions are shown in Fig. 3 for volunteers and patients. It shows excellent correlation ($R2 > 0.9$) and minimal bias (bias < 1) for intra-session repeatability, which was further validated by ICC values (>0.90) and wsCVs (<10%) (Fig. 4A). Lower reproducibility was observed among all analyses for 15 mins and 3 weeks inter-session reproducibility in volunteers as expected. However, the intra-session repeatability and 3 weeks inter-session reproducibility, which are more relevant for clinical analyses showed good correlation for both TSE-CASPR and GRASE.

Conclusions

3D pCASL with TSE-CASPR or GRASE provided high intra-session repeatability and 3 weeks inter-session reproducibility in both healthy volunteers and GBM patients at 3 T. While both readouts generated robust images, TSE-CASPR provided images with reduced distortion particularly in GBM patients (Figure 4B) and could be a better readout for pCASL measured perfusion in GBM patients (3).

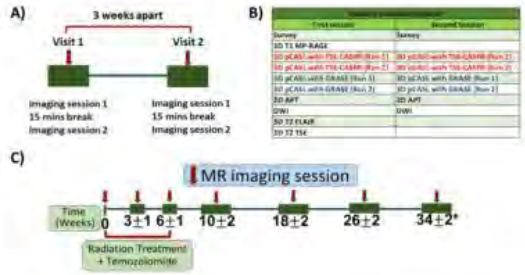

Figure 1: MR scan timelines and imaging protocol for healthy volunteers (A, B) and GBM patients (C). **A)** Each healthy volunteer was recruited for two visits at three weeks interval. Each visit included two imaging sessions with a 15 mins break. **B)** The MR imaging protocol for each visit of healthy volunteers. **C)** The MR scan timeline for GBM patients, with MR scans acquired before, during, and after the radiation treatment for a total of 78 imaging sessions. At each imaging session, two runs of 3D pCASL with TSE-CASPR readout was performed. In a subset of 33 imaging sessions, two runs of 3D pCASL with GRASE were also acquired.

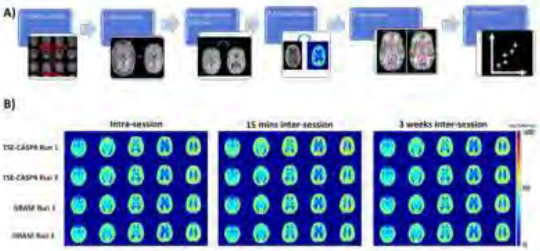

Figure 2: A) Data processing pipeline for healthy volunteers including skull stripping, co-registration to SRI24 atlas, ASL quantification, segmentation, and data analysis. For GBM patients, all images were co-registered to T1 post contrast images first and tumor ROIs were manually drawn by an experienced radiologist (M. P.). For regional perfusion extraction in GBM patients, all images and tumor ROIs were co-registered to SRI24 atlas such that Ipba40 labels could be used to extract normal appearing brain ROIs by subtracting the tumor regions that included whole tumor, cavity, and hemorrhage. **B)** Averaged ASL CBF maps among 20 healthy volunteers acquired with TSE-CASPR and GRASE readouts for three different conditions: intra-session, 15 mins inter-session and 3 weeks inter-session reproducibility.

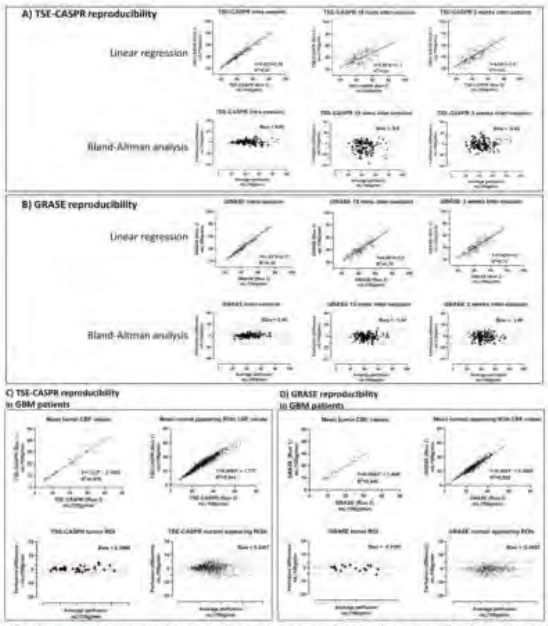

Figure 3: Linear regression and Bland-Altman analyses of 2 runs of CBF measurements in mL/100g/min using 3D pCASL for healthy volunteers with TSE-CASPR (Figure 3A) and GRASE (Figure 3B) from grey matter and white matter among three different conditions: intra-session (left), 15 mins inter-session (middle) and 3 weeks inter-session (right) reproducibility, and for GBM patients with TSE-CASPR (Figure 3C) and GRASE (Figure 3D) among tumor areas (left) and normal appearing ROIs (right) for intra-session reproducibility.

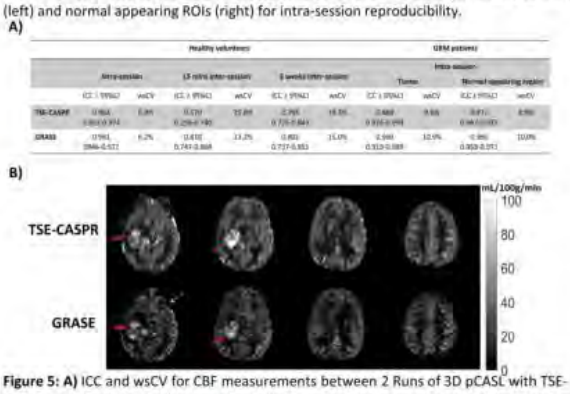

Figure 5: A) ICC and wsCV for CBF measurements between 2 Runs of 3D pCASL with TSE-CASPR and GRASE for healthy volunteers (intra-session, 15 mins and 3 weeks inter-session reproducibility) and GBM patients (intra-session reproducibility only). **B)** Representative CBF maps of a GBM patient acquired for 3D pCASL with TSE-CASPR (top row) and with GRASE (bottom row). CBF maps are visually very similar, including tumor (solid arrow). 3D TSE-CASPR images provided better tumor to background gray matter contrast and are more robust to B0 inhomogeneities compared with 3D GRASE (dashed arrow).

(Filename: TCT_761_FinalFigure.jpg)

494

Time to Tumor Regrowth, Temporal Rate of Response, and Temporal Rate of Regrowth Predicts Overall Survival in Recurrent Glioblastoma treated with Anti-VEGF Therapy

B Ellingson[1], A Hagiwara[2], C Morris[2], N Cho[2], S Oshima[2], F Sanvito[1], T Oughourlian[1], C Raymond[1], L Abrey[3], J Garcia[3], D Aftab[4], C Hessel[4], T Rachmilewitz Minei[5], S Shmueli[6], P Wen[7], T Cloughesy[8]

[1]University of California, Los Angeles, Los Angeles, CA, [2]David Geffen School of Medicine at UCLA, Los Angeles, CA, [3]Genentech, South San Francisco, CA, [4]Exelixis, Alameda, CA, [5]VBL Therapeutics, Modi'in, Israel, [6]VBL Therapeutics, Modi'in, None, [7]Dana Farber Cancer Institute, Boston, MA, [8]University of California, Los Angeles, 90095, CA

Purpose

Anti-angiogenic therapies, including agents targeting the vascular endothelial growth factor (anti-VEGF agents), are known to cause high radiographic response rates due to reduction in vascular permeability resulting in a lower degree of contrast extravasation. Previous studies have suggested the degree of tumor shrinkage combined with the duration of response might be a more meaningful measure of tumor control and may better reflect patient benefit. In the current study, we investigate the association between model-

derived parameters describing enhancing tumor volumetric dynamics and overall survival (OS) in recurrent glioblastoma treated with anti-VEGF therapy.

Materials and Methods

Pooled imaging, clinical, and outcomes data from N=276 patients in two completed phase II trials were used as training data. These trials included N=139 patients treated with bevacizumab with or without irinotecan1 (BRAIN Trial; NCT00345163) and N=137 patients treated with cabozantinib monotherapy2 (XL184-201; NCT00704288). Additionally, data from N=74 patients in the bevacizumab control arm in a phase III trial3 (GLOBE Trial; NCT02511405) were used as a validation dataset. Enhancing tumor volumes were estimated using T1 subtraction maps, and a biexponential model4 was used to model tumor regression (d) and regrowth (g) rates, as well as time to tumor regrowth (TTG), the inflection point where the tumor stops shrinking and starts to regrow after initiation of anti-VEGF therapy for each patient. Log-rank, univariate and multivariable Cox regression were used to quantify the relationship of these parameters with patient survival.

Results

Optimized thresholds based on maximum hazard ratio occurred at a regression rate of d=0.1 months-1 (P=5x10-9 training; P=0.01 validation); growth rate of g=0.07 months-1 (P=5x10-20 training; P=5x10-5 validation); and a TTG of 114 days (P=6x10-17 training; P=2x10-5 validation). Univariate and multivariable Cox regression controlling for age and baseline tumor volume confirmed that tumor regrowth rate (g) and TTG were significant and independent predictors of OS in both phase II training and phase III validation datasets (P<0.001).

Conclusions

Estimates of volumetric tumor regrowth rate (g) and time to regrowth (TTG) are significant and independent predictors of overall survival in recurrent glioblastoma treated with anti-VEGF therapy.

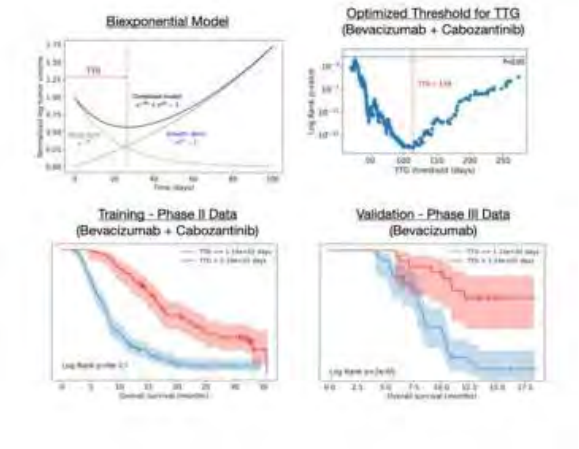

(Filename: TCT_494_Figure1.jpg)

Monday, May 1, 2023

1:00-2:00 PM

Scientific Abstract Session: Neurodegenerative Diseases

618

Accurate and automated detection of tap-test responsive normal pressure hydrocephalus using the ventricular to subarachnoid volume ratio in the largest NPH cohort to date

J Knittel[1], J Hoskin[2], D Hoyt[2], J Abdo[1], E Foldes[2], M McElvogue[2], D Keesler[3], M Borzage[4], J McComb[5], T Fife[2], K King[2]

[1]Creighton University School of Medicine Phoenix Regional Campus, Phoenix, AZ, [2]Barrow Neurological Institute, Phoenix, AZ, [3]Department of Radiology, St. Joseph's Hospital and Medical Center, Phoenix, AZ, [4]University of Southern California, Los Angeles, CA, [5]Children's Hospital Los Angeles, Los Angeles, CA

Purpose

The ability to identify those individuals with progressive dementia, gait disturbance and urine incontinence secondary to normal pressure hydrocephalus (NPH) as opposed to other forms of dementia is important as the former can often significantly improve with CSF diversion. (Kambara 2020). Additionally, NPH is a challenging disease to screen for with historically unreliable markers and many similar symptoms to other forms of dementia (Jaraj 2014, Miskin 2017, Borzage, 2022). There are no non-invasive means to identify patients with probable NPH; the only current but invasive test commonly used is to remove CSF via a spinal tap to determine if short term symptomatic improvement occurs. To that end, we hoped to identify a marker to diagnose probable NPH by non-invasive CT scans.

Materials and Methods

Although no data is yet available as to the outcome of patients shunted, a retrospective review of CT scans was done on 305 tap-test responsive suspected NPH patients between January 2015 and January 2022. The CT scans of this group were compared to a control group who presented to the Emergency Department between June 2021 and June 2022 whose only symptom was headache and whose CT scans were determined to be normal. From the CT studies of all these patients, the ventricular to subarachnoid volume (VSV) ratios were calculated by analyzing thin slice bone window scans and the ratios compared.

Results

The automatically calculated VSV ratios were able to distinguish between the two groups with a sensitivity and specificity of 93.1% and 98.4%, respectively. The area under the ROC curve was 0.995 (95% CI 0.99-1).

Conclusions

We developed an automated method to obtain a ventricular to subarachnoid ratio that correctly classifies NPH from control patients. We believe this marker is scalable and reliable due to the diagnostic accuracy in a cohort of 305 tap-test responsive NPH patients. Moreover, this study only used CT scans already being obtained as part of routine clinical care highlighting our marker's potential to cost-effectively screen patients for NPH. Further analysis of the positive tap-test responsive patients to shunting will be needed to confirm the accuracy of the VSV ratio as a means of helping identify those patients with NPH who would benefit from CSF diversion.

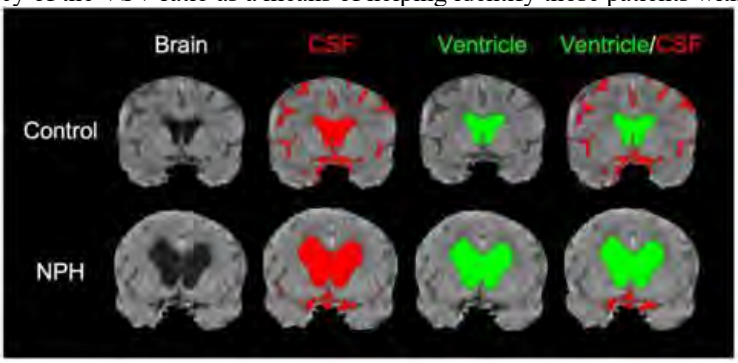

Figure 1. Visual representation of the ventricular to subarachnoid volume (VSV) ratio. Red highlights the supratentorial subarachnoid CSF. Green highlights ventricular volume. Ventricle/CSF represents the VSV ratio we used to differentiate Control (top) from NPH (bottom) patients.

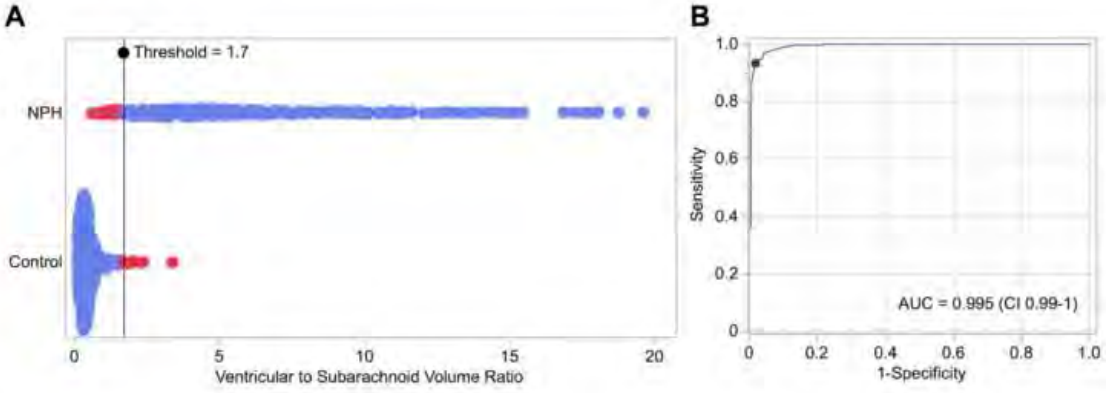

C

Actual State	Predicted Count	
	Control	NPH
NPH	21	284
Control	501	9

D

Measure	Estimate	Lower 95% CI	Upper 95% CI
Sensitivity	93.1%	89.7%	95.5%
Specificity	98.4%	96.9%	99.2%

Figure 2. Threshold analysis comparing ventricular to subarachnoid volume (VSV) ratio of NPH and Control patients. (A) Threshold of 1.7 optimally separated NPH from Control VSV ratios. Misclassified patients were labeled red and correctly classified in blue. (B) The area under the ROC curve was 0.995 with a 95% confidence interval between 0.99 and 1. (C) 21 of the 305 NPH patients and 9 of the 510 Control patients were misclassified (red). 284 or the 305 NPH patients and 501 of the 510 Control patients were correctly classified (blue). (D) VSV ratio differentiated between NPH and Control patients with a sensitivity of 93.1% (CI 89.7% - 95.5%) and specificity of 98.4% (CI 96.9% - 99.2%).

(Filename: TCT_618_ASNRAbstractFigures.jpg)

524

Association between Carotid Intraplaque Hemorrhage and Cerebral Beta-Amyloid Depostion

S Culleton[1], H Baradaran[1], S Kim[1], N Cole[2], D Parker[1], K Duff[3], J Hoffman[4], J McNally[1]

[1]University of Utah, Salt Lake City, UT, [2]MIM Software Inc, Beechwood, OH, [3]Center for Alzheimer's Care, Imaging, & Research, Salt Lake, UT, [4]University of Utah, Salt lake, UT

Purpose

Carotid atherosclerotic plaque increases the risk of dementia; however, the mechanism is unknown. A potential downstream consequence of carotid disease is beta-amyloid (AB) deposition, a known contributor to Alzheimer disease. Small studies showed brain AB deposition increases with >60% stenosis which was attributed to hypoperfusion (1,2). Another hypothesis is vulnerable plaque with intraplaque hemorrhage (IPH) is prone to cerebral microemboli, inflammation and AB deposition. This study investigated the association between cerebral AB deposition and carotid IPH.

Materials and Methods

This prospective study enrolled consecutive patients with carotid disease (≥1 carotid plaque >50% NASCET stenosis if symptomatic or >70% stenosis if asymptomatic), without known dementia. Imaging included a 3T carotid MRI (plaque assessment), 18F-Flutemetamol PET/CT (AB evaluation) and brain dynamic susceptibility contrast MRI (infarct and perfusion analysis). Baseline cognition was determined with the Repeatable Battery for the Assessment of Neuropsychological Status. Quantitative whole brain and regional/lobar AB analyses were performed with MIMNeuro. IPH(+) and (-) groups' 18F-Flutemetamol z-scores were compared against a 54-subject database of normal imaging. AB z-scores were evaluated at the 1- and 2-tailed 95% confidence thresholds of 1.65 and 1.96, respectively. Potential confounders (cerebrovascular risks, perfusion, plaque features, baseline cognition, white matter disease) were evaluated between groups using 2-tailed t-tests or chi-square tests.

Results

Forty-two patients [70.5±7.6 years, 36(85.7%) males] were assessed (Table 1). 17(40.5%) had IPH(+) plaque. AB was not significantly elevated in the IPH(-) group compared to controls, however, multiple areas were elevated in the IPH(+) group (Figure 1). A z-score of ≥2.0-2.5 was present in the posterior cingulate gyrus/precuneus region (largest volume of AB), left lingual gyrus, left fusiform gyrus, left insula, left inferior occipital gyrus, right putamen, right primary visual cortex, right middle occipital gyrus (Table 2). Potential confounders including stenosis were not significantly different between IPH(+) and (-) groups.

Conclusions

IPH(+) plaque was associated with elevated cerebral AB in multiple brain areas, particularly in the posterior cingulate/precuneus region. This finding was independent of the severity of stenosis. This association may have cognitive implications for patients with carotid disease and IPH.

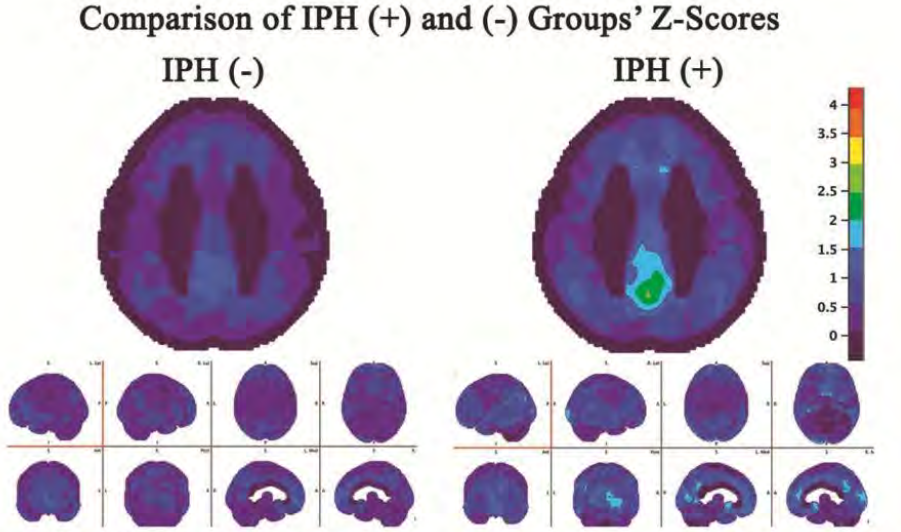

IPH(-)group (n=25) shows no areas of elevated beta-amyloid with z-scores ≥2.0

IPH(+) group (n=17) with elevated z-scores ≥2.0 (dark green) and ≥2.5 (light green) particularly in posterior cingulate/precuneus region

Parameter	All Participants n=42	IPH(+) n=17	IPH(-) n=25	P
Age, years	70.5±7.6	72.8±7.5	70.0±7.3	.114
Male	36(85.7)	16(94.1)	20(80.0)	.374
Caucasian	41(97.6)	17(100.0)	24(96)	1.00
BMI, kg/m²	31.1±7.3	31.7±7.0	30.8±7.7	.704
Education, years*	14.3±2.4	14.4±2.3	14.3±2.9	985
RBANS Total Scale score	90.8 ±14.1	91.6±17.3	90.3±12.0	.797
NASCET, %	50.1±18.8	47.0±22.2	52.8±16.1	.329
Comorbidities				
Hyperlipidemia	35(83.3)	13(76.5)	22(88.0)	.413
Hypertension	33(78.6)	11(64.7)	22(88.0)	.124
Diabetes	21(50.0)	10(58.8)	11(44.0)	.346
Ischemic stroke	11(26.2)	5(29.4)	6(24.0)	.733
Renal Failure	2(4.8)	2(11.8)	0(0.0)	.158
Current smoker	6(14.3)	1(5.9)	5(20.0)	.374
Prior smoker	26(61.9)	11(65.7)	15(60.0)	.758

Table 1: Potential confounders were not significantly different between the IPH(+) and IPH(-) groups

Mean Z-Score ± SD	Region	Volume (mls)
2.22±.13	Posterior cingulate gyrus/precuneus	6.09
2.06±.03	Left lingual gyrus	0.09
2.07±.04	Right primary visual cortex	0.09
2.05±.05	Right middle occipital gyrus	0.06
2.13±.11	Left fusiform gyrus	0.39
2.03±.01	Left insula	0.03
2.06±.04	Right putamen	0.15
2.01±.04	Left inferior occipital	0.04
2.50±.01	Precuneus	0.03

Table 2: Mean z-score map in IPH(+) patients compared to age-matched normal controls and corresponding volumes of interest for z-scores >2.0

(Filename: TCT_524_IPHASNRcopy.jpg)

643

Effect of MRI Volumetric Software on Neuroradiologists' Diagnostic Accuracy in Neurodegenerative Disease

M Lim[1], S Dash[1], J Pattee[2], A Thaker[1], B Steach[3], P Pressman[1], B Bettcher[1], V Potigailo[1], D Zander[1], J Honce[1], W Colantoni[1], J Tanabe[1]

[1]University of Colorado Anschutz Medical Center, Aurora, CO, [2]University of Colorado, Aurora, CO, [3]Icometrix, Boston, MA

Purpose

Dementia is a growing public health problem for which brain MRI remains the most widely used imaging tool. Visually assessing brain atrophy on MRI is unreliable and has prompted the introduction of automated quantitative software programs into clinical workflow. These tools can potentially augment the ability of the radiologist to suggest a diagnosis, but such studies are lacking [1,2]. We tested the hypothesis that availability of an Icometrix plot of age-normalized volumes over different brain regions would improve neuroradiologists' accuracy in diagnosing dementia.

Materials and Methods

60 patients - 21 cognitively intact (CI), 22 with Alzheimer's dementia (AD), and 17 with frontotemporal dementia (FTD) - were included in this study. The MRIs for these patients were assessed by 4 fellowship-trained neuroradiologists both with and without the use of Icometrix plots. Ratings were conducted over 2 sessions at least 1 week apart. For each session, raters classified each of the MRIs as either CI or neurodegenerative. If neurodegenerative, the rater was then asked to specify AD or FTD. Generalized linear mixed models were fit to assess whether use of Icometrix was associated with improved diagnostic accuracy, accounting for random effects of within-rater and within-subject variability. Two endpoints were assessed: "exact" correctness in diagnosing CI, FTD, and AD, and "rough" correctness in distinguishing CI from non-CI. A post-hoc analysis was conducted to test whether Icometrix use improved diagnostic accuracy within diagnosis groups.

Results

There was no significant effect of Icometrix use on either exact or rough diagnostic accuracy. Post-hoc analyses: Within the AD group, Icometrix use was associated with an increase in rough diagnostic accuracy (OR 2.77 [1.15 - 6.68], p=0.02). Within CI, Icometrix use was associated with a decrease in diagnostic accuracy (OR 0.25 [0.07-0.86], p=0.02). Within FTD, there was no change in accuracy with Icometrix use.

Conclusions

Icometrix plot availability did not improve overall diagnostic accuracy in a sample of AD, FTD, and CI. Post-hoc analysis showed that within AD, diagnostic accuracy improved with Icometrix use, suggesting a possible role for automated quantification in the clinical environment. Within CI, decreased diagnostic accuracy with Icometrix use may be related to the wide range of age-related atrophy or rater expectation bias. Future studies are needed to determine the context for optimizing the use of automated software.

358

Neuroimaging Features of Adult-Onset Leukoencephalopathy with Axonal Spheroids and Pigmented Glia (ALSP) and its Longitudinal Progression

R Rajagovindan[1], R O'Mara[2], A Meier[2], J MacDougall[3], E Finger[4], J Orthmann-Murphy[5], D Broderick[6], W Zbigniew[6], S Papapetropoulos[2]

[1]Vigil Neuroscience, Winchester, MA, [2]Vigil Neuroscience, Cambridge, MA, [3]Statistical Consultant, Cambridge, MA, [4]Western University, London, Ontario, [5]University of Pennsylvania, Philadelphia, PA, [6]Mayo Clinic, Jacksonville, FL

Purpose

ALSP is a rare, rapidly progressing fatal neurologic disorder commonly caused by mutations in the CSF1R gene. The pathological hallmarks include demyelination of white matter of the brain, swollen axons and pigmented glial cells. ALSP is characterized by a constellation of symptoms including personality changes, cognitive dysfunction and motor impairments, which can mimic several neurodegenerative diseases including Alzheimer's disease and thus is often misdiagnosed. There are currently limited treatment options. Further, limited natural history data is available to inform therapeutic development. The objective of the current work is to characterize the radiological features of ALSP and its progression to aid with accurate diagnosis and to inform the design of therapeutic intervention studies in ALSP.

Materials and Methods

This was a multicenter, retrospective, natural history study of patients diagnosed with ALSP. Data (demographics, medical history, diagnostic results, interventions/medications, original MRI when available) were acquired through retrospective review of EHRs/medical records of deidentified patients. MRI severity score for ALSP (Sundal et al 2012), white matter lesion and regional brain volume were derived by central analysis of available MRI exams.

Results

Records of 62 patients were reviewed. Brain MRIs were available for 19 patients, among which 16 had documentation of CSF1R gene mutation, 10 were women and the mean age at diagnosis was 48.7±12.9 years. Serial MRI scans were available in 9 of 19 patients. Brain MRI findings included white matter lesions (100%) with a fronto-parietal distribution, thinning of corpus callosum (79%), brain atrophy (84%) and enlarged ventricles (37%). The average MRI severity score was 14.3±6.5 (range: 3-25). Progression in MRI severity score, white matter lesion volume and regional brain volume loss were observed in most individuals with serial MRI scans.

Conclusions

Recognition of the differential MRI patterns of ALSP may improve diagnostic evaluation. The qualitative and quantitative measures of MRI disease severity may serve as sensitive outcome measures in therapeutic intervention studies in ALSP.

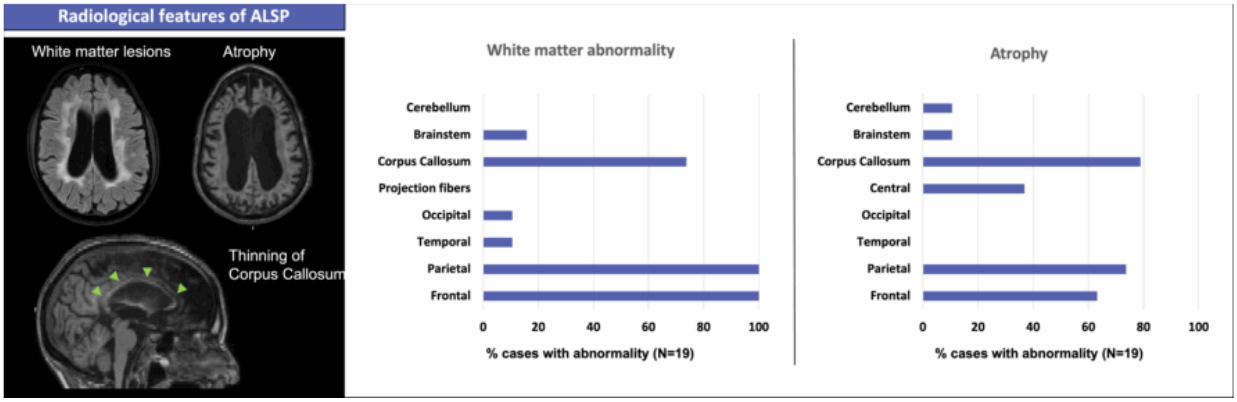

(Filename: TCT_358_ASNR_graphics.gif)

738

Normal Pressure Hydrocephalus; is Enlarged Brain Volume a Predisposing Factor?

D Hoyt[1], D Keesler[1], J Knittel[2], M Borzage[3], J McComb[4], K King[5], J Hoskin[5], T Fife[5], J Abdo[2], E Foldes[5], M McElvogue[5]

[1]Creighton University, Phoenix, AZ, [2]Creighton University School of Medicine Phoenix Regional Campus, Phoenix, AZ, [3]University of Southern California, Los Angeles, CA, [4]Children's Hospital Los Angeles, Los Angeles, CA, [5]Barrow Neurological Institute, Phoenix, AZ

Purpose

Normal pressure hydrocephalus (NPH) is a prevalent form of dementia, affecting an estimated 6-9% of individuals over the age of 80. NPH is reversible with early detection and treatment, though early detection is often challenging. Despite the prevalence of NPH, the etiology is poorly understood. In 2004, William Bradley proposed that benign external hydrocephalus of infancy may be a predisposing factor. We hypothesize that increased brain volume is one factor that might contribute to developing NPH. This study examines the intracranial volume and the brain volume in NPH patients versus normal individuals.

Materials and Methods

IRB approval was obtained for this retrospective study with a waiver of informed consent for creation and evaluation of a de-identified dataset. 305 patients with shunt-responsive NPH from Barrow Neurological Institute's clinic were included. 510 control patients with normal head CTs were included from patients who presented to the ED with headache. Image analysis was performed using the Functional Magnetic Resonance Imaging tool, the FMRIB Software Library or FSL to segment the ventricles and calculate the total intracranial volume and brain volume.

Results

The average intracranial volume for patients with NPH (n = 305) was 1.306±0.007L, compared with 1.239±0.005L for control subjects (n = 510). The NPH volume averaged 0.067L (5.4%) larger than the control volume (P<0.001). The average brain volume for patients with NPH was 1.173±0.006L, compared with 1.124±0.005L for control subjects. The NPH volume was 0.049L (4.4%) greater than the brain volume of controls (P<0.001). The ratio of brain volume to intracranial volume was 0.901±0.003 in NPH patients and larger (0.908±0.002) in controls (p=0.044).

Conclusions

Patients with NPH have significantly larger intracranial volumes when compared with healthy individuals, and it has been postulated that the initial insult may occur while the cranium remains malleable in infancy. This reasoning has led researchers to propose benign external hydrocephalus of infancy as a potential predisposing factor for NPH. Our data reveals that brain volume is also significantly larger in patients with NPH as compared with age-matched healthy control subjects, which cannot be inherently accounted for by benign external hydrocephalus of infancy.

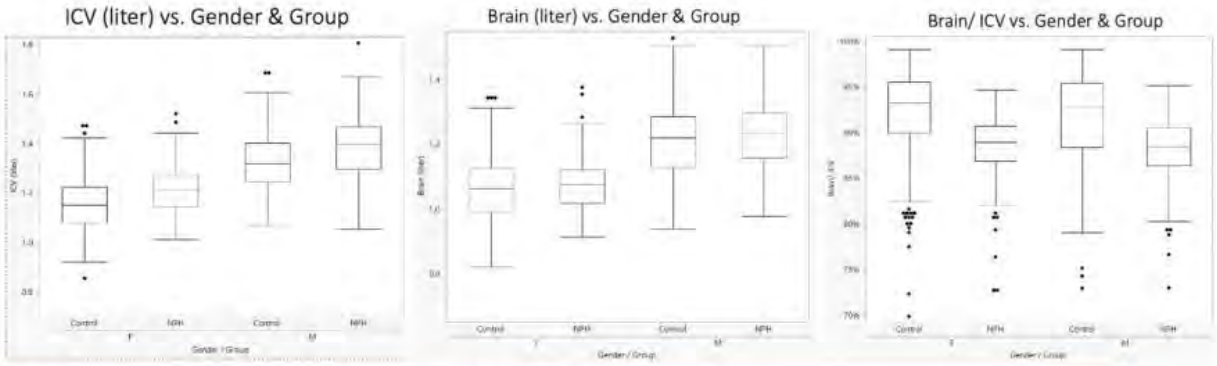

Group mean ICV, Brain Volume, and ratio adjusted for age and sex								
	ICV (L) mean		p	Brain (L) mean		p	Brain / ICV mean		p
Control (n=510)	1.239 ±	0.005	<.0001	1.124 ±	0.005	<.0001	0.908 ±	0.002	0.044
NPH (n=305)	1.306 ±	0.007		1.173 ±	0.006		0.901 ±	0.003	

Figure 1: The above figures and tables demonstrate that intracranial volume (ICV) is larger in NPH versus control patients, brain volume is larger in NPH versus control patients, and the ratio of brain volume to intracranial volume is smaller in NPH versus control patients, all with statistical significance.

(Filename: TCT_738_ASNRFigure1.jpg)

1052

Topographic evaluation of Semantic Dementia and its clinical mimics, Alzheimer's and Behavioral Variant Frontotemporal Dementia

S Nini[1], M Adly[2], A McKinney[3]

[1]University Of Miami, Miami, FL, [2]University Of Miami/ Jackson Memorial Hospital, Miami, FL, [3]University of Miami & Jackson Memorial Hospital, Miami, FL

Purpose

The study aimed to evaluate any imaging overlap as well as regional topographic relationships that exist, between Semantic Dementia (SD) and its clinical mimics, including Behavioral variant of Frontotemporal Dementia (BvFTD), and Alzheimer's (AD), which share neuropsychiatric symptoms.

Materials and Methods

Patients were identified utilizing proprietary institutional software (URIDE, University of Miami, FL), which collects deidentified data from the electronic records by filtering the diagnostic ICD codes; this search yielded diagnoses from the institutional "Memory Clinic". Additionally, an imaging report search software (Montage, Wilton, CT), was used to identify reports containing: "Semantic Dementia", "Alzheimer's with Temporal Atrophy", and "Behavioral variant Frontotemporal Dementia". Imaging data was then aggregated from both data sources for consensus review by two radiologists. This retrospective MRI review evaluated six brain regions: the anterior and posterior temporal lobes (ATL, PTL), amygdala (AD), hippocampi (HP), frontal lobes (FL), and insula (IN).

Results

Two software search algorithms resulted in 42 total patient's MRI being reviewed with one of these 3 disorders (mean age 72 years, 60% females). Of these 42 patients, 22 were diagnosed with AD [52%], 12 with SD [29%], and 8 with BvFTD [19%]. SD demonstrated propensity to affect the ATL's asymmetrically (predominantly right-sided SD 25% and predominantly left-sided SD 33%), as compared to BvFTD and AD. BvFTD patients demonstrated more severe and symmetric involvement of the FL's (88% of BvFTD patients had FL involvement, with 26% having severe atrophy) and incidentally the medial temporal lobe (MTL) when compared to AD and SD, most notably within the amygdala (n=8, 63% of BvFTD patients had amygdala involvement, 38% of whom had severe atrophy). Most AD patients (n=22, 86 %) had involvement of the hippocampi, with lesser in degree of severity compared to both SD and BvFTD.

Conclusions

Semantic Dementia has several clinical mimics with overlapping MRI findings, but with decernable differences on retrospective MR review. SD had a propensity for asymmetry, with increased severity of involvement of the ATL's. Meanwhile, BvFTD had similarly severe involvement of the ATL's, but more symmetrically and with more prominent FL atrophy; AD was most likely to affect the MTL, but to a much lesser degree of severity. Hence, these topographic observations during routine MR imaging interpretation may help contribute to the clinical diagnosis.

350

Utility of [18F] PI-2620 as Universal Biomarker for the A/T/N Classification of Dementia and Neurodegenerative Disease

A FRANCESCHI[1], S Peng[2], M Gordon[3], Y Ma[2]

[1]Northwell Health, New York, NY, [2]Feinstein Institutes for Medical Research, Manhasset, NY, [3]Donald and Barbara Zucker School of Medicine at Hofstra/Northwell, Manhasset, NY

Purpose

In this study, we implemented a data-driven scaled subprofile model (SSM)/principal-component analysis (PCA) to identify spatial covariance patterns of [18F]-PI-2620 PET scans of amyloid-positive neurodegeneration (AD) and healthy controls, and tested SSM/PCA pattern expression for its ability to predict amyloid status, with the aim of evaluating the efficacy of PI-2620 as a single, universal biomarker for the A/T/N classification of dementia and neurodegenerative disease.

Materials and Methods

Dual-phase [18F]-PI-2620 brain PET images were obtained on ECAT EXACT HR+ camera (early-phase: 0-5min post-injection [pi] for brain perfusion; late-phase: 45-75min pi for tau pathology). Late-phase [18F]-florbetaben (FBB) brain PET images 90-110 min pi were obtained on the same camera. T1 3D-MPRAGE images were acquired on a Siemens Espree 1.5 T scanner. Images of standard uptake value ratio (SUVR) were produced for PI-2620 (early-phase), Pi-2620 (late-phase) and FBB (late-phase) using cerebellar grey matter as reference region. Spatial covariance analysis was performed using our institutional public domain SSM/PCA toolbox, followed by post-hoc brain mapping analysis using SPM12.

Results

30 subjects (15 male, 10 female, mean age: 64.5 +/- 10.1, range 51-89) were analyzed; 15 patients with amyloid-positive AD (A+/T+/N+) and 10 controls (A−/T-/N-). We identified three distinct AD-related patterns of covariance for brain perfusion, tau and amyloid (Fig. 1: ADRP-tau5, ADRP-tau45, ADRP-FBB). ADRP expression scores discriminated AD from NC subjects (Fig. 2) and correlated positively with clinical ADAS-cognition scores in the combined group (Fig. 3). Moreover, group discriminant analysis revealed an accuracy of 92 %, 88% and 96 % respectively, with the combination of ADRP-tau5 and ADRP-tau45 scores yielding the same accuracy as ADRP-FBB score. These topographies were supported by known distributions of hypoperfusion and increased tau and amyloid depositions in AD (Fig. 4).

Conclusions

Preliminary analysis of AD-neurodegeneration and normal controls demonstrates the potential of PI-2620 to serve as a single biomarker ("one-stop-shop" approach) for the A/T/N classification of patients with cognitive impairment. Future work will include patients with amyloid-negative neurodegeneration (A−/T+/N+) in this analysis. Long-term goals of our single biomarker approach include the eventual use of PI-2620 in descriptive classification, patient selection, and monitoring of target engagement in disease-modifying treatment trials.

Figure 1: Topographic patterns of spatial covariance with SSMPCA

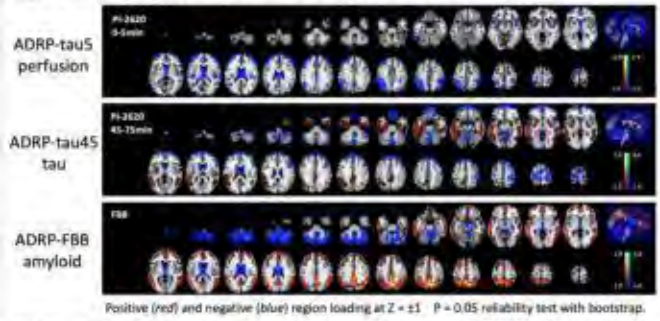

Positive (*red*) and negative (*blue*) region loading at Z = ±1 P = 0.05 reliability test with bootstrap.

Figure 2: Disease discrimination by ADRP expression

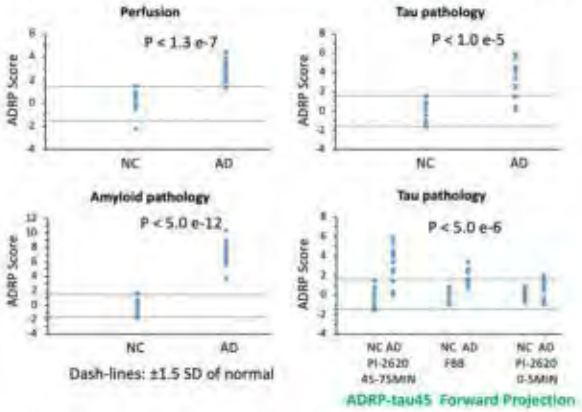

Dash-lines: ±1.5 SD of normal

ADRP-tau45 Forward Projection

Figure 3: Clinical correlations with ADRP expression

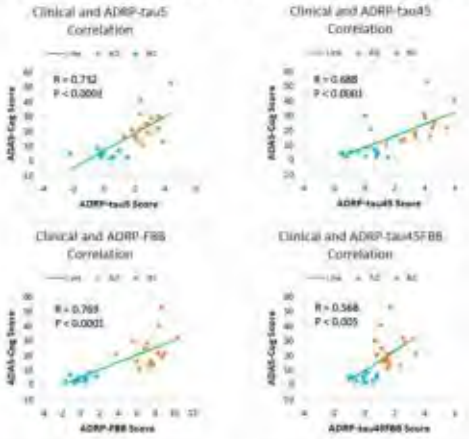

Figure 4: Topographic patterns of mean differences with SPM

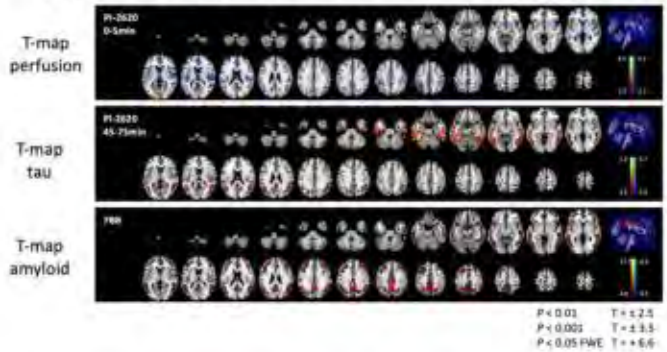

(Filename: TCT_350_ASNRFigureFINAL.jpg)

Monday, May 1, 2023

1:00-2:00 PM

Scientific Abstract Session: Spine Intervention

962

A Cohort Study of Spinal Cord Diffusivity After Treatment of Cervical Spondylotic Myelopathy with Instrumented Spinal Fusion

K Koch[1], A KLEIN[1], A Nencka[2], S Kurpad[1], A Vedantam[1], M Budde[1]

[1]Medical College of Wisconsin, Milwaukee, WI, [2]Medical College of Wisconsin, Wauwatosa, WI

Purpose

The present study provides the first large-cohort post-treatment diffusion MRI analysis of cervical spondylotic myelopathy (CSM) patients treated with metallic fusion for cord decompression. Using novel metal-artifact-suppressed DWI techniques, the study sought to test the hypothesis that routine decompression using metallic instrumentation reduces diffusivity relative to controls and non-instrumented levels in CSM subjects.

Materials and Methods

Post-surgical CSM (n=38) subjects treated with metallic instrumented fusion were recruited imaged between 3 and 36 months post-surgery. Asymptomatic non-instrumented control subjects (n=25) were also imaged. All subjects provided written consent to participate in a locally-approved IRB protocol. T1 and T2 weighted 3D-Multi-Spectral Images (3D-MSI)[1] were utilized for metal-artifact suppressed anatomic localization. To address metal artifacts, a prototype 2D-MSI PROPELLER-based diffusion weighted (DW) sequence (DW-MSI) [2] was utilized for axial diffusion-measurements of the spinal cord with b=600 m/s^2. Apparent diffusion coefficient (ADC) values of the cord were statistically modeled as a function of cohort (i.e. CSM vs control), vertebral level, decompressed (instrumented) level (yes/no), adjacent segment level (to instrumentation) (yes/no) age, BMI, cord area, duration between fusion surgery and imaging exam, and mJOA symptom score. Statistical tests were performed using linear mixed effects (LME) modeling with subject index modeled as a random effect.

Results

DW-MSI enabled cord ADC measurements near fusion hardware. CSM cases showed a reduction in ADC relative to controls for the entire cervical cord (p=0.005) and instrumented levels (p=0.004). Non-instrumented CSM levels (neglecting adjacent segments) did not show a statistically significant difference (p =0.107) from controls. Adjacent segments demonstrated reduced ADC at with duration since the fusion procedure (p=0.031). Vertebral level strongly correlated with ADC in all models (p<0.001).

Conclusions

Utilizing multi-spectral diffusion-weighted MRI techniques, the present study has revealed significant reductions in ADC within the post-surgical CSM spinal cord at levels at and adjacent to fusion instrumentation. This confirms the hypothesis that diffusivity of the spinal cord is reduced in post-surgical CSM patients at and near levels of metallic instrumented spinal fusion and agrees with previous observations of reduced ADC after non-instrumented cord decompression[3,4,5].

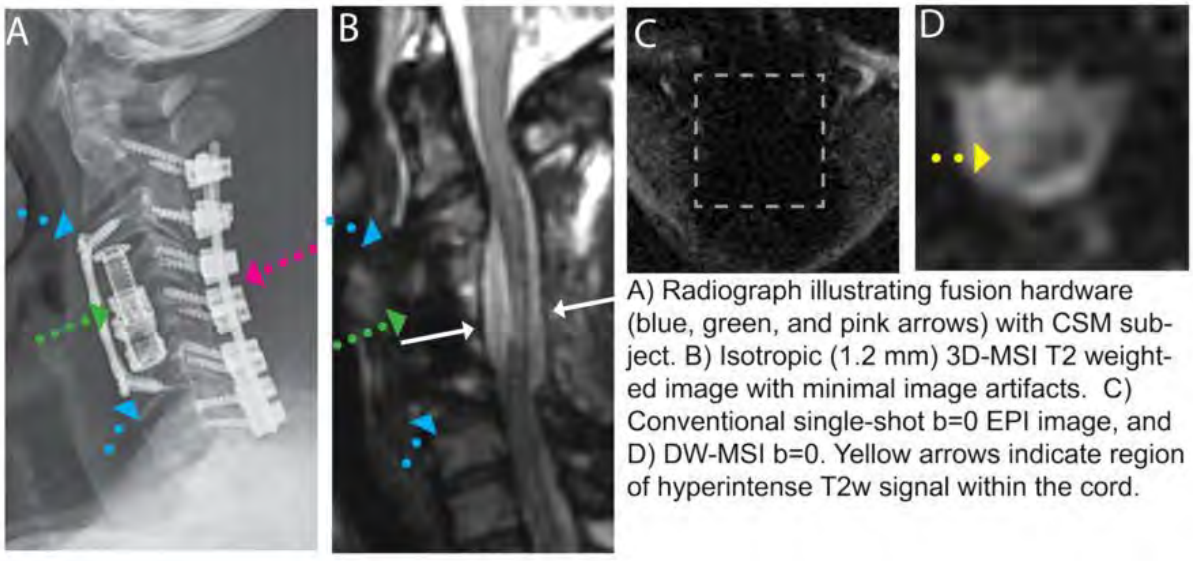

A) Radiograph illustrating fusion hardware (blue, green, and pink arrows) with CSM subject. B) Isotropic (1.2 mm) 3D-MSI T2 weighted image with minimal image artifacts. C) Conventional single-shot b=0 EPI image, and D) DW-MSI b=0. Yellow arrows indicate region of hyperintense T2w signal within the cord.

(Filename: TCT_962_MAV-DWI-C-Spine-Fig-1-ASNR2.jpg)

735

Efficacy of CT-guided indirect forceful facet injection for synovial cyst rupture; 10-year review at a single institution

A Yang[1], T Hutchins[2], L Shah[3], M Peckham[2]

[1]Rocky Vista University, Greenwood Village, CO, [2]University of Utah, Salt Lake City, UT, [3]University of Utah Health Care, Salt Lake City, UT

Purpose

Facet synovial cysts (FSCs) are benign, extradural outpouchings that arise from the facet joint capsule and can cause canal and nerve impingement [1, 2]. The effectiveness of fluoroscopic-guided indirect rupture has previously been investigated and found to have up to 81% efficacy [3]. However, CT-guided indirect rupture can unequivocally determine successful rupture and has not yet been performed. We sought to compare the efficacy of indirect CT-guided FSC rupture at our institution and determine if imaging markers and procedural technique were predictors of success.

Materials and Methods

A search for CT-guided FSC rupture procedures was conducted using the Nuance mPower search engine (Montage, Burlington, Massachusetts) over 10 years. Exported data included report text, sex, and age. The Picture Archiving and Communication System (PACS) was accessed to acquire further data on needle gauge used, successful rupture (determined by contrast spread into the epidural space), cyst size/T2 intensity, and presence of spinal hardware.

Results

86 FSC procedures were performed on 72 patients (28 M/44 F, 11 repeat procedures). 83/86 cases had unilateral, and 3/86 had bilateral FSCs. 14 patients had surgical hardware, all but one with the FSC at the directly adjacent or same level to hardware (92.9%). 65 cases (67 FSCs) were treated using only an indirect approach with 92.5% success (60/65). In 21 cases (22 FSCs) where indirect rupture failed it was followed by direct fenestration with 63.6% success (14/22). 18 gauge spinal needles were most commonly used in the indirect approach (75.7%). There was no significant difference in cyst size, T2 intensity, needle gauge used, and presence of surgical hardware (p=0.9, 0.7, 0.6, and 0.36 respectively) to predict success. There were no procedural complications.

Conclusions

CT-guided indirect forceful facet injection demonstrates moderate efficacy for FSC rupture and may be used as a more conservative initial approach to FSC treatment.

132

Efficacy of Epidural Blood Patching or Surgery in Spontaneous Intracranial Hypotension: A Systematic Review and Evidence Map

T AMRHEIN[1], J Williams[2], M Malinzak[1], L Gray leithe[3], S Cantrell[4], C Deline[5], C Carr[6], D Kim[6], K Goldstein[2], P Kranz[7]

[1]Duke University Medical Center, Durham, NC, [2]Duke School of Medicine, Durham, NC, [3]duke, Raleigh, NC, [4]Duke University Medical Center Library, Durham, NC, [5]Spinal CSF Leak Foundation, Spokane, WA, [6]Mayo Clinic, Rochester, MN, [7]Duke University Medical Center, Cary, NC

Purpose

Background: Spontaneous intracranial hypotension (SIH) is an important cause of treatable secondary headaches that leads to significant disability. Evidence on the efficacy of the two most common treatments, epidural blood patching (EBP) and surgery, has not been synthesized. Purpose: To identify evidence clusters and knowledge gaps about the efficacy of SIH treatments to prioritize future research.

Materials and Methods

Data Sources: MEDLINE (Ovid), Web of Science (Clarivate), and EMBASE (Elsevier) for published English language articles from inception until October 29, 2021. Study Selection: Experimental, observational, and systematic review studies that assessed the efficacy of EBP or surgery for the treatment of SIH. Data Extraction: Data extraction was performed by one author and verified by a second. Disagreements were resolved by consensus or adjudicated by a third author when consensus could not be reached.

Results

Data Synthesis: A total of 139 studies were included in this evidence map (14 median participants, range 3-298). The majority were published in the past decade and most assessed EBP outcomes. There were no studies that met level 1 evidence, and most were retrospective cohort or case series designs (92.1%, n=128). Few studies compared the efficacy of different treatments (10.8%, n=15). Most studies used objective methods for SIH diagnosis (62.3%, n=86), however, 37.7% (n=52) did not clearly meet ICHD-3 criteria. The specific type of CSF leak was not clear in 77.7% (n=108) of studies. Nearly all studies reported patient symptoms, using unvalidated measures (84.9%, n=118), almost no studies assessed quality of life (1.4%, n=2), and most did not include imaging-based outcomes (61.2%, n=85). Outcomes were rarely collected at uniform pre-specified time points. Limitations: Possible exclusion of some studies due to narrow search and not searching grey literature, although unlikely. Did not include venous embolization since this treatment was developed after study completion.

Conclusions

Conclusion: Evidence gaps in studies evaluating the efficacy of SIH treatment demonstrate the need for prospective study designs and clinical trials as well as more comparative studies. We recommend the use of ICHD diagnostic criteria, explicit reporting of CSF leak subtype, inclusion of key procedural details, and the use of objective validated outcome measures collected at uniform pre-specified time points.

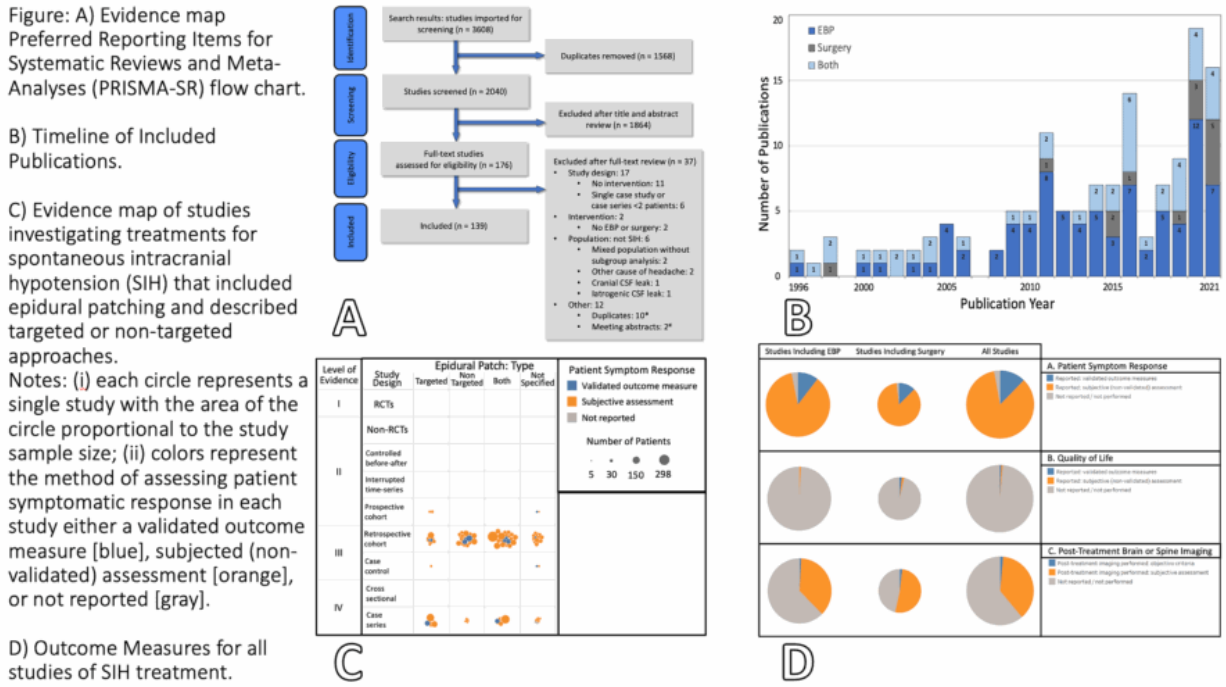

(Filename: TCT_132_Figure.gif)

393

Impact of Lowering Platelet Threshold Requirements for Fluoroscopy-Guided Lumbar Puncture

U Habib[1], K Buch[1], W Mehan[1]
[1]Massachusetts General Hospital, Boston, MA

Purpose
Fluoroscopic-guided lumbar puncture (LP) is a common diagnostic and therapeutic procedure performed by neuroradiologists. Traditionally, a minimum platelet count (MPC) of 50,000/μL for this procedure has been utilized1–3. Given recent national shortages of platelets and increased publication on platelet transfused related adverse events, we sought to lower our required MPC to 20,000 /μL for patients with hematologic malignancies and immune-mediated thrombocytopenia1–3. The purpose of this study was to compare adverse events in patients undergoing Fluoroscopic-guided LP with minimum platelet counts above and below the MPC of 50,000 /μL.
Materials and Methods
The patients with hematological malignancy (M/F=56/45) at our institute, who underwent fluoroscopically guided LP performed by neuroradiologist for chemotherapeutic, diagnostic or research purposes, were retrospectively analyzed between May 2021-April 2022. The pre-procedure MPC, need for platelet transfusion within 24 hours of procedure, number of platelet transfusions, presence of a traumatic tap (defined as >500 RBCs/HPF), procedure-related complications (including development of spinal hemorrhage), and any adverse event related to platelet transfusion was recorded. Basic descriptive statistics were used comparing these two groups.
Results
A total of 101 patients underwent LP, including 82 cases with a MPC above 50,000/μL, and 19 controls with a MPC between 20,000-50,000/μL. No post-procedural complications were encountered. A traumatic tap was found in 15 patients. A total of 17 patients received platelet transfusions within 24-hours prior to the procedure. One patient among the cases developed transfusion-related pruritic rash which was successfully treated with diphenhydramine.
Conclusions
Lowering the MPC threshold to 20,000 /μL for fluoroscopic-guided LP did not result in a higher incidence of post–lumbar puncture complications.

1486

Interim Results of a Prospective Registry Investigating Sacroplasty for Sacral Insufficiency Fractures

J Fleming[1], D NGUYEN[2], C Nelson[3], S Thomas[4], L Bastian[5]
[1]UT Southwestern, Addison, TX, [2]Neuroradiology & Pain Solutions of Oklahoma, Oklahoma City, OK, [3]Lewis Katz School of Medicine at Temple University, Snohomish, WA, [4]Des Moines University, Omaha, NE, [5]University of Texas Health Science Center in San Antonio, San Antonio, TX

Purpose
To evaluate the efficacy of sacroplasty for treating sacral insufficiency fractures, including the effect on pain relief, patient function, and complication rates in an as-treated on-label prospective data registry evaluation.

Materials and Methods
Observational data including patient reported outcomes (PROs), patient characteristics, osteoporosis treatment, fracture duration, cause of sacral fractures, and image guidance used for treatment were collected for patients undergoing sacroplasty. PROs were collected at baseline and at 1, 3, and 6 months following the procedure. Primary outcomes were pain as measured by the Numerical Rating Scale (NRS) and function as measured by the Roland Morris Disability Questionnaire (RMDQ). Secondary outcomes included adverse events, cement leakage, new neurologic events, readmissions, and death.
Results
Interim results for the first 102 patients included significant pain reduction with mean pain scores decreasing from 7.8 to 0.9 ($p < 0.001$) and significant improvement in function with mean RMDQ scores improving from 17.7 to 5.2 ($p < 0.001$). Most procedures were performed under fluoroscopy (58%). Cement leakage rate was 18%, but only one adverse event (new neurologic deficit) occurred as a result. Readmission rate was 16% mostly due to additional back pain and fractures. There were no subject deaths.
Conclusions
Sacroplasty with cement augmentation for acute, subacute, and chronic painful sacral insufficiency fractures caused by osteoporosis or neoplastic disorders results in highly significant improvements in pain and function with very low rate of procedural related adverse events.

1450

Intraosseous Basivertebral Nerve Ablation 3-Year Effectiveness and Safety Results: A Pooled Cohort Study of Two Prospective Clinical Trials

J Fleming[1], D NGUYEN[2], C Nelson[3], S Thomas[4], L Bastian[5]
[1]UT Southwestern, Addison, TX, [2]Neuroradiology & Pain Solutions of Oklahoma, Oklahoma City, OK, [3]Lewis Katz School of Medicine at Temple University, Snohomish, WA, [4]Des Moines University, Omaha, NE, [5]University of Texas Health Science Center in San Antonio, San Antonio, TX

Purpose
Vertebrogenic pain is a newly understood source of chronic low back pain (CLBP). Radiofrequency ablation (RFA) of the basivertebral nerve (BVN) was shown to be superior to sham-control and non-surgical care in randomized controlled trials. We report 3-year aggregated results of two prospective, single arm, open-label, multi-center, follow-up studies of BVN ablation-treated patients.
Materials and Methods
Aggregated results at 3-year post BVN ablation are reported with follow-up at 3, 6, 9, 12, 36, 48, and 60 months. Patient-reported Oswestry disability index (ODI) and numeric pain scores (NPS) were compared using two-sided paired t-test.
Results
95 patients who received BVN ablation and completed a 3-year visit were included in the analysis for an 84% retention rate. Patients reported pain and disability at baseline with a mean NSP of 6.7±1.2 and a mean ODI of 46.1±10.8. 71% had back pain for >5 years. Pain and functional improvements were significant at 3-years with a reduction in NPS of 4.3 points (95% CI 3.8, 4.8; $p<0.0001$) and a reduction in ODI of 31.2 points (95% CI 28.4, 34.0; $p<0.0001$) from baseline. Responder rates, using minimal clinically important differences of ≥ 15-points for ODI and ≥ 50% reduction in NPS from baseline were 85.3% and 72.6%, respectively. There were no serious device or device-procedure related adverse events reported through 3 years.
Conclusions
Intraosseous basivertebral nerve ablation demonstrates excellent safety results as well as significant, durable improvements in pain and function through 3 years in patients with vertebrogenic CLBP.

989

Outcomes of Percutaneous Vertebroplasty in Multiple Myeloma; A Tertiary Neurosciences Centre Experience with Long-term Follow Up

H Holmes[1], V Balian[2], S Kular[1], D Connolly[1], A Martin[1]
[1]Sheffield Teaching Hospitals, Sheffield, United Kingdom, [2]Sheffield Teaching Hospitals, Sheffield, South Yorkshire

Purpose
Multiple myeloma is diagnosed in 5,800 people in the UK each year with up to 64% of these having vertebral compression fractures at the time of diagnosis. Painful vertebral compression fractures can be of significant detriment to patients' quality of life. Percutaneous vertebroplasty is a management option which aims to provide long-term pain management and stabilise the fracture. This review aims to add to and compare with the current data. Outcomes will support evidence-based discussions about treatment options and informed consent for those diagnosed with myeloma who are referred for consideration of vertebroplasty.
Materials and Methods
Data was collected from all cases of percutaneous vertebroplasty in those with multiple myeloma from 2017 to 2019. Data sets included patient demographics, responses to the Oswestry Disability Index (ODI) and visual analogue scale (VAS) pre and post procedure and information on any complications. Patients were stratified into categories of "moderate" and "severe" pain. The primary outcome was pain score via ODI and VAS. An ODI and VAS were sent to patients in 2022 to obtain long-term follow up information, at a median time of 45 months post procedure.
Results
Total of 22 patients included, a total of 84 levels treated and 14 female and 8 male patients. Patients reported a significant

improvement in overall pain score with a mean pre-procedure ODI score on 60% and a mean post-procedure ODI score of 33%. There was a mean pre-procedure VAS of 7 and a mean post-procedure VAS of 3.5 ($p<0.0001$). There was improvement across multiple domains with a reduction in analgesia use. The most improved ODI domain scores were in the "social life" and "personal care" category with 82% showing an improvement. Outcomes were similar in patients who were categorised as having both moderate and severe pre-procedure pain. There was one incident of asymptomatic complication with cement embolus. When comparing these results with similar papers available, outcomes were found to be similar. There were 8 responders to the long term follow up questionnaire and this demonstrated an overall stable degree of pain relief in responders with a mean VAS of 3.5 and mean ODI of 20%.
Conclusions
At this centre, vertebroplasty has been shown to reduce pain scores across a multiple domains. The outcomes in this centre are comparable to those published elsewhere. Long-term follow up shows long lasting pain relief can be achieved.

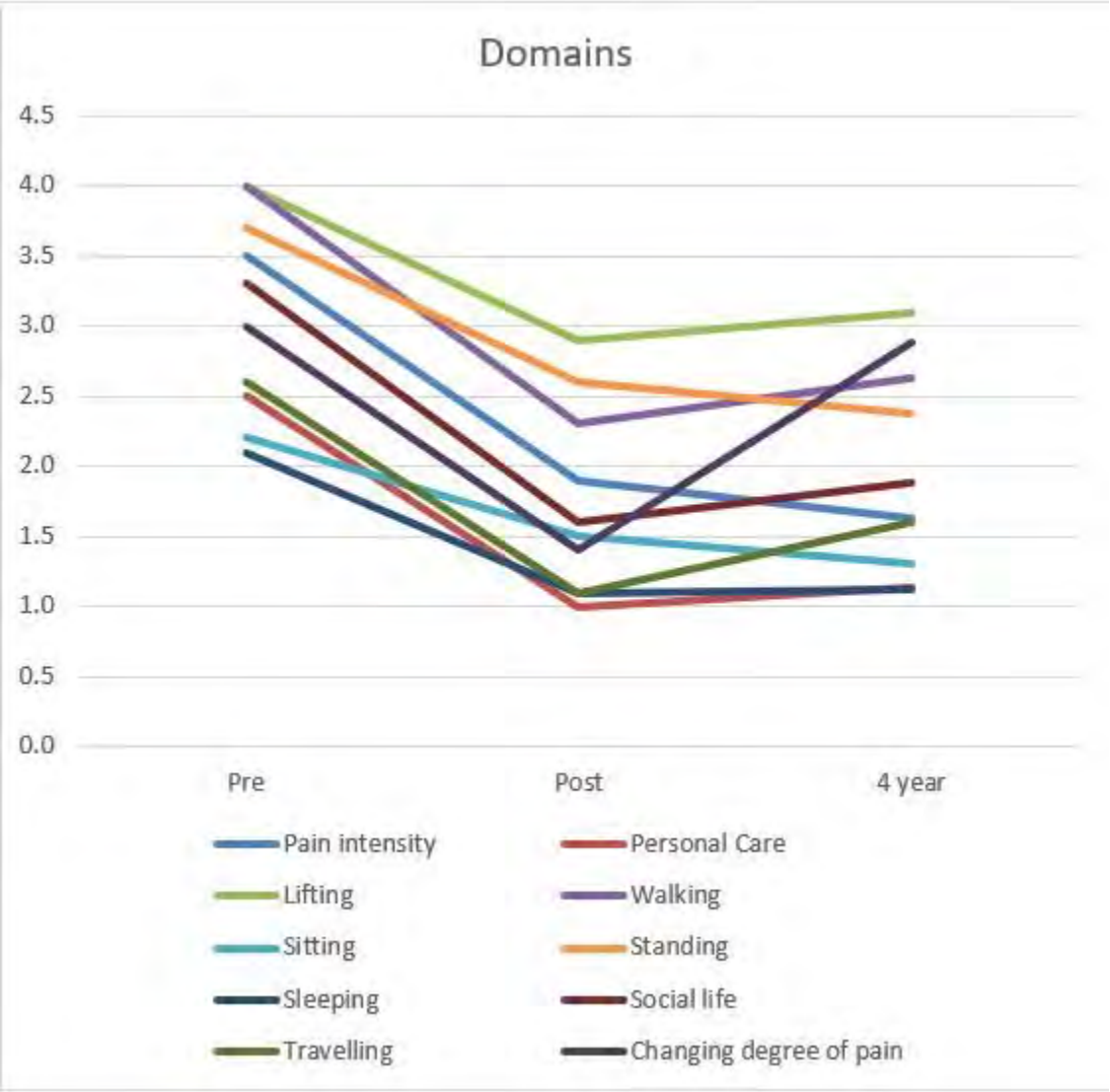

(Filename: TCT_989_PercutaneousvertebroplastyoutcomesODIdomainsvisual.jpg)

790

Who receives image-guided injections for low back pain? An in-depth chart analysis by race/ethnicity within a single healthcare system.

G Safazadeh[1], R Carlos[2], L Shah[1], T Hutchins[1], Y Anzai[1], M Peckham[1]
[1]University of Utah, Department of Radiology and Imaging Sciences, Salt Lake City, UT, [2]University of Michigan, Ann arbor, MI

Purpose
Low back pain (LBP) is a common debilitating condition. Lumbar spine imaging, conservative LBP therapy prior to imaging, and vertebral augmentation have demonstrated racial disparities (1-3). Image-guided injections (IGI) for LBP have yet to be evaluated. We investigated disparities in IGI receipt during a 12-month period in a single healthcare system.
Materials and Methods
Investigators performed a retrospective medical chart review of adult patients with a new LBP diagnosis (ICD 9-10 codes (724.2-M54.5)) in 2018 within a single healthcare system. Patients with diagnosis misclassification, pre-existing treatment, or unknown

race/ethnicity were excluded. Sociodemographic characteristics, presenting symptoms, provider seen, plans discussed, and IGI performed during a 12-month period were collected and comparison statistics performed.

Results

812 subjects met inclusion criteria (59% white non-Hispanic [WNH] and 41% non-white non-Hispanic [NWNH] or Hispanic). NWNH/Hispanic cohort were overall younger, single, and more often had Medicaid-only or self-pay. At the index LBP visit, NWNH/Hispanic patients more often saw generalists and non-physician providers compared to the WNH cohort (p<.04). LBP severity was reported higher in NWNH/Hispanic compared to WNH subjects in both generalist (p<.02) and specialist (p=.043) visits. Both cohorts were referred to a specialist at the same rate (p=.516), however, completion of referrals was noted less often, and time to complete longer, in NWNH/Hispanic patients (p<0.04, p=.007). At specialist visits, IGI treatment was discussed more with WNH than with NWNH/Hispanic patients (p<.02). More WNH patients had at least one IGI treatment within 12 months compared to People of Color patients (p<.02).

Conclusions

NWNH/Hispanic patients had more severe LBP on presentation but were offered, and received, IGI less often than WNH patients. Though both cohorts were referred to a specialist at the same rate, NWNH/Hispanic patients performed the referral less often or later than WNH patients.

Receipt of Image-Guided Injections for Low Back Pain by Race/Ethnicity.

	White Non-Hispanic (n= 479, 59%)	Non-White Non-Hispanic/Hispanic (n=333, 41%)	*P-value**
	Mean±(SD) / n%		
Female	56.58	57.36	.825
Age (years)	50.56 ± (18.20)	46.67 ± (16.67)	.002
Marital Status			.022
Single	27.56	33.03	
Married	53.86	45.65	
Medicaid Only (vs. commercial)	9.66	23.48	.000
Self-pay (vs. Insured)	3.55	7.21	.019
LBP Diagnosis Index visitǂ			
Seen by spine specialists	34.03	18.62	.000
Seen by physician providers	65.34	59.52	.034
Pain intensity ¡			
At generalist visit	5.95 ± (2.43)	6.68 ± (2.48)	.017
At specialist visit	5.27 ± (2.51)	5.96 ± (2.42)	.043
Treatment plans§			
Spine specialist referral	19.81	17.71	.516
Specialist referral fulfillment	77.78	60.42	.047
Time to fulfill referral (days)	29.22 ± (31.36)	67.79 ± (89.24)	.007
IGI discussed by specialist	19.21	12.61	.013
IGI refused by patient	4.12	4.35	1.00
IGI ordered after discussed	54.64	43.48	.212
During 12-month period			
Ever had IGI for LBP	12.53	7.21	.014

*Comparison using t-tests, chi-square tests, and Fisher Exact tests.

ǂ Presenting symptoms and provider seen (generalist and/or spine specialist).

¡By Numeric Rating Scale of 1-10.

§ Treatment plans were followed up from the LBP diagnosis index visit until an intervention for LBP was received.

(Filename: TCT_790_Table.jpg)

Monday, May 1, 2023

3:30-4:30 PM

Scientific Abstract Session: Epilepsy & Movement Disorders

856

7 Tesla multichannel sodium MRI of the brain in children with epileptogenic SCN1A sodium channel mutations – a pilot study

J Cleary[1], S Rot[2], M Eyre[3], P Bridgen[4], A Dokumaci[5], Y Blunck[6], W Syeda[6], B Solanky[2], S Malik[5], M Lim[3], C Gandini Wheeler-Kingshott[2], S Tang[3], D Carmichael[5]

[1]Imperial College Healthcare NHS Trust, London, United Kingdom, [2]UCL Queen Square Institute of Neurology, Faculty of Brain Sciences, London, United Kingdom, [3]Evelina London Children's Hospital at Guy's and St Thomas' NHS Foundation Trust, London, United Kingdom, [4]London Collaborative Ultra High Field System (LoCUS), London, United Kingdom, [5]King's College London, London, United Kingdom, [6]The University of Melbourne, Melbourne, Australia

Purpose

Epilepsy is the most common childhood neurological disorder(1), with sodium channel gene mutations the commonest genetic cause. SCN1A mutations (sodium channel NaV1.1) have a clinical spectrum(2). Most severe -Dravet syndrome- may have poor outcomes and sudden death. Prognostic biomarkers are needed to guide treatment. Sodium MRI, has given insights into adult epilepsy(3). To our knowledge, it has yet to be used in pediatric epilepsy, with pediatric applications thus far, limited(4). T2* relaxometry may offer insights into local sodium environment. Using a multi-echo sodium sequence(5) and multi-channel coil at 7T, we did a pilot study to assess relative total sodium concentration and sodium T2* in healthy children and with SCN1A mutations.

Materials and Methods

4 SCN1A mutation patients(Table 1) and 8 healthy children(9-17y) were imaged on a 7T Siemens Terra, with 32-channel 1H and 23Na head coils. T1 MP2RAGE images were acquired (0.65mm resolution, 7min). MERINA(5), was used for sodium acquisition (3.1mm resolution, 5mins, 38 echoes). 3x 5-min scans were averaged. Brain regions on T1 images were segmented with SynthSeg. T1 images were affine registered to sodium and transforms applied to segmentations. Biexponential T2* maps created for 10 subjects (2 controls had data quality issues). For first echo sodium images, peak vitreous humor signal was used to scale images, giving relative total sodium concentration maps (rTSC). Repeated measures ANOVA was used to assess variance. To assess patients more individually, Z-scores of regional patient T2* values were calculated using mean and standard deviation of controls.

Results

Fig.1: Typical control: (a)Segmented MP2RAGE images. (b)First echo sodium images. (c)Registered cortex and white matter segmentations from proton to sodium. (d)T2*short and (e)T2*long maps. Fig.2: rTSC was higher across brain regions in SCN1A patients (mean±SD,p=0.038). No group T2* difference was seen but comparing patients to controls using individualized Z-scores, high Z values in T2*short cerebral white matter were seen(Table 2).

Conclusions

rTSC in SCN1A patients was higher across brain regions. This is supported by focal epilepsy work with higher epileptogenic zone TSC(3). The biophysical basis for this may include tissue sodium accumulation or higher extracellular volumes, possibly due to cell loss. Possible trend of higher T2*short values, with high white matter Z-scores in patients, could reflect sodium environment change. Higher subject numbers are required to assess this.

Table 1

Patient	Age, Gender	SCN1A Mutation	Current Medication	Clinical Status
1	14 F	c.4078A>C p.(Ile1360)	• Topiramate	• Seizures controlled • Autism spectrum disorder and learning difficulties
2	8 M	c.4262G>C p.(Gly1421Ala)	• None	• Seizure free 7 years • On valproate until 2019 • Reduced educational attainment • ?ADHD difficulty focusing and restlessness.
3	10 F	Dravet syndrome with missense mutation	• Clobazam Valproate Topiramate	• Ongoing absence seizures despite medication • Autism spectrum disorder
4	9 F	c.5020G>A p.(Gly1674Ser) Also, c.379C>G p.(His127Asp) of uncertain significance	• Stiripentol Lamotrigine	• Seizure free for 4.5 years on medication.

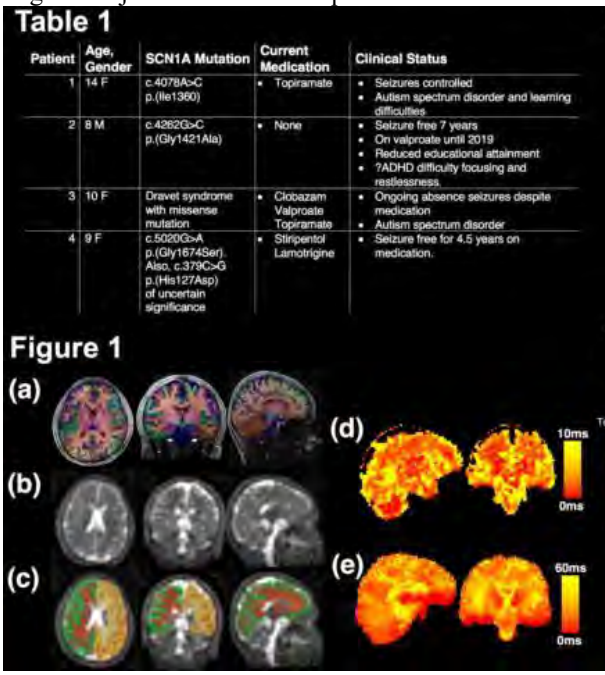

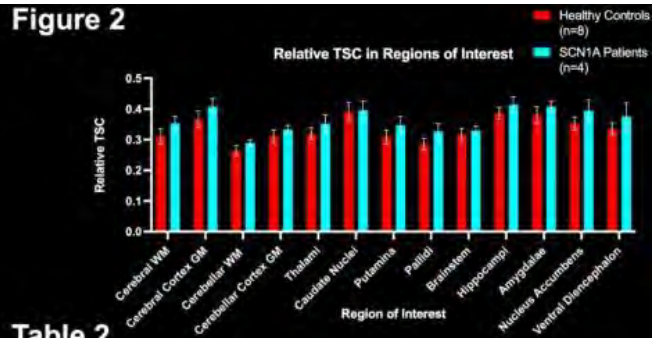

Table 2

Region of Interest	Patient 1 Mean T2*short (ms)	Patient 1 Z-score	Patient 2 Mean T2*short (ms)	Patient 2 Z-score	Patient 3 Mean T2*short (ms)	Patient 3 Z-score	Patient 4 Mean T2*short (ms)	Patient 4 Z-score	Controls (n=6) Mean T2*short (ms) ±SD
Total Cerebral WM	4.5	3.1	4.6	3.8	4.6	4.1	5.4	10.1	4.1±0.1
Total Cerebral Cortex	5.6	0.5	5.4	-0.4	6.0	1.5	6.8	4.2	5.5±0.3
Total Cerebellar WM	3.4	0.1	3.0	-0.8	3.5	0.5	4.8	3.7	3.3±0.4
Total Cerebellar Cortex	4.3	0.3	3.5	-1.4	4.0	-0.4	5.5	2.8	4.2±0.5
Thalami	3.4	-0.6	3.4	-0.7	4.2	1.9	6.2	7.8	3.6±0.3
Caudate Nuclei	5.3	-0.4	4.6	-1.0	6.0	0.2	7.1	1.2	5.7±1.2
Putamina	3.0	-1.8	3.6	0.7	4.3	3.6	4.8	5.5	3.4±0.3
Pallidi	2.0	-2.1	2.7	0.8	3.7	4.7	4.5	8.0	2.5±0.2
Brainstem	4.4	-0.9	3.8	-2.2	4.6	-0.4	5.4	1.4	4.8±0.5
Hippocampi	7.1	4.5	5.5	1.3	5.8	1.9	6.9	4.2	4.9±0.5
Amygdalae	6.3	2.8	4.5	-1.0	5.9	2.1	5.8	1.9	4.9±0.5
Nucleus Accumbens	8.0	0.8	5.6	-1.4	7.9	0.7	8.4	1.1	7.2±2.2
Ventral Diencephalon	4.4	0.5	4.4	0.5	6.1	3.0	5.5	2.1	4.1±0.7

(Filename: TCT_856_sodiumfigures2.jpg)

672

7T MRI Relates Thalamic Connectivity to Memory Performance and Huntington's Disease Stage

M Morrison[1], J Yao[1], A Jakary[1], T Driscoll[2], K Possin[2], M Geschwind[2], A Nelson[2], D Xu[2], C Hess[2], J Lupo[2]

[1]University of California, San Francisco, San Francisco, CA, [2]University of California San Francisco, San Francisco, CA

Purpose

Huntington's disease (HD) is a rare inherited neurodegenerative disorder caused by CAG nucleotide repeats in the huntingtin gene. Patients with confirmed HD typically experience symptom onset in their 30s and 40s starting with behavioral and cognitive changes followed by a progressive loss of motor abilities. Without any disease-modifying therapies for HD, there is currently a need for reliable markers of progression to support clinical trials. Here we aimed to characterize thalamic functional connectivity (FC) in HD based on our recent finding of progression-related changes in the volume and susceptibility of brain areas connected to thalamic nuclei.

Materials and Methods

Twenty-seven patients and 24 healthy controls consented to this prospective study. All subjects had resting-state functional MRI data acquired at 7T and their memory performance assessed. Patients also underwent motor evaluation. Analyses were performed in the CONN toolbox. We evaluated cross-sectional thalamic FC differences between controls and patients based on disease stage, as well as the relationship between thalamic FC and memory performance. Disease stage was classified based on total motor score (TMS) and function capacity (TFC) as pre-, early-, or full- manifest (PM, EM, FM). Patient groups were further divided by the predicted years to motor symptom onset (YTO).

Results

Predicted YTO correlated with TMS scores (Fig.1A). Thalamo-cerebellar connections were increased in patients compared to controls, revealing a trend of hyperconnectivity in early PM patients (>15 YTO) that gradually declined with progression returning to a hyperconnected state at the FM stage (Fig.1BC). When related to performance on a recall task, better scores were associated with stronger fronto-thalamic FC and weaker thalamo-cerebellar FC (Fig.1D). Further evaluation of individual group effects revealed fronto-thalamic FC changes with progression in a pattern suggestive of eventual functional recovery (Fig.1E). A similar trend was observed for performance scores (Fig.1F).

Conclusions

Thalamic connectivity is altered in HD and relates to the progression of symptoms. Hyperconnectivity prior to the onset of motor disability may reflect a compensatory mechanism to preserve. In FM HD, hyperconnectivity may reflect neuroplastic changes corresponding to a reemergence of cognitive abilities. Future work will characterize cross-sectional and longitudinal patterns of thalamic subnuceli FC to better understand their functional role in HD symptom manifestation.

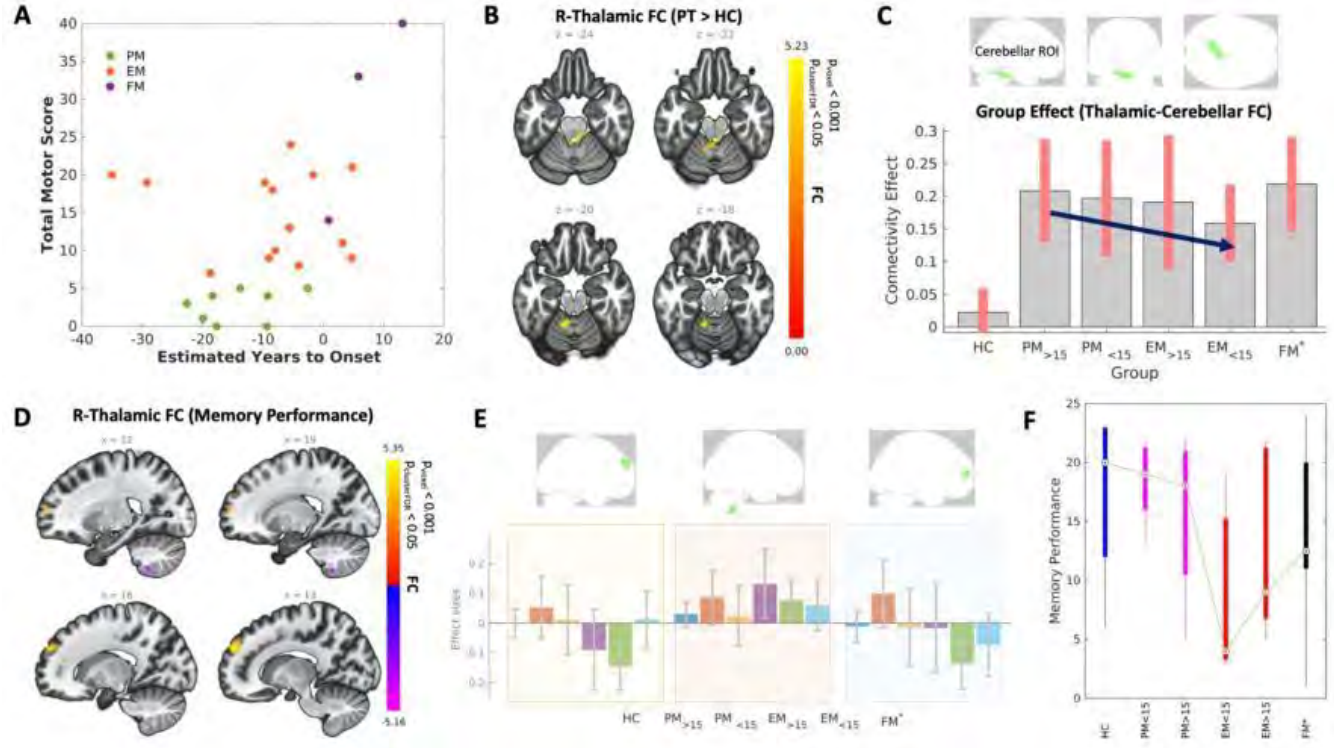

(Filename: TCT_672_figures_asnr2023.jpg)

986

Abnormal Iron Deposition and Microstructure in Striatum Correlate with Cognitive Decline in Huntington's Disease

J Yao[1], M Morrison[1], A Jakary[1], S Avadiappan[1], T Driscoll[1], M Geschwind[1], A Nelson[1], D Xu[1], C Hess[1], J Lupo[1]
[1]*University of California, San Francisco, San Francisco, CA*

Purpose
Huntington's disease (HD) is a neurodegenerative disorder caused by CAG repeat expansion in the huntingtin gene. Abnormal iron deposition in the striatum has been reported in both premotor (PM) and motor manifest HD using quantitative susceptibility mapping (QSM), and diffusion tensor imaging (DTI) studies have shown microstructural changes in the same region. This study used 7T QSM and DTI to investigate whether iron dysregulation and microstructure alterations in the striatum correlate with motor and cognitive impairments in HD.
Materials and Methods
We prospectively recruited 33 healthy volunteers (HC: 43.9±12.2yr), 14 PM (38.0±11.0yr), and 20 manifest HD patients (48.9±12.4yr) and evaluated their total motor scores (TMS) and cognitive performance on Danish Adult Reading Test (DART), Flanker, Match, and Set Shift. Subjects were scanned on a GE 7T scanner with a 3D multi-echo GRE sequence for QSM and a DTI sequence to calculate fractional anisotropy (FA) and mean diffusivity (MD). Volumes and median values of susceptibility, FA, and MD were extracted in caudate nucleus (CN), putamen (PU), and globus pallidus externa/interna (GPe/i), and compared across HC, PM, and HD. We performed Pearson correlations between imaging features in each ROI, and between imaging features and clinical variables, including disease burden (CAPS), years to onset (YTO), TMS, and cognitive test scores.
Results
We observed higher susceptibility and smaller volume in all ROIs and FA elevation in CN and PU in PM and manifest HD patients compared to HC (A). Across all subjects (HC, PM, and HD), volume and susceptibility were negatively correlated in CN, PU, and GPe. Positive correlations were observed between susceptibility and FA in CN, PU, and GPe, whereas negative correlations were found between FA and MD in PU and GP (B). A significant correlation was observed between striatal atrophy and higher disease burden, higher TMS, shorter YTO, and worse cognitive test scores (C,D). Higher susceptibility and FA in PU were correlated with worse cognitive test scores, whereas MD in CN was positively correlated with TMS and negatively correlated with Match and Set Shift scores.
Conclusions
We found significant iron deposition in CN, PU, and GP; increased FA in CN and PU; and atrophy in the GP in PM HD patients. Cognitive decline was most strongly correlated with increased iron and FA in the PU, where these metrics were highly correlated, whereas increased MD in CN was correlated with motor and cognitive dysfunction.

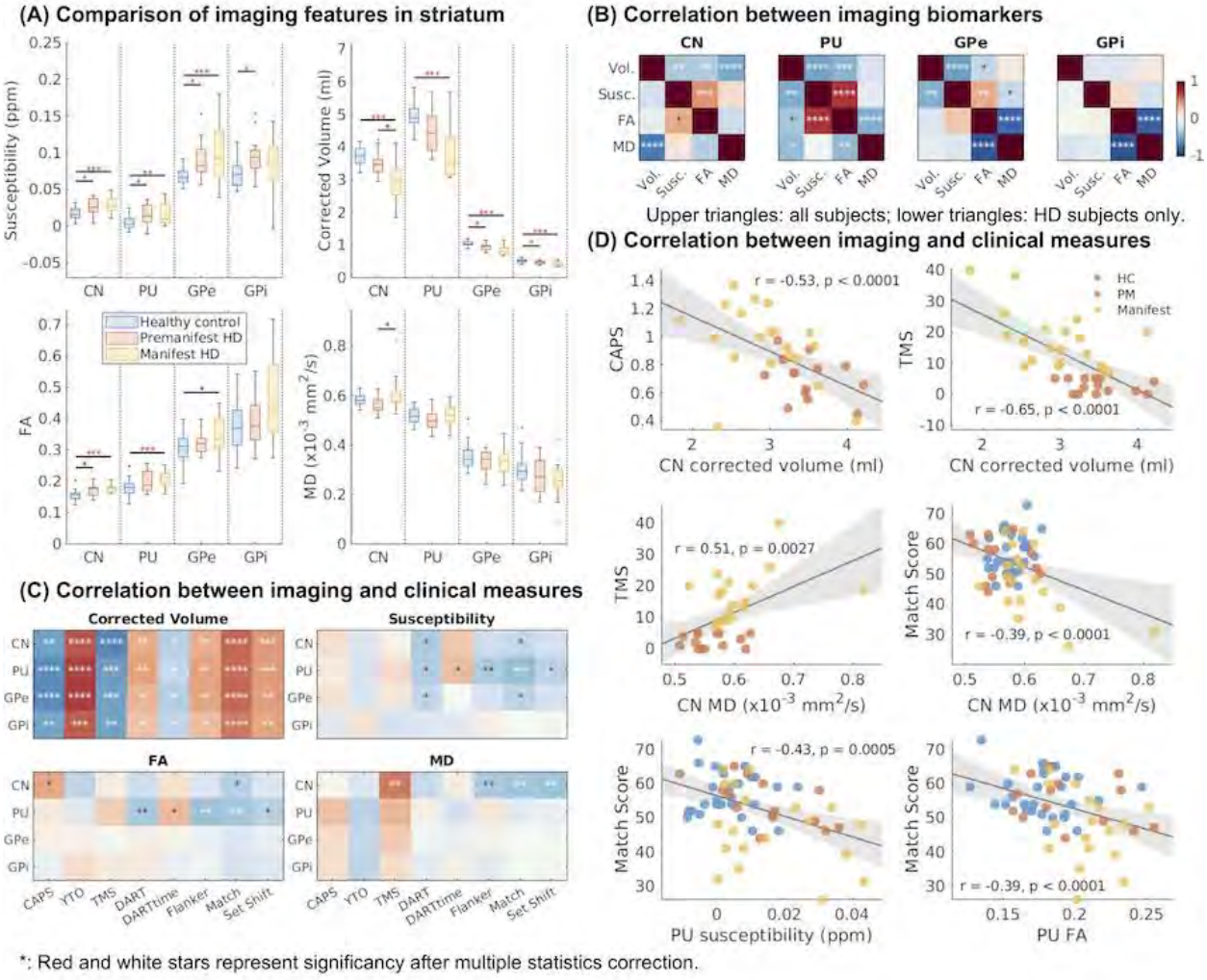

(Filename: TCT_986_Fig_HD_QSM_DTI.jpg)

1176

Mapping Resting Functional Networks in Awake and Sedated Pediatric Epilepsy Patients.

V Nair[1], T Choi[2], D CHU[3], J Hou[4], N Adluru[5], J Brucker[2], A Field[6], R AHMED[3], V Prabhakaran[7]

[1]University of Wisconsin-Madison, MADISON, WI, [2]UW Madison, MADISON, WI, [3]UW MADISON, MADISON, WI, [4]Fujian Normal University; UW Madison; Indiana University, Fujian province, China, [5]UW-Madison, Madison, WI, [6]University of Wisconsin School of Medicine and Public Health, Madison, WI, [7]Univ. Of Wisconsin Hospitals and Clinics, Madison, WI

Purpose

Mapping eloquent cortex in pediatric subjects is limited by challenges due to motion artifact, developmental and cognitive comorbidities and reduced compliance with instructional cues. This necessitates the use of pharmacological sedation to enable image acquisition. The impact of pharmacological sedation on acquisition and determination of resting state functional neuroimaging studies is not well understood. Here we compared standardized functional networks derived from resting-state functional MRI, acquired in pediatric subjects with and without pharmacological sedation.

Materials and Methods

Resting-state fMRI images from 62 pre-operative pediatric epilepsy patients (ages 1-20 years, 25 females, 29 non-sedated, 33 sedated) were analyzed. Standard preprocessing in the DPABI toolbox, based on SPM12 and MATLAB, included nuisance regression of head motion, and CSF and white matter signals using the CompCor method.1 Functional connectivity (FC) for any pair of two ROIs (in the 160-region Dosenbach atlas) was computed as the Pearson's correlation coefficient of the BOLD signals, transformed to z-scores. Network Based Statistic (NBS) analyses with two sample T tests (permutation-based, 5000 iterations, edge $p < .001$, component $p < .01$) were conducted to compare FC (sex, age as covariates).

Results

Mean FC maps in awake patients demonstrated, strong inter and intra-network connectivity in seven networks including the visual network (VN), somatosensory-motor (SMN), dorsal attention (DAN), ventral attention (VAN), subcortical (SCN), frontoparietal (FPN), and the default mode network (DMN)2 (Figure (a)). In contrast, mean FC in sedated patients was reduced in the sub-cortical, frontoparietal and default mode networks (Figure (b)). Group difference FC map demonstrated reduced intra-network (ventral attention, sub-cortical) and reduced inter-network connections (visual and dorsal attention) in sedated versus awake patients.

Conclusions
Our results suggest that standard functional networks can be extracted in pediatric patients using one sequence within standard MRI image acquisition. However, some of these networks may be more impaired in pediatric patients under pharmacological sedation. This may be due to effects of procedural sedation, neurological or cognitive comorbidities and medications in these patients. Interpretations regarding localization of function for clinical decision making should therefore be interpreted with caution.

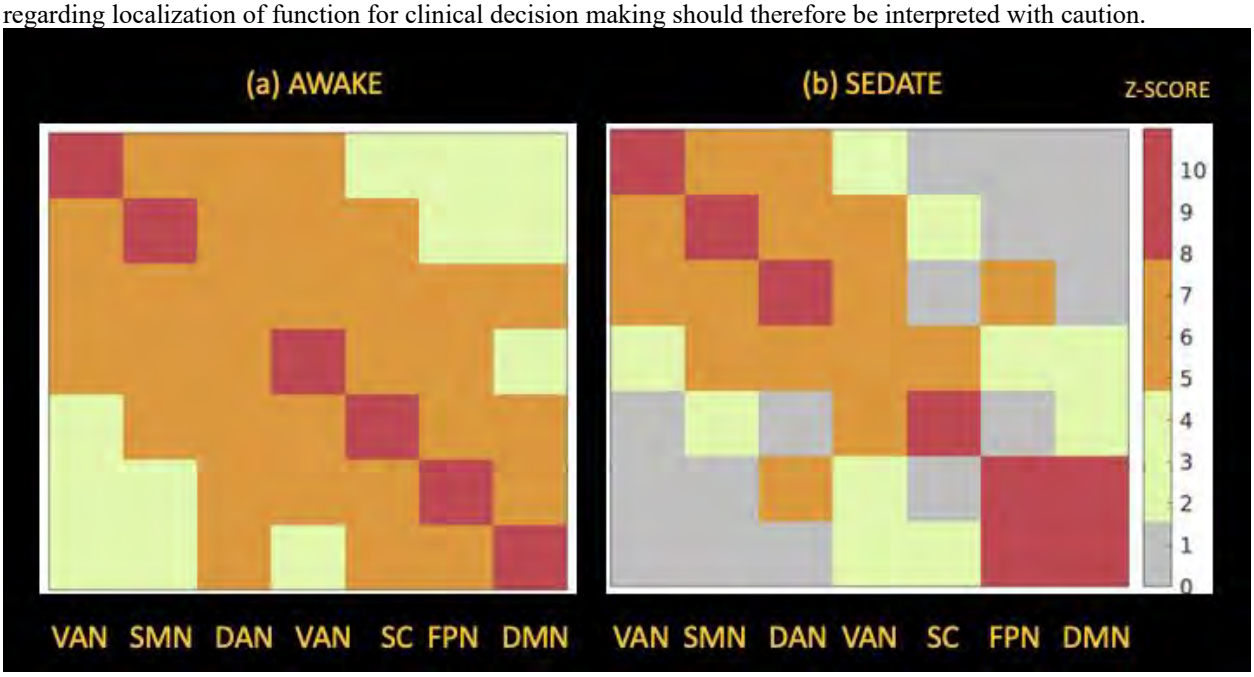

(Filename: TCT_1176_ASNR2022_figure.jpg)

721
Virtual Radiologist: A Novel High-performance MEG Dipole Atlas Viewer
N Cardoso da Fonseca[1], J Bowerman[1], P Askari[1], F Feltrin[1], A Proskovec[1], E Davenport[1], J Maldjian[1]
[1]*University of Texas Southwestern Medical Center, Dallas, TX*

Purpose
Magnetoencephalography (MEG) source estimation is a noninvasive technique with a key clinical application in epilepsy studies. However, it consists of a laborious and multi-step procedure that mobilizes a multi-disciplinary team(1). With the rising demand for MEG, pipelines have focused on automated analysis of sensor space data(2), leaving a gap for the anatomical identification step. Our lab developed a new program for a viewer, termed the "Virtual Radiologist," that labels each MEG dipole accordingly to its corresponding brain region. The main purpose of this study was to test its performance compared to radiologist identification.
Materials and Methods
We included patients with MEG scans for standard clinical care and a T1-weighted MRI. A radiologist blindly identified each dipole location, describing regions within reach in cases where they were in the sulcus, white matter (WM), or cerebrospinal fluid (CSF). The viewer application normalizes the patient's MRI to standard space utilizing one of three normalization techniques (FLIRT, FNIRT, and CAT12), reverse normalizes a variety of atlases to the patient's brain MRI, identifies the location of the dipole on the brain, and presents a list of identified dipoles along with the corresponding label in an assortment of atlases. We first chose FLIRT for segmentation and registration, and in cases of failure, we used CAT12 for registration (figure1). We evaluated the concordance of the atlas label for each dipole with the Radiologist's analysis.
Results
We compared the labeling of 180 dipoles from 7 patients (mean age 27y, ±13y). FLIRT normalization ran faster (20 – 120s) than CAT12 (10 - 12 min). FSL registration failed in 2 patients with T1 inversion recovery images. However, CAT12 registration was successful. There was an agreement between the atlas and radiologist labeling in 84% overall (table 1). The agreement was higher where there were minimal or no structural abnormalities on the MRI (90%). The cases with resection cavities and when the dipoles were within or borderline to a sulcus, WM, or CSF were more susceptible to being unlabeled or in disagreement.
Conclusions
We evaluated a novel and robust program for automating the identification and labeling of MEG dipoles, which was highly concordant with radiologist labeling, particularly in MRIs without significant abnormalities. We conclude that the Virtual Radiologist provides an opportunity to optimize the workflow in MEG clinical reporting and can also be a valuable tool for research purposes.

Table 1. Labeling accuracy for the Virtual Radiologist

	MRI with resection cavity		MRI without significant structural abnormality		Overall Performance	
	Concordant Dipoles	Unlabeled Dipoles	Concordant Dipoles	Unlabeled Dipoles	Concordant Dipoles	Unlabeled Dipoles
FLIRT	31/45 (68%)	12/ 57 (21%)	43/49 (88%)	9/58 (15.5%)	74/94 (78.7%)	21/115 (18.3%)
CAT12	x	x	57/62 (92%)	3/65 (4.6%)	57/62(92%)	3/65 (4.6%)
Overall	31/45 (68%)	12/ 57 (21%)	100/111 (**90%**)	12/123 (9.8%)	131/156 (**84%**)	24/180 13.3%

Figure 1. Virtual Radiologist User Interface. The left columns list the dipole cross-hair coordinates (top), the atlas labels (Found atlases), the Dipole group displayed (e.g., language evoked fields, somatosensory evoked fields, interictal discharges), and the individual dipoles in the group. The right side provides an interactive triplanar MRI display with color-coded dipole groups and the ability to interrogate individual dipoles.

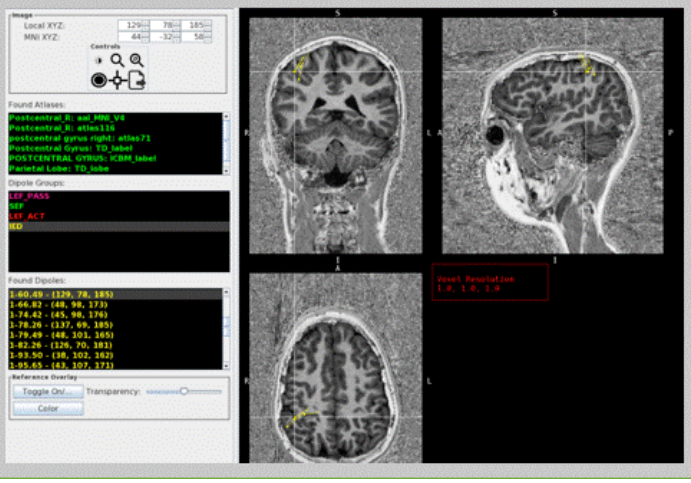

(Filename: TCT_721_Picture.gif)

Monday, May 1, 2023

3:30-4:30 PM

Scientific Abstract Session: Spine Imaging

390

CSF Venous Fistula Temporal Characteristics on Digital Subtraction Myelography

I Mark[1], A Madhavan[1], M Oien[1], J VERDOORN[1], J Benson[1], J Cutsforth-Gregory[1], W Brinjikji[1], P Morris[1]

[1]*Mayo Clinic, Rochester, MN*

Purpose

CSF-Venous Fistula (CVF) can be diagnosed with multiple myelographic techniques, however no prior work has characterized the time to contrast opacification and duration of visualization. The purpose of our study was to evaluate the temporal characteristics of CVF on digital subtraction myelography (DSM).

Materials and Methods

We reviewed the DSM images of 26 patients with CVF. We evaluated how long the CVF took to opacify after contrast reached the spinal level, and how long they remained opacified. Patient demographics, CVF treatment, brain MRI imaging findings, CVF spinal level, and CVF laterality were recorded.

Results

7 of the 26 CVF were seen on both the upper and lower field of view DSM, for a total of 33 CVF evaluated on DSM. The mean time to appearance was 9.5 seconds (range 0-30 seconds), and they remained opacified for a mean duration of 47.9 seconds (range 24-73 seconds). 22 (84.6%) of the CVF were on the right. The highest fistula level was C7, while the lowest was T13 (13 rib bearing vertebral bodies). The most common CVF levels were T6 (4 patients) followed by T8, T10, and T11 (3 patients each). The mean age was 58.3 years old (range 31.7-87.6). 16 were female (61.5%).

Conclusions
This is the first study to report the temporal characteristics of CVF using DSM. We found that on average, the CVF appeared 9.5 seconds after the intrathecal contrast has reached the spinal level and remained visible for an average of 47.9 seconds.

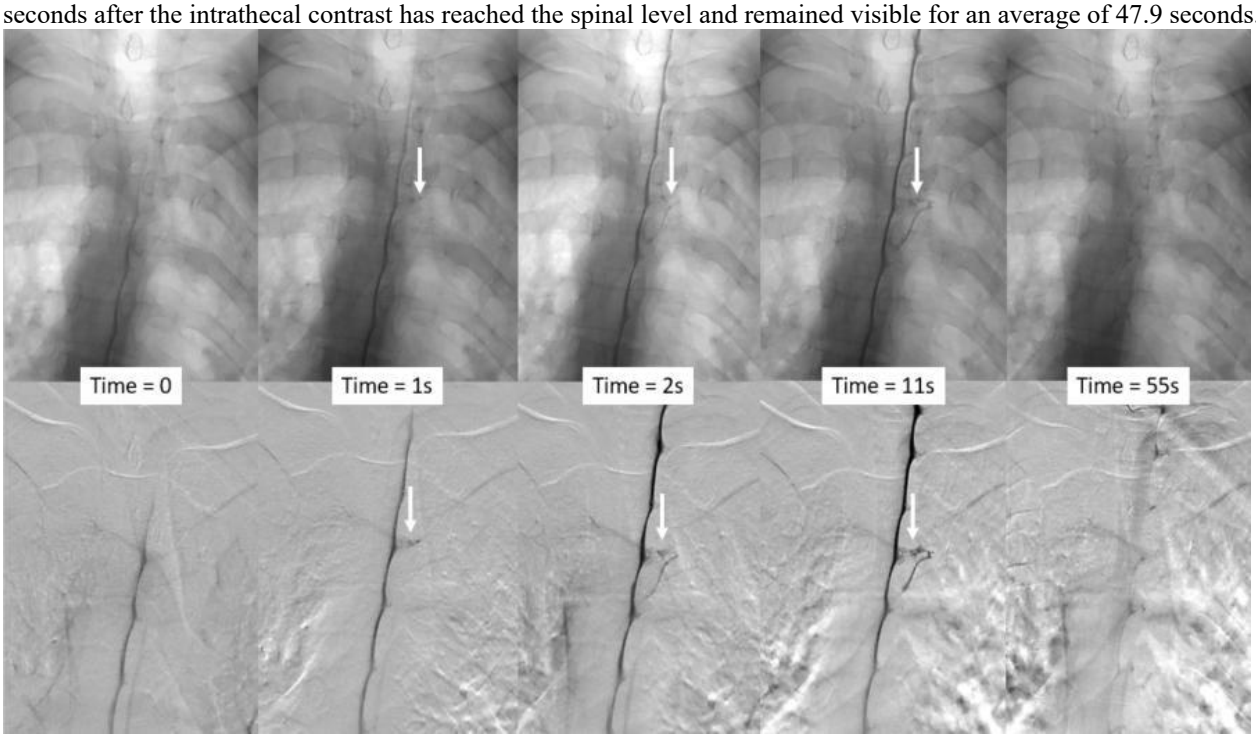

(Filename: TCT_390_Figforabstract.jpg)

1003

Diagnostic Efficacy and Clinical Utility of Image-Guided Core Needle Biopsy of Suspected Vertebral Osteomyelitis

W Winkler[1], J Fage[2], G Dettorre[2], J Jennings[2]
[1]Mallinckrodt Institute of Radiology, Bloomington, IN, [2]Mallinckrodt Institute of Radiology, Saint Louis, MO

Purpose
Purpose: The diagnostic yield (if biopsy specimens result in a histopathologic diagnosis of osteomyelitis and/or positive microbiological cultures) and impact on clinical management of image-guided core needle biopsy (ICNB) of suspected vertebral osteomyelitis in adults is heterogenous in published studies due to small sample size, indicating the need for large cohort studies1-5. In this study we examine the diagnostic yield of ICNB and determine the impact of ICNB on clinical management using a large cohort.
Materials and Methods
Materials and Methods: A retrospective analysis of ICNBs performed from 2010-2021 of clinically suspected vertebral osteomyelitis was completed. For each biopsy it was documented if histopathology was diagnostic of osteomyelitis and if microbiological cultures were positive. Additionally, it was recorded if and in what way the biopsy influenced clinical management regarding antimicrobial treatment.
Results
Results: A total of 570 biopsies performed on 527 patients (mean age, 60.8 years ± 13.5 [standard deviation]; 336 men) were included. A histopathologic diagnosis of osteomyelitis was made in 68.4% (359/525) of biopsies. Microbiological cultures from bone cores were positive in 27.1% (139/513) of biopsies, and microbiological cultures from sampled aspirate were positive in 28.1% (64/228). Clinical management was affected by ICNB in 37.5% (214/570) of cases. In 146 of these cases, cultures were positive and antimicrobial treatment was tailored to culture results. In 54 cases, antimicrobials were discontinued or not initiated because of negative cultures and histopathology. In 356 cases, clinical management was not affected by biopsy as the patient was started on empiric antimicrobial therapy before or shortly after biopsy without knowledge of biopsy results and was continued on this same therapy in the setting of negative cultures.
Conclusions
Conclusion: In this large cohort, ICNB yielded a histopathologic diagnosis of osteomyelitis in just over two-thirds of biopsies, and positive cultures in just over one-fourth. ICNB changed clinical management in over one-third of patients.

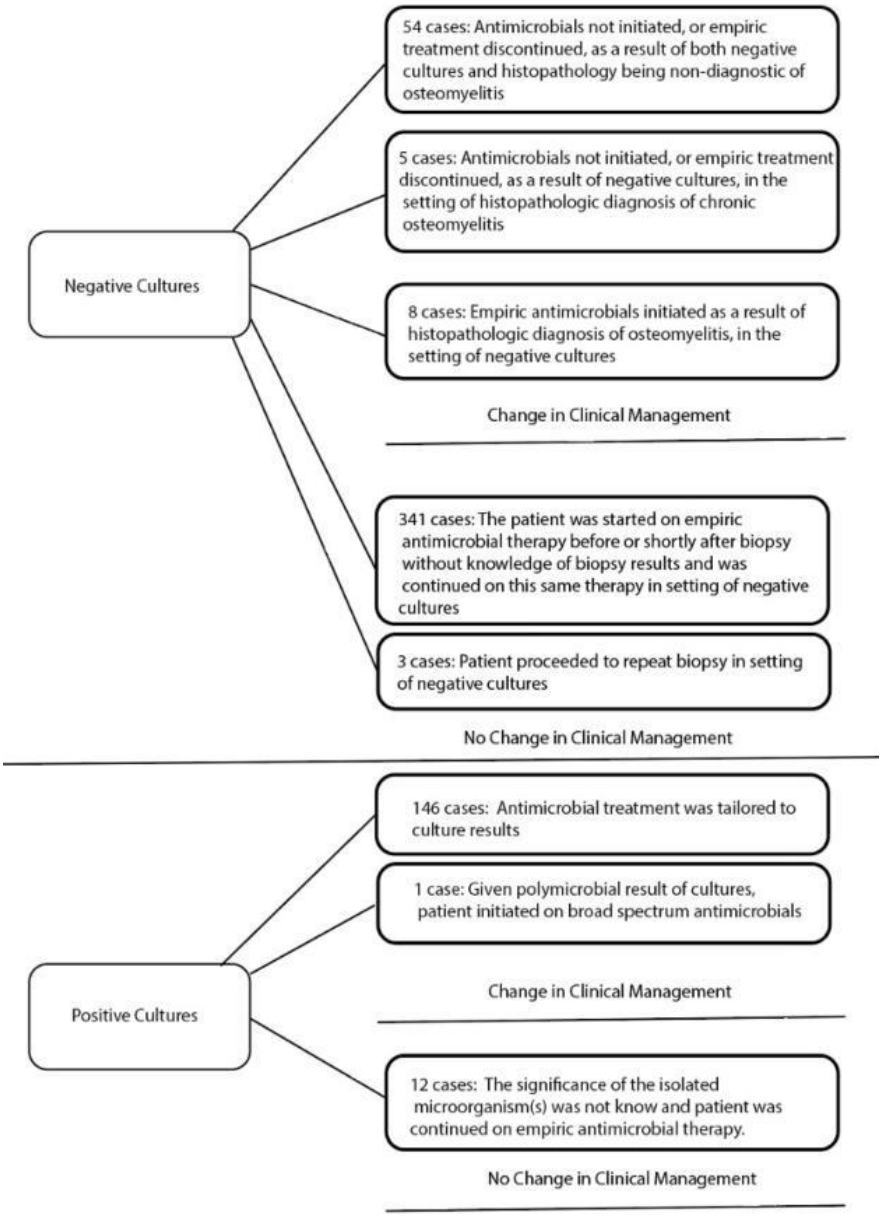

(Filename: TCT_1003_ASNRAbstract.jpg)

416

Diagnostic Utility of VIBE Sequence through the Filum Compared to Spin-echo T1 in Children with Concern for Tethered Cord

F Rafiee[1], K Buch[2], W Mehan[2]
[1]Mass General Hospital, Cambridge, MA, [2]Massachusetts General Hospital, Boston, MA

Purpose

Fatty intrathecal lesions (FIL) are a cause of tethered cord and detection of these on spinal MRI is paramount. Conventional T1 spin-echo (SE) sequences are the mainstay of detecting fatty elements, however, T1-like sequences e.g. VIBE are popular given increased motion resistance. We sought to evaluate the diagnostic accuracy of VIBE compared to T1SE for detection of FILs.

Materials and Methods

In this retrospective, IRB-approved study, 479 consecutive pediatric spine MRIs performed to evaluate for cord tethering between January 2016-April 2022 were reviewed. Inclusion criteria were patients who 1) were up to 20-years of age who 2) underwent spine MRIs containing both axial T1SE and VIBE sequences of the lumbar spine. Presence/absence of FIL was recorded for each sequence. If FILs were present, anterior-to-posterior (AP) and transverse (RL) dimensions were recorded. VIBE and T1SE sequences were evaluated at two separate instances (VIBEs first followed by T1SEs several weeks later) to minimize bias. Basic descriptive statistics compared FILs sizes on T1SEs and VIBEs. ROC curves were made to determine minimal FIL size detectable by VIBE.

Results

66 patients were included with 22 having FILs (mean age 7.3-years). T1SEs revealed FILs in 21/22 cases (95%), however, FILs on

VIBE were detected in 12/22 patients(55%). Mean AP and RL dimensions of FILs measured larger on T1SE compared to VIBE sequences (5.4x5.0mm versus 1.5x1.6mm, respectively (P-values: 0.039 AP; 0.027 RL).
Conclusions
While VIBE sequences may have decreased acquisition time and are more motion resistant than conventional T1SE sequences, they are less sensitive and may miss small FILs.

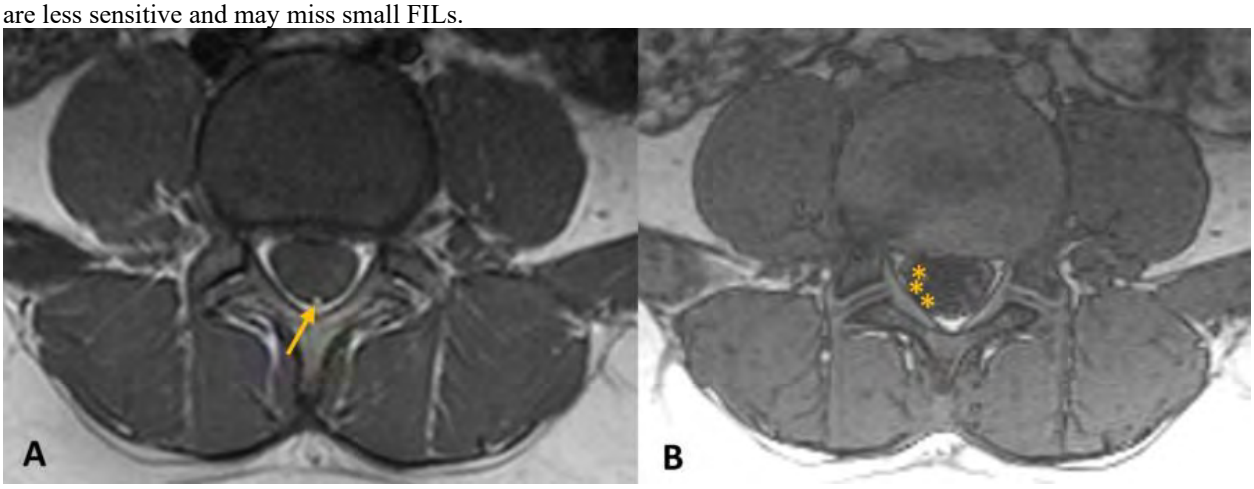

(Filename: TCT_416_ASNR2.jpg)

1260
Dynamic Lateral Decubitus CT Myelography with Novel Contrast Bolus Monitoring Technique for Detection of CSF-Venous Fistulas: High Diagnostic Yield Stratified by MRI Brain Bern Score
D Parizadeh[1], A Ahmed[1], O Fermo[2], K Brewer[1], C Gandia[1], P Vibhute[1], T Huynh[1]
[1]Mayo Clinic, Jacksonville, FL, [2]Departments of Radiology and Neurology, Mayo Clinic, Jacksonville, FL, Jacksonville, FL

Purpose
Optimizing imaging techniques to better detect cerebrospinal fluid-venous fistulas (CVF) is critical to management of patients with spontaneous intracranial hypotension (SIH). We aimed to evaluate the feasibility and diagnostic yield of dynamic lateral decubitus CT myelography (DLDCTM) with real-time bolus monitoring during contrast injection for detection of CVF in patients with SIH.
Materials and Methods
Retrospective review of consecutive suspected SIH patients evaluated with DLDCTM was performed. Patients without extradural fluid collection on spine MRI1 were excluded. Bern SIH score was calculated based on brain MRI to predict the probability of identifying a spinal CSF leak source and categorized as low (score 0-2), intermediate (score 3-4), and high (score 5-9) 2. DLDCTM was performed with the patient in lateral decubitus Trendelenburg position using angled foam wedges. Axial CT bolus monitoring was performed at a single level in the upper thoracic spine with 5 second acquisition intervals during manual intrathecal contrast injection; at least 3 CT acquisitions of the complete spine were obtained after contrast was visualized on bolus monitoring. Bilateral DLDCTM was performed for each patient on two separate days. Diagnostic yield of DLDCTM for CVF detection was assessed stratified by Bern SIH score and receiver operating characteristic (ROC) analysis was performed.
Results
Of the 49 patients included, DLDCTM was performed successfully in all and identified a CVF in 24 (49%). CVFs were located at T6-T11 (n=22), T4 (n=1), and L1 (n=1) and were more common on the right (n=17/24, 71%). CVF was identified in 100% (22/22) of patients with high Bern SIH score, 20% (2/10) of patients with intermediate score, and none of the 26 patients with low score. On ROC analysis, the area under the curve was 0.99 and the maximum value of Youden index was at a Bern SIH score of 5. Using a score of 5 or higher (high Bern SIH score), sensitivity and specificity were 92% and 100%, respectively.
Conclusions
DLDCTM with real-time contrast bolus monitoring is feasible and allows for standardized timing of imaging acquisition after intrathecal contrast injection. The novel technique has a high diagnostic yield for CVF identification and localization. Bern SIH score is strongly associated with probability of identifying CVF on DLDCTM and may be used as an effective tool to identify patients who will most likely benefit from DLDCTM.

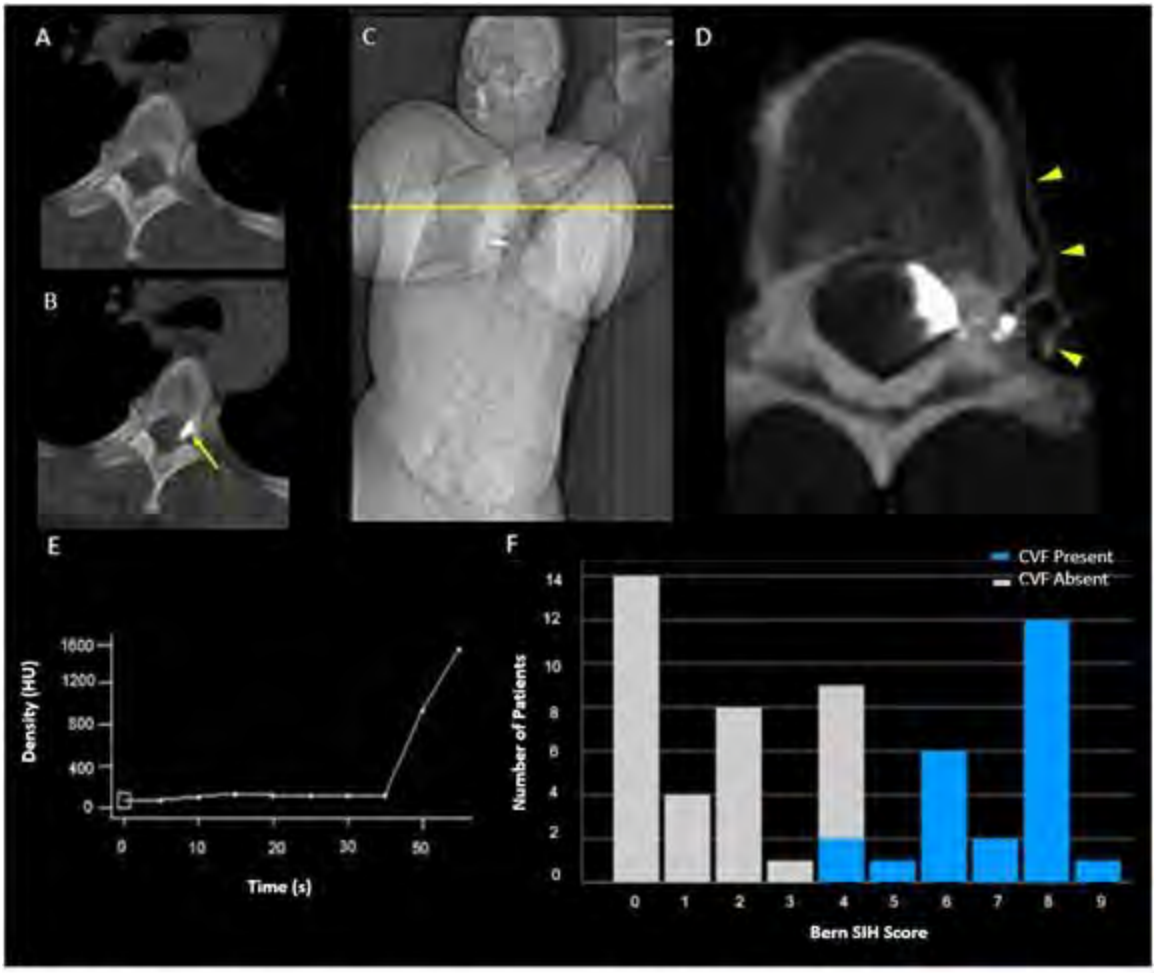

Figure 1. (A-E) Example of a patient in 50s presenting with new persistent daily headaches and a high Bern SIH score of 6 using left DLDCTM showing real-time contrast bolus monitoring images prior to injection **(A)** and during injection **(B)**. Monitoring performed at the level of T5 **(C, dashed line)**. DLDCTM acquisition shows contrast enhancement of paraspinal veins at left T7 consistent with a CVF **(D, arrow heads)**. Graph of density of monitored contrast bolus over time **(E,** region of interest placed at **arrow in B)**. Bar chart demonstrating presence/absence of CVF across Bern SIH scores in patients evaluated with DLDCTM **(F)**. (**SIH:** Spontaneous Intracranial Hypotension, **DLDCTM:** Dynamic Lateral Decubitus CT Myelography, **CVF:** CSF-Venous Fistula)

(Filename: TCT_1260_ASNR23-Abs1-2Fig6300.jpg)

1480

Dynamic Temporal Appearances of Cerebrospinal Fluid-Venous Fistulas Characterized with Dynamic Lateral Decubitus CT Myelography

D Parizadeh[1], A Ahmed[2], O Fermo[3], K Brewer[2], C Gandia[2], P Vibhute[2], T Huynh[1]

[1]Mayo Clinic Florida, Jacksonville, FL, [2]Mayo Clinic, Jacksonville, FL, [3]Departments of Radiology and Neurology, Mayo Clinic, Jacksonville, FL, Jacksonville, FL

Purpose

Lateral decubitus CT myelography is increasingly being used for detection of cerebrospinal fluid-venous fistulas (CVF) associated with spontaneous intracranial hypotension1,2 however the optimal timing and number of CT acquisitions after contrast administration for CVF detection remains uncertain. We sought to characterize the dynamic temporal appearances of CVFs using dynamic lateral decubitus CT myelography (DLDCTM).

Materials and Methods

A retrospective review of consecutive SIH patients with CVF identified on DLDCTM was performed at our institution. DLDCTM was performed using a bolus-monitoring technique allowing for real-time verification of contrast in the upper cervicothoracic spine. Once contrast was visualized during monitoring, at least 3 DLDCTM acquisitions were then obtained during contrast injection and with patient respiratory inspiration. All phases of DLDCTMs were reviewed for the presence of CVF and presence and size of adjacent diverticulum.

Results

Of 116 DLDCTMs performed, a CVF was identified in 24 (21%). CVFs were located at T6-T11 (n=22), T4 (n=1), and L1 (n=1) and were more common on the right (n=17/24, 71%). DLDCTM was performed with median (interquartile range, IQR) of 4 (3-5) acquisitions with the first, second, and third phases acquired at median (IQR) of 30 (25-34), 61 (48-96), and 141 (123-213) seconds after contrast was visualized on bolus-monitoring. 17 (71%) had additional phases acquired with median (IQR) of 552 (269-716)

seconds after monitoring. Of 24 CVFs, 15 (63%) were identified initially on the first DLDCTM phase while 9 (37%) were initially only identified on a later phase (second phase n=4, 17%; third or greater phase=5, 21%). Twelve (50%) CVFs were identified on all DLDCTM phases while 3/24 (13%) were identified only on 2 phases, and 6/24 (25%) only on a single phase. 9 (38%) CVFs dissipated in appearance on subsequent phases after initial detection. No CVFs re-appeared after dissipation. The third phase had the highest yield for CVF detection (83%), followed by second (75%) and first phase (63%). 88% of CVF were associated with a diverticulum. Delayed appearance of CVF (phase 3 or greater) was associated with larger diverticulum size (8.4 vs 2.0 mm, p=0.048).
Conclusions
CVFs have a transient dynamic temporal appearance on DLDCTM and multiple acquisitions and standardized timing after contrast bolus administration may be required to obtain high sensitivity for CVF detection. Delayed initial appearance of CVF was associated with larger diverticulum size.

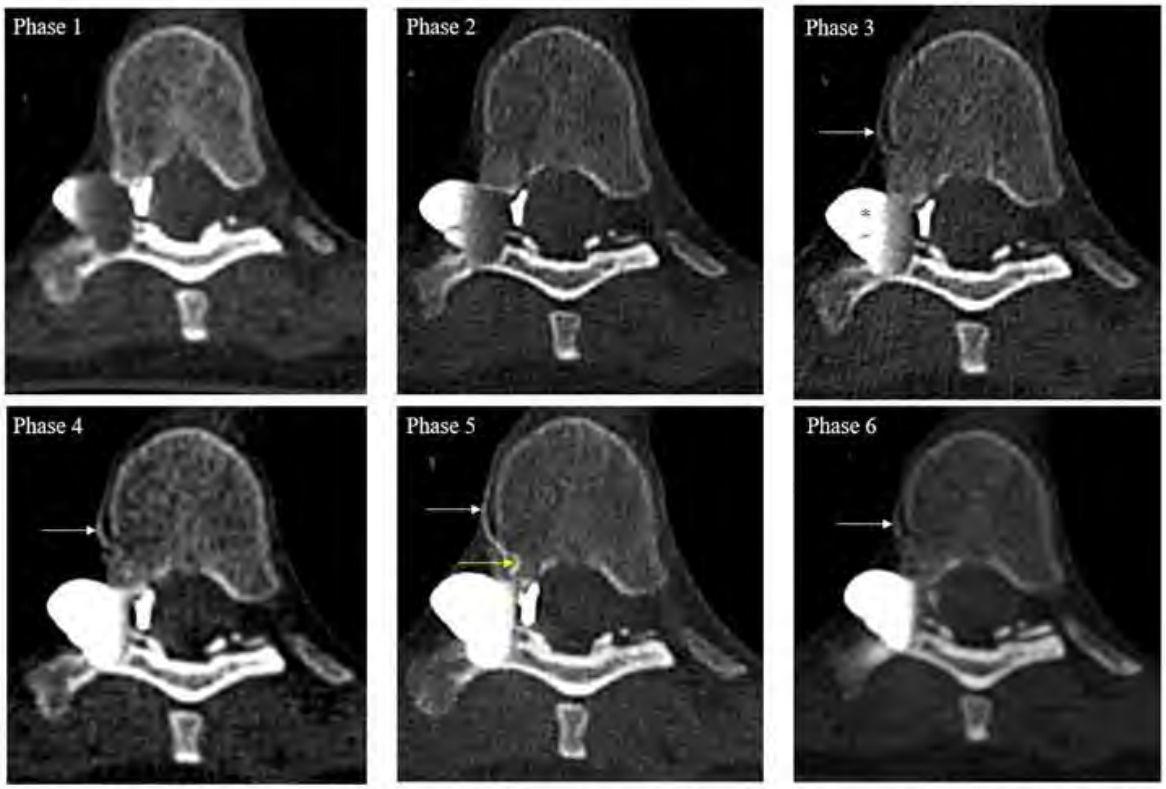

Figure 1. DLDCTM with 6 acquisitions (phases 1-6) performed in the right lateral decubitus position for evaluation of patient in 70s presenting with daily headaches and MRI findings highly suggestive of SIH. Paraspinal venous enhancement consistent with CVF (arrows) associated with a large diverticulum (asterisk, largest diameter = 16 mm) was identified beginning at phase 3, most conspicuous at phase 5, and visualized until the last phase (phase 6). The CVF was not apparent on phases 1 and 2. (**DLDCTM:** Dynamic Lateral decubitus CT myelogram, **SIH:** Spontaneous Intracranial Hypotension, **CVF:** CSF-Venous Fistula)

(Filename: TCT_1480_ASNR23-Abs2-Fig10in300.jpg)

914

Longitudinal Study of Metastatic Spinal Bone Marrow Response to Radiation Therapy Using T1 weighted Dynamic Contrast-Enhanced MRI Perfusion Imaging

M Behar[1], K Peck[1], O Yildirim[1]
[1]*Memorial Sloan Kettering Cancer Center, New York, NY*

Purpose
The skeletal system is the third most common location for tumor metastases, most frequently occurring within the spine. However, current imaging techniques have difficulty assessing the progression of metastatic spinal lesions. Research indicates that T1 weighted dynamic contrast enhancement (DCE) perfusion MRI detects changes in the tumor vasculature following radiation therapy (RT) and can non-invasively monitor treatment effect[1,2]. This study investigates the effect of RT on DCE-MRI perfusion parameters, namely, plasma volume (V_p) and vascular permeability (Ktrans), in metastatic spinal lesions. We hypothesize that reductions in V_p and Ktrans will correlate with improved clinical outcomes. Additionally, we compare DCE-MRI to traditional size measurements to determine which method better discriminates between clinical success and failure.
Materials and Methods
This is a prospective cohort study of 49 patients with metastatic spinal lesions treated with RT between 2013-2020. We divided the patients into two groups: clinical success (n=38) and clinical failure (n=11). Clinical failure was defined by either PET recurrence, biopsy-proven recurrence, or an increase in tumor size within 18 months. An absence of all trigger conditions defined clinical success. An unpaired T-Test was performed to assess differences between groups.

Results
There was a decrease in V_p and Ktrans after RT for the clinical success group. As hypothesized, these reductions were not observed within the clinical failure group. The mean change in V_p within the clinical success group was -57.3%, compared to +88.2% within the clinical failure group, p = .003. The mean change in Ktrans within the clinical success group was -11.7%, compared to +51.4% within the clinical failure group, p = .053. The change in V_p was a stronger predictor of clinical failure when compared with conventional size measurements. Using V_p to predict relapse yielded a sensitivity of 91% and a specificity of 87% (AUROC = .86), while conventional imaging yielded a sensitivity of 55% and a specificity of 71% (AUROC = .71).
Conclusions
After successful radiation therapy, V_p significantly decreased, suggesting that DCE MRI is a powerful tool to evaluate the success of RT and can be utilized as an indicator if further treatment is required. DCE-MRI can detect cases of tumor relapse with greater accuracy when compared with conventional size measurements.

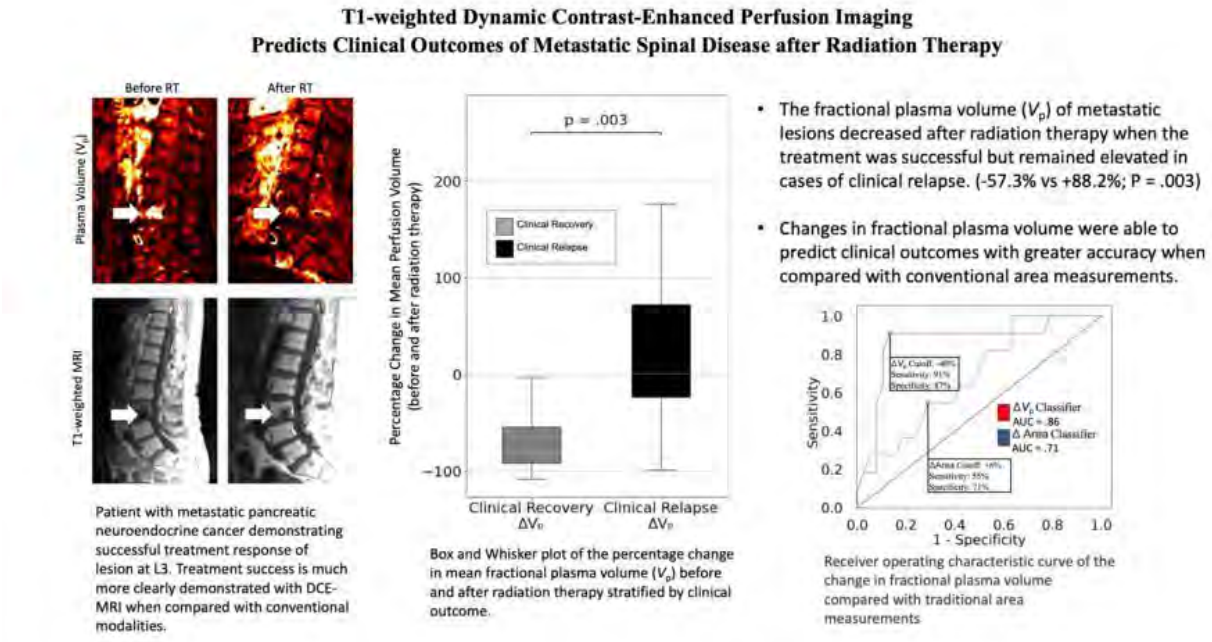

(Filename: TCT_914_ASNRGraphic.jpg)

1334

Opportunistic Prediction of Incident Fractures Based on Automatically Extracted vBMD from Routine Clinical MDCT Scans

J Bodden[1], M Dieckmeyer[2], E Burian[3], C Zimmer[4], J Kirschke[4], T Baum[5]
[1]Klinikum rechts der Isar, Technical University of Munich, Munich, Germany, [2]Klinikum rechts der Isar, Technical University of Munich, Bern, Bern, [3]Klinikum rechts der Isar, Munich, Germany, [4]Dept. of Neuroradiology, School of Medicine, Technical University of Munich, Munich, Germany, [5]Klinikum rechts der Isar, TU Munich, Munich, Bavaria

Purpose
To investigate the feasibility of opportunistic osteoporotic fracture prediction based on automated trabecular volumetric bone mineral density (vBMD), extracted from routine clinical multidetector computed tomography (MDCT) scans and to compare the model with prediction models based on baseline fracture prevalence.
Materials and Methods
Participants (n=420, 144 female) underwent two routine MDCT scans, with a mean time interval of 56 months (range 14-133) between scans. Vertebral labeling and segmentation as well as automated fracture and intravenous contrast phase detection was performed by a convolutional-neural network framework and all steps were supervised by a radiologist, specialized in spine imaging. Following an established algorithm to correct for intravenous contrast phase, trabecular vBMD was extracted automatically from each vertebra. Mean vBMD was calculated for three spine levels (T5-8; T9-12; L1-5). Logistic regression models were used to calculate the odds for incident fractures (ORs) as a function of vBMD (for each level, [mgHA/mm3]), baseline fracture incidence (yes/no), and number of baseline vertebral fractures (n), respectively. All models were adjusted for age and sex. ORs were inverted (1/OR) to simplify interpreting the results. Fracture prediction models were compared using the Akaike information criterion (AIC).
Results
Thirty-six participants (25 female) had prevalent fractures at baseline, and 24 (11 female) had incident fractures. Participants with lower vBMD at any spinal level were more likely to suffer incident fractures, and highest fracture odds were observed using the lumbar vBMD as predictor (L1-5: 1/OR, [95%-CI], p]; 1.03, [1.02 - 1.06], p < 0.001). Neither fracture status (0.46, [0.16, 1.39], p = 0.17) nor the count of fractures (0.73, [0.47, 1.12], p = 0.15) predicted fracture incidence. Model comparison revealed the lowest AIC

values for the lumbar vBMD-based model, indicating best fit (AIC; lumbar vBMD: 165.2; fracture status: 181.0; fracture count: 180.7).

Conclusions

Opportunistic fracture prediction based on automatically extracted vBMD from routine clinical MDCT is feasible and outperforms prediction models based on fracture status and fracture count at baseline.

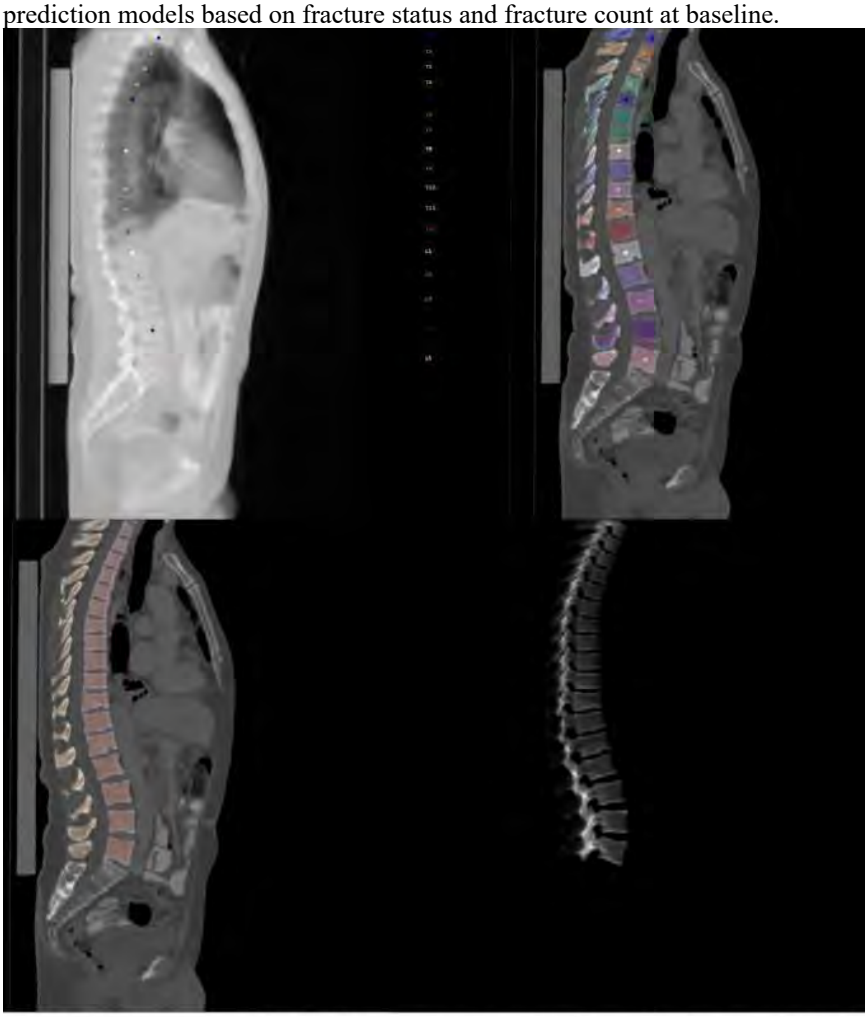

Steps of automated vertebral body segmentation, as performed by the convolutional neural network framework: **A** Automated vertebral body detection and labeling. **B** Segmentation of vertebral components, including posterior elements. **C** Separation of cortical and trabecular bone. **D** Three-dimensional reconstruction of segmented vertebra.

(Filename: TCT_1334_Fig1.jpg)

251

Validity of Bern Score as a Marker of Clinical Severity in Patients with Spontaneous Intracranial Hypotension

J Houk[1], S Morrison[1], S Peskoe[1], T AMRHEIN[1], P Kranz[2]

[1]Duke University Medical Center, Durham, NC, [2]Duke University Medical Center, Cary, NC

Purpose

The Bern Score is a quantitative scale characterizing the severity of brain MRI changes in Spontaneous Intracranial Hypotension (SIH).(1) Because these MRI changes may reverse after successful treatment, some investigators have proposed using the Bern score as an outcome measure for SIH. However, the relationship between clinical headache severity and Bern scores has not yet been evaluated. The purpose of this study is to determine the degree of correlation between pre-treatment Bern scores and headache severity in SIH.

Materials and Methods

Single-center, retrospective cohort meeting ICHD-3 criteria for SIH. Patients who completed a pre-treatment headache severity questionnaire (HIT-6, Headache Impact Test-6) and had an available pre-treatment brain MRI showing signs of SIH were included.(2) Bern scores were calculated using established methodology.(1) The Pearson correlation coefficient and 95% confidence interval (CI) for paired HIT-6 and Bern scores was calculated, and a regression line was fit to visualize the linear relationship between HIT-6 and Bern scores.

Results
Forty subjects were included in this study (mean age 54, 58% female). HIT-6 scores ranged from 51-78 (mean±SD, 65±6), representing clinical severity levels from "some impact" (score 50-55) to "severe impact" (score ≥60). Bern scores ranged from 2-9 (mean±SD, 6.1±2.1). There was low correlation (ρ=0.12, 95% CI: -0.20, 0.41) between paired HIT-6 and Bern scores.
Conclusions
Pre-treatment Bern scores show low correlation with clinical headache severity in patients with SIH. This suggests that Bern scores do not reliably reflect headache severity, and therefore should not replace clinical outcomes measures when determining effectiveness of SIH treatment.

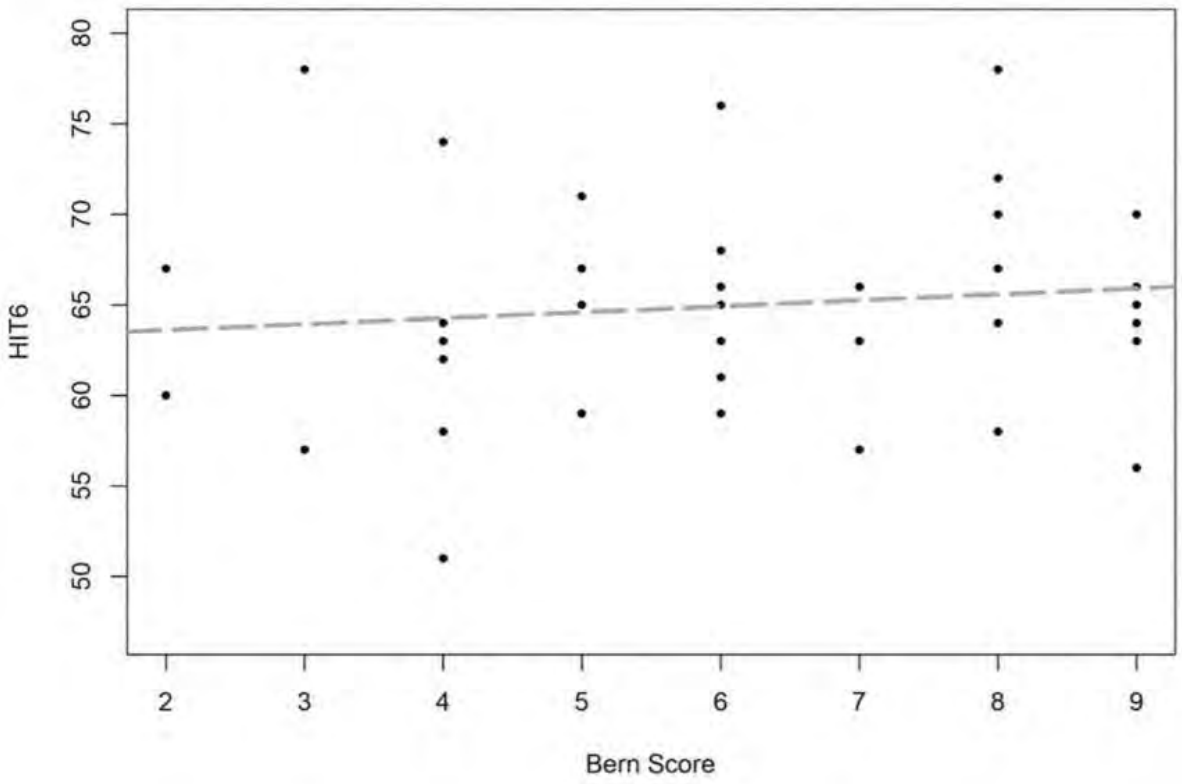

(Filename: TCT_251_FigureASNR.jpg)

Monday, May 1, 2023
3:30-4:30 PM
Scientific Abstract Session: Trauma

881

Association of Football Exposure with Brain Age in Former Professional Football Players

O Wu[1], R Grashow[2], M Weisskopf[2], J Dodelson[1], A Kulpanowski[1], B Hancock[1], D Marengi[2], M Doyle[3], W Copen[4], A Connor[5], A Baggish[4], R Zafonte[3], G Iverson[6]
[1]Massachusetts General Hospital, Charlestown, MA, [2]Harvard T. H. Chan School of Public Health, Boston, MA, [3]Harvard Medical School, Boston, MA, [4]Massachusetts General Hospital, Boston, MA, [5]Beth Israel Deaconess Medical Center, Boston, MA, [6]Spaulding Rehabilitation Hospital, Charlestown, MA

Purpose
Exposure to professional football might be a risk factor for later problems with brain health. A body of literature has examined imaging-based brain age estimation as a potential biomarker for individual brain health. We investigated the association of football exposure with premature brain aging in former professional football players.
Materials and Methods
Former professional football players who played since 1960 and who were less than 60 years old were enrolled [1]. The brainageR package was used to predict brain age from the players' 3D T1WI [2]. The predicted age difference was defined as the difference between the predicted brain age and the player's chronological age, with positive values indicating that the predicted brain age is older than the chronological age. Football exposure included position played (linemen vs. all other positions), total years played at the

professional level, and total years played non-professionally. Concussion signs and symptoms history scores were calculated [3]. Self-reported performance-enhancing drugs (PED) usage during playing years was recorded. Univariable linear regression was used to assess associations between predicted age difference and football exposure variables. Multivariable analysis was performed by stepwise backward regression.

Results

Data from 78 former professional football players were analyzed (mean±SD age was 49.0±7.7 years), 53% self-identified as white, 42% were former linemen, 15% reported PED use. Their median (IQR) total years of participation in football at the professional level was 5 (3, 7), whereas the median total years of non-professional participation was 11 (10, 14). Their median concussion history score was 30 (9.5, 58.3). Their median predicted brain age difference was -3.7 (-7.9, +1.5) years. The majority of players (68%) had a negative difference score. The results of univariable and multivariable analyses are shown in the Figure.

Conclusions

Former players had younger predicted brain age on average than their chronological age. This might be due to differences in several factors associated with brain health, e.g. history of exercise and physical activity across the lifespan, in the former players compared to the subject population comprising the training data used to develop brainageR. There was a significant univariable association between PED usage and older predicted brain age. Future studies with larger sample sizes are needed to better understand the association between football exposure and long-term brain health.

Figure: Univariable and multivariable factors associated with higher predicted brain age differences. Total number of datasets were from 78 participants unless otherwise noted.

Covariate	Univariable (95% CI)	P-value	Multivariable (95% CI)	P-value
Age	-0.16 (-0.34, 0.03)	0.10	NS	NS
Race, white	0.19 (-1.27, 1.65)	0.80	NS	NS
Concussion signs and symptoms history score (N=77)	0.04 (-0.00, 0.09)	0.054	0.04 (-0.008,0.08)	0.10
Main field position, lineman	1.16 (-0.29, 2.61)	0.11	1.29 (-0.12, 2.71)	0.072
Use of performance enhancing drugs during playing years, yes	2.13 (0.17, 4.08)	**0.034**	1.67 (-0.31, 3.65)	0.096
Total years of participation at the professional level	-0.29 (-0.68, 0.09)	0.13	-0.36 (-0.72, 0.01)	0.057
Total years of participation at the non-professional level (N=76)	0.24 (-0.22, 0.70)	0.31	NS	NS

NS=Not selected for the multivariable analysis by stepwise backward regression.

(Filename: TCT_881_figure.jpg)

304

Discovering the Symptom Burden-related Microstructure and Macrostructure Tissue Alterations of Mild Traumatic Brain Injury

S Chung[1], A Alivar[1], P Amorapanth[1], S Coelho[1], E Fieremans[1], D Novikov[1], J Rath[1], S Flanagan[1], Y Lui[1]
[1]*NYU Grossman School of Medicine, New York, NY*

Purpose

Mild traumatic brain injury (MTBI) is a major public health problem with potentially serious clinical sequelae. Here we attempt to understand white matter (WM) microstructural changes using advanced diffusion MRI including DTI, DKI, and the standard model, SM [1], and cortical changes that relate to symptom-burden after MTBI.

Materials and Methods

We studied 19 patients with high (37±12 yrs; RPQ total z-score, -3.52±0.96), and 21 patients with low symptom-burden (34±13 yrs; RPQ, 0.14±0.64) based on the Rivermead post-concussion symptom scale within 1 month of MTBI, and 39 normal controls (NC) (35±12 yrs; RPQ, 0.81±0.66). Multi-shell diffusion imaging with 6 b-values of 0-2.5ms/μm2 was performed on 3T MR scanners. We calculated 12 metrics of DTI and DKI (fractional anisotropy [FA], mean/axial/radial diffusivities [MD/AD/RD], kurtosis [MK/AK/RK]), and SM [1] (axonal water fraction [f], intra-axonal diffusivity [Da], extra-axonal axial/radial diffusivities [De,par/De,perp], ODF anisotropy [p2]). ComBat [2] was used to minimize scanner variability. MANCOVA was performed with age and sex as covariates.

Results

There are diffuse WM differences between high symptom-burden MTBI and NC (higher MD, AD, RD, Da, De,par, De,perp; lower FA, MK, AK) (Fig.1). Similar differences are not seen between low symptom-burden MTBI and NC. Cortical differences were found to be prominent in high symptom-burden MTBI, showing significantly higher cortical volume and thickness mainly in the inferior and posterior brain and lower values in more superior regions, while fewer differences were detected in low symptom-burden MTBI (Fig.2).

Conclusions

Our findings highlight widespread microstructural and macrostructural differences between high symptom-burden MTBI and NC. In particular, higher MD and lower FA have been previously seen chronically after injury believed to reflect reduced microstructural organization due to disruptions of healthy parenchyma structure, axon degeneration, or fiber disruption [3]. Increased De,perp may reflect demyelination [4], and decreased kurtosis reflects decreased tissue complexity and could also be associated with disrupted axonal integrity [5]. There are fewer differences between low symptom-burden MTBI and NC, suggesting that these diffusion metrics might specifically serve as good biomarkers for the clinically important group of symptomatic individuals. Further study delineating the relationship between symptom recovery and structural recovery is warranted.

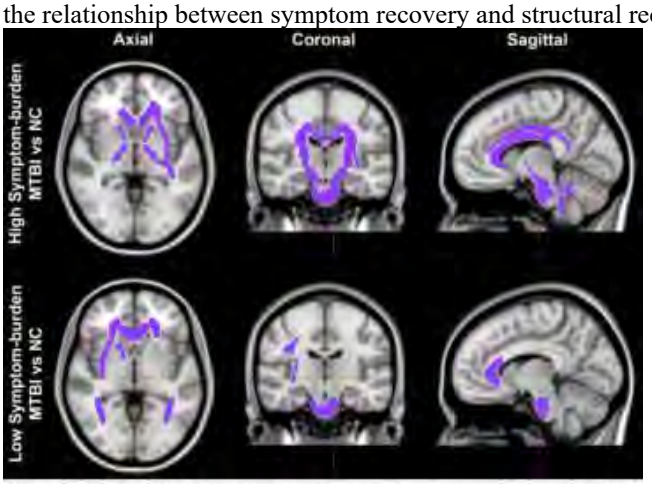

Figure 1. White matter ROI analysis results for diffusion measures comparing **(top)** high symptom-burden MTBI and NC groups and **(bottom)** low symptom-burden MTBI and NC groups. ROIs demonstrating significant differences in any of diffusion metrics (purple area, $p < 0.05$) are present mainly **(top)** in the middle cerebellar peduncle, genu and body of corpus callosum, left corticospinal tract, right/left inferior cerebellar peduncle, right/left superior cerebellar peduncle, right/left cerebral peduncle, right/left anterior/posterior limb of the internal capsule, left retrolenticular part of the internal capsule, right/left superior corona radiata, left external capsule and right/left cingulum (cingulate gyrus), and **(bottom)** in the middle cerebellar peduncle, genu of the corpus callosum, fornix, left corticospinal tract, right medial lemniscus, right superior cerebellar peduncle, right anterior limb of the internal capsule, right/left anterior corona radiata, right/left posterior thalamic radiation, right external capsule, right superior longitudinal fasciculus, right superior fronto-occipital fasciculus and right uncinate fasciculus. 48 WM ROIs are from the JHU-ICBM-DTI-81 WM atlas.

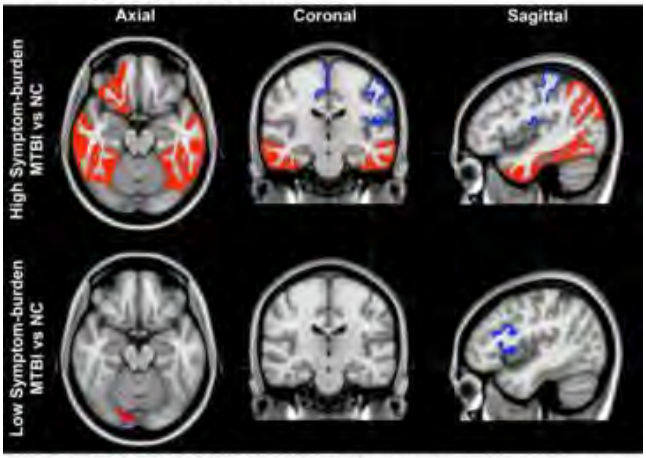

Figure 2. Gray matter ROI analysis results for cortical morphometry measures comparing **(top)** high symptom-burden MTBI and NC groups and **(bottom)** low symptom-burden MTBI and NC groups. ROIs demonstrating significant differences in cortical volume and/or thickness are present mainly **(top)** in the right/left fusiform, right paracentral, right/left inferiortemporal, right/left middletemporal, right lateralorbitofrontal, left inferiorparietal, left pericalcarine and left postcentral regions, and **(bottom)** in right/left pericalcarine, right/left caudalanteriorcingulate, right lingual, left parsopercularis and left cuneus. The red color represents higher cortical volume/thickness and the blue color represents lower cortical volume/thickness in MTBI. Cortical volume and thickness of 68 cortical ROIs were calculated using FreeSurfer.

(Filename: TCT_304_figure_final.jpg)

447

Feasibility Study of Computer Aided Detection of CT C-Spine Bone Fracture Using The YOLO Deep Learning Algorithm.

Y Cai[1], D Rao[2], V Agarwal[3], Y Chen[4], E Supsupin[5]

[1]Applicant for residency program, Houston, TX, [2]University of Florida College of Medicine Jacksonville, Jacksonville, FL, [3]University of Pittsburgh Medical Center, Pittsburgh, PA, [4]Burke Neurological Institute, White Plains, NY, [5]University of Florida College of Medicine at Jacksonville, Jacksonville, FL

Purpose

Computer-aided detection (CAD) of subtle cervical spine (C-spine) bone fractures is always desirable for radiologists. The You Only Look Once (YOLO) algorithm is a widely used deep learning algorithm for versatile object detection. As it is well established and supported, its feasibility in detecting C-spine fractures was investigated.

Materials and Methods

Total 235 C-spine fracture datasets with bounding box(BB) information were used from Kaggle. A YOLOv5 algorithm based on the PyTorch framework was customized. 25 datasets were used for validation and test data. The remaining 210 datasets were used as training data. The data was processed on Google Colab Pro platform. Based on the GPU power, 10 data sets were trained each time. 300 epochs were used per round. Each round of training took about 3h. After 21 rounds of training, the data was shuffled and repeated the above process, then compared the detection accuracy of the YOLO algorithm using the weights of the 21st and 42nd rounds of training. Figure 1 shows the evaluation flowchart we defined.

Results

25 testing datasets, by counting the blocks of continuous fracture slice numbers, yield a total 36 cervical fracture blocks and 60 normal blocks. It means some patients have multiple cervical fractures. Table 1 summarizes the detection results of the YOLO algorithm. Figure 2 compares between ground truth and YOLO detection results, showing the improvement at 42nd round of training. The YOLO algorithm also provides the calculated fracture probability. Figure 2B shows a case that the detection is not consistent across consecutive slices. Figure 2C shows a better way to label ground truth BBs based on Roboflow instruction.

Conclusions

The purpose of computer aided detection in radiology is to help radiologists quickly find abnormal lesions to reduce their search time. Our preliminary study suggests that the YOLO algorithm may show such promise in C-spine fracture detection based on 210 datasets. For satisfactory results, the guidelines for the YOLO algorithm recommend a minimum of 1500 datasets per class and at least 10000 labeled objects per class to train the algorithm. Therefore, there is still a large room for our study to improve. Compared to the weights trained at 21st round, the detection results at the 42nd training have more TP, FP, and number of "fractured" slices, indicating that detections become more stable and consistent across consecutive slices, an important quality assurance (QA) in our study.

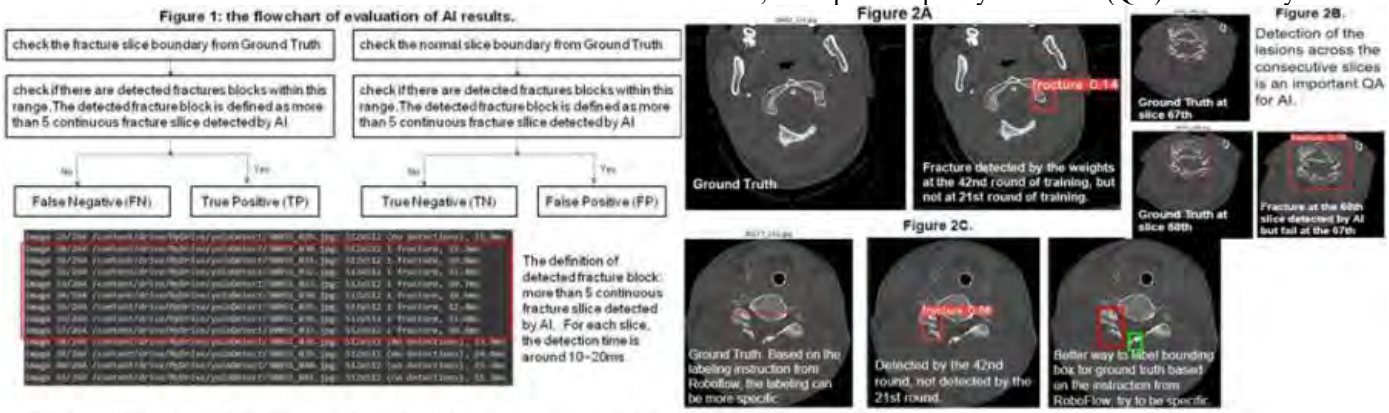

Table 1: The detection results of the YOLO algorithm using the weights at the 21st and 42nd rounds of training

	True Positive (TP)	False positive (FP)	False Negative (FN)	True negative (TN)	The total slice number of "fractures" detected
Weights at 21st round	3	10	33	50	323
Weights at 42nd round	8	17	28	43	577

(Filename: TCT_447_Figure.jpg)

630

Generalizability of Deep Learning Classification of Spinal Osteoporotic Compression Fractures on Radiographs Using an Adaptation of the Modified-2 Algorithm-Based Qualitative Criteria

Q Dong[1], G Luo[1], N Lane[2], L Lui[3], S Johnston[4], H Dabbous[5], M OReilly[6], K Linnau[1], J Perry[1], d haynor[7], J JARVIK[1], B Chang[1], J Renslo[8], N Cross[1]

[1]University of Washington, Seattle, WA, [2]UC Davis Health, Hillsborough, CA, [3]California Pacific Medical Center, San Francisco, CA, [4]University of Washington, seattle, WA, [5]Emory University, Atlanta, GA, [6]University Hospital Limerick, Limerick, Limerick, [7]univ of washington, seattle, WA, [8]Keck USC, Los Angeles, CA

Purpose

Spinal osteoporotic compression fractures (OCFs) can be an early biomarker for osteoporosis but are often subtle, incidental, and under-reported [1]. To ensure early diagnosis and treatment of OCF and osteoporosis, we aimed to build a generalizable deep learning vertebral body classifier for OCFs as a critical component of our future automated opportunistic screening tool.

Materials and Methods

We retrospectively assembled the local dataset, which included 1,790 subjects (~52% female) aged ≥65 years, 1,896 clinical spine radiographs, generated from 2000-2017, and 15,050 vertebral bodies (thoracic and lumbar). For the screening use case, the m2ABQ criteria [2] were simplified into a binary classification: normal/mild fracture/non-osteoporotic deformity vs. moderate or severe fracture. The Osteoporotic Fractures in Men (MrOS) Study dataset [3] collected the thoracic and lumbar spine radiographs of 5,994 men aged ≥65 years from six clinical centers. Five deep learning algorithms were used to classify the images of vertebral bodies extracted from the spine radiographs of the datasets. Classification performance was compared for the tuned models using multiple metrics including the area under the receiver operating characteristic curve (AUC-ROC), F1 score, sensitivity, specificity, and positive predictive value (PPV).

Results

On the local dataset's test set, our best model, which was trained on the local dataset's training set using the ensemble averaging algorithm, achieved an AUC-ROC of 0.948, an F1 score of 0.684, a sensitivity of 70.7%, a specificity of 98.3%, and a PPV of 66.2%. On the MrOS dataset's test set, this model achieved an AUC-ROC of 0.936, an F1 score of 0.729, a sensitivity of 64.3%, a specificity of 98.1%, and a PPV of 84.1%.

Conclusions

Our model built with the ensemble averaging algorithm achieved an AUC-ROC >0.90 on both the local dataset's test set and the MrOS dataset's test set. This testing shows some generalizability to real world clinical datasets and a suitable performance for a future opportunistic osteoporosis screening tool.

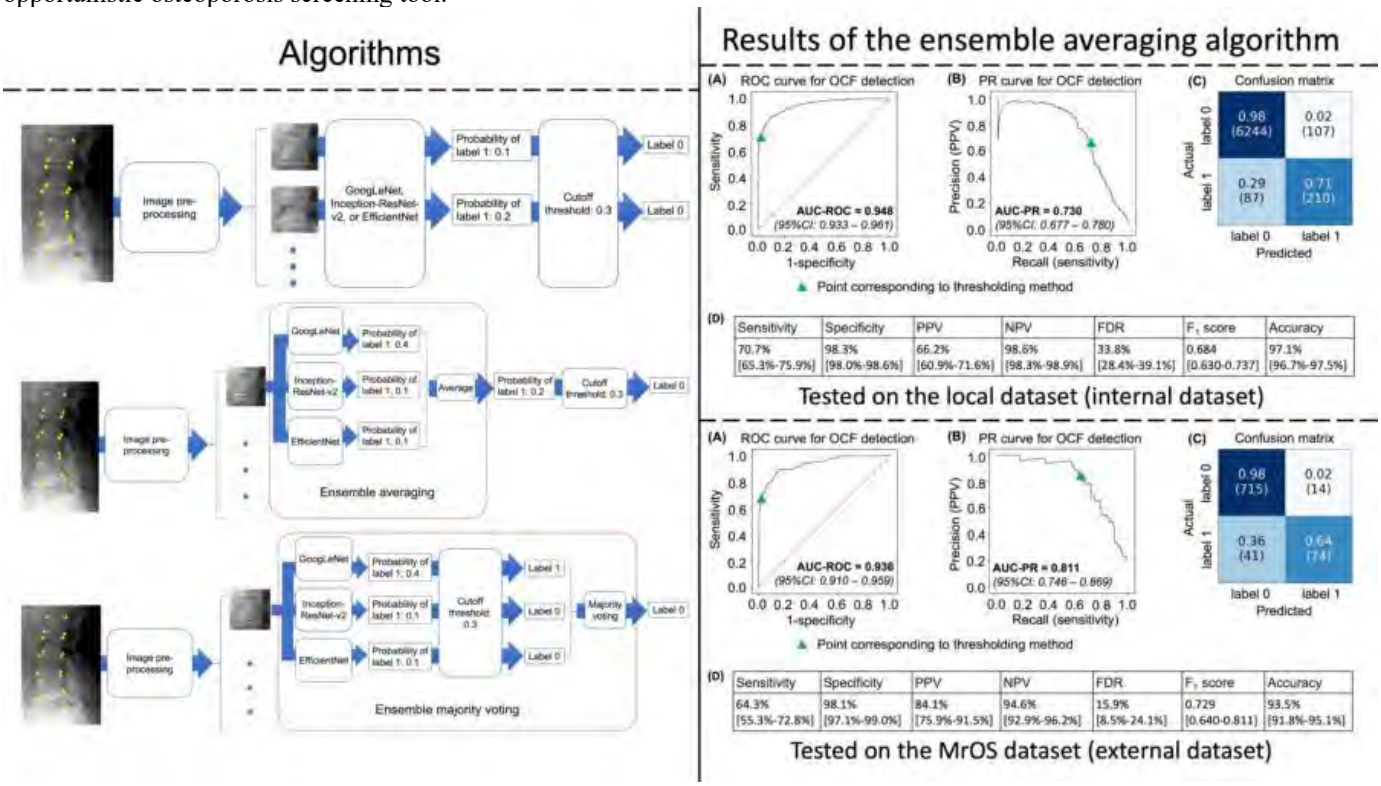

(Filename: TCT_630_graph_modified.jpg)

1438

Glymphatic Clearance Function as a Pathomechanism of Persistent Post-Concussive Working Memory Decline

Y Li[1], C CHEN[2]

[1]Taipei Medical University, Taipei, Taiwan, [2]TAIPEI MEDICAL UNIVERSITY HOSPITAL, TAIPEI, Taiwan

Purpose

The cerebral microbleeds (CMBs) and sleep disturbances (SD) has been reported to contribute to the persistent cognitive symptoms following mild traumatic brain injury (mTBI) but the pathogenesis remains unclear. This study aimed to elucidate the relationship between traumatic CMBs, sleep quality and glymphatic dysfunction in mTBI and to examine whether the glymphatic clearance function predicts persistent working memory decline.

Materials and Methods

Here we conducted a longitudinal MRI and neuropsychological study on mTBI patients (N=61) as well as demographically-matched controls (N=61) up to 1 year. The patients were divided into two groups: one with CMBs (N=18) and one without CMBs (N=43) based on the susceptibility-weighted MRI. The diffusion tensor imaging-analysis along the perivascular space (DTI-ALPS) technique (Figure 1) was performed on DTI to evaluate the glymphatic functioning. The Pittsburgh sleep quality index (PSQI) and digit span (DS) score were used to assessed the subject's sleep quality and working memory ability at both initial visit and 1-year follow-up, respectively. The patients were further divided to patient with SD (N=44) and without SD (N=17) according to a published cut-off threshold PSQI>5. Finally, the support vector machine regressor was trained using the DTI-ALPS index and PSQI assessed at initial visit along with patient's age and sex to predict the DS score at 1-year follow-up.

Results

Patients with CMBs appeared to have higher DTI-ALPS index compared to CMB negative patients and controls (Figure 2), suggesting that the traumatic CMBs may also lead to glymphatic dysfunction. Regardless of the presence or absence of CMB, patients had poorer sleep quality compared with controls. Both DTI-ALPS index and PSQI assessed at initial visit correlated significantly with the DS score at 1-year follow-up (Figure 3), whereas no significant correlation was found between these two factors, suggesting that they might be the independent factor affecting the glymphatic clearance efficiency and cognitive dysfunction. The DS score at 1-year follow-up can be satisfactorily predicted (RMSE=0.465, R^2=0.543, $p<0.001$), suggesting that DTI-ALPS index and PSQI can be used as surrogate biomarkers helpful for early prediction of permanent post-concussive working memory impairment.

Conclusions

The glymphatic clearance efficiency can be affected independently by glymphatic diffusivity (DTI-ALPS index) and sleep quality (PSQI) and predicts persistent working memory impairments after mTBI.

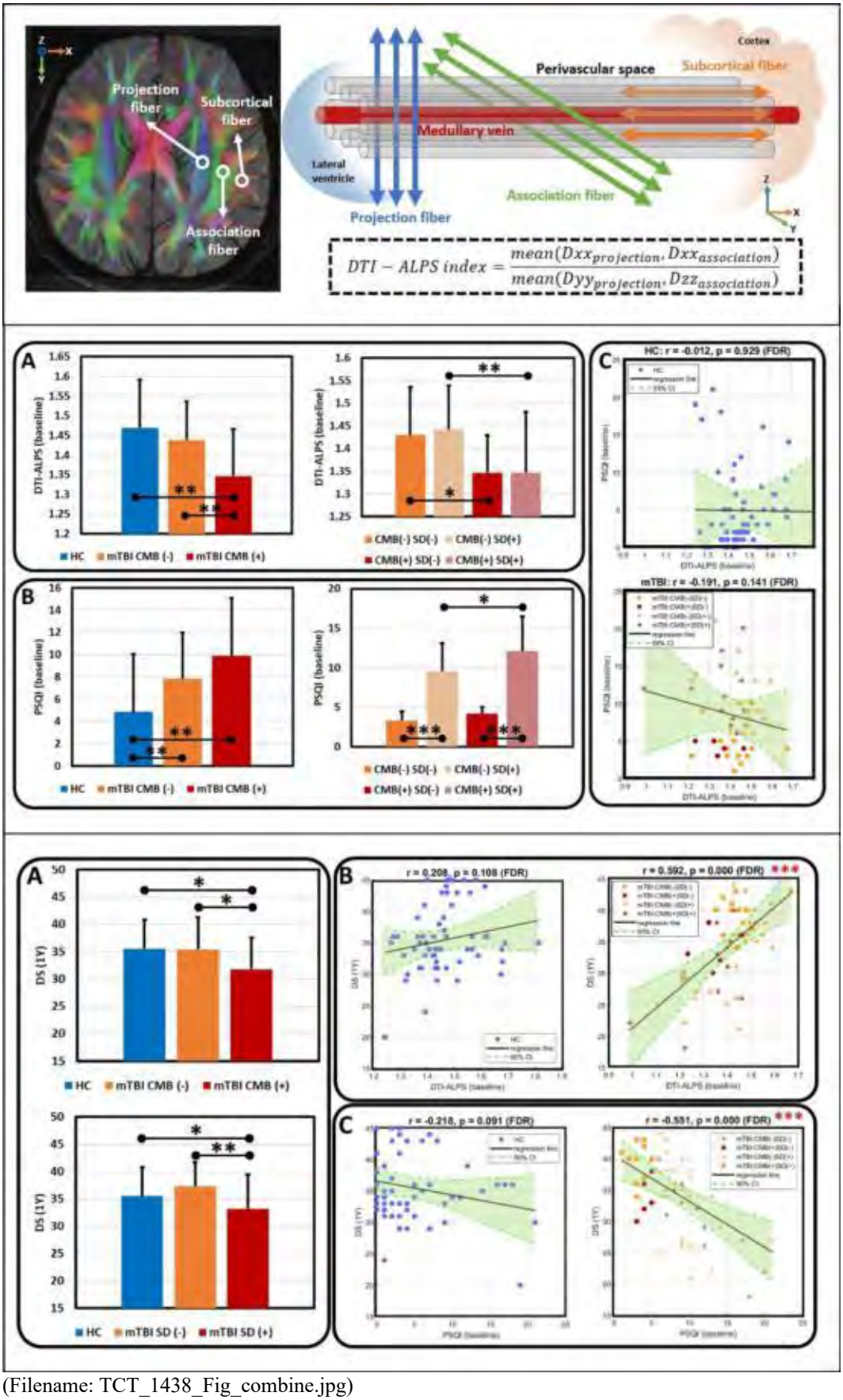

(Filename: TCT_1438_Fig_combine.jpg)

1030

Morphometric Changes of the Insula Between Acute and Chronic Phases of Sports-related Concussion are Associated with Changes in Measures of Physical and Psychological Symptoms

K Madi[1], C Whitlow[2], C Thibeault[3], C Sheridan[2]

[1]Wake Forest University/Atrium Health Wake Forest Baptist, Winston-Salem, NC, [2]Wake Forest School of Medicine, Winston-Salem, NC, [3]NovaSignal, Los Angeles, CA

Purpose

Autonomic dysregulation is common after sports-related concussion (SRC) and may contribute to symptoms in multiple domains.1 The insula plays a critical role in autonomic regulation;2 in previous work, we have shown that aberrant functional connectivity of specific subregions of the insula predicts acute and chronic symptoms. Shape analysis may be sensitive to pathophysiological changes such as swelling or blood distribution that may help elucidate the effect of SRC on specific brain structures. Here we deploy a novel automated pipeline for quantitative morphometry to determine if shape changes in the insula are independent predictors of symptom course after SRC.

Materials and Methods

Insular volumes were segmented from T1 images obtained from collegiate athletes (N=16, female=5) at 3 timepoints following an SRC: T1=1-4 days, T2=10-14 days, T3=2-3 months. Correspondent surface meshes of each insula were generated via spherical harmonics (SPHARM-PDM) in SlicerSALT.3,4 Vectorized distances between the T1 and T3 models were computed and projected onto surface normals at each vertex to obtain distances perpendicular to the surface—a direct measure of expansion or contraction. Projected distance vectors across the entire surface of the insula were incorporated into linear models alongside the T1-T3 delta scores on the Brief Symptom Inventory 18 (BSI-18) and the SCAT-3 Graded Symptom Checklist (GSC), and their respective subdomains. Results were mapped onto a template insula to visualize changes in surface regions significantly associated with changes in the symptom scores.

Results

For all symptom scales and subscales, there were multiple surface regions of L and R insula where the change in shape was significantly associated with the change in symptom scores. L insula exhibited an increased density of regions sensitive to symptom changes compared to R (Figure 1); L dorsal insula contained more regions sensitive to BSI-18 while L lateral and ventral anterior insula contained more regions sensitive to GSC severity scores (Figure 1E, 1G).

Conclusions

A novel pipeline for quantitative morphometry was successfully applied to the insula. The broad distribution of regions sensitive to symptom scores across the surface of the insula may reflect the distribution of shape changes over the cortical surface rather than concentration in a particular subregion. The increased density of sensitive regions on the lateral surfaces may indicate that a vascular or perivascular process underlies these shape changes.

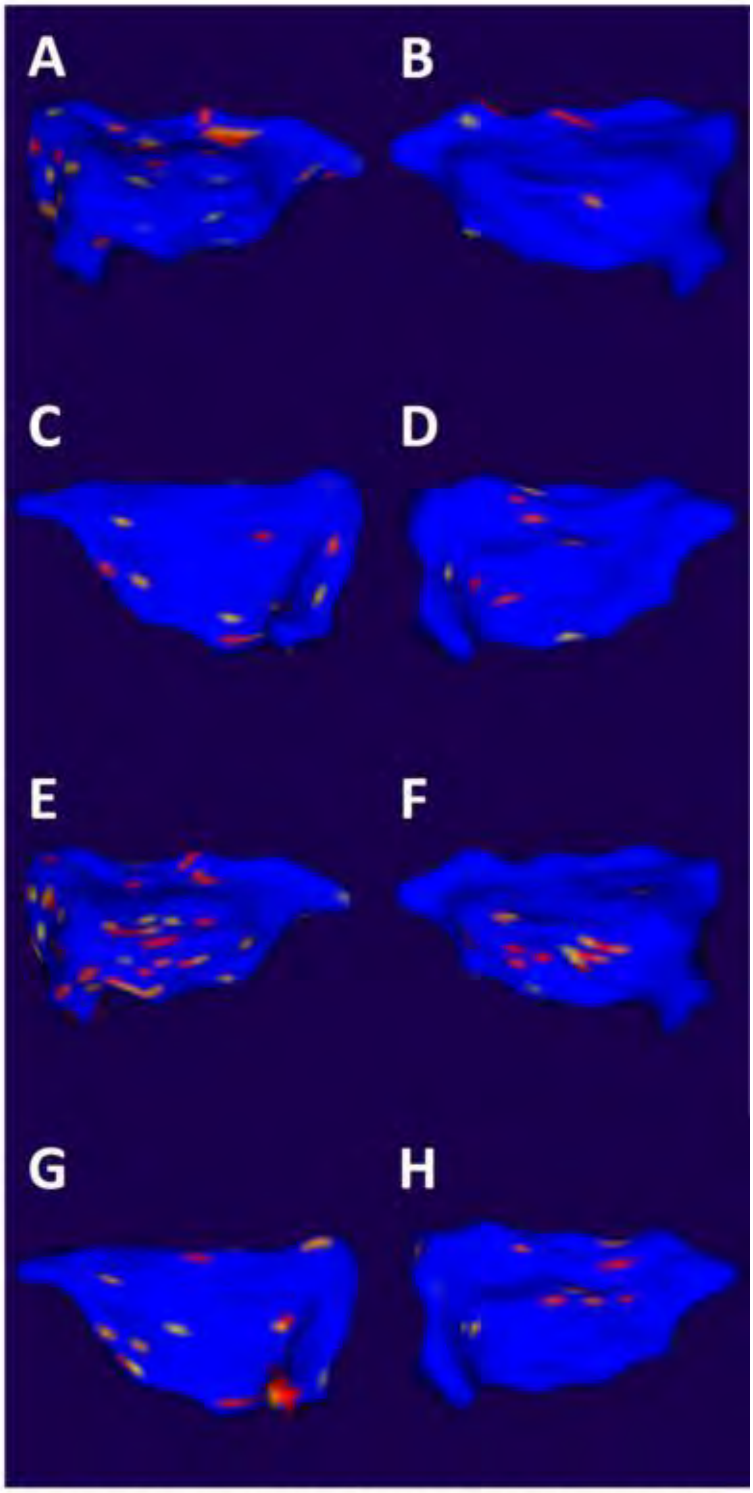

Figure 1: Significance maps of the left and right insula with respect to their associated change in symptom scores. Yellow-red areas indicate regions where $p \leq 0.05$. **(A)** Left insula, ΔBSI-18 total symptom score (lateral view). **(B)** Right insula, ΔBSI-18 total symptom score (lateral view). **(C)** Left insula, ΔBSI-18 total symptom score (medial view). **(D)** Right insula, ΔBSI-18 total symptom score (medial view). **(E)** Left insula, ΔGSC total score (lateral view). **(F)** Right insula, ΔGSC total score (lateral view). **(G)** Left insula, ΔGSC total score (medial view). **(H)** Right insula, ΔGSC total score (medial view).

(Filename: TCT_1030_ASNR_2023_figureJPG_KedarMadi.jpg)

1237

Participating in a Season of High School Football without Experiencing a Concussion is Associated with Increases in Functional MRI Measures of Neuroplasticity in Motor and Visual Brain Regions

M Kawas[1], K Atcheson[1], W Flood[1], J Kim[1], J Urban[1], E Davenport[2], J Maldjian[2], J Stitzel[1], C Whitlow[1]

[1]Wake Forest School of Medicine, Winston Salem, NC, [2]University of Texas Southwestern Medical Center, Dallas, TX

Purpose

Purpose: High school football, like other team sports, provides physical, mental, and social benefits. Still, the accompanying head impact exposure may cause harmful disruptions in brain function, and these disruptions are most studied and evident on fMRI after a concussion1. Therefore, we examined how some resting-state fMRI measures change after a season of high school football with no concussion.

Materials and Methods

Materials and Methods: Fifty-seven athletes (14-20 years, mean (SD) = 16.5 (1.1)) underwent fMRI before and after a single season of high school football. None of the participants reported a clinically diagnosed concussion before or during the season. BOLD time series data were pre-processed, de-noised, and band-pass filtered (0.008 – 0.1 Hz) using standard techniques in the CONN functional connectivity toolbox2. We computed the amplitude of low frequency fluctuation (ALFF, a measure of neural activity), intrinsic connectivity (IC, a measure of global connectivity), and local correlation (LCOR, a measure of local coherence) at each voxel to generate whole brain maps. Then, voxel-wise analyses of these maps were conducted to compare post- and pre-season scans. The thresholds of significant change were $p < 0.001$ at the voxel level and an FDR corrected $p < 0.05$ at the cluster level.

Results

Results: Post-season, there were multiple clusters with significant increases in ALFF. As shown in Figure 1, these clusters covered parts of the motor and vision areas, namely the bilateral precentral gyri, the bilateral postcentral gyri, and the bilateral occipital poles. Additionally, there were two clusters of significant IC increases over parts of the bilateral precentral gyri (Figure 2a). As for LCOR, there were also two clusters of significant increase that covered parts of the bilateral occipital poles, (Figure 2b).

Conclusions

Non-concussed football players showed significant increases in the intensity of spontaneous neural activity in multiple motor and visual areas as measured by ALFF. The concurrent increases in IC in motor areas as well as increases in LCOR in visual areas indicate increases in neuroplasticity that were associated improvements in motor function in other studies3, 4. To maximize the potential benefits of playing football, more studies are needed to explore these effects and how they interact with head impact exposure in the long term.

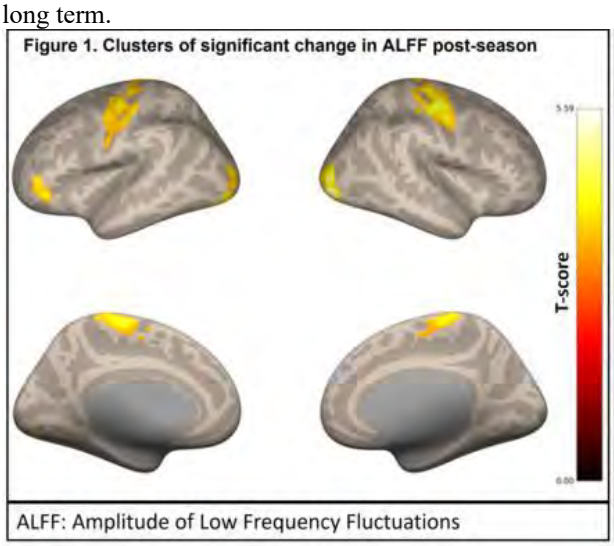

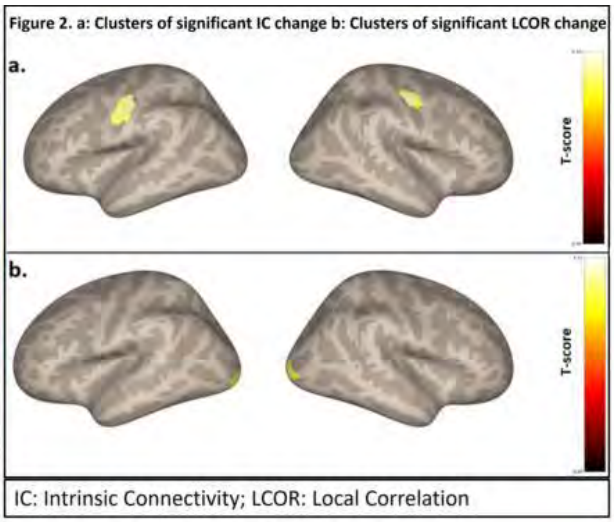

(Filename: TCT_1237_ASNRFigures_MKawas.jpg)

1067

Structural and Functional Imaging Group Differences Based on Rotational and Linear Head Impact Exposure Sustained Throughout a Single Season of Youth Football

N Bell[1], F Yu[2], J Urban[3], C Whitlow[3], J Stitzel[4], J Maldjian[5], E Davenport[6]

[1]UT Southwestern Medical Center, Dallas, TX, [2]UT Southwestern, Dallas, TX, [3]Wake Forest School of Medicine, Winston-Salem, NC, [4]Wake Forest University, Winston-Salem, NC, [5]University of Texas Southwestern Medical Center, Dallas, TX, [6]University of Texas Southwestern, Dallas, TX

Purpose

The purpose of this analysis was to investigate the effect of rotational and linear acceleration components on the brain. We compared structural and functional imaging metrics between a non-contact sport control group and youth football players that sustained the highest and lowest linear and rotational acceleration.

Materials and Methods

73 youth football players (all male; average age = 11.8 y) and 17 control participants (all male; average age = 11.2 y) were included in this analysis. Football players wore sensor-embedded helmets that detected HIE throughout the season. From this data, rotational and linear risk-weighted exposure (RWE) was calculated per subject. Control participants were assumed to have a 0 RWE value[1]. Four groups of 17 players each were created with this data: lowest rotational RWE (LR-RWE), lowest linear RWE (LL-RWE), highest rotational RWE (HR-RWE), and highest linear RWE (HL-RWE)[1]. No significant difference in age was present between groups. Diffusion Kurtosis Imaging (DKI), and 8 minutes of eyes-opened resting-state MEG data were acquired pre- and post-season for all participants. MEG data underwent standard pre-processing and source localization in Brainstorm[2]. The relative power per frequency band and mean kurtosis (kmean) images were normalized to MNI brain space. Voxel-wise difference (post-pre) maps were computed for all imaging metrics per subject[3]. Voxel-wise z-scores were computed and thresholded at 2 standard deviations above the mean[3]. A t-test analysis was performed comparing the 17 control participants to each group[4]. When evaluating the results, a Bonferroni correction was done to correct for multiple comparisons ($p<0.00625$).

Results

When evaluating the HR-RWE, alpha (p=0.00069), low gamma (p=0.0032) and high gamma (p=0.0029) frequency bands were significantly different from controls. However, when looking at the LR-RWE, none of the frequency bands were significantly different from controls. When looking at the HL-RWE; theta (p=0.0023), alpha (p=0.00069), beta (p=0.0032), low gamma (p=0.0028), and kmean (p=0.0027) imaging metrics were significantly different from controls. However, when looking at the LL-RWE; low gamma (p=0.0013), high gamma (p=0.0021), and kmean (p=0.0028) were the only neuroimaging metrics that significantly differed from controls.

Conclusions

These results suggest the type and magnitude of head impact sustained influence structural and functional brain measures.

Table 1. A comparison of neuroimaging measures between non-contact sport control athletes and football players sustaining the highest and lowest **rotational** head impacts.

	All Football	High RWE_{Rot} Football	Low RWE_{Rot} Football
	FB (n=73) vs. Control (n=17)	FB (n=17) vs. Control (n=17)	FB (n=17) vs. Control (n=17)
	P value	P value	P value
Delta	0.165	0.072931	0.214431
Theta	0.1011	0.007426	0.557887
Alpha	0.02803	**0.00069***	0.380211
Beta	**0.005158***	0.032341	0.031005
Low Gamma	**0.00003755***	**0.003215***	0.010973
High Gamma	**0.0002216***	**0.002909***	0.01339
Kmean	0.0079	0.12994	0.024453

*Indicates significance with Bonferroni correction (p-value < 0.00625).

Table 2. A comparison of neuroimaging measures between non-contact sport control athletes and football players sustaining the highest and lowest **linear** head impacts.

	All Football	High RWE_{Linear} Football	Low RWE_{Linear} Football
	FB (n=73) vs. Control (n=17)	FB (n=17) vs. Control (n=17)	FB (n=17) vs. Control (n=17)
	P value	P value	P value
Delta	0.165	0.999242	0.176052
Theta	0.1011	**0.00233***	0.841713
Alpha	0.02803	**0.000692***	0.259299
Beta	**0.005158***	**0.003294***	0.287009
Low Gamma	**0.00003755***	**0.002802***	**0.001311***
High Gamma	**0.0002216***	0.008689	**0.00218***
Kmean	0.0079	**0.002723***	**0.002877***

*Indicates significance with Bonferroni correction (p-value < 0.00625).

(Filename: TCT_1067_Table.jpg)

Monday, May 1, 2023

4:45-6:00 PM

Health Policy Programming: Transforming the Future of Neuroradiology: Real World Science

127

Scholarly Activity in Academic Settings Enabled by Point-of-Care Collaboration

A Mitchell[1], O Lopez[2], O Adaramola[2], C Polizzi[3], C Okoro[4], B Mathai[5], J Hefflefinger[3], Z Vardar[6], R Reeves[7], A Faghihimehr[8], Q Ng[3], M McArthur[9], M Gedrich[10], C Johnson[11], M Mehl[12], K Sweetwood[13], L llyang[14], A Tsibulski[15], E Hu-Wang[14], J Loo[9], V Patel[16]
[1]Spectrum Health/Michigan State University, Grand Rapids, MI, [2]Maimonides, Brooklyn, NY, [3]KPC/Hemet Global Medical Center, Hemet, CA, [4]Cedars-Sinai Medical Center, Los Angeles, CA, [5]Northwell Health, Manhasset, NY, [6]UMass Medical School, Worcester, MA, [7]Thomas Jefferson University, Philadelphia, PA, [8]Virginia commonwealth university, Henrico, VA, [9]University of California Los Angeles, Los Angeles, CA, [10]Cooper University, Camden, NJ, [11]Oregon Health & Science University, Portland, OR, [12]Arnot Ogden, Elmira, NY, [13]University of California, San Francisco, San Francisco, CA, [14]University of Chicago, Chicago, IL, [15]St. Joseph Mercy Oakland Hospital, Pontiac, MI, [16]University of Pennsylvania, Philadelphia, PA

Purpose
Mounting clinical pressures have resorbed dedicated academic time across departments, but scholarly activity is still required for residents, fellows, and faculty at ACGME-accredited programs. Simultaneously, growing considerations related to burnout and equity underscore the importance of protecting time outside of work. New mechanisms for scholarship are needed that enable meaningful contributions in the absence of dedicated academic time, during work hours. Existing methods for scholarship in academic radiology include traditional laboratory research, writing review articles, and clinical trials. With the exception of clinical trials, engagement in these methods of scholarship requires an uninterrupted focus that comes from dedicated time away from clinical service. This type of workflow may be impractical in many settings. In this work, we introduce the notion of point-of-care collaboration and demonstrate its application in the Human Disease Project, involving residents and faculty at 30+ radiology programs across the country.
Materials and Methods
This project aims to refine the differential diagnosis and provide imaging appropriateness guidance for more than 10,000 disease entities. Using a combination of crowdsourcing and natural language processing, we demonstrate a collaboration framework that recognizes differing levels of expertise between residents and faculty in order to harmonize concurrent edits made by individual contributors.
Results
Timecourse analysis of the pace of this collaboration is presented, demonstrating the refinement of differential diagnosis and imaging recommendations for more than 3,000 diseases occurred rapidly within a timeframe of 6 months. With the further introduction of automated worklists, micropilot data demonstrates feasibility of engagement from a cohort of radiology residents from multiple programs across the country with options that would satisfy ACGME requirements for scholarly activity.
Conclusions
By introducing a collaborative point-of-care framework in The Human Disease Project, we demonstrate that meaningful contributions to scholarly activity can be achieved at a rapid pace in a variety of academic settings by residents, fellows, and faculty. We conclude with future directions.

Tuesday, May 2, 2023

8:00-9:15 AM

ASHNR Programming: Technical Innovations in Head and Neck Imaging

1198

Comparison of 3T EPIC-DWI and MultiVane DWI TSE XD for Diagnosing Cholesteatoma

Y Lee[1]
[1]KOREA UNIVERSITY ANSAN HOSPITAL, Ansan-si, Korea (the Republic of)

Purpose
Due to its high degree of susceptibility, diagnostic value of EPI-DWI has been still disputed, rather non-EPI DWI has been regarded as a robust technique for identifying cholesteatoma. This study compares the diagnostic value of distortion-corrected EPIC DWI and MultiVane DWI TSE XD for cholesteatoma diagnostics.
Materials and Methods
A retrospective review was completed of consecutive patients who underwent 3T MR imaging for the evaluation of suspected cholesteatoma. Included patients had MR imaging examinations that included both EPIC DWI and MultiVane DWI TSE XD during the recent 6 months and confirmed cholesteatoma on a subsequent operation. Acquisition parameters of both DWI were as follows:

b=1000 s/mm, axial orientations, and section thickness of 2 mm. Image quality was evaluated by 2 readers on a 5-point Likert scale with respect to lesion conspicuity, air-bone susceptibility and overall subjective image quality. The ratio of signal to noise ratio (SNR), contrast to noise ratio (CNR) was also measured.
Results
Of 36 included patients, 10(27.8%) had surgically confirmed cholesteatoma. Lesion conspicuity and overall subjective image quality were comparable between both DWI studies, however, EPIC DWI showed better SNR and CNR despite of more pronounced air-bone susceptibility. Scan time of EPIC DWI and MultiVane DWI TSE XD was 1 min 50s and 5 min 24s.
Conclusions
EPIC DWI would be a more reliable imaging method than MultiVane DWI TSE XD to diagnose cholesteatoma in temporal bone

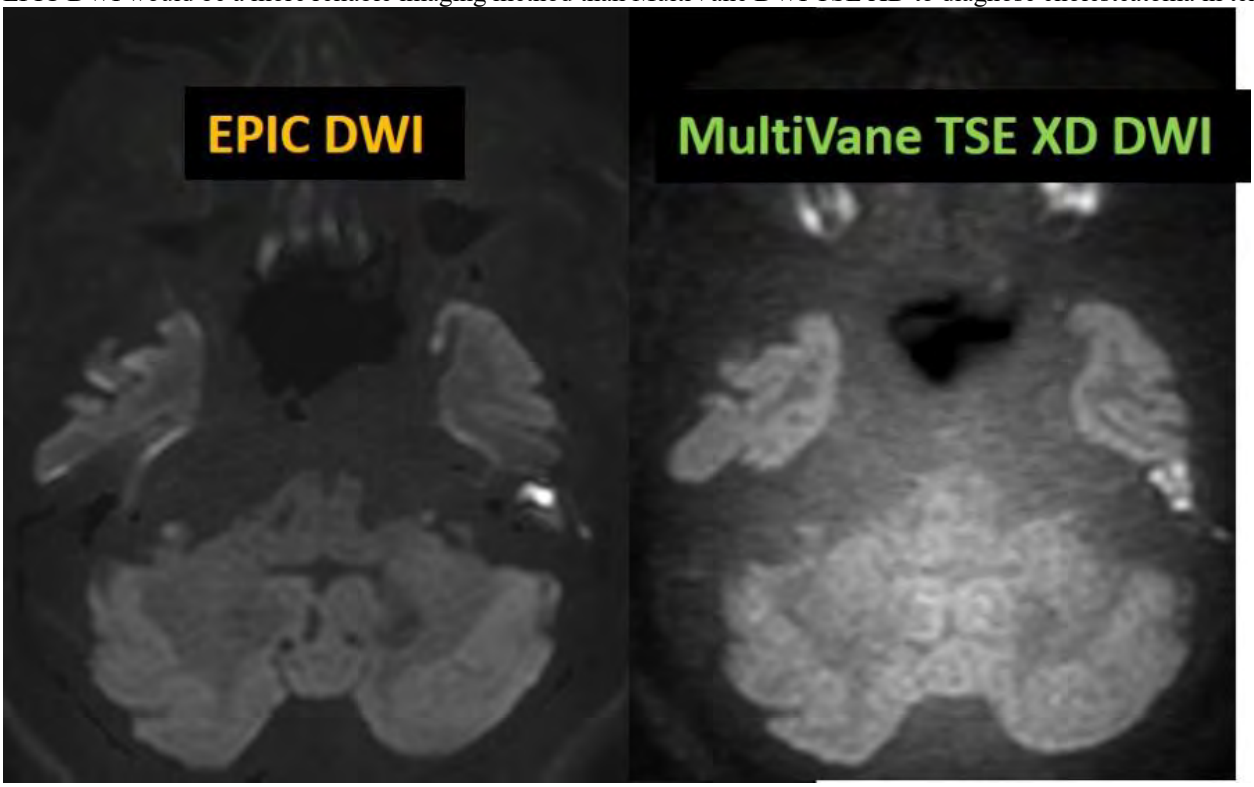

(Filename: TCT_1198_1.jpg)

301
Dynamic Contrast Enhanced (DCE) 3 Tesla MRI for Orbital Lesion Characterization
E O'Shaughnessy[1], C Le Cossec[2], N Mambour[3], A Lecoeuvre[4], J Savatovsky[5], M Zmuda[2], L Duron[6], A LECLER[5]
[1]Rothschild Foundation Hospital, PARIS 19, France, [2]Rothschild Foundation Hospital, Paris, France, [3]Rothschild Foundation Hospital, Paris 19, France, [4]Rothschild Foundation Hospital, Paris , France, [5]Foundation Adolphe de Rothschild Hospital, Paris, France, [6]Fondation Ophtalmologique A. Rothschild, PARIS, France

Purpose
Orbital lesions are rare but serious, especially because of the risk of functional impairment. Characterizing orbital lesions remains challenging clinically or with imaging. Diagnosis remains based on biopsy, an invasive procedure. It is necessary to develop non-invasive diagnostic tools. The goal of this study was to determine the diagnostic performance of Dynamic Contrast Enhanced (DCE) MRI at 3 Tesla when characterizing various orbital lesions.
Materials and Methods
This IRB-approved prospective single-center study enrolled participants presenting with an orbital lesion undergoing a 3 Tesla MRI prior to surgery from December 2015 to May 2021. Morphological, Diffusion-Weighted and Dynamic Contrast Enhanced MRI were assessed by two readers blinded to all data. A univariable analysis followed by a multivariable analysis were performed to distinguish benign from malignant lesions and orbital inflammations from lymphoma.
Results
One hundred and thirty-one participants (66/131 (50%) women and 65/131 (50%) men, mean age 52 ± 17 years [19-88]) were enrolled. Univariable analysis showed higher Ktrans and Kep medians in malignant versus benign lesion (1.1 min-1 versus 0.65 min-1, p=0.03 and 2.1 min-1 versus 1.1 min-1, p=0.01, respectively) and in lymphoma versus orbital inflammation (1.2 min-1 versus 0.6 min-1, p=0.001 and 2.3 min-1 versus 1.1 min-1, p<0.001, respectively). The best performing multivariable model in distinguishing malignant versus benign lesions included parameters from Dynamic Contrast Enhanced (DCE), Apparent Diffusion Coefficient (ADC) and morphology, and reached an AUC of 0.81 [0.67-0.96], yielding a sensitivity of 0.82 [0.55-1] and a specificity of 0.81 [0.65-0.96]. This same model reached an AUC of 0.84 [0.65-0.1], yielding a sensitivity of 0.83 [0.5-1] and a specificity of 0.85 [0.62-1] in distinguishing lymphoma from orbital inflammation.

Conclusions
Dynamic Contrast Enhanced MRI can be valuable when characterizing orbital lesions, either alone or in combination with morphological and diffusion weighted imaging.

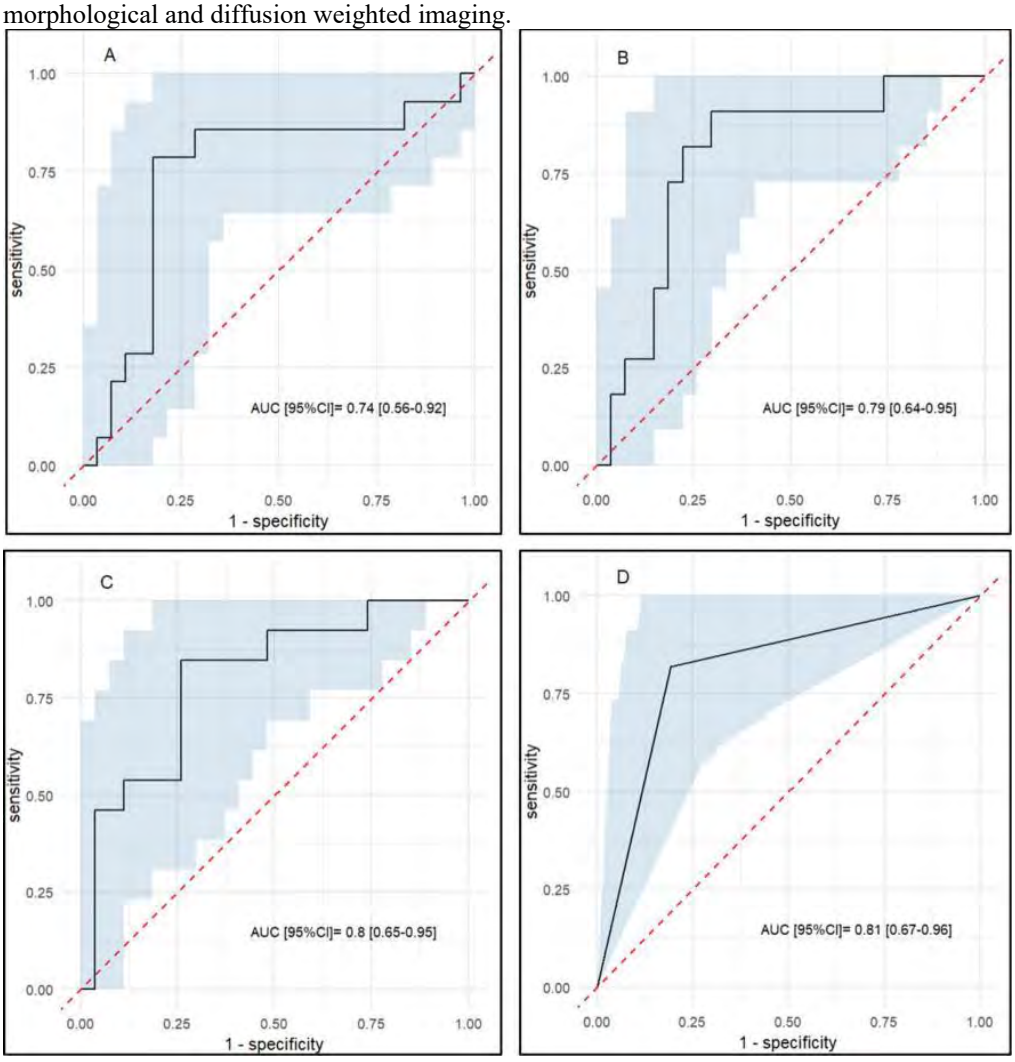

(Filename: TCT_301_Figure3.jpg)

Tuesday, May 2, 2023
9:30-10:30 AM
Scientific Abstract Session: Head and Neck

288

A signature of structural MRI features at 3 Tesla allows an accurate characterization of orbital cavernous venous malformation

S ELBAZE[1], L Duron[1], S KRYSTAL[2], J Savatovsky[3], A LECLER[3]
[1]Fondation Ophtalmologique A. Rothschild, PARIS, France, [2]Fondation ophtalmologique A de Rothschild, PARIS, france, [3]Foundation Adolphe de Rothschild Hospital, Paris, France

Purpose
ABSTRACT Objectives: To differentiate OCVM from other orbital lesions using structural MRI. Methods: This IRB-approved retrospective single-center analysis of a prospective cohort included consecutive adult patients presenting with an orbital lesion undergoing a 3T MRI before surgery from December 2015 to May 2021. Two readers blinded to all data read all MRIs assessing structural MRI characteristics. A univariate analysis followed by a stepwise multivariate analysis identified structural MRI features showing the highest sensitivity and specificity when diagnosing OCVM. Results: 191 patients with 30/191 [16%] OCVM and 161/191 [84%] other orbital lesions were included. OCVM were significantly more likely to present with a higher signal intensity than that of the cortex on T2WI: 26/29 (89.7%) versus 28/160 (17.5%), $p<0.001$, or with a chemical shift artifact (CSA): 26/29 (89.7%) versus 16/155 (10.3%), $p<0.001$, or to present with a single starting point of enhancement, as compared to other orbital lesions: 18/29

(62.1%) versus 4/159 (2.5%), p=0.001. The step-wise analysis identified 2 signatures increasing performances. The signature 1 combined a higher signal intensity than that of the cortex on T2WI and a CSA. Signature 2 included these two features and the presence of a single starting point of enhancement. Sensitivity, specificity and accuracy were 0.83, 0.94 and 0.92 for the signature 1 and 0.97, 0.93 and 0.93 for the signature 2, respectively. Conclusion: Structural MRI yields high sensitivity and specificity when diagnosing OCVM.
Materials and Methods
N/A
Results
N/A
Conclusions
Our study showed that structural MRI yields high sensitivity and specificity when diagnosing OCVM. We identified two signatures combining structural MRI features which might be used easily in routine clinical practice.

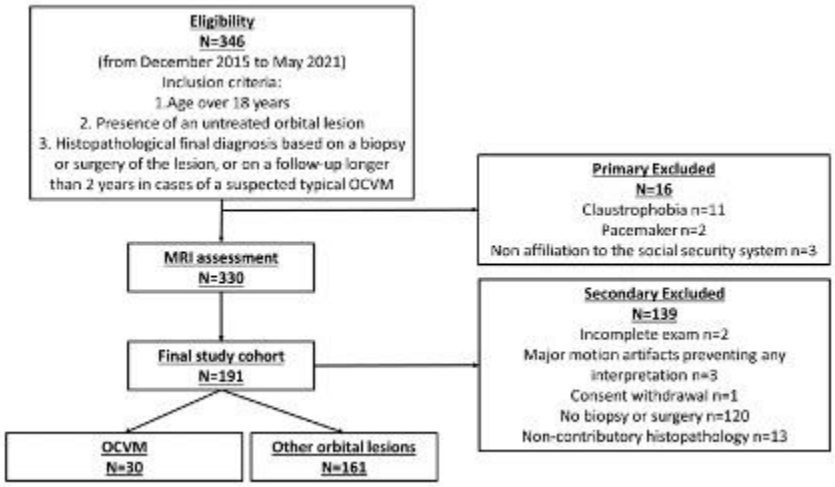

(Filename: TCT_288_Figure_1.jpg)

775

Effect of General Anesthesia on MR Optic Nerve Sheath Diameter in Pediatric Population

I Cohen[1], M Kraus[1], C Hoffmann[2], S Shrot[3]
[1]Sheba Tel Hashomer, Ramat gan, Israel, [2]Sheba Medical Center, Ramat-Gan, AK, [3]Sheba Medical Center, Ramat-Gan, Israel

Purpose
Papilledema is the hallmark of increased intracranial pressure. Associated distension of the subarachnoid space within the optic nerve sheath (ONS) is commonly reported in MR studies as a suggestive sign of increased intracranial pressure (1). However, sonographic ONS distention is well-described after general anesthesia (2). Our objective was to evaluate the effect of general anesthesia on ONS diameter as evaluated on MR.
Materials and Methods
We retrospectively evaluated 151 pediatric orbital MR studies. The anesthesia group included 97 studies, of which 22 patients had a clinical diagnosis of papilledema. The non-anesthesia group included 57 studies, of which 28 patients had a clinical diagnosis of papilledema. Patients without papilledema performed studies due to various indications such as blurred vision or strabismus. ONS diameter was measured on high-resolution T2-weighted images. A comparison of ONS diameter was performed between the anesthesia and non-anesthesia groups in patients with or without papilledema.
Results
In the non-anesthesia group, the average ONS diameter values were higher in papilledema patients compared to non-papilledema patients ($p<0.001$), with a positive correlation between ONS diameter and papilledema ($r=0.46$, $p<0.001$). In the anesthesia group, average ONS diameter values were similar in papilledema patients compared with non-papilledema patients ($p=0.06$). No significant correlation was found between ONS diameter and papilledema in the anesthesia group.
Conclusions
In the pediatric population, imaging findings of ONS distension might be related to general anesthesia rather than to increased intracranial pressure. Thus, the interpretation of ONS distention should be reported cautiously in conjunction with anesthesia status. Conversely, in non-anesthesia patients, ONS diameter correlates with a clinical diagnosis of papilledema.

567

Factors influencing a favorable outcome for radiofrequency ablation of huge benign thyroid nodules

C Chiu[1]

[1]Kaoshiung Chang Gung Memorial Hospital, Taiwan., Kaohsiung, Taiwan

Purpose

This study aimed to investigate the potential favorable factors influencing the therapeutic success of RFA of huge benign thyroid nodules (BTNs) (volume >100ml) and to evaluate the feasibility of RFA as an alternative treatment modality for patients unable or unwilling to undergo surgery.

Materials and Methods

This retrospective study evaluated a total of 868 patients, of which 22 patients had huge BTNs who underwent ultrasound guided moving shot technique RFA treatment between May 2017 and January 2022. The huge BTNs were categorized into two groups, according to a post-RFA treatment volume reduction ratio (VRR) of >80% and <80% at 6 months. Factors influencing these huge BTNs were reviewed, analyzed, and correlated with treatment effectiveness between the two groups.

Results

The mean VRR of the huge BTNs was 82.4 (66.6, 85.3) at the 6-month follow-up, indicating a notable treatment effect for relieving patient symptoms and cosmetic issues. Huge BTN characteristics, which included BTN on the left side (OR 7.875; 95% CI 1.11–56.1, p=0.03), and more heterogeneous echogenicity (OR 7.875; 95% CI 1.11–56.1, p=0.03), were the factors influencing an effective VRR.

Conclusions

RFA was effective in decreasing the volume of huge BTNs with an acceptable complication rate. Huge BTN characteristics, including BTNs on the left side and more heterogeneous echogenicity, showed a tendency toward a better VRR at the 6-month follow-up. This study indicates that RFA is a feasible alternative treatment modality for patients unable or unwilling to undergo surgery and assists clinicians to better educate and manage patient expectations prior to RFA treatment.

1443

Morning Glory Disc Anomaly: Expanding the MR Phenotype.

C Robson[1], F Dehghani Firouzabadi[2], V Rameh[3], J Rispoli[1]

[1]Boston Children's Hospital, Weston, MA, [2]Deprtment of Radiology, Children's Hospital, Harvard Medical School, Boston, MA, [3]Boston Children's Hospital, Boston, MA

Purpose

Morning glory disc anomaly (MGDA) is a congenital optic disc anomaly characterized by funnel shaped optic disc excavation with radiating vessels. The diagnosis is primarily clinical; imaging corroborates the diagnosis and reveals other associated findings referable to the optic pathway, skull base and intracranial vasculature. We sought to assess the incidence and type of associated optic nerve, chiasm, pituitary and central skull base anomalies in patients with MGDA.

Materials and Methods

We retrospectively searched a radiology database and reviewed medical records for all patients with MGDA at a tertiary children's hospital during the last 10 years. The inclusion criteria for our study cohort were: 1) clinical and radiological diagnosis of MGDA and 2) brain and/or orbit MRI. Imaging was reviewed by two pediatric neuroradiologists.

Results

Our study cohort consisted of 35 children (M:F=19:16; mean age=4 years, range=2 months-16 years). MGDA involved the right eye in 21, left eye in 11, and both eyes in 3 subjects. MR revealed the following: enlargement of the ipsilateral optic nerve in 16 (46%) patients, asymmetric optic chiasm in 21 (60%) patients with ipsilateral thickening in 19 (54%), and contralaterally small in 3 cases (8%). A persistent craniopharyngeal canal (CPC) was seen in 20 patients (46%) with opposed margins in 13, and 1–3 mm separated margins in 7 subjects. One patient had a ventral off midline cleft of the sphenoid body. Associated pituitary and infundibular anomalies included asymmetric position, angulation, and inferior displacement or a small beak of pituitary tissue projecting into the CPC. Two patients with CPCs had tubular fatty, enhancing pharyngeal lesions and 1 had a sphenoid cephalocele. Steno-occlusive vasculopathy was present in 7 patients. Two patients had ipsilateral anomalous oculomotor nerve origin with enhancement.

Conclusions

MGDA is associated with well described, characteristic ocular findings on MR which is primarily obtained to assess for associated vasculopathy and cephalocele. We have shown that thickening of the ipsilateral optic nerve and chiasm are frequently associated with MGDA and should not be misdiagnosed as optic glioma. In addition, MGDA is associated with a range of pituitary fossa anomalies from overt cephalocele to persistent CPC with varying degrees of pituitary and infundibular deformity and displacement as well as hamartomatous type lesions.

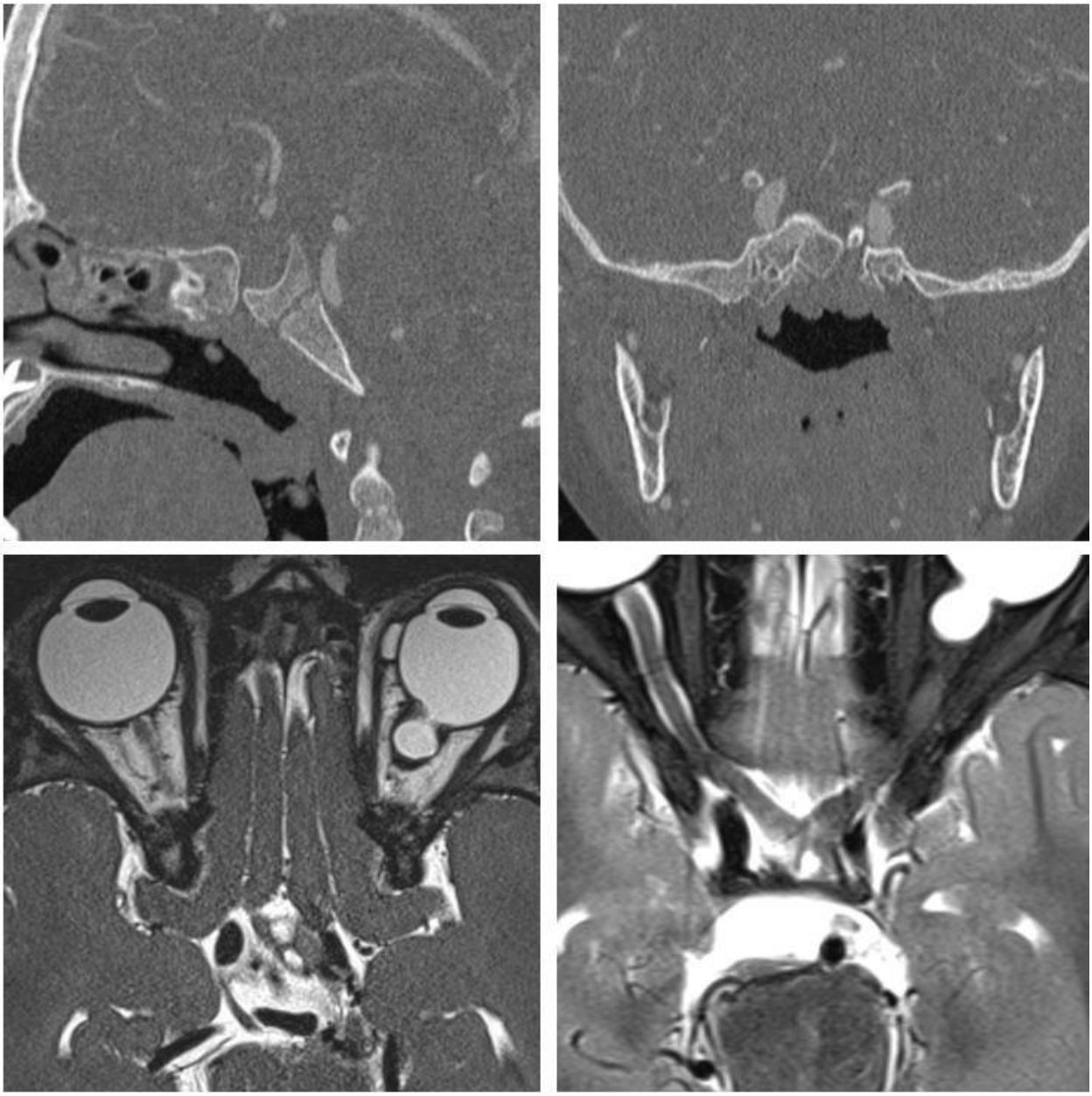
(Filename: TCT_1443_MGDA.JPG)

1265

Olfactory Function and Brain Structural Effects Following SARS-CoV-2 Infection

E O'Connor[1], T Zeffiro[1]
[1]*University of Maryland School of Medicine, Baltimore, MD*

Purpose

SARS-CoV-2 infection is accompanied by acute olfactory disturbance in as high as 70% of cases. This loss is associated with decreased olfactory bulb (OB) volume. Whle the anosmia tends to subside, the OB volume decrease does not. Volume reductions in primary and secondary olfactory cortex are also seen following SARS-CoV-2 infection. Nevertheless, concurrent SARS-CoV-2 infection effects on olfactory discrimination, olfactory bulb volume, primary olfactory cortex and its targets have not been investigated. To explore this possibility, we measured olfactory discrimination, olfactory bulb volume, primary olfactory cortex and basal ganglia volume in patients who had SARS-CoV-2 infection more than 12 weeks previously, who were then divided into COVID and long-COVID groups on the basis of self-reported fatigue, concentration, and memory complaints.

Materials and Methods

This cross-sectional study included 25 post-infection and 19 demographically-matched, no-COVID control participants. We investigated effects on olfaction using NIH Toolbox Odor Identification Test and the Monell Smell Questionnaire. GM structure was assessed with voxel-based morphometry and manual delineation of high resolution (1mm3), T1- and T2-weighted MRI data. Linear regression was used to model group effects on GM structure, adjusting for age, sex, education and total intracranial volume. CAT12/SPM12 and R were used for image processing and statistical modeling.

Results
The NIH Toolbox Odor Identification Test failed to show differences among the groups. In contrast, the Monell Smell Questionnaire revealed persistently diminished and distorted smell in 50% of the long-COVID sample. Olfactory bulb volume was lower in the long-COVID group (p=0.02). Primary olfactory cortex volume was reduced in the long-COVID group (p=0.004). Caudate volume was also lower in the long-COVID group (p=0.04).
Conclusions
In the absence of olfactory discrimination problems, long-COVID , but not COVID, patients experience persistent olfactory loss and distortion. These perceptual problems are associated with lower olfactory bulb, primary olfactory cortex and caudate volume, suggesting that the effects of SARS-CoV-2 infection can extend beyond the olfactory periphery to affect central targets.

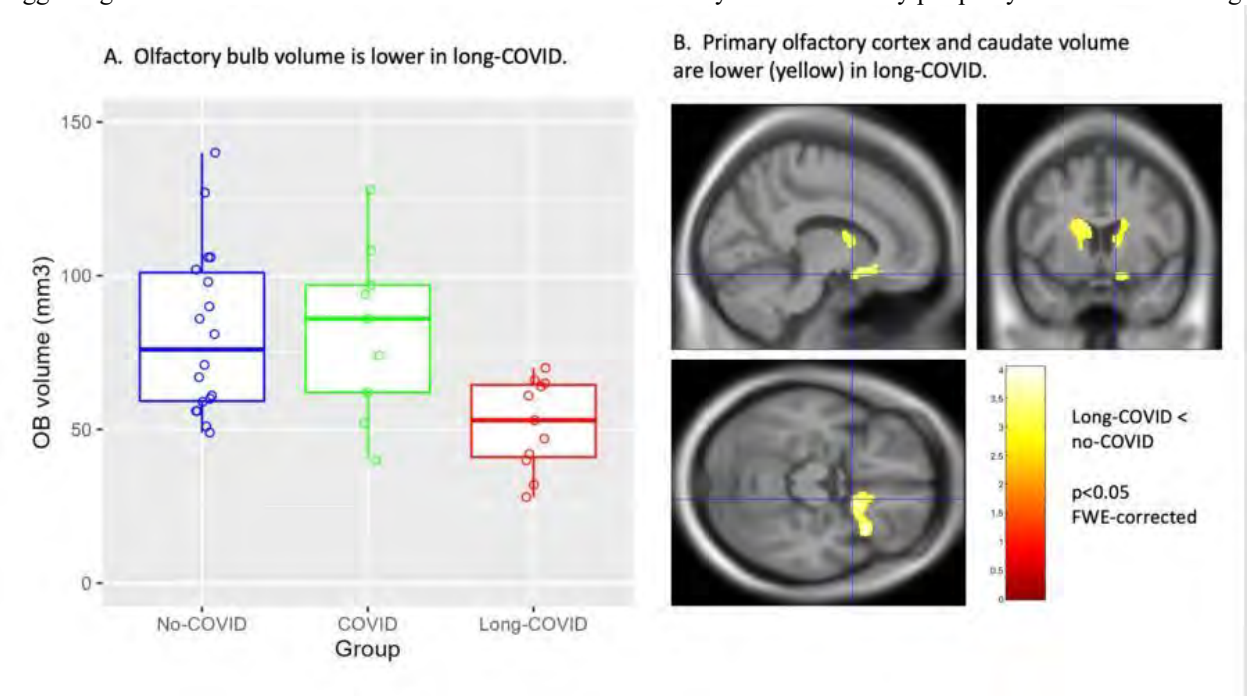

(Filename: TCT_1265_ASNRFig1.jpg)

402
Parathyroid 4D CT in Primary Hyperparathyroidism: Validation of Size Measurements for Predicting Multigland Disease
J Erickson[1], H Roeber[1], R Randle[1], P Bunch[1]
[1]*Wake Forest University School of Medicine, Winston-Salem, NC*

Purpose
Among patients with primary hyperparathyroidism (PHPT), minimally invasive parathyroidectomy is often preferred for single gland disease (SGD), and bilateral neck exploration is required for multigland disease (MGD). Accurate preoperative prediction of MGD versus SGD is therefore of substantial importance to parathyroid surgeons. Parathyroid 4D CT-derived candidate lesion estimated volume (EV) and maximum diameter (MD) have shown potential for accurately differentiating MGD from SGD. Specifically, for predicting MGD, second-largest high-confidence candidate lesion EV≥60 mm3 achieved 53% sensitivity (sens), 96% specificity (spec), 80% positive predictive value (PPV) and 85% accuracy (acc), and MD≥7 mm achieved 67% sens, 96% spec, 83% PPV, and 89% acc in a development cohort of 62 patients (1). However, these proposed thresholds have not been validated. The purpose of this study is to determine predictive performance of the proposed EV and MD thresholds for MGD versus SGD in an independent test cohort of surgically-treated PHPT patients.
Materials and Methods
This IRB-approved, HIPAA-compliant study reviewed consecutive PHPT patients undergoing preoperative 4D CT followed by parathyroidectomy at our institution between March 2021 and September 2022. Patients were excluded for 1) no high-confidence parathyroid lesion described on CT or 2) unsuccessful parathyroidectomy. A neuroradiologist reviewed 4D CT clinical reports to determine the EV (i.e., 0.52 x L x W x H) and MD of all described high-confidence parathyroid lesions. Independent surgeon review of operative notes, laboratory results, and pathology reports determined SGD versus MGD. Test performance characteristics of second-largest high-confidence candidate lesion EV≥60 mm3 and MD≥7 mm were calculated for predicting MGD.
Results
A total of 51 PHPT patients formed the study cohort (46 female, 5 male; mean age 66.1 years, SD 11.9). On 4D CT, a total of 99 high-confidence candidate lesions were described (mean 1.9 per patient, SD 1.1) – one in 24 patients (47%), two in 15 (29%), three in 3 (6%), and four in 9 (18%). At surgery, 34 (67%) patients were determined to have SGD and 17 (33%) to have MGD. For predicting MGD, second-largest high-confidence candidate lesion EV≥60 mm3 conveyed 65% sens, 97% spec, 92% PPV, and 86% acc; MD≥7 mm conveyed 71% sens, 91% spec, 80% PPV, and 84% acc.

Conclusions
Previously proposed parathyroid 4D CT-derived EV and MD thresholds are validated in this independent test cohort as accurate for predicting MGD.

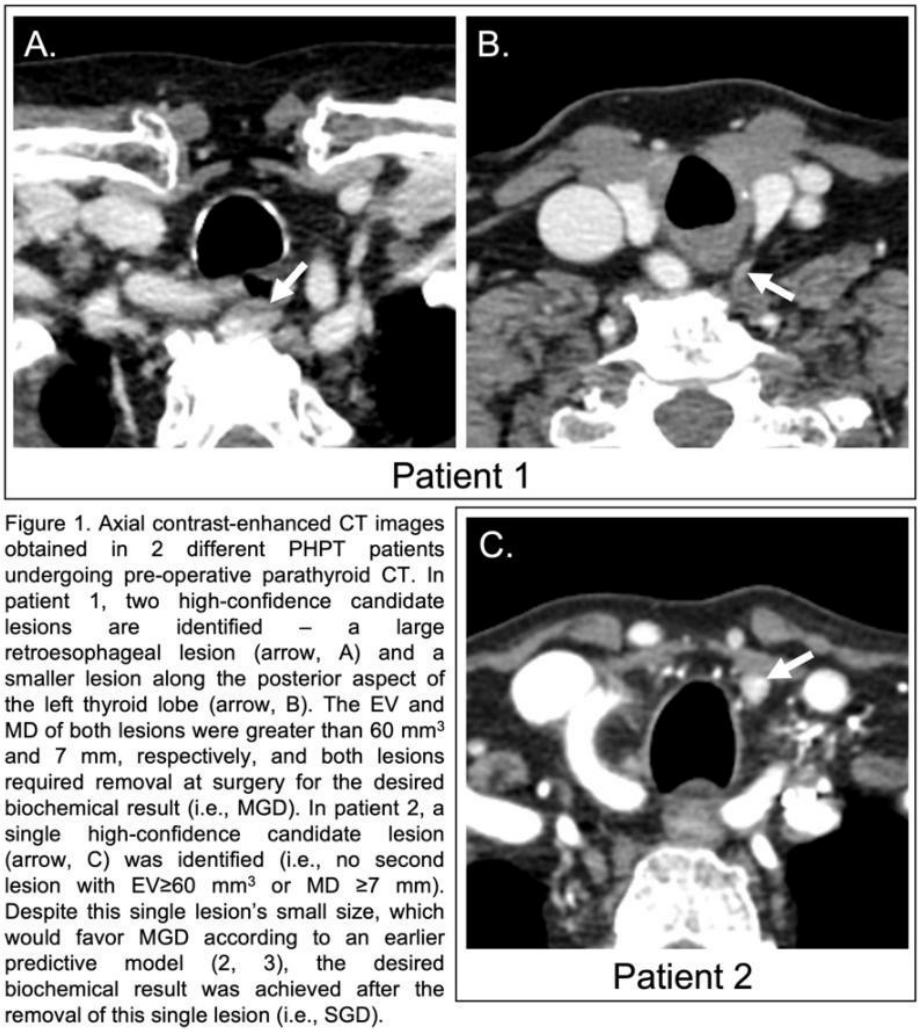

Figure 1. Axial contrast-enhanced CT images obtained in 2 different PHPT patients undergoing pre-operative parathyroid CT. In patient 1, two high-confidence candidate lesions are identified – a large retroesophageal lesion (arrow, A) and a smaller lesion along the posterior aspect of the left thyroid lobe (arrow, B). The EV and MD of both lesions were greater than 60 mm^3 and 7 mm, respectively, and both lesions required removal at surgery for the desired biochemical result (i.e., MGD). In patient 2, a single high-confidence candidate lesion (arrow, C) was identified (i.e., no second lesion with EV≥60 mm^3 or MD ≥7 mm). Despite this single lesion's small size, which would favor MGD according to an earlier predictive model (2, 3), the desired biochemical result was achieved after the removal of this single lesion (i.e., SGD).

(Filename: TCT_402_Figure1.jpg)

452
The Effect of Tumor Location and Size on Clinical Symptoms in Oculomotor Nerve Schwannomas.

Removed by author(s) instution request(s)

803

Ultrasound-guided Radiofrequency Ablation for Papillary Thyroid Microcarcinoma: Efficacy and Safety in a Cross-country Multicenter Retrospective Study

C CHEN[1], W Lin[1], M Wu[2], L My[3]

[1]Kaohsiung Chang Gung Memorial Hospital, Chang Gung University College of Medicine, Kaohsiung City, Taiwan, [2]National Taiwan University Hospital, Taipei City , Taiwan, [3]Vinmec Times City International Hospital, Hà Nội, Viet Nam

Purpose

This multicenter cross-country study aimed to assess and compare the short to long-term efficacy and safety of ultrasound (US)-guided radiofrequency ablation (RFA) for low-risk papillary thyroid microcarcinoma (PTMC).

Materials and Methods

This retrospective study included 150 patients (116 women, 34 men; mean age: 46 ± 13 years [range, 19-87]) who received US-guided RFA at 7 medical centers in 2 countries (Taiwan and Vietnam), between November 2017 and April 2022. Pre-RFA US and computed tomography (CT) were performed to assess the PTMC tumors and exclude cervical lymph node (LN) metastasis. Post-RFA follow-up US was performed at 1, 3, 6, and 12 months, and yearly thereafter. Complications, changes in tumor size, tumor disappearance rate, and disease progression were assessed and compared.

Results

A total of 167 PTMC tumors were treated. No patients reported complications post-ablation. All tumors demonstrated reduction in size ($p<0.001$) from 6 months after ablation compared with pre-ablation record. Fifty-two (31.0%) PTMCs had completely disappeared under US examination at the last-follow-up time. One patient had developed ipsilateral cervical LN metastasis at 6-month follow-up.

Conclusions

US-guided RFA proves to be effective and safe for patients with PTMC. Furthermore, we found no distinction of outcome under different background settings of treatment.

Tuesday, May 2, 2023
9:30-10:30 AM
Scientific Abstract Session: Vascular I

638

Calcification Contributes to Carotid Plaque Progression by Its Effect on Vessel Wall High-risk Components and Mechanical Properties

G Canton[1], D Geleri[1], D Hippe[2], J Sun[1], Y Guo[1], N Balu[1], K Pimentel[1], M Ferguson[1], T Kohler[3], G Tang[3], D Shibata[1], D Tirschwell[1], C Yuan[1], T HATSUKAMI[1]

[1]University of Washington, Seattle, WA, [2]Fred Hutchinson Cancer Research Center, Seattle, WA, [3]Seattle VA Puget Sound Healthcare System, Seattle, WA

Purpose

Carotid atheroma progression eventually leading to plaque rupture is a major cause of ischemic stroke. Intraplaque hemorrhage (IPH) is a risk factor for plaque progression and stroke risk[1]. Calcification often coexists with IPH but its role in plaque progression remains unclear[2]. Calcification may contribute to progression through its effect on plaque morphology and composition, as well as on the vessel wall's mechanical properties. In this study, we aimed at analyzing the relationship between the presence of calcification and IPH in a cohort of asymptomatic, medically managed subjects with known carotid atherosclerosis.

Materials and Methods

Participants underwent annual MR imaging resulting in 2-3 scans for each participant. Plaque morphology and composition was measured using standardized vessel wall image analysis. Blood pressure was measured at each visit. Plaque progression was defined as annualized change in percent wall volume between each pair of scans (a scan and its first successor). Generalized estimating equations-based regression was used to analyze predictors while accounting for multiple arteries and scan pairs per subject. Models were adjusted for sex, age, and statin use.

Results

There were 98 subjects with 162 carotid arteries measured across 267 serial scan pairs. IPH and calcification were present at baseline in 89 (33%) and 230 scan pairs (86%), respectively. The presence of IPH (β: 0.6 %/y, $p = 0.033$) and calcification (β: 1.2 %/y, $p = 0.028$) were each associated with faster plaque progression. Larger calcification was predictive of increasing pulse pressure (PP) over the next year (β: 1.4 mm Hg/year per 1-SD increase, $p = 0.040$). IPH developed in 7 arteries over follow-up. While the number was small, new IPH appeared to be associated with larger calcification (odds ratio [OR]: 2.6 per 1-SD increase, $p = 0.038$) and higher PP (OR: 2.3 per 1-SD increase, $p = 0.016$).

Conclusions

The presence of calcification in carotid atherosclerotic plaques may pose a double threat for plaque progression: its coexistence with IPH promotes faster plaque progression and its amount may lead to an increase in pulse pressure and the development of new IPH, further promoting plaque progression.

526

Extracranial Carotid Artery Atherosclerotic Plaque and APOE Polymorphisms: A Systematic Review and Meta-Analysis

S Culleton[1], M Alexander[1], J McNally[1], C Yuan[2], D Parker[1], H Baradaran[1]

[1]University of Utah, Salt Lake City, UT, [2]University of Utah, Salt Lake , UT

Purpose

Carotid atherosclerotic plaque is an important independent risk factor for stroke. Apolipoprotein E (APOE) influences cholesterol levels and certain isoforms are associated with increased carotid atherosclerosis, though the exact association between APOE and carotid plaque is uncertain (1,2). The study aimed to evaluate the association between APOE and carotid plaque.

Materials and Methods

A systematic review was performed to retrieve all studies which examined the association between carotid plaque and APOE. This study was conducted in accordance with the PRISMA guidelines. Independent readers extracted the relevant data from each study including the type of imaging assessment, plaque definition, frequency of APOE E4 carrier status and type of genotyping. Meta-analysis with an assessment of study heterogeneity and publication bias were performed. Results were presented in a forest plot and summarized using a random-effects model.

Results

After screening 838 studies, 17 studies were included for systematic review. A meta-analysis of 5 published studies showed a significant association between e4 homozygosity and carotid plaque (odds ratio [OR], 1.53; 95% CI, 1.16, 2.02; p=.003). Additionally, there was a significant association between patients possessing at least one e4 allele, heterozygotes or homozygotes, and carotid plaque (OR, 1.25; 95% CI, 1.03-1.52; p=.03). Lastly, there was no association between e4 heterozygosity and carotid plaque (OR, 1.03; 95%CI, 0.93, 1.26; p=.30).

Conclusions

APOE e4 allele is significantly associated with extracranial carotid atherosclerotic plaque, especially for homozygous individuals. While imaging currently plays an important role in identifying plaque and stratifying its severity, genetics could identify subgroups in need of closer imaging surveillance in the future.

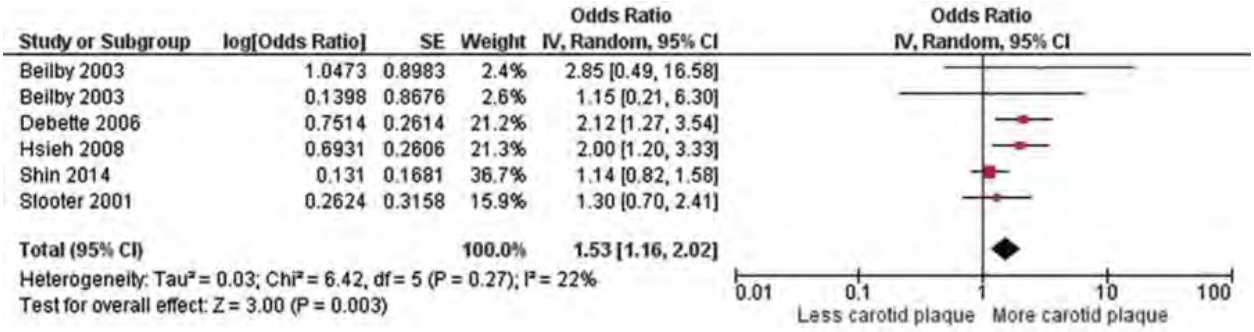

(Filename: TCT_526_Image1AssociationbetweenHomozygotesandCarotidPlaque1.jpg)

504

Flow Diversion using Pipeline Embolization Device for Intracerebral and Extracerebral Pseudoaneurysms: A Systematic Review and Meta-analysis

E Greco[1], J Rios-Zermeno[2], A Ghaith[3], S Kashyap[1], D Miller[1], T Huynh[1], C Perez-Vega[1], W Fox[1], W Brinjikji[3], E Middlebrooks[1], S Sandhu[1], R Tawk[1]

[1]Mayo Clinic, Jacksonville, FL, [2]Instituto Nacional de Neurología y Neurocirugía, Mexico city, Mexico, [3]Mayo Clinic, Rochester, MN

Purpose

Pseudoaneurysms are complex lesions associated with high incidence of rupture and mortality. Flow diverters have been proposed as an alternative treatment to preserve the flow through the parent artery. We investigated the safety and the short (< 1 year) and long-term (≥1 year) aneurysm occlusion rates following the treatment of intracerebral and extracerebral pseudoaneurysms using the Pipeline Embolization Device (PED).

Materials and Methods

An electronic database search for full-text English articles was conducted following Preferred Reporting Items for Systematic Reviews and Meta-Analysis guidelines. Studies of any design with at least 4 patients with intracranial or extracranial pseudoaneurysms treated with PED were included in our analysis. The primary safety endpoint was the incidence of post-procedural complications. The primary efficacy endpoint was the complete pseudoaneurysm occlusion rate.

Results

We included 9 studies with a total of 90 patients harboring 96 pseudoaneurysms. The mean age was 38.2 years, and 37.8% were women. The mean pseudoaneurysm size was 4.9 mm. Most pseudoaneurysms were unruptured, and the etiology was traumatic brain injury in 33.3%, spontaneous in 21.9%, and iatrogenic injury in 19.8%. Sixty-two (64.6%) pseudoaneurysms were intracranial, and 34 (35.4%) were extracranial. Twenty-nine (30.2%) pseudoaneurysms were located in the cervical ICA, while 15.5% and 12.5% were in the petrous and cavernous segments of ICA, respectively. Thirty-three pseudoaneurysms were treated with ≥ 2 devices, and 8 received adjunctive coils. The mean clinical and angiographic follow-ups were 10.6 and 12.8 months, respectively. The short-term and long-term complete occlusion rate was, respectively, 79% (95%, CI 66%-88%, p=0.82) and the 84% (95%, CI 70%- 92%, p=0.95). Complication rates were 8 % for iatrogenic dissection (95%, CI 3%-16%, p=0.94), 10% for silent thromboembolism (95%, CI 5%-21%, p=0.77) and 12% for symptomatic thromboembolism (95%, CI 6%-23%, p=0.48). No hemorrhage was noted following treatment at the last follow-up. The overall mortality rate was 14% (95%, CI 5% to 34%, p=0.02).

Conclusions

The complete occlusion rate of pseudoaneurysms treated with PED was high and increased over time. On the other hand, post-procedural complications and mortality were considerable, and further studies are required to clarify PED safety for treating intracerebral and extracerebral pseudoaneurysms.

Figure: Forest plot showing (A) the long-term silent stroke, (B) symptomatic stroke, (C) Aneurysm dissection, and (D) Mortality rates following PED placement in patients diagnosed with pseudoaneurysms.

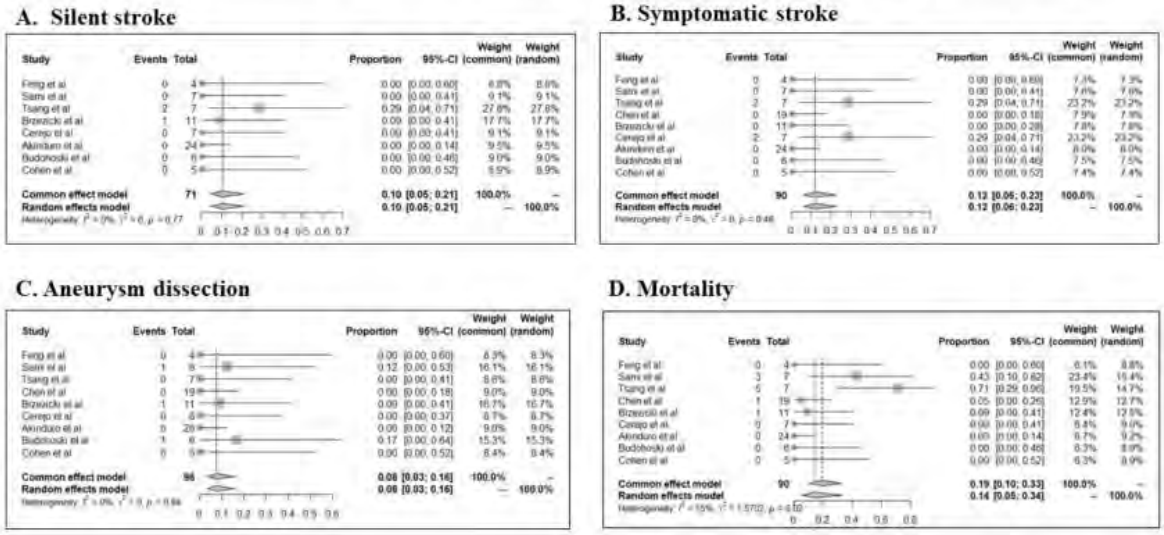

(Filename: TCT_504_ComplicationsPSEUDOANEURYSMS400.jpg)

715

Longitudinal Evaluation of Atherosclerosis Evolution on Intracranial Vessel Wall MRI Reveals Lumen-Side Arterial Wall Remodeling with Plaque Progression and Regression

Y Guo[1], G Canton[1], D Baylam Geleri[1], N Balu[1], D Tirschwell[1], T HATSUKAMI[1], C Yuan[1], M Mossa-Basha[1]
[1]*University of Washington, Seattle, WA*

Purpose
Intracranial atherosclerosis is a leading cause of ischemic stroke with a high risk of stroke recurrence. Intracranial atheromas are dynamic lesions showing progression and regression. However, few studies used serial vessel wall MRI (VWI) to characterize patterns of lesion development and vessel wall remodeling.
Materials and Methods
Participants were prospectively recruited in the WALLI study and underwent baseline and one-year follow-up VWI. TOF-MRA, pre- and post-contrast T1w- and PDw-VISTA sequences of both time points were jointly registered and pre-processed by a multi-time point, multi-contrast, and multi-planar viewing workflow (MOCHA). Plaques were detected and measured by expert readers as focal wall thickening compared to the proximal and/or distal segments. Based on annualized changes in percent wall volume, plaques were divided into progression (>2.5%/yr), stable, and regression (>-2.5%/yr) groups (threshold derived from estimation of measurement error from a reproducibility cohort). Baseline luminal stenosis was measured separately on TOF according to the WASID criteria. Generalized estimating equations-based models were used to compare groups while accounting for multiple arteries and scan pairs per subject.
Results
Among 37 participants, 120 plaques were identified, distributed as follows: 7 (6%) in petrous ICA, 31 (26%) in cavernous ICA, 26 (22%) in supraclinoid ICA, 20 in MCA (17%), 1 in ACA (1%), 17 in V4 (14%), 9 in BA (8%), and 9 in PCA (8%). In the regression group (30 plaques), minimum lumen area increased from 7.3mm2 to 8.1 mm2 ($p<0.001$) and maximum wall thickness decreased from 1.7mm to 1.5mm ($p<0.001$). In the progression group (12 plaques), minimum lumen area decreased from 6.0 mm2 to 4.9 mm2 ($p=0.01$) and maximum wall thickness increased from 2.0mm to 2.3mm ($p=0.02$). In the stable group (78 plaques), both measurements did not differ significantly from baseline to follow-up ($p=0.12$ and 0.70). However, in all three groups, the changes in mean total vessel area were not statistically different ($p=0.58$, 0.73 and 0.80). We also found no significant differences in degree of baseline stenosis among the three groups (odds ratio = 1.02 and 1.01, $p=0.11$ and 0.72).
Conclusions
Progressing plaques showed inward remodeling with lumen loss, while regression was accompanied by luminal expansion. Although plaque remodeling is more likely to happen at the lumen-inner wall boundary, the degree of baseline luminal stenosis did not predict future progression of lesions in this cohort.

TABLE 1. MRI Protocol

Sequence	Pre-T1 VISTA	PD VISTA	Post-T1 VISTA	3D-TOF
Orientation	**Coronal**	**Coronal**	**Coronal**	**Axial**
FOV (mm)	180 × 180 × 40	180 × 180 × 40	180 × 180 × 40	190 × 190 × 72
Resolution for acquisition (mm)	0.5 × 0.5 × 0.5	0.5 × 0.5 × 0.5	0.5 × 0.5 × 0.5	0.5 × 0.5 × 1
Resolution for reconstruction (mm)	0.25 × 0.25 × 0.25	0.25 × 0.25 × 0.25	0.25 × 0.25 × 0.25	0.25 × 0.25 × 0.5
Bandwidth (Hz/pixel)	620	625	620	289
TR (msec)	800	2000	800	15
TE (msec)	26	36	26	3.5
Flip angle (°)	Varies	Varies	Varies	18
Echo train length	30	60	30	NA
Averages	2	2	2	1
Scan time (min:sec)	5:03	5:38	5:03	5:15

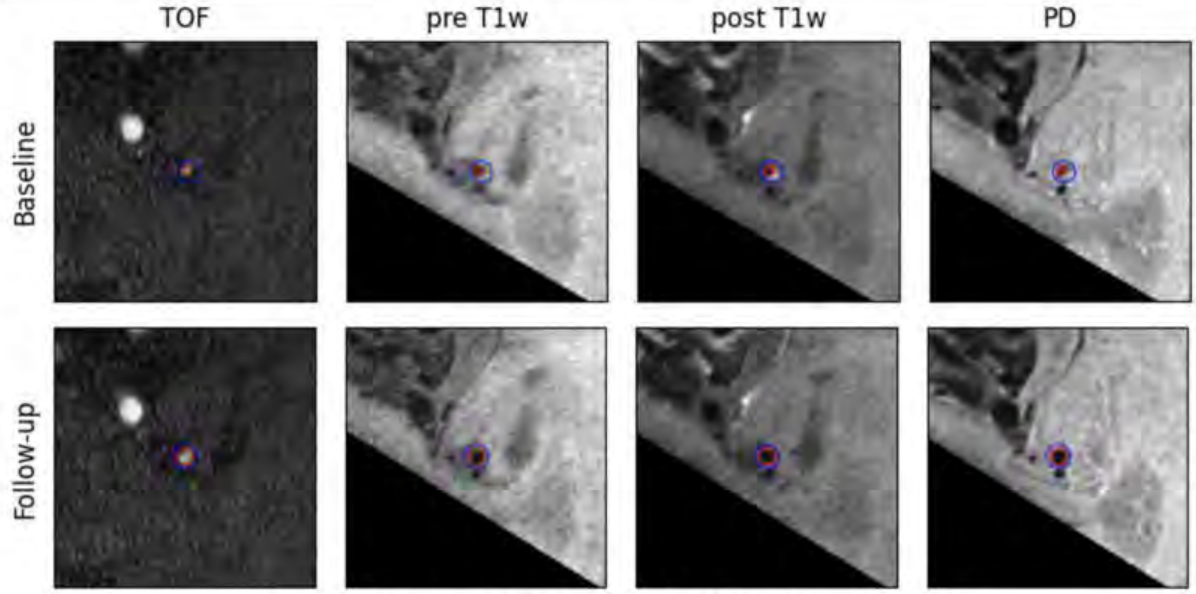

Multi-contrast cross-sections of a PCA plaque showing regression (thinning of arterial wall and expansion of lumen)

(Filename: TCT_715_ASNRFig1.jpg)

1521

Management of intracranial aneurysms in pregnant patients: U.S. national trends (2016-2020)

D Gandhi[1], M Khunte[2], S Payabvash[3], A Malhotra[4]

[1]University of Maryland School of Medicine, Baltimore, MD, [2]Yale University, New Haven, CT, [3]Yale, New Haven, CT, [4]Yale University School of Medicine, New Canaan, CT

Purpose

There is limited data regarding the frequency and outcomes of unruptured and ruptured intracranial aneurysms in pregnant patients. The impact of presence of unruptured aneurysms on mode of delivery is also poorly understood. This study explores the frequency of intracranial aneurysms and its correlation with subarachnoid hemorrhage and mode of delivery, and impact on outcomes.

Materials and Methods

Pregnancy- related hospitalizations for patients >18 years were identified from the National Inpatient Sample (NIS) for 2016 to 2020. The study cohort consisted of pregnant patients who had an unruptured intracranial aneurysm (UIA) and ruptured aneurysm/ subarachnoid hemorrhage (SAH). Treatment rates were determined and correlated with outcomes. Presence of IA was also correlated with modes of delivery. Logistic regression was used to determine impact of presence of unruptured aneurysm on rates of Caesarean section (C-section).

Results
19,426,240 pregnancy-related or postpartum hospitalizations were identified from 2016-2020, of which 93.6% were associated with labor and delivery. Subarachnoid hemorrhage was reported in 1445 hospitalization; 57.4% in antepartum and 22.5% during labor/delivery hospitalizations. 61.7% hospitalizations with unruptured aneurysm had a C-section compared to 32.3% in the overall population. Unruptured aneurysms were independently associated with higher odds of receiving C-section (OR 2.76 [95%CI 2.12 - 3.61], p<0.001). In hospitalizations with unruptured aneurysms, the average length of stay was 5.4 ± 17.0 for C-section and 2.8 ± 1.6 days for spontaneous birth.
Conclusions
The rate of subarachnoid hemorrhage in pregnant patients, especially during labor and delivery is low and may not justify higher use of C-section in patients with unruptured aneurysms.

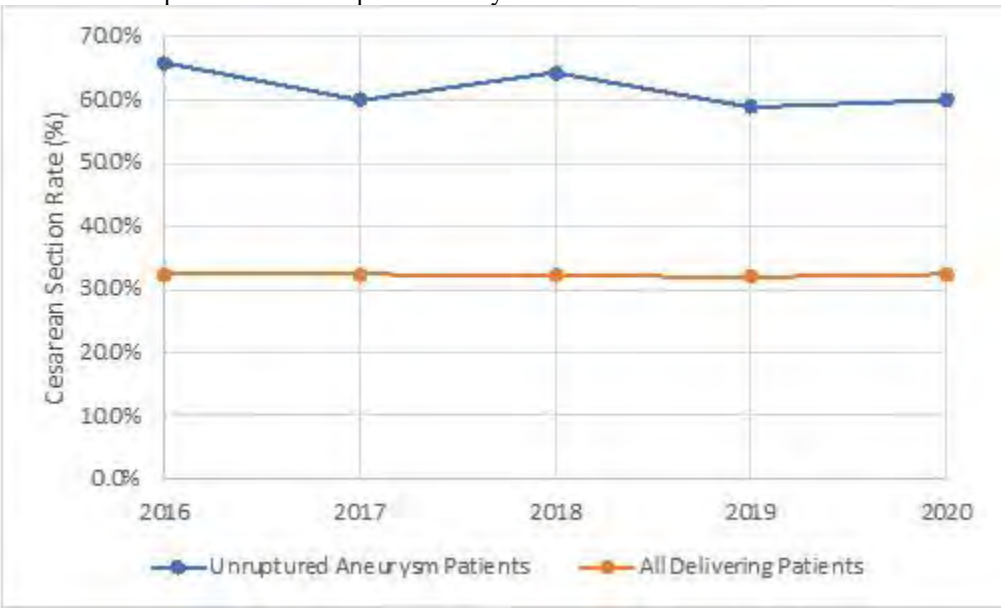

(Filename: TCT_1521_Picture1.jpg)

963
Nitrous Oxide Enhances MRI-guided Focused Ultrasound Mediated Blood Brain Barrier Opening
R Sultana[1], D Imphean[1], A Parchure[2], B Shah[3]
[1]UT southwestern, Dallas, TX, [2]UT Southwestern, Dallas, TX, [3]UT Southwestern, Irving, TX

Purpose
To investigate if the use of N2O could lower the MRI-guided focused ultrasound pressure or microbubble concentration required to open the BBB and if that in turn would improve efficacy of viral gene therapy delivery to the brain in region specific manner.
Materials and Methods
Swiss Webster mice ages 3 to 7 months were treated with MRI-guided focused ultrasound performed using either N2O (n = 20) or medical air (n = 6) as the anesthesia carrier. Hippocampus was targeted and the effect of the gas was first tested at different FUS pressures (0.39, 0.45 and 0.67 MPa) with standard microbubble dosing (20ul/Kg) then with varying conc. (standard dosing vs. dilution by a factor of 1000) while keeping the FUS pressure constant at 0.39 MPa. Further, for efficacy of viral delivery mice were treated and compared with the following conditions: N2O and MA at 0.39 MPa pressure (n=2), and medical air at 0.67 MPa (n=2). Contrast agent enhancement as well as immunofluorescent studies were performed to confirm the efficacy, specificity, and safety of viral expression in the targeted brain region.
Results
N2O improved BBB opening at all the pressures tested (for 0.39MPa at P<0.047, 0.45MPa at P<0.001 and 0.67MPa at P<0.0001 respectively) vs medical air. N2O gas also significantly meliorates the BBB opening as depicted by MRI contrast enhancement in the hippocampal region with lower dosages of microbubbles (at 2ul/kg, 0.2ul/kg and 0.02ul/kg) than medical air (at 20ul/Kg) at 0.67MPa pressure. N2O improved the delivery of viral vector vs medical air at 0.39 and 0.67 MPa pressure (at P<0.01 & P<0.03 respectively) as determined by the number of neurons transfected in the hippocampus. With the lower microbubble concentration at even lower FUS pressures, Nitrous oxide significantly reduced the damage at the targeted site as determined by lack of microgliosis and astrocytosis vs. medical air group.
Conclusions
Nitrous oxide significantly improved blood-brain barrier opening and viral gene therapy delivery with MRI-guided focused ultrasound at lower microbubble concentrations as well as lower FUS pressures compared to medical air. Our findings may help overcome limitations of injury and toxicity due to higher focused ultrasound pressures. This method has the potential to revolutionize FUS blood brain barrier applications in humans.

265

Revascularization Improves Vascular Hemodynamics in Moyamoya Patients

M Zhao[1], R Armindo[1], M Moseley[1], E Tong[1], G Steinberg[1], G Zaharchuk[1]
[1]*Stanford University, Stanford, CA*

Purpose

Cerebrovascular reserve (CVR) reflects the capacity of cerebral blood flow (CBF) to change [1]. Decreased CVR implies poor hemodynamics and is linked to a higher risk for stroke [2]. Revascularization has been shown to improve CBF in patients with vasculopathy such as Moyamoya disease [3]. Arterial spin labeling (ASL) is a non-invasive technique for CBF, CVR, and arterial transit time (ATT) measurements [4]. Here, we investigate the change in hemodynamics 4-12 months after STA-MCA direct bypass in 52 Moyamoya patients using ASL with single and multiple post-labeling delays.

Materials and Methods

Images were collected using 3T MRI systems (Discovery MR 750, GE Healthcare, Waukesha, WI, USA) a week before and 4-12 months after the patient's bypass surgery. During each imaging session, Diamox was administered to induce vasodilation. Single- and multi-delay (5 delays) ASL data were collected before and 15 minutes after the administration of Diamox. The scanning parameters were identical with our previous study [2]. CVR, CBF, ATT were measured in different flow territories. Two-tailed paired t-tests were conducted to compare the mean values of CVR, CBF, and ATT before and after revascularization in regions affected by vasculopathy under the null hypothesis that the value of these parameters was the same.

Results

Figure 1 shows the changes in CVR and CBF after bypass surgeries within the regions affected by vasculopathy. CVR in the affected regions increased significantly (by 16±11% and 25±13% [both $p<0.01$] for single- and multi-PLD PCASL) after bypass surgeries. A similar trend was observed in ΔCBF after vasodilation, whereby a significant increase (by 13±10% and 19±12% [both $p<0.01$] for single- and multi-PLD PCASL) can be found after bypass, as shown in Figure 1B. In terms of the CBF measurements, revascularization caused CBF to increase before and after vasodilation, as shown in Figure 1C. Revascularization caused ATT to reduce significantly by 11±7% ($p<0.01$) and 13±7% ($p<0.01$) pre- and post-vasodilation, respectively (not shown in Figure 1).

Conclusions

We demonstrated that revascularization improved hemodynamic parameters significantly in regions previously affected by vasculopathy and multi-PLD PCASL achieved a higher effect size in measuring these parameters than single-PLD PCASL. ASL could be an effective non-invasive modality to evaluate the vascular hemodynamic changes in longitudinal studies based on its strength in evaluating both perfusion and transit time directly and quantitatively.

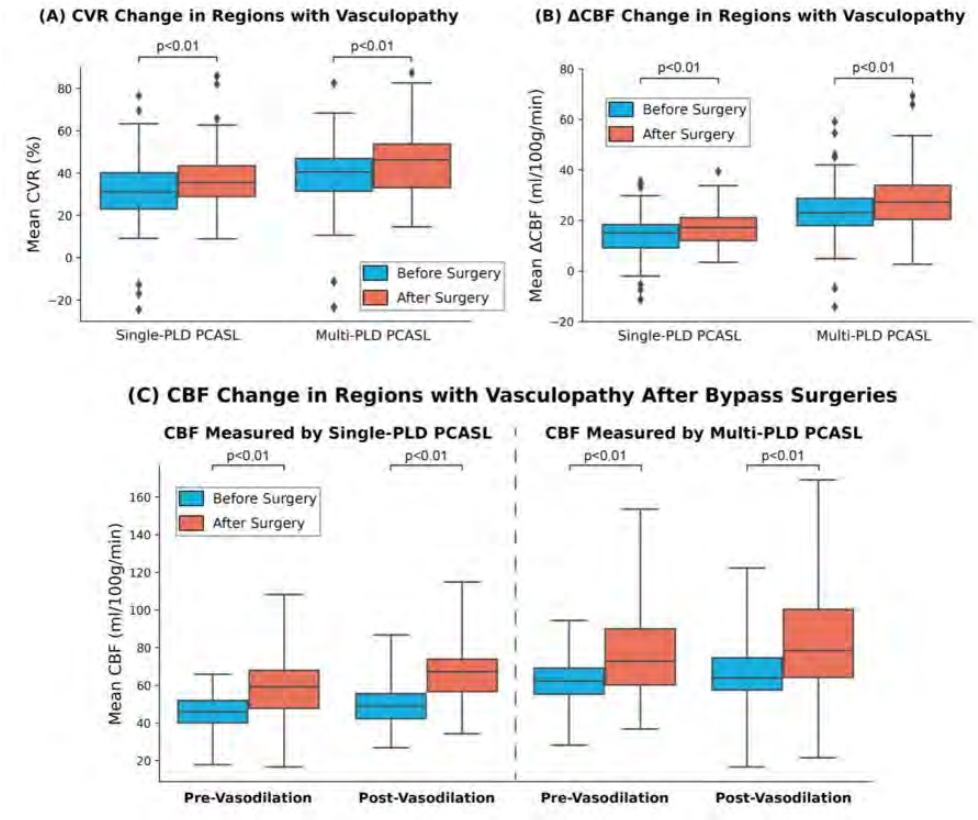

(Filename: TCT_265_Picture1.jpg)

Tuesday, May 2, 2023

10:45 AM-12:00 PM

Imaging Genomics & Radiomics Study Group Programming: Moving from Translation to Clinical Practice

514

Using Radiomics as a Computer-assisted Tool to Predict 1p/19q Co-deletion in Patients with IDH-1 Mutant Glioma: Added Value to the T2-FLAIR Mismatch Sign

S KIHIRA[1], E Tavakkol[1], A Derakhshani[1], M Leung[2], K Mahmoudi[1], A Bauer[3], H Zhang[1], J Polson[1], C Arnold[1], N Tsankova[4], A Hormigo[5], B Salehi[6], N Pham[7], B Ellingson[8], T Cloughesy[9], K Nael[1]

[1]UCLA, Los Angeles, CA, [2]University of California, Los Angeleles, Los Angeles, CA, [3]Kaiser Permanente, Fontana, CA, [4]Icahn School of Medicine at Mount Sinai, New York, NY, [5]Albert Einstein College of Medicine, Bronx, NY, [6]UCLA, Los angeles, CA, [7]Stanford, Palo Alto, CA, [8]University of California, Los Angeles, Los Angeles, CA, [9]University of California, Los Angeles, 90095, CA

Purpose

The T2-FLAIR mismatch sign has shown promise in determining IDH-mutant 1p/19q non-co-deleted gliomas with a high specificity and modest sensitivity (1). We aim to develop a multi-parametric radiomic model using MRI to predict 1p/19q co-deletion status in patients with newly diagnosed IDH-1 mutant glioma and to assess it's utility as a computer-assisted tool in determining T2-FLAIR mismatch sign.

Materials and Methods

In this retrospective study, patients with diagnosis of IDH-1 mutant gliomas with known 1p/19q status who had preoperative MRI were included. T2-FLAIR mismatch was evaluated independently by two board certified neuroradiologists. Texture features were extracted from glioma segmentation of FLAIR images. eXtremeGradient Boosting (XGboost) classifiers were used for model development. This model was then used to aid radiologist in determining presence of T2-FLAIR mismatch sign in equivocal cases.

Results

A total of 103 patients included for model development and 18 patients for external testing validation. The diagnostic performance (sensitivity/specificity/accuracy) in determination of 1p/19q codeletion status were 59%/83%/67% (training) and 62.5%/70.0%/66.3% (testing) for T2-FLAIR mismatch sign. This was significantly improved (p=0.04) using the radiomics model to 77.9%/82.8%/80.3% (training) and 87.5%/89.9%/88.8% (testing), respectively. Addition of radiomics as a computer-assisted tool resulted in significant (p=0.02) improvement in performance of neuroradiologist with 13 additional corrected cases in comparison to just using T2-FLAIR mismatch sign. (Figure)

Conclusions

The proposed radiomic model provides much needed sensitivity to the highly specific T2-FLAIR mismatch sign in determination of 1p/19q non-co-deletion status and improves overall diagnostic performance of neuroradiologists when used as an assisted tool.

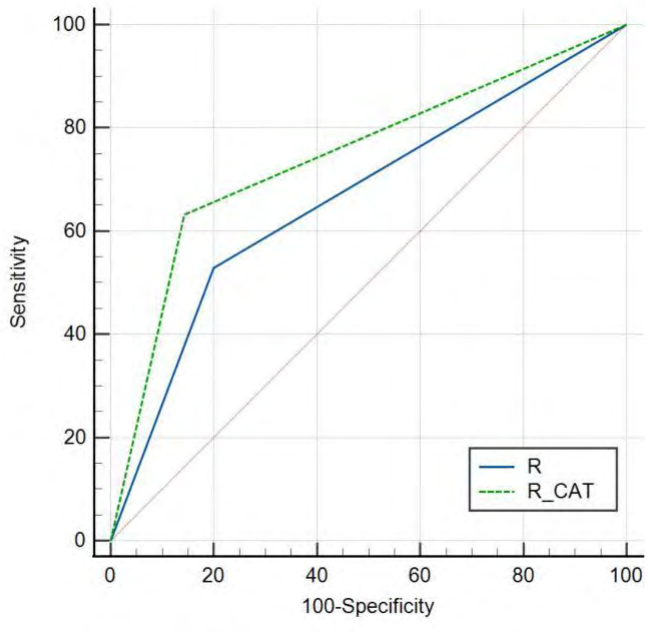

(Filename: TCT_514_ROC-R1vsR-CAT1.jpg)

Tuesday, May 2, 2023

10:45 AM-12:00 PM

Scientific Abstract Session: AI & Imaging Methods 1

161

A Deep Learning Approach for Automated Bone Removal from Computed Tomography Angiography of the Brain

M Isikbay[1], M Caton[2], E Calabrese[3]

[1]University of California, San Francisco, San Francisco, CA, [2]Mount Sinai Health System (Dept of Neurosurgery), New York, NY, [3]Duke University, Durham, NC

Purpose

Advanced visualization techniques such as maximum intensity projection (MIP) and volume rendering (VR) are useful for evaluating neurovascular anatomy on CT angiography (CTA) of the brain; however, interference from surrounding osseous anatomy is common. Existing methods for bone removal from CTA images to improve neurovascular visualization are hindered by poor performance at the skull base and/or in the presence of vascular pathology and postoperative findings. We present a new deep learning-based bone removal method, which addresses many of the limitations of existing bone removal methods.

Materials and Methods

A deep convolutional neural network was designed and trained for bone removal using 72 brain CTAs with a variety of neurovascular pathologies (aneurysms, hemorrhage, occlusions) and/or prior intracranial interventions (craniotomy, endovascular coiling, ventriculostomy catheters). The model was tested on 15 CTAs from the same data source and 17 CTAs from an independent external dataset. Bone removal accuracy was assessed quantitatively, by comparing automated segmentation results to manual segmentations using the Dice overlap coefficient, and qualitatively by evaluating VR visualization of the carotid siphons compared to a freely available method for automated bone removal.

Results

Average Dice overlap between automated and manual segmentations from the internal and external test datasets were 0.986 and 0.979, respectively. The proposed method yielded better VR visualization of the carotid siphons compared to the publicly available bone removal tool in 14 out of 15 CTAs (93%) from the internal test set and 15 out of 17 CTAs (88%) from the external test set. Visualization was equivalent between methods for the remaining cases. In addition, bone removal allowed subjectively superior MIP and VR visualization of vascular anatomy/pathology including in the presence of prior intracranial intervention.

Conclusions

The proposed brain CTA bone removal algorithm is rapid, accurate, and allows superior visualization of vascular anatomy and pathology compared to other available techniques Model performance was similar when evaluated on an independent external dataset suggesting that this method can be generalized to other CTA data sources.

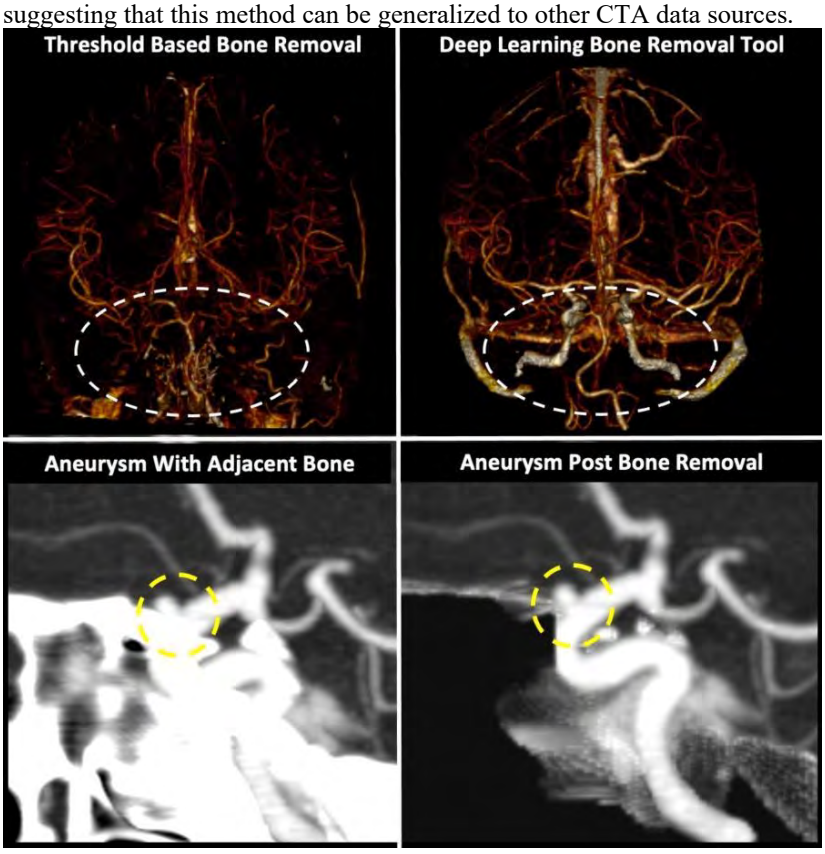

(Filename: TCT_161_ASNRFigure.jpg)

941

AI-Enhanced, Comprehensive, Quiet MR Neuroimaging

F Wiesinger[1], S mandava[2], X Wang[3], R Lebel[4], D Lythgoe[5], T Wood[5], M Bowdler[5], S Williams[5], A Solana[1]

[1]GE HealthCare, Munich, Germany, [2]GE HealthCare, Atlanta, GA, [3]GE HealthCare, Houston, TX, [4]GE HealthCare, Calgary, Alberta, [5]King's College London, London, UK

Purpose

Loud acoustic noise continues to be a fundamental limitation of MRI especially in case of hyperacusis subjects where it can lead to distress, anxiety, patient motion, or scan abortion. Even though silent and/or acoustic noise reduced MR scanning solutions exist and are commercially available [1,2], their clinical usage is still limited, primarily because of incomplete contrast coverage and/or trade-offs in terms of scan efficiency. Here, we present a quiet neuroimaging solution comprising standard anatomical scans [1,2], quantitative parameter mapping [3,4], and functional BOLD fMRI [4]; including optional DL-based image reconstruction [5].

Materials and Methods

The comprehensive, quiet neuroimaging encompasses several type of pulse sequences, including: 1) 3D ZTE (i.e., localizer, T1w-MPRAGE, MRA), 2) 2D Cartesian FSE (i.e., T2w, T2w-FLAIR, T1w-FLAIR), 3) 2D motion-robust PROPELLER FSE (i.e., Diffusion, T2w-FLAIR), 4) 3D ZTE-based quantitative Parameter Mapping (PD, T1, T2), 5) high-resolution Looping Star for structural T2* and susceptibility-weighted imaging (SWI), and 6) Looping Star BOLD fMRI. While ZTE-based pulse sequences (including Looping Star) are intrinsically silent, ART (Acoustic Reduction Technique based on gradient deration) was used for the 2D FSE-based methods. Healthy volunteer testing was performed on a GE 3T MR750w scanner using an 8-channel brain coil. 2D FSE (Cartesian and PROPELLER), and 3D ZTE acquisitions were processed using both standard and AIR Recon DL-based image reconstruction (GE Healthcare, Chicago, IL). Acoustic noise measurements were performed using a Bruel&Kjær (Nærum, Denmark) integrated sound level meter and microphone.

Results

The figure illustrates an exemplary quiet neuroimaging examination in a healthy volunteer including the localizer, structural scans (i.e., T1w-MPRAGE, T2w-FSE, T2w-FLAIR, MRA), PROPELLER Diffusion, quantitative parameter mapping (ADC, T2*, QSM, PD, T1, T2), as well as Looping Star BOLD fMRI using a visual checkerboard activation. AIR Recon DL improved overall image quality by denoising and sharpening the images. The complete neuroimaging examination (including prescan) was acquired at <100dBA (LAeq) in an ambient noise environment of ~67 dBA (LAeq) and was reported comfortable by all study participants.

Conclusions

In summary, quiet comprehensive MR neuroimaging appears well within reach but requires further clinical efforts to translate its benefits to patients and thereby further enhance the value and applicability of MR neuroimaging.

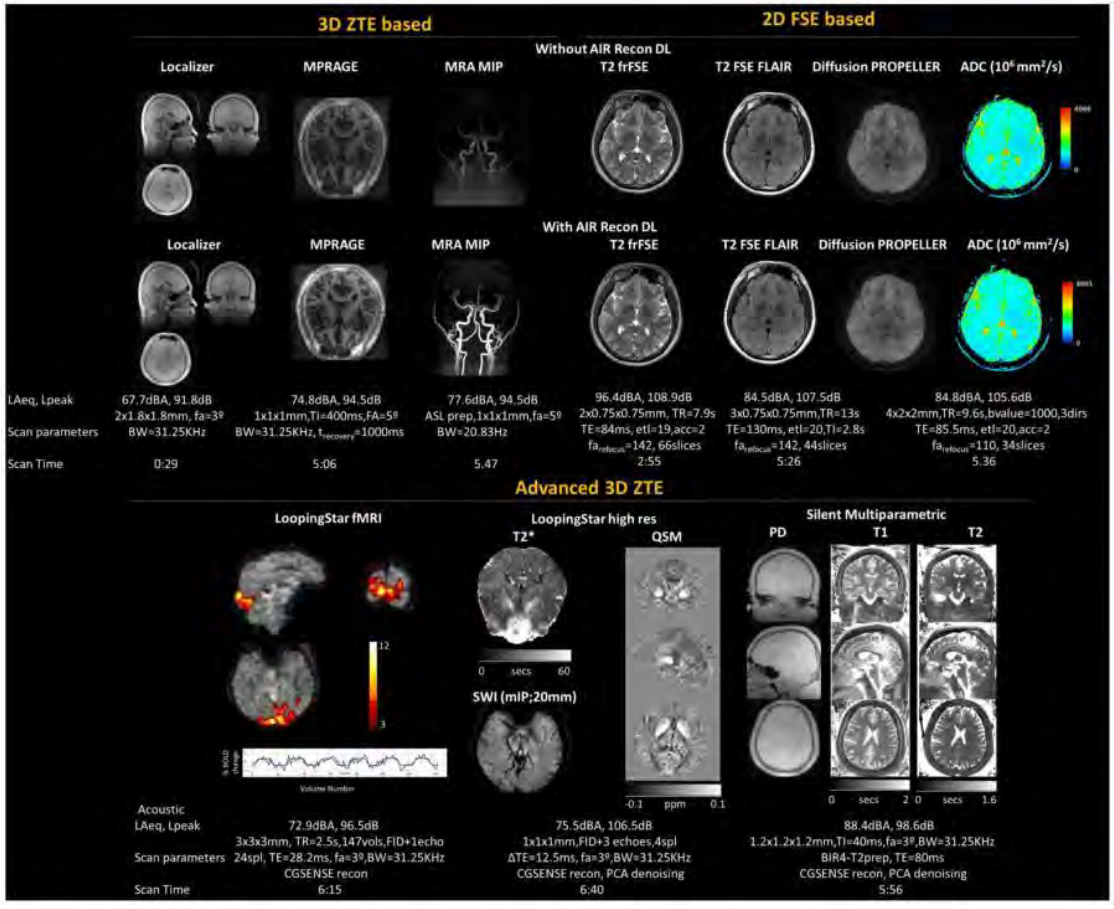

(Filename: TCT_941_FIG1_ASNR_Abstract.jpg)

1370

Benefits of Deep Learning-based Image Reconstruction in 3D Brain MRI – A Clinical Study at 3T

D Shin[1], E Calabrese[2], S Banerjee[1], R Lebel[3], S Kaushik[4], Y Liu[4], J Villanueva-Meyer[5]

[1]GE Healthcare, Menlo Park, CA, [2]Duke University, Durham, NC, [3]GE Healthcare, Calgary, Alberta, [4]GE Healthcare, Waukesha, WI, [5]University of California San Francisco, San Francisco, CA

Purpose

AIR Recon DL, a deep learning-based image reconstruction (DL Recon) has previously been shown to increase SNR efficiency and enhance resolution in 2D acquisitions of various contrast weightings across anatomies including neuroimaging applications [1,2]. In this work, we investigate the benefits of extending the DL Recon algorithm applied on routine 3D clinical brain MR images of various contrast weightings. Apparent SNR, lesion conspicuity for visualization of pathology, and overall image quality were assessed by neuroradiologists.

Materials and Methods

DL Recon used in our study is a deep convolutional residual encoder network trained to reconstruct images from raw complex MR data with reduced noise, reduced Gibbs ringing, and enhanced resolution [3]. MR complex data from 3D acquisitions in 44 cases (Females/Males=27/17, Mean age=59.3yr) were retrospectively reconstructed with DL Recon using 75% denoising level, and compared to images obtained with conventional reconstruction. Images of the brain were randomly sampled over a 4-week period from three clinical scanners (2 Discovery MR750s, 1 SIGNA Premier, GE Healthcare, Waukesha, WI) with various coil configurations. The reviewed cases (n=44) were acquired using 5 different 3D sequences, i.e., CUBE T2/T2 FLAIR (n=17), CUBE T1 (n=2), MPRAGE (n=15), black blood T1 for vessel wall imaging (n=7), and FIESTA (n=3). Two neuroradiologists performed a consensus review of the conventional and DL Recon with regards to Apparent SNR, lesion conspicuity (when pathology was present), and overall image quality on a 5-point Likert scale. Score differences between conventional and DL Recon images were assessed using paired t-test with statistical threshold set at $p<0.01$.

Results

Both raters assigned significantly higher scores on the DL reconstructed images for all three metrics, i.e., apparent SNR, lesion conspicuity for visualization of pathology, and overall image quality evaluated on the routine clinical images. The detailed scores are summarized in Table 1. Fig. 1 shows four pairs (conventional vs. AIR Recon DL) of representative clinical cases with different pathologies and varying image contrasts.

Conclusions

This work demonstrates the clinical benefit of using DL Recon on existing 3D neuro imaging protocols. Future work will include evaluation of this method on optimized highly accelerated 3D brain protocols to allow greater patient comfort and throughput as well as evaluation of diagnostic accuracy in DL versus standard reconstruction images.

	Rater 1		Rater 2	
	DL-	DL+	DL-	DL+
Apparent SNR	2.73 ± 0.54	3.73 ± 0.59*	2.93 ± 0.63	4.14 ± 0.63*
Lesion Conspicuity	3.09 ± 0.38	3.68 ± 0.63*	3.12 ± 0.48	3.70 ± 0.59*
Overall Image Quality	3.00 ± 0.43	3.75 ± 0.58*	3.00 ± 0.61	3.80 ± 0.70*

Table 1. Rater scores (mean ± SD) without and with AIR Recon DL; * denotes statistical significance based on paired t-test ($p<0.01$).

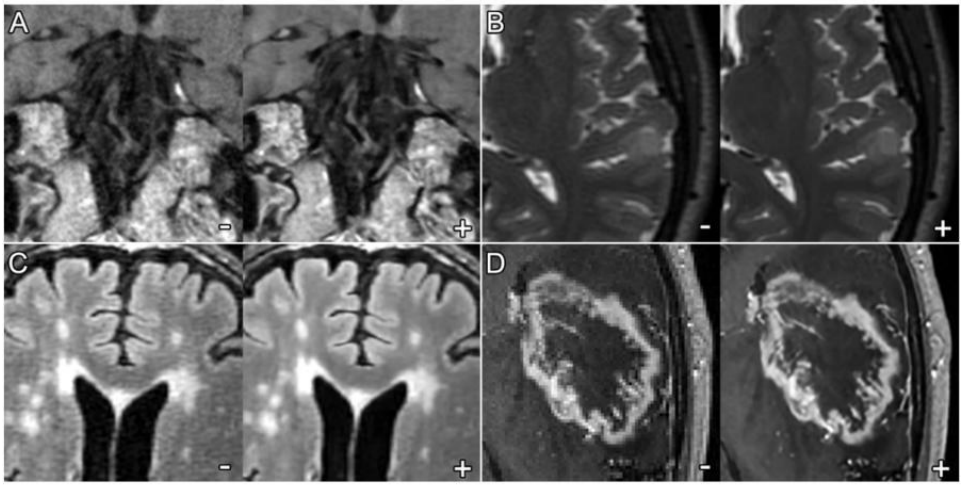

Figure 1. Side-by-side comparison of brain pathology using conventional (-) versus AIR recon DL (+) reconstruction of 3D MRI data acquired using 4 different sequences: (A) coronal T1 black-blood postcontrast (arterial wall imaging) of a patient with diffuse atherosclerotic vasculopathy of the basilar artery; (B) axial T2 fat saturated imaging of a patient with a non-enhancing cortically based tumor in the left posterior temporal lobe; (C) axial T2 FLAIR imaging of a patient with leukoaraiosis; (D) axial T1 fast gradient echo postcontrast imaging of a patient with a left frontoparietal glioblastoma.

(Filename: TCT_1370_FIG.jpg)

1319

Diagnostic evaluation of a deep learning accelerated lumbar spine MRI protocol

K Awan[1], A Tabari[2], B Applewhite[3], M Lang[1], W Lo[4], P Kollasch[5], R Sellers[6], B Clifford[7], S Cauley[1], P Schaefer[1], S Huang[8], J Conklin[1]

[1]Massachusetts General Hospital, Boston, MA, [2]Massachusetts general hospital, Boston, MA, [3]N/A, N/A, [4]Siemens Medical Solutions, Charlestown, MA, [5]Siemens Medical Solutions, Minnetonka, MN, [6]Siemens Medical Solutions, Pottstown , PA, [7]Siemens Medical Solutions, USA, Boston, MA, [8]Massachusetts General Hospital, Harvard Medical, Boston, MA

Purpose

To evaluate image quality and diagnostic performance of deep learning (DL) accelerated lumbar spine MRI compared to a conventional lumbar spine MRI protocol.

Materials and Methods

Patients undergoing non-contrast lumbar spine MRI were enrolled and imaged on a 3T MRI scanner (MAGNETOM Vida, Siemens) using a standard protocol (10 min 82 sec) and an accelerated protocol using a research deep learning-enabled reconstruction (4 min 70 sec). Both protocols included sagittal T1, T2 and STIR, and axial T2 weighted images. The deep learning reconstruction used an unrolled neural network [1] to mitigate noise and residual artifacts usually associated with high acceleration. Two blinded neuroradiologists with 3 & 5 years of experience reviewed all images for diagnostic performance and image quality. For diagnostic performance, they assessed foraminal stenosis, spinal canal stenosis, nerve root compression, and facet arthropathy using previously published grading scales. For image quality, they used a 5-point Likert scale to evaluate artifacts, SNR, visualization of anatomic structures, and overall diagnostic quality. Interrater agreement for diagnostic variables was evaluated using quadratically weighted Cohen's kappa. Categorical image quality variables were compared using the Wilcoxon signed rank test. ICCs were calculated to evaluate interobserver reproducibility. Disagreements between raters were adjudicated by a third neuroradiologist with >10 years of experience.

Results

36 patients were included (mean age 58±19 years; F:M 17:19). Indications for MRI were: low back pain with neurologic deficit or radiculopathy (n=19), low back pain with radiculopathy (n=13), low back pain without radiculopathy (n=15), and bone lesions (n= 2). Inter-observer reproducibility for all of the rated variables ranged from moderate to substantial (κ= 0.50-0.76). The two neuroradiologists rated the conventional protocol as superior for both SNR (97%) and artifacts (61%), and equivalent to the deep learning enabled reconstruction for overall diagnostic quality (97%).

Conclusions

Deep learning reconstruction in spine imaging can reduce the acquisition time and enable comparable diagnostic results to conventional spine MRI, with mild increases in image noise and image artifacts.

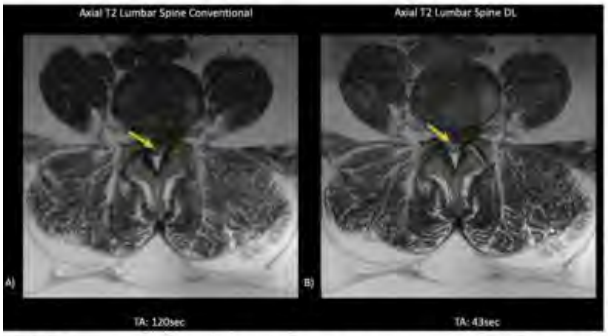

Fig 1. Axial images of a 43-year-old female with acute onset back pain with radiation. Both raters rated severe spinal canal stenosis. **(A)** Conventional **(B)** DL-Recon

Fig 2. Sagittal images of a 52-year-old female with lumbar radiculopathy showing shadowing artifacts on DL sequence. **(A)** Conventional **(B)** DL

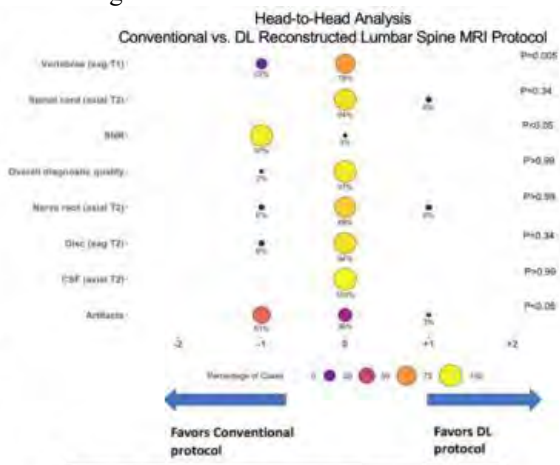

Fig 3. Balloon plot showing the results of the head-to-head comparison of conventional and DL sequences for visualization of nerve-root, disc, vertebrae, CSF, spinal cord, presence of artifacts, signal to noise ratio and the overall diagnostic quality by both raters. A zero-score indicates equivalency, negative scores (left) favors the conventional protocol, and positive scores (right) favor DL reconstructed lumbar spine.

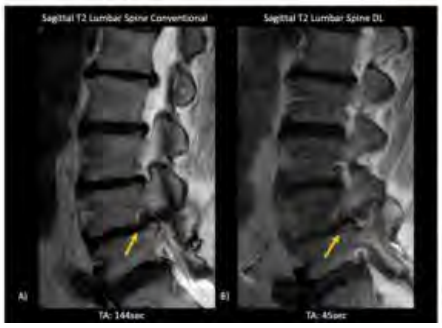

Fig 4. Sagittal images of evaluated left L4-L5 neural foraminal narrowing as severe on conventional **(A)** and on DL **(B)**. No high-grade spinal canal stenosis was present.

(Filename: TCT_1319_DL_figsub.jpg)

102

DICOM-based Deep Learning Generated Synthetic STIR Spine Images are Interchangeable with and Offer Better Quality than Conventional STIR MR Scans.

L Tanenbaum[1], S Bash[2], L Wang[3], A Shankaranarayanan[4], C Beaulieu[5], M Wintermark[6], M Novick[7], G Zaharchuk[8]

[1]RadNet, Riverside, CT, [2]RadNet, Woodland Hills, CA, [3]Subtle Medical, Menlo park, CA, [4]Subtle Medical Inc, Menlo Park, CA, [5]Stanford University, Palo Alto, CA, [6]Stanford, Stanford, CA, [7]All American Teleradiology, Bay Village, OH, [8]Stanford University, Stanford, CA

Purpose

Deep learning (DL) image reconstruction has the ability to allow faster MR acquisitions while matching or exceeding standard of care (SOC) quality. DL can also be used to create synthetic images from existing data sets. This retrospective, multicenter, multi-reader study was designed to evaluate the performance of synthetically created STIR images compared to standard of care STIR images of the spine.

Materials and Methods

With IRB approval and patient consent, 80 retrospective spine MR studies (sagittal T1, T2, STIR) were randomly selected from a multi-center, multi-scanner database of 200 cases classified into five categories of disease and normal by an experienced Neuroradiologist who did not participate as a reader. A DL, DICOM-based AI application trained on multi-vendor, multi-field strength MR data was then used to create a synthetic STIR data (Syn-STIR) set for each of the studies using the acquired Sag T1 and T2. Five experienced radiologists (3 neuroradiologists, 1 MSK radiologist, and 1 generalist) were presented with 160 data sets in a blinded and randomized fashion, consisting of acquired T1 and T2 and either acquired STIR (Acq-STIR) or Syn-STIR (480 series). Each reader classified the pathologies present and individually rated all STIR image quality on a 5-point Likert scale.

Results

A two-way model ICC analysis demonstrated that the decrease in inter-reader agreement expected by randomly introducing AI-generated STIR images was 0.94% (CI [-3.53, 5.22]), which indicates that AI-generated STIR images are significantly interchangeable with traditional STIR images. In addition, a Wilcoxon signed-rank test showed a significantly higher median IQ score for AI-generated STIR images compared to traditional STIR images (median difference = 0; $P < 0.0001$), and a t-test was also performed on the paired difference between IQ scores for AI-generated versus traditional STIR images, and this showed a significantly higher mean IQ score for AI-generated STIR images compared to traditional STIR images (average paired difference = 0.37, 95% CI [0.25, 0.49], $P < 0.0001$). The distribution of differences in IQ score across AI-generated and traditional STIR images is presented below.

Conclusions

DL generated synthetic STIR spine MR images were interchangeable with the conventionally acquired STIR, while providing significantly higher image quality, suggesting the potential for routine clinical practice utility.

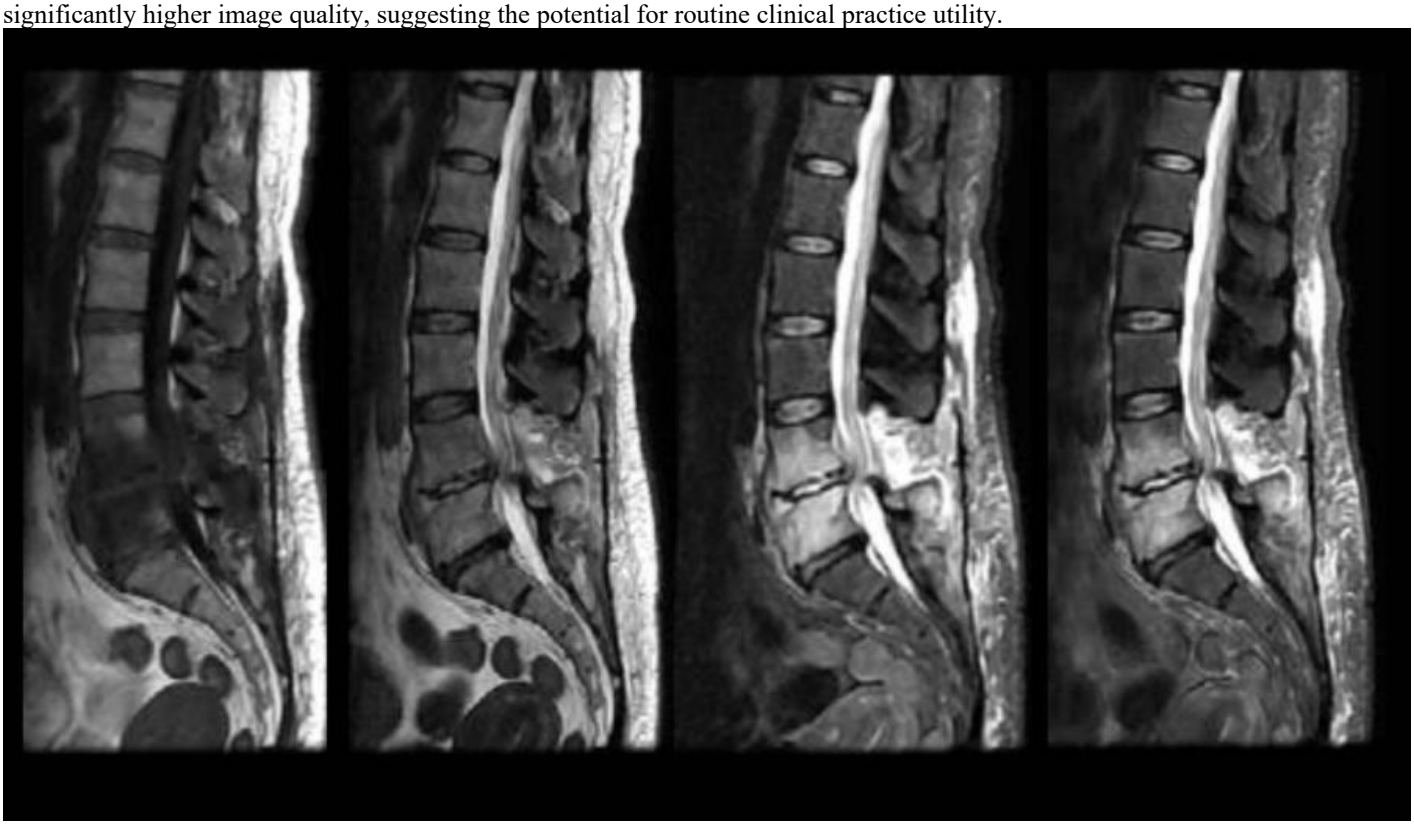

(Filename: TCT_102_nontraumaimage.jpg)

1325

Evaluation of Deep Learning Enhanced CAIPI Accelerated Contrast-Enhanced 3D T1 SPACE Compared to Standard 3D T1 SPACE for Neurovascular Imaging

Z Zhou[1], R Chamberlain[1], A Shankaranarayanan[1], M Mossa-Basha[2]

[1]Subtle Medical Inc, Menlo Park, CA, [2]University of Washington, Seattle, WA; University of North Carolina-Chapel Hill, Chapel Hill, NC

Purpose

Contrast-enhanced (CE) T1-weighted (T1w) intracranial vessel wall MRI (IVW) has mainly relied on 3D variable-refocusing flip-angle sequences, including T1-SPACE for evaluation of inflammatory changes of the arterial wall[1,2]. Accelerated CE 3D T1w SPACE enables high-resolution rapid whole-brain screening, but the image quality can be degraded with amplified noise/artifacts. In this work, a deep learning (DL) based image enhancement method is investigated to retrospectively enhance the CAIPI accelerated CE T1w SPACE images for noise suppression, and the diagnostic image quality is compared across the DL-enhanced, source CAIPI and fully sampled CE T1w SPACE.

Materials and Methods

MR Scans and Image Enhancement T1w SPACE scans with and without CAIPI acceleration (standard of care, SOC) were acquired sequentially after the contrast injection on a Siemens 3T scanner from 43 patients with informed consent. The major scan parameters include TR/TE=1000/11 ms, resolution=0.56x0.56x0.56 mm3, FOV=180x180x134 mm3, scan time without/with CAIPI = 8:08/5:11. CAIPI SPACE also used DANTE[3] for improved flow suppression[4]. CAIPI SPACE was processed by SubtleMR (Subtle Medical Inc) for DL based image enhancement (CAIPI+SMR). SubtleMR is a convolutional neural network trained on a separate MR dataset. To adapt for spatially variant noise reduction, the DL model was trained on image patches with augmentation of different noise levels. Image Analysis Image quality was qualitatively reviewed and compared across CAIPI, CAIPI+SMR and SOC. For each case, image quality was scored with four scales (Table notes) for overall quality, SNR, artifacts, flow suppression and lesion detection.

Results

Figure (A) illustrates an example of comparison across CAIPI, CAIPI+SMR, and SOC, where CAIPI+SMR image shows effective suppression of spatially variant noise particularly in the central brain region. Figure (B)/(C) shows the preference of overall image quality between CAIPI/CAIPI+SMR and SOC. SubtleMR largely reduces the number of cases with lower quality than SOC, and 90% of CAIPI+SMR cases can achieve similar or superior image quality compared to SOC. Detailed quality scores are summarized in the Table, which also demonstrates the improved quality of CAIPI+SMR.

Conclusions

DL enhanced CAIPI CE 3D T1 SPACE can effectively reduce the noise amplification and achieve similar diagnostic quality compared to SOC, which better serves the rapid neurovascular imaging without quality degradation.

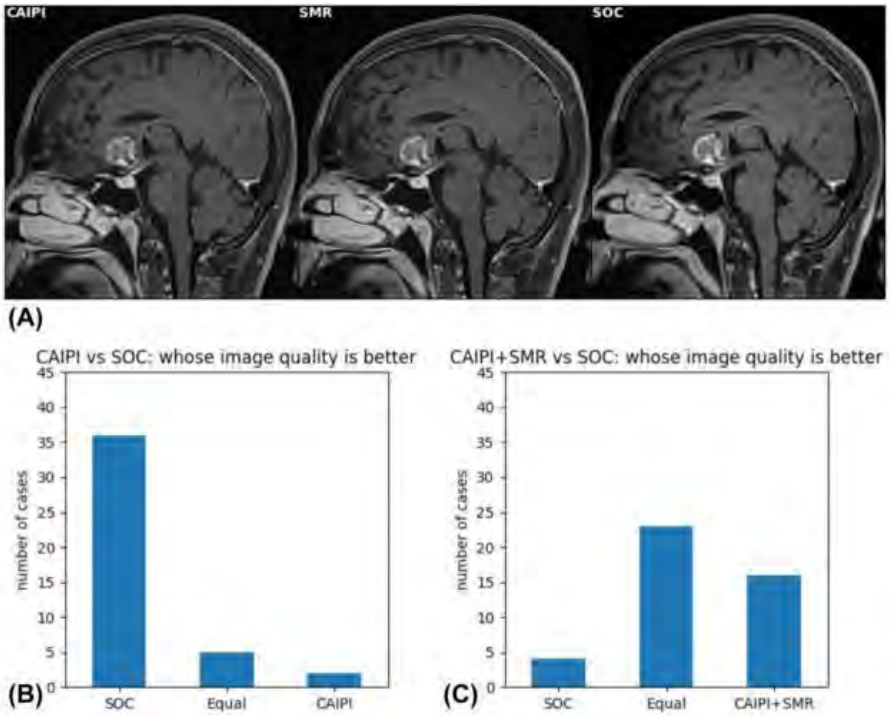

Figure: Image quality comparison of CAIPI, SubtleMR enhanced CAIPI (CAIPI+SMR) and standard of care (SOC) T1 SPACE. (A) Example image comparison of CAIPI, CAIPI+SMR, and SOC contrast-enhanced T1 SPACE images from another clinical case with enhanced lesion in the brain. (B) Image quality comparison between CAIPI and SOC T1 SPACE. (C) Image quality comparison between CAIPI+SMR and SOC T1 SPACE.

Table: Summary of image quality scores[a] on CAIPI, CAIPI+SMR, SOC T1 SPACE

T1 SPACE	Image quality	SNR[b]	Artifacts	Blood suppression	Lesion assessment[c]	Venous suppression
CAIPI	3.00 (2.00 - 3.00)	2.50 (2.00 - 3.00)	3.00 (2.25 - 3.75)	1.00 (1.00 - 1.00)	2.00 (1.25 - 2.00)	1.00 (1.00 - 1.00)
CAIPI+SMR	2.00 (1.25 - 3.00)	2.00 (1.25 - 2.00)	2.00 (1.25 - 3.00)	1.00 (1.00 - 1.00)	1.00 (1.00 - 2.00)	1.00 (1.00 - 1.00)
SOC	2.00 (1.25 - 2.00)	1.50 (1.00 - 2.00)	2.50 (2.00 - 3.00)	2.00 (2.00 - 2.00)	1.00 (1.00 - 2.00)	2.00 (2.00 - 2.75)

[a]Scores: 1- optimal quality; 2- minimally limited; 3- limited but interpretable; 4- non-diagnostic. Median and interquartile range of scores are provided.
[b]SNR: evaluation in the artery and perivascular region
[c]Lesion assessment: detection for arterial wall abnormalities

(Filename: TCT_1325_SMR_ASNR231.jpg)

1259

Evaluation of Deep Learning-based Reconstruction for Qualitative and Quantitative DW-MRI in Head and Neck Cancers

J Shin[1], R Paudyal[2], A Konar[2], N Bagchi[3], M Fung[1], A Shukla-Dave[2], S Banerjee[4]
[1]GE Healthcare, New York, NY, [2]Memorial Sloan Kettering Cancer Center, New York, NY, [3]Sidney Kimmel Medical College at Thomas Jefferson University, Philadelphia, PA, [4]GE Healthcare, Menlo Park, CA

Purpose

Diffusion-weighted (DW)-MRI has been used for tumor characterization and treatment response assessment in the head and neck (HN) region [1] but is challenged by susceptibility induced artifacts and low signal-to-noise ratio (SNR). A vendor-developed deep learning (DL)-based reconstruction (Recon) method [2], AIRTM Recon DL, has shown promise in enhancing the image signal-to-noise ratio (SNR) and sharpness in pituitary and prostate cancer patients. The present study is the first to evaluate its performance in multiple b-value DW-MRI for tumors in the Head and Neck (HN) region.

Materials and Methods

MRI data was acquired on a 3TR MRI scanner (SIGNA Premier, GE Healthcare) from six male, HN cancer patients) (median age 59 years, 2 HPV (+) positive, 1 HPV (-), and 3 with unknown primary tumor status) who then underwent chemo-radiation therapy (CRT) in this retrospective study. MRI protocol consisted of T1/T2 weighted imaging and multi-b-value diffusion (FOV=20-24 cm, matrix=128×128, slices=8-10, slice thickness=5mm, 2 averages, b=0,20,50,80,200,300,500,1000,1500,2000 s/mm2) at pre-treatment. The raw data from the DW-MRI scans were retro-reconstructed using the AIR Recon DL method in the GE reconstruction pipeline

(GE Healthcare) and labeled as DL recon DW images. The primary tumors and neck nodal metastases were delineated by an experienced neuroradiologist on DL-Recon (b = 0 s/mm2) images using ITKSNAP. Data analysis was performed using the MRI-QAMPER tool [3]. DW images with and without DL recon were compared using the Wilcoxon signed rank test (WSRT) for overall qualitative rating on Likert scale, as well as for SNR and percent change in ADC in a total of 10 tumor ROIs (i.e., 4 primary lesions and 6 metastatic nodes) in the six HN patients.

Results

For b=1000 s/mm2, DL recon DW images were rated at higher scores than those without DL (4.2± 0.4 vs. 3.7±0,5, P= 0.1) (Figure 2 and Table 1). The DL recon method improved overall SNR by 50% (143.0 vs. 71.0, P = 0.002, for b= 0 s/mm2) and 45% (63.0 vs. 34.0, P = 0.048, for b= 1000 s/mm2), compared to those without, the ROIs size ranging between 21- 81 mm2. Mean ADC values with and without DL for tumors in the HN region were not significantly different (P>0.05, Table 2).

Conclusions

The results suggest that DL recon on DW images improved the image sharpness, allowing better tumor delineation at a higher b-value and, after validation, could be included in the HN imaging workflow.

Figure 1. Representative DW images and ADC maps with and without DL-Recon. Exhibiting Bilateral metastatic nodes in nasopharyngeal cancer patient (40 years, male).

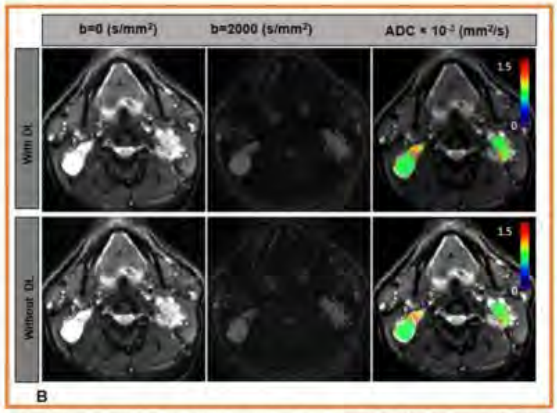

Figure 2. Bar plot showing the image rating score from six patients' DW images with and without DL-Recon. Error bars are SEM of the mean. The DL Recon showed a higher image rating than without DL for all b-values.

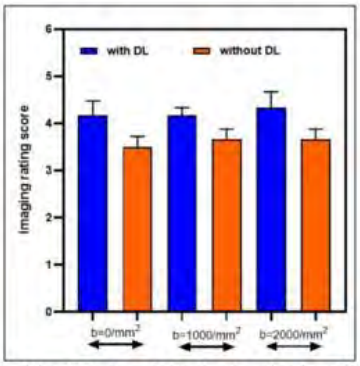

Table 1. Diagnostic qualitative image quality rating for DW images with and without DL-Recon

Diagnostic Quality of the Image (n =12)	DW Image b= 0 (s/mm²)		DW Image b=1000 (s/mm²)		DW Image b= 2000 (s/mm²)	
	With DL	Without DL	With DL	Without DL	With DL	Without DL
Excellent (rated 5)	2(33%)	0(0%)	1(17%)	0(0%)	3(50%)	0(0%)
Good (rated 4)	3(50%)	3(50%)	5(83%)	4(67%)	2(33%)	4(67%)
Acceptable (rated 3)	1(17%)	3(50%)	0(0%)	2(33%)	1(17%)	2(33%)
Poor and unacceptable (Rated 2 and 1)	0 (0%)	0 (0%)	0 (0%)	0 (0%)	0 (0%)	0 (0%)

Table 2. Summary of the ADC values obtained with and without DL-Recon of DWI patient data

Patient	ROI	ADC × 10⁻³ (mm²/s)		rΔADC (%)
		with DL	without DL	
1	Primary	1.008±0.138	1.015±0.148	-0.675
	Node	1.01±0.140	1.00±0.185	-0.169
2	Primary	1.43±0.339	1.446±0.361	-0.724
	Node	1.586±0.478	1.590±0.486	-0.013
3	Node	0.747±0.193	0.752±0.164	-0.735
4	Primary	0.898±0.303	0.899±0.303	-0.039
	Node	0.868±0.266	0.869±0.265	-0.130
5	Primary	1.124±0.429	1.13±0.415	-0.231
	Node	1.122±0.420	1.13±0.328	-1.350
6	Node	1.048±0.350	1.048±0.348	-0.048

(Filename: TCT_1259_DL_DWI_ANSR_Figure.jpg)

1477

How Deep Learning Can Make Short Half-Life 15O-Water Brain PET Imaging More Clinically Feasible?

A Sanaat[1], M Khalighi[1], R Hussein[1], M Zhao[1], h Zaidi[2], M Moseley[1], G Zaharchuk[1]

[1]Stanford University, Stanford, CA, [2]Geneva University Hospital, Geneva, Geneva

Purpose

Brain positron emission tomography (PET) imaging using the 15O-water radiolabel, has been accepted as the gold standard for measuring cerebral blood flow map (CBF) in humans. CBF maps depict the blood supply to a certain region of the brain in a given period of time with the unit of ml/100 g/min. Since the 15O-water has a very short half-life (~2 min), PET imaging is very challenging, requiring that 15O-water scans be performed only in sites with a co-localized cyclotron. In this study we enhanced extremely low dose 15O-water PET images with an MRI-guided deep learning model, to generate accurate PET CBF maps, simulating conditions in which the scanner and the cyclotron are not located in the same building, to ultimately enable more widespread 15O-water CBF imaging.

Materials and Methods

In this study, we used an attention-based deep learning model called Swin UNEt TRansformers (SwinUNETR)[1] to predict full-dose (FD) PET images from ultralow-dose (LD) PET and multi-contrast MRI including T1-weighted (T1w), T2-weighted fluid-attenuated inversion recovery (T2-FLAIR), multi-delay pseudo-continuous ASL (pCASL), proton density (PD), and quantified CBF/arterial transit time (ATT) maps derived from ASL (Figure 1). The LD images were generated by random undersampling of the FD list mode at a simulated dose of 5%. 5% dose is equivalent to ~10 min delay in injection. The dataset comprised 38 healthy controls and 8 patients (5 with Moyamoya disease and 3 with stroke), with a breakdown of 32/5/9 subjects for training/validation/testing sets.

Results

Visual qualitative assessment shows that our model can significantly improve the quality of predicted PET images (Figure 2). Quantitative assessment revealed improvements in the structural similarity index (SSIM), peak signal-to-noise ratio (PSNR), and root mean square error (RMSE) by 5%, 25% and 46%, respectively, in comparison with LD PET images (Table 1).

Conclusions

A deep learning model can make 15O-water PET imaging easier to perform by relaxing the time constraints between tracer production and imaging that has traditionally limited it to sites with a cyclotron. We found that scans simulated to represent a 10 min time-to-injection delay could be significantly de-noised to clinical quality levels.

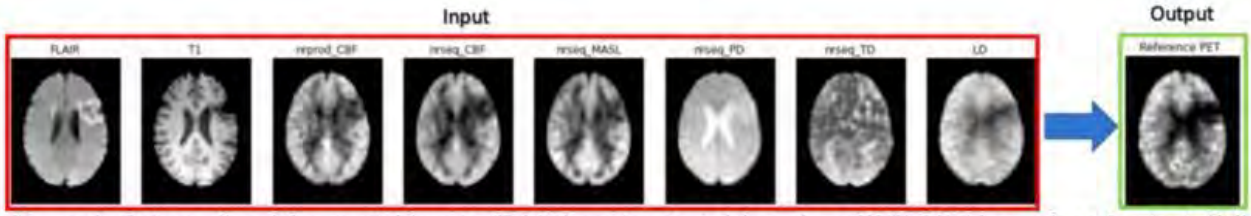

Figure 1: Schematic of the model inputs (7 MRI contrasts + 1 low dose PET CBF image) and output (full dose PET CBF image).

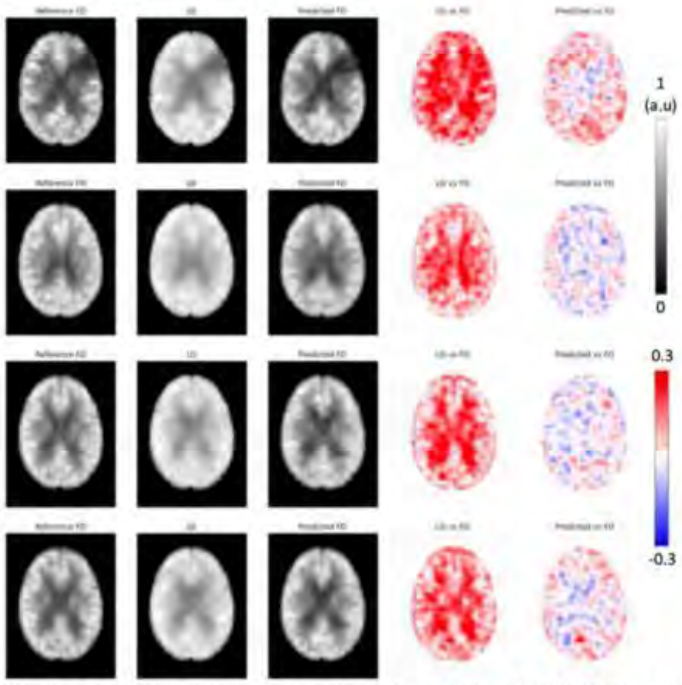

Figure 2: Reference FD (first column), LD (second column), predicted FD (third column) and corresponding error map between LD and FD and between prediction and FD (fourth and fifth column).

Table 1: The PSNR and SSIM calculated between the LD and predicted FD and reference FD respectively.

	PSNR	SSIM	RMSE
LD vs FD	22.77	0.88	0.061
Predicted vs FD	28.33 (Increase~25%)	0.92 (Increase~5%)	0.033 (Decrease 46%)

(Filename: TCT_1477_Presentation1.jpg)

463

Multi-Site Study: Novel Deep Learning Super-Resolution Algorithm Allows Substantial Improvement of Neuro MRI Image Quality and Scan Time

R Shreter[1], M Goldfeld[2], J Brace[3], G Stenoien[4], I Page[5], R Trindade[6], L Lucato[7], F Almeida[8], L Mori[9], T Aharoni[9], C Andrade[10]

[1]Hillel Yaffe Medical Center, Hadera, Israel, [2]WGH, Kiriat Motzkin, none, [3]Radiology Partners, El Segundo, CA, [4]Houston Medical Imaging, Houston, TX, [5]Monash Health, Melbourne, Victoria, [6]Alliar, Salvador, Bahia, [7]Instituto de Radiologia, Hospital das Clínicas da Faculdade de Medicina da Universidade de São Paulo, São Paulo, São Paulo, [8]Alliar, São Paulo, Sao Paulo, [9]Medic Vision, Tirat Carmel, Haifa, [10]Instituto de Radiologia, Hospital das Clínicas da Faculdade de Medicina daUniversidade de São Paulo, Sao Paulo, Sao Paulo

Purpose

To evaluate image quality, image resolution, and overall diagnostic sufficiency of low-resolution neuro MRI images processed by a novel deep-learning (DL) resolution enhancement algorithm, compared to images acquired with higher resolution from multiple sites and MRI scanners.

Materials and Methods

158 neuro sequences (73 Brain, 26 C-Spine, 30 L-Spine and 29 T-Spine) of 43 subjects (19-88 years) were obtained on 12 different clinical MRI scanners (1.2T, 1.5T and 3T) from different vendors (Philips, Hitachi, Siemens and GE) under multi-site IRB-approval (in USA, Israel and Brazil). Each patient was imaged using the site's routine high-resolution (HR) protocol and with 25-33% faster variants, solely compromising resolution in phase encoding direction. The low-resolution (LR) scans were processed by a novel convolutional-neural network (CNN) based super-resolution algorithm, trained on a vast amount of MRI images from scanners of multiple vendors with a variety of clinical indications, to produce enhanced resolution (ER) images. Independent, blinded, side-by-side comparisons of diagnostic quality, spatial resolution, noise level, artifacts appearance and contrast resolution were performed by 9 experienced neuroradiologists, using a 7-point Likert-scale (1=unacceptable, 7=excellent). An additional non-blind review by a highly experienced neuroradiologist (>15 years' experience) was performed comparing image details between the HR and ER scans. Statistical analysis was performed (using JASP 0.16.3) comparing (i) HR to ER scans and (ii) LR to ER scans. Statistical significance was determined by paired samples t-test testing for superiority of ER scans.

Results

Results (n=767 reads) exhibited superiority of the ER images over both the LR and HR images for diagnostic quality, spatial resolution, noise levels, contrast resolution and artifact appearance ($p<0.001$). 51 out of the 158 reviewed series showed pathologies. Statistical results were reinforced by the nonblinded review, demonstrating equality for image details and diagnostic confidence between the ER and HR images.

Conclusions

Results show that substantial improvement of neuro MRI Image quality and reduction in scan time can be achieved using a robust super-resolution DL-algorithm, resolving the trade-off between resolution and acquisition time on a variety of scanners.

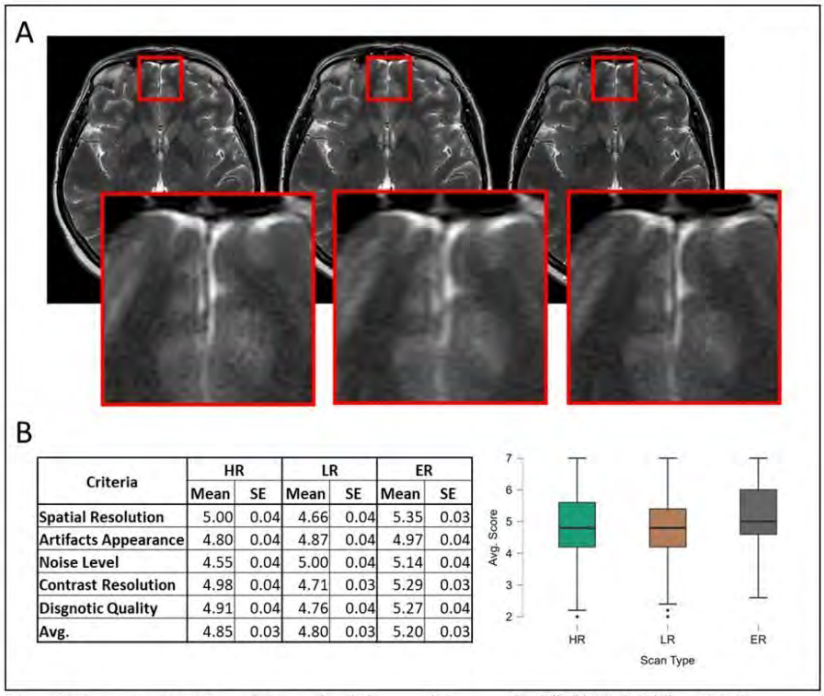

Figure 1 Comparing HR, LR and ER results. (A) example image of HR (left), LR (middle, 28% phase resolution reduction) and ER (right) of Axial T2 images from a Philips Ingenia 1.5T scanner, showing full reconstruction of the supraorbital frontal lobe in the ER image, not clearly visible in the LR image. (B) Descriptive statistics showing overall superiority of ER images over LR and HR images.

(Filename: TCT_463_asnr-abstract-figure-300dpi.jpg)

1516

Synthesizing MR Angiograms From Fast Quantitative Non-Angiographic Multi-Contrast MR Images: A Deep Learning-Based Approach

A Sanaat[1], M Zhao[1], R Hussein[1], h Zaidi[2], S Skare[3], M Moseley[1], G Zaharchuk[1]
[1]Stanford University, Stanford, CA, [2]Geneva University Hospital, Geneva, Geneva, [3]Karolinska University Hospital, Solna, Sweden

Purpose

Magnetic Resonance Angiography (MRA) imaging plays a critical role in diagnosing and assessing vascular abnormalities, such as aneurysms, stenoses, and occlusions. Angiographic information exists on conventional non-angiographic contrasts in various forms, including the presence of flow-voids on spin echo imaging. Previous work has suggested that non-angiographic multi-contrast MRI scans can be used to synthesize MRA using a deep learning framework[1]. MRA may be required in patients who cannot tolerate a standard-length MRI study or might be required after radiologists assess the conventional images, when the patient has already left the scanner. Synthesizing diagnostic MRA images from an ultra-fast MR sequence may be a valuable tool in emergency situations and for retrospective studies.

Materials and Methods

In this study, we used an attention-based deep learning model called Swin UNEt TRansformers (SwinUNETR)[2] to predict the MRA image from a fast 3T MR scan protocol called NeuroMix[3]. The NeuroMix protocol can simultaneously acquire whole-brain T1w, T2w, susceptibility-weighted (SWI), and T2 fluid-attenuated inversion recovery (T2-FLAIR) in 2.5 min (Figure 1). This sequence incorporates a motion-robust single-shot sequence using echo-planar imaging and fast spin echo readouts. A retrospective dataset of 350 cases with T1w, T2w, T2-FLAIR, and SWI acquired Neuromix and corresponding conventional MRA images were collected. The SwinUNETR model was adopted to generate MRA images from the combination of T1, T2, T2-FLAIR, and SWI. The SwinUNETR formulates this as a a sequence-to-sequence task wherein the four input images are projected into a 1D sequence and used as an input of a Swin transformer encoder. The encoder extracts five different representations of features by using shifted windows to estimate self-attention and is connected to a decoder by skip connections.

Results

The visual qualitative assessment revealed that our model can visualize the main intracerebral arteries (internal carotid and basilar arteries) well. Lower performance was noted for distal vessels, particularly the M1 segments of the middle cerebral arteries (Figure 2). Quantitative assessment demonstrated a structural similarity index of 0.92±0.05 and a peak signal-to-noise ratio of 28.75±3.2.

Conclusions

The proposed deep learning model can artificially synthesize MRA images directly from fast Neuromix MRI. This method may be valuable for unstable patients or retrospective studies.

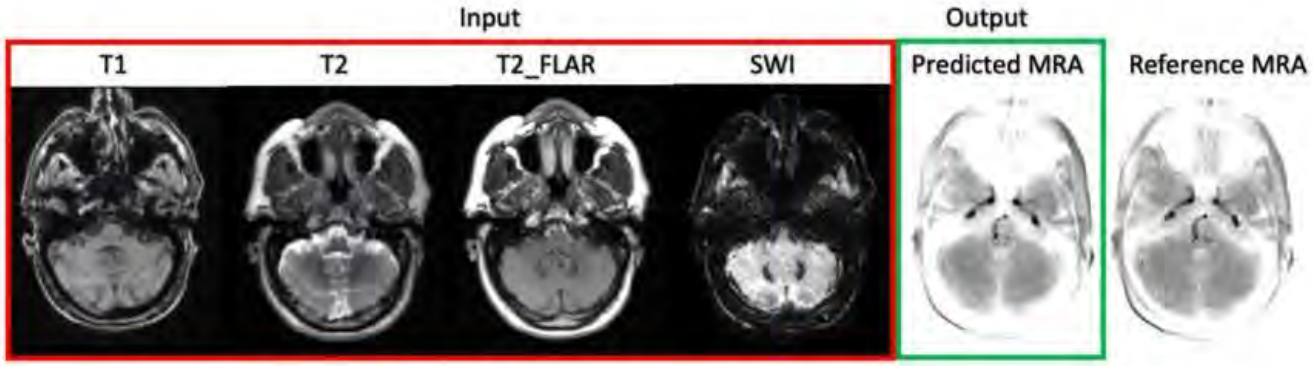

Figure 1: The model inputs and output with corresponding MRA (shown as an axial maximum-intensity projections (MIP)).

Figure 2: Two examples of coronal MIP MRA images showing both the reference (top) and predicted (bottom) images. The image on the left shows an occlusion of the left internal carotid artery, while the right shows a normal case.

(Filename: TCT_1516_Presentation3.jpg)

322

Using MRI-RSI to Predict Survival and Enhance Deep Learning-Based Brain Tumor Segmentation for Post-Operative Glioblastoma Patients

D Gupta[1], L Gagnon[1], N White[2], C McDonald[3], T Beaumont[4], T Seibert[5], J Hattangadi-Gluth[5], S Kesari[6], J Schulte[7], D Piccioni[7], N Farid[1], J Rudie[1]

[1]Department of Radiology, UC San Diego, San Diego, CA, [2]Cortechs.AI Inc., San Diego, CA, [3]Department of Psychiatry, UC San Diego, San Diego, CA, [4]Department of Neurological Surgery, UC San Diego, San Diego, CA, [5]Department of Radiation Oncology, UC San Diego, San Diego, CA, [6]Pacific Neuroscience Institute and Saint John's Cancer Institute at Providence Saint John's Health, Santa Monica, CA, [7]Department of Neurosciences, UC San Diego, San Diego, CA

Purpose

Multimodal MRI is used for the evaluation of tumor burden in glioblastoma (GBM) patients after surgical resection, radiation, and chemotherapy. However, it can be difficult to distinguish between residual/recurrent tumor and treatment-related changes (1,2). Restriction spectrum imaging (RSI), an advanced multishell diffusion technique, has shown promise in separating cellular tumor from edema and post-treatment enhancement (3,4). Here, we assessed the utility of RSI in developing a deep learning model for cellular tumor segmentation that could distinguish tumor recurrence from treatment effects and thereby predict overall survival (OS) for post-surgical GBM patients.

Materials and Methods

A cohort of 62 GBM patients with an RSI sequence from a brain tumor MRI protocol were identified from January 2011 to December 2014 at UC San Diego Health. 88 scans (79 post-resection and 9 pre-operative or post-biopsy) were manually segmented for cellular tumor volume by a neuroradiologist. We trained a nnU-Net neural network to segment cellular tumor using 68 randomly selected cases. The deep learning model was subsequently tested on the 20 remaining cases from unique patients. Model inputs included combinations of T1, T1 contrast-enhanced (T1CE), fluid-attenuated inversion recovery (FLAIR), RSI, and apparent diffusion coefficient (ADC) sequences. The volume of cellular tumor was correlated with OS for patients who had an RSI sequence performed within 180 days after surgical resection.

Results

Examples from the deep learning model applied to an individual patient are shown in Figure 1A. Adding RSI to T1, T1CE, and FLAIR sequences improved the segmentation Dice score from 0.51 ± 0.31 to 0.65 ± 0.24. Although adding ADC to T1, T1CE, and FLAIR sequences also increased the Dice score, the increase was less pronounced than with RSI (0.60 ± 0.31 vs. 0.65 ± 0.24). RSI was performed in twenty patients within 180 days after surgical resection. The volume of cellular tumor from manual segmentation was inversely correlated with OS ($r = -0.41$, $p = 0.07$) (Figure 1B).

Conclusions

Our preliminary results show the potential use of RSI as an imaging biomarker to identify and segment cellular enhancing and non-enhancing tumor and predict survival for post-operative GBM patients. The inclusion of RSI in the deep learning model improved segmentation performance. These findings may indicate that a combination of deep learning and RSI could improve longitudinal assessment of disease burden and treatment.

A

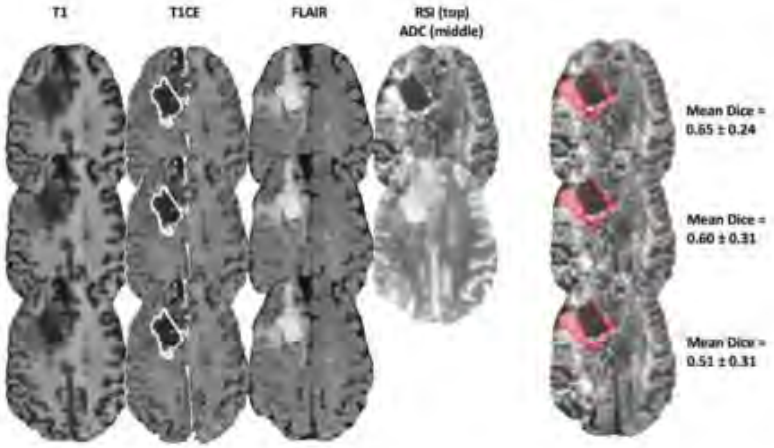

B

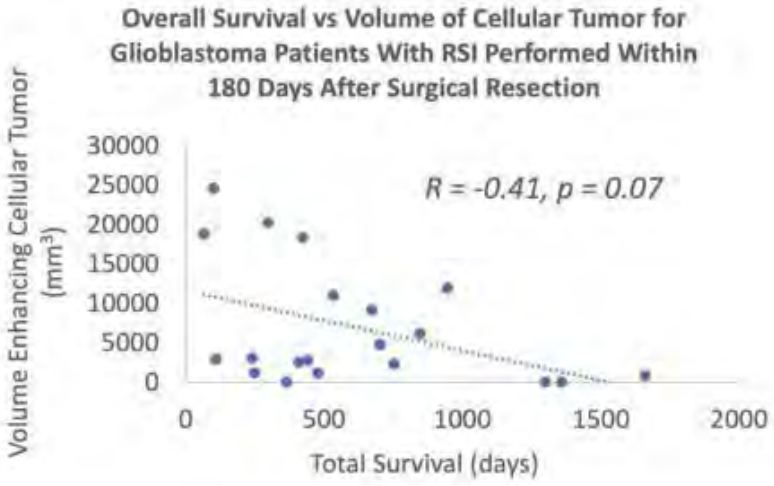

Figure 1A: Deep learning-based brain tumor segmentation with various multichannel inputs and respective segmentation Dice scores for an individual patient.
For row 1, inputs include T1, T1CE, FLAIR, and RSI with mean Dice score of 0.65 ± 0.24. For row 2, inputs include T1, T1CE, FLAIR, and ADC with mean Dice score of 0.60 ± 0.31. For row 3, inputs include T1, T1CE, and FLAIR with mean Dice score of 0.51 ± 0.31.
Figure 1B: Initial data demonstrating the potential of RSI as an imaging biomarker to predict survival for post-operative GBM patients.

(Filename: TCT_322_ImageASNRFinal.jpg)

1284

Validation and Machine Learning of New Method for Quantifying CBF with IVIM

M Liu[1], C Warioba[2], J Bertini[2], N Saadat[3], T Carroll[2], G Christoforidis[4]

[1]The University of Chicago, Chicago, IL, [2]University of Chicago, Chicago, IL, [3]University of Texas Southwestern, Dallas, TX, [4]Mount Carmel Health System, COLUMBUS, OH

Purpose

Quantification of cerebral blood flow (qCBF) proves critical at the clinical and research level for longitudinal and multicenter trials. Intravoxel Incoherent Motion (IVIM) is a non-contrast MR scan that measures various speeds of molecular motion, sidestepping problems of Gd-contrast or increased transit time in neurovascular disease. Questions remain of signal origin and whether IVIM returns quantitative and accurate perfusion in a setting of pathology. We test a new quantification method and compare against microspheres across three physiologic states (baseline, hypercapnia, and MCA occlusion) in a controlled animal model. Simulations and machine learning algorithms were studied to remove cerebrospinal fluid (CSF).

Materials and Methods

Seventeen subjects underwent a two-day controlled experiment of a pre-clinical canine model of normocapnia, CO2 induced hypercapnia, and middle cerebral artery occlusion (ischemic stroke) with IVIM (Fig 1a-c). Five subjects were measured with microsphere deposition. K-fold nested Leave-One-Out Cross-Validation (LOOCV) and segmentation via discriminant analysis (Fig 3) was written to remove CSF signal contamination (Fig 1d). IVIM perfusion was calibrated to quantitative flow by solving the 3D gaussian probability distribution as a function of σ(t) time at which 50% of the molecules have traveled half the voxel length from the center of the voxel. Hemispheric IVIM qCBF was compared to microsphere perfusion with linear regression, Wilcoxon signed-rank, and Bland-Altman analysis.

Results

Hemispheric IVIM with CSF removed via machine learning was compared to microsphere perfusion via linear regression, Bland-Altman, and Wilcoxon signed-rank showed strong correlation and agreement (Fig 2). K-fold LOOCV thresholding returned an outer-loop independent dice coefficient of .69. The linear discriminant analysis machine learning model built from baseline subjects performed best across all physiologic states (Fig. 4). Simulation of CSF suppression with Inversion Recovery reduced blood signal by 82% showing it should not be used in IVIM to remove CSF.

Conclusions

IVIM quantification using pseudo-diffusion mean transit time agreed with gold-standard microspheres across three physiologic states. Simulation suggested IR should not be used in IVIM to remove CSF. This suggests that CSF may be removed from IVIM with a simple machine learning model during post-processing, and that IVIM can be quantified to return signal strongly correlated with microsphere perfusion.

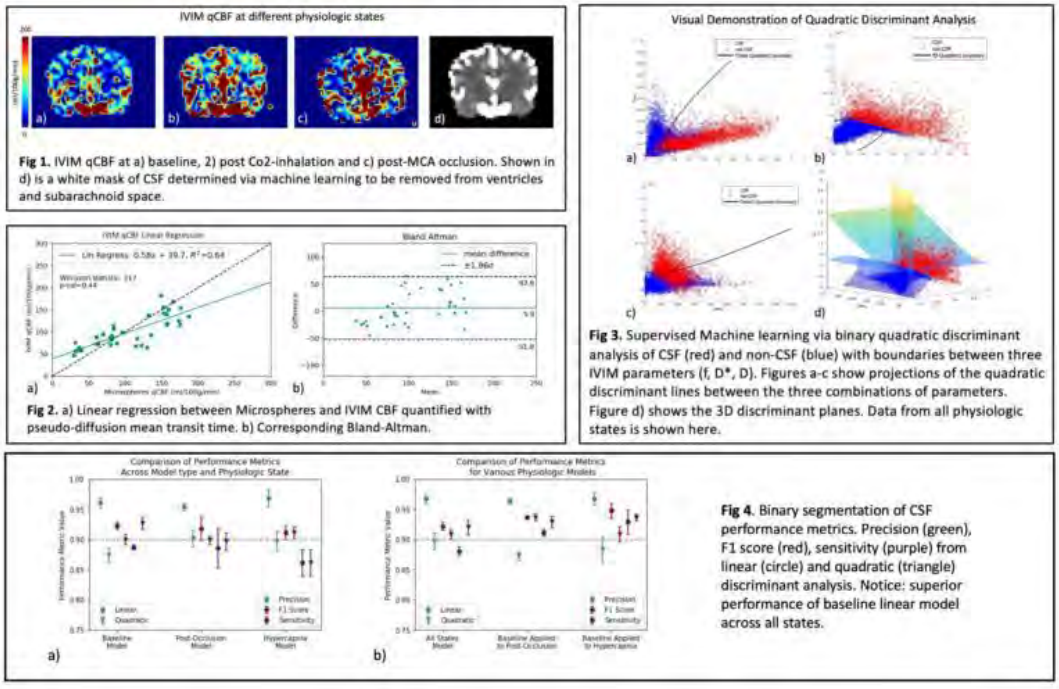

Fig 1. IVIM qCBF at a) baseline, 2) post Co2-inhalation and c) post-MCA occlusion. Shown in d) is a white mask of CSF determined via machine learning to be removed from ventricles and subarachnoid space.

Fig 2. a) Linear regression between Microspheres and IVIM CBF quantified with pseudo-diffusion mean transit time. b) Corresponding Bland-Altman.

Fig 3. Supervised Machine learning via binary quadratic discriminant analysis of CSF (red) and non-CSF (blue) with boundaries between three IVIM parameters (f, D*, D). Figures a-c show projections of the quadratic discriminant lines between the three combinations of parameters. Figure d) shows the 3D discriminant planes. Data from all physiologic states is shown here.

Fig 4. Binary segmentation of CSF performance metrics. Precision (green), F1 score (red), sensitivity (purple) from linear (circle) and quadratic (triangle) discriminant analysis. Notice: superior performance of baseline linear model across all states.

(Filename: TCT_1284_AbstractImages.jpg)

Tuesday, May 2, 2023
10:45 AM-12:00 PM
Scientific Abstract Session: Vascular 2

473

Comparative Analysis of CTP-based estimated Ischemic Core in a Multicenter Study

S KIHIRA[1], P Shahrouki[1], E Tavakkol[1], M McArthur[2], J Fifi[3], A Doshi[4], A Vagal[5], P Khatri[6], A Srinivasan[7], M Bahr-Hosseini[1], V Yedavalli[8], R Jahan[1], g duckwiler[9], N Salamon[2], J Villablanca[1], C Arnold[1], J Saver[1], J Mocco[10], D Liebeskind[11], K Nael[1]
[1]UCLA, Los Angeles, CA, [2]University of California Los Angeles, Los Angeles, CA, [3]Icahn School of medicine at Mount Sinai, New York, NY, [4]Mount Sinai Hospital, New York, NY, [5]University Of Cincinnati Medical Center, Cincinnati, OH, [6]University of Cincinnati, Cincinnati, OH, [7]University of Michigan, Ann Arbor, MI, [8]Johns Hopkins School of Medicine/Johns Hopkins Hospital, Baltimore, MD, [9]ucla, Los Angeles, CA, [10]Icahn School of Medicine at Mount Sinai, New York, NY, [11]UCLA Stroke Center, Los Angeles, CA

Purpose
CT Perfusion (CTP) is increasingly used to assess eligibility for endovascular therapy (EVT) in patients with large vessel occlusions (LVO). There remain variability and inconsistencies between available software packages in terms of estimation of ischemic core using CTP (1). We aimed to use heterogenous data from four geographically distant stroke centers to perform a comparative analysis for CTP-estimated ischemic core volumes between RAPID (iSchemaView) and Olea SIA (Olea Medical).
Materials and Methods
In this retrospective multicenter study, patients with anterior circulation LVO stroke were included if they had pretreatment CTP, underwent EVT, and had follow-up MRI. Automated CTP data analysis was performed using Olea SIA platform [rCBF<25% and differential time-to-peak (dTTP)>5s] and RAPID (rCBF<30%). In all patients who achieved successful recanalization (defined TICI ≥2b), the CTP estimated core volumes were compared against the final infarct volume on post treatment MRI-DWI.
Results
A total of 160 patients [92F; age (mean ± SD): 70.3 ±16.4; median NIHSS 16 [12-20] were included. The estimated ischemic core volume (mean ± SD) was 20 ± 19 mL on Olea and 10 ± 18 mL on RAPID, significantly different ($p<0.01$). Both software overestimated the ischemic core volume above 70 mL in 3 subjects (same patients) and each in one additional patient. In patients who achieved successful recanalization (n=153), the difference (mean ± SD) between CTP estimated core and final infarct was 26.2 ± 98.6 mL for RAPID and 18 ± 98 mL for Olea (Figure). There was moderate correlation between final infarct volume and CTP estimated ischemic core for both RAPID ($r=0.38$, $p<0.01$) and Olea ($r=0.39$, $p<0.01$).
Conclusions
Results of this multicenter study show substantial variation between Olea and RAPID CTP-estimated core volumes, though rates of overcalling of large core were low, 2.4%, for both. Both showed comparable core volume correlation to MRI infarct volume.

1220

Imaging endpoints of flow diverters for treatment of brain aneurysms with versus without coating - a matched pair analysis

G BROOCKS[1], L Meyer[2], M Bechstein[2], H KNIEP[2], A Kemmling[3]
[1]University Hamburg, Hamburg, NA, [2]University Medical Center Hamburg-Eppendorf, Hamburg, Hamburg, [3]University Marburg, Marburg, Hessen

Purpose
Evidence for benefit of aneurysm treatment using coated Flow Diverter (FD) devices compared to uncoated devices is limited. The aim of this study was to compare short term imaging endpoints of FD implants with and without coating for treatment of saccular aneurysms in a matched pair analysis.
Materials and Methods
We retrospectively included patients with incidental aneurysms who were treated with one or more FD. Coated FD included p64 HPC, p48 HPC, Derivo2 heal and PED2 shield. Uncoated FD included p64, Derivo2 and Evolve. Coated and uncoated FD were matched by location and diameters (within 20% difference) of distal and proximal landing zones and antiplatelet treatment (DAPT and SAPT). 7 patients were treated with 2 FD, 7 coated and 7 uncoated. Imaging endpoints included lumen diameter, stent diameter, neointimal thickness and neointimal ratio (stent – lumen diameter)/stent diameter), rate of occlusion and MRI lesions. Peri- and postprocedural complications and clinical outcomes were evaluated.
Results
71 patients with 90 aneurysms were included. Average early follow up was 4.3 months. Periprocedural lumen diameter decreased on follow up by 27% in uncoated vs. 18% in coated devices. Neointimal thickness on follow up was 0.33 mm in coated vs. 0.45 mm in uncoated devices. Neointimal ratio was 0.32 in uncoated vs. 0.18 in coated devices. There was no difference occlusion rate, complications or clinical outcomes.
Conclusions
Coated FD showed less lumen narrowing and neointimal thickness compared to uncoated devices. This did not affect outcome and occlusion rate on short term follow up.

1329

Longitudinal Changes in Cerebral Perfusion, Perivascular Space Volume, and Ventricular Volume in a Healthy Cohort Undergoing a Spaceflight Analogue

D Roberts[1], J Taylor[1], G Barisano[2], J Tidwell[1]

[1]Medical University of South Carolina, Charleston, SC, [2]University of Southern California, Los Angeles, CA

Purpose

A global decrease in brain perfusion has recently been reported during exposure to a ground-based spaceflight analogue (head-down tilt bedrest).1 Considering CSF and glymphatic flow are hypothesized to be propelled by arterial pulsations, it is unknown if a change in perfusion would impact these CSF compartments. The aim of the current study was to evaluate the relationship between changes in cerebral perfusion, ventricular volume, and perivascular space volume before, during, and after a spaceflight analogue.

Materials and Methods

11 healthy participants underwent 30-days bedrest at 6-degrees head-down tilt with 0.5% atmospheric CO2 as a spaceflight analogue. For each participant, six MRI brain scans, including perfusion and anatomical weighted T1 sequences, were obtained before, during, and after the analogue period. Global perfusion, ventricular volume, and perivascular space volume time courses were constructed and evaluated with repeated measures ANOVAs.

Results

Global perfusion followed a divergent time trajectory from ventricular and perivascular space volume, with perfusion decreasing during the analogue whereas ventricular and perivascular space volume increased, $p < .001$. (Figure: Grey shaded area represents duration of the HDT+CO2 intervention. Data points are represented with mean z-scores and SEM error bars.) These patterns subsequently reversed during the two-week recovery period.

Conclusions

The patterns of change in brain physiology observed in healthy participants suggest a relationship between cerebral perfusion and CSF homeostasis. Further study is warranted to determine if a causal relationship exists and if similar neurophysiological responses occur during spaceflight.

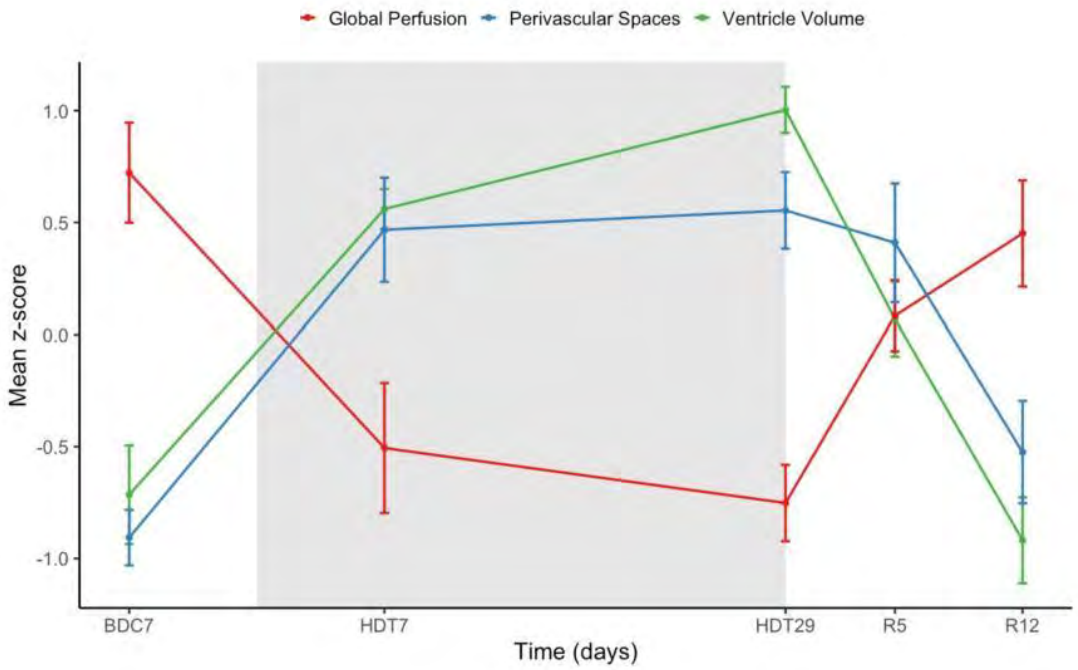

(Filename: TCT_1329_ASL_PVS_Bedrestpng.jpg)

1502

Optimization of Multi-Phase CT-Angiogram Acquisition Timing for Perfusion Imaging

C McDougall[1], R Sheronick[1], P Barber[1]

[1]University of Calgary, Calgary, Alberta

Purpose

Multi-phase CT angiograms (mCTA) have been shown to provide perfusion information similar to CT perfusion (CTP) acquisitions by applying the Simple Perfusion Reconstruction Algorithm (SPIRAL), which can be used to diagnose and determine severity of acute ischemic stroke (AIS)[1,2]. Existing mCTA acquisition protocols have been optimized for vascular visualization to locate clot location for endovascular therapy treatment, not for perfusion imaging. In the current work, the CTP acquisition is used as a surrogate to optimize mCTA slice timing for SPIRAL analysis by sampling specific phases of the CTP acquisition. The current work aims to provide an optimized three-phase mCTA acquisition timing protocol specifically for imaging of perfusion deficits.

Materials and Methods

75 AIS patients with occlusion visible on CTA were acutely imaged with a 24-phase CTP acquisition, with inter-phase timing of 2.8 seconds. The CTP raw data was analyzed using the logistic regression-based SPIRAL model [2]. The model was trained against a CTP gold standard, the General Electric (GE) – CTP T-MAX map, segmented for perfusion deficit defined as T-MAX = 9.9 seconds [3]. From the 24 CTP acquisition phases, multiple SPIRAL models are produced: 1) a 24-phase model to determine the upper limit of performance for SPIRAL analysis applied to the CTP acquisition; 2) Four 6-phase models to narrow the search range for the optimal mCTA acquisition; 3) A 3-phase model representing the "current" mCTA protocol using the 2nd, 5th and 8th phases of the CTP acquisition; 4) An optimal 3-phase model, using the same inter-phase timing of the "current" mCTA protocol, but varied overall timing. Performance was quantified using Area Under Curve (AUC) from Receiver Operating Characteristic (ROC) analysis.

Results

The optimal mCTA acquisition increased SPIRAL performance by approximately 5.5%, and is 15 seconds later, when comparing the current (AUC = 0.759) and optimal (AUC = 0.802) mCTA models. The upper limit for SPIRAL analysis on 24 phases was found to be AUC = 0.828, only 3.2% lower than the optimal 3-phase mCTA acquisition. The optimal 6-phase acquisition is between 16-33 seconds. These results are illustrated in Figure 1.

Conclusions

To achieve higher accuracy SPIRAL perfusion imaging, mCTA acquisitions should be acquired approximately 15 seconds later than the current protocol. Future work includes optimizing acquisition timing for identification of ischemic core and inclusion of cross-validation statistical analysis.

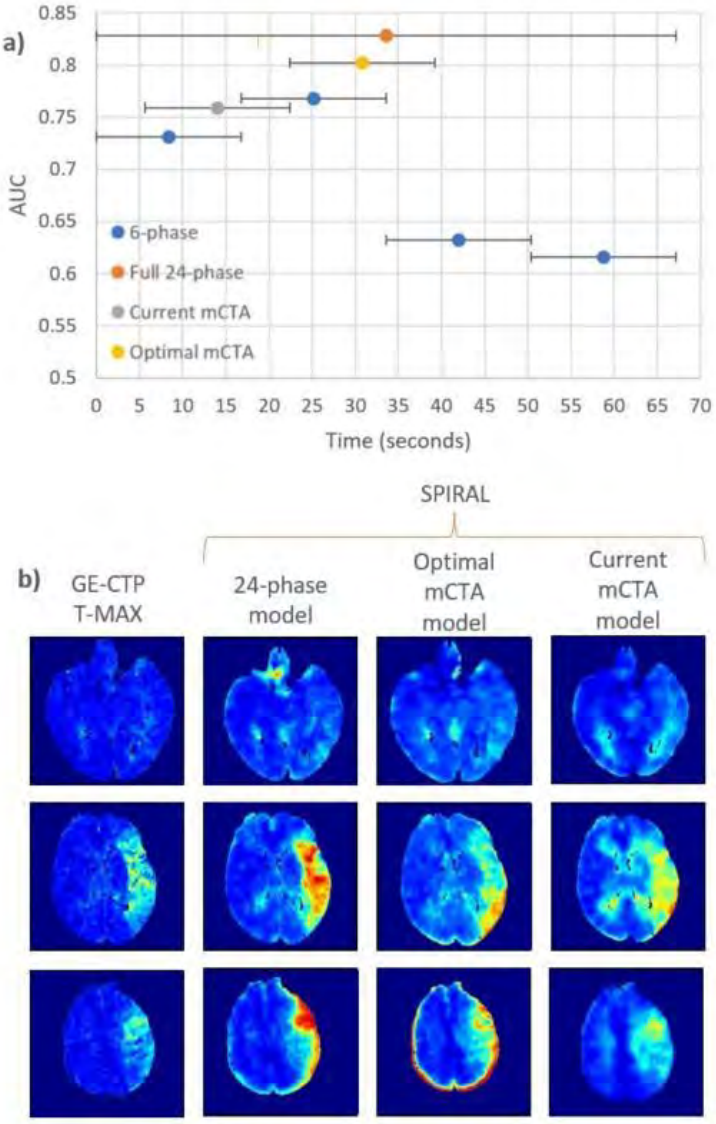

Figure 1. a) AUCs for each model tested, error bars represent the range of phases used from the CTP acquisition, b) example SPIRAL maps using models trained in the current work.

(Filename: TCT_1502_figure1.jpg)

1203

Penumbra Salvage versus Edema Reduction – Investigating Treatment Effects of Mechanical Thrombectomy in Ischemic Stroke

G BROOCKS[1], A Kemmling[2], L Meyer[3], U HANNING[4], H KNIEP[3], J Fiehler[5], R McDonough[6]

[1]University Hamburg, Hamburg, NA, [2]University Marburg, Marburg, Hessen, [3]University Medical Center Hamburg-Eppendorf, Hamburg, Hamburg, [4]UNIVERSITY MEDICAL CENTER HAMBURG-EPPENDORF, HAMBURG, Germany, [5]University Hospital Hamburg-Eppendorf, Hamburg, AS, [6]University of Calgary, Calgary, Alberta

Purpose

Despite the proven clinical benefit of mechanical thrombectomy (MT) in ischemic stroke, the pathophysiology of treatment effects is not yet well understood. The salvage of tissue-at-risk (i.e. penumbra) and reduction of ischemic edema are two major components known to be associated with successful reperfusion. The purpose of this study was to directly quantify how the effect of recanalization on functional outcome is mediated by penumbra salvage versus edema reduction.

Materials and Methods

Observational retrospective study of ischemic stroke patients triaged by multimodal-CT undergoing endovascular treatment. Edema reduction was defined as the difference of quantitative NWU (based on CT-densitometry) measured in admission and follow-up CT (=ΔNWU), and penumbra salvage volume (PSV) was defined as the difference between baseline penumbra volume and net infarct growth to follow-up. Mediation analysis was performed with recanalization as independent variable (defined as mTICI 2b-3), and penumbra salvage and edema reduction as mediator variables. End point was the modified Rankin Scale (mRS) score at day 90.

Results

715 patients were included, with 518 (71%) achieving successful recanalization. The median PSV was 66 ml (IQR: 8-124) and the median ΔNWU was 6.8% (IQR: 3.9-10.4). In ordinal regression analysis, ΔNWU, PSV and recanalization were independently associated with mRS at day 90. ΔNWU and PSV partially mediated the relationship between recanalization with mRS score. Treatment-induced edema reduction explained 66% of the relationship between recanalization and outcome, while 22% was mediated by penumbra salvage ($p<0.0001$).

Conclusions

Edema reduction was a stronger mediator of the effect of recanalization on functional outcome compared to penumbra salvage. Considering the currently running trials on adjuvant neuroprotection for stroke also targeting edema formation, the combination of reperfusion with neuroprotective agents may have synergistic effects leading to better functional outcomes in ischemic stroke patients.

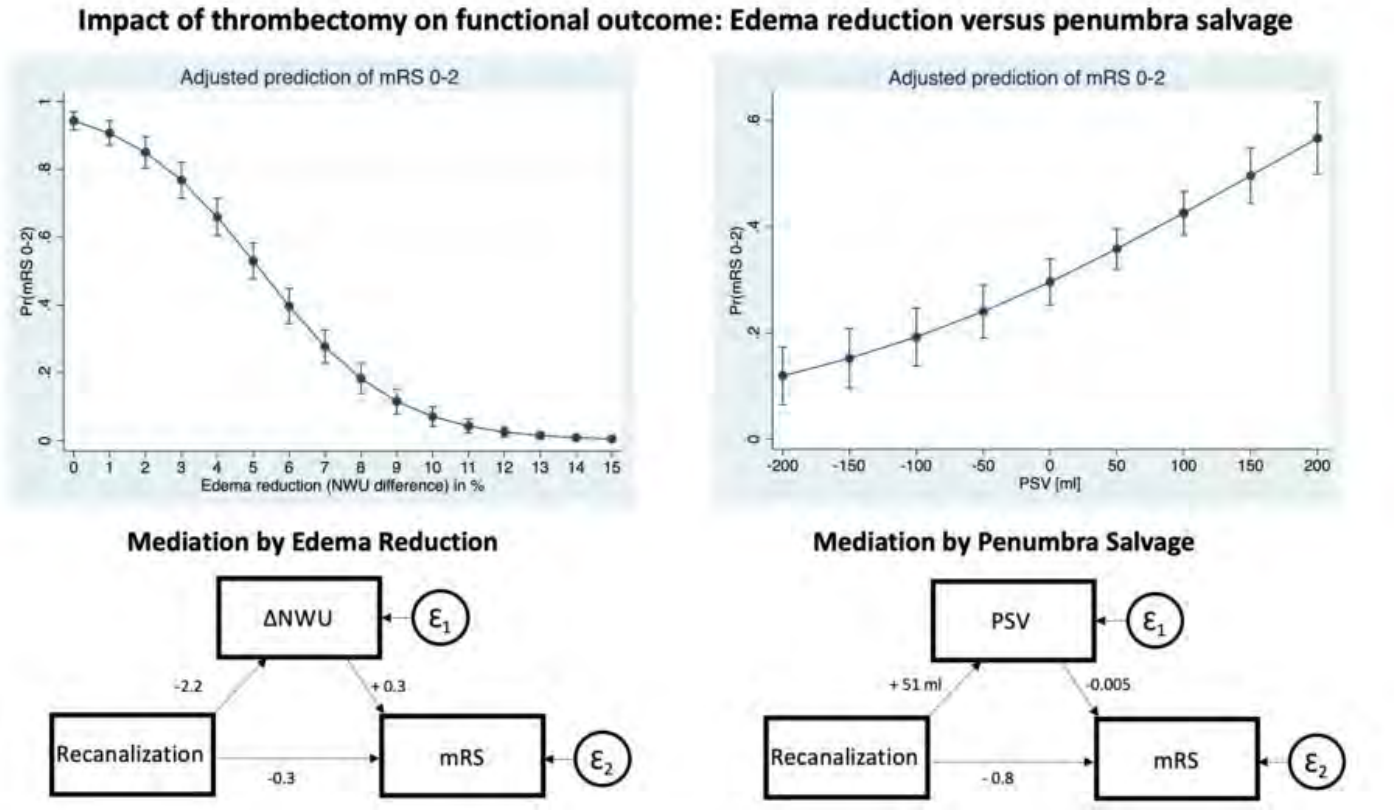

(Filename: TCT_1203_psv_fig_asnr.jpg)

1349

Predictors of Successful Recanalization after Mechanical Thrombectomy in M2 Occlusions

H KNIEP[1], L Meyer[1], G BROOCKS[2], M Bechstein[1], T Faizy[3], L Winkelmeier[4], F Flottmann[1], U HANNING[5], J Fiehler[6], S Gellissen[7]
[1]University Medical Center Hamburg-Eppendorf, Hamburg, Hamburg, [2]University Hamburg, Hamburg, NA, [3]University of Hamburg-Eppendorf, Hamburg, Germany, [4]University Medical Center Hamburg-Eppendorf, Hamburg, Germany, [5]UNIVERSITY MEDICAL CENTER HAMBURG-EPPENDORF, HAMBURG, Germany, [6]University Hospital Hamburg-Eppendorf, Hamburg, AS, [7]University Medical Hospital Hamburg-Eppendorf, Hamburg, Hamburg

Purpose
Patient-specific factors associated with successful recanalization in mechanical thrombectomy (MT) have been evaluated for acute ischemic stroke with large vessel occlusion (1). However, MT for medium-vessel occlusions is still a matter of debate. We sought to identify predictors of successful recanalization in MT for M2 occlusions.
Materials and Methods
All patients prospectively enrolled in the German Stroke Registry (GSR) from 05/2015 to 12/2021 were analyzed. Inclusion criteria were distal occlusion of the M2 segment of the middle cerebral artery and availability of the relevant clinical data. Standard descriptive statistics and multivariate logistic regression analysis was performed to identify factors associated with successful recanalization (Thrombolysis in cerebral infarction score (TICI) ≥ 2b) and full recanalization (TICI 3)
Results
1353 patients fulfilled the inclusion criteria, 1134 (84%) received a successful recanalization and 598 (44%) achieved good functional outcome. Patients with TICI ≥ 2b had a better neurological status at admission, higher ASPECTS, more general anesthesia, lower number of passes, lower rates of treatment related AEs and more good functional outcome with mRS 0-2 (Table 1). Patients with TICI 3 (N=672) vs TICI 2b (N=462) were older, had more often anti-thrombotic medication and suffered more often from hypertension, diabetes, dyslipidemia and atrial fibrillation. They had higher ASPECTS, more often general anesthesia, lower number of passes and less clot migration/embolization. Interestingly, 90d mRS was not significantly different com-pared to TICI 2b (Table 2). In a multivariate logistic regression analysis low pre-mRS, general anesthesia and low number of passes were associated with successful recanalization TICI ≥ 2b (Figure 1). Interestingly, TICI 3 recanalization was associated with older patients with comorbidities (Figure 2).
Conclusions
In patients with M2 occlusions, successful recanalization Tici ≥ 2b was associated with low pre-stroke mRS, general anesthesia, lower number of passes and less adverse events (AEs). Interestingly, higher age and comorbidities were predictors for TICI 3 recanalization. Further research is required to improve the understanding of factors associated with TICI 3 recanalization in M2 occlusions.

Table 1) Study polulation characterstics successful and incomplete recanalization

	Tici < 2b (N=97)	Tici ≥ 2b (N=490)	Total (N=587)	p value
Pre mRS	1.1 (1.4)	0.7 (1.2)	0.8 (1.3)	0.019
NIHSS admission	12.2 (6.0)	10.5 (5.8)	10.8 (5.8)	0.012
# of passes	2.4 (2.5)	1.8 (1.4)	1.9 (1.6)	0.002
Dissection/perforation	7 (7%)	13 (3%)	20 (3%)	0.024
Clot migration/embolization	8 (8%)	15 (3%)	23 (4%)	0.016
ICH during treatment	8 (8%)	13 (3%)	21 (4%)	0.007
Stroke during treatment	1 (1%)	0 (0%)	1 (0%)	0.024
NIHSS 24h	14.9 (9.2)	8.2 (8.2)	9.3 (8.7)	< 0.001
Malignant MCA 24h	3 (3%)	1 (0%)	4 (1%)	0.002
90d mRS	4.1 (1.9)	2.5 (2.1)	2.8 (2.1)	< 0.001

Table 2) Study polulation characterstics successful and full recanalization

	Tici 2b (N=194)	Tici 3 (N=296)	Total (N=490)	p value
Anti-thrombotic medication	89 (46%)	177 (60%)	266 (54%)	0.002
Comorbidity dyslipidemia	72 (37%)	157 (53%)	229 (47%)	< 0.001
Artrial fibrillation	74 (38%)	145 (49%)	219 (45%)	0.018
ASPECTS	8.6 (1.6)	9.0 (1.5)	8.8 (1.5)	0.013
Anesthesia				0.007
- beginning with local, change to general	7 (4%)	7 (2%)	14 (3%)	
- conscious sedation with local anesthesia	68 (36%)	69 (24%)	137 (28%)	
- general anesthesia	114 (60%)	216 (74%)	330 (69%)	
# of passes	2.2 (1.7)	1.6 (1.1)	1.8 (1.4)	< 0.001
ICH 24h	27 (14%)	19 (6%)	46 (9%)	0.005

Numbers are shown as mean (standard deviation) or N (%).
Only factors with significant differences ($p \leq 0.05$) are shown.

Figure 1) Predictors of successful recanalization Tici ≥ 2b (logistic regression)

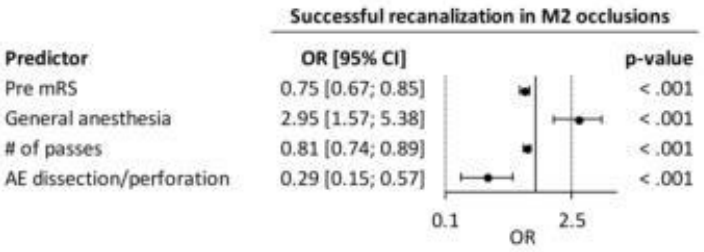

Figure 2) Predictors of successful recanalization Tici = 3 (logistic regression)

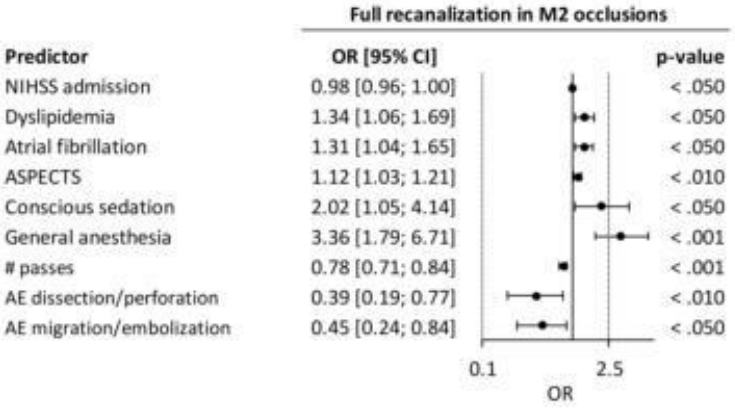

(Filename: TCT_1349_Tables_Figure.jpg)

1217

Quantification of the flow diversion effect provided by the braided intracranial stents

F CAY[1], A Arat[1]
[1]*Hacettepe University Medical School, Ankara, Turkey*

Purpose

The suggestion that braided stents (BS) act as flow diverters (FD) is based on literature data comparing stent-assisted coiling (SAC) with conventional flow diversion (without coiling) of cerebral aneurysms. Since coiling, not infrequently, leads to total aneurysm obliteration on its own, the extent of flow diversion provided purely by the BS has remained unknown. We aimed to determine the extent of flow diversion provided only by BS and eliminated the effect of coils on the occlusion rate by comparing the occlusion rate of only the aneurysms coiled with the assistance of FD, BS and laser-cut stents (LCS).

Materials and Methods

Saccular IAs treated with SAC and FD-assisted coiling were retrospectively evaluated. All of IAs were coiled as densely as possible by a single operator. Aneurysm occlusion was graded per the Raymond-Roy score and categorized as either stable/progressive occlusion (i.e. group A with "flow diverter effect") or recanalization/stable residual filling (group B; lacking a flow diversion effect). Factors predicting the flow diversion effect were evaluated.

Results

Of the 194 IAs included, LCS, BS and FDs were used in 70 (36.1%), 86 (44.3%) and FDS 38 (19.6%) IAs respectively. Aneurysms treated by FD were larger, had wider necks, and were located on larger parent arteries (p values were <0.01, 0.02 and <0.01, respectively). The mean imaging follow-up duration was 24.5 months. There were 29 (14.9%) IAs in group A and 165 (85.1%) IAs in group B. The change of RR score during the follow-up is listed in table 1. Among a spectrum of variables including sex, age, aneurysm size, neck width, parent artery sizes, follow-up duration, stent type, positive predictors for stable/progressive aneurysm occlusion were aneurysm size and placement of a FD or BS, p values were 0.01 and <0.01 respectively, (positive predictor over LCS with ORs of 6.29 [95% CI: 1.61 - 24.5] and 3.39 [95% CI: 1.27 – 9.06] respectively) in the multivariate logistic regression.

Conclusions

BS are flow diverting devices. The flow diversion effect was observed 3.3 times more commonly as compared to LCS but was approximately 50 × less than the FD suggesting that BS may be considered as "semi flow diverters".

Table 1: The change of RR score during the follow-up, n (%)

	LCS	*BS*	*FDS*
RR3 to 1	0	2 (2.3)	4 (10.5)
RR3 to 2	0	0	0
RR3 to 3	0	1 (1.2)	1 (2.6)
RR2 to 1	3 (4.3)	14 (16.3)	10 (26.3)
RR2 to 2	6 (8.6)	5 (5.8)	2 (5.3)
RR2 to 3	3 (4.3)	0	0
RR1 to 1	51 (72.9)	61 (70.9)	20 (52.6)
RR1 to 2	7 (10)	3 (3.5)	1 (2.6)
RR1 to 3	0	0	0
Total	70 (100)	86 (100)	38 (100)

(Filename: TCT_1217_Table1.jpg)

799

Radial versus Femoral Access for Diagnostic Cerebral Angiography: A Systematic Review and Bayesian Meta-Analysis of Randomized Trials

A Cyntia Lima Fonseca Rodrigues[1], D Tonetti[2]
[1]*Positivo University, Curitiba, Brazil,* [2]*Cooper Neurological Institute, Cooper University Hospital, Camden, NJ*

Purpose

This study aims to compare the radial and femoral access for diagnostic cerebral angiography with respect the efficacy and safety.

Materials and Methods

A systematic review and meta-analysis were performed according to the PRISMA guidelines. PubMed, Embase and Cochrane databases were searched from inception to November, 2022. Were included only randomized controlled trials (RCT) in which the participants were patients presenting only for diagnostic cerebral angiography to undergo radial or femoral access. The Cochrane risk-of-bias tool for randomized trials (RoB 2) was used to assess the quality of assessment of selected studies. Results were pooled by

Bayesian random effects models with stratification for radial or femoral access. We evaluated effects of the following priors: neutral moderate, pessimistic weak, optimistic moderate. The primary outcome studied was rate of technical success.
Results
We analyzed three RCTs involving 289 patients. Pooled technical success rates showed no difference when assuming neutral (natural logarithm of odds ratios, -0.08; 95% credible interval, -0.72–0.55), optimistic (lnOR, -1.11; 95% CrI, -1.11–0.29) and pessimistic priors (lnOR, 0; 95% CrI, -1.08–1.15), although the credible intervals were wide.
Conclusions
There is limited evidence to support whether radial access affects technical success when compared with the traditional femoral access, definitive conclusions are therefore not possible. Larger, randomized studies with longer follow-ups are needed to define the optimal role of radial access.

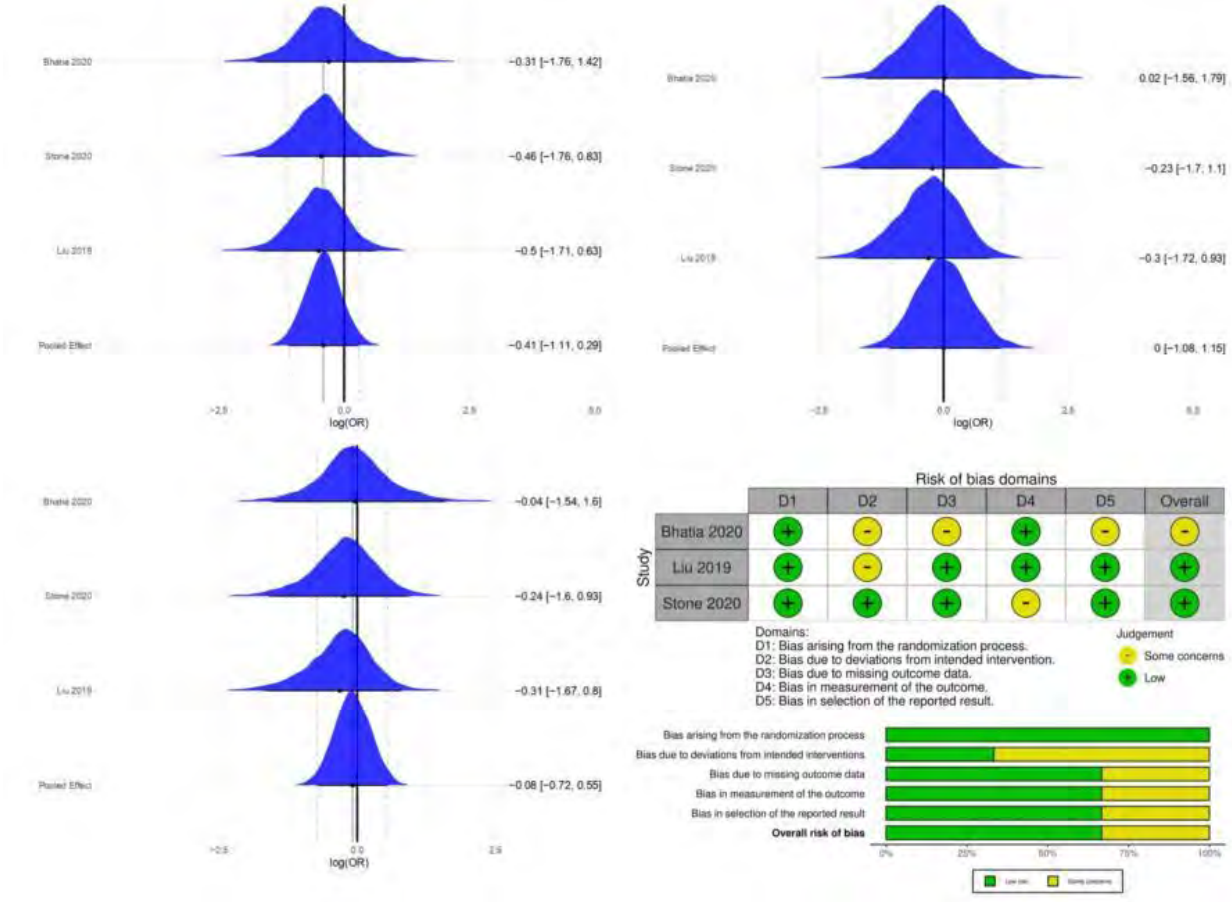

(Filename: TCT_799_Bayesian_Analysis_and_Risk_of_Bias_Radial_paper.jpg)

1511
The Accuracy of Perfusion Deficits on Multiphase CTA During Acute Ischemic Stroke Compared to CT Perfusion
R Sheronick[1], C McDougall[1], P Barber[1]
[1]*University of Calgary, Calgary, Alberta*

Purpose
Multi-phase CT angiograms (mCTA) can provide perfusion information during acute ischemic stroke (AIS), similar to CT perfusion (CTP) acquisitions1. mCTA can be acquired using less expensive equipment, lower radiation dose, and is more widely available than CTP infrastructure. Prior work has shown quantitative perfusion maps can be created using a logistic regression model trained on the mCTA acquisition using quantitative CTP maps as a gold standard2. The current work compares two additional machine learning models in place of logistic regression to determine which model is the most effective for producing perfusion maps from mCTA.
Materials and Methods
295 AIS patients were acutely imaged with a three-phase mCTA acquisition (Inter-phase timing of 8 seconds, inter-slice timing of approximately 30 milliseconds). Quantitative flow maps were generated from analysis of the mCTA phase data, then spatially-filtered using a 2D Gaussian function to produce Filtered Perfusion Base Maps (FPBMs). The FPBMs are used as inputs into multiple machine learning (ML) models assessed in the current work: 1) logistic regression (LR), 2) decision tree (DT) and 3) adaptive boosting (AB). General electric (GE) – CTP maps were generated from a CTP 24-phase acquisition (acquired acutely) producing T-MAX quantitative maps, which were thresholded at a T-MAX value of 9.9 seconds to produce a gold-standard segmentation of penumbra perfusion deficit, which is used to train the ML models3. The models were trained separately for different vascular regions using a registered vascular atlas, including Anterior Cerebral Artery (ACA), Posterior Cerebral Artery (PCA), Middle Cerebral Artery (MCA), Basal Ganglia (BG), and Cerebellum (CB) territories. Local vascular territory maps are amalgamated into a global Simple

Perfusion Reconstruction Algorithm (SPIRAL) map. Area Under Curve (AUCs) were produced during training through Receiver Operating Characteristic (ROC) analysis, while model accuracies were quantified using a 10-fold cross-validation.

Results

LR, DT and AB models performed similarly, as shown by the AUCs and cross-validated accuracies in Figure 1a. ROC curves are shown in Figure 1b for each vascular region for the DT model. Example SPIRAL maps generated using LR are shown in Figure 1c.

Conclusions

The SPIRAL perfusion maps generated by the LR, DT and AB models predicted CT penumbra perfusion deficits with high accuracy. Future work will optimize SPIRAL perfusion deficits for prediction of ischemic core.

a)

AUC (cross-validated accuracy)	MCA territory	ACA territory	PCA territory	BG territory	CB territory
LR model	0.785 (0.79)	0.766 (0.71)	0.786 (0.68)	0.785 (0.78)	0.787 (0.71)
DT model	0.787 (0.79)	0.793 (0.72)	0.788 (0.68)	0.789 (0.78)	0.788 (0.71)
AB model	0.791 (0.78)	0.789 (0.71)	0.790 (0.68)	0.793 (0.78)	0.794 (0.71)

Note: Accuracies in Brackets

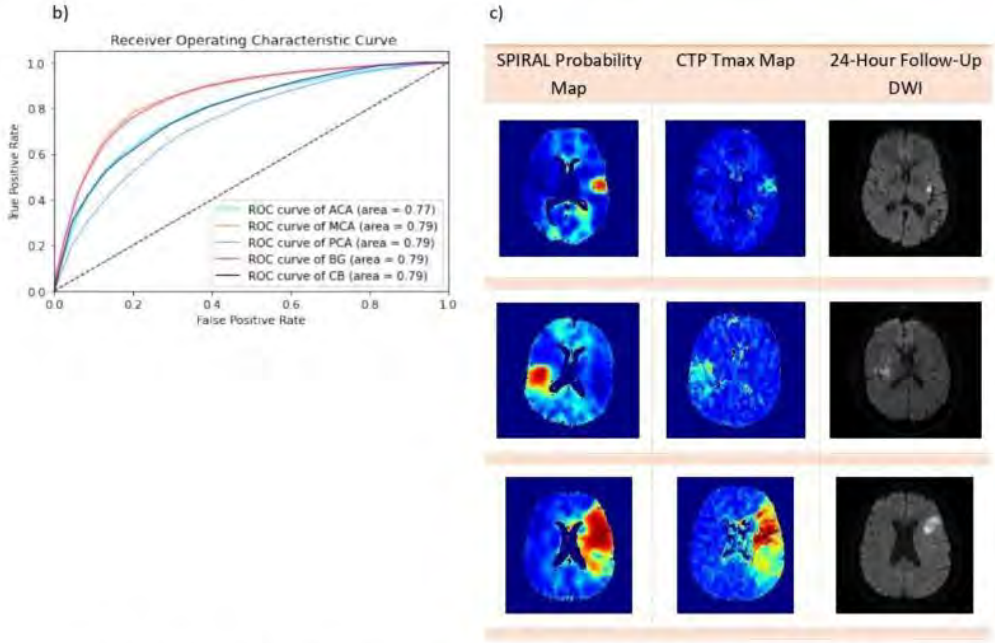

Figure 1. a) AUCs and cross-validated accuracies for each model & vascular region, b) AUCs for each vascular territory for the DT model, and c) example SPIRAL perfusion maps from the LR model.

(Filename: TCT_1511_figure-asnr.jpg)

823

The Association Between Acute Stroke and CT Cancer Screening

T Brown[1], P Duong[1], H Baradaran[1]

[1]*University of Utah, Salt Lake City, UT*

Purpose

Acute ischemic stroke can be seen in patients with cancer, thought to be related to underlying hypercoagulability. Within 2 years of having an ischemic stroke, nearly 10% of patients will be diagnosed with cancer. Colorectal, lung, and - to a lesser extent – breast cancers are the most strongly linked cancers with stroke. Despite this association between acute ischemic stroke and cancer, clear guidelines on additional imaging workup to evaluate for occult malignancy is unclear. Though additional imaging beyond age-appropriate cancer screening is not currently recommended, further workup for occult malignancy is sometimes performed using Abdominal/Pelvic and Chest Computed Tomography (CT) examinations. Since there are no clear guidelines of how to identify individuals for further malignancy workup, we sought to evaluate prevalence and incidence of malignancy in individuals presenting at our institution with acute ischemic stroke.

Materials and Methods

We retrospectively reviewed all patients at our institution between 1/1/16 and 12/31/2021 who were admitted to our hospital for acute ischemic stroke identified using ICD-9/10 coding for acute ischemic stroke. We identified a subset of patients with acute ischemic stroke presenting without preexisting cancer who received either a CT Abdomen/Pelvis, a CT Chest, or both within 30 days of acute

ischemic stroke diagnosis. A review of the patient's chart and imaging was conducted to determine if the initial CT scan(s) had evidence of malignancy present.
Results
15794 patients were identified that had a diagnosis of acute ischemic stroke. Of those, 2334 patients were excluded due to preexisting cancer. Of the remaining 13460 patients, 207 patients received either a CT Abdomen/Pelvis, a CT Chest, or both. Of the 219 patients, 111 patients had a diagnosis of cancer after their ischemic stroke. However, 18.8% (n=39) showed evidence of malignancy in their CT Abdomen/Pelvis, CT Chest, or both.
Conclusions
It is clear there is a link between acute ischemic stroke and cancer. When a patient presents with an ischemic stroke of unknown cause, cancer should be on the differential of potential underlying causes. A systemic cancer workup should be considered in these cases. A prioritized malignancy evaluation should be conducted, with a CT Abdomen/Pelvis and CT Chest performed if evidence of other neoplasms is not present.

712

White Matter Lesion Volume from T1-Weighted Magnetic Resonance Imaging Correlates with Hemorrhagic Transformation Following Thrombectomy

K Atcheson[1], M Kawas[1], C Whitlow[2], S Wolfe[2]
[1]Wake Forest University School of Medicine, Winston Salem, NC, [2]Wake Forest University School of Medicine, Winston-Salem, NC

Purpose
Endovascular thrombectomy for large vessel occlusion is a highly effective treatment to improve acute ischemic stroke outcomes. However, approximately a third of patients will suffer some degree of hemorrhagic transformation, making proper pre-procedural assessment and adverse risk prevention essential to prevent further injury. The goal of this study is to assess whether quantitative MRI analysis of white matter hypointensity volume (WMHV) can predict patients at risk for hemorrhagic transformation following thrombectomy.
Materials and Methods
We performed a retrospective analysis of the Atrium Wake Forest Stroke Thrombectomy Registry collected between 2015-2021 (n=602). Patients with large vessel occlusion who underwent thrombectomy with Thrombolysis in Cerebral Infarction (TICI) score of 2B or better were selected. Clinical T1-weighted images were transformed into high-resolution images using the convolutional neural network SynthSR. FreeSurfer software was then used to quantify baseline WMHV from the side of the brain contralateral to the stroke in order to minimize stroke interference. To correct for head size, white matter hypointensity volume was adjusted to the estimated total intracranial volume and then log-transformed to address skewness.
Results
Our analysis included 213 patients (mean age 67.5 ± 14.6, 49.3% female) who had MRI of sufficient quality collected within 14 days of the thrombectomy. Hemorrhagic transformation occurred in 103/213 (48.4%) patients as determined by CT imaging (ECASS - HH1&2: n=71; PH1: n=17; PH2: n=7; subarachnoid hemorrhage: n=7; intraventricular hemorrhage: n=1). A total of 13/103 (12.6%) were symptomatic. Univariate logistic regression analysis showed that WHMV significantly correlated with hemorrhagic transformation (X2 = 4.15, p = 0.045). When adjusting for covariates/comorbidities, there remained a trend towards significance for WMHV as a predictor for hemorrhagic transformation, (X2 = 2.76, p = 0.097), even with an underpowered sample size.
Conclusions
Increased white matter volume hypointensity correlates with hemorrhagic transformation of acute infarcts following thrombectomy. These findings build upon prior work which demonstrates that the use of neural networks can be applied to clinical management to quantify the effect of cerebrovascular disease. These techniques may have clinical implications for patient management and complication prevention as well as guiding future research avenues.

Figure 1: White Matter Hypointensity Volume (WMHV) Assessment

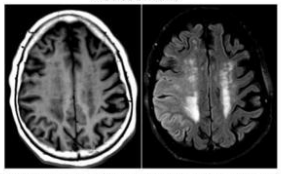

Axial T1 (Left) and T2 FLAIR (Right) through the level of the centrum semiovale demonstrating substantial white matter disease.

Figure 2: Hemorrhagic Transformation Post-Thrombectomy

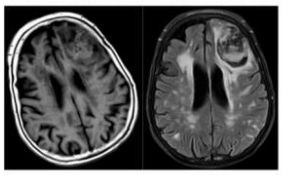

Axial T1 (Left) and T2 FLAIR (Right) showing a hemorrhagic transformation of a left frontal lobe infarct with a large space-occupying hematoma (PH2).

Table 1: White Matter Hypointensity Volume (WMHV) Correlates with Hemorrhagic Transformation Following Thrombectomy

Univariate Logistic Regression

Parameter	X^2	p-value
WMHV	4.15	0.042*

Multivariate Logistic Regression

Parameter	X^2	p-value
Sex	0.0141	0.906
Age	0.5908	0.442
Hypertension	0.2666	0.606
Admission NIHSS	3.6056	0.058#
HgbA1c	3.4149	0.065#
WMHV	2.7560	0.097#

*P values < 0.05 are considered statistically significant.
P values < 0.10 are considered trending towards significance.

(Filename: TCT_712_ASNR2023Figures_TablesKMA.jpg)

Tuesday, May 2, 2023
1:00-2:00 PM
Scientific Abstract Session: Stroke 2

353

Cerebral Arterial Air Emboli on Post-Endovascular Treatment Dual-Energy CT are Associated With Poor Short- and Long-Term Clinical Outcomes in Acute Ischemic Stroke Patients

F Pinckaers[1], I Huijberts[1], W van Zwam[1], H Boogaarts[2], R van Oostenbrugge[1], A Postma[1]
[1]Maastricht University Medical Centre+, Maastricht, Limburg, [2]Radboud University Medical Center, Nijmegen, Netherlands

Purpose
To determine the incidence and predictors of cerebral arterial air emboli (CAAE) on immediate post-endovascular treatment (EVT) dual-energy CT (DECT) and describe its association with clinical outcomes.
Materials and Methods
EVT records of patients treated in the Maastricht UMC+ from 2010 to 2019 were screened. Exclusion criteria included intracerebral haemorrhage on post-EVT DECT. Circular and linear (length ≥ 1.5*width) CAAE were counted in the affected middle cerebral artery (MCA) territory. Clinical data were collected from prospective stroke records. The modified Rankin Scale (mRS) at 90 days was the primary outcome measure. Multivariable linear, logistic, and ordinal regression was used as appropriate to analyse the association between each outcome measure and (1) linear and (2) isolated circular CAAE. Adjustments were based on univariate analyses.
Results
Out of a total of 651 records, 402 patients were included. In 65 patients (16%), at least one linear CAAE was found in the affected MCA-territory. Seventeen patients (4%) showed isolated circular CAAE. Considering procedural characteristics, patients with linear CAAE had a longer EVT duration (P<.001), more attempts (P<.001), higher rates of stent retriever usage (P<.001), lower recanalization rates (P<.001) and more procedural complications (P=.02). Multivariable regression analyses showed a significant association between both the presence and the number of linear CAAE in the ipsilateral MCA-territory and the mRS at 90 days (presence: adjusted (a)cOR 3.24, 95%CI 1.79-5.85; number: acOR 1.29, 95%CI 1.14-1.46), NIHSS at 24-48h (presence: aβ 4.02, 95%CI 1.72-6.32; number: aβ 0.82, 95%CI 0.37-1.27), mortality at 90 days (presence: aOR 3.17, 95%CI 1.4-7.19; number: aOR 1.24, 95%CI 1.07-1.43) and stroke progression (presence: aOR 3.66, 95%CI 1.75-7.67; number: aOR 1.28, 95%CI 1.11-1.47). Adjusted analyses for the dichotomized mRS (0-2 vs. 3-6) only reached significance for the presence of linear CAAE (aOR 2.42, 95%CI 1.05-5.57), but not for the number of linear CAAE (aOR 1.19, 95%CI 0.98-1.45). Isolated circular CAAE did not have a significant effect on any outcome measure on multivariable analyses.
Conclusions
CAAE are found frequently on post-EVT CT imaging. Procedural characteristics are significantly associated with the occurrence of CAAE. The presence and the number of linear CAAE, but not circular CAAE, are associated with unfavourable short- and long-term clinical outcomes.

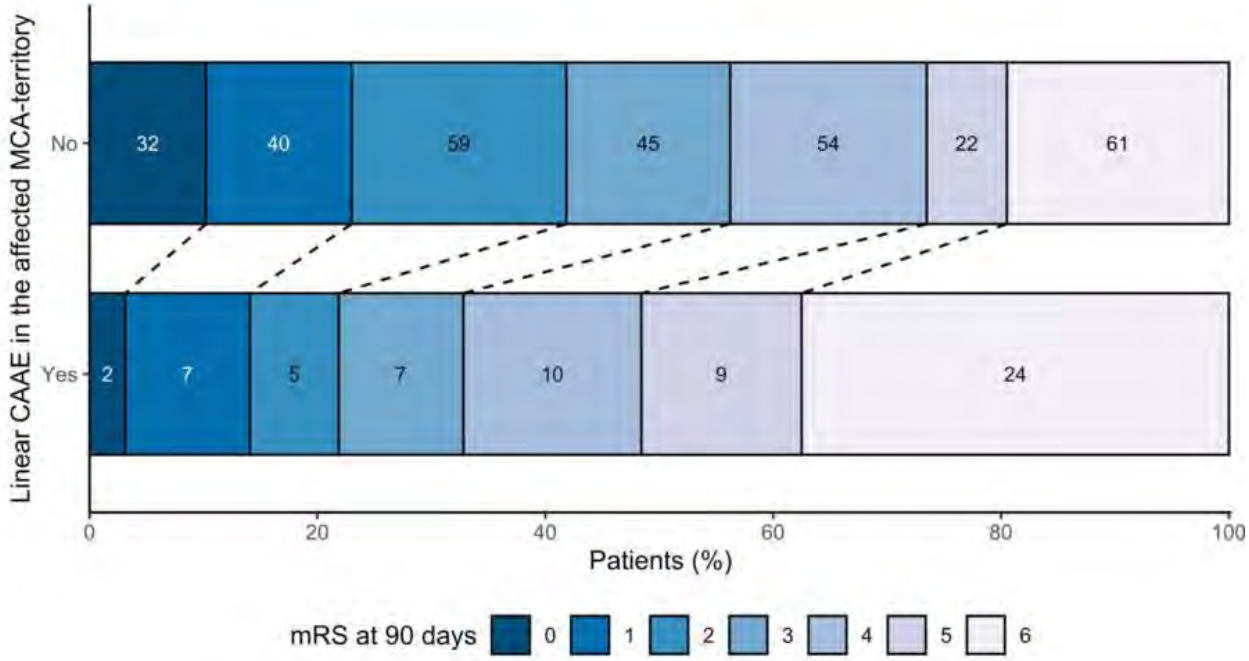

(Filename: TCT_353_mrsplot.jpg)

939

Effect of intravenous alteplase on early neurological improvement depends on lesion clock rather than time clock

G BROOCKS[1], L Meyer[2], M Bechstein[2], H KNIEP[2], L Winkelmeier[3], J Fiehler[4], A Kemmling[5]

[1]University Hamburg, Hamburg, NA, [2]University Medical Center Hamburg-Eppendorf, Hamburg, Hamburg, [3]University Medical Center Hamburg-Eppendorf, Hamburg, Germany, [4]University Hospital Hamburg-Eppendorf, Hamburg, AS, [5]University Marburg, Marburg, Hessen

Purpose

The time from symptom onset to imaging is directly associated with the clinical response to intravenous treatment with alteplase (IVT) and is therefore used to select patients for treatment. Alternatively, lesion progression may be estimated by neuroimaging to enable treatment in the uncertain or extended time window. We hypothesized that the estimation of the "lesion clock" using CT perfusion (CTP) or quantitative lesion water uptake (NWU) serve as equivalent predictors of early neurological improvement (ENI) and final functional outcome and modify the effect of IVT similar than the time clock.

Materials and Methods

Observational retrospective study of ischemic stroke patients triaged by multimodal-CT undergoing endovascular treatment. Quantitative NWU using an established threshold (11.5%) and CTP lesion-core mismatch (EXTEND criteria) were utilized to estimate the lesion progression and inverse-probability weighting analysis (IPW) was used to assess the treatment effect of IVT depending on the lesion and time clock. Endpoints were binarized early neurological improvement (ENI) and mRS 0-2 at day 90.

Results

409 patients were included, of which 223 (54.5%) received IVT. The rate of patients with early time window (<4.5h), low NWU, and CTP-mismatch were 45.0%/ 86.5%/ 80.3%. In IPW, IVT (+7.3%, p=0.02), early time window <4.5h (+11.0%, p=0.02), low NWU (+29.6%, p<0.001) and a CTP-mismatch (+16.8%, p<0.001) were significantly associated with ENI. The treatment effect of IVT on ENI, however, distinctively varied according to the presence of a CTP-mismatch (+9.6% versus -9.3%, p=0.004) and low NWU (+7.2% versus -7.3%, p=0.03) while the time window (<4.5h) did not significantly modifiy the effect of IVT (+5.8% versus -0.7%, p=0.56).

Conclusions

CT-based measures of the "lesion clock" in ischemic stroke triage might identify patients who benefit from IVT more accurately than the conventional time window of 4.5 hours. Considering the high number of patients with low lesion clock despite an extended time window, more patients might be treated when using CTP-mismatch or quantitative NWU to guide IVT.

Area under the curve (AUC) for ENI and mRS 0-2 at day 90 – Comparison of time from onset and lesion window parameters

	AUC *univariable* -ENI-	AUC *multivariable* -ENI-	AUC *univariable* -mRS 0-2-	AUC *multivariable* -mRS 0-2-
Time window	0.53	0.85	0.56	0.82
NWU	0.80	0.87	0.90	0.92
CTP lesion-core mismatch	0.59	0.84	0.63	0.89

	ENI	mRS 0-2	*ATE (95%CI) -ENI-	P Value
Early versus late time window	46.3% / 31.3% *(p<0.001)*	44.4% / 32.3% *p<0.01*	+11.0% (12.9-20.7)	0.02
Low versus high NWU	42.1% / 9.6% *(p<0.001)*	41.9% / 8.5% *(p<0.001)*	+29.6% (20.9-38.2)	<0.001
CTP lesion-core mismatch yes / no	40.4% / 23.6% *(p<0.01)*	39.6% / 26.4% *p<0.01*	+7.7% (-0.2-17.6)	0.12

*average effect on ENI adjusted for age, ASPECTS, and NIHSS as covariates using IPW analysis

Early Neurological Improvement (ENI) and distribution of time, quantitative NWU, and Mismatch Ratio

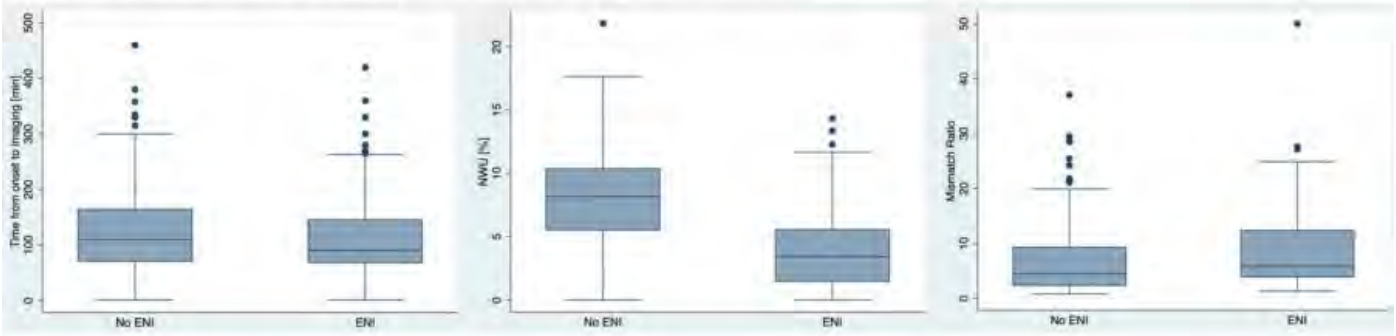

(Filename: TCT_939_fig_asnr_3.jpg)

758

How Often Do We Try? Patient-specific Factors Associated with Early Stopping without Successful Recanalization during Mechanical Thrombectomy

H KNIEP[1], L Meyer[1], G BROOCKS[2], T Faizy[3], M Bechstein[1], F Flottmann[1], L Winkelmeier[4], U HANNING[5], J Fiehler[6], S Gellissen[7]
[1]University Medical Center Hamburg-Eppendorf, Hamburg, Hamburg, [2]University Hamburg, Hamburg, NA, [3]University of Hamburg-Eppendorf, Hamburg, Germany, [4]University Medical Center Hamburg-Eppendorf, Hamburg, Germany, [5]UNIVERSITY MEDICAL CENTER HAMBURG-EPPENDORF, HAMBURG, Germany, [6]University Hospital Hamburg-Eppendorf, Hamburg, AS, [7]University Medical Hospital Hamburg-Eppendorf, Hamburg, Hamburg

Purpose
Successful recanalization has been shown to improve functional outcome in patients with ischemic stroke undergoing mechanical thrombectomy (MT) (1). However, successful recanalization defined as Thrombolysis in Cerebral Infarction Score (TICI) ≥ 2b is not achieved in 15% - 20% of the patients. This study aims to identify patient-specific factors associated with early stopping after 1 to 3 retrieval attempts without successful recanalization. We hypothesized that early stopping during MT is influenced by patient-specific factors.
Materials and Methods
All patients prospectively enrolled in the German Stroke Registry (GSR) between 06/2015-12/2021 were analyzed. Inclusion criteria were stroke in the anterior circulation and availability of relevant clinical data. For each retrieval attempt 1 to 3, patients with stopping of retrievals and failed reperfusion (TICI < 2b) were compared to all patients with continued retrieval attempts using descriptive statistics and multivariable logistic regression.
Results
2977 patients were included in the analysis. 350 patients had early stopping of retrievals after 1 to 3 passes without successful recanalization. These patients had a higher age (75.3 vs. 73.6), more nursing care (19% vs. 12%), higher mean pre-stroke mRS (1.0 vs. 0.7), less general anaesthesia (69% vs. 76%), a higher rate of distal occlusions (ACA, M2) (37% vs. 26%) and more adverse events. The rate of functional independence with mRS ≤ 2 was lower with 16% vs. 31% (Table 1). Multivariable logistic regression suggests that primary distal occlusions, dissection/perforation, higher age and nursing care are associated with higher probability for early stopping while general anesthesia increases probability for continuation. I.v. thrombolysis was associated with early stopping after the first pass while later admission years were associated with continuation (Figure 1).
Conclusions
Our study suggests that distal occlusions, higher age, nursing care and dissections/perforations increase risk of early stopping without successful recanalization, while general anesthesia is significantly associated with continued retrieval attempts. Stopping after a failed first pass is more likely in patients that received i.v. thrombolysis but generally decreased during the enrolment period from 2015 to 2021. Results may improve the understanding of clinical characteristic leading to early stopping without successful recanalization and may help to improve MT treatment strategies.

Table 1: Study cohort clinical characteristics

	Early stopping after passes 1-3 without successful recanalization			
	no (N=2627)	yes (N=350)	Total (N=2977)	p value
Age	73.6 (13.1)	75.3 (12.7)	73.8 (13.1)	0.019
Sex female	1439 (55%)	187 (53%)	1626 (55%)	0.634
Admission year	2019.1 (1.5)	2018.9 (1.6)	2019.1 (1.5)	0.016
Nursing	319 (12%)	65 (19%)	384 (13%)	< 0.001
Anti-thrombotic medication	1145 (44%)	157 (45%)	1302 (44%)	0.652
Pre-stroke mRS	0.7 (1.2)	1.0 (1.3)	0.8 (1.2)	< 0.001
NIHSS admission	14.3 (6.4)	14.5 (6.5)	14.3 (6.5)	0.502
Hypertension	1990 (76%)	266 (76%)	2256 (76%)	0.919
Diabetes	545 (21%)	65 (19%)	610 (20%)	0.344
Dyslipidemia	1052 (40%)	130 (37%)	1182 (40%)	0.297
Atrial fibrillation	1176 (45%)	157 (45%)	1333 (45%)	0.974
ASPECTS admission	8.3 (1.8)	8.1 (2.0)	8.2 (1.8)	0.146
I.v. thrombolysis	1221 (46%)	165 (47%)	1386 (47%)	0.815
General anaesthesia	1989 (76%)	240 (69%)	2229 (75%)	0.004
Occluded vessel right	1256 (48%)	157 (45%)	1413 (47%)	0.537
Primary distal occlusion (ACA, M2)	673 (26%)	130 (37%)	803 (27%)	< 0.001
AE vasospasm	160 (6%)	16 (5%)	176 (6%)	0.258
AE clot migration/embolization	148 (6%)	22 (6%)	170 (6%)	0.621
AE dissection/perforation	72 (3%)	42 (12%)	114 (4%)	< 0.001
AE ICH	101 (4%)	36 (10%)	137 (5%)	< 0.001
AE other	192 (7%)	47 (13%)	239 (8%)	< 0.001
Functional independence (90d mRS ≤2)	822 (31%)	57 (16%)	879 (30%)	< 0.001

Results shown in means (SD) and numbers (percentage). mRS: Modified Rankin Scale; NIHSS: National Institutes of Health Stroke Scale; ASPECTS: Alberta Stroke Program Early CT Score; ACA: Anterior cerebral artery; M2: M2 segement of the Middle cerebral artery; AE: Adverse event; ICH: Intracerebral hemorrhage

Figure 1: Factors accociated with early stopping without successful recanalization.

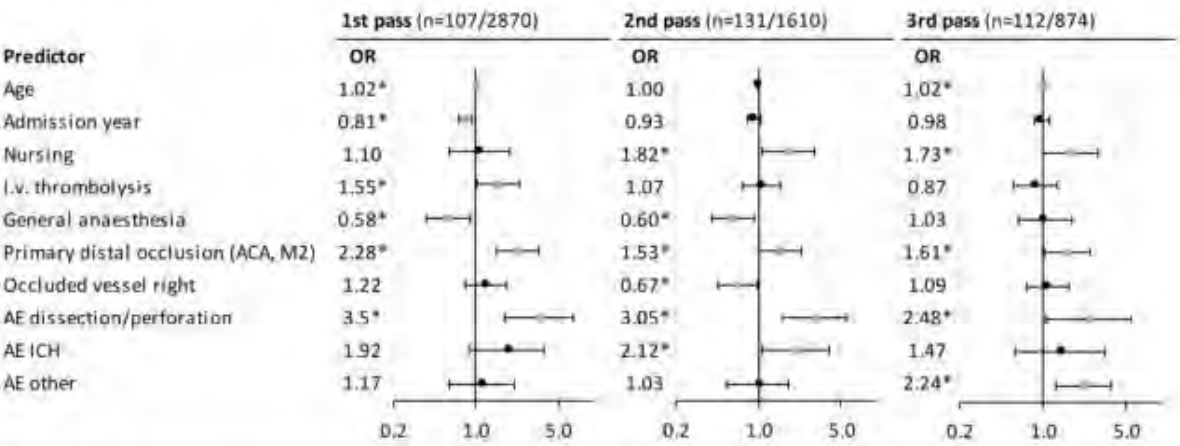

Orange markers indicate statistical significance with p-value < 0.05. ACA: Anterior cerebral artery; M2: M2 segement of the Middle cerebral artery; AE: Adverse event; ICH: Intracerebral hemorrhage

(Filename: TCT_758_Table_Figure.jpg)

851

In vivo analysis of selective intraarterial thiopental injection for neuroprotection in reversible cerebral ischemia

M Gökten[1], O Öcal[2], E Öcal[3], A Arat[4]

[1]Corlu State Hospital, Tekirday, Turkey, [2]Hacettepe University, Ankara, Turkey, [3]Ankara University, Ankara, Turkey, [4]Hacettepe University, Ankara, Eyalet/Yerleşke

Purpose

Neuroprotective agents are needed to reduce cerebral damage during surgical or neurointerventional procedures. This study aimed to evaluate whether intraarterially injected thiopental can be used as a neuroprotective agent in a transient ischemia model.

Materials and Methods

Twenty-four rabbits were divided into four groups with six animals: Group 1 served as the control group. Group 2 was administered thiopental intraarterially via the carotid artery. In group 3, transient ischemia was achieved via intracarotid administration of degradable starch microspheres (DSM). Group 4 (experimental group) received both thiopental and DSM intraarterially. DSM and thiopental were administered through a microcatheter placed into the common carotid artery via central ear artery access. After sacrifice, apoptotic cells in the cerebral tissues of the animals were evaluated in H&E and TUNEL stained slides.

Results

There was a significant increase in apoptotic glial or neuronal cells in group 3 compared to the control group and group 2. The mean number of both the apoptotic neuronal cells (6.8±2.1 vs. 2.5±1.3, $p<0.001$) and the apoptotic glial cells (9.4±3.1 vs. 4.6±1.6, $p<0.001$) were higher in group 3 compared to group 4. Additionally, a higher level of neurological improvement was observed in group 4 compared to group 3 based on the neurological assessment score.

Conclusions

Intraarterial low-dose thiopental administration has a protective effect on glial and neuronal cells during temporary cerebral ischemia.

691

Intravenous Thrombolysis improves Clinical Outcomes in Stroke Patients with Unsuccessful Endovascular Reperfusion

L Winkelmeier[1], J Heit[2], F Flottmann[1], G Albers[2], M Lansberg[2], J Fiehler[1], T Faizy[1]

[1]University Medical Center Hamburg-Eppendorf, Hamburg, Germany, [2]Stanford University Medical Center, Stanford, CA

Purpose

Purpose: Unsuccessful endovascular reperfusion is observed in 10-30% of patients who underwent endovascular treatment (EVT) with acute ischemic stroke due to large vessel occlusion (AIS-LVO).1, 2 It remains a matter of debate whether AIS-LVO patients may benefit from a combined treatment with intravenous thrombolysis (IVT) before EVT. We investigated whether IVT improves clinical outcomes in the subgroup of AIS-LVO patients with unsuccessful endovascular reperfusion.

Materials and Methods

Materials and Methods: Retrospective multicenter study to compare [1] IVT plus EVT versus [2] EVT alone in AIS-LVO patients in whom endovascular reperfusion was not achieved during EVT. Unsuccessful endovascular reperfusion was defined as failed or partial reperfusion (modified Thrombolysis in Cerebral Infarction (mTICI) score of 0/1 and 2a, respectively). Pairwise propensity score matching was used to adjust treatment arms for age, sex, and admission National Institutes Health Stroke Scale. The primary end point was good functional outcome defined as 90-day modified Rankin Scale score of 0-3. Stepwise multivariable logistic regression was performed to identify independent determinants of good functional outcomes.

Results

Results: A total of 136 out of 813 patients met the inclusion criteria. After 1:1 matching, 118 patients were compared by treatment arms. 31.6% in the IVT plus EVT group and 15.5% in the EVT alone group achieved good functional outcomes ($p=0.042$). The rate of good functional outcomes increased in case of partial compared to failed reperfusion in the IVT plus EVT group (50.0% vs 20.0%; $P=0.018$), but not in the EVT alone group (16.2% vs 14.3%; $p=0.845$; see Figure 1A). Higher age (adjusted odds ratio, 0.66 [95% CI, 0.44-0.93]), higher NIHSS (0.90 [0.82-0.98]), favorable arterial collateralization (4.05 [1.27-16.27]) and IVT (3.07 [1.16-8.79]) were independently as-sociated with good functional outcomes (see Figure 1B).

Conclusions

Conclusion: Our data suggest that IVT may improve functional outcomes in AIS-LVO patients with unsuccessful endovascular reperfusion. Particularly patients with partial reperfusion (mTICI 2a) might benefit from preceding IVT. Further research is required to validate our findings.

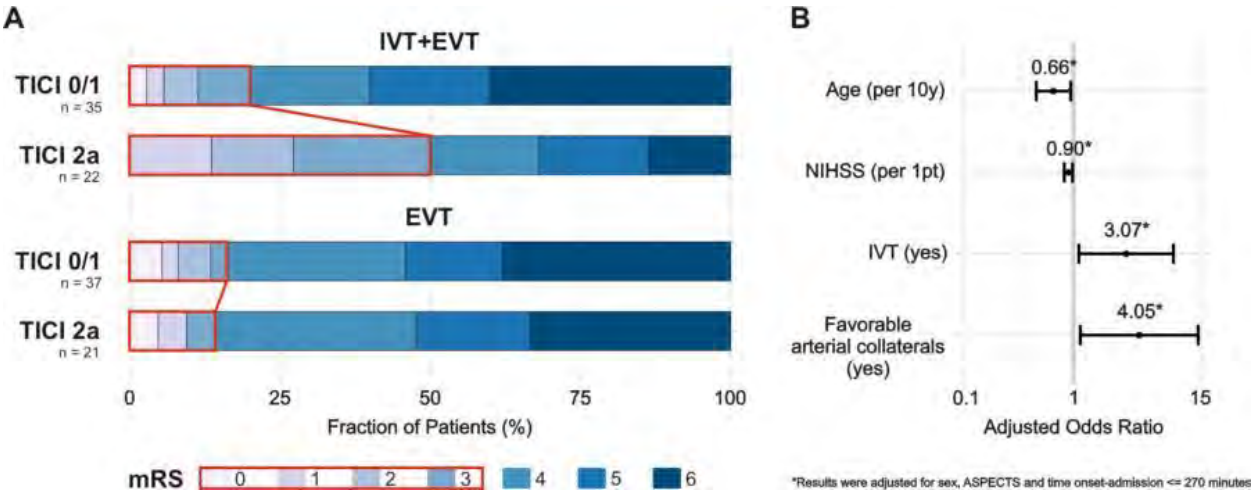

(Filename: TCT_691_Corel_FailedTPA.jpg)

380

Occurrence of Secondary Hemorrhage after Thrombolysis in Wake-Up Stroke Depends on Early Lesion Water Uptake

G BROOCKS[1], M Bechstein[2], L Meyer[2], J Fiehler[3], A Kemmling[4]

[1]University Hamburg, Hamburg, NA, [2]University Medical Center Hamburg-Eppendorf, Hamburg, Hamburg, [3]University Hospital Hamburg-Eppendorf, Hamburg, AS, [4]University Marburg, Marburg, Hessen

Purpose

In ischemic stroke with unknown time of onset, CT-based quantitative net water uptake (NWU) has recently been described as an alternative to MRI to guide intravenous treatment with alteplase (IVT). Symptomatic intracerebral hemorrhage (sICH) after IVT is a feared complication. As NWU directly indicates lesion progression, reflecting the severity of blood-brain barrier leakage, we hypothesized that the degree of NWU predicts secondary ICH in wake-up stroke patients.

Materials and Methods

All anterior circulation ischemic stroke patients with unknown onset who underwent CT on admission and endovascular treatment between 12/2016-10/2020 at a tertiary care center were consecutively analyzed. Quantitative NWU was measured in admission-CT. Primary endpoint was sICH. Inverse-probability weighting (IPW) analysis was performed to investigate the association of NWU and other baseline parameters to sICH.

Results

88 patients were included. The median NWU was 10.7% (IQR: 5.1-17.7). 46 patients (52%) received IVT. The rates of any hemorrhage and sICH were 35% and 12.5%, respectively. In patients with sICH, quantitative NWU at baseline was significantly higher (19.1% versus 9.6%, p<0.0001) and the median ASPECTS lower (5 versus 8, p<0.0001). In IPW analysis, IVT was not linked to sICH in unadjusted analysis. After adjusting for NWU and ASPECTS, however, IVT was significantly associated with sICH (+14.6%, 95%CI: 3.3-25.6%, p=0.01).

Conclusions

In wake-up stroke, high NWU in combination with IVT is associated with higher rates of sICH and poor functional outcome. Quantitative NWU might serve as imaging biomarker to indicate the severity of blood-brain barrier injury assessing the risk of sICH in wake-up stroke patients besides ASPECTS.

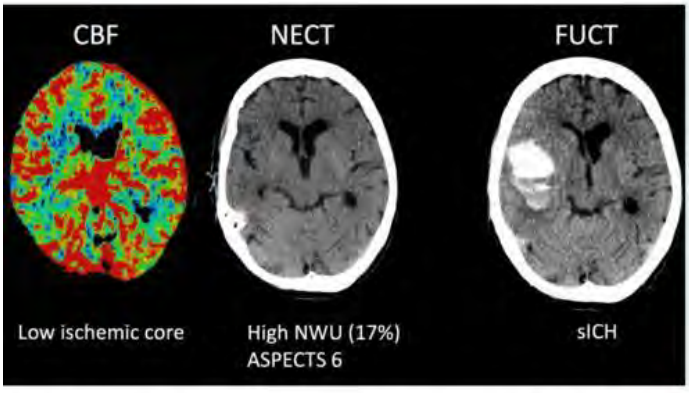

Figure - sICH in a patient with low ischemic core but high net water uptake (NWU) on admission

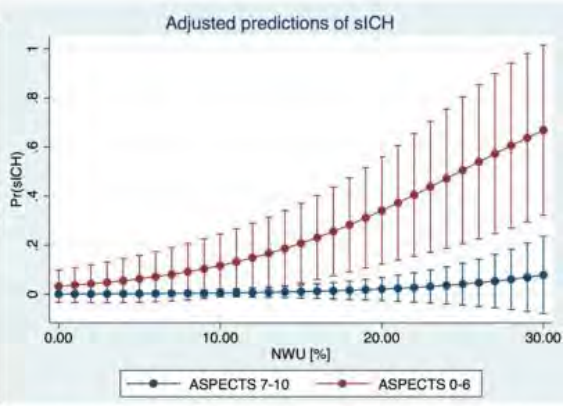

Graph - Association of NWU (x axis) and ASPECTS with sICH (y axis)

(Filename: TCT_380_ASNR_wakeup_FIG.jpg)

355

The association of blood pressure during endovascular treatment on immediate post-procedural intracranial hemorrhage on Dual-Energy CT in acute ischemic stroke patients

M Robbe[1], F Pinckaers[1], S Olthuis[2], R van Oostenbrugge[2], W van Zwam[1], J Staals[2], A Postma[1]

[1]Department of Radiology, Maastricht University Medical Centre+, Maastricht, Limburg, the Netherlands, [2]Department of Neurology, Maastricht University Medical Centre+, Maastricht, Limburg, the Netherlands

Purpose

Optimal blood pressure (BP) management during endovascular treatment (EVT) for acute ischemic stroke remains a topic of debate. Though elevated BP ensures the perfusion of potentially viable penumbra, it might be associated with an increased risk of intracranial hemorrhage (ICH). In this study, we aim to investigate the influence of BP during EVT on immediate post-procedural ICH on Dual-Energy CT (DECT).

Materials and Methods

We included all patients who underwent EVT for an anterior large vessel occlusion between 2010-2019, and received DECT post-EVT within 3 hours. Patients were excluded if an intracranial hemorrhage was present before EVT. All systolic BP (SBP) and diastolic BP measurements during EVT procedure were recorded. Mean arterial pressure (MAP) and SBPmax-min (maximum minus minimum) were calculated. Virtual native reconstructions of DECT were evaluated for ICH and classified as intra- or extraparenchymal ICH. If a patient demonstrated both, the ICH was classified as intraparenchymal. Symptomatic ICH at time of DECT was scored according to the Heidelberg criteria. The association between different BP parameters per 10mmHg and ICH was assessed using multivariable logistic regression models, adjusted for EVT duration and number of attempts, and presented as adjusted odds ratios (aOR). All analyses were performed on a multiple imputed dataset.

Results

478 patients met our inclusion criteria. 76 patients (15,8%) demonstrated ICH on DECT, of which 26 (5,4%) intraparenchymal ICH. Intraparenchymal ICH was symptomatic in 10 (38%) patients. SBPmax, SBPmean and MAPmean were associated with intraparenchymal ICH with an aOR of 1.19 (95% CI 1.02-1.39), 1.22 (95% CI 1.03-1.46), and 1.4 (95% CI 1.09-1.81) per 10mmHg increase, while SBPmax-min was not. There was no significant difference between blood pressures of asymptomatic and symptomatic ICH. No BP parameter was significantly associated with extraparenchymal ICH.

Conclusions

Procedural BP is significantly associated with immediate post-EVT intraparenchymal ICH, but not with extraparenchymal ICH.

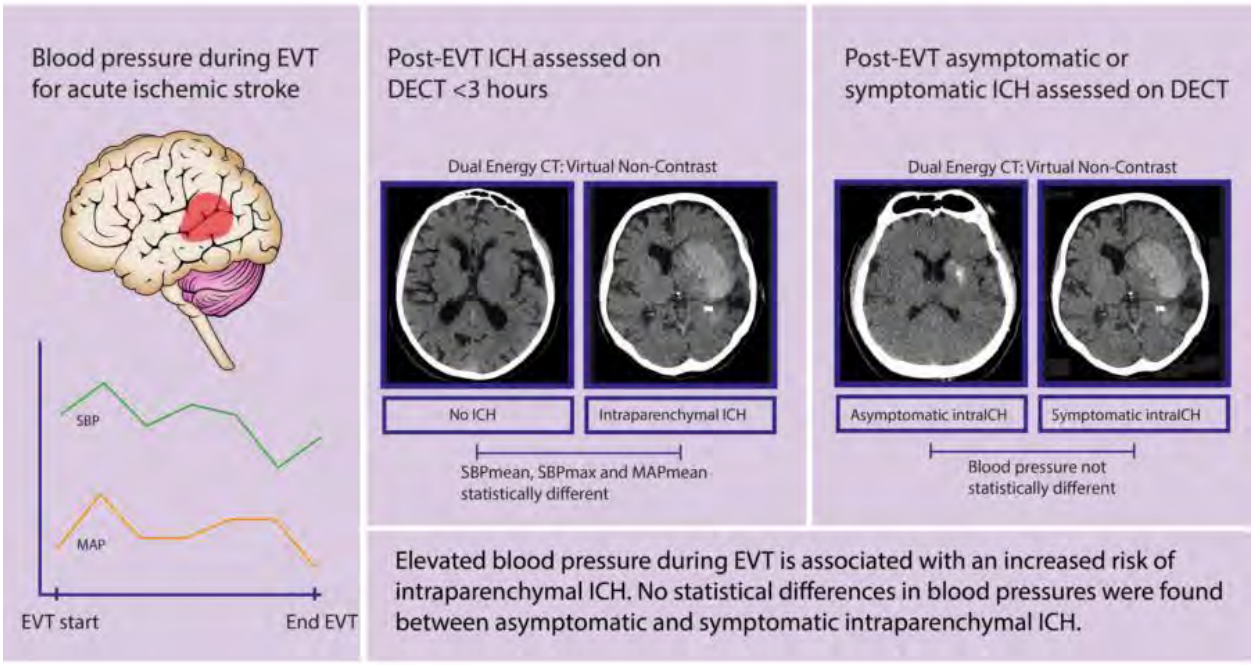

(Filename: TCT_355_AbstractBPvsHEMQuirienRobbe.jpg)

1150

Validating Heidelberg Ratings of Hemorrhagic Transformation After Mechanical Thrombectomy on MRI with SWI and GRE Sequences, with Comparison to CT

S Rogers[1], B Renshaw[1], C Reynolds[1], A Frazzitta[1], A Bhandari[1], S Vedantham[1]
[1]*University of Arizona, Tucson, AZ*

Purpose

Hemorrhagic transformation after reperfusion therapy in acute ischemic stroke has classically utilized CT for grading, both on the earlier ECASS and the later Heidelberg grading systems. To our knowledge, no studies have examined the application of the Heidelberg grading system of HT with MRI on SWI and GRE sequences. On CT, it has been recognized that the mildest grade of HT with Heidelberg, scattered small petechiae with no mass effect, is unlikely to represent symptomatic intracranial hemorrhage (sICH). Because SWI and GRE are more sensitive for detection of hemorrhage than CT, it is unclear if this increased sensitivity on MRI will lead to higher Heidelberg ratings, or how this correlates with sICH. The validity and interobserver agreement of Heidelberg ratings on MRI are also unknown.

Materials and Methods

IRB approval was obtained. We retrospectively reviewed consecutive patients with LVO treated with mechanical thrombectomy (MT) in our institution from January 2020 – August 2022. We included patients who had either MRI or CT after MT. Two observers independently evaluated the degree of HT on MRI using SWI or GRE according to Heidelberg rating (iHT), blinded to clinical information. This was also done for post-thrombectomy CT, if available. Symptomatic HT (sHT) was independently assessed according to joint commission guidelines of hemorrhage on imaging and worsening NIHSS (sHT). Detailed clinical information was recorded.

Results

156 patients underwent thrombectomy. Preliminary evaluation from one observer was performed on 62 patients, finally including 33 patients with post-thrombectomy MRI. 24 of these also had a concurrent CT. sICH was observed in 6 of these patients, all of which demonstrated a Heidelberg rating >1 on both CT and MRI. sICH was correlated with higher Heidelberg rating on both CT and MRI. MRI demonstrated similar Heidelberg ratings as CT, with 14/24 (58%) demonstrating the same score and 10/24 (42%) demonstrating a higher MRI rating by 1 point. Validity of the MRI Heidelberg rating will be assessed on the final analysis.

Conclusions

Both CT and MRI Heidelberg ratings of HT after thrombectomy correlate with sICH. MRI ratings are generally the same as CT or higher than CT by 1 point. Validity of MRI ratings will be assessed.

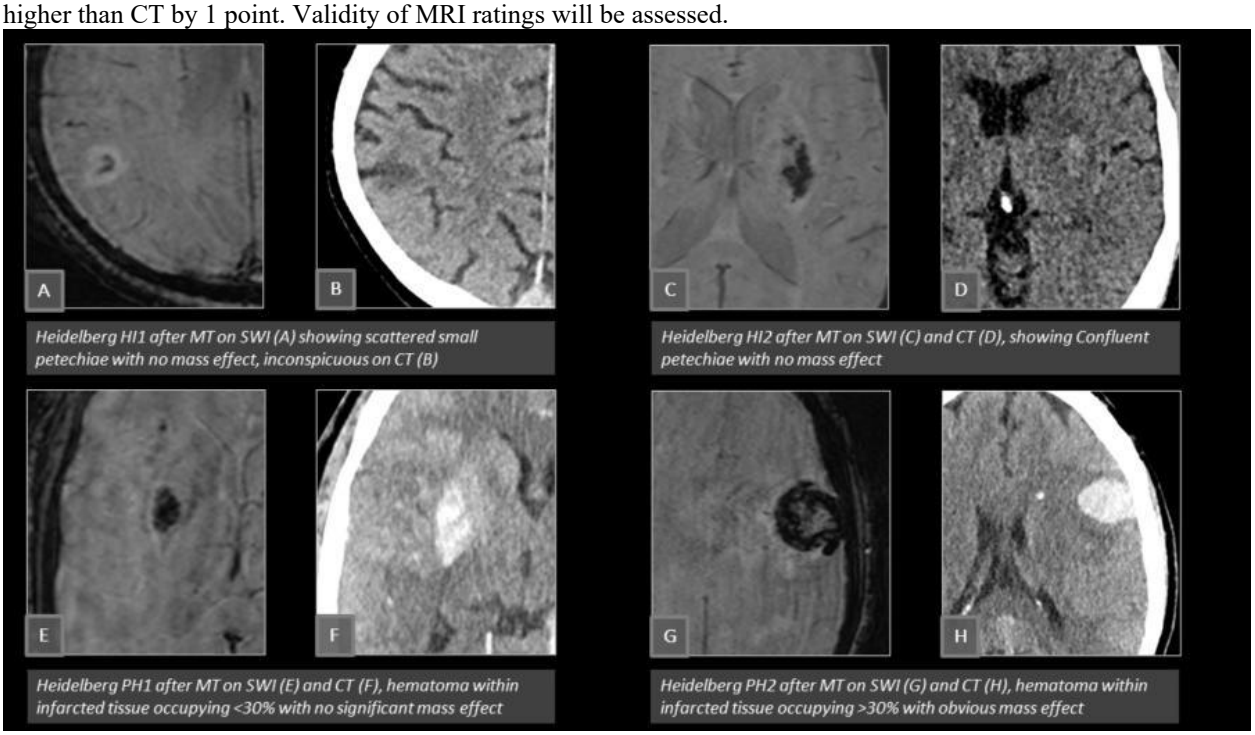

(Filename: TCT_1150_ASNRheidelbergfigure.jpg)

Tuesday, May 2, 2023

1:00-2:00 PM

Scientific Abstract Session: Tumor & Trauma

1445

IDH-wild type Glioblastoma: Predictive Value of Standard-of-care (SOC) MRI for Establishing MGMT Promoter Methylation Status

D Timaran[1], L Nunez[2], A Rodriguez[2], D Serrano[3], R Riascos[2]

[1]University of Texas Health Science Center Houston, Houston, TX, [2]The University of Texas Health Science Center at Houston, Houston, TX, [3]UT Houston, Sugar Land, TX

Purpose

Oxygen 6-methylguanine-DNA methyltransferase (MGMT) promoter methylation is associated with better response to chemotherapy and prognosis in patients with glioblastoma. Therefore, we aim to assess the prognostic value of standard-of-care (SOC) MRI findings to determine MGMT promoter methylation status.

Materials and Methods

A retrospective study was performed including 79 patients with histology confirmed IDH-mutant glioblastoma. Patients were divided in 2 groups: patients with MGMT promoter methylation (36[45.5%]) and unmethylated (43[54.5%]). MRI findings were assessed using the Visually Accessible Rembrandt Imaging lexicon (VASARI). Univariate analysis was performed using X2/ Fisher's test with Monte Carlo simulation for categorical variables. Independent predictors of MGMT promoter methylation status were determined using logistic regression analysis.

Results

Deep white matter invasion was more frequently seen in glioblastomas with unmethylated MGMT promoter (26 [60.4%] versus 11 [30.5%] in glioblastomas with MGMT methylation) (p=0.01). Intralesional cystic degeneration was observed in 9 patients (11.4%). Among them, 8[89%] were MGMT unmethylated lesions (p=0.03). Similarly, avid contrast enhancement was more frequently seen in unmethylated glioblastomas (40[60.6%] versus 26 [39.4%]) (p=0.04). Among glioblastomas with MGMT methylation, facilitated diffusion was more frequently seen (11[68.7%] versus 5[31.3%] in glioblastomas without MGMT promoter methylation) (p=0.01). In our multivariate analysis, cystic degeneration (OR, 9.89 [95% CI, 1.1-87]) (p=0.03) and white matter invasion (OR 1.85[95%CI, 1.04-3.13]) (p=0.03) were independent predictors of MGMT promoter methylation status.

Conclusions

Imaging characteristic on standard of care imaging may predict MGMT promoter methylation status in patients with glioblastomas. Furthermore, lesions with cystic degeneration and deep white matter invasion are independent predictors of non-MGMT methylation.

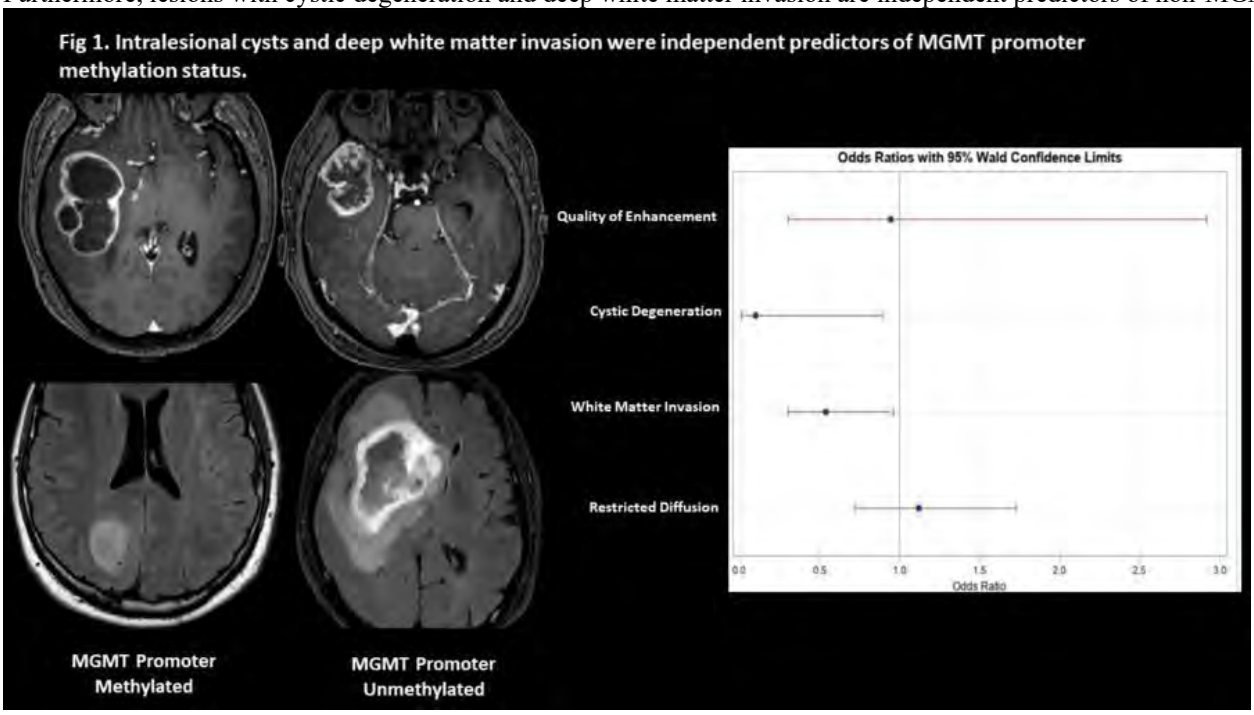

(Filename: TCT_1445_MGMT-Figure.jpg)

1463

Independent Predictors and Impact of the AO Spine Upper Cervical Classification System (AO Spine UCCS) on Spinal Cord Injury (SCI) Among Patients with Upper Cervical Spine Trauma (UCST)

D Timaran[1], L Nunez[2], J McCarty[3], S Khanpara[4], A Rodriguez[2], R Riascos[2]

[1]University of Texas Health Science Center Houston, Houston, TX, [2]The University of Texas Health Science Center at Houston, Houston, TX, [3]UTHealth Houston, Houston, TX, [4]University of Texas MD Anderson Cancer Center, Houston, TX

Purpose

To determine the incidence of spinal cord injury (SCI) in patients with upper cervical spine trauma (UCST). Furthermore, we investigated independent predictors of SCI including the impact of the AO Spine Upper Cervical Classification System (UCCS).

Materials and Methods

Over a 3-year period, an observational, single center study was performed at a level I trauma center. In total, 443 subjects with acute cervical spine trauma were reviewed. Only patients with UCST who were evaluated with cervical spine CT and MRI were included in the study (170 patients [38%]). Univariate analysis was performed using X2 test, Fisher exact test or Monte Carlo simulation test. Logistic regression analysis was used to determine independent predictors of SCI. Diagnostic performance of our model was assessed using the ROC method.

Results

In total, SCI was found in 26 patients (15%). Among them, spinal cord edema was seen in 11(42%), hematoma in 11 (42%) and in 4 patients (16%) mixed regions of edema and hematoma. In 8 patients (31%), concomitant lesions of the cervical subaxial spine ($p<0.01$) were observed. Only lesions at the AO Spine UCCS level I were associated with SCI (8 [31%] $p=0.05$). According to a multivariate analysis, combined injury of the upper cervical spine and subaxial spine was an independent predictor of SCI (OR of 6.5 [95% CI, 1.9-21.6] [$p<0.01$]). The area under the curve for this model was 0.758 with a sensitivity of 88%, specificity of 46%, PPV of 90% and NPV of 41%. A second model that included baseline clinical variables, the OR for subaxial spine injuries was 8.3 [95%CI, 2.5-28.1]) ($p<0.01$) and 1.4 for mode of trauma (95% CI, 1.08-2.02) ($p=0.01$). For this model, the ROC estimate was 0.77 with a sensitivity of 86%, specificity of 57%, PPV of 91% and NPV of 43%.

Conclusions

The incidence of SCI in patients with UCST reached 15%. Combined injuries of the upper and subaxial cervical spine were independent predictors of SCI, with an 8-fold increase in risk. Interestingly, lesions at the AO Spine UCCS level I were less frequently identified in patients with SCI. However, none of the AO Spine UCCS parameters demonstrated statistical significance on a multivariate regression model.

Table I. Baseline characteristics by presence and absence of SCI

Variables	Total n=170	Patients with SCI n=26 (15%)	Patients without SCI n=144 (85%)	p value
Gender				
Male	107 (63)	16(61)	91 (63)	0.8
Female	63(37)	10 (39)	53(37)	
Age (years)	41 +/- 20	50 +/- 21.7	39.3 +/- 19.5	0.02
BMI (kg/m^2)	25.6 +/- 5.5	26.9+/-5.5	25.4+/-5.4	0.2
Cause of trauma				
Motor vehicle accident	114(67)	13 (50)	101(89)	<0.01
Pedestrian/bicyclist struck by motor vehicle	22 (13)	0(0)	22(15)	
Fall less than 8 feet	17 (10)	8(31)	9(6)	
Fall greater than 8 feet	8 (5)	2(8)	6(4)	
All-terrain vehicle	6 (3.5)	1 (4)	5(3)	
Violent assault	2(1)	1 (4)	1 (0.6)	
Gunshot wound	1 (0.5)	1 (0.6)	0(0)	
BCVI	6 (3.5%)	1(4)	5(3)	>0.9
AO spine Upper Cervical Injury Classification				
Injury location				
I	84 (49)	8(31)	76(53)	0.05
II	59 (35)	11(19)	48 (81)	0.3
III	71(42)	11(15)	60 (84)	0.9
Injury type				
A	121(71)	18(69)	103(71)	0.8
B	32(19)	4(15)	28 (19)	0.7
C	27(16)	6(23)	21(14)	0.2

•BMI, body mass index
•BCVI, blunt cerebrovascular injury

(Filename: TCT_1463_SCI.jpg)

1039

Mechanisms to enhance immunotherapy in a rat model of medulloblastoma.

C Stateler[1], S Holland[1], J Stoller[1], D Wongsawaeng[1], L Muldoon[1], E Neuwelt[1], P Ambady[2], R Barajas[3]

[1]Oregon Health & Science University, Portland, OR, [2]Providence health, Portland, OR, [3]OHSU, Portland, OR

Purpose

Medulloblastoma is the most common malignant primary brain tumor in pediatric patients. Current treatment achieves long-term survival but can cause irreversible CNS damage. Clinical immunotherapies focus on activating adaptive immunity, but cells of the innate immune system comprise a significant portion of the cellular mass in brain tumors. Additionally, the tumor microenvironment

suppresses the activity of many critical defense mechanisms.(1) Our research aims to explore more efficacious treatments preclinically through use of targeted therapeutic techniques that leverage the innate immune system in the medulloblastoma microenvironment.
Materials and Methods
A group of 17 adult nude rats were implanted with serially passaged medulloblastoma orthotopic intracerebellar patient derived xenografts. At day 12 after tumor implantation, baseline gadolinium enhanced MRI (Gd-MRI) T1W and T2W images were used to estimate pre-therapy tumor volumes. The treatment groups consisted of untreated controls (N= 4), single fraction 2Gy irradiation to the tumor-bearing hemisphere with 20mg/kg temozolomide (CRT) orally x1 (N= 3), CRT combined with amphotericin B (AmpB) 0.2mg/kg IP daily x7 (N= 4), 2Gy radiation combined with both AmpB 0.2mg/kg IP daily x7 and CD47 antisense oligonucleotide 10.5mg/kg 24hrs post-radiation (N= 3), and 2Gy rad with CD47 oligo 10.5mg/kg 24hrs post radiation (N= 3). After 7 days of therapy (day 19), Gd-MRI was used to analyze percent change prior to euthanasia (statistical significance at $P \leq 0.05$).
Results
Figure 1 demonstrates post-therapy changes in enhancement volume compared to untreated controls. The untreated control group showed 14.4% and 4.0% growth respectively on T1W and T2W volumes. The CRT group showed a 4.0% and 2.0% growth (P= 0.07 and P= 0.12 compared to controls). The CRT+AmpB group grew 1.5% and 0.5% (P= 0.05 and P= 0.02). The 2Gy rad+anti-CD47+AmpB group displayed a 2.1% and 0.6% growth (P= 0.05 and P= 0.02). Lastly, the 2Gy rad+anti-CD47 showed a 7.6% and 5.3% growth (P= 0.14 and P= 0.21).
Conclusions
These observations suggest that combined irradiation and multimodal immunotherapy inducing an innate immune response may improve tumoricidal efficacy in preclinical medulloblastoma models as demonstrated by MRI. We are currently undertaking histological confirmation. Future studies will evaluate the efficacy of innate immune targeted therapies in larger sample sizes, with the eventual goal of progressing to the clinical environment.

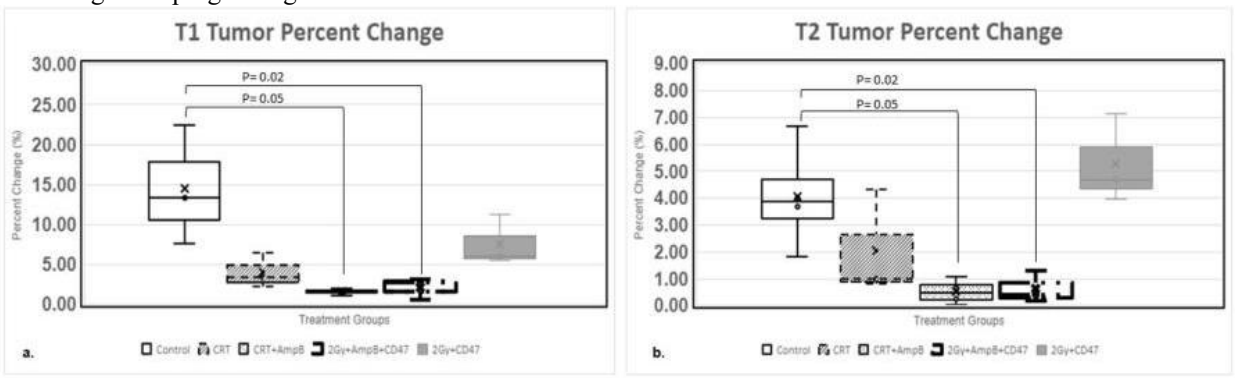

Figure 1: Tumor Volume Percent Change from Day 12 Start of Treatment to Day 19 Post Treatment. Tumor volumes were assessed by measuring areas of enhancement using Gd-MRI T1 and T2 weighted imaging following a seven-day treatment period. Figures 1a and 1b show the percent tumor volume changes for T1 and T2 respectively, beginning day 12 start of treatment to day 19 end of treatment.

(Filename: TCT_1039_Slide1.JPG)

315

Radiomics Analysis Predict Pseudoprogression vs. True Progression in Glioblastoma: a Multi-institutional Study

M Ak[1], P Mamindla[2], M Beker-Acay[3], V Peddagangireddy[1], M Er[4], S Zenkin[5], N Ak[1], T Idris[6], A Hassan[7], F Moron[8], R Colen[9]
[1]University of Pittsburgh, Pittsburgh, PA, [2]University of Pittsburgh, Cincinnati, OH, [3]UPMC, Pittsburgh, PA, [4]Rush university medical center, Chicago, IL, [5]Department of Radiology; University of Pittsburgh, Pittsburgh, PA, [6]Massachusetts General Hospital, Boston, MA, [7]MD Anderson Cancer Center, Houston, TX, [8]BCM, Houston, TX, [9]University of Pittsburgh Medical Center, Pittsburgh, PA

Purpose
To discriminate progressive disease (PD) vs. pseudoprogression (PsP) utilizing the radiomics analysis in glioblastoma (GBM).
Materials and Methods
We evaluated 686 patients from three institutions of which 487 were TP, and 199 were PsP. We segmented edema, contrast enhancement, necrosis, and hemorrhage for each patient. Their respective contralateral white matter (cWM) regions of interest (ROI). 205 texture features were extracted from each sequence's volume of interest (VOI), including 10 histogram-based first-order features and 195 second-order gray-level co-occurrence matrices features. After normalization, , the 195 second-order features were divided by their volume to produce 195 volume-independent—a total of 400 features extracted per VOI and 1600 features per patients. We removed features that are highly correlated (Pearson's correlation coefficient >0.80) and performed feature selection on the remaining features using the SHapley Additive exPlanations (SHAP) package that measures the feature importance. We split the cohort into 90% training and 10% testing. We used XGBoost algorithm to generate the radiomics model. The predictive performance of the models for classifying each lesion (PD versus PSP) was estimated using the receiver operating characteristic curve, summarized as the area under the curve.
Results
Out of the 1600 total features, 1491 features correlated greater than 0.80. These highly correlated features were removed from the total set, leaving 109 features. Feature selection with SHAP method on 109 features identified 86 that contribute highly to the outcome

prediction. 30 of the 86 were most relevant and were used for model building. Our model`s training set accuracy with 10-fold cross-validation was 80%, and the testing set accuracy was 81%, with sensitivity and specificity of 79% and 84%, respectively.
Conclusions
Our study presents a radiomics model that can successfully differentiate between PD vs. PsP in GBM patients.

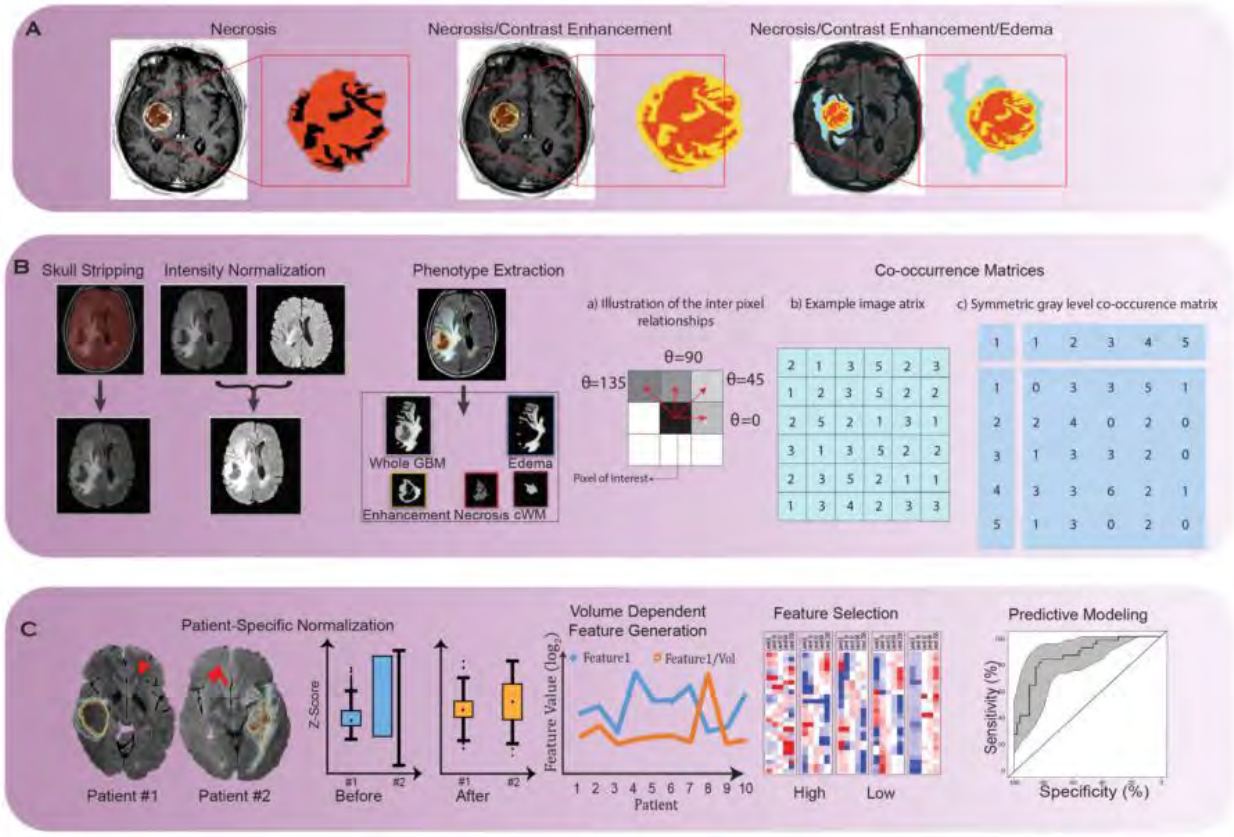

(Filename: TCT_315_psp-pipeline-01.jpg)

1455
Sex Differences in Insula-Prefrontal Connectivity After Sports-Related Concussion
M Xie[1], C Sheridan[2], C Whitlow[2]
[1]Wake Forest University School of Medicine, Raleigh, NC, [2]Wake Forest School of Medicine, Winston-Salem, NC

Purpose
We previously found distinct patterns of BOLD rsfMRI connectivity changes between the insula, PFC, and cingulate are associated with more severe acute and chronic symptoms after SRC. We hypothesized insula-PFC BOLD connectivity would exhibit within-group sex differences after SRC and that these differences may be predictive of acute and/or chronic clinical outcomes.
Materials and Methods
Seed-based connectivity values (Fisher's Z) were computed from BOLD rsfMRI acquisitions at 3 timepoints after SRC (T1=0-4days, T2=10-14days, T3=60-90days) in collegiate athletes (N=33,female=14) and two groups of demographic-matched controls (in-sport ISC, N=36,female=17; non-contact sport NCC N=37,female=15). 12 insula seed regions were selected from Brainnetome 264 Atlas (voxel threshold uncorrected $p<0.0001$, two-sided; cluster threshold FDR-corrected $p<0.0001$). ANOVA followed by Tukey's HSD was used to assess differences across group and time. Fisher's Z scores were correlated with SCAT-3 graded symptom checklist (GSC) and Brief Symptom Inventory 18 (BSI-18) scores at each timepoint.
Results
Compared to ISC and NCC, SRC athletes overall displayed hyperconnectivity between the left ventrolateral (VL) insula and right MFG at T1. Within SRC, male athletes displayed L VL insula-R MFG hyperconnectivity compared to females at T1, but not at T2 or T3. Over time, males displayed a decrease in L VL insula-R MFG connectivity and R dorsal insula-sgACC compared to females. Among male SRC athletes at T3, L VL insula-R MFG connectivity was positively correlated with GSC severity and its cognitive subscale; this relationship was also seen in female NCC athletes. R dorsal insula-sgACC connectivity was negatively correlated with BSI-18 severity and its depression subscale at T3; this was also seen in male NCC athletes.
Conclusions
Males seem to drive both longitudinal changes in insula-PFC connectivity & clinical symptoms in SRC and the correlation b/t connectivity & clinical sx at the chronic timepoint. Chronic hyperconnectivity b/t the L VL insula and R MFG is positively correlated with GSC severity and its cognitive subscale. Chronic hypoconnectivity between the R dorsal insula and cingulate gyrus is negatively correlated with BSI severity and its depression subscale. Response in connectivity with L insula regions may be useful for predicting

cognitive sx burden in male athletes 3 months after SRC. Response in connectivity with R insula regions may be useful for predicting affective sx burden in male athletes 3 months after SRC

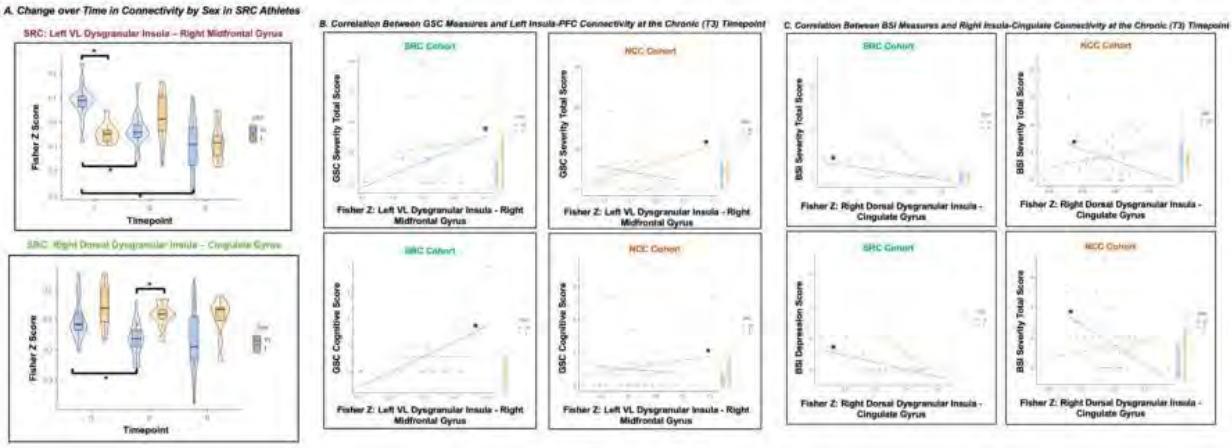

*(A) Violin plots representing changes in connectivity over the acute, intermediate, and chronic timepoints following SRC. *Indicate $p < 0.05$ (Tukey's HSD).*

*(B) Scatter plots representing the relationship between the SCAT-3 GSC Total Severity and Cognitive Domain subscale and connectivity between the left ventrolateral dysgranular insula and right midfrontal gyrus stratified by group and sex. R^2 values clockwise from top left for significant (*) linear regressions: 0.346, 0.135, 0.034, 0.346. *Indicate $p < 0.05$ (Tukey's HSD).*

*(C) Scatter plots representing the relationship between the BSI Total Severity and Depression Domain subscale and connectivity between the right dorsal dysgranular insula and cingulate gyrus stratified by group and sex. R^2 values clockwise from top left for significant (*) linear regressions: 0.369, 0.137, 0.24, 0.446. *Indicate $p < 0.05$ (Tukey's HSD).*

(Filename: TCT_1455_11152022_asnr_figures.jpg)

351

Utility of whole-body CT imaging for investigation of patients presenting with solitary brain tumors–experience of a national tertiary centre

J Cleary[1], D Mallon[2], K Miszkiel[2], S Bisdas[3]

[1]Imperial College Healthcare NHS Trust, London, United Kingdom, [2]University College Hospitals NHS Foundation Trust, London, United Kingdom, [3]University College London, London, United Kingdon

Purpose

There are limited standards for the use of whole-body CT (WBCT) in investigating patients with solitary brain tumors. UK guidance states that all patients with suspected intracranial metastasis should be offered body imaging to identify primary malignancy(1). As distinguishing them can be difficult, WBCT will be performed both in patients with metastatic and primary brain tumors. Limited studies have assessed diagnostic utility of WBCT in solitary brain tumors(2,3,4). WBCT also may expose the patient to unnecessary radiation, and reveal incidental findings, with increased patient anxiety and healthcare costs. We assessed the number and findings of WBCTs performed during workup of patients referred with solitary brain tumors to a tertiary neuro-oncology center. We also compared the baseline MRI report to the final tissue diagnosis of either metastasis or primary brain tumor. Determining the rate of WBCT primary body tumor detection, the number of scans performed for non-metastatic disease, and assessing radiologist confidence in brain tumor diagnosis, could help guide WBCT use.

Materials and Methods

We retrospectively identified patients with new solitary brain lesions referred to our neuro-oncology tumor board, with a tissue diagnosis from April'20-May'21. These were cross-referenced to available/documented PACS imaging and board discussion documentation. This captured: dates of internal and external imaging from referring hospitals, and initial brain MRI and WBCT findings (if available) and final histological diagnosis. Manual assessment of cases identified if the initial MRI brain report gave a likely diagnosis of a primary brain tumor and if WBCT identified a primary malignancy and any incidental findings.

Results

-Of 229 patients (18-84y, 99F) identified: 61% had an available WBCT(Fig.1) -56% of WBCT were performed in primary brain tumor patients -26% of WBCT found a primary malignancy (lung most common) -8% of WBCT found serious incidental findings(Fig.1) -There was high agreement for the MRI report diagnosis of primary brain tumor, when compared to final histology (89% overall) and good agreement for metastasis (75%) (Table1)

Conclusions

-Tissue-proven primary brain tumor patients had most WBCTs. -A quarter of WBCTs found body malignancy -WBCT in the UK are reimbursed at ~$122 (5): excessive WBCT scanning in primary brain tumors may represent a significant cost -Given high agreement between radiological and final diagnosis, WBCT could be selected on presenting tumor MRI characteristics

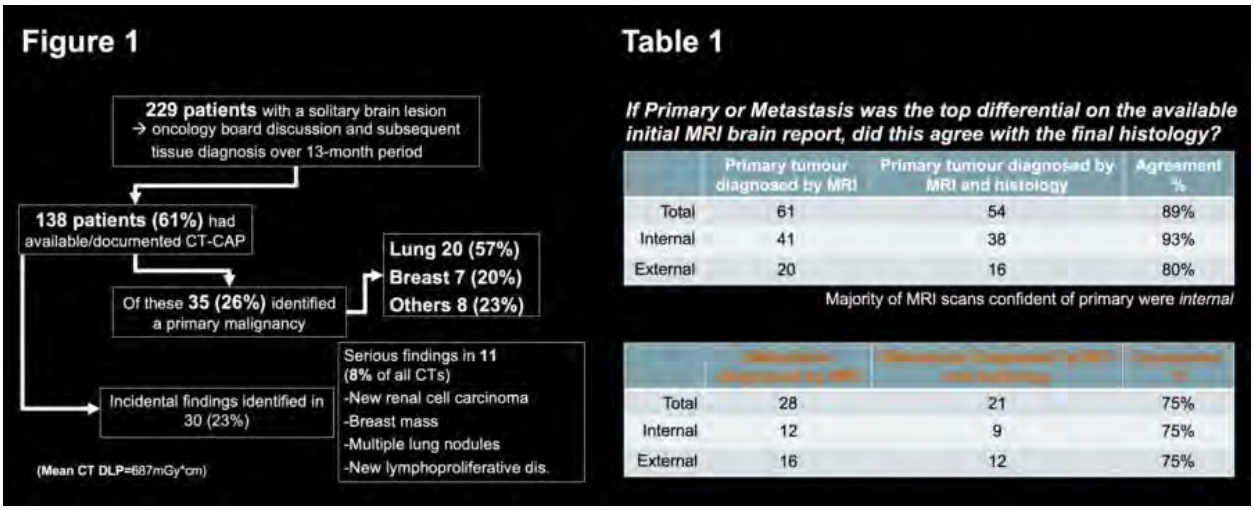

(Filename: TCT_351_Slide1.jpg)

907

Volume Measurement of Brain Metastases Using Artificial Intelligence and Correlation with the RANO Measurement

B Ozkara[1], F Ucisik[1], M Chen[1], D Pattnaik[1], M Wintermark[1], C Federau[2]

[1]The University of Texas MD Anderson Cancer Center, Houston, TX, [2]University of Zurich, Switzerland

Purpose

Contrast-enhanced MRI is the preferred imaging study for diagnosing and monitoring brain metastases (BMs) [1]. Treatment decisions are based on the RANO criteria, which is the single longest diameter of the lesion on contrast-enhanced MRI [2,3]. However, volumetric assessment of the tumor may be more precise. Historically, volumetric measurements were not practical for clinical workflow because this would require manual segmentation, a time-consuming process. Artificial intelligence (AI) has the potential to automate parts of the workflow, making it easier and faster. We aimed to compare the standard RANO measurement with the volume measurement of lesions with a semi-automatic, AI-based lesion segmentation algorithm to determine how consistent the longest diameter of lesions is with the actual volume.

Materials and Methods

We reviewed patients from January 1 to December 31, 2018, who had a brain MRI for cancer staging. Patients with at least one subcentimeter BM were selected for further review. Lesions were divided into ten groups based on their reported RANO measurement, from punctate (1 mm or less) to 9 mm. We stopped patient and lesion screening when there were ten lesions in each size group. The volumes of all included lesions were measured by a semi-automatic, AI-based lesion segmentation algorithm (Jazz software, AI Medical, Switzerland). Independent samples T-test was used to compare lesion volumes between the consecutive groups.

Results

Our study included 90 patients and 90 BMs. Significant differences in volume were found between the 3 mm group versus the 4 mm group, and the 5 mm group versus the 6 mm group with T-test ($p < 0.05$) (Figure 1). The mean measured volume in each group from punctate to 9 mm lesions was 0.015, 0.017, 0.031, 0.056, 0.078, 0.230, 0.187, 0.273, and 0.339 mL, respectively. Variations in volume were visualized using box and whisker plots for each group (Figure 2).

Conclusions

Our results indicate that reporting the BM RANO measurement of a lesion is a poor strategy for demonstrating their size since actual volumes of lesions can be quite different between lesions with the same longest diameter. Furthermore, our findings showed no significant volume differences between most consecutive groups stratified based on the BM RANO measurement, indicating that the longest diameter does not represent the volume correctly. Semi-automatic volume measurement of BM with a software tool could be a quick and efficient way to monitor BMs.

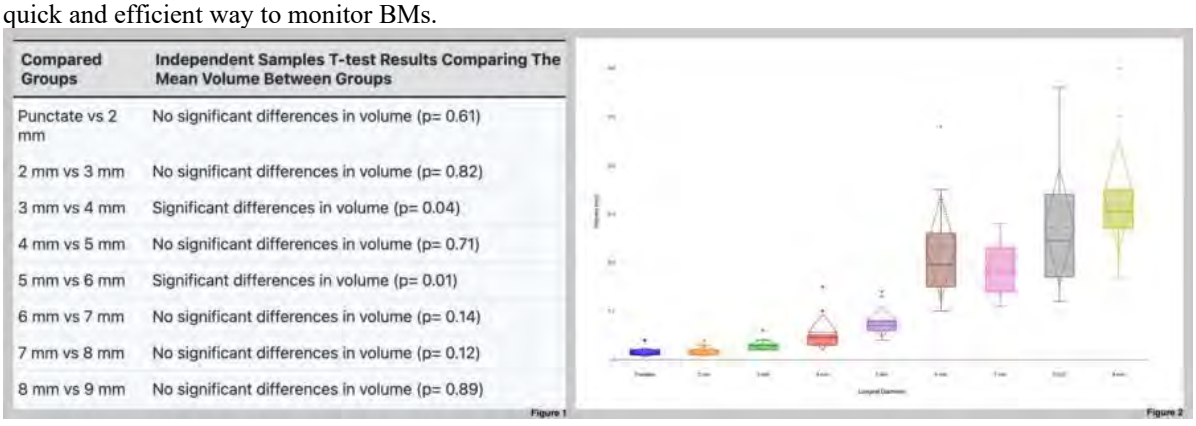

Compared Groups	Independent Samples T-test Results Comparing The Mean Volume Between Groups
Punctate vs 2 mm	No significant differences in volume (p= 0.61)
2 mm vs 3 mm	No significant differences in volume (p= 0.82)
3 mm vs 4 mm	Significant differences in volume (p= 0.04)
4 mm vs 5 mm	No significant differences in volume (p= 0.71)
5 mm vs 6 mm	Significant differences in volume (p= 0.01)
6 mm vs 7 mm	No significant differences in volume (p= 0.14)
7 mm vs 8 mm	No significant differences in volume (p= 0.12)
8 mm vs 9 mm	No significant differences in volume (p= 0.89)

Figure 1

Figure 2

(Filename: TCT_907_ASNRFigureFinal.jpg)

890

White Matter Lesion Burden is Associated with Football Exposure in Former Professional American-style Football Players

D Chung[1], M Etherton[1], R Grashow[2], M Weisskopf[2], G Iverson[3], J Dodelson[4], A Kulpanowski[4], B Hancock[4], D Marengi[2], M Doyle[5], W Copen[1], A Connor[6], A Baggish[1], R Zafonte[5], O Wu[4]

[1]Massachusetts General Hospital, Boston, MA, [2]Harvard T. H. Chan School of Public Health, Boston, MA, [3]Spaulding Rehabilitation Hospital, Charlestown, MA, [4]Massachusetts General Hospital, Charlestown, MA, [5]Harvard Medical School, Boston, MA, [6]Beth Israel Deaconess Medical Center, Boston, MA

Purpose

The possible long-term effects of repetitive head impacts experienced by former professional football players are poorly understood. White matter (WM) injury is a known sequela of head trauma. The goal of our study was to investigate the association of WM lesion (WML) burden with football exposure in former professional players.

Materials and Methods

Former professional football players who played since 1960 and who were less than 60 years of age were enrolled [1]. A semi-automated approach was used for WML segmentation. WML in 3D FLAIR MRI was first segmented using the combined results from two automated approaches (Samseg [2] and LST [3]). The combined WML masks were then manually edited by neurologists blinded to football exposure variables. The volumes were normalized by the estimated total intracranial volume and natural log-transformed. Football exposures were measured by career duration (years of professional play and years of non-professional play) and a concussion signs and symptoms history score [4]. Main playing position was dichotomized to linemen vs all other positions. Self-reported history of performance-enhancing drugs (PED) usage during playing years was recorded. Univariable linear regression was used to assess the association between WML and football exposure variables. Multivariable analysis was performed using stepwise backward linear regression.

Results

64 former players were evaluated. Median [IQR] WML volume was 0.91 [0.37-1.70] mm3. Summary statistics and the results of univariable and multivariable analyses are shown in the Figure.

Conclusions

In a multivariable stepwise backward regression model adjusting for age, self-reported concussion signs and symptoms history score and total years playing football at the non-professional level were independent predictors of white matter lesion burden. This result is consistent with antemortem findings showing more years of football play were associated with WML volume [5]. Our results reflect a basic association and should be interpreted cautiously because our analysis was not adjusted for comorbidities known to be associated with increased WML, such as hypertension and diabetes. Future studies with larger samples sizes are needed to better understand the association of WML with football exposure.

Figure: Univariable and multivariable factors associated with white matter lesion burden. Total number of datasets were from 64 participants unless otherwise noted. Summary statistics are reported as mean±SD or median [IQR].

Covariate	Summary Statistics	Univariable (95% CI)	P-value	Multivariable (95% CI)	P-value
Age, years	49.8±7.3	0.07 (0.03, 0.11)	**<0.001**	0.07 (0.04,0.11)	**<0.001**
Race, white	55%	0.12 (-0.18,0.42)	0.43	NS	NS
Concussion signs and symptoms history score	30 [9-60.5]	0.011 (0.002, 0.02)	**0.023**	0.009 (3e-4,0.02)	**0.042**
Main field position, lineman	41%	0.16 (-0.15,0.46)	0.31	0.19 (-0.08,0.47)	0.16
Use of performance enhancing drugs, yes	16%	-0.06 (-0.48,0.36)	0.78	NS	NS
Total years of professional participation	5 [3-7]	0.014 (-0.06,0.09)	0.72	NS	NS
Total years of non-professional football participation (N=63)	12 [10-14]	0.083 (-0.01,0.18)	0.087	0.09 (5e-3,0.18)	**0.038**

NS=Not selected in multivariable analysis by stepwise backward regression

(Filename: TCT_890_figure.jpg)

Tuesday, May 2, 2023

3:30-4:30 PM

Health Policy Programming: Payment Policy Update

1068

Visa Policies of Radiology Departments for Faculty Recruitment

P Khoshpouri[1], N Khalili[2], N Khalili[3], F Ghazi[4], D Yousem[5]

[1]Johns Hopkins Medical Institution, Coquitlam, British Columbia, Canada, [2]Johns Hopkins University School of Medicine, Baltimore, MD, [3]Children's Hospital of Philadelphia, philadelphia, PA, [4]Johns Hopkins, Baltimore, MD, [5]Johns Hopkins Medical Institution, Evergreen, CO

Purpose

We sought to elucidate the visa policies of American Radiology departments with regard to international faculty candidates.

Materials and Methods

A 14-question survey of all all radiology chairs of departments that are listed in the National Residency Match Program 2022 directory was created in Qualtrics and sent via an individual link by email. Four email reminders over a 6-week period were sent to improve survey completion. The data were analyzed for departments where Chairs knew the answers to the questions.

Results

The response rate to the survey was 65% (115/177). According to the chairs who knew their policies, over one third 45/116 (38.8%) of departments offered H-1B visas to non-American faculty applicants as their baseline policy, while 6/116 (5.2%) offered O-1. In 8.6% the radiology departments do not provide visas as an option and 31/116 (26.7%) departments offer positions preferentially to American citizens. 68/105 (64.8%) of Chairs answering said they frequently or sometimes sponsored H1-B visas to candidates but less than 1/3 (33/104 = 31.7%) do so for O-1 visas. The policy rarely varied whether the faculty candidate was clinical or research oriented (28/97 = 28.9%). In the past 10 years, about half (48/92= 52.2%) of the departments considered 0-4 faculty applicants who required visas and only 17/92 (18.5%) reviewed over 12 such applicants. The reasons why H-1B and O-1 visas were preferentially not offered included the process being time-consuming (H-1B: 26/167 = 15.5%, O-1: 22/136 = 16.2%), bureaucratic hassle and absence of candidates in that order (H-1B: 24/167 = 14.4%, O-1: 17/136 = 12.5%), avoiding expenses (H-1B: 22/167 = 13.2%, O-1: 13/136 = 9.5%), no visa requiring applicant to the program (H-1B: 14/167 = 8.4%, O-1: 11/136 = 8.1%), and a perceived desire to hire American citizen candidates preferentially (H-1B: 11/167 = 6.6%, O-1: 5/136 = 3.7%).

Conclusions

Most radiology departments (64.8%) offer the H-1B visa option for international faculty candidates with that being the baseline policy for 38.8% of programs. Resistance to offering different visas rested with the laboriousness, expense and a desire to hire American citizen candidates preferentially.

Field	Question 2 Choice Count	Question 3 Choice Count
We prefer to employ Americans	11 (6.6%)	5 (3.7%)
We cannot verify foreign qualifications	2 (1.2%)	2 (1.5%)
We wish to avoid the expense of the visa application	22 (13.2%)	13 (9.5%)
Foreign candidates are not as good as American citizens	1 (0.6%)	0 (0%)
We would have to pay foreign applicants more than Americans (prevailing wage)	3 (1.8%)	0 (0%)
We lack the expertise	5 (3.0%)	12 (8.8%)
There are not applicants for H-1B visas to our program	14 (8.4%)	11 (8.1%)
It is time consuming	26 (15.5%)	22 (16.2%)
It is not reliable as to starting time because of the embassy/immigration issues	24 (14.4%)	17 (12.5%)
Total	167	136

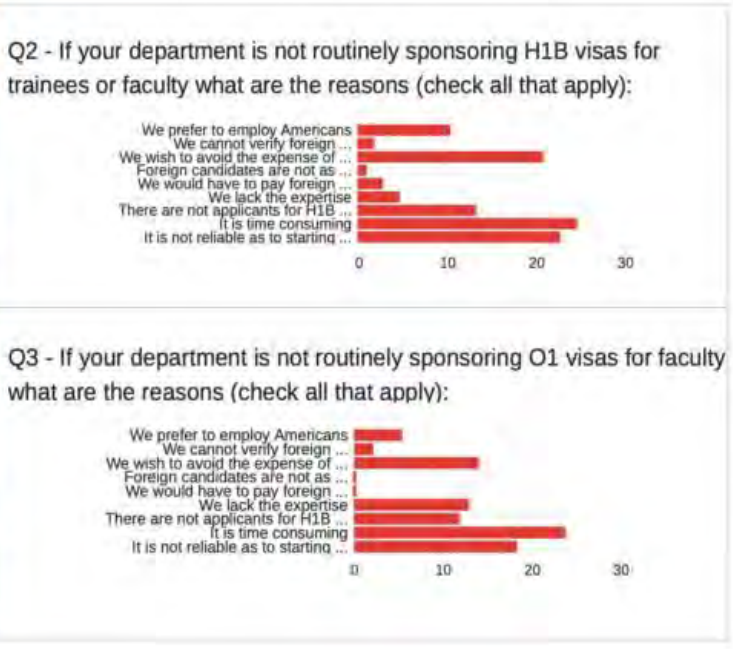

(Filename: TCT_1068_ASNR_graphs.jpg)

Tuesday, May 2, 2023

3:30-4:30 PM

Scientific Abstract Session: Neurorad Miscellaneous 1

1448

A comparison of image intensity normalization methods for harmonizing common MRI contrasts in brain cancer imaging studies

S Duenweg[1], S Bobholz[1], A Lowman[1], A Winiarz[1], F Kyereme[1], J Connelly[1], M Agarwal[1], P LaViolette[1]
[1]Medical College of Wisconsin, Milwaukee, WI

Purpose
Multi-parametric magnetic resonance imaging (MP-MRI) is a well-established tool for localizing and monitoring brain cancer. MP-MRI combines T1-weighted (T1), post-gadolinium contrast enhanced T1-weighted (T1+C), and fluid-attenuated inversion recovery (FLAIR) imaging to differentiate healthy tissue and lesions in the brain. These images are more often than not vary in intensity within and across patients and MR scanners (1). This study used T1, T1C, and FLAIR images collected from brain cancer patients across two scanner vendors to examine commonly used post-acquisition intensity normalization methods to identify which method produces images that are most comparable between scanners.
Materials and Methods
Data from 74 patients (26 female, mean age 60.6 years) with pathologically confirmed brain cancer were analyzed for this study. Patients underwent MP-MRI prior to initial treatment on a scanner from one of two vendors (General Electric n=50; Siemens n=24). Brain masks and cerebral spinal fluid (CSF) masks from each patient's T1-weighted imaging were created using SPM. Additionally, a 9-voxel radius circular ROI was defined within each eye on one slice of the T1. Each patient's clinical imaging was normalized using (1) no normalization, (2) the standard deviation of intensity within the brain mask, and the mean intensity within the (3) CSF and (4) eye masks. Mean and standard deviation of intensity was calculated across patients after normalization. Kruskal-Wallis tests were used to compare intensity distributions across each vendor for each image.
Results
Across all three imaging acquisitions, mean intensity of the three normalization methods all produced images that are compatible across scanners (T1: all $p > 0.5$, $\chi2 < 0.04$; T1C: all $p > 0.14$, $\chi2 < 2.2$; FLAIR: all $p > 0.29$, $\chi2 < 2.1$). Unnormalized intensity across all imaging acquisitions produced images that were not comparable. Figure 1 shows violin plots of T1, T1C, and FLAIR intensity distributions stratified by scanner vendor.
Conclusions
We demonstrate in a cohort of 74 patients, that intensity normalization of T1, T1C, and FLAIR is necessary to compare images across multiple clinical MR scanners. Specifically, using a standard deviation of intensity within the brain tissue produced the most equivalent image contrast distributions.

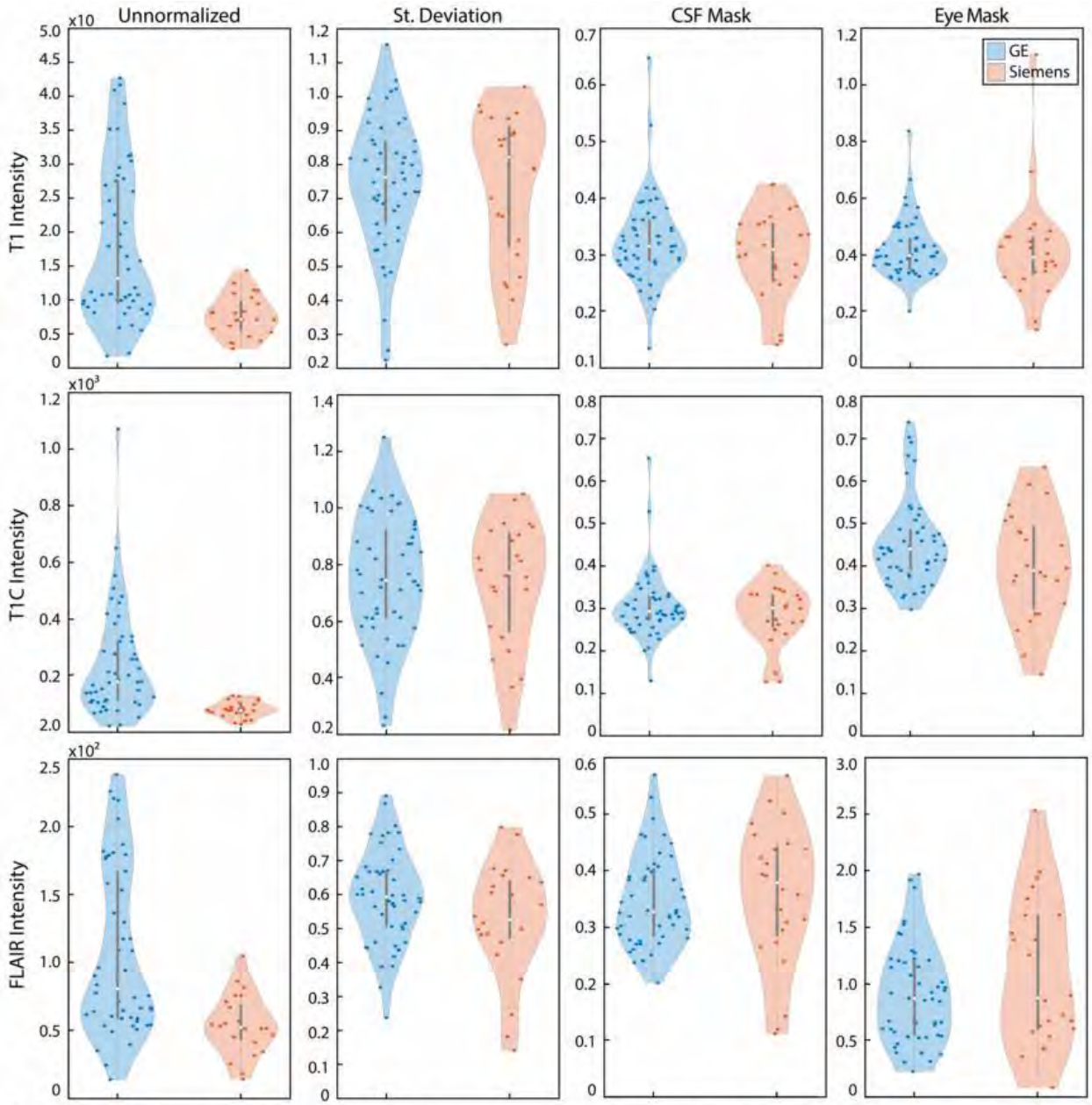

Figure 1. Violin plots showing the intensity distributions across the T1 (top), T1C (middle), and FLAIR (bottom) images

(Filename: TCT_1448_ASNR_AB2-f1-01.jpg)

386

Deep Learning-based Image Super-Resolution on a Portable Photon-Counting CT

B Yu[1], D Wu[1], D Lee[2], J Park[2], K Kim[1], I Bechwati[2], Q Li[1], R Gupta[1]

[1]Massachusetts General Hospital and Harvard Medical School, Boston, MA, [2]Neurologica, Danvers, MA

Purpose

A newly introduced photon-counting detector (PCD) based CT scanner (OmniTom PCD™, Neurologica, Samsung Electronics Co, Ltd, Danvers MA, US) is capable of ultra-high resolution of 0.12×0.14 mm2 in 1×1 binning mode. However, the ultra-high resolution mode increased bandwidth and/or increased data transfer time. We investigated a super-resolution (SR) neural networks to improve the spatial resolution of standard acquisition mode to ultra-high resolution mode.

Materials and Methods

A human cadaver head and temporal bone specimens were scanned by an OmniTom PCD at 120kVp and 20mA, using both 1×1 and 3×3 binning modes. The images were reconstructed by FBP with a slice thickness of 0.42 mm and a pixel size of 0.2×0.2 mm2. An image-domain ring artifacts reduction algorithm was applied [1]. A Wasserstein Generative Adversarial Network (WGAN) [2] was trained to map the 3×3 images to 1×1 images using 104 pairs of cadaver head data. In the WGAN that was trained, the generator network was a UNet, and the discriminator network used a CNN. A weighted L1 norm was added to the generator loss. The WGAN was trained for 100 epochs with a learning rate of 5×10-5. The bias in the SR generated images was further corrected by local linear fitting. The trained WGAN was tested on 52 slices of independently acquired 3×3 temporal bone images.

Results

While the SR images showed clear resolution improvement compared to 3×3 images, they were noisier. With 1x1 images as the groundtruth, the root-mean square error (RMSE) of SR and 3×3 were 84.3 HU and 69.3 HU, respectively. The increased RMSE in SR images was mainly due to the noise amplification in the SR process. Haralick texture features [3] were calculated to evaluate texture similarity by rescaling the pixel values between 0 to 255. When compared with 1×1, the L2 distances on the Haralick features were 116.7 and 199.0 for SR and 3×3, respectively. Therefore, SR images had closer texture similarity to 1×1 than 3x3. The residual images obtained by subtracting 3×3 from 1×1 showed edges and other image features. The same operation with the SR showed more uniformly distributed noise in the subtracted image demonstrating better edge preservation by the SR. The Fourier transforms also showed that SR was closer to 1×1, especially in the high-frequency domain where the fine image features reside.

Conclusions

A trained super-resolution network can improve the image resolution of a portable PCD CT, while preserving image texture and features, at the expense of increased image noise.

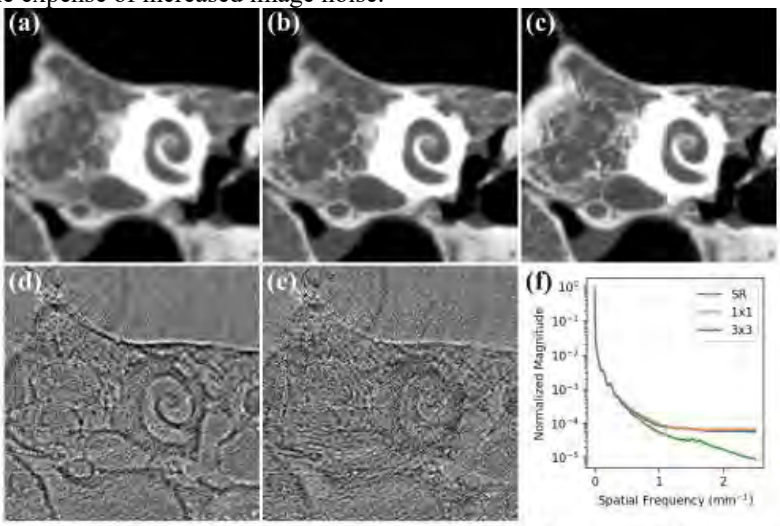

Fig. 1. Example SR results from the temporal bone specimen: (a) 3×3 image; (b) SR image; (c) 1×1 image; (d) residual image obtained by subtracting 1×1 from 3x3 image (i.e., (a) – (c)); (e) residual image obtained by subtracting 1×1 from SR (i.e., (b) – (c)); (f) normalized Fourier transform (FT) of SR, 1×1, and 3×3 images, where FT was averaged along all radial directions. The WW/WL for (a) – (c) are 2800/400 HU, and for (d) – (e) are 1000/0 HU. SR provids better structural details and clearer edges than 3×3. The residual image of SR is more uniform, whereas the residual image of 3×3 shows more obvious edges. It indicates that the SR images have less structural difference. The FT of SR almost overlaps with 1×1, especially in the high-frequency domain. It indicates the details reconstructed by SR are closer to 1×1.

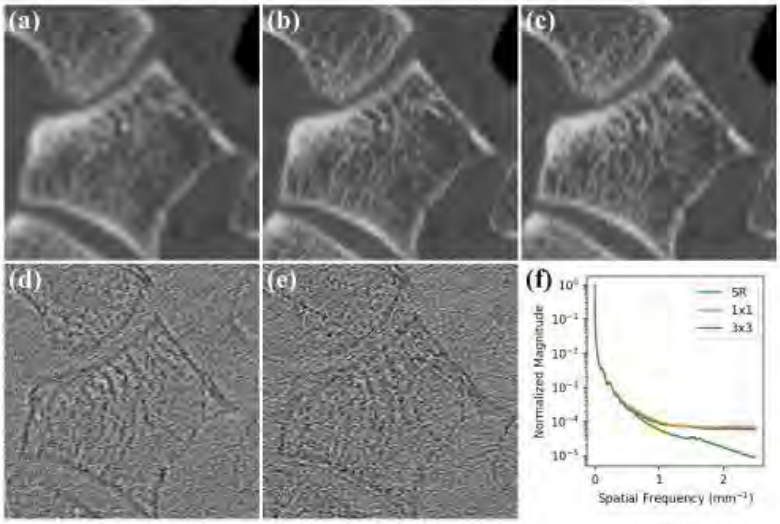

Fig. 2. Another example of the SR results from the temporal bone specimen: (a)-(f) are the same as in Fig. 1. SR provids better bony structure than 3×3. The residual image from SR shows fewer structural features than that from 3×3 demonstrating closer structural similarity between SR and 1×1. The FT image shows the same trend as in Fig. 1.

(Filename: TCT_386_fig1.jpg)

714

Effect of tumor genetics, pathology, and location on fMRI of language reorganization in brain tumor patients

L Pasquini[1], O Yildirim[2], P Silvera[1], M Jenabi[3], K Peck[4], A Holodny[5]

[1]Memorial Sloan Kettering Cancer Center, New York, NY, [2]Memorial Sloan Kettering Cancer Center, NYC, NY, [3]MSKCC, Great Neck, NY, [4]Department of Radiology, Memorial Sloan Kettering Cancer Center, New York, NY, [5]MEMORIAL SLOAN KETTERING CANCER CENTER, NEW YORK, NY

Purpose

Language reorganization may develop as a consequence of tumor invasion of the dominant hemisphere, with direct implications for patient care1. In tumors that invade eloquent language areas, functional reorganization may allow for a more complete resection2. Therapies that aim to enhance language reorganization may reduce postsurgical deficits3. However, the specific drivers of language plasticity are still unclear. Tumor location, grade, and genetics influence the communication between eloquent areas and tumor growth dynamics, which are drivers of language plasticity4,5. We evaluated language reorganization in brain tumor patients by studying the relationship of fMRI language laterality to tumor-related variables (grade, genetics, location), and patient-related variables (age, sex, handedness).

Materials and Methods

The study was retrospective cross-sectional. We included patients with left-hemispheric tumors and task-based language fMRI. We calculated five fMRI laterality indexes (LI) with a semi-automated threshold-independent method: hemispheric, temporal lobe, frontal lobe, Broca's area (BA), Wernicke's area (WA). We defined $LI \geq 0.2$ as left-lateralized and $LI < 0.2$ as atypical lateralized. Chi-square test ($p<0.05$) was employed to identify the relationship between LI and tumor/patient variables. For those variables having significant results, contingency coefficient, phi factor, and Cramer's V were computed

Results

We included 405 patients (235 males, mean age 51y, 106 low-grade gliomas - LGG, 242 high-grade gliomas – HGG, 57 metastases). Chi-square test demonstrated a significant correlation between BA LI and patient sex ($p=0.005$); frontal LI, BA LI, and tumor location in BA ($p<0.001$); tumor grade, BA, and hemispheric LI ($p<0.001$); hemispheric LI and epidermal growth factor receptor (EGFR) amplification ($p=0.042$); hemispheric LI and fibroblast growth factor receptor (FGFR) mutation ($p=0.019$); WA LI and O6-Methylguanine-DNA methyltransferase promoter (MGMT) methylation in high-grade gliomas ($p=0.016$).

Conclusions

Patients harboring left-hemispheric tumors present with significant fMRI activation in the right hemisphere, indicating the translocation of language function due to cortical plasticity. This phenomenon is well observed in HGG, LGG, and metastases. Increased fMRI activation in the right hemisphere, consistent with language reorganization, was seen in patients with tumors in the frontal lobe, BA and WA, EGFR amplification, FGFR mutation, and MGMT promoter methylation.

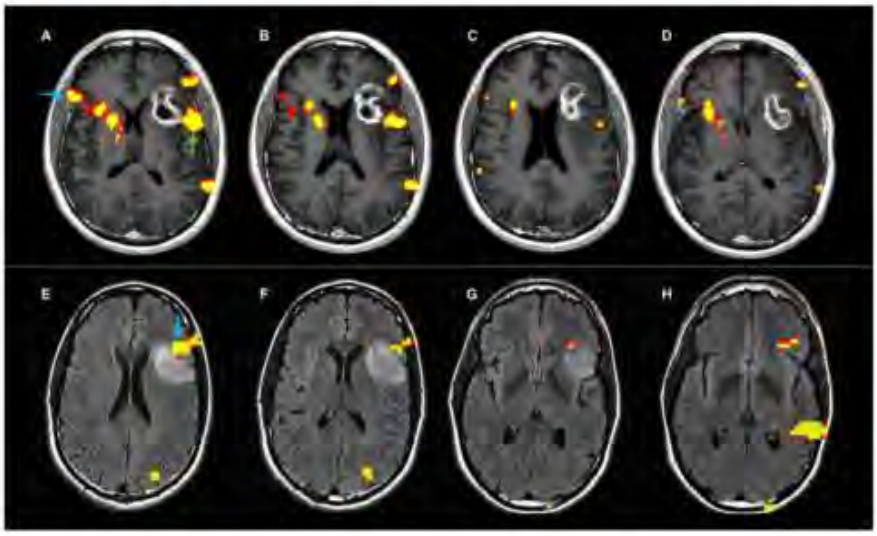

Figure 1. Exemplificative cases of language plasticity. Above, fMRI correlation map overlayed on post-contrast T1-w images of a 67-year-old man with glioblastoma affecting the left, lower-frontal lobe. The fMRI map shows co-dominant activation of Broca's area (left activation: green arrow in A; right activation: light blue arrow in A). Below, fMRI correlation map overlayed on axial post-contrast T1-w images of a 51-year-old man with glioblastoma affecting the left, lower-frontal lobe. This fMRI map shows left-dominant activation of Broca's area (light blue arrow in E).

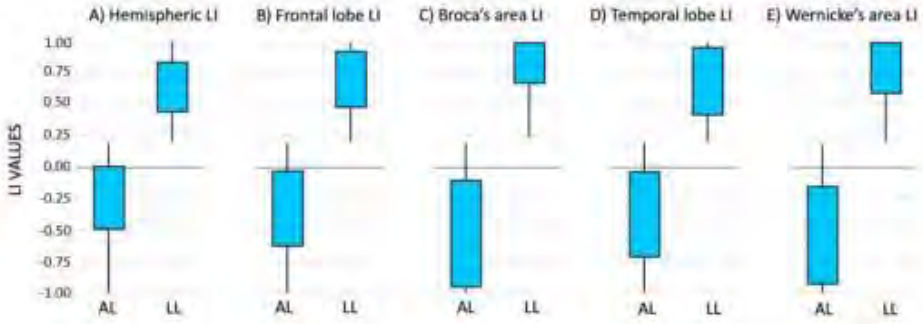

Figure 2. Distribution of the five laterality indexes (LI) calculated in the total population of our study: hemispheric LI (A), frontal LI (B), Broca's LI (C), temporal LI (D), and Wernicke's LI (E). AL = atypical lateralized; LL = left-lateralized.

Table 1. Patients' demographic data and tumor location

	HGG	LGG	METS
Age (mean and SD)	53 +/- 14	43 +/- 13	54 +/- 13
Sex	152M; 90F	56M; 50F	27M; 30F
Handedness	216R; 26L	92R; 14L	53R; 4L
Frontal lobe	126	59	37
Temporal lobe	88	40	12
Parietal lobe	65	14	18
Occipital lobe	8	2	2
Insula	45	36	1
BA	54	21	2
EA	28	19	3
SMA	30	12	8
WA	30	5	5
SMG	16	3	6
AG	18	3	4

AG=angular gyrus; BA=Broca's area; EA=Exner's area; SMA=pre-supplementary motor area; SMG=supramarginal gyrus; WA=Wernicke's area

(Filename: TCT_714_Presentation1.jpg)

1462

Fetal MR Neuroimaging in CHARGE Syndrome

C Robson[1], F Dehghani Firouzabadi[2], J Rispoli[1], K Al-Dasuqi[3], V Rameh[3]

[1]Boston Children's Hospital, Weston, MA, [2]Deprtment of Radiology, Children's Hospital, Harvard Medical School, Boston, MA, [3]Boston Children's Hospital, Boston, MA

Purpose

Fetal MRI is often performed in fetuses with CHARGE syndrome after discovery of craniofacial malformations, congenital heart defects and/or genitourinary anomalies on screening prenatal ultrasound. In this retrospective review of patients with a genetically confirmed postnatal diagnosis of CHARGE syndrome, we aimed to assess the reliability of fetal MRI in detecting the typical neuroimaging features that support a diagnosis of CHARGE syndrome.

Materials and Methods

Retrospective imaging review of fetal MR imaging in 11 patients with CHARGE syndrome was independently performed by 2 pediatric neuroradiologists. Only cases with confirmed CHD7 mutation on genetic testing and postnatal CT and/or MRI of the temporal bones/brain were included. Note was made of any findings missed by the interpreting neuroradiologist at the time of image acquisition.

Results

The gestational age of the fetuses at the time of fetal MRI acquisition varied between 19 – 38 weeks gestational age; all but 3 exams were at 3T. Postnatal MR was obtained in 9 patients (age 0 days – 33 months) with subsequent CT in 2, and CT alone was acquired in 2 patients. Small vestibules with absent semicircular canals were seen in all but 1 fetus. Cochlear anomalies (single turn, misshapen turns, absent cochlear aperture) were seen in most fetuses. Other findings visible on fetal MR included absent olfactory bulbs, pontine hypoplasia, uplifted vermis with inferior vermian hypoplasia, foreshortened or scalloped basiocciput, cleft lip and palate, choanal atresia, colobomas and ventriculomegaly. The typical findings of CHARGE seen postnatally were more likely to be occult on exams performed at 1.5T and when fetal imaging was obtained at an earlier gestational age. In many cases temporal bone, nasal cavity, brainstem and olfactory findings were overlooked at the time of the original interpretation and a differential diagnosis that included CHARGE syndrome was only suggested in a minority of patients prospectively.

Conclusions

For fetuses with multiple congenital anomalies heightened awareness of associated syndromes should prompt careful assessment of the brainstem, temporal bones, orbits and nasal cavity for additional findings that may suggest an underlying syndrome, help direct genetic testing and guide parental counseling. Our findings highlight the value of high resolution fetal MR in the identification of key features of CHARGE syndrome prenatally.

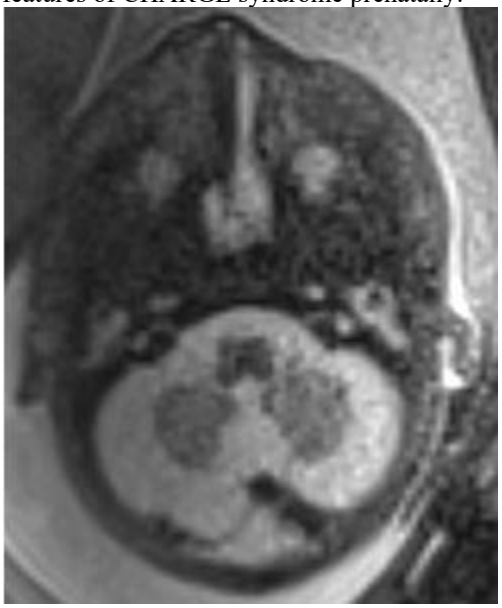

(Filename: TCT_1462_CHARGE.JPG)

1310

MR Perfusion Alterations Associate with Cognitive Deficits, Mood, Fatigue, and Dysautonomia in Post-COVID Brain Fog

S Dash[1], J Dyke[2], M Mahmud[2], G Chiang[3]

[1]New York Presbyterian Hospital Cornell, New York, NY, [2]Weill Cornell Medicine, New York, NY, [3]Weill Cornell Medicine/NewYork-Presbyterian, New York, NY

Purpose

Post-COVID brain fog is a poorly understood clinical syndrome, sometimes termed cognitive postacute sequelae of SARS-CoV-2 infection (PASC), that causes significant disability persisting months to years after the acute infection. However, no clear serologic,

CSF, or imaging biomarkers have been identified to diagnose cognitive PASC. The purpose of this analysis was to assess the utility of dynamic contrast-enhanced (DCE) MR perfusion as a biomarker of cognitive dysfunction in a cohort of cognitive PASC patients.
Materials and Methods
17 patients from the Weill Cornell Department of Neurology Post-COVID Brain Fog Clinic were included in this study and gave informed consent for inclusion. Mean age was 48 + 18 years (9 men, 8 women). Subjects underwent DCE-MR on the same 3 Tesla MRI 1.5 + 0.58 years after the initial COVID infection. Regions-of-interest were placed on the hippocampi and frontal, parietal, temporal, and occipital lobes. Quantitative measures of plasma volume (Vp) and permeability (Ktrans) were obtained, normalized by centrum semiovale white matter. Functional disability was assessed using the Center for Epidemiologic Studies Depression (CES-D) scale, Modified Fatigue Impact Scale (MFIS), Beck Anxiety Inventory (BAI), WHO ADHD self-report scale, the General Symptoms Questionnaire (GSQ), a measure of functional impairment, and COMPASS31, a measure of autonomic dysfunction. Associations between regional Vp and Ktrans and impairment scales were assessed using multivariate regressions, with age as a covariate.
Results
Lower Vp in the hippocampi was associated with higher GSQ impairment scores (coefficient=-2.37, p=0.005), higher MFIS cognitive (coefficient=-0.097, p=0.016) and total (coefficient=-0.040, p=0.028) subscores, and higher ADHD-Part B subscores (coefficient=-0.18, p=0.025). Lower Vp in the temporal lobes was also associated with higher total GSQ scores (coefficient=-0.038, p=0.014), higher BAI scores (coefficient=-0.11, p=0.003), higher COMPASS31 scores (coefficient=-0.074, p=0.025), and higher ADHD-Part B scores (coefficient=-0.25, p=0.045). Higher Vp in the frontal lobes was associated with higher CES-D scores (coefficient=0.57, p = 0.002). Ktrans measures were not significantly associated with disability scores.
Conclusions
Decreased perfusion in the hippocampi and temporal lobes may serve as an MR biomarker of functional impairment in patients with post-COVID brain fog. Further validation in larger cohorts is warranted.

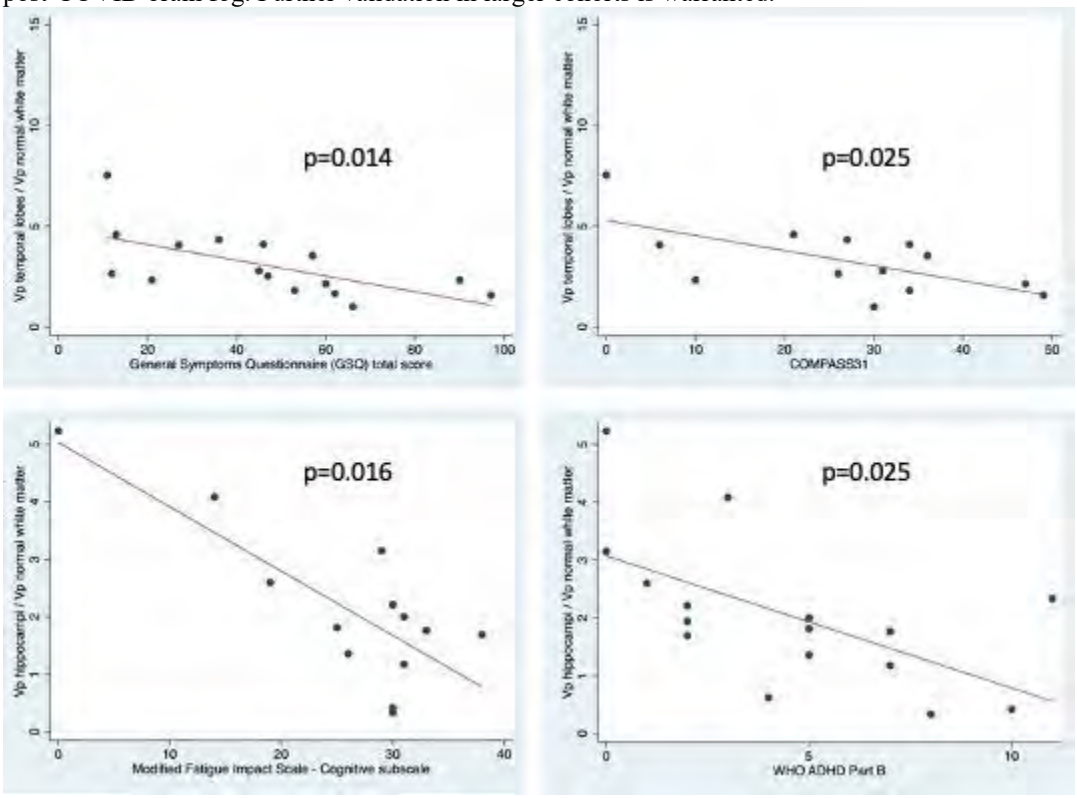

(Filename: TCT_1310_Fig1.jpg)

608

Perfusion Collateral Index can predict infarction growth in patients with successful thrombectomies.

S KIHIRA[1], H Zhang[1], P Shahrouki[1], E Tavakkol[1], J Polson[1], J Fifi[2], A Doshi[3], A Vagal[4], P Khatri[5], A Srinivasan[6], M Bahr-Hosseini[1], R Jahan[1], g duckwiler[7], C Arnold[1], J Saver[1], J Mocco[8], D Liebeskind[9], K Nael[1]
[1]UCLA, Los Angeles, CA, [2]Icahn School of medicine at Mount Sinai, New York, NY, [3]Mount Sinai Hospital, New York, NY, [4]University Of Cincinnati Medical Center, Cincinnati, OH, [5]University of Cincinnati, Cincinnati, OH, [6]University of Michigan, Ann Arbor, MI, [7]ucla, Los Angeles, CA, [8]Icahn School of Medicine at Mount Sinai, New York, NY, [9]UCLA Stroke Center, Los Angeles, CA

Purpose
In patients with large vessel occlusion (LVO), interval infarction growth occurs despite successful thrombectomy. Collateral status has been proposed as an important variable in determination of infarction growth (1). In this study we aimed to evaluate the association between baseline collateral status measured by recently defined Perfusion Collateral Index (PCI) (2) and infarction growth in a controlled setting of patients with anterior circulation LVO stroke who underwent timely successful thrombectomies.

Materials and Methods
In this retrospective multicenter study, patients with anterior circulation large vessel occlusions were included if 1) had baseline CTP, 2) underwent successful endovascular thrombectomy (TICI>=2B) within 2 hours of CTP, and 3) had post treatment MRI within 24 hours for determination of final infarction. PCI scores defined as volume of moderately hypoperfused tissue (arterial delay time between 2 and 6 seconds: delay 2-6sec) x relative cerebral blood volume were obtained from baseline CTP using Olea Sphere (Olea Medical). Infarct growth was determined by subtracting the pre-thrombectomy infarct volume on ADC from the 24 hr post-thrombectomy infarct volume on DWI.
Results
Thus far, 42 patients were included with age (mean ± SD) of 70 ± 13.7, 19M/23F, and NIHSS (median, IQR) of 14 (7-20). Initial and final infarct volumes (mean ± SD) were 4.8 ± 9.8 and 40.5 ± 50 mL, respectively. PCI showed a moderate negative correlation (r= -0.32, p=0.04) with infarction growth. Twelve patients (29%) had infarct growth > 30mL while 30 (71%) had infarct growth less than 30mL. ROC analysis showed a diagnostic performance (AUC/sensitivity/specificity) of 0.78/91.7%/70% for PCI at threshold of 60 ($p<0.001$) to predict infarction growth >30mL (Figure). The predictive performance of PCI for determination of infarct growth > 50mL was (AUC/sensitivity/specificity) of 0.83/100%/65% ($p<0.001$).
Conclusions
Baseline collateral status defined by CTP-PCI can predict infarction growth despite successful thrombectomy in patients with anterior circulation LVO stroke.

540

Post-COVID-19 Brain 18F-FDG-PET Findings: A Retrospective Single-Center Study in the United States

N Khalili[1], P Debs[1], H Sair[1], V Yedavalli[2], L Luna[1]
[1]Johns Hopkins University School of Medicine, Baltimore, MD, [2]Johns Hopkins School of Medicine/Johns Hopkins Hospital, Baltimore, MD

Purpose
To compare brain metabolic activity on [18F]-FDG-PET/CT scans between adult patients with a positive SARS-CoV-2 RT-PCR test (at least once before imaging) and control patients without a positive test for COVID-19 infection.
Materials and Methods
In this retrospective single-center study, we evaluated the brain metabolic findings in 45 adult patients with a confirmed history of COVID-19 infection, in comparison to 52 age- and gender-matched controls. We included patients who underwent routine [18F]-FDG-PET/CT imaging for any reason and had tested positive for COVID-19 any time before the PET/CT scan (on average 6.5 months). Of the included patients, six also had a pre-COVID scan. A group of 52 melanoma or lymphoma patients who underwent [18F]-FDG-PET/CT imaging between February-December 2019 was used as the control group. Clinical data was extracted from the individuals' medical records. Brain images were extracted from whole-body PET/CT scans, and whole-brain voxel-based analysis using statistical parametric mapping (SPM8) software was performed to identify clusters of hypometabolism and to compare brain metabolic activity between the groups.
Results
There was no significant difference between the two groups in terms of pre-PET glucose level, body mass index, and administered [18F]-FDG dose ($p>0.05$). In comparison to controls, patients with COVID-19 exhibited focal areas of hypometabolism in the right frontal lobe, bilateral parietal lobes, bilateral occipital lobes, left occipital fusiform gyrus, left lingual gyrus, bilateral precuneus cortex and bilateral lateral occipital cortex (p-voxel<0.05 uncorrected, p-cluster<0.05 FEW-corrected). There was a negative correlation between the clusters of hypometabolism and the number of days elapsed since the first positive test, with more pronounced hypometabolic clusters within the first two months of infection (Figure 1). In six patients, comparison of pre- versus post-COVID scans revealed hypometabolism in a widespread cerebral network including the right occipital and temporal cortex and left parietal cortex. Also, hypermetabolism was found in the left cerebellum, left frontal pole and right amygdala.
Conclusions
This study demonstrates a profile of brain PET hypometabolism in patients with confirmed SARS-CoV-2 infection compared to controls. The observed hypometabolism could serve as a potential biomarker to follow patients clinically and assess recovery.

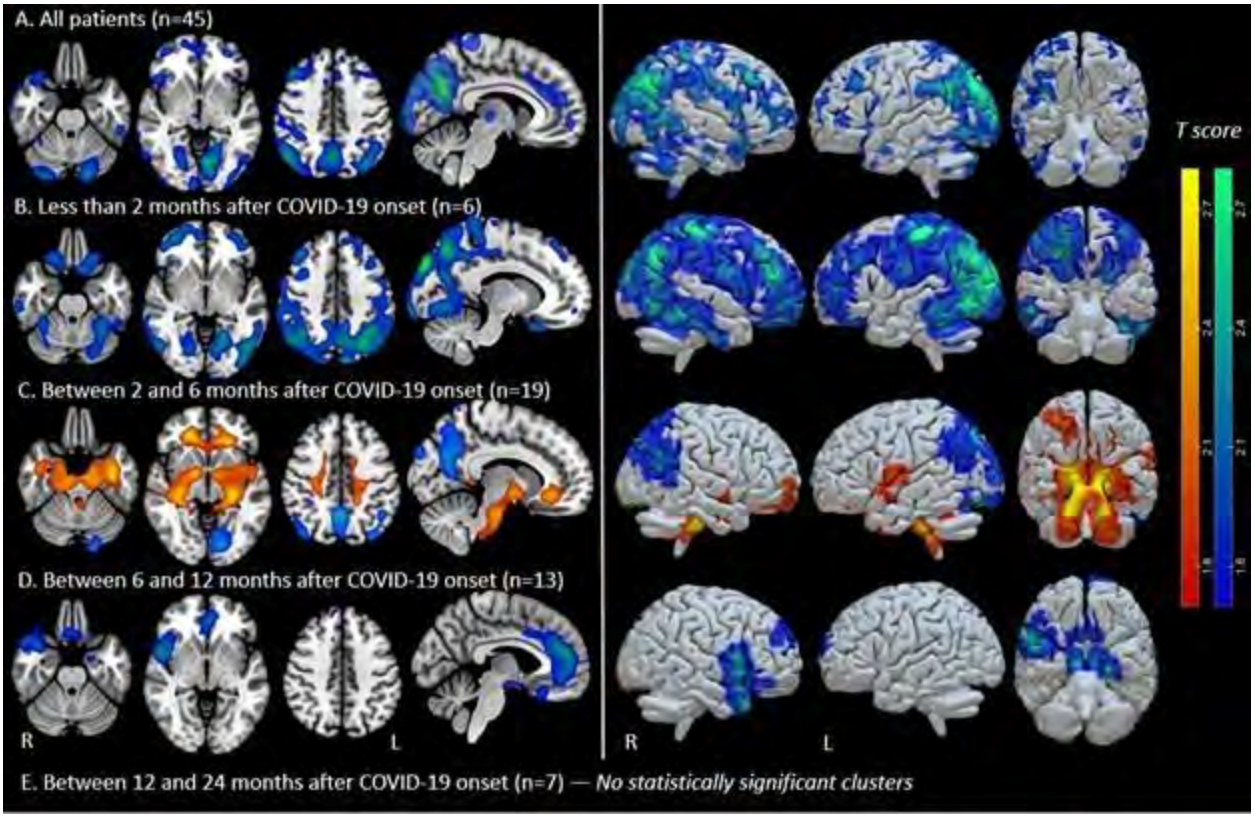

(Filename: TCT_540_Figure-1.jpg)

Tuesday, May 2, 2023
3:30-4:30 PM
Scientific Abstract Session: Vascular 3

831

5-Year Analysis of Intravenous Thrombolysis Related Intracranial Haemorrhage - Did Cerebral Microbleed Preclude Treatment in Patients with Acute Ischemic Stroke?

M Altibi[1], H Haseeb[2], V Sawlani[3]
[1]University Hospital Birmingham, Solihull, AL, [2]University Hospital Birmingham, Birmingham, AZ, [3]University Hospital Birmingham, Birmingham, AL

Purpose

Early treatment with intravenous thrombolysis (IVT) < 4.5 h from symptom onset increases the proportion of patients who survive with a favourable outcome after ischemic stroke. Intracerebral haemorrhage (ICH) is the most feared risk of systemic thrombolysis and may be secondary to haemorrhagic transformation or bleeding into an ischemic area following reperfusion. Although Cerebral microbleeds (CMBs) or cerebral amyloid angiopathy (CAA) are currently not contraindications to IVT, the former is associated with increased risk of thrombolysis-related ICH. The primary aim of this study is to examine the association between IVT in patients with acute ischaemic stroke and post IVT intracranial bleed. The secondary aim is to evaluate CMBs as an independent risk factor for post IVT intracranial bleed taking into account the presence, burden, location, and the likelihood of cerebral amyloid angiopathy.

Materials and Methods

Records from all patients presenting to the Queen Elizabeth Hospital Birmingham with acute ischaemic stroke treated with IVT over a 5-year period were retrospectively reviewed. Demographics, medical, and imaging variables were evaluated. Gradient Echo MRI sequences were used to evaluate the number and location of CMBs. Statistical models were used to determine the relationship between CMBs and symptomatic haemorrhagic transformation.

Results

Of 434 consecutive patients, the number of patients with intra or extra axial bleeding following IVT was 43 (9.9%) confirmed on post thrombolysis CT brain. Of those, 79.5% hadICH, 18.2% had SAH and 2.3% had SDH. Of patients with ICH, 30 (85.7%) patients had haemorrhagic transformation (HT). Old age, extensive small vessel disease, chronic infarcts and early cortical swelling were predisposing factors int he majority of these cases. Five patients (14.3%) patients had >10 CMB consistent with probable CAA according to the Boston Criteria 2.0. The distribution of the CMBs was described as lobar, deep and infratentorial.

Conclusions
The rate of post IVT ICH is approximately 1 in 10 in our cohort. Reliable risk assessment for probable CAA requires pre-existing MRI head prior to IVT treatment. This is a practical limitation of current practice. Whenever known,CMB burden of > 10 should be taken into consideration when stratifying the risk for symptomatic ICH, but even then the increased relative risk should be weighed against the risks of not treating with IVT.

862

Acute Ischemic Stroke Outcomes in COVID-19 Patients: A Systematic Review and Meta-analysis

S Ferrone[1], J O'Hara[2], T White[2], J Vialet[2], Z Lodato[1], J Jimenez[2], S Shahsavarani[3], M Sanmartin[1], J Katz[2], P Sanelli[2]
[1]Feinstein Institutes for Medical Research, Manhasset, NY, [2]Northwell Health, Manhasset, NY, [3]Donald and Barbara Zucker School of Medicine at Hofstra/Northwell, Manhasset, NY

Purpose
Since the COVID-19 pandemic, over 638 million people have been infected worldwide. Patients with COVID-19 have a higher risk of acute ischemic stroke (AIS). Our purpose was to determine the clinical outcomes of AIS associated with COVID-19 infection.
Materials and Methods
We performed a systematic review of the literature following the Preferred Reporting Items for Systematic Review and Meta-Analyses (PRISMA) guidelines. Our study protocol was registered with the International Prospective Register of Systematic Reviews (CRD42020211977). A senior medical librarian searched EMBASE, PubMed, Web of Science databases, Scopus, and CINAHL for studies published in English. Inclusion criteria: (1) Studies reporting outcomes on AIS patients with COVID infection, (2) Original articles published in year 2020 or later, (3) Study participants aged ≥18 years. Exclusion criteria: (1) Case reports, case series <5 patients, abstracts, letters, and review articles, (2) Studies analyzing any treatments or interventions, except IV-tPA and thrombectomy. PRISMA flow diagram (Figure 1) shows the selection of studies using a three-step process with independent review of abstracts, full-text, and data extraction by five blinded reviewers using Covidence software. Any discrepancies were resolved by a senior independent arbitrator. Following data extraction, an additional 10 studies were eliminated according to the exclusion criteria.
Results
A total of 43 studies were included; of which 56% (24/43) reported AIS patients without COVID as a comparison cohort. Study population: A total of 8,438 AIS with COVID (AIS-COVID+) and 159,579 AIS without COVID (AIS-COVID-) patients were included. Mean age ranged from 39.3-77.0 years for AIS-COVID+ and 58.7-75.2 years for AIS-COVID-. Males represented 58.0% (4,875/8,403) of AIS-COVID+ and 51.9% (82,159/158,401) of AIS-COVID-. Mean NIHSS scores ranged from 9.8-22.8 in AIS-COVID+ and 5.6-13.9 in AIS-COVID-. Stroke Outcomes: In-hospital mortality was 27.8% (1,990/7,152) for AIS-COVID+ and 7.0% (8,195/117,283) for AIS-COVID-. Modified Rankin scale (mRS 0-2) at discharge was 26.9% (67/249) in AIS-COVID+ and 39.3% (397/1,010) in AIS-COVID-. Home discharge was 37.6% (2,303/6,124) in AIS-COVID+ and 68.9% (77,136/111,888) in AIS-COVID-.
Conclusions
AIS-COVID+ patients overall suffered worse clinical outcomes with in-hospital mortality quadrupled and almost half less patients discharged home. These findings raise concern regarding the impact on the healthcare needs of the stroke population.

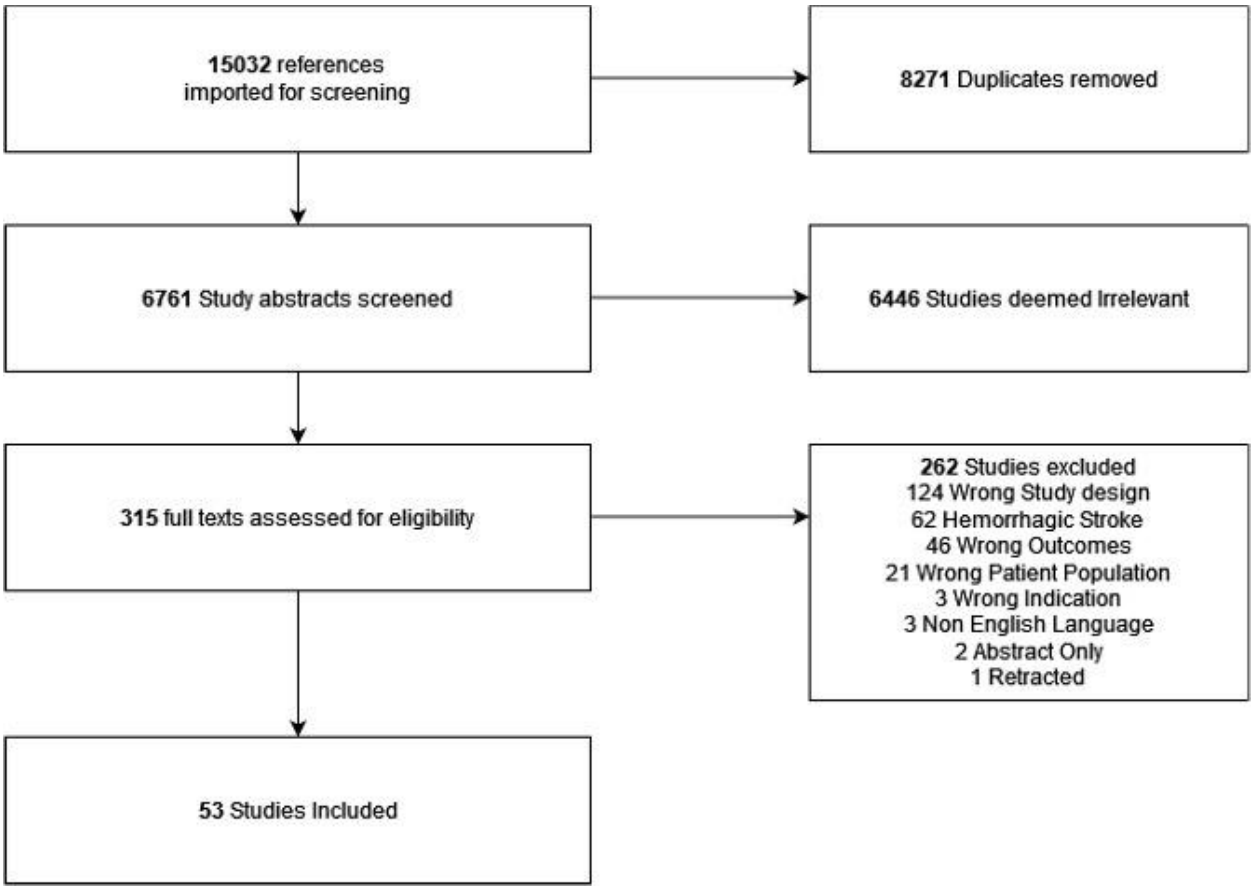

(Filename: TCT_862_Figure1.jpg)

1010

Changes in Quantitative Susceptibility Mapping on Magnetic Resonance Imaging During Prospective Follow-Up of Cavernous Angiomas with Symptomatic Hemorrhage in Trial Readiness Project

S Hage[1], A Stadnik[1], J Lee[1], K Flemming[2], H Kim[3], M Torbey[4], J Huang[5], C Mendoza-Puccini[6], J Koenig[6], R Thompson[7], T Carroll[1], R Girard[1], I AWAD[1]

[1]University of Chicago, Chicago, IL, [2]Mayo Clinic, Rochester, MN, [3]University of California San Francisco, San Francisco, CA, [4]University of New Mexico, Albuquerque, New Mexico, Albuquerque, NM, [5]Johns Hopkins University Medical Institutions, Baltimore, Maryland, Blatimore, MD, [6]NINDS, Bethesda, MD, [7]Johns Hopkins University Medical Institutions, Baltimore, Maryland, Baltimore, MD

Purpose

Quantitative susceptibility mapping (QSM) is a measure of iron content, and >6% increase in QSM has been correlated with new hemorrhage in previously stable cavernous angiomas[1]. Longitudinal changes in QSM are not known in cavernous angiomas with symptomatic hemorrhage (CASH) with high rates of rebleeding and are the targets of novel pharmacotherapies. In a prospective multisite Trial Readiness project [2-3] (clinicaltrials.gov NCT03652181), QSM is longitudinally assessed.

Materials and Methods

Trial eligible subjects with CASH in the prior year and not undergoing lesion resection or radiation, were enrolled. Mean QSM of CASH lesion was acquired at baseline and at 1 and 2 year planned follow-ups. Relative change in mean lesional QSM during each follow-up year was assessed, and any symptomatic hemorrhage (SH), asymptomatic changes (AC; defined as subclinical bleed or growth) in the lesion during the same epoch.

Results

Paired QSM assessments were completed to date in 99 CASH lesions (67 year 1, and 32 year 2) and are reported herein. Four SH and 6 ACs occurred during 1st follow-up year, and 3 SH during 2nd year. QSM increased in 54 lesion-years, decreased in 44, and remained stable in 1. The % lesional QSM change in year 1 was significantly higher than that observed in year 2 (mean +9.33, SD 37.52 vs. +5.20; SD= 24.86; p=0.05; Spearman correlation rho= -0.36). CAs with clinical SH or AC had a significantly higher % QSM change than lesions without (mean +28.03, SD 17.77 vs. +4.97, SD= 34.75; p=0.0014). All 13 lesions with SH/AC demonstrated a QSM increase ≥6% while 31 of 86 (36%) lesions with no clinical events had a >6% QSM increase.

Conclusions

QSM change of >6% is present in every CASH lesion manifesting a new SH or AC (100% specificity), and is more common than clinical events (3.4X higher sensitivity). The biomarker can hence be used as a more sensitive categorical outcome than SH or AC in clinical trials of novel therapies aimed at bleeding in CASH lesions. Effect of an intervention on % QSM change may also be

proposed as a time-averaged difference between 2 arms using a repeated measures analysis implemented as an unadjusted linear mixed model. These results are the basis of application for certification by the U.S F.D.A. of QSM as a monitoring biomarker of drug effect in CASH.

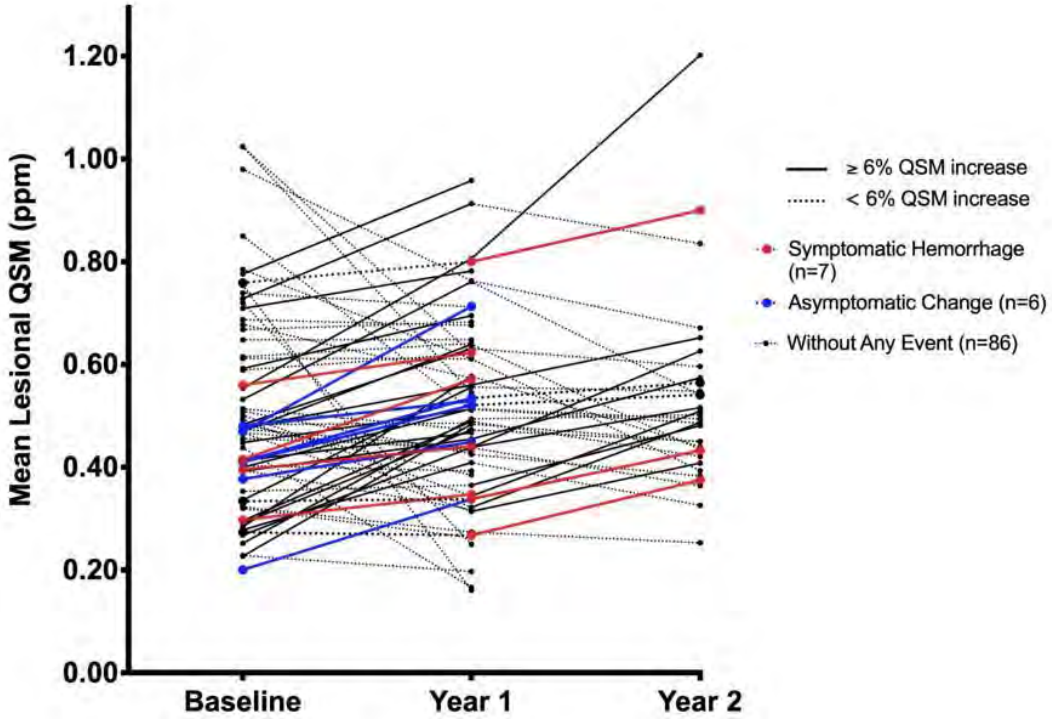

(Filename: TCT_1010_PairedQSM.jpg)

1300

Clinical Implications of Peri-Hematoma Edema Perfusion Fraction in Intracerebral Hemorrhage Intravoxel Incoherent Motion Imaging

G Abou Karam[1], M Aboian[2], A Malhotra[3], A De Havenon[1], G Falcone[4], S Payabvash[4]

[1]Yale School of Medicine, New Haven, CT, [2]Yale University, Woodbridge, CT, [3]Yale University School of Medicine, New Canaan, CT, [4]Yale, New Haven, CT

Purpose

Spontaneous intracranial hemorrhage (ICH) is a devastating cerebrovascular disease with less than 40% functional recovery and yet no effective treatment1. Perihematomal edema (PHE) (a manifestation of secondary brain injury (SBI)) appears within hours of ICH. However, the association between PHE volume and clinical outcome remains equivocal2. This led to evaluate PHE perfusion status. A reduced cerebral blood flow (CBF) in the PHE was found in some studies3. Some reported that reduced CBF was associated with poorer outcome independently from PHE volume4. IVIM imaging may be a better way to assess PHE perfusion (especially microperfusion) then classical imaging5. However, no study was done on IVIM metrics of PHE in patients with ICH. Given the equivocal association of PHE volume with clinical outcome, we aimed to evaluate potential prognostic value of IVIM diffusion and perfusion metrics of PHE in ICH patients.

Materials and Methods

We assessed PHE perfusion status in 24 patients with spontaneous supratentorial ICH who had clinical MRI with IVIM sequence within 1 week of ICH onset. The clinical data was retrieved prospectively. Both hematoma and PHE lesions were segmented manually on axial b-50 series with an overlay of T2-weighted images. The segmentation masks were overlayed on IVIM maps to calculate ICH and PHE volume as well as PHE average perfusion fraction, diffusion coefficient and pseudo-diffusion coefficient.

Results

Our population had 13 female (54%), a median age of 68.1±16.5 years, median (interquartile) baseline National Institute of Health Stroke Scale (NIHSS) of 8(4–12) and median 3-month modified Rankin Score (mRS) of 2(1–4). A longer interval gap between onset and MRI scan was associated with larger hematoma volume (rho=0.4692, p=0.0207); but no association was found with PHE volume. Higher PHE averaged perfusion fraction (rho=0.4732, p=0.0195), lower admission Glasgow Coma Scale, higher NIHSS and female sex were associated with worse outcome. Patient sex, age, admission NIHSS and the interaction product between PHE volume and perfusion fraction were independent predictor of outcome (table 1).

Conclusions

Our results suggest the presence of a higher microperfusion of the PHE which might further worsen blood-brain-barrier leakage2 (a potential target for future therapy) which consequently exacerbate the SBI. Also, IVIM perfusion fraction could play a potential major role in the assessment of PHE neurobiology and clinical prognostication in patient with spontaneous supratentorial ICH.

Table 1. Multivariate model of independent predictors of 3-month mRS

Variable	Odds ratio (95% CI)	P value
Sex	15.8 (1.8–142.7)	0.014
Age	1.08 (1.02–1.15)	0.008
Product of PHE volume and F perfusion fraction	1.01 (1.00–1.02)	0.046
Admission NIHSS	1.20 (1.02–1.42)	0.028

T1: In stepwise ordinal logistic regression, patients' sex, age, admission NIHSS, and production of PHE volume and F perfusion fraction were independent predictors of clinical outcome (higher 3-month mRS)

CI= confidence interval; mRS= modified Rankin Score; NIHSS= National Institute of Health Stroke Scale; PHE= peri-hematomal edema

(Filename: TCT_1300_Table1_IVIM.jpg)

725

Digital Subtraction Angiography Quantitative Analysis and Predictive Modeling of Obliteration in Cerebral Arteriovenous Malformation

M Jabal[1], M Mohammed[1], C Nesvick[1], C Graffeo[1], B Pollock[1], W Brinjikji[1]
[1]*Mayo Clinic, Rochester, MN*

Purpose
Individualized prediction of patient prognosis following therapy is becoming essential for the future of medical practice. This study aimed to investigate the potential of applying machine learning in modeling digital subtraction angiography (DSA) radiomic features for predicting obliteration of cerebral arteriovenous malformations (AVM) following radiosurgery compared to predictors in established scoring systems.
Materials and Methods
A prospective registry of patients with cerebral AVM was screened to include patients who have had DSA for stereotactic radiosurgery (SRS) planning purposes. Anteroposterior and lateral views were retrieved, and manual segmentation of the lesional region of interest was performed prior to radiomic features computation. Following feature selection, machine learning models were developed to predict unsuccessful 2-year total obliteration using processed radiomic features in comparison to combined clinical and radiosurgical features. Various evaluation metrics were used: AUROC, accuracy, AUPRC, F1-score, precision, and recall. The best performing model predictions on the test set were interpreted using shapley additive explanations (SHAP).
Results
From an initial cohort of 352 patients, DSA images of 100 included patients were retrieved and analyzed. Using clinico-radiosurgical features, the best performing model was gradient boosting classifier with an AUROC of 68% and a recall of 67%. When using radiomic variables as input, AdaBoost classifier had the best evaluation metrics with an AUROC of 79% and a recall of 75%. The most significant clinico-radiosurgical features, ranked by model contribution, were lesional volume, patient age, treatment dose rate, presence of seizure at presentation, and prior resection. The most important ranked radiomic features were: GLSZM Gray Level Non-uniformity, Kurtosis, Sphericity, Skewness, and GLDM Dependence Non-uniformity.
Conclusions
The combination of machine learning methods and quantifiable textural imaging analysis presents a promising approach to model outcomes in cerebral AVM managed with SRS and could complement and enhance classical prognostic tools. Our study's predictive findings were based on DSA features related to the diffuseness and angioarchitecture of AVM, in line with prior knowledge, with added precision in its assessment. Model interpretation is essential for building transparent models that give insight to potential new imaging biomarkers and establishing clinically valid radiomic signatures.

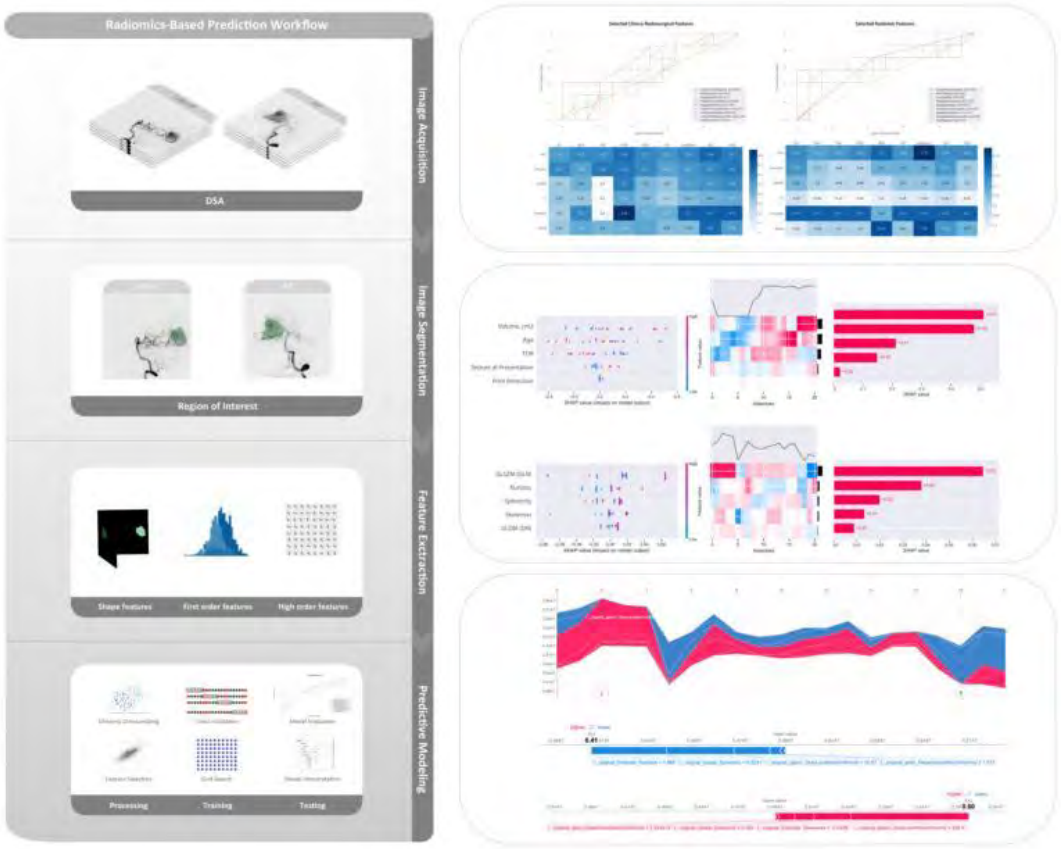

(Filename: TCT_725_Figures.jpg)

515

Plaque Contact Surface Area: A New High Risk Feature of Carotid Plaques Using CT-based Radiomics

F Shareef[1], L Alhilali[1], J Baranoski[1], S Fakhran[2], A Ducruet[1]

[1]Barrow Neurological Institute, Phoenix, AZ, [2]Banner Health System, Mesa, AZ

Purpose

Carotid plaques are associated with 30% of strokes. Associated stenosis from the plaque has long guided risk stratification. However, recent evidence indicates features suggesting unstable plaque offer better prognostication. Radiomics, the extraction of sub-visual, quantifiable shape and textural data from medical images, has the potential to identify imaging features of high-risk plaque better than traditional imaging metrics. MR-Radiomics has been applied to carotid plaques. Unfortunately, carotid imaging is primarily CT angiography (CTA). We sought to determine whether radiomics of carotid plaques on CTA may identify novel high-risk features to assist in therapeutic decision making .

Materials and Methods

Patients with unilateral anterior circulation embolic stroke with bilateral carotid atherosclerotic plaque on CTA were retrospectively analyzed from October 1, 2018-October 1, 2019. Carotid plaques ipsilateral and contralateral to the side of infarction were separately segmented in a semi-automated manner. Pyradiomics software was used to extract 12 shape and 13 first-order radiomic features from the segmented plaques on CTA. Comparison of radiomic features between plaque ipsilateral to the infarction and plaque contralateral to the infarction was performed within each patient, using the patient as their own internal control. A paired t-test was applied for each radiomic feature. False Discovery Rate was used to correct for multiple comparisons.

Results

33 patients (mean age 58, range 30-77, 44% male) were included. NASCET narrowing was not significantly higher ipsilateral to the stroke (67 vs 60%, p=0.11). After multiple comparisons correction, only two features, Surface Area (SA) and Maximum Superior-Inferior Length (MSIL) were significantly different between plaques ipsilateral and contralateral to the stroke (SA 1023 vs 802 mm2, p=0.048; MSIL 7.4 mm vs. 6.1 mm, p=0.049). Plaque volume and flatness trended towards significance (p=0.08 and p=0.07, respectively).

Conclusions

This is the first study to apply CT-radiomics to carotid plaques, using patients as their own internal controls to mitigate confounding demographic risk factors. Shape features indicating greater plaque contact with the vessel lumen (surface area, length of carotid wall

involvement) were greater risk factors than plaque size or gray scale features of plaque composition. This suggests large luminal contact area increases risk regardless of plaque volume or composition.

801

RAPID Aneurysm Accurately Measures Aneurysm Size on CTA Compared to Digital Subtraction Angiography

S Snyder[1], A Gauden[1], K Copeland[2], A Spiotta[3], J Heit[4]

[1]Stanford University, Palo Alto, CA, [2]Boulder Statistics, Steamboat Springs, CO, [3]Medical University of South Carolina, Charleston, SC, [4]Stanford University, Los Altos, CA

Purpose

Cerebral aneurysms are often identified and characterized on non-invasive CT Angiography (CTA) images, but digital subtraction angiography (DSA) is the gold standard for aneurysm evaluation. We compared cerebral aneurysm size measurements as measured from CTA processed by a semi-automated artificial intelligence software program (RAPID Aneurysm) and 3-dimensional rotational DSA.

Materials and Methods

We performed a retrospective cohort study of consecutive patients with a cerebral aneurysm who underwent CTA and DSA with 3-dimensional reformations. Patients with excessive motion on either CTA or DSA were excluded. CTA images were processed by RAPID Aneurysm to determine aneurysm height, width, and neck width. The reference standard for the measurements was determined on 3-dimensional DSA by a diagnostic and interventional neuroradiologist with 8-years of experience. An additional interventional neuroradiologist with 2-years of experience measured also measured 3-dimensional DSA images for comparison. Both readers were blinded to RAPID Aneurysm measurements. Correlation and bias between these measurements were determined.

Results

Results from 50 patients with 50 aneurysms were compared. 32 patients (64%) were female. Median age was 65 (IQR: 56.25 – 71.75). 37 patients (74%) presented with ruptured aneurysms. The aneurysms represented a range of aneurysm sizes (1.9-33.3 mm; IQR 3.6-7.2 mm). RAPID Aneurysm size measurements showed excellent correlation and low bias (correlation, mean difference) when compared to the reference standard for aneurysm height (0.98, -0.9mm), width (0.98, 0.1mm), and neck width (0.94, 1.1mm). The inter-reader comparison between the two interventional neuroradiologists was similarly excellent for aneurysm height (0.97, -0.4mm), width (0.98, -0.2 mm), and neck width (0.89, 0.8mm).

Conclusions

RAPID Aneurysm measurement of cerebral aneurysm height, width, and neck width on CTA is strongly correlated to expert interventional neuroradiologist measurements on 3-dimensional DSA. These findings suggest that neurointerventional aneurysm device sizing and treatment planning may performed prior to DSA, which may reduce procedure times.

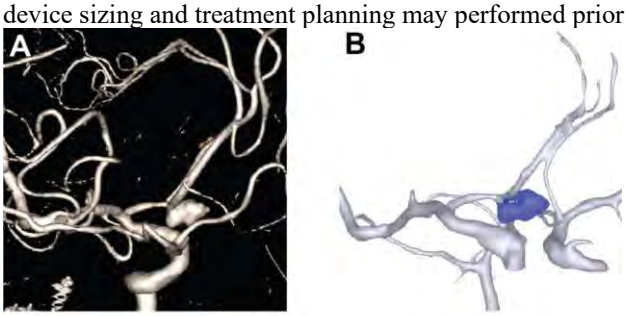

Figure 1. Ruptured Acom Aneurysm.
A 10.2 mm Acom aneurysm is shown on 3-D DSA (A) and on CTA images processed by RAPID Aneurysm. Measurements derived from these images showed an excellent agreement.

(Filename: TCT_801_Figure1.jpg)

Tuesday, May 2, 2023

4:45-6:00 PM

ASFNR Programming: Making Every Photon Count: A Must-know primer on Photon-counting CT for busy neuroradiologists (Essentials Track)

1336

Photon counting detector CT improves diagnostic confidence in temporal bone imaging

K Desai[1], J Benson[1], P Farnsworth[1], J Lane[1]
[1]*Mayo Clinic, Rochester, MN*

Purpose
Photon-counting detectors (PCDs) have the potential to change clinical CT by improving image quality and reducing radiation dose. This study sought to compare the diagnostic confidence between PCD-CT and conventional energy integrating CT (EID-CT) on temporal bone imaging.
Materials and Methods
A review was completed of prospectively recruited patients that underwent temporal bone CT examinations on both an investigational PCD-CT and clinical EID-CT. Two blinded neuroradiologists compared temporal bone imaging using conventional EID-CT and PCD-CT, side-by-side. The reviewers assessed both the ability to use each image set to achieve diagnostic confidence (either of identifying pathology or lack thereof), on a scale of 1-5. A Likert scale was used to assess preference of EID-CT or PCD-CT image quality. A post hoc analysis was used to adjust these scores: 1 = highly prefer EID, 2 = slightly prefer EID, 3 = no preference, 4 = slightly prefer PCD, 5 = highly prefer PCD.
Results
31 patients were included in the cohort, yielding 62 image sets (right and left sides). The average age of the patients evaluated was 55.7±17.1. 21 (67.7%) were female. 23/62 (37.1%) of temporal bones were normal. The most common pathology was otosclerosis (n=9), followed by superior semicircular canal dehiscence (n=7) and chronic otitis media (n=6). PCD-CT was preferred to EID-CT on Likert scales for both reviewers (4.5 for reviewer A, 5.0 for reviewer B). The average diagnostic confidence for PCD-CT and EID-CT were 4.71 and 3.98 for reviewer A and 5.00 and 3.69 for reviewer B, respectively. Together, diagnostic confidence was significantly higher on PCD-CT (4.9±0.4) than EID-CT (3.8±0.6) ($p<0.001$).
Conclusions
PCD-CT yields greater diagnostic confidence than EID-CT in temporal bone imaging.

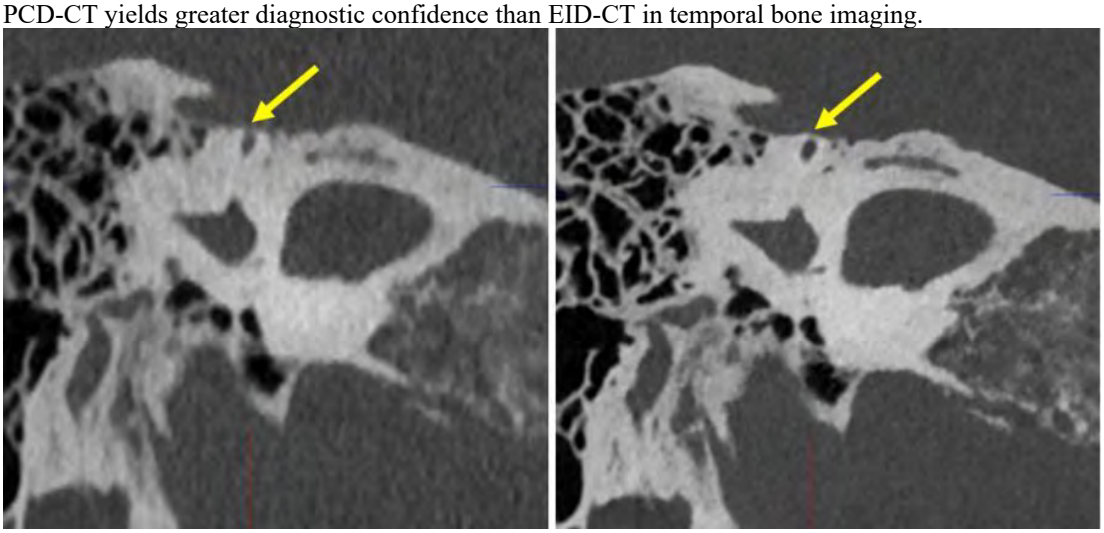

(Filename: TCT_1336_Snap1.jpg)

Tuesday, May 2, 2023

4:45-6:00 PM

ASPNR Programming: Interesting Pediatric Neuroradiology Case Session

759

Computational approach to assess cognitive outcome in pediatric patients with hepatic encephalopathy associated to a portosystemic shunt undergoing liver vascular shunt correction

G Sparacia[1], C Alms[2], G Parla[3], V Lo Re[3], A Iaia[2], R Miraglia[3], J de Ville de Goyet[3]

[1]IRCCS-ISMETT - UNIVERSITY OF PALERMO, Palermo, Italy, [2]Christiana Care Health System, Newark, DE, USA, [3]IRCCS-ISMETT, Palermo, Italy

Purpose

Pediatric patients with hepatic encephalopathy associated to a portosystemic shunt without underlying liver diseases presents variable degree of cognitive impairment mainly due to toxic brain catabolites deposition in the globi pallidi. The aim of this study was to assess cognitive outcome in pediatric patients undergoing liver vascular shunt correction by using a radiomic and connettomics approach.

Materials and Methods

From March 2021 to July 2022, 22 pediatric patients (13 males, 9 females; mean age 9.2 year, median age 9 years) underwent magnetic-resonance imaging (MRI) with resting-state functional MRI before and after (within 1 year from the first MR examination) liver vascular shunt correction obtained by meso-rex shunt (n=19 patients), or living-donor liver transplantation (LDLT) (n=3 patients). The vascular shunt was due to portal vein cavernoma, or to Abernethy syndrome, or to portal venous thrombosis (PVT) after liver transplantation. The SynthSeg neural network was applied for automatic brain MRI segmentation to extract 3D bilateral globi pallidi volume of interest (VOIs) from each patient. Matlab Radiomic Toolbox was used to perform texture analysis from the input VOIs and to perform multivariable analysis with feature set reduction and feature set selection from the input VOIs. Brain connectome was obtained by using FreeSurfer and the CONN Toolbox running under Matlab. General linear model and logistic regression analysis were computed to predict the cognitive outcome after treatment. Prediction of hepatic encephalopathy secondary to toxic catabolites deposition was assessed with the Matlab Radiomic Toolbox.

Results

The radiomic texture analysis model classified the presence of HE with a 94% of accuracy. Connettomics demonstrated a significant (p-FDR=0.05) global cognitive improvement in patients after liver vascular shunt correction.

Conclusions

Cognitive outcome in pediatric patients with hepatic encephalopathy associated to a portosystemic shunt undergoing liver vascular shunt correction can be predicted using a connettomics-based approach. Radiomic-based classification from automatic brain MRI segmentation of bilateral globi pallidi volume is feasible and can serve as additional tool to guide the therapeutic timing.

Fig. 1 - Automatic brain MRI segmentation to extract 3D bilateral globi pallidi volume of interest

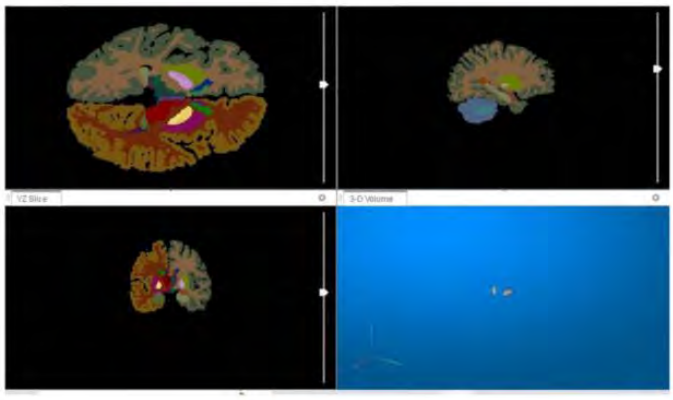

Fig. 2 - Comparison of brain connettome A) before and B) after liver vascular shunt correction demonstrated a significant (p-FDR=0.05) global cognitive improvement

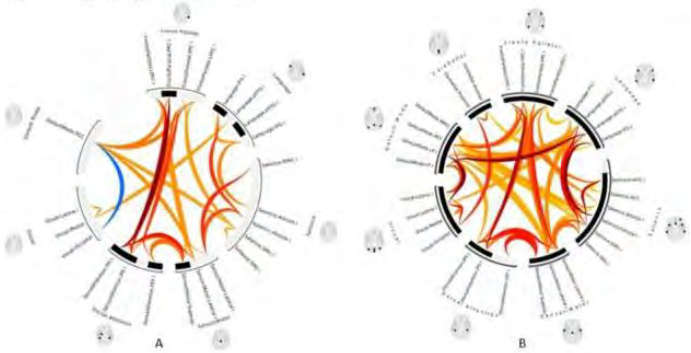

(Filename: TCT_759_ASNR2022.jpg)

532

Deep Cerebral Venous Anomalies in Premature Babies with GMH-IVH: an SWI MRI Retrospective Study

T Kent[1], V Sinha[1], E Ceyhan[2], L Sura[1], M Weiss[1], M ALBAYRAM[3]

[1]University of Florida College of Medicine, Gainesville, FL, [2]Auburn University, Auburn, AL, [3]U florida, Gainesville, FL

Purpose

Germinal Matrix Hemorrhage/Intraventricular Hemorrhage (GMH-IVH) is a multifactorial injury with both anatomic and hemodynamic involvement. Normal variants in preterm deep cerebral venous anatomy associated with GMH-IVH have been previously described using MRI susceptibility weighted imaging (SWI). The aims of this study were to use SWI to compare the deep venous systems of a cohort of preterm neonates with various grades of GMH-IVH to a group of age-matched controls without GMH-

IVH, to present novel retrospective SWI imaging findings, and to further the discussion regarding the complex pathogenesis of GMH-IVH.

Materials and Methods

A neuroradiologist retrospectively evaluated 3T MRI SWI and phase imaging of 56 preterm neonates with GMH-IVH (14 of each grade) and 27 controls or preterm neonates without GMH-IVH, scoring the venous irregularities according to three variables: decreased venous patency, increased lumen susceptibility, and the presence of collaterals. Eight different venous locations, including indicated bilateral components, were evaluated: straight sinus, vein of galen, internal cerebral, direct lateral, thalamostriate, atrial, and the anterior septal. Variables were analyzed for statistical significance.

Results

Deep venous anomalies were significantly more common in patients with GMH-IVH, with Wilcoxon Rank Sum Test demonstrating significant increase with GMH-IVH for total decreased venous patency (W=0, p <.0001), increased lumen susceptibility, and collateral formation. These venous anomalies were also positively correlated with increase in GMH-IVH grade from 1-4, not just GMH-IVH alone, with total decreased venous patency having a 0.782 correlation with increasing GMH-IVH grade.

Conclusions

Deep venous anomalies are significantly correlated with GMH-IVH alone and an increase in GMH-IVH grade. This study is the first to document these novel findings associated with GMH-IVH. Further study is needed to determine cause and effect, although in our discussion we suggest evidence for both.

Table 1: Venous Anomaly Scoring System

Score	0	1	2	3	4
Decreased Venous Patency	none	Contour irregularities, but no significant stenosis (<25%)	Stenosis <50%	Stenosis >50%	Occlusion
Collaterals	none	present			
Increased lumen susceptibility	none	Present, residual thrombotic changes			

Notes: If occlusion was found with a vein cast, decreased venous patency was scored a 4. If vein was missing, with no vein cast, vein was rate not applicable/NA.

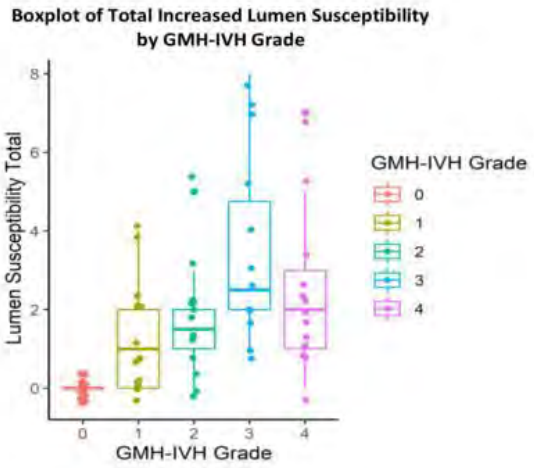

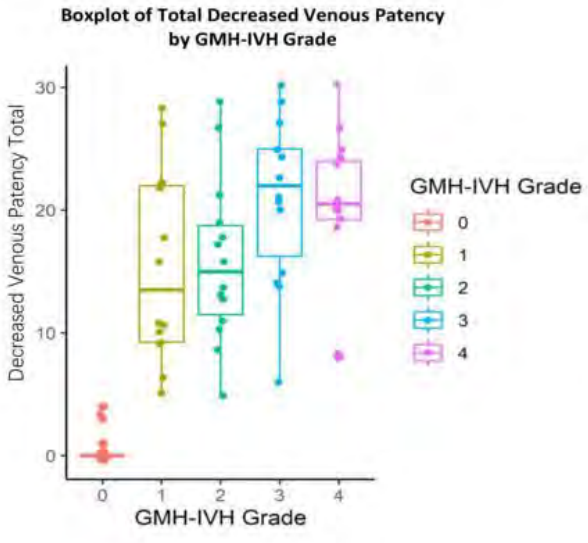

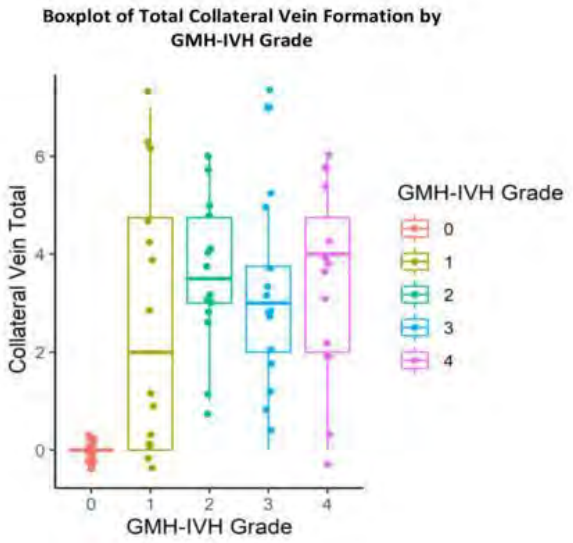

(Filename: TCT_532_KentASNR.jpg)

Tuesday, May 2, 2023

4:45-6:00 PM

SNIS Programming: From Diagnosis to Treatment – Stroke

668

Accuracy, Variability and Spatial Overlap of Infarct Core from Three CT Perfusion Packages vis-à-vis Diffusion Weighted Images: A Comparative Study

I Berglar[1], R Gupta[2], L Moser[3], J Vranic[1]

[1]Massachusetts General Hospital, Boston, MA, [2]Massachusetts General Hospital and Harvard Medical School, Bosten, MA, [3]ETH Zürich, Zürich, Switzerland

Purpose

In patients with acute ischemic stroke, estimation of infarct core volume is important to assess eligibility for endovascular therapy [1, 2]. Cerebral Blood Flow (CBF) below a certain threshold, measured using CT perfusion (CTP), is routinely employed as a surrogate for irreversibly infarcted core. We compared the accuracy and spatial localization of CTP derived infarct core from different commercially available CTP packages with diffusion weighted imaging (DWI) as the ground truth.

Materials and Methods

We included 48 consecutive patients with anterior circulation acute ischemic stroke who underwent admission CTP and DWI within 80 minutes of each other. The raw CTP dataset was processed by 3 post-processing settings designated at CTP-A, CTP-B, and CTP-C. Relative CBF (rCBF) <30% for CTP-A and CTP-C, and rCBF <20% for CTP-B of the contralateral side, as recommended by the vendor, was used to estimate infarct core for all settings. These 3 estimates were compared to DWI using correlation and Bland-Altman analyses. Spatial overlap of the CTP-derived core vis-à-vis DWI core was assessed by analyzing the co-registered MR and CT datasets using a custom developed Python script for all 3 CT settings. Intersection over union (IoU) and dice score measuring the spatial overlap were determined.

Results

For the 48 patients included (22 or 45.8% female), the mean age was 67 (±15) years, admission NIHSS median (IQR) was 15 (8-18), mean time (±SD) from symptom onset to CTP was 255 min (±212 min), mean time interval between CTP and MRI was 49 min (±17 min). When comparing DWI measurement of infarct volume with CTP, there was significant correlation ($r>0.7$, $p<0.0001$). Bland-Altman analyses revealed mean systematic bias in the CTP-derived infarct core of –15.2mL to 13.1mL and variability of +30.9mL (±1.96SD) compared to DWI. Spatial localization of CTP-derived and DWI-derived infarct volumes in a common coordinate system showed poor agreement in area of overlap, with median IoU and dice scores ranging from 0.18-0.24 and 0.31-0.38 respectively. In 8 cases (17%) at least one of the 3 settings failed to identify the stroke entirely.

Conclusions

Our study demonstrates that for all three CTP settings, the estimated volume and the degree of overlap disagreed considerably with the DWI ground truth. Strict adherence to CTP results could lead to incorrect triage decisions and influence patient treatment outcomes [3].

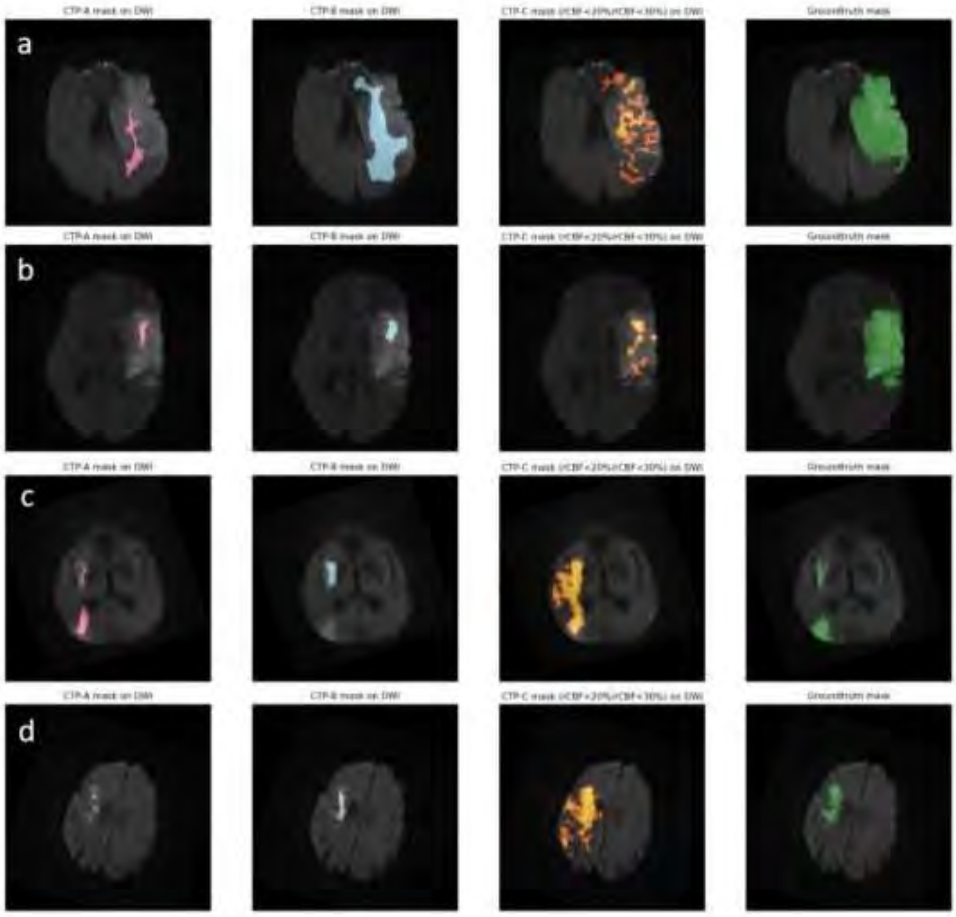

Figure 1. Examples of low concordance of all three CTP programs. The estimated ischemic core volume by CTP-A is shown in pink, CTP-B in blue and CTP-C with rCBF<30% in red, and CTP-C with rCBF<20% in orange. Intersection over Union (IoU) and dice score are shown for CTP-A, CTP-B, CTP-C with rCBF<30% and CTP-C with rCBF<20%, respectively.

a) Patient with left M1 and M2 occlusion. Total infarct core: 143.4ml. IoU: 0.18, 0.45, 0.30 and 0.00, respectively; Dice score: 0.29, 0.56, 0.45 and 0.16, respectively.
b) Patient with left M1 occlusion. Total infarct core: 132.8ml. IoU: 0.24, 0.27, 0.31 and 0.22, respectively; Dice score: 0.39, 0.42, 0.47 and 0.36, respectively.
c) Patient with right ICA and MCA occlusion. Total infarct core: 56.6ml. IoU: 0.40, 0.28, 0.31 and 0.34 respectively; Dice score: 0.57, 0.44, 0.47 and 0.51, respectively.
d) Patient with right M1 occlusion. Total infarct core: 27.7ml. IoU: 0.31, 0.29, 0.23 and 0.28 respectively; Dice score: 0.47, 0.45, 0.37 and 0.44, respectively.

(Filename: TCT_668_Supplement_figure.jpg)

648

Comprehensive Venous Outflow Predicts Functional Outcomes in Acute Ischemic Stroke Patients Treated by Thrombectomy

G Adusumilli[1], T Faizy[2], S Christensen[3], M Mlynash[3], G Albers[3], M Lansberg[3], J Fiehler[2], J Heit[3]
[1]Massachusetts General Hospital, Boston, MA, [2]University Hospital Hamburg-Eppendorf, Hamburg, Germany, [3]Stanford University, Stanford, CA

Purpose
Venous outflow (VO) has emerged as a robust measure of collateral blood flow in acute ischemic stroke patients with a large vessel occlusion (AIS-LVO).1-3 VO is commonly measured by the cortical vein opacification score (COVES), which represents only cortical venous drainage of the middle cerebral artery territory.4 The addition of deep venous drainage to VO assessment may provide valuable information to further guide the treatment of these patients.5 Our purpose was to develop a new comprehensive VO score, inclusive of deep venous drainage, and stratify patients by favorable (CVO+) versus poor (CVO-) comprehensive VO against angiographic and functional outcomes.
Materials and Methods
We performed a multicenter retrospective cohort study of AIS-LVO patients treated by thrombectomy. We quantified opacification of the internal cerebral veins on a scale of 0 to 2, analogous to the scoring system of COVES. This metric was combined to existing COVES scores in this patient cohort to create the comprehensive venous outflow score (CVO) from 0 to 8 and stratify patients by favorable (CVO+) versus poor VO (CVO-). The primary outcome was functional independence, defined as a modified Rankin Scale

(mRS) score of 0-2, at 90-day follow-up. The secondary outcome was excellent reperfusion, defined as thrombolysis in cerebral infarction scores of 2c/3.

Results

678 patients met inclusion criteria, and 315 were stratified into the CVO+ category and 363 into the CVO- category after deep venous scoring was added. There were significantly higher rates of functional independence (mRS 0-2; 194/296 vs. 37/352, 66% vs. 11%, $p < 0.001$) and excellent reperfusion (TICI 2c/3; 166/313 vs. 142/358, 53% vs. 40%, $p < 0.001$) in CVO+ patients compared to in CVO- patients. There was a significant increase in association of mRS with CVO compared to with COVES (-0.74 vs. -0.67, $p = 0.006$).

Conclusions

A new comprehensive VO score, inclusive of deep veins, was found to have a significantly greater association with functional independence at 90 days than COVES alone. A favorable CVO profile is strongly associated with functional independence and excellent post-thrombectomy reperfusion. Future studies should focus on patients with CVO status that is discrepant to eventual outcome.

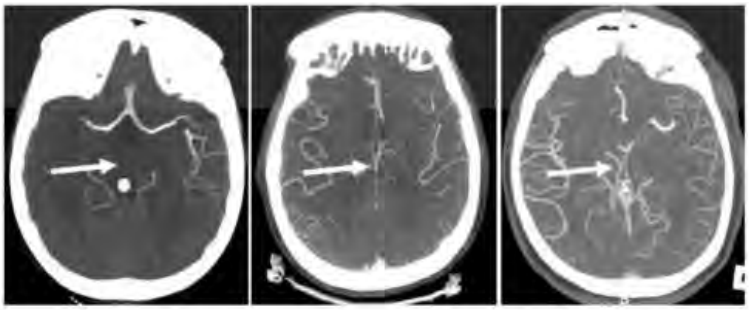

Table 1. Imaging metrics at baseline and follow-up by venous outflow status

	CVO+ (n = 315)	CVO- (n = 363)	p-value
ASPECTS, median (IQR)	8 (7 - 10)	7 (6 - 9)	<0.001
Baseline Infarct Volume, median (IQR) (N=309, 359)	5 (0 - 17.5)	18 (3 - 48)	<0.001
Follow-Up Infarct Volume, median (IQR) (N=304, 343)	12.4 (4.8 - 34.2)	54.3 (22.1 - 120.3)	<0.001
Change in Infarct Volume, median (IQR) (N=298, 340)	+5.9 (-0.4 - 22.1)	+32.1 (4.1 - 82.7)	<0.001

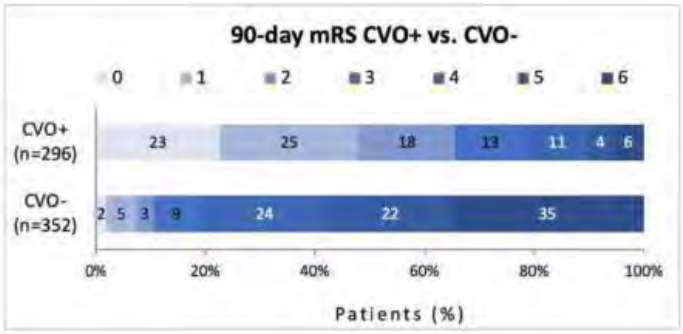

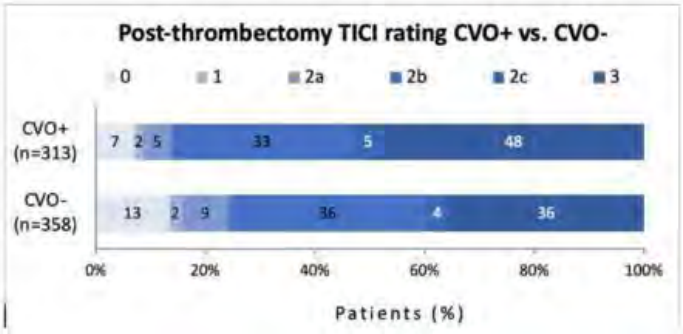

(Filename: TCT_648_GraphicsFileforASNR2023Abstract.jpg)

Wednesday, May 3, 2023

9:45-11:00 AM

ASFNR Programming: Big Data and Neuroradiology

724

Yale Brain Metastasis Dataset Is Ready for a Challenge: Preparing Large Annotated Brain Metastasis Dataset for #OpenScience

D Ramakrishnan[1], L Jekel[1], M Sala[1], M Kaur[2], A Janas[3], G Cassinelli Petersen[1], K Bousabarah[4], M Lin[5], S Merkaj[1], M von Reppert[6], M Aboian[7]

[1]Yale School of Medicine, New Haven, CT, [2]Ludwig Maximilians Universitat, Munich, NA, [3]Yale Medical School, New Haven, CT, [4]Visage Imaging GmbH, Berlin, CT, [5]Yale University School of Medicine and Visage Imaging, Inc., New Haven, CT, [6]Brain Tumor Research Group, Yale School of Medicine, New Haven, CT, [7]Yale University, Woodbridge, CT

Purpose

While several machine learning (ML) algorithms have been developed to classify brain metastases (BM), few have undergone external validation due to difficulty in obtaining secure and anonymized datasets from outside institutions. There are no US FDA-cleared AI algorithms to date with BM focus. We present the Yale Brain Metastasis database that includes annotated images of BM with clinical outcome information.

Materials and Methods

Our database includes 290 patients (1133 brain metastases) with T1 post-contrast images and corresponding survival data. Volumetric segmentations of enhancing tumor and peritumoral edema were generated in a semiautomatic workflow using nnUNet algorithm trained on an excluded subset. Segmentations were validated by a board-certified neuroradiologist. A subset of 228 patients from the database also had FLAIR images and information about qualitative imaging features and additional clinical features.

Results

nnUNET was trained using batches of 23 patients. DSC scores for segmentation of the contrast enhancing portion of the tumor reached a plateau of DICE 0.85 after 4 batches. The median overall survival for all 290 patients in our database was 3.4 years. The overall 1-year survival rate was around 77%, and the overall 5-year survival rate was around 45%. Of the 228 patients who had associated imaging and clinical outcome information available, the following was the breakdown of origin of brain metastases: breast (29), GI (16), SCLC (16), melanoma (41), NSCLC (106), and others (20). The mean number of metastases among all cancer origins was 3.4 per patient. 33.3% of patients had infratentorial involvement, 37.3% had intratumor susceptibility in at least one lesion, 61.8% had rim-like contrast enhancement pattern, and 14.9% had cystic degeneration. The mean age of the subset of 228 patients was 62.6 years with 60.2% female and 39.8% male. 47.8% of patients had extranodal metastasis. The mean pack-year smoking history for all patients was 15.5.

Conclusions

We demonstrate a BM dataset of 290 patients with individual segmentations on post-contrast MRI and a subset of 228 patients with FLAIR images, imaging features, and clinical information. Our database was generated in a streamlined approach involving direct clinical production to research server database using a forward-based hash to maintain a de-identified patient jacket. Open access of our database will aid in novel algorithm development of brain metastases.

		All	Breast	GI	SCLC	Melanoma	NSCLC	Others
Patients, n		228	29	16	16	41	106	20
NOM, mean (SD)		3.4 (4.6)	4.9 (8.3)	2.3 (2.1)	3.6 (4.6)	3.6 (3.5)	3.0 (3.8)	3.1 (3.9)
INFRA, n (%)	No	152 (66.7)	16 (55.2)	9 (56.2)	8 (50.0)	29 (70.7)	76 (71.7)	14 (70.0)
	Yes	76 (33.3)	13 (44.8)	7 (43.8)	8 (50.0)	12 (29.3)	30 (28.3)	6 (30.0)
ITSS, n (%)	No	143 (62.7)	22 (75.9)	9 (56.2)	11 (68.8)	24 (58.5)	66 (62.3)	11 (55.0)
	Yes	85 (37.3)	7 (24.1)	7 (43.8)	5 (31.2)	17 (41.5)	40 (37.7)	9 (45.0)
RIM, n (%)	No	87 (38.2)	14 (48.3)	2 (12.5)	4 (25.0)	24 (58.5)	36 (34.0)	7 (35.0)
	Yes	141 (61.8)	15 (51.7)	14 (87.5)	12 (75.0)	17 (41.5)	70 (66.0)	13 (65.0)
CYSTIC, n (%)	No	194 (85.1)	23 (79.3)	14 (87.5)	13 (81.2)	36 (87.8)	90 (84.9)	18 (90.0)
	Yes	34 (14.9)	6 (20.7)	2 (12.5)	3 (18.8)	5 (12.2)	16 (15.1)	2 (10.0)

Table 1: Segmentation features from qualitative imaging review. SD = Standard deviation. NOM = Number of metastases. INFRA = Infratentorial involvement. ITSS = Intratumoral susceptibility in at least one lesion. RIM = Rim-like contrast enhancement pattern. CYSTIC = Cystic degeneration.

		n/a	All	Breast	GI	SCLC	Melanoma	NSCLC	Others
Patients, n			228	29	16	16	41	104	20
Age, mean (SD)			62.6 (11.9)	56.7 (12.6)	68.2 (12.1)	62.8 (12.2)	62.7 (12.4)	63.5 (10.9)	61.1 (12.9)
Extranodal metastasis, n (%)	No	2	118 (52.2)	14 (48.3)	6 (37.5)	9 (56.2)	18 (43.9)	64 (61.5)	7 (35.0)
	Yes		108 (47.8)	15 (51.7)	10 (62.5)	7 (43.8)	23 (56.1)	40 (38.5)	13 (65.0)
Sex, n (%)	Female	2	136 (60.2)	28 (96.6)	9 (56.2)	11 (68.8)	16 (39.0)	63 (60.6)	9 (45.0)
	Male		90 (39.8)	1 (3.4)	7 (43.8)	5 (31.2)	25 (61.0)	41 (39.4)	11 (55.0)
Pack years, mean (SD)			15.5 (19.0)	3.5 (8.7)	15.0 (18.6)	22.9 (12.3)	7.7 (10.9)	22.2 (22.7)	13.8 (14.9)

Table 2: Basic demographics in patient cohort. SD = Standard deviation. Extranodal metastses refers to presence of metastatic foci outside of the cranium.

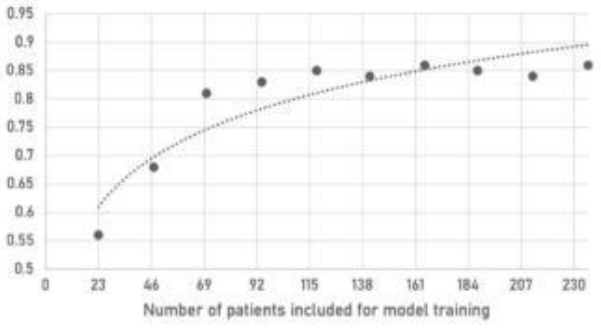

Fig 1. Training of nnUNet algorithm in batches of 23 reaches plateau of DICE 0.85.

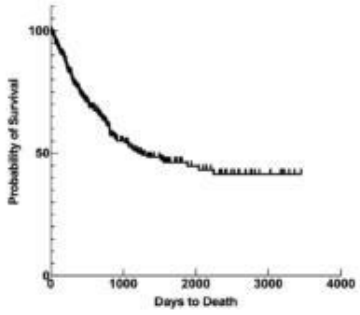

Fig 2. Survival for all 290 patients in Yale brain metastasis database

(Filename: TCT_724_BM_Database_figs.jpg)

Wednesday, May 3, 2023

9:45-11:00 AM

Scientific Abstract Session: AI & Tumors 2

697

AI based classification of three common tumors in Neuro-oncology: A Multi-institutional comparison of Machine Learning (ML) and Deep Learning (DL) methods

G Bathla[1], D Durjoy[2], Y Liu[2], M Sonka[3], S MOHAN[4], B Kassmeyer[1], N Larson[5], N Campeau[5], S Priya[6]

[1]Mayo Clinic, Rochester, Rochester, MN, [2]University of Iowa, Iowa City, IA, [3]The University of Iowa, Iowa City, IA, [4]UNIVERSITY OF PENNSYLVANIA, PHILADELPHIA, PA, [5]Mayo Clinic, Rochester, MN, [6]University of Iowa hospitals and Clinics, IOWA CITY, IA

Purpose

The purpose of the study was to determine if ML versus DL pipelines performed better in AI-based three-class classification of glioblastoma (GBM), metastatic disease (MD) and primary CNS lymphoma (PCNSL).

Materials and Methods

Institutional cancer registries were screened for index cases with pathologically proved GBM and PCNSL, as well as cases with known primary malignancy and neuroimaging compatible with MD. A total of 502 cases (208 GBM, 67 PCNSL and 227 MD) were included. External data from another institution consisted of 86 cases (27 GBM; 27 MD, 32 PCNSL). All cases were co-registered, resampled, denoised and intensity normalized using the same pipelines. Lesions were segmented using inhouse semi-automated software to 3D segment the enhancing tumor (ET) and peritumoral edema (PTE). 3D masks were used for DL pipeline. Radiomic features for ML pipelines were extracted using Pyradiomics. A total of 30 ML pipelines, consisting of 6 ML algorithms and 5 feature reduction techniques were evaluated and compared with the best DL pipeline. The pipelines were evaluated for basic MRI sequences (T1W, T2W, FLAIR, DWI and T1-CE), as well as combinations of different sequences. All pipelines were trained evaluated with 5-fold cross-validation on internal data followed by external validation.

Results

The best performing DL model achieved a multi-class AUC of 0.91 using a combination of T1-CE mask for tumor and T2 derived mask for PTE, with AUC of 0.85 (95% CI: [0.77,0.91]) on external data. The best performing ML model achieved a multi-class AUC of 0.92 using radiomics derived from the enhancing tumor of the CE sequence, XGBOOST pipeline with embedded feature selection. AUC on external dataset was 0.87 (95% CI: [0.80,0.92]).

Conclusions

Both ML and DL derived pipelines may achieve similar performance for three class classification in neuro-oncology, although ML pipelines may be logistically easier to implement as segmentation of PTE may not be needed.

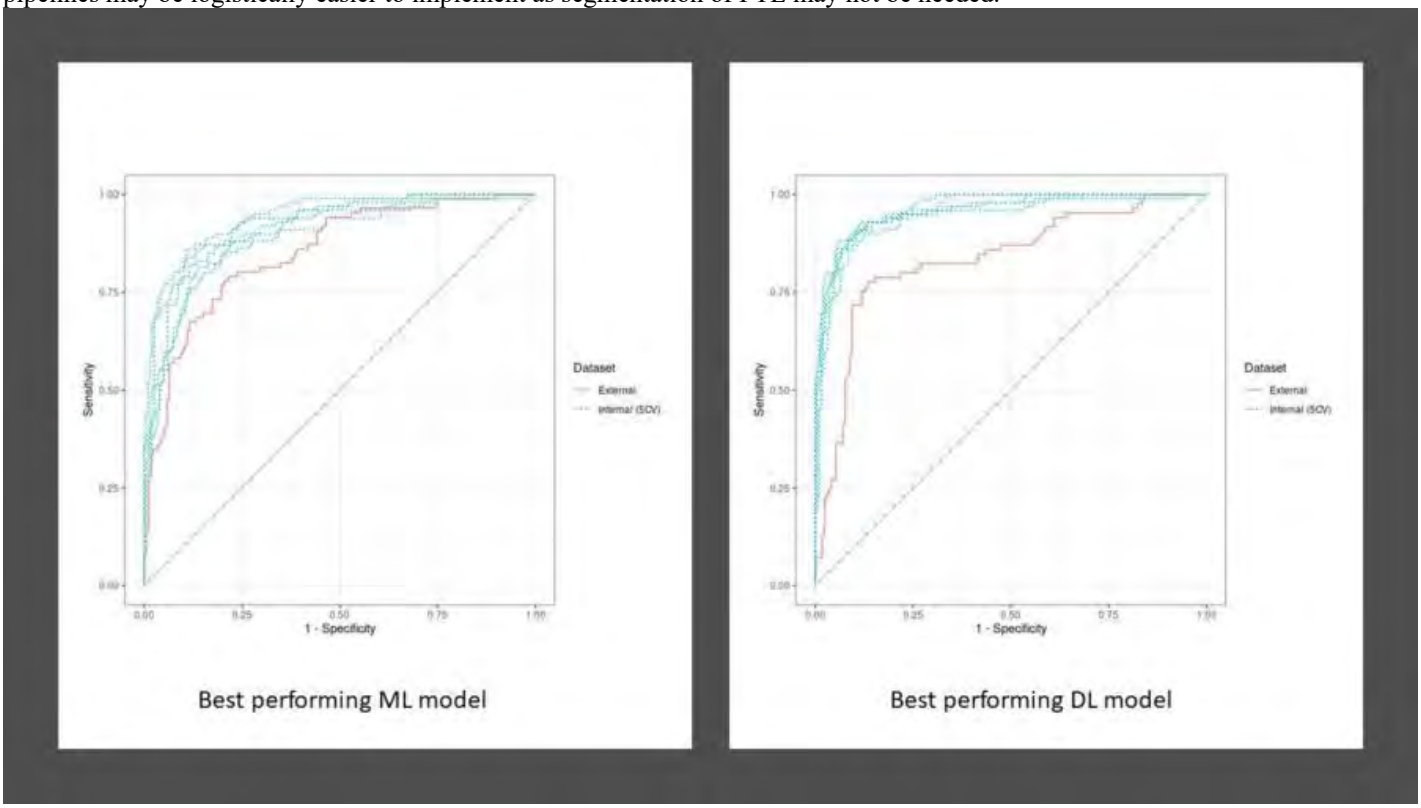

(Filename: TCT_697_ML-DL.jpg)

460

Comparison of Different Machine Learning Algorithms to Analyze MRI Features to Predict pTERT Mutation in IDH-wt GBM patients With Feature Selection Optimized By SHAP Algorithm

---

Removed by author(s) instution request(s)

397

Deep Learning for Detecting Brain Metastases on Magnetic Resonance Images: Systematic Review and Meta-analysis with a Critical Approach

B Ozkara[1], M Karabacak[2], M Chen[1], M Wintermark[1]

[1]The University of Texas MD Anderson Cancer Center, Houston, TX, [2]Mount Sinai Health System, New York, NY

Purpose

Contrast-enhanced magnetic resonance imaging (MRI) is the preferred imaging examination for diagnosing brain metastases (BMs).[1] Stereotactic radiosurgery (SRS) plays a more prominent role today in treating BMs. Before SRS, each BM must be correctly detected and manually delineated for treatment planning, which is time-consuming and subject to significant inter- and intra-observer variability.[2] While detecting and delineating BMs on MRI is critical for diagnosis and treatment planning there should be improvements. Research has been done to make this process automated using MRI studies and deep learning (DL). This study aimed to conduct a systematic review of this topic, assess the quality of the studies, and run a meta-analysis to evaluate the strength of the current evidence.

Materials and Methods

A systematic search of MEDLINE, EMBASE, and Web of Science was conducted until September 30, 2022. Inclusion criteria: patients with BMs included; DL and MRI images were used; adequate data was present regarding detective performance; and original research articles. Exclusion criteria: reviews, letters, or errata; case reports or series; studies with overlapping cohorts; inadequate data on detective performance; machine learning (not DL) was used; articles not in English. The quality was assessed with the Quality Assessment of Diagnostic Accuracy Studies-2 (QUADAS-2) and the Checklist for Artificial Intelligence in Medical Imaging (CLAIM). Two pooled proportion analyses of detectability were performed: for all the studies included in the quantitative analysis and for the studies reporting their sensitivity lesion-wise.

Results

Twenty-five studies were included. The pooled proportion of detectability of DL algorithms in all included studies was 89% (95% CI, 84-92%). The pooled proportion of DL algorithms' detectability in studies reporting lesion-wise sensitivity was 89% (95% CI, 83-93%). There was no statistical difference between the results of studies with a single MRI sequence and studies with multiple MRI sequences. The quality assessment showed that reporting was poor in some studies.

Conclusions

Our study revealed that DL algorithms effectively detect BMs with a pooled sensitivity of 89%. DL studies should adhere to CLAIM and QUADAS-2 checklists. There is a need for large-scale prospective studies. The results are auspicious, and while these models cannot be fully implemented into clinical practice today, they may serve as a robust assistant for radiologists.

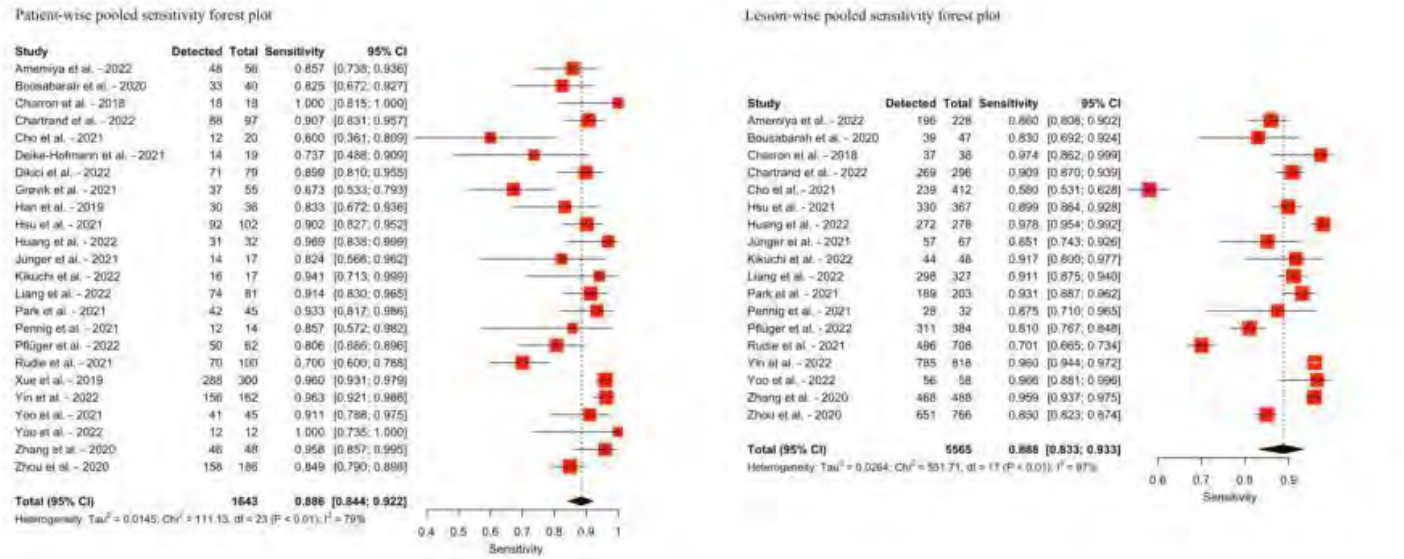

(Filename: TCT_397_ASNR-Figure.jpg)

816

Distinction of True-Progression from Pseudo-progression in Glioblastomas using Radiomics Model based on Diffusion and Perfusion MRI and Molecular Signatures

S Chawla[1], V Yadav[2], S MOHAN[3], L de Godoy[4], M Nasrallah[5], S Bagley[6], S Brem[6], L Loevner[5], A Singh[7]

[1]Perelman School of Medicine at the University of Pennsylvania, Philadelphia, PA, [2]Indian Institute of Technology, Delhi, PA, [3]UNIVERSITY OF PENNSYLVANIA, PHILADELPHIA, PA, [4]Perelman School of Medicine at the University of Pennsylvania, Philadelphia, USA, Philadelphia, PA, [5]Hospital of the University of Pennsylvania, Philadelphia, PA, [6]University of Pennsylvania, Philadelphia, PA, [7]Indian Institute of Technology, Delhi, DELHI

Purpose

To investigate the potential of radiomics features derived from diffusion tensor imaging (DTI) and dynamic susceptibility contrast (DSC)-perfusion imaging (PWI) and molecular signatures in distinguishing true-progression (TP) from pseudoprogression (PsP) in glioblastomas (GBMs).

Materials and Methods

Patients (n=75) with GBM exhibiting enhancing lesions within 6 months after completion of standard therapy underwent anatomical imaging, DTI and DSC-PWI on a 3T magnet. O6-methylguanine-DNA-methyltransferase (MGMT) promoter methylation status was available from these patients. Subsequently, these patients were classified as TP (n=55) or PsP (n=20) based on histological features obtained from tumor specimens following repeat surgery or mRANO criteria (1). DTI derived maps, CBV maps, and T2-FLAIR images were resliced and co-registered to post-contrast T1-weighted images. A semiautomatic approach was used to segment the contrast-enhancing regions of each lesion (2,3). Median values of DTI metrics (MD, FA, CL, CP, and CS), relative CBV and maximum rCBV (top 90th percentile) values were computed. To address the issue of imbalance sample size between two groups (TP and PsP), synthetic minority oversampling technique (SMOTE) was applied to augment the PsP cases from 20 to 35 resulting in a total sample size of 110 (4). A random forest (RF) algorithm was applied to select the optimized features using a sequential forward feature selection (SFFS) approach. The data were randomly split into training (n=90) and testing (n=20) sets. The 6-fold cross-validation approach was applied to training dataset for confirming our findings. To develop a robust prediction model in distinguishing TP from PsP, several machine learning classifiers were employed (5).

Results

The presentative images from a TP patient are shown in Figure 1. The frequency of GBMs harboring MGMT promotor methylation status was significantly higher in PsP than in TP ($p<0.01$, Figure 1). The medium neuronal network classifier provided the best discriminatory power in distinguishing TP from PsP with a training accuracy of 100%, cross-validation accuracy of 88.9% and testing accuracy of 85%. To avoid the issue of data overfitting, quadratic SVM classifier was selected to build the predictive model with a training accuracy of 90.9%, cross-validation accuracy of 85.5% and testing accuracy of 85%.

Conclusions

Machine learning using multi-parametric MRI and molecular signatures may be a promising approach to differentiate TP from PsP in GBMs.

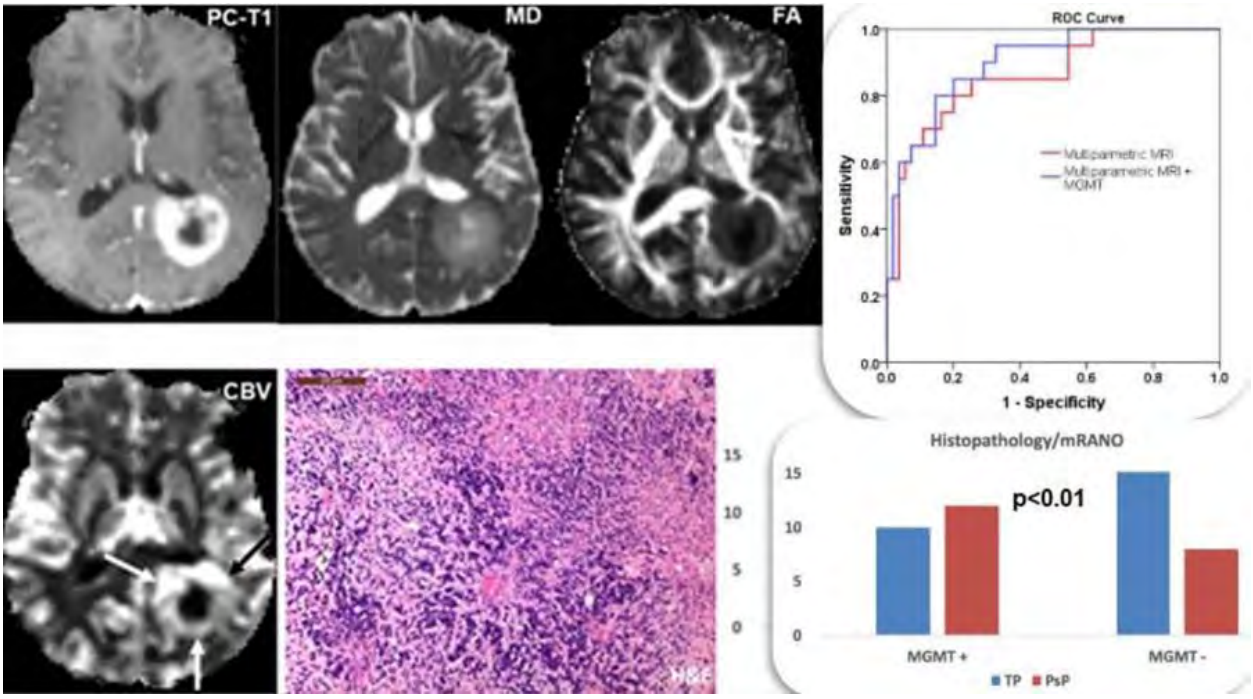

(Filename: TCT_816_Figure.jpg)

1129

IDH and 1p19q Diagnosis in Diffuse Glioma from Preoperative MRI Using Artificial Intelligence

H McHugh[1]

[1]*Auckland City Hospital, Auckland, New Zealand*

Purpose

Isocitrate dehydrogenase (IDH) mutation and 1p19q codeletion are key molecular markers in glioma and patients with IDH mutation and 1p19q codeletion have substantially better survival. In the 2021 WHO classification of CNS tumours IDH and 1p19q status determine the histological diagnoses of glioblastoma (IDH wild-type), astrocytoma (IDH mutant - 1p19q intact) and oligodendroglioma (IDH mutated - 1p19q co-deleted). (1) In the absence of a surgical brain biopsy, this information is unknown until after resection and there is evidence suggesting that molecular status affects the optimal surgical approach, (2) making non-invasive preoperative diagnosis desirable. Research supports the potential of MRI-based IDH and 1p19q diagnosis, however there is a paucity of external validation outside the widely used The Cancer Imaging Archive (TCIA) dataset. We present a combined IDH and 1p19q classification algorithm and assess performance on a local retrospective cohort (NZ) and the Erasmus Glioma Database (EGD).

Materials and Methods

2D convolutional neural networks were trained to provide IDH and 1p19q classification. Inputs are T1 post-contrast, T2, and FLAIR sequences. Training data consists of preoperative imaging from the TCIA dataset (n=184) and a locally obtained NZ dataset (n=349). Evaluation data consists of the most recent cases from the NZ dataset (n=205) and the EGD (n=420).

Results

IDH classification accuracy was 93.3% and 91.5% on the NZ and EDG, with AUC values of 95.4% and 95.8%, respectively. 1p19q accuracy was 94.5% and 87.5% with AUC values of 92.5% and 85.4% on the NZ and EGD datasets. Combined IDH and 1p19q accuracy was 90.4% and 84.3% on the NZ and EGD, with AUC values of 92.4% and 91.2%.

Conclusions

High IDH and 1p19q classification performance was achieved on the NZ retrospective cohort. Generalisation to the EGD was robust, demonstrating the potential for clinical translation. This method is able to non-invasively predict tumour histology according to the WHO 2021 classification with high accuracy using readily available imaging. This may better inform patients and clinicians prior to surgery and demonstrates the high potential impact in glioma diagnostics.

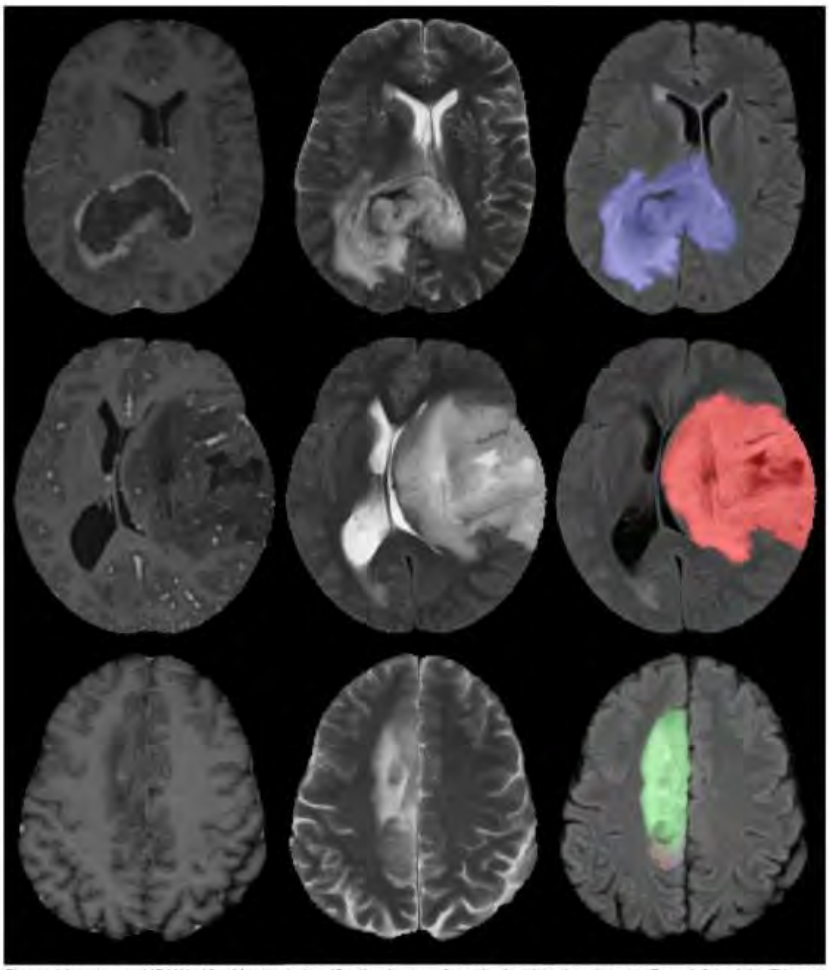

Figure 1 Images and IDH/1p19q AI output classification images from the local testing dataset. From left to right: T1 post-contrast, T2 and FLAIR with classification overlay. From top to bottom: IDH wild-type GBM (blue), IDH mutant - 1p19q intact astrocytoma (red), IDH mutant - 1-19q codeleted oligodendroglioma (green).

(Filename: TCT_1129_IDH-Figure.jpg)

490

MRI Based Differentiation Between Glioblastoma and Metastatic Disease Using 3D-Convolutional Neural Networks: Model Development and Validation

G Bathla[1], D Durjoy[2], Y Liu[2], S MOHAN[3], M Sonka[4], N Soni[5], A Nagelschneider[6], S Priya[7]

[1]Mayo Clinic, Rochester, Rochester, MN, [2]University of Iowa, Iowa City, IA, [3]UNIVERSITY OF PENNSYLVANIA, PHILADELPHIA, PA, [4]The University of Iowa, Iowa City, IA, [5]University of Rochester URMC, Rochester, NY, [6]Mayo Clinic-Rochester, Rochester, MN, [7]University of Iowa hospitals and Clinics, IOWA CITY, IA

Purpose

Imaging-based differentiation between glioblastoma (GBM) and brain metastases (BM) remains challenging despite the use of advanced imaging modalities. The aim of the current study was to evaluate the performance of 3D-convolutional neural networks (CNN) to address this binary classification task.

Materials and Methods

T1-CE, T2WI, and FLAIR 3D-segmented masks of 307 patients (157 GBM and 150 BM) were used for internal model development. The model was validated against an external set of 59 cases (27 GBM and 32 BM) from another institution. For all cases, images were co-registered, skull-stripped, denoised, normalized, down sampled and the lesion of interest segmented into whole tumor (WT) and peri-tumoral edema (PTE) masks using a semi-automated inhouse software. Four different mask-sequence combinations were evaluated using AUC, precision, recall and F1-scores. For each model, we performed a 10-fold cross-validation on the internal dataset, followed by validation on the external test set.

Results

3D-model using the T1-CE mask of the tumor showed the highest performance with AUC of 0.93 (95% CI 0.858-0.995) on an external test set. The precision, recall, and F1 scores were 0.90, 0.90, and 0.90 respectively. This was followed closely by the model using T1-CE WT mask and FLAIR mask of PTE which showed AUC of 0.91 (95% CI 0.834-0.986) on the external test set. The precision, recall, and F1 score are 0.89, 0.88, and 0.88 respectively. Both models using T2WI masks showed robust performance on the internal dataset (AUC: 0.93-0.94) but lower performance on the external test set (AUC: 0.82-0.85).

Conclusions

Even though the differentiation between GBM and BM remains challenging on conventional MRI imaging, various ML and DL-based approaches have shown promising results. Our study uses 3D-CNN, with improved classification performance than the previously reported literature using 2D-CNNs.

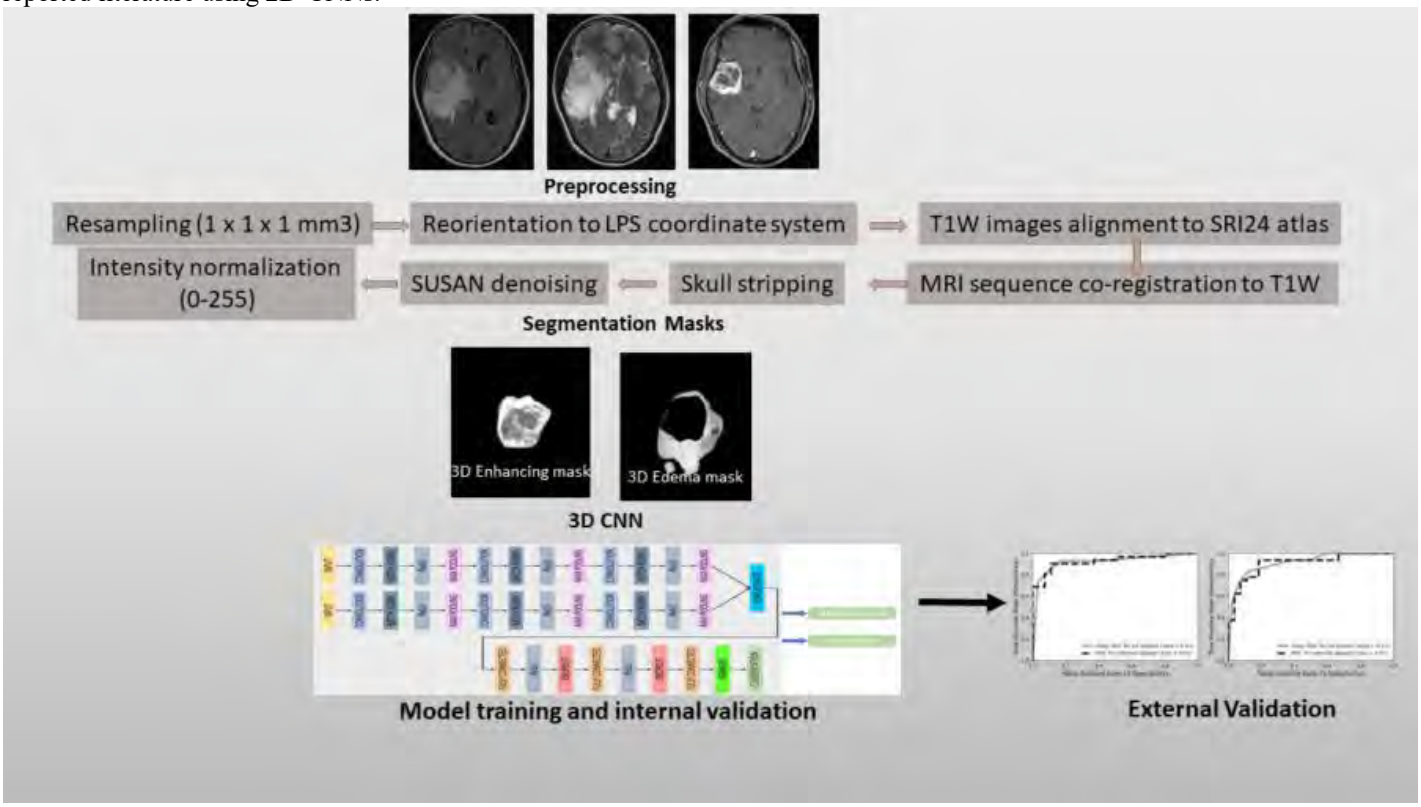

(Filename: TCT_490_Fig.jpg)

654

Predicting glioblastoma survival after radiotherapy in neuroimaging using deep learning

A Chelliah[1], H Shuaib[1], C Linares[2], A Bassiouny[1], T Young[2], C Dragos[3], A Swampillai[2], L Brazil[2], Y Lau[4], M Williams[5], Q Wang[5], S Currie[6], K Fatania[6], S Thust[7], S Wastling[7], M Modat[1], T Booth[1]

[1]School of Biomedical Engineering & Imaging Sciences, King's College London, London, UK, [2]Guy's and St Thomas' NHS Foundation Trust, London, UK, [3]Buckinghamshire Healthcare National Health Service Trust, Amersham, UK, [4]King's College Hospital, London, UK, [5]Imperial College London, London, UK, [6]Leeds Teaching Hospitals NHS Trust, Leeds, West Yorkshire, [7]University College London Hospitals NHS Foundation Trust, London, UK

Purpose

Glioblastoma is an aggressive brain tumour commonly investigated with MRI. Standard-of-care treatment involves resection followed by radiotherapy and chemotherapy(1). However the ability to use imaging as a prognostic biomarker predicting survival after treatment begins is unclear(2). This study aims to predict survival from MRIs obtained after radiotherapy using deep learning.

Materials and Methods

The sample is a retrospective dataset of 120 patients with glioblastoma at King's College Hospital. Models were trained/validated on 96 patients labelled as short-term survivors (≤32week survival post-radiotherapy;N=25(26%)), or long-term survivors (>32week;N=71(74%)). 24 patients (20%) were reserved as a test set. Dense convolutional neural networks were developed with three branches, each with separate loss functions. The image-only branch predicts survival from the first MR study after radiotherapy. The non-imaging branch inputs known data at time of imaging. A third branch concatenates outputs from the other branches to predict survival. Models were trained on a combination of T1 post-contrast(T1c), T2, FLAIR, and T1 MRIs, with stratified five-fold validation. Parameter tuning includes the number of dense blocks and linear layer sizes. 29 patients (30%) were missing data. A sparse matrix was used when T1/FLAIR MRIs were missing. Non-imaging variables were imputed with mean/mode or kNN imputation. Logistic regression, support vector classifier(SVC), and decision tree models were fit on non-imaging variables with bootstrap validation as a benchmark.

Results

The current best-performing imaging model has two dense blocks, with T1c and T2 inputs (lowest training loss=0.01,95%CI=0.001-0.02; weighted-ROC=0.84,95%CI=0.74-0.94; validation F1=0.68,95%CI=0.43-0.93). Among non-imaging machine learning models, the linear SVC benchmark model fit with mean/mode imputation of missing data performed best (weighted-ROC=0.62,95%CI=0.58-0.65; validation F1=0.41,95%CI=0.34-0.47). Combined model development is ongoing.

Conclusions

This is the first known model that uses imaging to predict patients who clearly do not respond to radiotherapy, and those who survive the adjuvant chemotherapy window. Initial results suggest that image-based models may outperform those without MRI inputs. Such survival models could prompt closer MRI surveillance and trial targeting of suspected short-term survivors, compared with patients expected to show longer survival (and so treatment response). Final holdout test results will be presented.

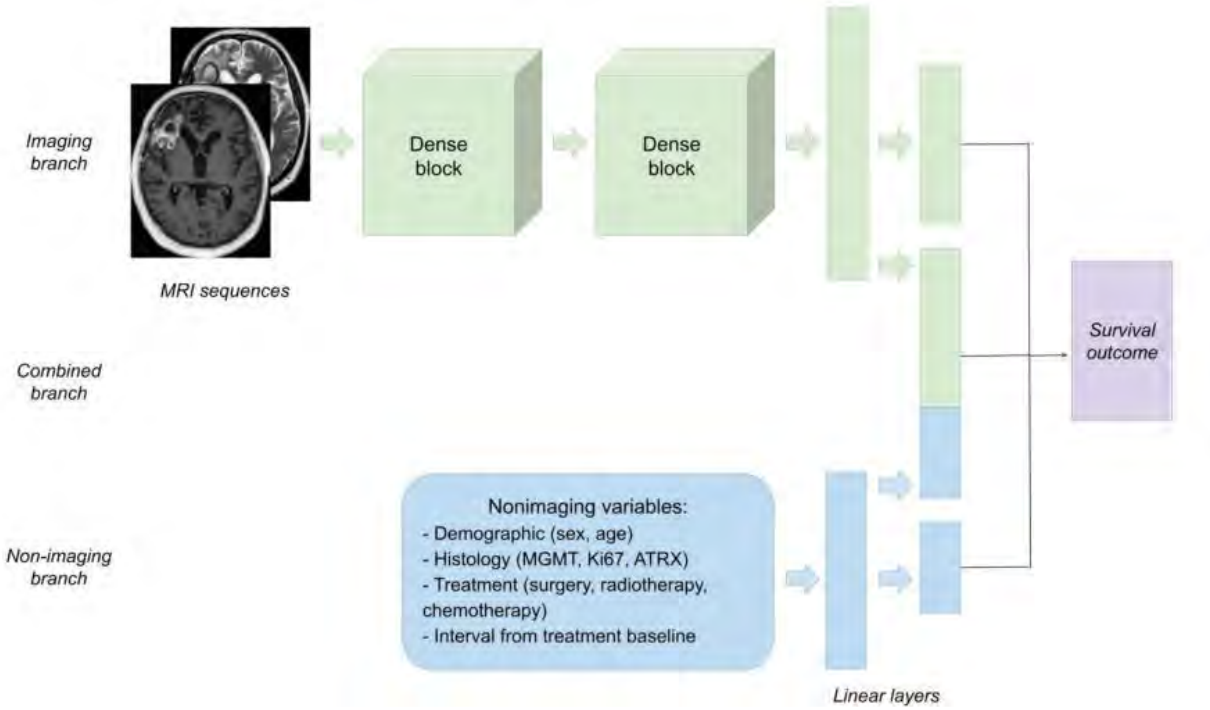

(Filename: TCT_654_model_diagram_achelliah.jpg)

915

Prediction of Treatment Response after Stereotactic Radiosurgery of Brain Metastasis using Deep Learning and Radiomics on Longitudinal MRI data

S CHO[1], W Cho[2], L Sunwoo[1], J Choo[2], S Baik[1], Y BAE[1], B Choi[1]

[1]Seoul National University Bundang Hospital, Seongnam, Gyeonggi, [2]Kim Jaechul Graduate School of Artificial Intelligence, KAIST, Daejeon, choong-cheong

Purpose

Timely assessment of treatment response after stereotactic radiosurgery (SRS) is crucial for the management of patients with brain metastasis (BM). However, prediction of treatment response after SRS is a challenging diagnostic task on conventional magnetic resonance imaging (MRI). We therefore developed and validated a deep neural network and radiomics models using serial contrast-enhanced MRIs to classify tumor progression from non-progression in BM patients after SRS.

Materials and Methods

The model was developed from the serial four-time (pre-SRS, and first to third post-SRS follow-up) MRIs of 194 BM patients, which included 369 target lesions according to modified Response Assessment in Neuro-Oncology Brain Metastases (modified RANO-BM) criteria. Ground-truth data was provided using the up-to-date clinical information upon consensus of two expert neuroradiologists. A total of 776 MRI data were divided into training and test datasets according to random split in a ratio of 8:2. The 3-dimensional (3D) patch of each BM nodule was cropped and used for training and testing. In addition, the 2D patches were derived from three orthogonal slices of each 3D patch. We generated three models for comparison, based on convolutional neural network (CNN), radiomics, and maximum axial diameter (size), respectively. In addition to simple CNN, we developed another CNN model based on gated recurrent unit (Conv-GRU) to capture characteristics of sequential data. The radiomic features were derived from XGBoost models. The area under the receiver-operating characteristic curves (AUCs) were compared among the models. Statistical analyses were performed using Youden's J statistics after Bonferroni correction.

Results

During the model development, the performance of Conv-GRU model was superior to simple CNN model both for 2D and 3D, thus Conv-GRU, radiomics, and size models were used for final comparison. As a result, the AUC of 2D Conv-GRU (0.88) was significantly higher than that of size (0.82) or radiomics (0.75) model ($P < 0.05$, respectively). The AUC of 3D Conv-GRU (0.83) was significantly higher than that of the radiomics model ($P < 0.05$). The AUCs of 2D Conv-GRU and 3D Conv-GRU showed no significance difference. Finally, the AUC of radiomics model was inferior to the size model ($P < 0.05$).

Conclusions

Deep neural network based on GRU showed excellent results in the prediction of treatment response after SRS of BM nodules using Serial MRI data.

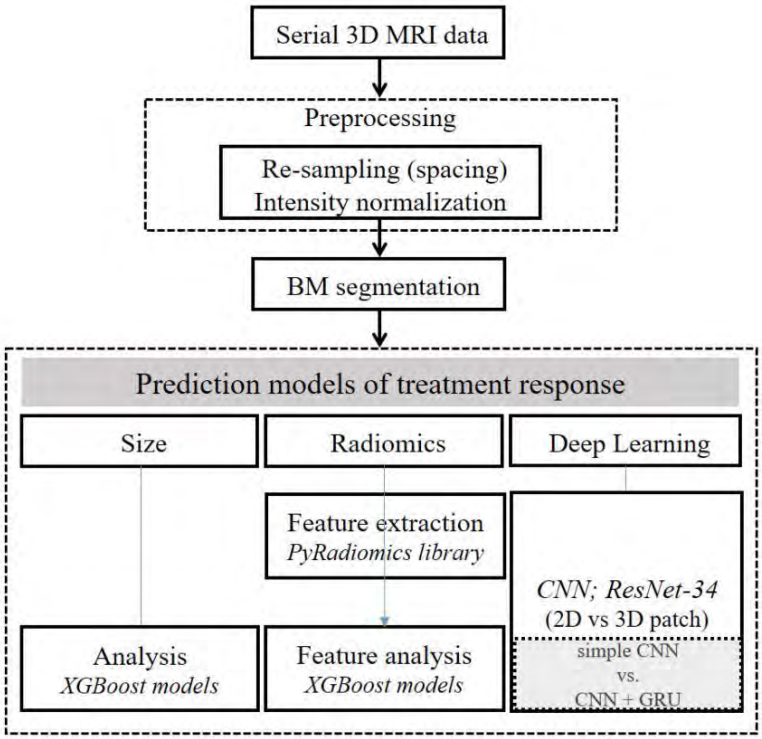

(Filename: TCT_915_Fig1.jpg)

Wednesday, May 3, 2023

9:45-11:00 AM

Scientific Abstract Session: Neuro IR

131

Connectomic Basis for Tremor Control in Stereotactic Radiosurgical Thalamotomy

D Lakhani[1], R Popple[2], E Greco[3], L Okromelidze[4], M Bredel[2], E Middlebrooks[4]

[1]West Virginia University, Morgantown, WV, [2]University of Alabama at Birmingham, Birmingham, AL, [3]Mayo Clinic in Florida, Jacksonville, FL, [4]Mayo Clinic, Jacksonville, FL

Purpose

Given the increased utilization of stereotactic radiosurgical (SRS) thalamotomy and other ablative therapies for tremor, new biomarkers are needed to improve outcomes. Using resting-state functional MRI (rs-fMRI) and MR tractography, we hypothesize that a "connectome fingerprint" can predict tremor outcomes and potentially serve as a targeting biomarker for SRS thalamotomy.

Materials and Methods

We evaluated twenty-seven patients who underwent unilateral SRS thalamotomy for essential tremor or tremor-predominant Parkinson. Percentage postoperative improvement in contralateral limb Fahn-Tolosa-Marin Clinical Tremor Rating Scale (TRS) was the primary endpoint. Connectome-style rs-fMRI and MR tractography were obtained prior to SRS. Using the final lesion volume as a seed, "connectivity fingerprints" representing ideal connectivity maps were generated as whole-brain R-maps using a voxel-wise nonparameteric Spearman correlation. A leave-one-out cross validation was performed with each subject using the generated R-maps.

Results

Mean improvement in contralateral tremor score was 55.1%±38.9% at a mean follow-up of 10.0±5.0 months. Structural connectivity correlated with contralateral TRS improvement (r=0.52; p=0.006) and explained 27.0% of the variance in outcome (Figure A and B). Functional connectivity correlated with contralateral TRS improvement (r=0.50; p=0.008) and explained 25.0% of the variance in outcome (Figure C and D). Nodes most correlated with tremor improvement correspond to areas of known network dysfunction in tremor, including the cerebello-thalamo-cortical pathway and the primary and extrastriate visual cortex.

Conclusions

SRS targets with a distinct connectivity profile predict improvement in tremor after treatment. Such connectomic fingerprints show promise for developing patient-specific biomarkers to guide therapy with SRS thalamotomy.

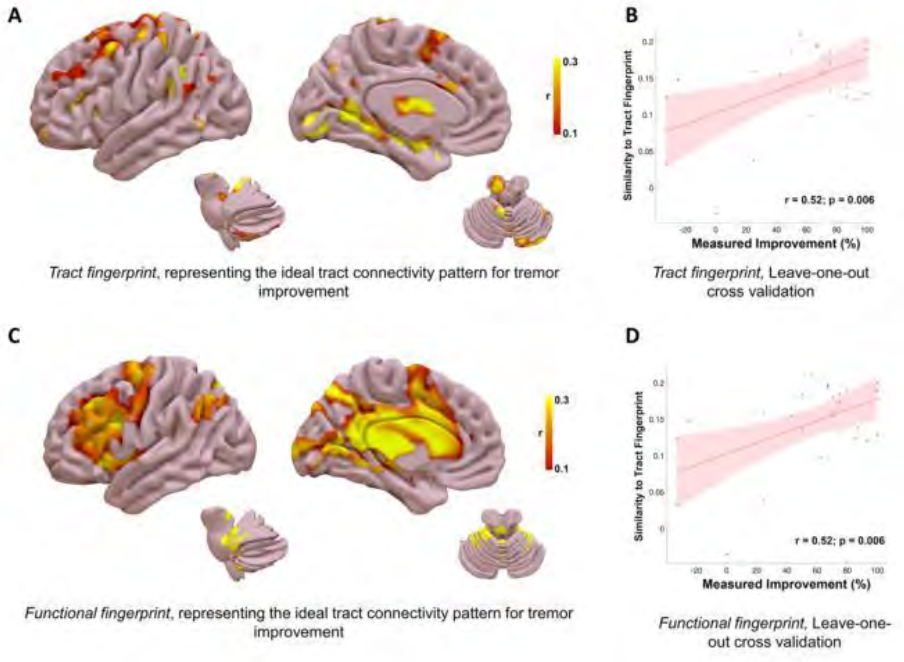

Tract fingerprint, representing the ideal tract connectivity pattern for tremor improvement

Tract fingerprint, Leave-one-out cross validation

Functional fingerprint, representing the ideal tract connectivity pattern for tremor improvement

Functional fingerprint, Leave-one-out cross validation

(Filename: TCT_131_Slide4.JPG)

947

Feasibility of Tele-Observerships in Neurointervention – Analysis of a Multi-Season European Program

M Bechstein[1], V Kalousek[2], J Fiehler[3], L Meyer[1], G BROOCKS[4], T Nawka[1], H Guerreiro[1], U HANNING[5]
[1]University Medical Center Hamburg-Eppendorf, Hamburg, Hamburg, [2]Clinical Hospital Center Sestre Milosrdnice, Zagreb, Croatia, [3]University Hospital Hamburg-Eppendorf, Hamburg, AS, [4]University Hamburg, Hamburg, NA, [5]UNIVERSITY MEDICAL CENTER HAMBURG-EPPENDORF, HAMBURG, Germany

Purpose
Virtual attendance of fellows during complex endovascular procedures via telestreaming has emerged as an additional method to acquire knowledge in interventional neuroradiology (ref. 1-2). The European EYMINT tele-observership (e-fellowship) was initially launched in 2020 and has since enrolled 56 neurointerventional fellows. These have live virtual access to procedures performed by individually assigned specialists (mentors) at geographically distant high volume neurointerventional centers for a period of 6-12 months while fulfilling their regular in-house fellowships. This study aims to quantitatively assess 1) Situational awareness during remote attendance of neurointerventional procedures and 2) Learning progress among participants.
Materials and Methods
Prospective evaluation of telestreamed cases from 2020 to 2022 via anonymous questionnaires for fellows and mentors.
Results
From 06/2020 to 05/2022 a total of 311 cases were transmitted to fellows using telestream technology. Although not being physically present, a high level of situational awareness for the procedure (levels 4+5 on a Lickert scale from 1-5) was reported by 81.9% of fellows. While 41.7% regarded the telestream technology as equal feasible to gain situational awareness compared to conventional in-room oberserverships, 8.3 % stated superior awareness with the streaming set-up. After graduation from the program, the general improvement of neurointerventional knowledge was evaluated to be substantial by 67 % of the participants. Remote attendance of complex aneurysm cases (intrasaccular devices, flow diversion) were reported to bring the most learning progress.
Conclusions
Tele-observerships may supplement neurointerventional hands-on training and facilitate learning progress, in particular of low-frequency high-complexity procedures.

1351

How Much of the Improvement in Functional Outcome after Successful Recanalization is Explained by Follow Up Infarct Volume Reduction?

H KNIEP[1], L Meyer[1], G BROOCKS[2], M Bechstein[1], F Flottmann[1], U HANNING[3], J Fiehler[4], S Gellissen[5]
[1]University Medical Center Hamburg-Eppendorf, Hamburg, Hamburg, [2]University Hamburg, Hamburg, NA, [3]UNIVERSITY MEDICAL CENTER HAMBURG-EPPENDORF, HAMBURG, Germany, [4]University Hospital Hamburg-Eppendorf, Hamburg, AS, [5]University Medical Hospital Hamburg-Eppendorf, Hamburg, Hamburg

Purpose
Mechanical thrombectomy (MT) has been shown to improve functional outcome in patients with anterior circulation stroke. However, previous works suggest only limited explanatory effect of infarct volume reduction on outcome in patients undergoing MT vs. standard medical care(1). The amount of improvement of functional outcome explained by follow-up infarct volume reduction after successful recanalization has not been investigated in detail. Results might allow quantification of pathophysiological effects and could improve the understanding of the value of follow-up infarct volume as imaging endpoint in clinical trials.
Materials and Methods
All patients from our institution enrolled in the German Stroke Registry from 05/2015 to 12/2019 with anterior circulation stroke, availability of the relevant clinical data and follow-up CT (2h-2 weeks) were analyzed. A mediation analysis was conducted to investigate the effect of successful recanalization (Tici≥2b) on good functional outcome (90d mRS≤2) with mediation through follow-up infarct volume.
Results
429 patients were included. Multivariate regression confirms significant association of successful recanalization with lower follow-up infarct volume and better functional outcome. Results of the mediation analysis suggest a 23 percentage points (pp) increase of probability of good function outcome (95%CI: 16pp-29pp) in patients with successful recanalization. 57% (95%CI: 38%-79%) of the treatment effect was explained by follow-up volume reduction (Figure 1).
Conclusions
57% of the improvement of functional outcome after successful recanalization is explained by follow-up infarct volume reduction. Results reflect established pathophysiological assumptions and confirm the value of infarct volume as imaging endpoint in clinical trials.

Figure 1: Mediation model layout

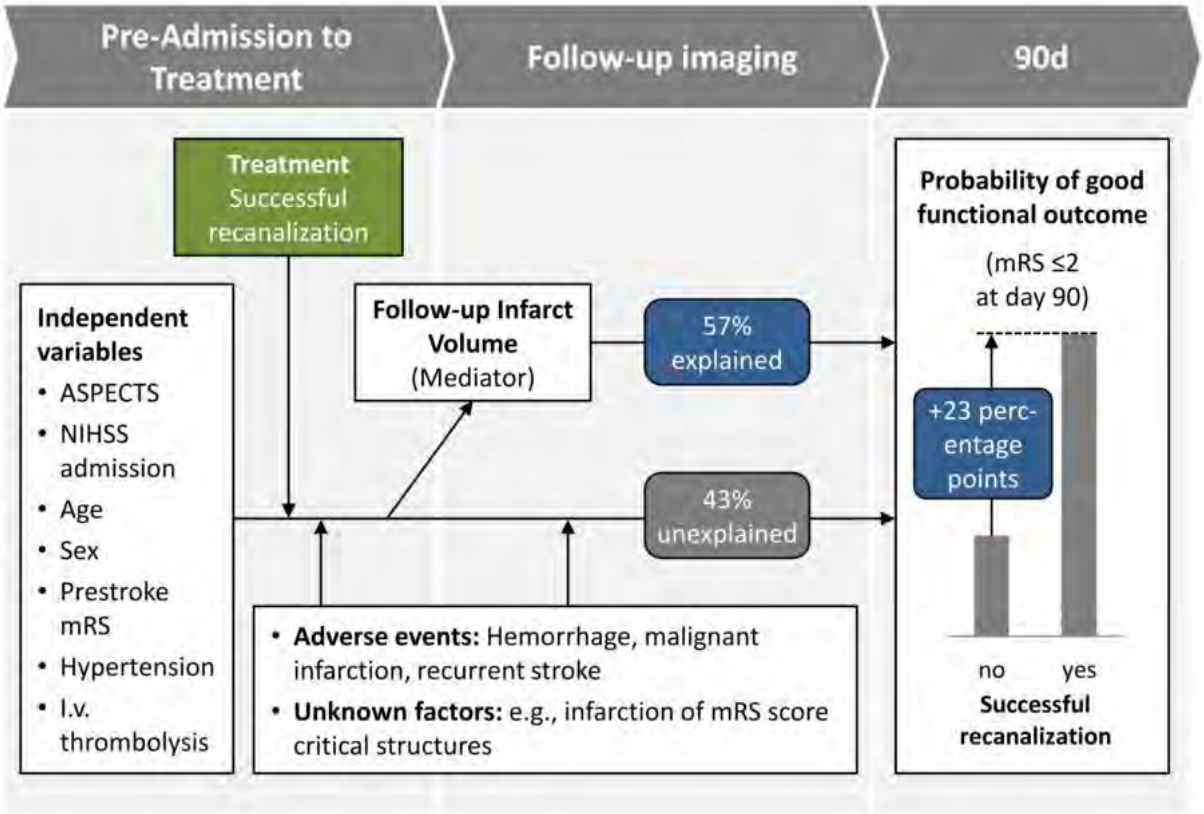

(Filename: TCT_1351_Figure_1.jpg)

979

Improving Tremor Response with Focused Ultrasound Thalamotomy

J Holcomb[1], F Feltrin[1], P O'Suilleabhain[1], J Maldjian[1], W Dauer[1], B Shah[1]
[1]*University of Texas Southwestern Medical Center, Dallas, TX*

Purpose
Thalamic ablation with MR-guided high intensity focused ultrasound (MRgHIFU) is an incisionless therapy for essential tremor (ET). To avoid injury to structures inferior to the anterior commissure-posterior commissure plane (ACPC), most centers target 2 mm superior to the standard indirect coordinates. At our center, we perform MRgHIFU targeting with four tract tractography to improve accuracy. In some patients, the dentatorubrothalamic tract (DRTT) merges with the corticospinal tract more proximally. In these patients, we typically target 1.2-1.5 mm superior to the ACPC to avoid eloquent structures. Post-procedure imaging in these patients demonstrates the focused ultrasound lesion to extend into the posterior subthalamic area (PSA), an important target for tremor control. The purpose of this study is to determine if patients with focused ultrasound lesions that extend into the PSA have greater tremor improvement.
Materials and Methods
20 ET patients underwent MRgHIFU and were classified into two groups. Group 1 (n=10) were those with MRgHIFU lesions extending into the PSA. Group 2 (n=10) were those without MRgHIFU lesions extending into the PSA. A movement disorder neurologist used The Essential Tremor Rating Assessment Scale to determine postural and kinetic tremor scores at baseline and at a 3-month follow-up for each patient. Additionally, baseline and follow-up Archimedes spirals were scored by movement disorder neurologists and a trained physician assistant. Two-tailed Wilcoxon rank sum tests were used to compare the improvement in ET scores, total number of sonications, thermal dose, and skull density ratio between groups.
Results
Group 1 had significantly greater tremor score improvement compared to Group 2 for postural, kinetic, and Archimedes spiral assessments (p=1.70x10-4, 2.22x10-4, and 1.66x10-4, respectively). Group 1 also required a significantly lower thermal dose to achieve tremor response and had significantly fewer total sonications during the procedure (p=1.24x10-4 and 6.30x10-4, respectively). No significant differences in skull density ratio were observed between groups (p=0.97).
Conclusions
MRgHIFU lesions that involve both the thalamus and PSA provide greater tremor control than lesions that do not. Targeting the confluence of decussating and non-decussating DRTTs at 1.5 mm rather than 2.0 mm superior to the ACPC improves response to MRgHIFU thalamotomy.

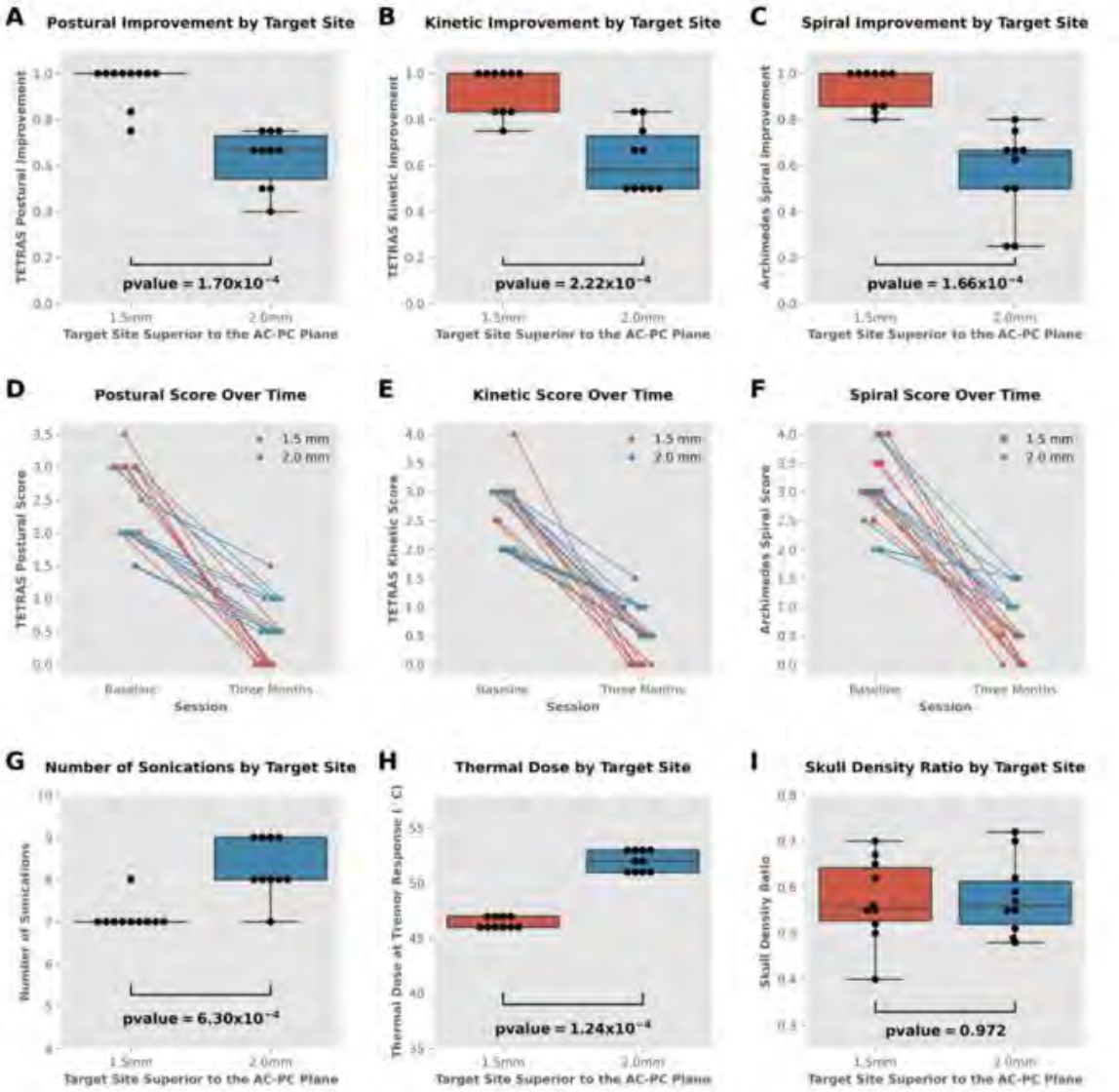

Fig. 2 (A–C) Tremor improvement comparisons for all tremor assessments. Orange boxplots on the left and blue boxplots on the right of each graph, respectively display the distribution of essential tremor improvement for the patients with focused ultrasound lesion targets placed 1.5 mm and 2.0 mm superior to the anterior commissure posterior commissure plane. Black dots indicate essential tremor improvement for each patient. **Fig. 2A** Distributions of essential tremor improvement as measured by the postural TETRAS assessment. **Fig. 2B** Distributions of essential tremor improvement as measured by the kinetic TETRAS assessment. **Fig. 2C** Distributions of essential tremor improvement as measured by the Archimedes spiral assessments. **Fig. 2 (D–F)** Essential tremor scores for each patient at baseline and three-month follow-up. Orange dots indicate scores for patients with focused ultrasound lesion targets placed 1.5 mm superior to the AC-PC plane. Blue dots indicate scores for patients with focused ultrasound lesion targets placed 2.0 mm superior to the AC-PC plane. Diagonal lines connect the baseline and follow-up scores for each patient. **Fig. 2D** Postural TETRAS assessment scores at baseline and three-month follow-up for groups with focused ultrasound lesions placed at 1.5- and 2.0-mm. **Fig. 2E** Kinetic TETRAS assessment scores at baseline and three-month follow-up for groups with focused ultrasound lesions placed at 1.5 and 2.0 mm. **Fig. 2F** Archimedes spiral assessment scores at baseline and three-month follow-up for groups with focused ultrasound lesions placed at 1.5 and 2.0 mm. **Fig. 2 (G-I)** Ultrasound parameter comparisons. **Fig. 2G** Number of sonications by target site. **Fig. 2H** Thermal dose by target site. **Fig. 2I** Skull density ratio by target site. The *p* values for each Wilcoxon rank-sum test (A-C) and (G-I) are displayed below each boxplot distribution.

(Filename: TCT_979_ASNR_2023.jpg)

1426

National trends in the utilization of cerebral venous sinus stenting for the treatment of idiopathic intracranial hypertension

D Gandhi[1], M Khunte[2], A Malhotra[3]

[1]University of Maryland School of Medicine, Baltimore, MD, [2]Yale University, New Haven, CT, [3]Yale University School of Medicine, New Canaan, CT

Purpose

To study the recent temporal trends of cerebral venous sinus stenting (VSS) and other surgical treatments for idiopathic intracranial hypertension (IIH) in the United States.

Materials and Methods

The 2016 to 2020 National Inpatient Sample databases were queried to identify hospital admissions of adult patients diagnosed with

IIH. Patient demographics, hospital characteristics, surgical procedures, medical comorbidities, and hospital lengths of stay were recorded and analyzed. Temporal trends of surgical procedure numbers for VSS, cerebrospinal fluid (CSF) shunts, and optic nerve sheath fenestration (ONSF) were assessed and compared.
Results
46,065 patients hospitalized for IIH were identified, of whom 7,535 patients (16.4%) received either VSS, CSF shunting, or ONSF procedures. The number of VSS procedures increased 80% over the 5-year study period, roughly accounting for 1 in 5 (270 of 1405) surgical IIH treatments in 2020. There were concurrent decreases in the number of CSF shunts and ONSF procedures (-19% and -54%, respectively). These temporal trends were seen across all hospitals, and they were particularly pronounced in smaller academic medical centers and community hospitals.
Conclusions
Practice patterns for surgical IIH treatment in the United States are rapidly evolving, and VSS is becoming an increasingly common treatment for IIH. These findings highlight the urgency of randomized controlled trials to investigate the comparative effectiveness and safety of VSS, shunts, ONSF, and standard medical treatments.

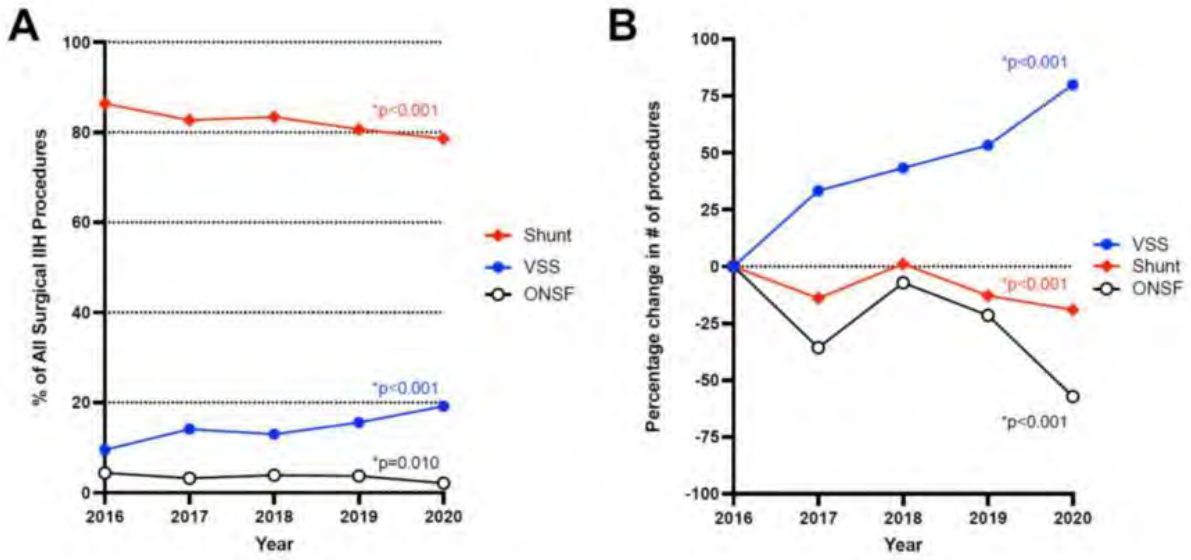

Figure 1. Temporal trends of surgical IIH treatments from 2016 to 2020. A) Percentage of shunt, VSS, and ONSF among all surgical IIH procedures over time; p-values derived from chi-squared analysis. B) Percentage change of number of procedures from 2016 to 2020; p-values derived from comparisons number of each procedure as a proportion of total procedures between 2016 and 2020 using Fisher's exact test.

(Filename: TCT_1426_IIH.jpg)

1286

Study of Vascular Dissection in the Treatment of Intracranial Atherosclerotic Stenosis with Balloon Angioplasty：Proposal of a New Angiographic Classification

Y Tang[1], Y He[1], W Liu[1], Q Ding[1], T Li[1]
[1]Zhengzhou University People's Hospital, Zhengzhou, Henan

Purpose
To investigate the characteristics of vascular dissection in the treatment of intracranial atherosclerotic stenosis with balloon angioplasty, propose a new classification of dissection in Angiographic, and explore the treatment methods for different dissection classifications.
Materials and Methods
Patients with symptomatic intracranial atherosclerotic stenosis who received balloon dilatation alone in People's Hospital of Zhengzhou University from January 2019 to August 2021 were retrospectively enrolled. They were divided into dissection group and non-dissection group, and the differences and clinical outcomes between the two groups were analyzed.A new classification method is proposed. Type I: The maximum residual stenosis ＜50%, and the blood perfusion rate of the diseased vessel is the same as that of the normal blood vessel on the same or opposite side. Type IIa: The maximum residual stenosis ＜50%, and the blood flow rate is less than 0.5s. Type IIb: The maximum residual stenosis of the lesion is >50%. Blood flow rate slowed down by 0.5-1s. Type III: The maximum residual stenosis >50%, and the blood flow rate was slower than 1s.
Results
Among 100 patients with symptomatic ICAS who underwent balloon angioplasty, 30 were in the dissection group and 70 were in the non-dissection group. There were more males and Mori C typing in the dissection group. In dissection group,there were 5 cases of

type I, 7 cases of type IIa , 15 cases of type IIb, and 3 cases of type III. 5 patients were not treated with type I. Tirofiban was used in type IIa, 2 cases turned into typeI and the other 5 cases developed into type IIb. Type IIb and type III were treated with stents. One patients with type IIb had ischemic stroke in perioperative period. Recurrent stroke was observed in 3 patients with type IIb during follow-up. Further analysis showed that the incidence of clinical adverse outcomes of type IIb and above were higher than those of type I~IIa, and the incidence of total adverse events were significantly higher than those of type I~IIa, with statistical significance (P=0.002).

Conclusions

Vascular dissection is the most common complication in the treatment of intracranial atherosclerotic stenosis with balloon angioplasty. The incidence of total adverse clinical outcomes in type IIb and above are higher than those in type I~IIa, which may require active remedial treatment. The new classification of vascular dissection provides a new idea for clinical decision-making.

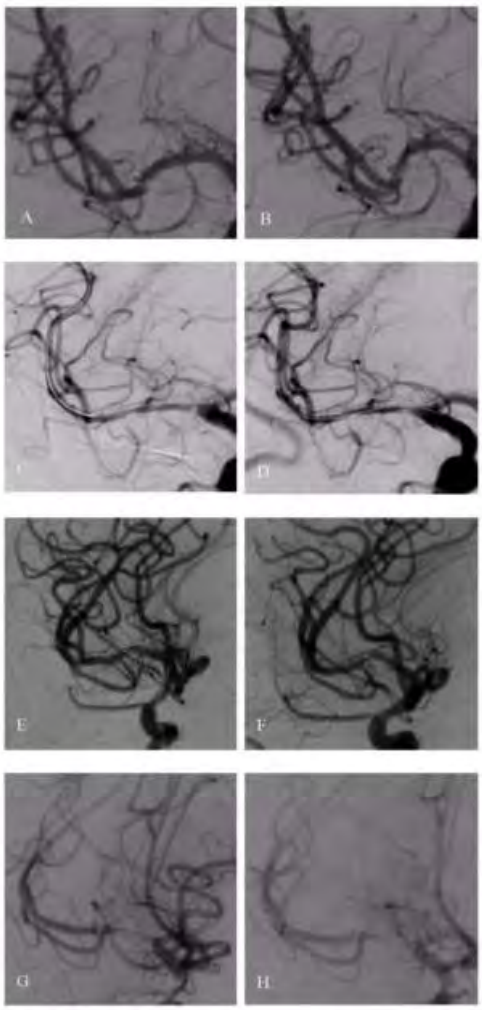

Typical vascular dissection: A~B: type I; C~D: type IIa; E~F: IIb; G~H: type III

(Filename: TCT_1286_Typicalvasculardissection.jpg)

1153

Transvenous Embolization of Dural Arteriovenous Fistulas Using the Dual Microcatheter Technique: Experience in 33 patients

M Marangoni[1], M Heran[2], B Rohr[3], A Rohr[2]

[1]UBC - Vancouver General Hospital, Vancouver, British Columbia, [2]Vancouver General Hospital, Vancouver, British Columbia, [3]University of British Columbia, West Vancouver, British Columbia

Purpose

Dural arteriovenous fistulas (dAVF) are complex vascular malformations that can be treated by surgical intervention, but endovascular treatment (transvenous +/- transarterial) is often preferred. Transvenous endovascular occlusion of the affected dural sinus is a favourable first-line treatment for many cases in which the sinus does no longer contribute to the normal brain venous drainage, avoiding some of the risks associated with transarterial treatment. However, if only incomplete occlusion of the sinus is achieved, dAVFs persist and venous access is blocked, limiting re-treatment options. The aim of this study is to describe the technique and

results of the transvenous approach using the relatively novel dual-microcatheter technique and its advantages over the conventional single microcatheter technique.
Materials and Methods
33 patients with dAVFs treated at our institution from 2013-2022 using a transvenous dual-catheter approach were reviewed. In each patient, two microcatheters were placed in the sinus draining the dAVF. Initial coil embolization was performed through one catheter, with the remaining microcatheter left in place for additional treatment with detachable coils (n=3) or ethylene vinyl-alcohol copolymer (EVOH) based embolic agent (n=30), with the goal of completing the obliteration of the fistula.
Results
16 Borden I and 17 Borden II dAVFs of the transverse and/or sigmoid sinuses (n=28), torcula (n=4) and superior sagittal sinus (n=1) were treated. In only 8/33 cases, complete dAVF occlusion was achieved using coils via the first microcatheter (24%). Of the 25 cases with residual dAVF after coil embolisation, n=20 dAVFs were successfully occluded using additional liquid embolic or coils via the second catheter, increasing the number of completely cured patients to 28/33 (85%). In the remaining 5 patients, complete transvenous cure of the dAVF was not achieved, but liquid embolization via the second catheter markedly improved the degree of occlusion when compared to coiling via the first catheter alone. No procedure-related complications were observed in any of the patients.
Conclusions
Transvenous dAVF embolization using the dual microcatheter technique has only been reported in a small number of patients. In our series of 33 patients (the largest series compared to the literature), this technique was safe and improved the cure-rate from 24% to 85% compared to using single-catheter technique.

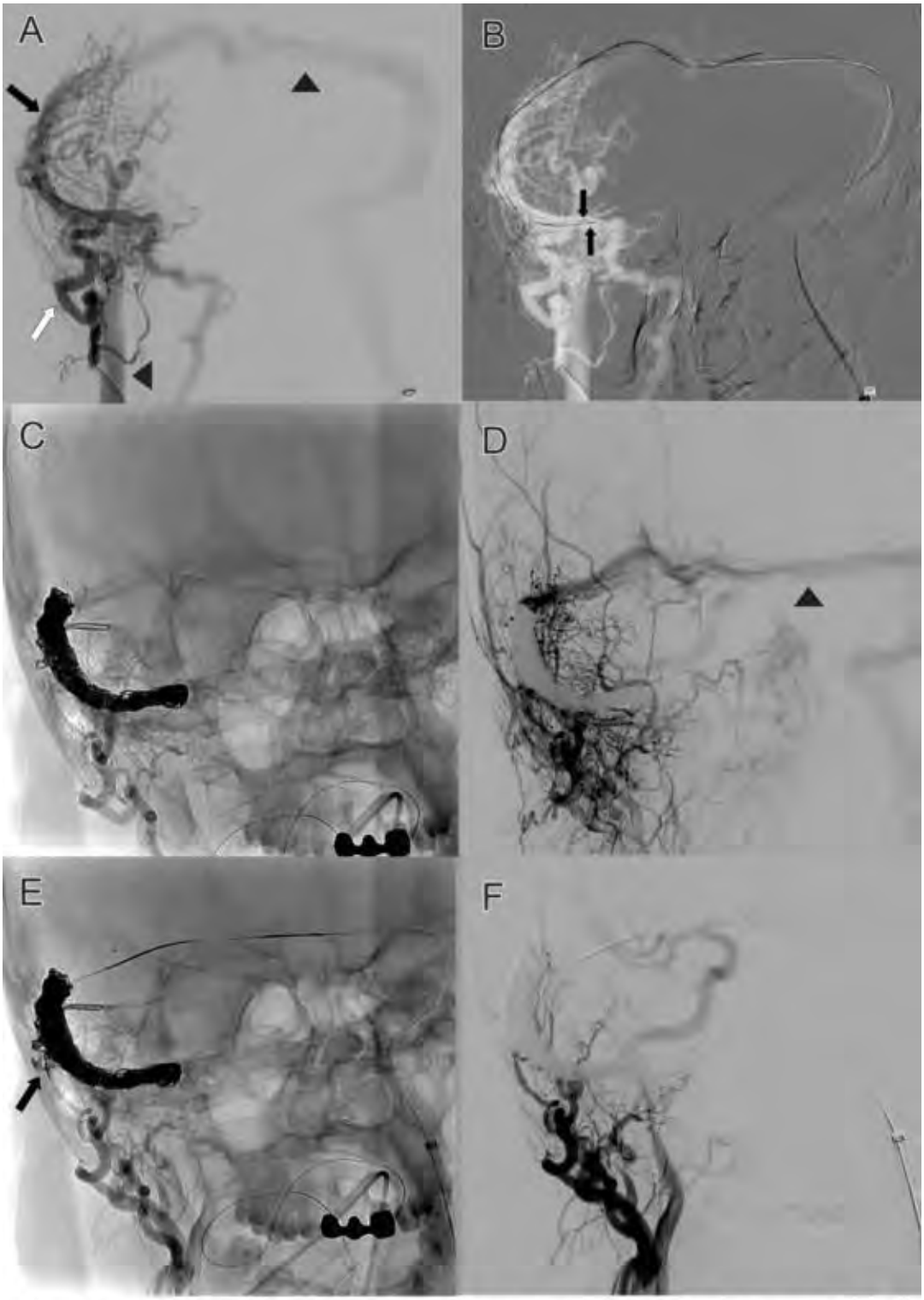

Figure 1. Borden type I dAVF of the right transverse and sigmoid sinus with antegrade and retrograde flow to the sinuses. **A:** AP angiogram of the right occipital artery (white arrow) demonstrates a right transverse and sigmoid sinus dAVF (black arrow) with antegrade and retrograde flow into the sinuses (arrowheads). **B:** AP roadmap image shows the placement of two microcatheters with the tips in the involved segment (arrows) via the left sinuses. **C:** AP unsubtracted flouroscopy image illustrating the coil mass delivered via the first microcatheter. **D:** Control AP angiogram of the right ECA shows significant residual dAVF with retrograde flow to the contralateral sinuses (arrowhead). **E:** AP unsubtracted flouroscopy image displaying the coil mass with the additional outline of the EVOH embolic agent (arrow) during the embolization via the second microcatheter. **F:** Final control AP angiogram of the right ECA demonstrates complete occlusion of the dAVF.

(Filename: TCT_1153_dAVFsDualMicrocatheterASNRabstract.jpg)

Wednesday, May 3, 2023

11:00 AM-12:00 PM

Evidence-Based Medicine Committee Programming: Head & Neck Cancer Surveillance imaging: What is the Evidence?

1401

Systematic Approach to Lacrimal Gland and Fossa Pathologies

B Hamilton[1]

[1]*Oregon Health & Science University, WEST LINN, OR*

Purpose

Few studies published to date have outlined a systematic approach for lesions involving the lacrimal gland and the adjacent soft tissues. We aim to use CT and MR characteristics of lacrimal gland and fossa pathologies to establish a pattern-based approach for building a relevant differential diagnosis.

Materials and Methods

This was a single institutional retrospective review of CT and MR performed for lacrimal gland and fossa pathologies over the past 22 years. Cases were identified using keyword searches of the radiology information system using institutionally developed software and teaching files. Imaging was reviewed by two neuroradiologists for lacrimal gland shape, internal morphology, unilateral vs. bilateral disease, extra-glandular and extra-orbital disease, bony changes and MRI signal characteristics including DWI. Discrepancies were resolved by consensus. Each case was reviewed for clinical, laboratory and/or histopathological diagnoses and classified into two clinically relevant categories: infection/inflammation (dacryoadenitis or DA) or neoplastic/tumor-like disorders (tumors).

Results

66 patients with 47 CT and 61 MRI were identified. 42/66 (63.6%) patients had dacryoadenitis (DA) and 24/66 (36.4%) were tumors. For DA, lacrimal gland shape was normal in 31/42 (73.8%) cases while abnormal shape was seen in 19/24 (79.2%) of tumors. Internal morphology was normal in 36/42 (85.7%) cases of DA and abnormal in 15/24 (60%) tumors. Unilateral disease was seen in 43/66 (65.2%) and bilateral disease in 23/66 (34.8%) patients. Unilateral disease was most common in infectious DA (3/3, 100%) and tumors (21/24, 87.5%) and seen in 20/39 (51.3%) of inflammatory DA. Extraglandular disease was identified in 29/42 (69.1%) of DA and 10/24 (41.7%) of tumors. Extraorbital disease was seen in 19/42 (45.2%) of DA and 8/24 (33.3%) of tumors. Bone changes were seen in 6/42 (14.2%) of DA compared to 11/24 tumors (45.8%). The most specific finding in neoplastic tumors was diffusion restriction, positive in 4/4 (100%) cases of lymphoma having DWI.

Conclusions

The presence of abnormal shape, morphology, and bone changes on imaging favor tumors over DA. These findings may help guide clinicians towards biopsy confirmation in suspected tumors while DA may be managed conservatively. Diffusion restriction favors lymphoma.

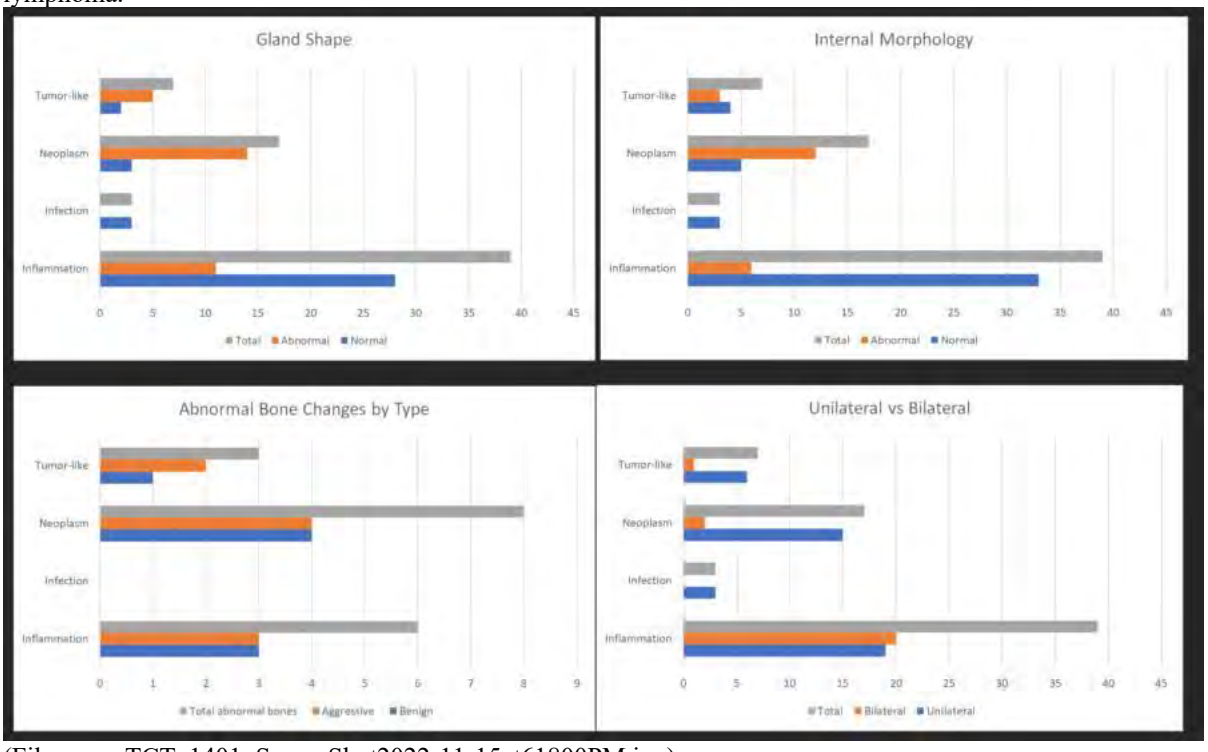

(Filename: TCT_1401_ScreenShot2022-11-15at61800PM.jpg)

Wednesday, May 3, 2023
11:00 AM-12:00 PM
Scientific Abstract Session: Tumors/Techniques

130

Clinical Application of Ultra-High-Resolution Time-of-Flight MR Angiography at 7T to Detect Small Vessel Pathology

D Lakhani[1], X Zhou[2], S Tao[2], S Sandhu[2], E Middlebrooks[2]
[1]West Virginia University, Morgantown, WV, [2]Mayo Clinic, Jacksonville, FL

Purpose

The Time-of-flight (TOF) imaging is the most commonly utilized non-contrast enhanced MR angiography (MRA) technique in clinical practice, with numerous clinical applications. The TOF sequence benefits from ultra-high field (UHF) imaging due higher signal-to-noise ratio (SNR) and inherently longer T1 relaxation constant of labeled blood, which improves the contrast between vessel and background parenchyma. Studies have shown the ability to visualize small caliber vessels on TOF MRA at 7T, yet employment of 7T MRA in clinical practice is currently limited. The main limiting factors include higher specific absorption rate (SAR), B1+ inhomogeneity, and increased image acquisition time. Compressed sensing (CS) techniques can accelerate the acquisition by under sampling of k-space, improving efficiency, and ultimately leading to widespread clinical utility of time intensive TOF sequence. In this technical note, we highlight the benefits of an UHF TOF MRA obtained at 7T utilizing CS acceleration in not only depicting small vessels, but also in diagnosing pathologies of small vessels.

Materials and Methods

A 7T Siemens Terra MR scanner was utilized. Technical parameters include TR=51 ms, TE=5.61 ms, slice thickness=0.3 mm, flip angle=20 degrees, Field-of-view = 220x174 mm, voxel size=0.3x0.3x0.3 mm, acceleration factor = 7.2, and acquisition time = 8.16 minutes. The combination of UHF scanner and CS allows a voxel volume over 90% smaller than commonly reported standard clinical TOF MRA at 3T and 88% smaller than TOF MRA with CS at 3T. This allows depiction of exquisite detail of the cerebral vasculature, including small caliber vessels with diameter less than 0.5 mm.

Results

TOF MRA at 7T provides the capability to assess small-caliber vessels, including those measuring less than 0.5 mm in diameter (Figure A-B). Pathologies including artery of Percheron stroke (Figure C) and lenticulostriate occlusion resulting in infarction (Figure D), can also be assessed. Assessment of these vessels is even difficult on digital subtraction angiography.

Conclusions

Clinical implications of MRA at 7T remain under investigation. Here, we demonstrate the feasibility of this technique for depiction of intracranial vasculature at 7T and highlight the exquisite detail gained with ultra-high-field-strength MRI, in addition to its ability to diagnosing pathologies of small vessel.

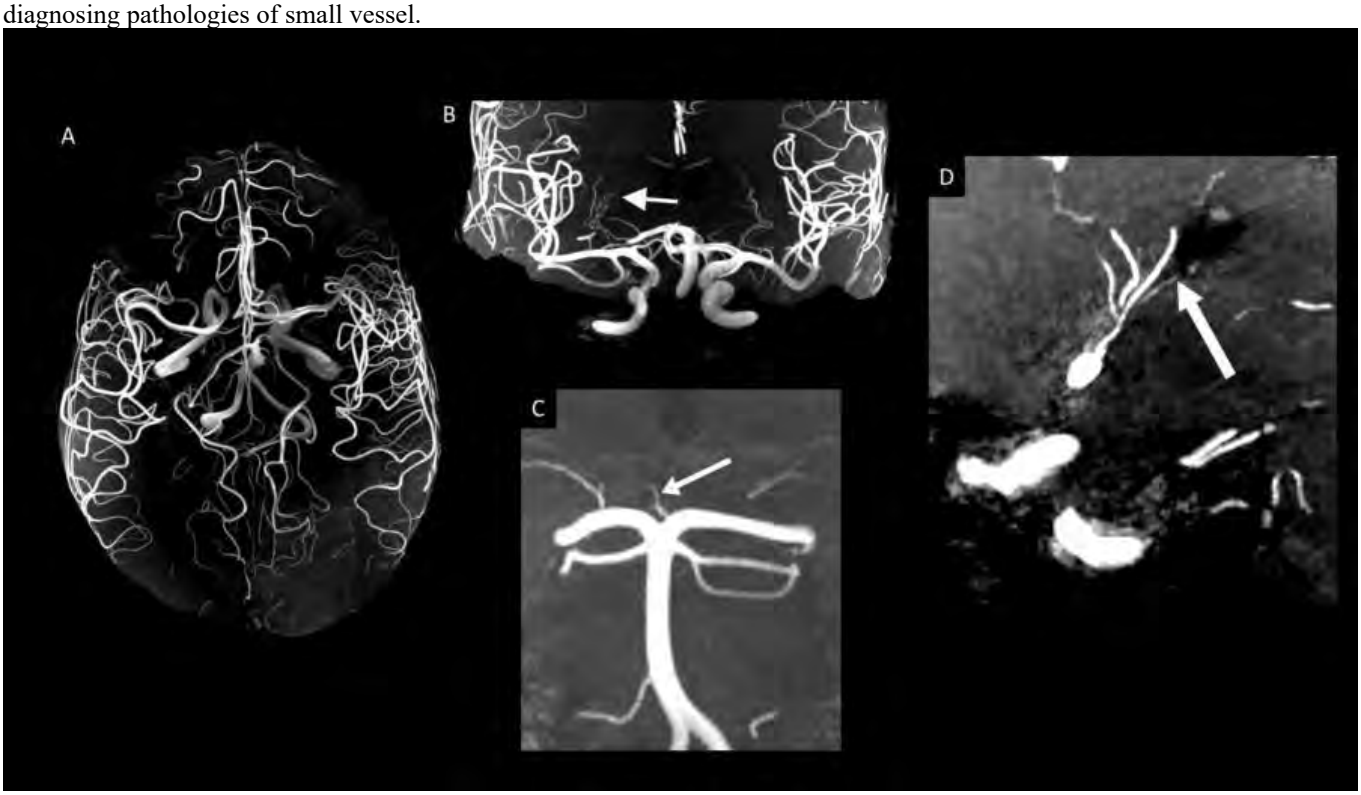

(Filename: TCT_130_Figure.jpg)

639

Dynamic Susceptibility Contrast (DSC) MRI and Arterial Spin Labeled (ASL) MRI Measured Perfusion in Glioblastoma: Are they Competitive or Complementary?

L Zhou[1], Y Wang[2], M Pinho[1], D Udayakumar[1], M Youssef[1], J Maldjian[1], A Madhuranthakam[1]
[1]UT Southwestern Medical Center, Dallas, TX, [2]Philips Healthcare, Shanghai, China

Purpose

The goal of this study is to evaluate whether arterial spin labeled (ASL) MRI is competitive or complementary to dynamic Susceptibility Contrast (DSC) in glioblastoma (GBM).

Materials and Methods

With IRB approval, 20 newly diagnosed GBM patients were recruited and imaged on a 3T MR scanner (Ingenia, Philips Healthcare) using 32-channel head coil for a total of 78 imaging sessions (Fig. 1A). Routine clinical imaging protocol including DSC were obtained using the recommended Brain Tumor Imaging Protocol (BTIP) (1) that also included preload contrast. ASL scans were acquired following the consensus paper (2) with two different readouts: TSE based Cartesian Acquisition with Spiral Profile Reordering (CASPR) (3) and GRASE. Processing pipeline is shown in Fig. 1B. Regions of interest (ROIs) were manually drawn by an experienced radiologist (M. P.).

Results

Mean cerebral blood flow (CBF) within enhancing tumor (ET) and tumor core (TC) showed good correlation between ASL-GRASE and ASL-CASPR, and hence ASL-CASPR was used for comparison with DSC-MRI (Figs. 2A & 2B). The scatter plot (Fig. 2C) and linear regression (Fig. 2D) between DSC and ASL-CASPR showed a relatively larger deviation from the diagonal, indicating a more complicated relationship. We observed both competitive and complementary relationships between ASL and DSC. In the competitive example (Figure 3A), both techniques were able to delineate the tumor well, although DSC was prone to vessel signal contamination and B0 inhomogeneity. In a complementary example (Fig. 3B), both methods delineated some lesions well (yellow arrow) but exhibited differences where ASL showed increased contrast in some lesions (red arrow), while exhibiting lower contrast in other lesions (blue arrow) compared to DSC. Figure 4 shows details about the competitive or complementary information for each specific MR scan. CBF maps were compared between DSC and ASL in our study due to the use of single post-label delay ASL. However, CBF maps were comparable to cerebral blood volume (CBV) maps and showed similar hyper-perfusion regions.

Conclusions

ASL was competitive to DSC in over 90% of the MR scans and in most cases, ASL was either equivalent or superior to DSC, making ASL a very attractive alternative to DSC in GBM patients. In some cases (less than 10%), ASL and DSC were complementary to each other and combining them together could generate a more comprehensive information of the whole tumor.

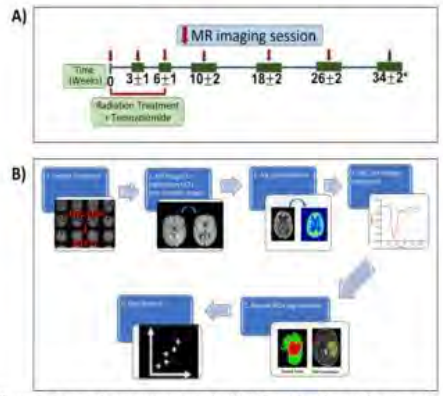

Figure 1: Magnetic resonance imaging (MRI) session time points in patients with glioblastoma (GBM) (A) and the processing pipeline (B). **A)** MRI including two variants of ASL and DSC were performed before, during, and after chemoradiation treatment at the indicated time points. **B)** The post-processing pipeline included the format transformation from DICOM to NifTI, co-registration to post-contrast T1-weighted images, quantification, manual segmentation, and data analysis.

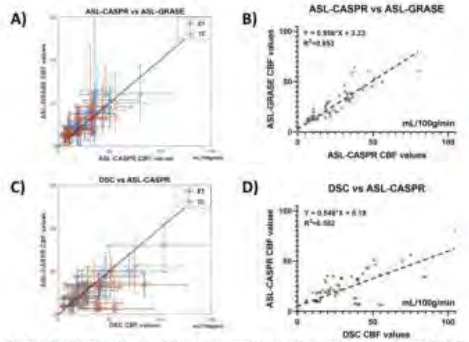

Figure 2: Scatter plots and linear regression analysis between ASL and DSC sequences. **A)** Scatter plot between ASL-CASPR and ASL-GRASE among enhancing tumor (ET) and tumor core (TC). The error bars are the standard deviation within the ROIs. **B)** Linear regression between ASL-CASPR and ASL-GRASE. **C)** Scatter plot between DSC and ASL-CASPR. **D)** Linear regression between DSC and ASL-CASPR.

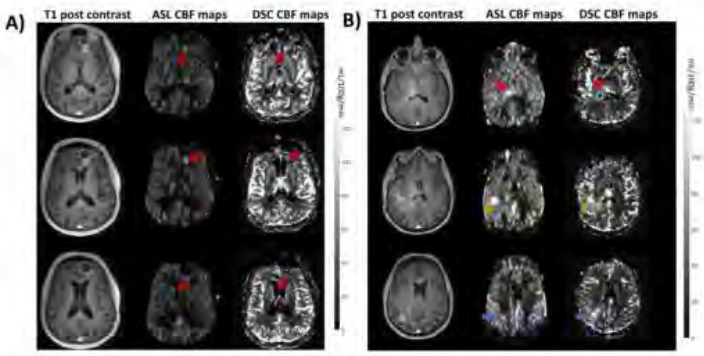

Figure 3: Both competitive and complementary relationships were observed. **A)** ASL is competitive to DSC. Either DSC or ASL can be used for tumor delineation in the first two slices (top & middle rows), but ASL outperforms DSC in third slice (bottom row). Although DSC shows lesion on the third slice, it is substantially obscured by the contamination of signal from large vessels and increased susceptibility due toB0 inhomogeneities. **B)** ASL and DSC are complementary to each other. In some lesions (yellow arrow), both ASL and DSC delineate tumor well. In other lesions, ASL has its advantages with increased conspicuity in some lesions (red arrow), while suffers from lower contrast in other lesions (blue arrow) compared to DSC.

Figure 4: Detailed table about the relationship between ASL and DSC in each specific MR scan. ASL is competitive to DSC in over 90% of the MR scans and in over 90% of the competitive cases, ASL is either equivalent or superior to DSC.

(Filename: TCT_639_FinalFIgure.jpg)

769

Early Volumetric Kinetics From Surgery to the Start of Radiotherapy and Association with Post-Treatment Response in High-grade Glioma

M Farhat[1], R Ivy[1], M Chen[1], M Gule-Monroe[2], W Talpur[1], L Nguyen[1], S Thrower[1], J Bronk[1], B Tran[1], H Langshaw[1], L Erickson[1], J Long[1], A Elliott[1], C Chung[1]

[1]The University of Texas MD Anderson Cancer Center, Houston, TX, [2]MD Anderson Cancer Center, Spring, TX

Purpose

To evaluate the prognostic value of volumetric progression before radiotherapy (RT) in predicting early post-treatment response of high-grade glioma (HGG).

Materials and Methods

We collected contrast-enhanced T1-weighted MRIs of patients enrolled on a prospective trial of adaptive 6-week RT and chemotherapy acquired post-operatively and then for RT treatment planning. Progressive disease (PD) was determined using bidimensional (2D) and volumetric assessment of the enhancing disease. 2D measurements were obtained by experienced radiologists following RANO criteria (25% increase in measurements). Volumetric assessment using semi-automated intensity-based segmentation of enhancing abnormality and volume extraction was performed on Raystation. Volumetric PD was defined by 40% increase in enhancing volume. The disease status at 6 months evaluated using clinical radiologic reports was used as an endpoint. Gender, age, molecular biomarkers, and the interval between the two imaging timepoints were collected for each patient. Fisher's Exact test and univariate analysis was used to analyze the results.

Results

Preliminary results for 43 patients show an incidence of PD was 53% and 47% using volumetric method and 2D, respectively. There was 44% (95% CI, 29%, 60%) disagreement between the volumetric and 2D PD. Univariate analysis of PD reported by volume and bidimensional had poor correlation with the 6 months PD (p=0.4) and (p=0.9), respectively. No significant correlation between age, gender, molecular characteristics, or time between the 2 MRIs and the volumetric progression between the post-operative and RT planning MRIs.

Conclusions

Preliminary results show a high incidence of progression in the enhancing abnormality between the postoperative MRI and RT

simulation MRI suggesting the value of a dedicated MR for RT treatment planning. However, the volumetric PD using 40% as a cutoff correlated poorly with the 2D PD and treatment response at 6 months, suggesting further evaluation of volumetric changes over a continuous scale.

Characteristic	N = 43[1]
Volume	
Progressed	23 (53%)
Stable	18 (42%)
Regressed	2 (4.7%)
Bidimensional	
Progressed	20 (47%)
Stable	23 (53%)
Regressed	0 (0%)
[1]n (%)	

Table 1: Incidence of progression between postop to RT planning MRI using volumetric versus bidimensional method.

		Bidimensional		
		Progressed	Stable	Regressed
Volume	Progressed	13	10	0
	Stable	7	11	0
	Regressed	0	2	0

Table 2: Correlation between postop to RT planning progression reported using volumetric and bidimensional methods.

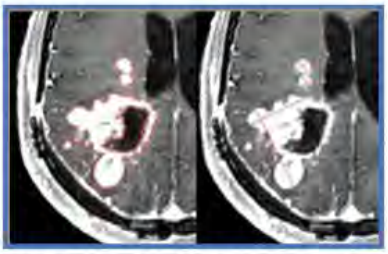

Figure 1: Example Measurements using volumetric (left) and bidimensional (right) methods.

Characteristic	Progressed, N = 23[1]	Stable, N = 18[1]	Regressed, N = 2[1]	p-value[2]
Gender				0.4
Female	9 (39%)	11 (61%)	1 (50%)	
Male	14 (61%)	7 (39%)	1 (50%)	
Age	60 (46, 64)	56 (51, 62)	53 (52, 54)	0.8
Days Postop MRI to RT MRI	25 (18, 34)	24 (16, 35)	32 (22, 43)	>0.9
IDH				>0.9
Mutant	5 (22%)	3 (17%)	0 (0%)	
Wildtype	18 (78%)	15 (83%)	2 (100%)	
MGMT				0.9
Indeterminate	1 (4.3%)	1 (5.6%)	0 (0%)	
Methylated	11 (48%)	6 (33%)	1 (50%)	
Unknown	1 (4.3%)	0 (0%)	0 (0%)	
Unmethylated	10 (43%)	11 (61%)	1 (50%)	

Table 3: Correlation between Volumetric Progression (postop to RT planning MRI) and gender, age, interval between 2 MRIs, IDH mutation, and MGMT methylation status.

(Filename: TCT_769_Slide1.JPG)

740

Improving the MRI Diagnosis of Leptomeningeal Disease

K Wierzbicki[1], J Herbst[2], O Yildirim[2], B Kalaycioglu[2], E Pentsova[2], R Young[2]
[1]Weill Cornell Medical College, New York, NY, [2]Memorial Sloan Kettering Cancer Center, New York, NY

Purpose

CSF tumor cell cytology via lumbar puncture is the current gold standard for diagnosing leptomeningeal disease (LMD). However, this assay has only a 60% sensitivity on initial puncture and often needs to be repeated in triplicate to confidently exclude LMD. MRI offers a noninvasive approach to diagnose and monitor LMD, but its application remains limited by inter-observer variability and the heterogeneity of leptomeningeal tumor appearance. We hypothesized that we could use specific MRI criteria to improve the diagnosis of LMD in patients with solid cancers.

Materials and Methods

A cohort (n=208) was selected from a database of consecutive patients with solid cancers and clinical suspicion of LMD who underwent CSF cytology analysis and brain and/or spine MR images <1 month apart. Blinded to the cytology report, two radiologists independently applied the Response Assessment in Neuro-Oncology criteria for leptomeningeal metastases. Adjunct parameters (e.g., subependymal spread, pial spread, hydrocephalus) were also applied to assess if these additional factors improved the sensitivity and specificity of LMD diagnosis. The CSF cytology results were used as the reference standard.

Results

Within the entire cohort, 24.5% (n=51) of patients had positive cytology LMD. Of those patients, positive MRI scans correctly detected 90.2% (n=46) of cases. Among the remaining 75.5% (n=157) of patients with negative cytology, positive MRI scans suggestive of LMD were present in 75.8% (n=119). Further statistical analysis showed that using MRI to diagnose LMD had a positive predictive value of 27.9% and a negative predictive value of 88.4%. Addition of the adjunct parameters did not improve LMD diagnosis ($p>0.05$).

Conclusions

We found MRI to have low positive predictive value due to many false positives. While this suggests a potential overdiagnosis by MRI using standard criteria, this difference may also be due to innate differences between CSF and MRI methods for the detection of leptomeningeal cancer cells that are floating (better suited to CSF analysis) versus adherent (better suited to MRI analysis). Further

precision approaches of CSF and MRI techniques and refinement of response criteria may improve patient evaluations, clinical trials, and hopefully outcomes.

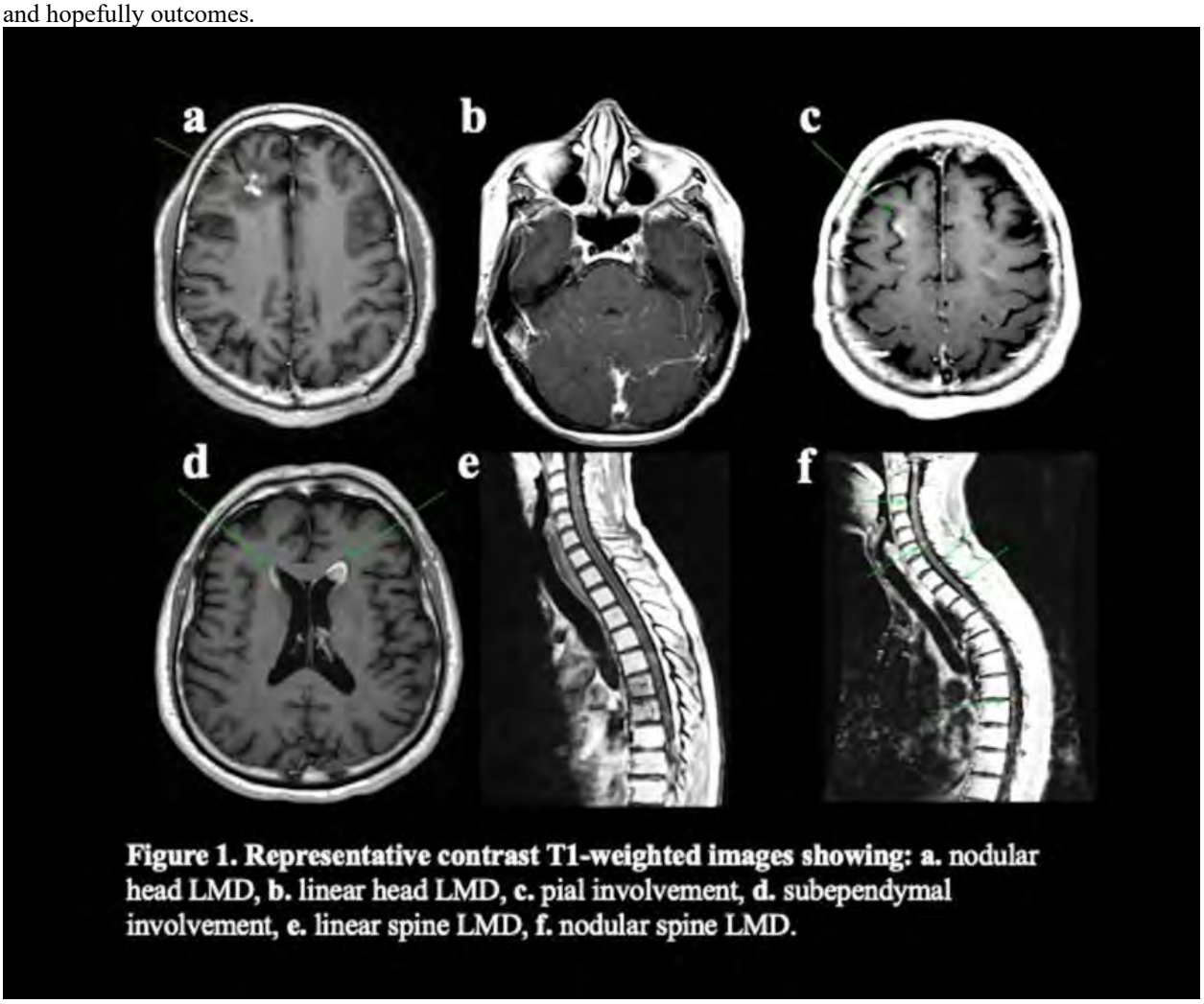

Figure 1. Representative contrast T1-weighted images showing: a. nodular head LMD, **b.** linear head LMD, **c.** pial involvement, **d.** subependymal involvement, **e.** linear spine LMD, **f.** nodular spine LMD.

(Filename: TCT_740_ASNRAbstractFigure1.jpg)

814

Iron and Non-iron Related Characteristic of Gliomas on 7T Quantitative Susceptibility Mapping

S Chawla[1], L de Godoy[2], M Nasrallah[3], S Bagley[4], A Desai[4], D O'Rourke[5], S Brem[4], L Loevner[3], S MOHAN[6]

[1]Perelman School of Medicine at the University of Pennsylvania, Philadelphia, PA, [2]Perelman School of Medicine at the University of Pennsylvania, Philadelphia, USA, Philadelphia, PA, [3]Hospital of the University of Pennsylvania, Philadelphia, PA, [4]University of Pennsylvania, Philadelphia, PA, [5]Perelman School of Medicine at the University of Pennsylvania, Philadelphia, PA, [6]UNIVERSITY OF PENNSYLVANIA, PHILADELPHIA, PA

Purpose

Abnormal accumulation of heme (deoxyhemoglobin) and non-heme (ferritin, hemosiderin) iron reflects a multiplicity of pathological and physiological processes in gliomas (1). On susceptibility weighted imaging (SWI), susceptibility-based signals within tumor beds are visible as low signal intensity with fine linear or dot-like structures with or without conglomeration (2,3). In comparison to SWI, quantitative susceptibility mapping (QSM) is a more sensitive tool for iron detection and quantification (4). The clinical utility of 7T QSM has not been reported in gliomas previously. The purpose of this study was to demonstrate the presence of distinct geometric patterns of iron deposition in high and low-grade gliomas using 7T QSM.

Materials and Methods

A total of 6 treatment naïve glioma patients (mean age=42.5±12.7years, M/F=2/4) were recruited. Based upon histopathological analyses, three patients had high-grade glioma (grade-4 astrocytoma) and two patients had low-grade glioma [(grade-2 astrocytoma (n=1) and grade-2 oligodendroglioma (n=1)]. One patient was diagnosed with a low-grade glioma by serial neuroimaging findings. All patients underwent MR imaging on a 7T scanner prior to surgical resection. The imaging protocol included conventional T1-weighted MPRAGE and T2-FLAIR sequences. Additionally, high-resolution, flow compensated 3D-susceptibility weighted imaging (3D-SWI) was acquired (in-plane resolution=0.5x0.5mm2, slice thickness=2mm). Susceptibility weighted imaging and mapping (SWIM) algorithm developed by Dr. Haacke's group (5) was used to reconstruct QSM maps from 3D-SWI data. Gliomas were classified as "iron-laden" if they demonstrated hypointensity on SWI and hyperintensity on QSM. Gliomas were classified as "non-iron-laden" if they were iso-intense/hyperintense on SWI and isointense on QSM.

Results
Three morphologically distinct patterns were observed in gliomas. All three high-grade gliomas were iron-laden and showed hyperintense signal intensity on QSM in the form of nodular areas of susceptibility. The mean QSM values from these nodules were 42±15ppb. On the other hand, two low-grade gliomas had no evidence of iron deposition. However, one low-grade glioma exhibited a hyperintense peripheral rim on the QSM with a corresponding value of 26.85ppb (Figure 1).
Conclusions
7T QSM may be helpful in distinguishing low from high-grade gliomas. However, correlative imaging and histochemical analyses from a larger patient population are required to confirm these findings.

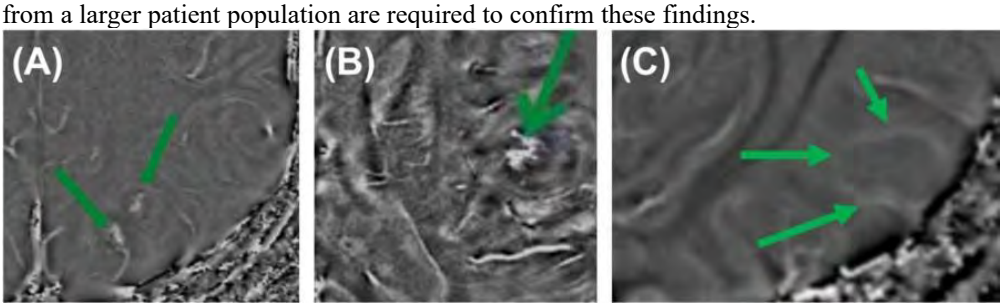

(Filename: TCT_814_Figure_Final_2.jpg)

1291
Local-AIF DSC Perfusion in Intracranial Atherosclerotic Disease
M Liu[1], S Prabhakaran[2], J Bertini[2], C Warioba[2], Y Pu[2], S Ansari[3], T Carroll[2]
[1]The University of Chicago, Chicago, IL, [2]University of Chicago, Chicago, IL, [3]Northwestern University, CHICAGO, IL

Purpose
Stroke is a leading cause of mortality and morbidity in the U.S. with 10% of ischemic strokes being due to intracranial stenosis. As the cause of a stroke is vital to targeted therapy of the underlying stroke mechanism, development and assessment of diagnostic tests regarding their ability to differentiate between atherosclerotic plaque and other pathologies can improve treatment outcome. Further, infarct pattern such as watershed infarction, multiple cortical infarcts, and single deep infarct has therapeutic implications regarding response and recurrence. As such, as a technical note towards improving diagnostic images and patient outcome we compare 1) single-photon emission computerized tomography (SPECT) perfusion, 2) dynamic susceptibility contrast (DSC) perfusion maps calculated from standard DSC via $Ct(t) = AIF(t)*R(t)$, and 3) perfusion calculated using a "local-AIF" with delay and dispersion effects corrected via $Ct(t) = AIF(t - t0)*R(t)$ where t0 represents the time-delay in arrival of the contrast bolus resulting from intracranial atherosclerotic disease.
Materials and Methods
Presented are preliminary results from an ongoing study studying intracranial hemodynamics with 6 subjects with ICAD analyzed. SPECT and DSC perfusion maps were acquired. DSC was post-processed into both standard DSC and "local-AIF" DSC. T1 anatomic scans were co-registered to vascular segmentation templates with code developed in-house (MATLAB) and DSC co-registered to the T1 anatomic scans (SPM) for automatic vascular segmentation. Asymmetry (hemispheric ratio of vascular territories) was compared between SPECT, standard DSC, and "local-AIF" DSC. The "local-AIF" effect was calculated on a voxel-by-voxel basis as the difference between the 'local-AIF' and standard DSC and compared to Tmax.
Results
Standard DSC appeared to overestimate perfusion deficit compared to reference standard SPECT (Fig 1a-b) and overestimate hemispheric asymmetry (Fig 2a-b). "Local-AIF" DSC returned perfusion maps and hemispheric asymmetry closer to SPECT (Fig 1c, 2c). "Local-AIF" effect did not match Tmax asymmetry patterns for all cases (Fig 3).
Conclusions
Tracer kinetics corrected with a "local-AIF" showed greater agreement with SPECT both visually and regarding asymmetry of vascular regions in 6 ICAD patients. Tmax agreed with SPECT hypoperfusion, while smaller Tmax (between 3-6s) may be removed using a "local AIF" to agree more with SPECT. DSC with a "local AIF" may function better for imaging perfusion asymmetry in intracranial stenosis.

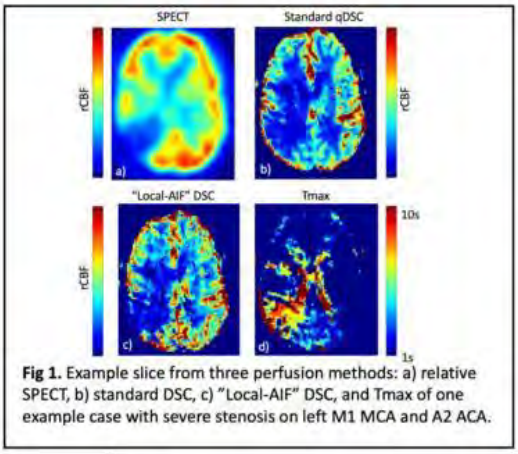

Fig 1. Example slice from three perfusion methods: a) relative SPECT, b) standard DSC, c) "Local-AIF" DSC, and Tmax of one example case with severe stenosis on left M1 MCA and A2 ACA.

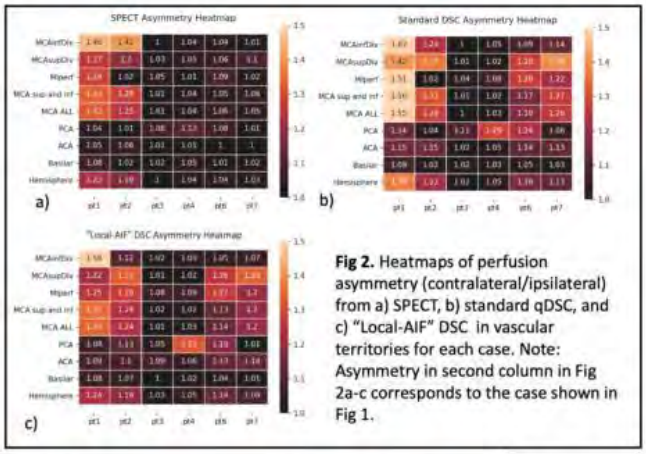

Fig 2. Heatmaps of perfusion asymmetry (contralateral/ipsilateral) from a) SPECT, b) standard qDSC, and c) "Local-AIF" DSC in vascular territories for each case. Note: Asymmetry in second column in Fig 2a-c corresponds to the case shown in Fig 1.

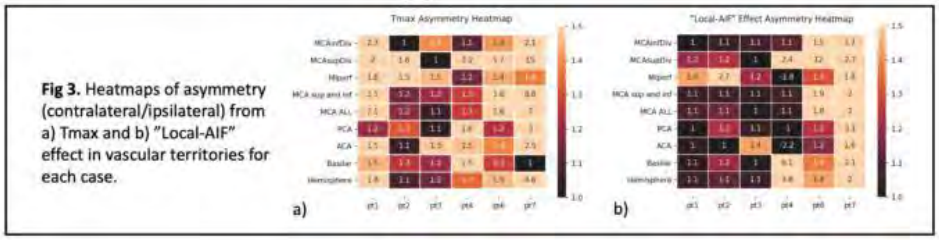

Fig 3. Heatmaps of asymmetry (contralateral/ipsilateral) from a) Tmax and b) "Local-AIF" effect in vascular territories for each case.

(Filename: TCT_1291_AbstractImages.jpg)

163

Morphological Atlas of the Three-Dimensional Vascular Network Architecture in the Entire Developing and Adult Mouse Brain at Ultra-High-Resolution

J Bisschop[1], A Miettinen[2], A Bonnin[3], M Schmeltz[3], V Novak[3], J Vogel[4], M Stampanoni[5], T Wälchli[1]

[1]University of Toronto, Toronto, Canada, [2]University of Jyväskylä, Jyväskylä, Finland, Jyväskylä, Finland, [3]Swiss Light Source, Paul Scherrer Institute, Villigen, Switzerland, [4]University of Zürich, Zürich, Switzerland, [5]ETH Zürich, Zürich, Switzerland

Purpose

The establishment of cerebrovascular networks is crucial during embryonic and postnatal brain development, acquires relative quiescence in the adult healthy brain, and plays critical roles during the initiation and progression of various CNS pathologies. Quantitative analysis of the morphology of the entire brain vasculature along the arterio-venous axis is important to better understand the three-dimensional brain vascular network across development, adulthood, and in disease. However, computational analysis and quantification of large brain vascular network datasets subdivided into specific brain regions remains challenging. We have constructed a morphological atlas of the three-dimensional vascular network architecture in the entire developing and adult mouse brain at ultra-high-resolution including all anatomical brain regions. We present results from hierarchical imaging and computational analysis of high-resolution vascular networks in postnatal- and adult mouse brains at a whole-brain level.

Materials and Methods

We developed a pipeline including resin-based vascular corrosion casting, scanning electron microscopy, synchrotron radiation/desktop µCT imaging and 3D computational reconstruction facilitating quantitative analysis of various vascular network parameters. Registration to the Allen Mouse Brain Atlas coordinate system enabled detailed comparisons of anatomical regions between the early postnatal stage of development and adulthood.

Results

We visualized and quantified the 3D brain vasculature in 19 animals (n=9 postnatal day 10 and n=10 adult wildtype mice). The network parameters feature vascular volume fraction, branch point density, vessel diameter, -length, -tortuosity, and -directionality as well as extravascular distance were obtained at both developmental stages, additionally subdivided into capillaries (diameter < 7µm) and non-capillaries (diameter > 7µm). Quantitative findings were interpreted in the context of biological functions of anatomical regions, e.g. brain vascular networks in grey versus white matter structures or vascular networks based on/correlated with the known neuronal density of a specific brain region.

Conclusions

Using vascular corrosion casting, SRµCT-imaging and 3D computational image analysis, we provide a 3D morphological atlas of the developing and adult mouse brain vasculature at high resolution generating absolute parameters, characterizing the entire 3D mouse brain vessel network at a previously unmet micrometer resolution.

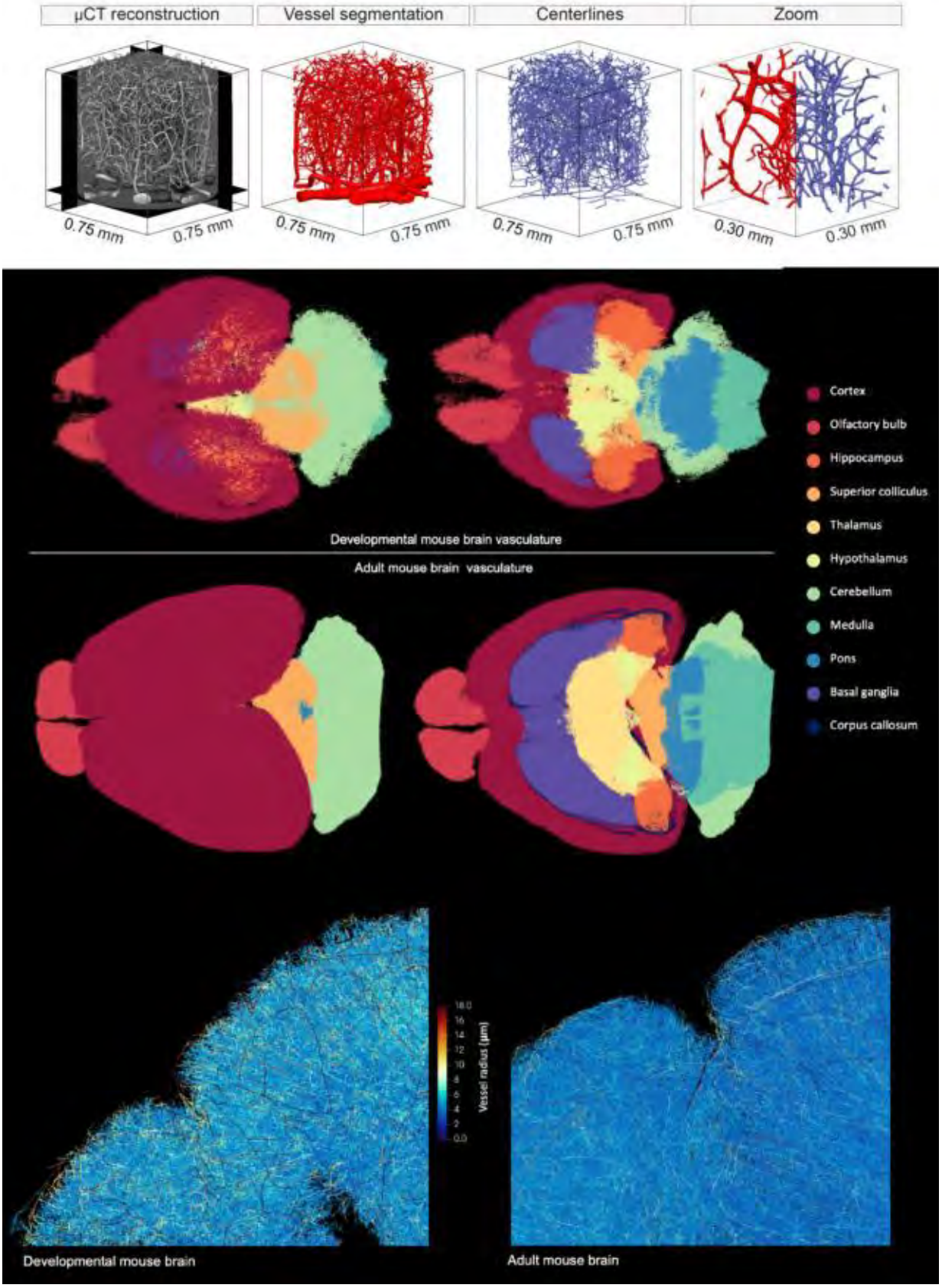

(Filename: TCT_163_Figure.jpg)

1009

Preoperative Determination of IDH Status and Grade in Gliomas using MRS

T Nguyen[1], N Zakhari[2], S Chakraborty[2], C Torres[2], M Brun-Vergara[2], G Melkus[3]

[1]The Ottawa Hospital, Ottawa Hospital Research Institute, Ottawa, ON, [2]The Ottawa Hospital, U. of Ottawa, Ottawa, ON, [3]The Ottawa Hospital, Ottawa, Ontario

Purpose

Edited MRS is a technique which can be used for the detection of 2-hydroxyglutarate (2-HG), which is a biomarker for the isocitrate dehydrogenase (IDH) mutation in gliomas[1]. We evaluated the diagnostic accuracy of preoperative MRS in the determination of the IDH status and grade in patients with newly diagnosed gliomas.

Materials and Methods

On a 3T scanner, MRS was performed using a regular PRESS sequence and a spectral editing sequence (MEGA-PRESS). MRS data were analysed using the LC Model[2]. Concentration of 2-HG was estimated from the subtracted spectra of the edited MRS sequence while NAA, choline and creatine concentrations were obtained from the regular PRESS sequence. Following surgery, gliomas were classified according to the 2016 WHO classification. IDH1 mutation status was assessed by immunohistochemistry for all patients. Patients with grade 2 and 3 gliomas and negative immunohistochemistry underwent further molecular testing for the detection of non-canonical IDH1 or IDH2 mutations using next generation sequencing. Differences in metabolite concentrations between IDH-mutant and IDH-wild type gliomas and between gliomas of various grades were assessed using non parametric tests. The areas under-the ROC curve (AUCs) for different metabolites were calculated with IDH mutation status or glioma grade as the outcome. Two radiologists evaluated the presence of T2/FLAIR mismatch in tumours which did not have central necrosis.

Results

There were 29 IDH-mutant gliomas and 52 IDH-wild type gliomas. Median 2-HG amplitudes were 1.33 I.U. (institutional units) (95% CI 0.17-2.09) for IDH-mutant and 0 I.U. for IDH-wild type gliomas (P= 0.0001). There was a significant difference in the NAA/Choline ratio among various glioma grades ($P<0.05$). The AUC for 2HG was 0.74 (95% CI 0.63-0.83) in the differentiation between IDH-mutant vs IDH-wild type gliomas. Using a 2-HG cut-off of >0.96 I.U., sensitivity was 59% and specificity was 90% for the identification of IDH-mutant gliomas. The AUC for the NAA/Choline ratio was 0.74 (95% CI 0.63-0.83) in the differentiation of high vs. low grade gliomas. Using a NAA/Choline cut-off ≤ 0.53, sensitivity was 45% and specificity was 100% for identification of high grade gliomas. Using the T2/FLAIR mismatch sign, both radiologists had a low sensitivity (6%) but a high specificity (94%) for the identification of IDH-mutant gliomas.

Conclusions

Preoperative MRS can identify IDH-mutant gliomas and high grade gliomas with high specificity.

Wednesday, May 3, 2023

1:15-2:15 PM

Alzheimer's, ARIA & Dementia Study Group Programming:

Update on Imaging in Alzheimer's, ARIA & Dementia: Cases, Roles and Workflows

722

Distinct Brain Morphometry Patterns are associated with Alzheimer's Disease Polygenic Risk Scores stratified using cell-level transcriptomics

P Rajagopalan[1], E Gleave[2], N Sahelijo[3], S Thomopoulos[4], G Jun[3]

[1]USC, Los Angeles, CA, [2]University of Southern California, Marina del Rey, CA, [3]Boston University, Boston, MA, [4]University of Southern California, Marina del Rey,, CA

Purpose

Alzheimer's disease (AD), the most common neurodegenerative disorder is a polygenic disorder with the greatest known common genetic risk factor being apolipoprotein E (APOE4), which is found in 40% of individuals diagnosed with AD and around 25% of elderly non-AD individuals. Recent GWAS studies identified over 75 genes associated with late-onset AD. Beyond APOE, additional sources of AD genetic risk are important to understand for more effective patient risk stratification and therapeutic targeting. AD polygenic risk scores (PRS) may more effectively explain heterogeneity in AD onset and progression. Prior work demonstrated a novel cell-based polygenic risk score strategy based on cell-level network analysis using single nuclei RNA-sequencing data where modules were identified based on variants previously associated AD genes expressed in specific pathways (Fig. 1a).

Materials and Methods

530 subjects (Fig. 1b) with MRI and genetic data across the Alzheimer's Disease Neuroimaging Initiative (ADNI1/GO/2) dataset were analyzed. For these participants, we mapped 3D brain atrophy patterns, assessed using brain-wide gray matter volume maps with voxel-based morphometry (VBM; https://sites.google.com/view/enigmavbm). PRS were also computed, based on genetic loci in

astrocyte and oligodendrocyte associated modules, M1 and M2 respectively, that were previously associated with faster rates of clinical decline.

Results

Voxel-wise whole brain analysis of gray matter density maps revealed that M1 and M2 PRS were associated with significantly greater atrophy in the medial temporal lobe, notably bilateral hippocampi, entorhinal cortex and amygdala. These regions of association survived false discovery rate (FDR) correction for multiple comparisons across all voxels using the critical p-value (q=0.05) of 0.0007 for module M1 (Fig. 1c) and 0.001 for M2 (Fig. 1d).

Conclusions

As far as we know, this study is the first to characterize brain signatures associated with cell-based PRS, facilitating understanding of the genetic contribution beyond APOE and demonstrating a strong translational potential to identify neurobiological mechanisms that may lead to targeted AD therapies.

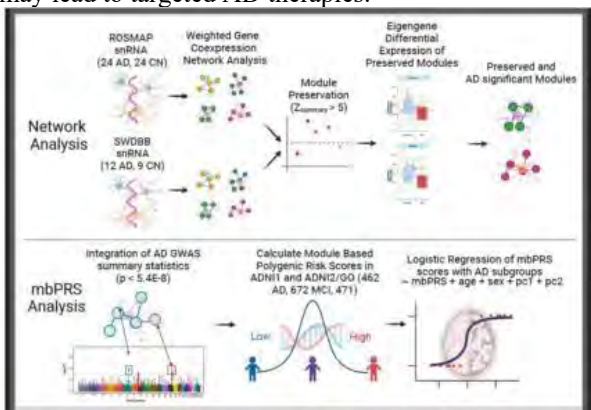

Figure 1a. Module-based Polygenic risk scores (mbPRS) based on cell-level network analysis using single nuclei RNA-sequencing data using Sahelijo et al. AAIC 2022, San Diego.

	N	Age [SD]	Sex (F%)	Dx (n=CN)	Dx (n=MCI)	Dx (n=AD)	TIV [SD]	Edu [SD yrs]	APOE (e4+)	FS (1.5/3T)
M1 PRS	530	74.1 [7.1]	211 (39.8%)	139	90	301	1.5 [0.2]	15.8 [2.8]	248	327/203
M2 PRS	527	74.2 [7.1]	212 (40.2%)	146	90	291	1.5 [0.2]	15.7 [2.8]	251	337/190

Figure 1b: Demographic data on subjects used in the analysis. SD=Standard Deviation, F%=Female percentage, Dx=diagnosis, CN=Cognitively Normal, MCI=Mild Cognitive Impairment, AD = Dementia, TIV=Total Intracranial Volume, Edu=Education in years and FS=MRI Magnetic Field Strength in Tesla.

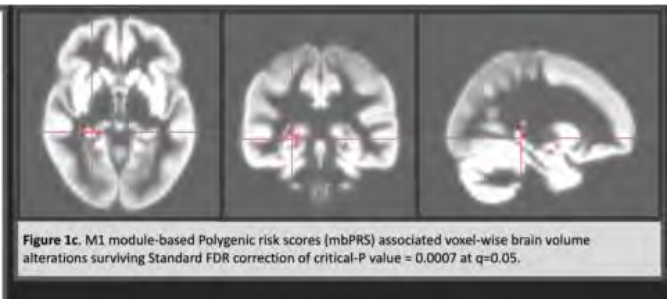

Figure 1c. M1 module-based Polygenic risk scores (mbPRS) associated voxel-wise brain volume alterations surviving Standard FDR correction of critical-P value = 0.0007 at q=0.05.

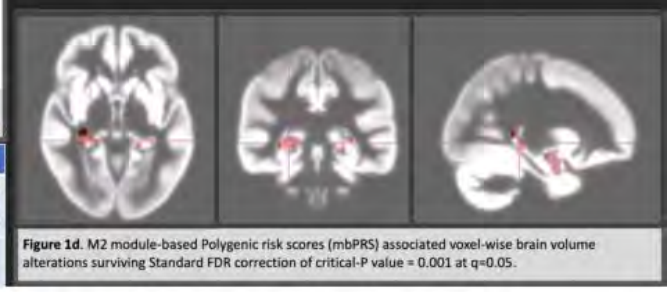

Figure 1d. M2 module-based Polygenic risk scores (mbPRS) associated voxel-wise brain volume alterations surviving Standard FDR correction of critical-P value = 0.001 at q=0.05.

(Filename: TCT_722_Fig1PRS.jpg)

1004

Imaging of Alzheimer Disease Pathology in Midlife Obese Participants with and without Insulin Resistance

M Dolatshahi[1], P Commean[1], C Nguyen[1], L Lloyd[1], N Hantler[1], T Benzinger[2], C Raji[3]

[1]Washington University in Saint Louis, Saint Louis, MO, [2]Washington University in St.louis, Saint Louis, MO, [3]Washington University in St. Louis, ST LOUIS, MO

Purpose

High body fat at midlife, as evidenced by obesity, is increasingly understood as a risk factor for Alzheimer disease (AD). Importantly, visceral fat is known to be associated with insulin resistance and proinflammatory state, the mechanisms involved in AD pathology. We compared amyloid and tau PET uptake across metabolically abnormal obese (MAO), metabolically normal obese (MNO), and metabolically normal non-obese (MNN) participants and assess their association with abdominal adipose tissue.

Materials and Methods

A total of 21 middle-aged, cognitively normal participants, underwent bloodwork, brain and abdominal MRI, as well as PiB and AV-1451 PET scan. Based on insulin resistance and obesity status, were categorized to three groups (MAO: 10, MNO: 6, MNN: 5). Visceral and subcutaneous adipose tissue (VAT, SAT) were automatically segmented using VOXel Analysis Suite (Voxa). FreeSurfer 7.1.1 was used for automatic segmentation of cortical and subcortical brain regions using a probabilistic atlas. Dynamic amyloid imaging was performed with a bolus injection of ~15 mCi of [11C]PiB, followed by a 60-min scan. A single intravenous bolus of between 7.2–10.8 mCi of AV-1451 was administered. Data from the 30–60 minute, and 80–100 minute post-injection window for PiB and AV-1451 were used for the analysis, respectively (4). PET data were registered to the brain MRIs and using FreeSurfer ROIs, standardized uptake value ratios (SUVRs) were calculated using the cerebellum as a reference region. PiB and AV-1451 SUVRs were compared across study groups using one-way ANOVA. Associations of VAT and SAT with brain imaging metrics were investigated using linear regression models.

Results

Higher left precuneus WM (p=0.037), left insula cortex (p=0.015), left and right lingual WM (p=0.027, p =0.035), and left inferior temporal WM (p=0.034) PiB SUVRs were observed in MAO compared to MNN group. Also, there was higher left pars orbitalis cortex and WM PiB SUVRs in MAO than MNO group (p=0.026, p=0.015). However, no significant differences were observed across these groups regarding AV-1451 SUVRs. The associations of PiB SUVR of right lingual, left precuneus, and left pars orbitalis WM with VAT volume (p=0.02, p=0.007, p=0.02), and PiB SUVR of left lingual WM with SAT volume (p=0.04) were significant.

Conclusions

We demonstrate a higher rate of early AD pathology in signature areas like precuneus, in middle-aged participants with obesity and insulin resistance in association with abdominal fat volumes.

	MNN (n=5)	MNO (n=6)	MAO (n=10)	P-value
Subject characteristics				
Age (year) [mean (SD)]	50.40 (6.80)	50.17 (7.57)	51.90 (6.49)	0.863
Education (year) [mean (SD)]	15.60 (2.88)	16.00 (1.79)	15.90 (2.42)	0.959
Gender (men) [N (%)]	3 (60.0)	2 (33.3)	4 (40.0)	
Race [N (%)]				0.07
Black/African American	2 (40)	4 (66.7)	5 (50.0)	
White/Caucasian	3 (60)	2 (33.3)	5 (50.0)	
BMI (kg/m^2) [mean (SD)]	22.12 (3.06)	33.73 (3.76)	37.47 (3.54)	**<0.001**
Waist circumference (cm) [mean (SD)]	84.75 (6.50)	111.87 (10.90)	106.16 (24.38)	0.099
Diabetes [N (%)]	0	1 (16.7)	0	NaN
Hypertension [N (%)]	1 (20)	1 (16.7)	4 (40.0)	0.465
Triglyceride (mg/dL) [mean (SD)]	72.40 (24.99)	74.83 (24.23)	137.30 (72.39)	0.048
Cholesterol (mg/dL) [mean (SD)]	181.60 (41.40)	169.17 (42.13)	178.90 (25.59)	0.811
LDL (mg/dL) [mean (SD)]	97.60 (32.54)	105.62 (31.54)		0.696
HDL(mg/dL) [mean (SD)]	69.60 (10.36)	58.50 (9.42)	42.80 (8.34)	**<0.001**
Cholesterol/HDL ratio [mean (SD)]	2.60 (0.55)	3.00 (0.63)	4.40 (0.97)	**0.001**
Fasting Glucose (mg/dL) [mean (SD)]	85.21 (20.04)	89.82 (2.78)	108.71 (31.21)	0.159
Glucose Tolerance (mg/dL) [mean (SD)]	135.10 (49.88)	103.00 (23.00)	162.90 (46.56)	**0.042**
HbA1C (%) [mean (SD)]	5.08 (0.31)	5.55 (0.48)	6.03 (0.79)	**0.038**
FastingInsulin (µU/mL) [mean (SD)]	4.12 (2.66)	5.30 (2.12)	26.39 (12.18)	**<0.001**
HOMA-IR [mean (SD)]	0.96 (0.73)	1.18 (0.48)	7.15 (3.57)	**<0.001**
MMSE score [mean (SD)]	29.60 (0.55)	29.33 (1.03)	29.20 (0.79)	0.679
Abdominal MRI Measures				
Subcutaneous Fat (cm3) [mean (SD)]	1187.16 (359.35)	3351.78 (1116.63)	3750.18 (1038.49)	**<0.001**
Visceral Fat (cm3) [mean (SD)]	554.63 (127.50)	828.01 (189.07)	1458.19 (551.42)	**0.001**
Visceral/Subcutaneous Fat ratio [mean (SD)]	0.48 (0.09)	0.26 (0.09)	0.43 (0.27)	0.176

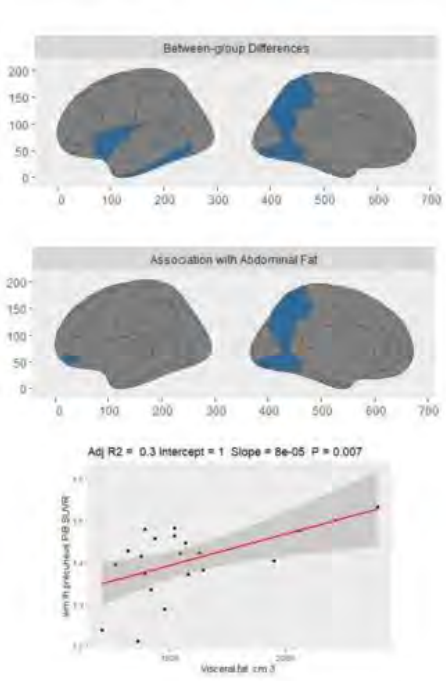

(Filename: TCT_1004_GraphicsPiB.jpg)

Wednesday, May 3, 2023

1:15-2:15 PM

ASSR Programming: Spine Imaging (Essentials Track)

1368

Detecting and Localizing Cervical Spine Fracture Using an End-To-End 3D Deep Learning Pipeline

B Khosravi[1], S Vahdti[1], P Rouzrokh[1], M Moassefi[1], S Faghani[2], B Erickson[1]

[1]Mayo Clinic, Rochester, MN, [2]Mayo Clinic (Rochester, MN, US), Rochester, MN

Purpose

Over 1.5 million spine fractures occur annually in the United States alone, resulting in over 17,000 spinal cord injuries. The most common site of spine fracture is the cervical spine, and computer tomography (CT) is the modality of choice for detecting these fractures. Commercial computer-aided diagnosis tools are being used to triage studies and prioritize patients with a suspected cervical spine fracture (CSFx). However, they come short when the patient has superimposed degenerative disease and osteoporosis and are reported to have variable sensitivity, ranging from 54% to 76%(1,2). This study aims to develop a deep learning algorithm that can robustly detect and localize cervical spine fractures on CT scans.

Materials and Methods

Data from the RSNA-ASNR Cervical Spine Fracture Challenge (n=2019) was used to train and validate the algorithm. This data was gathered from twelve different institutions that can lead to a more generalizable model. Inspired by the holistic view of the radiologists, an end-to-end 3D approach was used to prevent mistaking artifacts that mimic fracture in 2D slices (e.g., nutrition canals). We first used a weakly supervised approach to localize C1-C7 vertebrae by applying a trained model on the data and then trained a segmentation model to finetune the segmentation masks(3). The segmented vertebrae were then cropped out of the image and straightened in the z-axis to account for possible neck flexion. Finally, each 3D vertebrae volume was resized to 256x256x64 and used to train a 3D EfficientNetB4 to binary classify images as with or without fracture. The performance of the segmentation model is reported on the internal test set with human annotation groundtruth. We used 5-fold cross-validation to have a more robust classifier and their ensembled results are reported.

Results

The segmentation model reached a Dice Similarity Coefficient of 0.92. The vertebrae-level fracture detection model had an area under the receiver operating curve (AUROC) of 0.92. When ensemble, on a patient level, the model reached an AUROC of 0.93 with a sensitivity of 87% and specificity of 77%.

Conclusions
This work presents a 3D deep learning model to detect and localize CSFx in CT scans from multiple institutions. The high sensitivity of the model makes it a suitable candidate for screening. Additionally, the per-vertebrae nature of the workflow enables precise localization of the fracture, which can help speed up the evaluation by expert radiologists to verify or reject the model's prediction.

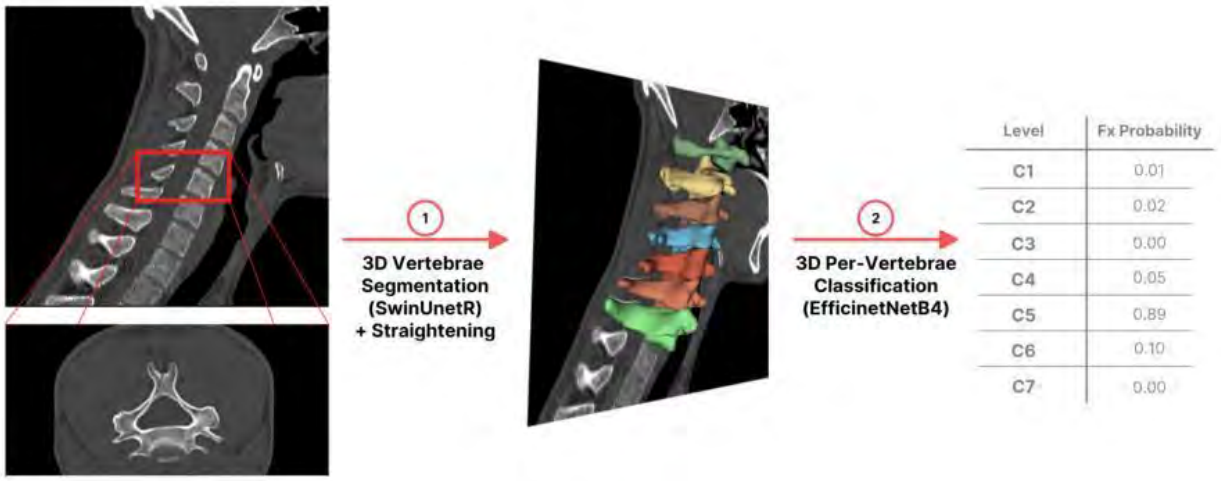

(Filename: TCT_1368_Figure1.jpg)

982

Trust, but Verify: Technical Efficacy, Safety, and Limitations of Surface Registered Electromagnetic CT-Navigation as an Adjunct Tool for CT-guided Percutaneous Vertebral Augmentation and Tumor Ablation in the Spine.

B Johnson-Tesch[1], J Morris[1]
[1]*Mayo Clinic, Rochester, MN*

Purpose
Percutaneous ablation with vertebral augmentation and vertebral augmentation alone are safe and effective palliative treatments for patients with pathologic and osteoporotic compression fractures, respectively [1,2]. Vertebral anatomy, kyphoscoliosis, and geometric limitations of the CT gantry add technical difficulties when performed under CT-guidance. The aim of this study was to report the safety and technical efficacy of incorporating a surface registered electromagnetic CT-navigation system into our busy spine ablation and vertebral augmentation practice, and to highlight the best use cases and limitations.
Materials and Methods
Retrospective review of a total of 22 patients (34 spinal levels; 5.9% cervical, 52.9% thoracic, 38.2% lumbar, and 2.9% sacral) treated with CT-guided percutaneous spinal intervention utilizing surface registered electromagnetic CT-navigation. Treatments consisted of percutaneous ablation for spinal metastases with or without vertebral augmentation (28 levels), and vertebral augmentation alone in the setting of osteoporotic compression fracture (6 levels). Ablation energies included radiofrequency (27 levels) and cryoablation (1 level). A total of 31 levels were stabilized with vertebral augmentation (16 kyphoplasty, 15 vertebroplasty/sacroplasty), and 3 levels were ablated without augmentation. Intraprocedural neuromonitoring was used for 10 patients undergoing ablation.
Results
Technical success was 100%. One patient had a self-limited complication manifesting as transient depression of motor evoked potentials. CT fluoroscopic guidance was essential in verifying the trajectory accuracy for pilot hole creation due to limitations including registration drift and small margins of error when working in the spine. Several benefits that were uniquely attributed to CT-navigation included the ability to obtain severe trajectories, placing ablation probes into pilot holes without ionizing radiation, and ability to plan out multiple trajectories across several levels while in a CT only interventional room.
Conclusions
Surface registered electromagnetic CT-navigation is a safe and effective adjunct tool for CT-guided percutaneous spinal ablation and vertebral augmentation, and is uniquely helpful in planning multiple needle trajectories, potentially reducing ionizing radiation exposure, and improving operator ergonomics, particularly when treating lesions that need severe angulations as seen in the thoracic spine of kyphotic patients and in the sacrum.

Wednesday, May 3, 2023

1:15-2:15 PM

Scientific Abstract Session: AI 3

1115

AI Assisted Diagnosis of Uncal Herniation in Brain CT: Training and Testing with Clinical Data

K Kuo[1]

[1]*Far Eastern Memorial Hospital, Taipei, Taiwan*

Purpose

Automatic monitoring of Uncal Herniation (UH) may help detect this subtle presentation for potentially life-threatening condition caused by the intracranial mass effect (IME). Despite UH being a focal sign, prior studies mainly focused on IME and used all slices of brain CT (1-3). Instead, we proposed in this study a cascade two-step model and used human-in the loop method to minimize the annotation and computation in building and testing an AI model of UH using large, real-world, clinical data.

Materials and Methods

We collected 134,348 scans of brain CT at Far Eastern Memorial Hospital from Jan 1, 2012, to Dec 31, 2021, and randomly selected them into training, validation, and test sets. Two-step model was designed to recognize UH. In step 1, we built a U-net model to identify dorsum sellae as the landmark to locate the single slice of suprasellar cistern where UH happened. In step 2, we further processed the slice image into three inputs in order to evaluate the influence of the size of region-of-interest: uncus only (input A), uncus and surrounding temporal lobe (input B), and uncus, surrounding temporal lobe, and simplified supratentorial brain (input C) (Figure). We then trained three ResNet models to classify UH separately. Finally, we tested and compared the two-step model of each ROI group with large clinical test set by evaluating recall, precision, F1-score, specificity, and accuracy.

Results

In step 1 model, 5,000 CTs (Train, Valid, Test = 700, 300, 4000) were used in building and testing the model. In step 2 model, randomly selected CTs (n=44,756) from 2012 to 2020 were used in building the model, and all CTs (n=9,830) in 2021 were used in testing the model. In step 1, The accuracy of identification of the slice of suprasellar cistern is 99.33%. In step 1+2, The F1-scores were 0.7500, 0.7742, 0.7857, 0.8131 for the three models of inputs A, B, C, and ensemble model from A-C respectively; meanwhile the accuracy were 0.9919, 0.9929, 0.9933, 0.9942 respectively.

Conclusions

We utilized a cascade two-step model and human-in-the-loop technique to annotate the large clinical data and to decrease the computation load. We proved that the larger the ROI, the better the performance in our UH classification task. Our ensemble model achieved fair result of F1-score and accuracy in large test set, which proved this model could work properly clinically.

Figure Illustration of three input strategies based on the dorsum sellae (the small red rectangles) recognized by step 1. (a) 50% cropped image from single slice of suprasellar cistern. (b) Full-sized image from single slice of suprasellar cistern. (c) Stacked full-sized image from three levels of brain according to relative location to suprasellar cistern.

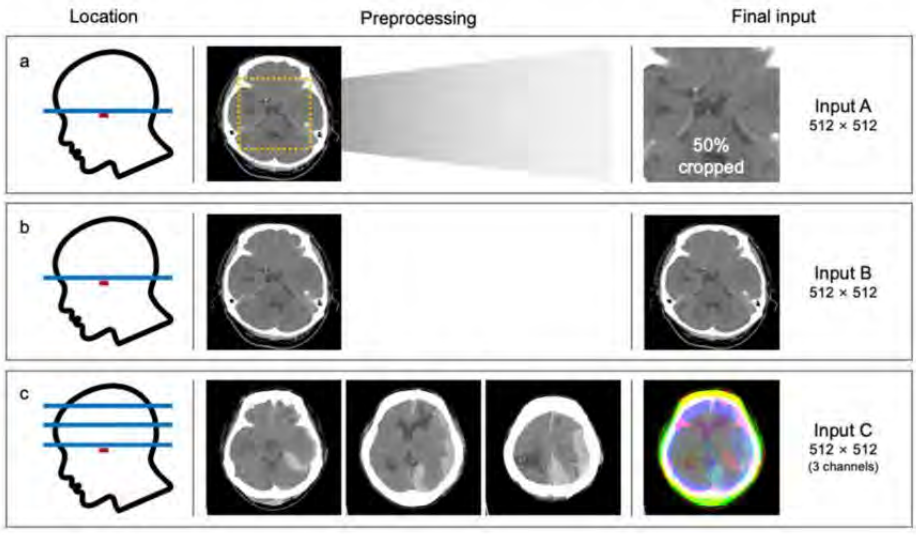

(Filename: TCT_1115_ASNRfigurecopy.jpg)

1031

All You Need is a Smartphone – An Interactive Demonstration of Low-Resource 3D Models for Neurosurgical Planning

S Panicker[1], L Lin[2], Z Wilseck[3], N Chaudhary[4], J Gemmete[4]

[1]University of Michigan Medical School, Troy, MI, [2]University of Michigan Hospital, Ann Arbor, MI, [3]UNIVERSITY OF MICHIGAN HEALTH SYSTEMS, CANTON, MI, [4]University of Michigan, Ann Arbor, MI

Purpose

Implementing 3D models in pre-operative planning is a non-standardized practice because of both the novelty and extensive computational resources required. In absence of an established model, we have demonstrated the usage of a low-resource 3D visualization tool for procedural planning. These interactive models optimize visual fidelity and clinical utility while minimizing file size and computational resource requirements. We hope to demonstrate the versatility of low-resource 3D visualization for neuroanatomical operative navigation, patient position, and pathology delineation.

Materials and Methods

3D acquisitions including rotational angiography axial reconstructions, MRI, and CT/CTA are registered using 3D Slicer. Models are constructed through Vitrea using segmentation with thresholding/region growing and exported as STL files. Files are imported to 3D Slicer for registration. Blender is used to combine the registered STL files into a comprehensive 3D model which is uploaded to a web-based viewing platform, Sketchfab. These 3D models are easily accessed by scanning the QR codes with any modern mobile device.

Results

Patient A with olfactory groove meningioma, with arterial supply from the ethmoidal and recurrent meningeal branches of the ophthalmic arteries as well as minor parasitized arterial feeders from the left anterior and middle cerebral arteries. A 3D model was created from angiography, MRI, and CT. Virtual pterional craniotomy was performed on the 3D model and additional extended exposures are displayed in a translucent manner including medial, temporal, and orbitozygomatic extensions. The model was then rotated in a surgical view for optimal visualization. Patient B with left L4 spinal dural arteriovenous fistula. The angiographic images were registered to CT L-spine to create a comprehensive model. Virtual L4 laminectomy was performed, and additional extended exposures are displayed in a translucent manner including L3 laminotomy, L5 laminotomy, and left medial L3-5 facetectomy.

Conclusions

These models concatenate structures that are typically visualized on different modalities to reveal anatomic relationships, i.e. vessels (best visualized on angiography) can be seen in relationship to tumor (best visualized on MRI) and bone (best visualized on CT). Additionally, virtual surgical exposures can be performed to reveal the best surgical approach in a fashion that is intuitive to neurosurgeons.

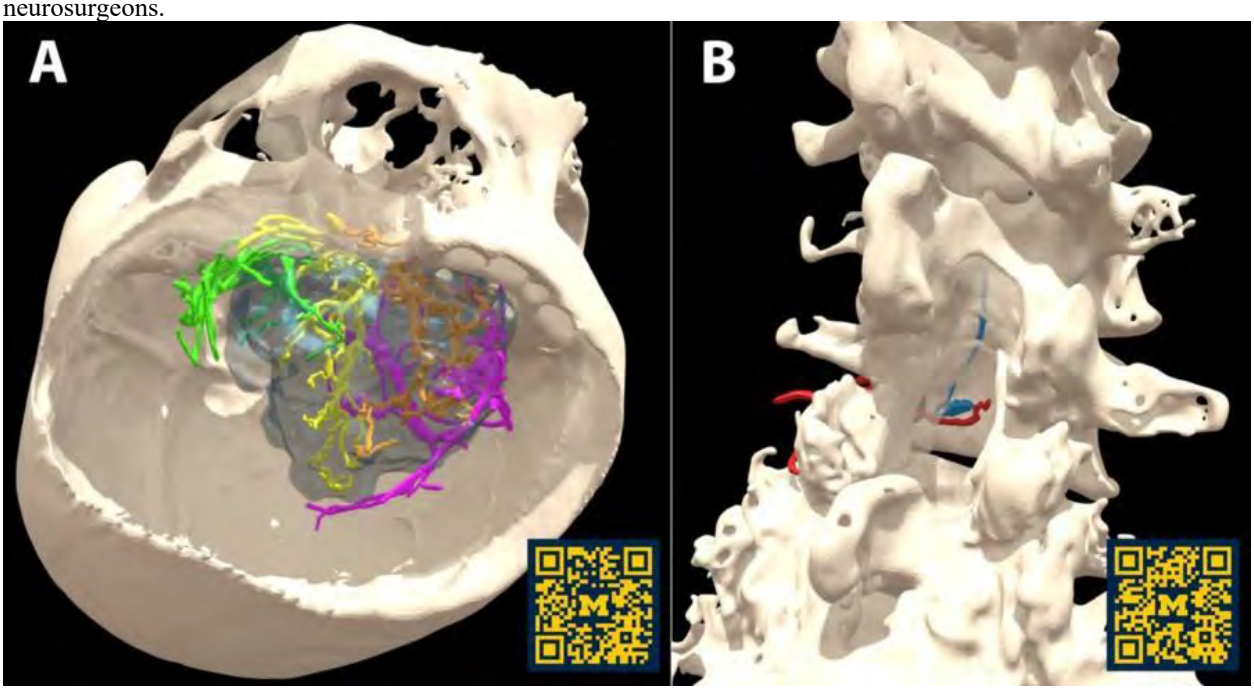

(Filename: TCT_1031_ASNR23ABSTRACT.jpg)

507

Artificial Intelligence Application in Skull Bone Fracture with Segmentation Approach

C Lu[1], W Lin[1], K Kuo[2]

[1]Kaohsiung Chang Gung Memorial Hospital, Kaohsiung, Taiwan, [2]Far Eastern Memorial Hospital, Taipei, Taiwan

Purpose

To develop a skull fracture AI model, which can autonomically perform binary classification and offer a segmentation AI mask on emergent cranial computed tomography (CT), offer screening supports, improve diagnostic loading, improve accuracy and clinical outcome.

Materials and Methods

This multi-center study was performed with the cooperation of two medical centers in Taiwan. Brain ERCT from Jan 1st, 2010, to Jan 14th, 2020, were retrospectively reviewed (131410 brain CT report pools). 125000 CTs were reported fracture-negative, and 5281 CTs were reported positives. The other 1129 CTs reported without the keyword "fracture" were also taken as negative. An independent dataset, including randomly selected 170 fracture-positive and 501 fracture-negative cases was prospectively collected for the testing dataset. Model 1 was trained using 1499 cases with training and validation datasets at a ratio of 1:1. Model 2 was trained in addition to "Hard negative cases" (post-craniectomy, atypical suture lines). Two denoising rules were applied to reduce the false positive rate. For the testing dataset (170 (+) and 501(-) cases), the reference standards were retrospectively reviewed and manually per patient labeled by 3 radiologists. Ground truth for segmentation was per-slice labeling using the tool of image annotation software (goman_assign). Confusion matrices and Dice coefficient scores were obtained for the models' binary classification and segmentation performance. A two-session observer study was conducted to compare the diagnostic performances of human readers before and after AI assistance. Confusion matrices and diagnostic duration were compared.

Results

Compared to Model 1, Model 2 has slightly elevated specificity (0.87 to 0.90) but marked decreased sensitivity (0.94 to 0.79). The false positive rate decreased after applying denoising rules. The best-performing combination is Model 1 plus Rule B (sensitivity 0.91, specificity 0.99, DICE 0.63). In the observer study, with the model's assistance, accuracy improvement was observed from 88.7% to 95.3%, and diagnostic duration decreased significantly from 48 ± 18.53 seconds/case to 30.44 ± 10.78 seconds/case (p=0.003).

Conclusions

The skull fracture detecting model using the segmentation approach achieved good sensitivity, specificity, and DICE score. AI model improved the performance of radiologists and clinical physicians and reduce the diagnostic duration. We believe the model is helpful in improving general accuracy and diagnostic environment.

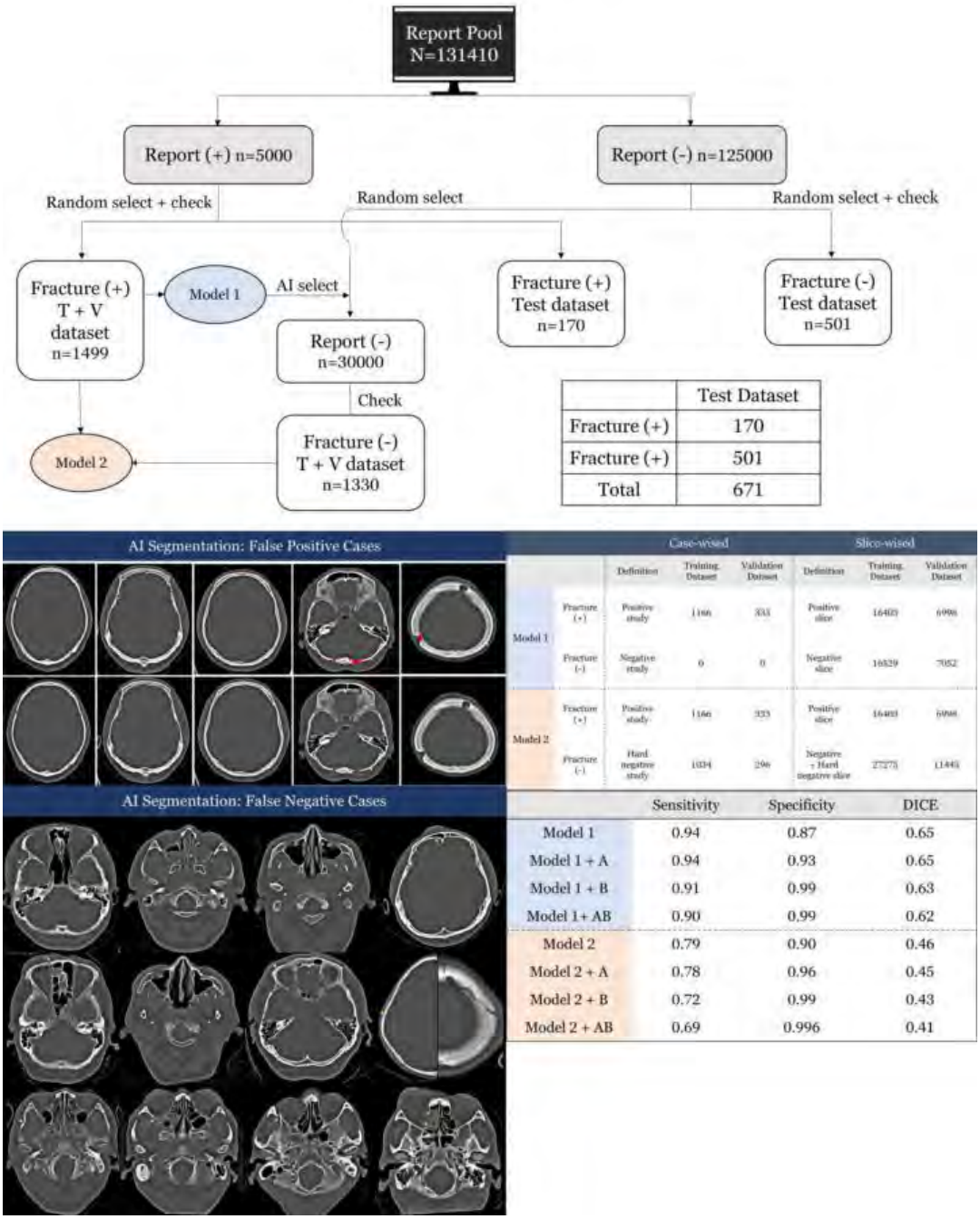

	Test Dataset
Fracture (+)	170
Fracture (+)	501
Total	671

	Sensitivity	Specificity	DICE
Model 1	0.94	0.87	0.65
Model 1 + A	0.94	0.93	0.65
Model 1 + B	0.91	0.99	0.63
Model 1+ AB	0.90	0.99	0.62
Model 2	0.79	0.90	0.46
Model 2 + A	0.78	0.96	0.45
Model 2 + B	0.72	0.99	0.43
Model 2 + AB	0.69	0.996	0.41

(Filename: TCT_507_ASNRimage.jpg)

897

Evaluation of Artificial Intelligence in Identifying Arterial Large Vessel Occlusion in the Head and Neck

M Gedrich[1], A Shahzad[2], H Shaikh[1], K Kazmi[1]

[1]Cooper University Health Care, Camden, NJ, [2]Cooper Medical School At Rowan University, Camden, NJ

Purpose

As medical imaging studies increase over the years, it is important to identify and prioritize studies with positive findings to aid clinicians in treating patients. Earlier interventions in cases of large vessel occlusion have been associated with better outcomes. Artificial intelligence (AI) is a useful tool for screening studies and notifying physicians. The purpose of this study is to evaluate the positive predictive value (PPV) and speed of AI in identifying large vessel occlusion within the head and neck arterial vasculature.

Materials and Methods

Computed tomography angiograms (CTA) and venograms (CTV) evaluated by Viz.ai™ software from April 2020 through August 2021 at Cooper University Hospital were included. Studies that were negative for arterial large vessel occlusion, as determined by AI, were excluded. The primary outcome was the PPV, determined by the comparison of studies marked positive by the software to the associated radiologist report. The secondary outcome was time-to-notification of the positive study by AI versus reporting time by

radiologists, as noted in dictation reports. Studies with no radiologist reporting time were excluded from the secondary outcome analysis.
Results
Of the 3,174 studies analyzed by AI, 299 studies were reported as positive for large vessel occlusions. Of the included studies, 156 were conducted on males and 143 on females. The median age of the study group was 63 (interquartile range, 51 to 75). Ninety-nine studies were positive for occlusions yielding a PPV of 33%. An additional fifty-six (19%) studies that were reported as positive by AI demonstrated moderate or severe stenoses rather than true occlusion. If those studies are added, the PPV increases to 52%. The median AI reporting time was 9 minutes (Interquartile range, 8 to 10) and the median radiologist reporting time was 31 minutes (interquartile range, 17 to 50). A total of 196 studies did not have a radiologist reporting time and were excluded from the secondary outcome analysis.
Conclusions
In our study, AI was significantly less accurate than the radiologist at detecting true large vessel occlusions. It did detect additional moderate to severe stenoses, which may be clinically important. It did also give faster alerts potentially providing utility as a screening tool, especially in high acuity, large volume centers. Therefore, it may be used to help radiologists and clinicians prioritize studies to decrease the time-to-intervention and improve patient outcomes.

578

Investigating the gene-brain relationship in heritable autism using transport-based learning

S Kundu[1], H Sair[2], P Mukherjee[3], G Rohde[4]
[1]The Johns Hopkins Hospital, Baltimore, MD, [2]Johns Hopkins University School of Medicine, Baltimore, MD, [3]UCSF, San Francisco, CA, [4]University of Virginia, Charlottesville, VA

Purpose
Copy number variation (CNV) at the 16p11.2 genetic locus is one of the most common causes of heritable autism and other neurodevelopmental disorders. However, its influence on brain morphology is largely unknown. This research investigates the gene-brain link using transport-based learning.
Materials and Methods
206 subjects with 16p11.2 CNVs (118 control, 48 deletion, and 40 duplication carriers) were selected from the Simons Variation in Individuals Project. Corresponding high-resolution T1 magnetic resonance images were analyzed. To correct for brain volume, images were affine registered and segmented into gray matter (GM) and white matter (WM) images. The structural variation linked to 16p11.2 CNVs was discovered using transport-based morphometry (TBM) in a fully automated manner. First, mass-preserving mappings were generated with respect to a common reference for each image. Then, 1000 iterations of stratified 10-fold cross-validation were used to train a penalized linear discriminant analysis (pLDA) classifier in the transport space. TBM's ability to visualize the macrostructural differences driving CNV discrimination through inverse transformation adds explainability to traditionally opaque machine learning models and is a key advance.
Results
The scatter plots in Figure 1 show that CNVs were highly separable in the TBM space. On unseen data, TBM enabled WM and GM discrimination of CNVs with 94.6% accuracy (kappa 0.91) and 88.5% accuracy (kappa 0.80), respectively. In contrast, age, gender, and brain volume enabled 61.6% accuracy (kappa 0.17). Next, visualizing the structural variation driving classification ability demonstrates reciprocal changes among duplication and deletion carriers. Deletion carriers were associated with an overgrowth of WM/GM and duplication carriers with an undergrowth of WM/GM matter across all ages (Figure 1). Specifically, TBM-generated images demonstrated macrostructural variations in GM (insula, orbital frontal, and posterior cingulate) and for WM (frontoparietal, occipital, corpus callosum, and cerebellum).
Conclusions
We report near complete penetrance of 16p11.2 CNVs on brain structural variations, enabling almost complete separability of genotypic classes on unseen data. 16p11.2 CNVs exert a dose-dependent influence on the brain, resulting in reciprocal variations among duplication and deletion carriers. Finally, there is future potential of 3D TBM to enable discovery and visualization of gene, brain, and behavior relationships in myriad diseases.

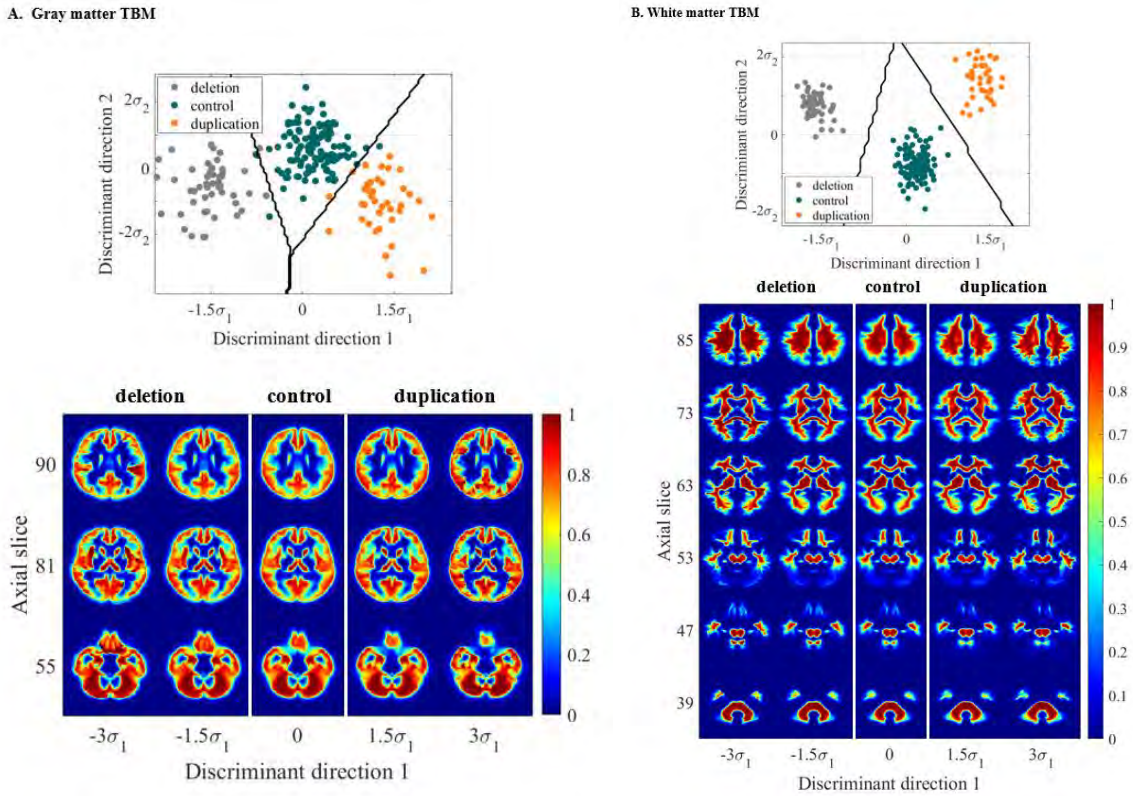

(Filename: TCT_578_ASNRFig1.gif)

1202

Longitudinal Changes of Opportunistically Assessed Vertebral BMD and Texture Features in Routine Clinical MDCT Using an Automated Segmentation Framework

J Bodden[1], M Dieckmeyer[2], E Burian[3], C Zimmer[4], J Kirschke[4], T Baum[5]

[1]Klinikum rechts der Isar, Technical University of Munich, Munich, Germany, [2]Klinikum rechts der Isar, Technical University of Munich, Bern, Bern, [3]Klinikum rechts der Isar, Munich, Germany, [4]Dept. of Neuroradiology, School of Medicine, Technical University of Munich, Munich, Germany, [5]Klinikum rechts der Isar, TU Munich, Munich, Bavaria

Purpose

To investigate longitudinal changes in thoracolumbar trabecular texture features (TFs) and volumetric bone mineral density (vBMD) at 6, 12, and 24 months in routine multidetector clinical computed tomography (MDCT) data in a single scanner setting.

Materials and Methods

Patients without bone diseases, who underwent two MDCT scans within 6 (n=13, 54-83 years, 7 females), 12 (n=73, 42-88 years, 26 females), or 24 months (n=26, 39-77 years, 10 females) were included. Vertebral body labeling and segmentation were performed using a convolutional neural network (CNN)-based framework, followed by asynchronous Hounsfield unit (HU)-to-BMD calibration with implemented correction for contrast phase. Trabecular vBMD and 6 TFs (Varianceglobal, Entropy, Short-run Emphasis (SRE), Long-run Emphasis (LRE), Run-length, Nonuniformity (RLN), and Run percentage (RP)) were extracted from the middle (T5-8) and lower thoracic (T9-12) and lumbar (L1-5) vertebrae. Relative annual changes in TFs and vBMD were calculated. Paired t-tests were used to test the statistical significance of the changes. RMSCV and RMSE were calculated as measures of variability.

Results

vBMD showed a nonsignificant decrease of approximately 2%/year in females. Entropy, SRE, RLN and RP increased at 12 and 24 months ($P<0.001$), while LRE decreased markedly (%/year, -1.35 - -2.11, $P<0.001$ and -0.90 - -1.02, $P<0.001$, respectively). vBMD variability exceeded that of TFs (L1-5, RMSCV=3.98% vs. RMSCV=0.02-2.55%).

Conclusions

Opportunistic assessment of longitudinal vBMD and TF changes is feasible in a single scanner setting. TF changes over 12 and 24 months co-occur with trabecular vBMD-loss and may reflect deterioration of bone microarchitecture due to aging.

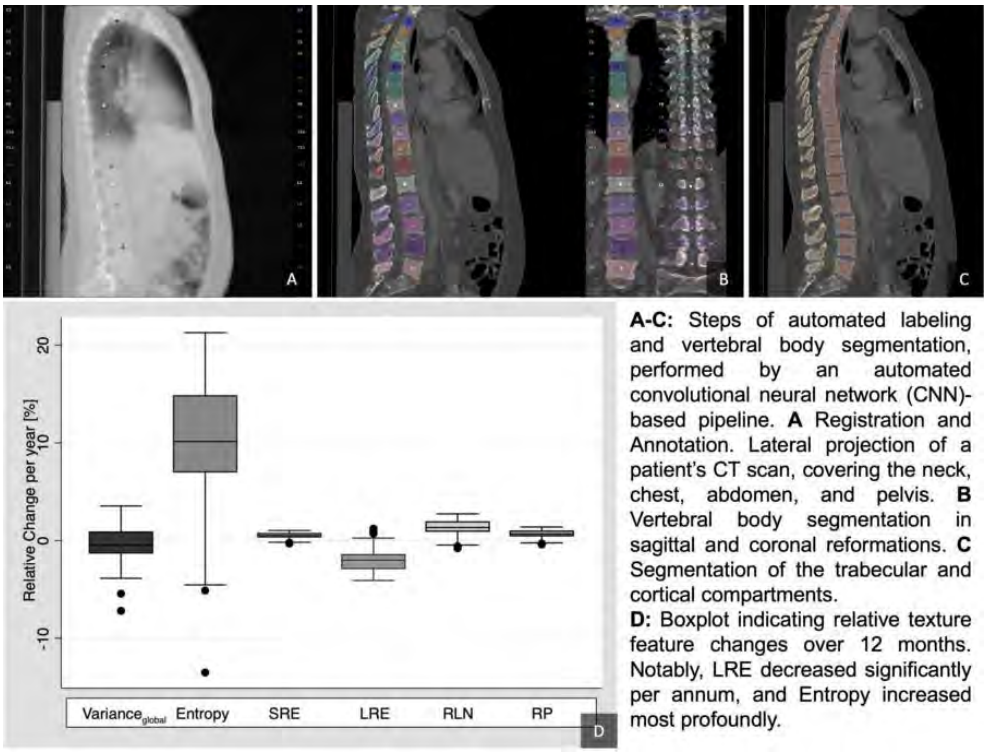

A-C: Steps of automated labeling and vertebral body segmentation, performed by an automated convolutional neural network (CNN)-based pipeline. **A** Registration and Annotation. Lateral projection of a patient's CT scan, covering the neck, chest, abdomen, and pelvis. **B** Vertebral body segmentation in sagittal and coronal reformations. **C** Segmentation of the trabecular and cortical compartments.
D: Boxplot indicating relative texture feature changes over 12 months. Notably, LRE decreased significantly per annum, and Entropy increased most profoundly.

(Filename: TCT_1202_figure_abstract_tf.jpg)

516

Machine Learning Based Determination of Ischemic Core Probability using CT Perfusion: A Multicenter Study

P Shahrouki[1], H Zhang[1], E Tavakkol[1], J Polson[1], J Fifi[2], A Doshi[3], A Vagal[4], P Khatri[5], A Srinivasan[6], M Bahr-Hosseini[1], R Jahan[1], g duckwiler[7], C Arnold[1], J Saver[1], J Mocco[8], D Liebeskind[9], K Nael[1]

[1]UCLA, Los Angeles, CA, [2]Icahn School of medicine at Mount Sinai, New York, NY, [3]Mount Sinai Hospital, New York, NY, [4]University Of Cincinnati Medical Center, Cincinnati, OH, [5]University of Cincinnati, Cincinnati, OH, [6]University of Michigan, Ann Arbor, MI, [7]ucla, Los Angeles, CA, [8]Icahn School of Medicine at Mount Sinai, New York, NY, [9]UCLA Stroke Center, Los Angeles, CA

Purpose

Estimation of ischemic core volume on CT perfusion (CTP) remains challenging due to low signal to noise of CTP data and variability in reported thresholds. Utilizing machine learning, we sought to establish CTP thresholds and provide a stepwise decision tree in determination of ischemic core probability.

Materials and Methods

In this retrospective multicenter study, patients with anterior circulation large vessel occlusions from 3 comprehensive stroke centers were included if they had baseline CTP, successful recanalization (TICI ≥ IIb), and follow up MRI. CTP analysis was performed using Olea Sphere (SP19, Olea Medical Solutions) by applying Bayesian probabilistic method to generate parametric maps including time to peak (TTP), mean transit time (MTT), relative cerebral blood flow (rCBF), relative cerebral blood volume (rCBV), and Delay (equivalent of Tmax in Bayesian model). Follow up MRI-DWI was used to draw infarction and non-infarction masks, followed by image coregistration to extract the corresponding voxels from baseline CTP. A leave-one-out cross-validation (LOOCV) analysis was performed to assess the binary outcome of voxel-based analysis (infarcted vs non-infarcted).

Results

Eighty-one patients (42 males; mean age 67.4 ±17.3) were included. The highest performing models were achieved by 1) step-wise and serial combination of Delayed (thresholds of 0.46 and 1.1s) and rCBF (30%) with AUC/sensitivity/specificity/accuracy (0.75/0.74/0.73/0.75) (Figure), and 2) step-wise combination of MTT (7.1s) and Delayed (1.7s) with AUC/sensitivity/specificity/accuracy (0.76/0.75/0.75/0.76).

Conclusions

Results show that using ML approach and LOOCV analysis, bayesian-based CTP thresholds from 2 parameters used in a step-wise decision tree can achieve an accuracy of 76% in predicting probability of ischemic core.

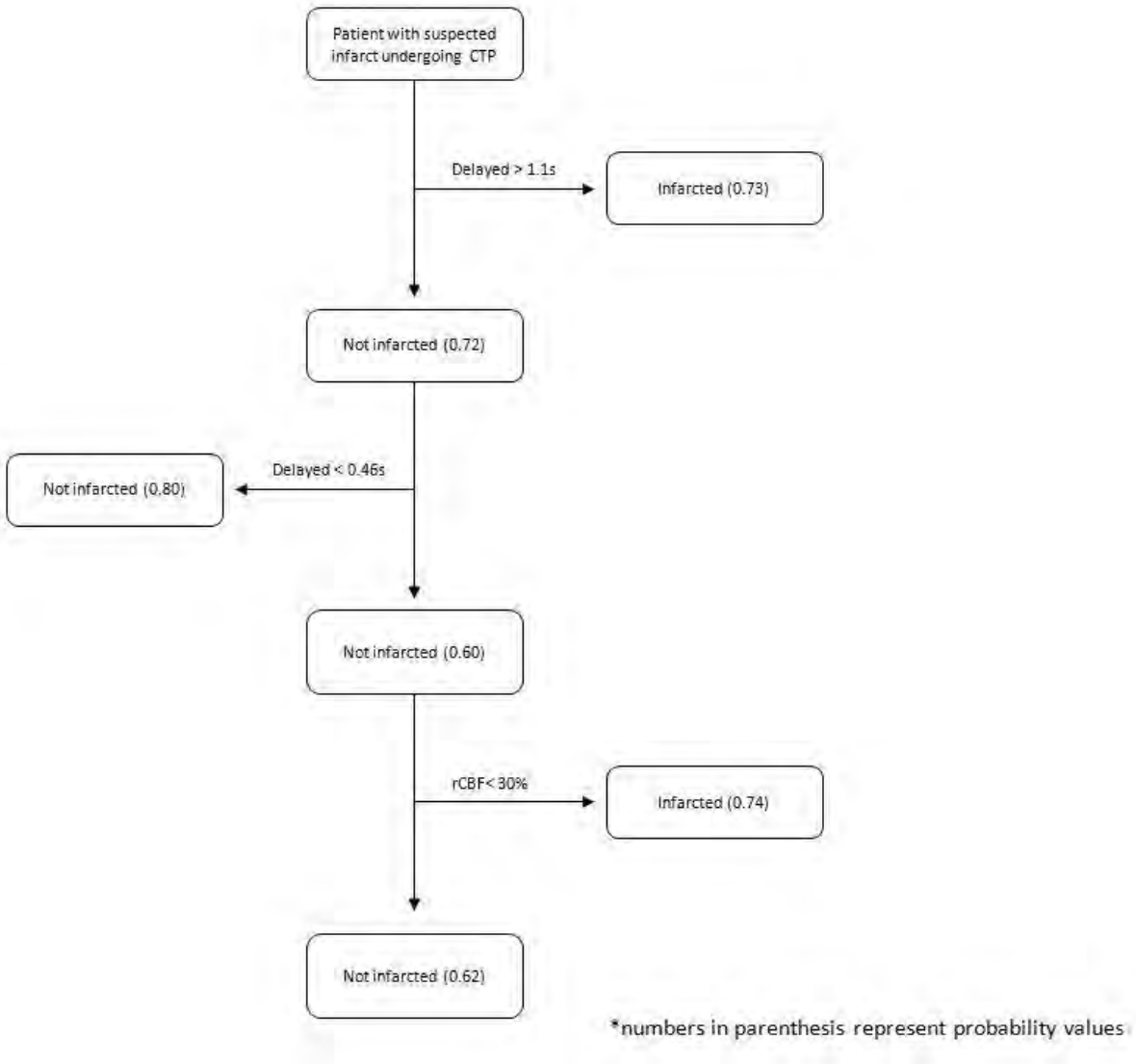

(Filename: TCT_516_ASNRworkflowabstractfigure.JPG)

1154

Multimodal Deep Learning for Predicting Cavernous Sinus Invasion

K Nernekli[1], B Sozer[2], L Adams[1], K Asmaro[3], K Yeom[1], JC Fernandez-Miranda[1]

[1]Stanford University, Palo Alto, CA, [2]Ankara University, Ankara, Ankara, [3]Henry Ford Hospital, Detroit, MI

Purpose

Cavernous sinus invasion (CSI) of pituitary adenoma can lead to incomplete resection, failure of endocrinological remission, and a higher tumor recurrence rate. Therefore, precise approaches toward CSI beyond Knosp grading may help guide treatment strategies and patient counseling. We propose utilizing both clinical and MRI data to train a robust deep learning (DL) model that can learn the complex dynamics behind this disease. Overall, we develop a multimodal DL approach that increases CSI prediction accuracy compared to Knosp grading(1).

Materials and Methods

135 patients (median age = 50.14±15.56; 1.05:1 male to female ratio) with pathologically confirmed pituitary adenoma were retrospectively identified. High-resolution, coronal T1-contrast enhanced pituitary MR images were used. The study cohort was separated into training (n=101) and testing (n=34) sets. Bounding box applied over the pituitary gland-cavernous sinus complex served to generate input image data. A 2D ResNet50V2 convolutional neural network (CNN) was used as the base architecture for the DL model. Intraoperative inspection of the cavernous sinus and histopathologic analysis of the cavernous sinus medial wall served as ground truths for CSI. Clinical data consisting of pathology, clinical diagnosis, age, gender, Knosp score were fed to a dense neural network, and the final decision was weighted between CNN and dense clinical neural network predictions.

Results

The receiving operating characteristic (ROC) and precision-recall (PR) curves were used to assess model performance. The model's average area under (AU) ROC was 80.6% compared to Knosp AU ROC %60. The model AU PR curve was 85.8% compared to Knosp AU PR curve of 66.3%. The sensitivity and F1 score of the model were 76% and 0.77, respectively, compared to Knosp

sensitivity and F1 scores of %40 and 0.50. The variables were further analyzed by multiple correspondence analysis which showed model's average was related to invasion more than Knosp Grading.
Conclusions
Inherent challenges exist regarding the pre-operative evaluation of CSI of pituitary adenoma on MRI and there is a need for supplementary methods other than variable interobserver classifications. Our study demonstrates the potential for multimodal deep learning methods that combine MRI and clinical data to predict CSI of pituitary adenomas. A future multi-site study that explores DL model generalizability could further examine the utility of integration of such DL methods in the clinical workflow

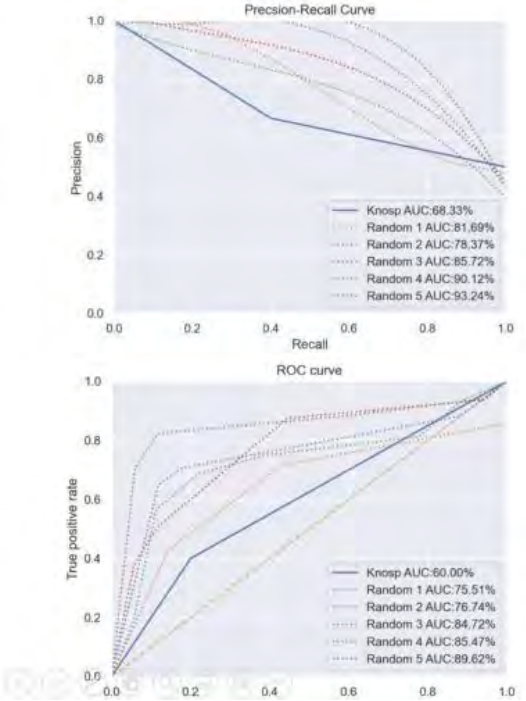

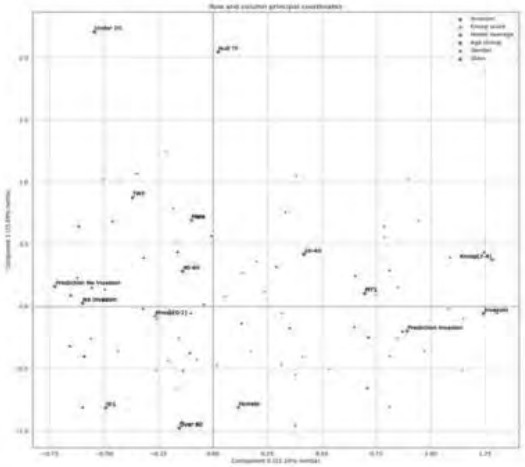

	Sensitivity	Specificity	F1 Score	Precision
Test Fold 1	0.63	0.57	0.67	0.62
Test Fold 2	0.73	0.78	0.71	0.73
Test Fold 3	0.86	0.61	0.80	0.86
Test Fold 4	0.82	0.82	0.82	0.82
Test Fold 5	0.88	0.88	0.85	0.86
Model Average	0.76	0.73	0.77	0.78
Knosp Score	0.4	0.8	0.5	0.66

(Filename: TCT_1154_Screenshot_1.jpg)

1092

Outcome Prediction in Patients with Acute Ischemic Stroke by fusing MRI-based Deep Learning and Clinical Information

Y Liu[1], J Ouyang[1], Y Yu[1], D Liebeskind[2], M Lansberg[3], G Albers[3], G Zaharchuk[1]
[1]Department of Radiology, Stanford University, Stanford, CA, [2]Department of Neurology, UCLA, Los Angeles, CA, [3]Department of Neurology, Stanford University, Stanford, CA

Purpose
The goal of this study is to predict 90-day modified Rankin scale (mRS) in AIS patients by combing deep learning model of follow-up DWI images and clinical information from the acute time period.
Materials and Methods
Data Acquisition and Preprocessing: 545 AIS patients with MRI in the 1-7 day time period following stroke and 90-day mRS were included. Specifically, 438 patients from four major multi-center clinical trials (114 patients from iCAS, 93 patients from DEFUSE2, 112 patients from CRISP, and 119 patients from DEFUSE3) were used to develop the proposed fused prediction workflow. An external dataset of 107 AIS patients scanned at the UCLA Medical Center were used to test the models. Method: The complete fused workflow consists of two sub-models, which are called the MRI-based Deep Learning model (MRI-DL) and the clinical model. In the MRI-DL, 16 slices with the largest probability of having the stroke lesion in each patient's follow-up DWI were firstly selected by a slice-selection DL model (SSDL), which were then fed into an outcome prediction (OPDL) deep learning model for the mRS prediction. SSDL is comprised of a spatially attentive deep residual network based on ResNet50 [1]. In OPDL, a 2.5D ResNet50 served as the backbone and the input dropout with a rate of 0.8 was added in front of the backbone. A support vector machine (SVM) model based on common patient biomarkers including age, baseline NIHSS, history of hypertension and diabetes, and pre-stroke mRS served as the clinical model. Ensemble stacking was employed to fuse the MRI-DL and the clinical model to yield the final mRS score prediction, as a continuous variable, which was rounded to the nearest integer number (0-6) to perform multinominal prediction of each patient's mRS score. The AUC for the most clinically relevant binary threshold of mRS>2 was obtained by thresholding at a predicted score of 2.5.
Results
On the external test set, 67%±2% of predictions of specific mRS scores made by the proposed fused model were within ±1 category, which was higher than 62±2% ($p<0.05$) for MRI-DL and 56±2% ($p<0.05$) for the clinical model. In addition, the fused method achieved an AUC of 0.81 for the most clinically relevant threshold of mRS >2, which was higher than that of MRI-DL (AUC = 0.79; $p=0.64$) and the clinical model (AUC = 0.74; $p<0.05$).

Conclusions
A deep learning-based fusion model combining MRI and clinical information from the first week after AIS has the potential to predict patient outcome at 90 days.

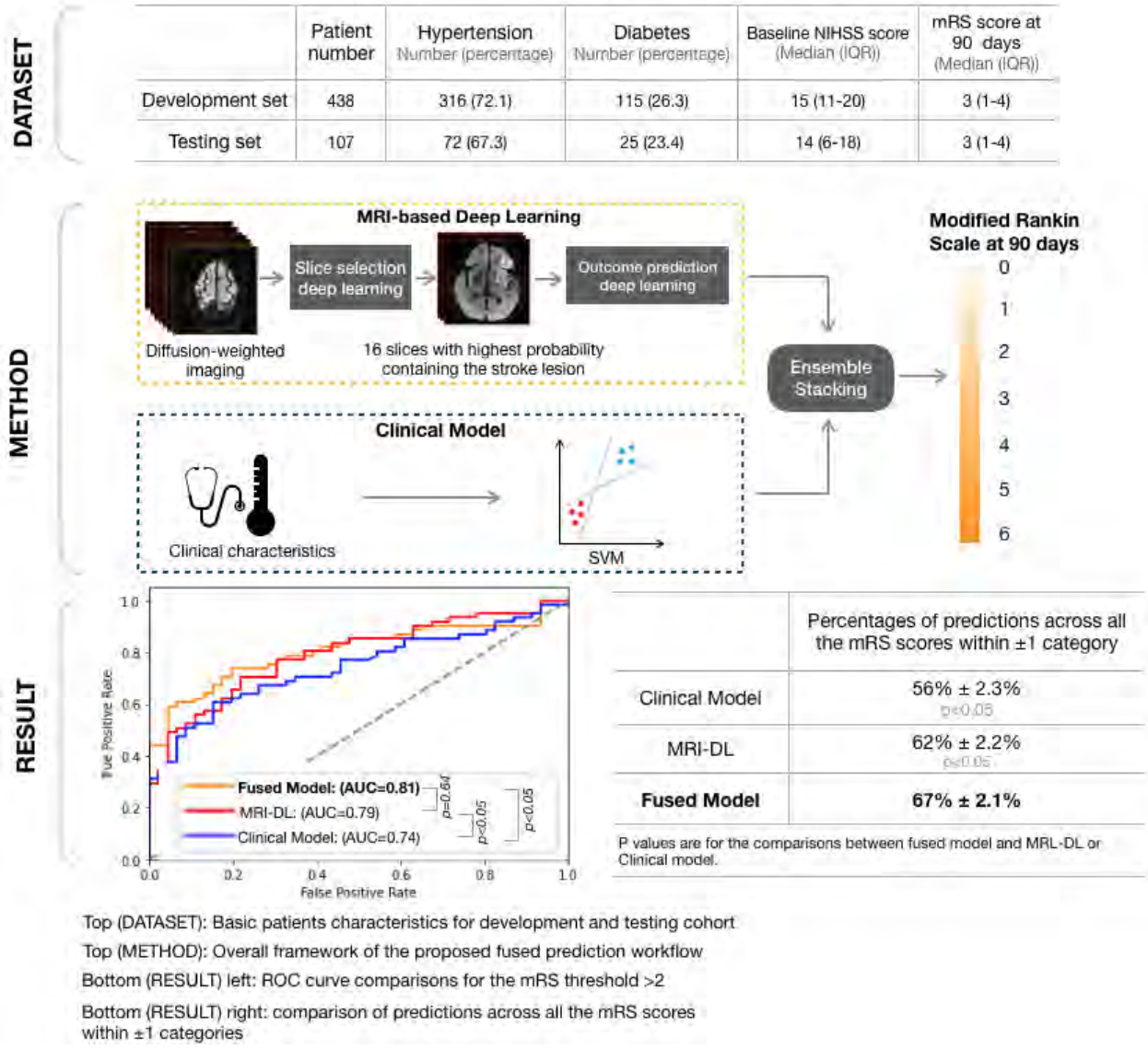

	Patient number	Hypertension Number (percentage)	Diabetes Number (percentage)	Baseline NIHSS score (Median (IQR))	mRS score at 90 days (Median (IQR))
Development set	438	316 (72.1)	115 (26.3)	15 (11-20)	3 (1-4)
Testing set	107	72 (67.3)	25 (23.4)	14 (6-18)	3 (1-4)

	Percentages of predictions across all the mRS scores within ±1 category
Clinical Model	56% ± 2.3% p<0.05
MRI-DL	62% ± 2.2% p<0.05
Fused Model	**67% ± 2.1%**

P values are for the comparisons between fused model and MRL-DL or Clinical model.

Top (DATASET): Basic patients characteristics for development and testing cohort
Top (METHOD): Overall framework of the proposed fused prediction workflow
Bottom (RESULT) left: ROC curve comparisons for the mRS threshold >2
Bottom (RESULT) right: comparison of predictions across all the mRS scores within ±1 categories

(Filename: TCT_1092_figure1.jpg)

159

Prediction of Spontaneous Basal Ganglia Hematoma Expansion; Clinical Data Versus Radiology signs Versus Radiomics; A Pilot Study

A Rezaei[1], R Godwin[2], M Tanwar[1], V Prattipati[3], A Singhal[1], M Sotoudeh[4], R Shahidi[5], P Shobeiri[6], M Alizadeh[7], H Sotoudeh[3]
[1]University of Alabama at Birmingham, Birmingham, AL, [2]University of Alabama at Birmingham (UAB), Birmingham, AL, [3]UAB, Birmingham, AL, [4]Azad University of Arak Branch, Arak, Iran, Arak, Arak, [5]School of medicine, Bushehr university of medical sciences, Bushehr, Iran, Bushehr, Bushehr, [6]School of Medicine, Tehran University of Medical Sciences, Tehran, Iran, Tehran, Tehran, [7]Iran University of Medical Sciences, tehran, Tehran

Purpose
Prediction of the hematoma expansion (HE) of spontaneous basal ganglia hematoma (SBH) from the first non-contrast CT can improve the patient outcome. This study has been designed to compare the performance of "Radiomics analysis," "radiology signs," and "clinical-laboratory data" for this task.
Materials and Methods
We collected clinical, demographic, and laboratory from medical records in patients with SBH. CT images were reviewed for the presence of radiologic signs, including Black hole, Blend, Swirl, Satellite, and Island signs, which may predict the hematoma expansion. Radiomic features from the SBH on the first brain CT were extracted, and the most predictive features were selected. Different machine learning models were developed based on clinical, laboratory, and radiology signs and selected Radiomic features to predict HE.

Results
The dataset used for this analysis included 116 patients with SBH. Among different models and different thresholds to define hematoma expansion (10%, 20%, 25%, 33%, 40%, and 50% volume enlargement thresholds), the Random Forest based on ten selected Radiomic features achieved the best performance (for 25% hematoma enlargement) with AUC of 0.9 on the training dataset and 0.89 on the test dataset. The models based on clinical-laboratory and radiology signs had deficient performance (AUCs about 0.5-0.6).
Conclusions
Based on our findings, Radiomic models outperform the radiology signs, clinical, laboratory, and demographic features to predict the HE. A twenty-five percent increase in the hematoma volume is likely the best threshold to predict HE by machine learning and Radiomics. The random forest models are probably the best models for this task.

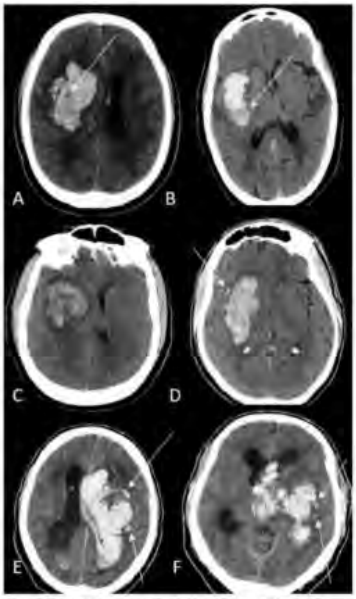

Figure 1. Radiology signs A.Black hole sign, B.Blend sign, C.Swirl sign, D.Satellite sign, E and F.Island sign

Definition of HE by volume enlargement	Best Model	AUC	Accuracy
10%	LR	0.54	63%
20%	KNN	0.5	67%
25%	SVM	0.5	78%
33%	SVM	0.46	83%
40%	SVM	0.46	87%
50%	LR	0.51	87%

Table 1. The performance of machine learning models to predict HE from 5 radiology signs of the baseline CT.

Definition of HE by volume enlargement	Best Model	AUC	Accuracy
10%	KNN	0.58	63%
20%	LR	0.54	61%
25%	GB	0.66	76%
33%	SVM	0.61	83%
40%	SVM	0.6	87%
50%	Ada Boost	0.6	83%

Table 2. the performance of different machine learning models to predict different thresholds of HE from the clinical data at the time of admission.

Definition of HE by volume enlargement	Best Model	AUC	Accuracy
10%	KNN	0.58	63%
20%	NN	0.53	66%
25%	GB	0.63	75%
33%	SVM	0.57	83%
40%	NN	0.57	81%
50%	NN	0.62	83%

Table 3. The performance of different machine learning models to predict different thresholds of HE from the "clinical" + "Radiology Signs" at the time of admission.

Definition of HE by volume enlargement	Best Model	AUC (train,test)	Accuracy (train,test)
10%	RF	0.759, 0.789	0.708, 0.792
20%	GBS	0.881, 0.815	0.824, 0.875
25%	RF^	0.9, 0.89	0.804, 0.875
33%	RF	0.858, 0.725	0.827, 0.833
40%	LGBM	0.711, 0.81	0.837, 0.792
50%	LR	0.719, 0.556	0.73, 0.833

Table 4. The performance of the Radiomic models to predict the different thresholds of HE.

(Filename: TCT_159_Abstractimage.jpg)

1218

Predictive modeling of acute stroke admissions based on meteorological weather systems to improve clinical resource allocation

M MAROS[1], N Santhanam[2], H Wenz[3], F Siegel[4]
[1]Heidelberg University, Medical Faculty Mannheim, Mannheim, Baden-Wuerttemberg, [2]Medizinische Fakultät Mannheim der Universität Heidelberg, Mannheim, Privatkunde, [3]Universität Heidelberg, Mannheim, Germany, [4]Medical Faculty Mannheim, Heidelberg University, Mannheim, Baden-Württemberg

Purpose
Due to global warming, weather variations and fronts are becoming more extreme and increasingly relevant stressors for the human body, which can cause cardiovascular stress and in combination with personal risk factors might lead to acute cerebrovascular disease [1-5]. Furthermore, extreme weather-related spikes in emergency admissions can overwhelm the healthcare providers [2,3]. Therefore, we investigated whether machine learning-based models can be utilized to predict the number of daily stroke admissions based on recent weather systems.
Materials and Methods
7914 (male: 4244, 53.6%) patients diagnosed with cerebral infarction (2015/01/01-2021/12/31) were extracted from the local data integration center (DIC) of the University Medical Center Mannheim, Heidelberg University with a catchment area of >500.000 patients in a ~50 km (30-40 mi) radius. Comprehensive weather parameters such as air temperature, humidity, pressure, sunshine duration and wind speed were obtained from the German Weather Service. Additionally, complex biometeorological features (heat- and cold-stress) [2,3] and atmospheric fronts (including lagged values from 3- up to 7-days) were also derived from these parameters. Patient-level clinical and geospatial weather data were matched based on the patient's location and time of admission to the hospital. Autoregressive neural network (ANN) and boosted trees (XGB) were fitted using a stratified cross-validation setting to predict the total number of ischemic stroke admissions per day as predictor value either as regression or multi-class classification (low: <3; moderate 3-7; high 7-10 and very high >10 admissions per day) models.
Results
The ANN model achieved a mean absolute error of 0.728 and Root mean square error of 0.926. For the daily model, mean air temperature was significantly negatively associated with the number of stroke cases resulting in 2.7% increased risk of stroke admission for each 1°C decrease in ambient temperature. This effect stayed significant to up to 5 days. The accuracy of the XGB

classification model on test data was 61.5%. We could quantify the effect of weather and seasonality (R^2~12%), which can be incorporated into risk scores and should be adjusted for in patient level models accordingly.
Conclusions
We could demonstrate highly significant associations between complex weather systems and the number of stroke admissions, which can be potentially exploited for resource allocation and optimized therapy planning of neuro/radiological emergencies.

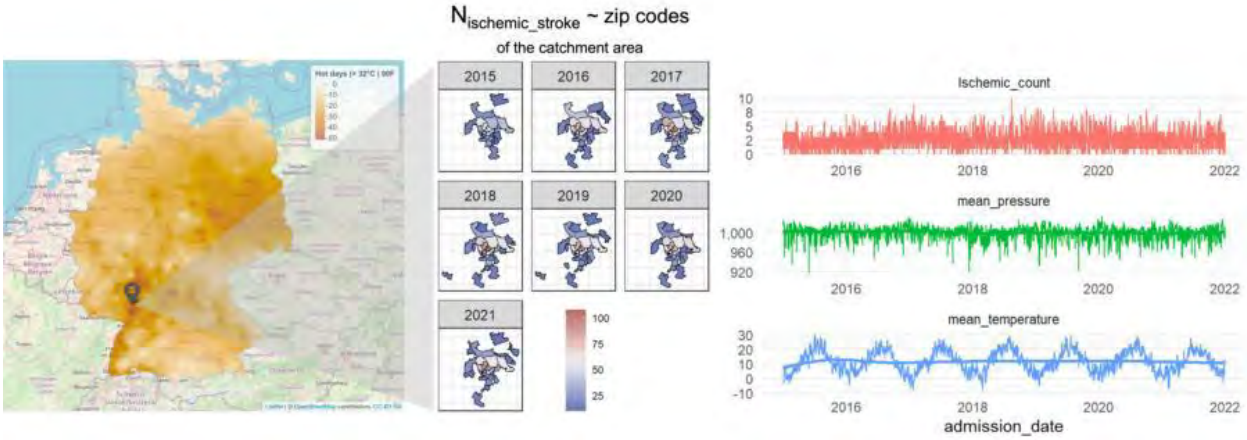

(Filename: TCT_1218_20221115-ASNR2023-FigureHeatmap-uploaded.jpg)

1322

Sequence selection for training neural network in brain metastasis segmentation on brain MRI

Y Yu[1], G Zaharchuk[2], J Rudie[3], A Rauschecker[1]
[1]UCSF Radiology, San Francisco, CA, [2]Stanford University, Stanford, CA, [3]Scripps clinic, San Diego, CA

Purpose
Accurate auto-segmentation of brain metastases could improve clinical efficiency and accuracy for radiation therapy planning. Previous studies showed variance in neural network performance on brain metastasis segmentation[1,2]. We aimed to investigate the importance of various MRI sequences routinely obtained in metastases studies on performance of an automated metastasis segmentation algorithm.
Materials and Methods
We used publicly available BrainMetShare dataset[3], which contained 156 patients (105 for training and 51 for testing) with brain metastasis and pre- and post-contrast gadolinium T1 -weighted 3D fast spin echo (CUBE), postgadolinium T1 -weighted 3D axial IR-prepped FSPGR (BRAVO), and 3D CUBE fluid attenuated inversion recovery (FLAIR). Three variations of the dataset were created: all available sequences, dataset without BRAVO, and dataset without BRAVO and FLAIR. The nnUNet[4] with default setting was used for training on the three dataset variations. Dice score coefficient, sensitivity, and positive predictive value (PPV) were calculated for voxelwise and lesionwise analyses comparing to expert human reference standard segmentations. T-tests and Mann-Whitney-U tests were used to compare models.
Results
Compared to a model trained without the post-gadolinium BRAVO sequence, the model trained with all available sequences has significantly higher sensitivity (77±42% vs 72±45%, p=0.02) and dice score coefficient (0.60[IQR 0.16-0.72] vs 0.43[IQR 0-0.64], p<0.001), similar positive predictive value (81±39% vs 79±40%, p=0.8). This benefit of the BRAVO sequence was more pronounced for small lesions (<3 mm diameter) (sensitivity 73±44% vs 66±47%, p<0.001; DSC 0.56 [IQR 0-0.68] vs 0.35 [IQR 0-0.57], p<0.001). However, there was no difference in performance between the model trained with and without FLAIR (sensitivity 72±45% vs 69±46%, p=0.50, DSC 0.43[IQR 0-0.64] vs 0.43 [IQR 0-0.64], p=0.66).
Conclusions
Training on data with a post-gadolinium BRAVO sequence outperformed the same model trained without BRAVO sequences, while the absence of the FLAIR sequence did not significantly impact model performance.

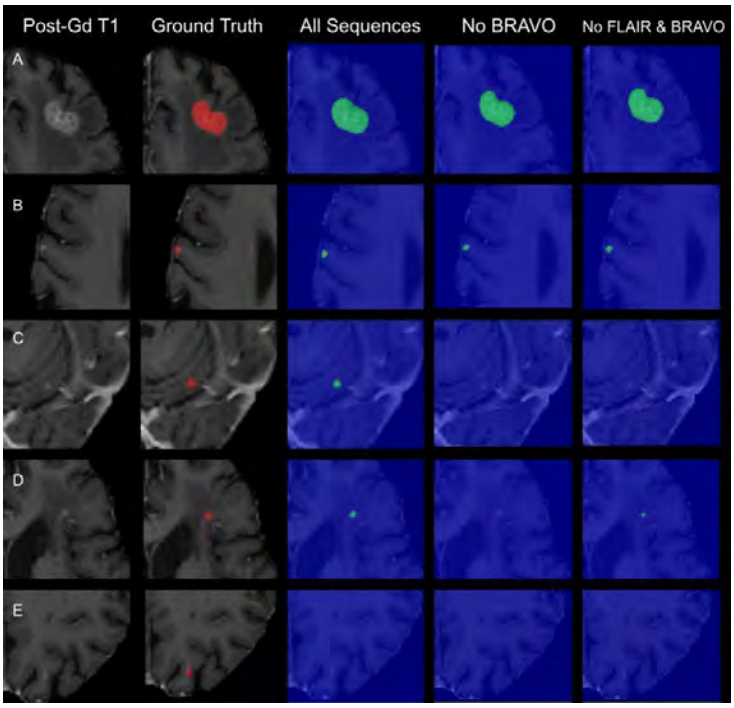

(Filename: TCT_1322_figure-sequence-compare.jpg)

Wednesday, May 3, 2023

1:15-2:15 PM

Scientific Abstract Session: Role of Functional/Advanced Imaging in Neuroradiology

371

Added Value of 64Cu/68Ga DOTATATE Brain PET/MRI in Clinical Practice

G Keir[1], J Rini[2], C Caravella[2], A Goenka[2], A FRANCESCHI[3]

[1]Northwell, Mineola, NY, [2]Northwell Health, New Hyde Park, NY, [3]Northwell Health, New York, NY

Purpose

Somatostatin receptors (SSTRs) are overexpressed in neuroendocrine tumors, and other tumors, including meningiomas. PET imaging with somatostatin analogue, TATE, radiolabeled with positron-emitting radionuclides, Ga-68 or Cu-64, via chelating agent DOTA (DOTATATE-PET), illustrates cell-surface expression of SSTRs. Due to its high sensitivity, DOTATATE-PET may detect small lesions that initially are overlooked on MRI, and may also detect more extensive disease, as MRI may be limited if lesions are infiltrative, trans osseous, or in the region of the skull base or cavernous sinus. In the post-treatment setting, DOTATATE-PET may differentiate residual disease from post-treatment changes more reliably than MRI.

Materials and Methods

In May 2022, we introduced a dedicated DOTATATE Brain PET protocol, replacing whole-body vertex to thigh imaging. Brain PET/CT was performed 50-60 minutes following intravenous administration of 4 mCi 64Cu-DOTATATE or 68Ga-DOTATATE (Table 1). Brain PET images were acquired in one bed position for 10 minutes. All 3D PET images were acquired and reconstructed using VUE Point FX TOF with a 256 matrix, 3 iterations, 8 subsets, 'standard' z-axis filter, and a post-filter cutoff of 7.0 mm FWHM. Attenuation corrected brain PET images were fused with separately acquired contrast-enhanced brain MRI using MIMneuro (version 7.1.6) for PET/MRI interpretation.

Results

Following IRB approval, we retrospectively reviewed DOTATATE brain PET studies scanned to date. 13 patients (10 F, 3 M, age range of 16-69 years) with SSTR-positive head and neck tumors (6 meningiomas, 4 head and neck paragangliomas [2 glomus jugulare, 1 glomus tympanicum, 1 glomus jugulotympanicum], 1 middle ear neuroendocrine adenoma, 1 sinonasal neuroendocrine carcinoma, 1 pituitary carcinoma) have been imaged with either 64Cu-DOTATATE (12) or 68Ga-DOTATATE (1 patient). More extensive disease was identified by DOTATATE PET/MRI compared to MRI brain alone in 3/13 (23%) patients. Additional lesions were identified in 5/13 (38%) patients including 5 meningiomas, 1 glomus jugulare paraganglioma, 1 pituitary microadenoma, and 1 suspected TMJ arthritis.

Conclusions

Our dedicated DOTATATE brain PET protocol decreased imaging time and was well-tolerated by patients. The superior soft tissue

resolution of MRI improved lesion localization and helped delineate fine anatomic details, while DOTATATE-PET detected extent of disease and additional lesions not identified by MRI alone.

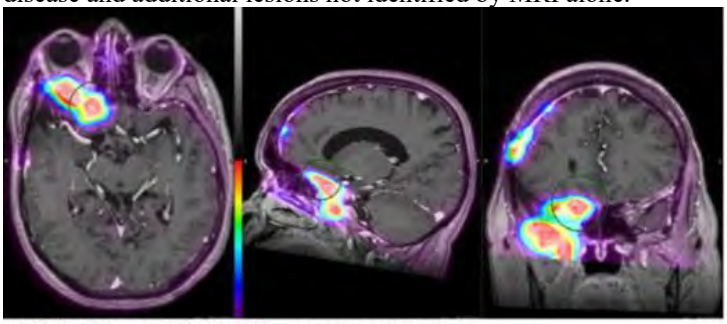

Patient 1. 63 year old female with recurrent meningioma.

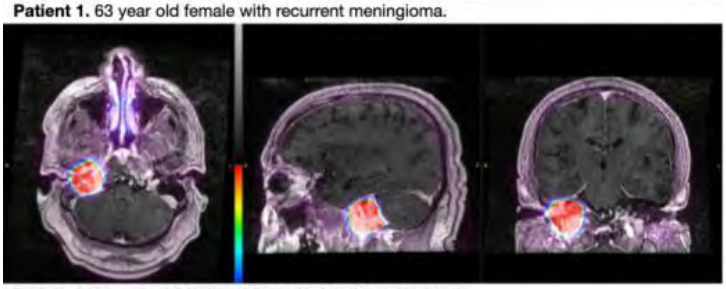

Patient 2. 55 year old male with glomus jugulotympanicum.

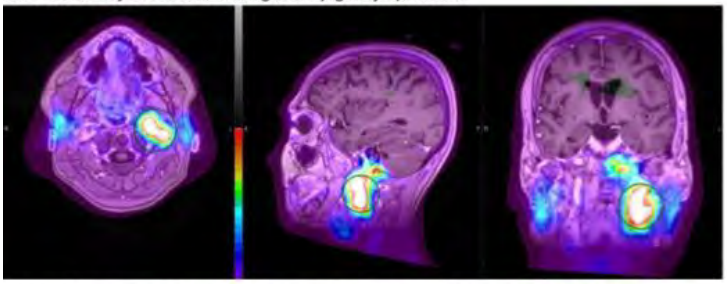

Patient 3. 66 year old female with petroclival meningioma with extra cranial extension.

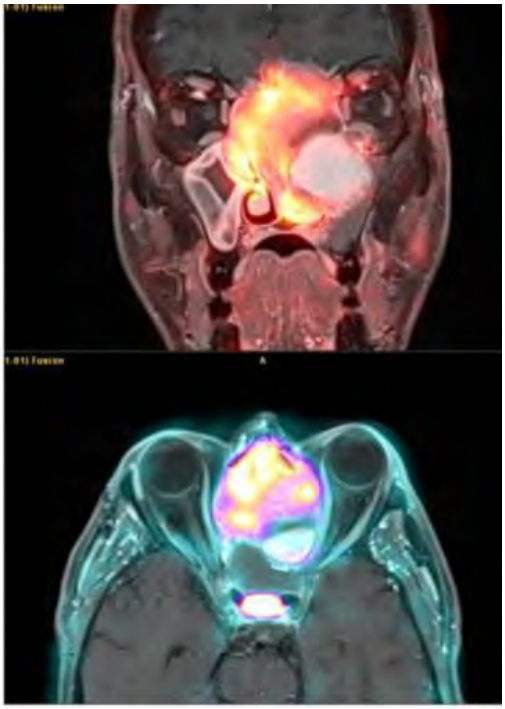

Patient 4. 56 year old man with sinonasal neuroendocrine carcinoma.

(Filename: TCT_371_ASNRFigure001.jpg)

844

Assessing Spatial Similarity Between Primary Language Areas of Brain Templates with Those Detected From Presurgical fMRI of Brain Tumor Patients

J Lee[1], V Kumar[1], J Teo[2], P Hou[2], R Eldaya[3], K Tran[4], K Noll[5], S Prabhu[6], H Liu[2]

[1]Department of Neuroradiology, The University of Texas MD Anderson Cancer Center, Houston, TX, [2]Department of Imaging Physics, The University of Texas MD Anderson Cancer Center, Houston, TX, [3]MD Anderson Cancer Center, Houston, TX, [4]Nordic Neuro Lab, Inc, Milwaukee, WI, [5]Department of Neuro-Oncology, The University of Texas MD Anderson Cancer Center, Houston, TX, [6]The University of Texas MD Anderson Cancer Center, Houston, TX

Purpose

Functional brain templates can help clinical fMRI analyses such as evaluating language lateralization and detecting functional networks with resting-state fMRI. This study aimed to determine which publicly available templates of primary language areas (PLAs) best represent those detected from presurgical fMRI of brain tumor patients.

Materials and Methods

We evaluated presurgical language fMRI studies of 38 brain tumor patients (16 females; 47.21 y ± 15.2 y; age range, 13-77 y) who performed a word generation and/or a sentence completion task paradigm. The fMRI data was analyzed using SPM12 following standard pre-processing procedures and the results were thresholded at $p<0.05$, FWE corrected. A board-certified neuroradiologist selected activated clusters in the PLAs, by constraining within the posterior inferior frontal gyrus, including pars triangularis and pars opercularis, for the anterior PLAs, and within the posterior superior and posterior middle temporal gyri for the posterior PLAs. The anterior PLAs from the following brain templates were studied: (1) anatomically determined with Harvard-Oxford Atlas [1] (Template A), (2) generated based on tb-fMRI study [2] (Template B), (3) generated based on rs-fMRI study [3] (Template C), and (4) obtained from Neurosynth [4] with anatomical constraints (Template D) (Fig. 1A). The posterior PLAs from Template B, C and D were studied (Fig. 1B). The templates were compared by evaluating their spatial similarity with the fMRI results using the Dice Similarity Coefficient (DSC). A nonparametric repeated-measure Friedman test and post hoc test with Bonferroni correction were performed to test the differences in the DSC.

Results

Total of 63 anterior and 61 posterior fMRI PLA results were analyzed. For the anterior PLAs, Template D yielded the highest mean DSC (0.26±0.17, $p<0.01$) (Fig. 2A). For the posterior PLAs, Templates B and D exhibited similar mean DSC (0.090±0.086 and

0.091±0.088, respectively, p=0.832) (Fig. 2B), which were both significantly (p<0.001) higher than that of Template C. The overall low DSC can be attributed to the stringent fMRI threshold applied.

Conclusions

Varied performances were found among the templates for representing PLAs of patients with brain tumors, with Template D and Templates B and D yielding the highest spatial similarity to the anterior and posterior PLAs respectively. This preliminary study provides recommendations for brain templates that may better inform PLAs for presurgical fMRI analysis.

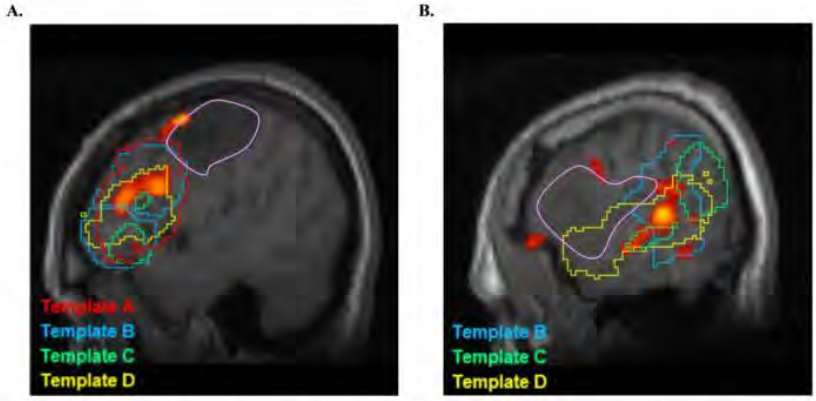

Figure 1. Areas with significant activations (t>5.0) detected from language fMRI of two patients overlaid with the anterior (a) and posterior (b) language templates on their normalized T1-weighted images. Gliomas are outlined in purple.

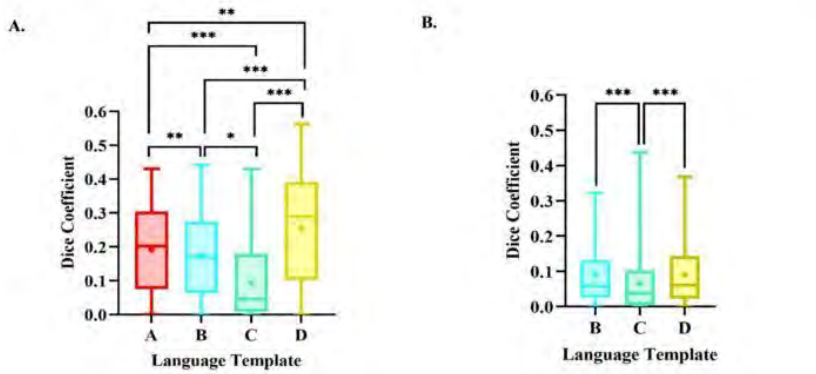

Figure 2. Box-and-whisker plot of the Dice coefficients between anterior (a) and the posterior (b) primary language templates and the language fMRI results from patients with brain tumors. The middle line of the box is the median, and the edges indicate the 25th and 75th percentiles. The whiskers are the maximum and minimum of data points and the plus (+) symbol is the mean. *p<0.05, **p<0.01, ***p<0.001.

(Filename: TCT_844_ASNRAbstractFINAL.jpg)

762

Can standard-delay ASL detect active plaques in multiple sclerosis?

E Piccirilli[1], C D'Orazio[2], E Spina[3], A Chiarelli[1], V Tomassini[1], L Ippoliti[4], M CAULO[1]

[1]University of Chieti, Chieti, Italy, [2]SS. Annunziata Hospital, Chieti, Italy, [3]ITAB - Institute for Advanced Biomedical Technologies, Chieti, Italy, [4]University of Chieti, Pescara, Italy

Purpose

Gadolinium uptake on post-contrast T1 sequences currently represents the reference standard in the identification of acute, active lesions in multiple sclerosis. We explored whether Cerebral Blood Flow (CBF) changes in active plaques measured with a standard-delay pseudo-Continuous Arterial Spin Labeling (pCASL) may serve as a surrogate of disease activity.

Materials and Methods

In this prospective study, the MRI scans of 148 relapsing-remitting MS (RRMS) adult patients performed at our Institution from January 2019 to September 2022 were considered. Patients were scanned on a 3T magnet (Philips Achieva) and the brain MRI protocol included pre and post contrast 3D-FFE T1, Axial and Coronal T2 TSE, 3D-FLAIR, SWI, DWI and the pCASL sequence (labeling duration:1800 ms; post-label delay: 2000 ms). The inclusion criteria were the presence of at least one enhancing plaque of at least 5 mm and the pCASL sequence. After the co-registration of post-contrast 3D-FFE T1, 3D-FLAIR and pCASL, the active plaque(s) and a chronic plaque (CP, greater than 5 mm) were manually segmented in each patient. Another ROI was manually placed in the contralateral normal-appearing white matter (NAWM). For each of these ROIs, CBF was automatically calculated using the manufacturer's software. Clinical data - including patients' age, Expanded Disability Status Scale (EDSS), corticosteroid pulse therapy

during the relapse, Disease Modifying Therapy (DMT) at the time of MRI - were also retrieved from medical records. Paired sample t-tests and ANCOVA were performed, setting the statistical significance at p=.05.

Results

A total of 80 APs from 42 patients were finally included. Median and mean CBF of APs were 19.25 and 20.70 ml/100g/min, respectively. The contralateral NAWM showed a median and mean CBF of 18.90 and 20.02 ml/100g/min respectively. CP had a median and mean CBF of 16.10 and 17.52 ml/100g/min respectively. The mean CBF of AP was significantly higher than that of CP (p=.0002) and contralateral NAWM (p=.08, with a significance of 10%). These differences remained statistically significant after controlling for the effect of clinical variables (F=4.21, p=2.53e-05).

Conclusions

Although hindered by an intrinsic lower SNR in the white matter, standard-delay ASL demonstrated to be highly sensitive to active inflammation in MS. As such, it may be a promising tool in monitoring disease activity as an alternative to contrast-enhanced MRI.

754

CSF Susceptibility Variation in Patient with Intracranial Hemorrhage: Implications for Quantitative Susceptibility Mapping Reference Selection.

S Wang[1], P Spincemaille[2], M Selim[1], A Thomas[3], A Filippidis[2], Y Wen[4], Y Wang[5], S SOMAN[6]

[1]Beth Israel Deaconess Medical Center, Harvard Medical School, Boston, MA, [2]N/A, N/A, [3]Cooper University Health Care, Cooper Medical School of Rowan University, Cherry Hill, NJ, [4]GE Healthcare, New York, NY, [5]Weill Cornell Medicine, New York, NY, [6]Beth Israel Deaconess Medical Center / Harvard Medical School, Boston, MA

Purpose

Quantitative susceptibility mapping (QSM) is an emerging technique with excellent sensitivity to microhemorrhage while having high specificity to magnetic susceptibility sources1. This technique has many potential impactable applications, especially in patients with brain pathologies. The QSM values resulting from blood mixing with CSF, as often occurs with intracranial hemorrhage patients, is not well documented.

Materials and Methods

Here, under an IRB approved protocol, we conducted a retrospective study to evaluate the effect of visible hemorrhagic CSF on QSM values. A total of 52 patients diagnosed with intraventricular and/or subarachnoid hemorrhage by non-contrast head CT and received concurrent brain MRI were recruited. Multiecho complex total field inversion (mcTFI) without CSF zero-referencing regularization were generated from the 3DMEGRE data and reviewed with FLAIR images2. Regions of hemorrhagic and non-hemorrhagic CSF where manually selected in reference to head CT and FLAIR images, Fig 1A. The relative QSM values were calculated by subtracting the non-hemorrhagic CSF from hemorrhagic CSF values.

Results

In patients with intraventricular hemorrhage (IVH) and subarachnoid hemorrhage (SAH), the unregularized QSM value measured at the hemorrhagic CSF are overall higher than that measured at the non-hemorrhagic CSF (Fig. 1C&D). Interestingly, the relative QSM values in patients with IVH (449±231 ppb) were significantly higher than that in patients with SAH (930±574 ppb), Fig 1B. This can be explained by the fact that CSF dilution and relatively small region of interest measurement area in cases of subarachnoid hemorrhage. Meanwhile, the CSF at the dependent areas within the ventricles likely had more concentrated blood products.

Conclusions

In conclusion, we demonstrated that QSM values are overall higher at the site of hemorrhagic CSF as determined by radiologist visual inspection of CT and MRI FLAIR images when compared with non-hemorrhagic CSF locations. These results suggest that the use of CSF as a QSM reference in intracranial hemorrhage patients should be made with caution since it can impact inter and intrasubject comparison of QSM values between studies.

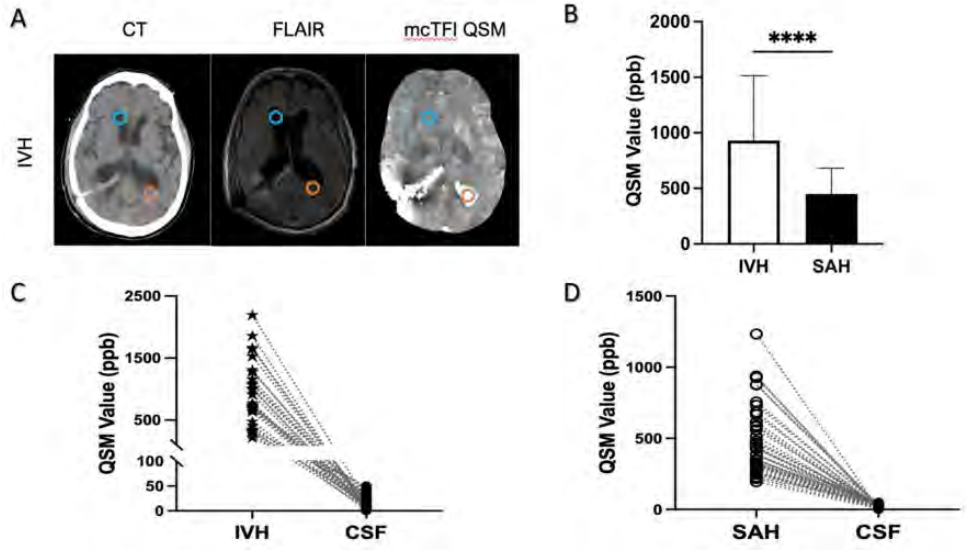

(Filename: TCT_754_ASNR_Fig.jpg)

1395

Diagnostic Utility of Delayed FDG-PET CT following Cerebral Stereotactic Radiosurgery of Brain Metastasis

B Ciavarra[1], M Gule-Monroe[1], M Chen[1], C Chung[1], S Ferguson[1], J Li[1], J Johnson[1]
[1]*The University of Texas MD Anderson Cancer, Houston, TX*

Purpose

Delayed 18F-FDG PET has been shown to increase the specificity of PET imaging for multiple types of cancer including lung, lymphoma, and high-grade gliomas. We sought to compare 1-hour and 5-hour imaging post injection in patients with metastatic brain cancer treated with radiation who developed MRI findings suspicious for recurrent disease.

Materials and Methods

Forty-one patients with suspicious enhancement following radiation were identified and imaged with this protocol. Diagnostic confirmation of progressive disease (PD) or radiation necrosis (RN) by radiographic follow-up (35 cases) and/or pathology (10 cases) identified 23 patients with RN and 18 patients with PD. Maximum standard uptake values (SUV) were calculated for suspicious areas of MR enhancement (lesion) and compared to normal appearing brain (background) at both time points.

Results

The mean L/B (lesion/background) for PD at the early time point (1.30+0.61) was significantly higher than L/B for the early time point for RN (0.94+0.30), ($p=0.0299$). Additionally, the mean L/B (lesion/background) for PD at the later time point (1.89+0.52) was significantly higher than L/B for the later time point for RN (1.11+1.06), ($p=0.0092$). Lesion to background ratios in cases with PD showed significantly higher SUV at the delayed time point compared to early time points ($p=0.0497$). Lesion to background ratios in cases with RN were not significantly different between early and delayed time points ($p=0.161$). Notably, there were two PD patients who had a L/B ratio < 1 on the initial time point who revealed a L/B ratio > 1 on the delayed time point.

Conclusions

Contrary to conventional teaching, we observed significant hypermetabolism associated with cases of proven radiation necrosis with a mean SUV of 8.75. Thus, the presence of increased metabolism associated with suspicious enhancement alone is not specific for PD. Our experience with the addition of delayed FDG imaging improves overall study accuracy and reduces FP and FN. Sixty-one percent of PD patients on the initial time point, and 72% of PD on delayed time point were correctly identified by L/B > 1. Further investigation is warranted including assessing algorithms that include both MRI (perfusion, spectroscopy, diffusion imaging) and PET metrics.

1019

Distinguishing Between Cognitively Impaired and Unimpaired Adults using fMRI Graph Theory

D Ahmed[1], J Holcomb[1], P Srivastava[1], E Davenport[1], J Maldjian[1], M Cullum[1], F Yu[1]
[1]*University of Texas Southwestern Medical Center, Dallas, TX*

Purpose

Graph theory (GT) is used to mathematically represent complex networks. When applied to functional imaging, GT metrics are used to describe the connectivity between distinct brain regions. The purpose of this study was to identify differences between those with and without cognitive impairment using functional MRI (fMRI) GT metrics. Secondary aims sought to compare fMRI GT measures with the results from the Patient-Reported Outcomes Measurement Information System (PROMIS) Cognitive Function (CF) scale to determine the relative strength of each in predicting impairment classification.

Materials and Methods

Resting-state fMRI, CF, and the Montreal Cognitive Assessment (MoCA) scores were acquired on adult subjects from UT Southwestern Medical Center. Two board-certified neuropsychologists used the MoCA to classify participants as cognitively impaired (mean MoCA score = 22.28) or unimpaired (mean MoCA score = 25.81). Each of 32 subjects (12 male and 20 female) aged 48-81 years old (mean age = 62.19 years old, SD = 7.77 years, mean BMI = 9.31, SD = 5.12) with cognitive impairment were compared to cognitively normal participants who were similar in terms of race, sex, age and BMI. 31 participants self-identified as Caucasian Non-Hispanic, 2 as Caucasian Hispanic, 30 as African American and 1 as American Indian. Global efficiency (GE) values at statistically significant nodes were then used in a logistic regression model with covariates of age, sex, race, BMI, CF, and years of education. Post-hoc analyses were additionally performed for GT measures of local efficiency, betweenness centrality, cost, average pathlength, clustering coefficient, and degree.

Results

Cognitively impaired subjects had significantly greater GE ($p<0.001$), shorter average pathlength ($p<0.001$), and higher degree ($p<0.001$) in the anterior cingulate cortex (ACC) than unimpaired subjects. GT measures were the strongest predictor in each model and CF scores were not predictive in this sample.

Conclusions

ACC GT measures identified connectivity differences between cognitively impaired and unimpaired subjects. GT measures outperformed PROMIS CF scores in determining cognitive impairment classification. Findings are promising for the use of GT approaches to fMRI analysis in aging populations with and without cognitive impairment.

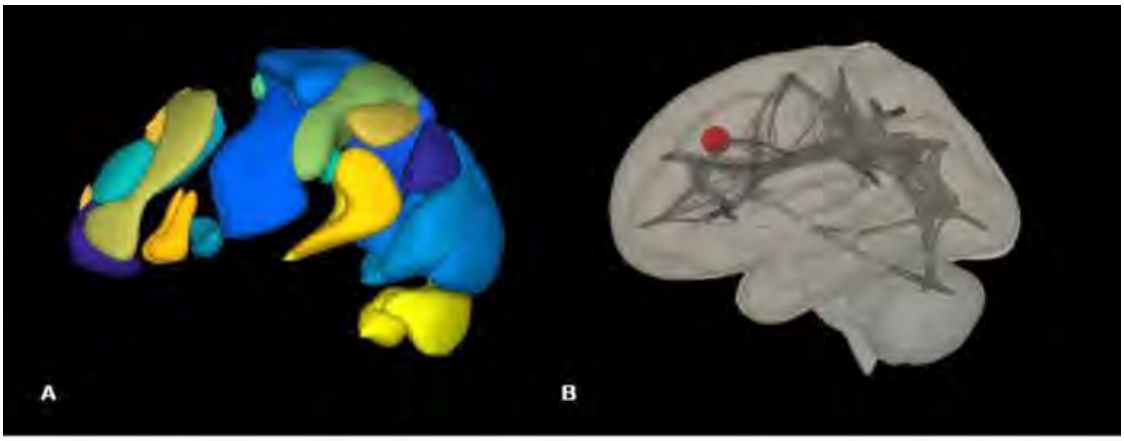

FIG 1. (A) Functional Regions of Interest to define nodes. (B) Graph theory network on glass brain. Dark regions define edges between nodes. Red sphere identified the node (anterior cingulate cortex) where there were significant differences in graph theory measures between groups.

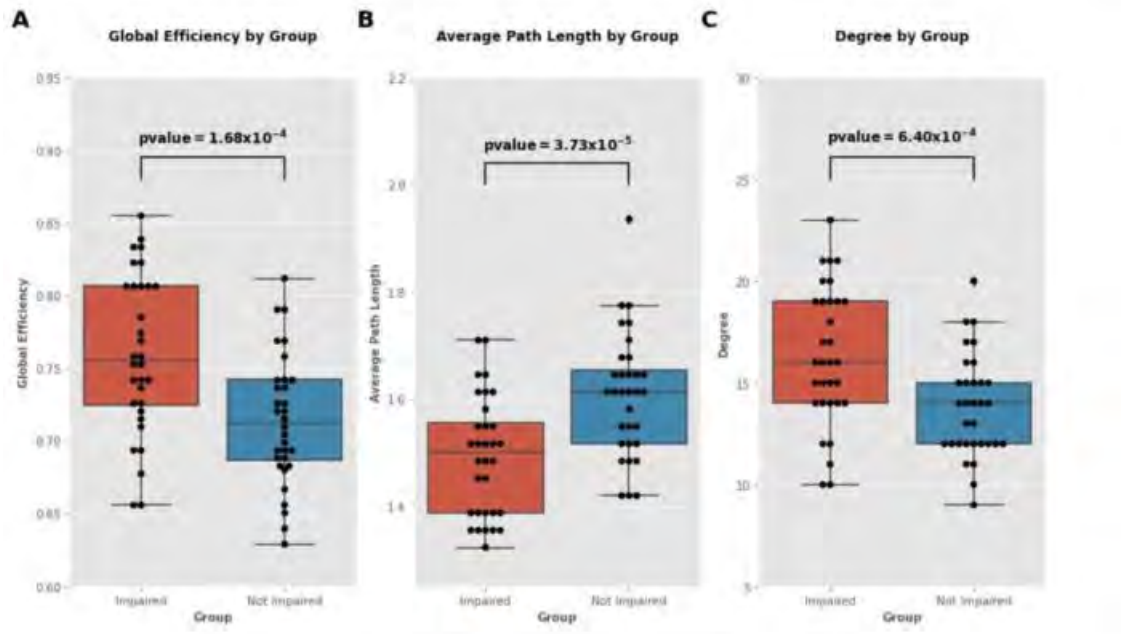

FIG 2. (A-C) Graph theory comparisons that were significantly different between groups at the anterior cingulate cortex node. Orange boxplots on the left and blue boxplots on the right of each graph respectively display the distribution of graph theory measures for the impaired and unimpaired groups. Black dots indicate graph theory values for each subject. The p-values for each Wilcoxon Rank- sum test are displayed above the boxplot distributions. (A) Distributions of global efficiency by group. (B) Distributions of average path length by group. (C) Distributions of degree by group.

(Filename: TCT_1019_AbstractFigures.jpg)

1513

Glioblastoma Versus Solitary Brain Metastasis: Utility of Intralesional Distribution of SWI Susceptibility Artifacts.

Y Munir[1], D Timaran[2], A Rodriguez[3], L Nunez[3], R Riascos[3]

[1]University of Texas at Houston Health Science Center, Houston, TX, [2]University of Texas Health Science Center Houston, Houston, TX, [3]The University of Texas Health Science Center at Houston, Houston, TX

Purpose

Metastasis and glioblastoma are the two most common malignant tumors of the brain with similar characteristics on conventional MR imaging. Both type of lesions can present with necrosis, peripheral-rim enhancement, and surrounding T2 hyperintensity. However, the use of newer sequences and advanced imaging may help to differentiate between high grade primaries versus secondary lesions. Therefore, we aim to evaluate the use of Susceptibility-Weighted imaging (SWI) to differentiate unifocal glioblastomas from solitary brain metastasis.

Materials and Methods
Over 24-month period, 30 patients with histopathologic confirmation of glioblastomas (15 [50%]) and solitary metastasis (15 [50%]) were enrolled in this study. Lesions were eligible if MRI studies were performed on a 3T scanner with adequate SWI sequences. Additionally, lesions included in this study measured were larger than 3 cm, demonstrated peripheral rim enhancement without large acute/subacute intralesional hemorrhage. All images were reviewed by 2 reviewers blinded to the pathology result. Interobserver agreement, sensitivity, specificity positive predictive value (PPV), negative predictive value (NPP) and likelihood ratios (LR) of SWI patterns were calculated.
Results
Overall, 23 lesions (76.6%) demonstrated predominantly central distribution of susceptibility artifacts on SWI. The remaining 7 lesions (23.4%) demonstrated peripheral distribution of the susceptibility artifacts. Almost perfect agreement was obtained between the 2 observers differentiating lesions with peripheral versus central distribution of susceptibility artifacts (kappa=0.87[95% CI 0.76-0.98]). In the diagnosis of glioblastoma, the sensitivity of lesions with centrally distributed susceptibility was 93.3%, with a specificity of 40%, PPV of 60.8%, NPV of 85.7% and LR of 1.5.
Conclusions
Central distribution of SWI susceptibility artifacts of solitary lesions with peripherally-rim enhancement may help to differentiate glioblastomas from metastasis. In fact, the sensitivity of centrally distributed susceptibility was 93.5% with a likelihood ratio of 1.5 and a NPV of 85.7%.

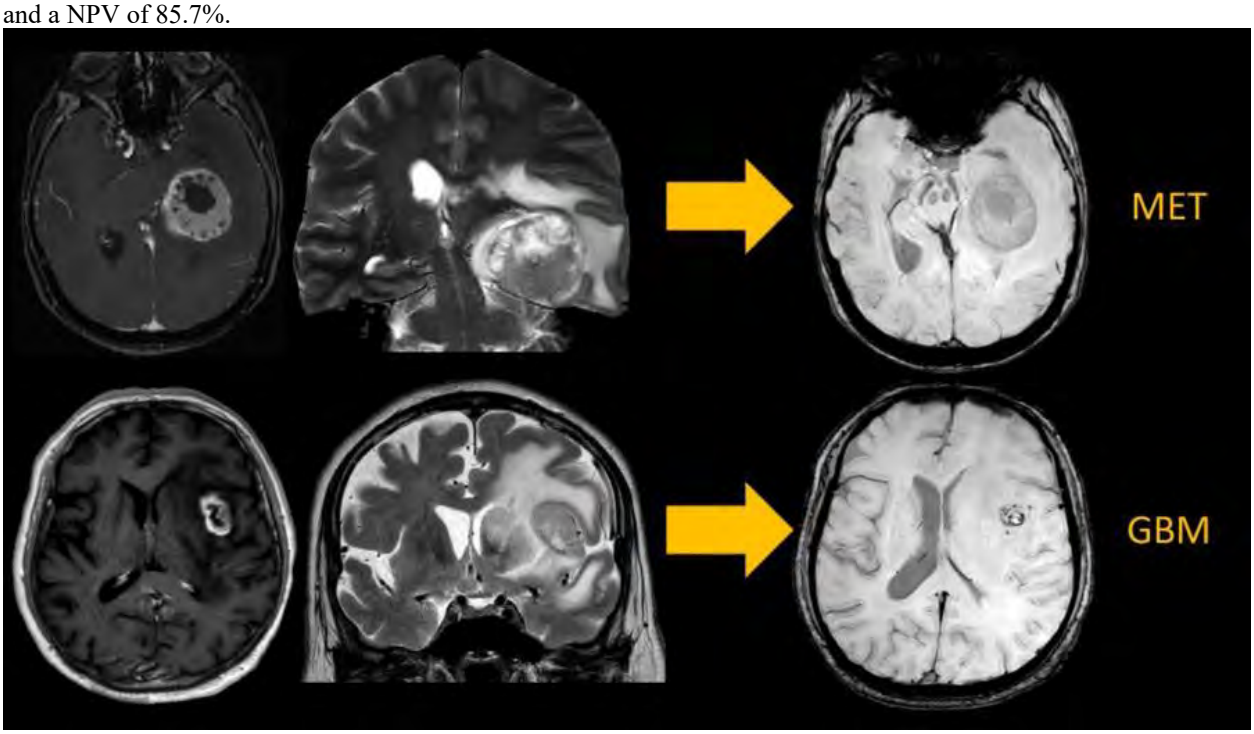

(Filename: TCT_1513_GBMMET.jpg)

952

Microstructural White Matter Changes in Subacute Postconcussion Vestibular Dysfunction (PCVD) as Assessed with NODDI

J Behnke[1], V Ahluwalia[2], J Smith[1], B Risk[3], R Gore[4], J Allen[3]
[1]Emory University School of Medicine, Atlanta, GA, [2]Georgia Institute of Technology, ATLANTA, GA, [3]Emory University, Atlanta, GA, [4]Shepherd Center, Atlanta, GA

Purpose
Vestibular symptoms are frequently reported following mild traumatic brain injury (mTBI) and are associated with protracted recovery [1], yet the underlying neuroanatomical substrates remain unclear. The present study utilized advanced diffusion MRI techniques to examine microstructural changes in white matter integrity following mTBI and their relationship to postconcussion vestibular dysfunction (PCVD).
Materials and Methods
Multi-shell, multi-directional diffusion-weighted imaging (DWI) acquired from 37 control and 23 patients with subacute (4-12 weeks post injury) PCVD was corrected for susceptibility- and eddy current-induced distortions as well as subject movements using 'eddy' in FSL toolbox [2]. Neurite orientation dispersion and density imaging (NODDI) metrics were derived using the NODDI-Bingham model [3]. Group-level, voxelwise analysis was performed on skeletonized diffusion metric maps using TBSS. Comparisons between subacute PCVD and controls were performed using voxelwise GLM analysis adjusted for age and corrected for multiple comparisons at $p(fwe) \leq 0.05$ by permutation testing using 'randomise' tool in FSL. To assess the relationship between anatomical changes in diffusion metrics and symptom severity, linear regression was performed using composite vestibular ocular motor screening (VOMS) [4] as a predictor measure regressed over ROI-extracted metrics, adjusted for age, gender, and time since injury.

Results

Voxelwise statistics revealed significant changes in two NODDI parameters: 1) the intracellular volume fraction (Fin), also known as the neurite density index (NDI), and 2) free water (isotropic) volume traction (Fiso). Compared to controls, the subacute PCVD group exhibited an increase in both Fin and Fiso (pfwe≤0.05). Increased Fin involved the left corticospinal tract (CST), internal and external capsules, and super longitudinal fasciculus. Increased Fiso involved the left internal capsule, corona radiata and superior longitudinal fasciculus. Linear regression revealed that increased Fin within the internal/external capsules, and CST was significantly correlated with symptom severity as measured using the composite VOMS.

Conclusions

Increases in Fiso within subacute PCVD patients, relative to controls, may represent extracellular tissue edema within the subacute injury period. Fin, which corresponds to axonal density, is also increased in the subacute PCVD group, and may represent a dynamic remodeling of axonal white matter microstructure within the subacute injury period[5].

A

Table 1 Demographic & Clinical Measures Summary

	Control (HC)	Subacute mTBI (ST)	P-value* ST vs HC
Demographics			
N	37	23	-
Female	19 (51%)	12 (52%)	-
Age, years	28 (5)	22 (5)	$p \leq 0.0001$
Days since injury	-	35 (23)	-
Subjective Measures			
PCSS	0 (0)	32 (32)	$p \leq 0.0001$
DHI	0 (0)	36 (18)	$p \leq 0.0001$
VVAS	0 (1.8)	20.3 (27.5)	$p \leq 0.0001$
VOMS (minus baseline)			
Smooth pursuit	0 (0)	0 (1.0)	$p \leq 0.05$
Horizontal saccade	0 (0)	1 (2.0)	$p \leq 0.0001$
Vertical saccade	0 (0)	2 (2.0)	$p \leq 0.0001$
Near-Point Convergence	0 (0)	2 (3.5)	$p \leq 0.001$
Horizontal VOR	0 (1)	4 (3.5)	$p \leq 0.0001$
Vertical VOR	0 (0)	4 (4.5)	$p \leq 0.0001$
VMS	0 (1)	4 (5.0)	$p \leq 0.0001$

Note, unless otherwise indicated, values correspond to median with interquartile range (IQR) within parenthesis. Abbreviations: PCSS, post-concussion symptom scale; DHI, dizziness handicap scale; VVAS, visual vertigo analog scale; VOMS, vestibular/ocular motor screening; VOR, vestibular-ocular reflex; VMS, visual motion sensitivity. *Mann-Whitney U test w/ Bonferroni correction

C

NODDI metric-roi_side	β	std.error	P-value (FDR-corrected)
Fin-cst_R	0.633	0.184	0.007
Fin-ilf_L	0.540	0.157	0.007
Fin-cst_L	**0.626**	**0.183**	**0.007**
Fin-ext_cap_R	0.542	0.161	0.008
Fin-unc_fasc_R	0.647	0.203	0.013
Fin-cing_L	0.640	0.201	0.013
Fin-ilf_R	0.485	0.159	0.018
Fin-ant_ic_L	**0.640**	**0.214**	**0.021**
Fin-ant_ic_R	0.593	0.201	0.023
Fin-ext_cap_L	**0.467**	**0.162**	**0.027**
Fin-fwm_R	0.480	0.178	0.040
Fin-slf_R	0.467	0.175	0.044

Cst, corticospinal tract (superior corona radiata); ilf, inferior longitudinal fasciculus; ext-cap, external capsule; unc_fasc, uncinate fasciculus; ant_ic, anterior internal capsule; fwm, frontal white matter (anterior corona radiata); slf, superior longitudinal fasciculus; R, right; L, left

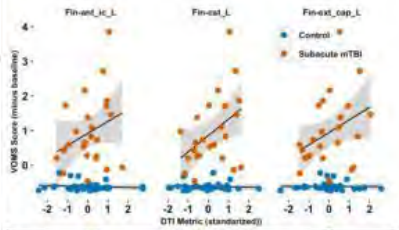

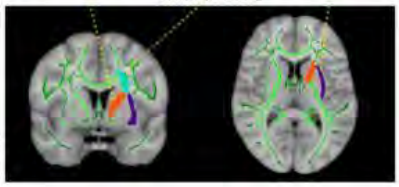

B

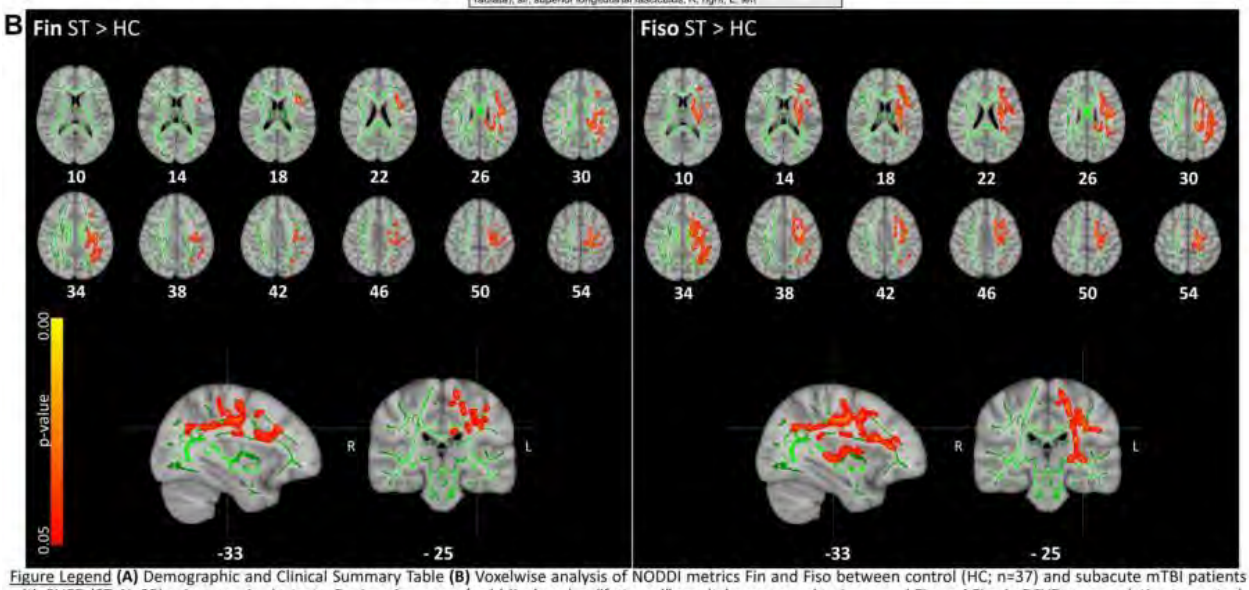

Figure Legend **(A)** Demographic and Clinical Summary Table **(B)** Voxelwise analysis of NODDI metrics Fin and Fiso between control (HC; n=37) and subacute mTBI patients with PVCD (ST; N=23) using unpaired t-tests. Regions in orange/red (displayed as "fattened" results) correspond to increased Fin and Fiso in PCVD group relative to control. Results corrected for multiple comparisons using TFCE-FWE at p ≤ 0.05.; representative images shown in radiographic orientation with MNI coordinates below **(C)** ***(left)*** Results of linear regression model assessing relationship between standardized composite VOMS scores and JHU atlas-based, ROI-extracted NODDI measures for subacute PCVD comparisons. Model is adjusted for age, gender, and time since injury. Results corrected for multiple comparisons using FDR at p ≤ 0.05. ***(right),*** Representative scatter plots of significant linear regression results (**bolded** results from table on left).

(Filename: TCT_952_final_figure.jpg)

568

Prediction of Bevacizumab Therapy Effect on Meningiomas: Utility of Diffusion-Weighted and Dynamic Susceptibility Contrast Perfusion MR Imaging

Y Ota[1], E Liao[1], G Shah[2], A Srinivasan[1]

[1]University of Michigan, Ann Arbor, MI, [2]Univ. Michigan Health System, Ann Arbor, MI

Purpose

Bevacizumab, an anti-angiogenic agent, has been used for treatment-refractory meningiomas, but imaging assessment of its treatment effect has not been fully investigated. The focus of this study was hence to assess imaging biomarkers to predict the response of treatment-refractory meningiomas to Bevacizumab using diffusion-weighted (DWI) and dynamic susceptibility contrast perfusion MRI (DSC-MRI).

Materials and Methods

This single-center retrospective study included 30 patients with treatment-refractory meningiomas (median 67 years, 20 females)

treated with Bevacizumab from May 2015 to November 2021. All included patients had DWI and DSC-MRI as well as conventional MRI before Bevacizumab treatment (5-15mg/kg). The treatment response was defined as a greater than 20% decrease in tumor size by volumetric MRI analysis. The patients were divided into groups with or without the treatment response, and the last follow-up MRI was performed median 5 months (range, 3-12 months) after induction of Bevacizumab. As an internal control, a region of interest was placed on the normal-appearing white matter at the level of the centrum semiovale. All quantitative parameters were normalized by dividing them by the corresponding parameters of the normal-appearing white matter. Pretreatment normalized mean ADC (nmADC), relative cerebral blood volume (nrCBV), and relative cerebral blood flow (nrCBF) as well as patient demographics and conventional imaging features were compared between the 2 groups.

Results

The group with a treatment response constituted 13 patients (median 71 years; 8 females), while that without a treatment response consisted of 17 patients (median 54 years; 12 females). The patient demographics were not significantly different between the 2 groups. nrCBV and nrCBF were higher in the group with a treatment response than in the group without a treatment response (nrCBV, median 5.68 vs 3.26; P<0.001, nrCBF, median 5.42 vs 2.88; P=0.001), while nmADC was not significantly different between the 2 groups (nmADC, 1.16 vs 1.08; P=0.094). Based on ROC analysis, nrCBV and nrCBF showed 0.89 and 0.86 area under the curve, 0.92 and 0.85 sensitivities, and 0.77 and 0.77 specificities, with cut-off values of 3.95 and 3.64.

Conclusions

DSC-MRI can provide predictive values for the response to Bevacizumab treatment in treatment-refractory meningiomas.

Table 1. Patient demographics of treatment-refractory meningiomas

	Total (30)	Treatment response (13)	Treatment failure (17)	P value
Age	67 (40-73)	71 (41-73)	54 (36-70)	0.27
Sex (male/total)	10/30	8/13	12/17	0.71
Pretreatment volume (ml)	5.65 (3.22-17.1)	5.01 (3.25-19.1)	7.15 (2.25-17.1)	0.88
Posttreatment volume (ml)	5.03 (2.55-19.3)	2.67 (2.55-5.03)	7.54 (4.4-35.7)	0.052
Follow-up (month)	5 (3-6)	5 (4-6)	4 (3-6)	0.33
WHO Grade	Grade 1 (10) Grade 2 (13) Grade 3 (7)	Grade Ⅰ (3) Grade Ⅱ (6) Grade Ⅲ (4)	Grade Ⅰ (7) Grade Ⅱ (7) Grade Ⅲ (3)	NA

Note-Values are presented as the median (IQR).

Table 2. DWI and DSC-MRI parameters between treatment response and failure

	Treatment response	Treatment failure	P value
nmADC	1.16 (1.09-1.30)	1.08(0.97-1.18)	0.094
nrCBV	5.68 (4.32-8.69)	3.26 (1.76-3.67	<0.001
nrCBF	5.42 (3.64-8.09)	2.88 (2.30-2.93)	0.001

Note-Values are presented as the median (IQR).

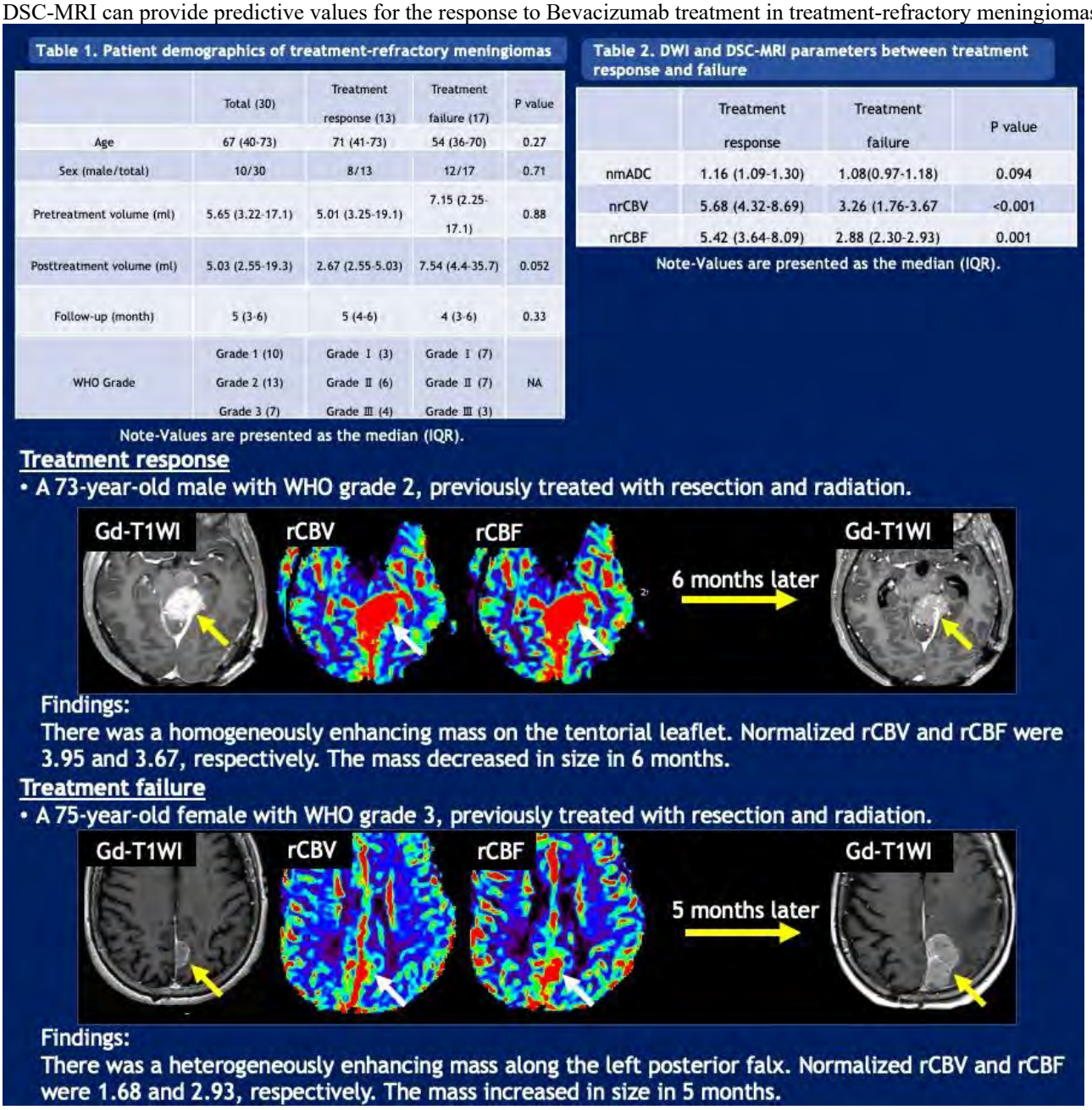

(Filename: TCT_568_Bevacizumabtreatment7.jpg)

1095

The Glioblastoma Immune Microenvironment Differs Between Gadolinium Enhancing, Ferumoxytol Enhancing, and Non-enhancing T2 FLAIR Hyperintense Biopsy Locations

J Stoller[1], C Kersch[2], L Muldoon[2], P Ambady[3], C Harrington[1], E Neuwelt[2], R Barajas[4]

[1]Oregon Health and Science University, Portland, OR, [2]Oregon Health & Science University, Portland, OR, [3]Providence health, Portland, OR, [4]OHSU, Portland, OR

Purpose

MRI with gadolinium contrast (GBCA) is standard of care for monitoring glioblastoma tumor response but is of limited utility for defining the cellular constituents of the immune microenvironment. Developing a noninvasive approach to detect a neuroinflammatory response is critical in the era of immunotherapies. Prior investigations have demonstrated ferumoxytol (Fe) nanoparticle MRI contrast to be clinically useful for defining neuroinflammatory pseudoprogression after standard of care chemoradiotherapy. We hypothesized that ferumoxytol enhancement may improve upon the clinical ability to discriminate the glioblastoma tumor immune microenvironment.

Materials and Methods

Eight patients with IDH-wild type glioblastoma underwent GBCA-MRI and Fe-MRI immediately prior to tumor resection. Tissue sampling from regions of T1- and T2-flair signal characteristics was performed using a stereotactic image guided technique. RNA was extracted from the tissue samples and analyzed by gene expression array for transcript identification by the Oregon Health & Science University Gene Profiling Shared Resource. The gene identifications were dichotomized based on tissue MRI characteristics; T1-enhancing (CEL) or not (NCEL). Transcriptomic data was analyzed using Cibersortx a digital cytometry software that allows for characterization of tissue cell composition from their gene expression profiles. We calculated immune cell fractions present in CEL and NCEL samples. T-test of unequal variance was performed to assess for cellular composition differences between imaging features. A p-values of 0.05 was considered statistically significant.

Results

A total of 57 tissue samples were analyzed (35 GBCA-CEL/22 NCEL and 41 Fe-CEL/17 NCEL). Fe-CE tissue demonstrated significantly increased M2 Polarized Macrophages. Fe-NCEL tissue showed significantly elevated Natural Killer and Neutrophil immune cells. GBCA-CEL tissue only showed significantly elevated Neutrophils.

Conclusions

Unlike GBCA, Fe-enhancing tissues demonstrated significantly elevated M2 polarized macrophages. This is consistent with the proposed macrophage phagocytosis mechanism by which Fe-MRI signal is generated. Macrophages comprise up to 40% of the cellular mass within glioblastoma. This suggests that Fe-MRI may be improve upon GBCA by localizing the cell specific neuroinflammatory component of the glioblastoma immune microenvironment.

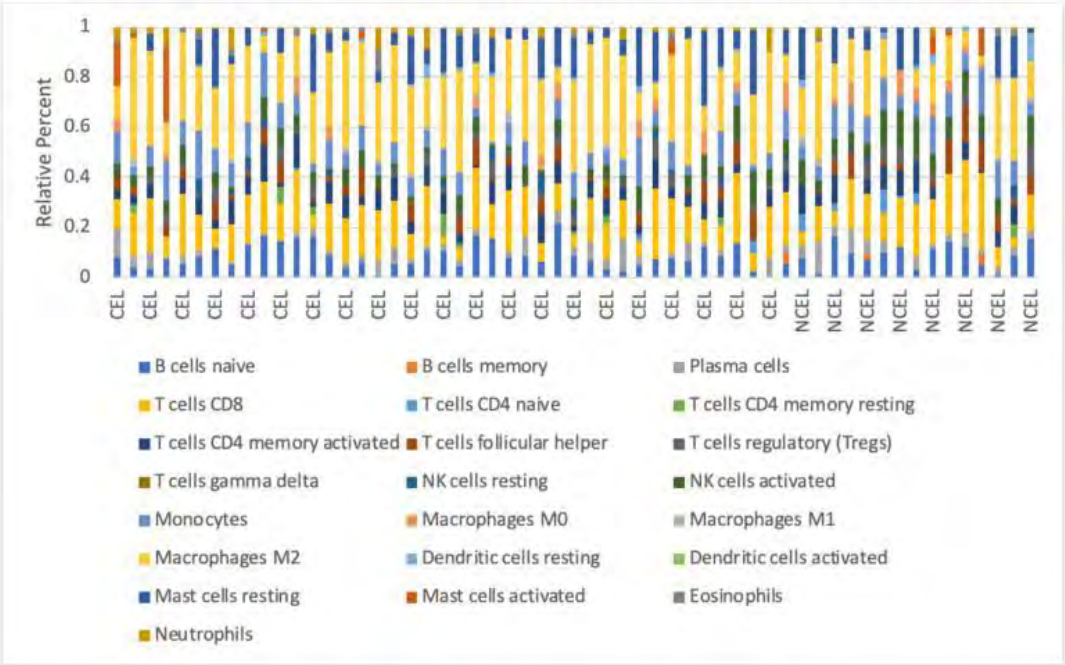

Figure 1: Anonymized results comparing ferumoxytol enhancing (CEL) and non-enhancing (NCEL) samples and relative percent of immune cells present within the sample.

(Filename: TCT_1095_Screenshot2022-11-14at91636PM.jpg)

Wednesday, May 3, 2023

2:45-4:00 PM

ASHNR Programming: Bad to the Bone: Infection and Neoplasia of the Temporal Bone, Skull Base and Facial Bones (Essentials Track)

227

Diffuse Basisphenoid Enhancement: Possible Differentiating Feature for Granulomatous Hypophysitis

I Mark[1], C GLASTONBURY[2]
[1]Mayo Clinic, Rochester, MN, [2]UCSF, SAN FRANCISCO, CA

Purpose

Granulomatous hypophysitis (GH) is a rare inflammatory condition of the pituitary with an imaging appearance that can overlap with that of pituitary adenoma. Differentiating between the two prior to surgical resection can have important treatment implications. The purpose of our study was to determine whether it was possible to differentiate between GH and pituitary adenoma based on diffuse enhancing infrasellar basisphenoid bone marrow.

Materials and Methods

We present three cases, initially thought to be pituitary adenomas, that were pathology-proven GH. The pre-operative MRI were reviewed for diffuse enhancing infrasellar basisphenoid bone marrow. For comparison, we reviewed 100 cases of pathology-proven pituitary adenoma for the same finding. Additionally imaging findings including the sphenoid sinus pneumatization pattern, clinical history, laboratory values, and pathology results were reviewed.

Results

All three cases of GH had diffuse enhancing infrasellar basisphenoid bone marrow. Conversely, this was not seen in any of the 100 pituitary adenomas. The GH patients were all female. Two patients were idiopathic GH, and one was secondary GH with sarcoidosis. Of the 100 pituitary adenoma patients, 67 were female. The basisphenoid pneumatization patterns was as follows: 15 (type 2), 40 (type 3), and 45 (type 4).

Conclusions

We present three cases of GH with diffuse enhancement of the infrasellar basisphenoid bone marrow that was not seen in our 100 cases of pituitary adenomas. This imaging feature may be valuable to suggest a diagnosis of GH and avoid surgical resection of what might otherwise be misdiagnosed as a pituitary adenoma.

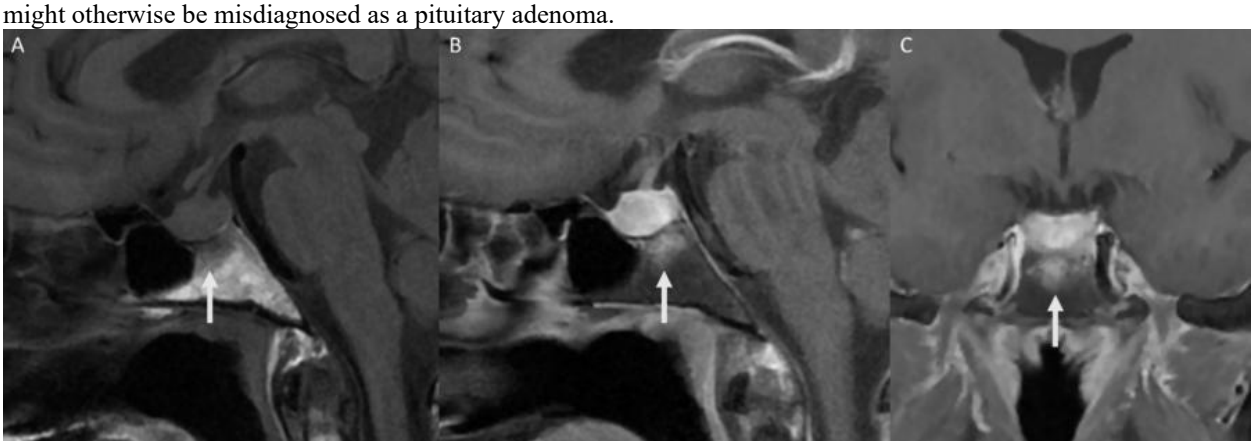

(Filename: TCT_227_GHfig.jpg)

817

Proposal of a magnetic resonance imaging follow-up protocol after cholesteatoma surgery: a prospective study

A Romano[1], A Romano[2], S Palizzi[1], G Moltoni[1], E Covelli[3], M Barbara[4], a bozzao[5]
[1]La Sapienza University of Rome, Sant'Andrea teaching Hospital, Rome, Lazio, [2]Sant'Andrea Hospital, La Sapienza University, Rome, Italy, [3]Università, Roma, RI, [4]Azienda Ospedaliero-Universitaria Sant'Andrea, roma, rome, [5]Sant'Andrea Hospital, La Sapienza University, Roma, ROMA

Purpose

Non-echo planar (EPI) diffusion weighted (DW) MRI has become an effective tool for the follow-up after cholesteatoma surgery and decreased the rate of second-look surgeries. The objective of the study is to shed light on the optimal imaging follow-up protocol to detect postoperative residual or recurrent cholesteatoma.

Materials and Methods

64 patients were included in this prospective study. Three different surgical procedures were considered: canal-wall-up (26 patients), canal-wall-down (20 patients), and obliterative (18 patients). The imaging follow-up protocol included non-EPI DW MRI during the following postoperative periods: 1 month, 6 months, and 1, 3, 5, and 7 years after the primary surgery.

Results
MRI-positive lesions were present in 18.75% of patients. 50% of the MRI-positive findings occurred at the 1-month follow-up. The other peak of MRI positivity occurred at the 3-year follow- up. The last MRI-positive finding appeared at the 5-year follow-up.
Conclusions
The timing for the imaging protocol proposed by this prospective study to detect recidivism after cholesteatoma surgery stressed the importance of performing non-EPI DW MRI for detecting residual, though rare, disease. Likewise, extending the follow-up to a least 5 years after primary surgery was also recommended to detect any recurrent cholesteatoma that would appear unlikely to be present beyond this time set.

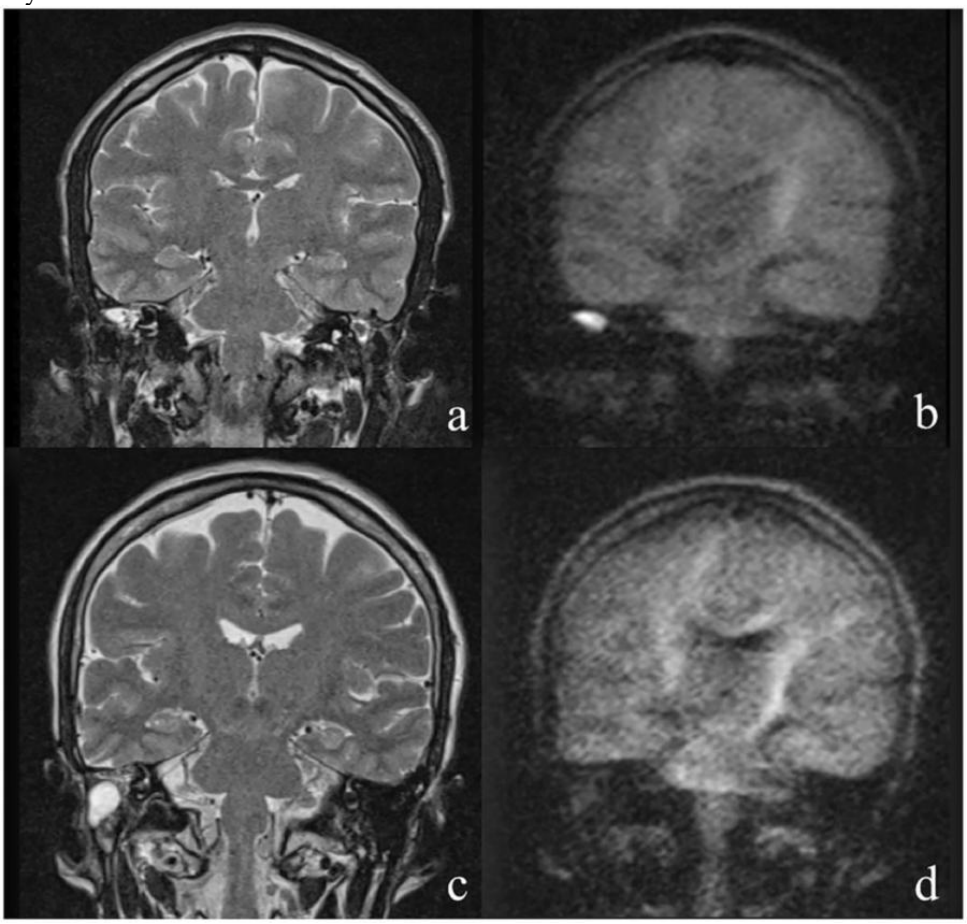

(Filename: TCT_817_Figure1.jpg)

Wednesday, May 3, 2023

2:45-4:00 PM

Evidence-Based Medicine Committee Programming: Adoption of Artificial Intelligence into Clinical Practice: 2023 Update

1001

Advancing Clinical AI Technologies in Neuroimaging with Academic-Industrial Partnerships

L Penn[1], J Nguyen[1], T Kennedy[2], J Yu[1], R Bruce[3]
[1]University of Wisconsin School of Medicine and Public Health, Madison, WI, [2]The University of Wisconsin, Middleton, WI, [3]University of Wisconsin - Madison, Madison, WI

Purpose
The variability of medical imaging AI algorithm performance in clinical workflows is a well known phenomenon.[1] This is most frequently attributed to differences in exam acquisition protocols and differences in patient populations relative to the training data. We evaluated the clinical performance of two commercially available FDA approved (for triage) AI algorithms. We hypothesized that collaboratively working with the commercial solution provider primarily by providing our local data would improve the performance of the AI algorithms.

Materials and Methods

A total of 693 non-contrast CT head and 683 serial comprehensive stroke code CT/CTA exams (non-contrast CT head, CTA head & neck, CT perfusion) were evaluated. Realtime output from triage ICH and ASPECTS AI algorithms was available at the time of clinical radiologist interpretation. The triage output was collated with findings from the radiologist final reports. The imaging datasets and collated algorithm and report output was provided to the commercial algorithm provider. Triage ICH and ASPECTS output was evaluated following incorporation of our data and model retraining in a new version of the algorithms.

Results

Clinical triage performance of the initial ICH algorithm was deemed to be poor with a sensitivity and specificity of 57.9% and 89.3% (respectively) for the ICH detection algorithm. Similarly, for ASPECTS 65.3% of cases differed by >1 point and 14.8% differed by >2 points versus the radiologist interpretation. The most common difference for ASPECTS was when the radiologist reported a normal ASPECTS score (10/10) and the algorithm reported an abnormal ASPECTS score (<10). There were 71/683 cases reported by the radiologist with a non-normal ASPECTS score versus 474/683 reported by the algorithm. After incorporation of our data into the algorithm training data along with other algorithm improvements, the triage ICH algorithm improved to a sensitivity of 94.7% and a specificity of 97.9%, a marked improvement. The ASPECTS algorithm improved to differing 10.7% with >1 point difference and only differed 5.0% for >2 point differences relative to the radiologist score.

Conclusions

We are at the dawn of clinical adoption of medical imaging AI. Even well developed commercial AI solutions can have poor results with local acquisition protocols and data. Our results show that a collaboration with the solution provider can significantly improve the algorithm robustness.

ICH:

The tables below show the difference between what we have been using (ICH v1, thick slices) to the version after incorporation of our data (ICH v3.3.6, thin slices). Sensitivity goes from 57.9% to 94.7%. Specificity goes from 89.3% to 97.9%. Pretty dramatic improvements.

*Version/slice thickness used at site previously.

Thick	5.00 mm
True Positive ICH 1.0	11
True Negative ICH 1.0	602
False Positive ICH 1.0	72
False Negative ICH 1.0	8
Total # Cases Processed Successfully	693
Sensitivity ICH 1.0	0.5789
Specificity ICH 1.0	0.8932
PPV ICH 1.0	0.1325
NPV ICH 1.0	0.9869

Thin	1.25 mm
True Positive ICH 1.0	12
True Negative ICH 1.0	633
False Positive ICH 1.0	41
False Negative ICH 1.0	7
Total # Cases Processed Successfully	693
Sensitivity ICH 1.0	0.6316
Specificity ICH 1.0	0.9392
PPV ICH 1.0	0.2264
NPV ICH 1.0	0.9891

Thin	1.25 mm	
True Positive ICH 3.3.6	18	
True Negative ICH 3.3.6	660	
False Positive ICH 3.3.6	14	
False Negative ICH 3.3.6	1	
Total # Cases Processed Successfully	693	
Sensitivity ICH 3.3.6	0.9474	*TP/(TP+FN)*
Specificity ICH 3.3.6	0.9792	*TN/(TN+FP)*
PPV ICH 3.3.6	0.5625	*TP/(TP+FP)*
NPV ICH 3.3.6	0.9985	*TN/(FN+TN)*

*Version/slice thickness used at site previously.

Correlation ICH Reported/ICH 1.0 Thick?	0.23744
Correlation ICH Reported/ICH 1.0 Thin?	0.35069
Correlation ICH Reported/ICH 3.3.6?	0.72098

*Removed tech. inadequate imaging from analysis.

ASPECTS:

We see an improvement as well in the ASPECTS numbers. In our data within the 683 cases that were able to be evaluated, there were 71 "positive" ASPECTS scores (score <10) based on the reports. Overall there is a dramatic drop in the number of false positives with the total ASPECTS <10 dropping from 474 to 168.

*Version/slice thickness used at site previously.

	# <10	# Yes	Total # Successful Scans	%
>2 Pt Difference ASPECTS V1, Thick?	474	101	683	14.79%
>2 Pt Difference ASPECTS V1, Thin?	373	76	683	11.13%
>2 Pt Difference ASPECTS V3+ Thick?	223	63	683	9.22%
>2 Pt Difference ASPECTS V3+ Thin?	168	34	683	4.98%
ASPECTS Reported	71		683	

Thin = 1.25 mm
Thick = 5.00 mm

*Version/slice thickness used at site previously.

	# <10	# Yes	Total # Successful Scans	%
>1 Pt Difference ASPECTS V1, Thick?	474	446	683	65.30%
>1 Pt Difference ASPECTS V1, Thin?	373	158	683	23.13%
>1 Pt Difference ASPECTS V3+, Thick?	223	117	683	17.13%
>1 Pt Difference ASPECTS V3+ Thin?	168	73	683	10.69%
ASPECTS Reported	71		683	

Thin = 1.25 mm
Thick = 5.00 mm

Correlation ASPECTS Reported/ASPECTS v1 Thick?	0.46882
Correlation ASPECTS Reported/ASPECTS v1 Thin?	0.54811
Correlation ASPECTS Reported/ASPECTS v3+ Thick?	0.44551
Correlation ASPECTS Reported/ASPECTS v3+ Thin?	0.63919

*Removed tech. inadequate imaging and cases with hemorrhage from analysis.

(Filename: TCT_1001_abstracttables.jpg)

590

Real-World Performance of Large Vessel Occlusion CADt Artificial Intelligence Algorithms - What Radiologists Need to Know.

M Kunst[1], R Gupta[2], J Delfino[3], P Noonan[3], J Fang[3], L Gillis[4], I Berglar[5], B Kozak[5], J Small[6], K Dreyer[5], C Wald[6]

[1]Lahey Hospital and Medical Center, Winchester, MA, [2]Massachusetts General Hospital and Harvard Medical School, BOSTON, MA, [3]Food and Drug Administration, Silver Spring, MD, [4]American College of Radiology, Reston, VA, [5]Massachusetts General Hospital, Boston, MA, [6]Lahey Hospital and Medical Center, Burlington, MA

Purpose

To evaluate the real world performance of 2 FDA approved AI CADt LVO detection devices and compare them with the manufacturer reported performance testing in the Instructions for Use.

Materials and Methods

Clinical performance of two FDA-cleared CADt LVO devices was retrospectively evaluated at two separate stroke centers (RAPID LVO from IschemiaView, Inc. at Lahey Hospital & Medical Center (Lahey), ContaCT from Viz at Massachusetts General Hospital (MGH)). Consecutive "code stroke" CTA exams from 2020 to 2022 at both stroke center were included. Data elements collected included patient demographics, scanner manufacturer and model, presence/absence of CADt result and output, Radiologist LVO presence and location. LVO segments included ICA, M1, M2, A1, A2, VA, BA, P1 and P2 A study Radiologist extracted the above data elements from the imaging exam and Radiology report. A Board-certified and CAQ-certified Neuroradiologist or Board-certified Emergency (ER) radiologist interpreted the original exam at each medical center, which served as the reference standard.

Results

For both RAPID and Viz, the manufacturer reported performance testing listed in the Instructions for Use (IFU) are summarized in Table 1. For RAPID at Lahey, 79 cases did not return a CADt result, including 14 LVO. In these cases, Radiologists detected 14 LVO (12 in ICA, M1 or M2 (of these, 8 in ICA or M1); and 1 each in the VA and P1 PCA). The real-world performance testing for processed cases were similar to IFU for ICA and M1 segments only (Table 2a). For Viz at MGH, 23 cases did not return a CADt result, including 4 LVO. In these cases, Radiologists detected 4 cases with LVO (1 in M2; 1 in ICA, M1 and A2; 1 in M1; 1 in basilar). The real-world performance testing for processed cases were similar to IFU for ICA, M1 and M2 segments only (Table 2b).

Conclusions

Real-world testing of 2 CADt LVO detection algorithms identified gaps in the detection and communication of potentially treatable LVOs when considering vessel segments beyond the ICA and M1 segments, and in cases with absent and uninterpretable data. Even after the installation of CADt, there must be continued vigilant, perhaps even redundant, communication of every potentially treatable LVO by Radiologists to members of the treatment team to ensure no gap in optimal clinical care.

Table 1. Device performance of LVO CADt devices reported by the manufacturer

Algorithm	N	Measure	Estimate	Lower 95% CI	Upper 95% CI
RAPID	217	Sensitivity	97.0	93.3	98.7
RAPID	217	Specificity	95.6	91.9	97.7
Viz	300	Sensitivity	87.8	81.2	92.5
Viz	300	Specificity	89.6	83.7	93.9

Table 2a. CADt device Performance by Vessel Location: RAPID

		LVO Truth			Other
Vessel Location	Algorithm	Yes	No	Total	
ICA, M1	Yes	87	36	123	
	No	15	410	425	
	Total	102	446	548	
		Sensitivity: 85.3%	Specificity: 91.9%		
ICA, M1 and M2	Yes	100	36	136	
	No	46	410	456	
	Total	146	446	592	
		Sensitivity: 68.5%	Specificity: 91.9%		
ICA, M1, M2 and Other	Yes	103	36	139	PPV: 73.05 (0.66, 0.81)
	No	69	410	479	NPV: 85.59 (0.82, 0.88
	Total	172	446	618	
		Sensitivity: 59.9%	Specificity: 91.9%		

Note: Other includes A1, A2, BA, P1, P2, VA, V4

Table 2b. CADt device Performance by Vessel Location: Viz

		LVO Truth			Other
Vessel Location	Algorithm	Yes	No	Total	
ICA, M1	Yes	39	11	52	
	No	4	509	513	
	Total	43	520	563	
		Sensitivity: 90.7%	Specificity: 97.9%		
M2	Yes	55	11	66	
	No	17	509	526	
	Total	72	520	592	
		Sensitivity: 76.4%	Specificity: 97.9%		
ICA, M1, M2 and Other	Yes	57	11	15	PPV 83.8 (0.72, 0.91)
	No	41	509	533	NPV 92.5 (0.90, 0.94
	Total	98	520	618	
		Sensitivity: 58.2%	Specificity: 97.9%		

Note: Other includes A1, A2, BA, P1, P2, VA, V4

(Filename: TCT_590_Slide1.JPG)

Wednesday, May 3, 2023

2:45-4:00 PM

Scientific Abstract Session: Neurorad Miscellaneous 2

861

Absolute Volumetry of deep Gray Matter in Extremely Preterm Children and Adolescents

A Elzieny[1], R McNaughton[1], R Abushaigah[1], B Setty[1], O Sakai[1], R Joseph[1], S Hooper[2], R Fry[2], J Frazier[3], S Kim[3], S Gogcu[4], D Kennedy[3], L Douglass[1], K Kuban[5], M O'Shea[2], H Jara[1]

[1]Boston University School of Medicine, Boston, MA, [2]University of North Carolina School of Medicine, Chapel Hill, NC, [3]University of Massachusetts Medical School, Worcester, MA, [4]Wake Forest School of Medicine, Winston-Salem, NC, [5]Boston Medical Center, Plymouth, MA

Purpose

Extremely preterm (EP) birth (gestational age <28 weeks) can disrupt brain development leading to a greater risk of life-long adverse neurocognitive outcomes. Structures of deep gray matter (dGM) form complex functional networks with the cerebral cortex and modulate a wide range of brain functions such as motor, cognitive, and emotional. The main objectives of this study were: (1) to assess the longitudinal trajectory of dGM volumes in EP-born participant males and females, (2) to evaluate the relationship between dGM volume with neurological impairment at age 15 in EP participants, (3) to compare EP participants at ages 10 and 15 to full-term (FT) children at age 10 regarding dGM volumes.

Materials and Methods

Subjects included 70 participants of a prospective multicenter longitudinal study of children born EP, who underwent 3.0T brain MRI at both near age 10 and near age 15, and 20 matched full-term dGM volumes at near age 10. Manual segmentation of dGM was performed by a single examiner blinded to clinical outcome, using Fiji-ImageJ 2.3.0, and verified in a sub-sample by an expert neuroradiologist. Segmental volumes were calculated (Figure 1). Neurological impairment was defined by the presence of one or more of the following disorders: autism spectrum disorder, cerebral palsy, epilepsy, or full-scale IQ <85.

Results

70 EP participants had a mean gestational age of 26±1 weeks and half of both groups (EP and FT) were males. dGM volume increased in EP participants between ages 10 and 15 (46.9±5.5 vs 51.7±6.6; p <0.001). Notably, volumes at both 10 and 15 years were lower than volumes in the age 10 FT comparison group (54.9±6.0) (Table 1). Participants without neurological impairment (n=46) had significantly higher dGM volumes than those with such impairment (n=24) (48.7±3.7 to 53.6±6.9 vs. 43.4±3.7 to 48.1±4.1 respectively; p <0.001) (Table 2, Figure 2). Boys had higher dGM volumes than girls at 15 years and in both outcome groups.

Conclusions

Among participants born EP, dGM volumes at ages 10 and 15 years were smaller when compared to the full-term group, and dGM volumes were smaller in females compared to males and in participants with neurological impairment compared to those without. Results await confirmation with adjustment for total brain volume.

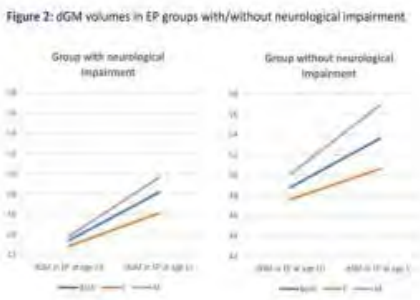

Table 1: dGM volume in EP participants and FT group

	Sex	N	Minimum	Maximum	Mean ± SD
EP dGM at age 10		70	36.14	59.24	46.9 ± 5.5
EP dGM at age 15			38.49	66.08	51.7 ± 6.6
			t -9.737		p <.001
FT dGM at age 10		20	37.61	64.86	54.9 ± 6.0
EP dGM at age 10	F	34	36.14	56.78	47.0 ± 5.5
	M	36	36.71	59.24	46.8 ± 5.5
EP dGM at age 15	F	34	38.49	64.35	49.2 ± 6.4
	M	36	42.38	66.08	54.0 ± 5.9
FT dGM at age 10	F	10	37.61	58.60	51.4 ± 5.9
	M	10	53.20	64.86	58.4 ± 3.9

Table 2: dGM volumes in EP groups with/without neurological impairment

		N	Minimum	Maximum	Mean ± SD	t	p
dGMv in EP with neurological impairment							
dGM at age 10		24	36.14	48.54	43.4 ± 3.7	-6.404	<.001
dGM at age 15			38.49	55.40	48.1 ± 4.1		
dGM at age 10	F	10	36.14	48.45	42.8 ± 4.3	-3.186	.011
dGM at age 15			38.49	51.05	46.1 ± 4.2		
dGM at age 10	M	14	39.10	48.54	43.7 ± 3.3	-6.003	<.001
dGM at age 15			42.38	55.40	49.8 ± 3.5		
dGMv in EP without neurological impairment							
dGM at age 10		46	37.98	59.24	48.7 ± 5.4	-7.441	<.001
dGM at age 15			39.70	66.08	53.6 ± 6.9		
dGM at age 10	F	24	37.98	58.28	47.5 ± 4.9	-3.593	.002
dGM at age 15			39.70	64.35	50.5 ± 6.8		
dGM at age 10	M	22	40.07	59.24	50.0 ± 5.7	-8.212	<.001
dGM at age 15			46.97	66.08	56.8 ± 5.5		

(Filename: TCT_861_Graph.jpg)

287

Cerebral Nocardiosis: Clinical, Laboratory, and Imaging Findings in 33 cases

J REES[1], K Pierre[2]
[1]University of Florida, Gainesville, FL, [2]University of Florida, Gainesville , FL

Purpose

Nocardiosis is an uncommon opportunistic bacterial infection with multiple clinical manifestations. CNS involvement is most typically multiple small brain abscesses. Clinical knowledge of this entity is important given the increasing use of medical therapies which produce immune suppression and because many of its features may be nonspecific and misdiagnosed.

Materials and Methods

We will present a retrospective single institutional review analyzing the imaging, clinical, and microbiological characteristics of Cerebral Nocardiosis in 33 patients with review of the literature.

Results

We have identified 33 cases of proven intracranial CNS Nocardiosis over approximately 19 years at the University of Florida. Our data collection and analysis are ongoing but will be completed by Jan 2023. The imaging features are nonspecific consisting of multiple small ring enhancing lesions scattered throughout the brain with exuberant perilesional edema, and central diffusion restriction. In addition, we have identified 3 cases of head and neck nocardiosis; sinus and/or cervical adenitis, and one case of spinal nocardiosis. Clinically, many of our patients are immune compromised for a variety of reasons, but some were apparently immune competent. Many of our patients had preexisting or concomitant pulmonary nocardia and a small number had other foci of infection, however a certain percent had no documented involvement at other sites. We document a variety of Nocardia subspecies which exhibit a range of antibiotic susceptibilities. Many of our patients required neurosurgical intervention for definitive diagnosis which was not suspected a priori.

Conclusions

This the largest single institution study of the clinical and imaging features of CNS Nocardiosis in the world literature. In addition, we have studied the phenotype and antibiotic susceptibility of several atypical and less well known nocardia subspecies. Given the broad range of new immunomodulatory therapies for neoplasm, autoimmune disorders, and the rising number of somatic allograft transplants requiring long term immune suppression, awareness of and aggressive diagnostic intervention including neurosurgical biopsy is of increasing clinical importance and relevance.

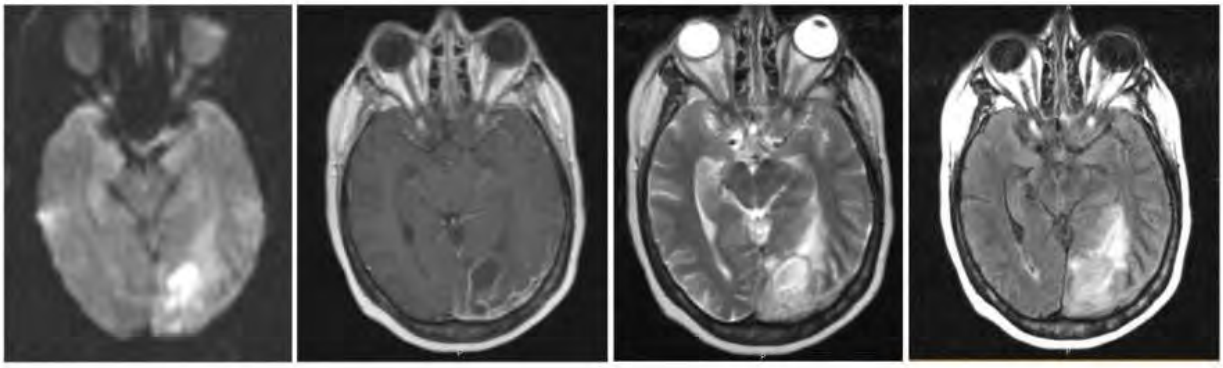

Cerebral Nocardiosis – DWI, Post Gad T1, T2, and FLAIR

(Filename: TCT_287_CerebralNocardiosisCompositeforASNR2023Abstract.JPG)

828

Evaluation of Scout Accelerated Motion Estimation and Reduction (SAMER) MPRAGE for Visual Grading and Volumetric Measurement of Brain Tissue

N Gil[1], W Lo[2], B Clifford[2], M Lang[1], K Awan[1], D Splitthoff[3], D Polak[4], S Cauley[1], S Huang[1]
[1]Massachusetts General Hospital, Harvard Medical School, Boston, MA, [2]Siemens Medical Solutions, USA, Boston, MA, [3]Siemens Healthineers, Erlangen, Germany, [4]Siemens Healthineers, Erlangen, AL

Purpose

To evaluate the recently-developed Scout Accelerated Motion Estimation and Reduction (SAMER) [1] method for correcting motion artifact in volumetric brain MRI with T1-weighted MPRAGE [2], which is important in the clinical evaluation of dementia. We used 90 3D T1-weighted-MPRAGE reconstructed images derived from ten volunteers and demonstrated that SAMER effectively corrects even severe motion with non-diagnostic image quality, greatly increasing the accuracy of volumetric brain measurements.

Materials and Methods

Ten adult volunteers underwent five MPRAGE scans. The first was a Wave-CAIPI-MPRAGE [3] sequence defined as the reference standard. The remaining four were acquisitions performed with a SAMER-MPRAGE research sequence with varying degrees of deep-

breathing-induced motion corruption: "no", "mild", "moderate", and "severe" [4]. Motion-corrupted scans were motion-corrected with SAMER, producing four additional reconstructions. For the resulting nine reconstructed images from each volunteer, Freesurfer [5] measured cortical volume for 11 brain regions (listed in Fig. C/D; "WM" = white matter), which were then averaged across all volunteers. Percent-error of the mean cortical volume for each region of each motion corrupted/corrected scan relative to Wave-CAIPI-MPRAGE was computed.

Results

Representative cases show the effect of each degree of motion and SAMER-correction on the ability to delineate sulci and gyri (Fig. A, arrow), as well as the smoothness of Freesurfer segmentation of inner and outer cortical surfaces (Fig. B, yellow/red outlines). Errors introduced by motion resulted in general underestimation of the reference volume (Fig. C) in a manner directly proportional to the degree of motion. The percent-error values were highest for the temporal lobe (38%) and the cerebral WM (32%) (Fig. D). SAMER considerably reduced the percent-error across all anatomical areas, including the temporal lobe (19%) and cerebral WM (10%). Illustratively, the effect of severe motion correction on volume measurement was statistically significant across all anatomical areas except the brain stem: e.g., the temporal lobe median volume was 72,895 mm3 for motion-corrupted scans versus 93,259 mm3 for motion-corrected scans (Bonferroni-corrected Wilcoxon rank sum test $P < 0.004$).

Conclusions

SAMER can turn non-diagnostic-quality scans into ones that allow for accurate volumetric measurements. SAMER has strong potential for evaluation in practical clinical settings and can contribute to diagnosing dementia.

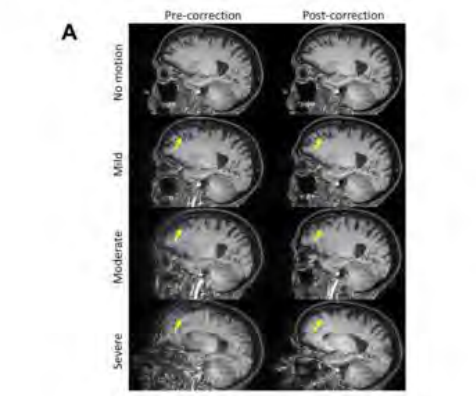

Figure A. Example scans of a single subject representing four motion states: no motion, mild motion, moderate motion, and severe motion, along with effect of motion correction showing the improvement in delineation of sulci and gyri (arrow).

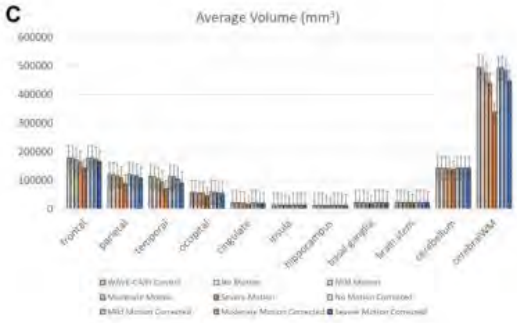

Figure C. Cortical volume for the 11 anatomical regions examined in this work, averaged over all the volunteers for Wave-CAIPI-MPRAGE (gray), motion corrupted (orange shades), and SAMER-motion-corrected (blue shades) scans.

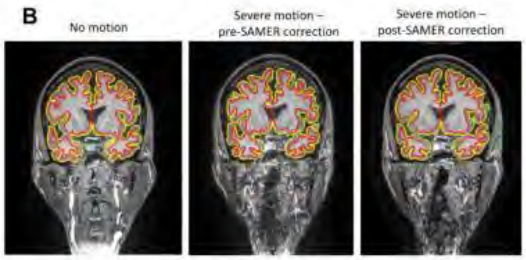

Figure B. Representative Freesurfer segmentation on a coronal slice demonstrating the inner and outer cortical surface on a representative subject's no motion and severe motion scans, before and after SAMER correction.

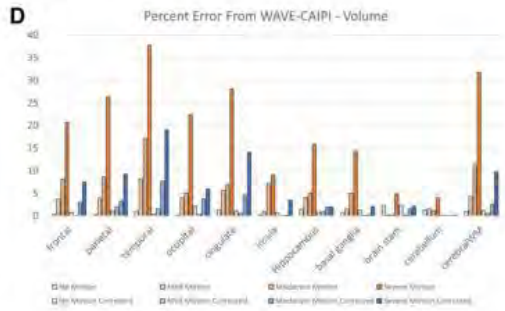

Figure D. Percentage error for the volume, with Wave-CAIPI-MPRAGE serving as the reference standard. Overall, SAMER motion correction results in significant reduction of the percentage error across almost all anatomical areas.

(Filename: TCT_828_SAMER_Figure_ASNR_2023_NG_Rearranged_with_Caption.jpg)

1043

Exploring the Genetic Contribution to Oxidative Stress in Myalgic Encephalomyelitis/Chronic Fatigue Syndrome

N Hampilos[1], A Germain[2], X Mao[1], M Hanson[2], D Shungu[3]

[1]Weill Cornell Medicine, New York, NY, [2]Cornell University, Ithaca, NY, [3]WEILL CORNELL MEDICAL COLLEGE, NEW YORK, NY

Purpose

Strong evidence has implicated oxidative stress as a disease mechanism in myalgic encephalomyelitis/chronic fatigue syndrome (ME/CFS) (1,2). The study aim was to assess whether a C>T single nucleotide polymorphism (SNP) (rs1800668), which reduces the activity of glutathione peroxidase 1 (GPX1), is associated with brain oxidative stress in patients with ME/CFS (3).

Materials and Methods

Study population: The study enrolled 20 patients with ME/CFS diagnosed according to Canadian Consensus Criteria, and 11 healthy control (HC) subjects. Genotyping: DNA was extracted from whole blood samples, amplified by PCR, and purified. Sanger sequencing was used for genotyping. 1H MRS: Proton magnetic resonance spectroscopy (1H MRS) was used to measure levels of

glutathione (GSH) — a primary tissue antioxidant and oxidative stress marker — in a 3x3x2 cm3 occipital cortex (OCC) voxel. GSH spectra were recorded in 15 minutes with the standard J-editing technique. The resulting GSH peak area was normalized to tissue water level in the voxel(1). Statistical Analysis: T-tests were used to compare OCC GSH levels between ME/CFS and HC groups, and between the study's genotype groups (group 1: CC, group 2: combined TC and TT).
Results
Clinical characteristics: ME/CFS and HC groups were comparable on age and BMI but not on sex (p = 0.038). Genotype frequencies: Genotype frequencies in the ME/CFS group were 0.55 (CC), 0.25 (TC) and 0.2 (TT); and 0.636 (CC), 0.364 (TC), and 0 (TT) in the HC group. GSH levels: There was a trend-level lower mean OCC GSH in ME/CFS than in HC (0.0015 vs 0.0017; p = 0.076). GSH levels by genotype group interaction: Within the ME/CFS group but not in the combined ME/CFS and HC group or HC group alone, GSH levels were lower in the TC and TT genotypes than in CC genotypes (0.00143 vs 0.00164; p = 0.018).
Conclusions
This study found that the presence of a C>T SNP in GPX1 is associated with lower mean GSH levels and, hence, brain oxidative stress, in ME/CFS patients. If validated in a larger cohort, this finding may support targeted antioxidant therapy based on their genotype as a potentially effective treatment for patients with ME/CFS.

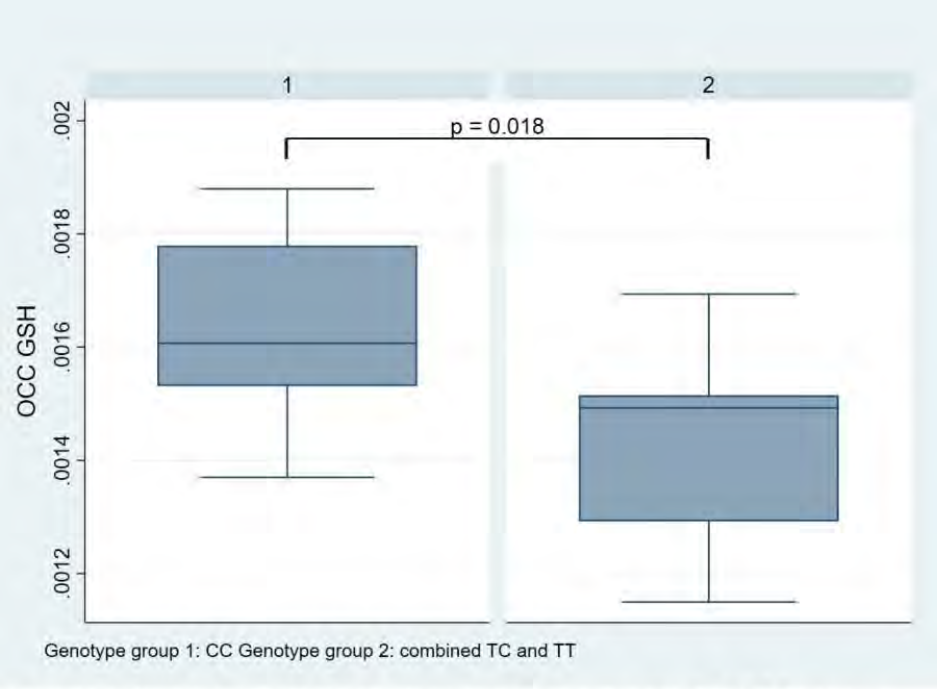

Figure 1: Boxplots of OCC GSH by genotype group in the ME/CFS group

(Filename: TCT_1043_Figure1.jpg)

1359
Flow Artifact Mitigation for Post-Contrast Wave-CAIPI MPRAGE Imaging of the Brain
A Tabari[1], K Awan[2], M Lang[2], B Clifford[3], W Lo[4], D Splitthoff[5], S Cauley[2], P Schaefer[2], S Huang[6], J Conklin[2]
[1]Massachusetts general hospital, Boston, MA, [2]Massachusetts General Hospital, Boston, MA, [3]Siemens Medical Solutions, USA, Boston, MA, [4]Siemens Medical Solutions, Charlestown, MA, [5]Siemens Healthcare GmbH, Erlangen, Germany, [6]Massachusetts General Hospital, Harvard Medical, Boston, MA

Purpose
Vascular flow-related artifacts are common in post-contrast Wave-CAIPI T1 MPRAGE images of the brain. We developed and tested a flow-mitigated Wave-CAIPI T1 MPRAGE acquisition, and tested the protocol in a flow phantom and in patients undergoing contrast-enhanced brain MRI examinations.
Materials and Methods
MRI was performed on a flow phantom, which used pineapple juice to provide T1 shortening1, while the flow was controlled by a peristaltic pump to simulate vascular flow in the cerebral arteries (~200 mL/min). Flow compensation techniques included 1) addition of flow compensation gradients and 2) use of a radial reordering of the k-space data acquisition, both of which were incorporated into the Wave-CAIPI protocol2. Readout bandwidth of the flow-compensated protocol was increased to compensate for increased echo time and to preserve tissue contrast. The flow-mitigated Wave-CAIPI MPRAGE protocol was then evaluated in 17 consecutive patients undergoing contrast-enhanced brain MRI (Siemens Vida). The MRI protocol included Wave-CAIPI post-contrast T1 MPRAGE (without flow-compensation) and the optimized flow-mitigated version of the Wave-CAIPI T1 MPRAGE sequence3. Two

neuroradiologists, blinded to sequence type, independently evaluated the imaging data sets for presence of artifacts, signal-to-noise ratio (SNR), gray-white matter contrast, enhancing lesion contrast, and image blurring on a 3-point Likert scale.
Results
In the phantom experiment, maximal flow artifact reduction was achieved with the combination of flow compensation gradients and radial reordered k-space acquisition. In the 17 clinical cases (F:M 12:5, mean age 54±17 years), the optimized flow-mitigation protocol reduced flow-related artifacts in 15 of 17 (88%) cases and 16 of 17 (94%) cases for raters 1 and 2, respectively. SNR, gray-white contrast, and enhancing lesion contrast were rated as equivalent for standard Wave-CAIPI MPRAGE flow-mitigated Wave-CAIPI MPRAGE in all subjects. The optimized flow-mitigation protocol was the preferred sequence for reduced flow-related artifacts by both raters (P<0.001).
Conclusions
Flow-mitigation was successful at reducing flow-related artifacts in most cases without sacrificing SNR, gray-white matter contrast, or enhancing lesion conspicuity. As fast MRI becomes increasingly adopted in clinical practice, this study highlights the need to minimize unexpected artifacts that may be associated with highly accelerated imaging techniques.

Table 1: Acquisition protocols for Wave MPRAGE with and without flow mitigation

	Wave MPRAGE routine	Wave MPRAGE hybrid flow mitigation
Resolution(mm³)	1x1x1	1x1x1
Acceleration	4	4
Turbo factor	192	192
Acquisition time (min)	2:15	2:11
TE/TI/TR (ms)	3.47/900/2000	4.26/900/2440
FOV (mm)	256/256	256/256
Bandwidth (Hz/px)	200	350
# of Wave cycles	10	09
Reordering	Linear	Radial
Elliptical Scanning	No	Yes
Flow Compensation	Off	On

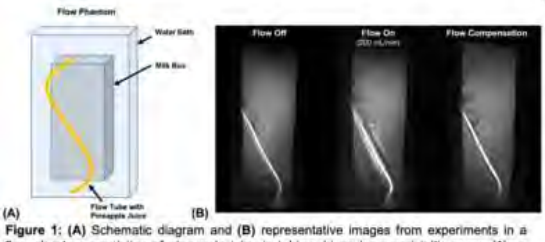

Figure 1: (A) Schematic diagram and (B) representative images from experiments in a flow phantom consisting of pineapple juice in tubing driven by a peristaltic pump. Wave MPRAGE images with flow demonstrate pronounced flow-related artifact, which is improved with flow compensation as described in the proposed flow mitigation protocol (see Table 1).

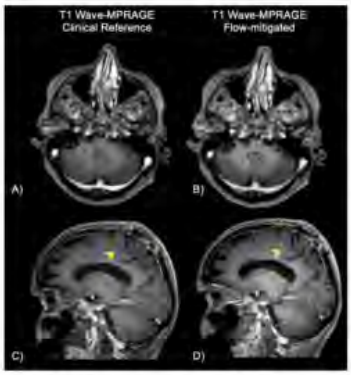

Figure 2: Representative images of an 82-year-old female with progressive multifocal leukoencephalopathy (PML) showing a small focus of apparent enhancement (arrows) on A) axial and C) sagittal views of conventional T1-weighted post-contrast Wave-MPRAGE imaging. No enhancement was noted on the corresponding B) axial and D) sagittal flow-mitigated Wave-MPRAGE images, suggesting that the area of apparent enhancement was consistent with flow-related artifact. Curvilinear enhancement is also seen in the posterior frontal lobe subcortical U-fiber (arrowhead) corresponding to a white matter demyelinating process associated with the patient's known diagnosis of PML.

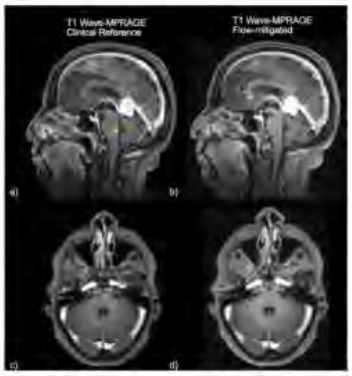

Figure 3: Representative images of a 64-year-old female with a pineal region meningioma. A & C) Conventional T1-weighted Wave-MPRAGE images in sagittal and axial planes demonstrating an enhancing pseudo-lesion in the inferior pons, likely arising from flow in the basilar artery/venous plexus. B & D) Flow-mitigated T1-weighted Wave-MPRAGE images demonstrate no abnormal enhancement in the pons, confirming that the enhancement seen on the conventional Wave-MPRAGE images was artifactual.

(Filename: TCT_1359_Figures.jpg)

1479

Gray and white matter integrity in migraine patients with aura

K Eikermann-Haerter[1], L Eskandarian[2], K Gaudet[3], M Li[4], S Huang[5]
[1]New York University, New York, NY, [2]Massachusetts General Hospital, Harvard Medical School, Boston, MA, [3]Massachusetts General Hospital, Boston, MA, [4]New York University Grossman School of Medicine, New York, NY, [5]Massachusetts General Hospital, Harvard Medical, Boston, MA

Purpose
Migraine is a debilitating headache disorder and one of the most common neurological conditions. Thirty percent of migraine patients develop transient neurological symptoms, the so-called migraine aura. There is increased incidence of white matter lesions (WML) in migraine patients with aura. Our understanding of the microstructural substrate of WMLs in migraineurs [1, 2] is still incomplete.
Materials and Methods
Here, we utilize Soma and Neurite Density Image (SANDI) [3] as an advanced diffusion magnetic resonance imaging signal model to characterize in vivo microstructure of gray matter (GM) and white matter (WM) in 16 migraine patients with aura and 16 age- and sex-matched healthy controls (HC). MR imaging was performed on a 3T Connectome scanner (MAGNETOM Connectom, Siemens Healthcare, Erlangen, Germany) using a diffusion multi-shell acquisition protocol and the MGH-USC Human Connectome project's data preprocessing pipeline [4, 5], including the Freesurfer (http://surfer.nmr.mgh.harvard.edu) and FMRIB Software Library (https://fsl.fmrib.ox.ac.uk) toolboxes for analysis.
Results
We find reduced WM and GM soma radius and intra-neurite signal fraction maps in migraine patients compared to HC ($p < 0.0001$, $p = 0.015$, $p = 0.28$, and $p = 0.0002$, respectively). WM cell body signal fraction was increased in patients compared to HC ($p = 0.001$). Moreover, intra-neurite signal fraction, apparent soma radius, and cell body signal fraction of white matter lesions increased significantly compared to HC and NAWM of the same subjects ($p < 0.04$), while extra-neurite signal fraction increased significantly ($p < 0.0001$). These findings were replicated in several deep gray structures that have been previously reported to show volume loss in

migraine, notably the thalamus, putamen, hippocampus, and amygdala. Healthy controls showed a positive correlation between cell body signal fraction and cortical thickness ($r = 0.7$ and $p = 0.003$) and a negative correlation between intra-neurite signal fraction and cortical thickness in GM, while this relation was not present in migraine patients.
Conclusions
Our data suggest occult changes in microstructural gray and white matter integrity in migraine patients with aura that may precede the development of white matter lesions seen on conventional T2-weighted MRI. Microstructural alterations in gray and white matter integrity in migraine patients with aura suggest a common underlying mechanism driving observed increases in cellular density and neurite loss.

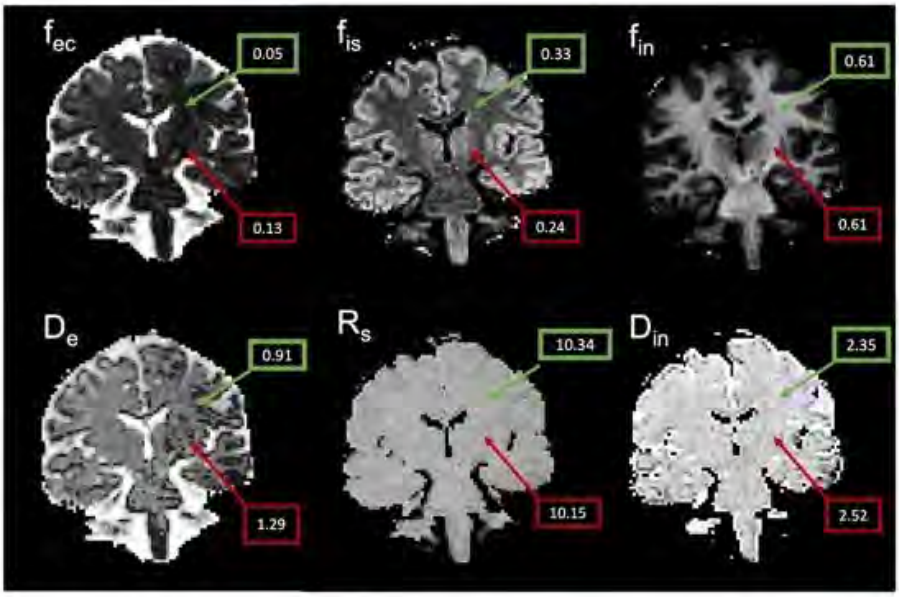

Figure 1. SANDI parameter maps derived from DWI data in a representative migraine patient.

f_{ec} = extra-cellular signal fraction; f_{is} = intra-soma signal fraction; f_{in} = intra-neurite signal fraction; R_s = apparent soma radius. Green boxes indicate representative values in cerebral white matter; red boxes indicate representative values in the accumbens (gray matter).

(Filename: TCT_1479_sandi.jpg)

1245

Introducing the Calloso-Forniceal Distance: A Surrogate Marker for Ventricular Volume

L Nunez[1], D Timaran[2], R Riascos[1], W Zingg-De Jongh[3]
[1]The University of Texas Health Science Center at Houston, Houston, TX, [2]University of Texas Health Science Center Houston, Houston, TX, [3]UTHealth McGovern Medical School, Houston, TX

Purpose
Ventricular enlargement represents a non-specific, common imaging finding that can be associated with both physiologic and pathologic conditions. In an effort to improve radiologic evaluation, several measurements and relative indexes have been proposed as surrogate markers of ventricular volume. However, the lack of appropriate definitions regarding section planes and measurement techniques, have led to inconsistent results limiting the use of imaging biomarkers in clinical practice. Because the sagittal plane is more consistent than the axial and coronal planes, the aim of this study is to introduce the calloso-forniceal (CF) distance as a novel surrogate marker of ventricular volume.
Materials and Methods
Through a retrospective case collection, multiple magnetic resonance (MR) examinations were gathered and classified into three different groups based on the radiology reports, as either normal, brain atrophy, or hydrocephalus. Evans index, Callosal angle, mammillo-pontine distance, and CF distance, were measured in all scans. Ventricular volume was calculated through semi-automatic segmentation and was considered as the gold standard. Spearman correlation coefficient (SCC) was used to compare ventricular volume and imaging biomarkers; a p-value lower than 0.05 was considered significant.
Results
A total of three hundred subjects were included, one hundred in each group. The median ventricular volume across all 3 groups was 39080.00 mm3. The 75th and 25th percentile volumes were 87350 and 19030 mm3, respectively. Among all the imaging biomarkers, CF distance was most closely correlated to our gold standard across all three groups, with a SCC of 0.79, 0.90, and 0.58 in the hydrocephalus, brain atrophy, and normal groups, respectively, with a P value = <0.0001 among all groups. EI was the second closest

biomarker with a SCC of 0.75, 0.83, and 0.43 in the hydrocephalus, brain atrophy, and normal groups, respectively, with a P value = <0.0001 among all groups. Both MP distance and CA had correlations below 0.3 across all three groups.
Conclusions
Widely known markers such as MP and CA demonstrated no correlation with ventricular volume. CF distance showed the higher correlation with ventricular volume among all the imaging biomarkers, followed by EI. As plane angulation poses a significant bias in axial measurements, sagittal plane reproducibility may explain a better diagnostic performance of CF.

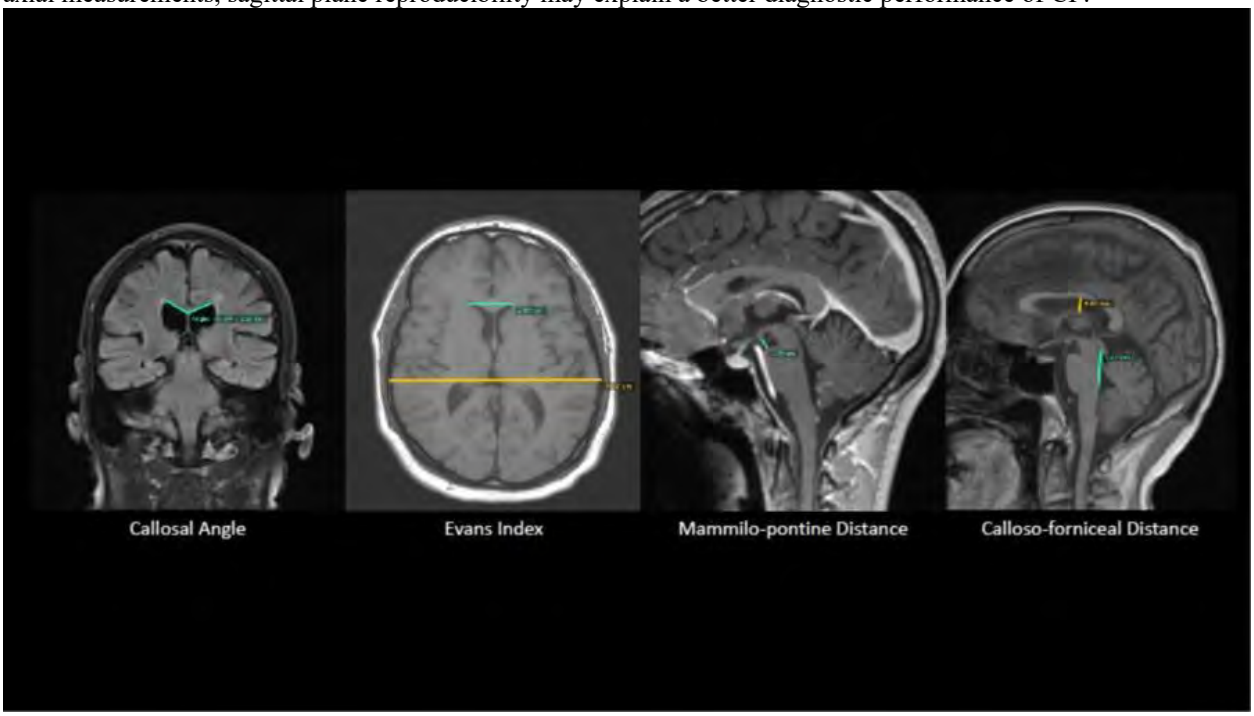

(Filename: TCT_1245_Fig2.jpg)

357

Safety of Gadopiclenol for Magnetic Resonance Imaging (MRI): a Pooled Analysis of Eight Studies

D Roberts[1]
[1]*Medical University of South Carolina, Charleston, SC*

Purpose
Gadopiclenol (Elucirem®, Guerbet) is a high relaxivity macrocyclic gadolinium-based contrast agent (GBCA) [1], approved by the FDA and currently under review by the EMA. The aim of this analysis was to evaluate the global safety of gadopiclenol based on pooled data from all completed clinical studies.
Materials and Methods
Data were obtained from eight phase I to III clinical studies with 1047 patients or healthy volunteers (median [range] age: 55 [2 88] years) receiving gadopiclenol intravenously at doses from 0.025 to 0.3 mmol/kg. In one pediatric study, 80 patients aged 2 17 years received a dose of 0.05 mmol/kg. In cross-over studies, 791 patients also received another GBCA (gadobenate dimeglumine or gadobutrol), administered at 0.1 mmol/kg. Safety data included post-injection adverse events (AEs), all available laboratory measures (biochemistry and hematology), vital signs, and electrocardiograms (ECG).
Results
Most subjects (67.6%) received gadopiclenol at 0.05 mmol/kg. AEs were reported after gadopiclenol in 23.6% of the subjects and were considered related to gadopiclenol for 8.5%. Similar rates of AEs were reported with the other GBCAs in comparative studies. The most common AEs related to gadopiclenol were injection site pain (1.9%), headache (1.3%), nausea (0.7%) and injection site coldness (0.6%). Most AEs were of mild (83.3%) or moderate (12.8%) intensity. Three severe AEs were related to gadopiclenol: injection site pain (2 patients) and upper abdominal pain (1 patient). One serious AE was assessed as related to gadopiclenol (blood creatinine increase of mild intensity). All resolved. Among the pediatric patients, 2 (2.5%) experienced AEs related to gadopiclenol: a mild QT interval prolongation and a moderate maculopapular rash. A good safety profile was also observed in other sensitive populations, such as elderly patients, and patients with renal impairment. No safety concerns were raised from vital signs, laboratory parameters, and ECG data. The thorough QT study confirmed the cardiac safety of gadopiclenol.
Conclusions
Gadopiclenol showed a good safety profile consistent with other GBCAs when used for MRI of the central nervous system and other body regions in adults and pediatric patients aged 2-17 years.

367

Semi-Supervised Learning with Spatial Pseudo Labeling for Peritumoral Infiltration Prediction in Glioblastoma using MR Fingerprinting

W Zhao[1], X Wang[2], C Tippareddy[3], H Akbari[4], A Fathi Kazerooni[4], C Davatzikos[4], M Couce[5], D Ma[1], C Badve[6]

[1]Department of Biomedical Engineering, Case Western Reserve University, Cleveland, OH, [2]Department of Quantitative Health Sciences, Cleveland Clinic, Cleveland, OH, [3]Department of Radiology, University Hospitals Cleveland Medical Center, Willowick, OH, [4]Department of Radiology, Perelman School of Medicine, University of Pennsylvania, Philadelphia, PA, [5]Department of Pathology, University Hospitals Cleveland Medical Center, Cleveland, OH, [6]Department of Radiology, University Hospitals Cleveland Medical Center, Cleveland, OH

Purpose

Standard clinical magnetic resonance (MR) imaging of glioblastoma (GB) cannot identify malignant infiltration into the peritumoral non-enhancing region. We develop a semi-supervised MR fingerprinting (MRF)-based model for tumor infiltration prediction that integrates pretraining based on the near-far heuristic [1,2] with finetuning and spatial pseudo labeling [3] using infiltration ground truth.

Materials and Methods

Pre-operative MRF (T1 and T2) and multiparametric MRI (mpMRI; T1w, T2w, T1w-Gd, FLAIR, and ADC) from GB patients (n = 25) were analyzed. Two edema ROIs were defined on pre-operative FLAIR by a radiology resident (CT) and reviewed by a board-certified neuroradiologist: a "near" ROI (NEAR) adjacent to enhancing tumor margin, and a "far" ROI (FAR) located further than 3 cm from enhancing tumor margin [1]. For subjects with pathologically confirmed infiltration (n = 10), infiltration ROIs (n = 40) identified by targeted biopsy or intra-operative 5-ALA fluorescence-guided resection [4] were annotated by a board-certified neuroradiologist (Figure A), reviewed in collaboration with the operating neurosurgeon, and labeled as "infiltration" (INF). The near-far heuristic was used for initial pretraining and infiltration data was incorporated for model finetuning and spatial pseudo labeling (Figure B). For pretraining (Figure 3A), voxel-based features were extracted from each image's NEAR and FAR voxels (1549 near voxels, 1611 far) using a 3D 5x5x5 voxel sliding kernel. Following MRMR [5] feature selection, a combined MRF and mpMRI model was developed (Figure C). Finetuning was performed by training on INF and FAR voxel features from infiltration data (40 ROIs, 2593 voxels). Spatial pseudo labeling was performed to incorporate unlabeled edema voxels (25787 total) adjacent to infiltration and far ROIs.

Results

The model's LOOCV classification performance on infiltration data was compared following pretraining, finetuning, and spatial pseudo labeling (Figure D). Following finetuning and spatial pseudo labeling (AUC = 0.81), significant improvements to sensitivity (51% to 76%) and accuracy (67% to 71%) were observed.

Conclusions

We introduce a semi-supervised learning scheme to improve GB infiltration prediction using infiltration MRF data that improves classification following model finetuning and spatial pseudo labeling. These findings indicate the potential in employing MRF-based models to guide GB diagnosis and treatment.

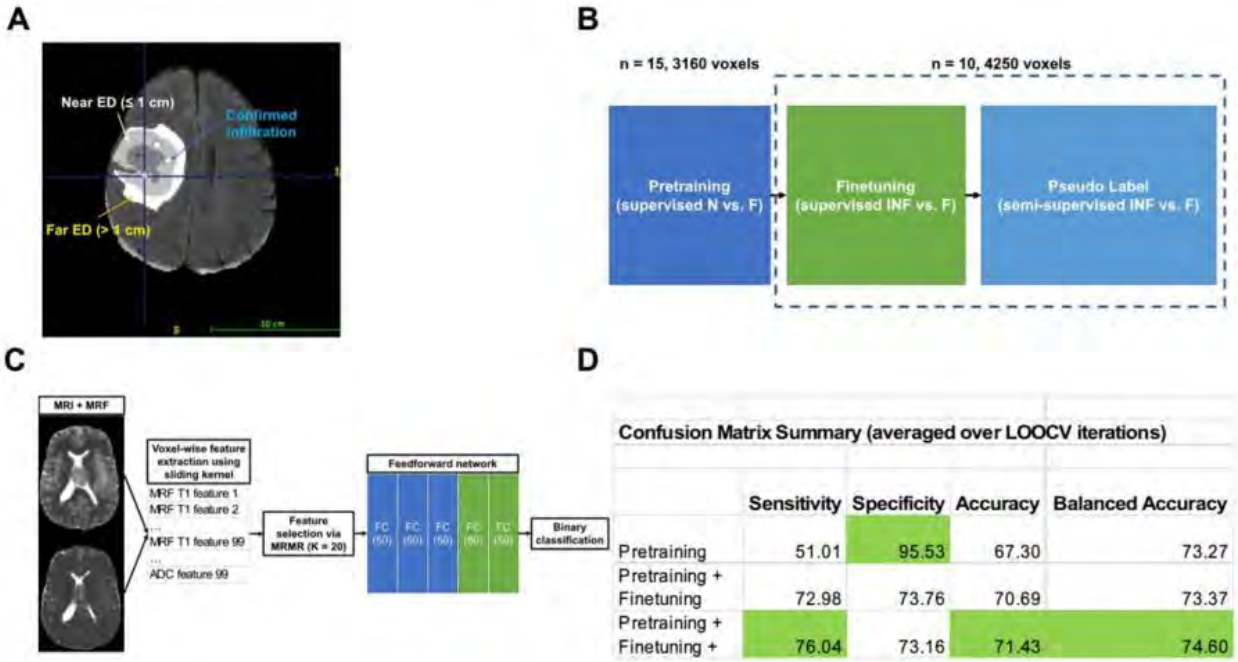

	Sensitivity	Specificity	Accuracy	Balanced Accuracy
Pretraining	51.01	95.53	67.30	73.27
Pretraining + Finetuning	72.98	73.76	70.69	73.37
Pretraining + Finetuning +	76.04	73.16	71.43	74.60

(Filename: TCT_367_2023ASNR.jpg)

809

Transient subcortical T2 hypointensity in SMART syndrome: a possible biomarker of glymphatic inflow dysfunction in cortical and leptomeningeal disease processes.

K Krecke[1], D Black[1], P COGSWELL[1]
[1]*Mayo Clinic, Rochester, MN*

Purpose

T2 signal hypointensity is an occasional finding in white matter deep to cortical and leptomeningeal disease processes, documented in several published case reports. We hypothesize that obstruction of peri-arterial CSF influx or dysfunction of aquaporin-4 channels leads to decreased interstitial fluid as a principal cause of decrease in T2 signal intensity. SMART syndrome consistently demonstrates this T2 phenomenon transiently during the active phase of superficial vascular enhancement and cortical swelling and enhancement. This archetype is a regional asymmetric disease process, allowing for contralateral baseline comparison.

Materials and Methods

Nineteen patients with clinical and MRI evidence of active SMART syndrome were ascertained from a clinical database. MRI exams were inspected for classic SMART cortical and leptomeningeal findings and single exams were selected for evident low T2 signal subjacent to superficial disease. On FLAIR sequences, ROIs were fitted to regions of subcortical white matter low T2 signal and the contralateral, putatively normal, subcortical white matter. Intensity values were recorded. When available, T2* sequences where similarly interrogated with matching ROIs. Percentage differences were computed with the normal side as denominator. Range, median and mean was computed separately for FLAIR and T2* series.

Results

18 of 19 patients with active cortical encephalopathy of SMART syndrome had measurable transient T2 signal decrease in subjacent white matter at the time of MRI examination. The percent decrease in relative T2 signal averaged -21% (range: -3 to -39%, median -21%). T2* signal intensity decrease in matched ROIs averaged -11% (range: -1 to -22%, median -8%). Anecdotal examples of patients with subarachnoid hemorrhage (T2: -26%) bacterial leptomeningitis (T2: -20%, T2*: -3%) and MOG cortical encephalitis (T2: -19%, T2*: -9%) showed quantitatively similar effects.

Conclusions

Subcortical white matter low T2 signal is a consistent transient finding in active SMART syndrome. T2* effects are muted, suggesting that decreased intraparenchymal water outweighs the effects of paramagnetic metabolites. We hypothesize that the mechanism of signal loss is interference with glymphatic fluid influx in SMART and other leptomeningeal and cortical pathologies.

168

Workflow Interruptions in an Era of Instant Messaging: A Detailed Analysis

C Pierson[1], R Bruce[1], T Kennedy[1], J Yu[1]
[1]*University of Wisconsin School of Medicine and Public Health, Madison, WI*

Purpose

The complex practice environment and myriad of clinical responsibilities incumbent on diagnostic radiologists create workflows that are uniquely susceptible to disruption. To reduce the number and effect of interruptions on radiologists, new communication platforms such as instant messaging have rapidly emerged as an efficient and potentially asynchronous communication tool; however, a quantitative understanding of the effect of this new mode of communication on radiologist workflow remains unknown. The overall objective of this retrospective study is to quantify the number and frequency of interruptions experienced by radiologists using a newly deployed instant messaging platform at our institution.

Materials and Methods

Instant messaging logs (Webex, Cisco, San Jose, CA) of neuroradiology fellows staffed to our main reading room from 7/5/2021-12/31/2021 were collected. Messages included in our study include only those sent Monday-Friday between the hours of 0600-2100. Messages were categorized by sender and time of day (0600-1000; 1000-1200; 1200-1500; 1500-1800; 1800-2100). Interruptions per shift, defined as a message sent or received by the main reading room neuroradiology fellow(s), were calculated based on month, week, and day of the week.

Results

14,424 messages were sent across 289 total shifts during the study period. 6 neuroradiology fellows assigned to the main reading room sent 3,258 messages and received 10,260 messages from technologists and other staff. There was an average of 50 interruptions per shift when examined by month (range 48 – 53), and an average of 52 interruptions per shift when examined by day of the week (range 40 – 60).

Conclusions

In keeping with prior studies examining interruption rates with phone calls, neuroradiology fellows experienced an equivalent to increased number of interruptions during clinical shifts from an instant messaging platform [1-2]. These disruptions, when considered in conjunction with other non-interpretative tasks such as phone calls, case consultations, and examination protocoling, may have negative implications for workflow efficiency, diagnostic accuracy, and patient safety [3-4].

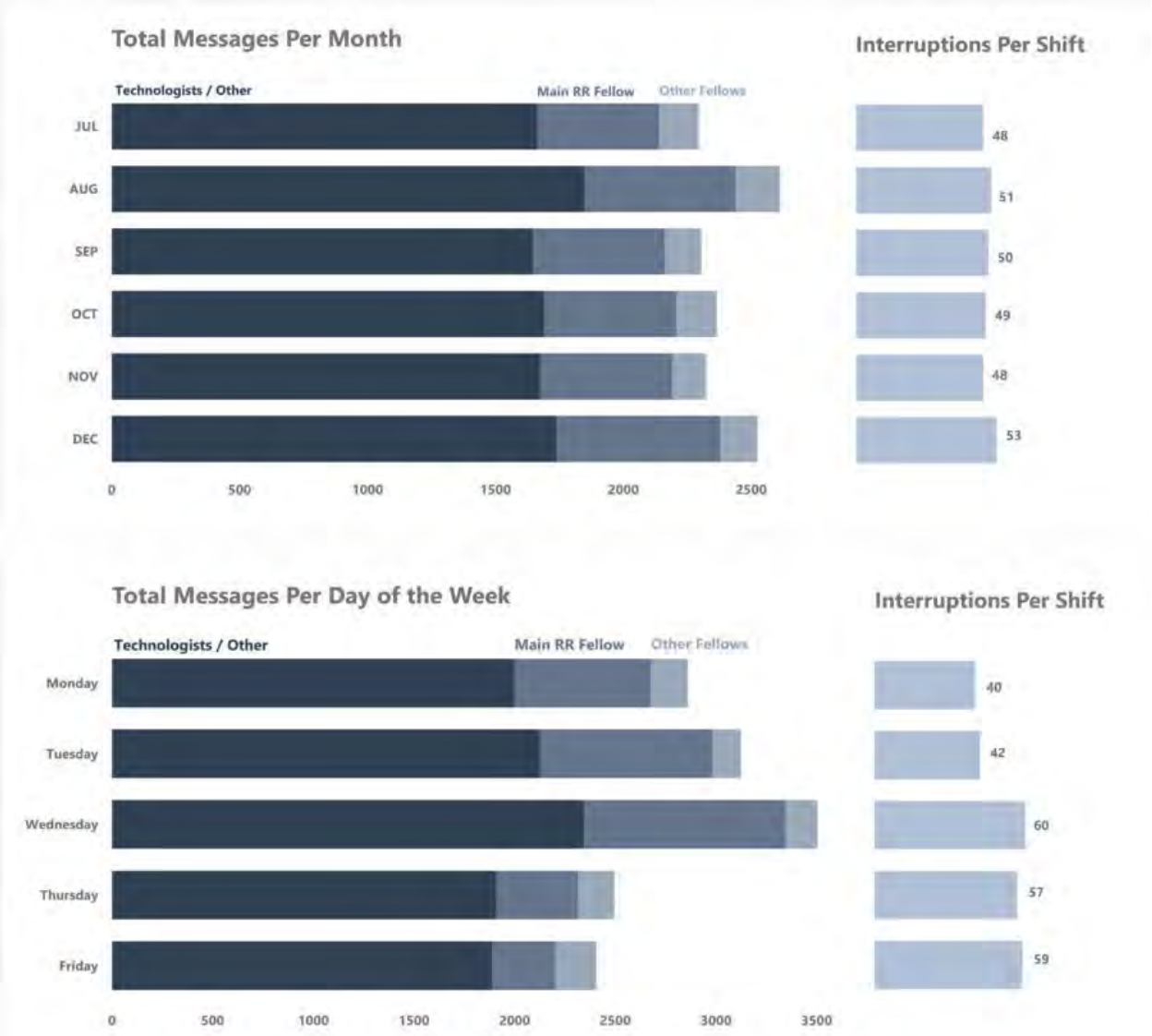

(Filename: TCT_168_ASNRFig1.jpg)

Sunday, April 30, 2023
2:50-3:30 PM
Live Educational Exhibits Session 1

694

A Primer on Blockchain in Neuroradiology — Data Ownership and Beyond

M Haider[1], M Aboian[2], I Ikuta[3], S Merkaj[1], M Farhat[1]
[1]Yale School of Medicine, New Haven, CT, [2]Yale University, Woodbridge, CT, [3]Mayo Clinic Arizona, Phoenix, AZ

Purpose

1. Introduce blockchain as a decentralized system that can make patient data more secure and portable. 2. List the applications of blockchain in the field of Neuroradiology. 3. Elaborate on the utility of blockchain databases in management of imaging data in clinical practice. 4. Highlight the role of blockchain in complementing the functions of AI in image processing and analysis, and securing clinical trials.

Materials and Methods

Latest facial recognition software demonstrates ability to fully reconstruct faces of patients whose MRIs underwent removal of facial features. Multiple states in the US are considering to follow strict recommendations of EU's GDPR and to grant patients more rights over their data, which may affect imaging research and the concomitant use of Al in research. This educational exhibit presents background information on blockchain which is a digital ledger popularized by cryptocurrency, and can be used as an alternative to building traditional databases.

Results

PubMed review of 38 articles searched with "blockchain", "imaging", "radiology" was performed; information on potential uses of blockchain in radiology was compiled; and definitions of DAO and governance structures used in decentralized data were obtained from finance literature.

Conclusions

This exhibit describes blockchain as a tool for storing, transmitting and analyzing imaging data in Neuroradiology. Through ingenious use of metadata, blockchain can gauge the amount of radiation exposure incurred by the patient at each procedure; adjudicate billing claims for radiological workup; determine levels of contribution in comprehensive radiology reports and annotations (fig.1); and even permit cross-institutional 'dynamic consenting', giving patients the unique ability to modify consent without having to repeatedly fill forms to report important details, e.g. allergies to contrast material, at every admission. The shared ledger keeps track of all events in a systematized way. This allows for imaging data to be stored locally while metadata can be uploaded on the blockchain, secured through a private key owned by the patient and subsequently used as a pointer to locate the stored image once patient grants access to it. Such advancements in processing imaging datasets augment the amount of high quality data available for training phase of AI algorithms. Superimposing blockchain on AI algorithms further allows for human oversight over the workings of AI. Clinical trials, similarly, can also be rendered tamper-proof.

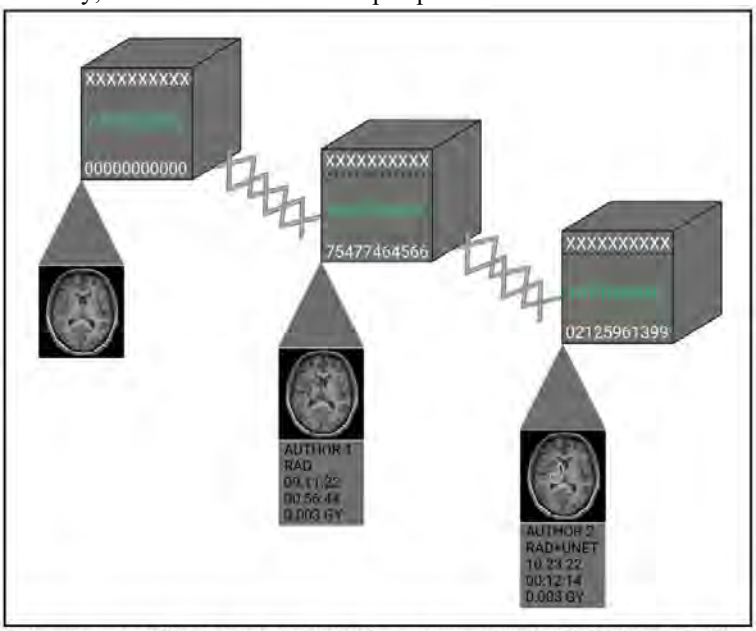

Fig. 1 shows concept map of blockchain structure in relation to its functions: stores metadata within a "block", locks it with a "hash" (an alphanumeric key), adds a new block in a decentralized manner – only once consensus is reached between the nodes across the system; and block by block, creates an immutable "chain". Application: Blockchain provides the distinct ability to measure the contribution of each neuroradiologist in the form of an annotation on a scan (e.g. Boodoo et al.) through use of metadata generated as a result of each action, and to even determine if the said contribution is from a human or an AI algorithm – down to its version.

(Filename: TCT_694_BlockchainEEASNR4.jpg)

1065

Effective atomic number as a novel quantitative CT imaging marker to differentiate primary CNS lymphoma from brain metastasis

T NAKANO[1], M Nakajo[2], T Hasegawa[3], K KAMIMURA[4], T Yoshiura[2]

[1]Kagoshima university, Kagoshima, Japan, [2]Kagoshima University Graduate School of Medical and Dental Sciences, Kagoshima, Japan, [3]Kagoshima University graduate school of medical and dental sciences, Kagoshima, Kagoshima, [4]Kagoshima University Graduate School of Medical and Dental Sciences, Kagoshima, Select a State or Province

Purpose

To determine whether dual-energy CT parameters including electron density (ED) and effective atomic number (Zeff) could be quantitative imaging markers to differentiate primary CNS lymphoma from brain metastasis.

Materials and Methods

This study included 39 consecutive patients with pathologically proven CNS lymphoma (n=18) and brain metastasis (n=21). For all patients, preoperative dual-energy CT examination was performed using a spectral detector CT scanner. ROIs were drawn to fill the solid parts within each tumor avoiding cystic and calcified areas with reference to conventional MR images, and placed onto exactly the same locations in the images of conventional poly-energetic CT value (CT), ED and Zeff. The mean CT, ED, and Zeff values were compared between CNS lymphomas and brain metastases using the Mann-Whitney U test. Receiver operating characteristic (ROC) curve analysis was carried out to assess the ability of CT, ED and Zeff values to differentiate CNS lymphomas from brain metastases. Sensitivity and specificity were calculated with a threshold criterion that would maximize the average of sensitivity and specificity.

Results

The mean Zeff value of CNS lymphoma (7.41±0.07) was significantly higher than that of metastatic tumor (7.32±0.05) (p=0.0005), whereas no significant differences were shown in CT or ED (p=0.0965 and 0.4220, respectively). The areas under the ROC curves for differentiating CNS lymphomas from brain metastases were 0.656, 0.575 and 0.827 for CT, ED, and Zeff, respectively. With a cut-off value of 7.34, the sensitivity and specificity of Zeff for differentiating CNS lymphomas from metastatic tumors were 88.89% and 66.67%, respectively.

Conclusions

Zeff derived from dual-energy CT may be useful for differentiating primary CNS lymphoma from brain metastasis. Zeff could be a new quantitative CT imaging marker for characterizing brain tumors.

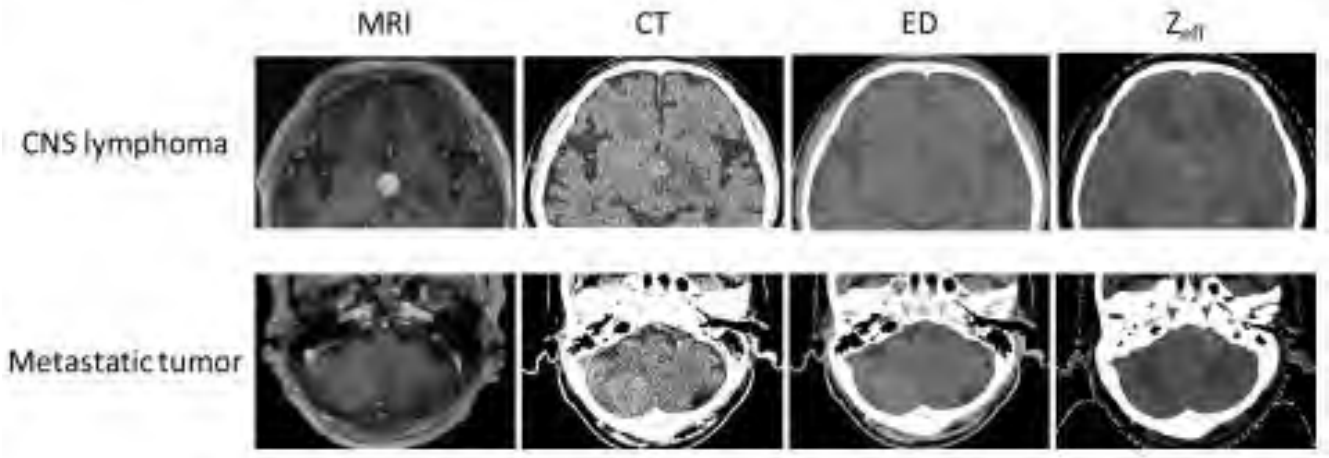

CT, ED and Z_{eff} values of CNS lymphomas and metastatic tumors

	CNS lymphomas (n=18)	Metastatic tumors (n=21)	*P* value*
CT (HU)	36.10 ± 5.23	26.58 ± 6.50	0.0965
ED (%EDW)	103.07 ± 0.57	102.52 ± 0.70	0.4220
Z_{eff}	7.41 ± 0.07	7.32 ± 0.05	0.0005

ROC curves

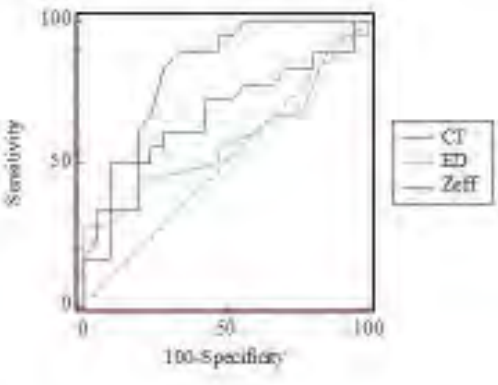

(Filename: TCT_1065_ASNR.jpg)

716

Let There Be Light: PET Imaging of Synaptic Density in Alzheimer's and Epilepsy

D Ramakrishnan[1], T Toyonaga[2], B Khazai[3], M Sala[1], J Cai[2], M Aboian[4]

[1]Yale School of Medicine, New Haven, CT, [2]Yale University, New Haven, CT, [3]Norwalk Hospital-Yale School of Medicine, Norwalk, CT, [4]Yale University, Woodbridge, CT

Purpose

PET imaging using synaptic vesicle glycoprotein 2A (SV2A) tracer has been described in the literature as a promising avenue to study in-vivo synaptic density changes in Alzheimer's and epilepsy. EDUCATIONAL OBJECTIVES: • Describe the studies that established the correlation between SV2A PET and post-mortem measurement of synaptic density. • Compare the different properties of 11C and 18F-labeled SV2A tracers • Review the published literature on findings of SV2A PET imaging in Alzheimer's and epilepsy. • Propose the future applications of SV2A PET tracers in neurodegenerative disease and epilepsy imaging.

Materials and Methods

To discuss the correlation between synaptic density measured by SV2A PET imaging and post-mortem analysis of brain tissue, compare the pharmacodynamics of 11C and 18F-labeled SV2A tracers, present studies of SV2A PET imaging in Alzheimer's and epilepsy, and discuss future applications of SV2A tracers.

Results

Literature review of the development and types of SV2A PET tracers and animal/human studies of SV2A PET imaging in Alzheimer's and epilepsy.

Conclusions

Our educational exhibit highlights the potential of using SV2A PET tracers in studying in-vivo synaptic density changes in Alzheimer's and epilepsy. First, we discuss the development of the [11C] UCB-J SV2A PET tracer and its correlation with in-vitro SV2A protein levels in primate brain tissue using immunohistochemistry (IHC) and western blotting. Next, we discuss the advantages of a novel [18F] SynVesT-1 over the [11C] UCB-J SV2A PET tracer, which include its larger binding potential (BPND) and longer half-life of isotope. We present findings from studies that have used SV2A PET imaging to reveal a significant decrease in synaptic density in the hippocampus of Alzheimer's patients. We also discuss the role of SV2A PET in studying rat models of epilepsy, which have found that SV2A loss can lead to epileptogenesis and drug resistance. We discuss preliminary human studies using SV2A PET that have demonstrated decreased SV2A levels in the ipsilateral mesial temporal lobe of patients with temporal lobe epilepsy. Finally, we discuss potential future applications of SV2A PET imaging, including early detection of Alzheimer's, treatment response assessment of new Alzheimer's drugs, and pre-surgical identification of seizure onset zone in epilepsy.

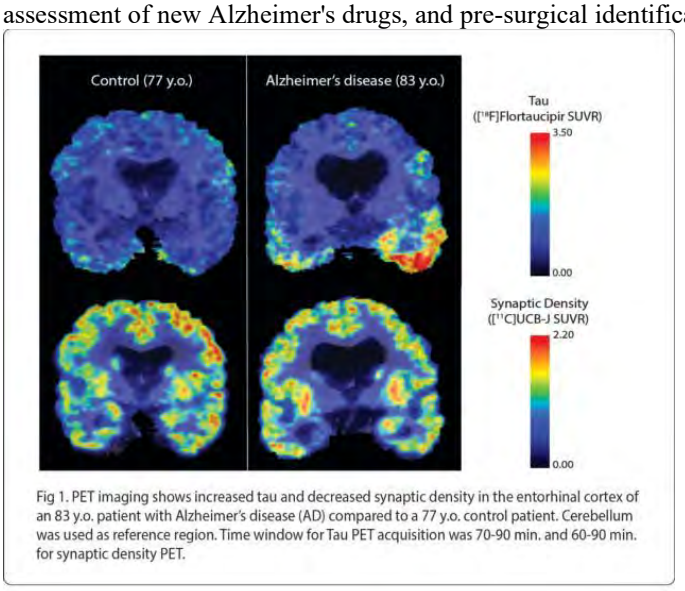

Fig 1. PET imaging shows increased tau and decreased synaptic density in the entorhinal cortex of an 83 y.o. patient with Alzheimer's disease (AD) compared to a 77 y.o. control patient. Cerebellum was used as reference region. Time window for Tau PET acquisition was 70-90 min. and 60-90 min. for synaptic density PET.

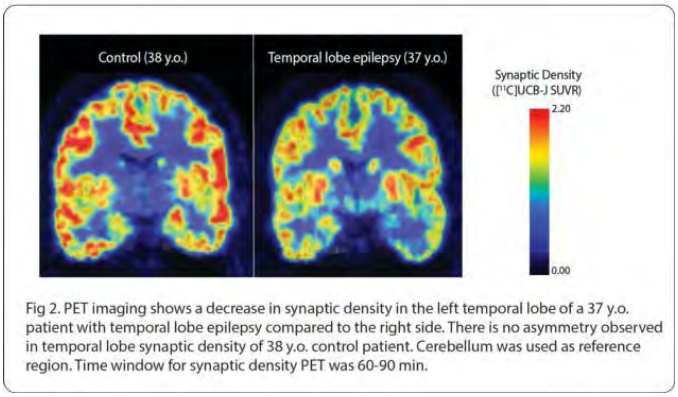

Fig 2. PET imaging shows a decrease in synaptic density in the left temporal lobe of a 37 y.o. patient with temporal lobe epilepsy compared to the right side. There is no asymmetry observed in temporal lobe synaptic density of 38 y.o. control patient. Cerebellum was used as reference region. Time window for synaptic density PET was 60-90 min.

(Filename: TCT_716_Synaptic_density_figs.jpg)

1269

The Brainstem Stroke Atlas: What Every Neuroradiologist Needs to Master the Anatomy and Expertly Diagnose Brainstem Stroke Syndromes

A Frazzitta[1], C Reynolds[2], S Rogers[1]

[1]University of Arizona, Tucson, AZ, [2]University of Arizona - Tucson, Tucson, AZ

Purpose

We provide a novel, color-coded atlas overlaid onto high-resolution MRI, allowing for expert reference of brainstem tracts, nuclei, and microvasculature. The atlas is detailed but not overly cumbersome, providing the framework radiologists need to quickly achieve higher mastery. The atlas overviews the cervicomedullary junction, lower medulla, mid medulla, pontomedullary junction, lower pons, mid pons, upper pons, high pons, lower midbrain, mid midbrain, and midbrain thalamic junction. Using case-based examples we apply the atlas to and describe the classic brainstem stroke syndromes. These include lateral medullary syndrome (Wallenberg syndrome), medial medullary syndrome (Déjerine syndrome), Babinski-Nageotte syndrome, hemimedullary syndrome (Reinhold syndrome), facial colliculus syndrome, medial pontine infarcts & Foville syndrome, lateral pontine syndrome (Marie Foix syndrome), Locked-in syndrome, medial midbrain infarct (Claude syndrome), and ventrolateral midbrain infarcts (Weber syndrome). We also provide clinical pearls on the clinical presentation of posterior circulation infarcts and helpful localizing signs such as crossed sensory and crossed motor deficits. In summary, this Brainstem Stroke Atlas will serve as the neuroradiologist's trusty companion, empowering radiologists to continue their vital role in comprehensively describing complex anatomy with clinical symptoms. This will only get more important with time, as ongoing advances in clinical MRI will demonstrate the tracts and nuclei ever more clearly. 1. Review the clinical presentation of posterior circulation infarcts 2. Overview the brainstem stroke atlas and master major nuclei, tracts, and microvasculature 3. Review common brainstem stroke syndromes by applying cases to the atlas to explain clinical symptoms

Materials and Methods

Brainstem anatomy is difficult to master and challenging to apply real time in the heat of an acute stroke MRI. Both neuroradiologists and neurologists may have difficulty correlating a patient's symptoms with brainstem lesions, which are often subtle. Classically described brainstem stroke syndromes do serve as a guide, however the variability of affected nuclei and tracts can complicate the diagnosis. Detailed knowledge of both brainstem neuroanatomy and classic stroke syndromes is therefore essential for the neuroradiologist to help clinicians comprehensively and confidently explain a patient's symptoms.

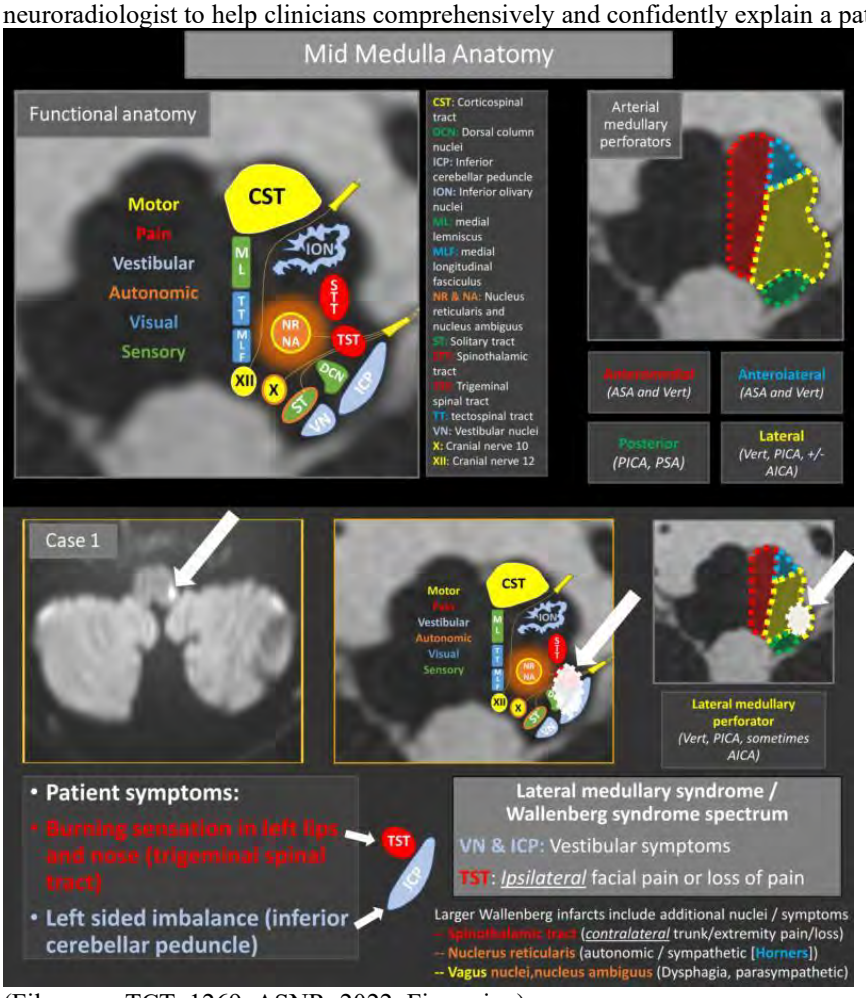

(Filename: TCT_1269_ASNR_2022_Figure.jpg)

Monday, May 1, 2023
2:50-3:30 PM
Live Educational Exhibits Session 2

214

CT and MR Imaging Findings of Lingual Nerve Perineural Spread

M Prenc[1], S Sozio[2], A Tjan[3], S Kim[4], S Mukherji[5]
[1]UHC Sisters of Mercy, Zagreb, Grad Zagreb, [2]Rutgers Cancer Institute of New Jersey, New Brunswick, NJ, [3]Siloam Hospital Banjarmasin, Banjarmasin, South Kalimantan, [4]Rutgers-Robert Wood Johnson Medical School, New Brunswick, NJ, [5]ProScan Imagng, Carmel, IN

Materials and Methods

Retrograde perineural spread is a well-described entity involving many major nerves including the inferior alveolar, facial and branches of the trigeminal nerves. However, isolated perineural spread along the lingual nerve (LNPNS) has not been well-described in the literature and is often overlooked. The intent of this paper is to describe the CT and MR imaging findings of LNPNS and provide imaging landmarks that help the neuroradiologist identify lingual nerve involvement and assist radiation oncologists plan initial treatment in patients with high risk of LNPNS.

Results

This is a retrospective review of CT and MR of patients with recurrent squamous cell carcinoma and adenoid cystic carcinoma with initially unrecognized LNPNS. The presentation will 1. Review the anatomy of the lingual nerve and is enhanced with original anatomic illustrations 2. Describe the characteristic findings of LNPNS and 3. Identify anatomic "anchor points" that help radiologists identify potential LNPNS and assist radiation oncologists contour the lingual nerve pathway in patients at risk for LNPNS.

Conclusions

LNPNS is characterized by thickening and enhancement along the course of the lingual nerve which extends from the lateral floor of mouth (between the mylohyoid and hyoglossus muscles) proximally along the medial aspect of the mandibular ramus to the main trunk of V3. We also identify and illustrate 5 unique "anchor points" (1. foramen ovale, 2. lateral pterygoid muscle, 3. transition between lateral & medial pterygoid muscles, 4. pterygomandibular space, 5. posterolateral FOM) to help radiologists identify potential LNPNS and assist radiation oncologists contour the lingual nerve pathway. LNPNS is a potential pathway of recurrent floor of mouth cancers which is often clinically occult. This educational presentation will help radiologists diagnose patients with LNPNS and help radiation oncologists plan treatment in patients who are at high risk for LNPNS.

270

Fetal Ear Anatomy and Anomalies

M Soldatelli[1], S Hiremath[2], P Krishnan[3], B Ertl-Wagner[4], S Cushing[1], D Chitayat[5], P Shannon[6], S BLASER[7]
[1]The Hospital for Sick Children (Sickkids), Toronto, Ontario, [2]The Hospital for Sick Children, Toronto, Ontario, [3]The Hospital for Sick Children, University of Toronto, Toronto, ONTARIO, [4]The Hospital for Sick Children, University of Toronto, Toronto, Ontario, [5]Mount Sinai Hospital, Toronto, Ontario, [6]University of Toronto, Toronto, Ontario, [7]HOSP. FOR SICK CHILDREN, TORONTO, ON

Purpose

Ultrasound is the gold standard for prenatal imaging, and although 3D-ultrasound helps delineate the pinna, its visualization of the middle and inner ear is limited. In contrast, MRI is capable of high spatial resolution and can trace the development of the temporal bone structures during gestation. It is possible to fully delineate the cochlea, vestibule, semicircular canals, and the middle ear using MRI as early as 13 weeks of gestational age (GA). This review aims to: - Investigate the ability of the fetal MRI to depict the normal ear anatomy between 16 and 41 weeks of GA and ear malformations of the pinna, external auditory canal, middle ear, and inner ear in both syndromic and non-syndromic patients. - Understand the additional benefit of fetal MRI over fetal US in identifying the ear structures. - Illustrate normal and abnormal ear anatomy on postnatal or post-mortem fetal MRI obtained in selected cases - Identify additional extra-labyrinthine features to aid in phenotype-genotype correlation. For example: o Small pons, ocular coloboma, choanal atresia and absent olfactory bulbs accompany semicircular canal atresia in CHD7/CHARGE o Bicoronal synostosis and syndactyly accompany lateral semicircular canal anlage (absent bone islands) in Apert Syndrome

Materials and Methods

Review the ease of visualization of the pinna, external auditory canal, cochlea, modiolus, vestibule and semicircular canals at different gestational ages. Describe ear malformations in both syndromic and non-syndromic patients and identify extra-labyrinthine clues, such as facial and extremity abnormalities, to show how evaluation of the fetal ear aids in phenotype-genotype prediction and prognostication. Serve as a comprehensive review for neuroradiologists and pediatric radiologists working with fetal MRI.

Results

Retrospective study approved by the institutional review board of our terciary academic pediatric institution. The MRI protocol included 1.5 and 3T imaging with SSFSE and T2* sequences in all cases. 3D skin-surface reconstructions and postnatal or post-mortem imaging in selected cases. The imaging data was reviewed from 2000 to 2022 by a senior pediatric neuroradiologist with 35 year of experience.

Conclusions

• Evaluation of the fetal ear can be performed on routine fetal MRI and augmented with 3D surface reconstructions. • Identification of ear abnormalities and extra-labyrinthine anomalies aids in phenotype-genotype correlation.

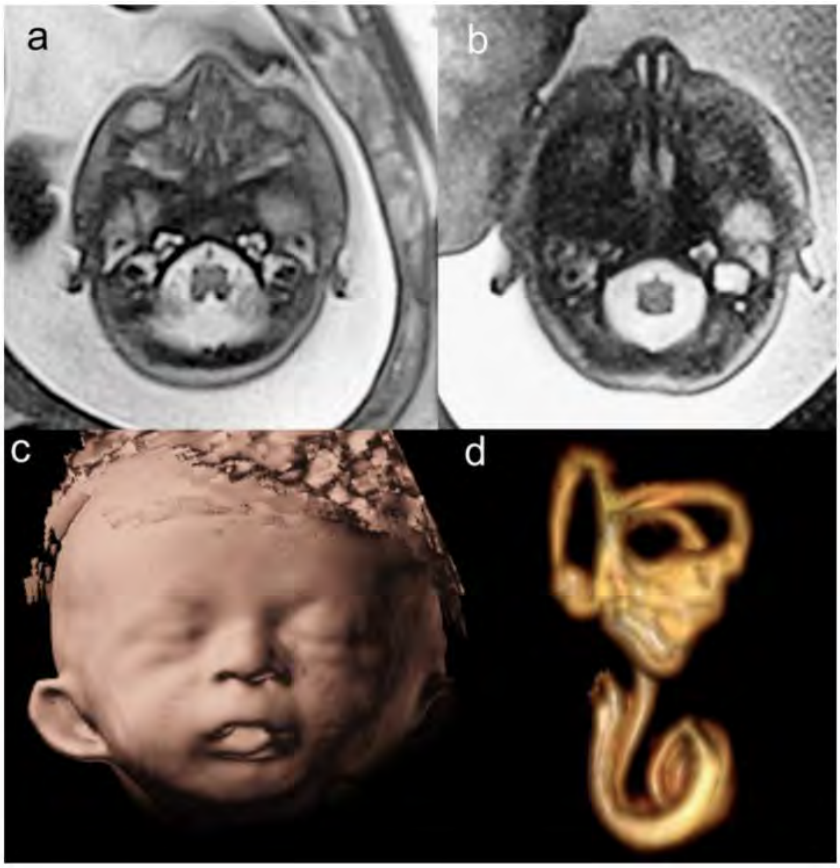

Legend: (a) SSFSET2 demonstrates normal inner ear, GA 25+5. (b) SSFSET2 reveals left LSCC anlage (absent bone island) in Apert Syndrome GA 25+5. (c) MRI 3D surface reconstruction shows cup pinna deformity in Emmanuel Syndrome GA 31+4. (d) Fetal autopsy specimen, high-resolution MRI.

(Filename: TCT_270_Figure.jpg)

480

Incidence of hypersensitivity reactions and anaphylaxis after epidural patching with fibrin glue

M Kim[1], M Malinzak[2], P Kranz[3], L Gray leithe[4], T AMRHEIN[5]

[1]Duke University, Raleigh, NC, [2]Duke University Medical Center, durham, NC, [3]Duke University Medical Center, Cary, NC, [4]duke, Raleigh, NC, [5]Duke University Medical Center, Durham, NC

Purpose

Spinal CSF leaks result in debilitating symptoms and are effectively treated with epidural blood patching (EBP). Historically, EBP used only autologous blood. Recently, CSF leak referral centers have added fibrin glue, a hemostatic agent used in surgery, to improve efficacy. However, the complications of EBP with fibrin glue have not been investigated. Aprotinin, a component within fibrin glue, is allergenic with estimated allergic reaction rates of 0.1-5.8% during thoracic surgery (1).

Materials and Methods

The purpose of this study was to determine the incidence of hypersensitivity and anaphylactic reactions after EBP with fibrin glue and to identify patient and procedural characteristics that may predispose to such reactions.

Results

This retrospective cohort study included patients that underwent EBP with fibrin glue to treat CSF leaks at Duke University from 1/1/09-6/5/22. Cases were identified via manual review of procedure logs in the electronic health record (EHR) with supplemental EHR query system searches including DEDUCE/SLICER DICER. Factors including patient demographics, presence and degree of hypersensitivity reactions and procedural and disease characteristics were recorded. Anaphylaxis was defined by clinically significant cardiovascular, respiratory, neurologic, or mucosal symptoms (2).

Conclusions

A total of 2956 EBPs with fibrin glue in 1334 patients were identified. 66.9% (n=892) of the patients were female. A total of 13 hypersensitivity reactions were recorded, establishing a per procedure incidence of 0.04% (13/2956) and per population incidence of 9.7/1,000. Anaphylactic reactions occurred in 53.8% (7/13) of the hypersensitivity reactions for a per procedure incidence of 0.02% (7/2956) and per population incidence of 5.2/1,000. Mean age of the hypersensitivity cohort was 41+/-14.7 (16-64) years. No hypersensitivity reactions took place on the first exposure to fibrin glue. Median duration of time since prior exposure to fibrin glue

was 84 days (IQR:193.5, Range 24-3072). Hypersensitivity reactions after EBP with fibrin glue for the treatment of CSF leaks are rare but potentially life-threatening since greater than half lead to anaphylaxis. Such events only occurred after re-exposure to fibrin glue.

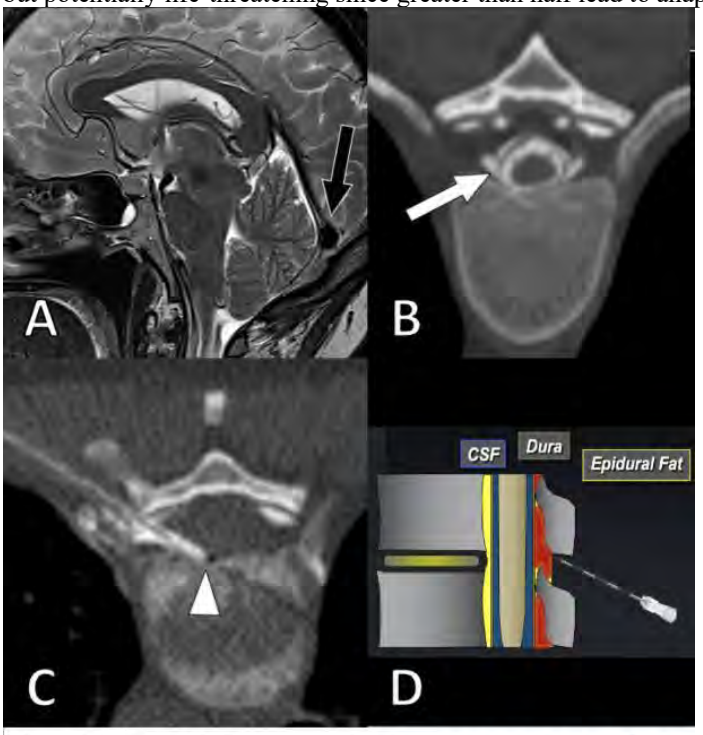

Figure: Example of a CT fluoroscopy guided epidural patch using blood and fibrin glue in a patient with confirmed spontaneous intracranial hypotension (SIH). A) Sagittal T2 weighted image from an MRI of the brain demonstrates inferior cerebellar tonsillar ectopia, venous sinus distension (black arrow), and decreased mamillopontine distance consistent with SIH. B) Axial image from CT myelogram demonstrates ventral extradural contrast confirming spinal CSF leak. C) CT guided transforaminal approach ventral epidural blood and fibrin glue patch at T7/8 to treat the CSF leak. D) Diagram demonstrating the concept of epidural patching. Percutaneous needle delivers patching material (red) into epidural space.

(Filename: TCT_480_Figures.jpg)

883

Neuroradiology Blind Spots! A Primer Before Your Next ER Rotation

A Tejani[1], A Hussien[2]

[1]UT Southwestern Medical Center, Frisco, TX, [2]UT Southwestern, Garland, TX

Purpose

Context: The rapid pace needed to interpret cases in a timely manner during an emergency radiology (ER) shift can be overwhelming, enabling premature closure or satisfaction of search in study interpretation. Consequently, radiologists and residents may miss findings that they would otherwise detect in less pressing settings. A proactive approach involving review of potential misses, common blind spots, and cognitive biases will help minimize mistakes. A systematic approach to learning these blind spots will enable the radiologist to build a mental "checklist" that guides efficient, thorough interpretation despite pressure to jump to the next case. Educational Objectives: 1. Understand common sources of error in evaluating ER neuroimaging. 2. Review cognitive bias and diagnostic errors in reviewing ER neuroimaging. 3. Review blind spots in reading CT and MRI head and neck images. 4. Provide examples of the most common blind spots in neuroimaging to prepare residents and attending radiologists before their next ER shift. Presentation Summary: 1. Introduction a. Demands in ER (i.e., short turnaround time) and consequent sources of error in imaging interpretation 2. Brief review of bias contributing to errors in ER neuroimaging interpretation a. Satisfaction of search b. Premature closure c. Availability bias d. Blind spot bias 3. Case-based review of blind spots on CT and MRI head and neck Images a. Brain parenchyma (beyond acute trauma) b. Vascular structures I. Dural venous sinuses II. Arterial structures on non-contrast enhanced CT and MR studies c. Basal Cisterns d. Orbits e. Parotid/Salivary Glands f. Osseous structures I. Leveraging reformatted images for subtle fractures g. Visualized soft tissues 4. Leveraging MRI sequences for a targeted approach 5. Example search pattern to guide ER image review a. CT Brain b. MR Brain

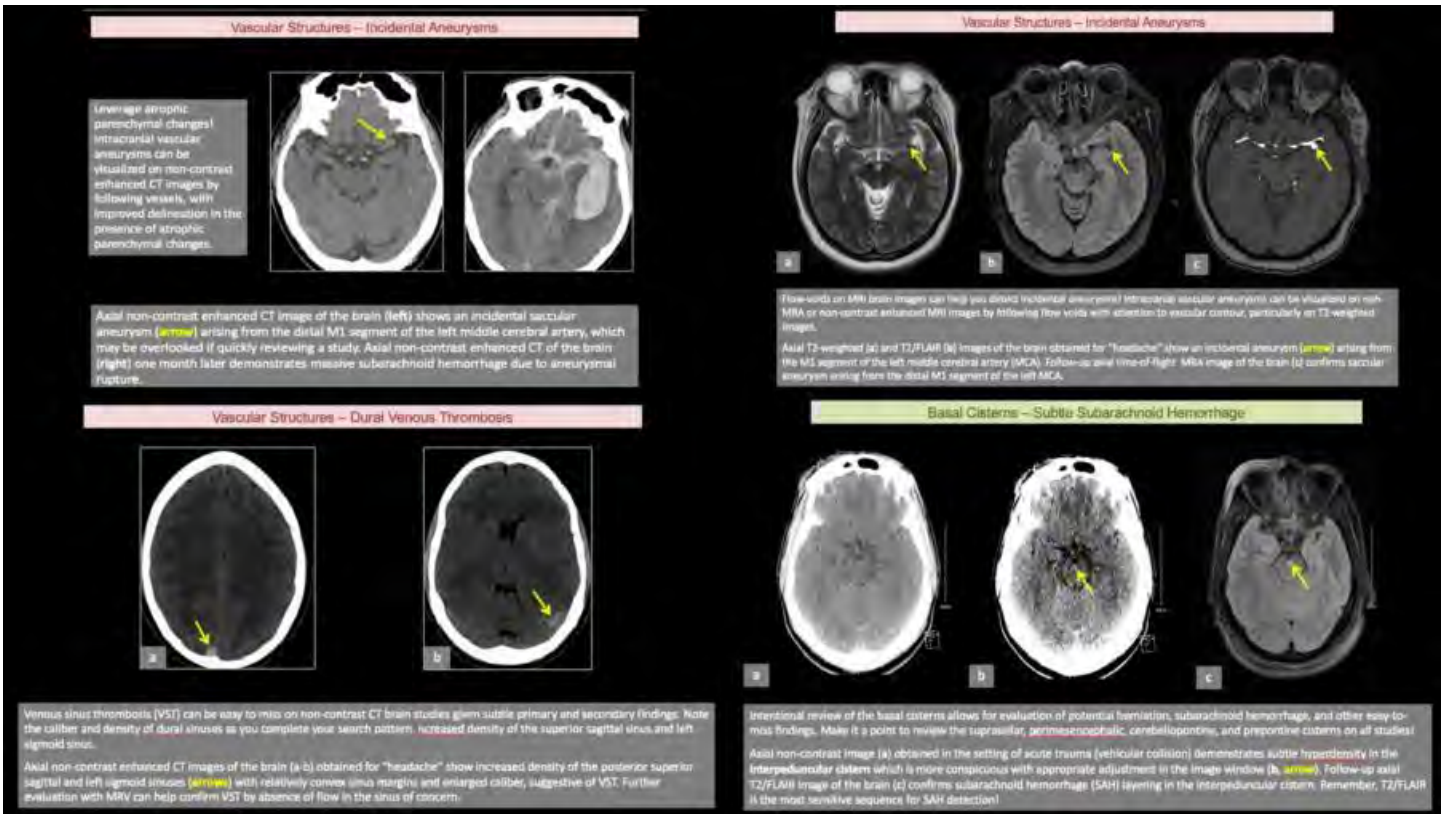

(Filename: TCT_883_Tejani_BlindSpots.jpg)

Tuesday, May 2, 2023
2:50-3:30 PM
Live ePoster Session

1303

Diffusion Tensor Imaging (DTI) Analysis of Neural Networks in Patients with Drug Resistance Temporal Lobe Epilepsy (TLE)

M Alberti[1], G Vatti[2], S Bartalini[2], M Angelozzi[2], D Momi[3], G Mazza[2], T Casseri[4], L Monti[5], A Rossi[2]
[1]Neuroimaging Unit, Siena, Siena, [2]Neurology Unit, siena, siena, [3]Krembil Centre for Neuroinformatics, Toronto, Toronto, [4]Radiology Unit, Siena, Tuscany, [5]NEUROIMAGING UNIT AOUS, SIENA, ITALY, siena, siena

Purpose

Rising evidence highlights the importance of white matter damage in epilepsy (1).Diffusion tensor imaging (DTI) and its analytical wings, have demonstrated microstructural alterations in tracts usually involved in Temporal lobe epilepsy (TLE).The aim of our study is to analyze and quantify microstructural alterations able to predict the prevalent neural networks in drug resistant TLE through the involved tracts.

Materials and Methods

Ten normal subjects and sixteen patients with TLE (mean age 44,4 yrs; M9:W7) underwent MR examination. Morphological and DTI sequences were acquired by using 1.5T Siemens Aera machine using a 2D EPI diffusion sequence. TE=90 ms, and TR=7244 ms. A total of 64 diffusion sampling directions were acquired and the b-value was 1000 s/mm². The slice thickness was 2.3 mm. DTI analysis and tractography were processed by DSI Studio (2,3). Arcuate Fasciculus (AF), Fornix (F), Superior Longitudinal Fasciculus (SLF), Inferior Longitudinal Fasciculus (ILF), Uncinate Fasciculus (UF) and Spine-cortical tracts were tracked by using DSI Studio and compared between healthy and age-matched subjects. Anderson & Pearson test was used to identify normality distribution. Mann Whitney U test and Unpaired t-test were used for the data analysis.

Results

Spine-cortical tracts did not result statistically different while all other studied fascicles (healthy right/left hemisphere vs epileptic right/left hemisphere) resulted statistically different. Comparison between healthy subjects and epileptic patients demonstrated that the tracts involved in language and memory were highlighted by statistical analysis: FA values of AF (p=0.0002 Left; p=0.0174), F (p=0.0058 Right; p=0.0004 Left), SLF (p=0.0001 Right; p=0.0001Left) , ILF(p=0.0001 Right; p=0.0001 Left), UF(p=0.0012 Left; p=0.0003Right).

Conclusions

Drug-resistant TLE patient presents an alteration of the language and memory networks, and this translates into a picture of greater

complexity which should drive the therapeutic choice and therefore the patient management. The use of DTI can contribute to the understanding of seizure propagation networks to facilitate the choice for increasingly less invasive surgery, such as thermal ablation or deep brain stimulation.

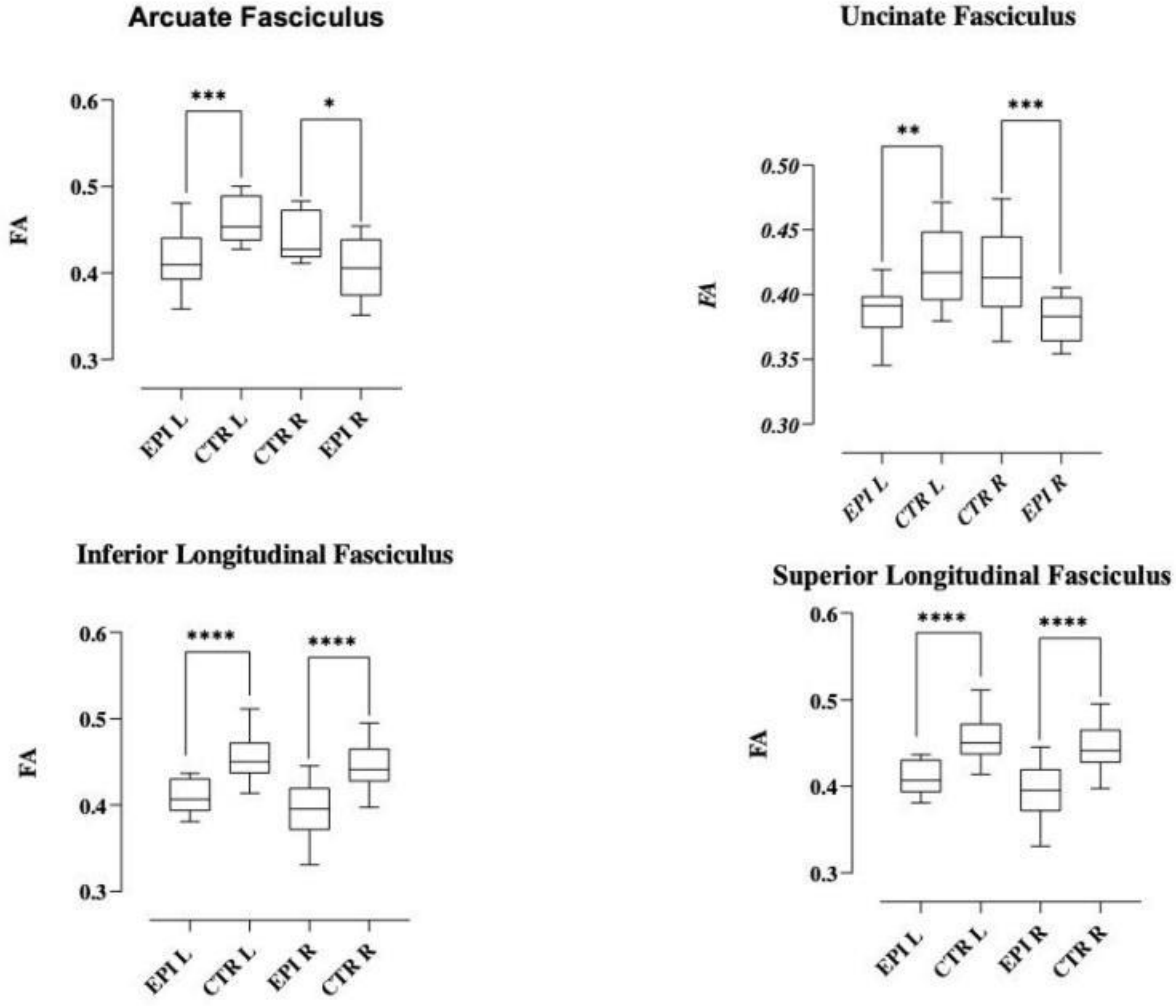

(Filename: TCT_1303_unnamed.jpg)

234

Early [18F]-Florbetaben (eFBB) Can Measure Cerebral Blood Flow in Patients with Memory Concerns: a Comparison Study using Simultaneous Gold-standard [15O]-Water PET/MRI

A Fettahoglu[1], M Zhao[1], M Khalighi[1], E Mormino[1], M Moseley[1], K Chen[2], G Zaharchuk[1]
[1]Stanford University, Stanford, CA, [2]National Taiwan University, Taipei, Taiwan

Purpose

[18F]-Florbetaben (FBB) PET is a β-amyloid plaque radiotracer for neurodegenerative dementias such as Alzheimer's disease (AD). Due to its lipophilicity and high first-pass extraction, early phase FBB (eFBB) may be used to measure cerebral blood flow (CBF), another important dementia biomarker. Using simultaneous PET/MRI, we compared gold standard [15O]-PET CBF to eFBB reconstructions from time of injection to 5 minutes to determine the optimal frame duration for perfusion extraction.

Materials and Methods

Data were collected from 14 subjects (age 69±8.7 yrs, 8 Aβ+ and 6 Aβ-) using simultaneous 3T PET/MRI (GE Healthcare). Subjects received 775 MBq of [15O]-water followed 25 min later by 330 Mbq of [18F]-FBB. Images were reconstructed with OSEM at 3 iterations, 28 subsets, and a 4 mm Gaussian post-reconstruction filter. eFBB images were reconstructed from time of injection (TOI) to 30s, 60s, 120s and 300s post-injection, yielding four early duration uptake images for comparison. [15O]-water CBF quantification was performed using the phase-contrast PET method (1). eFBB images were normalized and scaled to phase-contrast total blood flow measurement. All images were registered to the MNI-152 template. Whole brain correlation was calculated for each subject. A qualitative comparison of images was also performed.

Results

The optimal time reference of eFBB that relays perfusion was determined to be 120s post TOI to balance flow sensitivity and signal-

to-noise ratio. The mean correlation coefficient (R) for 120s eFBB for all the cohort was 0.96, and did not depend on β-amyloid pathology. Images demonstrated high similarity visually to gold standard [15O]-water CBF imaging.

Conclusions

Early imaging of [18F]-FBB is a promising method to measure CBF, as indicated by the high correlation reported for the whole brain and qualitative similarities observed. While a 120s reconstruction demonstrates high correlation, this may depend on the sensitivity of the PET scanner being used. The ability to acquire both CBF and amyloid burden from a single examination would expedite the workup and provide valuable information for research studies in dementia patients.

Recon Time	30s	60s	120s	300s
Correlation (R)	0.73±0.19	0.94±0.03	0.96±0.03	0.96±0.03

Correlation coefficient vs. reconstruction time.

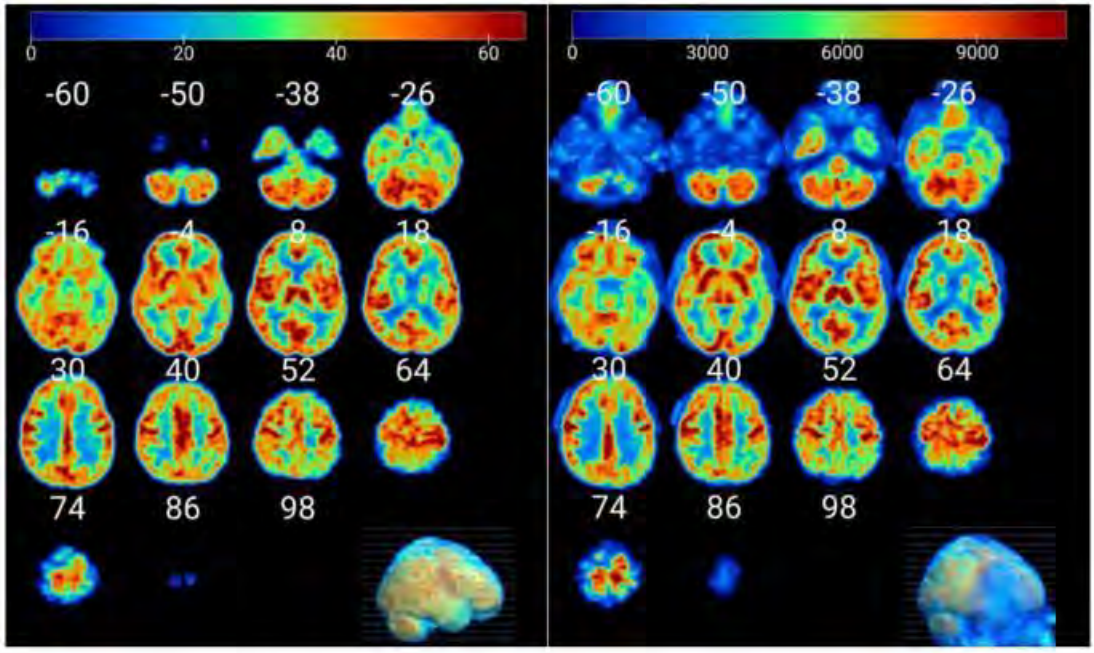

A representative image of [^{15}O]-water CBF (ml/100g/min) and 120s eFBB (AD Subject).

(Filename: TCT_234_ASNR_fig.jpg)

1087

ulti-threshold Mapping of 18F-Fluorethyltyrosine Positron Emission Tomography (18F-FET PET) Improves Tumor Detection in Primary Malignant Brain Tumor Patients

A Gauger[1], M Veronesi[1], N Smith[1]

[1]*Indiana University School of Medicine, Indianapolis, IN*

Purpose

The purpose of this project was to analyze whether volumetric mapping of various TBR thresholds would yield information beyond typically reported threshold cutoffs (i.e. TBRmax >2.5 or TBRmean >2.0) for distinguishing progressive disease from treatment induced changes.

Materials and Methods

Hybrid 18F-FET PET/MRI was obtained in patients during routine clinical care with tissue confirmed high grade glioma (HGG) when the prior MRI was equivocal for progressive disease (POD) versus treatment related changes (TRC). 43 patients with grades III or IV were imaged via a Siemens 3T Biograph mMR PET/MRI unit from Aug 6th, 2020-Apr 14th, 2022, and retrospectively analyzed. A 1 ml region of interest was drawn around the lesion of interest and a ratio was determined relative to a crescentic volume on the

contralateral normal side of the brain (TBR). The TBRmax threshold, TBRmean threshold, and TBRmax volumes above 1.6, 2.0, 2.5, and 3.0 were recorded following 18F-FET PET acquisition. Change in lesion volume on conventional post-contrast MRI relative to prior exam were also included in the analysis. All patients were monitored for at least 6 months, where subsequent pathology, imaging, and clinical reports helped establish a final diagnosis. Any patient who died before 6 months was counted as POD.

Results

Table 1 summarizes accuracy, specificity, and sensitivity of volumetric MRI, static 18F-FET TBRmax and mean values used in clinical practice, and 18F-FET TBRmax volumes (both less than and greater than 1 ml). TBRmax > 2.5 and TBRmean > 2.0 was more accurate for detecting POD than conventional MRI assessment. The greatest accuracy was achieved (100%) when TBRmax activity exceed 2.5 with a volume > 1 ml. Figure 1 shows an example of the method used for volumetric analysis of a patient segmented based on four different 18F-FET PET TBRmax thresholds (1.6, 2.0, 2.5, and 3.0).

Conclusions

18F-FET PET volumetric information increased diagnostic accuracy when TBRmax exceeded a 2.5 threshold at a volume greater than 1 ml. Stratification of tumor activity with regard to 18F-FET volumes may lend additional valuable information than simply reporting static TBRmax and mean values during clinical management of patients with high grade glioma.

Table 1. Analysis of volumetric measurements for discriminating POD from TRC in high grade glioma (HGG) patients. 43 total patients were assessed by the three parameters, where values under threshold (TBR_{max},TBR_{mean}, or MRI change in volume) were assigned as TRC while those surpassing threshold were assigned as POD. Predicted assignments were compared to established diagnoses, where 34 total patients experienced POD. Accuracy was provided for the stratified subpopulations, while combined accuracy, sensitivity, and specificity values were included for the parameters as a whole.

Parameter	Accuracy	Specificity	Sensitivity
MRI change in volume	63%	89%	56%
Size increase > 25% (n=20)	95%	-	-
Size increase < 25% (n=23)	35%	-	-
Static TBR_{mean}	84%	64%	91%
TBR_{mean} > 2.0 (n=33)	88%	-	-
TBR_{mean} < 2.0 (n=10)	70%	-	-
Static TBR_{max}	86%	78%	88%
TBR_{max} < 2.5 (n=11)	64%	-	-
TBR_{max} > 2.5 (n=32)	94%	-	-
TBR_{max} > 2.5 and volume < 1 ml (n=11)	82%	-	-
TBR_{max} > 2.5 and volume > 1 ml (n=21)	100%	-	-

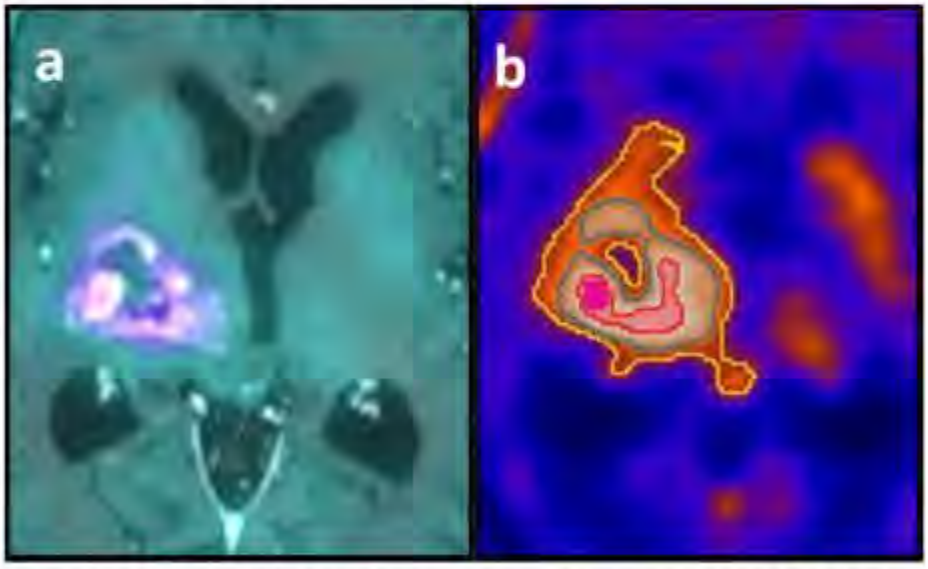

Figure 1: ^{18}F-FET PET TBRmax volumetric determination in a patient with a right thalamic Glioblastoma. (A.) PET/MR fusion image shows enhanced ^{18}F-FET PET uptake in the area of contrast enhancement on MRI. Static ^{18}F-FET analysis revealed a TBRmax of 3.1. (B.) TBRmax volumes were determined using cutoffs of TBR 1.6 (yellow outline), 2.0 (blue outline) , 2.5 (red outline), and 3.0 (pink outline). The volumes were 42.41 mL, 18.69 mL, 2.91 mL, and 0.53 mL respectively.

(Filename: TCT_1087_FinalASNRFigures1024_1.jpg)

272

U-Net for Spine Segmentation - Towards Osteoporotic Fracture Detection

J Renslo[1], B Chang[2], Q Dong[2], d haynor[3], S Johnston[4], G Luo[2], J Perry[2], N Lane[5], J JARVIK[2], N Cross[2]

[1]Keck USC, Los Angeles, CA, [2]University of Washington, Seattle, WA, [3]univ of washington, seattle, WA, [4]University of Washington, seattle, WA, [5]UC Davis Health, Hillsborough, CA

Purpose

Screening for osteoporosis (OP) is strongly recommended by the USPSTF. Incidental spinal fractures are diagnostic of prevalent OP and are currently underreported. Automated screening of radiographs could facilitate detection of these fractures that do not come to medical attention. To build such a tool to do so, the location of vertebral bodies (VB) must be identified. The U-Net deep learning model has been well studied for its segmentation efficacy. It has not yet been evaluated on certain large-scale medical corpora. This work explores how U-Net may be used to identify VB location on lateral and thoracic and lumbar spine radiographs using the Osteoporotic Fractures in Men Study (MrOS).

Materials and Methods

Lateral thoracic and lumbar radiographs were obtained from 4,461 men participating in MrOS. Radiographs were obtained using standardized procedures at baseline and a four-year follow-up visit. We used annotated radiographs (n=15,521) to train a U-Net deep learning model to segment VBs. We split images randomly into train, validation, and test sets (70%/15%/15%), preprocessed with contrast limited adaptive histogram normalization, then resized and zero-padded to 512x512 pixels. Output was a map of each pixel's likelihood of including a VB. This map was binarized, and bounding boxes (BB) were drawn automatically around VB candidates. We used the Jaccard score to evaluate performance for our primary analysis. Secondary analysis evaluated F1 score, failure analysis of image confounders, and BB mean-centroid-distance on random subsamples of test set images.

Results

The mean Jaccard score for test radiographs was 76%±0.23%, n=2,329 (background vs. any vertebral body). The model also found unannotated VBs as demonstrated in Figure 1. Failure analysis revealed significant Jaccard score losses due to lettering on the image (n=155, p=0.04). BB centroid-distance analysis revealed an average of 5.89±0.03 pixel displacement (n=100 images, 632 VBs), or 10.5% of the mean endplate length. F1 score for object detection was 96.1% (0.99 PPV, 0.93 sensitivity, n=632 VBs).

Conclusions

Our study demonstrates that a semantic vertebra segmentation model can be generated with U-Net and a large high quality training dataset. This model, with some postprocessing, will inform future work on automated vertebral segmentation of spine radiographs providing a vital component of an automated pipeline.

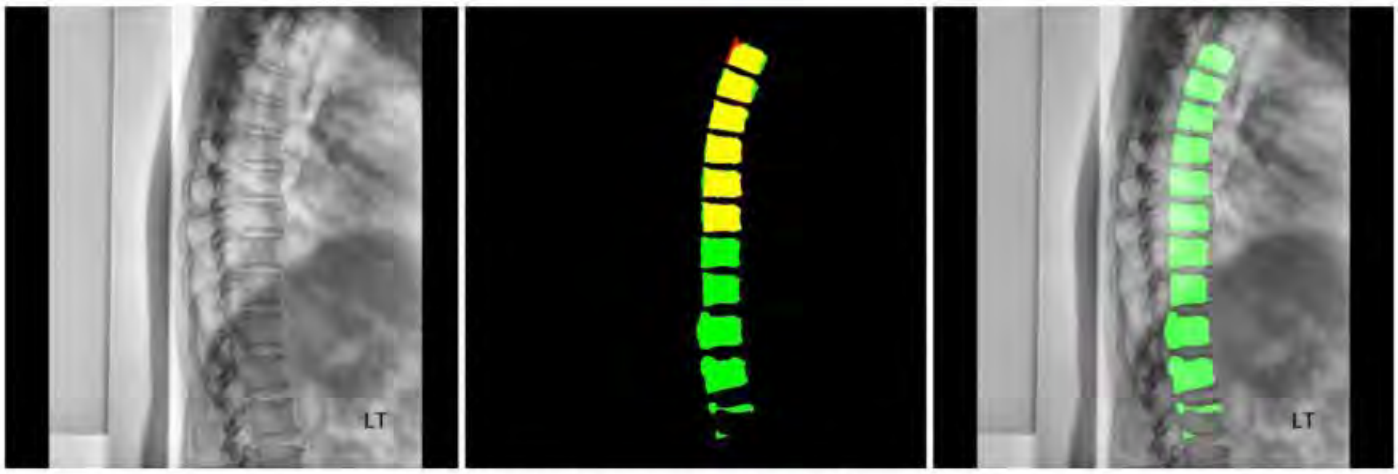

Figure 1: Image used for failure analysis. Left – preprocessed image. Center – overlayed prediction (green channel) on ground truth (red channel). Overlap is yellow. Right – Prediction overlayed on preprocessed image

(Filename: TCT_272_Figure1-FA_v2.jpg)

235

3D Machine Learning Algorithm for Characterizing the HPV Status of Oropharyngeal Cancers

E Qiu[1], M Vejdani Jahromi[1], A Kaliaev[1], D Gaberz-Mah[1], N Fujima[2], O Sakai[1]
[1]Boston University School of Medicine, Boston, MA, [2]Hokkaido University Hospital, N/A

Purpose
Oropharyngeal Squamous Cell Carcinomas (OPSCCs) are among the major head and neck cancers causing substantial morbidity and mortality worldwide. HPV status as a biomarker has been shown to have a major role in predicting the survival of OPSCC patients and is used for TNM staging of these tumors. In this study, we have developed a 3-dimensional machine learning algorithm to characterize the HPV status of OPSCCs noninvasively based on CT images.
Materials and Methods
CT images of patients with OPSCC from a single institution and their HPV statuses were used from The Cancer Imaging Archive database (TCIA), OPC-Radiomics. Full 3D CT images were used to train a DenseNet-121 model via transfer learning to predict HPV-p16 status. With 10% of the dataset held out as the testing set, the remaining CT images were split into training and validation sets by 10-fold cross-validation. Final model predictions were computed by voting of the 10 sets with equal weights given to each set. Model performance was evaluated on ROC Curve (AUC), accuracy, specificity, and sensitivity. Programming and analysis were performed on Python with the MONAI and PyTorch-Ignite libraries.
Results
A total of 499 patients were included in this study, of which 356 (71%) and 143 (29%) were HPV-p16 positive and negative, respectively. The final trained algorithm achieved an AUC of 0.89 on the training set. Specifically, 34 of the 36 HPV-p16 positive patients (sensitivity = 0.94) and 6 of the 13 HPV-p16 negative patients (specificity = 0.46) were classified correctly. The overall accuracy of this classification model was 81.6%.
Conclusions
In this study, we have developed a 3D machine learning algorithm to characterize the HPV status of OPSCC patients. This algorithm can provide radiologists and clinicians with a major biomarker noninvasively for clinical management planning as well as survival prediction.

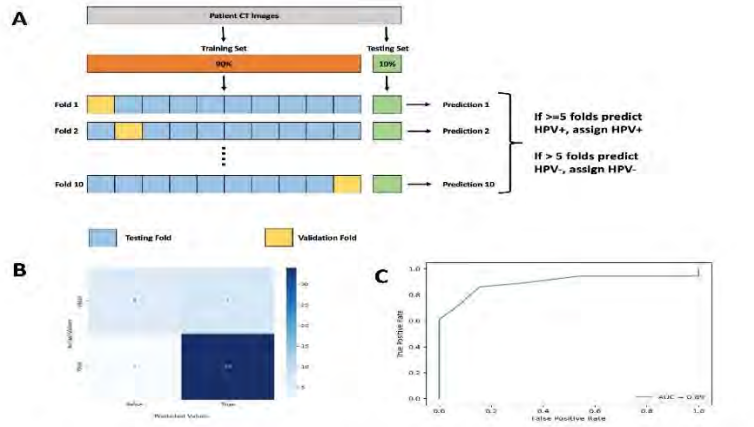

Fig. 1. Overall architecture for the HPV machine learning classifier (**A**). A confusion matrix of model predictions on the testing set (**B**) and AUC (**C**) were used to analyze performance.

(Filename: TCT_235_figure.jpg)

837

4DCT Parathyroid Scans: Is There Added Value From a Second Read?

L Mercado[1], J Varghese[2]
[1]Northwell Health, Manhasset, NY, [2]Northwell Health, New Hyde Park, NY

Purpose
Parathyroid 4DCT has become an essential tool in the workup of patients with a diagnosis of primary hyperparathyroidism. It allows for localization of parathyroid adenomas prior to surgery and makes minimally invasive surgery for adenoma resection possible. However, these exams can be challenging to interpret due to varied potential locations for lesions, potential beam hardening artifact,

presence of thyroiditis as well as variable expertise between readers. We studied the added benefit of a second read by a head and neck radiologist for 4DCTs performed at our institution after primary interpretation.
Materials and Methods
118 parathyroid 4DCT scans with second read recommendations available for review from a head and neck radiologist were retrospectively identified from December 2021 to October 2022. 86 of these cases went to surgery and had available surgical and pathology reports, which were reviewed.
Results
Mean age of patients was 63.0 years (SD ±12.8) and 80.5% were female. At least one additional potential adenoma was added by the second read in 18.6% (22/118) of cases. Of the cases with an additional lesion added by second read and for which a subsequent surgical report was available, 33.3% (4/12) were confirmed adenomas by pathology. Overall, of all 4DCTs with a second read performed that went to surgery, 4.7% (4/86) led to a pathology proven adenoma identified only by the second read.
Conclusions
This study suggests that second reads for parathyroid 4DCT examinations can increase accuracy and yield as well as further facilitate minimally invasive parathyroid exploratory surgery.

366

A 13 Month Retrospective Review of Emergency Department Code Stroke Head CT at Martin Luther King Jr Hospital Emergency Department with Emergency Medicine Physician Perspectives.

R Homer[1], Y Gelman[2], S Dua[3]
[1]University of California Los Angeles, Santa Monica CA, CA, [2]Martin Luther King Jr Medical Center, Los Angeles, CA, [3]University of California Los Angeles, Santa Monica, CA

Purpose
To evaluate the acute stroke positivity, serious finding and incidental findings rates of non contrast head CT code stroke protocol performed in the emergency department (ED) at Martin Luther King Jr Community Hospital (MLKCH), a large urban county hospital in Los Angeles, California with perspectives from an emergency medicine (EM) physician.
Materials and Methods
The medical record was reviewed retrospectively from July 2020-July 2021 for emergency department code stroke head CTs. Images of positive cases were reviewed to confirm findings.
Results
411 code stoke CTs were performed in the ED. 369 (90%) were interpreted as normal. There were 12 (3%) acute ischemic infarcts. There were 6 cases of intraparenchymal cerebral hemorrhage, one thought to be due to hemorrhagic conversion of a prior ischemic infarct. There were 2 cases of subarachnoid hemorrhage and 3 subdural or epidural hemorrhages. There were 2 multi compartment intracranial hemorrhages, one due to blunt trauma and one due to gunshot. Intracranial hemorrhage was identified in 13 (3%) of the exams. There were 3 intracranial masses, 3 cases of hydrocephalus and 1 colloid cyst identified. In 3 cases, the findings led to a differential diagnosis. Including all of the above findings, there were 35 (8.5%) "major" findings identified. Incidental "minor" findings were noted in 7 (1.7%) cases including 3 incidental meningiomas, 2 parotid nodules and a case of prior parenchymal hemorrhage. Overall, there were 42 (10.2%) exams with a major or minor finding identified over this 13 month period. There were no discrepancies.
Conclusions
There were 12 (3%) acute infarcts and a total of 35 (8.5%) major findings, including hemorrhage, mass and hydrocephalus. Routine head CTs are reported to have serious findings at a rate between 4.3-13.8% in retrospective studies of 10,000-30,000 ED head CTs. From an EM physician perspective, the code stroke CT is ordered to prioritize rapid scanning and interpretation to expedite potential thrombolysis or thrombectomy and to expedite further CTA or MRI/MRA imaging. While focal neurologic deficits have the highest positive predictive value, altered mental status (AMS) with an onset within treatment window is still the most common indication for code stroke CT in EM practice. Given that AMS is one of the most common presentations to the ED, the relatively low positivity of these code stroke CTs at the same rate as routine head CT is not surprising but does not diminish their importance for patient care.

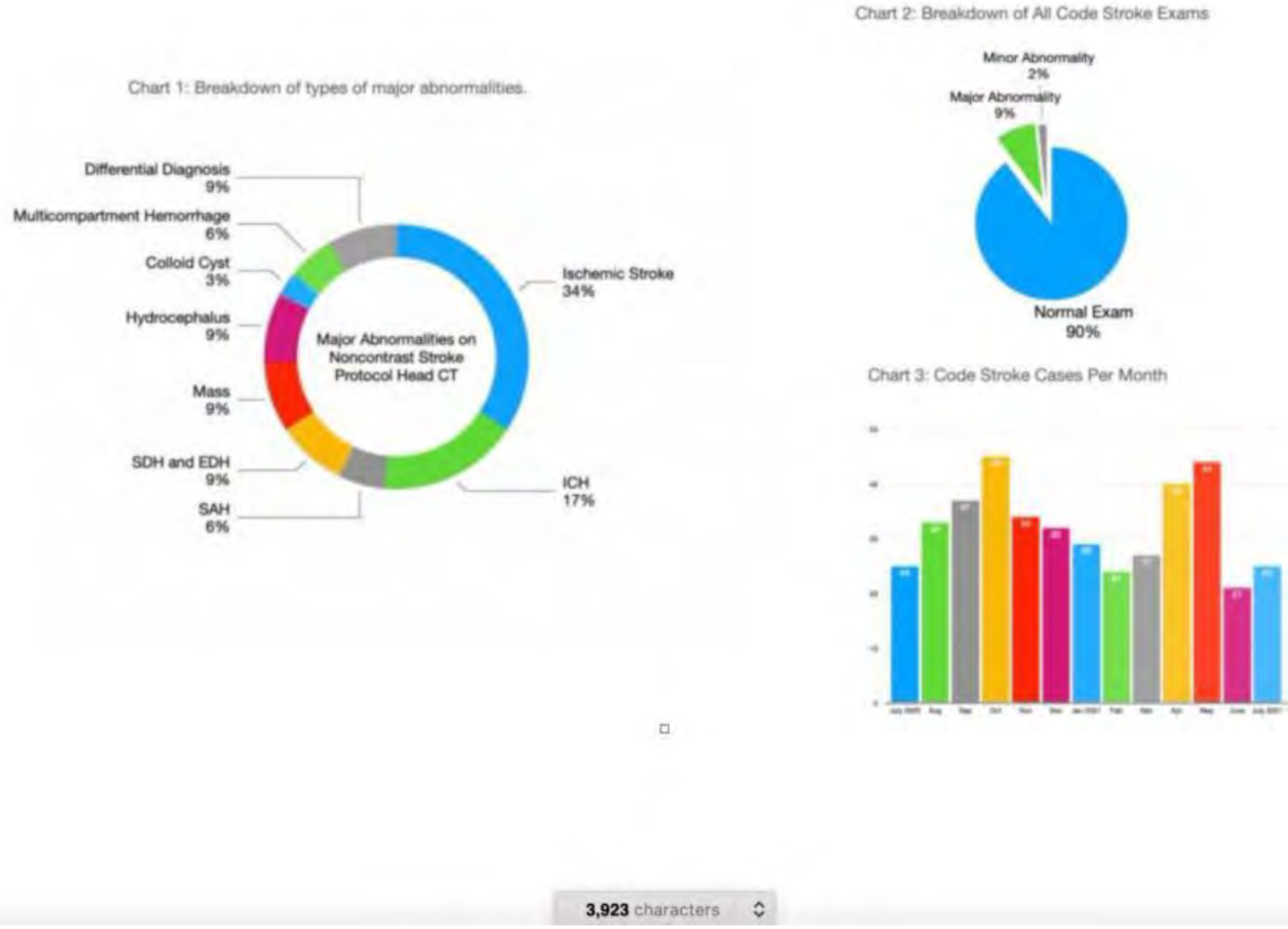

(Filename: TCT_366_ScreenShot2022-10-24at121141PM.jpg)

1382

A Deep Learning Model for Discriminating True Progression from Pseudoprogression in Glioblastoma Patients

M Moassefi[1], G Conte[1], S Faghani[2], B Erickson[1]

[1]Mayo Clinic, Rochester, MN, [2]Mayo Clinic (Rochester, MN, US), Rochester, MN

Purpose

Glioblastomas (GBMs) are highly aggressive tumors. Despite chemoradiation treatment effectiveness, it may cause the clinical challenge of treatment-related changes that appear like tumor progression, also known as pseudoprogression(PsP). Usually, PsP resolves or stabilizes without further treatment or a course of steroids, whereas true progression(TP) requires more aggressive management. Differentiating PsP from TP will affect the patient's outcome(1). Human interpretation of MRI cannot distinguish them. A method that could reliably and non-invasively distinguish PsP from TP in glioblastoma(GBM) patients, after initial treatment would be highly beneficial. This study investigated using deep learning to distinguish PsP magnetic resonance imaging (MRI) features from progressive disease in GBM.

Materials and Methods

We included newly diagnosed GBM patients who met our inclusion criteria, including a new or increasing enhancing lesion size within the original radiation field and who had clinical, medication, and any histopathology available. The interpretation of the MRI at the image inclusion time point had to be indeterminate—that is, the neuroradiologist had to have definite uncertainty about the lesion being PsP or TP. Clinical notes and radiology reports were reviewed to confirm initial tumor location, new/enlarging lesions location, clinical history, and medication. We labeled those who subsequently were stable or improved on imaging and clinically as PSP and those with clinical and imaging deterioration as TP. A subset of subjects underwent a second resection. We labeled these subjects as PSP or TP based on the histological diagnosis. We performed skull stripping, coregistered contrast-enhanced T1 MRIs with T2-weighted images for each patient and used them as input to a 3-D Densenet121 model. We used several augmentation techniques and five-fold cross-validation to achieve more robust predictions.

Results

We included 124 patients who met the criteria, and of those, 63 were PsP and 61 were TP. We trained a deep learning model that

achieved 76.4%(range 70%-84%, SD 5.122) mean accuracy over the 5 folds, 0.7560(range 0.6553-0.8535, SD 0.069) mean AUROCC, 88.72%(SD 6.86) mean sensitivity, and 62.05%(SD 9.11) mean specificity.
Conclusions
We report the development of a deep learning model that distinguishes PsP from TP in GBM patients treated per the Stupp protocol. Further refinement and external validation are required prior to widespread adoption in clinical practice.

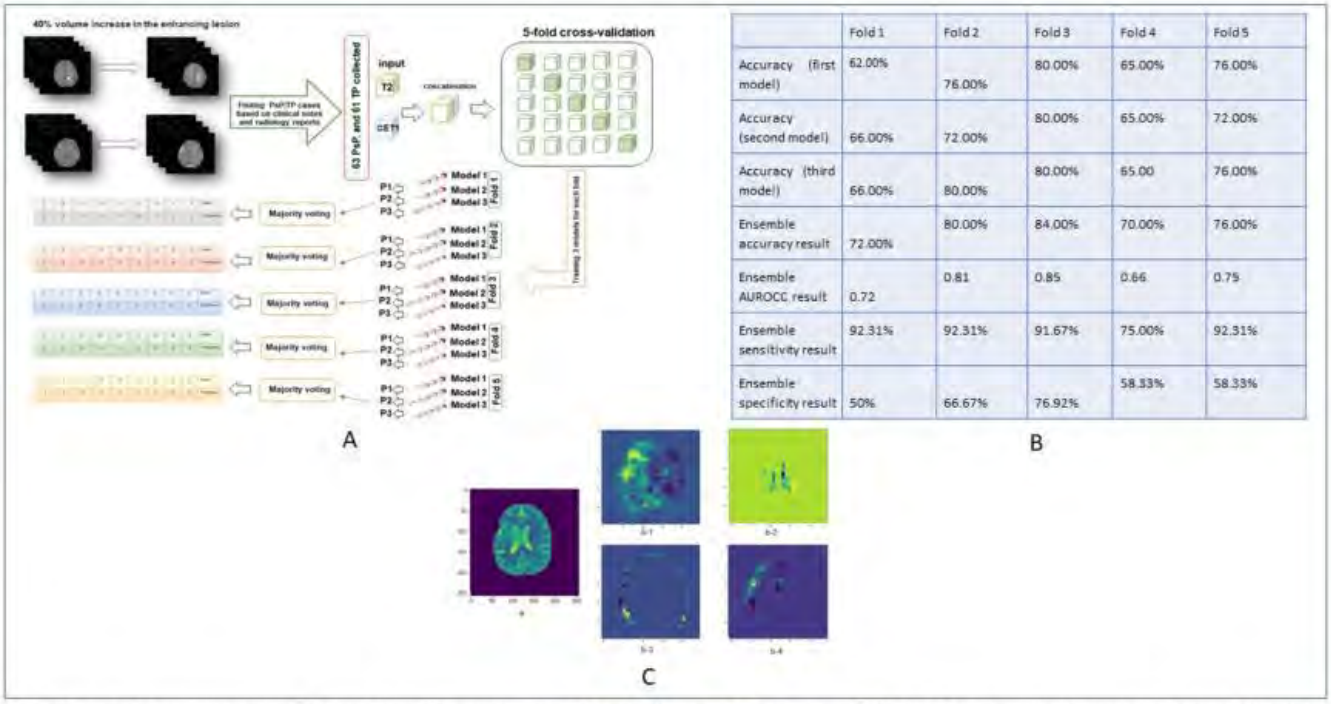

	Fold 1	Fold 2	Fold 3	Fold 4	Fold 5
Accuracy (first model)	62.00%	76.00%	80.00%	65.00%	76.00%
Accuracy (second model)	66.00%	72.00%	80.00%	65.00%	72.00%
Accuracy (third model)	66.00%	80.00%	80.00%	65.00	76.00%
Ensemble accuracy result	72.00%	80.00%	84.00%	70.00%	76.00%
Ensemble AUROCC result	0.72	0.81	0.85	0.66	0.75
Ensemble sensitivity result	92.31%	92.31%	91.67%	75.00%	92.31%
Ensemble specificity result	50%	66.67%	76.92%	58.33%	58.33%

A- Brief schema of our prediction pipeline. B- Outcome of the CNN prediction model in the validation group. C- a- A skull-stripped T2 MRI slice of a random patient demonstrating the tumor's presence in the temporal lobe. b- plotted feature maps of the 4 different channels of the 6th convolutional layer within the first dense block of the trained deep learning model. b-1 highlights the whole brain. b-2 highlights the lateral ventricles. b-3 highlights the brain edges. b-4 highlights the tumor area.

(Filename: TCT_1382_IMAGE.jpg)

225
A Large Retrospective Analysis of the Imaging Features of Craniofacial Giant Cell Granulomas
R Chanda[1], M Kandagaddala[1], S Regi[1], A Irodi[1]
[1]*Christian Medical College, Vellore, Tamil Nadu*

Purpose
This presentation aims to describe the imaging features of craniofacial giant cell granulomas which are rare lesions with varied appearances on imaging.
Materials and Methods
A retrospective analysis of the clinical and imaging features of 20 histopathology-proved cases of craniofacial giant cell granulomas, dating from 2006 to 2022, was performed.
Results
Of the 20 cases, 10 each were in men and women. The lesions varied in location: maxilla in 8; mandible in 5; temporal bone in 3; sphenoid/clivus in 3; and orbit in 1 patient. On the radiographs, the lesions were well-circumscribed, expansile, and lytic. On CT, the lesions were predominantly multiloculated, with thin septa, a soft-tissue component, and with expansion and remodeling of the underlying bone. On MR imaging, the solid component of the lesions was isointense on T1WI and hypointense on T2WI, with heterogeneous enhancement of the solid component and rim enhancement of the locules. Fluid-fluid levels were present in 3 patients.
Conclusions
Giant cell granulomas are locally aggressive, expansile, multiloculated lytic lesions, with solid and cystic areas. Certain key imaging features of giant cell granulomas can aid the radiologist in narrowing the differential diagnosis.

1371
An Artificial Intelligence Algorithm for Detection of Brain Metastases
C Paton[1], A Rahman, MD; DO[2]
[1]*University of Rochester, Rochester, NY,* [2]*University of Rochester Medical Center, Rochester, NY*

Purpose
Artificial Intelligence programs are designed to learn feature representations in radiographic images and aid in detection of abnormalities. Typically, a new algorithm is trained with supervised learning of annotated images to accomplish a specific task, usually segmentation or classification in the medical imaging field. After training, the algorithm is tested with unseen data in an

unsupervised manner to check its generalization capability. Our AI program has undergone a round of supervised training and the initial assessment of its performance shows high accuracy in the diagnosis of neurological metastases on MRI images, approaching the accuracy of board-certified radiologists (89%). These initial results state a baseline that could be further improved by the addition of larger volumes of annotated images and advanced techniques that could improve the accuracy. This program has the potential to improve clinical detection accuracy of metastases, reduce the burdensome caseload of easily-detected metastases, and identify new features associated with brain metastases on MRI imaging.

Materials and Methods

A TensorFlow based deep learning algorithm, specifically a convolutional neural network (CNN) using transfer learning was used to train our AI model for semantic segmentation. We used a 2D UNet architecture with inception v3 backbone and initialized with weights pretrained using ImageNet dataset for faster and better convergence. Three separate models were created for three axes: axial, coronal and sagittal. The training: validation images for axial, coronal and sagittal models are 1821:203, 4378:487 and 2331:259, respectively. The model was evaluated using sensitivity, accuracy and Intersection over Union score (IoU).

Results

On axial model, our training IOU score was 68.84%, validation IOU score 80.14%, validation sensitivity 79% and validation accuracy 69%. On sagittal model, our training IoU score was 89.98%, validation IoU score 85.34%, sensitivity 82% and accuracy 72%. On coronal model, validation IoU score 82.27%, sensitivity 79% and accuracy 68%.

Conclusions

This novel AI program is the first iteration of our algorithmic testing, serving as a baseline for our continued refinement and assessment with larger volumes of images. Our model could be employed alongside practicing radiologists to improve detection, to train radiology residents or fellows, and to identify novel features of interest for further research.

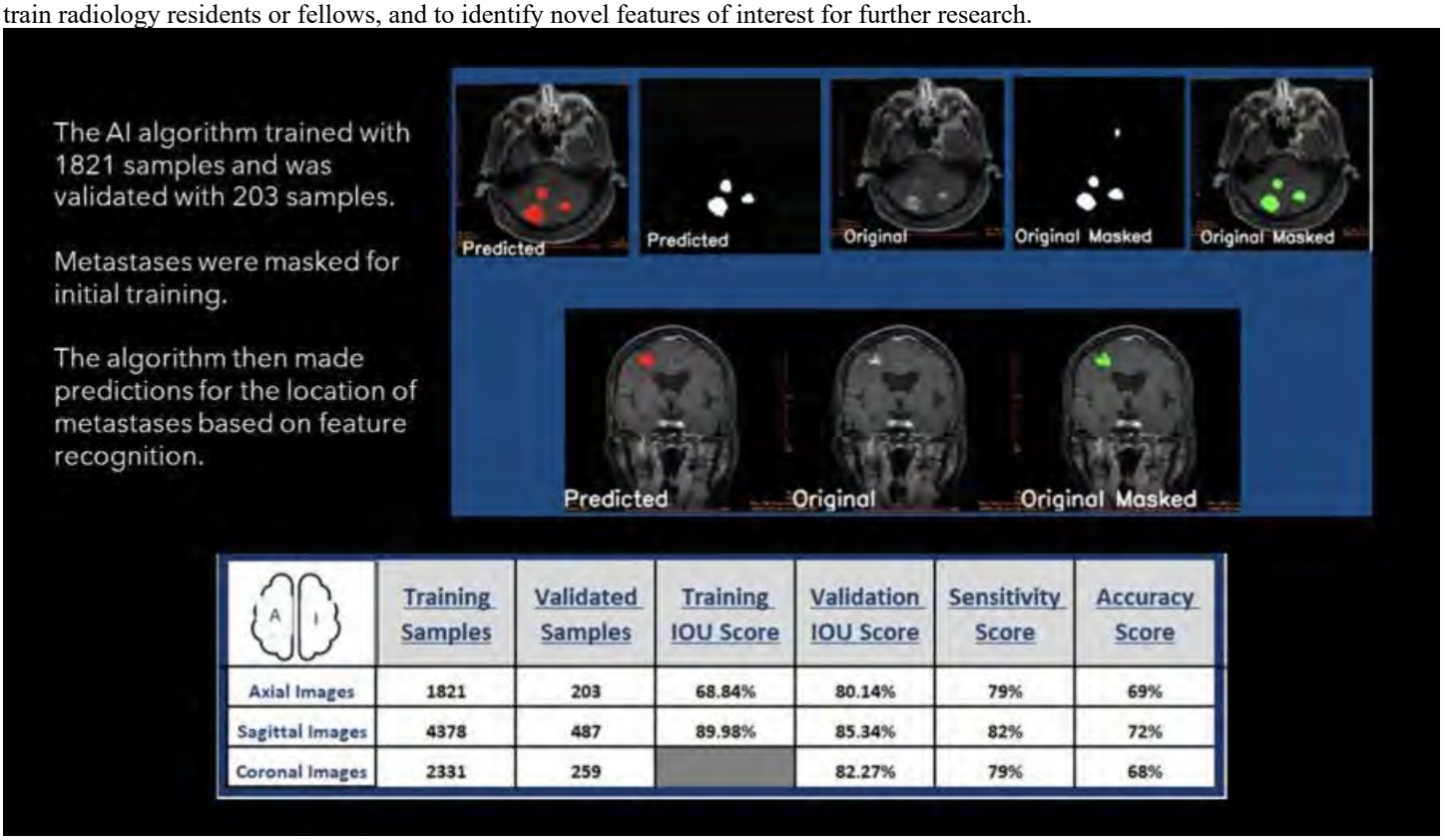

	Training Samples	Validated Samples	Training IOU Score	Validation IOU Score	Sensitivity Score	Accuracy Score
Axial Images	1821	203	68.84%	80.14%	79%	69%
Sagittal Images	4378	487	89.98%	85.34%	82%	72%
Coronal Images	2331	259		82.27%	79%	68%

(Filename: TCT_1371_ASNRAIImage.jpg)

802

Analysis of Procedural Requirement of Neuroradiology Job Advertisements

V Thumar[1], J Chen[2]

[1]UC San Diego, San Diego, CA, [2]San Diego VA Medical Center/UC San Diego Health System, La Jolla, CA

Purpose

Radiology fellowship is an integral component of training for current sub-specialized practices. As practices are becoming more sub-specialized, a radiologist is valued as a subspecialty expert rather than a "jack of all trades." The Accreditation Counsel for Graduate Medical Education (ACGME) in coordination with American Society of Neuroradiology (ASNR) task force created guidelines for Neuroradiology training, for example 100 image-guided procedures and 3000 total examinations, which aims to prepare fellows for their future careers. The purpose of this study is to present patterns in current job requirements that can guide Neuroradiology fellows' approach to training to best prepare them for the job market.

Materials and Methods

ASNR and American College of Radiology (ACR) job boards were queried for Neuroradiology positions or Neuroradiology preferred

general Radiology positions from 8/12/2022 to 11/12/2022 on the ASNR job board and from 10/12/2022 to 11/12/2022 on the ACR job board. Positions were categorized into academic and private practice and job descriptions were categorized into general diagnostic radiology, hybrid remote/onsite, outpatient, inpatient/emergency, general interventional radiology (IR) procedures, and Neuroradiology procedures. Exclusion criteria included Neurointerventional only, remote only, pediatric Neuroradiology only, no preference for Neuroradiology, and duplicate posts. Additional exclusion criteria for the ACR jobs included posts overlapping with the ASNR job board.

Results

A total of 1735 jobs were posted on the ACR and ASNR job boards. After exclusion criteria was applied, 44 jobs were academic and 96 jobs were private practice. A significantly higher proportion of private practice jobs required general diagnostic reads (80% vs 21%), a higher proportion of academic jobs required Neuroradiology procedures (54% vs 25%), and a higher proportion of private practice jobs required general IR procedures (20% vs 0%). Only 33% of all jobs required Neuroradiology procedures and 14% required general IR procedures.

Conclusions

Since there was a significant difference between general radiology reading and procedure requirements between academic and private practice positions, tailoring fellowship training for the career aspirations of Neuroradiology fellows should be considered to adapt to the skills needed for the evolving job market. This data should help provide leadership with information to guide decisions on how to harmonize training and job requirements.

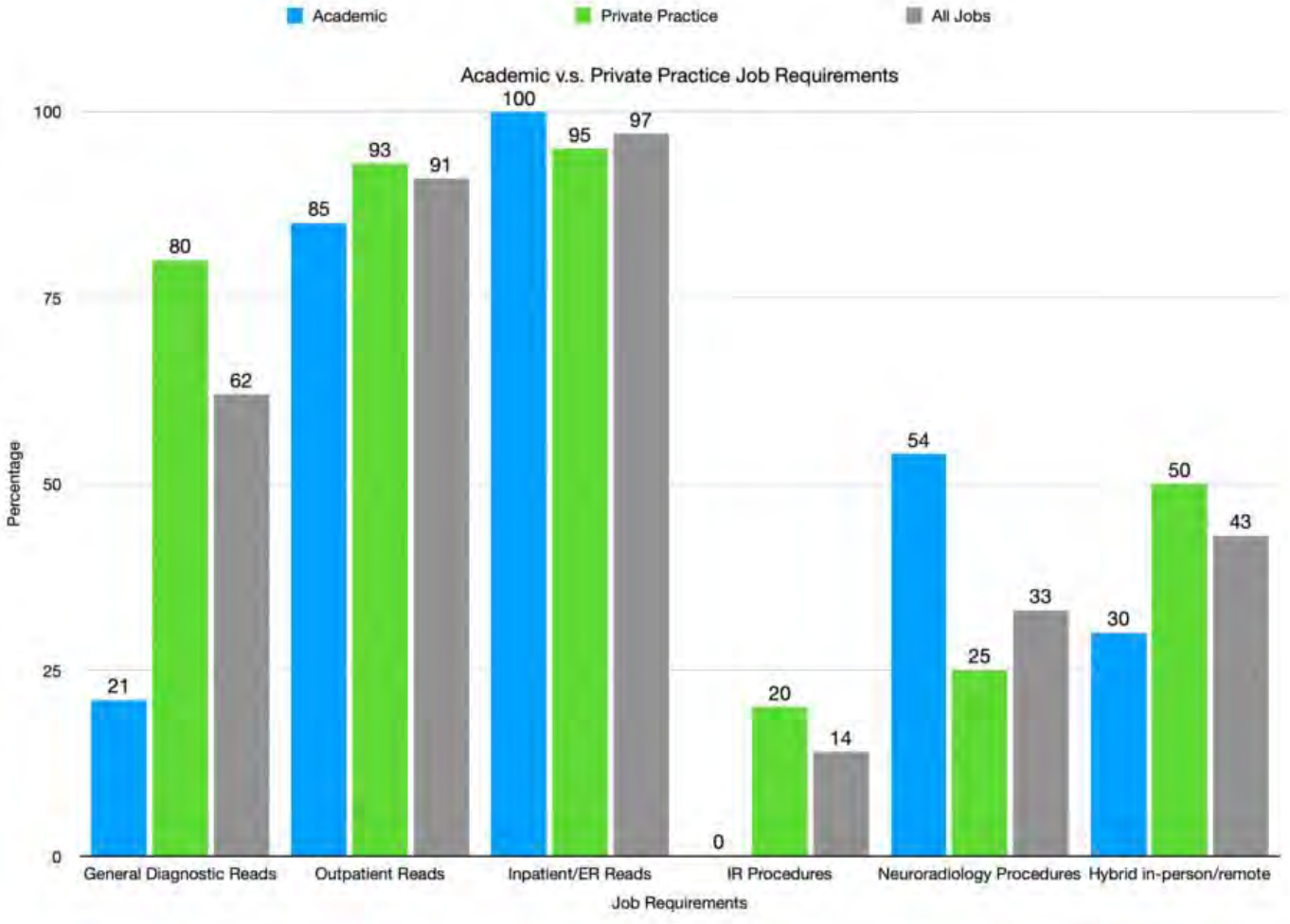

(Filename: TCT_802_BarGraphjpeg.jpg)

1326

Analysis of Routine Biopsies During Percutaneous Kyphoplasty for Vertebral Compression Fractures

M Finkelstein[1], A Yang[1], H Bilal[1], A Tieu[1], M Chen[1], P Marcadis[1], M Umphlett[1], A Doshi[1]

[1]Icahn School of Medicine at Mount Sinai Hospital, New York, NY

Purpose

Percutaneous kyphoplasty has emerged as a commonly performed and efficacious treatment for pain related to vertebral compression fractures (VCF), most commonly caused by osteoporosis. With increasing utilization of this procedure, there is ongoing debate concerning the utility of routine biopsy during kyphoplasty. Prior studies have shown varying rates of reported malignancy depending on site and population. The purpose of this study was to report the rates of positive findings at a major tertiary care center.

Materials and Methods
A retrospective cohort study was performed. An institutional pathology dataset was queried for all vertebral biopsy results performed across the health system for January 1st 2016 to October 1st 2022. Findings were then linked to corresponding procedures as identified in the institutional PACS. Images and procedure notes were reviewed to ensure kyphoplasty was performed. Procedure, pathology, and chart notes were reviewed to ascertain suspicion for or presence of a history of malignancy. Findings were further categorized by vertebral body level. All analysis was completed using R version 3.6.3 (R Foundation for Statistical Computing, Vienna, Austria).
Results
A total of 663 biopsy results were reviewed of which 241 were found to be related to kyphoplasty procedures. There were 134 lumber (56%) and 107 thoracic body samples within a population consisting of 155 females (64%). Of the 241 biopsy results, 101 (42%) were found to exhibit a known history of for malignancy with an additional 9 (4%) found to be suspicious for malignancy based on prior imaging without definitive diagnosis. Of those with a known history of malignancy, 1 (2%) was found to have resulted in a malignancy discordant with history. Within the group with no known history of or stated suspicion for malignancy, 6 (5%) resulted in non-benign pathology. Of these 4 (67%) were found to be consistent with plasma cell neoplasm, 1 was consistent with a breast primary, and another was consistent with osteomyelitis. For the group with known history of or stated suspicion for malignancy, 59 (54%) were found to be consistent with malignancy.
Conclusions
Within the population analyzed at a major urban health system, we have found routine biopsies to reveal unexpected malignant pathology in a clinically significant portion of all concurrent kyphoplasties performed without stated suspicion or knowledge of malignancy as well as those with a history of prior malignancy.

1196

Application of deep learning reconstruction to short echo derived magnetization transfer prepared neuromelanin MR imaging from multiecho GRE acquisition

H Lee[1], J Lee[2], S Gho[2], R Lebel[3], S Banerjee[4], Y KANG[5]
[1]Inje University Haeundae Paik Hospital, Busan, [2]GE HealthCare, Seoul, [3]GE HealthCare, Calgary, Alberta, [4]GE HealthCare, Menlo Park, CA, [5]Inje University Haeundae Paik Hospital, BUSAN, Busan

Purpose
It has been known that short-echo-time magnitude image derived from multiecho gradient echo (ME-GRE) acquisition, with or without magnetization transfer (MT) preparation can be used for neuromelanin (NM) imaging [1]. In a previous study by Oshima et al., deep learning reconstruction (DLR) has been applied to 2D GRE based NM imaging for improved image quality [2]. The purpose of this study is to test whether DLR can improve image quality of short echo derived MT prepared neuromelanin image from multiecho gradient echo (ME-GRE) acquisition.
Materials and Methods
Images were acquired on a 3T scanner (Signal Architect, GE Healthcare, Waukesha, WI) with a 48-channel head coil. 3D ME-GRE images were acquired with the following parameters. TR/TE, 38.7/6.4/14.3/22.2 ms; 64 slices; slice thickness/gap, 1.2/0.6 mm; in-plane resolution, 0.8x0.8 mm, flip angle, 20°; and scan time, of 4 minutes 52 seconds. The MT preparation was achieved with a similar approach by Rua et al.[3]. A 3D enabled DLR was performed with 75% denoising level (prototype version of AIR Recon DL, GE Healthcare, Waukesha, WI)[4]. 10 subjects (M:F = 6:4; age 68.3±8.37 years, 4 Parkinson's disease (PD) patients and 6 non-PD patients) in which the DLR was performed were included for analysis. Region of interests were placed at substantia nigra (SN) and decussation of cerebellar peduncle (SCP) at level of SCP as in Figure 1 in each image. Signal intensities (SI) from SN, and SCP, and standard deviation (SD) from SCP was recorded. SI from SN was averaged and used for calculation. Signal to noise ratio (SNR) and contrast to noise ratio (CNR) were as follows: SNR = meanSI_SCP / SD_SCP, CNR = (meanSI_SN – SI_SCP) / SD_SCP and calculated for images with and without deep learning reconstruction. The SNRs and CNRs were compared with paired t-test. Statistical analysis was performed with Jamovi version 2.2 [5].
Results
SNR and CNR after deep learning reconstruction was significantly higher as compared to conventional reconstruction (41.7±7.33 vs 26.8±3.22, 13.6±2.4 vs 8.62±1.63, respectively, $p<0.001$ for both tests).
Conclusions
In this preliminary work, SNR and CNR of short echo derived MT prepared NM image from ME-GRE acquisition for SMWI was improved by DLR.

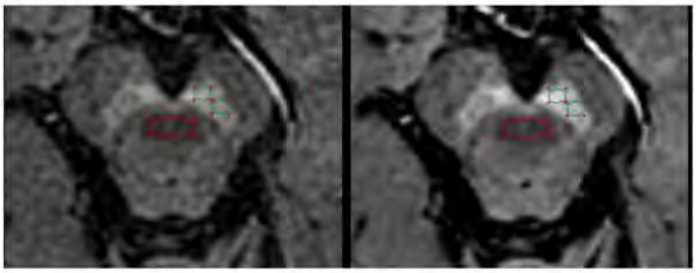

Figure 1. Region of interests within the substantia nigra (SN; green circles), and decussation of superior cerebellar peduncle(SCP; red oval) for signal to noise (SNR_{SCP}) and contrast to noise (CNR) calculation.

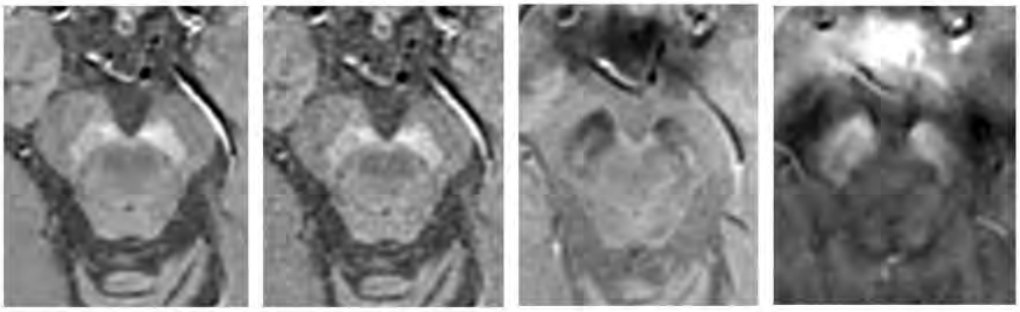

Figure 2. Short echo time images with neuromelanin contrast after and before deep learing based reconstruction (DLR), susceptibility map weighted image (SMWI), and quantitative susceptibility map in a 73 year old female patient with tremor. Preserved "swallow tail sign" is seen on SMWI. The SNR_{SCP} / CNR for the DLR applied and non-applied image was 44.1/16.4, 31.9/11.4 respectively.

(Filename: TCT_1196_graphic.jpg)

1223

Application of Hometown Walking Paradigm to localize BOLD memory network in epilepsy patients undergoing pre-surgical evaluation in clinical settings

V Sawlani[1], U Chaudhary[2], S Bose[3], N Davies[3], R Flintham[3], A Hawkins[3], S Samarasekra[3], R Chelvarajah[3]

[1]University Hospital Birmingham, Birmingham, West Midlands, UK, [2]University Hospitals Birmingham, Birmingham, UK, [3]University Hospitals Birmingham, Birmingham, West Midlands

Purpose

To use hometown walking paradigm in clinical settings to localize memory function in patients undergoing pre-surgical evaluation.

Materials and Methods

Pts. undergoing pre-surgical evaluation for temporal lobe epilepsy were selected from multidisciplinary meeting from Jan 2015 to April 2022. All patients had detailed clinical assessment, video-telemetry, structural imaging of brain and neuropsychological assessments for memory functions. We used a hometown walking paradigm during fMRI acquisition for memory localization which required mental navigation through one's hometown by using landmarks given by pts themselves. We performed fMRI acquisitions on two consecutive days. fMRI data was acquired on a Siemens scanner, and analysed using BOLD processing package (Siemens MAGNETOM Skyra, VE11e). Images were processed for motion correction and temporal high-pass filter, analysed using a block design in General Linear Model, and activation t-maps were produced. Activation t-maps are threshold for minimum allowable t-value and voxel cluster size by neuroradiologist and MRI physicist, in order to exclude clusters likely representing motion-related artefact, and fused to 3D T1 W MPRAGE images using Syngo.VIA software.

Results

246 fMRI studies were performed for 177 patients. 108 patients had repeated scans atleast twice and 14 patients had additional follow up scans. Ninety out of 117 (76%) patients showed BOLD activation in the para-hippocampal gyrus for at least one of the days. BOLD activation were seen more commonly in the para-hippocampal and fusiform gyri as compared to hippocampus. Bilateral BOLD activation in the para-hippocampal gyrus were seen in 57% of the patients. Patients with lesions in the temporal lobes had stronger activation in the contralateral para-hippocampal gyrus. Additional activation were seen in the posterior cingulate cortex, bilateral superior parietal cortex and dorsolateral prefrontal cortex reflecting visuospatial mental navigation and sequencing of task during hometown walk.

Conclusions

Implementation of hometown walking paradigm during fMRI can show consistent and reproducible BOLD activation in medial temporal lobes to localize memory in patients undergoing pre-surgical evaluation, which can be used as an adjunct to neuropsychological memory assessment.

1327

Assessment of Lenticulostriate Artery Using Vessel Wall MRI in a Population-based Study

x zhou[1], M Caughey[2], z Huang[3], C Wang[4], D Ling[5], B Wasserman[6], Y Qiao[7]

[1]Johns Hopkins Hospital, Baltimore, MD, [2]University of North Carolina & North Carolina State University, Raleigh, NC, [3]the university of Maryland, Baltimore, MD, [4]The Bryn Mawr School, Baltimore, MD, [5]Dulaney High School, Lutherville, MD, [6]University of Maryland School of Medicine, Baltimore, MD, [7]Johns Hopkins University, Baltimore, MD

Purpose

Lenticulostriate arteries (LSA) represent the major microvasculature of the middle cerebral arteries, and are known to be involved in silent strokes, which contribute to progressive cognitive impairment. The morphology of LSA (e.g. branch number) show significant differences between subjects with subcortical vascular dementia and healthy controls as well as between hypertensive and normotensive subjects. We propose to report the basic characteristics of LSAs in older individuals from a general population.

Materials and Methods

705 Atherosclerosis Risk in Communities (ARIC) study participants (age 72-95 years; 401 women; 186 black) who underwent brain MRI from 2017 to 2019 were included in this study. All brain MRI exams were acquired on 3.0 T Siemens scanners using a standardized protocol including a 3D high-resolution vessel wall MRI (VWMRI) with optimized contrast using a flip angle evolution 1. The parameters were:1200 ms/24 ms; turbo factor, 60; parallel imaging (GRAPPA) acceleration, 2; FOV,180 x 180 x 64 mm3; matrix, 360 x 360 x 128; acquired resolution, 0.5×0.5×0.5 mm3; slice number,128; acquisition time, 6.44 minutes. LSAs were evaluated on the coronal minimum intensity projection of VWIMRI images with 10 mm thickness. The visualization of LSAs was graded as low/non-existent visibility, and clear visibility (Figure). The number of bilateral LSA stems and branches was quantified. Stems were defined as the portion of the LSAs that originated directly from the MCA. Branches are defined as daughter vessels originating from parent LSA stems or as stems with no branches (single vessel).

Results

Among the 705 participants, 650 demonstrated clear visualized LSAs on VWMRI. On average, each participant had 4.5 stems (range 1-11) and 1.4 branches (range, 1-6), bilaterally. When stratified by sex and race, more LSA branches were identified in blacks than whites (1.8 ± 1.3 vs 1.4 ± 1.1, p<0.001). No significant difference on number of stems between gender and race groups (Table).

Conclusions

3T VWMRI can identify LSA and the morphological measurements may insight into cerebral small vessel degeneration during aging across a US community-based population.

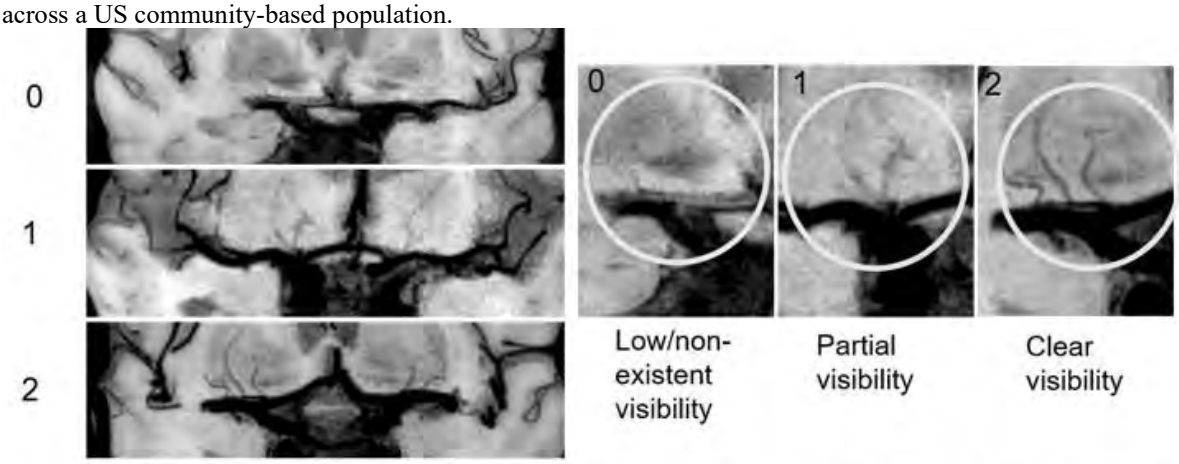

Figure: assessment scale for lenticulostriate arteries on coronal minimum intensity projection of VWIMRI images with 10 mm thickness.

Table: Assessment of Lenticulostriate arteries by Race and Gender (mean ± SD).

Sex Stratified	Women	Men	P-value
Number of Stems (bilateral)	4.6 ± 2.3	4.5 ± 2.3	0.5
Number of Branches (bilateral)	2.9 ± 2.5	2.8 ± 2.5	0.7
Race Stratified	Black	White	
Number of Stems (bilateral)	4.4 ± 2.3	4.6 ± 2.3	0.2
Number of Branches (bilateral)	3.5 ± 2.9	2.6 ± 2.4	0.003

(Filename: TCT_1327_FigureTable.jpg)

688

Association between angioarchitecture and hemodynamic parameters by 4D flow MR in unruptured and ruptured arteriovenous malformation: a pilot study

Y Wang[1], H Wei[2], M Cheng[3], Y Wang[3], R Li[2]

[1]Sichuan Provincial People's Hospital, Chengdu, China, [2]Tsinghua University, Beijing, Beijing, [3]Sichuan Provincial People's Hospital, Chengdu, Sichuan

Purpose

The hemodynamics of cerebral arteriovenous malformation (AVM) could hardly be reflected by conventional morphology-based imaging and clinical grading. The objective was to investigate the association between the angioarchitecture and hemodynamics in both unruptured and ruptured cerebral AVM.

Materials and Methods

Consecutive patients with DSA diagnosed cerebral AVM were prospectively enrolled. Lesion angioarchitecture were assessed by DSA. 4D flow MR was performed to assess the hemodynamics with the voxel size 1.0mm (isotropic). 3D velocity filed was calculated from 4D flow MRI. We also calculated wall shear stress (WSS) of the feeding artery adjacent to the nidus and dynamic pressure (DP). Hemodynamics were compared between groups with different angioarchitectures and rupture status. Correlations between multiple flow-derived parameters were examined.

Results

Hemodynamic evaluation was achieved in 9 out of 11 patients. Nine patients (4 male, age range: 19~58 years old) include 5 with ruptured and 4 with unruptured AVM. There was no significant association between rupture status and Spetzler-Martin grade. Feeding by multiple arteries was associated with unruptured status ($p<0.001$). Deep vein drainage was associated with diffusely distributed nidus (compared with compact nidus, $p=0.011$), and also with higher WSS (3.13pa vs. 1.71pa, $p=0.033$). The total flow in cases with Spetzler-Martin grade II (4.38 to 8.34 ml/s) showed substantial overlap with that in grade III (4.03 to 15.34 ml/s). The flow was 8.02±5.01 ml/s in unruptured group and 2.88±3.50 ml/s in ruptured group ($p=0.111$). The flow of the two cases that required a second embolization later were the greatest among all cases (15.34ml/s and 8.34ml/s). There were no significant differences in the arterial velocity or flow between AVM with deep and superficial vein drainage, or between AVM with or without aneurysms in the nidus. Among the hemodynamic parameters, mean and maximal flow of the feeding artery were highly correlated with nidus DP and with nidus volume (both $p=0.037$).

Conclusions

Cerebral AVM tend to have heterogeneous hemodynamics even with similar clinical grade or angioarchitecture, which could be quantified by 4D flow MR. In this pilot study, AVM tend to have smaller flow in ruptured lesions. AVM with deep vein drainage tends to have diffusely distributed nidus and higher WSS adjacent to the nidus. Higher flow of the feeding artery was associated with higher DP and larger volume of the nidus.

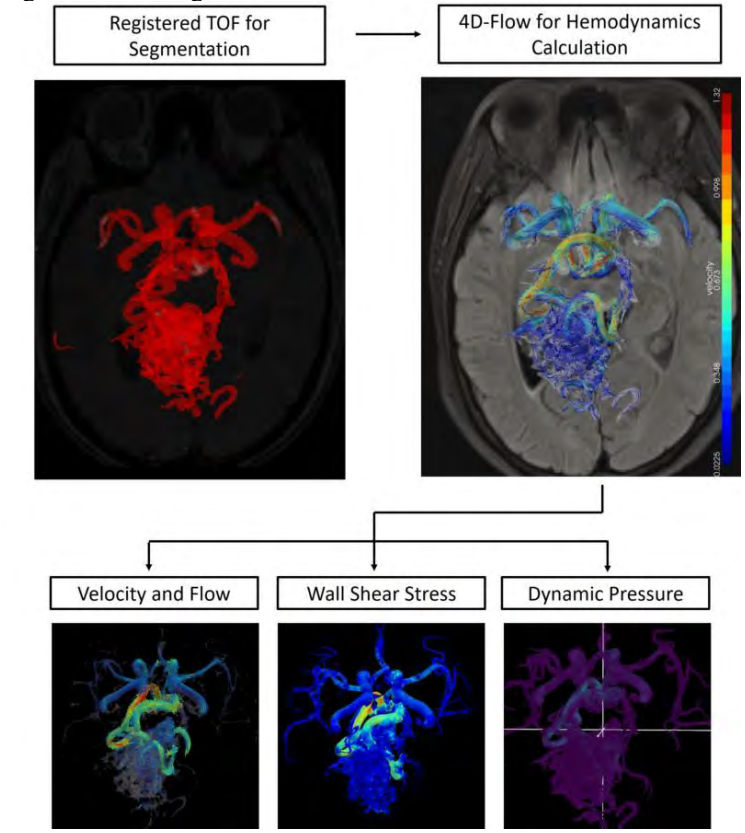

(Filename: TCT_688_Figure1.jpg)

588

Automated detection of Multiple Sclerosis Lesions with Artificial Intelligence-powered, Cloud-based Software

W Dennis[1], E Ye[2], J Chamberlin[1], D Roberts[1], M Spampinato[3]

[1]Medical University of South Carolina, Charleston, SC, [2]Medical University of South Carolina, Charleston , SC, [3]MUSC, Charleston, SC

Purpose

The purpose of our investigation was to test the use of an Artificial Intelligence (AI) convolutional neural network (CNN) software for the detection and quantification of white matter T2 hyperintense (WMH) lesions in patients with multiple sclerosis (MS). We then evaluated the association between MS plaque burden and the patient's degree of disability as described by the Kurtzke Expanded Disability Status Scale (EDSS).

Materials and Methods

MPRAGE and 3D FLAIR DICOM images were post-processed using AI-powered, cloud-based CNN software. The software generated a DICOM annotated lesion distribution map, and a report of WMH lesion count and volume in four brain regions (periventricular, deep, juxta-cortical, infratentorial white matter). We compared WMH volumes and white matter (WM) lesion counts (periventricular, deep, juxta-cortical, infratentorial WM, and total lesion count) between MS patients and age-matched normal controls using the Independent-Samples Mann-Whitney U test. We evaluated the association between the Kurtzke Expanded Disability Status Scale and total WMH volume and total WM lesion number using Spearman's rho correlation coefficient. Results were considered significant when $p < 0.05$ after Bonferroni correction for multiple comparisons.

Results

We included in the study 26 MS patients (5 males and 21 females, both groups with an average age of 35) and 13 normal controls (6 males with an average age of 34, and 7 females with an average age of 35). Periventricular, deep, juxta-cortical, and total WMH volumes were significantly different between MS patients and normal controls (all p-values <0.001). Periventricular, deep, juxta-cortical, and total WM lesion numbers were also significantly different between MS patients and normal controls (all p-values <0.001). There were no significant differences in infratentorial WMH volume and lesion count between MS patients and normal controls. There was a significant association between EDSS and total WMH ($rho = 0.476$, $p = 0.014$) in the MS group, but not between EDSS and total WM lesion number.

Conclusions

AI-powered post processing software may be a useful adjunct to the interpretation of brain MRIs for patients with MS. The information gleaned regarding cumulative lesion volume correlated with the degree of disability as measured by the Expanded Disability Status Scale and creates a quantitative metric of the disease status.

1142

Automated Protocol Assignment for Neuroimaging Studies

S Talebi[1], E Tong[2]

[1]University of California, Berkeley, Berkeley, CA, [2]Stanford University, Stanford, CA

Purpose

MRI protocol assignment is typically done manually, and can be tedious and time-consuming. The aim of this study is to develop an interpretable natural language processing (NLP)–based classifier to automate the assignment of image protocol. In addition to assessing the performance of our model, we also measure the word importance by attributing the classification output to every word through a gradient based method.

Materials and Methods

A dataset with more than 50,000 neuroradiology orders with corresponding imaging protocols was collected. Each recorded entry contains anonymized patient ID, age, gender, the reason for study, and the recommended protocol (assigned manually by experienced radiologists). The dataset was limited to the 10 most common imaging protocols for this study. We formulate a classification task as predicting which class corresponds to a specific text. We utilized a pre-trained BERT model for the classification task. The data is randomly split into a 70:20:10 training, evaluation, and test sets. The model's performance is evaluated by calculating precision and recall scores for each class and a weighted average of all classes. Model interpretation is done by appraising the contribution of each word to the final prediction, i.e. "word importance". We investigate the effectiveness of word importance weights on model prediction by applying synthetic perturbations. Specifically, we erase the most (or least) important word from the input sentence and measure the resulting model accuracy.

Results

The F1 scores of the 10 protocols range from 0..87 to 0.97 (average F1 score of 0.94). There is little impact on performance when up to 4 least important words were removed from the reason of the study. However, when up to 4 most important words were omitted, the performance was substantially degraded (Figure 1).

Conclusions

Our NLP classifier demonstrated excellent performance in protocoling neuroradiology orders. We also have better understand how our NLP model made its decisions. By using word importance, we can understand how the model makes decisions and use this information to investigate systematic errors. By interpreting the model's mistakes, we found that the largest source of errors was due to

the model not understanding the hierarchy of protocol assignments. Another large contribution of mistakes was due to potential limitations or biases in the dataset that can be addressed with a more diverse dataset.

F1 Score	BERT
MR NASOPHARYNX OROPHARYNX	0.95
MR BRAIN MASS/METS/INFECT	0.91
MR STROKE	0.92
MR SELLA	0.97
MR BRAIN SEIZURE	0.96
MR BRAIN DEMYELINATING	0.95
MR BRAIN MOYA-MOYA DIAMOX	0.96
MR SKULL BASE	0.87
MR VASCULAR MALFORMATION	0.91
MR ORBIT SINUS FACE	0.91

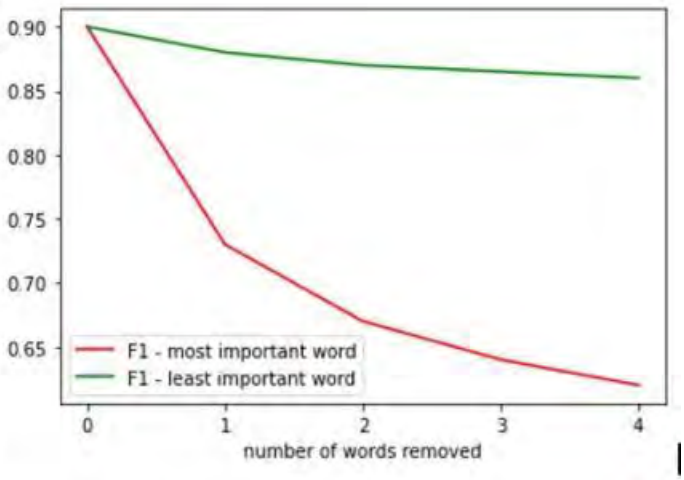

(Filename: TCT_1142_figure1.jpg)

388

Baseline Risk Factors for Developing ARIA-E From the SCarlet RoAD and Marguerite RoAD Open-Label Extension Studies

M Lyons[1], A Neve[2], Z Huang[3], B Das[2], J Wojtowicz[2], S Bullain[2]
[1]Roche Products Ltd, Welwyn Garden City, UK, [2]F. Hoffmann-La Roche Ltd, Basel, Switzerland, [3]F. Hoffmann-La Roche Ltd, Shanghai, China

Purpose

Treatment-induced amyloid-related imaging abnormalities-edema (ARIA-E) are identified risks of N-terminus anti-amyloid antibodies, with reported overall incidence in Alzheimer's disease trial participants of up to 40%. Known risk factors for developing ARIA-E include apolipoprotein E ε4 (APOE ε4) carrier status, higher anti-amyloid antibody dose, and baseline microhemorrhage burden [1,2]. SCarlet RoAD (NCT01224106) and Marguerite RoAD (NCT02051608) open-label extensions were designed to investigate the long-term safety and biomarker impact of gantenerumab 1,200mg every 4 weeks. To generate safety data that would inform future pivotal study design (GRADUATE trials [NCT03444870, NCT03443973]), 5 titration regimens were studied (Figure 1). ARIA-E incidence varied across treatment arms; here we investigated potential baseline risk factors for ARIA-E.

Materials and Methods

Baseline risk factors were selected for analysis based on those previously reported in the literature as potential individual characteristics. Univariate logistic analysis was used to identify baseline risk factors and multivariate logistic analysis was used to assess the independence of identified risk factors.

Results

In univariate logistic analysis, identified baseline risk factors for ARIA-E in both studies were APOE ε4 carrier status and presence of one or more microhemorrhage (Tables 1 & 2). Homozygous APOE ε4 carriers were at higher risk than heterozygotes (Tables 1 & 2). Multivariate logistic analysis showed that presence of APOE ε4 alleles or one or more microhemorrhage at baseline were independent risk factors (Table 3). Participants with both risk factors had a higher ARIA-E onset risk than those with one risk factor or no risk factors. Age, race, sex, and body mass index were not identified as baseline risk factors for ARIA-E (Tables 1 & 2).

Conclusions

APOE ε4 carrier status, in particular homozygous status, and microhemorrhage presence were identified as independent, nonmodifiable, and cumulative baseline risk factors for ARIA-E. Taking into consideration these nonmodifiable and modifiable (speed of titration) risk factors as well as the convenience of a universal regimen for all participants, an optimized trial design with a single 9-month titration was selected for GRADUATE trials. This optimized trial design aims to maximize exposure for all participants, including individuals at higher ARIA-E risk, while offering a simple regimen for all. Topline results of the GRADUATE trials will be presented in Nov. 2022.

Figure 1. Scarlet and Marguerite RoAD OLE titration regimens

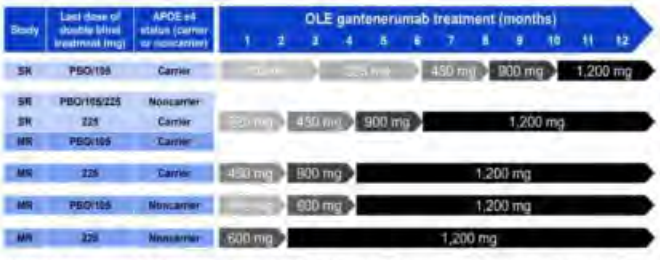

APOE ε4, apolipoprotein E ε4 allele; MR, Marguerite RoAD; OLE, open-label extension; PBO, placebo; SR, Scarlet RoAD

Table 1. Univariate logistic analysis for baseline risk factors in SR OLE

Risk Factors	Parameter Estimate	Standard Error	Odds Ratio	Wald 95% CI	p-value
Age (years) at start of OLE	-0.028	0.025	0.97	(0.93, 1.02)	0.2676
Sex					
Reference F, n=91					
M, n=63	-0.286	0.361	0.75	(0.37, 1.52)	0.4286
BMI at baseline	-0.009	0.052	0.99	(0.90, 1.10)	0.8650
APOE ε4 carrier status					
Reference noncarrier, n=45					
Carrier, n=109	1.146	0.457	3.15	(1.29, 7.70)	0.0121
APOE ε4 status					0.0169
Reference 0ε4, n=45					
1ε4, n=89	1.015	0.468	2.76	(1.10, 6.91)	0.0302
2ε4, n=20	1.692	0.608	5.43	(1.65, 17.86)	0.0054
Maximum microhemorrhage at OLE baseline					
Reference 0, n=114					
≥1, n=40	1.17	0.385	3.22	(1.51, 6.86)	0.0024

APOE ε4, apolipoprotein ε4; BMI, body mass index; CI, confidence interval; F, female; M, male; OLE, open-label extension; SR, SCarlet RoAD
Footnote: Univariate logistic analysis was not performed on race in SR OLE because the numbers of participants of Asian (n=2) and Other (n=7) races were small.

Table 2. Univariate logistic analysis for baseline risk factors in MR OLE

Risk Factors	Parameter Estimate	Standard Error	Odds Ratio	Wald 95% CI	p-value
Age (years) at start of OLE	-0.005	0.017	1.00	(0.96, 1.03)	0.7719
Race					0.9271
Reference White, n=175					
Asian, n=37	-0.133	0.394	0.88	(0.40, 1.90)	0.7366
Other, n=7	-0.189	0.852	0.83	(0.16, 4.40)	0.8248
Sex					
Reference F, n=127					
M, n=92	-0.209	0.296	0.81	(0.45, 1.45)	0.4802
BMI at Baseline	0.026	0.033	1.03	(0.96, 1.09)	0.4415
APOE ε4 carrier status					
Reference Noncarrier, n=81					
Carrier, n=138	0.649	0.316	1.91	(1.03, 3.55)	0.0401
APOE ε4 status					0.0169
Reference 0ε4, n=81					
1ε4, n=100	0.238	0.344	1.27	(0.65, 2.49)	0.4886
2ε4, n=38	1.610	0.423	5	(2.18, 11.46)	0.0001
Maximum microhemorrhage at OLE baseline					
Reference 0, n=196					
≥1, n=23	1.154	0.449	3.17	(1.31, 7.64)	0.0102

APOE ε4, apolipoprotein ε4; BMI, body mass index; CI, confidence interval; F, female; M, male; OLE, open-label extension; MR, Marguerite RoAD

Table 3. Multivariate logistic analysis for identified baseline risk factors in SR and MR OLE

Risk factor	Parameter Estimate	Standard Error	Odds Ratio	Wald 95% CI	p-value
Scarlet RoAD OLE					
APOE ε4 status					0.0298
Reference 0ε4, n=45					
1ε4, n=89	0.977	0.479	2.66	(1.04, 6.79)	0.0413
2ε4, n=20	1.604	0.624	4.97	(1.46, 16.90)	0.0102
Maximum microhemorrhage at OLE baseline					
Reference 0, n=114					
≥1, n=40	1.112	0.397	3.04	(1.40, 6.62)	0.0050
Marguerite RoAD OLE					
APOE ε4 status					0.0010
Reference 0ε4, n=81					
1ε4, n=100	0.225	0.347	1.25	(0.63, 2.47)	0.5177
2ε4, n=38	1.516	0.429	4.55	(1.96, 10.56)	0.0004
Maximum microhemorrhage at OLE baseline					
Reference 0, n=196					
≥1, n=23	0.956	0.472	2.61	(1.03, 6.57)	0.0422

APOE ε4, apolipoprotein ε4; CI, confidence interval; OLE, open-label extension

(Filename: TCT_388_ASNRSRMRARIARiskFactorsFigure_v1.jpg)

1227

Brain MR image synthesis using denoising diffusion probabilistic models.

M Moassefi[1], B Erickson[1], S Faghani[2], G Conte[1], B Khosravi[1]
[1]Mayo Clinic, Rochester, MN, [2]Mayo Clinic (Rochester, MN, US), Rochester, MN

Purpose

Deep learning-based methods for computer-aided diagnosis (CAD) have widespread applications nowadays and are a fast-growing field in medicine. The training of deep learning algorithms is, however, dependent on utilizing large medical imaging datasets. Prior literature has demonstrated that various generative paradigms, such as GANs or autoregressive models can be used to extract and generate the representations for common imaging modalities. Recent studies have shown that the diffusion probabilistic model (DDPM) outperforms alternative approaches to modeling natural image distributions both in terms of realism and diversity[1]. DDPMs are capable of generating new samples of the data, as well as representing the distribution of the real data. In this paper, we provide an affirmative answer to the question of if DDPM can also serve as representation learners and assist the generation of medical imaging. We intend to release all generated MRI files. In the case of using DDPMs in generating images, researchers might have a private dataset that can be used to generate new images based on that. Since the generated images are derived from patients' private images (not exactly them), they can be shared with no harm to patient confidentiality.

Materials and Methods

For our generative task, from the publicly available BRATS 2021 dataset which is an ample multi-institutional routine clinically acquired scans of glioma, we used post-contrast T1-weighted (T1Gd) Magnetic resonance imaging (MRI)s. From original images(x0), we consecutively introduced Gaussian noise to each pixel in t steps to create the noisy version of the image at step t(xt), using the noise-inducing function (x0 → xt) q(xt|x0). Then we used a noise predictor which is a U-Net network that approximates the Markov step of the reverse diffusion process in DDPM on a specific diffusion step t.

Results

Based on our primary results in figure-1, we showed that these activations effectively capture the spatial information from an input image and appear to be excellent image-level representations for the generation task.

Conclusions

We concluded that DDPMs have the potential for the synthesis of brain MRI data and to improve the application of CAD in the diagnosis of glioma. For our future direction, we will evaluate our images by radiologists' visual assessment and report Frechet Inception Distance (FID)which is a metric for evaluating the quality of generated images.

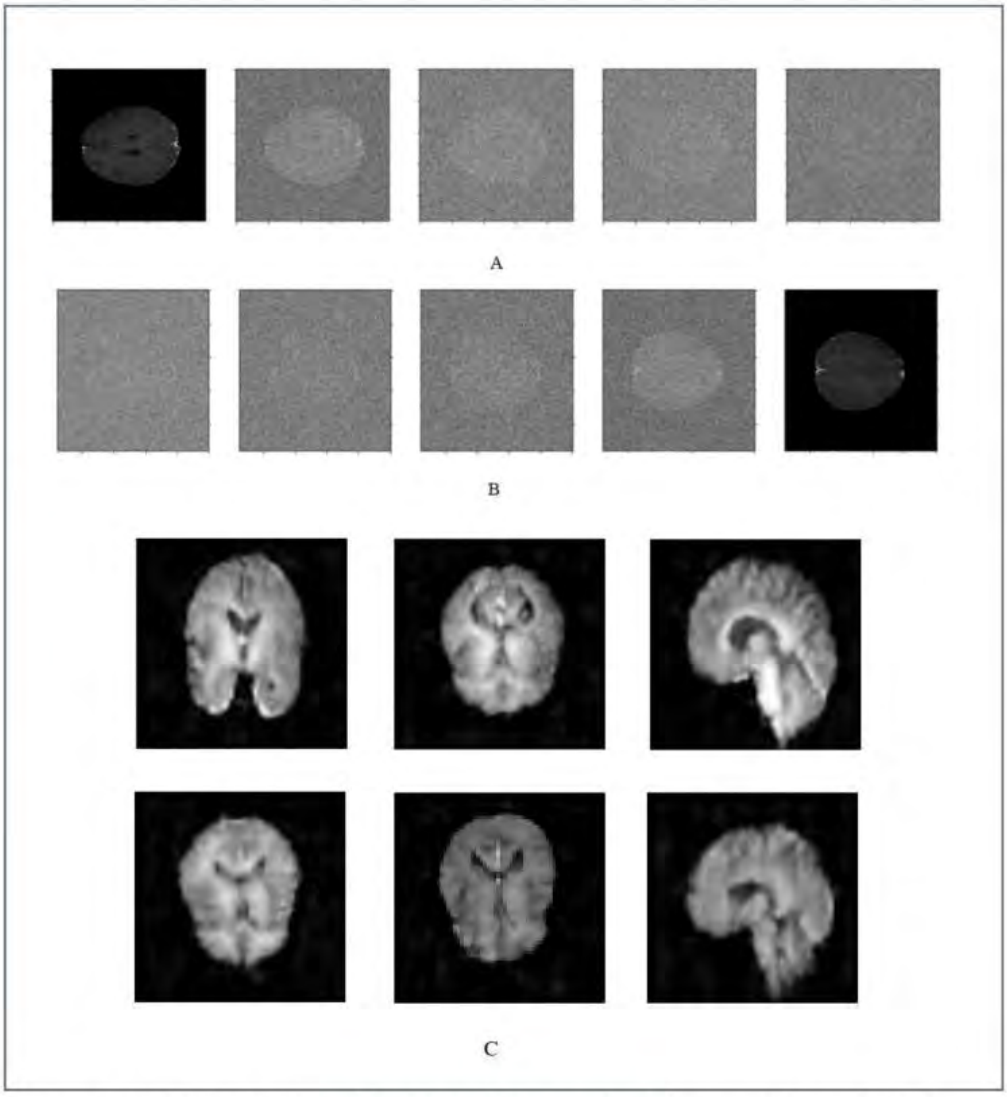

Figure 1- A and B shows noising and denoising on 2 slice examples. C demonstrates 2 examples of 3D brain MRIs generated by denoising using the U-Net model.

(Filename: TCT_1227_Image1.jpg)

953

Brain tumor segmentation from missing MR sequences: A meta-learning approach

G Singh[1], A Konwer[2], S Jambawalikar[1], A Lignelli[1], P Prasanna[2]
[1]Columbia University Irving Medical Center, New York, NY, [2]Stony Brook University, Stony Brook, NY

Purpose

Multi-modal magnetic resonance (MR) imaging remains the mainstay for diagnosing and assessing treatment plans for brain tumors. MRI scans provide diagnostic and prognostic information by defining different sub-regions of tumors from a combination of different multimodal sequences, such as T1-weighted, contrast-enhanced T1-weighted (T1c), T2-weighted, and Fluid Attenuation Inversion Recovery (FLAIR) images. Each of these subregions provides key information defining underlying phenotypic characteristics and genotypic alterations, as well as intrinsic heterogeneity of gliomas. Accurate segmentation of these sub-regions is crucial for extracting features for any diagnostic/prognostic applications or for predicting survival outcomes. Many algorithms have achieved human-level performance for image-segmentation tasks using all four structural MR sequences (T1, T1c, T2, FLAIR); however, in clinical practice, due to various reasons (patient movements, erroneous settings, allergy to contrast mediums, limited scan times), only a subset of sequences may be available for a patient. Contemporary deep learning (DL) models cannot handle missing MRI sequences for tumor segmentation and classification tasks. Our goal is to build a modality-agnostic DL network to segment brain tumors, even when full modality data is not available for model training.

Materials and Methods

We propose a novel approach to learn enhanced modality-agnostic representations by employing a novel meta-learning strategy in training, even when only a fraction of patients with full modality data are available. Meta-learning enhances partial modality representations to full modality representations by meta-training on partial modality data and meta-testing on limited full modality

samples. Additionally, we co-supervise this feature enrichment by introducing an auxiliary adversarial learning branch. More specifically, a missing modality detector is used as a discriminator to mimic the full modality setting.
Results
We leverage MRIs of 285 patients from the BraTS 2018 dataset to perform the segmentation task. Our method significantly outperforms previous segmentation approaches, such as heMIS, U-HVED and RFNet. Quantitative and qualitative results are shown in Figure (1).
Conclusions
We present a novel framework that efficiently performs tumor segmentation task, even when MRI sequences are missing for training purposes.

M																	
	FLAIR	○	○	○	●	○	○	●	○	●	●	●	●	●	○	●	Avg
	T1	○	○	●	○	○	●	●	●	○	○	●	●	○	●	●	
	T1c	○	●	○	○	●	●	○	○	○	●	●	○	●	●	●	
	T2	●	○	○	○	●	○	○	●	●	○	○	●	●	●	●	
WT	HeMIS [22]	79.85	60.32	55.76	66.20	81.63	65.39	75.41	81.70	82.56	76.25	79.82	84.58	86.27	82.74	85.06	76.23
	U-HVED [10]	81.06	58.74	52.37	82.65	80.88	66.21	83.70	82.83	86.44	84.92	86.33	87.56	87.84	83.47	88.25	79.55
	D2-Net [32]	76.58	43.79	19.43	85.06	84.62	65.37	86.18	82.56	86.35	87.94	87.31	88.59	89.12	83.78	88.94	77.04
	ACN [30]	85.24	79.16	78.65	86.72	85.87	79.27	86.33	85.21	86.69	87.54	86.92	88.22	87.51	86.38	89.14	85.25
	RFNet [13]	84.92	73.41	72.57	87.93	86.22	78.31	89.43	**86.81**	89.98	89.23	89.80	90.22	90.16	86.95	90.32	85.75
	mmFormer [31]	84.73	76.10	75.39	**88.53**	86.75	79.24	89.57	86.61	90.05	89.69	89.64	90.11	90.20	87.11	90.09	86.25
	Ours	**86.52**	**79.23**	**78.66**	87.45	**86.77**	**79.60**	**89.94**	86.71	**90.82**	**90.13**	**90.38**	**90.74**	**90.63**	**88.09**	**91.26**	**87.12**
TC	HeMIS [22]	49.63	53.75	24.80	32.91	70.28	64.29	45.62	54.36	54.93	69.40	72.57	62.38	75.51	73.94	74.18	58.57
	U-HVED [10]	56.62	64.50	36.77	54.38	74.46	65.29	59.03	58.66	62.57	73.14	75.85	63.72	73.52	76.81	72.96	64.55
	D2-Net [32]	59.87	64.29	20.32	50.84	81.06	77.96	62.54	64.18	61.70	82.45	79.38	67.52	81.47	80.23	80.94	67.65
	ACN [30]	67.24	84.35	70.49	67.38	84.70	83.92	70.61	**73.58**	70.66	82.17	84.35	67.08	81.94	84.32	84.73	77.16
	RFNet [13]	67.72	78.87	64.39	67.85	83.04	80.84	72.80	71.65	73.32	83.76	84.09	74.89	84.26	82.98	84.40	76.99
	mmFormer [31]	65.92	77.50	62.94	66.10	80.58	79.35	72.31	69.89	71.39	79.72	81.53	73.30	80.68	80.56	81.62	74.89
	Ours	**68.12**	**84.57**	**71.24**	**68.75**	**85.67**	**84.39**	**73.48**	72.90	**73.71**	**84.97**	**85.43**	**75.62**	**84.75**	**86.56**	**86.77**	**79.12**
ET	HeMIS [22]	22.47	56.20	7.89	9.64	64.07	65.66	17.73	26.95	27.42	65.83	70.35	30.18	68.97	69.52	73.80	45.11
	U-HVED [10]	27.82	61.24	11.06	22.35	68.93	65.79	24.57	24.46	35.80	69.31	71.42	32.14	70.66	69.98	71.20	48.44
	D2-Net [32]	22.83	69.52	15.34	12.96	70.45	71.38	14.06	19.32	17.79	69.25	68.31	23.66	67.14	68.56	67.72	45.22
	ACN [30]	43.26	**78.57**	40.89	42.14	74.95	75.88	42.73	**47.80**	44.39	76.72	76.33	41.61	75.54	75.27	76.79	60.85
	RFNet [13]	40.62	69.73	37.62	38.08	75.42	71.55	45.67	43.44	45.36	75.18	**76.52**	47.14	76.75	75.26	76.71	59.67
	mmFormer [31]	39.65	66.23	37.08	38.72	68.70	67.84	45.15	42.61	43.69	68.42	68.36	45.33	68.45	69.81	68.16	55.88
	Ours	**44.87**	78.09	**41.12**	**43.94**	**77.16**	**77.58**	**45.81**	46.25	**48.63**	**77.29**	76.04	**48.22**	**77.92**	**76.71**	**78.30**	**62.53**

Table 1. Comparison with state-of-the-art (DSC %) for the different combinations of available modalities on BRATS2018. Dice scores are computed for three nested tumor subregions - Whole tumor (WT), Tumor core (TC), Enhancing tumor (ET). The best and second best scores are **highlighted** and underlined. Modalities present are denoted by ●, the missing ones by ○.

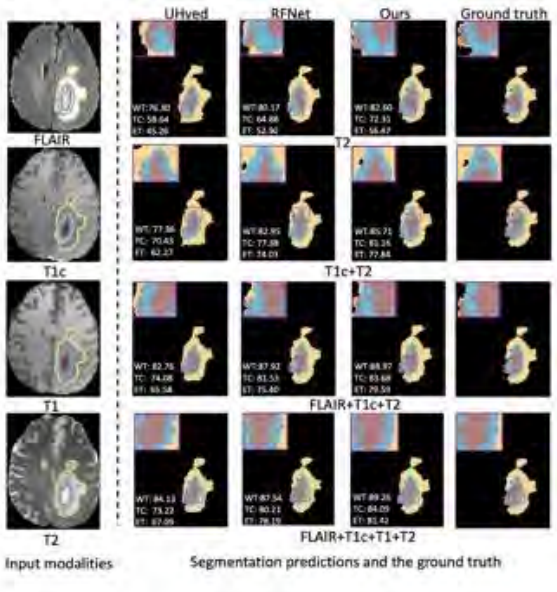

(Filename: TCT_953_Figure1.jpg)

476

Brainstem Atrophy across the AD Spectrum and its Correlation with Markers of Cognitive Decline, Sleep, and Mood Disturbance: An Automated Volumetric MRI study.

D Bhalla[1], B Bendlin[2], E Granadillo[3]
[1]Medical College of Wisconsin, Wauwatosa, WI, [2]UW-Madison, Madison, WI, [3]Medical College of Wisconsin, Milwaukee, WI

Purpose
Alzheimer's disease (AD) is the most common dementia that causes progressive problems with memory, critical thinking, and behavior. Studies have shown brainstem displaying earliest signs of AD progression (2,3). Midbrain structural changes are linked to AD symptoms i.e., memory impairment, sleep disorders, and emotional disturbances (4,5). The purpose of this study is to investigate changes in brainstem volumes (BS-V) and elucidate the differences in BS atrophy patterns across the AD spectrum utilizing MRI automated volumetric assessment (NR). Potential correlations between BS-V and biomarkers of cognition, sleep, and mood disturbances are evaluated.
Materials and Methods
A retrospective review of 60 AD spectrum patients who had NR, and sleep and cognitive tests was performed. BS-V and Hippocampal volumes (Hip-V) for 3 groups of 20 patients each: Subjective cognitive impairment (SCI), Mild cognitive impairment (MCI) and AD were collected. Multiple regression models corrected for age and gender were obtained, to determine group-wise differences in BS-V and Hip-V with SCI set as the comparison group. Pearson correlations between BS-V, sleep biomarker, and cognitive test scores was assessed.
Results
No difference in BS-V or BS-V corrected for total intracranial volume (BS-VM) across AD spectrum compared to SCI. Hip-V difference between AD and SCI remained significant after adjustment for age (p=0.014). Female gender was a significant predictor of lower brainstem volumes (β =-0.382, p=0.004) but when corrected for total intracranial volume (BS-VM), male gender was associated with lower brainstem volumes (β =-0.356, p=0.009). Female gender was also a significant predictor of lower raw hippocampal volumes (β =-0.403, p=0.002), consistent with AD literature suggesting a differential gender-based susceptibility to AD pathology (1). Inverse correlation between SE and BS-V noted, contrary to prevailing literature that needs further exploration.
Conclusions
Significant results obtained from this study can be explored further towards establishing a few non-invasive clinical biomarkers that could be utilized for early AD detection as well as assessing AD progression. Characterizing the brainstem atrophy rate in AD spectrum patients and correlating with accompanying clinical manifestations such as sleep and mood disorders could refine the diagnostic algorithm leading to earlier diagnosis, appropriate change in care, and possible treatments of patients.

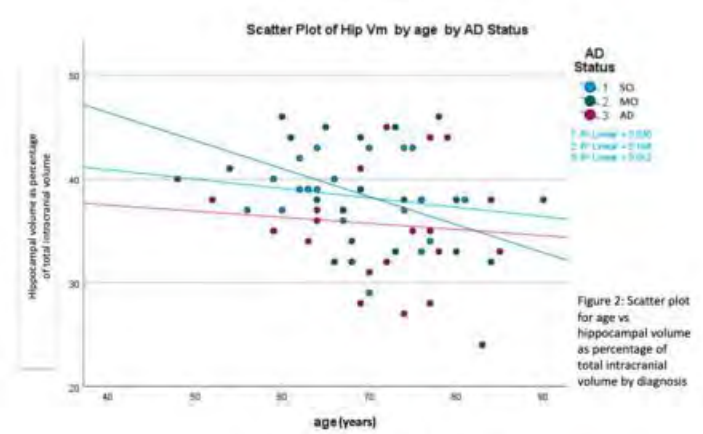

Figure 2: Scatter plot for age vs hippocampal volume as percentage of total intracranial volume by diagnosis

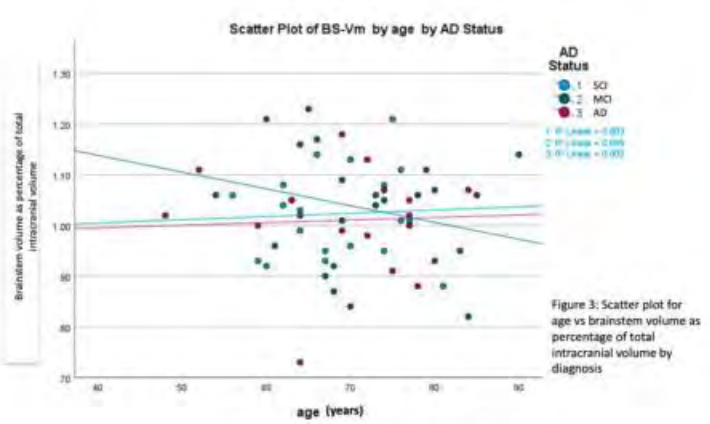

Figure 3: Scatter plot for age vs brainstem volume as percentage of total intracranial volume by diagnosis

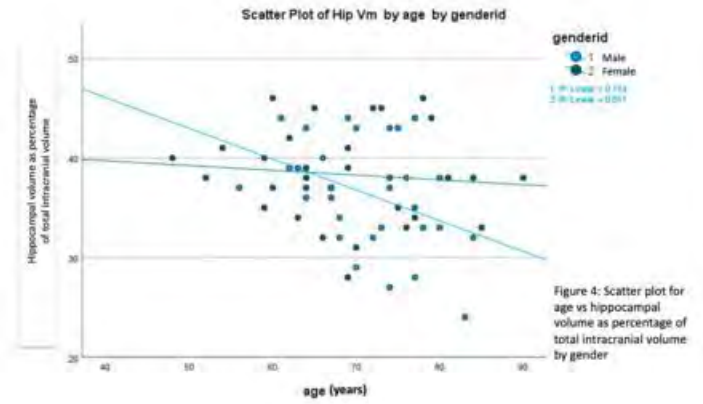

Figure 4: Scatter plot for age vs hippocampal volume as percentage of total intracranial volume by gender

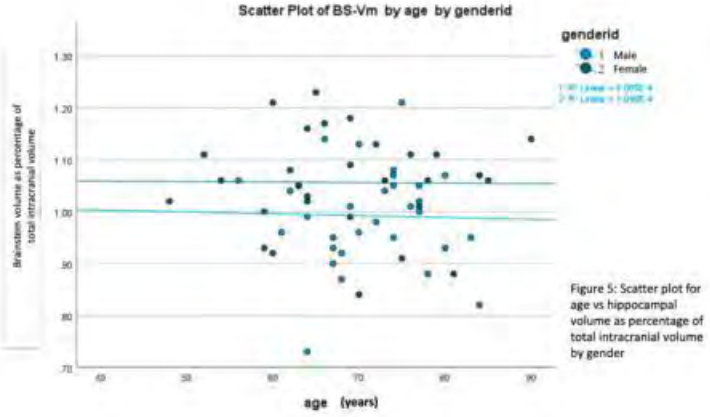

Figure 5: Scatter plot for age vs hippocampal volume as percentage of total intracranial volume by gender

(Filename: TCT_476_Abstract2022graphs.jpg)

990

Can Imaging Predict L1CAM Status in Supratentorial Ependymomas?

G PADMASRI[1], C Prasad[1], K Kulanthaivelu[1], N B N[2]

[1]National Instituite of Mental Health and Neurosciences, Bangalore, Karnataka, [2]National Instituite of Mental Health and Neurosciences, Bangalore , Karnataka

Purpose

Supratentorial ependymomas associated with ZFTA fusion(previously named RELA fusion) are the most aggressive subgroup with poor prognosis. L1CAM(Cell Adhesion Molecule L1/CD171, a 200kDa glycoprotein), even though not a specific marker, is a surrogate and relatively easily available IHC marker for presence of ZFTA/RELA fusions. The purpose of this study is to establish the efficacy of the imaging features in predicting this aggressive subgroup on imaging which plays a significant role in pre surgical prognostication.

Materials and Methods

23 cases of histologically proven supratentorial ependymomas, operated over one and half year duration at our institution were analyzed. 2 cases were excluded due to non availability of L1CAM status. MRI features of 21 molecularly proven cases of L1 CAM and Non-L1CAM supratentorial ependymomas were retrospectively evaluated, conforming to the institutional research protocols. Conventional and advanced MR imaging features (including Diffusion, Susceptibility weighted imaging) were observed wherever feasible. MRI features were mainly described along the lines of tumor definition, cortical invasion, enhancement pattern, extent of edema, degree of hemorrhage.

Results

Among the 21 cases, 11 cases were L1CAM positive and 10 were L1CAM negative. No significant difference in age or sex between both the groups. 20 among the 21 tumors, were Anaplastic Ependymomas with Grade 3 histology. One tumor with Grade 2 histology was L1CAM negative. L1CAM tumors predominantly showed solid cystic appearance with well defined margins, relatively less perilesional edema and micro hemorrhages without gross cortical invasion. Non L1CAM tumors predominantly were solid with infiltrative margins into the adjacent cortex, showed heterogeneous enhancement with enhancing and non enhancing components as well as more intratumoral hemorrhage. All the L1CAM positive lesions were located over cerebral convexities and superficially located. Two thalamic lesions mimicking midline glioma and one suprasellar lesion mimicking craniopharyngioma on imaging were L1CAM negative. However, larger studies are required to establish the statistical significance.

Conclusions

Analysis of MRI features have a potential role in discriminating L1CAM status in suspected cases of supratentorial ependymomas, aiding in pre operative prognostication.

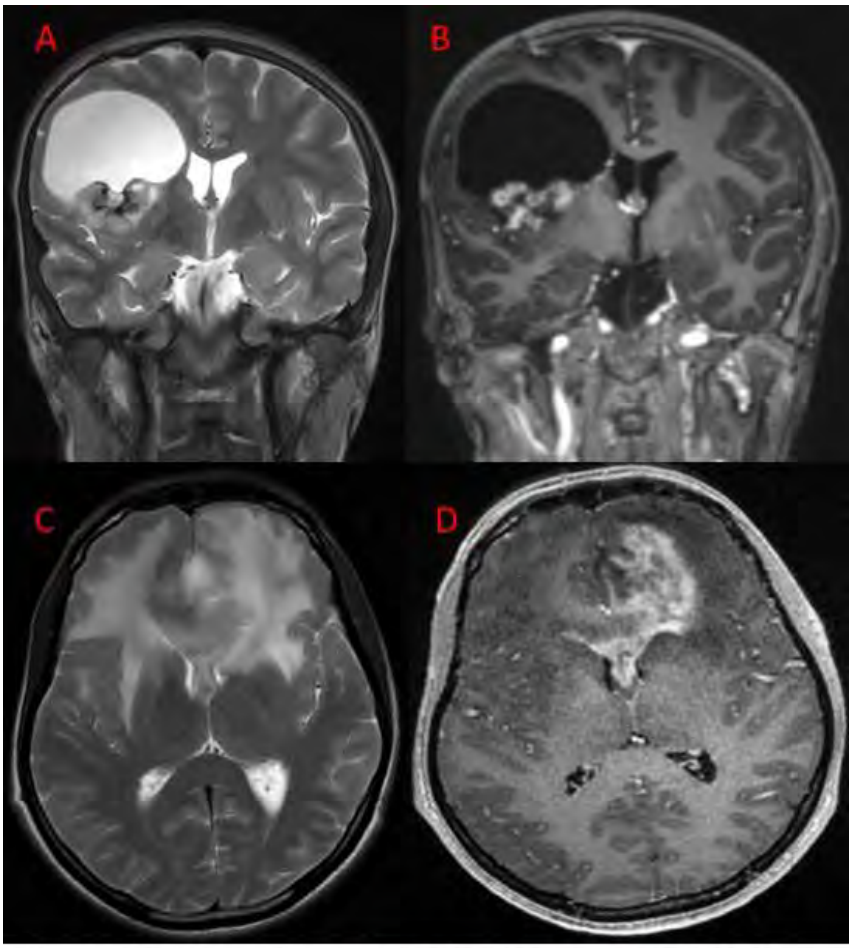

Figure; A and B shows L1CAM positive Supratentorial Ependymoma with well defined solid cystic lesion.
C and D shows L1CAM negative lesion with ill defined margins and heterogeneous enhancement

(Filename: TCT_990_ASNR.JPG)

945

Can simultaneous MR PET serve as a tool for virtual biopsy in gliomas ? - A histopathological correlation study .

S Ahmed[1], s mangalore[2], P KUMAR[3]

[1]NIMHANS, Bangalore, KS, [2]NIMHANS, Bangalore, India, [3]National Instituite of Mental Health and Neurosciences, Bangalore , Karnataka

Purpose

We live in the era of non invasive prediction of the genotype of cerebral gliomas. Radiomics has served well in this development. However, the accuracy of conventional MRI markers such as T2/FLAIR mismatch has underscored the efficacy of conventional sequences in predicting the genotype of cerebral gliomas. In this pilot study we aimed to explore if the pattern of methionine PET uptake of gliomas could aid in prediction of the genotype of gliomas.

Materials and Methods

Prospective recruitment of all cases of treatment naïve gliomas that fulfilled the inclusion criteria comprising of availability of i) T2/FLAIR, DWI, SWI and post contrast T1 images. ii) good quality perfusion imaging. iii) methionine PET imaging. iv) Histopathological genotyping of tumor type, grade and IHC markers-i.e IDH status, presence of p53 mutation, ATRX loss of expression/ retention and miB index. 13 cases were included in this pilot study. Descriptive analysis of common patterns of uptake, conventional MRI imaging surrogates and correlation with genetic markers was performed. Results : Of the 13 cases recruited in this pilot study the tumor type comprised of the following :2 diffuse astrocytomas, 3 anaplastic astrocytomas,2 anaplastic oligodendrogliomas, 2 oligodendrogliomas , 2 high grade gliomas- one with astrocytic and one with oligoastrocytic morphology – the above were IDH mutant. One case of IDH wild type astrocytoma was included. In this cohort, 3 cases were grade II, the remaining were of higher grade- i.e III.

Results

(Grade II) gliomas – 2/3 showed avid homogenous PET uptake ,1/3 case showed no uptake on PET. PET-perfusion match , PET-enhancement and PET-DWI(TRACE) match was observed Of 10 high grade gliomas-9/10 demonstrated DWI-PET match,9/10 perfusion –PET match and 8/10 PET-enhancement match. 3/13 cases showed concordance with T2/FLAIR mismatch hypotheses. IDH

wild and mutant variants showed similar pattern of methionine uptake. No difference in uptake was observed with p53 mutant/wildtype. All oligodendrogliomas showed uptake on PET,2/7 astrocytic tumors showed no uptake on PET.
Conclusions
Preliminary observations point towards the possibility of developing a biomarker of virtual biopsy on METHIONINE PET coupled with diffusion and perfusion match for predicting the genotype and grade of gliomas.

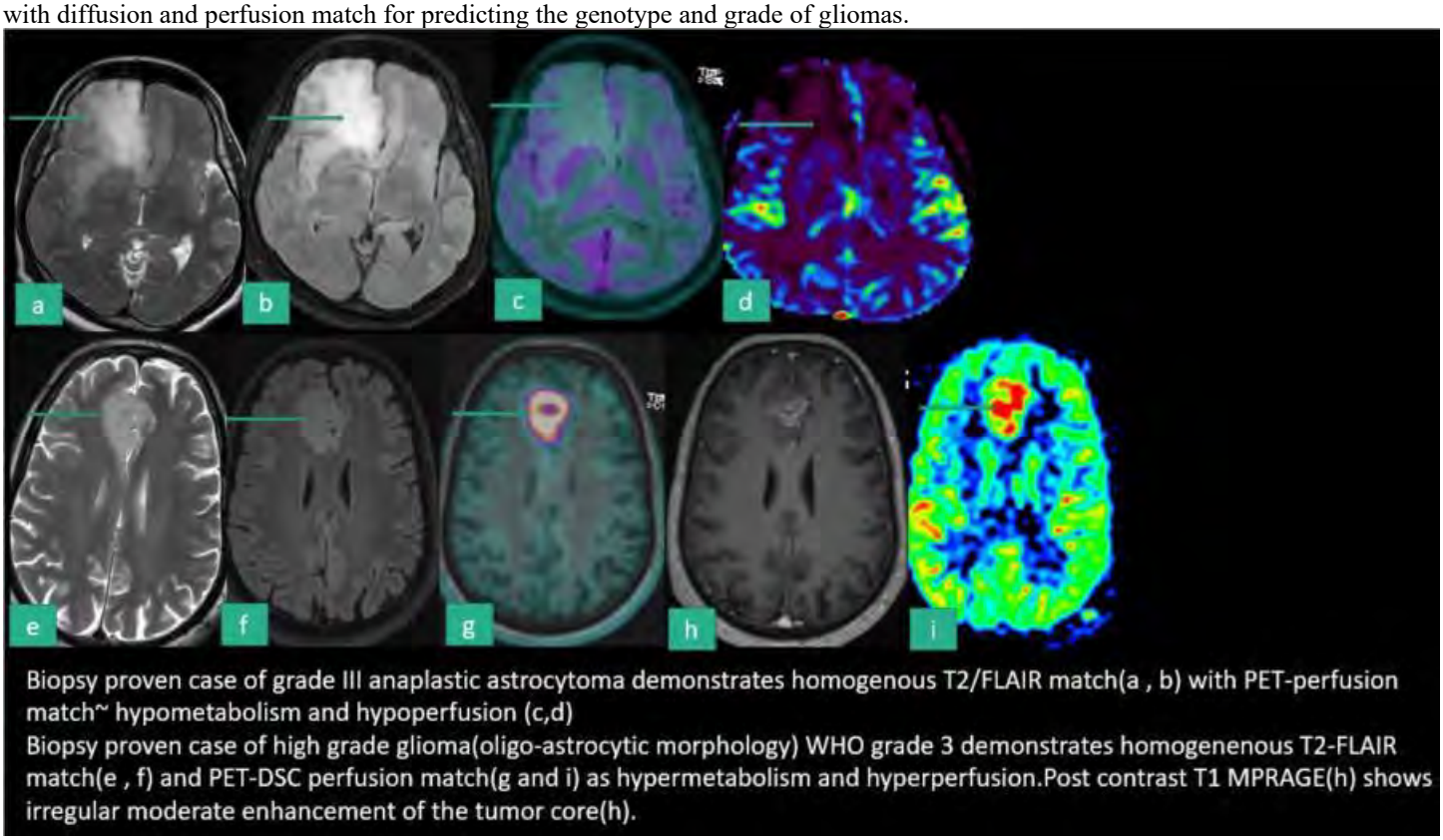

Biopsy proven case of grade III anaplastic astrocytoma demonstrates homogenous T2/FLAIR match(a , b) with PET-perfusion match~ hypometabolism and hypoperfusion (c,d)
Biopsy proven case of high grade glioma(oligo-astrocytic morphology) WHO grade 3 demonstrates homogenenous T2-FLAIR match(e , f) and PET-DSC perfusion match(g and i) as hypermetabolism and hyperperfusion.Post contrast T1 MPRAGE(h) shows irregular moderate enhancement of the tumor core(h).

(Filename: TCT_945_HYBRIDMRPET.JPG)

1340

Cerebellar Involvement in Term Perinatal Hypoxic-Ischemic Injury and Association with the Thalamic-Cerebellar Circuit

L Tierradentro-García[1], S Venkatakrishna[1], P Sharma[1], C ALVES[1], M Elsingergy[1], F Worede[1], S Andronikou[1]
[1]*Children's Hospital of Philadelphia, Philadelphia, PA*

Purpose
Profound hypoxic-ischemic injury (HII) affects metabolically active regions (e.g. basal ganglia [BGT]), but cerebellar injury is believed to be uncommon. Intrathalamic nuclear involvement has been associated with global patterns of injury (e.g. ventrolateral [VLN] with BGT pattern), but their association with cerebellar injury has not been elucidated. We aimed to determine the associations between cerebellar and thalamic injury in children with HII.
Materials and Methods
This is an IRB-approved, retrospective, observational study. We used a dataset of children aged 0-18 years with a history of term HII as demonstrated on delayed magnetic resonance imaging (MRI). We included those with cerebellar injury defined as signal abnormality and/or atrophy in either of the cerebellar hemispheres, or vermis. We assessed the presence of thalamic injury as: 1) VLN, 2) pulvinar, 3) anterior, 4) medial. Qualitative data are reported as counts and percentages; quantitative data are reported as median (IQR). We used chi-square to test associations between categorical variables and calculated odds ratio (OR).
Results
252 of 1175 children (21%) with term HII had cerebellar injury, mean age at delayed MRI 6 (3-9) years. 145 (58%) had cerebellar atrophy. The most commonly cerebellar injured region was the vermis (n=209, 83%). 226 (90%) children had a concomitant thalamic injury: most commonly VLN (n=97, 39%). Vermian injury was associated with VLN injury ([OR 35.7 (CI 4.8-264.1), p<0.001]). Injury in any hemisphere was associated with pulvinar ([OR 3.9 (CI 2.3-6.9), p<0.001]), anterior ([OR 3.4 (CI 1.6-6.1), p<0.001]), median ([OR 2.3 (CI 1.3-4.3), p<0.006]) or any thalamic region other than the VLN ([OR 3.3 (CI 1.9-5.7), p<0.001]) injury.
Conclusions
Over a fifth of children with term HII demonstrate cerebellar injury on delayed MRI - mostly involving the vermis (83%), and presenting more frequently in the setting of VLN thalamic injury, likely due to profound insults. Cerebellar hemispheric injury is more likely associated with injury to other thalamic nuclear groups. These connections could help explain the dysfunction in upstream or downstream synaptic networks in HII depending on the severity and duration of the ischemic insult.

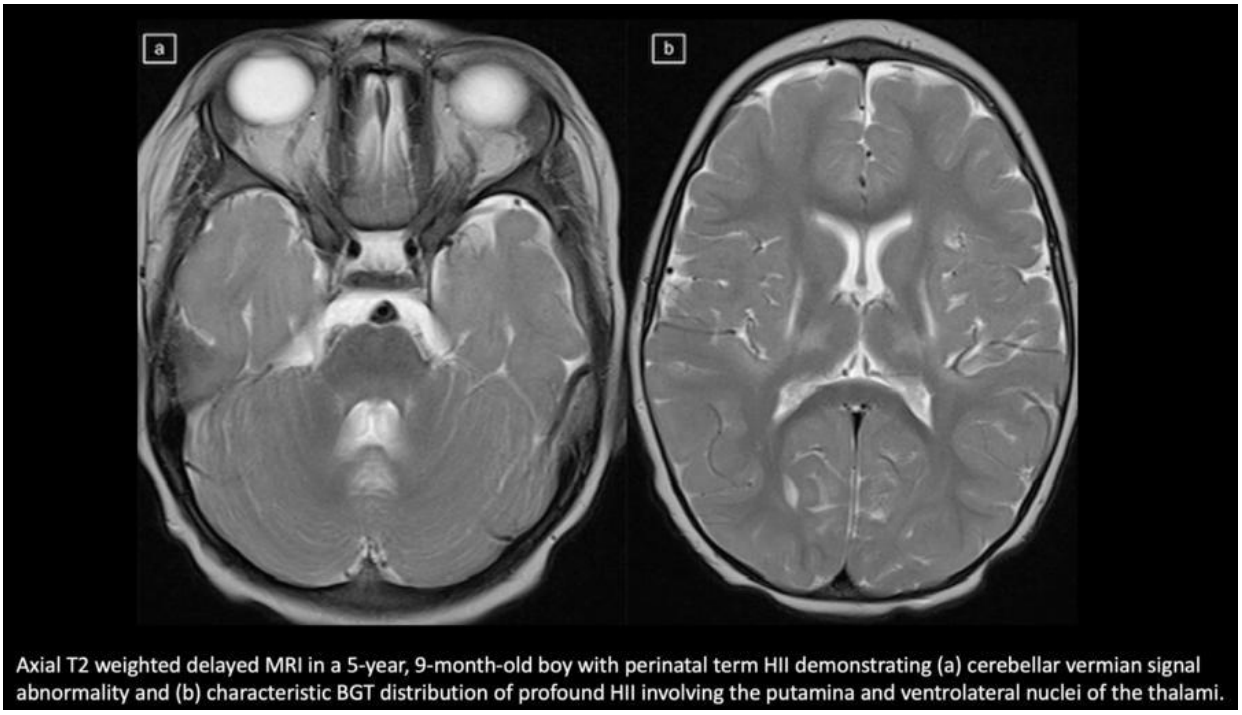

Axial T2 weighted delayed MRI in a 5-year, 9-month-old boy with perinatal term HII demonstrating (a) cerebellar vermian signal abnormality and (b) characteristic BGT distribution of profound HII involving the putamina and ventrolateral nuclei of the thalami.
(Filename: TCT_1340_Tierradentro_ASNR2023.jpg)

838

Chemotherapy-induced Brain Glucose Metabolism Patterns in Patients with Advanced Non-Small-Cell Lung Cancer ：a Retrospective 18F-FDG PET Study

X Cao[1], J Yu[2], Q Chen[2], Y Wang[3]

[1]Department of Nuclear Medicine, The Fifth Affiliated Hospital of Sun Yat-sen University, Zhuhai, Guangdong, AK, [2]Department of Nuclear Medicine, The Fifth Affiliated Hospital of Sun Yat-sen University, Zhuhai, Guangdong, China, [3]The Fifth Affiliated Hospital of Sun Yat-sen University, Zhuhai, Guangdong， China

Purpose

Currently, chemotherapy remains the standard-of-care for most patients affected by advanced non-small-cell lung cancer (NSCLC). However, survivors often complained that they have cognitive problems during treatment or even after therapies, which we called chemotherapy-related cognitive impairment (CRCI) or chemo-brain. This study was designed to investigate: (1) the acute or chronic post-chemotherapy effect on brain glucose metabolism; (2) different chemotherapy cycles effect on brain.

Materials and Methods

73 patients with advanced NSCLC after chemotherapy who underwent whole body 18F-fluorodeoxyglucose positron emission tomography/computerized tomography (18F-FDG PET/CT) scan at our department from September 2017 to August 2022 were included. 72 healthy controls were included as they had underwent whole-body 18F-FDG PET/CT scan at our department without any evidence of malignancy or mental illness and were further confirmed by follow-up visit. Advanced NSCLC patients were classified in six arms: short-to-long course (chemotherapy cycles under 4, between 5 to 8 or more than 8) in acute chemotherapy effect(AC) group (scanned PET/CT within 6 months post-chemotherapy) or chronic chemotherapy effect (CC) group (the interval between scanning and the last chemotherapy more than six months). Statistical parametric mapping (SPM) analysis on 18F-FDG PET was performed (uncorrected $p < 0.001$ with cluster size above 20 contiguous voxels).

Results

There were no significant differences between patients' groups and healthy controls in age, sex and BMI. SPM 18FDG PET analyses detected anomalous metabolic activity in specific regions in different groups ($p < 0.001$). Short-course + AC group showed hypermetabolism was in the cerebellum and large hypometabolism regions in bilateral frontal lobe predominantly. Only hypometabolic brain regions in middle-course + AC patients were reported. In long-course + AC group, we found more abnormal brain metabolism regions. But the abnormal brain metabolism regions of patients in CC group tend to reduce in all courses.

Conclusions

In this study, we found that abnormal brain metabolism patterns in patients with advanced NSCLC who received chemotherapy treatment, the brain metabolic pattern of the patient with advanced NSCLC is related to the chemotherapy cycles and the anomalous regions trend to recover after received chemotherapy 6 month.

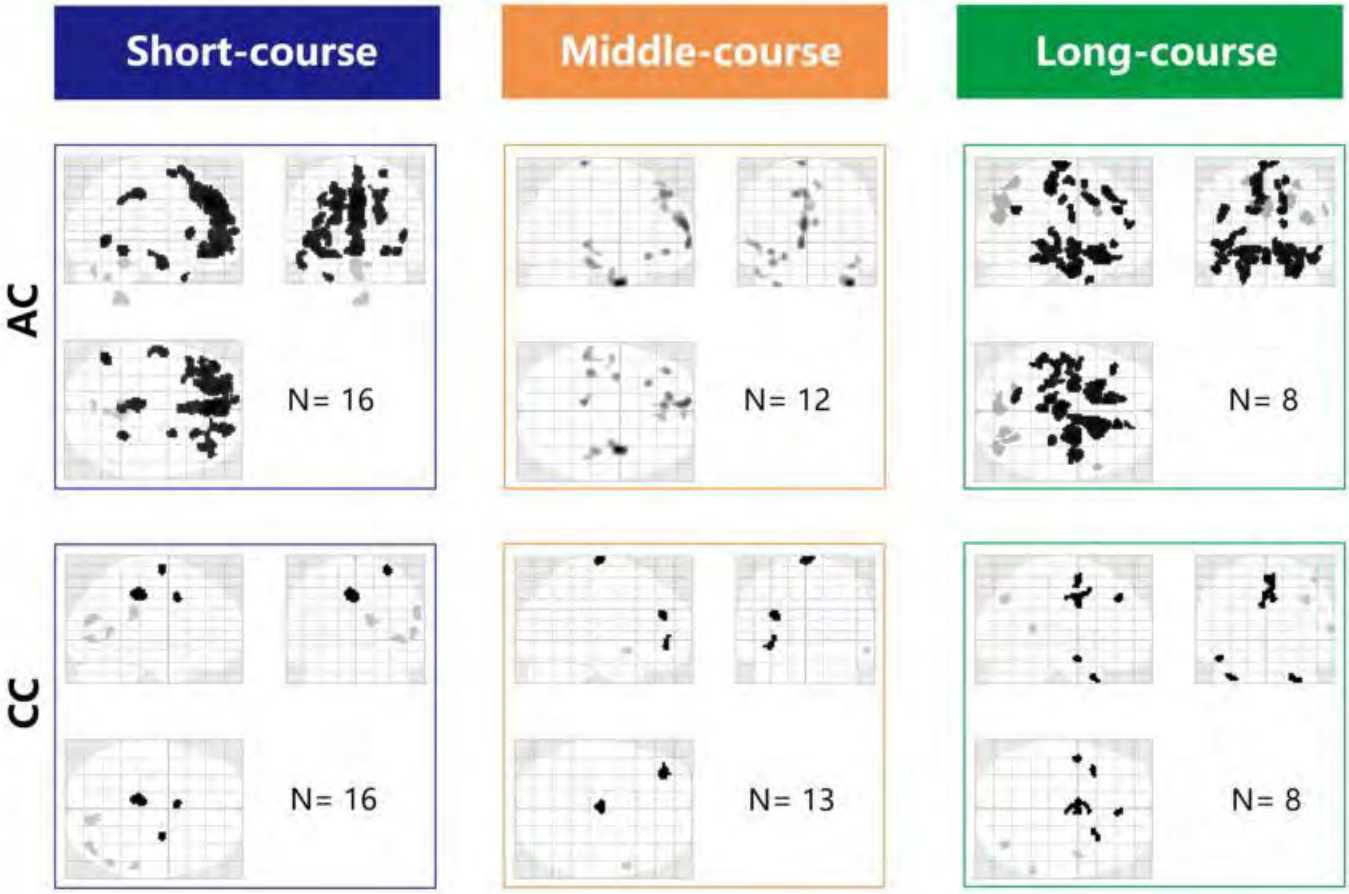

(Filename: TCT_838_MIPofchemo.jpg)

698

Clinical Neuroradiology: Radiology Rounds Reinvented

R Singh[1], G Virador[1], A Ahmed[1], Y Alami Idrissi[1], M Hardman[1], A Desai[1], P Vibhute[1], V Gupta[1], K Barrett[1], W Freeman[1], T Shaw[1], J McKinney[1], S Sandhu[1]

[1]*Mayo Clinic, Jacksonville, FL*

Purpose

The presence of a neuroradiologist on a neurology clinical rounding team could lead to improvements in patient care and a reduction of unnecessary costs via imaging study optimization. Prior studies have demonstrated that large percentages of inpatients can receive inappropriate imaging.1 We seek to quantify the value of a neuroradiologist on neuroscience clinical rounds teams.

Materials and Methods

A board-certified neuroradiologist joined the neurology team on their inpatient rounds to both interpret patient imaging findings and evaluate new imaging orders. If "suboptimal imaging" was identified in the patient care plan, potential adjustments were discussed with the neurology team. "Suboptimal imaging" was defined by neuroradiology as either imaging orders with a low probability of answering the clinical question posed by the neurology team or which would be adjusted to be more appropriate for the patient's current circumstances. The American College of Radiology Appropriateness Criteria were consulted as guiding principles when evaluating each patient's case, but most of the encountered scenarios did not have a corresponding structured indication.

Results

The neuroradiologist was present while the neurology team reviewed the cases of 100 inpatients. The neurology team planned to order new imaging in 30 (30%) of the patients. In these patients, the neurology team planned to have 42 new imaging studies, 32 of which were MR, 6 of which were CT, 3 were angiograms, and 1 was a PET-CT. Of the new imaging studies the neurology team planned to perform, 25 (60%) were found to be suboptimal. These included 21 MRIs, 3 CTs and 1 DSA (Table 1). One additional CT scan was recommended which increased utilization. There was a significant difference between the neurology team and the neuroradiologist new inpatient imaging recommendations ($p<0.001$) and inpatient MRI recommendations ($p<0.001$).

Conclusions

An embedded neuroradiologist on clinical rounds improves appropriate imaging utilization and timely management. This can ensure

the patient receives the necessary imaging studies for their treatment while potentially decreasing length of stay, patient radiation exposure and unnecessary costs.

Table 1

	New Imaging Studies	MRI/MRA	CT	DSA	PET-CT
Neurology imaging orders	42	32	6	3	1
Suboptimal imaging per neuroradiology	25 (60%)	21 (65%)	3 (50%)	1 (33%)	0 (0%)

Figure 1

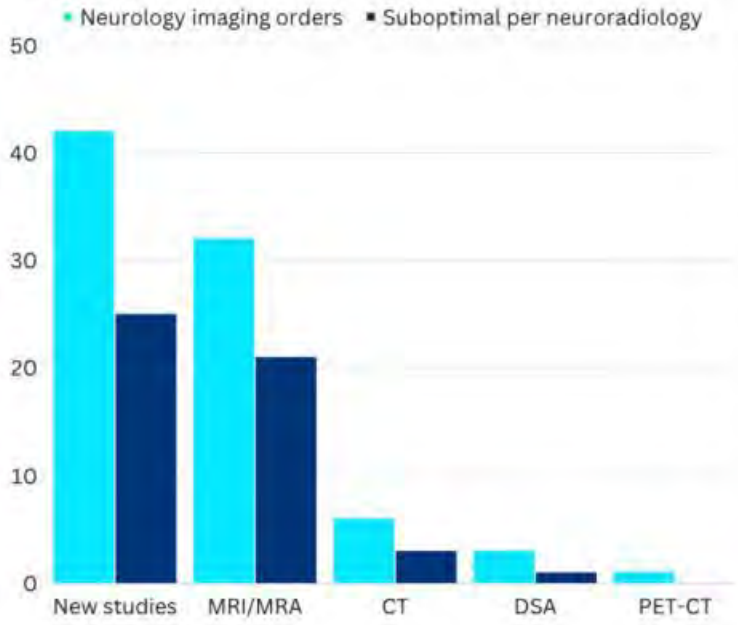

Figure 2

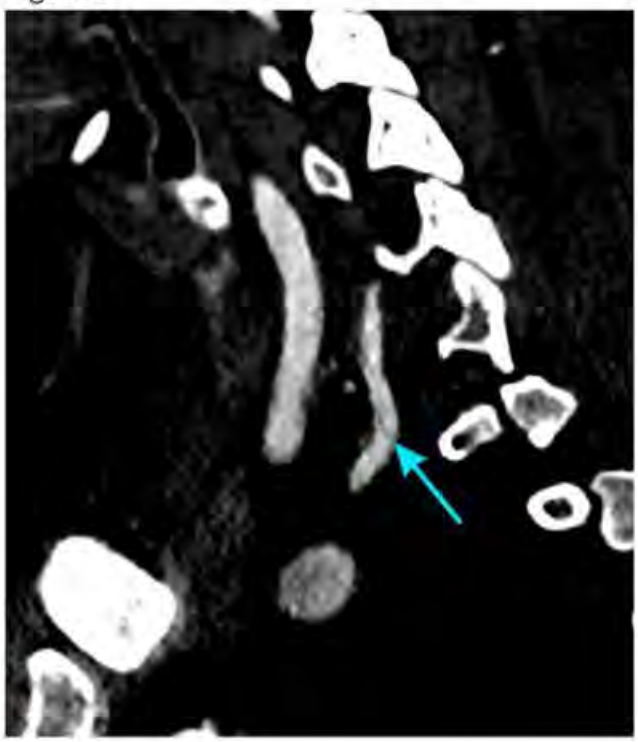

Table 1: Imaging studies ordered by the neurology team and those deemed suboptimal by the neuroradiologist.
Figure 1: Imaging studies ordered by the neurology team and those deemed suboptimal by neuroradiologist.
Figure 2: Patient who received overnight imaging orders for MRI/MRA head and neck for suspected dissection. Rounding neuroradiologist cancelled the MRI/MRA orders after deeming dissection unlikely.

(Filename: TCT_698_ASNRCNRImages.jpg)

1514

Comparison Between Postcontrast T1-Weighted Thin-slice 2D Spin Echo and 3D SPACE Sequences in Detection of Brain Metastases at 1.5T and 3T

A Rulseh[1], J Vymazal[2]
[1]Na Homolce Hospital, Prague, Czech Republic, [2]Na Homolce Hospital, Prague, CT

Purpose

The accurate detection of metastatic brain lesions (MBL) before radiotherapy is critical. Although spin echo (SE) are superior to gradient echo sequences in detecting small MBL, thin-slice whole-brain coverage is time-consuming. The sampling perfection with application optimized contrasts using different flip angle evolution (SPACE) sequence shares many advantages with SE, but with faster acquisition and greater resolution while achieving whole-brain coverage.

Materials and Methods

Fifty-six patients with MBL were included and underwent a standard protocol (1.5T n=37, 3T n=19), including postcontrast T1-weighted SE and SPACE (postcontrast order: SE first n=26, SPACE first n=30). Rating was performed by 3 raters in 2 sessions >6 weeks apart; images were de-identified and order randomized, only SE or SPACE per-subject per- session. The true number of MBL was determined using all available imaging including follow up. Intraclass correlations were determined; consistency for intra-rater (SE vs. SPACE) and agreement for inter-rater (same sequence). A paired t-test was used to evaluate postcontrast sequence order.

Results

A total of 135 MBL were identified (mean/subject 2.41, SD 6.4). Relatively fewer lesions were identified on the first postcontrast sequence (SE/SPACE), however the difference was not significant (p=0.08). Intra-rater consistency (SE vs. SPACE) was excellent (ICC: R1, 0.984; R2, 0.971; R3, 0.946), as was inter-rater agreement, with ICC values of 0.984 and 0.969 for SE and SPACE sequences, respectively. Finally, agreement between individual sequences and the true number of lesions was excellent (SE ICC: R1, 0.981; R2, 0.973; R3, 0.977; SPACE ICC: R1, 0.984; R2, 0.971; R3, 0.965).

Conclusions
The emergence of fast computer-assisted treatment planning of targeted radiosurgery techniques in the management of brain metastases requires precise, fast and reliable MRI workup. The reliable detection of MBL with MRI depends on a number of factors, particularly pulse sequence and contrast agent type, dose and application delay. Although SE sequences are superior to gradient echo sequences in the detection of small brain metastases, they have relatively long acquisition times and are prone to artifacts. To our knowledge this is the first comparison between thin-slice T1-weighted SE and SPACE sequences in the detection of brain metastases at 1.5 Tesla and 3 Tesla. Our results show that T1-weighted SPACE is not inferior to standard thin-slice SE sequences in the detection of brain metastases.

868

Comparison of neuroradiologist versus A.I. for detection of new multiple sclerosis lesions within a real-world clinical setting

A Saremi[1], S Jones[2], H Kitzler[3]
[1]Case Western Reserve University, Cleveland, OH, [2]Cleveland Clinic, Cleveland, OH, [3]University Hospital Carl Gustav Carus Dresden, Dredsen, Dresden

Purpose
MSPie (MS PATHS Image Evaluation) is a new machine-learning prototype software developed by Siemens Healthcare as part of the MS PATHS initiative.[1,2] It is designed to automatically analyze standardized T1-MPRAGE and 3D-FLAIR for brain parenchymal fraction, T2 lesion volume, and new/enlarged T2 lesion (NEL) count. Previous studies have validated MSPie's performance in lesion and volume detections within a selected sample.[3,4] Our objective was to evaluate how MSPie performed compared to a group of clinical neuroradiologists evaluating MS studies within a real-world clinical setting.
Materials and Methods
Standardized 1mm isotropic 3D images (MPRAGE: TR=2300ms, TE=2.98ms, TI=900ms; FLAIR: TR=5000ms, TE=393ms, TI=1800ms) acquired on a 3T Siemens Skyra were collected as part of routine care at the Cleveland Clinic. Images were analyzed by MSPie to measure NEL count, defined as lesion size of >=2mm. n=160 MS patients were selected. Inclusion criteria included having an established diagnosis of MS, at least one prior MS PATHS study available for longitudinal evaluation, and a matching neuroradiologist report that compares the same studies. Studies were labeled as either congruent or discordant with the report based on number and site of lesions. MSPie results were then individually assessed by an expert neuroradiologist to determine true (TP) and false positive (FP) lesions. False negatives (FN) were determined using described lesions from neuroradiologist reports. A target threshold of FP+FN ≤ 3 had been used in previous MSPie validation studies.3 Therefore, readopted for consistency in determining accuracy.
Results
Chi-square test determined that negative studies are more likely to be congruent with neuroradiologist reports ($\chi 2$ (2, N=160) = 30.1747, $p < 0.001$). For T2 lesion detection, 8% (13/160) of the cases exceeded the pre-defined criteria, an improvement from previously reported rate of 25%. [3] Sensitivity of MSPie was calculated to be 82.8% with a positive predictive value of 34.8%. Compared to neuroradiologist, MSPie had a higher TP count for 14% of studies (23/160), with a lower count for only 4% (7/160).
Conclusions
The high sensitivity and TP count demonstrate MSPie can serve as an invaluable tool for neuroradiologist in triaging for (in)active disease and the presence of lesions. Neuroradiologists need to be aware of the high FP rate of MSPie and troubleshoot when appropriate. This work increases diagnostic confidence in the chosen approach for its transition to the point of care.

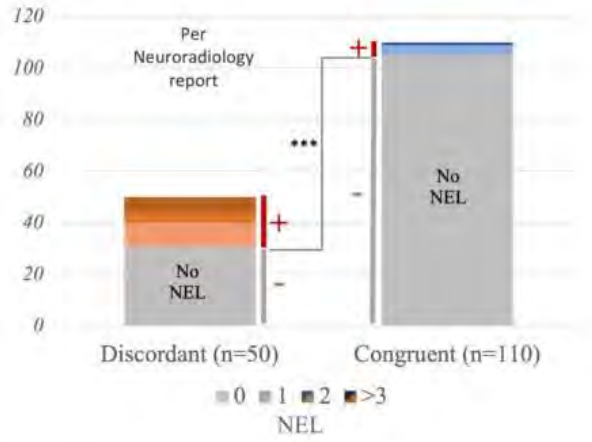

Figure 1. Variability of MSPie compared to neuroradiologist. Congruent (blue) and discordant (orange) represent number of matching and non-matching results between them, respectively. Red "+" denotes portion of positive studies with ≥ 1 detected lesion per report. Gray "-" for negative studies with 0 lesions. Patients are further grouped within each category based on number of detected lesions. "***" denotes highly significant p<0.001 chi-squared tests. **NEL**= New/ Enhancing Lesion.

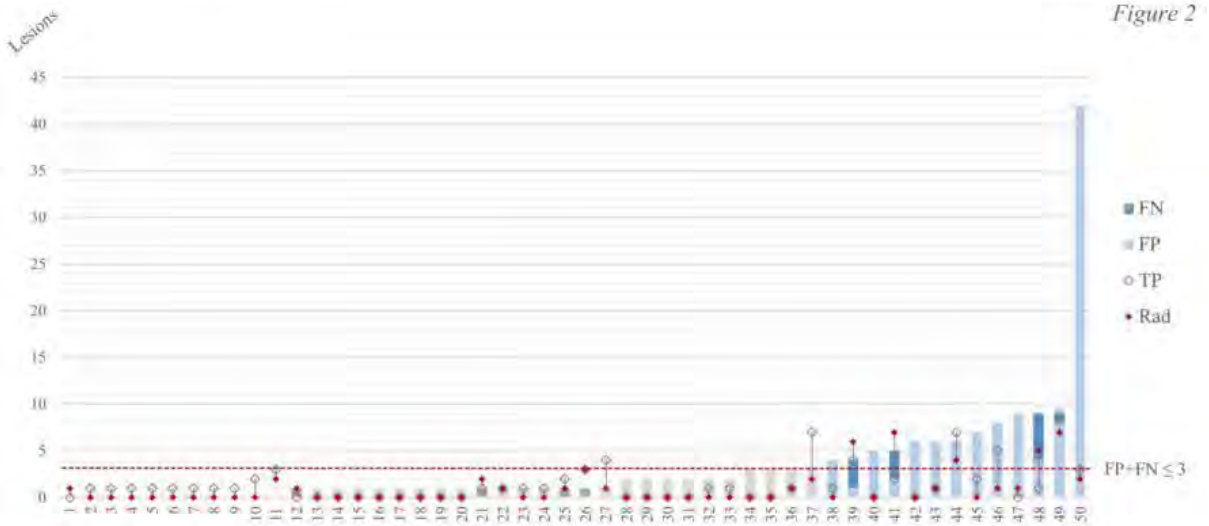

Figure 2. MSPie performance for new/enlarged T2 lesion detection for discordant studies (n=50). Blue/gray bars depict # of FP and FN lesions. Red and hollow-gray diamonds represent # of the neuroradiologist (Rad) and MSPie TP lesions, with a gray line in between for easier visualization of their difference. Criteria for high accuracy (FP+FN≤3) is depicted by the red dashed line; blue bars are studies that failed this criterion. Congruent patients are not included in this chart (n=110).

(Filename: TCT_868_ASNR2023-MSPieAbstractFigures.jpg)

904

Complications of Mechanical Thrombectomies for Large Vessel Occlusions and Ischemic Stroke: An Educational Review

M Hayat[1], T Massoud[2], N Telischak[2]
[1]Stanford University, Los Altos, CA, [2]Stanford University School of Medicine, Stanford, CA

Purpose

Judicious use of thrombolysis and endovascular mechanical thrombectomy (MT) have dramatically improved ischemic stroke treatments and outcomes. MT has been shown to improve overall patient outcome at 90 days post stroke, and DEFUSE 3 and DAWN trials have shown the safety of MT even up to 16-24 h. However, complications during and after MTs for large vessel occlusions are not insignificant. We review the incidence, risk factors, implications, as well as illustrate imaging appearances of MT complications and their management.

Materials and Methods

We provide a pictorial review of various intraprocedural and postprocedural complications of mechanical thrombectomies and their respective management relative to an organized treatment algorithm.

Results

Careful pre-procedural patient selection is essential to help avoid MT complications. These complications have been reported to occur in 11% of patients, and can be either intraprocedural or post-procedural, occurring extracranially or intracranially. Extracranial complications generally include groin hematoma, groin infection, and neurovascular injury. Vessel vasospasm and arterial dissection can occur extracranially or intracranially secondary to catheter and device manipulations. While distal embolic events are the most frequent intracranial complications, especially with greater number of device passes and terminal carotid or tandem occlusions, the

most feared complications are arterial perforations. These are also significantly associated with terminal carotid or tandem occlusions. Consequent vessel ruptures and subarachnoid extravasation of contrast medium are especially associated with poor outcomes. Hemostasis may be achieved using detachable coils or liquid glue. Early recognition of post MT complications including reperfusion hemorrhage (in 4.4% of patients, usually in the first 24 h when dual-energy CT may help distinguish true hemorrhage from iodinated contrast staining), vessel re-occlusion (in 3% of patients, usually in the first 48 h), cerebral edema (nonmalignant and malignant), and large space occupying infarcts is imperative to improve neurological outcomes.
Conclusions
Mechanical thrombectomies have dramatically improved ischemic stroke outcomes, but they are not without their complications. Awareness and early recognition of the various intra- and postprocedural complications and their subsequent management can help improve patient care and long-term outcomes.

965

Correlation between Same-Procedure Cerebral Venous Pressures and Cerebrospinal Fluid Opening Pressure in Idiopathic Intracranial Hypertension

B Ryu[1], A Bui[1], T White[2], K Shah[2], A Patsalides[2]
[1]Donald and Barbara Zucker School of Medicine at Hofstra/Northwell, Hempstead, NY, [2]Northwell Health, Manhasset, NY

Purpose
Venous sinus stenting (VSS) presents an effective treatment strategy for idiopathic intracranial hypertension (IIH) and relies on the presence of transverse venous sinus stenosis [1]. Clinical work up typically warrants venous manometry and lumbar puncture to measure opening pressure (CSF-OP). The purpose of the present study was to determine the diagnostic accuracy of venous manometry in the assessment of intracranial pressure when using CSF-OP as the gold standard [2].
Materials and Methods
A retrospective review of patients undergoing venous manometry and lumbar puncture at the same setting was done. Demographic information, CVPs (mmHg) from superior sagittal sinus (SSS), proximal and distal transverse sinus (PTS, DTS), and proximal and distal sigmoid sinus (PSS, DSS), and CSF-OP (cmH2O) were collected. The trans-stenotic gradient (TSG) was calculated as the difference in pressure between DTS and PSS. Correlation analysis was conducted using the Pearson correlation coefficient. The diagnostic accuracy of venous manometry was assessed using receiver-operating characteristic curves.
Results
CSF-OP was found to have the highest correlation with TSG (r = 0.76), in comparison to 0.60, 0.58, 0.48, 0.01, and 0.07 for SSS, PTS, DTS, PSS, and DSS, respectively. The correlations with TSG, SSS, PTS, and DTS were statistically significant, while those with PSS and DSS were not. SSS and TSG as a combined assessment maintained excellent diagnostic accuracy for IIH with an AUC of 0.95. SSS >25 and TSG >8 led to an overall sensitivity of 0.89 and specificity of 0.93 for elevated CSF-OP >20.
Conclusions
TSG combined with SSS on venous manometry is a reliable predictor of CSF-OP. The optimal parameters associated with elevated CSF-OP are SSS>25 and TSG>8. If this is found during manometry the addition of an LP may be unnecessary.

1143

Correlation Between White Matter Hyperintensity Volume and Intracranial Eccentric Vessel Wall Enhancement on High-Resolution Vessel Wall Imaging

A Honarmand[1], J Javier m Romero[2]
[1]Massachusetts General Hospital, Harvard Medical School, Boston, MA, [2]MassGH, Boston, MA

Purpose
Cerebral small vessel disease (CSVD) corresponds to variety of clinical, neuroradiological, and pathological findings. Typical neuroimaging representation of CSVD include white matter hyperintensities (WMH) (1). Recent advances in high-resolution vessel wall imaging (HR-VWI) paved the way to investigate underlying vascular contributors to CSVD more objectively (2); however, the relationship between intracranial atherosclerosis and CSVD remains to be established. This study aims to determine the association between WMH volume on FLAIR sequence as a marker of CSVD and intracranial atherosclerotic lesions representing as eccentric vessel wall enhancement on HR-VWI.
Materials and Methods
We retrospectively reviewed a single-institution database of HR-VWI. Demographic data and underlying medical risk factors, including hypertension, hyperlipidemia, and diabetes, were obtained. HR-VWI studies (with spatial resolution of 0.6 x 0.6 x 0.6 mm) were evaluated to detect the eccentric vessel wall enhancement. Patients with WMH due to other etiologies including CNS vasculitis, CNS infection, and neoplastic lesions causing WMH were excluded. Subsequently, patients were divided into a control group (without eccentric vessel wall enhancement) and a test group (with eccentric vessel wall enhancement involving at least one vascular segment of the circle of Willis). WMH volume measurement was performed using an automated segmentation program on FLAIR images using an image processing framework. Finally, statistical analysis was performed appropriately. A P-value of <0.05 was considered statistically significant.
Results
Seventy-five cases were enrolled including 38 cases in the control group, and 37 cases in the test group. Both groups were matched in gender and underlying medical comorbidities, including hyperlipidemia, hypertension, and diabetes (P>0.05). however, patients in the

control group were significantly younger compared to test group (mean age: 56.9 vs. 66.1, P= 0.02). The WMH volume in the test group was significantly higher than the control group (median volume: 9685.4 mm3 vs. 363.1 mm3, P=0.01).
Conclusions
White matter hyperintense volume was significantly higher in patients with intracranial atherosclerotic lesions representing as eccentric vessel wall enhancement compared to control group without enhancement independent of underlying comorbidities. This finding may indicate an imaging biomarker to for estimation of CSVD.

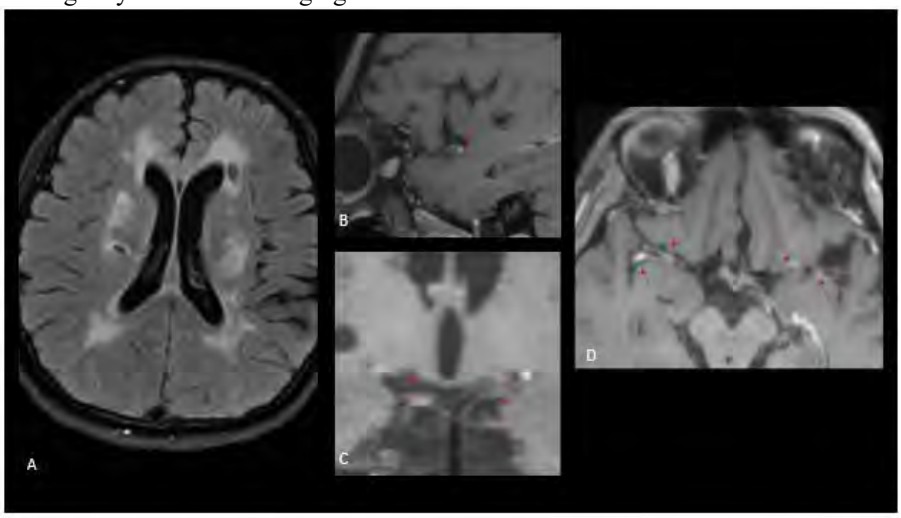

Representative case with WMH volume of 36137.2 mm^3 (A) and intracranial eccentric vessel wall enhancement in multiple vascular segments of circle of Willis including proximal right MCA (B), bilateral PCAs (C) and multifocal bilateral MCAs (D).

(Filename: TCT_1143_ASNRVWI.jpg)

1333
Correlation of Quantified Aneurysm Wall Enhancement MR-VWI with ELPASS Score for Evaluation of Unruptured Intracranial Aneurysms.
A Patel[1], S Faruqui[1], R Abdalla[1], A Malik[1], C Zhou[1], J Moore[1], B Jahromi[1], M Potts[2], A Shaibani[1], V Rayz[3], M Markl[4], T Carroll[5], D Cantrell[1], S Ansari[1]
[1]Northwestern University, Chicago, IL, [2]Northwestern University - Feinberg School of medicine, Chicago, IL, [3]Purdue University, West Lafayette, IN, [4]Northwestern University McCormick School of Engineering, Chicago, IL, [5]University of Chicago, Chicago, IL

Purpose
The incidence of Intracranial Aneurysms (IAs) is estimated to be between 3% and 5% globally. While the rupture rate remains low at approximately 3-50/100000, mortality and morbidity remain high in these patients.1 Risk stratification scores such as PHASES, UIATS and ELPASS are used to guide clinical decision-making in patients with IAs. MR-Vessel Wall Imaging (VWI) has gained traction in evaluation of neurovascular pathologies, including IAs recently. Typically, qualitative evaluation of aneurysm wall enhancement (AWE) is used as a marker of wall instability.2 We investigate the potential of quantitative assessment of AWE in conjunction with the ELAPSS score as a marker of wall instability.
Materials and Methods
We conducted an IRB approved study of patients with multiple IAs scanned using VWI protocol between January 2018 to June 2022 at an academic hospital. AWE was evaluated qualitatively on T1-SPACE sequences. DSA or CTA studies were used to evaluate the IA Wall Morphology (IAWM). Furthermore, AWE was evaluated quantitatively using Aneurysm Wall to Pituitary Infundibulum ratio (AWPI ratio) obtained using a mean of 3-point ROIs on the aneurysm wall and a 2mm circular ROI on the PI. IAs were grouped into small (<3.9mm), medium (4-7mm) and large (>7.1mm) sizes. IAs were also grouped into three subgroups of ELAPSS scores 0-13, 14-26, 27-40. Pearson correlation test, unpaired t-test and ANOVA were used to assess statistical correlations with AW-PI ratio, ELAPSS scores, AWM and other variables in SPSS v28.
Results
We evaluated 126 IAs in 56 patients (Age: 63.37 +/- 13.11, 27-88, 42 female). The mean size of IAs was 5.15mm +/- 4.34 mm, 2-30 and the mean ELAPSS score was 15.42 +- 8.43, 4-35. Qualitatively, AWE was seen in 62 (49.2%) IAs and irregular IAWM in 44 (52.3%) out of 126 IAs. The AWPI ratios of IAs with and without irregular AWM were 0.584 and 0.755, ($p<0.0001$).AWPI ratios in IAs of sizes small(n=62), medium(n=43) and large(n=21) were 0.559, 0.660 and 0.864 ($p < 0.001$).. ELAPSS score showed a moderately strong correlation to AW-PI ratio, r = 0.492, 95% CI (0.3432, 0.6114). IAs in ELAPSS groups 0-13 (n=72), 14-26(n=39) and 27-40(n=15), showed mean AWPI ratios of 0.573, 0.679 and 0.895($p<0.001$). The mean ELAPSS score for IAs with AWE was 19.82 and 11.02 in IAs without AWE. ($p<0.0001$)

Conclusions

Our findings demonstrates a correlation between increased AWPI and higher ELAPSS score, suggesting possible use of both approaches for patient management and aneurysm growth risk stratification.

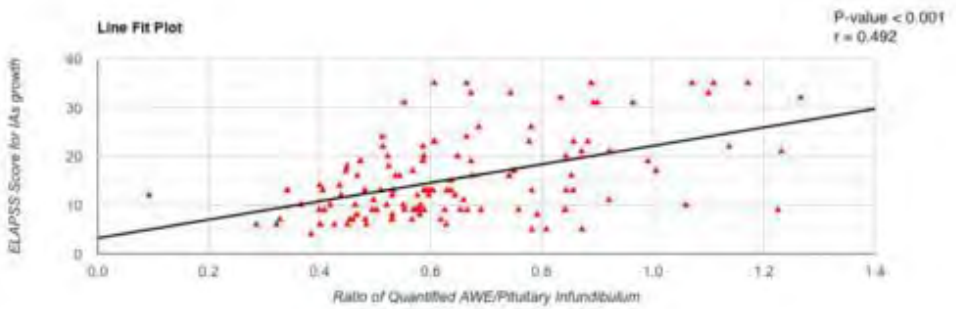

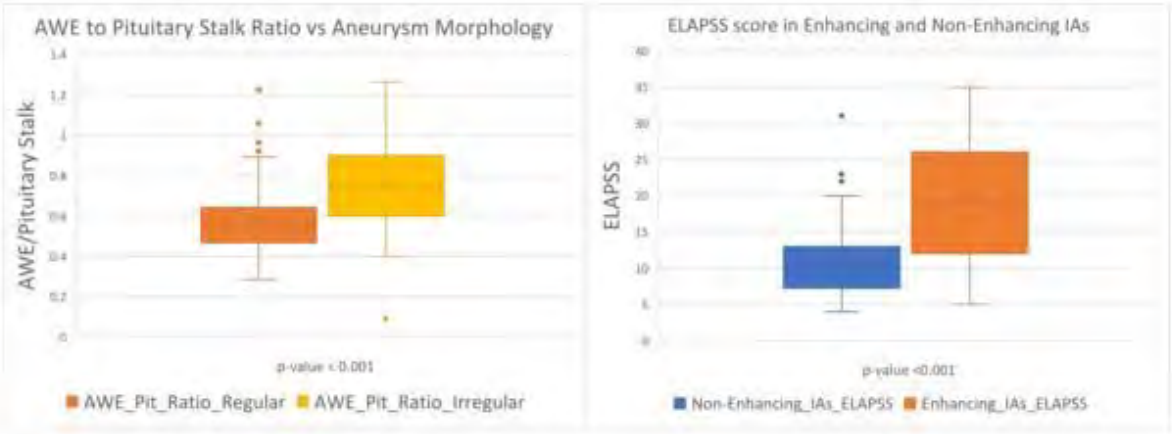

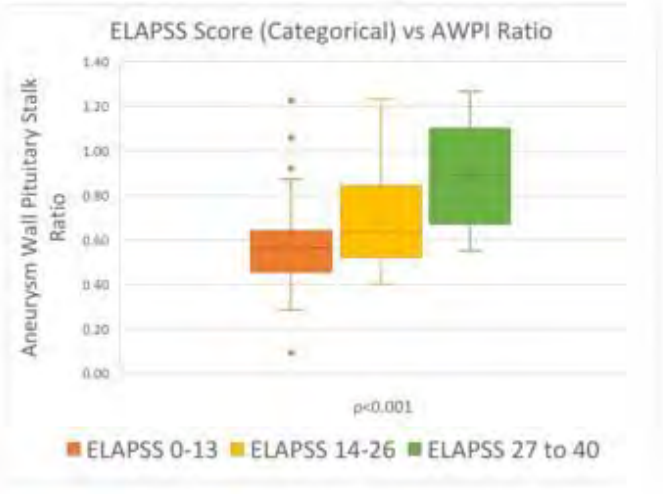

(Filename: TCT_1333_ASNR1.jpg)

872

Creating a Top Gun Approach to Radiology Education - Stroke Imaging

L Penn[1], J Yu[1], T Kennedy[2]

[1]University of Wisconsin School of Medicine and Public Health, Madison, WI, [2]The University of Wisconsin, Middleton, WI

Purpose

Strokes are common and place a significant burden, both physically and financially, on individuals and health care systems in the United States. An essential component of acute stroke management is stroke code CT examination and accurate interpretation by the on-call radiologist or radiology resident. In other areas of radiology, such as breast imaging, large volume practice databases have been shown to increase radiology resident diagnostic accuracy; however, no such database currently exists for stroke code CT scans.[1,2]

Materials and Methods

We analyzed 3,162 consecutive code stroke examinations from UW Health, an academic level I trauma center, over a 4.25-year period (March 2017 – May 2021). A key piece of this analysis was recording Alberta Stroke Program Early CT Scan (ASPECT) scores reported by the neuroradiologist at the time of examination. We then manually reviewed the corresponding patient electronic health records to gather characteristics (age, sex, self-reported ethnicity, and risk factors of stroke [hypertension, diabetes, smoking, etc.]), indication for imaging including the NIH stroke scale (NIHSS) score, hospital course including other further imaging (MRI) or treatment (IV tPA or mechanical thrombectomy), and final diagnosis/ disposition following imaging.

Results

Within the 3,162 studies, we identified 705 studies concerning for acute ischemic stroke, 146 intracranial hemorrhages, 368 large vessel occlusions, and 293 non-stroke neurologic pathology diagnoses. Of the patients with studies concerning for acute ischemic stroke and large vessel occlusions, 364 went on to receive IV tPA and 371 went on to undergo mechanical thrombectomy. There was additionally a broad range of both NIHSS and ASPECT scores across the studies.

Conclusions

Currently, we have compiled a large and diverse cohort of stroke code CT examinations and have created a training database for learners. With this comprehensive data set, we are additionally afforded the opportunity to explore other research avenues related to stroke code imaging, such as how artificial intelligence impacts stroke code CT examination and how treatment outcomes differ based on ASPECT scores and site of large vessel occlusion.

1069

Deep Learning Algorithm For Detection of Cervical Spine Fracture: Failure Mode Analysis:

D Shakoor[1], A Malhotra[2]

[1]Yale University, New Haven, CT, [2]Yale University School of Medicine, New Canaan, CT

Purpose

Artificial intelligence (AI) algorithms have been developed to assist radiologists manage high clinical volumes while maintaining diagnostic accuracy. While AI algorithms has shown promising results for detection of fracture in extremities, poor diagnostic performance of AI algorithms particularly with high rate of false positive cases has been reported for cervical spine fracture. The purpose of this study is to assess the performance of AI system implemented in our institution, Aidoc, for the detection of cervical spinal fracture.

Materials and Methods

Over a three-month period, consecutive cervical spine CT studies which were performed in our institution were reviewed. For the purpose of this study, only positive studies which were flagged by our AI algorithm AiDoc were selected. The demographic information of patients were extracted. The final reports of these studies were reviewed to determine the final status of the fracture. The images were again reviewed by a PGY-3 radiology resident to confirm the results and identify the etiologies for the false positive results. The findings were also reviewed and confirmed by the neuroradiology attending.

Results

377 cervical spine CTs were flagged positive by Aidoc and reviewed. Among them, 251 (66.6%) studies were true positive and 126 (33.4%) were false positive. The positive predictive value was 66.5%. Of all cases, 57 (15%) had IV contrast and 42 (11.2) scans had metal hardware. Among the false positive cases, 29 (23%) and 28 (22%) cases were due to degenerative facet disease and pannus formation of C1 (figure 1). Mean age of false positive cases was not statistically significantly different than true positive cases (67.25 (95% CI: 64.8, 69,7) vs 69.2 (95%CI: 65.9, 72.3), P-value=0.3). The odds of false positive cases were not higher among cases with IV contrast (odds ratio: 0.45, (P-value:0.1) or hardware (odds ratio:0.013, P-value:0.9)

Conclusions

Approximately one third of cervical spine CTs were falsely detected positive which limits AI accuracy and its generalizability. Given the concerns over the generalizability of this algorithm, rigorous studies are required to address its weaknesses before its widespread adaptation.

978

Deep Learning for Model-free Prediction of Perfusion Maps

S Gai[1], S Talebi[1], E Tong[2], A Sossin[3]

[1]University of California, Berkeley, Berkeley, CA, [2]Stanford University, Stanford, CA, [3]Stanford University, New York City, NY

Purpose

Dynamic susceptibility contrast MR perfusion (DSC-MRP) is a non-invasive method that assesses the passage of blood through the brain parenchyma by using an exogenous contrast agent. Perfusion parameters, such as cerebral blood volume (CBV), cerebral blood flow (CBF), and time-to-max (TMAX), derived from DSC-MRP, are used in the assessment of cerebrovascular disease and CNS pathologies. Many commercial software are available to compute the perfusion parametric maps. We developed a deep learning model to generate these perfusion maps from the DSC-MRP dataset.

Materials and Methods

Our models are based on a modified U-net architecture trained with 126 subjects, validated with 5 subjects, tested in 10 subjects. We compared the predicted CBF and TMAX perfusion maps with the ground truth maps generated by a commercial software.

Results

Qualitatively, the Tmax, CBV, CBF maps predicted by our models are comparable with the ground truth. The mean MAE for the predicted Tmax Maps were 0.29s (2.41% error). The mean MAE for the predicted CBF Maps were 1.91 mL/100g/min (2.38% error). Attached figure shows patient presented with left sided weakness, NIHSS 20, found to have an acute infarct from right middle cerebral artery occlusion, which affected the right frontotemporal regions. (A) Predicted Tmax map generated from a commercial software and (B) Tmax map predicted by the DL model. The areas with Tmax > 6s as predicted by the DL model is comparable to the ground truth. (C) Predicted CBF map generated from a commercial software and (D) CBF map predicted by the DL model. The areas with reduced CBF as predicted by the DL model is comparable to the ground truth.

Conclusions

DL-based method may act as an accurate and dependable alternative for generating perfusion parametric maps from DSC-MRP.

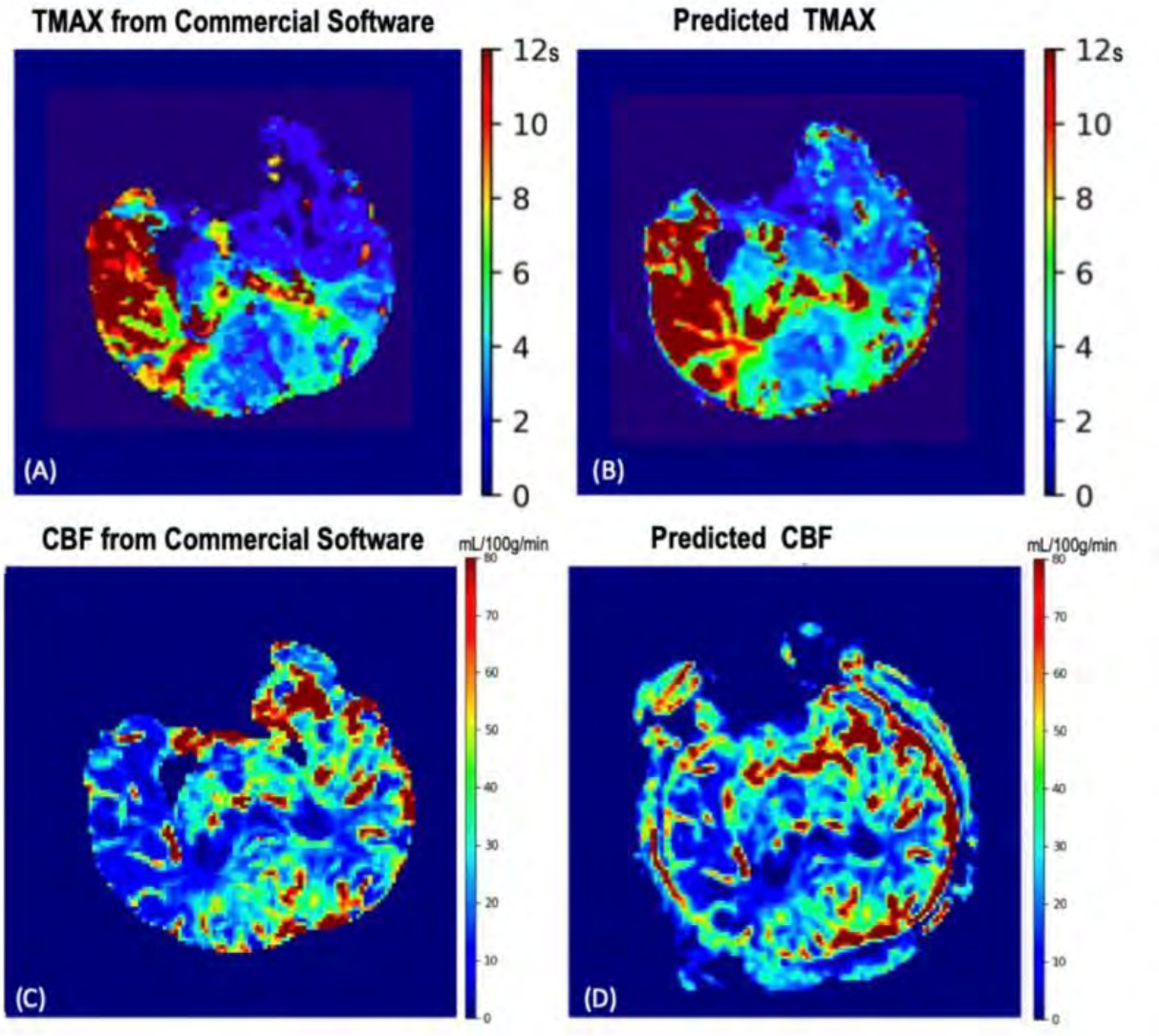

(Filename: TCT_978_ASNR_MRP.jpg)

246

Determining Foramen Magnum Crowdedness and Dimensions of Chiari I Patients Compared to Controls

L Eisenberg[1], A Eisenberg[2], K Arnautovic[1]
[1]Semmes-Murphey Clinic, Memphis, TN, [2]Mid-South Imaging and Therapeutics, Memphis, TN

Purpose

The study of foramen magnum (FM) structure and contents in patients with Chiari malformation type I (CMI) has been incomplete. Since this condition may be asymptomatic or produce disabling symptoms leading to surgical intervention, identification of objective differences in the FM of these patients may be helpful.

Materials and Methods

97 CMI patients and 30 Control patients had MRI exams and clinical records available for analysis. This population was evaluated for FM linear dimensions, area, crowdedness (%FM taken up by neural tissue), clinical symptomatology, ectopia length, and the performance of surgery. The statistical tests used on these data were Pearson correlation and Welch's t-tests.

Results

There is a correlation between symptomatology, crowdedness, and tonsil ectopia length with surgical treatment. There is a statistically significant difference between the CMI and Control groups' longest CSF segment and CNS delineation at the FM and crowdedness. A difference in the FM dimensions between female CMI patients and female Controls was found, but not for males. The control group, but not the CMI patients demonstrated a gender difference in FM area.

Conclusions

The presence of symptoms, tonsil ectopia length, and FM crowdedness can be used to help determine the need for cranial cervical decompression surgery. There is a difference in CSF space in the FMs of CMI patients and Controls. Differences in FM dimensions between Control and CMI groups only exists for females.

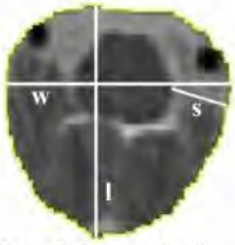

Figure 3| Representation of how the dimensions of the FM were measured. Width: w; length: l; longest CSF segment: s.

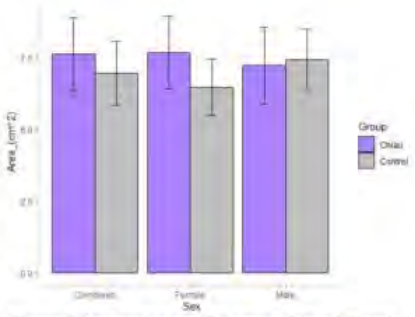

Figure 5| Comparing the FM areas of the CMI and Control patients. Averages for the different sexes were: 7.7±1.3cm (F CMI), 6.5±1.0cm (F Control), 7.2±1.3cm (M CMI), 7.4±1.1cm (M Control).

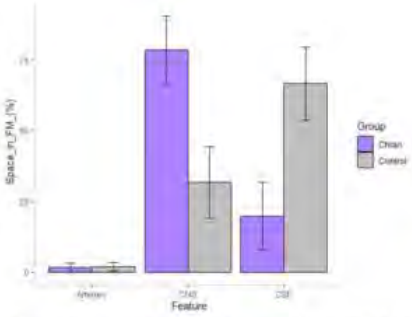

Figure 6| Comparing the region percentage of Chiari I and Control patients.

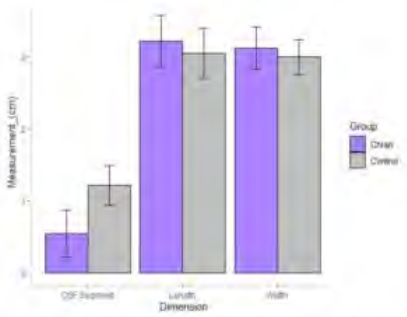

Figure 7| Comparing the FM dimensions of the Chiari I and Control patients.

(Filename: TCT_246_GraphicforFMAbstractASNRSubmission.jpg)

548

Diagnosis and Localization of Discitis Osteomyelitis Using a Deep Learning Approach and Gradient Class Activation Map (GradCAM) Localization

D Warren[1], A Mian[1], J Shimony[1], W Wang[1]
[1]Washington University School of Medicine, St. Louis, MO

Purpose

Discitis osteomyelitis has a mortality ranging from 5-34% and delayed diagnosis more than triples the rate of persistent motor weakness to 45% (1,2). Early detection of discitis osteomyelitis may lead to better outcomes. This study intends to develop a deep learning algorithm to detect discitis osteomyelitis in MRI imaging and aid the radiologist by highlighting areas needing closer review.

Materials and Methods

MRI lumbar spine imaging studies were retrospectively selected from a health system consisting of 12 midwestern academic and community hospitals to train and evaluate a deep learning network for discitis osteomyelitis detection. Keras TensorFlow Python

package was used to train VGG-16, ResNet, Inception version 3, Inception-ResNet, and DenseNet architectures using transfer learning and a grid search method to optimize hyperparameters. The trained networks were evaluated on sensitivity, positive predictive value, and F1 score. The three highest-performing networks were combined in an ensemble method to create final predictions. The final trained model with the largest final convolution layer dimensions was used to generate a gradient class activation map (GradCAM) to aid in the localization and interpretability of detected abnormalities.
Results
The deep network was able to achieve a sensitivity of 0.96, a positive predictive value of 0.90, and an F1 score of 0.93 on clinical MRIs of lumbar spines. Generated GradCAM overlays confirmed that the network was using relevant portions of the image to categorize the images.
Conclusions
This research demonstrated that a deep learning network was effective for the detection of discitis osteomyelitis in lumbar spine MRIs and GradCAM method was an effective method to indicate areas needing additional radiologist review.

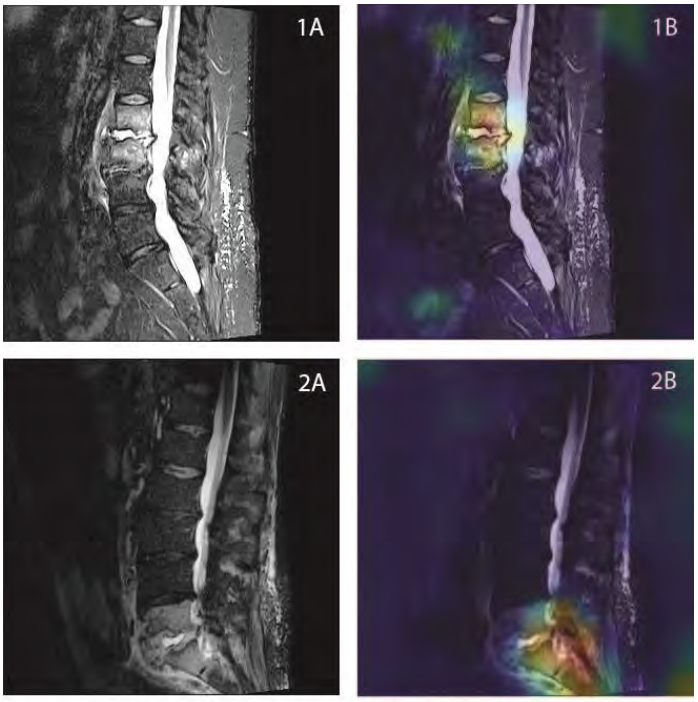

Figure 1: Left column demonstrates the original lumbar spine MRI STIR images and the right column demonstrating gradCAM overlay indicating identified discitis osteomyelitis.

(Filename: TCT_548_Gradcamfigure.jpg)

1474

Diagnostic Performance of Ultra-low Field Portable MRI in Acute Stroke – A Preliminary Study

R Gallagher[1], D Boulter[2]
[1]The Ohio State University, Columbus, OH, [2]The Ohio State University Wexner Medical Center, Columbus, OH

Purpose
To evaluate the diagnostic performance the Hyperfine Swoop Portable 0.064T MRI in patients presenting with acute stroke symptoms, compared to reference standard high field 1.5T or 3T MRI.
Materials and Methods
We performed portable point-of-care 0.064T MRI with DWI and FLAIR in 10 patients who presented with acute stroke symptoms between December 2021 and April 2022. All patients also received a conventional high field 1.5T or 3T MRI with DWI and FLAIR within 48 hours. Image diagnostic quality was assessed for all exams. Prospective clinical interpretations were compared.
Results
The portable 0.064T MRI DWI images were poorly diagnostic in the majority of cases due to severe artifacts and low signal to noise ratio. Multiple acute infarcts were not clearly visible on the portable MRI prospectively. Intracranial hemorrhage was also not well assessed prospectively.
Conclusions
Portable 0.064T MRI has poor diagnostic performance in acute stroke compared to reference standard high field MRI.

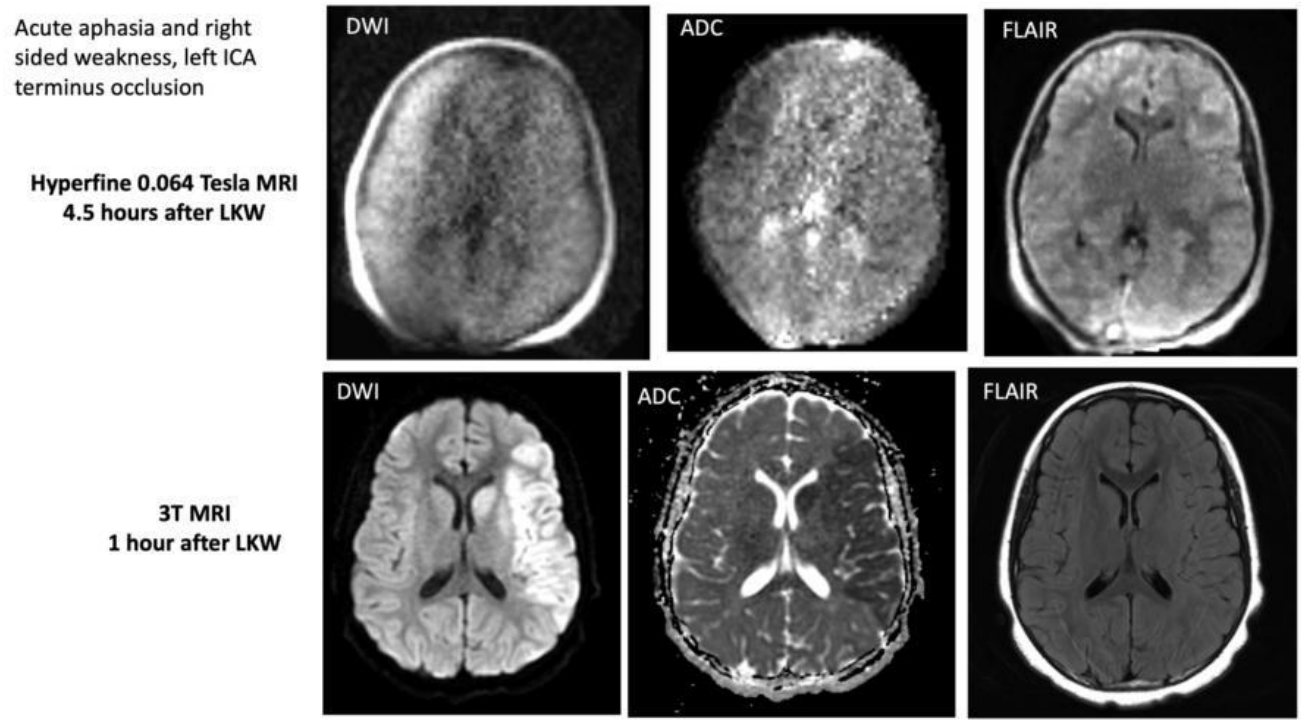

(Filename: TCT_1474_Hyperfinecases.jpg)

1211

Differential Assessment of Internal Jugular Vein Stenosis in Patients Undergoing CT and MRI with Contrast

M Miller[1], H Dabbara[1], B Setty[2], T Nguyen[2], O Sakai[2], M Abdalkader[2]

[1]Boston University School of Medicine, Boston, MA, [2]Boston Medical Center, Boston, MA

Purpose

Internal Jugular Vein Stenosis (IJVS) is hypothesized to play a role in the pathogenesis of diverse neurological diseases [1-3] and must also be considered in patients undergoing neurointerventional venography or therapy. In this context, cross-sectional imaging using CT or MRI with contrast plays an important role in assessing IJVS during diagnosis and treatment planning. Herein, we document differences in IJVS between these two modalities in a retrospective patient cohort.

Materials and Methods

From January 2022 to September 2022, we included 35 patients who underwent consecutive MRI with contrast and CT with contrast of the head and neck. Patients were included if they had normal T1-weighted MRI of the brain and normal CT venogram or angiogram of the head and neck. MRI and CT examinations were evaluated by two board-certified radiologists. The maximal stenosis on both the right and left sides was selected on sagittal images and measured in corresponding axial sections. For all internal jugular veins, the degree of IJVS was categorized into four groups: 0 to 24%, 25% to 49%, 50% to 74%, or 75% to 99%.

Results

Among 35 patients undergoing both CT and MRI with contrast, 15 (42.9%) had a visible degree of IJVS on at least one side. McNemar-Bowker testing of categorical stenosis groups across all internal jugular veins (n=70) demonstrated discordance in apparent IJVS distributions measured by CT and MRI, respectively ($p<0.001$). Among those with visually-apparent IJVS, we also compared continuous stenosis measurements between modalities, finding mean IJVS of 50.4% (std. deviation=29.1%) on CT versus 85.8% (std. deviation=15.6%) on MRI. MRI measurements of IJVS were significantly greater than paired CT measurements per Wilcoxon Rank Sum testing ($p < 0.001$).

Conclusions

MRI with contrast may overestimate the degree of IJVS compared to CT with contrast. This discrepancy between neuroimaging modalities should be considered in diagnosis and treatment planning for neurointerventions.

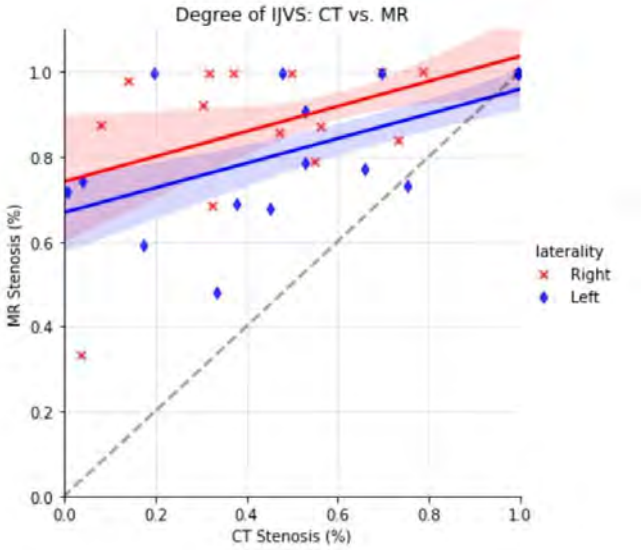

(Filename: TCT_1211_ScreenShot2022-11-15at63626AM.jpg)

426

Drug-Coated Balloon Versus Conventional Balloon Angioplasty for the Treatment of Symptomatic Intracranial Atherosclerotic Stenosis

Y He[1], Y Tang[2], W Liu[3], Q Ding[1], T Li[4]

[1]Zhengzhou University People's Hospital, Zhengzhou City, Henan Province, [2]Zhengzhou University People's Hospital, Zhengzhou, Henan, [3]河南省人民医院, Zhengzhou, Henan, [4]Henan Provincial People's Hospital, Zhengzhou, Henan

Purpose

To compare the safety and efficacy of DCB with conventional balloon angioplasty for the treatment of symptomatic ICAS.

Materials and Methods

A prospective, non-randomized, single-center cohort study of 66 patients with symptomatic ICAS treated with DCB or conventional balloon was performed at a tertiary stroke center from 2019 to 2021. The periprocedural events and long-term outcomes were reported.

Results

Twenty-three patients (36.5%) received DCB. Technical success (＜50% residual stenosis) was achieved in all cases (100%) with the DCB group and 42 cases (97.7%) with the conventional balloon group. Median clinical follow-up was 6 months. No differences were found in the clinical baseline characteristics. The rates of stroke and mortality in the perioperative (4.3% [1/23] vs 4.7% [2/43], P=1), recurrent ischemic events (4.3% [1/23] vs 7.0% [3/43], P=1) were not statistically significant between the two groups. The restenosis incidence (4.3% [1/23] vs 25.6% [11/43], p=0.446) in the DCB group was significantly lower than that in the conventional balloon group.

Conclusions

In this study, DCB was feasible and safe in the treatment of symptomatic ICAS. Compared with conventional balloon angioplasty, DCB dilation can effectively lower restenosis risk. Further studies will be needed to definitively elucidate the role of DCB in the management of symptomatic ICAS.

1155

Dual-energy computed tomography material decomposition improves the accuracy of predicting hematoma expansion in traumatic intracranial hemorrhage

J LEE[1], S Park[2], J Kim[3]

[1]SOONCHUNGHYANG UNIV HOSPITAL, BUCHUN, Gyeonggi-do, [2]Soonchunhyang University Seoul Hospital, Seoul, Seoul, [3]CHA Bundang Medical Center, Seongnam, CA

Purpose

This study aimed to evaluate the diagnostic performance of predicting hematoma expansion using dual energy computed tomography (DECT) angiographic spot sign (AS) in traumatic intracranial hemorrhage.

Materials and Methods

We recruited participants with intracranial hemorrhage confirmed via computed tomography (CT) angiography for suspected traumatic cerebrovascular injury. We evaluated AS on both conventional-like and fusion images of DECT. AS was grouped into three: intralesional enhancement without change (NC), delayed enhancement (DE), and growing contrast leakage (GL). Hematoma expansion was evaluated by measuring hematoma size on DECT and a follow-up CT. Logistic regression analysis evaluated whether

the AS on the fusion image was a significant risk factor for hematoma expansion. Diagnostic accuracy was calculated, and results from conventional-like and fusion images were compared.
Results
Thirty-nine hematomas in 24 patients were included in the study. Of these, 18 hematomas in 13 patients showed expansion on follow-up CT. Among the expanders, AS and GL on fusion images were noted in 13 and 5 hematomas, respectively. In non-expanders, 10 and 1 hematoma showed AS and GL, respectively. In the logistic regression model, GL on the fusion image was a significant independent risk factor for predicting hematoma expansion. However, when AS on conventional-like images was used, no factors significantly predicted hematoma expansion. In the receiver operating characteristic (ROC) curve analysis, the AUC of AS on the fusion images was calculated as 0.71, with a sensitivity and specificity of 66.7% and 76.2%, respectively.
Conclusions
GL on the fusion images of DECT in traumatic intracranial hemorrhage is a significant independent radiologic risk factor for predicting hematoma expansion. AS of the DECT fusion images has improved sensitivity than that of the conventional-like images.

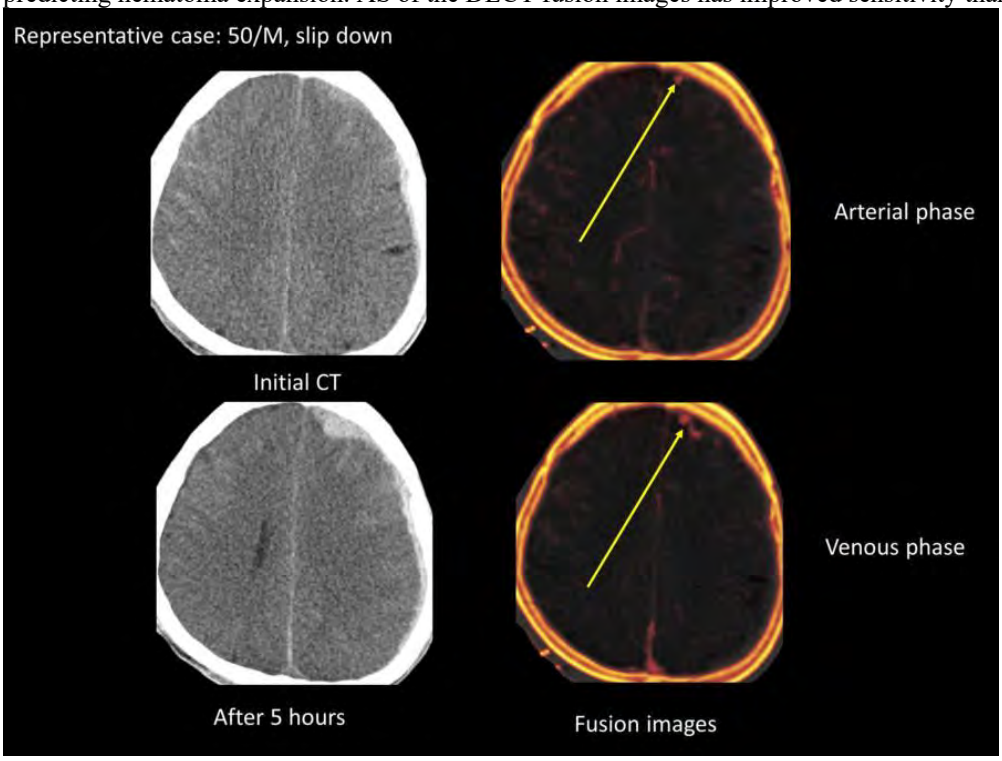

(Filename: TCT_1155_SE-2022-0466_JungbinLee.jpg)

181
DWI DETECTED ISCHEMIC LESIONS FOLLOWING ENDOVASCULAR TREATMENT: SYSTEMATIC REVIEW AND META-ANALYSIS
A Habtezghi[1], D Kallmes[1], S Ghozy[1], C Bilgin[1]
[1]*Mayo Clinic, Rochester, MN*

Purpose
Diffusion-Weighted Imaging(DWI)-detected Ischemic lesions are some of the non avoidable complications of endovascular procedures for intracranial aneurysms. We present an updated systematic review and meta-analysis to identify the occurrence of DWI-detected lesions following endovascular procedures for intracranial aneurysms.
Materials and Methods
A systematic literature search of PubMed, web of science, Embase, and Scopus between 2000 to June 2022 of post-endovascular procedures for intracranial aneurysms studies were done. Nested-knowledge software was used to screen and extract the studies. The principal outcome was DWI detected lesions within five days of the procedures, and associated risk factors such as type of procedure, patient demographics, and aneurysm characteristics were sought. We calculated the pooled incidence rates with the 95% confidence intervals (95% CI). The random model was used to pool the data due to the heterogeneity among the included studies. Heterogeneity was assessed using Q statistics and the I2 test, where P-value < 0.05 or I2> 50% were considered significant 8.Publication bias was investigated using Egger's regression test 9, 10. All data were analyzed using R software version 4.2.0. and the "meta" package.
Results
Twenty eight Studies with 2488 patients were included. The overall incidence of DWI lesions was 47.4%(95% CI= 39.7-56.6). The highest rate of lesions were seen with flow diversion at 62.4% (95% CI= 48.4-80.5), complex procedures 57.86% (95% CI= 34.3-97.7), stent-assisted coiling with 49.1 (95% CI= 35.0-68.7), simple coiling at 47.3% (95% CI= 35.5-63.7), followed by balloon-assisted coiling 33.12% (95% CI= 22.77-48.18). The differences among different techniques were not statistically significant; however, there was significant heterogeneity and a significant risk of publication bias.

Conclusions
Many patients who undergo endovascular procedures for intracranial aneurysms present with new post-procedural DWI detected ischemic lesions regardless of the endovascular procedure used. Using flow diversion has the highest risk of DWI-detected infarcts. As our metanalysis had a high risk of bias due to the heterogeneity of studies included, further studies are needed to investigate these early outcomes and the long-term outcomes of such small infarcts.

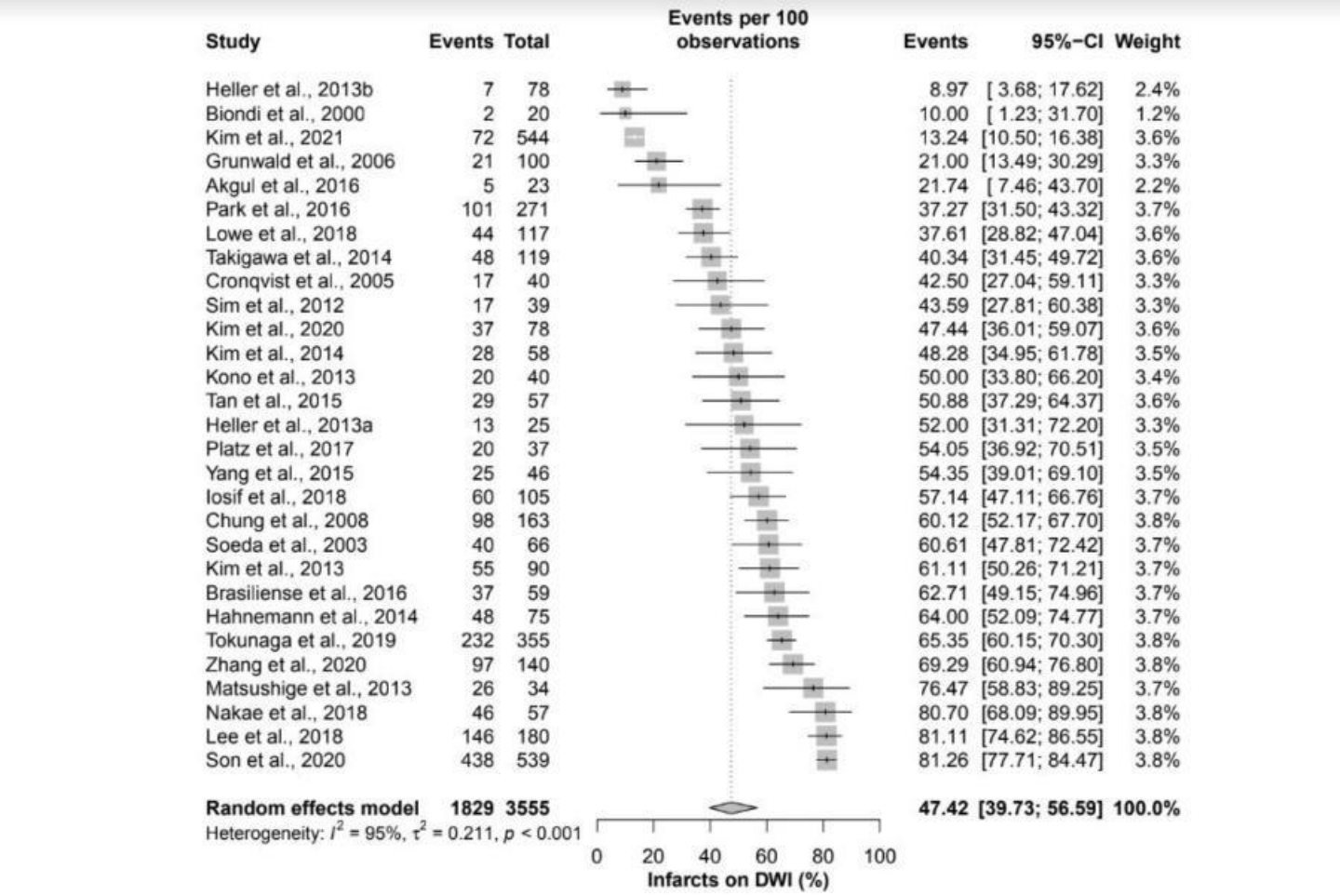

(Filename: TCT_181_overalldwi.JPG)

1466

Early vs Delayed Change in Aneurysm Wall Enhancement and Intracranial Structures on High Resolution MR Vessel Wall Imaging.

A Patel[1], R Abdalla[1], C Zhou[1], S Faruqui[1], J Moore[1], M Potts[2], B Jahromi[1], V Rayz[3], M Markl[4], T Carroll[5], D Cantrell[1], S Ansari[1]
[1]Northwestern University, Chicago, IL, [2]Northwestern University - Feinberg School of medicine, Chicago, IL, [3]Purdue University, West Lafayette, IN, [4]Northwestern University McCormick School of Engineering, Chicago, IL, [5]University of Chicago, Chicago, IL

Purpose
Vessel Wall Imaging is increasingly utilized in evaluation of neurovascular pathologies such as Intracranial Aneurysms (IAs), Intracranial Atherosclerotic Disease (ICAD), Vasculitis, Dissections, and Moyamoya, which resulted in a significant heterogeneity in equipment, protocols, and technique.1 The optimum time for acquiring post-contrast sequence has not been standardized and varies depending on contrast biodistribution across cranial structures. We aim to study contrast distribution in IA walls compared to intracranial tissues at early (5-15 min) and delayed (20-30 min) post-contrast scans.
Materials and Methods
An IRB approved study for evaluation of aneurysms using pre-contrast, early post-contrast (5-15 min), and delayed post-contrast (20-30 min) T1-SPACE sequences was conducted. ROIs of standardized diameter (2mm) were used to measure the signal intensities (SI) of the Cavernous Sinus (CS), Temporalis (TM), Pituitary Infundibulum (PI), and Choroid Plexus (CP). Point ROIs were used for IA Wall. These SIs were normalized with white matter SI obtained using ROIs of 10mm diameter. Measurements were acquired in pre-contrast, early post-contrast, and delayed post-contrast T1-SPACE sequences for each patient. Means were compared using one-way repeated ANOVA in SPSS v28.
Results
40 IAs in 42 patients were analyzed. IAs and reference structures demonstrated a statistically significant increase in SI from pre-contrast scans to both early and delayed post-contrast scans on T1-SPACE sequence. While IAs demonstrated a 9.61% increase in

signal intensity on delayed vs early post-contrast scans, (p<0.001), the PI and CS showed a 9.56% and -7.74% decrease in SI (p<0.001). However, SI intensity of IAs remained lower than CS and PI even on delayed imaging at 20-30 mins. IAs smaller than 5mm in size showed an increase of 8.96% (p=0.048) on early to delayed post-contrast sequences whereas IAs larger than 5mm increased in SI by 10.1% (p<0.001).

Conclusions

The relative increase in contrast uptake on the delayed compared to the early post contrast scans likely reflects increased contrast permeability over time. This poses the question of whether intense contrast enhancement should only be considered a sign of instability on early post contrast images as this may reflect increased permeability secondary to ongoing inflammation rather than cumulative contrast deposition in aneurysm's wall.

Location	Pre	Early (5-15 mins)	Delayed (20-30 mins)	Early to delayed	Early to delayed percent change	P-value
Cavernous Sinus n = 41	**0.819**	**1.874**	**1.729**	**-0.145**	**-7.74%**	**<0.001**
Pituitary infundibulum n = 40	**0.987**	**1.925**	**1.741**	**-0.184**	**-9.56%**	**<0.001**
Temporalis Muscle n=42	0.531	0.785	0.765	-0.020	-2.55%	0.833
Choroid Plexus n=42	0.788	1.520	1.474	-0.047	-3.02%	0.383
Aneurysms n = 40	**0.844**	**1.218**	**1.335**	**0.117**	**+9.61%**	**<0.001**
Aneurysms >5 mm n = 21	**0.837**	**1.279**	**1.408**	**0.130**	**10.1%**	**0.001**
Aneurysms <5 mm n = 19	**0.853**	**1.150**	**1.253**	**0.103**	**8.96%**	**0.048**

Total number of patients = 42
Patients with aneurysms = 33 (40 aneurysms)

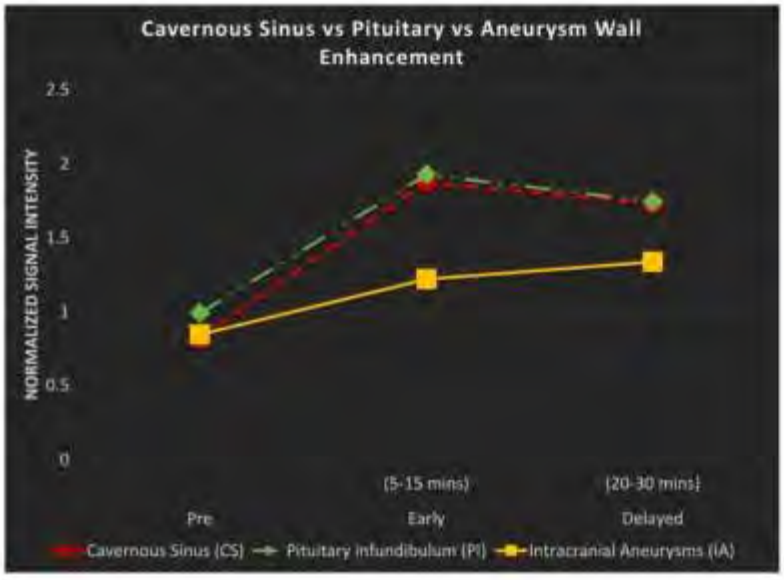

(Filename: TCT_1466_EarlyvDelayed.jpg)

971

Effect of reduced contrast bolus volume on head and neck CTA study quality during the global iodinated contrast shortage

K Cardenas[1], S Armstrong[1], K Hiatt[1], P Bunch[1], J Sachs[1], M Zapadka[1], C Lack[1]
[1]*Wake Forest School of Medicine, Winston-Salem, NC*

Purpose

The recent global iodinated contrast media shortage forced difficult decisions about rationing of contrast-enhanced studies and contrast media doses (1). In our health system, a dose reduction was recommended for many studies. To evaluate the potential effects of dose reduction on head and neck CT angiography (CTA) study quality, we evaluated CTAs performed prior to and during the shortage.

Materials and Methods

We reviewed 100 sequential head and neck CTA studies from March 2022 (i.e, before the shortage) and 100 studies from June 2022 (i.e., during the shortage). 18 studies were excluded due to missing patient body mass index (BMI) or contrast media dose, leaving 93

"pre" and 89 "during" studies. Demographics, route and dose of contrast media administered, and mean Hounsfield unit (HU) measurements in the cervical internal carotid arteries (ICAs), internal jugular veins (IJs), internal carotid termini, basilar artery, and sigmoid sinuses were recorded. The largest mean HU values of the cervical ICAs, IJs, intracranial arteries, and sigmoid sinuses from each study were used for analysis. Previously derived measures of CTA study adequacy, established by an internal quality improvement project, were applied to classify studies as "good" (maximum intracranial arterial attenuation > 242.25 HU AND artery to sigmoid sinus difference of > 10.75 HU) or "poor" in quality (not meeting criteria for "good"). Student t-tests were used to compare means, with statistical significance defined as $p < 0.05$.
Results
Comparing means from the "pre" and "during" data, we found that "pre" studies used a significantly larger contrast media dose (mean 72.15 mL "pre" versus 62.96 mL "during"; $p < 0.005$), had significantly higher attenuation in the cervical ICAs (429.2 HU "pre" versus 393.8 HU "during"; $p < 0.05$) and intracranial arteries (408.5 HU "pre" versus 375.2 HU "during"; $p < 0.05$), and were more often of "good" quality (95.70% "pre" versus 80.90% "during"; $p < 0.005$). There were no statistically significant differences in patient age, BMI, or contrast media injection site between the groups.
Conclusions
Rationing contrast media dose can decrease the study quality for head and neck CTAs. These findings should be considered when discussing measures to combat future contrast media shortages.

1026

Emerging tropical Spinal Infections: An Update in MRI findings

A Lima Júnior[1], M Castillo[2], E Garcon[3], L Lucato[4], L Freitas[5]
[1]Mount Sinai Hospital, New York, NY, [2]Radiology, Chapel Hill, NC, [3]Columbia NYPH, New York, NY, [4]Instituto de Radiologia, Hospital das Clínicas da Faculdade de Medicina da Universidade de São Paulo, São Paulo, São Paulo, [5]BP - A Beneficência Portuguesa de São Paulo, São Paulo, SP

Purpose
Tropical illnesses are often forgotten, once their more prevalent in poor and underserved areas. We aimed to widen scientific literature available and aid doctors in diagnosis of these conditions.
Materials and Methods
A narrative review based on literature research from PubMed, SciELO, and Scholar Google. English and Portuguese language filters were applied. Only articles that addressed spine infections (tropical and non-tropical diseases) and imaging diagnostic methods were selected.
Results
Schistosomiasis is one of the most prevalent human parasitic infections. Usually presents as acute/subacute myelopathy. MRI shows imaging patterns, such as edema of conus medullaris with T1-weighted low-intensity signal, T2-weighted high-intensity signal, and heterogeneous contrast enhancement at granuloma sites, mimicking a tumor. Also known as Tropical Spastic Paraparesis, it is caused by HTLV-1. Pathophysiological hypothesis is that HTLV-1 infection results in an immune/autoimmune response leading to axonal and myelin injury in spinal cord. Localized or confluent lesions of the cerebral white matter and spinal cord atrophy with T2-weighted increased signal are found in HTLV-1-associated myelopathy. In the spinal cord, there is a predilection for lateral columns and white matter. Conus medullaris may be swollen and with T2-weighted increased signal and peripheral contrast enhancement. Chikungunya myelitis is caused by an alphavirus whose vectors are tropical mosquitoes Aedes aegypti. Encephalitis, myopathy, neuropathy, polyneuropathy, myeloradiculopathy, and longitudinally extensive transverse myelitis cases have been reported. Brucellosis is a worldwide zoonosis caused by gram-negative bacillus. Transmission occurs through consumption of contaminated animal meat and milk. It is estimated that 1 out of 10 patients have neurological involvement. MRI shows heterogeneous vertebral body bone marrow with T1-weighted decreased signal and T2-weighted increased signal. Advanced cases display loss of intervertebral disc space, as well as T2-weighted decreased signal, which reflects fibrosis.
Conclusions
As conclusion, many patients clinical and laboratory findings are mild or even absent, diagnostic imaging, especially magnetic resonance imaging plays a fundamental role in diagnosis establishment. Radiologists must be familiar with these diseases' imaging aspects, and biopsy should not be postponed when necessary.

289

Evaluating the Utilization and Utility of the NIH Stroke Scale in the Workup of Stroke with Imaging

M Isikbay[1], J Talbott[2]
[1]UCSF, San Francisco, CA, [2]UCSF and ZSFG, San Francisco, CA

Purpose
The prompt identification of stroke is essential given new interventions that prevent long term disability and death if administered in a timely manner. A core component in the workup of stroke is performing the NIH stroke scale (NIHSS) to effectively triage patients. We present data from one of our high-volume stroke centers to draw attention to the fact that many patients are not evaluated with the NIHSS prior receiving "code stroke" imaging.
Materials and Methods
A retrospective analysis at a single center was performed of 225 patients who received "code stroke" imaging. The documentation of a

NIHSS prior to obtaining imaging was noted. Additional clinical variables (such as presentation vitals and relevant past medical history) were also documented. Chi square analysis and logistic regression (controlling for the collected covariables) was performed comparing patients who had a documented NIHSS vs. those who did not. Additionally, for the patients with a NIHSS documented, an ROC curve was created, and the sensitivity/specificity was calculated for each NIHSS value cutoff.

Results

Out of the 225 cases of "code stroke" imaging performed and analyzed, only 122 (54%) cases had a NIHSS documented prior to obtaining imaging. The stroke positivity rate in patients without a NIHSS was approximately 14% (14/103) and was approximately 40% in those with a documented NIHSS (47/122) which after Chi square analysis revealed a odds ratio of 3.9 (P<.001). Logistic regression analysis revealed that only presentation blood pressure and prior history of hypertension were statically significant co-variables in our patient dataset, and analysis controlling for these variables redemonstrated these findings (odds ratio, 3.75; 95%CI, 1.92–7.53; P<.001) ROC curve analysis of stroke positivity by NIHSS score demonstrated an area under the curve of 0.79 and a sensitivity/specificity of 100%/28% if using a stroke scale cutoff of < 3 to rule out a stroke.

Conclusions

Despite its validated clinical utility, we note that a NIHSS was not performed prior to ordering "code stroke" imaging in roughly half of our analyzed patients. As expected, patients with a documented NIHSS had a significantly higher stroke positivity rate. Notably in our analyzed dataset no patient had a stroke with a stroke scale under 3. Future work supporting ordering providers to perform the NIHSS prior to ordering stroke imaging seems prudent given these findings.

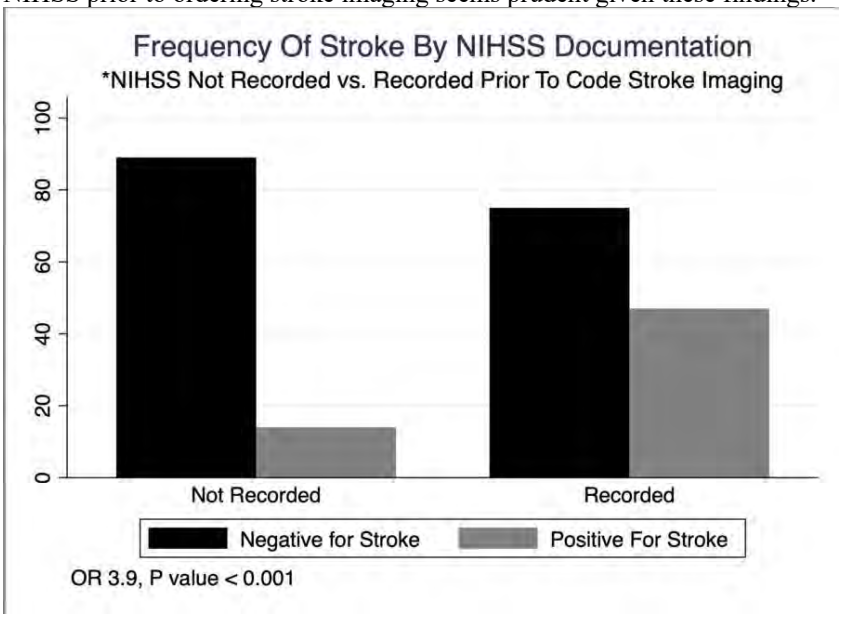

(Filename: TCT_289_ASNRAbstractFigure1.jpg)

763

Extraocular Muscle Displacement on MRI in Sagging Eye Syndrome

R Mashayekhi[1], W Plum[1], S Jambawalikar[2], G Moonis[3]

[1]Columbia University, New York, NY, [2]Columbia University Medical Center, NY, NY, [3]NYU Langone, New York, NY

Purpose

Sagging Eye Syndrome (SES) is strabismus caused by degeneration of orbital connective tissue predominantly among the elderly. There has been ongoing research to find objective measurements to diagnose SES on orbital Magnetic Resonance Imaging (MRI). Our study evaluates the position of the lateral rectus (LR) muscle and the medial rectus (MR) muscle using three angle measurements to provide radiologists with tools to better evaluate for SES on MRI.

Materials and Methods

This retrospective study compared 11 subjects with clinical diagnosis of SES to 11 control subjects. We used axial FIESTA-C sequence to create oblique coronal reconstructions with the plane parallel to a line joining the lacrimal crest and zygoma. Image-J software was used to measure three angles: (1) the vertical angle from the midpoint of the LR relative to the midpoint of the MR; (2) the vertical angle of the midpoints of the LR and MR muscles relative to the optic nerve; (3) and the vertical tilt angle of the LR and MR muscles. A Mann Whitney U test was performed to compare the angle measurements between the two groups.

Results

The 11 subjects with SES had an average age of 69 and 73% were female. The 11 control subjects had an average age of 60 and 64% were female. The average vertical angle from the midpoint of the LR relative to the midpoint of the MR was on 4.7 degrees in the SES group and 0.5 degrees in the control group (P<0.001). The vertical angle of the midpoints of the LR and MR muscles relative to the optic nerve were not significantly different between the two groups. The two groups did have a statistically significant difference of their LR muscle tilt angle ($p < 0.01$).

Conclusions
This study demonstrates that vertical displacement angle between the midpoint of the LR and MR muscles and the tilting of the LR muscle may be useful tools for evaluating for SES on MRI.

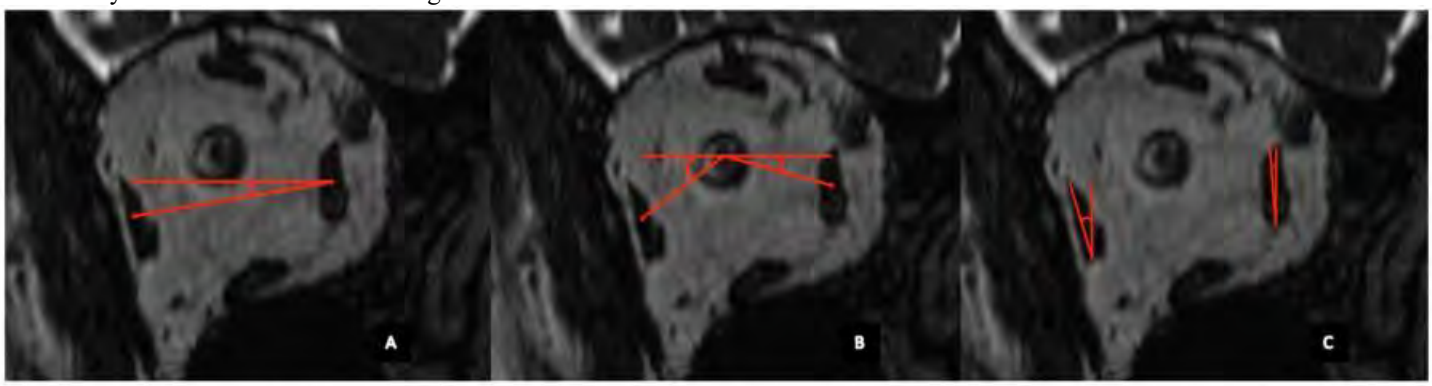

Angle measurement for SES. Figure A demonstrates LR muscle vertical angle displacement relative to the MR muscle. Figure B shows LR and MR muscle vertical angles relative to the optic nerve. Figures C is an example of the tilt angle of the LR and MR muscles.

(Filename: TCT_763_SESASNR.jpg)

470

FDA-Approved Machine Learning Algorithms in Neuroradiology: A Systematic Review of the Current Evidence for Approval

A Yearley[1], C Goedmakers[2], A Panahi[3], A Rana[2], J Doucette[4], K Ranganathan[2], T Smith[2]
[1]Harvard Medical School, Boston, MA, [2]Brigham and Women's Hospital, Boston, MA, [3]The George Washington University School of Medicine and Health Sciences, Washington D.C., [4]MCPHS University, Boston, MA

Purpose
We aim to determine the relationship between artificial intelligence algorithm development and clinical adoption by evaluating the evidence supporting the FDA-approval of machine learning (ML) "neuroalgorithms," the largest subcategory of FDA-approved ML algorithms, and subsequent translation to clinical care applications.
Materials and Methods
This systematic review was conducted according to the PRISMA guidelines (1). Articles covering the 52 FDA-approved algorithms with applications in the central nervous system published in PubMed, EMBASE, Google Scholar and Scopus between database inception and January 24, 2022 were identified. Of the 1,505 studies screened, 92 articles met criteria for extraction and inclusion. Data related to study design, performance metrics, external validation, clinical application, strengths, and limitations were extracted for each algorithm by two separate authors. A quality assessment was conducted for all 85 papers that validated a surveyed algorithm against an accepted gold standard or another machine learning algorithm with an identical function.
Results
Performance metrics were available for 15 algorithms and external validation studies for 24 algorithms (Table 1). For 16 of the 24 algorithms at least one study could be identified in which the algorithm's performance was rated as "good." Multiple algorithms, including Aidoc BriefCase-CSF triage, AutoMIStar, CINA, CT CoPilot, DeepCT, Health VCF, QyScore, RAPID ICH, Stroke VCAR, and SubtlePET had only a single peer-reviewed paper published, mostly studying algorithm performance. Only 7 of the 52 surveyed neuroalgorithms had been studied in clinical practice. Papers studying the clinical utility of these algorithms focused on three domains: workflow efficiency, cost savings, and clinical outcomes. Viz LVO had been the most extensively studied in clinic, with multiple studies analyzing the clinical integration of the algorithm into the stroke workflow at 9 medical centers over a total of 27 months (2,3).
Conclusions
Our analysis suggests that there is a meaningful gap between the FDA-approval of machine learning algorithms and their clinical utilization. We make recommendations as to how the process can be improved to provide compelling evidence that algorithms work as advertised, including mandating a minimum set of performance metrics, minimum cohort sizes, adequate exploration of algorithm limitations, well-controlled studies of algorithms in clinical practice, and interpretable code sharing.

Algorithm	Performance Metrics	External validation performance		Risk of Bias†
		Validation w/ ground truth	*Validation w/ other algorithm*	
Aidoc BriefCase- CSF triage	*Detection of Cervical Spine Fractures* Sensitivity - 54.9 Specificity - 94.1 PPV - 38.7 NPV - 96.8	[illegible]	-	Low
Aidoc BriefCase-ICH	*Detection of ICH* Sensitivity - 88.4-95.0 Specificity - 98.2-99.0 PPV - 73.7-96.0 NPV - 96.3-98.0	[illegible]	-	Low
AutoMINing	-	[illegible]	[illegible]	Moderate
Brainance MD	-	[illegible]	[illegible]	Moderate
CINA	*Detection of ICH* Sensitivity - 91.4 Specificity - 97.5 PPV - 80.2-97.3 NPV - 91.9-99.0 *Detection of LVO* Sensitivity - 98.1 Specificity - 98.2 PPV - 85.8-98.2 NPV - 98.1-99.8	[illegible]	-	Low
CT CoPilot	-	[illegible]	-	High
FastStroke, CT Perfusion 4D	-	[illegible]	[illegible]	Moderate
Health VCF	*Detection of VCFs* Sensitivity - 54.0 Specificity - 92.0 PPV - 69.0 NPV - 87.0	[illegible]	-	Low
IB Neuro	*Classification of Survival in GBM* Sensitivity - 80.0 Specificity - 63.0 *Differentiation of DIGG and PA* Sensitivity - 100.0 Specificity - 76.7	[illegible]	[illegible]	High
icobrain	-	[illegible]	[illegible]	Moderate*
InferRead CT Stroke.AI	-	-	[illegible]	Low
LesionQuant	*Identification of New MS Lesions* Sensitivity - 53.0 Specificity - 75.0	[illegible]	[illegible]	Moderate
NeuroQuant	*Identification of Alzheimer's* Sensitivity - 63.0-88.5 Specificity - 66.0-92.0 *Identification of MCI* Sensitivity - 48.9-60.2 Specificity - 80.0-80.6	[illegible] [illegible] Poor	[illegible] [illegible] Poor	Moderate*
Neurovrender	*Identification of Mesial Temporal Sclerosis* Sensitivity - 89.0 Specificity - 71.0-78.0	[illegible] [illegible]	Poor	High
QuantiB Brain	*Diagnosis of Dementia* Sensitivity - 95.0-97.5 Specificity - 60.0	Poor	-	Moderate
QyScore Software	-	[illegible]	-	Low
Rapid ASPECTS	*ASPECTS Score Generation* Sensitivity - 24.0-54.0 Specificity - 87.0-93.0	[illegible] [illegible] Poor	[illegible]	Moderate*
RAPID ICH	*ICH Detection* Sensitivity - 95.6 Specificity - 95.3 PPV - 95.6 NPV - 95.3 [122]	[illegible]	-	Moderate
Rapid LVO 1.0	*LVO Detection* Sensitivity - 96.0 Specificity - 98.0	-	-	Low
Stroke VCAR	-	Poor	-	Moderate
SubtleMR	-	[illegible]	-	Moderate
SubtlePET	-	[illegible]	-	Moderate
Syngo.CT Neuro Perfusion	*Detection of Ischemic Core Volumes* Sensitivity - 93.0-97.0 Specificity - 97.0-100.0	[illegible]	[illegible]	Moderate
Vitrea CT Brain Perfusion	*Detection of Ischemic Stroke* Sensitivity - 70.0 Specificity - 80.0 PPV - 98.8 NPV - 10.2 *Detection of Intracranial Aneurysms* Sensitivity - 90.9-96.3 Specificity - 100.0	[illegible]	[illegible]	Moderate*
Viz LVO (ContaCT)	*Detection of LVO* Sensitivity - 74.6-93.8 Specificity - 88.5-91.1 PPV - 34.4-94.4 NPV - 65.0-99.7	[illegible]	-	Low

Table 1: Summary of performance metrics and external validation studies in the primary literature for all studied algorithms.
* Consider a lower risk of bias given a larger number of validation studies.
† Green columns are associated with an aggregated low risk of bias, yellow columns a moderate risk of bias, and red columns a high risk of bias based on the calculated mode risk of bias for all the papers studying the given algorithm

(Filename: TCT_470_Table_1.jpg)

1324

Frequency, Patterns and Intracranial Associations of Cystic Encephalomalacia on Delayed MRI Scans of Children with Term Hypoxic Ischemic Injury

D Alkhulaifat[1], S Venkatakrishna[1], F Worede[2], M Elsingergy[1], S Andronikou[1]

[1]Children's Hospital of Philadelphia, Philadelphia, PA, [2]Mercy Catholic Medical Center, Darby, PA

Purpose

Perinatal hypoxic ischemic injury (HII) is the leading cause of encephalopathy in neonates. In total hypoxia or anoxia, or catastrophic HII, a condition known as multicystic encephalomalacia (MCE) may develop, where the injury extends beyond the watershed zones and involves major vascular territories. In this condition, there is progressive loss of cerebral volume with extensive irreversible damage with large cystic spaces separated by gliotic strands visible on MRI. This condition has been poorly described. We aim to describe a variety of cystic encephalomalacia patterns in children with term HII by magnetic resonance imaging (MRI) and determine any associated intracranial lesions that reflect severity of injury.

Materials and Methods

We retrospectively reviewed a database of 1233 delayed brain MRI in children with a diagnosis of term perinatal HII and extracted those with cystic encephalomalacia. These were classified into MCE (large hemispheric areas with little residual parenchyma) vs. focal cysts. For children with focal injury, regions distribution was extracted as well as the overall pattern of HII: Watershed (WS), Basal Ganglia Thalamus (BGT), Combined BGT/WS. We also calculated the frequency of thalamic and cerebellar involvement and the presence of ulegyria, and compared the two main subgroups.

Results

Out of 1233 patients evaluated with term HII, 32% (n=388) had cystic encephalomalacia on delayed MRI. 47% demonstrated typical extensive MCE (n=181), while 53% had focal cystic injury (n=207) which was most frequently bilateral (79%). The most common underlying HII injury pattern in children with focal cystic injury was combined BGT/WS (51%) and the Peri-Sylvian regions were most commonly involved (68%). Other MRI findings included: ulegyria, present in 196 patients (51%): MCE 52/181 (29%) vs. focal 144/207 (70%); thalamic injury, present in 343 (88%): MCE 161/181 (90%) vs. focal 182/207 (88%); and cerebellar injury, present in 69 (18%): MCE 38/181 (21%) vs. focal 31/207 (15%).

Conclusions

Cystic breakdown is common (32%) in patients with term HII on delayed MRI, with similar prevalence of focal cystic injury (53%) and classic multicystic encephalomalacia (47%). Both patterns are associated with other indicators of severity such as thalamic injury (88%) and cerebellar injury (18%). Focal cystic injury was distributed most often in the perisylvain watershed and showed a significantly higher frequency of ulegyria confirming a prolonged insult.

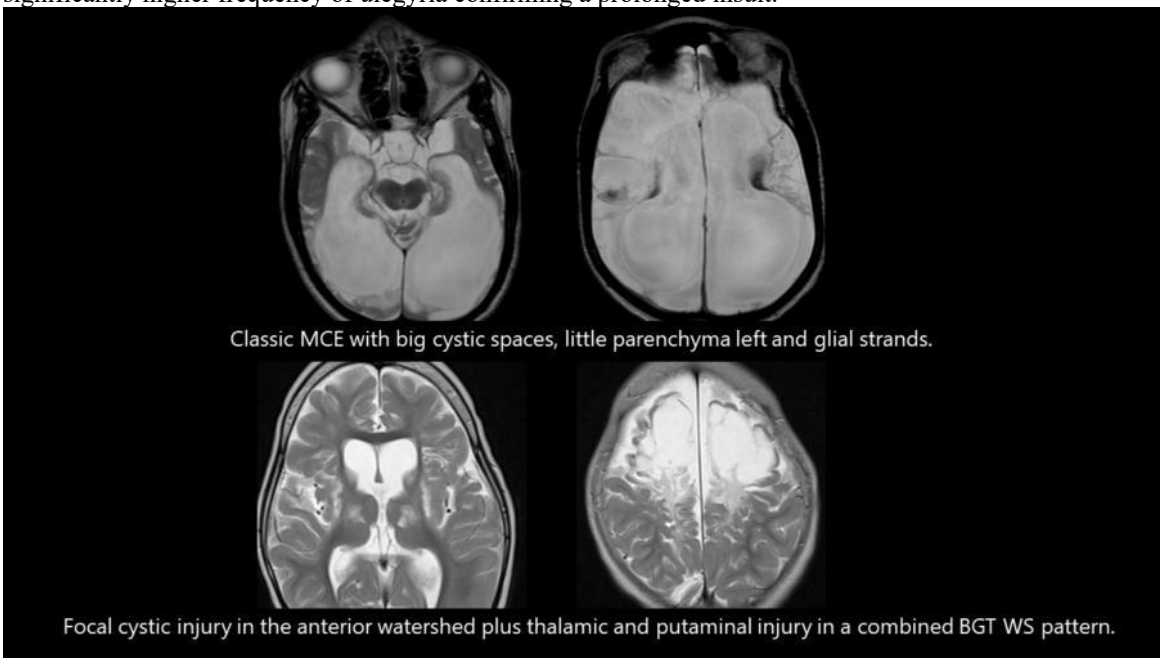

(Filename: TCT_1324_CysticEncephalomalaciaSelectedImages.jpg)

1341

GRADUATE I and II: Imaging Findings From Two Phase III Trials of Subcutaneous Gantenerumab in Early Alzheimer's Disease

F Barkhof[1], G Klein[2], M Tonietto[2], T Bittner[2], S Ahlers[3], R Abbas[2], J Smith[4], N Fox[5], S Black[6], O Hansson[7], R Doody[2]
[1]Amsterdam Neuroscience, Amsterdam UMC, Vrije Universiteit, Amsterdam, Netherlands, [2]F. Hoffmann-La Roche Ltd, Basel, Switzerland, [3]Excelya Germany GmbH, Mannheim, Germany, [4]Roche Products Ltd, Welwyn Garden City, UK, [5]Dementia Research Centre, Queen Square Institute of Neurology, University College London, London, UK, [6]Sunnybrook Health Sciences Centre, Toronto, Ontario, Canada, [7]Lund University, Lund, Sweden

Purpose
Gantenerumab, a subcutaneous fully human monoclonal antibody targeting aggregated forms of amyloid-beta (Aβ), is a potential disease-modifying treatment for Alzheimer's disease (AD). The global Phase III GRADUATE I (NCT03444870) and II (NCT03443973) studies aimed to assess the efficacy and safety of gantenerumab in early AD. Previous amyloid positron emission tomography (PET) substudies of SCarlet RoAD (NCT01224106) and Marguerite RoAD (NCT02051608) Phase III trials suggested that gantenerumab treatment can lead to robust Aβ removal below threshold levels [1]. GRADUATE I and II included amyloid and tau PET substudies and volumetric magnetic resonance imaging (vMRI) measures to investigate the effects of gantenerumab treatment on these imaging biomarkers in participants with early AD.
Materials and Methods
Eligible participants (50–90 years) with mild cognitive impairment (MCI) due to AD or mild AD dementia were randomized 1:1 to subcutaneous gantenerumab or placebo, administered at the study site or at home. Gantenerumab was up-titrated over 36 weeks to a target dose of 510 mg every 2 weeks in all participants, irrespective of apolipoprotein E ε4 (APOE ε4) genotype. Imaging biomarkers were assessed at baseline and annually. Changes in centiloid levels were obtained from [18F]Florbetaben and [18F]Flutemetamol PET. Regional changes in tau standardized uptake value ratio (SUVR) were obtained with [18F]GTP1 PET. Whole brain and regional atrophy were assessed via vMRI.
Results
Amyloid and tau PET findings as well as initial vMRI data will be presented.
Conclusions
Imaging findings from GRADUATE I and II and the PET substudies provide further insights into the effects of subcutaneous gantenerumab on amyloid and tau load, and regional brain volume in early AD.

359

High-speed datalink-enabled remote deep-learning reconstruction of T2-weighted brain magnetic resonance imaging results in enhanced acquisition speed without sacrificing diagnostic quality

C Koo[1], C Welch[1], A Yang[1], X Cai[2], J Lee[1], M Mostapha[3], L Fleysher[1], M Bush[2], N Janardhanan[3], K Chow[4], L Lazar[5], S Arberet[3], G Paladini[3], J Guehring[6], H Meyer[6], M Nadar[3], D Comaniciu[3], P Belani[7], A Doshi[7], Z Fayad[1]
[1]Icahn School of Medicine at Mount Sinai, New York, NY, [2]Siemens Medical Solutions USA, Inc., New York, NY, [3]Digital Technology & Innovation, Siemens Healthineers, Princeton, NJ, [4]Siemens Medical Solutions USA, Inc., Chicago, IL, [5]Siemens S.R.L, Brasov, Romania, [6]Healthcare GmbH, Erlangen, Germany, [7]Mount Sinai Hospital, New York, NY

Purpose
Deep Learning (DL) image reconstruction algorithms have been shown to maintain or improve image quality with significant time savings. Deployment of these AI algorithms can be limited as they often require significant local computational power. A remote high-performance reconstruction computer connected via high-speed network can overcome this problem. We evaluated the feasibility and diagnostic performance of accelerated MR scans with DL reconstruction deployed on such a system.
Materials and Methods
We connected four MR scanners with a novel infrastructure to a remote supercomputing system via a high-speed datalink, allowing streamlining of data from the MR scanners concurrently. A prototype DL reconstruction was deployed on the supercomputer and reconstructed images are returned to the scanner in real-time. Data transfer was anonymized. We evaluated the performance of this infrastructure in 54 patients obtaining brain MRI on 1.5T and 3T scanners. In addition to the standard clinical T2-Weighted TSE-BLADE sequence (acquisition time 1:45), we acquired a TSE sequence with rate-4 acceleration (acquisition time 0:31) which was reconstructed locally (standard GRAPPA) and remotely (DL). All images were blindly evaluated by two experienced neuroradiologists for diagnostic quality (Likert scale 1-5, 5 = excellent), legibility of deep gray structures (Likert scale 1-5), and presence of pathology. White matter signal-to-noise ratio (SNR), gray matter SNR, and white/gray matter contrast-to-noise ratio (CNR) were measured on a central slice.
Results
Datalink-enabled reconstruction was successful in all subjects. Server execution time ranged 11-20 seconds. DL TSE images was non-inferior to the standard T2-weighted BLADE sequence in diagnostic quality and legibility ($p > 0.05$). There was 100% concordance in detection of pathology between BLADE and DL reconstruction. SNR and CNR were comparable between BLADE and DL. Spearman rank correlation coefficient was 0.48 for inter-reader variability.
Conclusions
Remote DL reconstruction via a high-speed datalink is a feasible method for DL imaging reconstruction and is non-inferior to

standard T2-weighted BLADE sequence in qualitative and quantitative assessment. This may allow for faster imaging without the need for in-house high computational powered hardware.

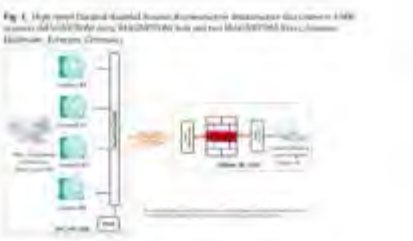

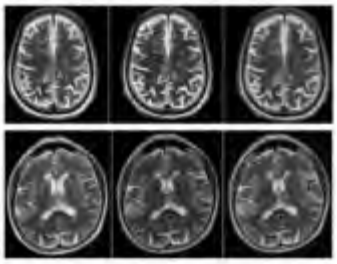

(Filename: TCT_359_359images.jpg)

1506

Identifying Predictors of Intracranial Aneurysm Wall Enhancement and Associated Rupture Risk using Bayesian Network Analysis

S Faruqui[1], A Patel[1], C Zhou[1], R Abdalla[1], M Potts[2], B Jahromi[1], V Rayz[3], M Markl[4], T Carroll[5], A Shaibani[1], S Ansari[6], D Cantrell[1]
[1]Northwestern University, Chicago, IL, [2]Northwestern University - Feinberg School of medicine, Chicago, IL, [3]Purdue University, West Lafayette, IN, [4]Northwestern University McCormick School of Engineering, Chicago, IL, [5]University of Chicago, Chicago, IL, [6]Northwestern University, CHICAGO, IL

Purpose

Bayesian Networks (BNs) are probabilistic models that can represent the relationships among factors and target variables within their structure. BNs allow for quantitative reasoning by estimating the probability of different events given observed conditions and may be useful tools in clinical decision-making. Intracranial Aneurysms are found in 3-5% of population globally. While the rupture risk is less than 1%, mortality and morbidity in patients with ruptured IAs remains high. 1 In this work, we propose the use of a BN to analyze the patient demographics and cerebrovascular risk factors affecting aneurysm wall stability, it's relationship with quantified Aneurysm Wall Enhancement (AWE) on High Resolution MR Vessel wall Imaging (VWI), and Subarachnoid Hemorrhage (SAH).

Materials and Methods

An IRB approval was obtained for a single-cohort, retrospective, patient level study. A total of 214 IAs in 174 patients (mean age 62.50 (22 - 87), 74% female) with 19 (9.09%) SAH were utilized for this study. AWE was evaluated both qualitatively and quantitatively. Quantitative evaluation of AWE was performed using three-point ROIs on the aneurysm wall at the areas of maximum intensity on pre- and post-contrast T1-SPACE sequences (percentile Increase). The quantified data was normalized with white matter signal intensity and a percentage increase from pre to post contrast sequences was calculated. Patient demographics, risk factors, IA size, and morphology were also considered for the study. IAs were grouped into small (<3.9mm), medium (4-7mm), and large (>7.1mm) sizes. The structure (DAG) of the BN model was developed manually by consulting relevant clinical literature. Finally, the developed model was evaluated to identify the factors that affect the growth of AWE and SAH.

Results

BN model parameters were learned from data via maximum-likelihood estimation, and the model results were compared to a standard logistic regression model. The BN model found SAH to be strongly associated with age, IA location, IA size and percentile increase of AWE. Regression analysis confirms this finding (age, $p = 0.03$; IA location (PICA, ICA/Pcomm, ACA) $p = 0.0012$; IA size, $p = 0.06$; and percentile increase of AWE, $p = 0.02$).

Conclusions

This study develops a BN model to investigate the relationship between clinical factors that affect the Intracranial Aneurysm Wall Enhancement and Associated Rupture Risk.

598

Image Quality Assessment of Virtual Monoenergetic and Polyenergetic Reconstructions for Head and Neck CT Angiography: Initial Experience with a Photon-Counting CT

W Lee[1], J Rodgers[1], M Matheus[2], U Schoepf[1], J O'Doherty[1], M Spampinato[1]
[1]Medical University of South Carolina, Charleston, SC, [2]MUSC, Charleston, SC

Purpose

The recent introduction of photon-counting detectors (PCDs) is a breakthrough in CT technology. Traditional energy-integrating detectors (EID) convert x-ray photons into light photons, which are then converted into electrical signal. Instead PCDs directly convert incident x-ray photon into electrical signal, resulting in separate measurements of the incident photons, including the number of pulses and their energies. This technique improves soft tissue and iodine contrast, decreases beam hardening artifact, and improves discrimination between iodine and dense structures such as calcified plaque. We describe preliminary experience with the first photon-counting CT approved for clinical use.

Materials and Methods

After informed consent, three patients who had undergone standard-of-care EID CTA for cerebrovascular disease were recruited. Within 30 days of the standard-of-care CTA, patients underwent head and neck CTA using an FDA-cleared photon-counting CT scanner. Three types of images were included in the analysis: 1. Standard EID-CT polyenergetic reconstructions; 2. PCD-CT polyenergetic reconstructions obtained using PCD-CT data with x-ray energies >20 keV to simulate EID-CT; 3. PCD-CT virtual monoenergetic images (VMI) ranging from 40-100 keV at 5-10 keV increments. ROIs were placed in the common carotid artery, petrous internal carotid artery, and trapezius muscles. The standard deviation of the CT attenuation of muscle ROI was used as image noise. Contrast-to-noise ratio (CNR) was calculated (average attenuation vessel - attenuation muscle) / noise. Signal to noise (SNR) was calculated (mean HU vessel) / noise.

Results

Three patients were included in the study. Average noise was 13.2 HU for EID-CT polyenergetic reconstructions, 13.0 HU for the PCD-CT polyenergetic reconstructions, and ranged from 9.8-15.5 HU for PCD-CT monoenergetic images. Average CNR was 35.7 for the EID-CT polyenergetic reconstructions, 39.9 for the PCD-CT polyenergetic reconstructions, and ranged from 20.4-93.2 for the PCD-CT VMI. Average SNR was 39.8 for the EID-CT polyenergetic reconstructions, 44.3 for the PCD-CT polyenergetic reconstructions, and ranged from 26.2-96.6 for the PCD-CT VMI.

Conclusions
We have preliminarily investigated image quality of PC-CT CTA of the head and neck. Our initial results suggest that VMI at 70 keV and lower provide better SNR and CNR than EID-CT and PCD-CT polyenergetic reconstructions for head and neck CTA.

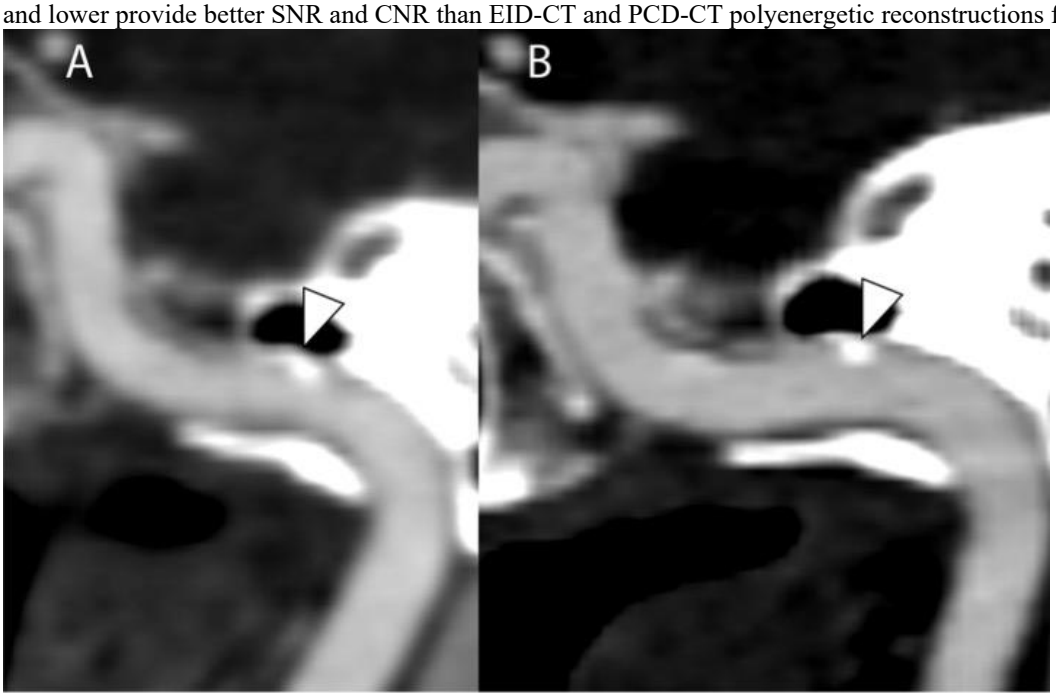

Petrous segment of the left internal carotid artery. A. EID-CT standard polyenergetic reconstruction; B. PCD-CT 70 keV virtual monoenergetic angiographic images.

(Filename: TCT_598_Figure1.jpg)

1285

Imaging-based Prediction of Histological Clot Composition and Its Impact on Vascular Recanalisation By Mechanical Thrombectomy in Patients of Acute Ischemic Stroke.

P Bharti[1], V Agarwal[2], A Singh[3]
[1]Christian Medical College, Ludhiana, Punjab, [2]Christian Medical College, Ludhiana, UT, [3]Christian medical college, Ludhiana, ludhiana, PUNJAB

Purpose
Currently, only two Food and Drug Administration approved treatment options are available for acute ischemic stroke, intravenous thrombolysis and mechanical thrombectomy. Mechanical thrombectomy is the optimal therapy for acute stoke patients with large vessel occlusion. It also provides the opportunity for histopathological analysis of clot composition. We propose to undertake this study to assess the correlation between early imaging findings and clot composition with the number of passes required for revascularisation in patients undergoing mechanical thrombectomy
Materials and Methods
This will be a cross sectional study to be conducted on a total number of 50 patients of acute ischemic stroke undergoing mechanical thrombectomy in the Department of radiodiagnosis in collaboration with division of neurointervention and pathology department at Christian Medical College and Hospital, Ludhiana After the procedure, the clot obtained will be sent to pathology lab for the histopathological compostion and results obtained will be analysed and documented in a excel sheet.
Results
Perviousness significantly positively and negatively correlated with the percentage of fibrin/platelet aggregates (P = .001) and the percentage of red blood cells (P = .001), respectively. clots with greater fibrin/platelet aggregate content has higher permeability(P = .042). Cases that achieved a first-pass effect (n = 14) had lower perviousness, though not significantly (P = .055). The percentage of red blood cells was significantly higher (P = .028) and the percentage of fibrin/platelet aggregates was significantly lower (P = .016) in cases with a first-pass effect. The similar RBC rich clot was correlated well with suseptibility vessel sign on SWI.
Conclusions
Clot perviousness on CT is associated with a higher percentage of fibrin/platelet aggregate content. Histologic data and, to a lesser degree, perviousness help to value in predicting first-pass outcome. Imaging metrics that more strongly reflect clot biology than perviousness may be needed to predict a first-pass effect with high accuracy along with suceptibility vessel sign on SWi for RBC rich clots

641

Impact of high field strength (3T and 7T) on dynamic susceptibility contrast (DSC) perfusion MRI using Gadolinium and Ferumoxytol as contrast agents in primary brain tumors

D Wongsawaeng[1], R Barajas[2], D Schwartz[3], X Li[3], L Muldoon[4], J Stoller[5], C Stateler[6], S Holland[4], E Neuwelt[7]

[1]Department of Radiology, Faculty of Medicine Siriraj Hospital, Mahidol University, Bangkok, Thailand, [2]Department of Radiology, Advanced Imaging Research Center, Knight Cancer Institute, OHSU, Portland, OR, [3]Advanced Imaging Research Center, Oregon Health & Science University, Portland, OR, [4]Department of Neurology, Oregon Health & Science University, Portland, OR, [5]Department of Radiology, Oregon Health and Science University, Portland, OR, [6]School of Medicine, Oregon Health & Science University, portland, OR, [7]Department of Neurology, Department of Neurosurgery, Veterans Affairs Medical Center, OHSU, Portland, OR

Purpose

Dynamic susceptibility contrast (DSC) MRI, widely used for brain tumor perfusion evaluation, relies on T2*-effect induced signal loss resulting from the passage of a bolus of gadolinium (Gd) or a long-circulating iron oxide nanoparticle, Ferumoxytol (Fe). It is predicted that DSC will have superior performance at high magnetic field strength. This study aimed to investigate the impact of ultra-high field strength (7T) on DSC perfusion scan using Gd or Fe as a contrast agent.

Materials and Methods

A total of 18 primary brain tumor lesions, including 11 GBM, 3 anaplastic astrocytoma, 3 oligodendroglioma and 1 astroblastoma, were scanned at 3T (7 lesions) and at 7T (11 lesions). DSC was performed with axial 2D gradient echo echo-planar imaging (EPI) (TE20/TR1500/FA45). All patients received 0.1 mmol/kg gadoteridol (Gd) on day 1 and low or high dose Fe on day 2 (0.6-1.8 mg/kg) at a rate of 3 mL/sec. DSC scans were processed using NordicICE software. Leakage-correction was done in analyzing Gd-derived cerebral blood volume (CBV)1 but not for Fe2. Volumes of interest were defined on enhancing tumor, non-enhancing hyperintense T2W brain and contralateral normal appearing white matter. The contrast to noise ratio (CNR) was calculated.

Results

There was significantly higher CNR using Gd compared to Fe on 7T at either low dose (0.6 mg/kg) or high dose (1.0-1.8 mg/kg) Fe ($P<0.05$) (Table 1, 2, Figure 1). This finding was not detected at 3T. There was no significant difference comparing the CNR of Gd nor the CNR of Fe between the 2 MRI field strengths, but there was a trend toward a higher CNR for Fe on 3T versus 7T (Table 3).

Conclusions

Gd-based contrast had higher image conspicuity as measured by CNR than Fe on 7T MRI. Extreme T2* effect from higher magnetic field strength together with Fe itself might induce more image noise rather than enhance performance on DSC scans.

Table 1 : Comparison between contrast to noise ratio of gadolinium (CNR-Gd) and contrast to noise ratio of 1.0 -1.8 mg/kg Ferumoxytol (CNR-Fe) at two MRI field strengths

MRI Field strength	Number of lesions	CNR-Gd (mean ± SD)	CNR-Fe (mean ± SD)	p-value
3 Tesla	7	1.02 ± 0.65	1.07 ± 0.82	0.911
7 Tesla	11	0.96 ± 0.55	0.55 ± 0.26	**0.016**

Table 2 : Comparison between contrast to noise ratio of gadolinium (CNR-Gd) and contrast to noise ratio of 0.6 mg/kg Ferumoxytol (CNR-Fe) at two MRI field strengths

MRI Field strength	Number of lesions	CNR-Gd (mean ± SD)	CNR-Fe (mean ± SD)	p-value
3 Tesla	4	1.05 ± 0.90	0.77 ± 0.42	0.49
7 Tesla	10	1.02 ± 0.51	0.50 ± 0.35	**0.023**

Table 3 : Comparison of contrast to noise ratio of gadolinium (CNR-Gd) or contrast to noise ratio of 1.0 -1.8 mg/kg Ferumoxytol (CNR-Fe) between 3T and 7T MRI scanners (mean ± SD)

Contrast agent	3T	7T	p-value
CNR-Gd (mean ± SD)	1.02 ± 0.65	0.96 ± 0.55	0.846
CNR-Fe (mean ± SD)	1.07 ± 0.82	0.55 ± 0.26	0.154

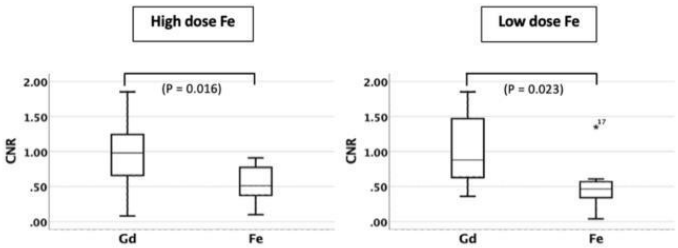

Figure 1 : Comparison contrast to noise ratio (CNR) between gadolinium (Gd) and Ferumoxytol (Fe) at 7T MRI

(Filename: TCT_641_TablesfigureDSC3T-7TabstractASNR2023.jpg)

980

Importance of MR Spectroscopy in Pediatric Patients with Suspected Neurometabolic Disorders.

P Sharma[1], S Serai[2], S Andronikou[1], S Venkatakrishna[1], A Vossough[3], C ALVES[1], M Whitehead[4]

[1]Children's Hospital of Philadelphia, Philadelphia, PA, [2]Children's Hospital of Philadelphia, Phiiladelphia, PA, [3]CHOP-UPENN, Philadelphia, PA, [4]Children's Hospital of Philadelphia, Philadelphia, PA

Purpose

MR Spectroscopy (MRS) is an underutilized, yet powerful clinical tool that can impact the diagnosis, prognosis, and treatment for pediatric patients with suspected neurometabolic disorders. We sought to determine the yield of MRS in the context of diagnosing and treating neurometabolic disorders, to determine its clinical importance.

Materials and Methods

All available MRS on both 1.5 and 3.0 Tesla systems, with single or multivoxel spectroscopy technique (SVS), and 2D (chemical shift imaging) CSI technique, performed for clinical purposes at a large tertiary children's hospital were considered. Protocol parameters generally included a short echo time, TE (TR/TE: 1500-1800/20-35 msec; scan time of around 5 to 6 mins) for SVS and intermediate or long TE (TR/TE: 1500-1900/135-288 msec; scan time of around 6-8 mins) for the 2D CSI. We included and retrospectively reviewed studies with clinically suspected neurometabolic disease over a 20-year period, spanning 2001 to 2022. A pediatric neuroradiologist conducted a double-blind review of the first MRS following MR imaging and performed a detailed evaluation of baseline imaging. TE and voxel location had small variability of 4% among areas evaluated. Areas of brain evaluation included left or right basal ganglia, left parietal lobe and cortex at the level of the posterior cingulum. MRS was reviewed for abnormal diagnostic peaks. Analyzed data was classified into sub-cohorts separately for both the MRS and MRI findings as either (a) typical diagnostic features, (b) suggestive diagnostic features, (c) nonspecific features, or (d) normal.

Results

Out of 600 clinically suspected neurometabolic disorder subjects with a brain MRI and MRS, 128 (21.3%) were molecularly confirmed with a neurometabolic disorder. Of these confirmed neurometabolic disorders, 48 (37.5%) had typical diagnostic features on both brain MRI and MRS; 42 (32.8%) had normal brain MRI but typical diagnostic features on MRS; 34 (26.6%) suggested features of neurometabolic disorders on brain MRI with MRS upgrading overall diagnostic ability of the routine MRI.

Conclusions

This study represents a large cohort of subjects with clinically suspected neurometabolic disease, with 21.3% confirmed molecularly. Data demonstrates clinical importance of MRS by providing typical diagnostic features in 32.8% of a specific neurometabolic disease, where routine MRI was normal. It further provided additional diagnostic support in 26.6% when features on routine MRI were only suggestive of neurometabolic diseases.

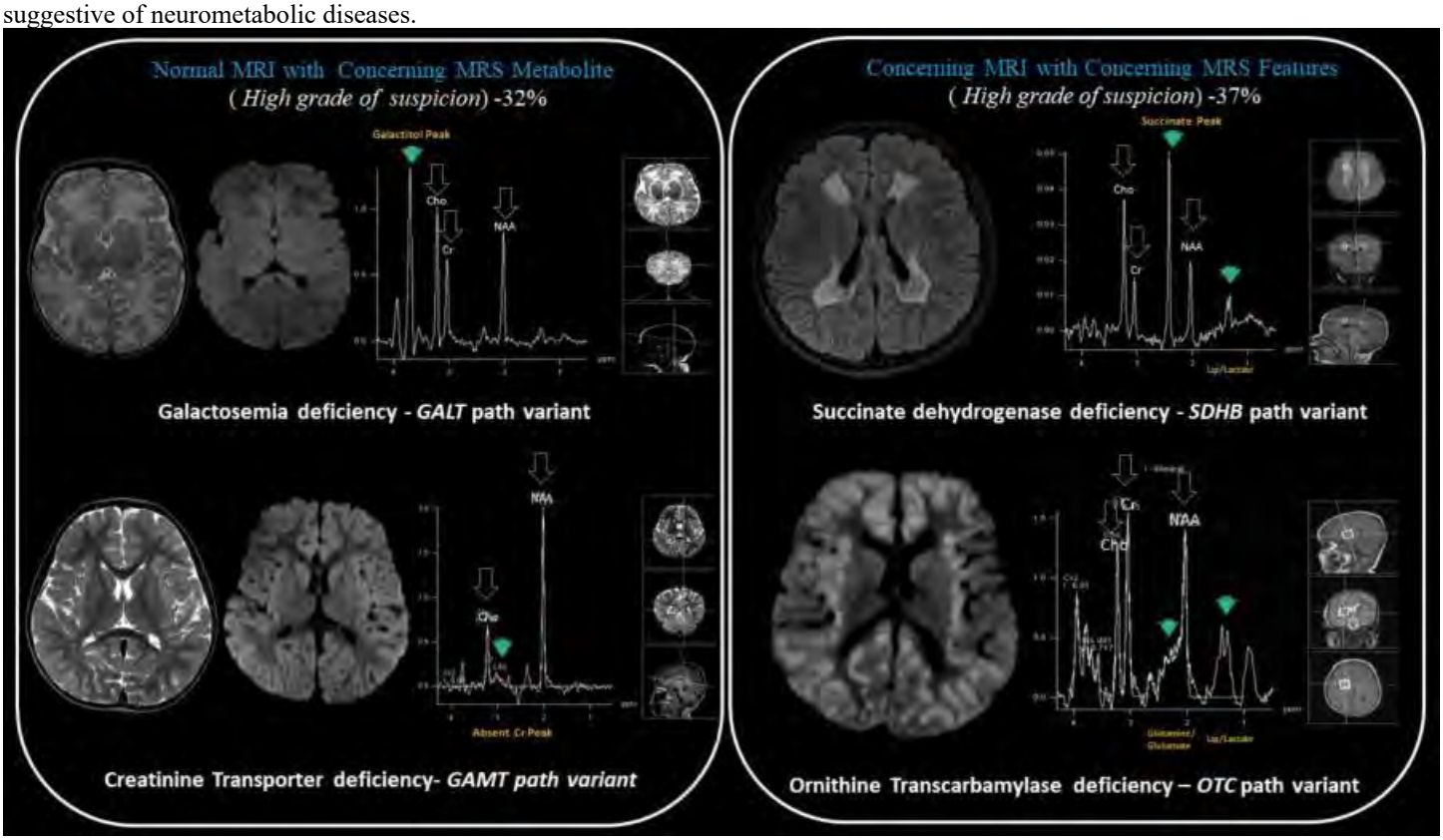

(Filename: TCT_980_CAA_FinalfiguremodelsforMRSProjectASNR.jpg)

677

Inferior frontal junction connectivity is associated with vestibular symptom severity after concussion

J Smith[1], V Ahluwalia[2], J Benke[1], R Gore[3], J Allen[4]

[1]Emory University School of Medicine, Atlanta, GA, [2]Georgia Institute of Technology, ATLANTA, GA, [3]Shepherd Center, Atlanta, GA, [4]Emory University, Atlanta, GA

Purpose

Recent research suggests vestibular syndromes, particularly post-concussive vestibular dysfunction (PCVD), may be associated with an over-reliance on visual cues.1 The aims of the present study were to examine (1) if resting-state functional connectivity (RSFC) is associated with vestibular symptom severity in subacute patients; (2) whether these associations implicate vestibular and visual areas; and (3) whether such connections can differentiate control from subacute participants using a classifier.

Materials and Methods

30 control (19F, age 28.78±1.04yrs) and 25 subacute PCVD subjects (4-12wks post-concussion; 13F, 22.96±4.76yrs) participated; inclusion and exclusion criteria are described elsewhere.2 Clinical assessment included the VVAS, a self-report of evoked vestibular symptom severity. SMS-EPI resting-state MRI (rsfMRI, 7:30 run) was acquired on a 3T Siemens Prismafit MRI and subjected to minimal preprocessing, including 8mm FWHM blur and 10-250mHz bandpass.2 Bivariate ROI-ROI RSFC was computed for all ROIs in the EAGLE vestibular compilation.3 Associations between RSFC strength and VVAS Z-scores were assessed by GLM, covarying participant age and log-transformed days since injury. The resulting VVAS-correlated network was FWER-corrected using ROI-based multivariate parametric statistics. Suprathreshold ROI-ROI correlations were then imported into MATLAB for feature selection and machine classification with 10-fold cross-validation.

Results

48 connections, all originating in the right inferior frontal junction (R IFJ), survived analysis. VVAS Z-scores were negatively correlated with R IFJ connectivity to vestibular, sensorimotor, insular, and brainstem areas, and positively correlated with orbitofrontal, ventral visual, cerebellar, and cingulate areas. Feature selection algorithms consistently ranked R IFJ connections with ipsilateral inferior olivary nucleus and vestibular/sensorimotor cortex as factors discriminating HC from ST participants, and the best classifier (Gaussian Naïve Bayes; validation accuracy 72.6%) successfully classified participants with a validation accuracy of 72.6%.

Conclusions

Connections of the R IFJ – a cognitive control component associated with visual processing4 and postural instability5 – are significantly associated with VVAS scores. Symptom severity in subacute PCVD may thus be associated with greater reliance on ventral visual and executive areas, and less reliance on vestibular cortex, as mediated through the R IFJ control region.

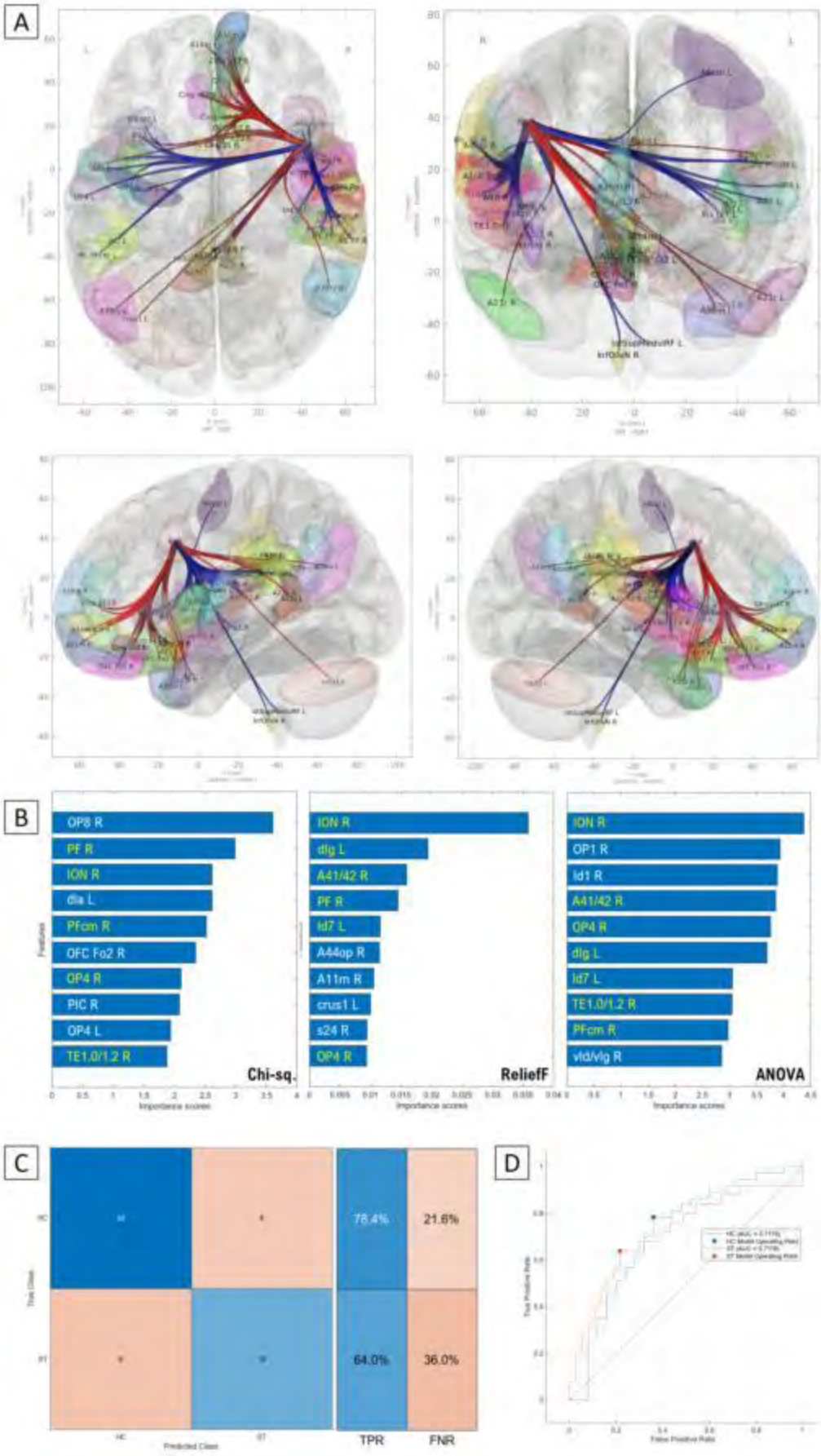

(Filename: TCT_677_JLS_figure_for_ASNR_JPG.jpg)

1055

Inner Ear Anomalies in Treacher Collins Syndrome

D Homuth[1]
[1]*Indiana University, Indianapolis, IN*

Purpose

Treacher Collins Syndrome (TCS) is a genetic disorder resulting in craniofacial malformation. Anomalies of the external and middle ear have been described but there is hardly any literature on inner ear anomalies. Anecdotally, inner ear anomalies have been noted in TCS patients. This project seeks to retrospectively look at inner ear anomalies in TCS patients.

Materials and Methods

Retrospective study of 47 patients with Treacher Collins Syndrome with thin section imaging through the ears. Imaging was reviewed by two neuroradiologists for a consensus on the presence of inner ear anomalies.

Results

An inner ear anomaly was detected in 22/47 patients with most of the anomalies involving the semicircular canals. To a lesser extent oval window atresia and round window atresia was noted, especially in patients with severe middle ear hypoplasia.

Conclusions

Despite the lack of literature, inner ear anomalies are present in a significant proportion of TCS patients.

1530

Intracerebral Hemorrhage Markers and the Dynamic Spot Sign

M Truong[1]
[1]*Royal Adelaide Hospital / Jones Radiology, Adelaide, South Australia*

Purpose

Intracerebral hemorrhage (ICH) has a high mortality rate of >40% at 30 days. Enlargement of the hematoma, termed hematoma expansion, is a well documented determinant of mortality and poor clinical outcome. There remains an unmet need for reliable imaging predictors of HE, particularly on non-contrast computed tomography (NCCT), which is requisite for the acute diagnosis of ICH. Our study is the first to assess the association between the non-contrast CT hematoma markers and the dynamic spot sign on CT perfusion (CTP). Recently, CTP has been shown to have greater sensitivity and specificity for the spot sign than single phase CTA. Our secondary outcomes were the associations of hematoma expansion, poor clinical outcome and in-hospital mortality.

Materials and Methods

Over an 18 month period, 282 consecutive patients presented with ICH to our comprehensive stroke centre. Of these, 85 patients underwent the stroke imaging protocol and were included in the study. 55 of these patients had a follow up NCCT within 24 hours and were included in our expansion analysis. Two raters independently assessed the baseline NCCT for hematoma markers. CTP scans were assessed concurrently by both raters on a MIStar workstation for the presence of the dynamic spot sign. A dynamic CTA was reconstructed from the whole brain CTP and time-density curves at specific regions of interest were generated. Multivariate logistic regression analyses were performed with adjustment for known ICH expansion predictors.

Results

Heterogeneous density was the only NCCT haematoma marker to be associated with the dynamic spot sign after multivariate analysis (odds ratio, 58.61; 95% confidence interval, 9.13–376.05; $P < 0.001$). All patients who had a dynamic spot sign also had a concurrent swirl sign. The dynamic spot sign was the most important predictor of significant haematoma expansion (odds ratio, 36.6; 95% confidence interval, 2.51–534.2; $P = 0.008$). The co-located spot sign was the greatest predictor of in-hospital mortality (odds ratio, 6.17; 95% confidence interval, 1.09-34.78; $P = 0.039$).

Conclusions

Heterogeneous density and the swirl sign were the most significant predictors of the dynamic spot sign. The swirl sign requires prospective validation and has the potential to guide patients to additional post contrast imaging. A co-located hypodensity and dynamic spot sign is an ominous combination, predictive of in-hospital mortality

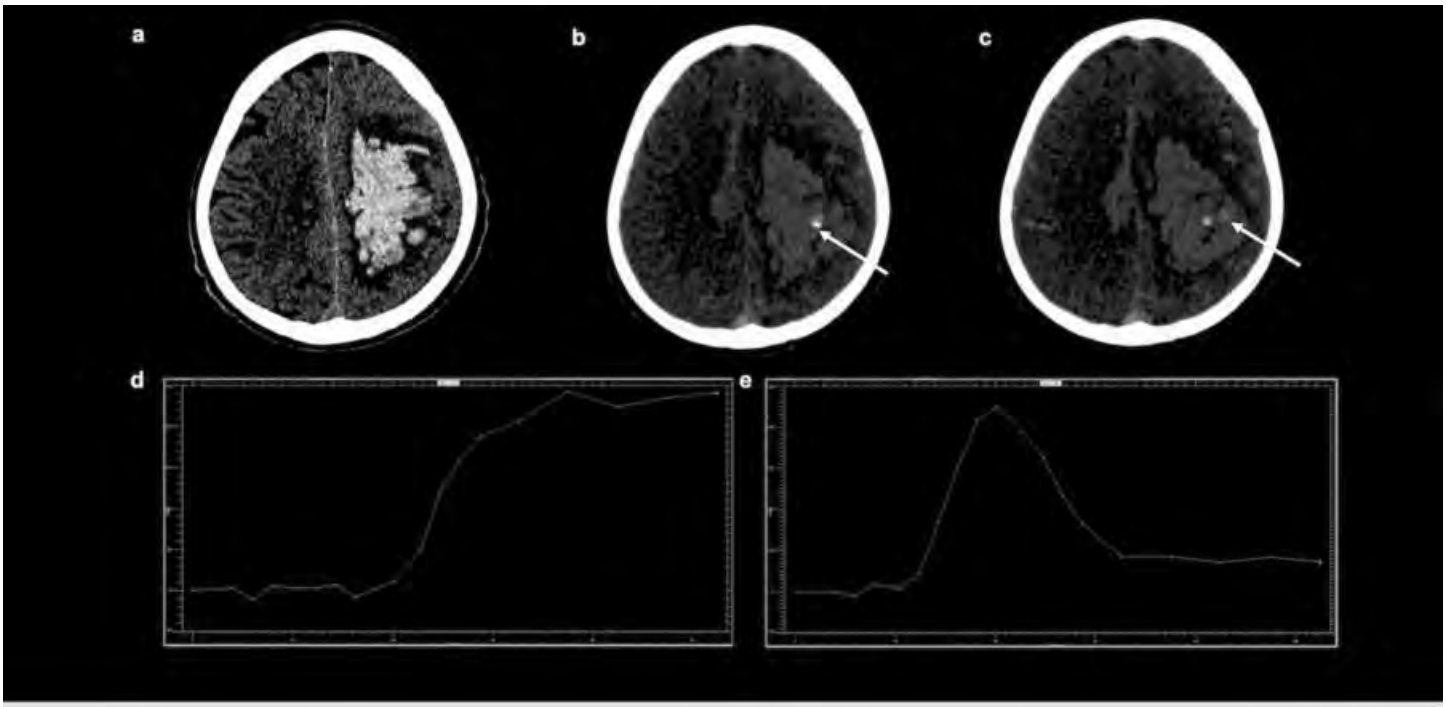

This is an example in which CT perfusion is able to discriminate between a dynamic spot sign and its mimics.
An intracerebral hemorrhage (**a**) demonstrates two foci of contrast enhancement on CTP (shown in b and c).
The medial focus (arrow in b) is further scrutinized with a region of interest and the density is measured over time. The attenuation pattern (shown by the graph in d) is a crescendo of increasing density throughout the scan period suggestive of active contrast extravasation and characteristic of a dynamic spot sign.
In contradistinction, the second focus of contrast (arrow in c), demonstrates a rapid increase and decrease in density that returns to the baseline Hounsfield unit (**e**) and is consistent with a vessel

(Filename: TCT_1530_Imageexample.JPG)

1195

Intravoxel Incoherent Motion (IVIM) MRI: Evaluation of the Effect of Intravenous Gadolinium-Based Contrast Media

L Wang[1], Z Cai[1], Q Ai[2], A Jill[1], Z Yu[1], W Chen[1], T So[1]
[1]The Chinese University of Hong Kong, Shatin, New Territories, [2]The Hong Kong Polytechnic University, Hung Hom, KLN

Purpose
Intravoxel incoherent motion (IVIM) imaging is a quantitative imaging technique which measures diffusion and perfusion parameters using a multi-b-value diffusion weighted imaging (DWI) acquisition [1]. Similar to DWI, IVIM is usually performed before injection of intravenous contrast media. Prior studies have investigated whether the magnetic susceptibility of contrast may alter DWI apparent diffusion coefficient (ADC) values, with conflicting results. The effect of contrast on IVIM parameters has yet to be explored. The purpose of this study was to investigate the effect of intravenous gadolinium-based contrast on measured IVIM parameters (D, D*, f).
Materials and Methods
This study included 10 patients with multiple sclerosis (MS) and 10 healthy volunteers as controls. IVIM with 14 b-values was performed at 3T, immediately prior, immediately after, and 10 minutes after gadoteric acid contrast in patients with MS, and immediately after, and 10 minutes after the initial IVIM scan in controls. IVIM parameters (D, D*, f), and ADC were measured in regions of interest (corpus callosum, thalamus, caudate, pons, cerebellum). Repeated measures analysis of variance (ANOVA) and within-subject coefficient of variation (wCoV) were used to determine the differences between the parameters measured at the different timeframes.
Results
In the control group, IVIM parameters (D, D*, f and ADC) showed no significant differences between the three scans in all measured brain regions (all $p>0.05$). In the patient group, ADC values in the corpus callosum ($p = 0.02$), thalamus ($p = 0.001$) and cerebellum ($p = 0.001$) and values of f ($p= 0.03$) in the thalamus significantly altered with contrast administration.
Conclusions
No significant changes in ADC, f, D*, D measurements were observed in the control group with low wCOVs, indicating good baseline reproducibility of the technique. ADC and f showed significant difference after contrast, suggesting specific components of perfusion and perfusion may be affected by contrast administration.

1399

Investigating microstructural and macrostructural changes in association with postconcussive symptoms following mild traumatic brain injury: a longitudinal study

A Alivar[1], S Coelho[2], J Rath[1], P Amorapanth[1], E Fieremans[1], D Novikov[3], S Flanagan[1], Y Lui[4], S Chung[1]

[1]NYU Grossman School of Medicine, New York, NY, [2]NYU School of Medicine, Center for Advanced Imaging and Research, New York, NY, [3]New York University School of Medicine, New York, NY, [4]NYU Langone Health, New York, NY

Purpose

Mild traumatic brain injury (MTBI) can lead to troubling long-term consequences such as lasting postconcussive symptoms[1]. This study investigated brain microstructural and cerebral cortical changes along with postconcussive symptoms from baseline to 6 months post injury.

Materials and Methods

12 MTBI patients within 1 month of injury and 13 normal controls (NC) were studied at baseline and 6 months post injury. Symptom burden was assessed using the Rivermead Post Concussion Symptoms Questionnaire (RPQ) and Fatigue Severity Scale (FSS). Multi-shell diffusion imaging was performed using a 3T MR scanner (Prisma, Siemens) with 6 b-values (0-2.5 ms/μm2, 2.5mm iso-image resolution) and MPRAGE (1mm iso-image resolution) was performed to assess cortical volume. We calculated 11 diffusion maps of DTI and DKI (fractional anisotropy [FA], mean/axial/radial diffusivity [MD/AD/RD] and kurtosis [MK/AK/RK]) as well as compartment-specific standard model (SM) metrics (axonal water fraction [f], intra-axonal diffusivity [Da], extra-axonal axial/radial diffusivities [De_par/De_perp]) [2]. Statistical analyses were performed using tract-based spatial statistics (TBSS)[3] and MANCOVA with age and sex as covariates.

Results

RPQ and FSS values showed significant improvements at 6 months (Fig.1). Significant correlations were found diffusely between RPQ and MD, MK (Fig.2a) and also between FSS and FA, AK, RK mainly in capsular regions (Fig.2b). We also found significant differences between MTBI baseline and NC (Fig.3 Top; lower FA, higher MD,MK, De_par, De_perp,Da) as well as between MTBI baseline and 6 months (Fig.3 Middle; higher FA, lower MD,MK, De_par, De_perp,Da), while there was no difference between MTBI 6 months and NC (Fig.3 Bottom). Significant cortical volume changes were observed between MTBI baseline and NC, which appeared predominantly resolved at 6 months (Fig.4).

Conclusions

We showed that both microstructural and macrostructural brain changes were dynamic over time during a period of recovery after injury. In particular, lower FA and higher MD and De_perp in MTBI baseline are in keeping with the previous literature and likely serve as indicators of disrupted white matter integrity during this period. Though few patients remained symptomatic at 6 months, in most patients these long-term changes occurred concurrently with postconcussive symptoms, suggesting that diffusion measures along with macrostructural features serve as promising biomarkers for symptom recovery.

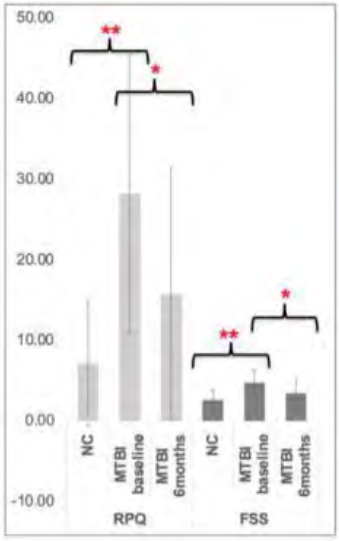

Figure 1. Changes in RPQ and FSS values over time at MTBI baseline and 6 months post injury against normal controls (NC). Rivermead Postconcussion Questionnaire (RPQ) and Fatigue Severity Scale (FSS). **(*: p<0.05, **: p<0.01)**

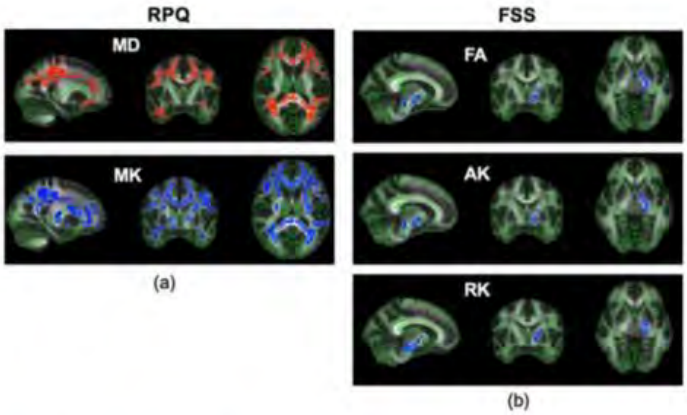

Figure 2. TBSS Correlation results of **(a)** RPQ and diffusion metrics (MD, MK) in MTBI 6months, **(b)** FSS and diffusion metrics (FA, AK, RK) in MTBI baseline. No other metrics showed significant correlation. Color indicates FA skeleton (green), significant positive correlation (Blue), and significant negative correlation (Red).

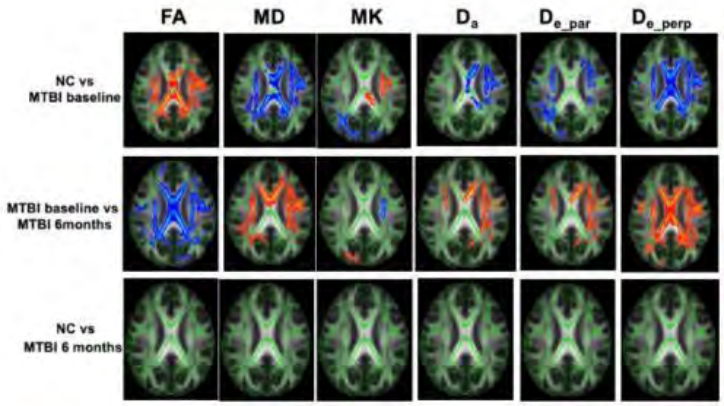

Figure 3. TBSS Comparison results of diffusion metrics (FA, MD, MK, D_a, D_{e_par}, D_{e_perp}). Blue indicates statistically significant regions where NC < MTBI baseline (**Top**), MTBI baseline < MTBI 6months (**Middle**), and NC < MTBI 6months (**Bottom**), while red indicates NC > MTBI baseline (Top), MTBI baseline > MTBI 6months (Middle), and NC > MTBI 6months (Bottom). No significant differences between NC and MTBI 6months showed, suggesting longitudinal recovery progression.

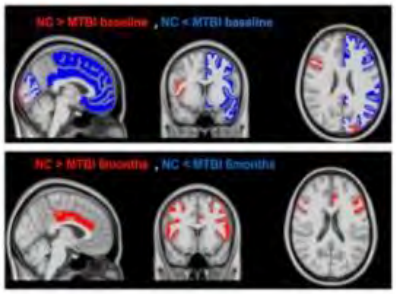

Figure 4. ROI analysis results for cortical volume changes between NC and MTBI baseline (Top) and between NC and MTBI 6months (Bottom). ROIs demonstrating significant changes at MTBI baseline (Top) included mainly the left hemisphere, while significant decrease in MTBI 6months (bottom) was found in Caudalmiddlefrontal, Parsopercularis, Caudalanteriorcingulate, and Posteriorcingulate on the left and Caudalmiddlefrontal, Parsopercularis on the right hemisphere.

(Filename: TCT_1399_Figure.jpg)

623

Large-Scale Analysis of Structure-Function Associations across Human Cortex

E Collins[1], O Chishti[2], S Obaid[3], A King[4], H Zaveri[2], D Spencer[2]

[1]MIT, Cambridge, MA, [2]Yale University, New Haven, CT, [3]University of Montreal, Montreal, QC, [4]University of California, Berkeley, Berkeley, CA

Purpose

Prior research has modeled the structure-function association of the brain using different statistical and biophysical approaches. These models have traditionally predicted whole-brain functional connectivity (FC) based on whole-brain structural connectivity (SC), assuming that structure-function association is governed by a uniform mechanism. Altogether, this motivated us to analyze how structure-function association varies across both specific cortical structures and across specific functions. We developed algorithms to merge large-scale fMRI and connectome data into a novel anatomical atlas, executed linear models to assess the extent to which SC predicts FC, and furthermore assessed how structure-function associations relate to rsfMRI and cortical thickness.

Materials and Methods

We used large-scale data repositories to analyze structure-function associations across healthy cortex. We localized fMRI activation data from Neurosynth and white matter connectivity data from Human Connectome Project into high-resolution atlas space. FC data was calculated with a custom metric that uses z-scores and word embeddings of functional terms to quantify functional similarity

between parcels. SC data was computed as a group-consensus matrix of streamline counts between parcels. We executed linear models to assess the extent to which SC predicts FC at a global level, parcel level, and functional term level.
Results
Diffusion maps of our FC data demonstrated a continuum of function, particularly along sagittal and axial directions. Moreover, FC was found to significantly correlate with rsfMRI connectivity. Globally, we found that SC variables, namely, white matter streamline count, predict FC. We found that structure-function association varies across cortex, with higher associations in unimodal cortex and lower associations in transmodal cortex. We found that structure-function association varies by functional term, with terms related to complex judgement having higher associations. Structure-function association negatively correlates with cortical thickness.
Conclusions
In the most comprehensive analysis to date, we show structure predicts function to varying degrees across cortex. We used large repositories to compute patterns of structure-function association, with higher associations in unimodal primary sensory and motor cortex and lower associations in transmodal default mode network cortex. We moreover identified a group of judgement-related functional terms with higher structure-function associations.

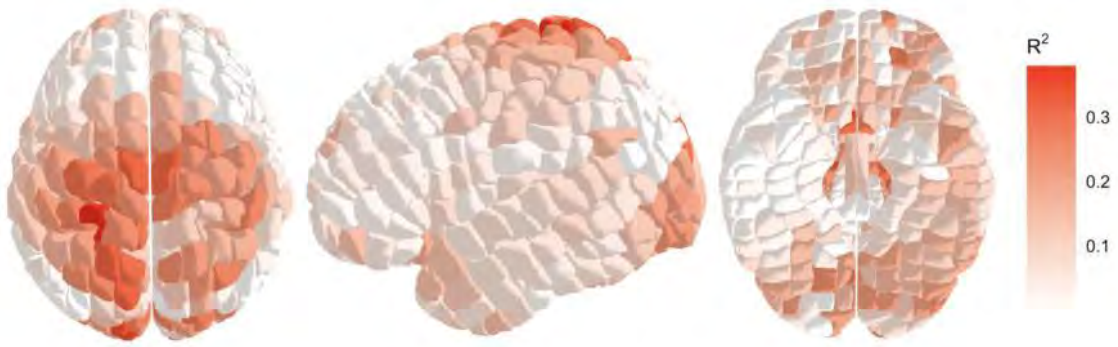

Figure 1: *Structure-function association varies by cortical localization*. The color intensity of each of the 696 parcels reflects the adjusted R^2 value for a linear model testing for the relationship between functional distance (FC) and number of white matter tracts (SC). Higher structure-function associations are primarily shown to be in unimodal primary sensory and motor cortex. Lower structure-function associations are primarily shown to be in transmodal default mode network cortex.

(Filename: TCT_623_ASNR_2023_Evan_Collins_Fig1.jpg)

553

Machine Learning Based on MRI Radiomics Features for the Diagnosis of Autism Spectrum Disorder

Q Chen[1], J Yu[1], X Cao[2]
[1]Department of Nuclear Medicine, The Fifth Affiliated Hospital of Sun Yat-sen University, Zhuhai, Guangdong, China, [2]Department of Nuclear Medicine, The Fifth Affiliated Hospital of Sun Yat-sen University, Zhuhai, Guangdong, AK

Purpose
This study explored the accuracy of radiomics analysis based on MRI images for the diagnosis of autism spectrum disorder (ASD) to provide additional data for clinical intervention.
Materials and Methods
A total of 242 participants, including autism spectrum disorder and typically developing (TD) children were enrolled in the study. T1-weighted (T1W) and T2-weighted (T2W) MRI images from before treatment were obtained. Two experts manually segmented the bilateral hippocampus, thalamus, caudate nucleus, and lenticular nucleus (putamen and globus pallidus) in the Radcloud platform. Radiomics features were extracted in four categories: first-order, shape, textural, filter, and wavelet. Least absolute shrinkage and selection operator regression analyses were used to select features. A fivefold cross-validation strategy was used to distinguish ASD children from TD children using logistic regression (LR), multilayer perceptron (MLP), and support vector machine (SVM). Three models were built: model 1 (T1WI), model 2 (T2WI), and model 3 (T1WI+T2WI). The average area under the curve (AUC) for the validation set was calculated to assess the diagnostic accuracy.
Results
Each participant had 4013 radiomics features extracted from the T1WI and 2900 radiomics features extracted from the T2WI. The mean classification accuracy achieved with LR classifiers to discriminate ASD patients from control subjects was 81.2%. Furthermore, radiomics features associated with clinical scale scores of ASD are primarily found in the left thalamus and right lenticular nucleus.
Conclusions
These findings support the hypothesis that radiomics analysis can detect MRI changes associated with ASD core symptoms. Therefore, the radiomics-based machine-learning model offers a promising new biomarker for the diagnosis of autism spectrum disorder.

1050

Machine Learning to Predict Hearing Preservation After Middle Cranial Fossa Approach for Sporadic Vestibular Schwannomas

L Wojdyla[1], M McDonald[1], M Schwartz[1]
[1]UC San Diego Health, San Diego, CA

Purpose

The primary advantage of the middle cranial fossa (MCF) approach in the context of microsurgery for vestibular schwannomas (VS) is in hearing preservation for small intracanalicular tumors. Identifying patients most likely to benefit is critical to achieving an ideal outcome, which includes gross total resection, preservation of hearing and facial function, and avoidance of complications. Factors considered in the selection of MCF approach candidates includes tumor size and location, patient age, and pre-operative hearing (1-4). In reality, the probability of a good outcome is influenced by complex and often non-linear interactions between these and other factors that are difficult to characterize with traditional statistical techniques. We sought to apply supervised machine learning techniques to identify patient and tumor characteristics associated with hearing preservation after MCF approach for sporadic VS.

Materials and Methods

144 patients underwent MCF approach resection of an untreated sporadic VS at a single tertiary referral center. Supervised machine learning algorithms were used to predict whether the patient experienced hearing preservation. 39 patient and tumor characteristics measured prior to surgery were considered as candidate predictors for machine learning models, including tumor dimensions and position within the internal auditory canal (IAC). The primary outcome was hearing preservation. Model performance was evaluated with classification accuracy in an independent validation sample. Variable importance for the random forest model is reported according to entropy, a measure of mean decrease in model accuracy incurred by excluding each variable from the model.

Results

Hearing preservation was achieved in 60% of patients (86/144). The classification and regression tree model identified more posterior tumor positions and baseline pure tone average with a cut point of 30 dB HL to be the most important prognostic features for hearing preservation (model accuracy 0.68). The random forest model identified anteroposterior tumor position, baseline pure tone average, and word recognition score among the most influential features for hearing preservation prediction (model showed perfect accuracy).

Conclusions

Machine learning algorithms have the potential for accurate prediction of hearing preservation rates after MCF approach for VS at a single institution. These models have the capacity for continued refinement with ongoing addition of data.

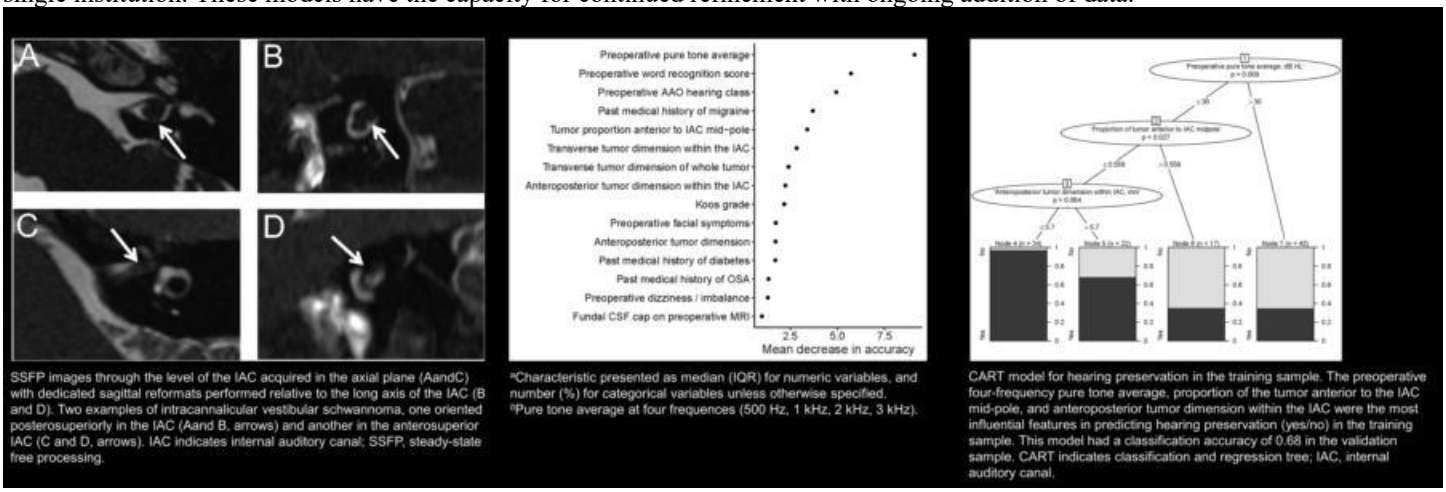

SSFP images through the level of the IAC acquired in the axial plane (AandC) with dedicated sagittal reformats performed relative to the long axis of the IAC (B and D). Two examples of intracannalicular vestibular schwannoma, one oriented posterosuperiorly in the IAC (Aand B, arrows) and another in the anterosuperior IAC (C and D, arrows). IAC indicates internal auditory canal; SSFP, steady-state free processing.

[a]Characteristic presented as median (IQR) for numeric variables, and number (%) for categorical variables unless otherwise specified. [b]Pure tone average at four frequences (500 Hz, 1 kHz, 2 kHz, 3 kHz).

CART model for hearing preservation in the training sample. The preoperative four-frequency pure tone average, proportion of the tumor anterior to the IAC mid-pole, and anteroposterior tumor dimension within the IAC were the most influential features in predicting hearing preservation (yes/no) in the training sample. This model had a classification accuracy of 0.68 in the validation sample. CART indicates classification and regression tree; IAC, internal auditory canal.

(Filename: TCT_1050_Graphic.jpg)

626

Meningioma Grading via Diagnostic Imaging - A Systematic Review and Meta-Analysis

T Upreti[1], S Dube[2], V Pareek[1], A Chin[1], N Sinha[1], J Shankar[1]
[1]University of Manitoba, Winnipeg, Manitoba, [2]University of Winnipeg, Winnipeg, Manitoba

Purpose

Meningioma grading is essential in determining disease course for patients; with high grade (HG) having a worse prognosis. Current World Health Organization (WHO) grading depends on histopathological analysis of tumour. Radiology based grading can overcome the surgical risk of sampling and can expedite treatment planning to improve outcomes. Therefore, our study aims to systematically review reports on diagnostic imaging used to differentiate HG from LG meningioma.

Materials and Methods

Three databases were searched for primary research that reported either magnetic resonance imaging (MRI) or computed tomography (CT) use in grading pathologically WHO graded meningiomas. Preferred Reporting Items for Systematic Reviews and Meta-Analyses checklist was followed. Two investigators independently screened and extracted data from included studies with conflicts resolved via consensus. Data for each identified imaging feature was pooled into HG or LG category for measuring diagnostic accuracy.

Results
24 studies met our inclusion criteria. We identified 13 significant ($p<0.05$) CT and MRI features for differentiating HG from LG meningioma. Mass effect had the highest sensitivity (80.95%) and negative predictive value (90.7%) of all imaging features. Cystic change had the highest specificity (93.44%) and irregular tumour-brain interface had the highest positive predictive value (65.00%). The heterogeneity of tumour was most accurate at identifying HG meningioma (80.58%). Irregular tumour-brain interface and heterogeneity of tumour had the highest AUC values of 0.788 and 0.766, respectively.
Conclusions
Our study identified numerous significant CT and MRI features that can differentiate HG from LG meningioma. Although multivariable analysis was not performed, some features individually showed high measures of diagnostic accuracy. Thus, highlighting the potential of diagnostic imaging in prompt the grading of meningioma and prevent any delay in treatment planning for HG meningioma.

Table 1. The diagnostic accuracy of identified imaging features at differentiating high grade from low grade meningioma.

Imaging Feature	Sensitivity	Specificity	Positive Predictive Value	Negative Predictive Value	Accuracy	AUC
Peritumoral Edema*	70.13%	56.05%	31.4%	86.74%	59.19%	0.631
Location*	70.75%	47.37%	29.41%	83.94%	52.90%	0.591
Tumour Enhancement*	62.67%	76.32%	53.71%	82.33%	72.15%	0.695
Irregular Margins*	45.6%	85.02%	46.63%	84.48%	76.23%	0.653
Calcification of Tumour*	26.56%	87.17%	36.56%	81.01%	73.98%	0.569
Dural Tail Sign*	72.73%	45.18%	22.86%	88.12%	50.21%	0.589
Cystic Change*	29.17%	**93.44%**	63.64%	77.03%	75.29%	0.613
Hyperintense on DWI*	79.59%	59.87%	38.24%	90.38%	64.56%	0.697
Heterogeneity of tumour*	67.86%	85.33%	63.33%	87.67%	80.58%	**0.766**
Capsular Enhancement*	43.24%	25.57%	19.63%	51.72%	30.80%	0.344
Mass effect*	**80.95%**	47.56%	28.33%	**90.7%**	54.37%	0.643
Irregular Tumour-Brain Interface*	76.47%	81.21%	**65.00%**	88.32%	**79.72%**	**0.788**
Tumour Necrosis*	44.07%	88.41%	61.9%	78.71%	75.13%	0.662
Hypointense on T1 MRI	45.31%	63.64%	37.66%	70.59%	57.65%	0.545
Hyperintense on T2 MRI	66.67%	32.2%	29.82%	69.09%	42.60%	0.494
Reactive Hyperostosis	26.42%	63.19%	17.28%	74.68%	54.89%	0.448
Skull Invasion	18.52%	84.81%	22.06%	81.77%	72.33%	0.517

Abbreviations: DWI = Diffusion weighted imaging, ADC = Apparent diffusion coefficient
* Imaging feature with p-value <0.05 for differentiating high grade from low grade meningioma

(Filename: TCT_626_MeningiomaSRTableImage.jpg)

1432
Modelling the Discriminative Value of rCBV in Distinguishing Pseudoprogression and Progression in Glioblastoma
E Gaudette[1], M Schmidt[2]
[1]Faculty of Medicine, Dalhousie University, Halifax, Nova Scotia, [2]Department of Diagnostic Radiology, Dalhousie University, Halifax, Nova Scotia

Purpose
Glioblastoma multiforme (GBM) is the most common primary brain tumor in adults. After treatment, up to 30% of patients display new gadolinium enhancement on MRI that closely resembles tumor progression (TP). This is termed "pseudoprogression" (PsP).1,2 Perfusion-weighted MRI helps to distinguish between PsP and TP. However, the interpretation of perfusion-weighted MRI is usually qualitative, and diagnostic performance is variable. The goal of this project was to segment enhancing tissue after treatment, measure the relative cerebral blood volume (rCBV) within this tissue and assess its ability to classify the enhancement correctly as TP or PsP.
Materials and Methods
This study was approved by the local research ethics board and made secondary use of data collected from the University of

Pennsylvania GBM Cohort (UPenn-GBM), made available through The Cancer Imaging Archive.3-5 The subset of data from the UPenn-GBM cohort that was used included all patients who had follow-up MRI scans within 15 days of a second surgical resection, due to radiographic changes concerning for tumor recurrence. Histopathologic confirmation of tumor status was completed by board-certified neuropathologists. ITK-SNAP software (version 3.8.0) was used to segment enhancing tumor and to quantify the mean rCBV intensity in the segmented volume. Values from each scan were normalized to the corpus callosum. A receiver operating characteristic curve (ROC) analysis was performed to assess the ability of mean rCBV to classify enhancement correctly as PsP.
Results
After excluding participants with poor image quality and missing perfusion scans, the total sample size was N=48. The sample contained 5 cases of PsP and 43 cases of TP. The area under the ROC (AUC) was 0.754 (p=0.001), demonstrating moderate classification ability. The cut-off for mean rCBV value was 52.7 a.u. below which PsP was the predicted outcome with a sensitivity of 0.55 and a specificity of 1.
Conclusions
Measurement of rCBV in enhancing portions of treated GBM has moderate ability to classify the enhancement as TP versus PsP. Incorporation of additional contrasts such as apparent diffusion coefficient may improve classification. The small number of confirmed PsP cases that were available for analysis is a limitation of this study.

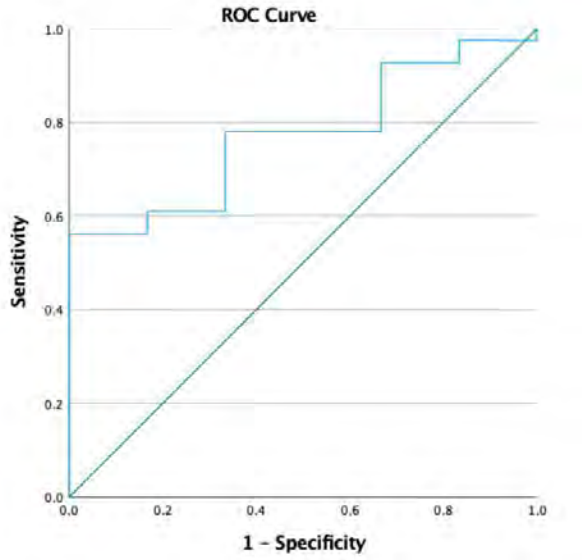

(Filename: TCT_1432_MeanrCBVETROCCurve.jpg)

632

MR Perfusion Collateral Index Predicts Infarct Growth in Acute Ischemic Stroke

M McArthur[1], S KIHIRA[2], E Tavakkol[2], B Salehi[3], M Linetsky[2], L Ledbetter[4], M Bahr-Hosseini[2], J Villablanca[2], R Jahan[2], g duckwiler[5], J Saver[2], D Liebeskind[6], K Nael[2]

[1]University of California Los Angeles, Los Angeles, CA, [2]UCLA, Los Angeles, CA, [3]UCLA, Los angeles, CA, [4]David Geffen School of Medicine, Los Angeles, CA, [5]ucla, Los Angeles, CA, [6]UCLA Stroke Center, Los Angeles, CA

Purpose
Collateral status is an important variable in patients with acute ischemic stroke (AIS) and correlates with infarction growth (1). The Perfusion Collateral Index (PCI) obtained from MR perfusion has been shown to assess angiographic collaterals (2). In this study, we aim to evaluate the ability of PCI to predict infarction growth in a cohort of patients who underwent timely successful recanalization.
Materials and Methods
AIS patients with anterior circulation large vessel occlusion (LVO) who underwent endovascular treatment were included if they met the following inclusion criteria: 1) pre-treatment MRI including perfusion, 2) successful recanalization (TICI >2a) within 2 hours from MRI, and 3) post-treatment MRI to calculate final infarction volume. PCI defined as the volume of moderately hypoperfused tissue (2 sec < delay time < 6 sec) multiplied by its corresponding relative cerebral blood volume (rCBV) was calculated from pretreatment MR perfusion data using Olea Sphere® software (SP.23, Olea Medical) (2). Infarct growth was determined by subtracting the pre-thrombectomy infarct volume on ADC from the 24 hr post-thrombectomy infarct volume on DWI. The association between infarct growth and PCI was assessed.
Results
Thus far, 39 patients are included: 16 male; age (mean +/- SD): 70.6 +/- 12.2 years; NIHSS (median, IQR) 14, 7-21. The mean +/- SD was 118.2 +/- 90 for PCI and 19.3 +/- 55.4 mL for the infarct growth. Despite successful recanalization (TICI >2a) in less than 2 hours from MRI, 14 patients (36%) showed infarction growth of >20mL. ROC analysis of PCI for determination of infarction growth >20mL revealed 0.80/85.7%/84% (AUC/sensitivity%/specificity%) at threshold of 60 (figure). Infarction growth more than 20 mL was noted in 2/23 patients (9%) with good collaterals (PCI >60) and 12/16 (75%) among patients with inadequate collaterals (PCI <60) (p=0.001).

Conclusions
Collaterals evaluated by baseline MR-PCI predict infarction growth in AIS patients with anterior circulation LVO stroke despite timely and successful recanalization.

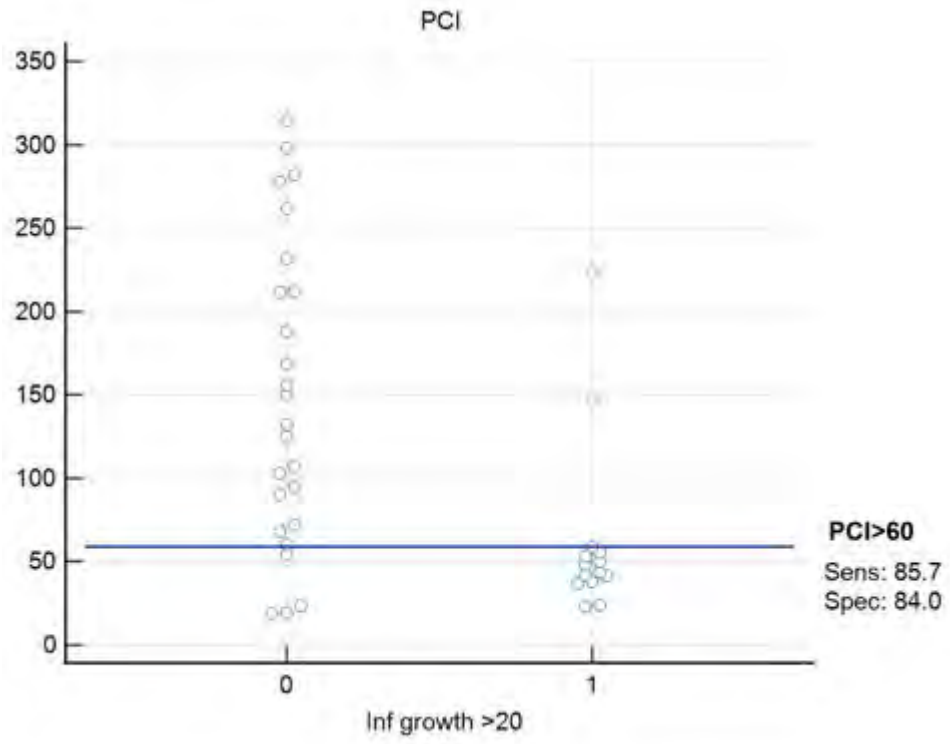

(Filename: TCT_632_MR-PCIGraphic.jpg)

1422

MRI-Based Prediction of Clinical Improvement Following Ventricular Shunting for Normal Pressure Hydrocephalus (NPH) using Artificial Intelligence: Assessment of Model Performance in 241 Patients

O Leary[1], Z Jiao[1], Z Zhong[1], L Bi[1], S Sayied[1], G Riccardello[1], H Bai[2], P Klinge[1], J Boxerman[3]
[1]Warren Alpert Medical School of Brown University, Providence, RI, [2]Johns Hopkins Univeristy School of Medicine, Baltimore, MD, [3]Rhode Island Hospital / Brown University, Providence, RI

Purpose
Here, we propose an imaging-based artificial intelligence (AI) method to assess the likelihood of symptomatic improvement of normal pressure hydrocephalus (NPH) patients from pre-treatment T2- and FLAIR- weighted MRI scans. Improvement is assessed across multiple functional outcome categories important to disease prognosis and outcome.
Materials and Methods
241 NPH patients who underwent ventricular shunt placement and baseline MRI scanning at a single institution between March 2014 and December 2021 were retrospectively identified. Functional improvement in global modified Rankin Scale (mRS) and in each component of the classical symptom triad for diagnosis of NPH (continence, gait, and cognition) was determined based on clinical documentation by the treating surgeon ≥ 12 months postoperatively. For the T2-based and FLAIR-based models, 40 and 56 patients were excluded, respectively, due to a lack of MRI scans or one-year follow-up results. All scans were pre-processed by the standard steps to get skull-stripped brains. Then, state-of-the-art 3D deep residual neural network models were built on T2 and FLAIR images for each improvement category. Finally, the prediction based on two sequences was fused by additional network layers to obtain combined results. For all models, patients who were scanned from 2014 to 2019 were used for parameter optimization, while scans of 2020 and 2021 were used for independent testing.
Results
The T2-based models achieved AUROC values of 0.5899, 0.7386, 0.6689, and 0.5713 on the prediction of mRS, continence, gait, and cognitive tasks, while the FLAIR-based models achieved AUROC values of 0.6607, 0.7611, 0.7611, and 0.6627. The combination of T2 and FLAIR imaging into a fused model further improved these values to 0.7299, 0.8158, 0.8414, and 0.6925.
Conclusions
Application of an AI algorithm leveraging baseline T2-weighted and FLAIR MR imaging together offered optimized imaging-based prediction of postoperative shunt outcome in NPH. Across the four outcomes of interest, models generally performed best for prediction of gait and continence improvement, and worst at predicting improvement in overall function status and cognition. Future models should incorporate clinical variables such as comorbidity burden and baseline symptom severity to further optimize performance.

912

Multi-delay Arterial Spin Labelling technique - A Novel paradigm in the evaluation of flow patterns in Chronic Cerebral Venous Sinus Thrombosis.

s mangalore[1], K Kulanthaivelu[2], P G V N[3]

[1]NIMHANS, bangalore, India, [2]National Instituite of Mental Health and Neurosciences, Bangalore, Karnataka, [3]NATIONAL INSTITUTE OF MENTAL HEALTH AND NEUROSCIENCES, BANGALORE, KARNATAKA

Purpose

To evaluate the role of the Multi-delay ASL technique in the evaluation of flow dynamics in chronic CVT cases which can provide guidance to the clinician in deciding the duration of the anti-coagulation treatment.

Materials and Methods

ASL protocol: Multi- labelling delay(MLD) was applied with MLD timings(in milliseconds) were T1=1500, T2=2500, T3=3500, T4=4500 & 36 slices were acquired to cover the whole brain with 8 averages per time point. Sections at the level of Superior sagittal sinus(SSS) and Straight sinus were reviewed. Structural Contrast-enhanced MRI with Phase contrast MR Venogram was done in all cases and gives the details on site of CVT, with or without Hematoma, collateral status, Whether sinus is fully/partially recanalized or there is persistent thrombus or development of Dural AV fistula. MLD-ASL findings were correlated with the clinical symptoms.Total 11 cases for which MLD-ASL data was available were included in the study and by looking at the four time points we segregated patients into 5 groups, which is as follows:Group 1-Chronic CVT with full recanalization and functionally normal or equal to the baseline,Group 2-Partially recanalized and slightly worse than the baseline,Group 3-Complete block with no recanalization but with adequate collaterals,Group 4-Complete block with no recanalization but with adequate collaterals and additional dural arteriovenous fistula,Group 5-Complete block with collaterals with retrograde venous flow,Group 6-Acute CVT cases.

Results

Described in table figure

Conclusions

Clinically group 4 & 5 cases constitute high risk groups with tendency to rupture, Structural MRI has limitations in identifying these groups and hence the need for functional imaging techniques such as Dynamic susceptibility contrast (DSC) and ASL. DSC is a semi-invasive technique and requires contrast and is contraindicated in few conditions like pregnancy and pediatric age groups etc. Hence, ASL has an important role in the work of the chronic CVT. Multi-delay ASL technique is a simple non-invasive technique in evaluating the flow dynamic changes in chronic CVT cases and can guide the neurologist in decision making about the treatment and can assess the treatment response & can identify the high risk patients.

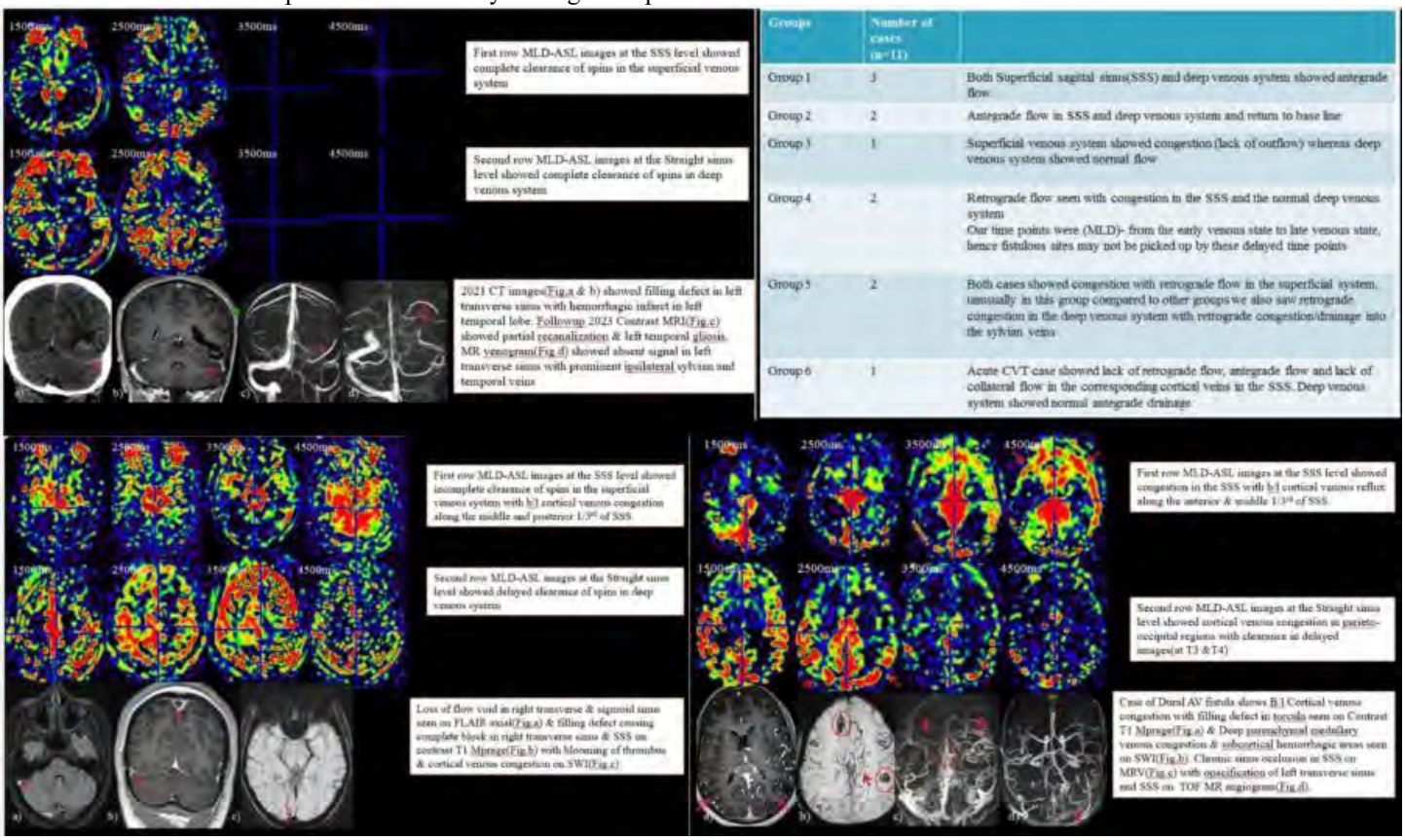

(Filename: TCT_912_final.JPG)

1157

Multiparameter 3D Image-based deep learning models for Pituitary Macroadenoma Surgical Planning and Outcomes

W Mohammed[1], Z Khokhar[2], J Kus[3], J Cunningham[4], M Kim[5], A Mallik[6]

[1]Midwestern University (CCOM), Downers Grove, IL, [2]Loyola University, Maywood, IL, [3]Loyola University Medical Center, Maywood, IL, [4]Loyola Stritch School of Medicine, Maywood, IL, [5]Loyola Medical Center, Maywood, IL, [6]Loyola University Medical Center - Strich School of Medicine, Maywood, IL

Purpose

MRI is a crucial tool for pituitary macroadenoma (PA) resection planning. Pituitary imaging is the basis for current clinical criteria to assess complexity of cases and extrapolate patient outcomes, e.g., Knosp criteria for predicting cavernous sinus invasion (CSI). We apply an image-based 3D deep learning model to predict the following factors correlated with resection: including CSI, tumor hardness, adherence to other structures, gross total resection itself, as well as the most common intraoperative complication which is CSF leak. To our knowledge, this is the first imaged based predictive model for predicting multiple factors for affecting resection and complications.

Materials and Methods

Data from 87 patients was extracted after inclusion and exclusion criteria were applied to consecutive PA patients operated by 3 neurosurgeons. Pre-operative images and operative data were reviewed, and the Knosp criteria and percent encasement of the internal carotid artery (PEICA) were assessed. Presence of CSI, tumor hardness, adherence to adjacent structures, gross total resection and CSF leaks during endoscopic surgery were used as the primary predictive outcome. Tumor hardness was also evaluated with masson trichrome histologic staining. Keras/Tensorflow (Python) was used to design 3D convolutional neural network (CNN) models, with standard 70/30% training and test cohorts.

Results

Our 3D CNN models demonstrated high accuracy (< 90%) for CSI, intermediate accuracy for CSF leak (>80%, <90%), and modest accuracy (>70%, <80%), for other predictive parameters.

Conclusions

Variability in predictive parameters may be due to the relative impact of tumor intrinsic factors (CSI, tumor hardness), versus extrinsic factors (operating neurosurgeon). The performance of deep learning models with relatively few cases is promising for a rapid, accurate multiparameter patient profile that can be used for operative planning and stratification. This also lays the groundwork more broadly applicable models validated with larger, multisite data sets.

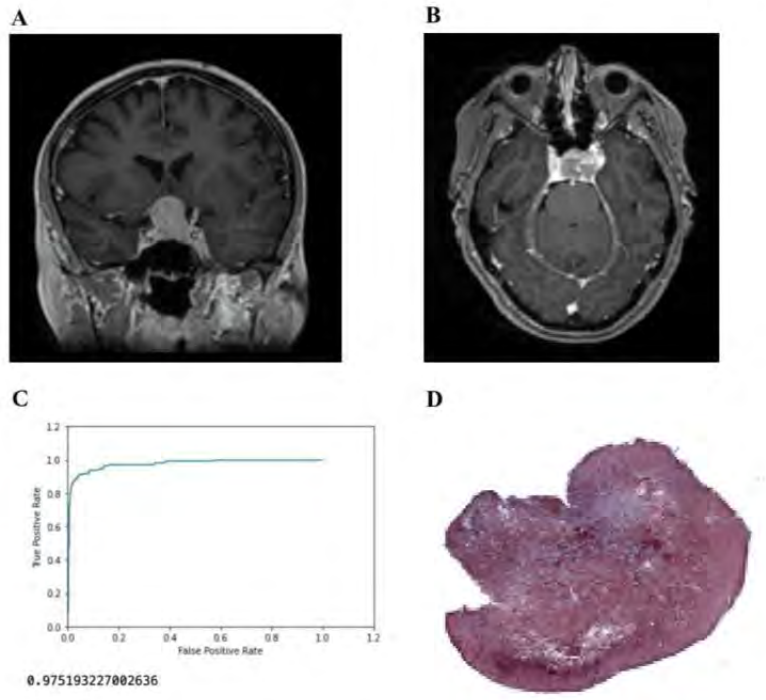

Figures: A. Coronal 3D postcontrast image demonstrates a pituitary macroadenoma with left cavernous sinus invasion. **B.** Axial 3D postcontrast image demonstrates the field of view for the image-based CNN models. **C.** Sample validation ROC curve for the Cavernous Sinus Invasion CNN model. Test accuracy is reported in the Findings. **D.** Masson trichrome stain demonstrates (blue) collagen corresponding with a fibrous, hard tumor that was difficult to resect

(Filename: TCT_1157_CSIabstractfigure.jpg)

403

Multiparametric Machine Learning Algorithm for Head CT Outcome Prediction in Pediatric TBI Utilizing Social Determinants of Health

M Vejdani-Jahromi[1], A Gunawan[1], A Kaliaev[1], M Abdalkader[1], B Setty[1], C Farris[1], C Takahashi[1], A Mian[1]
[1]*Boston University Medical Center, Boston, MA*

Purpose
Considerable socioeconomic disparities exist among pediatric traumatic brain injury (TBI) patients. The aim of this study is to create a novel machine learning algorithm that incorporates social determinants of health to accurately predict the likelihood of a clinically relevant trauma-related finding on head computed tomography (CT). This algorithm would guide clinical decision-making regarding the use of CT in high-risk populations of pediatric patients.
Materials and Methods
A cohort of blunt trauma patients under age 15 who presented to Boston Medical Center between January 2006 and December 2013 (n=210) was included in this study. Multiple socioeconomic determinant variables were collected, including race, language, zip code, and insurance type as well as additional variables like Injury Severity Score (ISS), age, sex, and mechanism of injury. Feature selection was performed with the minimum-redundancy maximum-relevance (mRMR) algorithm. The cohort was split into 80% training and 20% testing held out datasets. A wide range of machine learning algorithms (total of 23 methods) was developed, trained, and tested with cross fold validation to identify the highest performing method in this setting.
Results
The greatest predictors of head CT outcome included ISS, age, insurance type and mechanism of trauma. Age of the subjects with a clinically relevant trauma-related head CT finding (mean= 4.3 years) was significantly different compared to patients without such findings (mean= 8.7 years), $p < 0.05$. These predictors were utilized for training the machine learning models. The Naïve Bayes model demonstrated the highest testing accuracy in cross fold validation (75.0%) and was used on the held-out test dataset, demonstrating an accuracy of 71.4% and an AUC of 0.79.
Conclusions
ISS and age are among the highest predictors of clinically relevant head CT findings in pediatric TBI. Younger patients less than 5 years old have a higher likelihood of clinically relevant head CT results. A novel coarse tree model was trained and tested with promising results in predicting head CT outcomes. This would be a helpful tool in guiding clinical decision making and optimizing radiation exposure for pediatric patients.

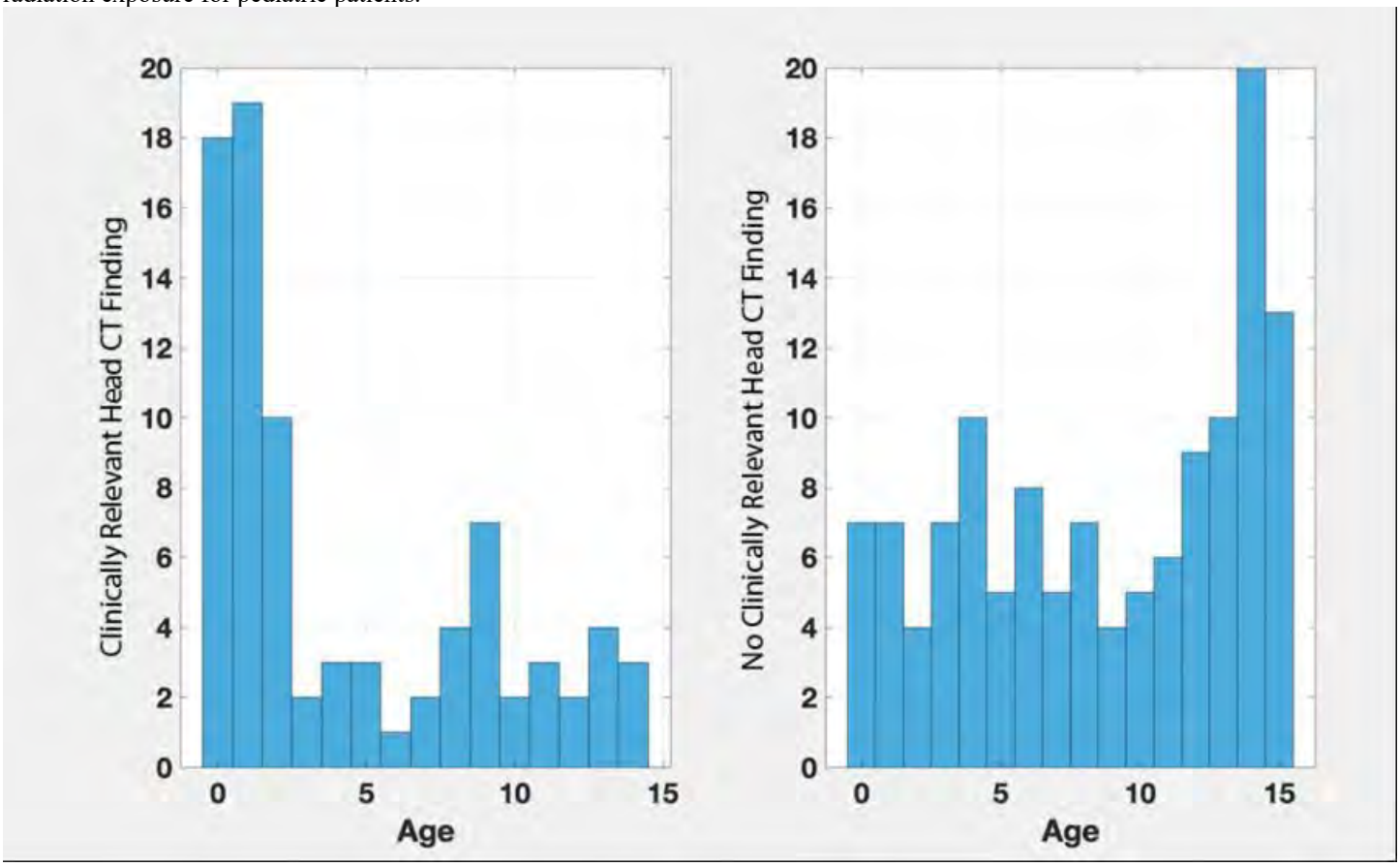

(Filename: TCT_403_Figure1.jpg)

399

Multiparametric Machine Learning Algorithm to Predict Human Papillomavirus Status and Outcomes in Oropharyngeal Cancer Patients

S Fazelpour[1], M Vejdani Jahromi[2], A Kaliaev[2], V Andreu Arasa[2], N Fujima[3], O Sakai[2]

[1]Boston University School of Medicine, Boston, MA, [2]Department of Radiology at Boston Medical Center, Boston, MA, [3]Hokkaido University Hospital, Sapporo, Hokkaido

Purpose

Oropharyngeal cancers (OPCs) originate from squamous cells, primarily from human papillomavirus (HPV), tobacco smoke, and alcohol use. Despite their high prevalence, OPCs have a comparatively poor long-term prognosis due to late detection, enabling extensive growth, lymph involvement, and metastasis. HPV status is a major factor in determining TNM staging, generally indicating a lower stage. Thus, models capable of identifying high-risk patients are critical to individualizing and improving treatment. We aim to provide a noninvasive readily available opportunity for clinical management and treatment planning of OPC patients by developing and training multiple machine learning pipelines to determine the best model for characterizing the p16/HPV status and survival of these patients utilizing multiple clinical and imaging parameters.

Materials and Methods

Multi-parametric machine learning algorithms were designed in MATLAB using a TCIA database with 492 OPC patients (58 ± 9 years, 423 men, from 2005 to 2012). Age, sex, smoking status and pack-years, drinking habits, primary tumor volume, and cancer stage according to the AJCC 7th edition classification system were incorporated for HPV status prediction. OPC outcome, determined by whether patients died from OPC complications, considered all the HPV model inputs plus HPV status. Parameter impactfulness was determined utilizing random forest. Patients were broken between 80% training and 20% testing. No significant differences were present between the training and test sets in any parameters. Algorithm efficacy was assessed through the positive and negative predictive values (PPV and NPV), accuracy, and area under the receiver operator characteristic curve (AUC). The highest testing accuracy model types from MATLAB were selected.

Results

HPV status ensemble model most depended on age, smoking pack-years, and sex, and had 90.2% TP, 50.0% TN, 74.3% PPV, 76.0% NPV, AUC of 0.79, with 74.7% accuracy. The OPCs outcome linear discriminant model considered age, smoking pack-years, and tumor volume most impactful and yielded 90.3% TP, 75.5% TN, 84.4% PPV, 84.1% NPV, AUC of 0.90, with 84.3% accuracy.

Conclusions

The model could distinguish HPV status in OPC patients and achieve high accuracy in outcome prediction, reinforcing the ability of artificial intelligence to be used for tumor characterization and outcome prediction successfully. Utilizing these algorithms enables radiologists to provide clinical guidance and optimize patient care noninvasively.

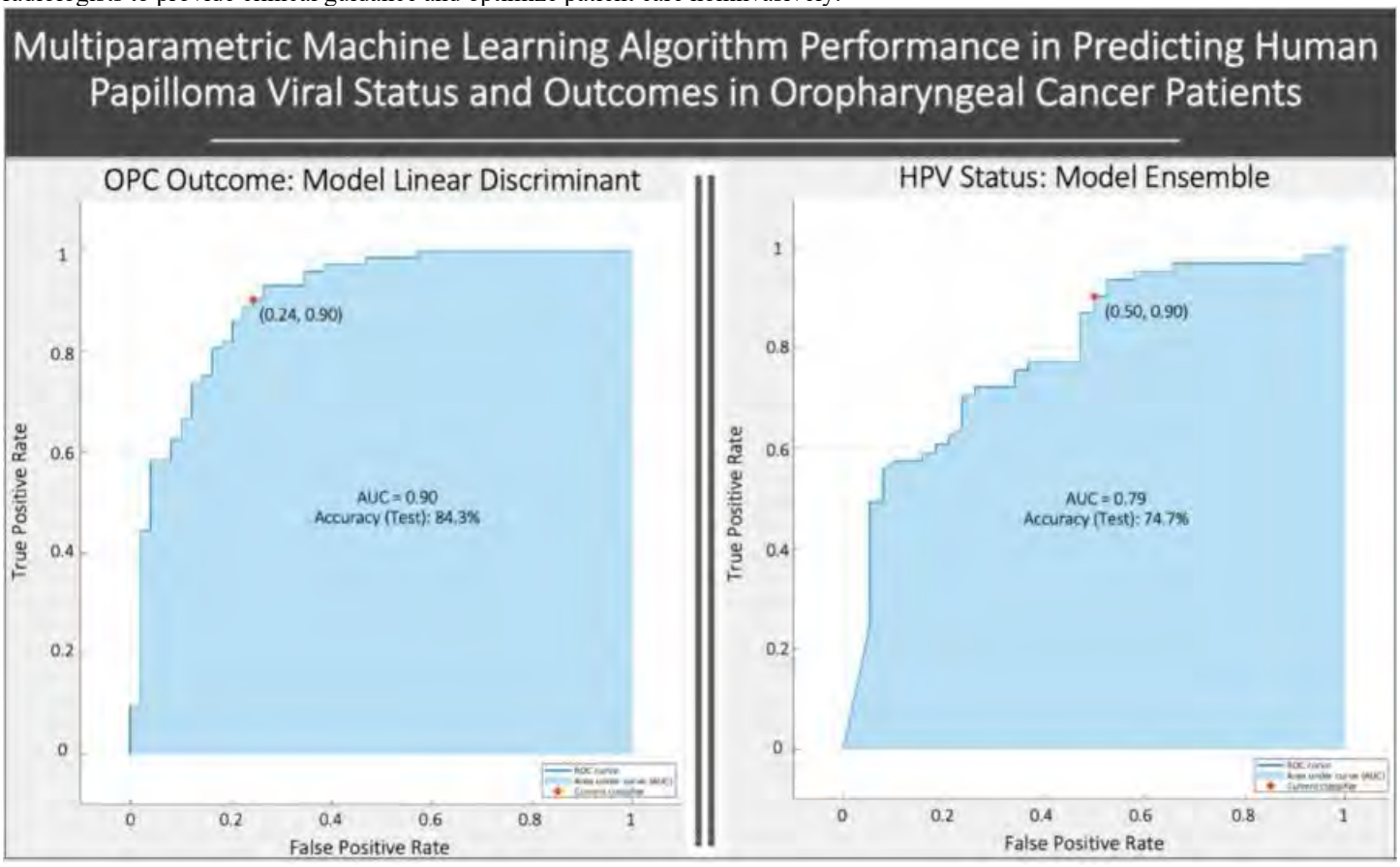

(Filename: TCT_399_AbstractMachineLearningFigure.jpg)

1413

Oculomotor Nerve Cisternal Segment Variants: MRI Mining Study

A Ahmed[1], L Tanke[2], A Desai[1], E Eggenberger[1], R Singh[1], V Gupta[1], P Vibhute[1]

[1]Mayo Clinic, Jacksonville, FL, [2]Mayo Clinic College of Medicine and Science, Rochester, MN

Purpose

The third cranial nerve, the oculomotor nerve (OMN), originates from the oculomotor nucleus, including the Edinger-Westphal subnucleus in the midbrain. It travels to the orbits via the subarachnoid space (cisternal segment), cavernous sinus (cavernous segment), and supraorbital fissure (orbital segment). Within the orbits, It is then divided into two divisions: superior and inferior (1). OMN dysfunction can be caused by a variety of conditions, including ischemia and mass lesions, the location of which can be determined based on clinical presentation (2). Here we describe four variants of the OMN cisternal segment found following MRI mining.

Materials and Methods

Our institution's MRI database was searched using Illuminate Insight™ using the terms "MRI," "Brain OR Head OR Face," and "CISS." A list of 196 MRIs were reviewed. Variants were only assessed using the 3 Tesla MRI due to its higher resolution. They were assessed on the T2-weighted constructive interference in steady-state (CISS) sequence with 0.4 – 0.75 mm slice thickness acquired in the sagittal, coronal, or axial plane. After that, multiplaner reconstruction was utilized for additional characterization.

Results

Four OMN cisternal segment variants were unraveled. The first one (the most common) was the OMN emerging as a single trunk. The second variant (seen in 2 cases) was a complete splitting of the cisternal segments. The OMN emerged as two separate roots with distinct origins form the midbrain and remained separated throughout the cisternal course until they reached the porus for OMN. The medial root was more prominent and placed slightly inferior on both sides. The third variant (seen in 3 cases) resembled the second one except that the roots rejoined just proximal (or at the level) to the posterior cerebral arteries (PCA). The fourth variant (seen in one case) was a focal OMN split at the level of the PCA.

Conclusions

The cisternal segment of the OMN has many variants with different patterns of root splits. Knowing these may explain the different presentations of OMN palsies, especially the compressive ones.

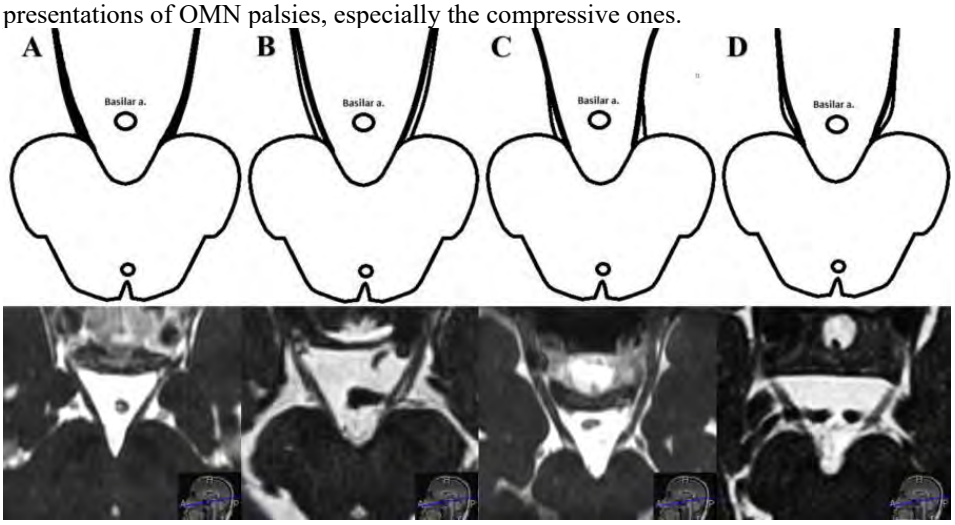

(Filename: TCT_1413_OMN_ASNR23_300dpi2.JPG)

930

Osteomyelitis/Discitis After Treatment for Head and Neck Cancer

A Bhatt[1], P Vibhute[1], X Wu[2], E Escott[3], C Chung[4], P Rhyner[5]

[1]Mayo Clinic, Jacksonville, FL, [2]UCSF Health, San Francisco, CA, [3]University of Kentucky, Lexington, KY, [4]NYU Langone Medical Center, New York, NY, [5]Mayo Clinic Jacksonville, Atlanta, GA

Purpose

Laryngectomy or pharyngectomy, surgical resection options for advanced laryngeal or pharyngeal squamous cell carcinoma (SCCA), may be closed by primary closure or with flap reconstruction. Neopharyngeal breakdown and ulceration with subsequent fistula formation, with or without recurrence, is a rare and underrecognized complication. Osteomyelitis and discitis may result especially when the ulceration occurs on the posterior neopharyngeal wall. The purpose of this retrospective clinical series is to describe 9 patients who developed discitis/osteomyelitis following laryngectomy for tumor resection, reconstruction, and adjuvant radiation.

Materials and Methods

IRB approval was obtained. Databases were searched for "laryngectomy," "pharyngectomy," "discitis" or "osteomyelitis." EMR were reviewed and confirmed cervical osteomyelitis/discitis after laryngectomy or pharyngectomy.

Results
9 patients were identified, 7 M/ 2 F, age range 60-78 years, average age 65.9 years. All patients had undergone surgical resection for SCCA of the larynx (8/9) or hypopharynx (1/9). All were treated with adjuvant radiation. 6/9 required post-treatment esophageal or neopharyngeal stricture dilatation. Most presented years after surgery with new compression fracture, neck pain, or arm pain. All had serologic evidence for infection. Delay to diagnosis following signs/symptoms of infection was as long as 18 months. Imaging showed edema and phlegmonous changes around the flap. Extraluminal air was misinterpreted as neopharyngeal air, but reformations showed air in small prevertebral collections. Characteristic CT and MRI findings of osteomyelitis and discitis were present in all. In 5 cases the findings were missed, or misinterpreted as recurrent tumor.
Conclusions
Osteomyelitis/discitis is a rare but frequently underrecognized complication of laryngectomy/pharyngectomy. Neck pain, fever and serologic evidence for infection should prompt careful assessment for extraluminal air, and soft tissue or osseous infections. In our series, most patients with neopharyngeal perforation and spinal infections had undergone prior esophageal or neopharyngeal dilatations for post-treatment stricture.

1123

Overestimation of Ischemic Core on Baseline MRI in Acute Stroke: A Case Series

M McArthur[1], S KIHIRA[2], E Tavakkol[2], J Villablanca[2], M Bahr-Hosseini[2], R Jahan[2], g duckwiler[3], J Saver[2], D Liebeskind[4], K Nael[2]
[1]University of California Los Angeles, Los Angeles, CA, [2]UCLA, Los Angeles, CA, [3]ucla, Los Angeles, CA, [4]UCLA Stroke Center, Los Angeles, CA

Purpose
Overestimation of ischemic core on CT perfusion, also known as ghost core, has been reported in acute ischemic stroke (AIS) particularly within a short time-window from stroke onset (1). In addition, overestimation of ischemic core on baseline diffusion MRI has been described but primarily in regions with mild (e.g. 621-760 x10−6 mm 2/s) rather than "severe" ADC ≤620 x10−6 mm 2/s that is currently used in clinical practice (2). We aimed to assess the possibility of "ghost core" on pretreatment MRI in regions with severe ADC hypointensity in AIS patients with successful recanalization.
Materials and Methods
In this retrospective study, AIS patients with anterior circulation large vessel occlusion who had pretreatment MRI, underwent successful recanalization (mTICI >2a), and had follow up MRI within 24 hours from treatment were reviewed. Baseline ischemic core volumes were evaluated with RAPID (iSchemaView) software using ADC ≤620 x10−6 mm 2/s as part of routine clinical practice. Due to rise of ADC following reperfusion, final infarction volume was assessed by manual segmentation on follow-up MRI using DWI (B1000) images. The ghost ischemic core was described as an overestimation of final infarct volume by baseline MRI of more than 10 mL (1). Baseline clinical, demographic, imaging, and procedural data were assessed in patients who had ischemic core overestimation.
Results
Out of 157 patients reviewed, six patients (4%) had overestimation of ischemic core >10mL. The baseline clinical and demographic data were: sex (4 female, 2 male); age (mean+/-SD: 57.3+/-15.5 years); NIHSS [median (IQR): 17 (5-29]; time-to-stroke symptom (TSS) [median (IQR): 73 (61-85) min]; time-to-recanalization [median (IQR): 81 (37.5-124.5) min]. All patients had TSS less than 90 minutes. Estimated ischemic core volume on baseline MRI was 110.6+/-100 mL (mean+/-SD) and final infarct volume on follow up MRI was 59.8+/-54.3 mL (mean+/-SD). The mean difference between baseline estimated core and final infarct was 50.8 mL (95%CI: -115 to +14 mL). In 2/6 patients the estimated ischemic core overestimation on initial MRI was >70mL (figure), which would have resulted in exclusion from thrombectomy using DEFUSE 3 guidelines (3).
Conclusions
Overestimation of ischemic core, also known as ghost core, is rare on low-ADC threshold MRI, but does occur in about 1 of every 25 patients in the hyperacute setting with TSS <90 minutes. Awareness of this phenomenon carries therapeutic implication for inadvertent exclusion from thrombectomy.

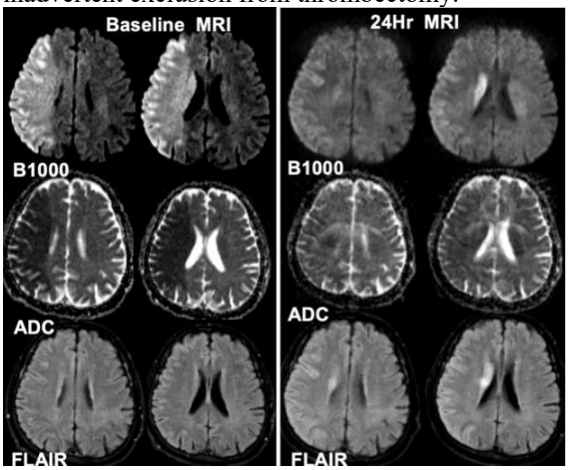

(Filename: TCT_1123_OverestimationGraphic.jpg)

693

Percutaneous Angioplasty and Stenting of Intracranial Artery Stenosis: Comparison of Wingspan Stent and Credo Stent - a Preliminary Result

T LIN[1], C Wu[2], F Chang[3]

[1]Taipei Veterans General Hospital, Taipei, Taiwan, [2]Taipei Veterans General Hospital, Taipei, Taipei, [3]Taipei Veterans General Hospital, Taipei, CA

Purpose

Compare the technical safety and outcome of Credo and Wingspan stent systems in percutaneous angioplasty and stenting (PTAS) of severe intracranial artery stenosis.

Materials and Methods

We prospectively enrolled patients of severe ICAS in our hospital receiving Wingspan and Credo intracranial stenting. All patients had received aggressive medical treatment but were refractory before PTAS evaluated. We use (1) technical success, (2) periprocedural complications, and (3) post-procedure restenosis to compare the outcome. The technical success was defined as successful stenting. The periprocedural complications include any intracranial hemorrhage and postinterventional lacunar infarction. The intracranial hemorrhage was detected by cone-beam CT immediately after stenting. The postinterventional lacunar infarction was defined as newly developed infarction, sized less than 1.5cm, located over the same vascular territory to the stenting. The post-procedure restenosis is defined as increased stenosis to more than 30% at the stenting site within 1 year after the procedure. The stenosis degree was evaluated by MRI or CT angiography by an interventional neuroradiologist with a 30-year experience.

Results

A total of 37 patients, 21 receiving Wingspan stenting and 16 receiving Credo stenting, are included. The average ages of the two groups are about 60 years old. The population is male predominance in both groups. There were no significant differences in age and gender between the two groups. The technical success was 95% in Wingspan stent, with one patient failed stenting, and 100% in Credo stent. Periprocedural complications including intracranial hemorrhage and post-procedure lacunar infarction tended to be more often in the Wingspan group compared with the Credo group, although still not reach statistical significance. The restenosis rate within one year was slightly higher in Wingspan group (19%) than the Credo group(13%).

Conclusions

In this preliminary result, the Credo stent is non-inferior to Wingspan stent in percutaneous angioplasty and stenting of severe intracranial artery stenosis, considering the technical success, periprocedural complications, and restenosis rate within one year.

	Wingspan stent group (n=21)		**Credo** stent group (n=16)		P value
Baseline demographic characteristics					
Patient no	21		16		
Age (year) (mean±SD)	59.5±18.6		60.2±14.6		0.91
Sex					0.43
Male	15	71%	14	88%	
Female	6	29%	2	13%	

	Wingspan stent group (n=21)		**Credo** stent group (n=16)		P value
Outcome					
Technical success	20	95%	16	100%	1.00
Neurological complications					
Intracranial hemorrhage	2	10%	0	0%	0.50
Periprocedural MRI (DWI)					0.39
no infaction	5	24%	7	44%	
infaction 1~5 foci	8	38%	5	31%	
infaction >=6 foci	9	43%	4	25%	
Occlusion rate during the one-year follow-up period					
restenosis after discharge from hospital (>50%)	4	19%	2	13%	0.68

(Filename: TCT_693_table.jpg)

423

Performance of an AI-based Automated Identification of Intracranial Hemorrhage in Real Clinical Practice.

A Ayobi[1], A Bani-Sadr[2], Y CHAIBI[1], S Quenet[1], M Scudeler[1], M Marx[1], F Cotton[2], P Chang[3]

[1]Avicenna.AI, La Ciotat, France, [2]Hospices Civils de Lyon, Lyon, France, [3]University California Irvine, Irivne, CA

Purpose

To evaluate the real-world performance of an FDA-cleared and CE-marked Artificial Intelligence (AI) based software for intracranial hemorrhage (ICH) detection on head non-contrast-CT (NCCT) scans at a large emergency teleradiology network.

Materials and Methods

A retrospective assessment of head NCCTs from patients admitted to several emergency departments over a time period of 2 weeks

was performed. The data was received by a teleradiology company (Telediag, Lyon, France) for interpretation. CINA-ICH v1.0 (Avicenna.AI, La Ciotat, France) was integrated into the workflow in order to flag suspected ICH findings immediately after NCCT reception. Only the data automatically processed by the device was selected. The results of the algorithm were compared to the final report of senior radiologists used as reference standard. Finally, an independent neuroradiologist reviewed the false positive and false negative cases and established the causes that could have influenced the device performance.
Results
A total of 300 NCCTs were included in the study. Of these, 2 post-contrast NCCTs were excluded. The comparison of the device's outputs (298 cases with 38 positive ICH) with the reference standard yielded a sensitivity of 97.4% [95%CI: 86.5%-99.9%], a specificity of 96.1% [95%CI: 93.%-98.1%], a PPV of 79.2% and a NPV of 99.6%. Only 1 ICH was missed (false negative) corresponding to a very subtle subarachnoid hemorrhage. Moreover, incorrect detection of ICH (10 false positives) was due to streak/motion artifacts (n = 3), hyperintense venous sinus (n = 2), parafalcorial meningioma (n = 1), falx cerebri (n = 1), chronic stroke area with no acute ICH (n = 1) and indeterminate (n = 2).
Conclusions
This study provides significant real-world data that demonstrate the potential of CINA-ICH to accurately identify life-threatening conditions such as ICH. Indeed, AI-automated ICH detection may have a positive effect on early diagnosis leading to an improvement in patient management and clinical workflow.

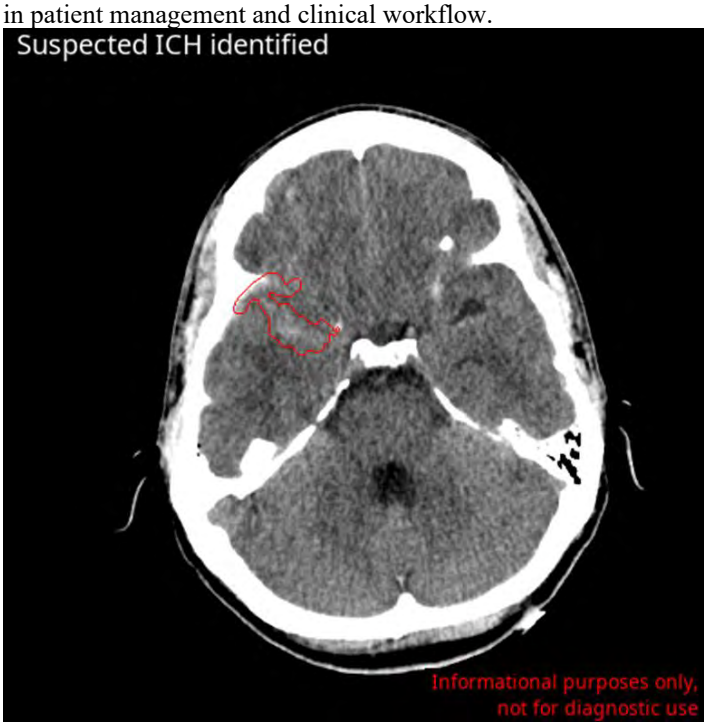

(Filename: TCT_423_image14.jpg)

1343
Postoperative Lumbar Fusion Bone Morphogenic Protein-Related Epidural Cyst Formation
F Abel[1], E Tan[1], D Sneag[1], D Lebl[1], J Chazen[1]
[1]Hospital for Special Surgery, New York, NY

Purpose
Bone morphogenetic protein (BMP) is broadly used in spinal surgery to enhance fusion rates [1]. Several complications have been associated with utilization of BMP, including postoperative radiculitis, seroma/hematoma formation, and vertebral bone osteolysis [2]. Presence of epidural cysts following BMP-augmented lumbar fusion may represent a not widely reported complication with characteristic findings on postoperative MRI.
Materials and Methods
Patients with postoperative 1.5 Tesla MRI that underwent lumbar spinal fusion and decompression surgery with rhBMP-2 bone grafting were retrospectively identified. Postoperative MRI was obtained for ongoing or new lumbosacral pain or radiculopathy. A consensus interpretation was established regarding presence of epidural cysts/fluid collections and concurrent imaging findings on the postoperative lumbar spine MRIs between 2 board-certified radiologists. Ethical approval to retrospectively review clinical, pathologic, and imaging findings was obtained at the local Institutional Review Board.
Results
Between 2016 – 2022, 16 patients (mean age: 60.1 years ± 7.7 (SD); BMI 25.8 kg/m2 ± 3.7 (SD); 7 females) with epidural cysts (Figure 1) were identified. The epidural cysts demonstrated fluid-fluid levels in 9 (56.3%) patients. In 8 (50%) patients, mass effect on the thecal sac or lumbar nerve roots was noted. Of these, 6 (37.5%) patients developed new postoperative lumbosacral radiculopathy. All of the patients with symptomatic mass effect of epidural cysts underwent either transforaminal (4/16, 25.0%) or posterior interbody lumbar fusion (4/16, 25.0%). Over the study period, the majority of patients were managed conservatively, and 1 patient

required dedicated revision surgery to remove the cyst due to persistent lumbosacral radiculopathy. Concurrent imaging findings included reactive endplate edema in 14 (88.0%) patients, vertebral bone osteolysis in 11 (69.0%) patients, and dorsal seroma formation in 11 (69.0%) patients.
Conclusions
Epidural cyst formation following BMP-augmented spinal fusion may represent an important postoperative complication with characteristic MRI findings.

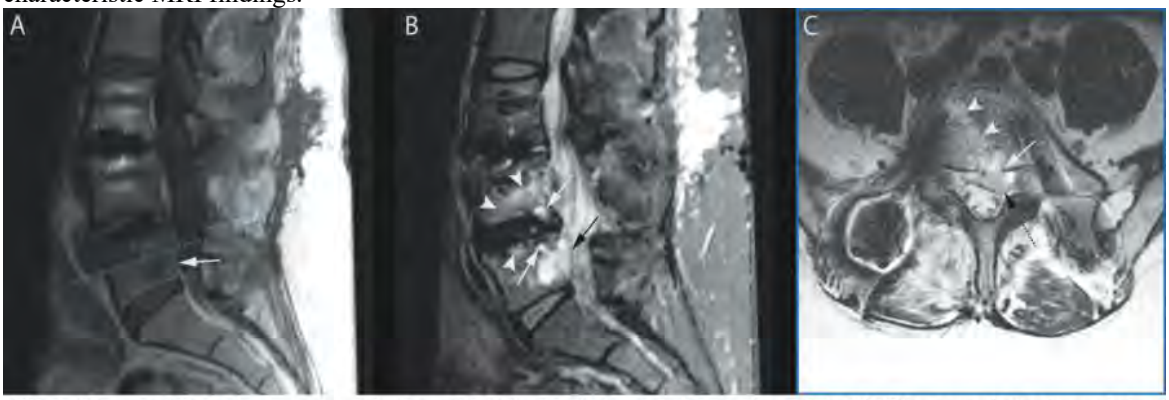

FIG 1: 56-year-old female approximately 5 months following bone morphogenetic protein (BMP)-augmented extreme lateral and transforaminal lumbar interbody fusion L3-4 to L4-5 with persistend left-sided L5 radiculopathy. A, Sagittal T1-weighted MR image of the L-spine demonstrates a hypointense epidural collection along the posterior margin of the L5 vertebral body (arrow). B, Corresponding, sagittal short-tau inversion recovery sequence shows the epidural cyst at L5 (black arrow), cystic osteolysis of the L4 and L5 vertebral bodies (white arrows) with surrounding stress reaction (arrowheads). C, Axial T2-weighted image at the L5 level (blue dashed line, A) illustrates the cyst (dashed black arrow) with a fluid-fluid level that narrows the left subarticular recess. Note the connection of the cyst to resorptive changes within the vertebral body (arrowheads) and focal interruption of the posterior longitudinal ligament (white arrow).

(Filename: TCT_1343_Fig1asnr3.jpg)

1309

Prediction of MGMT promoter methylation status in glioblastomas- Comparison of ensemble convolution neural network frameworks with transformer models

G Singh[1], M Bhattacharya[2], V Spektor[1], S Jambawalikar[3], A Lignelli[1], P Prasanna[2]
[1]Columbia University Irving Medical Center, New York, NY, [2]Stony Brook University, Stony Brook, NY, [3]Columbia University Medical Center, NY, NY

Purpose
Glioblastoma Multiforme (GBM) is a highly aggressive neoplasm and accounts for over 45% of all primary malignant tumors in the brain. Surgery followed by Temozolomide and radiation is standard of care for GBM. The efficacy of Temozolomide may be affected by the methylation status of O6-methylguanine methyltransferase (MGMT) at promoter and enhancer regions. Surgical sampling with or without resection is the gold standard for detecting these genetic alterations. However, depending on patient comorbidities or location of neoplasm-for example in brain stem or eloquent area, an in vivo MGMT imaging marker is desired. Currently, the prediction of MGMT status on conventional imaging is a challenging task. In the past, we explored the efficacy of an ensemble neural network framework in predicting MGMT methylation status on treatment-naive multiparametric MRI. Given the potential of transformers in the vision community, we further experimented with using transformer models with advanced complex architecture and compared their performance with our previous deep learning model.
Materials and Methods
We trained a shifting window (Swin) transformer model, which was pre-trained on Brain Tumor Segmentation (BRATS) 2021 dataset for the segmentation task, in a 5-fold cross-validation setting. We froze the five-model ensemble and trained a classifier layer for the Radiogenomics classification. We also compared this model with Vision Transformer (ViT) and Swin Transformer models trained from scratch. 400, 60, and 117 cases were used for training, validation, and testing. We normalized all input images to have zero mean and unit standard deviation according to non-zero voxels. Random patches of 128 × 128 × 128 were cropped from 3D image volumes during training. We applied a random axis mirror flip with a probability of 0.5 for all 3 axes. We used the 3D Swin and ViT models and pre-trained models for BRATS segmentation from MONAI.
Results
We report an accuracy of 58.12% for the linear probing experiment. For comparison, we report an accuracy of 54.70% for the Swin transformer trained from scratch and 53.85% for the ViT model trained from scratch. Our previous CNN-based model had achieved a final testing Area-under-Curve (AUC) value of 91.38% with a training loss of 0.0013 for the similar task.
Conclusions
Based on a preliminary comparative analysis, we conclude that CNN models are better suited for the radiogenomic classification task.

1316

Predictive Modeling of Regional Neuroradiology CT and MRI Utilization from Population Variables

N Takacs[1], S Schlotter[1], X Nguyen[2]

[1]The Ohio State College of Medicine, Columbus, OH, [2]Ohio State University Wexner Medical Center, Columbus, OH

Purpose

Accurate prediction of future health care utilization may facilitate optimal resource planning and budgeting (1). In this study, we seek to better understand how changes in incidence of common diagnoses in a population or recent imaging volumes may affect near-term future utilization of neuroradiology CT and MR exams within large geographically defined populations.

Materials and Methods

In this retrospective study, data were obtained from COSMOS, a large national multi-institutional, multi-payor dataset. We queried monthly counts of procedures for selected neuroradiology CT and MR exam types within the study period (Jan 2016 to Dec 2021), partitioned by state. To capture patient population characteristics, we identified the top ten diagnosis codes for neuroradiology exams within the study period (e.g., hyperlipidemia, hypertension) and queried monthly counts of encounters of any type associated with these ten diagnoses. The 72 months of data were grouped into 24 triplets of timepoints spaced three months apart, with the third timepoint of each triplet representing the target timepoint for prediction. In addition to historical exam counts and state-wide encounter volumes at the initial two timepoints, predictor variables also included the target timepoint calendar month to account for seasonal variation. Data were fitted to a standard least-squares linear regression model, with R2 used to assess model performance.

Results

Neuroradiology CT exams occur at a frequency of 0.69% +/- 0.33% of total encounters, and neuroradiology MR exams occur at 0.32% +/- 0.15%. Linear regression models for three-month future volume prediction satisfactorily predicted utilization of head CT, spine CT, and head/neck CTA, each with R2 of 0.96. Fit statistics were mildly poorer for soft-tissue neck CT and orbit/face/ear CT, with R2 of 0.94 and 0.92, respectively, and for brain MRI, spine MRI, and orbit/face/neck MRI, yielding R2 of 0.94, 0.92, and 0.90, respectively.

Conclusions

Linear regression models applied to exam volumes and population characteristics from two prior timepoints can predict future neuroradiology volumes one calendar quarter in advance. This method of modeling population-level neuroimaging utilization from a small number of easily obtainable historical data could be helpful for predicting changes in subspecialty radiology needs at a regional level based on shifts in population characteristics.

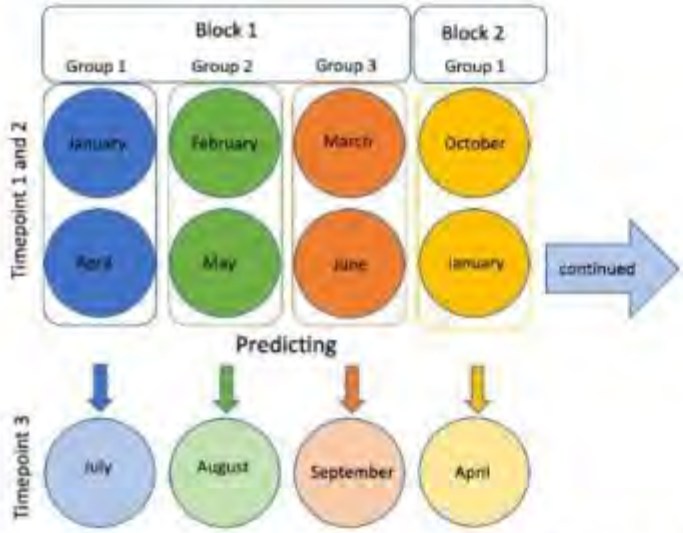

Fig 1. *Figure showing how the monthly data were grouped into blocks and then subsequent groups using time point one and two to predict the time point three.*

Top 10 ICD-10 Diagnosis Codes Used	
I25.10	Atherosclerotic heart disease of native coronary artery without angina pectoris
R42	Dizziness and giddiness
I10	Essential (primary) hypertension
K21.9	Gastro-esophageal reflux disease without esophagitis
R51	Headache
E78.5	Hyperlipidemia, unspecified
Z79.82	Long term (current) use of aspirin
F17.210	Nicotine dependence, cigarettes, uncomplicated
Z79.899	Other long term (current) drug therapy
Z87.891	Personal history of nicotine dependence
	None of the above

Table 1. *Table showing the top 10 ICD-10 codes and diagnoses used to collect the procedure data for the regression analysis.*

	With Imaging Volumes from Timepoints 1 and 2		Without Imaging Volumes from Timepoints 1 and 2	
	Linear R^2	P-Value	Linear R^2	P-Value
CT Head	0.96	<0.0001	0.93	<0.0001
CT Neck	0.94	<0.0001	0.91	<0.0001
CT Spine	0.96	<0.0001	0.93	<0.0001
CT Orbit, Face, Ear, Post Fossa	0.92	<0.0001	0.90	<0.0001
CTA Head Neck	0.96	<0.0001	0.93	<0.0001
MRI Orbit Face Neck	0.90	<0.0001	0.83	<0.0001
MRI Brain	0.94	<0.0001	0.92	<0.0001
MRI Spine	0.92	<0.0001	0.85	<0.0001

Figure 2. *Results showing the model fit from linear regression analysis*

(Filename: TCT_1316_FiguresVolume.jpg)

1099

Predictive Performance of Linear and Non-linear Models for Meningioma Tumor Grade Prediction Based on Multiparametric MRI

Z Cai[1], Y Wong[1], L Wang[1], L Wong[1], T So[1]
[1]The Chinese University of Hong Kong, Shatin, New Territories

Purpose
Meningioma is a common brain tumor. High-grade (WHO grade 2 and 3) meningiomas grow aggressively and frequently recur, resulting in higher mortality rates and poor prognosis (1). Preoperative assessment of tumor grade may help decide the type of surgery and resection (2). Logistic regression models have been widely used to predict tumor grade from a range of clinical variables and MRI features in prior studies. Nonlinear models can determine complex discriminative patterns from multiple variables in a dataset without assuming linearity. We hypothesized that nonlinear models can achieve greater predictive performance for prediction of meningioma grade than linear models.
Materials and Methods
We retrospectively reviewed 164 meningiomas (133 cases, low-grade; 31 cases, high-grade) and assessed 81 factors from clinical variables and MRI features. Univariate analysis was used to select features for machine learning (ML) models. We compared the average prediction performance over 5-fold cross-validation of several ML classifiers (logistic regression, random forest, support vector machine, and XGBoost) based on the significant features.
Results
The gaps in the mean accuracy between logistic regression and the nonlinear models (random forest, support vector machine, and XGBoost) were 0.01, 0.03, and 0.01 respectively. Meanwhile, the gaps in the average area under curve between logistic regression and the nonlinear models were -0.02, 0.04, and 0, respectively.
Conclusions
In this study, all nonlinear models could predict tumor grade with higher prediction accuracy than the linear model. Support vector machine prediction achieved significant improvement in accuracy and area under curve in predicting tumour grade using the binary selected features.

1164

Preliminary evaluation of a deep learning based metric for head motion artifact grading on a publicly available dataset

H Lee[1], S Gho[2], S Banerjee[3], Y KANG[4], S Joel[5]
[1]Inje University Haeundae Paik Hospital, Busan, [2]GE HealthCare, Seoul, [3]GE HealthCare, Menlo Park, CA, [4]Inje University Haeundae Paik Hospital, BUSAN, Busan, [5]GE HealthCare, Bangalore, Karnataka

Purpose
The purpose of this study is to evaluate the performance of a motion artifact grading deep learning network on a publicaly available dataset.
Materials and Methods
48 subjects from the Movement-related artefacts (MR-ART) dataset, which is a publicly available dataset consisting of matched motion-corrupted and clean images, were included in this preliminary study [1,2]. In this dataset, healthy adult volunteers underwent three MPRAGE scans with different frequency of motion tasks, standard setting without motion (STAND) and with low (HM1) and high levels of head motion (HM2) on a single 3T scanner at isotropic 1mm cubic resolution. The image quality was rated using a 3 point visual scoring system, which was good (1), medium (2) and bad (3; clinically unusable) by 2 experienced neuroradiologists, blinded to the motion state (Figure 3). A deep learning network was trained to grade motion artifacts on various 2D and 3D brain sequences including T1, T2, FLAIR and SWAN, by a separate group or researchers in partnership with Mass General Brigham, and shared for evaluation. The network was an ensemble of 4 inception V3 models, each trained for one of four annotator's score which was then ensembled by XGBoost. A metric is given for each slice. Average of the metric over multiple slices ("average") was used for analysis. The "average" metric was compared according to each motion state, and visual score, with ANOVA . Post-hoc analysis was performed with Bonferroni correction. Correlation waas assessed with Kendall's Tau-b [3]. The statistical analysis was performed with Jamovi version 2.2 [4].
Results
The "average" metric was significantly different between each score, notably between clinically unusable image (score 3) and medium quality with some artifacts (score 2). However, the "average" metric was significantly different between standard image and low and high levels of head motion, but not different between low and high levels of head motion. The correlations for "average"-score and "average"-motion showed strong correlation (Figure 1). This can be expected since the scores and the level of head motion were not always concordant or correlated (Figure 2). Potential explanations may be that the subject did not follow the directions correctly, or the image artifacts were confounded by other factors such as degree or timing of motion.
Conclusions
Based on this preliminary result, a deep learning based metric for head motion artifact grading is significantly different according to visual scoring levels.

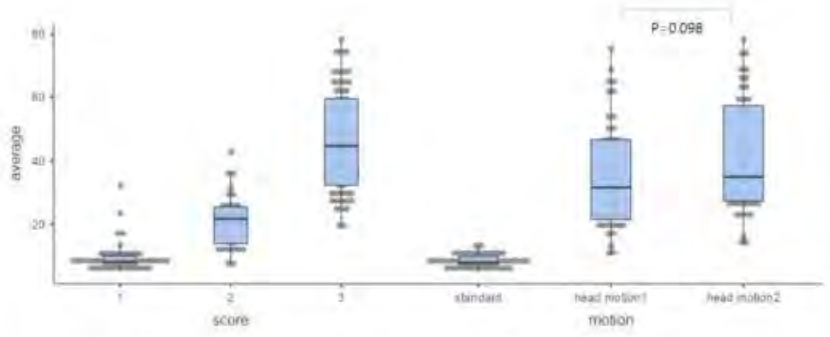

Mean±SD	9.13±4.70	21.3±8.25	45.8±16.0	8.57±1.93	34.9±16.7	41.1±17.7
Kendall's Tau B	0.732	p<0.001		0.605	p<0.001	

Figure 1. Bar plot of average metric according to score and motion levels, mean and standard deviation(SD) values, and correlation between average metric and each ordinal variables. Average metrics were significantly different (p<0.001) for all pairs except for head motion 1 vs head motion 2 (p=0.098).

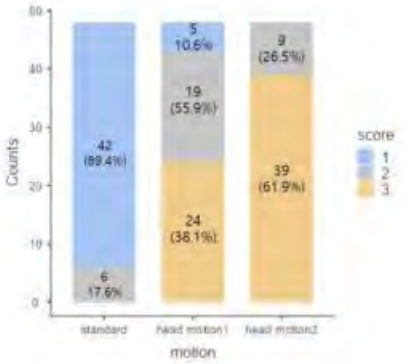

Figure 2. Frequency of allocated scores for each motion level. The plot shows that some of the standard motion group had a score of 2 while some in head motion 1 group had score of 1

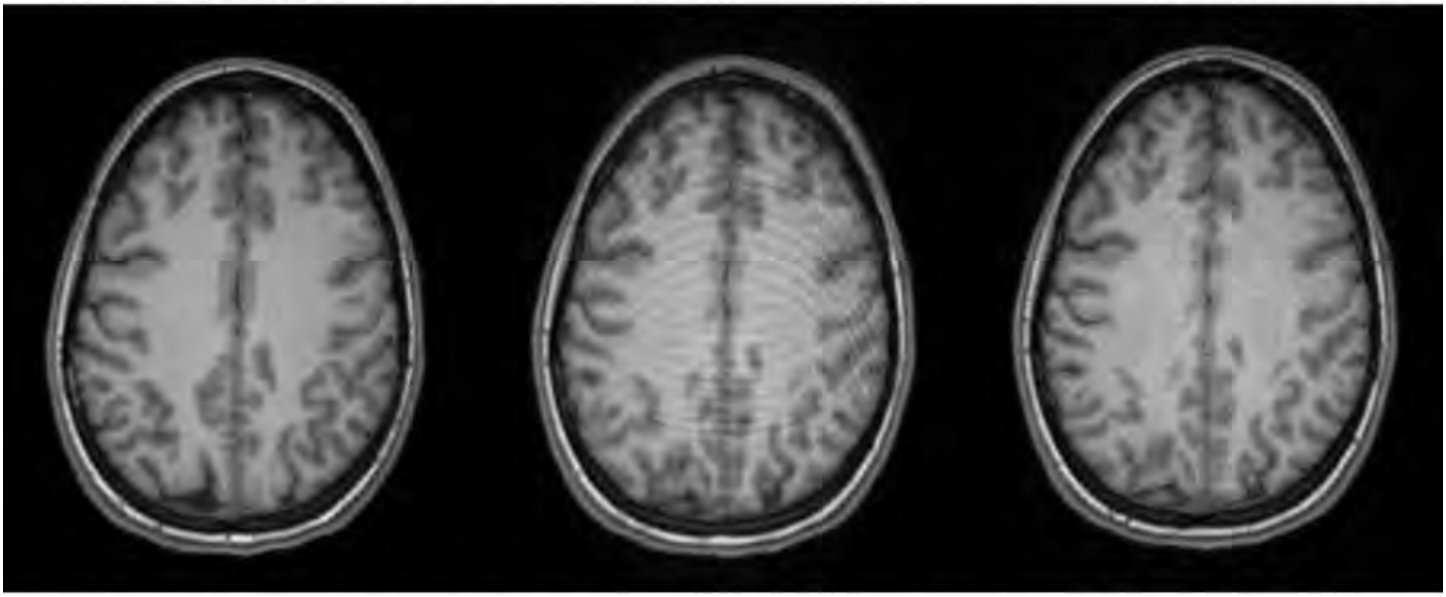

Figure 3. Example of images acquired with different image levels, standard(STAND), low head motion (HM1), and high head motion (HM2). Scores of 1(good), 3(bad), and 2(medium) were given by the radiologists, respectively. The average metric were 10.27 , 47.27, and 25.51 correctly reflecting the visual scores.

(Filename: TCT_1164_Graphic.jpg)

396

Pretreatment MR-based radiomics in patients with glioblastoma: a systematic review and meta-analysis of prognostic endpoints

Y CHOI[1]

[1]*Asan Medical Center, Seoul, Korea, Republic of*

Purpose

Recent studies have shown promise of MR-based radiomics in predicting the survival of patients with untreated glioblastoma. This study aimed to comprehensively collate evidence to assess the prognostic value of radiomics in glioblastoma.

Materials and Methods

PubMed-MEDLINE, Embase, and Web of Science were searched to find original articles investigating the prognostic value of MR-based radiomics in glioblastoma published up to March 6, 2022. Concordance indexes (C-indexes) and Cox proportional hazards ratios (HRs) of overall survival (OS) and progression-free survival (PFS) were pooled via random-effects modeling. For studies aimed at classifying long-term and short-term PFS, a hierarchical regression model was used to calculate pooled sensitivity and specificity. Between-study heterogeneity was assessed using the Higgin inconsistency index (I2). Subgroup regression analysis was performed to find potential factors contributing to heterogeneity. Publication bias was assessed via funnel plots and the Egger test.

Results

Among 596 abstracts, 17 studies were included. Respective pooled C-indexes and HRs for OS were 0.65 (95% confidence interval

[CI], 0.58–0.72) and 2.88 (95% CI, 2.28–3.64), whereas those for PFS were 0.61 (95% CI, 0.55–0.66) and 2.78 (95% CI, 1.91–4.03). Among 4 studies that predicted short-term PFS, the pooled sensitivity and specificity were 0.77 (95% CI, 0.58–0.89) and 0.60 (95% CI, 0.45–0.73), respectively. There was a substantial between-study heterogeneity among studies with the survival endpoint of OS C-index (n=9, I2=83.8%). Publication bias was not observed overall.

Conclusions

Pretreatment MR-based radiomics provided modest prognostic value in both OS and PFS in patients with glioblastoma.

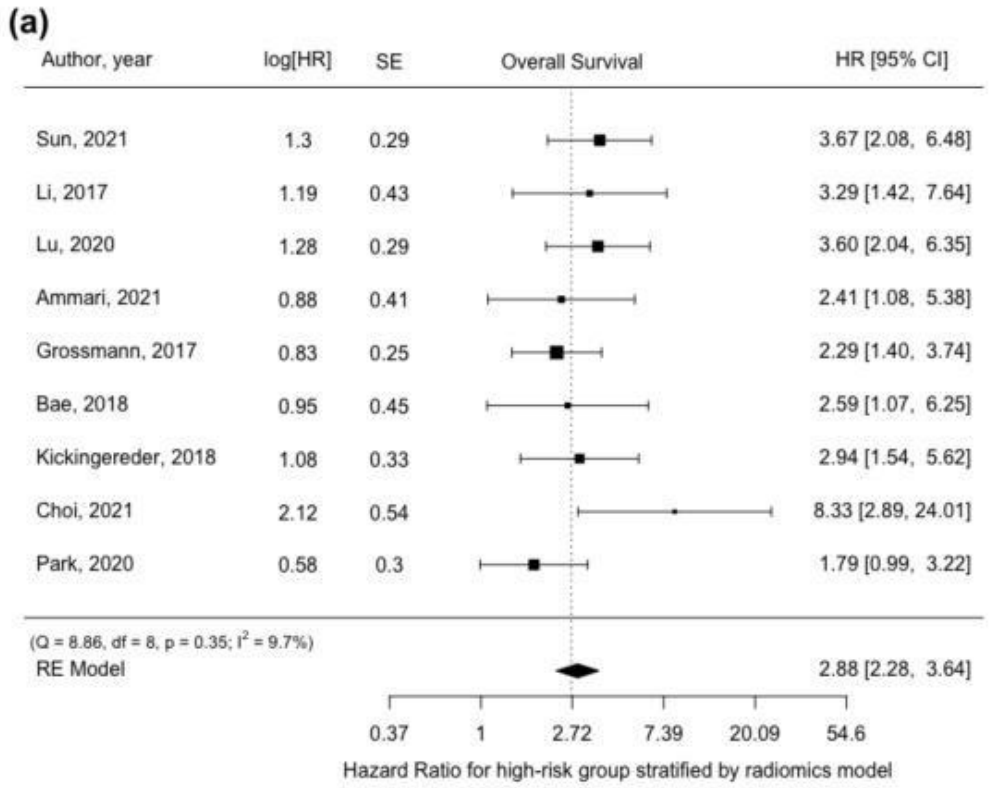

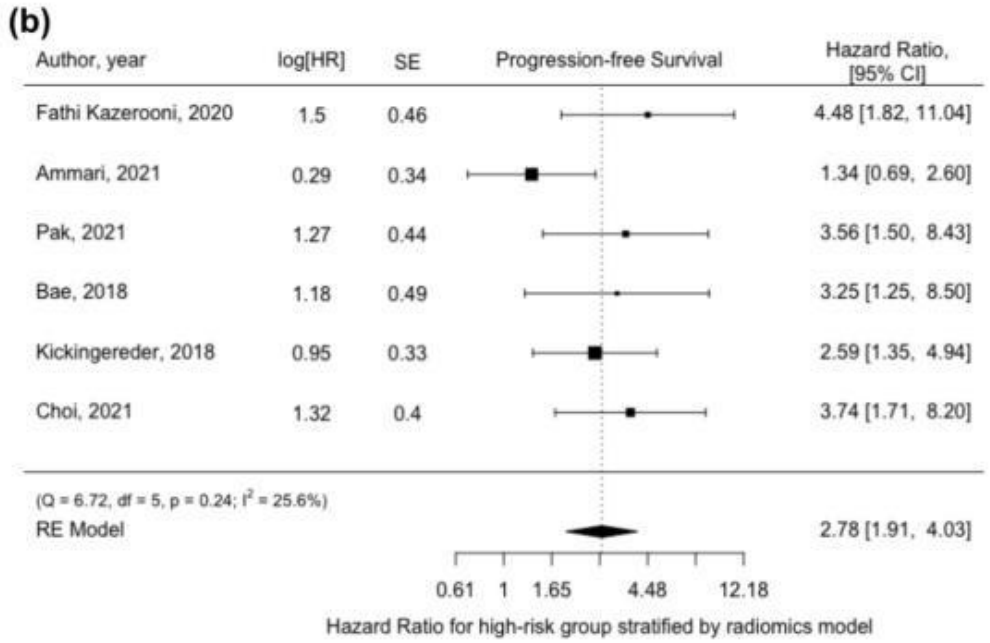

(Filename: TCT_396_FIG3_forest_os_pfs_0804_labelled.jpg)

1306

Proposed diagnostic volumetric bone mineral density thresholds for osteoporosis and osteopenia at the cervicothoracic spine in correlation to the lumbar spine

S Rühling[1], J Kirschke[2]

[1]University Hospital rechts der Isar of the Technical University Munich, Munich, Germany, [2]Dept. of Neuroradiology, School of Medicine, Technical University of Munich, Munich, Germany

Purpose

To determine the correlation between cervicothoracic and lumbar volumetric bone mineral density (vBMD) in an average cohort ofadults and to identify specific diagnostic thresholds for the cervicothoracic spine on the individual subject level.

Materials and Methods

In this HIPPA–compliant study, we retrospectively included 260 patients (59.7 ± 18.3 years, 105 women), who received a contrast-enhanced or non-contrast-enhanced CT scan. vBMD was extracted using an automated pipeline. The association of vBMD between each vertebra spanning C2–T12 and the averaged values at the lumbar spine (L1–L3) was analyzed before and after semiquantitative assessment of fracture status and degeneration, and respective vertebra-specific cut-off values for osteoporosis were calculated using linear regression.

Results

In both women and men, trabecular vBMD decreased with age in the cervical, thoracic, and lumbar regions. vBMD values ofcervicothoracic vertebrae showed strong correlations with lumbar vertebrae (L1–L3), with a median Pearson value of r =0.87 (range: rC2 =0.76 to rT12 = 0.96). The correlation coefficients were significantly lower ($p < 0.0001$) without excluding fractured and degenerated vertebrae, median r = 0.82 (range: rC2 = 0.69 to rT12 = 0.93). Respective cut-off values for osteoporosis peaked at C4 (209.2 mg/ml) and decreased to 83.8 mg/ml at T12.

Conclusions

Our data show a high correlation between clinically used mean L1–L3 values and vBMD values elsewhere in the spine, independent of age. The proposed cut-off values for the cervicothoracic spine therefore may allow the determination of low bone mass even in clinical cases where only parts of the spine are imaged.

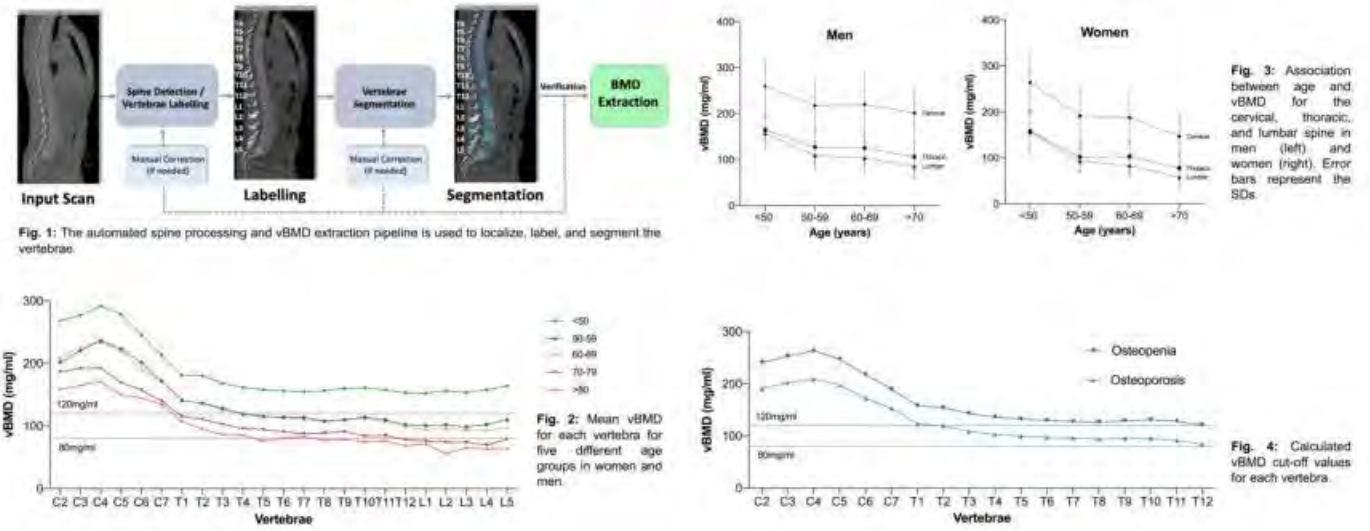

Fig. 1: The automated spine processing and vBMD extraction pipeline is used to localize, label, and segment the vertebrae.

Fig. 3: Association between age and vBMD for the cervical, thoracic, and lumbar spine in men (left) and women (right). Error bars represent the SDs.

Fig. 2: Mean vBMD for each vertebra for five different age groups in women and men.

Fig. 4: Calculated vBMD cut-off values for each vertebra.

(Filename: TCT_1306_Figures_1_2_3_4.jpg)

1131

Quantitative assessment of the systemic levels of Tau, Aβ, NfL and inflammatory biomarkers in patients with Essential Tremor and cognitive impairment undergoing High-Intensity Focused Ultrasound therapy

N Saez Calveras[1], B Stopschinski[1], M Diamond[1], B Shah[1]

[1]University of Texas Southwestern, Dallas, TX

Purpose

Patients with Essential Tremor (ET) have a higher incidence and prevalence of both mild cognitive impairment and dementia (1-3). The postmortem examination of these patients has revealed the presence of Tau aggregates with a unique isoform profile (4), and preliminary data from seeding assays has also shown increased levels of pathologic Tau capable of forming self-propagating aggregates in ET patients with dementia (Figure 1). MR guided high intensity focused ultrasound (MRgHIFU) is a technique that has been FDA approved for the management of tremor in patients with ET. Thermal ablation by HIFU also causes a transient disruption of the blood brain barrier (BBB) in the treated area (5). This transient BBB opening can potentially lead to the egression of intraparenchymal proteins into the systemic circulation. Profiling these factors could provide an insight into the local environment of ET patients' brains, which is of particular interest in those cases with cognitive impairment. The primary goal of our study is to determine whether patients with ET who are cognitively impaired have significantly higher levels of total Tau and phospho-Tau

species in the peripheral blood when compared to those patients with ET who were cognitively intact at the time of treatment. We also seek to quantify whether the levels of Aβ species, neurofilament light chain (NfL), GFAP and proinflammatory cytokines are significantly increased in the systemic circulation of patients with ET with MCI/dementia before and after focused ultrasound, when compared with patients with normal cognition.
Materials and Methods
All patients with known ET undergoing MRgHIFU were stratified according to their known neuropsychological score (MOCA testing) into non-cognitively impaired, mild cognitive impairment and demented. Plasma samples are collected from subjects at two time points: 10 minutes before undergoing HIFU, and 30 minutes after the delivery of high intensity sonication. The quantitative measurement of systemic biomarkers in these samples will be done with the use of a multiplex assay.
Results
The study is finalizing its collection stage and the results from this analysis will be available at the end of this year.
Conclusions
This study will help better elucidate the role of Tau pathology and neuroinflammation in ET. It will also serve to inform the development of early biomarkers that could predict the risk of progression to cognitive impairment in this population, and to categorize patients for potential future treatment trials.

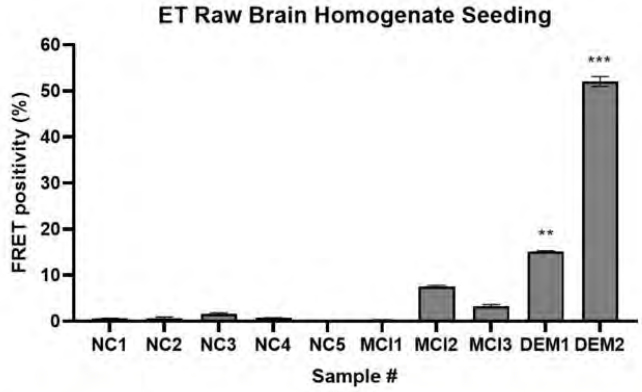

Figure 1: *Essential Tremor patient brain homogenates were incubated with biosensor cells and the % Tau aggregation was measured. Tau % aggregation in ET patients was associated with the presence of dementia.*

(Filename: TCT_1131_Figure1-EssentialTremorseeding.jpg)

348

Radiographic Findings of Papilledema in the Pediatric Population

W Chen[1], S Mahmoud[1]
[1]*Saint Louis University School of Medicine, St Louis, MO*

Purpose
Differentiating between papilledema and pseudopapilledema in the pediatric population is challenging for neuro-ophthalmologists. Prevalence of well characterized signs of intracranial hypertension (IIH) has not been specifically tested in children with pseudopapillledema. We aimed to study if imaging differences in children with papilledema and pseudopapilledema could help differentiate the two, thereby avoiding lumbar puncture.
Materials and Methods
We performed a retrospective chart and imaging review of patients <18 years old with a diagnosis of papilledema and pseudopapilledema who were seen at our institution from June 2012 through September 2018. The determination of pseudopapilledema was decided upon clinical judgment including a normal intracranial pressure (ICP) and/or stability of exam on serial testing. There were 17 patients with pseudopapilledema [age (SD) 11.56 (4.32) years; 9 females] and 29 patients [mean (SD) age 12.37 (4.28) years; 23 females] with papilledema and opening pressure greater than 28 cm H2O. Presence of signs of IIH on brain MRI, as determined by a masked neuro-radiologist, were compared between the two groups.
Results
In our IIH cohort, flattening of the posterior poles was seen in 41% (12/29), distention of the optic nerve sheath in 41% (12/29), tortuosity of the optic nerve in 21% (6/29), sellar changes in 34% (10/29), and tonsillar descent in 17% (5/29). Flattening of the globe was seen statistically significantly less often (5.9% versus 41%) in pseudopapilledema group (p=0.007). Prevalence of distention of the optic nerve sheath, tortuosity of the optic nerve, sellar changes, and tonsillar descent was not found to be significantly different between the two groups (p= 0.087, 0.575, 0.195, and 0.270 respectively).
Conclusions
Presence of flattening of the globe on MRI should suggest raised ICP and consideration for workup for IIH when clinical differentiation between pseudo-papilledema and papilledema is difficult.

Figure 1. Comparison of Pseudopapilledema and Papilledema. **A,** Axial MRI of an 11-year-old male diagnosed with pseudopapilledema depicts normal appearance of globes and extraocular muscles, bilaterally. **B,** Axial MRI of an 11-year-old female diagnosed with papilledema depicts inversion of the optic discs and flattening of the posterior globes, bilaterally (red arrows). The extraocular muscles and optic nerves are normal.

(Filename: TCT_348_ASNRFigure.jpg)

1032

Re-emerging tropical diseases and Spinal Infections: An Update in Image findings

A Lima Júnior[1], M Castillo[2], L Freitas[3]

[1]Mount Sinai Hospital, New York, NY, [2]Radiology, Chapel Hill, NC, [3]McGill University, Montreal, Quebec

Purpose

Narrative review of infectious disorders that affect the intervertebral discs, vertebrae, and the spinal column, especially reemerging diseases, are inconsistent. We aimed to widen scientific literature available and aid doctors in diagnosis of these conditions.

Materials and Methods

A narrative review based on literature research from PubMed, SciELO, and Scholar Google. English and Portuguese language filters were applied. Only articles that addressed spine infections (tropical and non-tropical diseases) and imaging diagnostic methods were selected.

Results

Tuberculous spondylodiscitis is caused by Mycobacterium tuberculosis that leads to osteomyelitis of the vertebral body and discitis. Lower thoracic and upper lumbar spine segments are involved. Pathophysiology involves hematogenous dissemination through Batson's venous plexus. There is the development of epidural granulation tissue, leading to spinal cord compression. CT-Scan and mostly MRI, provide a better assessment of the extent of spine involvement. Findings such as irregularity of the endplates corners associated with edema and increased signal of the bone marrow are often seen. Spinal, sub-ligament, and disc contrast enhancement can be seen in post-gadolinium T1-weighted images. Paravertebral collections are circumscribed, with central liquefaction and well-defined highlighted margins (so-called "cold abscesses"). Cysticercosis is the most common parasitic infection of the CNS. Clinical signs of spinal neurocysticercosis depend upon mechanisms of compression, edema, and inflammatory reaction. MRI is the diagnostic imaging method of choice and reveals cysts with signal intensity similar to the cerebrospinal fluid. The scolex (bearer of low signal on T1 and T2 sequences) may be seen as an eccentric nodule close to the cyst wall and its identification helps establish the diagnosis. Tabes dorsalis, the most common late presentation of tertiary syphilis. Progressive demyelination may arise, especially in the posterior spinal cord tracts. MRI shows a T2-weighted hyperintense signal at the posterior spinal cord columns. On imaging, it can present as a neuropathic arthropathy or Charcot's column.

Conclusions

As conclusion, many patients clinical and laboratory findings are mild or even absent, diagnostic imaging, especially magnetic resonance imaging plays a fundamental role in diagnosis establishment. Radiologists must be familiar with these diseases' imaging aspects.

602

Recurrent Glioblastoma vs Pseudoprogression: the utility of arterial spin labeling (ASL) and dynamic susceptibility contrast (DSC) in differentiating these two entities.

D Pozivilko[1], C Lu-Emerson[2], F Lucas[2], F Weng[2], C Lewis[2]
[1]Maine Medical Center, Portland, ME, [2]Maine Medical Center, Portland , ME

Purpose

To evaluate the value of arterial spin labeling (ASL) and dynamic susceptibility contrast (DSC) perfusion imaging in helping to differentiate disease progression (Pr) from pseudoprogression (PsPr) in patients with glioblastoma (GBM).

Materials and Methods

A retrospective analysis was performed evaluating 26 GBM patients at Maine Medical Center between 2009-2019 who received the standard of care surgical resection and chemoradiotherapy who then subsequently demonstrated imaging findings reflective of Pr versus PsPr and underwent a second resection for pathological analysis. For ASL perfusion estimation of cerebral blood flow, we used a qualitative analysis and a semi-quantitative grading system: 0- darker than white matter, 1- same as white matter, 2- same as cortex, 3- brighter than cortex. For DSC perfusion estimation of cerebral blood volume, we used a quantitative analysis by placing an ROI in the region of most avid contrast enhancement as well an ROI in an area of normal appearing white matter in the contralateral hemisphere; a ratio of these two ROI values was obtained. Sensitivity and specificity of the ASL grades and DSC ratios were calculated and compared between the Pr and PsPr patients.

Results

Of our 26 patients with GBM status post standard treatment with resection and chemoradiotherapy who displayed findings concerning for Pr vs PsPr and underwent re-resection, 23 had pathology consistent with Pr and 3 had pathology consistent with PsPr. Mean ASL grade was 2.4 for Pr patients and 1.3 for PsPr patients (p=NS). ASL grades of 2 or higher had a sensitivity of 62% (95% CI [36,83%]) and specificity of 33% (95% CI [6,79%]) in differentiating Pr from PsPr patients. Both Pr and PsPr had similar mean DSC ratios (Pr 2.098, PsPr 2.200 PsPr, p=NS). DSC ratio's of 1 or greater had a sensitivity of 96% (95% CI [80,99%]) and specificity of 0% (95% CI [0, 66%]) for Pr versus PsPr patients. When using the combination of both DSC ratio's of 1 or greater and ASL grade 2 or higher the sensitivity was 91% (95% CI [62,98%] and specificity of 0% (95% CI [0,66%]).

Conclusions

Although limited by a small patient cohort our results support the use of DSC and ASL perfusion imaging to help aide in differentiation between tumor recurrence and pseudoprogression in treated GBM patients.

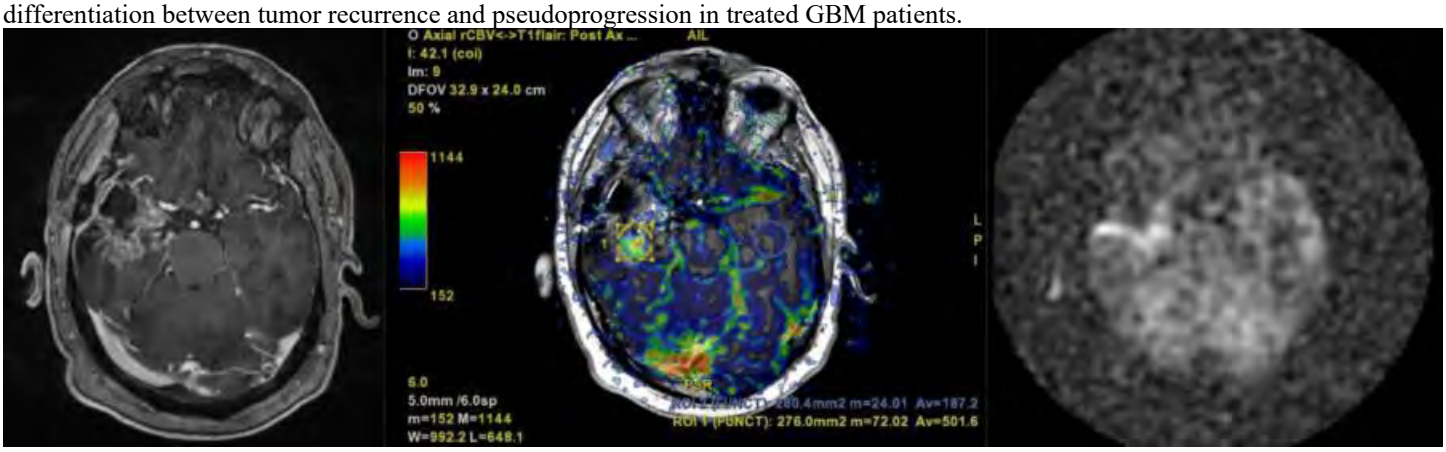

(Filename: TCT_602_Graphic.jpg)

908

Reduced Glymphatic Flow in Recreational Marijuana Users Associated with the Age of First Use and Cognitive Decline

C Andica[1], K Kamagata[2], K Takabayashi[2], Z Mahemuti[2], M Owaki[2], A Hagiwara[2], K Sato[2], T Akashi[2], A Wada[2], S Aoki[2]
[1]Faculty of Health Data Science, Juntendo University, Chiba, Japan, [2]Department of Radiology, Juntendo University Graduate School of Medicine, Tokyo, Japan

Purpose

The recreational use of marijuana is increasing, partially due to shifts in legal and societal attitudes toward its use. Marijuana use is associated with impairments of cognitive functions; however, little is known about its effects on the glymphatic system, a glial-based perivascular network that promotes brain metabolic waste clearance [1]. The present study aimed to assess the changes in the glymphatic system in marijuana recreational users using the index of diffusion tensor imaging along the perivascular space (DTI-ALPS) [2].

Materials and Methods

We assessed 250 subjects (age range, 22-37 years) from the latest S1200 release from the WU-Minn HCP Consortium, including 125 marijuana recreational users and 125 non-users (see Figs. 1 and 2; Table 1 for inclusion criteria and the characteristics of study participants). The ALPS index was calculated using 3T diffusion MRI data (b = 1,000; Fig. 3). The mean ALPS index was compared between users and non-users using a general linear model while controlling for age, sex, sleep quality index, alcohol usage, and

tobacco usage. The associations between the ALPS index and the number of times used, age of first use, or cognitive function scores were also assessed in marijuana users using multiple linear regression analysis with backward elimination method. A p-value (two-tailed) < 0.05 was considered statistically significant in all analyses.

Results

After adjusting for age, sex, sleep quality index, alcohol usage, and tobacco usage, we found no significant difference in the ALPS index between non-users and users (Fig. 4) or between users with varying ages of first use or the number of uses. The linear regression analysis showed the association between lower ALPS index (unstandardized B, -0.036; p = 0.014) and younger age of first marijuana use after controlling for age and sex (Fig. 5). Lower ALPS index was also associated with lower number of the Penn matrix test correct responses (unstandardized B, 0.005; p = 0.048) and poorer working memory task accuracy in the 0-back condition (unstandardized B, 0.003; P = 0.024) after covarying for age, sex, and education.

Conclusions

The present study extended the potential use of DTI-ALPS, as a noninvasive indirect indicator of the glymphatic system in young adults. Our findings provide evidence of the adverse effect of younger use of marijuana on glymphatic system function (indexed by lower ALPS index), which is associated with impaired working memory efficiency and fluid intelligence.

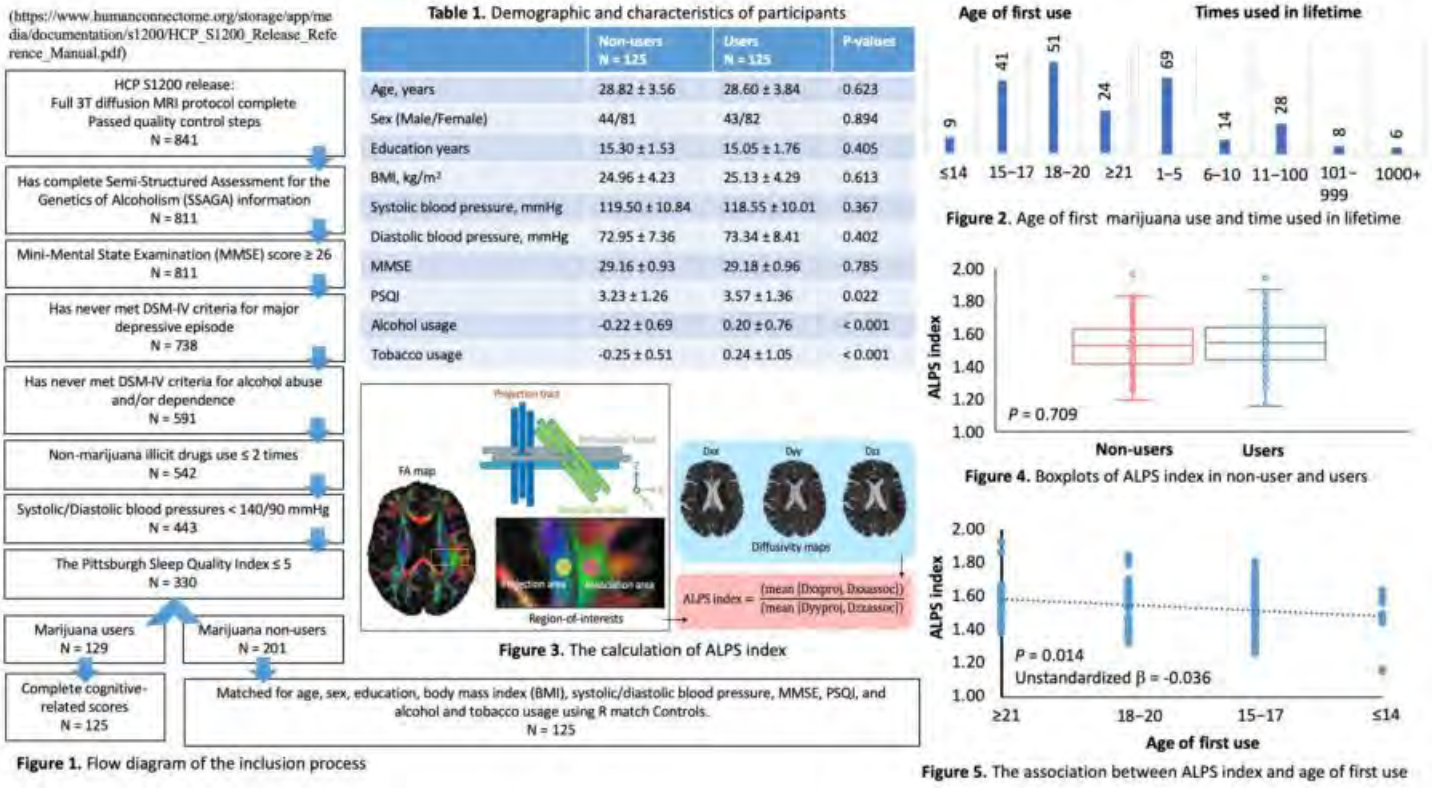

(Filename: TCT_908_Figure_ASNR2023_Andica.jpg)

1390

Relationship between perivascular spaces and plasma inflammatory biomarkers in ADNI data in different scanner magnetic fields

F Sibilia[1], N Sheikh-Bahaei[2], J Choupan[1]

[1]USC Mark and Mary Stevens Neuroimaging and Informatics Institute, University of Southern California, Los Angeles, CA, [2]University of Southern California, Irvine, CA

Purpose

Perivascular spaces (PVSs) are fluid-filled spaces surrounding blood vessels in the brain. They facilitate the cerebrospinal fluid drainage from the interstitial space, allowing the outflow of waste soluble proteins(1). PVS volume increases with age, especially in basal ganglia and centrum semiovale (CSO) regions. Physiological factors such as stress and hypertension contribute to the brain inflammation state(2), potentially leading to PVS enlargement. We used ADNI-1 data to investigate associations between plasma inflammatory biomarkers and PVS volume fraction assessed at two different magnetic fields.

Materials and Methods

Participants were older adults (age range=56-89 years old) that had T1w at 1.5T (n=465) and 3T (n=108) and all the inflammatory markers. Voxel resolution for 1.5T was 1.19x0.9375x0.9375, and 1.19x1x1 at 3T. PVS was segmented within white matter volume by using a pipeline developed by our team3. Plasma inflammatory markers were matrix metallo-proteinases (MMPs) 2 and 9, tumor-necrosis-factor (TNF) alpha, receptor-like-2 (TNFr2), TNF-apoptosis-ligand (TRAIL), interleukin-6-receptor and C-reactive-protein (CRP). Cortisol was used as a stress measure and Angiotensin-converting-enzyme (ACE) as a hypertension marker. Generalized linear

models were used to test the association of PVS volume fraction with plasma biomarkers, as well as the interaction between them. We controlled for age, sex, hippocampal volume and body mass index.
Results
In 1.5T data, PVS in the CSO showed a significant inverse association with TNFr2, which was stronger with higher levels of ACE. The effect of Cortisol on the PVS volume fraction became significantly inverse with higher levels of CRP, MMP9 and the TNF biomarkers. Basal ganglia PVS was positively associated with TRAIL, whereas the relationship with Cortisol was significantly inverse when CRP levels were higher. TRAIL showed a significant positive association with PVS volume fraction in the 1.5T data; the opposite was seen in 3T data (inverse association). In the 3T data, the effect of ACE on PVS basal ganglia was significant and weaker if MMP2 was included in the model. No significant association was seen in the CSO.
Conclusions
This study showed that the scanner magnetic field strength and sample size influence the relationship between PVS and plasma biomarkers. On a clinical level, results highlighted how the levels of cytokines and physiological biomarkers can contribute to PVS structural alterations indicating neuroinflammation in older people.

172

Resting State fMRI Differences in Self-Reported Anxiety Among Healthy Young Adults

S Sundara Raj Sreenath[1], H Sandoval[1], V Calhoun[2]
[1]Texas Tech University Health Sciences Center - El Paso, El Paso, TX, [2]Georgia Institute of Technology, Atlanta, GA

Purpose
Anxiety disorders are characterized by excessive feelings of fear or worry that are difficult to control and interfere with daily functioning. Resting state fMRI has been an important tool to study various neurocognitive disorders. This study therefore aims to look at resting state fMRI changes in a sample of healthy young adults with self-reported anxiety without comorbidities or other neurological disorders.
Materials and Methods
Participant MRI data was obtained from the S1200 release of the Human Connectome Project, consisting of healthy young adults between the ages of 22-37 yrs. Based on their Achenbach self-report (ASR) anxiety scores, 38 participants were stratified into either a clinically significant anxiety (n = 19) or a healthy control (n=19) group. The NeuroMark automated fMRI ICA pipeline was used to identify brain network differences between the two groups1. Seven functional domains and its independent components (ICs) were identified: Sub-cortical (5 ICs), Auditory (2 ICs), Sensorimotor (9 ICs), Visual (9 ICs), Cognitive-control (17 ICs), Default-mode (7 ICs), and Cerebellar domain (4 ICs) as shown in the spatial correlation matrix in Figure 1.
Results
Differences in static functional network connectivity (sFNC) measures were analyzed using two tailed t-tests ($p < .05$). Increased connectivity differences in the clinical anxiety vs HC group were observed between the subthalamus/hypothalamus and L, R-postcentral gyrus, paracentral lobule and middle temporal gyrus. Decreased connectivity was observed between the middle temporal gyrus and L, R-postcentral gyrus and paracentral lobule as well as between the R-inferior frontal gyrus and L, R- postcentral gyri.
Conclusions
Connectivity differences in the paracentral lobule as well as pre and post central gyri have been reported not only in anxiety related disorders but in several other neurocognitive disorders such as Alzheimer's and Post Traumatic Stress Disorder as well, highlighting the potentially important role of the somatosensory cortex in these disorders2-4. Detailed understanding of these neuroanatomical and functional underpinnings of anxiety disorders could allow for more targeted therapeutic interventions.

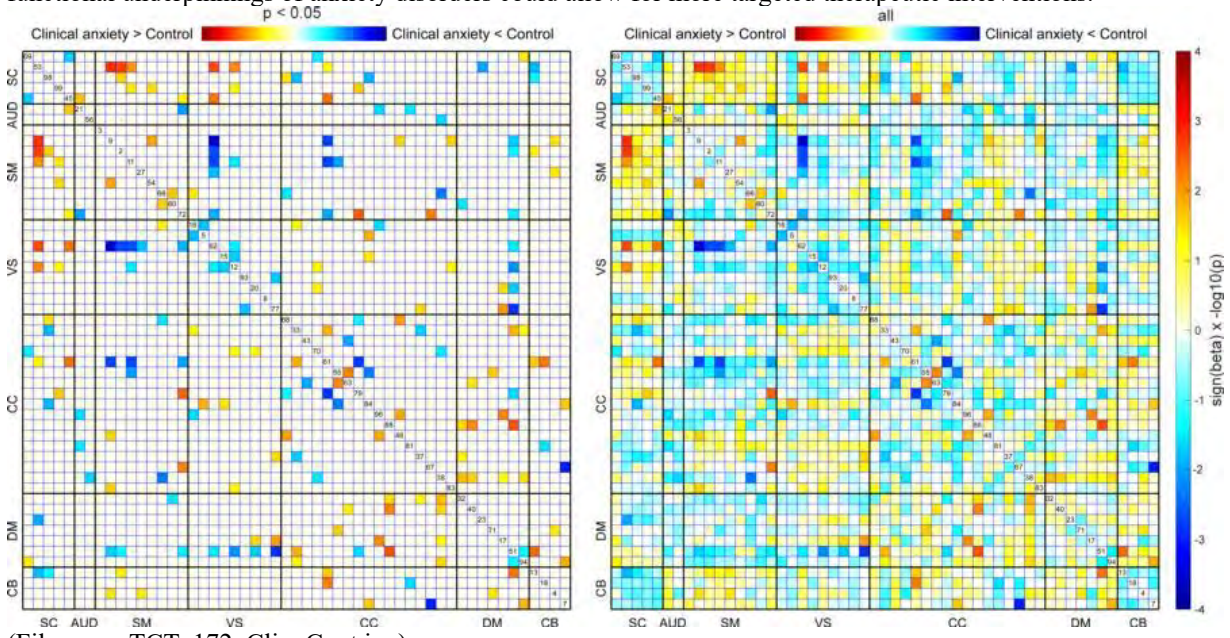

(Filename: TCT_172_Clin_Cont.jpg)

1409

Retrospective Evaluation of MR Vessel Wall Imaging Performance Following Treatment of Intracranial Aneurysm with Flow Diverter Stent

A Goncalves Filho[1], M dos Santos[2], S Chakraborty[3], R Aviv[4], E Portela de Oliveira[4]

[1]University of Ottawa, Ottawa, Ontario, [2]The Ottawa Hospital, University of Ottawa, Ottawa, ON, [3]The Ottawa Hospital, U. of Ottawa, Ottawa, ON, [4]The Ottawa Hospital, Ottawa, Ontario

Purpose

To evaluate the performance of vessel-wall MRI (VWMRI) on the early and long-term post-treatment examination of patients with intracranial aneurysms treated with Flow Diverter (FD) stent in comparison to standard Digital Subtraction Angiography (DSA) or CT Angiogram (CTA).

Materials and Methods

We retrospectively reviewed patients with intracranial aneurysms treated with FD, who underwent post-treatment follow-up VWMRI for the detection of in-stent stenosis between January 1, 2020, to December 31, 2021. We collected demographic and treatment-related data from patient's charts, including sex, age, comorbidities, aneurysm size and location, model of FD used, presence of subarachnoid hemorrhage and post-treatment assessment of the patency of the vessel lumen within the flow diversion stent, grade of in-stent stenosis, and grade of aneurysm occlusion. Interrater agreement was reported using Cohen κ statistic.

Results

We included 30 patients. Interrater agreement was strong for the evaluation of in-stent stenosis, aneurysm occlusion grade and post-treatment complications (ranging from $\kappa = 0.81$ to 0.97).

Conclusions

The non-invasive follow-up of these cases using VWMRI is an innovative method that could replace DSA in the lifetime assessment of the angiographic performance of FD. Information about stent patency and stenosis is crucial for management of associated dual antiplatelet therapy. In addition, this technique can lead to a substantial reduction in hospital costs compared to the standard invasive procedures. VWMRI demonstrates high interobserver agreement for the assessment of FD patency following endovascular treatment of intracranial aneurysms. It has proven to be a safe, effective and reliable method for evaluation of aneurysmal occlusion and post-procedural complications such as in-stent stenosis.

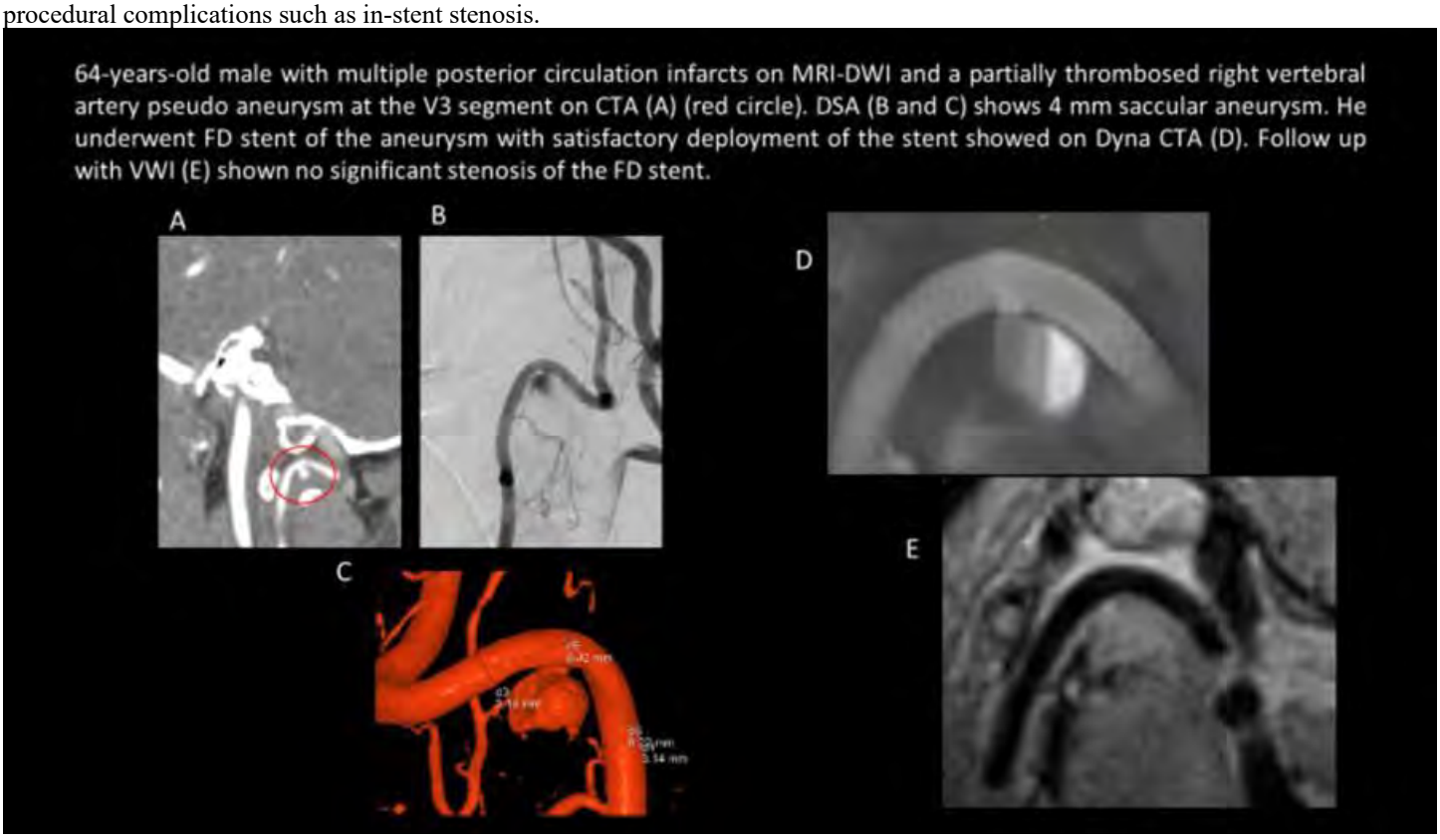

(Filename: TCT_1409_ASNR-VWMRI_FD.jpg)

1209

Robust Artificial Intelligence Image Modality Recognition With Minimal DICOM Size

M Bardis[1], D Chow[2], P Chang[3]

[1]University of California Irvine, Orange, CA, [2]University of California Irvine, IRVINE, CA, [3]University California Irvine, Irivne, CA

Purpose

As artificial intelligence becomes more incorporated into radiology workflow with continuously increasing imaging volumes, a software tool that identifies imaging modalities efficiently will be highly desirable. A deep learning neural network that effectively examines DICOM images and identifies their modality could be used at the beginning stage of any device that further manipulates specific modalities. In this study, a convolutional neural network was created that accurately identified the modalities of CT, PET, MR, and X-Ray.

Materials and Methods

This IRB approved study used CT, PET, MR, and X-Ray data from patients at UC Irvine. These DICOM images were gathered from 1,035 accessions from 2018 to 2020. Out of the 1,035 accessions, 744 were collected on a single day in January of 2020 to best mimic the distribution of these modalities on a typical, single day. DICOM is a tag based standard and the tag named, "Modality", was used to identify each accession's modality. When the tag's text contained, "CT", "PT", "MR", or "CR", the DICOM file was identified as CT, PET, MR, or X-Ray. When the tag's text did not contain "CT", "PT", "MR", or "CR", the DICOM file was excluded from the study. For each accession's image that was labeled as CT, PET, MR, or X-Ray, the matrix was downsampled and compressed to a 28x28 matrix. All images were then randomly placed in a training set or validation set. A deep learning algorithm was then implemented in this study with 3 layers. Each layer successively downsampled the matrix and convolved it with filters for feature identification. The logits values were used to calculated before applying the Softmax function for the three types of classification. Adam optimization was used to update the weights and the network ran for 30 epochs. The CNN performance was defined as classification accuracy of the modality on the validation set.

Results

A total of 415,663 images were classified as either CT, PET, MR, or X-Ray. The number of CT, PET, MR, and X-Ray images used were 253255, 10055, 151117, and 1236 respectively. The CNN used 332,531 (80%) images for training and 83,132 (20%) of images for validation. In validation, the CNN accurately classified 81,877 out of 83,132 images for an accuracy of 98.5%.

Conclusions

A single CNN algorithm accurately identifies an image's modality with a significantly compressed version of the original accession.

Figure 1: Image Modality Recognition

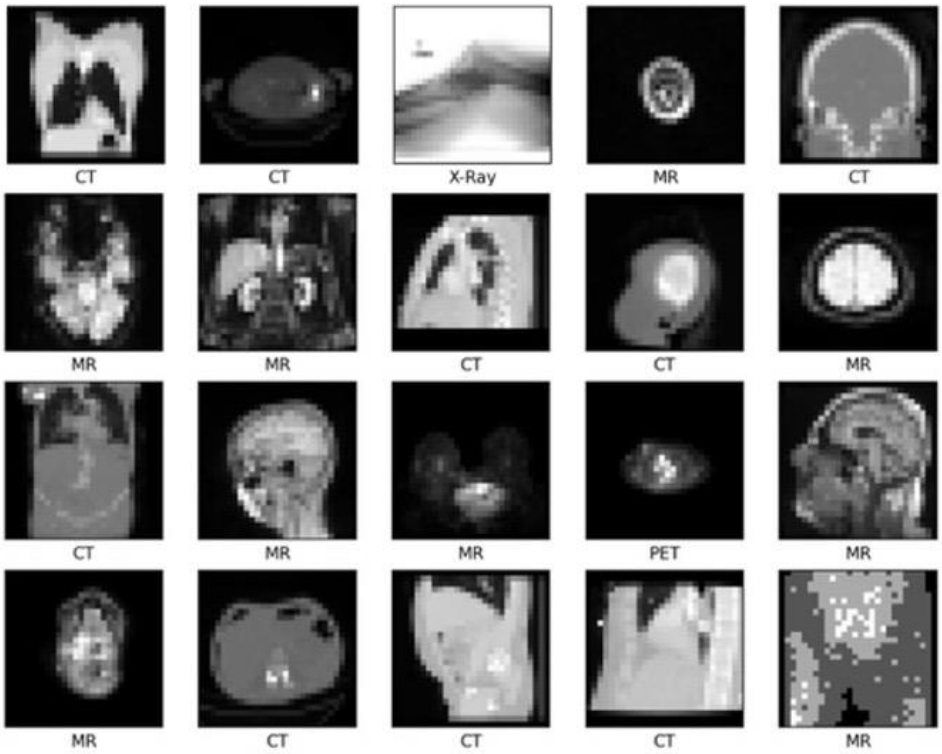

Figure 1: The CNN efficiently recognizes imaging modalities by using a compressed DICOM image as an input. The small DICOM images are 28x28 matrices that contained enough information for a neural network to recognize its modality.

(Filename: TCT_1209_Slide1.jpg)

1064

Role of Artificial Intelligence in Detection of Intracranial Aneurysms: Clinical Applications

D Shakoor[1], A Malhotra[2]

[1]Yale University, New Haven, CT, [2]Yale University School of Medicine, New Canaan, CT

Purpose

Intracranial aneurysms (IA) are a major health concern. An efficient method for early detection of IAs is required to provide appropriate radiological screening guidelines. Application of artificial intelligence (AI) for detection of neuroradiology emergencies such as aneurysms has received recent attention. Several studies have reported the high sensitivity of AI for detection of small aneurysms, however, data regarding its specificity are scarce. Besides, the rupture prediction model and the clinical impact of identifying AI detected small aneurysms are unknown. Therefore, we intend to evaluate the size of AI detected aneurysms which were not mentioned in the radiology report and assess the inter-reader agreement of second reads by different readers.

Materials and Methods

2100 consecutive CTAs, performed in our center, were reviewed and the studies which were flagged positive by the AI software (AiDoc) were extracted. The reports of these studies were reviewed to identify those studies which the radiology report did not mention the aneurysms. The identified 30 studies were read anonymously by 3 neuroradiology attendings and a neuroradiology fellow. The average of the size of each aneurysm was calculated and inter-reader agreements were calculated using the Intra-class correlation (ICC)

Results

R1 identified 21 (70%) aneurysms, with the mean and range of 2.4±0.7 (1.5-4) mm. R2 detected 14 (47%) aneurysms, with the mean and range of 2.5±1.3 (1-5) mm. R3 found 6 (20%) aneurysms with the mean and range of 2.3±0.8 (2-4) mm and R4 noted 15 (50%) aneurysms with the mean and range of 1.7±1 (1.5-5) mm. The ICC between readers was 55.2% (95%CI:25%-76%, P-value=0.001). In 6 (20%) cases, none of the readers identify any aneurysm, while in 5 (17%) cases, three readers did not identify any aneurysm. In 4 (13%) cases, no reader identified the same area, concerning for aneurysms.

Conclusions

Further attempts should be made to improve diagnostic accuracy of AI for detection of aneurysm, with emphasis on specificity. The focus of future AI research should be made on the improving prediction model for aneurysm rupture, which will be of more clinical significance.

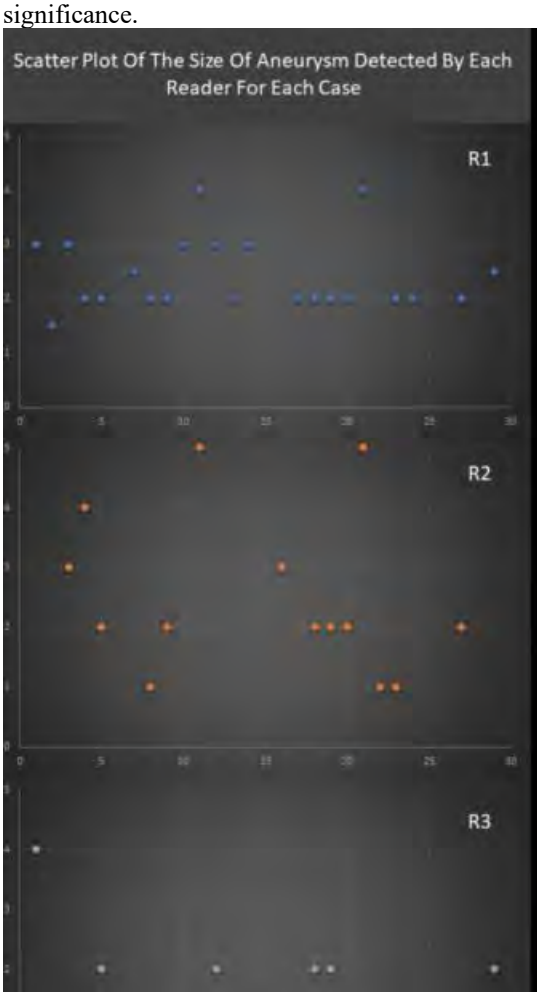

The median and interquartile range of the sizes of aneurysms identified by each reader

Case	Reviewer 1		Reviewer 2		Reviewer 3		Reviewer 4	
	Location	Size	Location	Size	Location	Size	Location	Size
1	Rt VA	3	None	-	Rt VA	4	Basilar	3
2	Rt Ophthalmic	1.5	None	-	None	-	None	-
3	Rt ICA	3	Rt ICA	3	None	-	Rt ICA	3
4	Rt ICA	2	Lt ICA	4	None	-	Lt ICA	2.5
5	Lt ICA	2	Lt ICA	2	Lt ICA	2	Lt ICA	1.5
6	None	-	None	-	None	-	None	-
7	Lt Pcom	2.5	None	-	None	-	Lt ICA	3
8	Lt ACA	2	Lt ACA	1	None	-	Lt ACA	1.5
9	Rt ICA	2	Rt ICA	2	None	-	Rt ICA	3
10	Rt ICA	3	None	-	None	-	None	-
11	Rt ICA	4	Rt ICA	5	None	-	Rt ICA	5
12	Lt ICA	3	None	-	Left ICA	2	Lt ICA/Pcom	2

(Filename: TCT_1064_Screenshot2022-11-14194538.jpg)

208

Role of Whole Brain Spectroscopy(EPSI) in Unilateral Mesial Temporal Sclerosis (MTS) - an MR/PET correlation study

s mangalore[1], M KUMAR[2], N Pradhan[2], P Bairwa[2], S Sinha[3], R Kenchaiah[2], A Asranna[2], R Mundlamuri[2], L Viswanathan[2]
[1]NIMHANS, bangalore, India, [2]National Institute of Mental Health and NeuroScience, BENGALORE, KARNATAKA, [3]National Institute of Mental Health and Neurosciences, Bengaluru, Karnataka

Purpose
Role of 3D echo planer spectroscopic imaging (EPSI) is well established in tumors but not in epilepsy. This first-time study explores whole brain metabolic mapping in healthy control versus unilateral MTS correlated with FDG PET. Distribution of Metabolites maps in MTS and healthy control compared to surrounding parenchyma. Lateralizing the MTS using whole-brain MR spectroscopy. Severity scoring of Unilateral MTLE on PET with grade 1 reflecting hypo-metabolism in the medial temporal lobe, grade 2 in the lateral temporal lobe, and grade 3 extending up to the parietal lobe.
Materials and Methods
12 Patients with unilateral MTS -right(10) left(2) and 9 healthy control subjects. Age range between 18-50 years. Patient underwent the EPSI scan in a 3T clinical MRI (mMR Biograph, Siemens Health System) scanner along with structural (T1-MPRAGE) sequence. Anatomical images were used for placing grid of voxels after anatomical registration in MIDAS pipeline. Visual analysis of in-vivo metabolic concentration using metabolic maps of Glx, NAA, Creatine, Choline, Lactate, Myo-inositol was done.The maps were generated from EPSI on MIDAS pipeline to visually analyzed the data and observed a pattern with a affected subject between affected and unaffected temporal lobes and also in healthy controls.
Results
The pattern noted in healthy controls in the temporal lobe as compared to surrounding parenchyma was equivocal for NAA, creatine. mI, choline and Glx were increased and lactate was found be decreased in MTL patients as compared to surrounding parenchyma.On visual analysis, the affected side that is either right/left MTS when compared to the unaffected side showed decreased NAA, creatine, Glx and have a role to lateralize epilepsy. Equivocal myo-inositol, choline, lactate and hence these maps have no lateralizing value in interictal epilepsy cases.On comparing EPSI with PET metabolism in unilateral MTS and labelling as grade 1 to 3, we found that decreased NAA and Cr on metabolite map correlated with hypo-metabolism in FDG-PET appropriate to the severity shown on PET scan.
Conclusions
The EPSI NAA and Cr metabolite maps generated are correlating with FDG-PET uptake in this study. Hence EPSI may act as an additional parameter of advanced MRI in epilepsy imaging.

1507

Sacroplasty for Pain Management in Cancer Patients: A Tertiary Centre Experience

M Nasralla[1]
[1]Toronto Western Hospital, Toronto, Ontario

Purpose
Sacroplasty is an increasingly utilised treatment in the management of patients with painful sacral insufficiency fractures, a technique which is predicated on experience from vertebral augmentation. Sacral pain may also occur in cancer patients resulting from direct tumour infiltration, pathological fractures, or insufficiency fractures related to previous cancer therapy. The use of sacroplasty for treating cancer-related pain however is less established with relatively small cohorts in the literature. Published reports also offer differing opinions with regards to optimal technique and inclusion criteria. We aim to review the technical considerations, efficacy, and safety in a large cohort of cancer patients who underwent sacroplasty at our institution. We also review our technical evolution towards the use of a trans-iliac approach to provide minimally invasive sacroplasty.
Materials and Methods
This is a retrospective review of all cancer patients who underwent sacroplasty at our institute over an 11-year period (01.01.2009 to 31.12.2020). Patients underwent preprocedural clinical assessment with follow up at 30 days post-procedure. Clinical variables included pre- and post-procedural Numerical Pain Rating Scale (NRS) and symptomatic complications. Preprocedural CT and MR imaging was reviewed to define the extent of bone infiltration, extraosseous tumour, and grade fractures. Procedural and postprocedural imaging was reviewed to assess technique, cement distribution and volume, and complications
Results
We identified 145 cancer patients who underwent sacroplasty over the study period. The study population comprised of patients with solid organ malignancies (n=81), lymphoma (n=2), leukaemia (n=1) and multiple myeloma (n=61).
Conclusions
Sacroplasty is becoming an increasingly utilised technique for treatment of painful insufficiency fractures. Nevertheless, its use in treating cancer-related pain is less well established, with the published literature tending towards small cohorts of patients and offer differing opinions regarding technique, modality, and treatment indications. We review the technical considerations, efficacy and safety, and consider its overall role in the management of cancer patients.

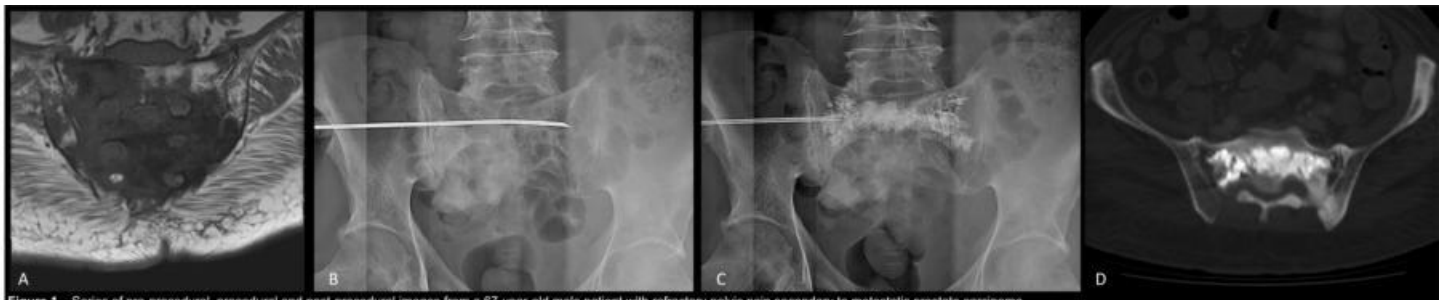

Figure 1 – Series of pre-procedural, procedural and post-procedural images from a 67-year-old male patient with refractory pelvic pain secondary to metastatic prostate carcinoma.
The coronal T1-weighted image (A) demonstrate extensive metastatic infiltration of the sacrum with involvement of the cortical margins and foraminal tumour infiltration. The posteroanterior procedural fluoroscopic image shows the appropriate position of an 11G needle inserted via the left transiliac approach (B) with the subsequent image (C) showing the final pattern of cement filling resulting from intermittent cement injection during needle withdrawal. (C). The post-procedural coronal CT image (D) demonstrates excellent cement filling within the sacral body and ala.

(Filename: TCT_1507_Sacroplastyfigure1ASNR.jpg)

1250

Sensitivity of Vocal Cord Sign on Initial Computed Tomography in Detection of Acute Lateral Medullary Syndrome: A Cross-Sectional Retrospective Single-Centre Study

B Tahan[1], N Badrawi[2], A Alfalahi[3], M Siddiqui[4], M Almulla[4], T Alnour[4]

[1]Dubai Health Authority, Dubai, Dubai, [2]Dubai Health Authority, Dubai, United Arab Emirates, [3]University of Toronto, Toronto, Ontario, [4]N/A, N/A

Purpose

To evaluate the sensitivity of vocal cord paralysis that may be detected on an initial CT angiogram of the head and neck in predicting lateral medullary syndrome prior to performing an MRI. The study also aims to investigate different types of imaging modalities in identifying this condition since it may improve early detection of this specific kind of stroke which may lead to significant life-threatening clinical complications.

Materials and Methods

Retrospective cross-sectional study conducted in the Radiology Department at Rashid Hospital & Trauma Centre in Dubai, which is a major tertiary hospital in the nation providing 24/7 emergency access as a stroke center. 83 Patients included, all were above 18 years old with clinical presentation of acute posterior circulation stroke and underwent CT angiogram of the brain according to the specific stroke protocol followed at Rashid Hospital that includes the head and neck and follows the great branches from the aorta to the circle of Willis and confirmed to be LMS on follow up MRI scan of the brain. All eligible patients were identified from the electronic medical records section. CTA images were evaluated by two experienced radiologists to detect the presence of standardized VCP sign in scored data collection sheet. Readers were blinded for the MRI result at the time of CTA evaluation, the CTA was always reviewed before the DSA. Following the initial analysis, a representative subset of 30 CTA records were selected and independently evaluated by the third experienced radiologist in the exact same way as the initial analysis. For baseline data, mean and standard deviations were used for continuous variables. Categorical variables were expressed as counts and percentages. Sensitivity of the CT scan compared with MRI findings (gold standard) to diagnose lateral medullary syndrome was estimated with 95% confidence intervals to evaluate its significance. All statistical analyses were performed with assistance of a statistician and SPSS statistical software, setting the level of significance of p-value of <0.05.

Results

Positive vocal cord sign in initial CTA of head and neck was highly sensitive and specific in LMS patients. Therefore, CT scan showed a high significance (reached up to 80%) in shortening the median time of diagnosis of lateral medullary syndrome.

Conclusions

Detection of Vocal cord sign on CTA is the new gold standard tool of early diagnosis of LMS, enabling prompt management; therefore reduce complications rate and saving life.

352

Sequential and Hybrid PET/MRI Acquisition in Follow-Up Examination of Glioblastoma Show Similar Diagnostic Performance

J Ziegenfeuter[1], I Yakushev[2], M Metz[3], B Wiestler[4]

[1]Klinikum rechts der Isar, TU Munich, Germany, Munich, Germany, [2]Dept. of Nuclear Medicine, Klinikum rechts der Isar, TU Munich, Germany, Munich, Bavaria, [3]Technical University of Munich, Munich, Germany, [4]TU Munich University Hospital, Munich, Germany

Purpose

Both positron emission tomography (PET) and magnetic resonance imaging (MRI) including dynamic susceptibility contrast perfusion (DSC-PWI) are crucial for treatment monitoring of patients with high-grade glioma.[1] In clinical practice, however, they are usually acquired at separate time points. If this affects their diagnostic performance is presently unclear.

Materials and Methods

To answer this question, we retrospectively reviewed 38 patients with pathologically confirmed glioblastoma (IDH wild type) and suspected tumor recurrence after radiotherapy. All patients received both a PET-MRI (where DSC perfusion was acquired simultaneously with a FET-PET) as well as a separate MRI exam (including DSC perfusion). Tumors were automatically segmented

into contrast-enhancing tumor areas (CET), necrosis and edema. To compare the simultaneous as well as the sequential DSC perfusion to the FET-PET, we calculated Dice overlap, global mutual information as well as voxel-wise spearman correlation of hotspot areas. For the joint assessment of PET and MRI, we computed logistic regression models for the differentiation between true progression (PD) and treatment-related changes (TRC) using simultaneously or sequentially acquired images as input data.
Results
We observed no significant differences between Dice overlap (p = 0.17; paired t test), mutual information (p = 0.17, paired t test) and Spearman correlation (p = 0.9) when comparing simultaneous PET-MRI and sequential PET/MRI acquisition. This held true also for the group of patients with > 14 days between both exams. Importantly, for the diagnostic performance, ROC analysis showed similar AUCs for differentiation of PD and TRC (AUC simultaneous PET: 0.77; AUC sequential PET: 0.76; p = 0.83, DeLong's test.).
Conclusions
We found no relevant differences between simultaneous and sequential acquisition of FET-PET and DSC perfusion, in particular for their diagnostic performance. Given the increasing attention to multi-parametric assessment of glioma treatment response, our results reassuringly suggest that sequential acquisition is clinically and scientifically acceptable.

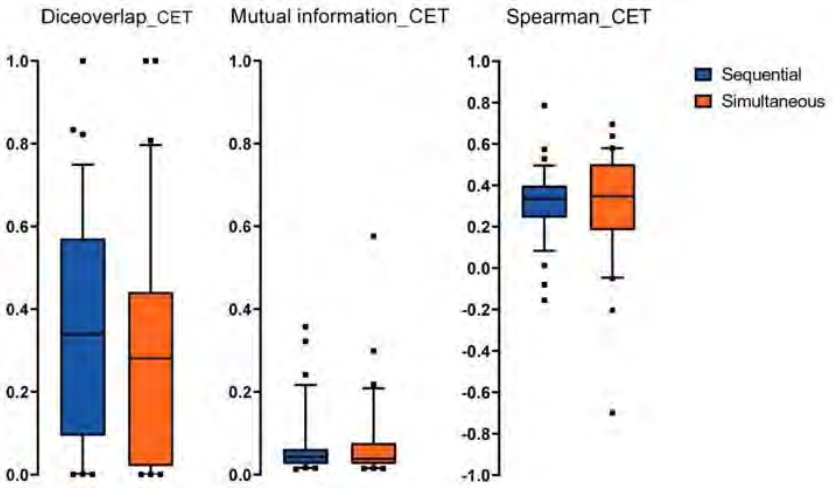

(Filename: TCT_352_CETtest.jpg)

1185

Simultaneous MRI-PET correlation of radiologic and histopathological changes with associated amygdala volumetry in patients diagnosed with mesial temporal sclerosis

S Malla[1], s mangalore[2], S Sinha[1], A Mahadevan[1], K Sitani[3]
[1]National Institute of Mental Health and Neurosciences, Bengaluru, Karnataka, [2]NIMHANS, bangalore, India, [3]National Institute of Mental Health and Neurosciences, bengaluru, Karnataka

Purpose
Patients with refractory mesial temporal epilepsy undergo extensive surgical resection in view of widespread abnormalities in neuronal synchronization involving mesial or neocortical structures. On structural imaging of brain, in addition to FLAIR hyperintensities involving hippocampus,signal changes in amygdala and uncus have been identified. The nature of the additional signal changes remains unknown with various theories attributing to gliosis or dysplastic changes. Here,we explored the pathologic findings pertaining to the abnormal signal changes in background of structural and metabolic imaging.
Materials and Methods
We retrospectively reviewed the preoperative imaging data of patients with medically intractable temporal lobe epilepsy and segmented the temporal lobe segmented into hippocampus, amygdala, uncus/ anterior temporal pole and lateral temporal lobe (STG/ MTG/ LTG). FLAIR signal changes in an ordinal scale, 18F-FDG PET metabolism (SUV quantification) and histopathology were correlated to assess for the cause of abnormal signal changes on structural imaging in addition to volumetric analysis of amygdala.
Results
Nineteen patients (right MTLE: 13, left MTLE: 6) were evaluated. FLAIR hyperintensities in hippocampus (19/19) and amygdala (16/19) had a significant association with neuronal loss and reactive gliosis on histopathology respectively. FLAIR hyperintensities seen in temporal pole/ uncus (11/19) did not show any evidence of cortical dysplasia. FDG-PET showed significant decrease in hypometabolism on the affected side. Volumetric analysis revealed no significant difference in amygdala volume between affected and unaffected side, however significant association (positive correaltion) was found between FLAIR hyperintense signal changes on affected side and volume of amygdala on the unaffected site.
Conclusions
Microscopic-necrosis due-to-underlying energy-failure leading to structural damage to myelination process could be causative mechanism for FLAIR-hyperintense signal changes rather than any cortical-developmental-malformation. Widespread hypometabolism could signify decrease in neuronal glutaminergic activity due to underlying subpial gliosis as found in histopathological studies. Larger-volume of amygdala seen on the side opposite to the ictal focus could be possibly due to ongoing-

neuro-inflammation on opposite-amygdala with an underlying potential network. This study could serve-as-a-template to understand the nature of MTLE from histopathological point of view.

1163

Styloidogenic Jugular Venous Compression May Contribute to 'Benign Jugular Reflux' Manifesting as ASL-MRI Skull Base Venous Hyperintensity: Image Analysis and Anatomical Considerations

T Geisbush[1], T Massoud[1]
[1]Stanford University School of Medicine, Stanford, CA

Purpose

Demonstration of MRI arterial spin-labeling (ASL) signal hyperintensity at the left jugular bulb (JB) is often misdiagnosed as a dural AVF when this may just be 'benign jugular venous reflux' (JR). The exact mechanisms for JR are not fully understood, but could include anatomico-physiological asymmetries in internal jugular veins (IJVs) causing flow reversal through increased valvular resistance or retrograde flow. However, the potential contribution of JB flow stasis owing to styloidogenic jugular venous compression (SJVC) has not been evaluated previously. We studied this possible mechanistic link between SJVC and JR by image analysis of patients with presumed JR on ASL-MRI.

Materials and Methods

We retrospectively reviewed MRIs of 60 criteria-selected adult patients (30 JR+ on ASL, and 30 age and sex near-matched JR- controls). For both cohorts, we measured ASL signal intensity at bilateral JBs, and calculated percentage increase in ASL signal in the higher-signal JB relative to the lower-signal one, also noting sidedness and IJV relative dominance. We measured IJV axial areas at and 2cm below maximum SJVC, categorizing this as mild (0-50%), moderate (51-80%), or severe (81-100%). We performed within group category comparisons using a non-parametric Kruskal-Wallis test to assess differences in percentage ASL signal increase compared to severity of SJVC.

Results

For JR+, 29 patients had left JR (ASL higher signal intensity) and 1 had right JR. Their IJVs were right/left/co-dominant in 28/1/1 patients, and SJVCs were mild/moderate/severe in 12/14/4 patients. For JR-, none of the 30 patients had visually detectable ASL hyperintensity, and when measured, ASL increases were marginal. Their IJVs were right/left dominant in 23/7 patients, and SJVCs were mild/moderate/severe in 12/13/5 patients. For JR+ there was a significantly higher increase in ASL-hyperintense JR with severe compared to mild SJVC (p=0.044), and a trend toward significantly higher increase in ASL-hyperintense JR with severe compared to moderate SJVC (p=0.094). In comparison, for JR- there was no statistical difference or trend toward a difference between mild, moderate, or severe SJVC.

Conclusions

In JR, the hyperintense ASL signal is predominantly in the left JB. Severe SJVC contributes to ASL-hyperintense JR when observed but does not solely explain its presence. Severe SJVC alone may not result in ASL-hyperintense JR. Further studies of structural and functional etiologic factors for this clinically important entity are ongoing.

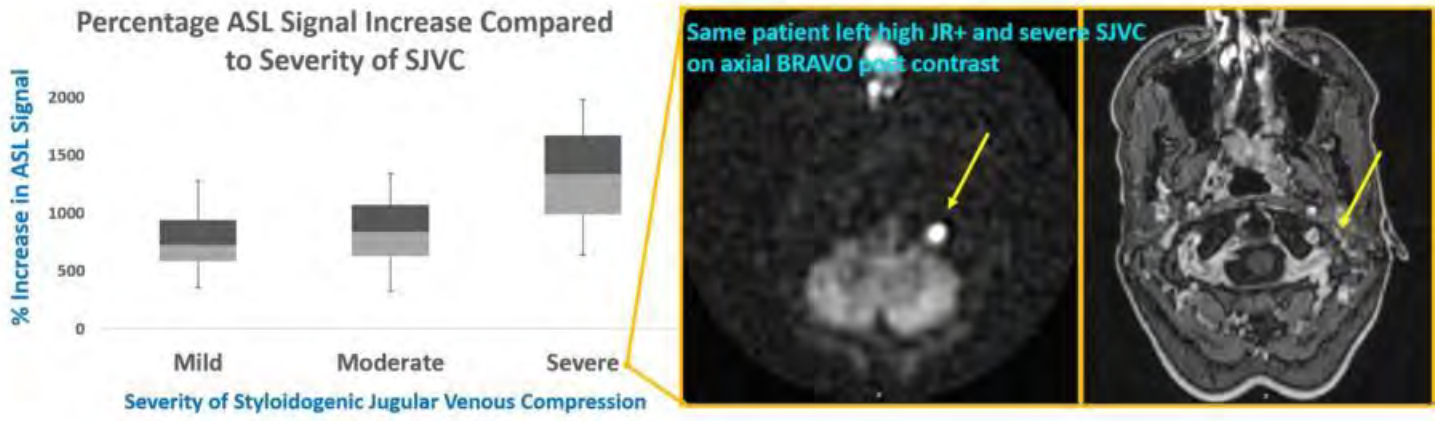

(Filename: TCT_1163_ASNRabstractfigure.jpg)

157

Subcortical Signal Alteration of Corticospinal Tracts. A Radiologic Manifestation of ARIA

M Alizadeh[1], R Shahidi[2], P Shobeiri[3], M Natelson Love[4], A Singhal[5], H Sotoudeh[6]
[1]Iran University of Medical Sciences, tehran, Tehran, [2]School of medicine, Bushehr university of medical sciences, Bushehr, Iran, Bushehr, Bushehr, [3]School of Medicine, Tehran University of Medical Sciences, Tehran, Iran, Tehran, Tehran, [4]University of Alabama at Birmingham, BIRMINGHAM, AL, [5]University of Alabama at Birmingham, Birmingham, AL, [6]UAB, Birmingham, AL

Purpose

Patients with Alzheimer's disease who have been given monoclonal antibodies targeting amyloid-β (Aβ) for scientific purposes may demonstrate a spectrum of abnormal brain MRI findings known as amyloid-related imaging abnormalities (ARIA). ARIA may exhibit as brain edema or sulcal effusion (ARIA-E) or as hemosiderin deposits caused by brain parenchymal or pial hemorrhage (ARIA-H).

The current study explores two cases with interval development of FLAIR hyper signal intensity along the bilateral corticospinal tracts in the motor cortex/precentral gyri after treatment by aducanumab. We believe this manifestation is a subtype of ARIA-A that has not been explored earlier.

Materials and Methods

Our first case was a 72-year-old woman with a history of HTN and kidney transplant (polycystic kidney) who presented with mild cognitive impairment with clinical findings consistent with early Alzheimer's disease. Second case was an 85-year-old woman with a history of Small Lymphocytic leukemia who was treated 20 years earlier and manifestations of dementia and anterograde amnesia from two years ago with failure of Aricept and Namenda therapy. Baseline MRI and baseline Amyloid PET/MR imaging delineated brain structural details before initiation of treatment for case1 and case 2, respectively. Also, safety MRIs were performed due to the registered guidelines. Moreover, further safety MRIs were carried out whenever a side effect presented (Case 1 manifested dizziness and vertigo). Follow-up MRI demonstrated interval spontaneous resolution of FLAIR hypersignal intensities along the corticospinal tract.

Results

Case 1 Baseline MRI demonstrated microvascular angiopathy without acute findings. Due to the reported dizziness and vertigo, the following safety MRI demonstrated new FLAIR hyper signal intensity in subcortical regions of precentral gyri (motor cortex) symmetrically and trace subarachnoid hemorrhage at the vertex compatible with ARIA-E and ARIA-H. Following MRI demonstrated stable ARIA-H and resolution of FLAIR hyper signal intensity of corticospinal tracts. Case 2 Initial Amyloid PET/MR imaging showed diffuse cerebral Amyloid deposition. After tolerating six doses of treatment, a safety MRI on day 154 of treatment revealed new bilateral symmetric FLAIR hyper signal intensity in the subcortical motor cortex. The follow-up MRI showed interval resolution of abnormal signal intensity.

Conclusions

New ARIA with unusual MR findings of symmetrical FLAIR hyper signal intensities in the subcortical corticospinal tracts.

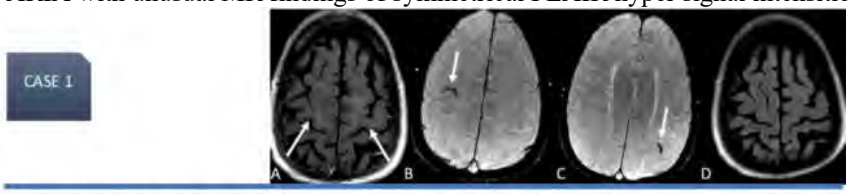

Fig 1. Day 84 brain MRI of the first case. New symmetric subcortical FLAIR hyper signal intensity in the subcortical motor cortex (A, Axial FLAIR sequence arrows) and trace SAH in bilateral cerebral hemispheres (B, and C Axial SWI sequence, arrows). Day 116 follow-up brain MRI demonstrates interval resolution of subcortical FLAIR hyper signal intensities (D, Axial FLAIR sequence).

Date	Event	Comments
Day 0	Dose #1 1mg/kg	No side effects noted
Day 28	Dose #2 1mg/kg	No SE effect
Day 56	Dose #3 3mg/kg	No SE effect
Day 84	Safety MRI #1 (Fig 1, A-C)	Done due to the patient's complaint of "Things running through her brain that takes her breath away momentarily". Consistent with FLAIR hyper signal intensity in subcortical motor cortex bilaterally and ARIA-H.
Day 116	Safety MRI #2 (Fig 1, D)	interval resolution of subcortical FLAIR hyper signal intensity of subcortical motor cortex) ARIA-H stable, . OK to restart
Day 139	Dose #4 3mg/kg	Reported Gastrointestinal discomfort and headache
Day 146	ED visit because of headache	CT Head negative, headache treated by Tylenol
Day 150	Safety MRI #3	Stable ARIA-H
Day 174	Dose #5 6mg/kg	No side effects- pretreated with Tylenol
Day 202	Dose #6	No side effect

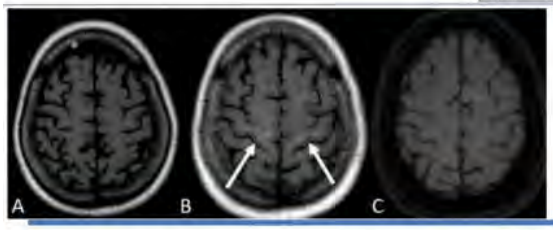

CASE 2

Fig2. A: Baseline MRI in FLAIR sequence. B: FLAIR sequence on day 154 demonstrates symmetric FLAIR hype signal intensity in the subcortical motor cortex, arrows. C: Follow-up MRI on day 203 shows interval spontaneous resolution of abnormal signal changes

Date	Event	Comments
Day 0	Dose #1 1mg/kg	No side effect
Day 14	ED trip	Dizziness and blurred vision 10/1-10/5, normal CT Head
Day 24	ED visit because of confusion/MRI	No acute finding on MRI
Day 29	Dose #2 1mg/kg	No side effect
Day 57	Dose #3 3mg/kg	No side effects except brief headache several days later
Day 91	Dose #4 3mg/kg	No clear side effect except continued decline with confusion
Day 113	Dose #5 6mg/kg	No obvious side effects, just worsened appetite and confusion
Day 142	Dose #6 6mg/kg	No side effects, but started having neck pain
Day 154	Safety MRI	New subcortical FLAIR hyper signal intensities in the bilateral motor cortex
Day 203	Contrasted MRI	Interval resolution of FLAIR hyper signal intensities, but daughter wanted to stop aducanumab because of lack of symptom improvement

(Filename: TCT_157_ARIACASESPIC.jpg)

256

Susceptibility Vessel Sign (SVS) for Assessment of Intra-Arterial Thrombus and Thrombus burden in Patients with Acute Ischemic Stroke: an institutional study

S PAUDEL[1]

[1]*Nepalese Army Institute Of Health Sciences, Bharatpur, Bagmati*

Purpose

SWI can help in the diagnosis of thrombus within the vessel in acute ischemic stroke (AIS) known as susceptibility vessel sign (SVS) and detection of SVS within the vessel can predict treatment modality and outcome. In this study, the purpose is to correlate the SVS on SWI with different parameters of stroke.

Materials and Methods

It was a retrospective cross-sectional study, where consecutive stroke patients with vessel occlusion on magnetic resonance angiography (MRA) were included for the study for one year. The relation of SVS on SWI with risk factors and territory involved and length of thrombus was correlated with the NIH stroke scale (NIHSS).

Results

A total of one hundred and five patients were enrolled for this study. 62% (66 out of 105) of patients showed SVS on SWI with MRA positive occlusion. A positive correlation was observed between SVS on SWI with the risk factor (p=0.003) with 86% of heart disease and 47% of hypertension had SVS. A positive correlation was also observed between the SVS on SWI with territorial occlusion (p =0.000). There was moderate positive correlation was observed between the NIHSS and thrombus length (p=0.002) with a Pearson coefficient of 0.367.

Conclusions

SWI can be useful in identifying the location of the thrombus, and NIHSS can determine the thrombus length in acute stroke. A higher incidence of SVS can be associated with risk factors and it also depends upon the site of occlusion of the vessel.

Table 1: Demographics of all the patients included in study

Total no of patients (n=105)	**Number of patients (%)**
Sex	
Males	66(62.8)
Females	39(37.2)
Age (years)	
Mean	58 (22-87)
Risk Factor	
Hypertension	44 (41.9)
Heart Disease	30(28.5)
Tobacco use	22(20.9)
Type 2 Diabetes Mellitus	3(2.8)
Others	6(5.7)
Territory involved	
MCA M1	42(40)
MCA M2	15(14.2)
MCA M1+M2	15(14.2)
T occlusion (ICA bifurcation)	19(18.1)
Others	15(14.2)
NIHSS Score (National Institutes of Health Stroke Scale)	
Maximum	23
Minimum	2
Mean	11
SVS on SWI with MRA showing occlusion	
Present	66(62.9)
Absent	39(37.1)

MCA- Middle cerebral artery, SVS- susceptibility vessel sign, MRA- MR angiography, T occlusion-ICA bifurcation

(Filename: TCT_256_figuref.jpg)

704

Teaching Complex Skull Deformities with 3D-Printed Models

L Amundson[1], D Nascene[1], Y Huang[1]
[1]University of Minnesota, Minneapolis, MN

Purpose

New learning modalities have become available for teaching three-dimensional (3D) anatomic topics including virtual 3D models, 3D printed models, augmented reality, and virtual reality. 3D printed models improve memory retention, enhance anatomic spatial awareness, and increase student satisfaction compared to traditional two-dimensional learning (1-3). One topic that could benefit from the application of 3D modeling is craniosynostosis, a common disorder occurring in one in every 2,200 live births (4). While 3D modeling is being used for surgical simulation of craniosynostosis repair, there is limited data on the efficacy of 3D models for identification of craniosynostosis (5). Since early recognition is vital for surgical consultation, primary care providers must be able to identify the presentations of craniosynostosis. We hypothesize that adding 3D models to learning will enhance diagnostic accuracy and user confidence in recognizing craniosynostosis.

Materials and Methods

From existing CT data, the following types of pediatric skulls with craniosynostosis were segmented and 3D printed: sagittal, bilateral coronal, unilateral coronal, unilateral lambdoid, and metopic. Additionally, a normal, ping-pong fracture, and positional plagiocephaly skull were also printed. Positional plagiocephaly is an important craniosynostosis lookalike, and the ping-pong fracture represents a distractor diagnosis. An introductory presentation was created to provide a brief overview of craniosynostosis in addition to individual online modules for the 3D models. The introductory lesson was given to six medical students followed by the 3D model + module portion. Modules featured an interactive mini lesson utilizing the 3D model to answer questions. Afterwards, a posttest was given, and the results were qualitatively analyzed.

Results

Five qualitative responses were obtained in this preliminary study (Figure 1). Overall, respondents found the lesson improved their understanding and recognition of craniosynostosis. All participants favored an interactive lesson over a lecture-based presentation and noted the physical 3D models improved their understanding of craniosynostosis.

Conclusions

Physical models may provide benefit over traditional, lecture-based learning for understanding complex 3D anatomy such as craniosynostosis. Further studies are needed with learners of all levels to collect both qualitative and quantitative data comparing in-person learning incorporating physical 3D models versus virtual learning.

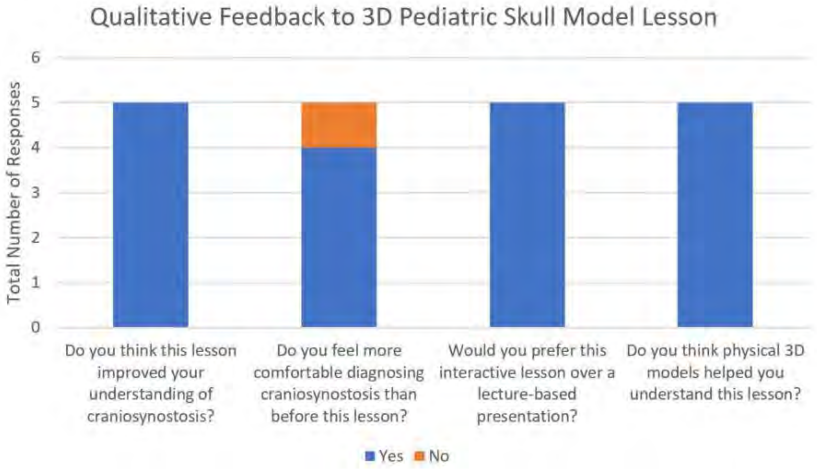

(Filename: TCT_704_QualitativeFeedbackto3DPediatricSkullModelLesson.jpg)

956

Textural Radiomic Features from Multiparametric MRI can predict Alzheimer's Disease Progression: A Proof-of-Concept Study

G Singh[1], T Kainth[2], X Xu[2], V Spektor[1], P Prasanna[2]
[1]Columbia University Irving Medical Center, New York, NY, [2]Stony Brook University, Stony Brook, NY

Purpose

An estimated 6.5 million Americans aged 65 and older are affected by Alzheimer's dementia (AD) in 2022. Progression of Alzheimer's disease occurs in a continuum divided into three components: a) Preclinical Alzheimer's disease, b) Mild Cognitive Impairment (MCI), and c) AD. It is crucial to identify individuals with MCI that are more likely to develop dementia. In this study, we perform a comparative analysis of sub-visual imaging features (radiomics) extracted from structural MRI. Our goal is to identify features that potentially predict the progression of dementia.

Materials and Methods

Our dataset comprised 65 cases from the Alzheimer's Disease Neuroimaging Initiative database. We selected preprocessed 3D T1w

MRI sequences in the MCI group within ADNI 1, ADNI 2, and ADNI GO projects. Selected patients were divided into two groups based on Clinical Dementia Rating (CDR): 1) Converters (C) (23 out of 65), whose baseline CDR of 0.5 changed to 1 at the latest diagnoses, and 2) Non-Converters (NC) (42 out of 65), whose baseline CDR of 0.5 remained 0.5 at the latest diagnosis. We used FreeSurfer software to segment 41 subcortical structures. The segmented subcortical structures were then used to extract gray-level co-occurrence matrix (GLCM) radiomic features using Pyradiomics. Out of 65 patients, five patients in the NC group were excluded due to erroneous segmentation and feature extraction. Using the Student's T-test, we compared 24 radiomic features from 41 subcortical segmentations in C and NC groups.
Results
The regions with the highest number of statistically significant different radiomic features ($p<0.05$) between the C and the NC groups were: a) left hippocampus (20/24), b) left lateral ventricle (17/24), c) middle-anterior corpus callosum (10/24), d) right hippocampus (9/24), and e) right lateral ventricle (9/24).
Conclusions
Our results demonstrate the textural radiomic feature differences in converters (C) and non-converters (NC) groups diagnosed with MCI. As our next step, we will use the extracted radiomic features to train a machine learning model for prognostic prediction in Alzheimer's disease. Clinical Relevance/Application: Identifying radiomic signature differences on MRI can help us characterize different groups of patients with MCI. Using these features with machine classifiers can aid in the management of Alzheimer's disease.

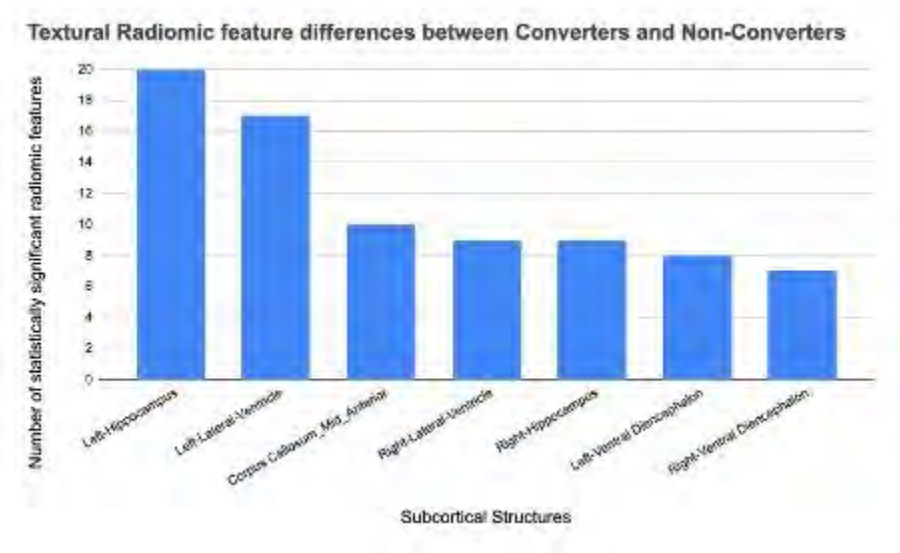

(Filename: TCT_956_Figure1.jpg)

886

The Circle of Willis in a New Dimension: How 3D Printing Offers a Nuanced Approach to Procedure Simulation

S Patel[1], J Kirsch[1], E Moon[1], H Chong[1], E Dunning[1], R Richardson[1]
[1]*Creighton University, Phoenix, AZ*

Purpose
To determine the cost-effectiveness of 3D printing vasculature models for procedure simulation and training. We aim to delineate the process of converting a head tomography angiogram (CTA) into a 3D printed model for simulations like Circle of Willis navigation and large artery embolization.
Materials and Methods
CTA image was converted into a 3D digital model and saved as a .stl file using GE Healthcare AW Volumeshare 7. A free automated computer-aided design software 3D Slicer was used to hollow out the arterial model and erase artifacts. The final digital version was printed on Formlabs Form3 3D printer using Elastic 50A resin. The 3D printed models were further processed by manually removing support structures, washing residual resin off with 100% isopropanol, and treating in UV light at 60˚C for 20 min (1).
Results
The Circle of Willis and its neighboring branches were 3D printed using a CTA brain image. The model was hollow, elastic, and transparent with varying vessel sizes. We found that the diameter of the arteries varied from 0.7-3.6 mm throughout the entirety of the model with an average wall thickness of around 1 mm. The Form3 printer at the price of $3,499 printed our model at a resolution of 100 um layer thickness using a total resin volume of 52 mL. With the current price of resin at $0.15/mL, our single print costs about $7.80 of resin.
Conclusions
Our 3D printed high-fidelity model of the Circle of Willis was produced at a significantly lower cost than many models currently sold for simulation training. Preservation of haptic feedback was maintained as our model is both hollowed and transparent allowing for direct visualization of catheter and wire advancement. We specifically aimed to 3D print this model as it not only demonstrates the ability to accurately create both large and small vessels, but also acts as a tangible method of visualizing the anatomical complexity of

a significant neurovascular structure. Simulation-based training allows individuals to learn new skills and become more proficient and confident, ultimately resulting in better patient outcomes (2). Currently, training opportunities for settings such as interventional radiology are limited due to cost and availability. 3D-printed models offer not only a cost-effective possibility but also patient-specific anatomical models to simulate the diversity within vascularity. Additionally, these files have the unique property to be shared, so different institutions may utilize and print models for the benefit of trainees.

319

The development and application of a cost-effective cervical spine phantom for use in fluoroscopically guided lateral C1-C2 puncture training

V Risner[1], B Huang[2], K McCullagh[3], T Benefield[3], Y Lee[4]

[1]University of North Carolina at Chapel Hill, Durham, NC, [2]University of North Carolina, Chapel Hill, NC, [3]University of North Carolina at Chapel Hill, Chapel Hill, NC, [4]UNC Chapel Hill, Chapel Hill, NC

Purpose

Lateral C1-C2 puncture is a rare procedure performed by neuroradiologists for various purposes, including CSF collection and contrast injection, when lumbar puncture is not available. Due to the infrequency of this procedure, there are limited opportunities to learn and practice the technique. We aimed to develop and assess the efficacy of a low-cost, reusable cervical spine phantom for use in fluoroscopically guided lateral C1-C2 puncture training.

Materials and Methods

Model Construction: The phantom was constructed using a modified PVC cervical spine model, an outer latex tubing with a 12.7mm inner diameter representing the spinal canal, an inner latex modeling balloon with 5mm outer diameter representing the spinal cord, and alginate encompassing the model to replicate soft tissue. The total cost of materials for one model was approximately $65. The outer tube was filled with water and the inner balloon filled with dyed water so the spinal tap would reveal dyed water if the "spinal cord" was punctured. A valve was placed on one end of the outer tubing and a hemostat was used to secure the other end to maintain pressure and seal the canal. This enabled refilling of the canal and replacing of the latex balloon if the balloon was punctured in a previous attempt. Assessment of Training Efficacy: Residents and fellows were provided with a pre- and post-survey assessing for comfort level in performing a puncture, confidence in having a successful puncture, and perception of current knowledge of the steps in a puncture. Training sessions were led by neuroradiology faculty at a single institution using the phantom model under fluoroscopic guidance. Survey questions were assessed on a 5-point Likert scale.

Results

The sample size of the training group was 21. Comfort level was improved by 2.00 points (standard deviation [SD]: 1.00, p-value <0.0001), confidence by 1.52 points (SD: 0.87, p-value <0.0001), and perception of current knowledge by 2.19 points (SD: 0.93, p-value <0.0001). 81% of participants found the model to be "very helpful" (5/5 on Likert scale), and all participants were "very likely" to recommend others to sign up for this workshop.

Conclusions

This cervical phantom model is a low cost, replicable, and demonstrates clinical training utility to better prepare residents for lateral C1-C2 puncture. Lateral C1-C2 punctures are rare procedures, so the use of a phantom model prior to patient encounters will be invaluable to resident education and training.

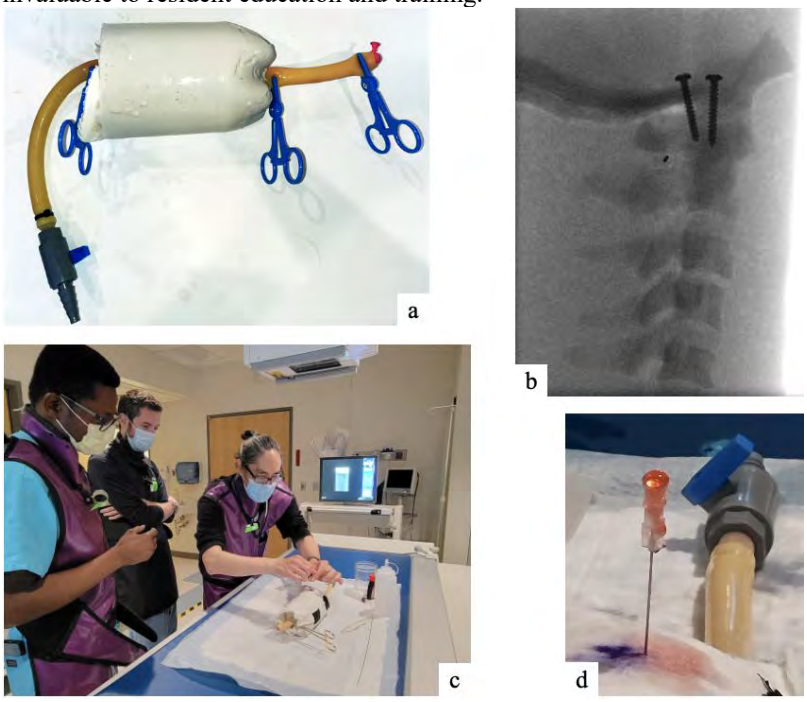

(Filename: TCT_319_graphic.jpg)

713

The Effect of Chronic Traumatic Brain Injury on Cerebral Blood Flow as Measured by Arterial Spin Labeling MRI And Metabolism as Measured by Fluorodeoxyglucose Positron Emission Tomography.

J Heholt[1], R Patel[2], F Vedaei[3], J Muller[3], D Middleton[3], M Alizadeh[3], A Bazzan[4], D Monti[3], A Newberg[3], Z Wang[5], F Mohamed[3]
[1]State University of New York Downstate Medical Center, Brooklyn, NY, [2]Rutgers Robert Wood Johnson Medical School, New Brunswick, NJ, [3]Thomas Jefferson University, Philadelphia, PA, [4]Thomas Jefferson Unviersity, Philadelphia, PA, [5]University of Maryland, Baltimore, MD

Purpose
To simultaneously observe and compare the changes in relative cerebral blood flow (rCBF) measured using arterial spin labeling functional magnetic resonance imaging (ASL fMRI) to metabolism measured using Fluorodeoxyglucose positron emission tomography (FDG-PET) in chronic traumatic brain injury (TBI) patients as compared to healthy controls (HC).
Materials and Methods
56 chronic TBI patients (age 18-71) and 40 HC with no prior history of TBI (age 28-67) underwent both ASL fMRI and FDG-PET via a Siemens mMR (simultaneous PET/MRI) scanner. Images were processed using statistical parametric mapping software relevant to each modality (ASLtbx or PETPVE12). CBF and glucose uptake values were normalized to the whole brain of each patient to generate relative values; rCBF and glucose standard uptake value ratios(SUVR). Using these rCBF and SUVR maps a voxel-wise two-sample T-test between TBI patients and HC was performed over grey matter regions for each modality using DPABI_V5.1_20120. The regions that survived two-tailed Gaussian random field (GRF) correction for multiple comparisons with a voxel P-value < 0.01 and cluster size > 50 voxels were identified.
Results
Both FDG-PET (Figure 1) and ASL (Figure 2) identified areas of change in rCBF and SUVR in the TBI patients as compared to the controls. More areas were identified using FDG-PET than ASL but both showed an increase in rCBF and glucose uptake in the right thalamus and a decrease in rCBF and SUVR in bilateral occipital lobes and calcarine sulci (Table 1 and 2). Regions in the left frontal lobe were found to have an increase in rCBF but a decrease in SUVR. The left Precuneus and regions in the right temporal lobe were found to have a decrease in rCBF but an increase in glucose SUVR.
Conclusions
Uncoupling of blood flow and metabolism is a well-documented phenomenon following traumatic brain injury. Our study shows that both ASL fMRI and FDG-PET can identify changes in brain function and that this uncoupling still persists in a chronic TBI population (>3 months post-TBI). This uncoupling may explain why even though ASL fMRI and FDG-PET identified common regions of change, FDG-PET identified more regions of functional disturbance than ASL fMRI. Even with a normal structural MRI scan, individual or combination ASL fMRI and FDG-PET images show changes in brain function that can lead to a better understanding of the pathophysiology of chronic TBI.

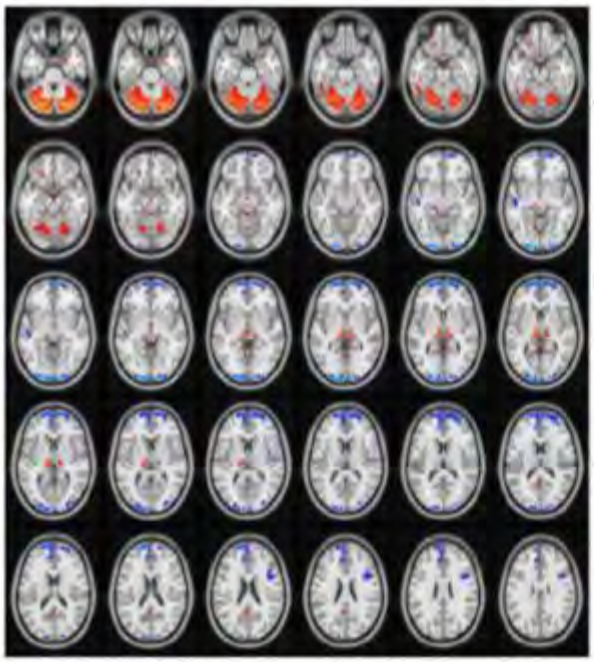

Figure 1: Results of FDG PET Two Sample T-Test TBI Patients vs HC Two Tailed GRF Corrected Voxel p<0.01 Cluster >50 Controlled for Sex and Age

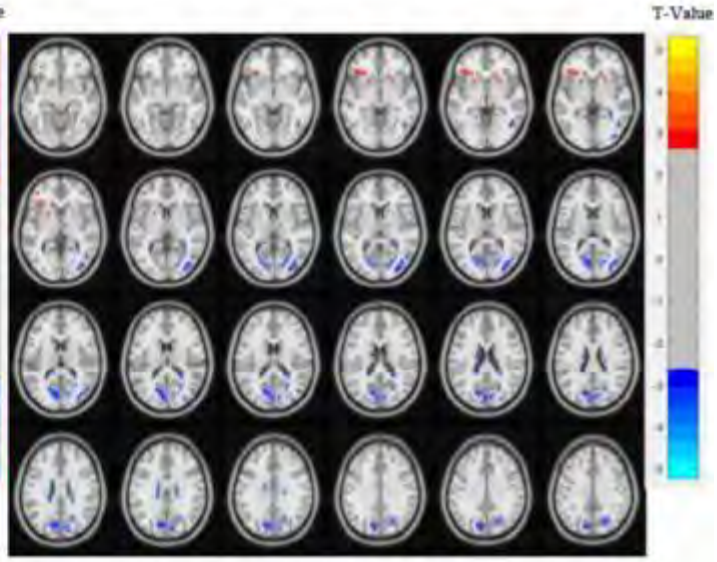

Figure 2: Results of ASL fMRI Two Sample T-Test TBI Patients vs HC Two Tailed GRF Corrected Voxel p<0.01 Cluster >50 Controlled for Sex and Age

Significant Clusters (aal atlas)	No. of Voxels	Peak MNI Coordinate	Peak Intensity (T Value)
Left Cerebellum Right Cerebellum Left Fusiform Left Inferior Temporal	9276	-30 -70 -44	6.6601
Left Thalamus	360	-14 -22 2	4.9487
Left Precuneus	101	-6 -56 20	3.736
Right Middle Temporal Pole Right Parahippocampus	285	20 2 -34	3.7328
Right Thalamus	171	12 -20 0	3.5292
Left Middle Temporal	107	-48 -20 -8	-3.4663
Right Inferior Frontal Operculum	165	38 8 24	-3.583
Right Calcarine **Right Middle Occipital** Right Inferior Occipital	361	26 -96 -8	-4.218
Left Superior Medial Frontal Left Superior Frontal Left Anterior Cingulum Left Medial Orbital Superior Frontal	1029	-10 60 22	-4.2679
Right Superior Frontal Right Superior Medial Frontal Right Medial Orbitofrontal Right Superior Orbitofrontal	790	18 68 2	-4.3395
Left Middle Occipital **Left Superior Occipital** Left Inferior Occipital **Left Calcarine**	789	-18 -100 -8	-5.5176

Table 1: Results of two sample T-tests between standard uptake value ratio (gSUVR) in the grey matter of cTBI vs HCs. Two-tailed GRF corrected voxel p<0.01 and clusters >50 voxels shown. Regions in **bold** were also identified as significant on PASL-fMRI scanning. Yellow shading indicates an increase in gSUVR, while blue shading indicates a decrease in gSUVR in cTBI patients as compared to controls.

Significant Clusters (aal atlas)	No. of Voxels	Peak MNI Coordinate	Peak Intensity (T Value)
Right Thalamus	52	10 -8 6	5.303
Left Frontal Inferior Triangularis	199	-42 28 0	4.201
Left Putamen	61	-22 12 0	3.5942
Left Precuneus	55	-2 -66 50	-4.1846
Right Cuneus Right Superior Occipital **Right Calcarine** Right Precuneus	677	6 -82 26	-4.4511
Right Middle Occipital Right Middle Temporal	427	30 -86 0	-4.4583
Left Cuneus **Left Calcarine** **Left Superior Occipital**	785	-20 -80 6	-4.5339

Table 2: Results of two sample T-test between relative cerebral blood flow (rCBF) in the grey matter of cTBI vs HCs. Two tailed GRF corrected voxel p<0.01 and clusters >50 voxels shown. Regions in **bold** were also identified as significant on FDG PET scanning. Yellow shading indicates increase in rCBF, while blue shading indicates decrease in rCBF in cTBI patients as compared to controls.

(Filename: TCT_713_ASNRABSTRACTIMAGES.jpg)

596

The effects of time to repeat head CT among TBI patients with anticoagulant reversal

J Hudson[1], S Jarvis[2], D Hamilton[3], R Landin[1], D Bar-Or[2]

[1]Saint Anthony Hospital, Lakewood, CO, [2]Injury Outcomes Network (ION) Research, Englewood, CO, [3]Penrose Hospital, Colorado Springs, CO

Purpose

There is controversy surrounding the timing of routine repeat head computed tomography (CT) for traumatic brain injuries (TBI), especially for patients taking anticoagulants requiring reversal, who have a higher risk of bleeding.(1, 2) The study objective was to examine the effect of having a repeat head CT scan ≤ 2 hours of arrival among TBIs with anticoagulant reversal.

Materials and Methods

This retrospective cohort study at two level I trauma centers included adult TBIs who had their pre-injury anticoagulants reversed and had 2+ head CTs (1/1/19-11/30/21). Patient's whose repeat head CT was ordered ≤ 2 hours of the initial CT (termed "≤ 2 patients") were compared to patient's whose repeat head CT was ordered > 2 hours after arrival (termed "> 2 patients"). Outcomes included hospital length of stay (HLOS), intensive care unit (ICU) admission, worsening intracranial hemorrhage (ICH), and readmission. Analyses were also conducted among only patients whose repeat head CT was not used for post-procedure follow-up. Fisher's exact, chi-squared, Wilcoxon, and Student's t-tests were used, $\alpha<0.05$.

Results

There were 112 patients, 98 were > 2 patients and 14 were ≤ 2. Overall patients were a mean of 74 y/o and 66% male. The groups were similar in their baseline characteristics. The ≤ 2 patients were admitted to the ICU significantly less often than > 2 patients, 79% vs 96%, p=0.04, but the median HLOS was similar, 4 days vs. 5, p=0.29. The ≤ 2 patients had CT evidence of ICH worsening significantly more often than > 2 patients, 62% vs 22%, p=0.01. The median time to surgery was significantly shorter for ≤ 2 patients, 1 hr vs 9, p=0.02. The total number of scans was 3 for both groups, p=0.33. The ≤ 2 patients had a statistically similar readmission rate to the > 2 patients, 29% vs 14%, p=0.24. In a subset of patients excluding those whose repeat head CT was a post-procedure scan, the ≤ 2 patients were still more likely to have CT evidence of ICH worsening, 80% vs 25%, p=0.02, and a faster time to surgery, 4 vs 32, p=0.03, but there were no differences in ICU admittance, p=0.15, HLOS, p=0.47, or readmission, p=0.12.

Conclusions

Conducting a repeat head CT ≤ 2 hrs for TBI patients with anticoagulant reversal may lead to a faster diagnosis of worsening ICH and earlier surgery without significantly impacting HLOS or readmission.

944

The intrinsic functional neural pathway underlying thirst behavior

Y TSAI[1]

[1]CHANG-GUNG MEMORIAL HOSPITAL, CHIAYI CITY 600, CHIAYI CITY

Purpose

Goal-directed behaviors responding to physiological needs is essential to organismal well-being and survival. An example is thirst behavior, where the physiological need to maintain water balance drives the basic instinct to drink. However, the neural basis underlying how this spontaneous behavior remains unclear. Determining the neural basis of thirst behavior can provide insights into how a brain-wide system transforms sensory inputs into behavioral outputs.

Materials and Methods

Here, we designed an experiment that simultaneously collects MRI scans and diverse psychological data under different hydration statuses within 13 hours in a longitudinal manner. We used functional connectivity analysis on resting-state functional magnetic resonance imaging data of volunteers (n = 20) to determine the dynamic changes in functional interactions among medical preoptic nucleus (MnPO) and high-level cognition systems across different dehydration statuses. We then use serial-multiple mediation analysis to discover the underlying functional pathways for thirst regulation.

Results

We provide a model for the neural basis of human thirst behavior (Fig. 1), where the physiological need for water is first detected by the medical preoptic nucleus, which then regulates the intention of drinking via serial large-scale spontaneous thought related intrinsic network interactions that includes the default mode network, salience network, and frontal-parietal control network.

Conclusions

This study used functional connectivity analysis and serial-multiple mediation analysis, to provide a model for the neural basis of human thirst behavior, where the physiological need for water is first detected by the MnPO which then regulates the intention of drinking via serial large-scale spontaneous thought related intrinsic network interactions that includes the default mode network, salience network, and frontal-parietal control network. Our study provides evidence that large-scale intrinsic brain networks underlie the transformation of sensory inputs from physiological needs to human spontaneous behavioral responses.

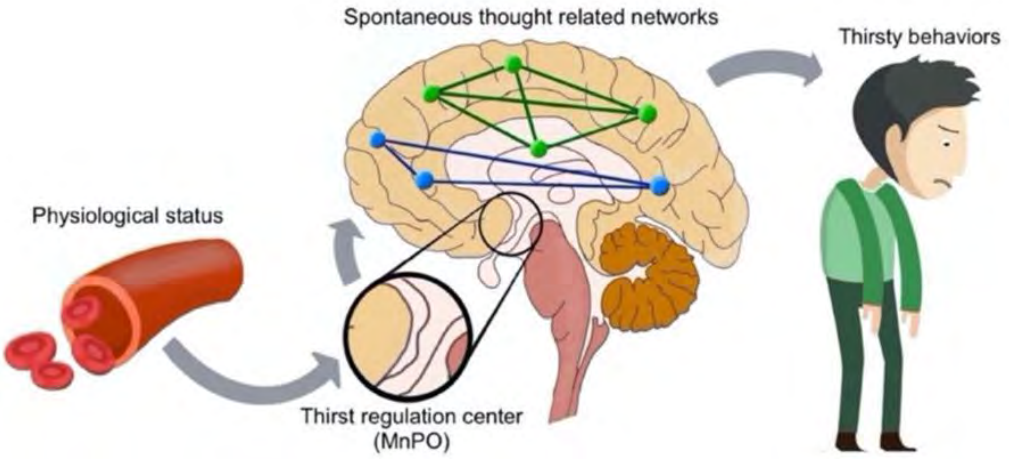

(Filename: TCT_944_Figure.jpg)

525

THE PRESENCE OF PACHYMENINGEAL HYPERINTENSITY ON NON-CONTRAST FLAIR IMAGING IN PATIENTS WITH SPONTANEOUS INTRACRANIAL HYPOTENSION

R O'Cearbhaill[1], R Willinsky[1], R Farb[1], P Nicholson[1]
[1]*University Health Network, Toronto Western Hospital, Toronto, Ontario*

Purpose

Traditionally, in the work up of patients for spontaneous intracranial hypotension, T1 post-contrast imaging is performed in order to assess for pachymeningeal enhancement.1 The aim of this study is to assess whether pachymeningeal hyperintensity can be identified on a non-contrast FLAIR sequence in these patients, as a surrogate sign for pachymeningeal enhancement.

Materials and Methods

The patient cohort was identified from a prospectively maintained database of patients with a clinical diagnosis of intracranial hypotension. Patients who had both a post contrast T1 sequence brain as well as non-contrast FLAR sequence of the brain were reviewed. Imaging was retrospectively reviewed by 3 independent neuroradiologists. Each study was assessed for the presence or absence of pachymeningeal hyperintensity on the FLAIR sequence.

Results

From January 2010 to July 2022, 177 patients were diagnosed with spontaneous intracranial hypotension. 121 were excluded as post contrast imaging was not performed during their work up. 24 were excluded as the FLAIR sequence was performed after administration of contrast. 6 were excluded as there was no pachymeningeal thickening present on T1 post-contrast imaging, although there were other signs of intracranial hypotension. The study group therefore consisted of 26 patients. Pachymeningeal thickening was correctly identified on the non-contrast FLAIR sequence in all patients (100%).

Conclusions

Where present, diffuse pachymeningeal hyperintensity can be accurately identified on a non-contrast FLAIR sequence in patients with spontaneous intracranial hypotension. This obviates the need for gadolinium based contrast agents in the work up of these patients.

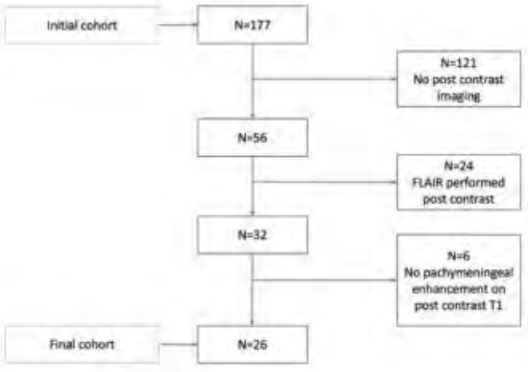

Figure 1: Flow chart demonstrating the inclusion/exclusion criteria.

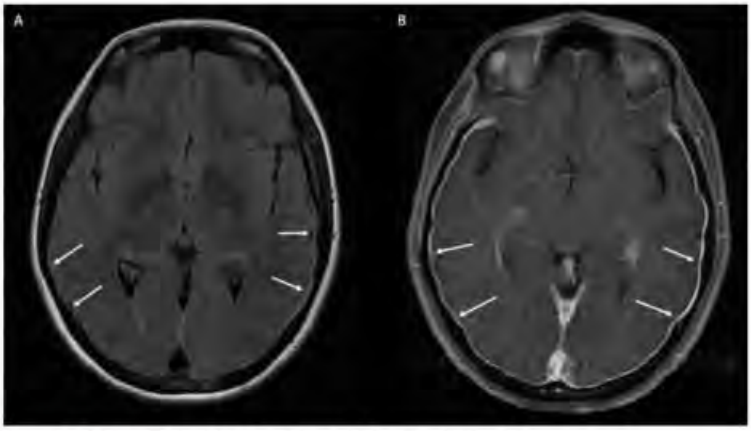

Figure 2: MRI brain imaging of a 41 year old female patient with symptoms of intracranial hypotension. A, axial non-contrast FLAIR sequence demonstrates diffuse pachymeningeal hyperintensity (arrows) and B, axial T1 post-contrast, shows diffuse pachymeningeal enhancement (arrows).

(Filename: TCT_525_Screenshot2022-11-03at112227.jpg)

230

The Usefulness of the New MR-Neurography Sequences in the Evaluation of the Parsonage Turner-Syndrome

M Jiménez de la Peña[1], A Maldonado[2], A Fernández Alonso[1], J Carrascoso Arranz[3], V Martínez de Vega[1]

[1]Hospital QuironSalud Madrid, Madrid, Spain, [2]Hospital Universitario de Getafe, Madrid, Spain, [3]Hospital QuironSalud Madrid, Madrid,Spain

Purpose

- We show a case series of Parsonage Turner-syndrome evaluated with the new isovolumetric 3D-DIR-STIR sequences after endovenous gadolinium contrast - This sequence evidence the individual nerve or nerves fascicle constrictions supporting the suspected clinical diagnosis and providing a presurgical neurography map in patients with no improvement after conservative treatment

Materials and Methods

We evaluated 8 patients (6 males,2 females) with clinical and electromyographic findings of neuralgic amyotrophy. All patients were imaged by an MR 3TPremier (GE), using an aircoil multichannel to improve the magnetic homogeneity and the fat suppression of this complex anatomic area. Patients were evaluated in all planes with a tse-t1 and t2-weighted sequences, and with a postgadolinium high resolution MR-neurography and a fat-suppressed t1-weighted sequence. the 3D-DIR-STIR parameters were: R:3000ms;TE:85ms;TI:280ms;BW:1,67,etl:110;nex:1; fov:260x260;matrix:352x352;slice:1,2;gap:0.The acquisition time was <6 min

Results

Muscular denervation was observed in 7 patients, with diffuse muscle edema and/ or variable degree atrophy affecting the supraspinatus, infraspinatus, anterior serratus, teres minor, scalenes and extensor muscles. The nerves structures involved with radiologic findings were: C5, C6 and C7 roots, superior and middle brachial plexus trunks and suprascapular, axilar, radial and musculocutaneous nerves. In 6 cases nerve constrictions were noted with focal stenosis with hourglass morphology or punctual absence of signal intensity in the nerve trajectory. All patients evidenced focal enlargement of the fascicle nerve or the whole nerve.Two patients were bilaterality affected. Post-gadolinium T1 sequence showed variable degree of muscular or nerve enhancement in all patients.

Conclusions

The new MR-Neurography sequences combined with the new multichannel air coils allow high resolution images of the brachial plexus and nerves structures, improving the prompt diagnosis of diseases as Parsonage Turner-syndrome. These sequences may provide a presurgical nerve constrictions mapping for patients with no improvement.

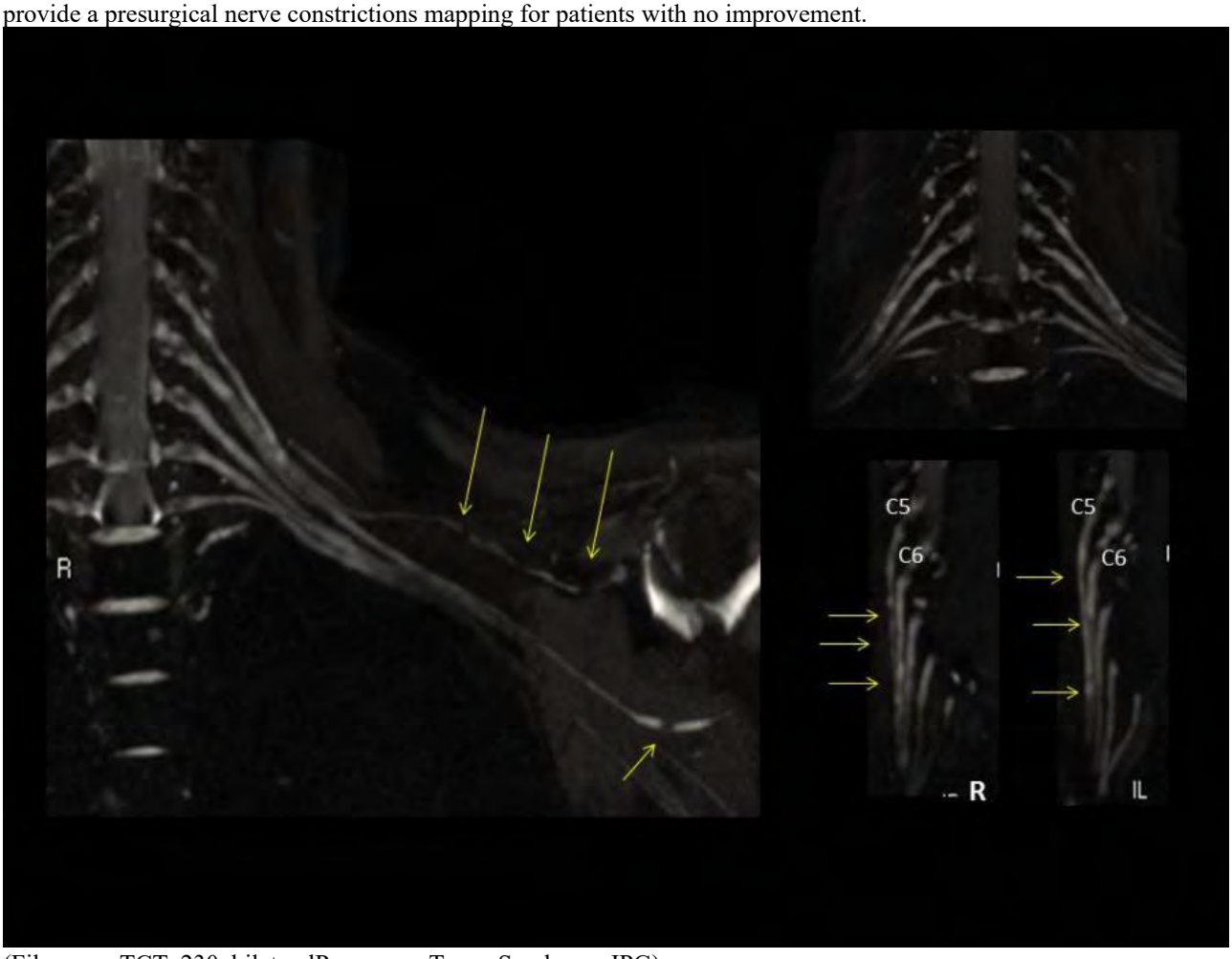

(Filename: TCT_230_bilateralParsonage-TurnerSyndrome.JPG)

1496

The utility of F18-FET PET/MRI in differentiating necrotic changes from recurrence/residual in Glioma.

P KUMAR[1], K Sitani[2]

[1]National Instituite of Mental Health and Neurosciences, Bangalore, Karnataka, [2]National Institute of Mental Health and Neurosciences, bengaluru, karnataka

Purpose

Amino acid positron emission tomography (PET) imaging is a choice of modality when it comes to diagnose brain tumors. Especially when MRI is inconclusive, FET-PET can add onto the information and helps in making better diagnosis. We are sharing our experience of using simultaneous FET-PET-MRI in differentiating recurrence from necrosis in glioma patients.

Materials and Methods

Thirty patients were included in the study, who underwent [18F]-FET PET/MRI at our centre. A radioactivity of 6 ± 1 mci (220 ± 40 MBq) was injected intravenously to each patient. The PET-MRI scan was acquired 30 minutes post injection. Standard MRI sequences like 3D FLAIR, T1-MPRAGE were added to the scan protocol. PET imaging reconstruction was done using iterative reconstruction with 512 matrix, 5 iterations, FWHM-2. The standard uptake value (SUV) and tumor to background (TBR) was calculated in all the case for analysis.

Results

The study has 30 patients (10 males and 20 females), whose tumor classification was confirmed by histopathological analysis as shown in Table-1. There was concordance found in 28 cases between PET and MRI findings and discordance noted in 2 cases where PET findings were suggestive of recurrence and MRI findings suggestive of post-operative changes. Three cases had multiple PET/MRI scans available over multiple time points, where no recurrence was noted in either PET or MRI. Out of 30 cases, 24 cases were of high-grade tumors (III/IV), 3 were low grade I/II and in 3 cases grade was not specified. In high grade tumor, SUVmax was greater than 2.5 (figure 1) and TBR greater then 2.0 (except two cases). In low-grade tumors, two of the cases showed a SUV of < 2.5 (figure 2) and TBR <2.0 while two shoed higher than this. A representative image of [18F]-FET PET/MRI shown in figure-1.

Conclusions

[18F]FET PET/MRI is superior to [18F]FDG (in view of low background in [18F]FET) and MRI in differentiating post operative changes from recurrence/residual disease. Simultaneous [18F]-FET-PET-MR adds on to the diagnostic value and can be a useful tool as well to ascertain the grade of tumors though it needs larger sample size to further validate the study.

Tumor type	Numbers
Glioblastoma	14
Parieto-occipital Ewing's sarcoma	1
Oligodendrogliomas	8
Solitary fibrous hemangiopericytoma	1
Thalamo-peduncular neoplasm	1
Grade I ganglioglioma	1
Anaplastic astrocytoma	3
Pilocytic astrocytoma	1

Table 1: showing tumor classification of the subjects.

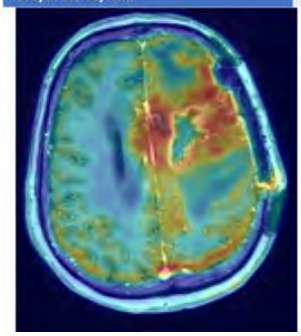

Figure-1: The hypermetabolic activity was seen in left frontal lobe, corpus callosum, and basal ganglia. It suggested recurrence in the left frontal lobe.

(Filename: TCT_1496_FET.jpg)

1331

The utility of multiparametric MRI in reducing diagnostic uncertainty for primary CNS lymphoma

A Goel[1], V Sawlani[2]

[1]University Hospitals Birmingham, Birmingham, United Kingdom, [2]University Hospital Birmingham, Birmingham, AL

Purpose

One of the key limitations in early treatment initiation in primary CNS lymphoma is the delay in diagnosis caused by lack of recognition of a lesion as a suspected lymphoma, initiation of steroid treatment, lesion involution, and often a subsequent inconclusive biopsy. Inability to distinguish a probable lymphoma from a glioma on standard MRI imaging may lead to unnecessary surgical resection of this chemosensitive tumour. We demonstrate that multiparametric MRI (MPMRI), which incorporates diffusion weighted imaging (DWI), perfusion weighted imaging (PWI) and magnetic resonance spectroscopy (MRS) is a valuable tool in addition to standard MRI modalities in resolving diagnostic uncertainty for PCNSL.

Materials and Methods
We present a series of 8 patients with histology-proven diffuse large B-cell lymphoma who underwent multiparametric imaging prior to biopsy at our centre (Queen Elizabeth Hospital Birmingham) due to equivocal appearances for lymphoma on standard MRI sequences, and describe the typical imaging features we note.
Results
Appearances on MPMRI shared similar features that increased the diagnostic likelihood of PCNSL - very low apparent diffusion coefficient (ADC) on DWI reflecting dense cellularity and low perfusion on PWI reflecting low angiogenesis. MRS demonstrated a high choline-creatine ratio reflecting high cellular membrane turnover, a high lipid peak due to macrophage infiltration, and very low NAA levels. This pattern of high choline and high lipid on MRS gives a 'twin tower' appearance, typical for PCNSL.
Conclusions
We propose multiparametric MRI as a tool to reduce the imaging-based diagnostic uncertainty for PCNSL. Concordance between two of three imaging multiparametric modalities could be used as a radiological predictor for PCNSL. We feel this could make histological confirmation redundant in selected cases – those with biopsy confirmed systemic high-grade lymphoma and a lesion typical for CNS involvement, patients with poor performance status suitable only for palliative chemotherapy and those with previous biopsy-confirmed PCNSL with a suspected relapse on imaging. Further, MPMRI may reduce the rate of steroid initiation for suspected lymphoma, provide a more accurate target for biopsy, and result in quicker tissue diagnosis and treatment initiation.

1301

Title: Randomized dropout of brain MR input series increases model flexibility, generalizability, and performance.

J Urbain[1], K Schmainda[2]
[1]ImagingBiometrics LLC, Mequon, WI, [2]Medical College of Wisconsin, Milwaukee, WI

Purpose
Develop a brain MR image segmentation and image synthesis model to perform optimally given the presence or absence of standard input series channels Flair, T1, T1 with contrast, and T2. Second, develop higher performing deep learning models less prone to overfitting limited training data and less susceptible to input image noise and quality. All standard brain MR imaging series, Flair, T1, T1 with contrast, and T2, are not always available. In addition, image quality can vary across different imaging series. In these cases, it would be beneficial to have deep learning models perform well over the presence or absence of different input series channels and to have models more robust to input image quality. Further, existing models have a tendency to overfit their training data and do not generalize well. Deep learning models have a large number of parameters and are powerful machine learning systems. Their huge capacity for learning makes overfitting a serious problem. Dropout and bootstrap aggregation are techniques for addressing overfitting. In dropout, the key idea is to randomly drop neural units and their connections during training. This prevents units from co-adapting too much. In bootstrap aggregation, the idea is to randomly select different sets of inputs and aggregate the results of models trained on each set. To address these issues, we developed a training algorithm that adapts the ideas of dropout and bootstrap aggregation to imaging input series channels. During training, Flair, T1c and T2 are randomly dropped (independently) from the training input following a training schedule.
Materials and Methods
A deep conditional deep convolutional generative adversarial network (cGAN) was developed to perform image segmentation and image synthesis of brain MR images. The model was trained using two methods: 1) Using all input image series channels (Flair, T1, T1c, T2), and 2) using a randomized algorithm that always selects T1 and randomly selects Flair, T1c, and T2 independently.
Results
Use of the randomized dropout algorithm significantly outperformed the same model trained without using randomized dropout. Further, the results with limited input channels provided high quality results.
Conclusions
We hypothesize that the model was trained to never become overly dependent on the presence or absence of different input image series. The high performance of a model with limited inputs opens up areas of future research to explore learning methods to limit dependence on input channels.

Results:

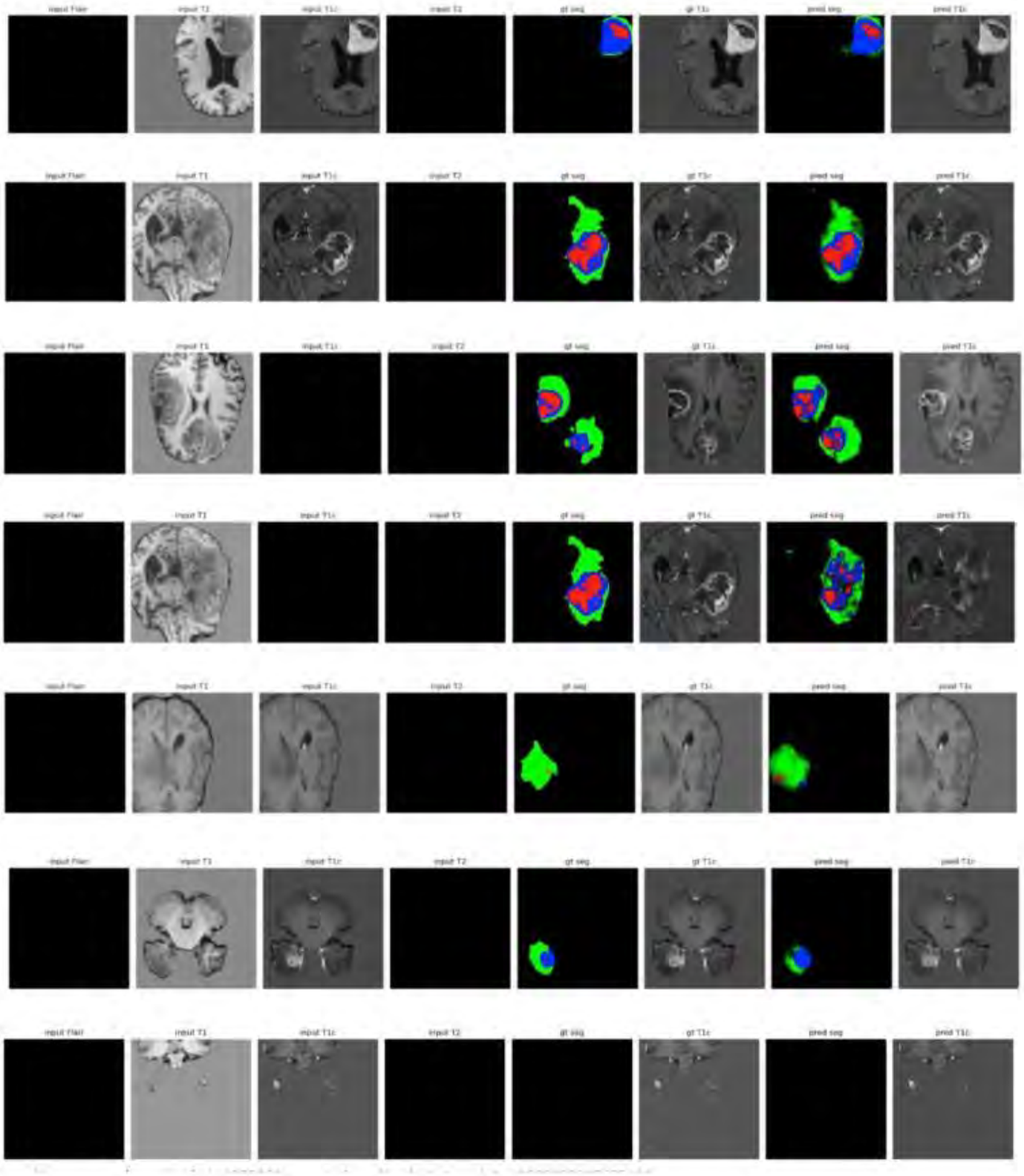

(Filename: TCT_1301_randomdropoutresults.jpg)

1033

Traditional Spinal Infections: An Update in Image findings

A Lima Júnior[1], M Castillo[2], L Freitas[3]

[1]Mount Sinai Hospital, New York, NY, [2]Radiology, Chapel Hill, NC, [3]McGill University, Montreal, Quebec

Purpose

Narrative review of infectious disorders that affect intervertebral discs, vertebrae, and spinal column, as traditional diseases. We aimed to widen scientific literature available and aid doctors in diagnosis of these conditions.

Materials and Methods

A narrative review based on literature research from PubMed, SciELO, and Scholar Google. English and Portuguese language filters were applied. Only articles that addressed spine infections (tropical and non-tropical diseases) and imaging diagnostic methods were selected.

Results

Pyogenic spondylitis and spondylodiscitis infections tend to occur during 5th decade of life and vertebral disc and body are the most involved sites. Staphylococcus aureus and Enterobacter are responsible for up to 90% of cases. CT-Scan is sensitive to demonstrate lysis, fragmentation, cortical erosions, sclerosis, hypodensities, reduced intervertebral space, edema, and infiltration of paraspinal soft tissues. Initially, there is an increase in the height of affected disc and T2-weighted hyperintensity. Followed by a reduction in disc height, loss of the normal signal of intranuclear cleft, and contrast enhancement. There are three primary pathological manifestations of HIV infection in spinal cord: vacuolar myelopathy, HIV myelitis, and aseptic leptomeningitis. Classic triad includes progressive spastic paraparesis, sensory ataxia, and neurogenic bladder. Typical imaging finding is spinal cord atrophy more commonly situated in dorsal cord, with T2-weighted hyperintensity, which is considered very specific to HIV spine infection. Transverse myelitis has been reported during acute phase of HIV infection and chronic phase, sometimes mimicking multiple sclerosis and neuromyelitis optica. Neurotoxoplasmosis is caused by reactivation of latent infection, usually in individuals with immunodeficiency, particularly those coinfected with HIV. Lesions have been described as T1-weighted isointense and T2-weighted increased signal intensity, focally enlarging spinal cord, commonly involving thoracic segment. Contrast enhancement is conventional, with variable patterns. Coexisting lesions in the brain are common and may help to define diagnosis.

Conclusions

As conclusion, many patients clinical and laboratory findings are mild or even absent, diagnostic imaging, especially magnetic resonance imaging plays a fundamental role in diagnosis establishment. Radiologists must be familiar with these diseases' imaging aspects.

995

Treated Glioblastomas: Tumor Progression is not Always Related to High rCBV Values

Hilario[1], E Salvador[2], A Cardenas[3], J Romero[3], Z Chen Zhou[4], A Martinez de Aragon[5], C Lechuga[4]

[1]Universitary Hospital 12 de Octubre, Madrid, Spain, [2]Hospital 12 de Octubre, Madrid, Madrid, SPAIN, [3]Hospital 12 de Octubre, Madrid, AK, [4]Hospital 12 de Octubre , Madrid, Madrid, Madrid, [5]Hospital 12 de Octubre, Madrid, Madrid, Madrid

Purpose

Standard treatment for glioblastomas is chemoradiotherapy with Temodal. During follow-up, perfusion MRI is used to differentiate tumor progression from post-treatment changes. In our experience, tumor recurrence is not always associated with high relative cerebral blood volume (rCBV) values. Our objectives are: 1) to correlate rCBV values at diagnosis and at tumor progression, 2) to determinate the relationship between rCBV values at progression with tumor volume and with time passed since the end of RT.

Materials and Methods

Inclusion criteria were: 1) age >18 years, 2) tumor resection, 3) histologically confirmed glioblastomas treated with STUPP regimen, 4) progression according to RANO criteria >12 weeks after the end of RT. Using Olea Sphere software, we calculated DSC (rCBVcorrected) and DCE (Ktrans, Ve, Vp, Kep) perfusion parameters, both at diagnosis and at tumor progression. We also correlated perfusion parameters at tumor progression with volume (enhancing tumor) and with time elapsed since the end of radiotherapy. STATA software was used for statistical analysis (significant test result $p<0.05$).

Results

We included 67 glioblastomas (age rage 33-76 years). At tumor progression, 68.66% of glioblastomas showed mean rCBVcorrected values <2. Changes in mean rCBVcorrected values between diagnosis and tumor progression were statistically significant ($p<0.001$). In the group of 47 patients with mean rCBVcorrected values ≥2 at diagnosis, 65.96% showed mean rCBVcorrected values <2 at tumor progression. At progression, rCBVcorrected values decreased by a mean of 1.125 (95%CI, 0.742-1.508). We have shown no relationship between rCBV, enhancing tumor volume or time elapsed since the end of RT. Quantitative analysis of DCE perfusion MRI did not help in the characterization of tumor progression.

Conclusions

rCBV values may be decreased at tumor progression. Decrease in rCBV values is independent of time delay from end of radiotherapy to tumor progression.

835

Ultra-high field 7T MRI detects the iron accumulation in patients with Amyotrophic Lateral Sclerosis: whole-brain QSM

C Otgonbaatar[1], H Song[2], Y Jeon[3], K Lee[3], C Sohn[3]

[1]Department of Radiology, Seoul National University College of Medicine, Seoul, Korea, Republic of, [2]Biomedical Research Institute, Seoul National University Hospital, Seoul, Korea, Republic of, [3]Department of Radiology, Seoul National University Hospital, Seoul, Korea, Republic of

Purpose

Amyotrophic lateral sclerosis (ALS) is a devastating neurodegenerative disease that entails upper and lower motor neurons. Accumulation of irons has been found to associate with its pathology. QSM is a recently introduced MRI technique that uses phase data to provide quantification of tissue iron content at a voxel-level and better demonstration of deep gray matter fibers and shows highly specific and sensitive to magnetic susceptibility sources compared with other sequences(1-2). However, the assessment of the iron accumulations with QSM at ultra-high field 7T MRI in the whole-brain has not been performed. Therefore, the aim of this study was to investigate the whole-brain QSM values at 7T MRI in patients with ALS.

Materials and Methods

For this prospective study, 21 patients with ALS (mean age, 55 years; 14 men) and 11 healthy control subjects (mean age, 50 years; 6 men) were recruited from local communities between February 2022 and July 2022. All patients underwent imaging with a 7T MRI scanner (Magnetom Terra 7T, Siemens Healthcare, Erlangen, Germany) using a 32-channel head coil (Nova Medical, Inc., MA, USA). The three-dimensional (3D) T1-weighted image was acquired using MP2RAGE and susceptibility weighted imaging was obtained with 4 echoes (Fig. 1a-b). Median susceptibility values were extracted from subcortical regions and pre-, postcentral cortex.

Results

Regionally, significantly higher median susceptibility values were obtained in right caudate nucleus ($p < 0.05$), left thalamus ($p < 0.01$), pre- (right, $p < 0.01$; left, $p < 0.01$) and postcentral (right, $p < 0.01$; left, $p < 0.05$) cortex in patients with ALS compared to that of control subjects. In contrast, the susceptibility values for globus pallidus, right thalamus, substantia nigra, and red nucleus showed no significant differences between patients with ALS and control subjects (Fig. 1c).

Conclusions

Our study demonstrates that there are differences in the concentration of iron in the precentral and postcentral cortex between ALS patients and healthy controls.

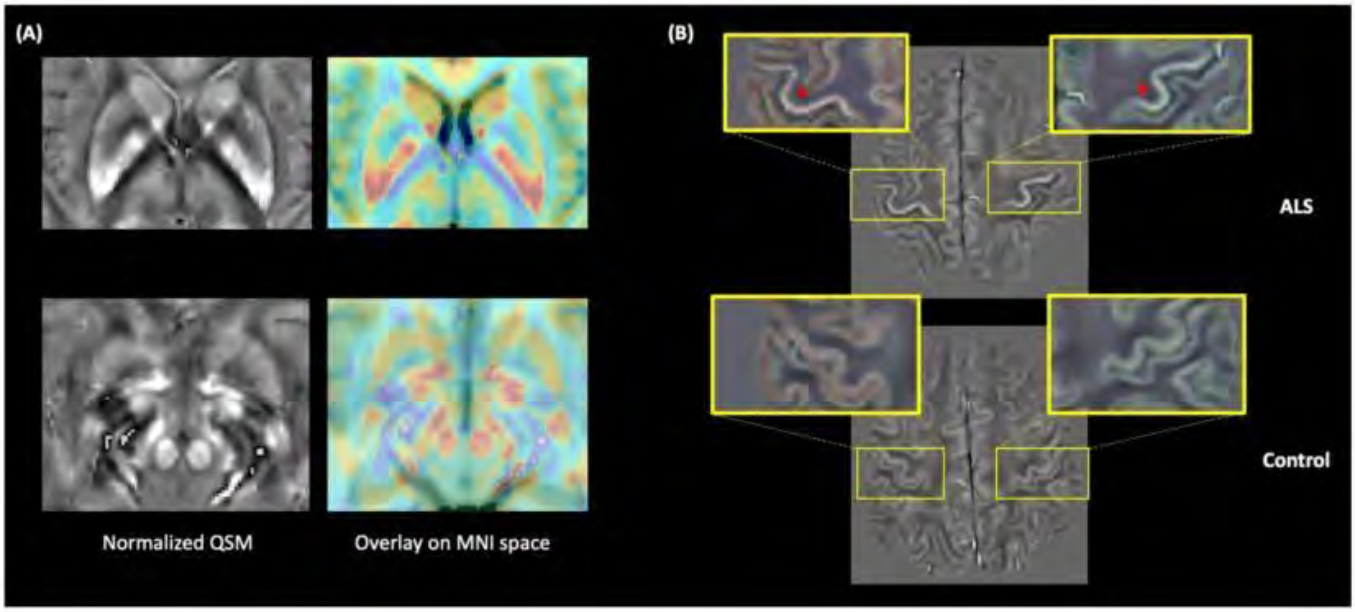

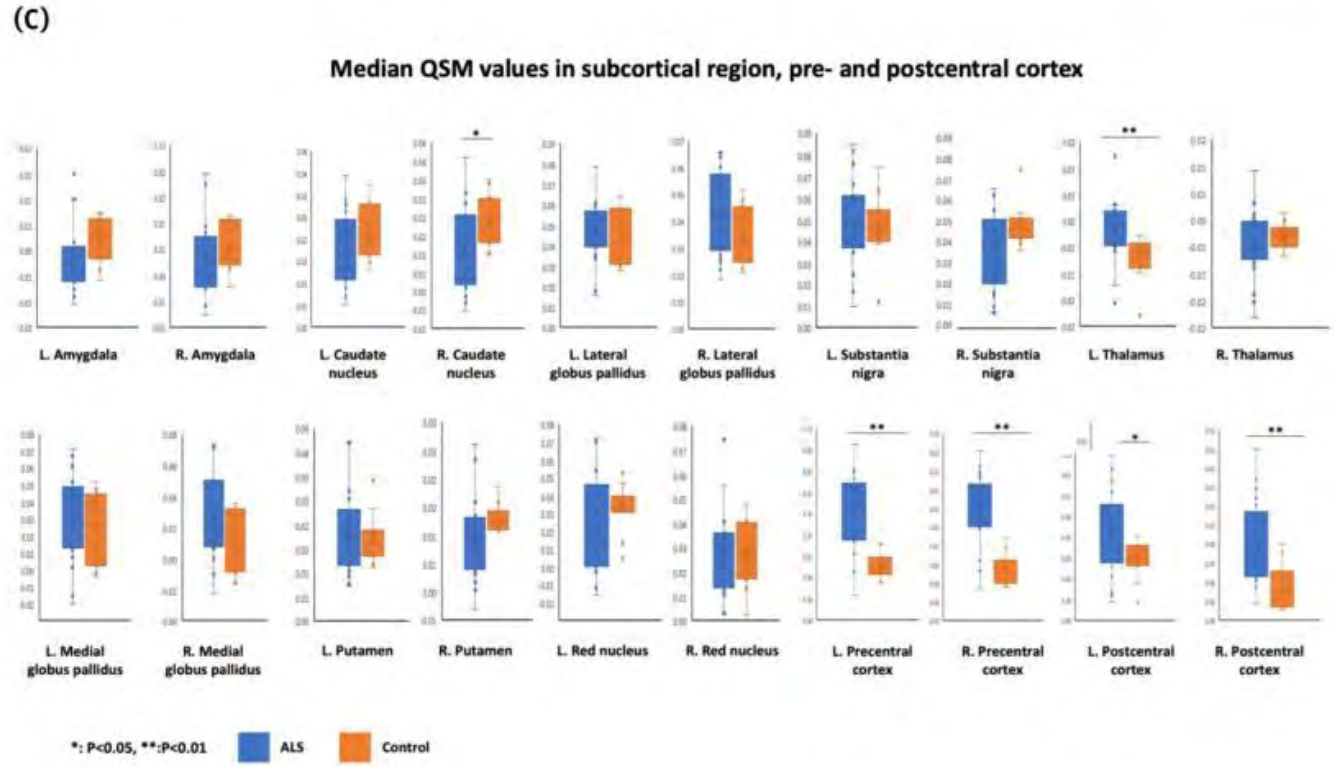

(Filename: TCT_835_Figure-ASNR.jpg)

660

Unilateral Cerebral Arterial Tortuosity: Associated with Aneurysm Occurrence, but Potentially Inversely Associated with Aneurysm Rupture

R Li[1], P Zhou[2], E Kao[3], Y Wang[4]

[1]Sichuan Provincial People's Hospital, University of Electronic Science and Technology of China, Chengdu, China, [2]Sichuan Provincial People's Hospital, University of Electronic Science and Technology of China, Chengdu,China, [3]University of California San Francisco, San Francisco, CA, [4]Sichuan Provincial People's Hospital, Chengdu, China

Purpose

To investigate the association of extracted quantitative tortuosity of main cerebral arteries with aneurysm occurrence and rupture, and explore the underlying mechanism. To investigate the relationship between arterial tortuosity and aneurysm morphology as well as conventional risk factors of vascular diseases.

Materials and Methods

We matched ruptured-aneurysm patients (group1) with unruptured-aneurysm patients (group2) and healthy people (group3) based on sex and age using tendency score matching, and collected their MRA images retrospectively. The intracranial arterial structures were segmented from the images by Python, yielding five segments: basilar artery (BA), intracranial segment of left and right internal carotid artery (LICA,RICA), M1 segment of left and right middle cerebral artery (LM1,RM1). The centerline of the three-dimensional arterial structure was extracted to form the skeleton of the arteries.The artery's tortuosity was calculated by dividing the path length by the Euclidean (shortest) distance and iterating through every voxel along the path. Arterial tortuosity was compared between different groups.Bonferroni correction was performed as to the multi-segmental comparison.Correlation analysis was conducted between arterial tortuosity and clinical risk factors as well as aneurysm morphology.

Results

After matching, 40 subjects in each group were enrolled (mean age, 67.5 years; 60% female). The parent artery's tortuosity was significantly greater than the contralateral artery's in both groups 1 and 2 ($p<0.001$). But parent artery's tortuosity didn't differ significantly between groups 1 and 2 (ICA: $p=0.127$, MCA: $p=0.133$). Between group(1+2) and group3, the arterial tortuosity was only significantly different in the LM1 segment ($p=0.001$). There was no significant association between clinical risk factors (history of hypertension, hyperlipidemia, diabetes, smoking, and alcohol use) and arterial tortuosity. There were significant negative correlations between parent artery tortuosity and aneurysm morphological features such as aneurysm maximal diameter ($p=0.001$), aneurysm neck diameter ($p<0.0001$), aneurysm maximum height ($p=0.002$), and size ratio ($p=0.027$).

Conclusions

The occurrence of cerebral aneurysm correlated to an increase in unilateral arterial tortuosity, but the risk of aneurysm enlargement/rupturing decreases with greater arterial tortuosity.The abnormal tortuosity may be congenital as tortuosity has no clear connection with acquired common risk factors of vascular diseases.

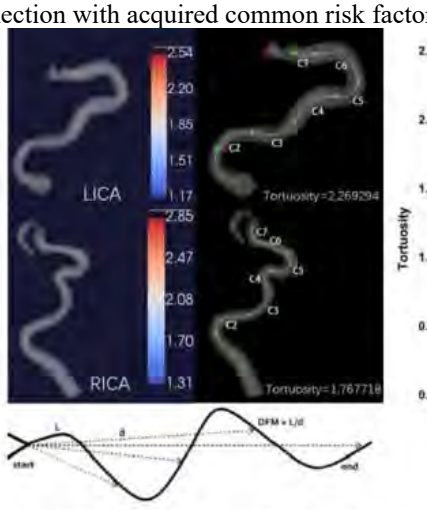

The ruptured intracranial aneurysm subject: tortuosity of the parent artery (LICA) was greater than that of the contralateral artery (RICA).
Schematic diagram of calculation principle of arterial tortuosity.

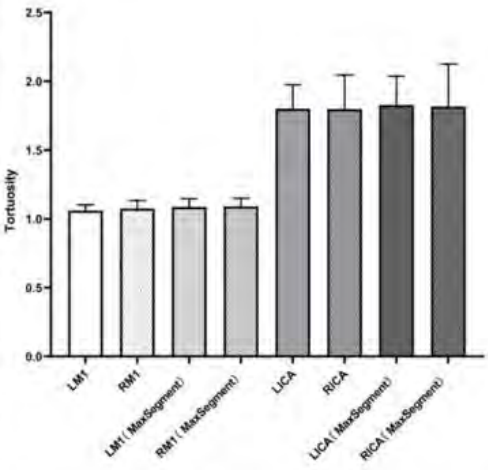

The healthy control group: there was no significant difference in the tortuosity of the left and right symmetrical arteries (LICA vs. RICA, p= 0.420; LM1 vs. RM1, p=0.192)

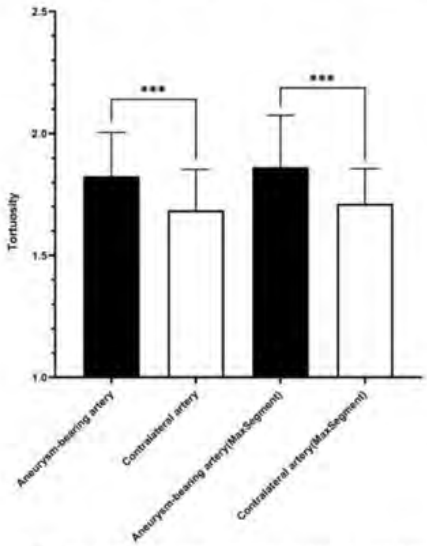

The ruptured aneurysm group: tortuosity of the parent artery was significantly greater than that of the contralateral artery (p<0.001).

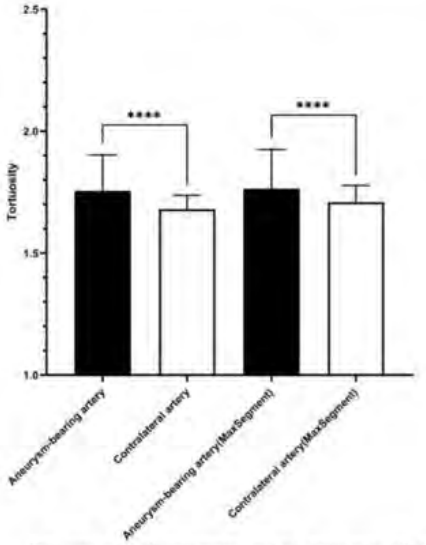

The unruptured aneurysm group: tortuosity of the parent artery was significantly greater than that of the contralateral artery (p<0.001).

(Filename: TCT_660_figures.jpg)

877

Usefulness of 4D Ultrashort-TE MR Angiography for Assessing Intracerebral Aneurysms Treated with Flow-Diverter Stenting

H UETANI[1], K Iwashita[1], K MORITA[2], Y Kaku[1], Y Yamashita[3], M KITAJIMA[1], A MUKASA[4], T Hirai[4]

[1]Kumamoto university, Kumamoto, Kumamoto, [2]Kumamoto University Hospital, Kumamoto, Kumamoto, [3]Canon Medical Systems Corporation, Kawasaki-shi, Kanagawa, [4]Kumamoto University, Kumamoto, Kumamoto

Purpose

Residual flow in intracranial aneurysms after flow diverter (FD) placement is sometime difficult to evaluate with time-of-flight MR angiography (MRA) owing to susceptibility artifacts. To overcome this issue, 3D MRA by using an ultrashort TE (UTE) combined with an arterial spin-labeling (ASL) technique has been developed. The purpose of this study was to evaluate the usefulness of the 4D UTE-MRA for evaluating aneurysm occlusion state of intracranial aneurysms after FD placement.

Materials and Methods

This study included 18 patients (17 women and one man; age range 45-85 years; mean age 67 years) with intracranial aneurysms treated with FD stenting. Immediately after treatment, all patients underwent digital subtraction angiography (DSA) and 3T 4D UTE-MRA within 8 days. Twelve patients underwent follow-up 4D UTE-MRA approximately 3 months after FD placement and then DSA within 3 months. Two neuroradiologists assessed the 4D UTE-MRA images and scored the aneurysm occlusion state with reference to the O'Kelly-Marotta occlusion classification as follows: no filling, neck remnant, incomplete filling and complete filling. DSA images were also evaluated by a neuroradiologist. The level of intermodality agreement in the evaluation was analyzed by weighted κ statistics.

Results

Immediately after treatment, DSA revealed 15 incomplete filling and 3 complete filling aneurysms. The intermodality agreement in aneurysm occlusion state between DSA and 4D UTE-MRA by two observers were perfect (κ = 1.0) and very good (κ = 0.77). At follow-up, 4D UTE-MRA showed 1 no filling, 4 neck remnants, 6 incomplete filling, and 1 complete filling, consistent with DSA in 10 of 12 cases. The intermodality agreement between DSA and 4D UTE-MRA was very good (κ = 0.80).

Conclusions

4D UTE-MRA is a useful follow-up tool in the evaluation of the aneurysm occlusion state of intracranial aneurysms after FD placement.

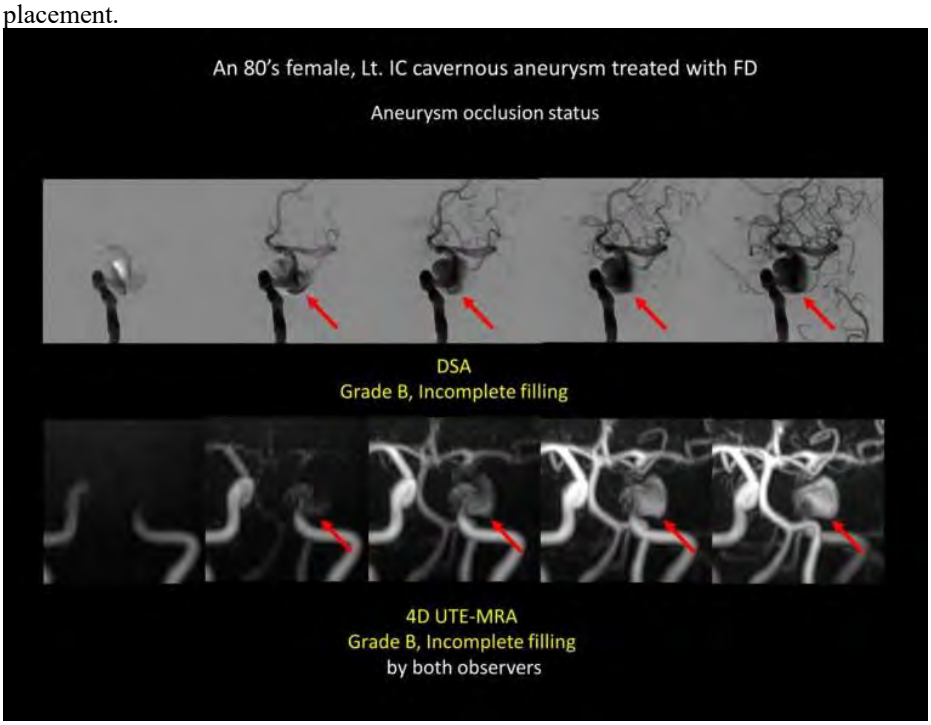

(Filename: TCT_877_2023ASNRabstractimageUTE4DMRA.jpg)

278

Using Super Resolution MRI to Perform Quantitative Assessment of the Fetal Optic Pathway

E Juang[1], N Rubert[2], J Greer[3], L Goncalves[4], P Cornejo[5]

[1]Creighton University School of Medicine, Phoenix, AZ, [2]Phoenix Children's Hospital, Scottsdale, AZ, [3]Phoenix Children's Hospital, Phoenix, AZ, [4]Pheonix Children's, Pheonix, AZ, [5]phoenixchildrens hospital, Phoenix, AZ

Purpose

To assess the use of three-dimensional slice-to-volume reconstruction magnetic resonance imaging (3D SVR MRI) for fetal optic pathway (FOP) evaluation. Currently, there is no consensus on an optimal imaging method to assess the FOP, which if defective can

lead to permanent visual disturbances. Prenatal ultrasound is efficacious but limited by issues with fetal presentation and reproducibility. Fetal brain MRI exams with fast sequences – T2-weighted single-shot fast spin-echo (T2 SSFSE) and balanced turbo field echo (BTFE) – are limited by motion artifacts and inadequate spatial resolution. 3D SVR MRI can address these challenges. Our goals are to (1) demonstrate 3D SVR MRI; (2) compare 3D SVR MRI to T2 SSFSE and BTFE in their reliability in capturing the FOP; (3) generate reference nomograms for FOP segments (i.e., pre-chiasmatic optic nerve width (ONW) and optic chiasm width (OCW)) in neurodevelopmentally normal fetuses.

Materials and Methods

Retrospective review was done on all fetal MRI scans from 01/01/2020 to 08/01/2022 at Phoenix Children's Hospital. MRI scans of fetuses without brain pathologies ranging from 23 to 38 weeks gestational age with sufficient image quality were selected. 3D SVR, as described by Kuklisova-Murgasova et al., was applied to the selected scans. FOP measurements (ONW and OCW) were gathered from post-reconstruction images. 3D SVR MRI and conventional fast sequences were compared in their ability to capture the FOP. Nomograms of ONW and OCW were created using linear regression fit and Pearson correlation coefficient to estimate the contribution of gestational age to FOP growth.

Results

The FOP visualization rate was higher at 78.6% (55 out of 70 cases) when using 3D SVR MRI compared to 12.8% (9 out of 70 cases) when using T2 SSFSE or BTFE. Among the 55 cases where the FOP was visualized with 3D SVR MRI, the ONW was measured in 53 out of 55 cases, and OCW was measured in all 55. Linear regression fit performed on optic nerve width and gestational age yielded an estimate of ON=0.04×GA+0.24 (R^2=0.34), where ON is the pre-chiasmatic optic nerve width in millimeters. The relationship between optic chiasm and gestational age was estimated as OC=0.11×GA+2.0 (R^2=0.30), where OC is optic chiasm width in millimeters.

Conclusions

3D SVR MRI is more effective than T2 SSFSE or BTFE for FOP evaluation due to improved spatial resolution and motion compensation. Reference nomograms of ONW and OCW were successfully generated using 3D SVR MRI, although a larger sample size is preferred.

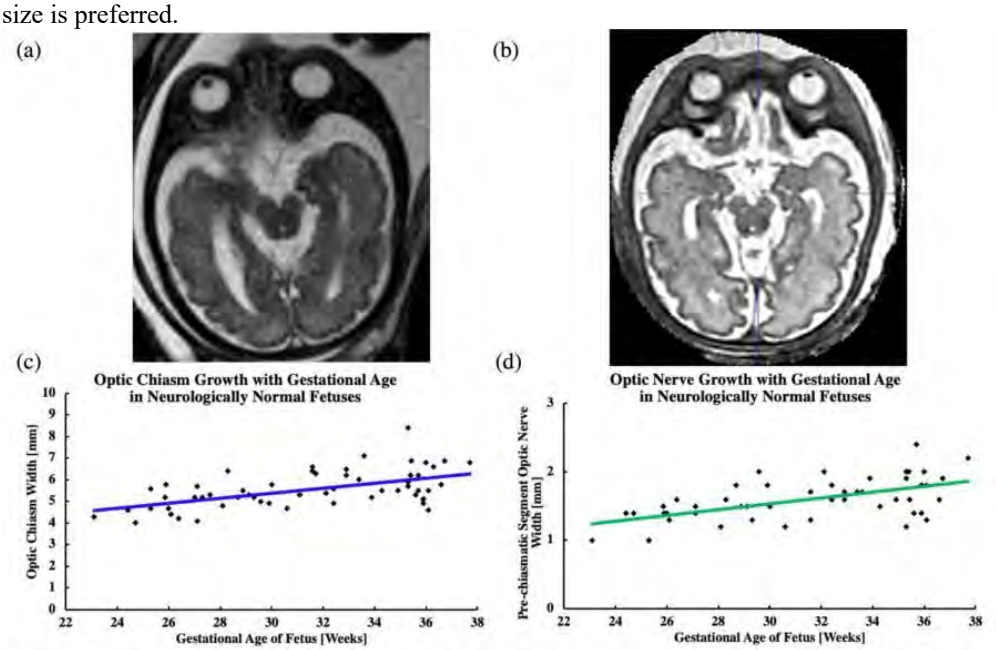

Figure. BTFE (a) and 3D SVR MRI (b) images of the same fetus (gestational age = 33. 4 weeks) at the slice that allowed the best available visualization of the optic chiasm. Nomograms of optic nerve width (c) and optic chiasm (d) in fetuses with no reported brain pathologies between 22 to 38 weeks of gestational age.

(Filename: TCT_278_ASNR_FOP_fig.jpg)

1210

Utility of conventional MRI features to differentiate isolated brainstem tuberculomas from brainstem gliomas and pilocytic astrocytomas.

S Ahmed[1], A Arora[2], N Sadashiva[2], J Saini[3]

[1]NIMHANS, Bangalore, KS, [2]National Institute of Mental Health and Neurosciences, Bangalore, Karnataka, [3]NATIONAL INSTITUTE OF MENTAL HEALTH & NEURO SCIENCES, BANGALORE, India

Purpose

The multifarious radiologic phenotype of isolated brainstem tuberculomas oftentimes mislead the neuroradiologists and clinicians into diagnosing these lesions as neoplastic. The rarity of isolated brainstem tuberculous lesions also serves as a confounding factor in this diagnostic dilemma. The purpose of this study is to establish specific imaging tell tales of brainstem tuberculomas. Additionally we aim to highlight the distinguishing conventional MRI features of brainstem gliomas and pilocytic astrocytomas which more often than not appear eidetic.

Materials and Methods
A retrospective review of conventional MRI features comprising of a)morphology b)T1, T2 signal intensity c)Susceptibility characteristics d) diffusion characteristics e)pattern of enhancement of 15 cases of isolated brainstem tuberculomas, 28 biopsy proven cases of diffuse midline glioma(DMG) of brainstem and 20 cases of biopsy proven brainstem pilocytic astrocytomas (PA) from June 2014 to July 2022 were documented. Descriptive analysis of common structural features, signal intensity and enhancement pattern of the above 3 cohorts was performed.
Results
Unanimously all the brainstem tuberculomas showed characteristic hypointensity on T2 WI (14/15) as compared to the grey matter.Brainstem gliomas and pilocytic astrocytomas demonstrated variable T2 hyperintensity with the latter subgroup showing solid cystic morphology in 90% cases. DWI-enhancement match, i.e 40% of cases of DMGs showed corollary diffusion restriction and mild enhancement. Avid nodular and ring enhancement was demonstrated by all tuberculomas. Nodular heterogenous enhancement was a feature of all PAs. Intratumoral bleed was a feature of 15% of PAs and 30% of DMGs. The cases with multiple conglomerated lesions showed extensive vasogenic edema but this could be differentiated from diffuse midline gliomas by selective involvement of white matter and non inherent expansile contour of the afflicted brainstem.
Conclusions
Conventional MRI features in particular T2WI and post contrast sequences can successfully differentiate between brainstem tuberculomas and glial neoplasms.

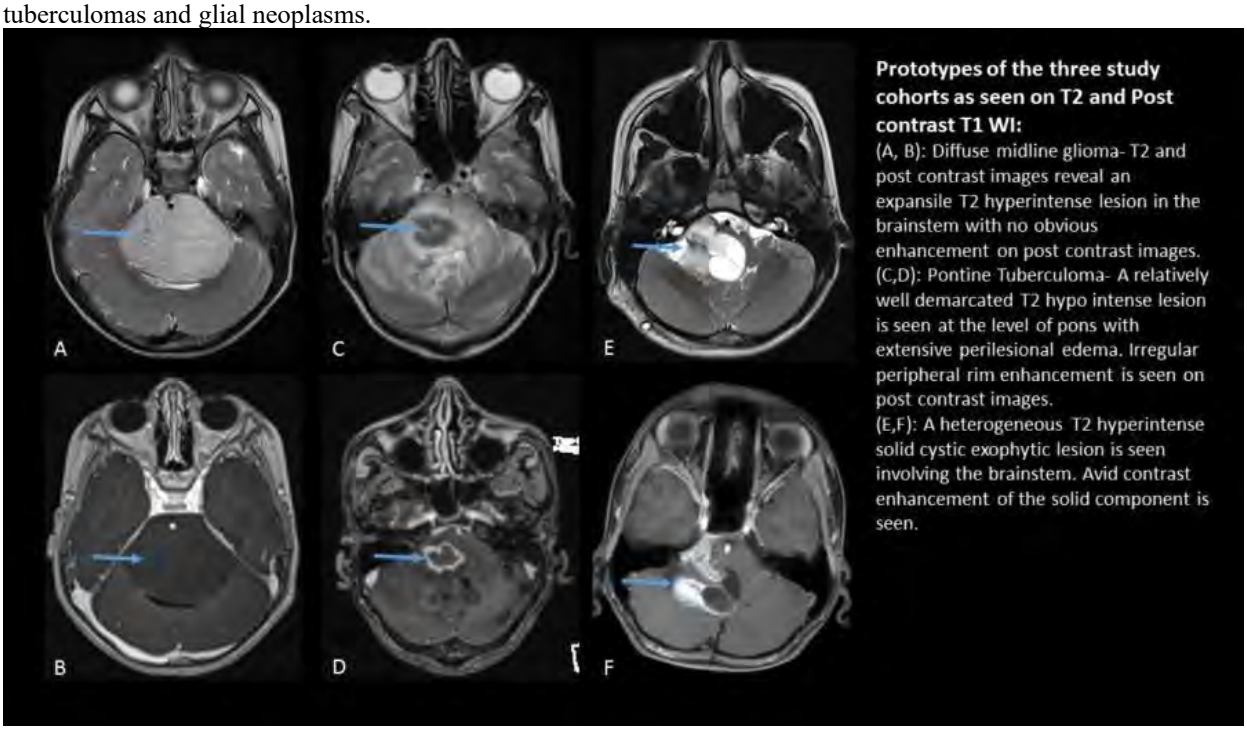

(Filename: TCT_1210_Presentation1.jpg)

1307
Utilizing a Fully Convolutional Neural Network to Predict Myelogram Contrast Pattern from Non-Contrast Computed Tomography Spine Imaging: A Feasibility Study
N Takacs[1], H Stecko[1], T Mallela[1], E Dikici[1], X Nguyen[2]
[1]The Ohio State College of Medicine, Columbus, OH, [2]Ohio State University Wexner Medical Center, Columbus, OH

Purpose
While Computer Tomography (CT) offers excellent assessment of bony structures, visualization of the intraspinal soft tissue contents is often suboptimal on non-contrast imaging. Myelography using intrathecal injection of iodinated contrast is often performed to evaluate these structures (1). In this study, we create and employ a fully convolutional neural network (FCNN) with a U-net architecture to synthetically generate predicted post-contrast images from a non-contrast input deck. We hypothesize that a FCNN, trained on a previously 3D co-registered stack of non-contrast and post-myelogram spine CT images of the same patient, can perform the image-to-image translation task of generating a simulated post-myelogram CT image from an input non-contrast CT image.
Materials and Methods
In this study, we identified 11 post-myelogram CT lumbar spine exams from 2016 to 2019 for which a non-contrast CT lumbar spine exam of the same patient had been performed within 50 days. 3-D spatial co-registration was performed using sequential application of center-of-mass, translation, rigid, and affine transforms to align the post-myelogram images of each pair to the corresponding non-contrast CT images, creating a pooled set of over 2000 2-D image pairs. A FCNN with U-net architecture was developed and trained on these pairs of 2-D non-contrast and contrast CT image pairs using a mean squared error (MSE) loss function. Programming was

performed in Python using the Keras library as an interface with the open-source TensorFlow AI platform. Output accuracy was calculated by isolating the spinal canal in ImageJ and binarizing both the model produced and contrast images.

Results

Affine registration was performed on 11 pairs of non-contrast and post-myelogram lumbar spine CT images, with mean MI score of 0.095, resulting in generation of over 2000 2-D image pairs. Following limited training on a subset of 1000 images (20 epochs, batch size = 20), contrast shading was generated with an average of 82.3% accuracy.

Conclusions

This study applies a novel post-processing technique to improve visualization of intraspinal soft tissue contents without requiring an invasive procedure or an alternative modality like MRI. This study demonstrates the feasibility of a fully convolutional approach to predict image contrast.

Figure 1: Generating the Ground Truth

Using ImageJ, the section of the CT image constituting contrast was isolated. The output image was converted to a binary map/2D array with class 1 denoting CSF and class 0 denoting "all other tissue". This binary map was used to assign class values to each of the pixels in the non-contrast image via a data generator. This served as the ground truth for the segmentation task.

This figure illustrates the Fully Convolutional Model employed in this project, a modified model from Santini et al. (2018). A grayscale non-contrast image acts as the input.

General layer information:

- *Kernel size: 3 x 3*
- *Activation function: Rectified Linear Unit*
- *Downsampling function: MaxPooling*
- *Batch Normalization employed*
- *Output Layer Activation Function: Sigmoid (Development), Softmax (Final)*

Loss Function: Binary Cross-Entropy (Development); Mean Square Error (Final)

Figure 2: Our Encoder-Decoder Model

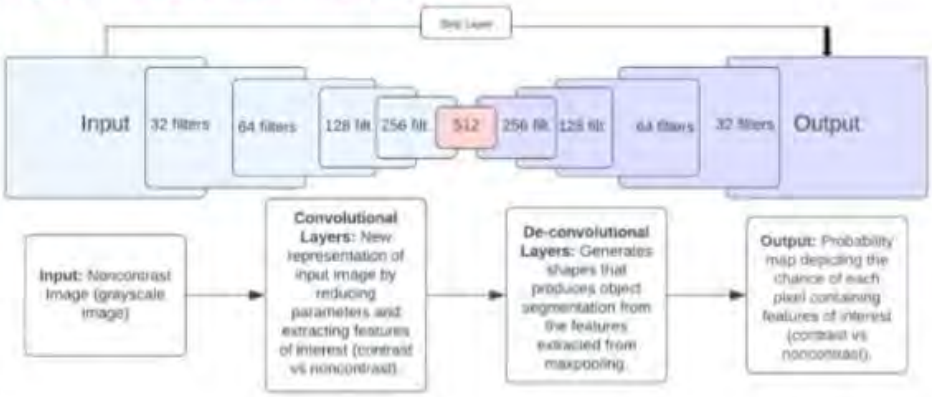

Figure 3: Preliminary Results

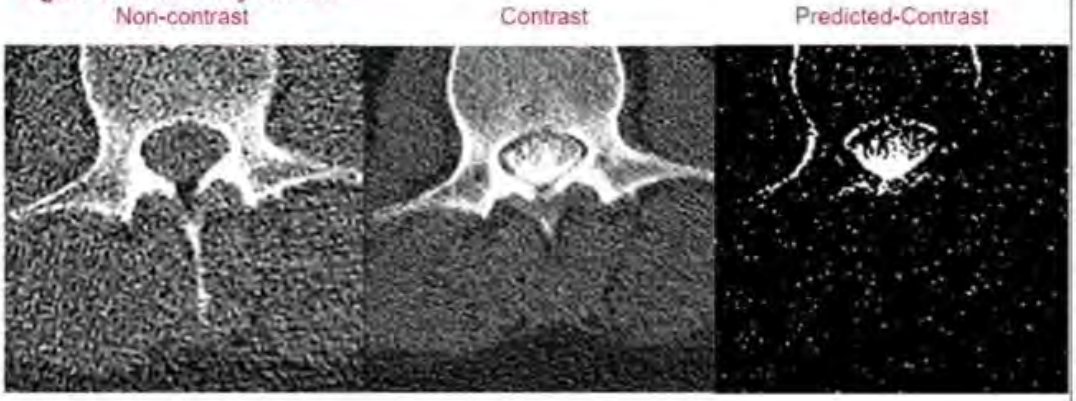

A singular patient's image stack was utilized to generate these preliminary results (batch = 10, epochs = 10). The 229 images within this singular patient's image stack were randomly assigned to the training and testing deck. The training deck and testing deck consisted of 220 images and 9 images, respectively. Across the 9 image pairs, there is a region of interest (spinal canal) accuracy of 67.4% with a range of 51.2% - 82.3%. The binary prediction, converted to image form, with 82.3% ROI accuracy is on the far right of this figure.

(Filename: TCT_1307_Figures.jpg)

1441

Utilizing Radiological Imaging Metrics to Define Epidemiological and Diagnostic Characteristics of Neck Lesions During the COVID-19 Pandemic

L Larsen[1], C Stateler[2], J Stoller[3], J Nickerson[4], B Hamilton[5], R Barajas[6]

[1]OHSU, portland, OR, [2]School of Medicine, Oregon Health & Science University, Portland, OR, [3]Oregon Health and Science University, Portland, OR, [4]Oregon Health Sciences University, Portland, OR, [5]Oregon Health & Science University, WEST LINN, OR, [6]OHSU, Portland, OR

Purpose

Reports of head and neck symptoms and clinical manifestations of Corona Virus Disease 19 (COVID-19) are well documented in a broad population of patients and include but are not limited to, sore throat, increased sputum production, rhinorrhea, rhinitis, sneezing, cough, and headache (1). However, there is a paucity of data about the relationship between these infectious symptoms and non-malignant, inflammatory neck lesions in patients infected with COVID-19. Evaluation of these specific patient populations with radiological imaging over recent, specific time courses may provide valuable information about the possible shifting epidemiology of these lesions. The purpose of this study is to investigate the incidence of non-malignant, inflammatory neck lesions before and during the COVID-19 pandemic.

Materials and Methods

We performed a retrospective review of electronic medical records and Magnetic Resonance Imaging (MRI) and Computed Tomography (CT) imaging to identify multiple types of inflammatory lesions and patient COVID-19 status between 2018 to present at Oregon Health and Science University (OHSU). The total number of neck CTs performed at OHSU Emergency Department during that time frame was used to represent the population at risk.

Results

The incidence proportion of patients with non-malignant, inflammatory neck lesions with a positive COVID-19 test in 2020, 2021, and 2022 was 4.305%, 46.97%, and 19.138%, respectively. Chi-squared test: 2.08263E-09.

Conclusions

An increase in incidence proportion of patients with non-malignant, inflammatory neck lesions and COVID-19 infection may indicate a relationship between the lesions and viral infection, clinically and/or radiographically. Future investigation for each specific disease process will involve whether morphologic and physiologic metrics predict clinical outcomes.

420

Validation of a Deep Learning AI-based Software for Automated ASPECTS Assessment

P Chang[1], D Chow[1], C Filippi[2], A Ayobi[3], S Quenet[3], M Tassy[3], Y CHAIBI[3]

[1]University of California Irvine, Irvine, CA, [2]Tufts University Medical Center, Boston, MA, [3]Avicenna.AI, La Ciotat, France

Purpose

The primary objective aims to evaluate physicians' ability to assess Alberta Stroke Program Early CT Score (ASPECTS) when assisted by an AI-based automated software designed to identify hypodense regions on head non-contrast CT (NCCT) exams, compared with the unassisted readings. Secondly, this study aims to evaluate the standalone performance of the device.

Materials and Methods

139 retrospective, consecutive and multicenter baseline NCCT from patients with acute middle cerebral artery and/or internal carotid artery occlusion were collected. The ASPECTS ground truth (GT) was established by consensus reading between 3 expert neuroradiologists. 40 cases were randomly selected from the main dataset for a multi-reader-multi-case (MRMC) study, conducted by 3 additional readers (radiologists different from the ground truthers) who assessed each exam first without software assistance and, after a washout period, with the assistance of CINA-ASPECTS (Avicenna.AI, La Ciotat, France). The readers used a 6-point confidence scale for the assessments of each ASPECTS region. Improvement in reader's performance was determined by the percentage of the individual ASPECT regions where agreement was achieved between the reader and the GT, for both the unassisted and assisted reads. Moreover, the difference in the Receiver Operating Characteristic (ROC) Area Under the Curve (AUC) following the Obuchowski-Rockette-DBM-MRMC methodology was calculated. Finally, the standalone region-based performance of the device was evaluated against the GT for the 139 patients.

Results

Regarding the MRMC study, all readers increased their agreements when assisted by the software: 79.8% vs 73.8% for reader 1 ($p<0.05$), 78.5% vs 76.5% for reader 2 ($p>0.05$) and 77.3% vs 71.8% for reader 3 ($p>0.05$). The overall difference among all readers was statistically significant: 78.5% vs 74.0% ($p<0.05$). Similarly, the use of CINA-ASPECTS significantly increased the average ROC AUC of all readers to 0.824 compared to a baseline average ROC AUC of 0.776 without software assistance ($p<0.05$). For the standalone performance, comparison of CINA-ASPECTS with the GT yielded a region-based sensitivity of 76.6% [95%CI: 72.4%–81.1%] and a specificity of 88.7% [95%CI: 87.4%–89.9%].

Conclusions

CINA-ASPECTS can identify hypodense brain regions with high concordance to expert neuroradiologists. In addition, the conjunctive use of the software as a diagnostic aid significantly improves the accuracy of physicians' interpretations in a realistic clinical workflow.

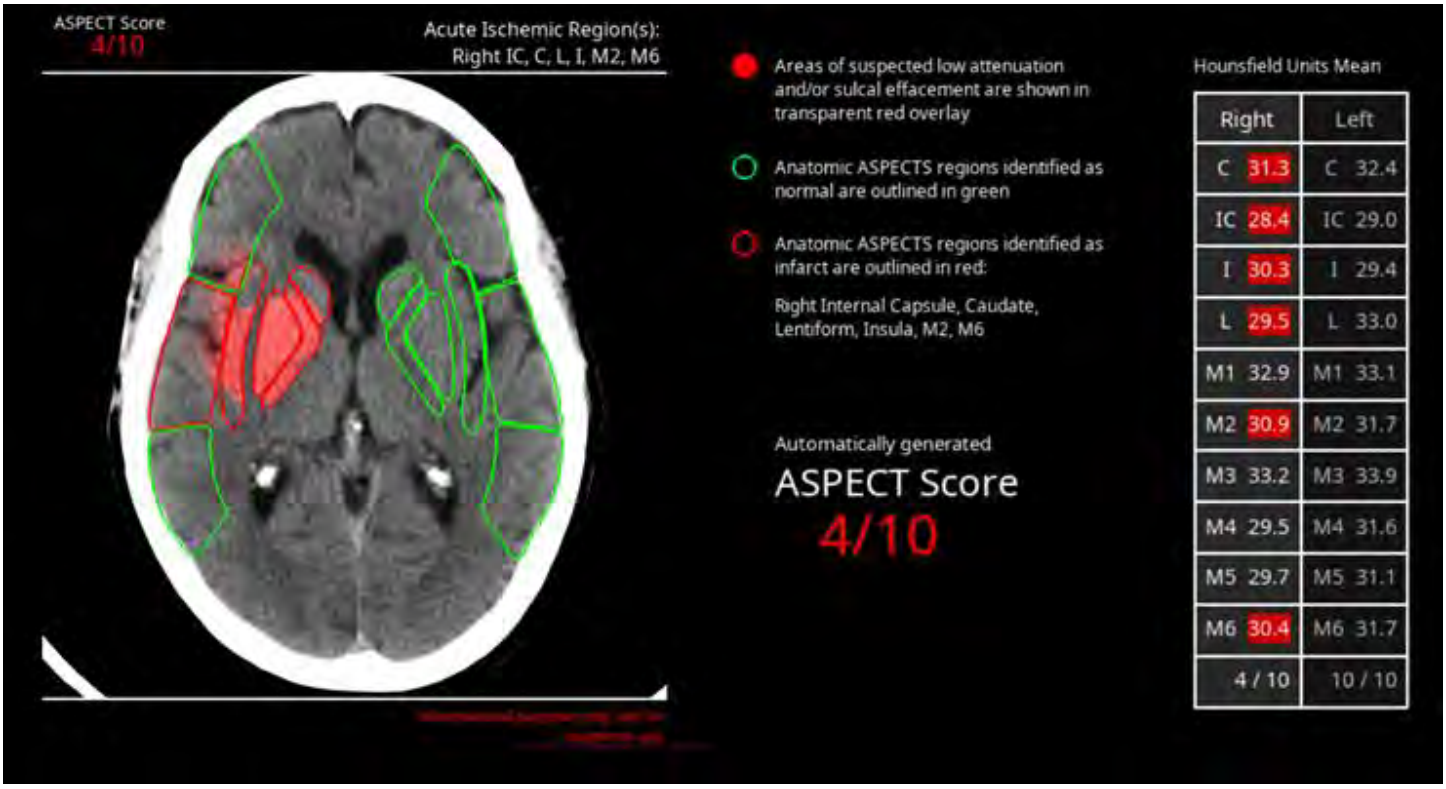

(Filename: TCT_420_image14.jpg)

576

Validation of a low flip angle DSC-MRI perfusion protocol for brain tumor evaluation at 1.5T.

N Chasen[1], M Gule-Monroe[2], B Taylor[3], P Hou[4], M Wintermark[5], R Stafford[1], C Chung[1], H Liu[6]

[1]The University of Texas MD Anderson Cancer Center, Houston, TX, [2]MD Anderson Cancer Center, Spring, TX, [3]The University of Texas M. D. Anderson Cancer Center, Houston, TX, [4]MD Anderson Cancer Center, Houston, TX, [5]MD Anderson, Houston, TX, [6]UT MD Anderson Cancer Center, Houston, TX

Purpose

The goal of this study is to compare a low flip angle dynamic susceptibility contrast magnetic resonance imaging (DSC-MRI) protocol without the preload dose of gadolinium (1) to a standard DSC-MRI protocol with preload (2) at 1.5T.

Materials and Methods

24 patients with intracranial neoplasms underwent evaluation with MRI of the brain at a single institution as part of a quality improvement project. The imaging was performed on three 1.5 Tesla scanners in the outpatient setting. All patients were imaged with DSC perfusion sequences without (P-) and with (P+) a preload gadolinium bolus in addition to routine sequences. DSC-MRI (single dose Gadavist, single-shot gradient-echo EPI, TR/TE = 1500 ms/45 ms, iPAT=2, 18 slices, voxel size = 2.3x2.3x5.0 mm3) was performed twice for each patient. Initial DSC was performed using a flip angle of 30° and was used for the preload for the second DSC with flip angle of 60°. Two patients were excluded from the analysis secondary to confounding intralesional susceptibility artifact. Relative CBV (rCBV) and standardized CBV (sCBV) maps were generated after the leakage correction (C+) (3) using IB Neuro software. A 0.4-0.6 cm² region of interest (ROI) was drawn within the enhancing lesion on the registered T1 post contrast images, which was then mapped onto the four CBV maps (rCBV and sCBV x 2 DSC). A 2cm² ROI was placed on normal appearing frontal or occipital white matter (WM) on two registered T1 post image slices and mapped to rCBV maps for each patient. Normalized CBV (nCBV) was derived by dividing the lesion rCBV by the WM rCBV for each of the two DSC sequences for all patients. Lin's concordance correlation coefficient (LCCC) and Bland-Altman plots were used to compare the CBV results obtained from the first (P-C+) vs. the 2nd (P+C+) DSC-MRI.

Results

The nCBV and sCBV results from the first DSC were not significantly different than those from the 2nd DSC (p=0.70 and 0.10, respectively). Scatter plots demonstrate a substantial correlation between the two DSC-MRI scans with a high LCCC for both nCBV (0.986) and sCBV(0.955). Bland-Altman analysis resulted in limits of agreement (LOA = bias +/- 1.96 SD) of (-55.2%, 51.4%) for nCBV and (-59.7%, 45.7%) for sCBV.

Conclusions

Although prior studies have shown consistent CBV measurements at 3T when comparing a low flip angle without preload and the standard high flip angle with preload, our study is the first to evaluate the utility of this new DSC-MRI protocol at 1.5T.

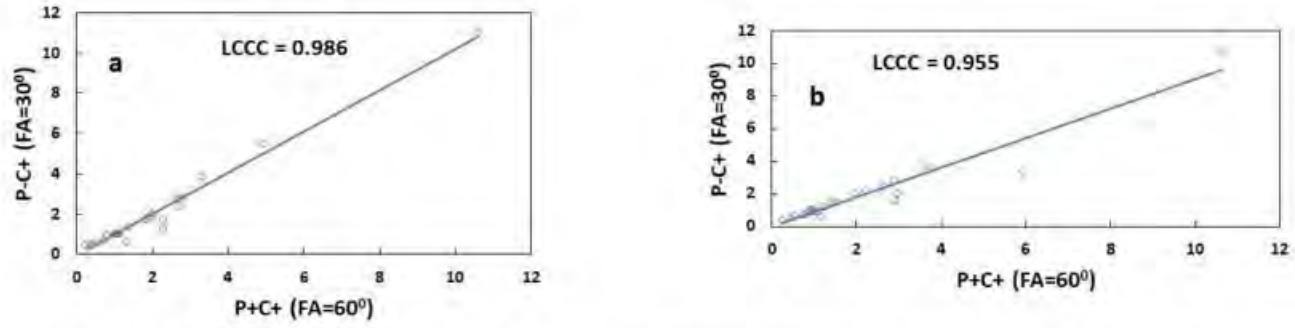

Figure 1: Scatter plots of nCBV (Lesion/WM) (a) and sCBV (b). LCCC: Lin's concordance correlation coefficient.

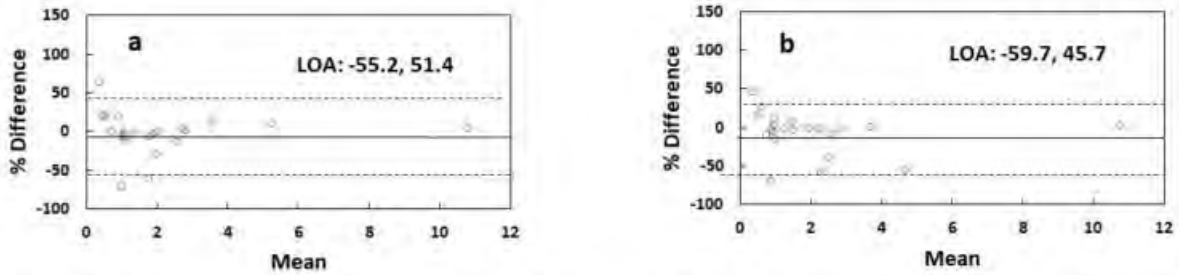

Figure 2: Bland-Altman plots of nCBV (Lesion/WM) (a) and sCBV (b). LOA: Limits of Agreement = bias ± 1.96 SD.

(Filename: TCT_576_300dpijpeg.jpg)

746

Validation of Computed Tomography based Risk Stratification System and Biopsy Criteria for Cervical Lymph Nodes in Preoperative Patients with Thyroid Cancer

Y Jeon[1], J Lee[1], J Kim[1], R Yoo[1]
[1]Seoul National University Hospital, Seoul, Korea, Republic of

Purpose
To validate the current CT-based risk stratification system (RSS) and biopsy criteria for LNs proposed by the Korean Society of Thyroid Radiology (KSThR).
Materials and Methods
In total, 277 LNs from 228 consecutive patients were included between December 2006 and June 2015. Preoperative CT images of cervical LNs were retrospectively analyzed and categorized according to the KSThR RSS for cervical LNs on a node-by-node basis. The diagnosis of metastatic LNs was confirmed if they met at least one of the following criteria: (1) confirmation based on cytology or histopathology, or (2) FNA-Tg cutoff >8.3 ng/mL or greater than serum Tg levels for cystic LNs. The malignancy risk and diagnostic performance for each category were calculated. The size cutoff proposed in KSThR guidelines varied, and the diagnostic performance and unnecessary biopsy rates were calculated.
Results
A total of 277 LNs in 228 patients were analyzed and 147 (53.1%) LNs were diagnosed with metastasis by biopsy. According to the KSThR RSS, probably benign (12.5%, 95% confidence interval [CI 2.6–36.5%]) and indeterminate LNs (7.5%, [CI 3.0–15.5%]) showed similarly low malignancy risks (P = 0.468), while suspicious LNs showed a significantly higher malignancy risk (85.6%, [CI 71.9–100.0%]) compared to other categories (P < .001). When LNs were further categorized by size, the malignancy risk of indeterminate LNs (0–20.0%) and probably benign LNs (0–33.3%) tended to be low, even when their sizes were large. In contrast, the malignancy risk of suspicious LNs was high overall (78.8–100.0%), even when their sizes were smaller than 5 mm. While biopsy criteria covering both suspicious and indeterminate LNs showed a relatively low specificity (16.2–51.5%) and high unnecessary biopsy rate (33.5–43.1%), the criteria covering only suspicious LNs showed a significantly higher specificity and lower unnecessary biopsy rates, while maintaining sensitivity.
Conclusions
CT indeterminate LNs have low malignancy risks; therefore, additional biopsies may not generally be required for these LNs. Performing biopsy for only suspicious LNs would reduce unnecessary biopsies with improved specificity compared to the current biopsy criteria, including both suspicious and indeterminate LNs. These results could potentially contribute to refinement of the current RSS for cervical LNs in patients with thyroid cancer.

Table 1. Simulated different biopsy size thresholds for cervical lymph nodes in thyroid cancer

Classification	Size stratified criteria	Description
Suspicious LNs only	(1)	Any suspicious LNs
	(2)	Suspicious LN > 3mm in SD
	(3)	Suspicious LN > 5mm in SD
Indeterminate LNs only	(4)	Any indeterminate LNs
Suspicious and indeterminate LNs	(5)	Any suspicious and indeterminate LNs
	(6)	Suspicious >3mm and Indeterminate > 5mm
	(7)	Suspicious >5mm and Indeterminate>5mm

LN, lymph nodes; SD, short diameter

Table 2. Malignancy risk of CT classified LNs according to size thresholds

Categories	Suspicious LNs			Indeterminate LNs			Probably benign LNs		
Size thresholds	Malignant LNs, N (%)	All LNs, N (%)	Malignancy risk (%)	Malignant LNs, N (%)	All LNs, N (%)	Malignancy risk (%)	Malignant LNs, N (%)	All LNs, N (%)	Malignancy risk (%)
All	137 (100.0)	160 (100.0)	85.6 (71.9, 100.0)	7 (100.0)	93 (100.0)	7.5 (3.0, 15.5)	3 (100.0)	24 (100.0)	12.5 (2.6, 36.5)
SD <3mm	1 (0.7)	1 (0.6)	100	1 (14.3)	5 (5.4)	20.0	1 (11.1)	4 (16.7)	25.0
3≤ SD <5m	26 (19.0)	33 (20.6)	78.8	3 (42.9)	38 (40.9)	7.9	0 (0.0)	6 (25.0)	0.0
5≤ SD <8m	54 (39.4)	64 (40.0)	84.4	3 (42.9)	44 (47.3)	6.8	1 (11.1)	8 (33.3)	12.5
8 SD <10mm	19 (13.9)	20 (12.5)	95.0	0 (0.0)	3 (3.2)	0.0	0 (0.0)	3 (12.5)	0.0
SD ≥10mm	37 (27.0)	42 (26.3)	88.1	0 (0.0)	3 (3.2)	0.0	1 (11.1)	3 (12.5)	33.3

Note- Comparison of malignancy risks: Benign vs. indeterminate, $P = .468$, probably benign vs. suspicious, $P = .001$, indeterminate vs. suspicious, $P < .001$

Numbers in parentheses indicate 95% confidence intervals.

Table 3. Diagnostic Performance of CT based risk stratification criteria according to various biopsy size thresholds

Classification	Size stratified criteria	Sensitivity	Specificity	PPV	NPV	Accuracy	AUROC	Unnecessary biopsy rate
Suspicious LNs	**(1)**	93.2 (87.9, 96.7)	82.3 (74.7, 88.4)	85.6 (80.4, 89.6)	91.5 (85.4, 95.1)	88.1 (83.7, 91.7)	0.878 (0.833, 0.914)	14.4 (9.1, 21.6)
	(2)	92.5 (87.0, 96.2)	82.3 (74.6, 88.4)	85.5 (80.3, 89.6)	90.7 (84.6, 94.5)	87.7 (83.3, 9.4)	0.874 (0.829, 0.911)	14.5 (9.0, 21.7)
	(3)	74.8 (67.0, 81.6)	87.7 (80.8, 92.8)	87.3 (81.2, 91.7)	75.5 (69.8, 80.4)	80.9 (75.7, 85.3)	0.813 (0.762, 0.857)	12.7 (7.0, 20.6)
Indeterminate LNs	**(4)**	4.8 (1.9, 9.6)	33.8 (25.8, 42.7)	7.5 (3.8, 14.5)	23.9 (19.8, 28.6)	18.4 (14.1, 23.5)	0.193 (0.148, 0.245)	92.5 (74.0, 100.0)
Suspicious and Indeterminate LNs	**(5)**	97.9 (94.2, 99.6)	16.2 (10.3, 23.6)	56.9 (55.0, 58.8)	56.9 (55.0, 58.8)	87.5 (68.1, 95.8)	0.571 (0.51, 0.63)	43.1 (35.4, 52.0)
	(6)	94.6 (89.6, 97.6)	46.2 (37.4, 55.1)	66.5 (62.8, 70.1)	88.2 (78.9, 93.8)	71.8 (66.2, 77.1)	0.704 (0.646, 0.757)	33.5 (26.1, 42.3)
	(7)	76.9 (69.2, 83.4)	51.5 (42.6, 60.4)	64.2 (59.5, 68.6)	66.3 (58.4, 73.4)	65.0 (59.1, 70.6)	0.642 (0.583, 0.699)	35.8 (27.5, 45.8)

Numbers in parentheses indicate 95% confidence intervals.

CT, computed tomography; LNs, lymph nodes; PPV, positive predictive value; NPV, negative predictive value; AUROC, area under receiver operating characteristics

* Criteria (1) Any suspicious LNs. Criteria (2) Suspicious LNs >3mm in short diameter (SD). Criteria (3) Suspicious LNs > 5mm in SD. Criteria (4) Any indeterminate LNs. Criteria (5) Any suspicious and indeterminate LNs. Criteria (6) Suspicious LNs > 3mm and indeterminate LNs > 5mm in SD. Criteria (7) Suspicious LNs > 5mm and indeterminate LNs > 5mm

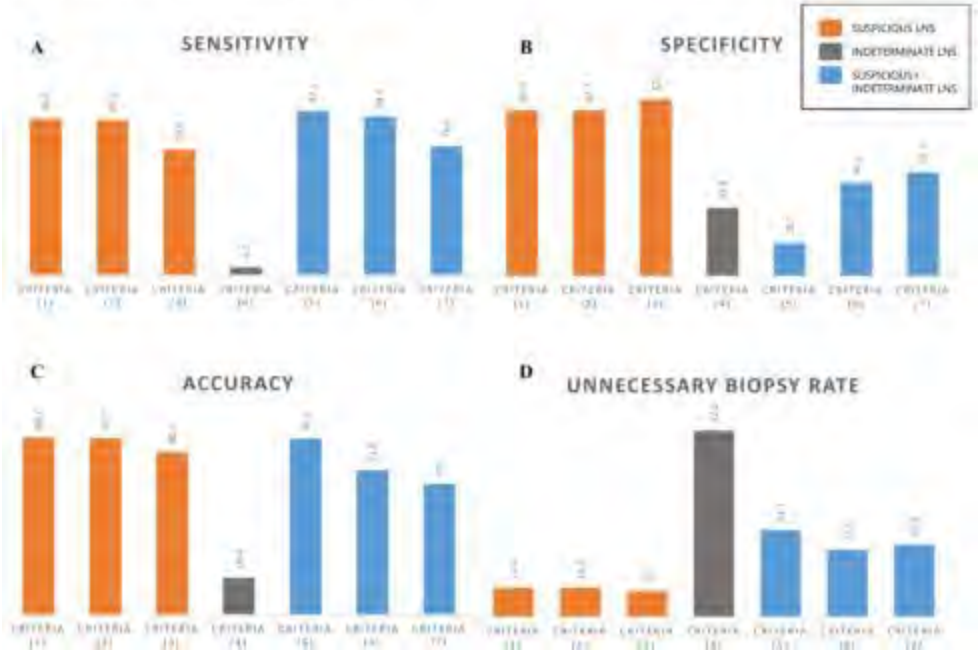

(Filename: TCT_746_Figures.jpg)

1231

Validation of Language fMRI-detectedBOLD Activation In The Right VentralPremotor Cortex (vPMC) using Intra-Operative Direct Cortical StimulationFindings In Right Sided Brain Tumours.

A Vijan[1], A Sahu[2]

[1]Tata Memorial Hospital, MUMBAI, MAHARASHTRA, [2]Tata Memorial Hospital, Mumbai, MAHARASHTRA

Purpose

To assess the concordance of pre-operative language functional MRI (fMRI) for localization of theright ventral premotor cortex (vPMC) in comparison with Direct Cortical Stimulation.

Materials and Methods

Prospective analysis was performed for 11 (n=11) patients with right-sided tumours who underwent language mapping by fMRI, followed by awake neurosurgery and intra-operative mapping by DirectCortical Stimulation (DCS). Multi-paradigm language fMRI was performed using a standard 3-paradigm language protocol, with additional tongue movement paradigm on a Phillips Ingenia, 1.5TScanner. The vPMC was identified as BOLD signal activation seen in at least two paradigms anterior to and discrete from the motor orofacial cortex. Pre-operative fMRI findings were validated intra-operatively using DCS with the intra-operative responses of anarthria (speech arrest) and dysarthria recorded separately.

Results

vPMC detection by fMRI shows good concordance (sensitivity) with anarthria responses on Direct Cortical Stimulation. Thus, fMRI serves as a useful non-invasive tool in pre-operative planning for maximal safe resection of brain tumors.

Conclusions

The ventral pre-motor cortex is represented bilaterally. Right vPMC activations seen on fMRI show concordance with intra-operative speech arrest responses, reinforcing the criticality of this often-under-recognized right-sided eloquent area. Thus, vPMC mapping must be incorporated in routine pre-operative fMRI workflow for right sided tumors as well.

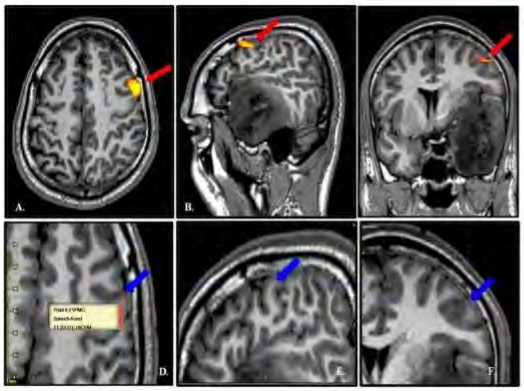

Left sided vPMC : fMRI-DCS concordance. Axial (A), Sagittal (B), and Coronal (C) BOLD fMRI images using verb generation paradigm with a 3D-T1 underlay. The red arrow shows BOLD signal activation within the left ventral pre-motor cortex as seen pre-operatively. Small field-of-view Axial (D), Sagittal (E), and Coronal (F) images have been imported from Brain Lab and depict the intra-operative site of speech arrest (marked by blue arrows). These images show almost exact one-to-one correspondence in all three planes. Thus, fMRI and DCS findings match and represent concordance.

(Filename: TCT_1231_ASNR1.jpg)

1007

Within Patient Contrast Adjustment Through a Self-Consistent Deep Learning Model when Imaging Near Metal: An Example in Angiography

A Nencka[1], K Koch[2]

[1]Medical College of Wisconsin, Wauwatosa, WI, [2]Medical College of Wisconsin, Milwaukee, WI

Purpose

When metallic foreign bodies disrupt image quality in regions necessary for diagnosis, multi-spectral acquisitions are added to standard exams to reconstruct images near the foreign bodies. This results in significant regions of artifact-free overlap between multi-spectral and standard acquisitions. A method is described to train a patient-specific neural network to modify contrast of multi-spectral acquisitions to be consistent with standard cerebral angiography acquisitions in regions where standard acquisitions fail.

Materials and Methods

A human participant gave consent and was imaged at 3.0T with T1, T2, and PD weighted 3D-multi-spectral imaging and time of flight imaging under an approved IRB protocol. A ferroshim chip was placed at the location of a cochlear implant magnet, affixed to the 48-channel head coil, and separated from the participant with a dielectric pad. This safely simulates artifact arising from a MRI-conditional cochlear implant magnet. A subject-specific U-Net was trained to highlight the vasculature. The U-Net ingested multi-contrast 3D-MSI images and predicted a thresholded TOF acquisition with training only in artifact-free regions of the TOF acquisition. Slices were randomly split into train and validation datasets, and the model with best performance on the validation dataset inferred a vascular image from the full set of acquired multi-spectral data--including in the region of signal loss of the TOF angiographic image.

Results

Vascular images were generated from the time of flight and 3D-MSI acquisitions. While the right middle cerebral artery is visible in

the time of flight acquisition, field inhomogeneity significantly disrupts the spatial encoding of the acquisition on the left half of the brain. Conversely, the multi-spectral inferred vascular image shows recovered vascular signal in both the left and right MCAs.
Conclusions
Multi-spectral imaging near metallic implants allows subject-specific deep learning because both standard acquisitions and multi-spectral acquisitions are performed with significant regions of artifact-free overlap. A neural network trained in that region within a single patient yields a contrast transform achieves similar contrast to traditional acquisitions where those acquisitions obscured by metal artifacts. An example of synthesizing time of flight-like contrast from a multi-spectral acquisition with vascular flow voids was shown.

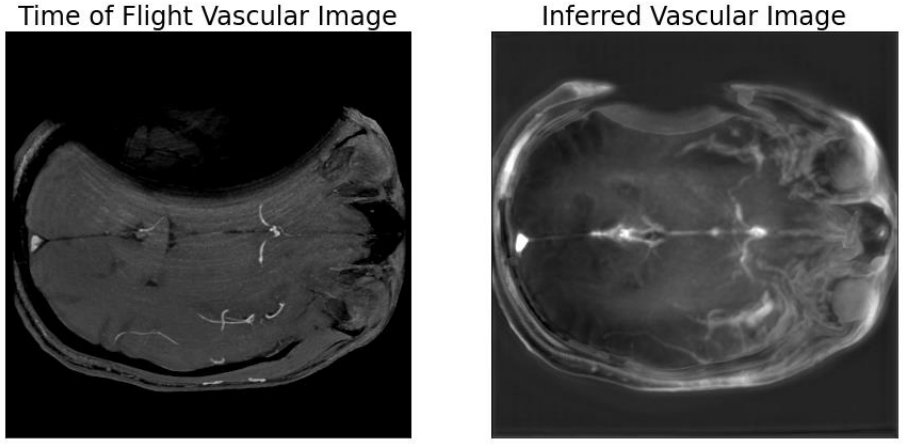

(Filename: TCT_1007_MavAngio.jpg)

1098

Yield of Neuroimaging in Children with Acute Acquired Comitant Esotropia (AACE)

V Rameh[1], F Dehghani Firouzabadi[2], C Robson[3], S Prabhu[4]
[1]Boston Children's Hospital, Boston, MA, [2]Department of Radiology, Children's Hospital, Harvard Medical School, Boston, MA, [3]Boston Children's Hospital, Weston, MA, [4]Boston Children's Hospital, Boston, MA

Purpose
Acute acquired comitant esotropia (AACE) is an infrequent presentation of strabismus in children, characterized by sudden comitant esotropia with diplopia after infancy. Neuroimaging is increasingly requested in these children, as the acute presentation with diplopia raises concern for intracranial abnormalities. In this retrospective study, we reviewed neuroimaging studies in young children aged > 1 year of age with AACE to determine the frequency of clinically significant findings. We used this data to define the ideal imaging protocol including extent of coverage (orbits/brain/both), need for sedation, and need for gadolinium-based contrast administration.
Materials and Methods
We retrospectively reviewed the clinical records and neuroimaging of children presenting with acute comitant esotropia at a large tertiary children's hospital over a ten-year period (8/2012-8/2022). The inclusion criteria for our study were: (i) no prior history of strabismus or hyperopia (ii) age at presentation greater than 1 year (iii) no family history of strabismus in first-degree relatives, and (iv) neuroimaging study obtained for the indication of AACE.
Results
Our study cohort consisted of 66 children (M: F=34:32); Mean age at presentation was 3 years (range 1-18 years). All the patients underwent magnetic resonance imaging (MRI) studies, of which 66 underwent MRI of the brain and 35 patients underwent an MRI of the brain with dedicated orbit imaging sequences. Thirty-three patients (50%) were scanned with sedation. Gadolinium-based contrast medium was administered in 32 studies (48%). New clinically significant abnormal findings were identified on neuroimaging in 5/66 (7.6%) children, Specific etiologies included smaller 6th cranial nerve and lateral rectus muscle in 2 patients, enhancement of the 3rd cranial nerve in 1 patient, Chiari type 1 malformation in 1 patient, and tectal glioma in 1 patient. Contrast-enhanced images revealed an abnormality not seen on non-contrast imaging in only 1 patient, who was subsequently diagnosed to have Lyme disease.
Conclusions
A substantial minority of children presenting with acute onset comitant esotropia after infancy have abnormal findings on neuroimaging. MRI of the brain without contrast is the preferred imaging modality after a careful history and thorough clinical examination. Gadolinium-based contrast medium administration may be reserved for patients with history or clinical signs of infection or a focal abnormality on the screening non-contrast images.

584

A case of a septal dysembryoplastic neuroepithelial tumor associated with obstructive hydrocephalus

W McLean[1], C Soto[2], C Stevens[1], O Arevalo[1]
[1]LSU Health Shreveport, Shreveport, LA, [2]National University of Colombia, Shreveport, LA

Clinical History

5-year-old Caucasian male who presents with new-onset seizures, recurrent headaches and back pain. Past medical history is significant for prior behavioral disorder with increased aggression and developmental delay.

Imaging Findings

A non-enhancing T2 hyperintense mass is seen arising from the septum pellucidum, demonstrating partial signal suppression on FLAIR and no significant enhancement. There is no associated restricted diffusion or hemorrhage. Of note, there is obstructive hydrocephalus associated with transependymal CSF migration (yellow arrowhead).

Discussion

Septal dysembryoplastic neuroepithelial tumors (sDNET) is an uncommon tumor that can initially present as headaches but can present with seizures which is more commonly associated with cortical DNETs. DNET's are the second most common tumor that has surgical resection for associated refractory epilepsy, with at least 90% of patients presenting with seizures (1). Other symptoms include behavioral disorder such as in our case at around 10-20% of the time (2). Median time to progression of the tumor was around 19 months in a review of 20 cases, and mean age of diagnosis of the tumor was approximately 23 years old (1). MR characteristics for sDNET are mostly anterior-inferior aspect of the septum pellucidum and homogeneous T2-weighted hyperintensity and FLAIR hypointensity with peripheral hyperintensity (3). Differential for septal masses in these suspected sDNETs can be vast, with the low-grade gliomas and central neurocytomas being grade II neoplasms versus the grade I neoplasms such as sDNEts or the other mimics such as subependymomas or colloid cyst (3). Clinical history and imaging of these uncommon tumors can aid the treating team in proper medical and surgical management to avoid unnecessary complications that are potentially caused by treatment.

Teaching Point

Dysembryoplastic neuroepithelial tumors (DNETs) are uncommon neural tumors presenting most often in children and young adults and associated with intractable seizures. Septal DNETs harbor different genetic alterations from those of cerebral DNETs and have a distinct methylome profile and anatomical location.

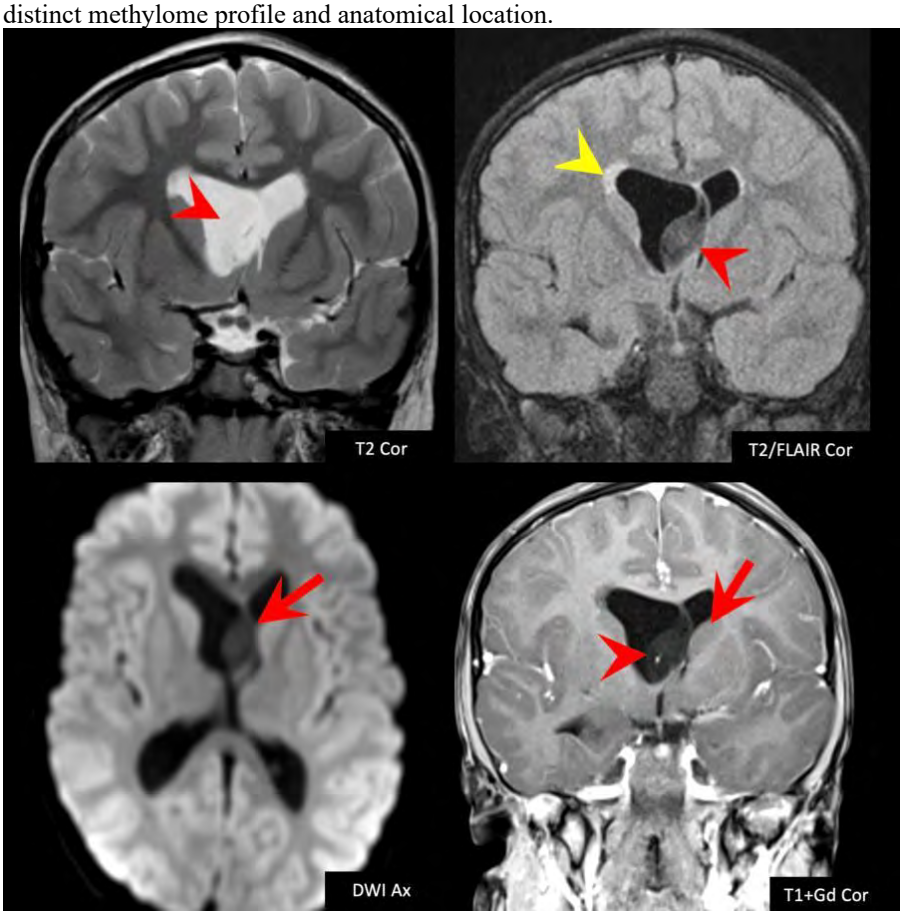

(Filename: TCT_584_sDNET.jpg)

1247

A Case of Cranial Nerve III Cavernous Malformation

A Kamali[1], L Nunez[2], A Rodriguez[3], R Patel[4], R Riascos[3], A Kamali[1]

[1]University of Texas Health Science Center Houston, Houston, TX, [2]University of Texas Health Science Center at Houston, Houston, TX, [3]The University of Texas Health Science Center at Houston, Houston, TX, [4]Texas Children's Hospital, Houston, TX, Houston, TX

Clinical History

A 59-year-old female who presented with diplopia, blurry vision and vertigo for 1 day. Physical exam demonstrated a left cranial nerve III palsy. Past medical history included history of multiple cavernous malformations and a thoracic hemangioblastoma resected in 2009 with residual paraplegia. An enhancing lesion was detected involving the left oculomotor nerve in MRI brain and orbits. Biopsy was performed with histologic diagnosis of cavernous malformation.

Imaging Findings

There is a well-defined T1 isointense, T2 hyperintense mass in the left posterior suprasellar cistern, which demonstrates homogenous postcontrast enhancement. Susceptibility-weighted imaging shows numerous blooming artifacts in both cerebral hemispheres, consistent with history of multiple cavernous malformations.

Discussion

Cavernous venous malformations consist of dilated vascular sinusoid channels lined by endothelium without associated feeding arteries or draining veins, and account for up to 20% of all vascular malformations of the central nervous system. Extra-axial cavernous malformations, however, account for only 2% of all intracranial vascular malformations. Previous cases of cavernous malformations arising from cranial nerves have been reported to affect the II, V, VII, and VIII cranial nerves. Imaging appearance can resemble more common tumors such as schwannoma, neurofibroma or meningioma.

Teaching Point

-- Cavernous venous malformations are benign lesions that can have an extra-axial location. When evaluating a dural-based lesion without evidence of a dural tail or adjacent bone hyperostosis, cavernous malformation should be suspected. -- In the presence of multiple brain parenchymal cavernous malformations, any lesion involving the cranial nerves, should be scrutinized for cavernous malformation alongside the nerve sheath tumors such as schwannoma.

Axial FLAIR, SWI, T1 pre and post contrast sequences of brain MRI. A FLAIR hyperintense enhancing lesion is seen involving the left oculomotor nerve. SWI showed multiple periventricular and subcortical cavernous malformations. The enhancement places nerve sheath tumors in the differential diagnosis as well.

(Filename: TCT_1247_CNCavMal.jpg)

631

A case of diffuse metastatic infiltration of thyroid from colon carcinoma mimicking lymphoma

L Nunez[1], S Khanpara[2], P Rabiei[3], R Patel[4], T Vu[5], R Riascos[1]

[1]The University of Texas Health Science Center at Houston, Houston, TX, [2]University of Texas MD Anderson Cancer Center, Houston, TX, [3]University of Texas Health Science Center at Houston, Houston, TX, [4]Texas Children's Hospital, Houston, TX, [5]M.D. Anderson Cancer Center, Houston, TX

Clinical History

53-year-old female who presented with trouble swallowing and recent voice change. She also complained of fatigue, cold intolerance, shortness of breath and cough. On physical exam, she was found to have palpable thyroid nodules with laboratory testing showing profound hypothyroidism. Past medical history was significant for colonic adenocarcinoma diagnosed on 2014, treated with surgical resection and chemoradiation

Imaging Findings
Thyroid ultrasound demonstrated minimal but globular enlargement of both lobes with diffuse homogeneously hypoechoic signal. No focal abnormality was noted. Doppler ultrasound did not demonstrate increased vascularity. Few scattered enlarged hypoechoic lymph nodes were seen along the inferior aspect of the left lobe of thyroid, right superior neck and left inferior neck. Postcontrast CT chest corroborated the findings of diffuse involvement with few slivers of hyperdensity which was believed to represent normal thyroid tissue. Lymphoma and thyroiditis were suggested as possible differential diagnosis. However, US guided fine needle aspiration of the left lobe was consistent with metastatic disease from the known colon primary
Discussion
Despite its rich vasculature, metastasis to thyroid gland is uncommon. Thyroid metastases represent 3% of all thyroid neoplasms with majority presenting as solitary or multiple nodules on imaging. Lung, kidney and colon/rectum are the most common sites for primary tumor. Diffuse infiltrative metastasis of the thyroid is rare and often mimic non-neoplastic disorders such as thyroiditis and neoplastic conditions such as lymphoma. The lack of significant internal vascularity with no prior history of thyroid abnormality made thyroiditis less likely in this patient. However, the presence of enlarged hypoechoic cervical lymph nodes raised suspicion for lymphoma. No ultrasound or CT features were found to be specific/typical for diffuse metastatic infiltration. We believe diffusion weighted MRI would been useful in differentiating diffuse metastatic infiltration from lymphoma
Teaching Point
Diffuse metastatic infiltration of thyroid is rare with no specific imaging findings. Fine needle aspiration is often required to make the diagnosis

(Filename: TCT_631_Fig1600.jpg)

411
A Case of Dural Plasmacytoma
S Grasso[1], E Yekeler[1], T Baldwin[1], A Kolluri[1], M ALBAYRAM[2]
[1]University of Florida, Gainesville, FL, [2]U florida, Gainesville, FL

Clinical History
A previously healthy 42-year-old woman with no significant past medical history initially presented with an acute onset of neurologic symptoms, including numbness and weakness in left upper and lower extremities, difficulty with balance, headache, nausea and blurry vision in the left eye. MR imaging showed a large extra-axial mass with an underlying mass effect on the brain parenchyma (Fig 1). The patient was consulted by a neurosurgery with a subsequent resection of the tumoral lesion. The pathology revealed the diagnosis of plasmacytoma.
Imaging Findings
Figure 1. (a) Coronal T2-weighted SE image demonstrates the classic appearance of an extra-axial mass with "CSF Cleft" sign (arrows). (b-d) Coronal, axial, and sagittal contrast-enhanced 3D T1-weighted GRE images demonstrate a multi-lobulated and somewhat irregular (arrows) extra-axial dural-based mass lesion with an impression and mass effect upon the underlying right frontal high convexity.
Discussion
Plasmacytoma is a plasma cell dyscrasia which can be subdivided into two separate types(1). Paraskeletal plasmacytomas are soft tissue lesions which arise from the paraskeletal soft tissues; whereas extramedullary plasmacytomas are soft tissue masses with an osseous contact. Dural-based plasmacytomas belong to the latter category and present as an extra-axial masses in the head and spine. As such, they can mimic meningiomas and should remain on the differential diagnosis of extra-axial masses. There are no definitive characteristic features to differentiate the dural-based plasmacytomas from meningiomas; however, in the current case, we noticed that the lesion is more lobulated and irregular in shape than would be expected for a typical meningioma.
Teaching Point
Dural Plasmacytoma can present in the presence or absence of multiple myeloma. While it is an uncommon neoplasm, it remains an important part of the differential diagnosis for extra axial mass.

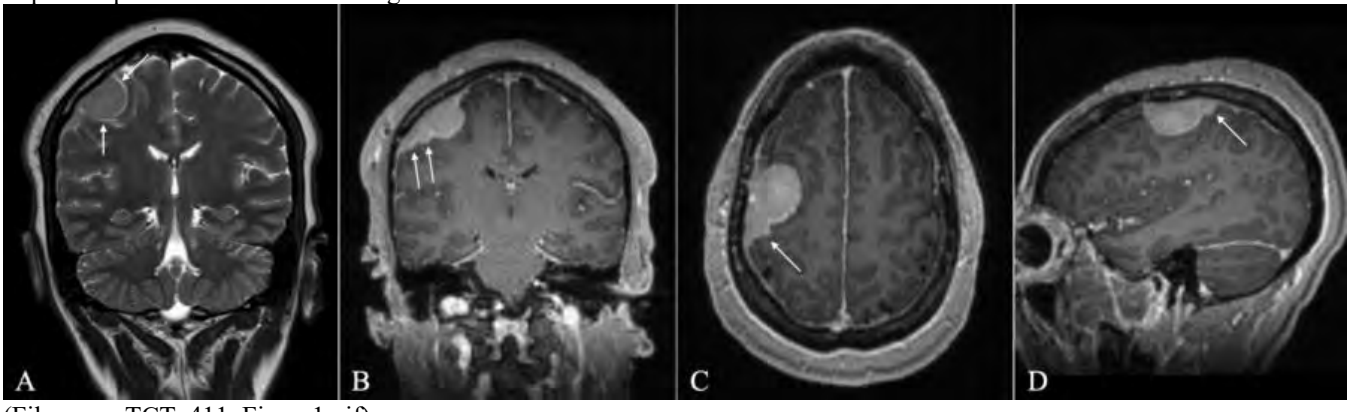

(Filename: TCT_411_Figure1.gif)

686

A case of growing Traumatic intracranial internal carotid artery aneurysm treated with covered stent graft.

S Tadisetty[1], A Guntamukkala[2], S Kokkula[3], K Sajja[4]

[1]University of Kentucky, Lexington, KY, [2]Life hospital, Guntur, Andhra Pradesh, [3]Guntur medical college, Guntur, Andhra Pradesh, [4]Life hospital, Guntur, Guntur, Andhra Pradesh

Clinical History

A 25-year-old male with no prior medical history was brought to the emergency department after a motor vehicle accident. He had a subarachnoid hemorrhage. A DSA showed a left sided extradural ICA aneurysm which was not thought to be the cause of the SAH and the SAH was thought to be traumatic. However, a follow up DSA within 14 days showed increase in size of the aneurysm. The patient was in a minimally conscious state throughout the hospital admission. He also had multiple injuries including right clavicular fracture.

Imaging Findings

On Computed tomography (CT) Imaging, there was a sub arachnoid hemorrhage. A diagnostic angiogram was done to rule out intracranial lesions causing the SAH. On the angiogram (done at outside hospital) showed a traumatic aneurysm of left intracranial Internal carotid artery which not the cause of subarachnoid hemorrhage as this aneurysm is not intradural. He presented to our hospital a few weeks after the initial event for further neurovascular options. By this time, a tracheostomy was done. We did a follow up DSA with a 3D angiogram and also a balloon occlusion test to evaluate for treatment options. The aneurysm was found to be growing rapidly in size. We reviewed treatment options with the family. Flowdiverter was out of the question due to the financial situation. We also discussed about parent artery occlusion. However, the patient failed the balloon occlusion test. We then discussed about using a Covered stent which was cheap and financially feasible. He was started on dual antiplatelets- Aspirin and Ticagrelor 5 days prior to the procedure and the aneurysm was stented using a Abbott Graftmaster stent graft. The patient was discharged home a few days later when his secretions and the tracheostomy wound was manageable. His mental condition improved a month later and he came back to the clinic. A follow up angiogram is planned in 6 months.

Discussion

Rapidly growing traumatic aneurysms need treatment to reduce the risk of stroke and further neurologic deterioration.CTA and DSA have good sensitivity and specificity for diagnosing this condition. Prior literature showed the utility and effectiveness of endovascular therapy with covered stents. Endovascular therapy has the additional utility of being economically viable in low income settings or when surgical options are limited by anatomy or other reasons.

Teaching Point

Coved grafts are a good option of treatment for Traumatic intracranial aneurysms, especially in a low economic setting.

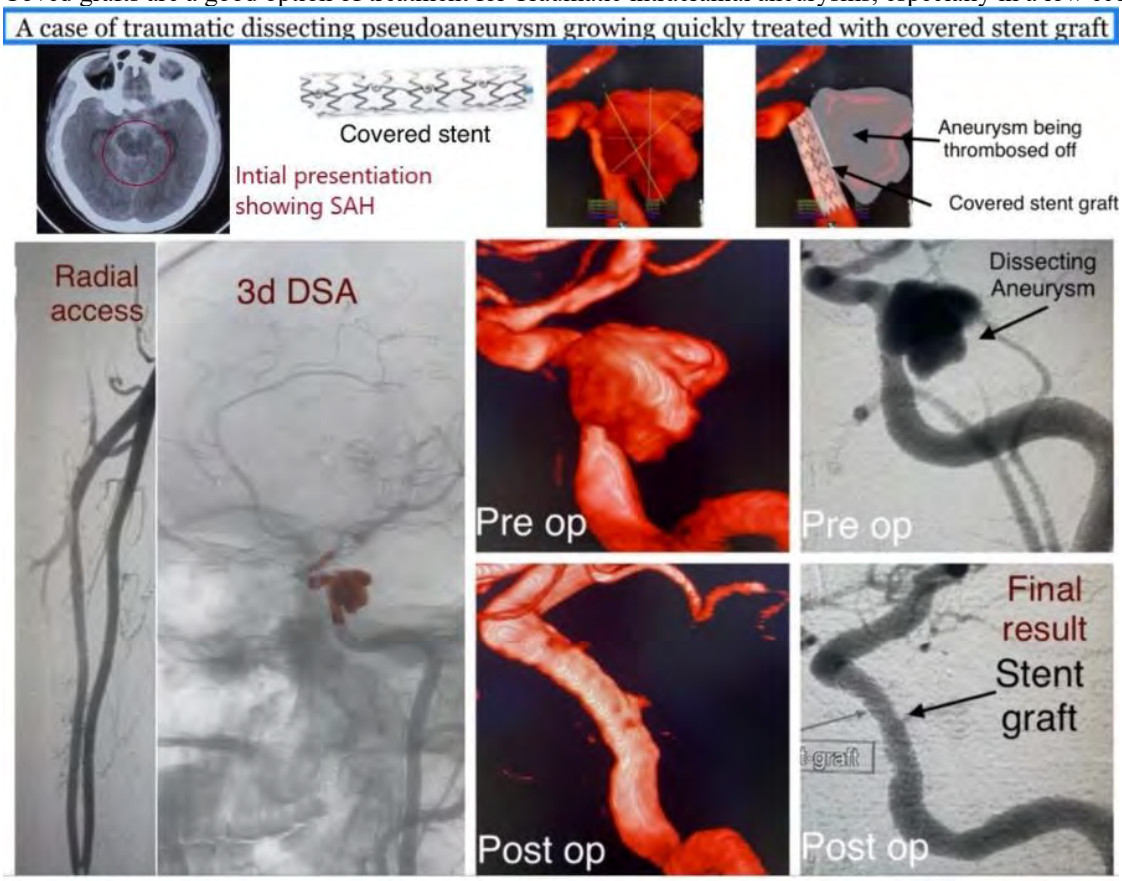

(Filename: TCT_686_TIPAC.jpg)

384

A Case of Olivopontocerebellar Degeneration (MSA-C) with Imaging and Genetic Testing Results Potentially Supporting Inherent Susceptibility to Sporadic MSA

D Ledet[1]
[1]*MUSC, Charleston, SC*

Clinical History

The patient is a 50-year-old Hispanic male with no significant past medical or past surgical history who presented to neurology clinic after approximately 15 months of progressive symptoms including: headache, difficulty with balance, and difficulty with ambulation.

Imaging Findings

Initial imaging in 2020 including CT head without contrast and MRI brain without contrast showed no significant abnormalities. Subsequently, repeat MRI brain without contrast two years after symptom onset demonstrated marked volume loss involving the pons, medulla, and cerebellum, as well as increased T2/FLAIR signal involving the transverse pontine fibers. No significant abnormality or volume loss involving the cerebral hemispheres was identified.

Discussion

Multiple system atrophy is a well-known progressive neurodegenerative disease with three recognized subtypes: MSA-C, MSA-P, and MSA-A. MSA has a prevalence of 2-5 cases per 100,000 people. MSA-C is also known as olivopontocerebellar atrophy. While the cause of this disease process is multi-factorial, there are certain genes which have been implicated in a rare presentation of genetic etiology causing MSA-C. In this case, the patient was referred to a genetics counselor, where a comprehensive ataxia panel was performed. Results described two heterozygous variants of uncertain clinical significance involving the COQ2 gene. Loss of function in COQ2 mutations results in primary CoQ10 deficiency. Some studies have suggested a link between specific heterozygous variants involving the COQ2 gene and susceptibility to sporadic MSA. As the laboratory could not decipher whether the variants were on a single or both chromosomes, a discussion ensued about testing the patient's daughter for further clarification. If genetic testing showed that the patient's daughter had one variant, then in theory, the patient's mutation would involve both chromosomes, thus suggesting inherent susceptibility to MSA.

Teaching Point

While causes of MSA-C are multi-factorial, there is a rare genetic variant involving the COQ2 gene which suggests a link between genetic mutation and inherent susceptibility to MSA. Imaging findings are well-known and include atrophy of the pons, medulla, and cerebellum, as well as increased T2 signal involving the transverse pontine fibers (also known as the hot cross buns sign).

Figure 1: Axial T2 and Sagittal T1 imaging showing normal appearance of the pons, medulla, and cerebellum. Images were acquired at the onset of symptoms.

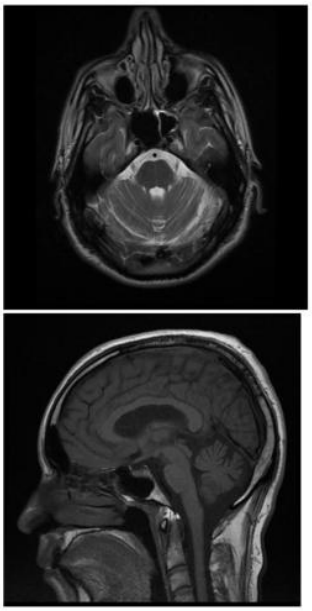

Figure 2:
Axial T2 and Sagittal T1 demonstrate imaging findings suggestive of MSA-C. Axial T2 through the pons demonstrates pontine and cerebellar atrophy, as well as increased T2 signal involving the transverse pontine fibers (hot cross buns sign). Sagittal T1 through at midline demonstrates diffuse atrophy involving the pons, medulla, and cerebellum. Images were acquired approximately two years after symptom onset.

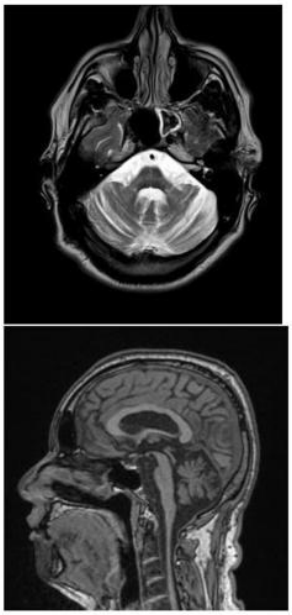

(Filename: TCT_384_ASNRgraphics.jpg)

1437

A Case Series of Owl-Eyes in Cervical Spondylotic Amyotrophy

N Hwang[1], M Branston[1], O Tong[1]
[1]*University of California, Davis, Sacramento, CA*

Clinical History

The owl-eyes sign, also known as the snake-eyes sign, refers to the circular foci of high T2-weighted signals in the anterior horn of the spinal cord on MR imaging. It is a unique finding commonly associated with anterior spinal artery ischemia. It can also be seen in chronic compressive myelopathy, specifically cervical spondylotic amyotrophy (CSA), which presents with muscle atrophy in the upper extremities with no sensory symptoms or involvement of the lower extremities. This is a case series of four patients (3 male and

1 female) with ages ranging from 57-75 years who were followed over a three-year time period (2019-2022) at University of California, Davis Medical Center for CSA. All four patients presented with years of asymmetric bilateral upper extremity weakness, with symptoms worse on the nondominant side for all patients. On exam, 100% of patients had distal greater than proximal muscle weakness and had documented atrophy of the intrinsic hand muscles. Half of the patients' presentations were also consistent with concurrent radiculopathy.

Imaging Findings

MRI of the cervical spine revealed the characteristic owl-eyes sign. All of the patients had owl-eyes in the lower cervical region involving multiple levels, 50% had involvement down to the level of T1, and 25% involved up to the level of C3.

Discussion

Three of four patients had undergone spinal surgery. Of those who had spinal surgery, only one patient endorsed improvement in his hand coordination; the other subjects demonstrated decline of function over time. The patient who was managed conservatively also had progressive worsening of his symptoms.

Teaching Point

CSA is not a commonly associated condition with the owl-eyes sign on MRI, but it should be considered as a possibility in the right clinical context, including patients who present with chronic and progressive asymmetric upper extremity weakness. This case series suggests that this imaging finding is associated with poor outcomes even with surgical intervention, which may at best stabilize symptoms.

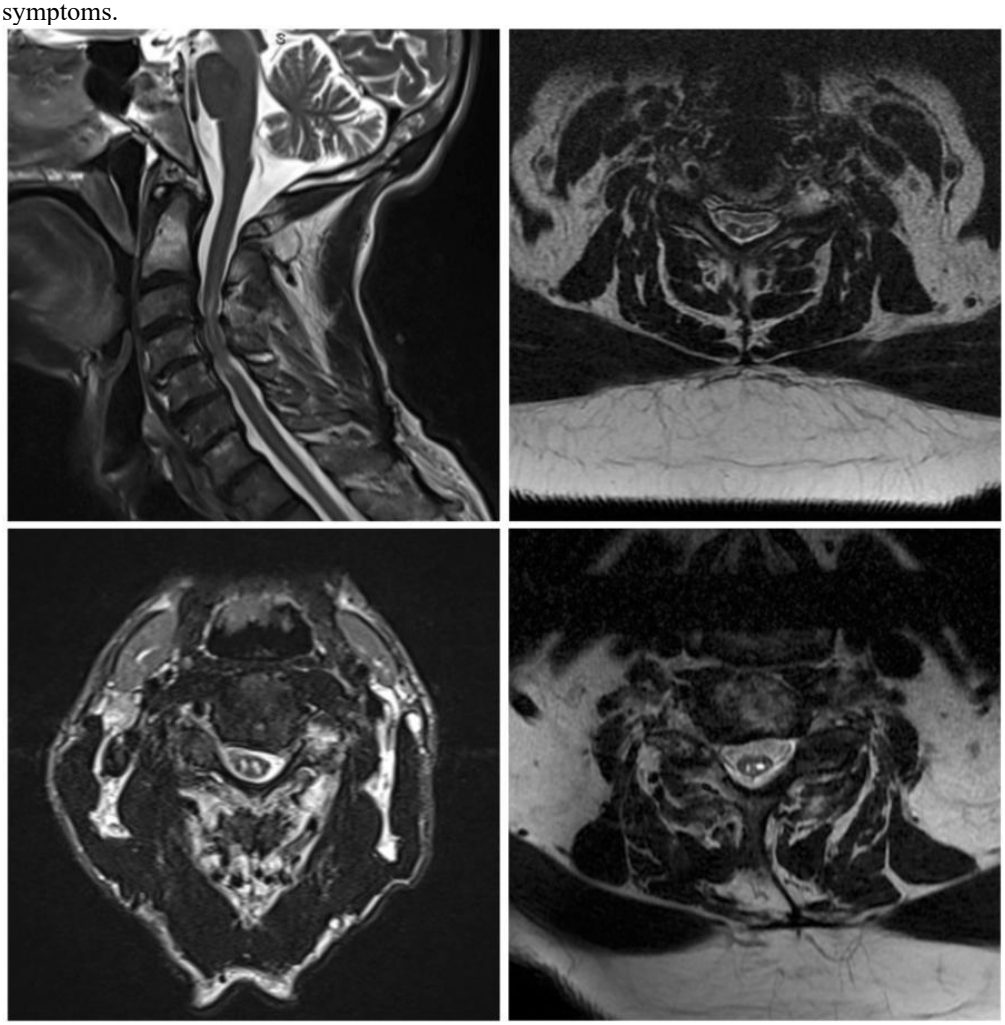

(Filename: TCT_1437_Images.jpg)

792

A Peculiar Case of Diffusion Restriction in Valproate-Induced Hyperammonemia

E Shin[1], S Girn[1], J Soun[2], E CHU[3], E KUOY[2], C Li[4]

[1]UC Irvine Medical Center, Orange, CA, [2]UC Irvine, Orange, CA, [3]UNIVERSITY OF CALIFORNIA, IRVINE, ORANGE, CA, [4]University of California, Irvine, Orange, CA

Clinical History

Patient is a 23-year-old female with no significant prior history who presented with convulsive status epilepticus. These seizures were preceded by a flu-like illness, for which the patient drank an herbal tea mixture almost immediately before developing seizures. After extensive laboratory workup, the patient was ultimately diagnosed with new-onset refractory status epilepticus (NORSE) without clear etiology. The patient had a prolonged hospital course, during which she was initiated on a multitude of anti-epileptic drugs including

valproic acid. This was discontinued after four days due to rising liver function test lab values. Ammonia was also found to be elevated, which steadily dropped after valproic acid cessation.

Imaging Findings

(A) Initial MRI Brain obtained about two weeks after admission demonstrated no significant T2/FLAIR signal abnormalities. (B) MRI Brain obtained a few days after cessation of valproic acid demonstrated diffuse symmetric edema and gyriform cortical diffusion restriction with sparing of the (C) occipital lobes and (D) perirolandic regions. Suspicion for severe hepatic encephalopathy was raised based on these findings.

Discussion

Hyperammonemia has a wide variety of clinical manifestations that is most commonly seen in patients with liver failure. However, hyperammonemia may be attributed to several non-hepatic etiologies such as valproic acid. While valproic acid can cause hepatotoxicity, as in this case, clinical hyperammonemia and elevated serum ammonium can manifest without evidence of liver injury. MRI findings of hyperammonemia often include edema and diffusion restriction within the cerebellar white matter, globus pallidus, as well as within the grey matter, especially within the insular and cingulate cortices. Often, the severity on MRI correlates with plasma ammonia level. A proposed mechanism for this phenomenon is inhibition of an enzyme within the urea cycle which hinders conversion of ammonia to urea. Other MRI findings of valproate induced hyperammonemia include focal T2/FLAIR hyperintensity in the cerebellar white matter and globus pallidus.

Teaching Point

Valproate-induced hyperammonemia is a process which can be seen with or without evidence of liver injury that manifests most strikingly as cortical grey matter diffusion restriction and edema.

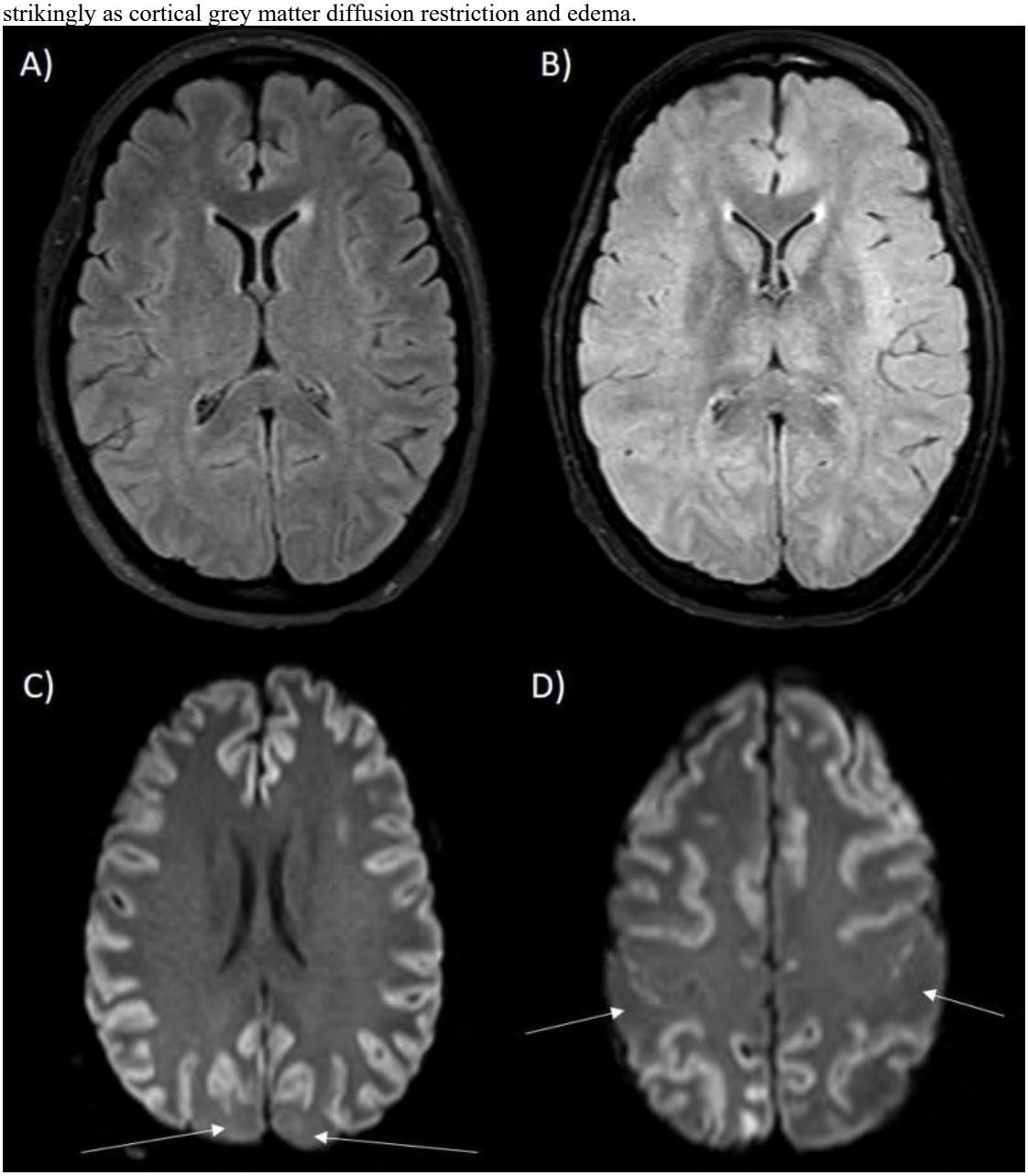

(Filename: TCT_792_ASNR2023submission2.JPG)

583

A rare case of a Glioblastoma, IDH-wildtype with FGFR3-TACC3 fusion

C Soto[1], W McLean[2], C Stevens[2], O Arevalo[2]

[1]National University of Colombia, Shreveport, LA, [2]LSU Health Shreveport, Shreveport, LA

Clinical History

32-year-old male patient with no significant past medical history presenting to ED with a one-week history of generalized tonic-clonic seizures with a short postictal period.

Imaging Findings

There is an ill-defined T2/FLAIR hyperintense mass centered at the left parietal white matter, extending into the subcortical white matter and the splenium of the corpus callosum. Of note, there are gyriform and dystrophic calcifications (yellow arrowhead) surrounded by areas of nodular enhancement (red arrowhead). No restricted diffusion or hemorrhage are noted.

Discussion

Adult glioblastomas comprise a molecularly and histopathologically heterogeneous spectrum of neoplasms characterized by poor prognosis. Actionable fibroblast growth factor receptor 3 (FGFR3)–transforming acidic coiled-coil protein 3 fusions (F3T3) are oncogenic drivers found in approximately 3% of gliomas; they encode a protein that causes a loss of the normal chromosomal segregation and stimulates aneuploidy (1)(4). There are unique characteristics of F3T3-positive gliomas that include morphological features (monomorphous ovoid nuclei, nuclear palisading and thin parallel cytoplasmic processes, endocrinoid network of thin capillaries, frequent microcalcifications, and desmoplasia) associated with a rich vascularization (2). Among IDH wildtype tumors, F3T3 gliomas have a more favorable clinical outcome, especially when associated with 12q13.15 amplicons. They have MRI findings such as the preferential involvement of non-eloquent areas, poorly defined margins for contrast-enhancing and non-contrast-enhancing tumors (3).

Teaching Point

In-frame FGFR3-TACC3 fusions confer to glioblastomas, IDH-wild type some unusual histologic features, including monomorphous rounded cells with ovoid nuclei, nuclear palisading, endocrinoid network of "chicken-wire" vessels, microcalcifications and desmoplastic stroma. Although no specific imaging biomarkers have been identified, the presence of calcifications, ill-defined borders and the preferential involvement of non-eloquent areas might suggest the diagnosis on preoperative MRI.

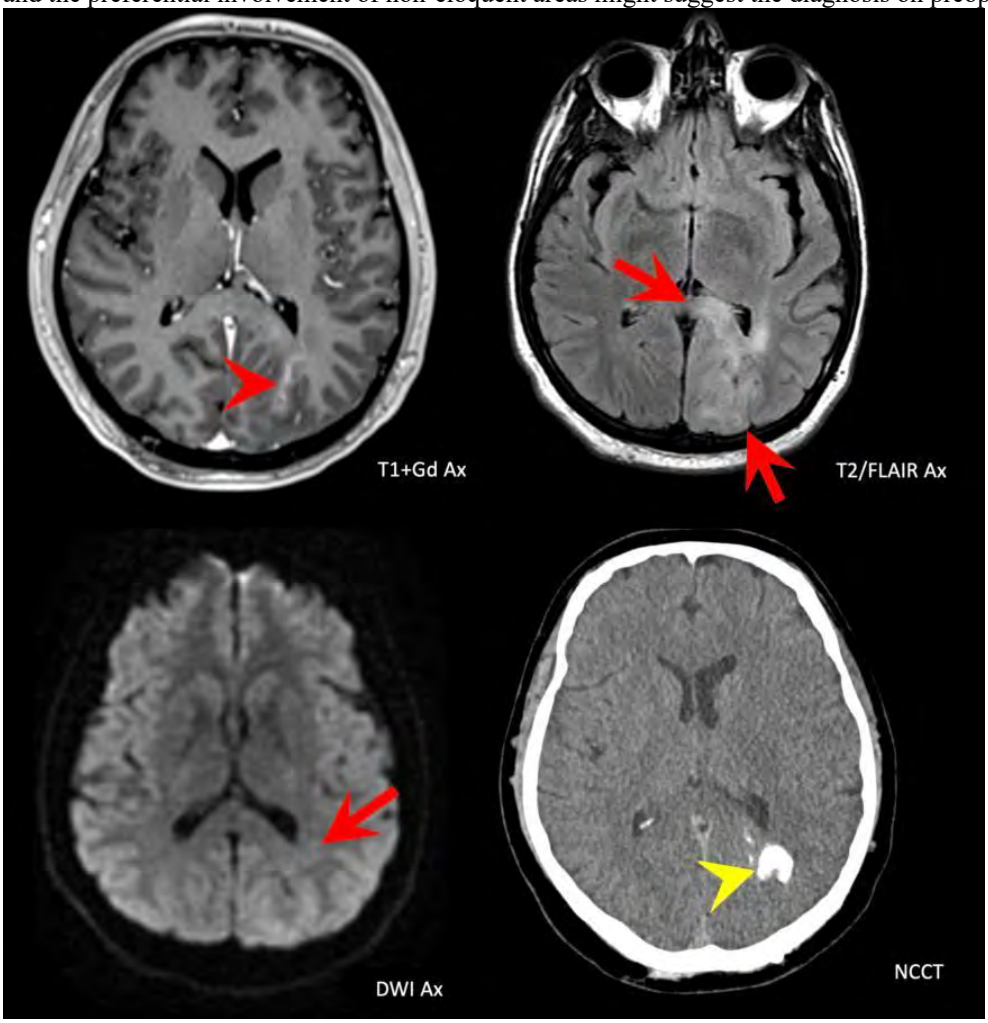

(Filename: TCT_583_GBM.jpg)

110

A rare case of Cerebral Fat Embolism Syndrome in the setting of Sickle Cell Crisis

A Patel[1], S Peterson[1], R Hynecek[1]
[1]*Hartford Hospital, Hartford, CT*

Clinical History

A 30-year-old female with a history of sickle cell disease, previously well-controlled on hydroxyurea and folic acid supplementation, presented to the ED in sickle cell crisis. She was initially treated with IV hydration, pain control, hydroxyurea and folic acid. She subsequently developed acute anemia and thrombocytopenia, and underwent RBC transfusion and platelet replacement. She became increasingly lethargic, with initial head CT negative for acute findings. She later became tachypneic and tachycardic and underwent CTA chest which showed pulmonary emboli and bilateral airspace opacities suspicious for ARDS. Despite aggressive efforts, mental status continued to decline. MRI, MRA, and MRV of the head were obtained. MRA/MRV demonstrated patent vasculature. MRI findings as discussed.

Imaging Findings

A. Gradient recalled echo imaging demonstrates innumerable symmetrically distributed punctate foci of susceptibility artifact with a predilection for white matter. B. Diffusion weighted imaging demonstrates extensive restriction primarily involving the supratentorial white matter (the Starfield pattern) and basal ganglia, with corresponding low signal on ADC (C), consistent with acute infarct.

Discussion

Fat Embolism Syndrome (FES) is a rare, under-recognized, and often fatal complication of sickle cell disease. In the setting of sickle cell crisis, vaso-occlusion secondary to RBC sickling can result in bone infarcts, triggering the release of fat molecules and pro-inflammatory free fatty acids into systemic circulation. In end-organ capillary beds, fat molecules result in mechanical occlusion of vessels, while free fatty acids incite a cytokine mediated inflammatory reaction, ultimately leading to endothelial cell injury and vessel destruction(1). Though the exact mechanism by which fat molecules enter cerebral circulation is unknown, it is hypothesized that emboli traverse the pulmonary capillary bed or enter via a patent foramen ovale(2). Imaging plays a crucial role in the diagnosis of cerebral FES, with DWI characteristically showing the Starfield pattern of innumerable punctate foci of high signal on a relatively hypointense background(3). Treatment of FES is mainly supportive(4), though multiple published case reports boast hopeful outcomes following prompt diagnosis and early red cell exchange transfusion(5).

Teaching Point

Recognition of the Starfield pattern on MRI will facilitate prompt diagnosis and early intervention of cerebral fat embolism syndrome in the setting of sickle cell crisis.

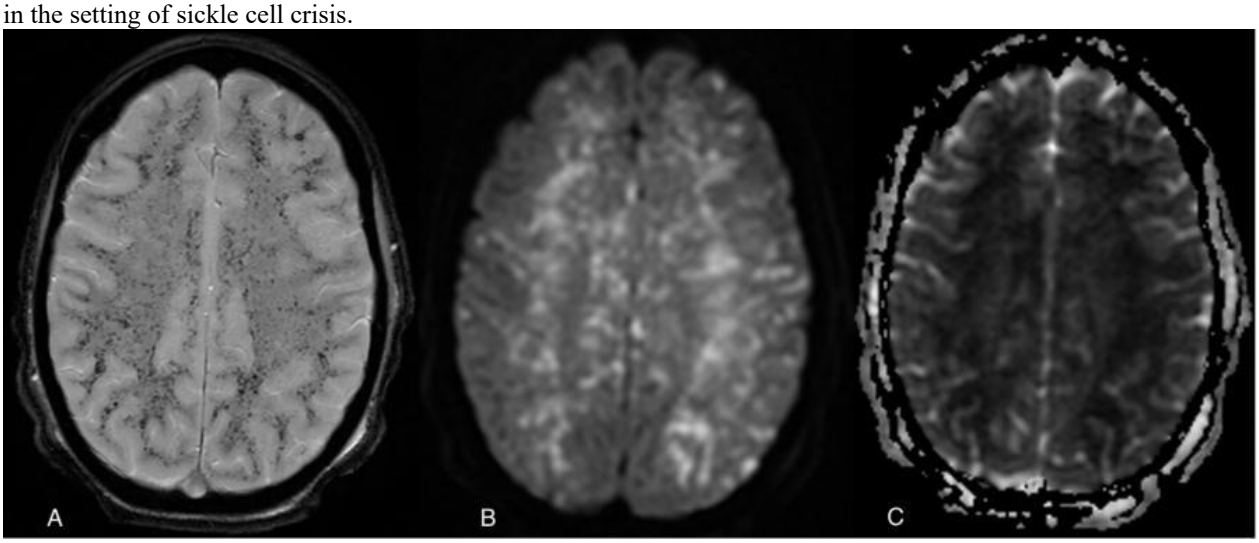

(Filename: TCT_110_FESinSCD.jpg)

737

A rare case of Frontonasal Dysplasia (Median Cleft Facial Syndrome)

A Vij[1], K Oguz[1], J Huynh[1], O Raslan[1], L Hacein-Bey[1], M Bobinski[1], A Ozturk[1]
[1]*University of California Davis, Sacramento, CA*

Clinical History

We report a rare case of Frontonasal Dysplasia in a full-term female infant via spontaneous uneventful delivery. Prenatal Ultrasound revealed a left frontal meningocele in the fetus. Early postnatal physical exam was notable for 1 x 1 cm soft tissue protrusion above the left frontal region, broad base of nose with cleft of left nares, bilateral preauricular ear tags, hypertelorism, sacral dimple, and anterior displacement of anus with anorectal fistula. The patient also had left upper lid coloboma. There was no history of consanguinity and no family history of similar conditions.

Imaging Findings

Postnatal computerized tomography (CT) of head and face demonstrated a large left frontal supraorbital osseous defect partially overlying the area of left frontal meningocele (upper red arrow, Figure 1), median cleft along the left nares and palate (lower red

arrow, Figure 1), and oblique laterally oriented bilateral sutures of the frontal bone (yellow stars) extending rostrally from a large anterior osseous defect without separately visualized open anterior fontanelle. Magnetic Resonance Imaging (MRI) showed the left frontal meningocele and pericallosal lipoma (Figure 2). The patient had other abnormalities including scoliotic spine and multiple segmentation abnormalities (Figure 1).

Discussion

Frontonasal Dysplasia can present as various clinical anomalies with associated imaging findings including midline defects in the face, head, and CNS (see Table 1); three types of frontonasal dysplasia have been described so far. Associated clinical findings include accessory nasal tags, coloboma, cataracts, preauricular tags, low-set ears, and conductive hearing loss. The exact pathogenesis of Frontonasal Dysplasia is unknown but likely related to primary defects in the nasofrontal process that prevents midline migration. There has been a documented association with loss of function in the ALX homeboy gene family. It is understood that remodeling defects in the nasal capsule lead to the key features of Frontonasal Dysplasia (Sharma et. al).

Teaching Point

Frontonasal Dysplasia is a rare entity with a spectrum of clinical and imaging findings. Radiologists should be aware of additional midline intracranial abnormalities to determine neurological status for accurate medical care and prognostication.

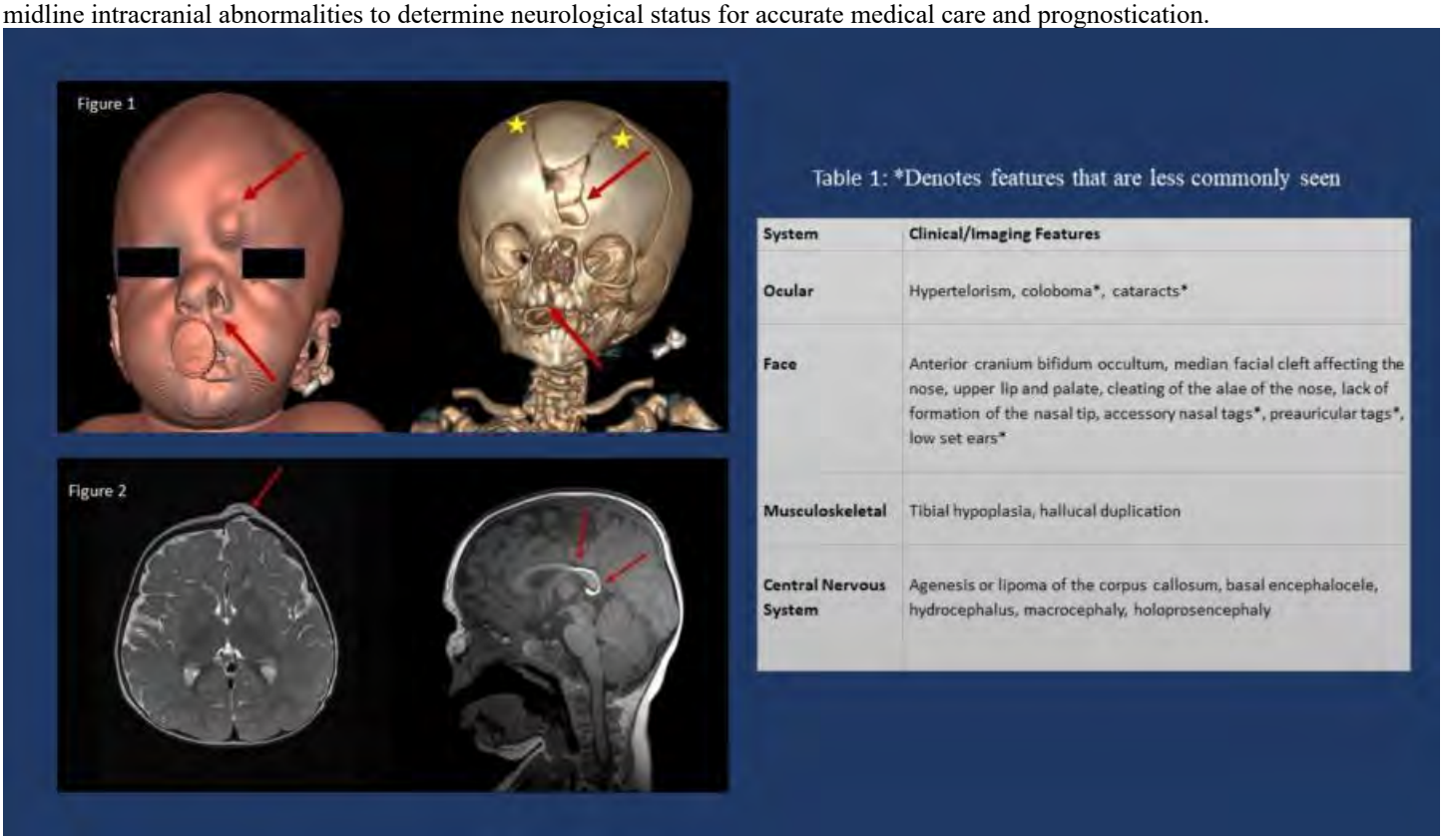

(Filename: TCT_737_MCSYND.jpg)

458

A Rare Case of Hemifacial Spasm Secondary to Pontine Microhemorrhage

A Kamali[1], A Ali[2], L Nunez[3], A Rodriguez[4], R Patel[5], A Kamali[1]

[1]University of Texas Health Science Center Houston, Houston, TX, [2]UTHealth McGovern Medical School, Houston, TX, [3]University of Texas Health Science Center at Houston, Houston, TX, [4]The University of Texas Health Science Center at Houston, Houston, TX, [5]Texas Children's Hospital, Houston, TX, Houston, TX

Clinical History

A 52-year-old male, with past medical history of hypertension, who presented with 4 week history of twitching muscles of the right face which was gradually progressive. No history of headache or shooting pain in the face. Patient presented to ED with worsening of the symptoms. Blood pressure at arrival was 173/98. Physical exam showed right ptosis with subtle upward lateralization of right mouth. The brain MRI was performed at ED.

Imaging Findings

Only seen on gradient echo sequences of the brain MRI, was a focus of hemosiderin deposition compatible with chronic microhemorrhage in the right aspect of the pons. No mass or lesion was detected in the high resolution FIESTA sequences along the cisternal and temporal courses of the cranial nerve VII. Additional chronic punctate microhemorrhages were seen in bilateral thalami and basal ganglia compatible with history of hypertensive microangiopathy. No vascular structure was detected to impose mass effect over the root exit zone of the cisternal segment of the cranial nerve VII causing neurovascular compression.

Discussion

Irritation of the cranial nerve (CN) VII at the root exit zone by an aberrant vascular structure is usually the cause of hemifacial spasm.

In one study, more than 100% of subjects had a vessel contacting the nerve in symptomatic patients. CN VII, facial nerve, nucleus is located in the posterior pons. The fascicular segment of the CN VII originates from the nucleus, makes a circular course around the nucleus of CN VI and subsequently continues laterally towards the cerebellopontine cistern. Pontine microhemorrhage is a rare cause of hemifacial spasm causing mass effect over the fascicular fibers of the facial nerve and clinically manifests as an isolated facial nerve palsy or spasm. Other causes of hemifacial spasm are tumors such as schwannoma, cerebellopontine angle meningioma and rarely demyelinating plaques of multiple sclerosis.
Teaching Point
Hemifacial spasm is mostly caused by neurovascular compression of the cisternal segment of CN VII at the root exit zones - CN VII, facial nerve, nucleus is located in the posterior pons - the fascicular segment of the CN VII makes a loop around the nucleus of CN VI and then courses laterally towards the cerebellopontine angle - demyelinating plaques and punctate hemorrhages are rare causes of involvement of the fascicular segment of CN VII in the pons - presents with painless spasm of the orbicularis oculi gradually spreading in extent and severity to involve the majority of the face,

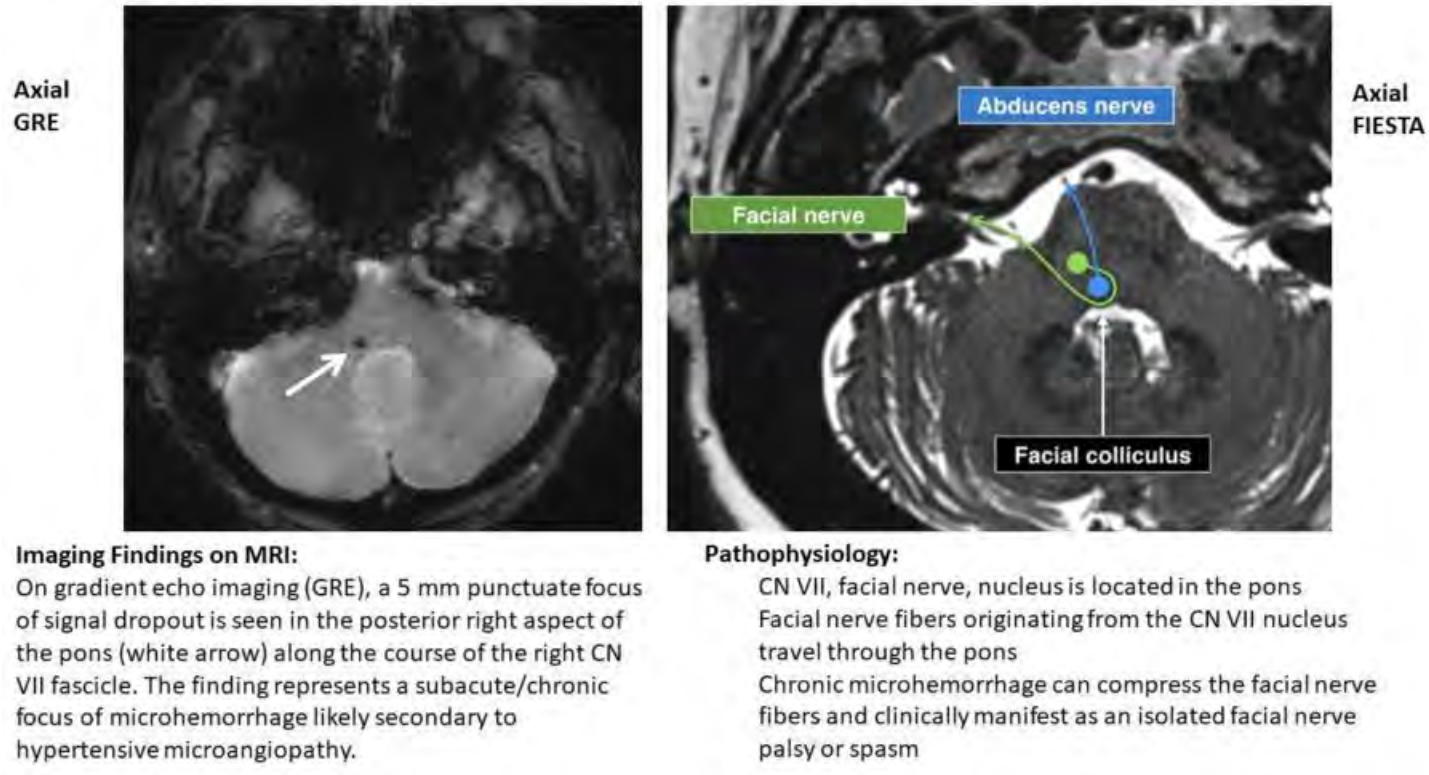

(Filename: TCT_458_hemifacialspasm1.jpg)

233

A rare case of IDH-mutant astrocytoma with primitive neuronal component and disseminated extracranial metastasis

P Rabiei[1], S Khanpara[2], O Arevalo[3], R Patel[4], K Shah[2], T Vu[2]
[1]University of Texas Health Science Center at Houston, Houston, TX, [2]University of Texas MD Anderson Cancer Center, Houston, TX, [3]LSU Health Shreveport, Shreveport, LA, [4]Texas Children's Hospital, Houston, TX

Clinical History
Our patient is a 43 y/o male with an initial diagnosis of right frontal lobe IDH mutant astrocytoma, WHO grade 2 (resected in 2007). Local recurrences were treated with surgery and temozolomide. A surgery in 2019 showed progression to IDH mutant astrocytoma, WHO grade 4. In 2021, further rapid progression and disseminated metastatic disease involving the scalp, dura, leptomeninges, left parotid gland, cervical lymph nodes, and osseous structures were noted. Stereotactic biopsy of a dural-based mass showed features of astrocytoma, WHO grade 4 with high grade small round blue cell morphology (suggesting primitive neuronal component) and expression of synaptophysin, NCAM CD-56, with negative GFAP. Molecular analysis yielded IDH1/IDH2 mutation, loss of ATRX, TP53/RB1 alteration, and unmethylated MGMT. Cervical lymph node biopsy showed identical histopathological features as seen in the dural-based mass.
Imaging Findings
Fig A. Serial axial FLAIR brain MR images show gradual minimal growth of the non-enhancing recurrent tumor in the right precentral gyrus over 7 years. Fig B. Axial T2 Flair image shows rapid enlargement of the tumor within 4 months with mild enhancement and restricted diffusion. Fig C. Axial 3D postcontrast images show dural-based masses (along right temporal and occipital convexities with mass effect upon the torcula and transverse sinus) and metastatic right cervical lymph node. Fig D. Postcontrast T1 fat-saturated lumbar spine image shows numerous bony metastasis and leptomeningeal disease. PET MIP shows bilateral cervical adenopathy, left parotid, and diffuse osseous metastases.

Discussion
Major features of the tumor progression and recurrences of IDH mutant diffuse astrocytoma are recognized and have been reported in the literature, including the presence of a primitive neuronal component which increases the tendency for CSF dissemination, extracranial metastasis, and poor survival. In addition, RB1 mutation has been recently recognized as an important driving alteration in grade 4 diffuse astrocytoma which develops a primitive neuronal component.
Teaching Point
The presence of primitive neuronal component on pathology in IDH mutant astrocytoma imparts a propensity towards rapid progression, widespread metastatic disease, and poor prognosis. Early detection of this variant, prompt investigation of any symptoms related to possible systemic involvement, and multimodal treatment may improve the prognosis of this disease.

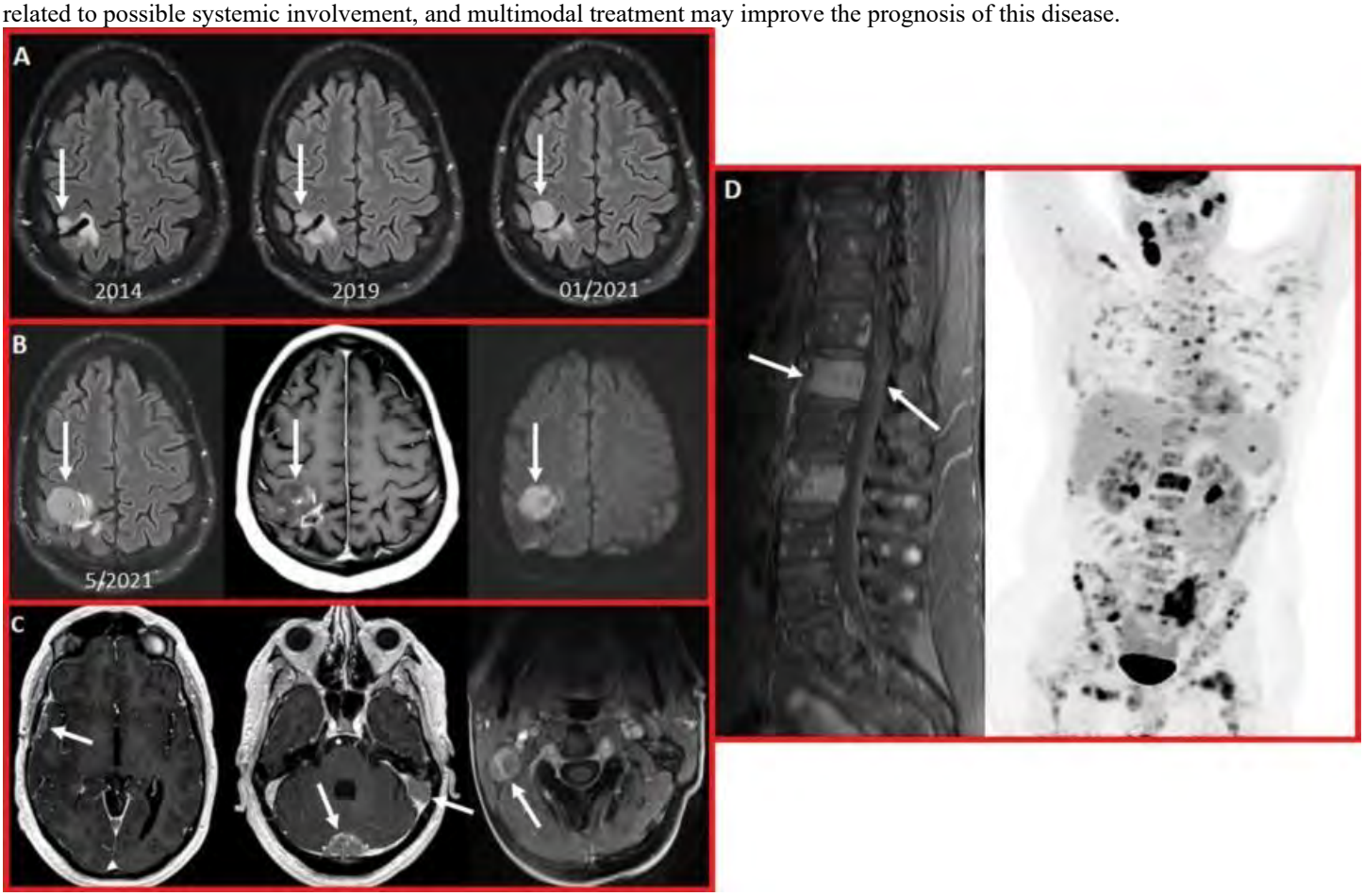

(Filename: TCT_233_ASNR_GBM.jpg)

1062
A Rare Case of Intraosseous Cranial Myxoma in a Pediatric Patient
A Sureen[1], A Dutta[2], F Zerpa[3]
[1]Cooperman Barnabas Medical Center, Weehawken, NJ, [2]Cooperman Barnabas Medical Center, WEST ORANGE, NJ, [3]Cooperman Barnabas Medical Center, Livingston, NJ

Clinical History
A fourteen year-old boy was sent to the ED in Dominican Republic by an ophthalmologist after being found to have papilledema and elevated intracranial pressure. An MRI of the skull base was performed at that time and a left extra-axial temporo-parietal lesion was identified. The patient underwent ventriculoperitoneal (VP) shunt placement and partial resection and biopsy of the lesion in late 2020 which ultimately diagnosed intraosseous cranial myxoma (ICM). After undergoing a total of 3 debulking procedures and radiation due to rapid tumor growth, the patient was referred by his neurosurgeon for further evaluation within the United States. He reported that his symptoms included headaches, intermittent left inner ear pain and hearing loss, left-sided blurred vision, and left sporadic eyelid and facial droop that lasted a few minutes.
Imaging Findings
MRI with and without contrast demonstrated a 7cm extra-axial heterogenous, calcified lesion with areas of avid enhancement arising from the left temporal bone and extending into petrous and mastoid portions of the left temporal calvarium. There was significant mass effect on the left cerebellar hemisphere, pons, and cerebrum. Compression of the left sigmoid dural venous sinus and the 7th and 8th nerve complexes were noted. There was severe narrowing of the fourth ventricle with the distal tip of a VP shunt seen in the right lateral ventricle.

Discussion
Myxomas are masses that arise from mesenchymal origins. The few case reports published on ICM typically show lesions arising from the mastoid, ethmoid, or sphenoid air cells as they are locations of primitive embryonic mesenchymal tissue. Myxoma's characteristic findings on MRI are T1 hypointensity, T2 hyperintensity. Peripheral enhancement is the most common presentation on contrast enhanced studies; however they can also have patchy, linear, or heterogenous internal enhancement. Early resection of these benign but locally aggressive lesions greatly improves prognosis of the patient, though myxomas have a recurrence rate of approximately 30% within 10 years.
Teaching Point
Intraosseous cranial myxoma is an extremely rare manifestation of myxoma. This lesion often requires radical resection and possible radiation therapy to minimize risk for reoccurrence; therefore early identification is paramount for prompt surgical intervention and further treatment.

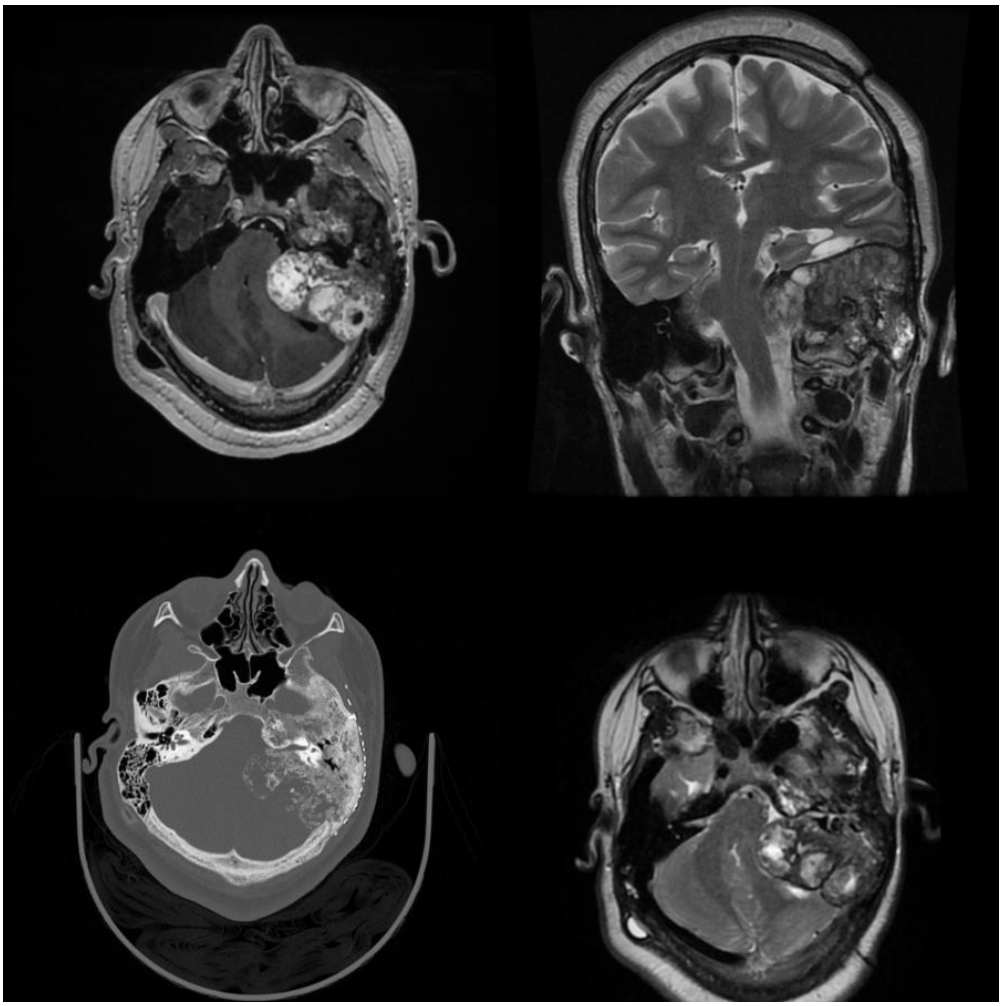

(Filename: TCT_1062_ICMImages.jpg)

566
A rare case of migrating intraventricular neurocysticercosis
P Rabiei[1], J McCarty[1]
[1]*University of Texas Health Science Center at Houston, Houston, TX*

Clinical History
A 40 y/o female patient with nausea, vomiting, and worsening headaches was noted to have noncommunicating hydrocephalus with an obstructing cystic lesion at the foramen of Monro. A provisional diagnosis of neurocysticercosis was made and the patient received antiparasitic, anticonvulsant, and corticosteroid medications. A follow up brain MRI after EVD placement showed migration of the cysticercus from the foramen of Monro to the right lateral ventricle. The patient underwent endoscopic ventriculostomy which revealed deformity of the foramen of Monro and scarring tissue at the floor of the 3rd ventricle. The lateral ventricles were thoroughly irrigated after septostomy. Subsequently, the patient's symptoms gradually improved.
Imaging Findings
Fig A. Axial FLAIR and coronal post contrast images show obstructive hydrocephalus and a non-enhancing cystic lesion within the foramen of Monro. Fig B. Axial and sagittal head CT show focal tiny calcification, hydrocephalus, transtentorial herniation, and known intraventricular cysticercus at the foramen of Monro. Fig C. Axial FLAIR images after placement of a right transfrontal EVD

show the previously seen cysticercus has moved and now resides in the right lateral ventricle. Fig D. Axial and coronal head CT after endoscopic ventriculostomy and irrigation of the ventricles show persistent hydrocephalus with an EVD in place.

Discussion

Neurocysticercosis is the most common CNS parasitic infection and intraventricular cysticerci can be seen in up to 20% of cases. These cysts can freely circulate in the ventricles and may cause hydrocephalus by physical obstruction or scar formation. In the absence of other typical findings of parasitic infection, diagnosis of interventricular cysticerci could be challenging due to similarities with other entities such as colloid or ependymal cysts. T1W and proton density MR sequences have shown better diagnostic values for evaluation of these cystic lesions. FLAIR is considered the best sequence for visualization of the cysticercus wall and its internal hyperintense scolex. The role of contrast enhanced MRI is very limited.

Teaching Point

Prompt diagnosis of intraventricular cysticerci would offer timely surgical management and prevent recurrent admissions due to hydrocephalus. Radiologists should be aware of possible migration of the intraventricular cysticerci which can occur spontaneously or secondary to sudden pressure change in the ventricular system during ventriculostomy.

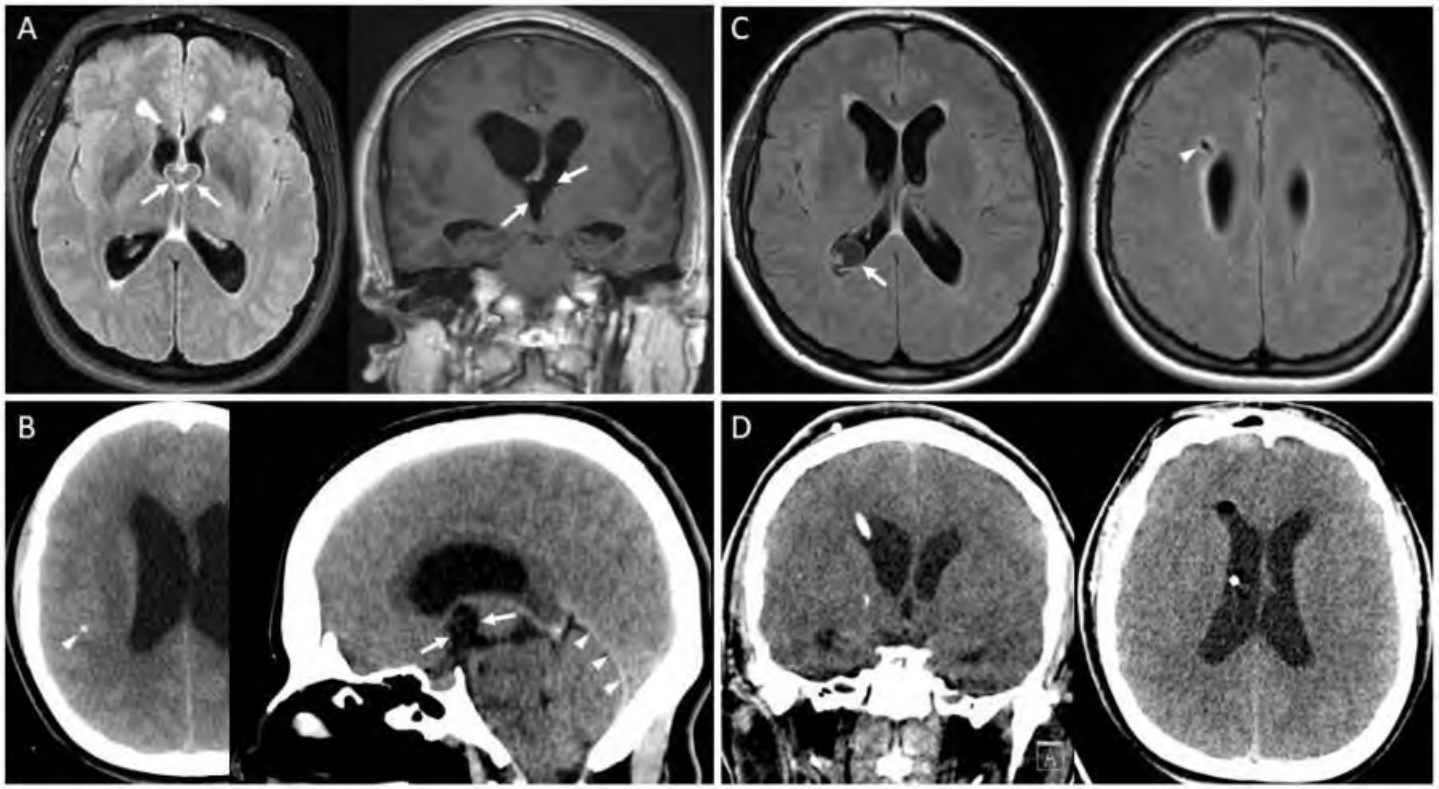

(Filename: TCT_566_cysticercus_300.jpg)

678

A rare case of synovial osteochondromatosis of temporomandibular joint and radiological correlation

W Wang[1], A Primoazen[2], T Fredericks[2], M Jenson[3], D Rao[3]

[1]UF Health Jacksonville - - Jacksonville, FL, Jacksonville, FL, [2]UF Health Jacksonville, Jacksonville, FL, [3]University of Florida College of Medicine Jacksonville, Jacksonville, FL

Clinical History

A forty-six-year-old female with a past medical history of seronegative arthritis presented with painful swelling around the right TMJ (temporomandibular joint) with associated crepitus and difficulty chewing. Patient underwent MRI (magnetic resonance imaging) which showed joint effusion of right TMJ with synovial enhancement suggestive of septic or inflammatory arthritis. Corticosteroids were given for presumed flare of seronegative arthritis without relief. Follow-up MRI showed persistent synovial enhancement and inflammatory changes. CT (computer tomography) was ordered which revealed multiple small loose bodies within the joint space. Tissue biopsy was then performed confirming the diagnosis of osteochondramatosis. She underwent total right TMJ replacement and postoperatively she reported significant improvement of TMJ symptoms.

Imaging Findings

MRI revealed marked synovial enhancement and joint effusion of right TMJ, multifocal loose bodies within the joint space as well as anterior and posterior recesses. Follow-up MRI in one year showed persistent inflammatory changes and increased amount of loose bodies. Subsequent CT demonstrated extensive stippled calcifications adjacent to the right mandibular condyle and osseous irregularity as well as sclerosis along the mandibular condyle and minimal changes of the glenoid fossa. Post-operative CT showed postsurgical changes from right condylectomy and right total TMJ replacement with surrounding stippled calcifications.

Discussion
Synovial osteochondromatosis is a benign proliferative process involving the articular cartilage featured by loose bodies. It typically affects the large joints such as hips and knees, and rarely the TMJ. Prompt diagnosis and intervention is crucial to improving prognosis. Reported radiological features include preferential involvement of superior joint space, destruction and sclerosis of the glenoid fossa, joint space widening, post-contrast enhancement of the synovium, and various types of calcifications (loose bodies) in the form of stippled, ring-and-arc, popcorn, or flocculent patterns. Given its proximity to the skull base, intracranial extension is a potential complication. CT and MRI findings are instrumental in assessing the extent of the disease and facilitating pre-operative planning.
Teaching Point
TMJ involvement is rare manifestation of synovial osteochondromatosis. Presence of synovial loose bodies is a hallmark feature. CT and MRI are complementary in establishing the diagnosis and guiding treatment.

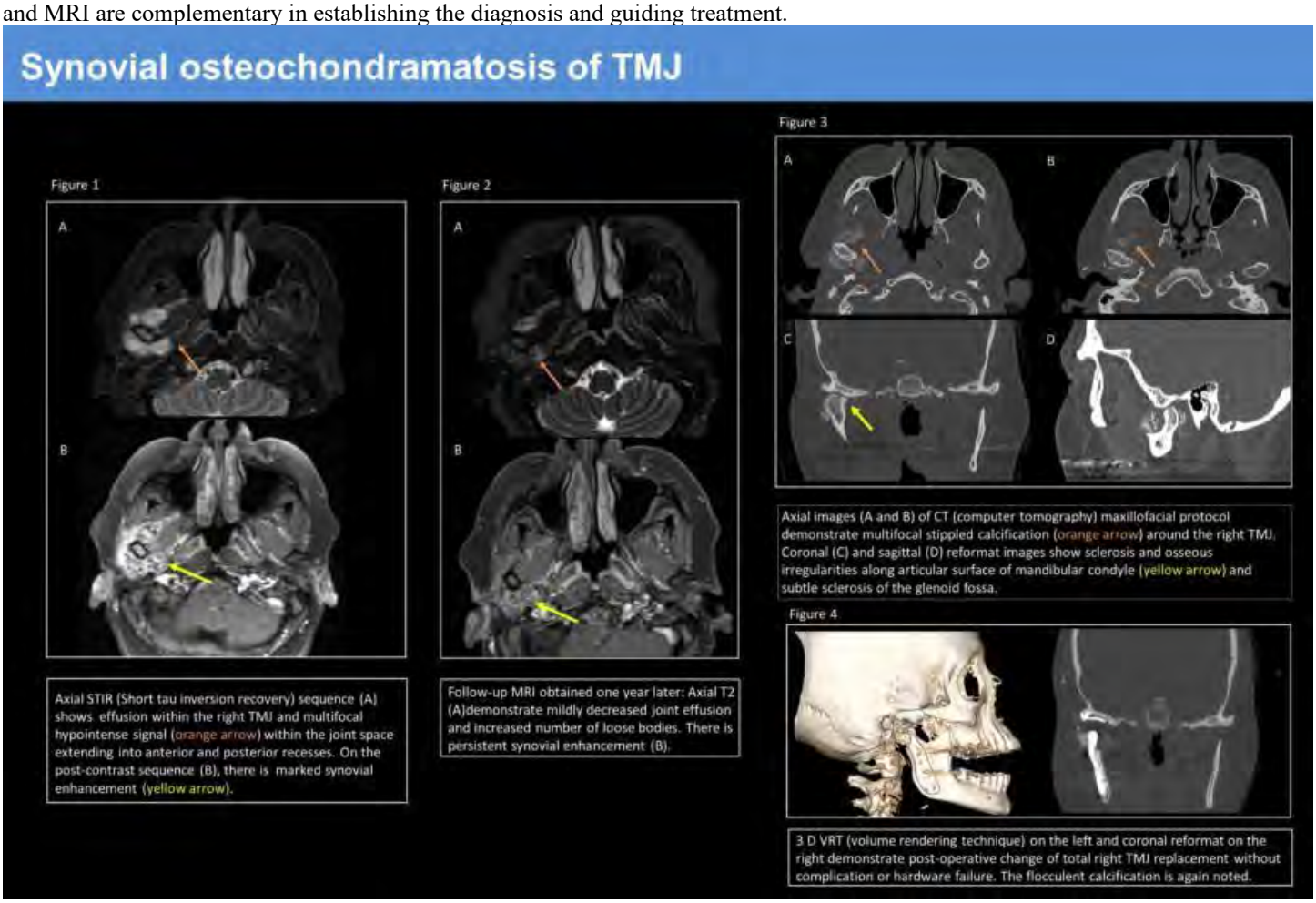

(Filename: TCT_678_Imagefileww.jpg)

1374
A sting into the eye: Traumatic orbit injury with a stingray barb
A Paydar[1], T Abdulsalam[2], S Saith[3], O Raslan[4], M Bobinski[4], L Hacein-Bey[5], A Ozturk[2]
[1]University of Califronia-Davis, Sacramento, CA, [2]UC Davis Medical Center, Sacramento, CA, [3]UC Davis Medical Center, Redondo Beach, CA, [4]UC Davis, Sacramento, CA, [5]University of California Davis, Sacramento, CA

Clinical History
A 54-year-old male presented with left eye swelling and decreased vision 10 days after being stung by a stingray when he was swimming in the ocean. He had noticed a puncture wound below the left eyelid with bleeding on the day of injury. He had nausea and vomiting following the incident, with persistent pain, gradual eye swelling, and blurred vision when he visited the Emergency Department. Computerized Tomography (CT) of the face confirmed penetrating traumatic injury to orbit with a retained foreign body. The neurosurgery, otolaryngology, and ophthalmology evaluated the patient for treatment management. Due to the location of the two major fragments, a direct orbital approach was not possible, so a transcranial operation was performed, and gross pathology confirmed the foreign body as the stingray barb.
Imaging Findings
CT Orbit demonstrates linear high-density intraconal foreign body within the left orbit, with another broken detached fragment extending through the superior rectus muscle complex into the orbital apex with the probability of the left optic nerve sheath

impingement at the orbital apex (Figure). There was also a small amount of retrobulbar hemorrhage and proptosis of the left globe, with some resultant traction on the left optic nerve.
Discussion
Stingray injuries usually happen when a person steps into one, resulting in the attack of the fish introducing a sting into the feet or leg in a defensive manner, causing significant pain and inflammation due to the venom. Here, we present imaging findings of a traumatic orbital injury, the first in the literature to the best of our knowledge. There is low percentage of retained stingray barbs during fish attacks (1). Imaging has a pivotal role in the diagnosis of foreign bodies, particularly in orbital injury. Imaging reduces the complication and duration of disease and helps with the planning for treatment along with post-foreign body removal confirmation. There are reports of patients suffering from debilitating sequela of a long time retained stingray barb due to delayed use of imaging (2,4). The optimal imaging is not specified in stingray injuries (3), but due to radiopaque barb and spine, X-rays and CT have been used in most cases with reported high sensitivity.
Teaching Point
This case report aims to present CT imaging findings of a retained stingray barb within the orbit as the first case in the literature. Awareness of the radiological appearance of stingray barbs is essential for surgical treatment planning.

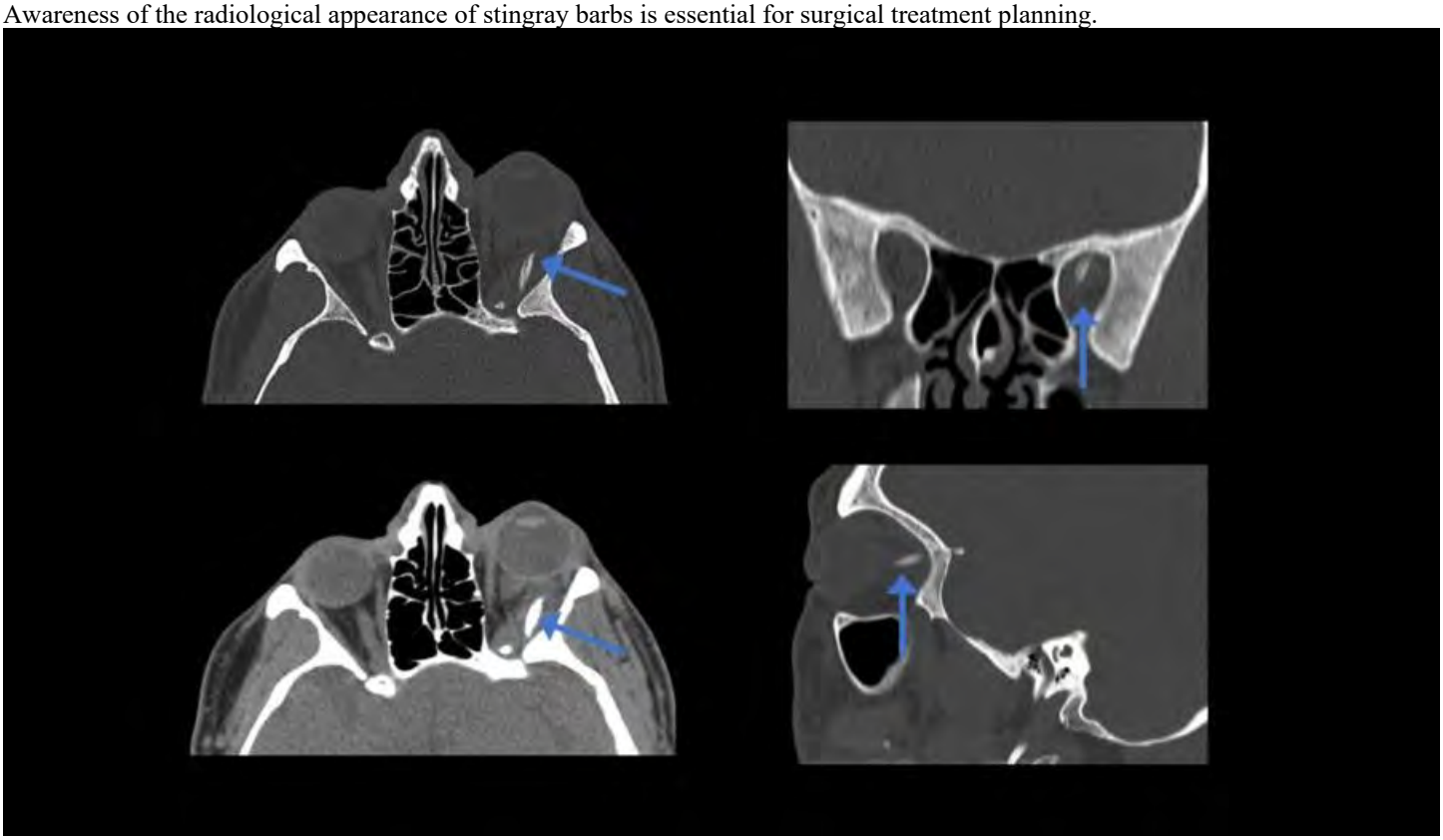

(Filename: TCT_1374_stingaybarb.jpg)

1096

Absence of Meckel Cave, a Cause of Refractory to Treatment Trigeminal Neuralgia.

Y Mateo-Camacho[1], E López López[2], H Maya-García[3]
[1]Hospital Universitario Dr. José Eleuterio González, Monterrey, Nuevo León, Nuevo León, [2]Hospital Universitario Dr. José Eleuterio González, Monterrey, Nuevo Leon, [3]Universidad Autónoma de Nuevo León, Monterrey, Nuevo León

Clinical History
A 52-year-old woman comes with chronic trigeminal neuralgia without response to symptomatic treatment.
Imaging Findings
Brain contrast-enhanced MR imaging and a skull CT were performed. The FIESTA sequence shows thinning of the right trigeminal nerve in its cisternal segment (A, C) with the absence of the affected side Meckel's cave (B, C). The left trigeminal nerve and Meckel's cave have normal morphology (B, D). Foramen ovale and foramen rotundum were normal and symmetrical. There is height loss of the pituitary gland and CSF protrusion into the sella turcica (B). There is no other compressive mass lesion.
Discussion
Trigeminal neuralgia (TN) is an entity that seriously compromises the quality of life of affected people. A rarely reported entity, the absence of Meckel's cave, has been described in some patients with TN, including 2 case reports and three patient case series. In some reports, patients presented trigeminal neuropathy early in life. Other reports suggested a potentially acquired etiology; however, the etiology remains unknown. The absence of a Meckel cave is associated with atrophy of the trigeminal nerve and TN. Understanding the etiology of patients' symptoms leads to a specific treatment.

Teaching Point
The absence of a Meckel cave is poorly understood and rarely reported, and the etiology remains unknown. Recognition of this entity as a potential cause of TN may have important diagnosis and treatment considerations.

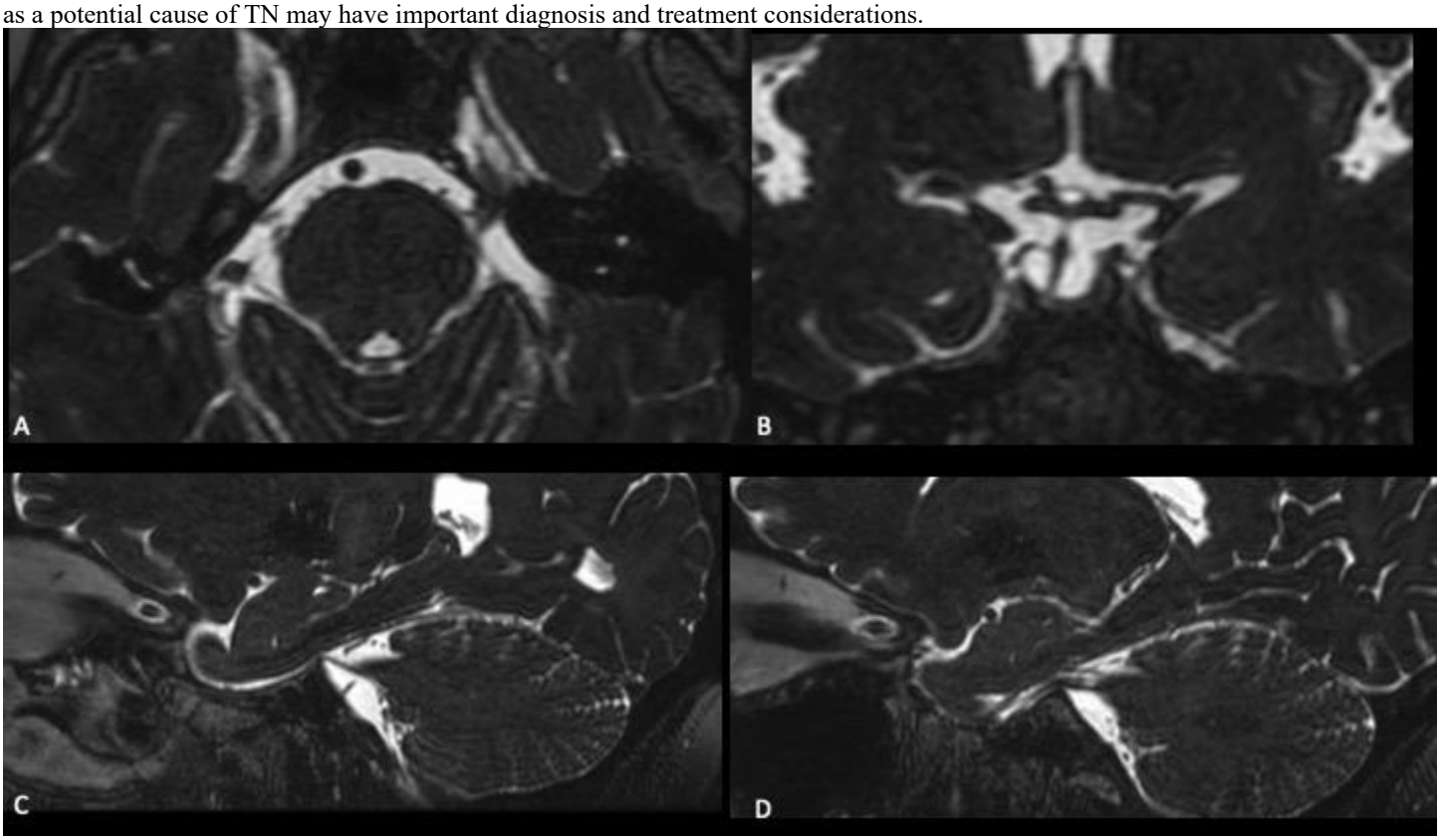

(Filename: TCT_1096_CAVUM.jpg)

1141

Acquired Cortical Dysplasia in a Patient with Treated GBM

M Anteet[1], C Zuraski[2], M Alsaggaf[3], V Goodwill[4], N Farid[2]
[1]UCSD, San Diego, CA, [2]UCSD, La Jolla, CA, [3]King Abdulaziz University, Jeddah, KSA, [4]UCSD, La jolla, CA

Clinical History
55-years-old male initially presented with headache. Brain MRI showed a 4.5 cm rim-enhancing mass in the right frontal lobe with associated hemorrhage and mass effect. He underwent gross total resection (GTR) with pathology compatible with GBM, MGMT methylated. The patient was subsequently treated with standard chemoradiation therapy. 6 years following resection, the patient presented with new episodes of witnessed generalized tonic-clonic seizure. MRI at this time demonstrated a new region of cortical thickening along the anterior and paramedian aspect of the right frontal lobe with associated marked hyperperfusion. Imaging findings were attributed to seizure activity and radiation necrosis, without convincing evidence of recurrent tumor. Electroencephalogram revealed frequent runs of right frontal spikes. Patient continued to have episodes of breakthrough seizure activity despite medical treatment with antiepileptic medications. Ultimately, the region of cortical thickening and heterogenous enhancement in the right frontal lobe was resected for seizure control. Pathology revealed cortical dysplasia in the right anterior frontal lobe, corresponding to the region of cortical thickening seen on MRI. Additionally, pathology demonstrated radiation necrosis, with no evidence of recurrent tumor.
Imaging Findings
N/A
Discussion
Radiation therapy plays an essential role in the treatment of patients with high grade glioma. There are well-known and well-documented sequela of brain radiation therapy, both acute and late sequela. These include edema, radiation necrosis, vasculopathy, vascular malformations, and secondary neoplasm. Another less known and much less common sequela of radiation therapy is acquired cortical dysplasia. Only four cases of "neuronal gigantism" following radiation therapy have been reported in the literature and only one of these was in the radiology literature. The pathology in these cases was essentially compatible with findings of cortical dysplasia, like what was found in the case described here.
Teaching Point
We present an uncommon late complication of radiation therapy in a patient with treated GBM- acquired cortical dysplasia- with radiologic-pathologic correlation.

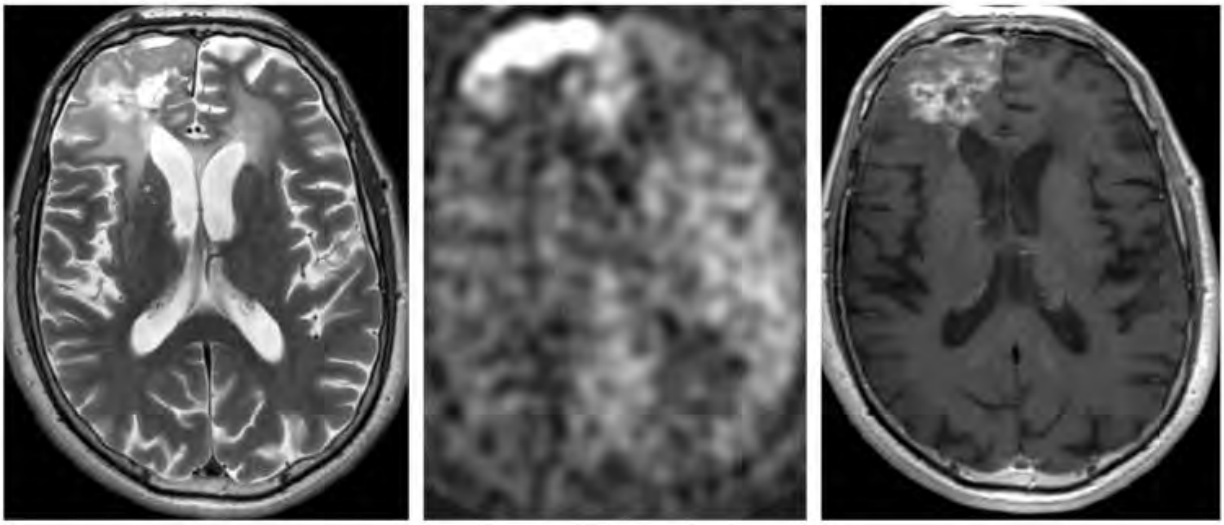

New cortical thickening and FLAIR hyperintensity of the right anterior frontal cortex with marked hyperperfusion, compatible with pathologically proven cortical dysplasia. Similar heterogeneous enhancement in the right frontal lobe compatible with radiation necrosis.

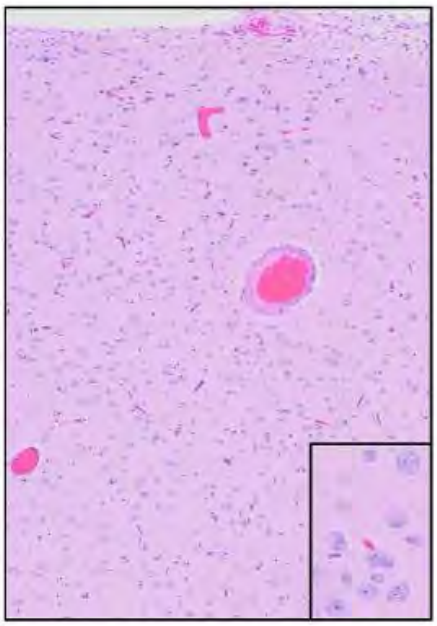

Areas of loss of normal six-layered cytoarchitecture with tangential dyslamination attributable to aberrant clustering of enlarged, cytologically dysplastic neurons (right inset, high-power), a histopathology similar to isolated focal cortical dysplasia (type IIA).

(Filename: TCT_1141_image.gif)

1436

Acute Large Territory Iatrogenic MCA Cerebral Fat Embolism Status Post TKA

m sochacki[1], k diaz[2]

[1]hartford hospital, hartford, CT, [2]Hartford Hospital, hartford, CT

Clinical History

77F presented to ED as an activated stroke with acute onset right-sided weakness, aphasia, and left gaze status post right TKA. LKN at 11:15 pre-sedation with: Propofol/Ketamine as well as right knee nerve block. Patient reevaluated at 12:15 PM, was noted to be nonverbal with right-sided weakness and leftward gaze. Patient transferred to ED for further evaluation. In ED, NIH 22. HR 126, SBP 110, NSR.

Imaging Findings

Non-con CT: Loss of gray-white matter differentiation of the left MCA territory with associated proximal M1 hyperdense sign as well as hypoattenuating distal M1 segment. The Hounsfield units of this finding correspond with subcutaneous fat embolism which demonstrates suppression on lung windows. CTA head/neck: The left cervical internal carotid artery is occluded just beyond its origin and remains occluded throughout the cervical and intracranial segments to the point of fat density embolus. Fat density embolism

extending from the left supraclinoid ICA segment through the left M1 MCA segment resulting in occlusion of the left middle cerebral artery. MRI Brain Non-con: Fat embolus exhibits high T1 signal intensity and suppresses on fat-suppressed imaging.

Discussion

Cerebral fat embolism syndrome (CFE) is a rare condition that occurs most commonly in the setting of traumatic long bone fracture. Although incidence of CFE ranges from .9%-11%, symptoms only manifest in only 0.9%-2.2% of patients. After a bone traumatic fracture or during orthopedic surgery (from high pressures within marrow) fat globules can pass into venous sinuses that drain the marrow and then into the systemic circulation. There are two proposed mechanisms for fat globules entering the arterial circulation. Fat globules can enter the left atrium via shunt (PFO) from the right heart through; or globules may filter directly through the lung capillaries to reach the arterial system. Although the prevalence of PFO at autopsy in the general population is approximately 27.3% a PFO was found only in 12% of all cases of CFE" (Mijalski, 2015).

Teaching Point

Comprehensive imaging demonstrated a large volume fat embolism affecting the left internal carotid artery up to the level of the proximal left M1 segment. Retrospective review showed that the patient had family history of PFO (mother and sister). Subsequent Echo completed showed, EF 62% with no PFO, no cardiac cause of stroke identified. Although PFOs exist in many cases of CFE, the presence of a PFO is not necessary to manifest a post traumatic large volume CFE.

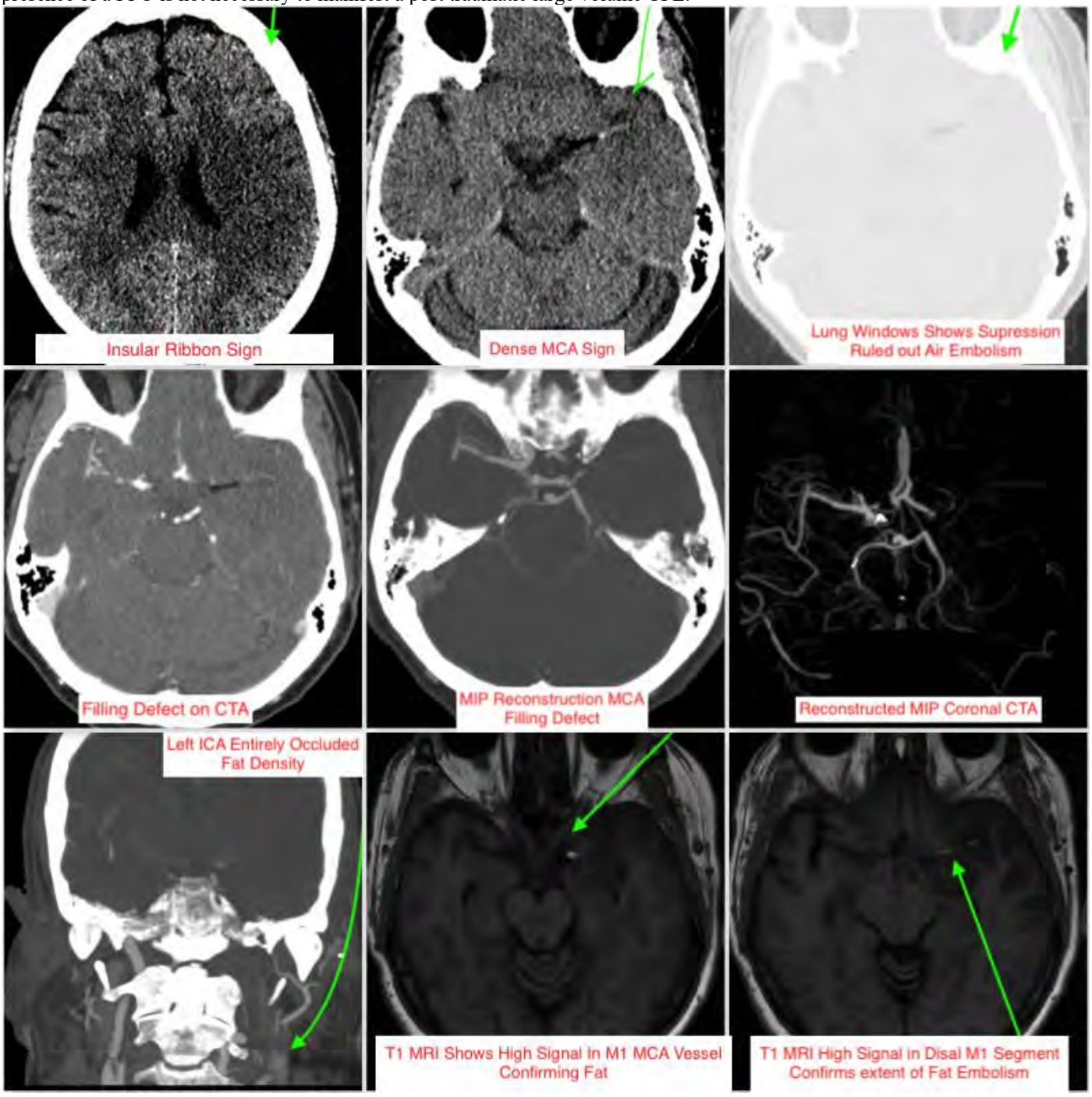

(Filename: TCT_1436_CerebralFatEmbolism.jpg)

1076

Adult Presentation of Disseminated Pilocytic Astrocytoma with Extensive Leptomeningeal Metastases: A Case Report

J Wright[1], E CHU[1], E Kuoy[1]
[1]*University of California Irvine Medical Center, Orange, CA*

Clinical History

A 30-year-old woman presented with headaches, nausea, and vomiting. MRI imaging revealed a mass centered in the right lateral ventricle and extensive leptomeningeal disease of the brain and spinal canal. A bifrontal craniotomy with excision of the intraventricular tumor was performed without complication. Histopathology and molecular analysis were consistent with pilocytic astrocytoma. Due to persistent communicating hydrocephalus, a ventricular drain was placed in the right lateral ventricle and a ventriculoperitoneal shunt was created. Multiple cycles of chemotherapy were administered. To date, there is no clinical or radiographic evidence of disease progression.

Imaging Findings

MRI Brain without and with gadolinium contrast demonstrates a mixed cystic and solid mass in the anterior right lateral ventricle with mild hydrocephalus and leftward midline shift (Figure 1A, B). There are enhancing nodular components within the predominantly cystic lesion. Nodular leptomeningeal enhancement is seen throughout the infratentorial and supratentorial brain, most prominent in the cerebellum, left sylvian fissure, and third ventricle (Figure 1B). MRI of the whole spine is significant for diffuse, nodular leptomeningeal enhancement of the cervical, thoracic and lumbar spine (Figure 1C, D). In the cervical spine, there is dorsal nodular leptomeningeal enhancement (Figure 1C). In the thoracic spine, the ventral leptomeningeal lesions exert mass effect on the spinal cord with associated scalloping and spinal canal stenosis at T9-T12 (Figure 1D).

Discussion

Pilocytic astrocytoma (PA) is a common pediatric brain tumor but is rarely seen in the adult population. PA most often presents in the posterior fossa and is a slow-growing tumor with a generally good prognosis [3]. Rare cases of disseminated PA have been reported in the pediatric and adult populations with the majority involving leptomeningeal spread through the ventricles and subarachnoid spaces [1,2,4,5]. These patients have a worsened prognosis as evidenced by a review of 58 cases, which found a median survival of 65 months [3].

Teaching Point

Although pilocytic astrocytoma is classically an indolent pediatric tumor, there are rare cases with disseminated leptomeningeal metastases, which have a poorer prognosis. This case illustrates that leptomeningeal dissemination may be seen at initial presentation and can cause hydrocephalus. Despite widespread disease, this patient remains clinically and radiographically stable with treatment.

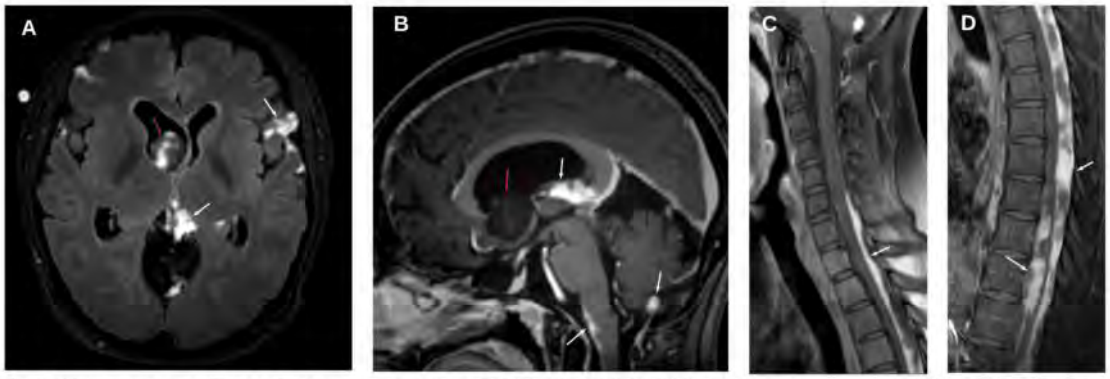

Fig. 1 MRI brain and spine without and with intravenous contrast: (A) Axial brain T2 FLAIR, (B) Sagittal brain T1 post-contrast (C) Sagittal cervical spine T1 post-contrast, (D) Sagittal thoracic spine T1 post-contrast. Red arrows (A,B) indicate the intraventricular mass. White arrows (A-D) show several areas of leptomeningeal disease.

(Filename: TCT_1076_Figure1.jpg)

1083

Aggressive Plasmacytoma in CNS. A case Report.

A Sosa[1], B Reyes Palmero[2], P Soto Garcia[2], A TORRES MONARREZ[3], J Rubalcava Ortega[4], J Higuera-Calleja[5], G Romero Sanchez[6]
[1]*Instituto Nacional de Ciencias Medicas y Nutricion Salvador Zubiran, Ciudad de Mexico, Not Applicable,* [2]*Instituto Nacional de Ciencias Medicas y Nutricion Salvador Zubiran, Mexico, Ciudad de Mexico,* [3]*INSTITUTO NACIONAL DE CIENCIAS MEDICAS Y NUTRICIÓN SALVADOR ZUBIRAN, CIUDAD DE MEXICO, CIUDAD DE MEXICO,* [4]*Instituto Nacional de Ciencias Medicas y Nutricion Salvador Zubiran, Mexico City, Not Applicable,* [5]*Instituto Nacional de Ciencias Médicas y Nutrición Salvador Zubirán, Mexico City, Mexico City,* [6]*Instituto Nacional de Ciencias Médicas y Nutrición Salvado Zubirán, Mexico City, Mexico*

Clinical History

A 31-year-old male with a history of HIV presented with paresthesia in the left pelvic and thoracic limbs, and the ipsilateral side of the face.

Imaging Findings

Brain MRI. FLAIR demonstrated hyperintense extra-axial dural rounded lesions associated to vasogenic edema located in the right

parietal and frontal regions. T1+Gd showed strong homogeneous enhancement of the lesions. DWI demonstrated restricted diffusion in the lesions located in the parietal and frontal regions.

Discussion

A plasmacytoma is a mass of neoplastic plasma cells either in the bone marrow or at various extramedullary sites (1). Extramedullary presentation is extremely rare and represents less than 4% of all cases. MRI is the modality of choice for the evaluation of extramedullary sites, and CT is for the evaluation of bone abnormalities, but both show nonspecific findings (2-3). Histological examination of tumor tissues acquired after brain biopsy is critical for achieving a clear diagnosis.

Teaching Point

Extramedullary presentation (EMP) is extremely rare and represents less than 4%. The extra-axial lesion with contrast enhancement, restricted diffusion, and the clinical history may suggest the diagnosis. However, it is the biopsy that establishes the ultimate diagnosis.

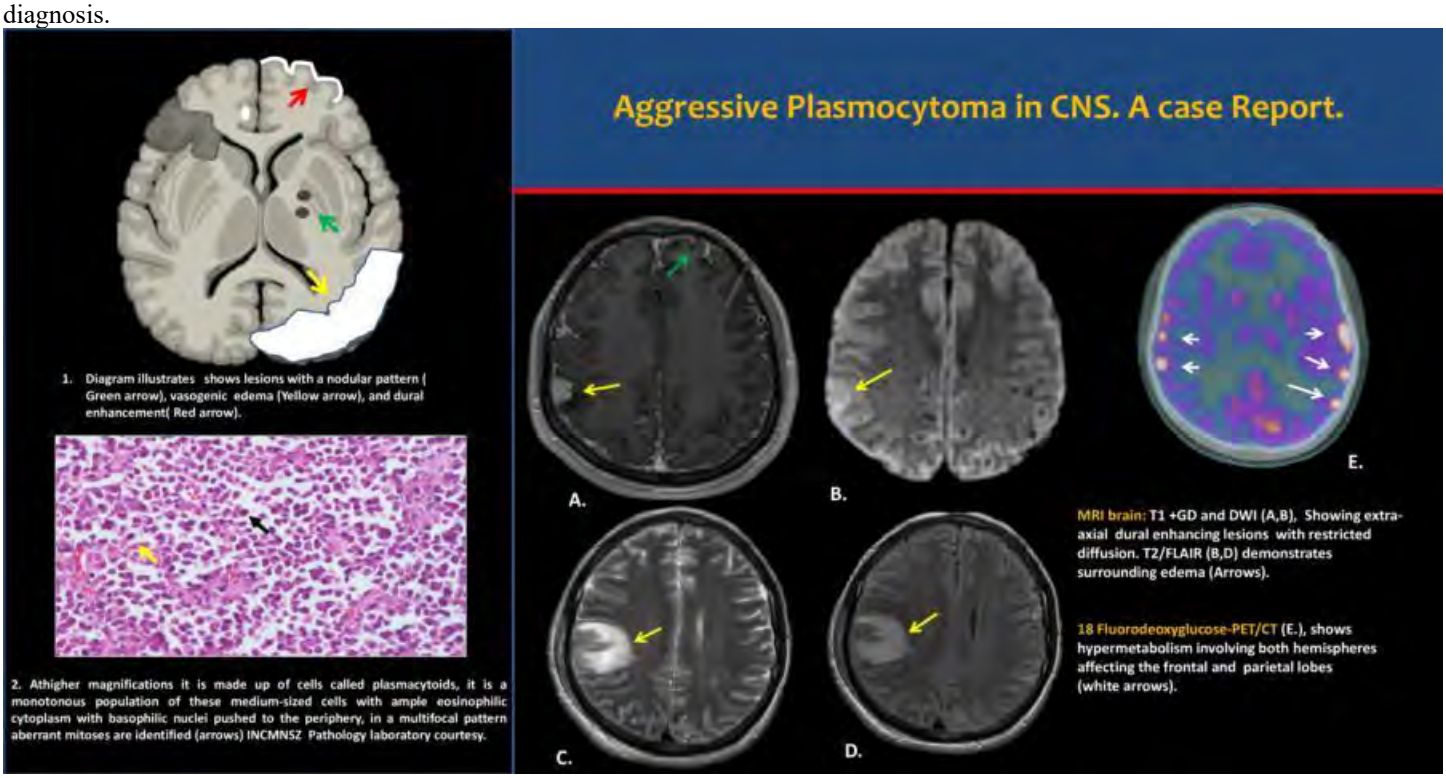

(Filename: TCT_1083_Plasmocytoma.JPG)

1113

An Abnormal Enhancement of Oculomotor nerves in a Patient with Multiple Sclerosis

R Gupta[1], R Samant[2]

[1]UTHealth, Houston, TX, [2]UT Health, McGovern School of Medicine, Texas Medical Center, Houston, TX

Clinical History

A middle-aged man in his 50s with multiple sclerosis for more than 15 years presented to neurology clinic for routine follow-up and complained about blurry vision but denied diplopia. Neurological exam showed upper motor neuron signs consistent with multiple sclerosis. There were no pupillary or extraocular movement abnormalities. Magnetic Resonance Imaging (MRI) of brain showed abnormal contrast-enhancement of right more than left oculomotor nerves.

Imaging Findings

Magnetic Resonance Imaging (MRI) of brain showed abnormal contrast-enhancement of right more than left oculomotor nerve.

Discussion

Peripheral nerve involvement is uncommon in MS. Oculomotor nerve involvement is rare seen on imaging. The oculomotor nerve is clinically affected in 2% of patients with Multiple Sclerosis. Any peripheral nerve involvement would suggest combined central as well as peripheral demyelination, and would raise possibility of chronic inflammatory demyelinating polyradiculoneuropathy (CIDP), a disorder that has different treatment modalities.

Teaching Point

This case report highlights the importance of commenting on any cranial nerve involvement if seen on imaging of multiple sclerosis patients as that may warrant further testing for disorders of combined central and peripheral demyelination by testing autoantibodies against nodal/paranodal proteins, such as neurofascin 155 (NF155), contactin 1, and contactin-associated protein 1.

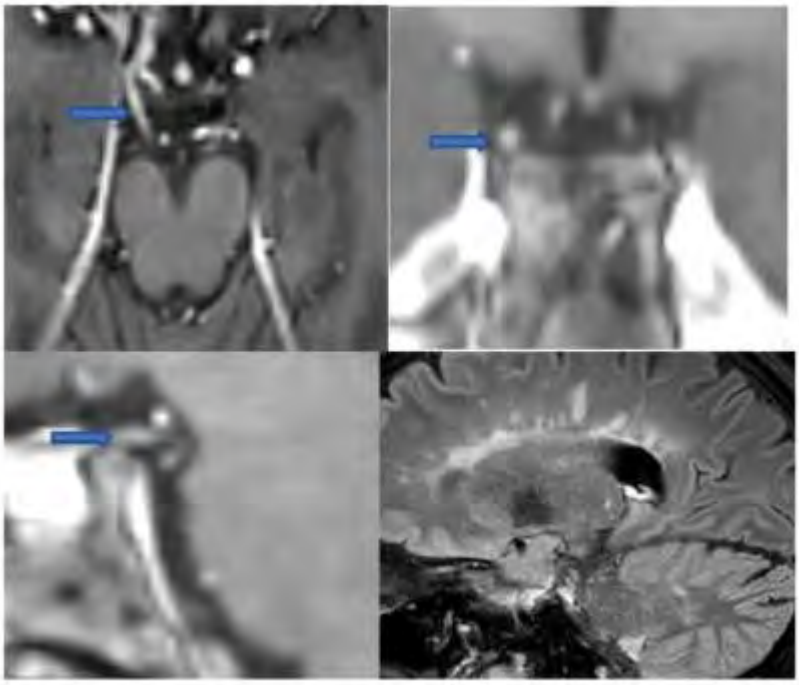

(Filename: TCT_1113_finalfor3rdnerve.jpg)

854

An Interesting Case of Neonatal HSV II Encephalitis

A Kamali[1], A Ali[2], D Timaran[1], R Patel[3], A Kamali[1]

[1]University of Texas Health Science Center Houston, Houston, TX, [2]UTHealth McGovern Medical School, Houston, TX, [3]Texas Children's Hospital, Houston, TX, Houston, TX

Clinical History

A 7 month old female baby with history of natural delivery from a mother with past history of HSV II infection presented to ED with poor feeding, fever, lethargy and decreased level of consciousness. She was started on acyclovir for diagnosis of HSV II meningoencephalitis during the hospital stay. However the treatment was delayed followed by antibiotic therapy and did not receive a complete course pf acyclovir. The HSV II encephalitis was confirmed by CSF PCR test. Initial MRI showed diffuse leptomeningeal enhancement compatible with leptomeningitis/encephalitis with no evidence of complications. She developed seizures during the hospital stay and found to have large cystic lesions in bilateral frontal lobes on the follow up MRI 18 days later.

Imaging Findings

Initial MRI showed diffuse leptomeningeal enhancement without evidence of complications such as ischemia, subdural/epidural empyema or cerebritis. Follow up CT brain for new onset seizures showed extensive areas of hypoattenuation and loss of gray-white differentiation in bilateral frontal lobes during the hospital stay. Repeat MRI scan showed large areas of cystic encephalopathy in bilateral frontal lobes with no evidence of intracranial hemorrhage, midline shift or herniation.

Discussion

HSV can be transmitted from mother-to-child in utero, postnatally, or most commonly during the peri-partum period. In a mother with active genital lesions or prodromal symptoms, cesarean delivery is recommended. In patients with a history of HSV II but no active genital lesions, vaginal delivery is still recommended. Immediate initiation of acyclovir should be started in neonates with suspected HSV meningitis, with repeat CSF HSV PCR test at the end of treatment regimen. Transmission can happen in both primary viral outbreak and secondary outbreak. However, transmission is significantly less likely in secondary outbreak due to mother's IgG antibodies crossing the placenta and providing passive immunity to the neonate. Our case stands out due to the severity of encephalomalacia seen with interval of 18 days in the follow up MRI due to delayed outbreak of HSV II encephalitis.

Teaching Point

- untreated neonatal HSV encephalitis can lead to encephalomalacia with neurologic sequelae - HSV encephalitis may have a clear pattern on imaging in adults (involvement of the limbic system/medial temporal lobes with or without hemorrhage) - in infants, imaging findings can be more ambiguous due to immature myelin

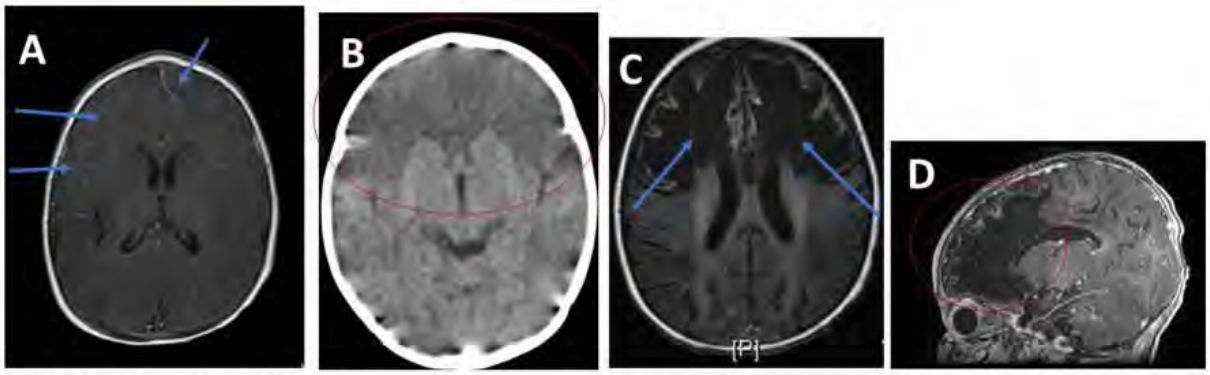

A) axial T1-weighted first MRI showed diffuse leptomeningeal enhancement (long blue arrows)

B) axial CT shows extensive areas of hypoattenuation, and loss of gray-white differentiation seen in bilateral frontal lobes (red circle) 15 days after the first MRI

C, D: Axial and sagittal T1-weighted MRI images, 18 days after the first MRI, showed cystic encephalomalacia (long blue arrows in C and red circle in D) in frontal lobes.

Teaching pont:
HSV encephalitis may have a clear pattern on imaging in adults (involvement of the limbic system/medial temporal lobes with or without hemorrhage). Imaging findings of HSV infection can be more ambiguous and devastating in infants due to immature myelin.

(Filename: TCT_854_HSVencephalitis.jpg)

459

An Interesting Case of Thalamic Diffuse Midline Glioma in a Child Presenting with Double Visions

A Kamali[1], A Ali[2], V Kumar[3], L Nunez[4], A Rodriguez[5], R Patel[6], A Kamali[1]

[1]University of Texas Health Science Center Houston, Houston, TX, [2]UTHealth McGovern Medical School, Houston, TX, [3]UTHealth Houston, Sugar Land, TX, [4]University of Texas Health Science Center at Houston, Houston, TX, [5]The University of Texas Health Science Center at Houston, Houston, TX, [6]Texas Children's Hospital, Houston, TX, Houston, TX

Clinical History

A 7-year-old male, previously healthy with no past medical history, who presented with 4 week history of nausea, vomiting, neck pain, and headache with recent double vision. He had been to the ED with only abdominal workup done by an abdominal x-ray which was unremarkable. After experiencing episodes of intermittent double vision alongside his previous symptoms, the patient presented to the ED and underwent head imaging.

Imaging Findings

CT head showed a large heterogeneous mass arising from the left thalamus protruding into the left aspect of the midbrain and left lateral ventricle. MRI with and without contrast showed a large heterogeneously enhancing mass arising from the left thalamus and protruding into the left lateral ventricle and effacing the third ventricle posteriorly. Areas of central necrosis were present, and the mass was hemorrhagic. A non-enhancing solid component of the mass demonstrated diffusion restriction indicating increased cellularity.

Discussion

The diffuse midline glioma seen in this patient is classically associated with the Histone H3-K27M mutation, altering a crucial site of post-translational modification in the histone protein H3 leading to p53 overexpression and uncontrolled proliferation. Diffuse midline gliomas are considered aggressive tumors and are WHO grade 4. This tumor carries a poor prognosis, a 2-year survival less than 10%. Most diffuse midline gliomas are seen in children and are located in the pons but can also be seen in other midline structures of the central nerves system including the thalamus and spinal cord. The clinical presentation depends on the location of the tumor and can often manifest as cranial nerve palsies. The tumor in our case resulted in mass effect over the cranial nerves III and IV nuclei within the midbrain and caused diplopia. Increased intracranial pressure is also generally present in these patients, causing early morning vomiting and headache.

Teaching Point

Diffuse midline glioma is an aggressive WHO grade 4 pediatric tumor - associated with the Histone H3-K27M mutation - involving the midline structures of the central nerves system including the brainstem, spinal cord or thalami - the clinical presentation depends on the location of the tumor and may manifest as cranial nerve palsies or increased intracranial pressure

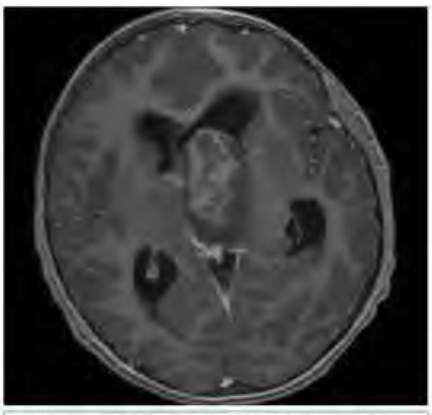

Fig A: Axial T1-weighted C+ image showing large heterogeneously enhancing mass arising from the left thalamus.

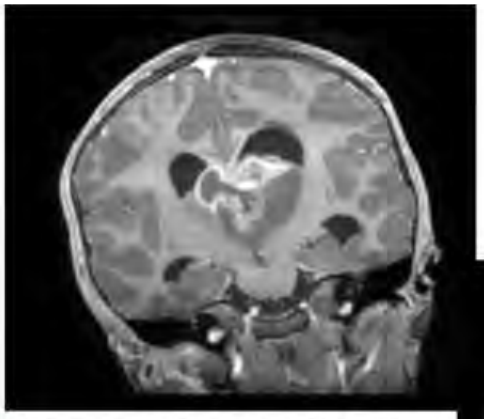

Fig B: Sagittal T1-weighted C+ image showing large heterogeneously enhancing mass arising from the left thalamus protruding into the left lateral ventricle and superior left midbrain.

Imaging findings: Contrast enhanced MRI showed a large heterogeneously enhancing mass arising from the left thalamus and protruding into the left lateral ventricle and effacing the third ventricle posteriorly. Areas of central necrosis were present, and the mass also protrudes into the left aspect of the midbrain. A non-enhancing solid component of the mas is seen within the left thalamus and superior left midbrain.

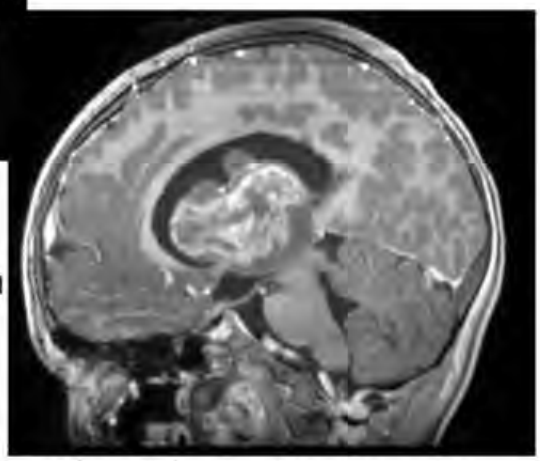

Fig C: Sagittal T1-weighted C+ image showing heterogeneously enhancing mass arising from left thalamus.

(Filename: TCT_459_Diffusemidlineglioma.jpg)

1416

Arterialized Developmental Venous Anomaly: How Useful is Arterial Spin Labeling?

I Brown[1], K O'Connell[1], L Hacein-Bey[1], K Oguz[1], A Ozturk[1]
[1]*University of California, Davis, Medical Center, Sacramento, CA*

Clinical History

A cerebellar developmental venous anomaly (DVA) with an enlarged vermian vein was found in a 75 yo female patient undergoing routine non-contrast enhanced MRI as part of a research protocol. No nidus or surrounding edema were present. Post-contrast and Arterial Spin Labeling (ASL) perfusion MR were then obtained, showing enhancement and elevated CBF, suspicious for an arterialized DVA. Final confirmation with cerebral angiography was however not obtained.

Imaging Findings

Non-contrast MR showed left cerebellar dilated vessels converging into a dilated vermian vein. There was no suggestion of hemorrhage or cavernoma susceptibility imaging. Post-contrast MRI demonstrated avid enhancement. ASL and 3D TOF demonstrated focally elevated flow in corresponding areas.

Discussion

DVAs are the most common cerebral vascular congenital malformations, consisting of dilated medullary veins that drain in a collector, then either into a dural venous sinus or deep ependymal veins. DVAs may rarely demonstrate early arteriovenous shunting, best depicted on DSA, referred to as "arterialized" DVAs or Transitional Venous Anomalies (TVAs)(1). ASL and 3D TOF provide a noninvasive method for evaluating arterialized DVAs(1). 3D TOF is sensitive to localized increases in flow due to the inflow effect. ASL provides quantitative cerebral blood flow values. Hyperintense signal on venous ASL is a predictor of the presence of arteriovenous shunt on DSA(2). A study showed that the presence of ASL signal intensity predicted the presence of early shunting (early venous or parenchymal filling) on DSA in 71% (5/7) of cases, confirming these lesions are not typical DVAs(1), suggesting that ASL may be overly sensitive, leading to false positive diagnosis. DSA remains the gold standard for "arterialized" DVAs; however DSA may result in complications, such that its use should be weighed out given the low annual hemorrhagic risk with DVAs, estimated at less than 1% versus 4% for AVMs.

Teaching Point

Arterialized DVAs are characterized by early shunting, which may be detected on non-invasive imaging, i.e. 3D TOF and ASL. However, it has been suggested these modalities may be overly sensitive compared to DSA which remains a topic for future research.

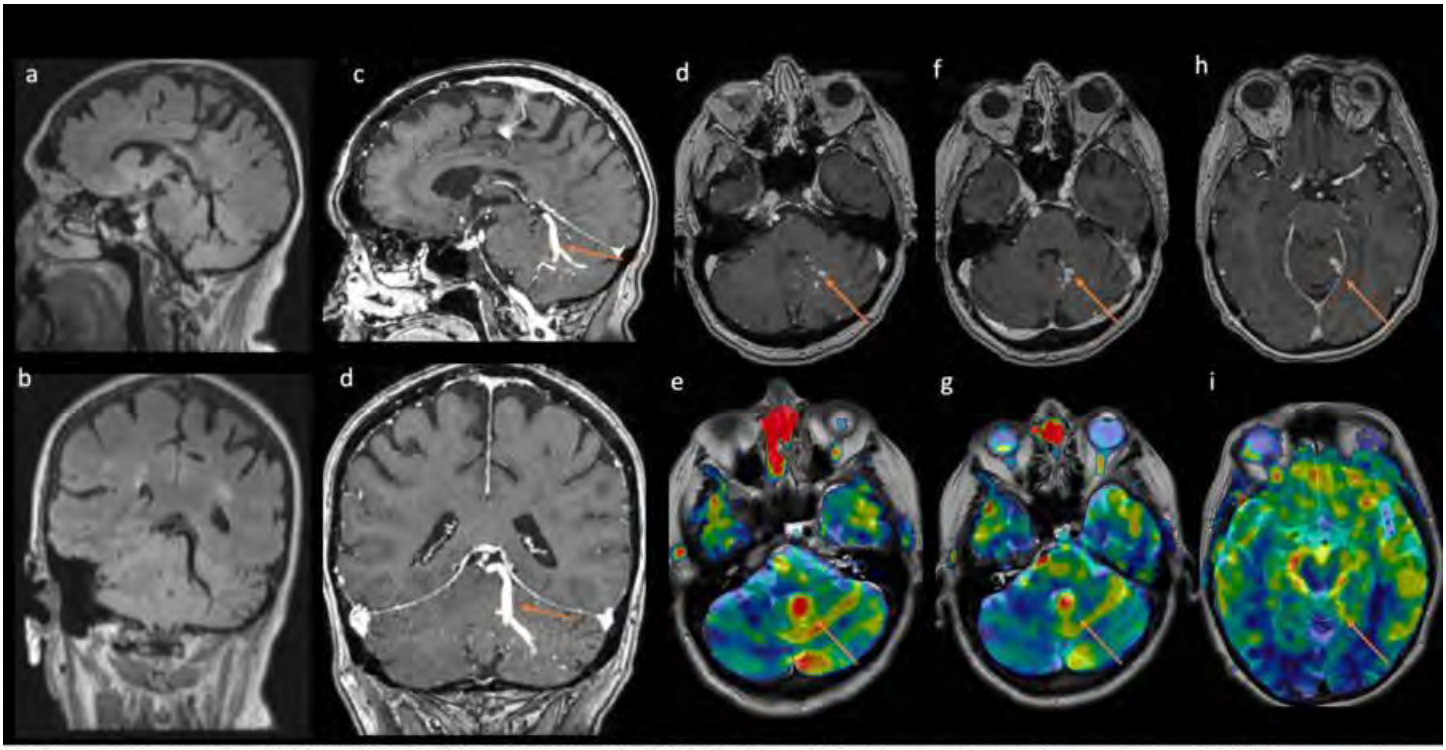

Left cerebellar arterialized DVA annotated with orange arrow. (a,b) 3D FLAIR sagittal and coronal multi-planar reformats, (c,d) T1 post-contrast sagittal and coronal multi-planar reformats, (d,f,,h) top row demonstrates axial post contrast T1W images with corresponding ASL and T2/FLAIR fusion images at same level. The ASL fusion images demonstrate apparent focally elevated flow both in the DVA (orange arrow) and in the surrounding the parenchyma.

(Filename: TCT_1416_FinalImages.jpg)

1379

Atypical Intraventricular Subependymoma

A Reda[1], M Brun-Vergara[2], E Portela de Oliveira[3], N Zakhari[4]

[1]university of Ottawa, ottawa, Ontario, [2]THE OTTAWA HOSPITAL, OTTAWA, ONTARIO, [3]The Ottawa Hospital, Ottawa, Ontario, [4]THE OTTAWA HOSPITAL, OTTAWA, ON

Clinical History

43-year-old woman presented with severe worsening headache and papilledema.

Imaging Findings

MRI showed a large multilobulated heterogeneously enhancing lesion in the atrium and occipital horn of the right lateral ventricle, with surrounding vasogenic edema and blooming on gradient-echo images related to calcification. Another smaller lesion in the left atrium is seen with no enhancement. MR perfusion demonstrated peripheral increased relative cerebral blood volume with mildly decreased NAA and mild increase in choline levels on MR spectroscopy. The lesion extends to the contralateral ventricle and is causing mass effect, midline shift, and brain herniation. Patient underwent biopsy and resection of the mass that demonstrated intraventricular subependymoma.

Discussion

Subependymomas are benign (WHO grade 1) tumors. They are slow-grow tumors and are often discovered incidentally. Patients typically are middle-aged and asymptomatic. They commonly arise from the subependymal layer of the fourth ventricle and lateral ventricle, with a predilection to the frontal horns. They are typically homogeneous on T1 isointense to the white matter, T2 hyperintense and without enhancement. Atypical large lesions can be heterogeneous with calcifications and areas of enhancement. Main differential considerations include other intraventricular neoplasms, such as ependymoma, choroid plexus papilloma and central neurocytoma.

Teaching Point

•Most of the subependymoma lesions are slow growing, cause no symptoms, and show no or minimal enhancement. •Atypical supratentorial subependymoma shows large tumor, avid heterogeneous enhancement and significant symptoms. •The atypical appearance of subependymoma can mimic other intraventricular lesions. However, it should be considered within the differential diagnosis for supratentorial interventricular lesions. •The goal of the surgical resection of the supratentorial subependymoma is for symptomatic treatment.

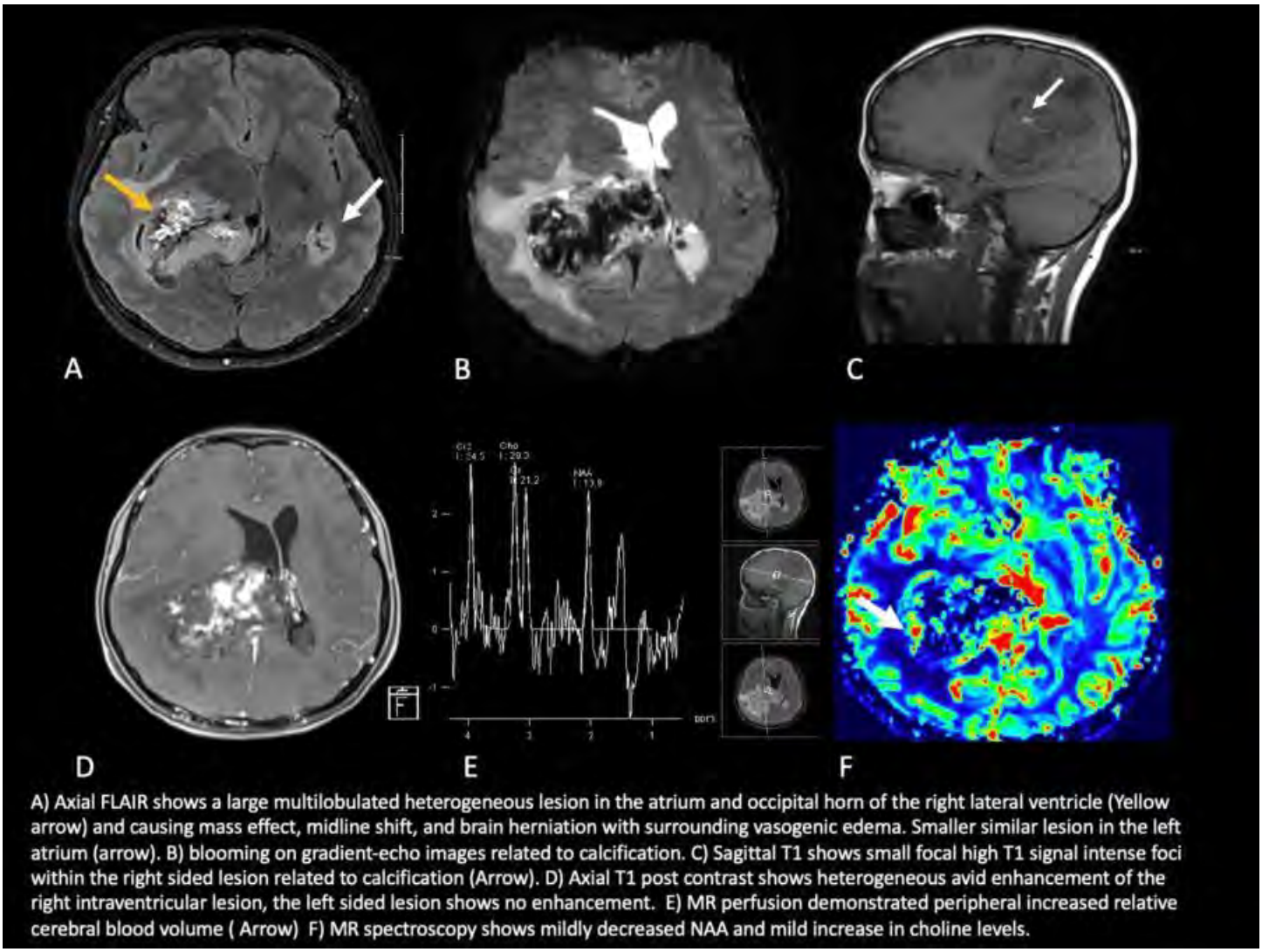

A) Axial FLAIR shows a large multilobulated heterogeneous lesion in the atrium and occipital horn of the right lateral ventricle (Yellow arrow) and causing mass effect, midline shift, and brain herniation with surrounding vasogenic edema. Smaller similar lesion in the left atrium (arrow). B) blooming on gradient-echo images related to calcification. C) Sagittal T1 shows small focal high T1 signal intense foci within the right sided lesion related to calcification (Arrow). D) Axial T1 post contrast shows heterogeneous avid enhancement of the right intraventricular lesion, the left sided lesion shows no enhancement. E) MR perfusion demonstrated peripheral increased relative cerebral blood volume (Arrow) F) MR spectroscopy shows mildly decreased NAA and mild increase in choline levels.

(Filename: TCT_1379_Screenshot2022-11-15at185031.jpg)

283

Autoimmune Glial Fibrillary Acidic Protein (GFAP) Astrocytopathy

M Brun-Vergara[1], N Zakhari[1]
[1]*THE OTTAWA HOSPITAL, OTTAWA, ON*

Clinical History

A 42-year-old male presents with a 3-week history of dizziness, severe headache, tingling in bilateral limbs, and progressive worsening sense of disequilibrium and unsteady gait. His family noted confusion and inability to elaborate further. His past medical history included ADHD, Asthma, Bipolar disorder, ETOH abuse, and hypertension. Patient stated significant weight loss of 70lb in the last year. On physical examination, patient was encephalopathic, with bilateral upper motor neuron signs, and significant sensory ataxia and length-dependent sensory loss of large fiber modalities. CSF analysis showed elevated protein, pleocytosis and high IgG index. Extensive additional diagnostic workup, including ANA, Hepatitis, Anti-AMPA/GABAb, syphilis, mycobacteria, cryptococcal, HIV, Lyme, Anti-NMO/MOG, and other paraneoplastic antibodies were all negative.

Imaging Findings

MRI of the brain and whole spine revealed extensive and diffuse supra and infratentorial signal abnormality with bilateral symmetric periventricular and deep supratentorial, brain stem, brachium pontis and cerebellar linear and nodular enhancement. Diffuse nodular enhancement and T2 hyperintensity in the cervical spinal cord with more patchy and confluent enhancement and T2 hyperintensity in the thoracic spinal cord.

Discussion

Given the clinical course and associated imaging findings, a diagnosis of autoimmune GAFP was suggested, which prompted further CSF analysis, confirming the presence of GFAP-IgG. Tissue indirect immunofluorescence was compatible with anti-GFAP. Patient started on IV pulse steroids and immunoglobulin, with significant improvement in his clinical condition with gradually improving balance. Patient was discharged one month after admission, after being complicated by SARS-CoV2 infection and IVIg-induced hemolysis.

Teaching Point
*Novel CNS disorder characterized by a monophasic/relapsing immunotherapy-responsive meningoencephalomyelitis commonly presenting with subacute symptoms. Since its initial description, less than 300 cases have been reported in the literature. *Presumably mediated by GFAP peptide-specific cytotoxic CD8+T cells. *MRI striking pattern of radial linear periventricular enhancement supports the diagnosis. *Diagnosis confirmation is made by CSF GFAP-IgG detection. Further confirmation can be made with tissue-based and cell-based IFA. *Treatment requires high-dose steroids, IV immunoglobulin, or plasma exchange. *Patients usually have a rapid clinical and imaging improvement after treatment.

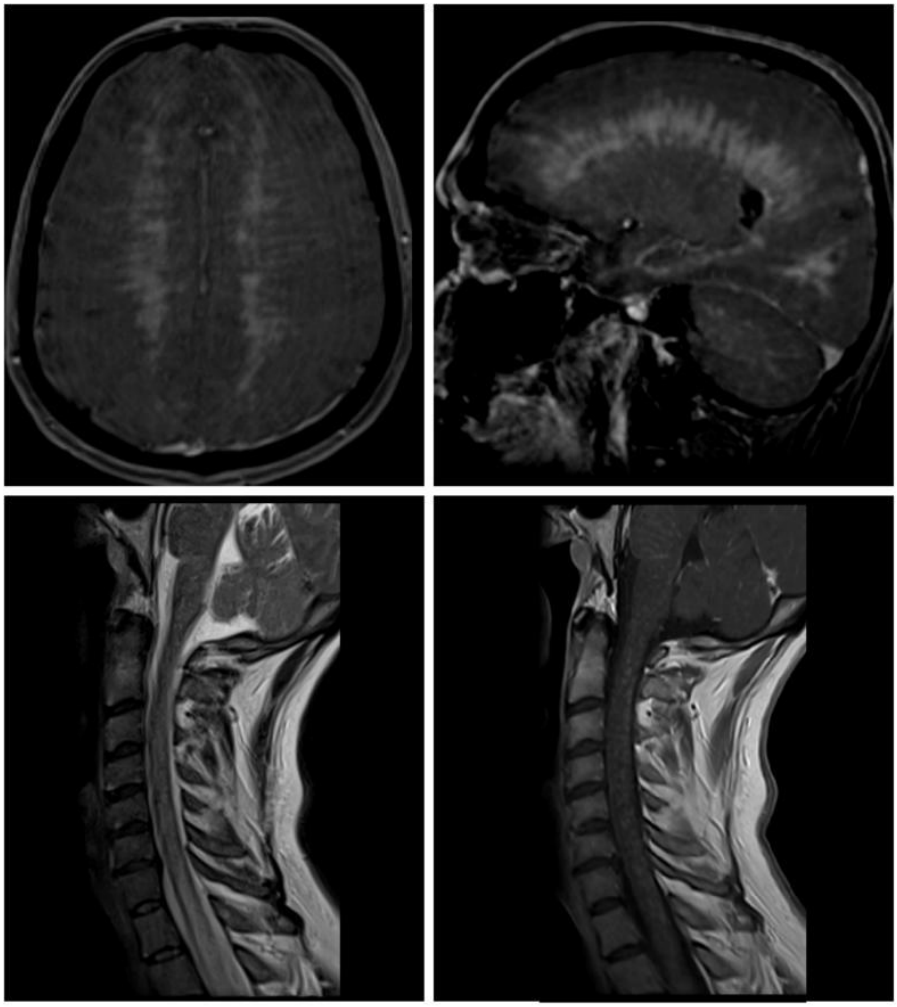

(Filename: TCT_283_Fig_1.jpg)

1392
Beyond Lipomatosis: Unsuspected Angiolipoma of the Cervicothoracic Junction
L Wojdyla[1], M McDonald[2]
[1]UC San Diego Health, San Diego, CA, [2]UCSD, San Diego, CA

Clinical History
26-year-old female presenting with slowly progressive right-sided posterior neck and upper thoracic pain in the setting of migraine headaches and lupus nephritis.
Imaging Findings
MRI imaging of the cervicothoracic junction revealed an extramedullary lesion spanning from the level of C7 inferiorly to T4 (sagittal T1W imaging in A) with a distinct spindle-cell configuration. Two distinct components were visualized on pre-contrast imaging, including a homogenously T1-hyperintense dorsal component (A, arrows) and a relatively T1-hypointense ventral component (A, arrowheads) intimately associated with the dorsal surface of the adjacent cord parenchyma. Post-contrast T1W fat-saturated imaging was then performed confirming macroscopic fat in the peripheral components of the lesion (B and D, arrows). Although no significant contrast enhancement was noted on initial post-contrast imaging (B), a 5-min delay revealed heterogeneous enhancement within the medially directed, relatively T1-hypointense components (C and D, arrowheads), raising suspicion for underlying vascularity.
Discussion
Spinal angiolipomas are rare spinal neoplasms, accounting for only 1.2% of spinal tumors but up to 22% percent of epidural tumors (1, 2). They most commonly occur in mid-thoracic region and are histologically comprised of a combination of fat and abnormal vascular tissue. The clinical symptoms of spinal angiolipomas are predominantly related to mass-effect and associated impingement

upon the cord parenchyma and/or spinal nerve roots. MRI is the imaging modality of choice for detecting and characterizing spinal angiolipomas, with common imaging findings including a spindle shaped lesion located in the posterior epidural space extending longitudinally along the spine. The MR signal of angiolipomas reflects their underlying dual composition with internal adipose components confirmed on fat-suppression sequences. Given the heterogeneous composition of the underlying vascular components, variable degrees of enhancement have been reported in the literature (3). Ultimately, although rare, it is important to consider this entity in the interrogation of fat-containing epidural lesions to help guide surgical management and prevent complications related to unsuspected vascular components.

Teaching Point

To identify the key imaging features of spinal angiolipomas in contrast to other fat-containing epidural lesions, with an eye towards surgical management.

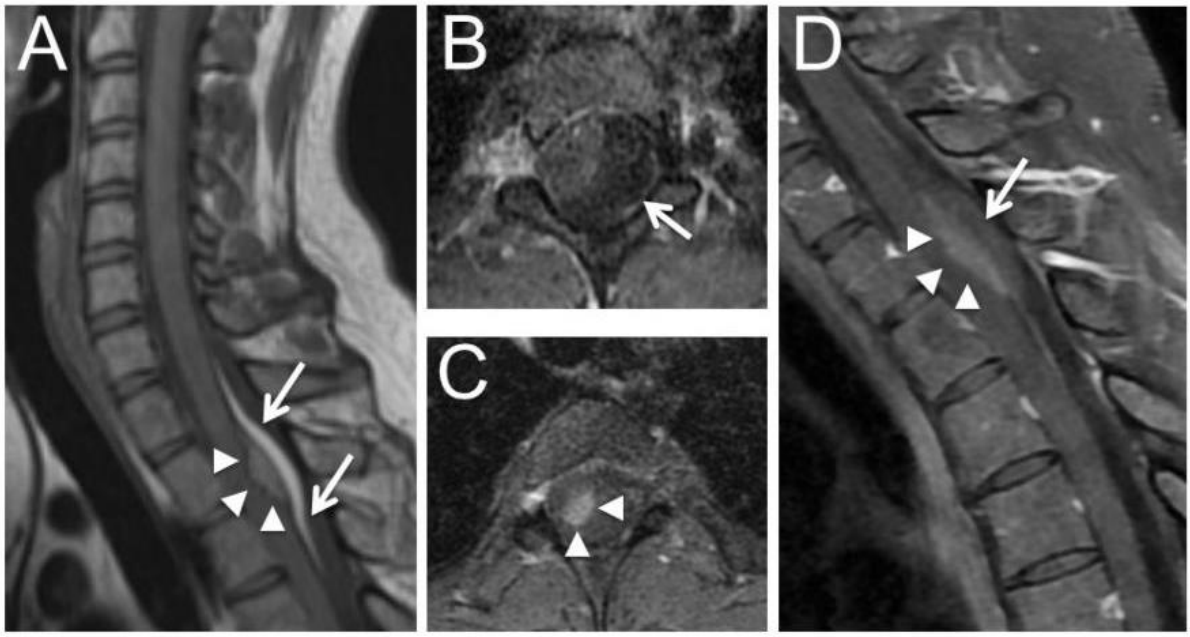

(Filename: TCT_1392_Figure1.jpg)

167

Bilateral Mandibular Arteriovenous Malformation: An Illustrative Case

K Young[1], S Kejriwal[2], A Ozturk[3], K Oguz[3], M Shahrzad[3], O Raslan[3]

[1]001087961215, Foster City, CA, [2]John A. Burns School of Medicine, University of Hawaii at Manoa, Honolulu, HI, [3]UC Davis Medical Center, Sacramento, CA

Clinical History

A 17-year-old patient presented to the current institution after a routine wisdom tooth extraction resulted in massive hemorrhage. The patient was determined to be hemodynamically stable after arrival, and the decision to observe the patient was made in lieu of more invasive management strategies. However, on the third hospital day, the patient developed a massive oral cavity hemorrhage which required emergent intubation. The patient was subsequently brought to the interventional radiology suite for emergent endovascular embolization.

Imaging Findings

Contrast-enhanced computed tomography (CT) images from an outside hospital revealed an expansile mass within the right mandible, with involvement of the right masticator and parotid spaces. Through angiography, the patient was found to have a large venous lake extending throughout the entire right mandible, with additional AVM involvement of the right maxilla and skull base Seven months after discharge, the patient was reassessed via diagnostic angiogram for his right-sided mAVM for residual disease. However, an additional left-sided AVM was noted in the left anterior mandible, supplied predominately by the left facial artery.

Discussion

While the main focus for unilateral mAVMs is to eradicate the nidus of the AVM to prevent residual or recurrent disease, this may not be feasible in more extensive cases that extend bilaterally through the mandible. Unilateral embolization procedures are generally well-tolerated, but bilateral embolization of the branches of the ECA may lead to iatrogenic sequelae including tissue necrosis. For similar reasons, the ligation of the bilateral external carotid arteries should not be pursued, especially since this procedure does not prevent the recruitment of collateral vessels from the vertebral system. Furthermore, ligation of this vessel is not recommended since this will render endovascular access through the external carotid artery impossible. Surgically, near-total mandibulectomy is not an acceptable option in most cases due to the functional limitations of the resultant defect and tremendous difficulties associated with reconstruction.

Teaching Point
Bilateral mAVMs may lead to life-threatening hemorrhages, and treatment should not be delayed. The most common imaging modalities used in diagnosis are angiography, CTA, and ceCT. Embolization and surgery are the definitive modes of treatment. More rigorous research is needed before more formal guidelines in the management of mAVMs are established.

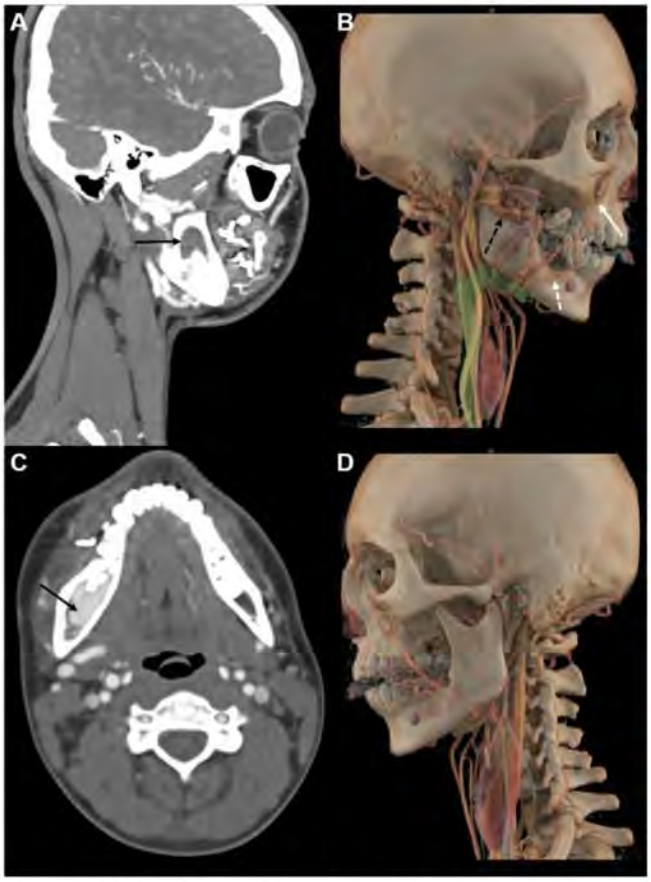

Figure 1. Axial Sagittal (A) and Coronal Axial (C) contrast enhanced CT of the mandible with corresponding 3D volume illumination rendered images (B, D), demonstrating an expansile lytic homogenously intensely enhancing AVM (black solid arrows) in the right mandible extending from the angle to the roots of tooth #6. Dilated and tortious inferior alveolar (black dashed arrow), angular (white solid arrow), and mental (white dashed arrow) arteries are present on the right side, and an enlarged facial vein emptying into a dilated internal jugular vein is highlighted in green. The left-sided 3D volume rendered image depicts normal appearing vasculature.

(Filename: TCT_167_Picture1.jpg)

1058

Case of Biopsy Proven Progressive Multifocal Leukoencephalopathy- Immune Reconstitution Inflammatory Syndrome (PML-IRIS)

A Monga[1], S Jain[1]
[1]*Detroit Medical Center, Detroit, MI*

Clinical History
A 41-year-old male with medical history of HIV, not on antiretroviral therapy, presented from a homeless shelter with altered mental status. After admission the patient's mentation gradually improved. He was started on antiretroviral therapy and discharged. The patient presented approximately two months later with seizures. Brain biopsy was performed, which demonstrated PML-IRIS.
Imaging Findings
Brain MR from initial presentation showed asymmetric subcortical white matter demyelinating lesions (FLAIR hyperintense) with sparing of the periventricular white matter (Fig. 1). The lesions showed no enhancement (Fig. 2). Brain MR from the subsequent presentation showed an increase in the extent of the previously seen demyelinating lesions (Fig. 3) which now demonstrated enhancement (Fig. 4).
Discussion
PML is a demyelinating encephalopathy that is caused by JC virus reactivation in immunosuppressed patients. The patient presented in this case was immunosuppressed due to untreated HIV. Brain MR at the initial visit shows typical imaging features of PML, which include: asymmetric subcortical white matter demyelinating lesions without enhancement. Diffusion restriction is seen mostly in

regions of active demyelination. Brain MR at the second visit shows the typical imaging features of PML-IRIS, which include: enhancement, diffusion restriction, and increased extent of the T2 hyperintense lesions. PML-IRIS in HIV patients started on antiretroviral therapy is a paradoxical phenomenon where with the reconstitution of the immune system the patient's clinical status deteriorates. Steroids are the mainstay of treatment for PML-IRIS and the patient presented in the case improved after a course of steroids. CNS-IRIS in HIV patients is most commonly associated with PML, but it can also be associated with other infections such as cryptococcal meningitis, toxoplasmosis and tuberculosis. Imaging features such as enhancement and diffusion restriction are shared among the various causes of CNS-IRIS, but each cause may have unique imaging features that could allow differentiation. Awareness of PML-IRIS is important for radiologists as prompt treatment with steroids can control the inflammatory response and improve morbidity and mortality.

Teaching Point

It is important to consider PML-IRIS in an HIV patient diagnosed earlier with PML, who is clinically worsening despite rising CD4 count, decreasing HIV viral load, history of recent initiation of antiretroviral therapy and developing enhancing white matter lesions on MR.

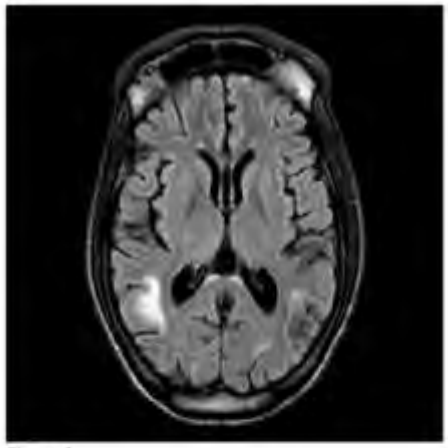
Figure 1

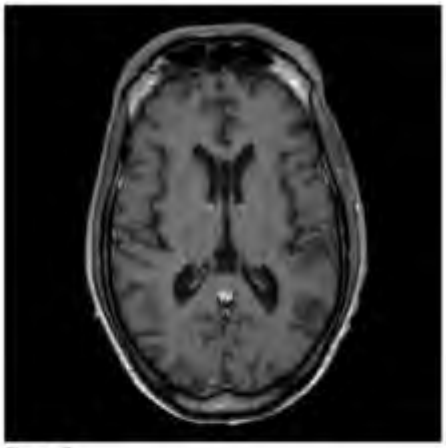
Figure 2

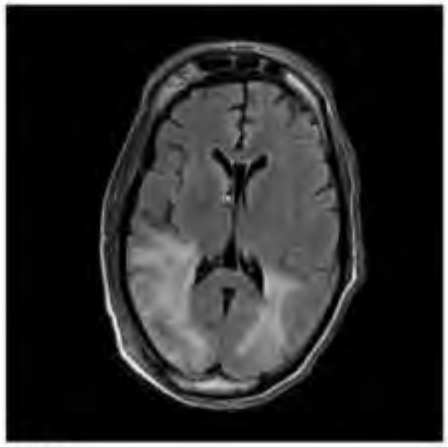
Figure 3

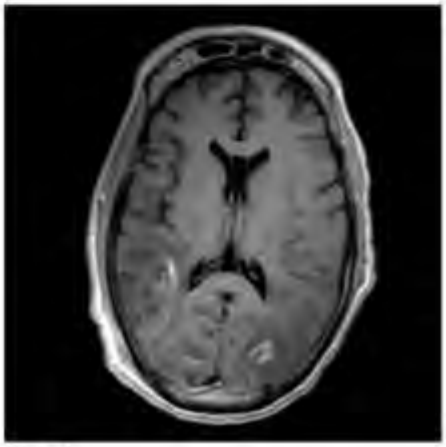
Figure 4

(Filename: TCT_1058_Figures.jpg)

457

Cauda Equina Paraganglioma: An Uncommon Radiologic Presentation of a Rare Neuroendocrine Tumor

E DAMLE[1], V HILL[2]

[1]Tulane University, New Orleans, LA, [2]Northwestern University Feinberg School of Medicine, Chicago, IL

Clinical History

66 year-old male with history of diabetes mellitus, obesity, benign essential hypertension, hyperlipidemia, and prostate cancer came in for sciatic pain in the left leg/gluteal area without weakness or bowel/bladder issues. Lumbar spine MRI revealed a 16x22x37 mm intradural lesion at the L3 level appearing to be a meningioma and patient underwent spinal angiogram, which showed an early blush, to attempt embolization. However, because the anterior spinal artery supplied the mass, the tumor was resected instead. DNA methylation profiling identified the cauda equina mass as a spinal paraganglioma, a WHO Grade I neuroendocrine tumor.

Imaging Findings

On spinal MRA, the mass enhanced considerably with contrast. Angiography revealed blood supply to be a large vessel coming off the T10 segmental artery. The tumor was more homogenously enhancing than most paragangliomas and was initially thought to be a meningioma. An atypically subtle "salt and pepper" appearance was noted on contrast-enhanced T1-weighted and T2-weighted imaging, with the "salt" being enhancing parenchyma and the "pepper" being flow voids in a rich capillary network. The supplying vessel was visible on sagittal images and a vascular structure at the posterior margin of the mass was visible on axial images.

Discussion

Paragangliomas of the cauda equina are rare WHO Grade I neuroendocrine tumors associated with the non-chromaffin, non-neuronal, neural crest-derived cells of the paraganglia that tend to form highly vascular, well-defined intradural masses (1,2,3). Representing about 3% of tumors of the cauda equina, only a few hundred have been documented since 1970 (4). Common symptoms include lower back/extremity pain plus possible sensory/motor loss and/or bowel/bladder dysfunction. Differential diagnosis for paraganglioma includes myxopapillary ependymoma, schwannoma, neurofibroma, and meningioma, with anatomic location and pathological findings being the primary differentiators (5). Pathologically, paragangliomas appear as soft, red-brown, encapsulated tumors that are richly vascular. Typical treatment is surgical resection, sometimes with pre-operative embolization to minimize blood loss, or radiotherapy. Post-resection recurrence rate is less than 5%, so surgical excision is usually curative.

Teaching Point

Paragangliomas of the spine are rare neuroendocrine tumors that have interesting characteristics in imaging studies. This case discusses clinical and radiologic features of an atypically-presenting paraganglioma of the cauda equina.

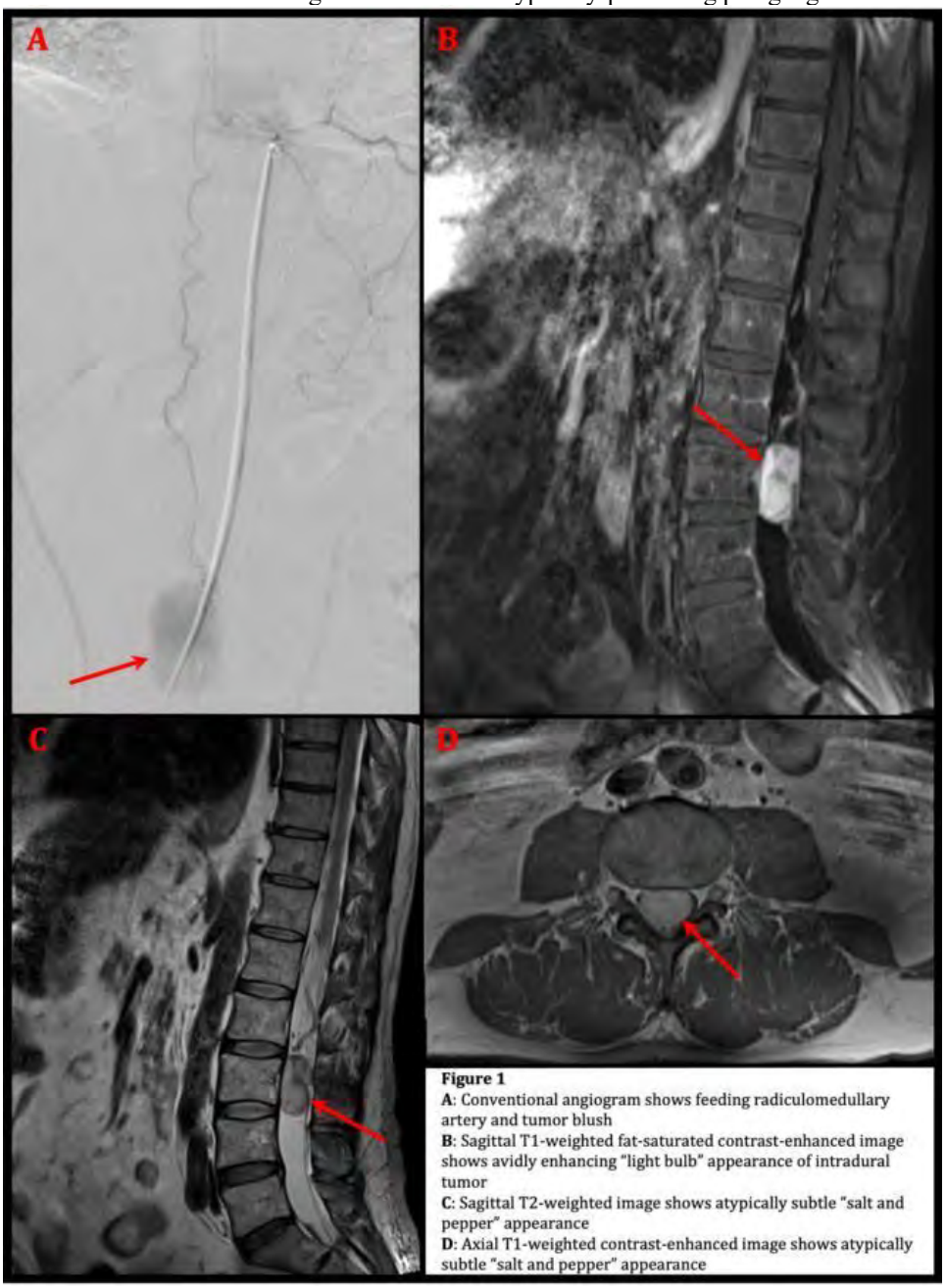

Figure 1
A: Conventional angiogram shows feeding radiculomedullary artery and tumor blush
B: Sagittal T1-weighted fat-saturated contrast-enhanced image shows avidly enhancing "light bulb" appearance of intradural tumor
C: Sagittal T2-weighted image shows atypically subtle "salt and pepper" appearance
D: Axial T1-weighted contrast-enhanced image shows atypically subtle "salt and pepper" appearance

(Filename: TCT_457_ImagesLayoutFinal.jpg)

711

Cavernous Sinus Hemangioma: a Rare Lesion with Characteristic Imaging Findings

R Fernandes[1], G Watanabe[1], N Casimiro[1], R Fava[1], L Feltrin[1], R Rossini[1], A Mamere[1]
[1]Barretos Cancer Hospital, Barretos, SP

Clinical History

- Patient 1: 55 year-old female presented with a 4-month history of left facial paresthesia, blurred vision, diplopia and left-sided ptosis. - Patient 2: 46 year-old female referring presented with a 3-month history of nausea and daily headaches. - Patient 3: 39 year-old male presented with a 3-year history of progressive vision loss on the left eye and intracranial lesion. Al these 3 patients showed unilateral intracranial masses on Magnetic Resonance Imaging (MRI) examination, centered on the parasellar region, with imaging features suggestive of cavernous sinus hemangiomas. Only patient 3 was submitted to surgical biopsy and presented profuse intraoperative bleeding.

Imaging Findings

The imaging features of cavernous hemangiomas are: - Extra-axial parasellar growing lesion with remodeling of bone structures and occasional encasement of the internal carotid artery without lumen narrowing. - On Computed Tomography (CT), it can be iso or hyperdense and have an intense post-contrast enhancement. Calcification foci may be present, although more commonly seen in meningiomas. - On MRI, it presents as a mass with very high signal intensity on T2-weighted image (WI) lesion, similar to cerebrospinal fluid, and iso/hypointense on T1WI. On Dynamic Contrast-Enhancing (DCE) sequences, the contrast enhancement pattern is characteristically progressive and centripetal.

Discussion

Cavernous sinus hemangioma is a non-encapsulated vascular malformation composed by numerous dilated vascular channels. In spite of having characteristic radiological features, it can be difficult to differentiate from other parasellar lesions such as meningioma, schwannoma and chondrosarcoma. The clinical presentation matches the usual cavernous sinus symptomatology: impairment of the cranial nerves that rout through the cavernous sinus (diplopia, ptosis) and occasional ipsilateral proptosis. The preoperative diagnosis is key to patient management on cavernous sinus hemangiomas, since it is reported to have a troublesome intraoperative bleeding tendency.

Teaching Point

- The cavernous sinus hemangioma is a rare but important differential diagnosis for T2WI hyperintense parasellar lesions. - The DCE progressive and centripetal filling of the lesion plays an important role in differentiating hemangiomas from other parasellar lesions. - The preoperative diagnosis is important since cavernous sinus hemangiomas are reported to exhibit intense intraoperative bleeding.

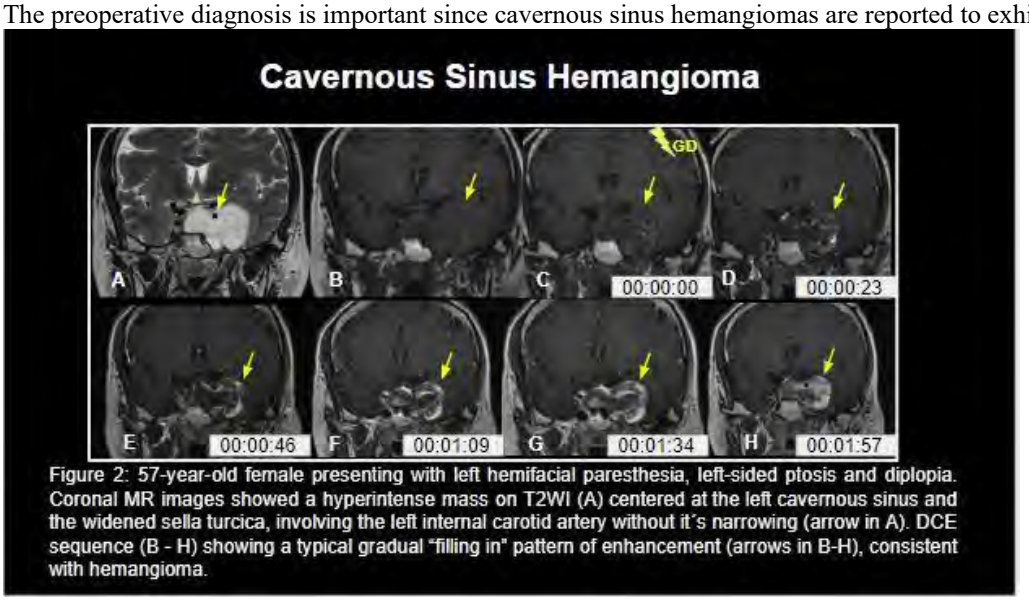

Figure 2: 57-year-old female presenting with left hemifacial paresthesia, left-sided ptosis and diplopia. Coronal MR images showed a hyperintense mass on T2WI (A) centered at the left cavernous sinus and the widened sella turcica, involving the left internal carotid artery without it´s narrowing (arrow in A). DCE sequence (B - H) showing a typical gradual "filling in" pattern of enhancement (arrows in B-H), consistent with hemangioma.

(Filename: TCT_711_Hemangioma.JPG)

1273

Cerebral Venous Sinus Thrombosis in a Pediatric Patient Related SARS-CoV-2 Infection: Case report

Q Nguyen-Duong[1], C Tran[1], M Ngo[1], T Bui[1], T Vo[1], L Nguyen[1], T Quach[1], H Truong[1], D Nguyen[1], M Le[1], H Duong[1]
[1]Can Tho Stroke International Services General Hospital, Can Tho, Viet Nam

Clinical History

A 4y boy was admitted emergency department with seizures. He experienced headache and vomiting during the last 7 days before admission with none of the treatment. Severe progression of symptoms happened to seizures. His personal history: he had suffered the severe acute respiratory syndrome coronavirus 2 (SAR-CoV 2) 10 months ago. Except for SAR-CoV2, no other known risk factor of cerebral venous sinus thrombosis could be identified. The level of SAR-CoV 2 IgG II was 885.7 AU/ ml. He was diagnosed with cerebral venous sinus thrombosis (CVST) by MRI and DSA images. He was treated by thrombectomy and anticoagulation drug with good clinical outcomes.

Imaging Findings
The results of non-contrast CT brain showed the hypodense of right and left thalamus, the hyperdense of the right transverse sinus, the straight sinus, vein of Galen, inferior sagittal sinus. Images on MRI 3 Tesla revealed a remarkable increase of the sign in both two thalamus on FLAIR, DWI, ADC. The occlusion of the right transverse sinus, the straight sinus, vein of Galen, inferior sagittal sinus due to thrombosis was seen clearly on SWI, MRV. Then, DSA was used for a patient. CVST was suggested for our patient and he was treated by thrombectomy. The imaging on MRV after treatment has been still remained some blood clots at these sinuses. He continued to be treated with the anticoagulation method.
Discussion
CVST is an uncommon condition. There are several known genetic and acquired risk factors for CVST. COVID-19 disease has multi-systemic manifestations, one of which includes a high prevalence of venous thromboembolism. Our patient was admitted the hospital with neurological manifestations. Neuroimaging with cranial CT shows some abnormal images of venous sinus but it is not enough for diagnosing CVST. By MRI imaging, especially MRV imaging, the diagnosis of CVST was confirmed. Because he had a medical history with SAR-CoV 2 and no evidence of other risk factor could be found, we present this case as a potential association between CVST and SAR-CoV 2.
Teaching Point
COVID-19-related CVST should also be suspected in pediatric patients, although rare in this group of patients, but it can be a cause of stroke. CVST has a good prognosis when treated promptly but can be fatal when not treated. Pediatric patients with neurological manifestations should be scanned with MRI techniques to provide exactly diagnosis. With abnormal imaging of the cerebral sinus appeared on MRI, the patient should be scanned by neurovascular DSA for treatment.

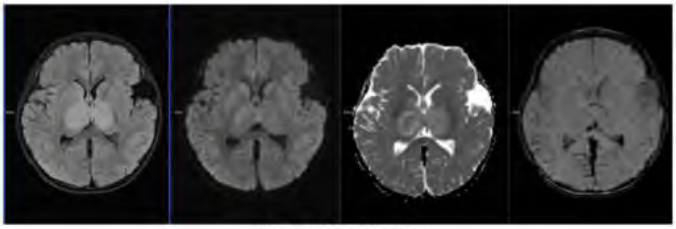
Fig 2. MRI

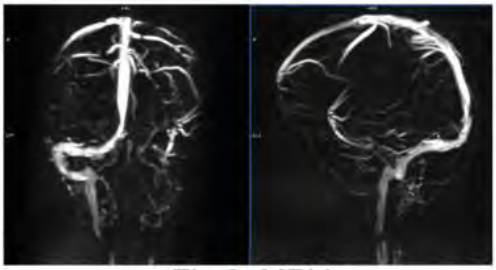
Fig 3. MRV

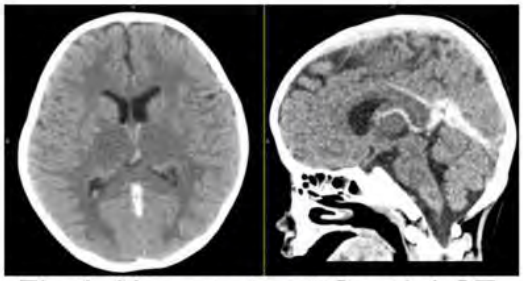
Fig 1. Non-contrast Cranial CT

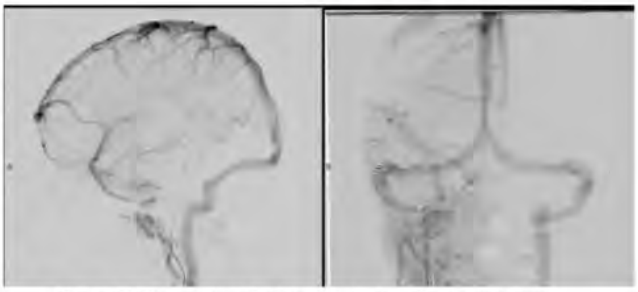
Fig 4. DSA images: before and after thrombectomy

(Filename: TCT_1273_Untitled.jpg)

550
Cervical Myelopathy After Electrical Trauma, a Case Series
D Murphy[1], M Peckham[1], T Hutchins[1], L Shah[2]
[1]University of Utah, Salt Lake City, UT, [2]University of Utah Health Care, Salt Lake Cty, UT

Clinical History
Patient 1 A 73-year-old male presented with extensive burns after contact with a high voltage electrical line. Immediately following the trauma, the patient displayed absent lower extremity clonus, hyperreflexia, and absent proprioception. Patient 2 A 34-year-old female was struck by lightning and suffered cardiac arrest, extensive burns, and multifocal injuries. Six weeks later, the patient noted progressively worsening extremity paresthesias, lower extremity spasticity, and upper extremity impaired proprioception and fine motor skills. Patient 3 A 27-year-old male landed on high voltage electrical wires after jumping from a building and sustained extensive burns and cervical spinal fractures. At admission, the patient noted difficulty walking and intermittent left-hand numbness.
Imaging Findings
Cervical spine MRI of patients 1 and 2 obtained 4 and 6 weeks after injury, respectively, demonstrated long segment of T2 hyperintensity in the corticospinal tracts and dorsal columns. Of note, a cervical MRI of patient 1 one week after injury was negative for cord signal abnormality. Cervical MRI of patient 3 demonstrated long segment T2 hyperintense lesions of the cervical spinal cord involving the dorsal columns and dorsolateral cord.
Discussion
This series of cases of electrical injury demonstrate a specific imaging pattern of predominantly white matter T2 hyperintensity,

particularly involving the corticospinal tracts. Other case reports have demonstrated a predilection of corticospinal tract and dorsal column involvement, as in these cases. Symptom onset varies and can be immediate or delayed. Recovery is also variable, as one patient had symptomatic improvement one month after onset while the others had persistent signs and symptoms. The pathogenesis of electrical injury is not entirely understood but may relate to direct thermal injury of the tissues or to the supplying blood vessels. Alternatively, the conducted electricity may disrupt cellular membrane potentials and result in pore formation, a process known as electroporation.

Teaching Point

- Neurologic injury in electrical trauma has a predilection of corticospinal tract and dorsal cervical spinal cord involvement - Symptom onset and recovery are variable

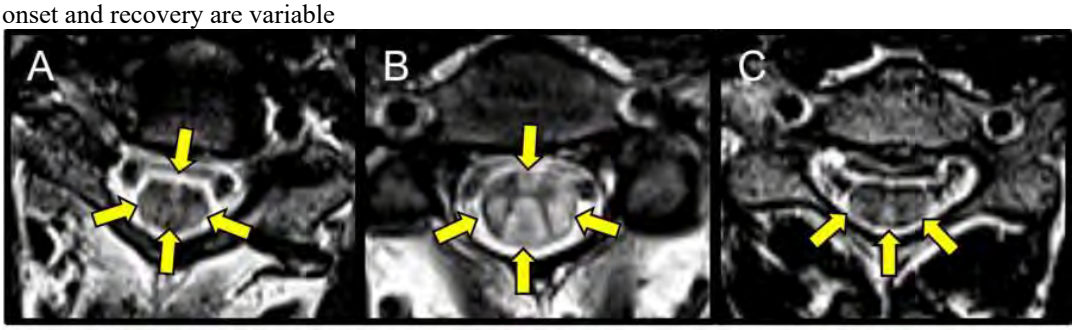

Figure 1: T2 weighted cervical spine MRI findings for patient 1 (A), patient 2 (B), and patient 3 (C) demonstrates hyperintense T2 signal of the cervical spinal cord involving the corticospinal tracts and dorsal columns. (yellow arrows).

(Filename: TCT_550_ASNRFinal300.jpg)

323

Challenges and Potential Pitfalls of RAPID AI

N Thackar[1], J Bansal[1], S Forseen[1]

[1]*Medical College of Georgia at Augusta University, Augusta, GA*

Clinical History

We reviewed five cases at our institution of patients presenting with stroke-like symptoms, who were evaluated with either CT angiography or noncontrast CT of the head. The images were then interpreted with RAPID AI software.

Imaging Findings

Patient 1 – Meningioma erroneously tagged as 'suspected hemorrhage' by RAPID IPH. Patient 2 – A chronic right MCA territory infarct was tagged as a region of concern by RAPID ASPECTS. This patient also had a simultaneous acute left territory MCA infarct which was not tagged. Also, on the noncontrasted CT head, the dural venous sinuses were opacified due to a previous contrasted exam. RAPID ICH analysis erroneously attributed an opacified torcular herophili as an area of hemorrhage. Patient 3 – RAPID ASPECTS software erroneously labeled a portion of the right sylvian fissure as the insular cortex, resulting in an area of concern in the right MCA territory. Subsequent MR did not show evidence of acute infarct. Patient 4 – Subdural hematoma erroneously interpreted as infarcted tissue by RAPID CTP. Patient 5 – Patient with large right hemorrhagic infarct with RAPID APSECTS erroneously indicating presence of left ischemic infarct.

Discussion

RAPID AI is a commercially available software package that is commonly utilized for interpretation of head CTs for evaluation of stroke. While this comes with many advantages, it is important to not rely exclusively on software-guided interpretation of images. The RAPID AI software package includes several subset applications, each with their own utility. In this review, we describe pitfalls of the RAPID ASPECTS, RAPID ICH, and RAPID CTP tools. RAPID ASPECTS: We show two cases in which there was an erroneous ASPECTS score output due to errors in software guided post-processing. Another case is shown, in which a large right hemorrhagic infarct was erroneously interpreted a large left hemispheric ischemic infarct. RAPID ICH: We describe cases in which a partially calcified meningioma and an opacified dural venous sinus were both tagged as ICH. RAPID CTP: We show a case of a subdural hematoma which was tagged as ischemic tissue.

Teaching Point

There are several commercially available software applications that aim to aid in the evaluation of stroke. We evaluated the use of RAPID AI software analysis of several stroke cases and highlighted potential pitfalls of using AI in acute stroke imaging. It is important for interpreters to evaluate the source images as well, and not rely solely on the assistance of AI generated images.

(Filename: TCT_323_RAPIDAIImages.JPG)

239

CIC-Rearranged Intracranial Sarcoma with Recurrence

S Khan[1], A Lignelli[1]
[1]*Columbia University Irving Medical Center, New York, NY*

Clinical History

A 34-year-old female without significant past medical history presented with two weeks of worsening headaches and nausea/vomiting. Workup was initiated with computed tomography (CT) and magnetic resonance imaging (MRI) of the brain demonstrating an intraparenchymal mass. The mass was resected. Surgical pathology confirmed the tumor to be a malignant undifferentiated small round blue cell tumor with molecular pathology characterizing it as a CIC (Capicua transcriptional repressor gene)- rearranged genotype sarcoma. Two months later, patient presented with complaint of daily headaches, along with left eye vision "darkness", after being lost to follow up. MRI of the brain demonstrated new extra-axial enhancing lesions along the bilateral optic nerves, with significant mass effect, compatible with recurrence of disease.

Imaging Findings

Contrast enhanced MRI of the brain demonstrated an intra-axial, heterogeneously enhancing mass with solid and cystic components within the left frontal lobe. Significant mass effect was seen upon adjacent structures. Postoperative contrast enhanced MRI demonstrated gross total resection. Two month follow up MRI demonstrated no intraparenchymal enhancement. New extra-axial nodular enhancing lesions were seen along the bilateral pre-chiasmatic segments of the optic nerves, left greater than right. This resulted in compressive atrophy of the left optic nerve when correlated with ophthalmology exam. Infectious/inflammatory etiologies were considered; however, patient's workup was negative. Imaging findings were attributed to recurrence.

Discussion

CIC-rearranged sarcoma is a rare, aggressive undifferentiated sarcoma with round cell phenotype, predominately seen in soft tissues. This entity was considered a Ewing-sarcoma subtype given the similarity in histopathology; however, quite different in its genetic composition. Most tumors occur in the soft tissue (86%), predominantly deep-seated and equally divided among trunk and extremity, followed by visceral locations, including brain, (12%) and rarely in the bone (3%). Given this aggressive type of sarcoma, studies have shown that recurrence is quite common.

Teaching Point

We present a unique case of intracranial CIC-rearranged sarcoma which is a rare diagnosis in head and neck imaging. When such heterogeneous intracranial masses are seen in this demographic group of young adult females, it is important to consider this rare entity. It is also important to note the propensity of recurrence with these tumors.

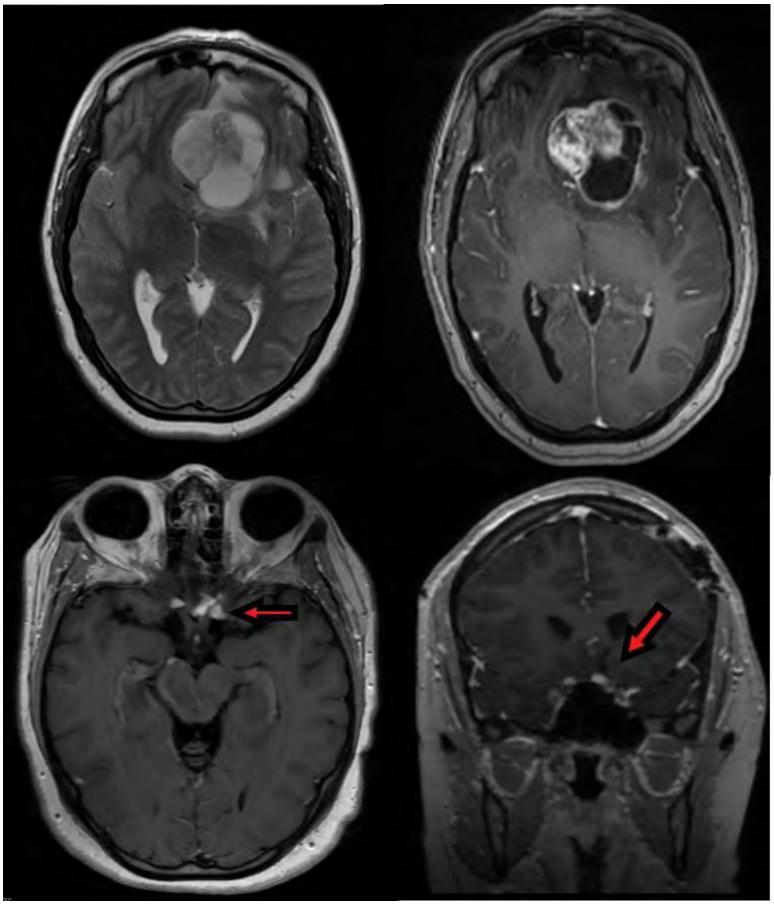
(Filename: TCT_239_ASNRimages.jpg)

1355

Claudication Secondary to Ischemic Lumbosacral Plexopathy: A Rare Third Type of Claudication in the Setting of Pelvic Arterial Disease.

N Kan[1], J Maw[1], J Go[2], P Rajagopalan[3]
[1]University of Southern California, Los Angeles, CA, [2]Keck Medicine of USC, Los Angeles, CA, [3]USC, Los Angeles, CA

Clinical History

The patient is a 52-year old male with history of hypertension and bilateral common and internal iliac artery aneurysms status post EVAR and right internal iliac artery coil embolization one year ago, presenting with progressive right low back and groin pain with L2-L4 distribution right lower extremity weakness and sensory loss, and new onset L2-L4 distribution left lower extremity sensory loss. The patient was admitted for open right common femoral aneurysm repair.

Imaging Findings

CTA showed stable type 2 endoleak of a repaired 3.3 cm infrarenal abdominal aortoiliac aneurysm with retrograde filling from the inferior mesenteric artery. The patient also had bifurcated stents within stable bilateral common iliac and internal iliac aneurysms with chronic occlusion of the right internal iliac artery and distal reconstitution. Multiple MRI lumbar spine were obtained to rule out spinal canal stenosis and demonstrated no compressive spinal canal lesion. Eventually, patchy denervation edema and enhancement of the bilateral iliopsoas muscles and right greater than left posterior paraspinal musculature was demonstrated. MR neurography of the lumbosacral plexus showed an edematous and enlarged right lumbar plexus. Electromyography performed three months later showed active denervation changes in the bilateral L3-L4 myotomes and right lower paraspinal muscles, suggestive of moderate to severe right greater than left L3-L4 radiculopathy and possible mild involvement of the right L5-S1 levels.

Discussion

Extensive denervation edema of the iliopsoas and posterior paraspinal musculature, as well as a lack of imaging evidence for nerve compression or compressive spinal canal lesion to explain the patient's claudication symptoms, leads us towards a diagnosis of ischemic lumbosacral plexopathy. Lumbosacral plexus has a rich pelvic arterial supply from the artery of Adamkiewicz, lumbar arteries and internal iliac arteries. Ischemic lumbosacral plexopathy is extremely rare, but has been reported in the literature after aortic interventions or vascular stenosis and occlusion interrupting blood supply, especially with demands from muscular activity.

Teaching Point

Symptoms of claudication with weakness and paresthesias should remind us to look for other causes such as pelvic arterial ischemia, in addition to spinal canal stenosis. Knowledge will prevent misdiagnosis, help with timely intervention by radiology and may help restore the blood supply to improve function in patients.

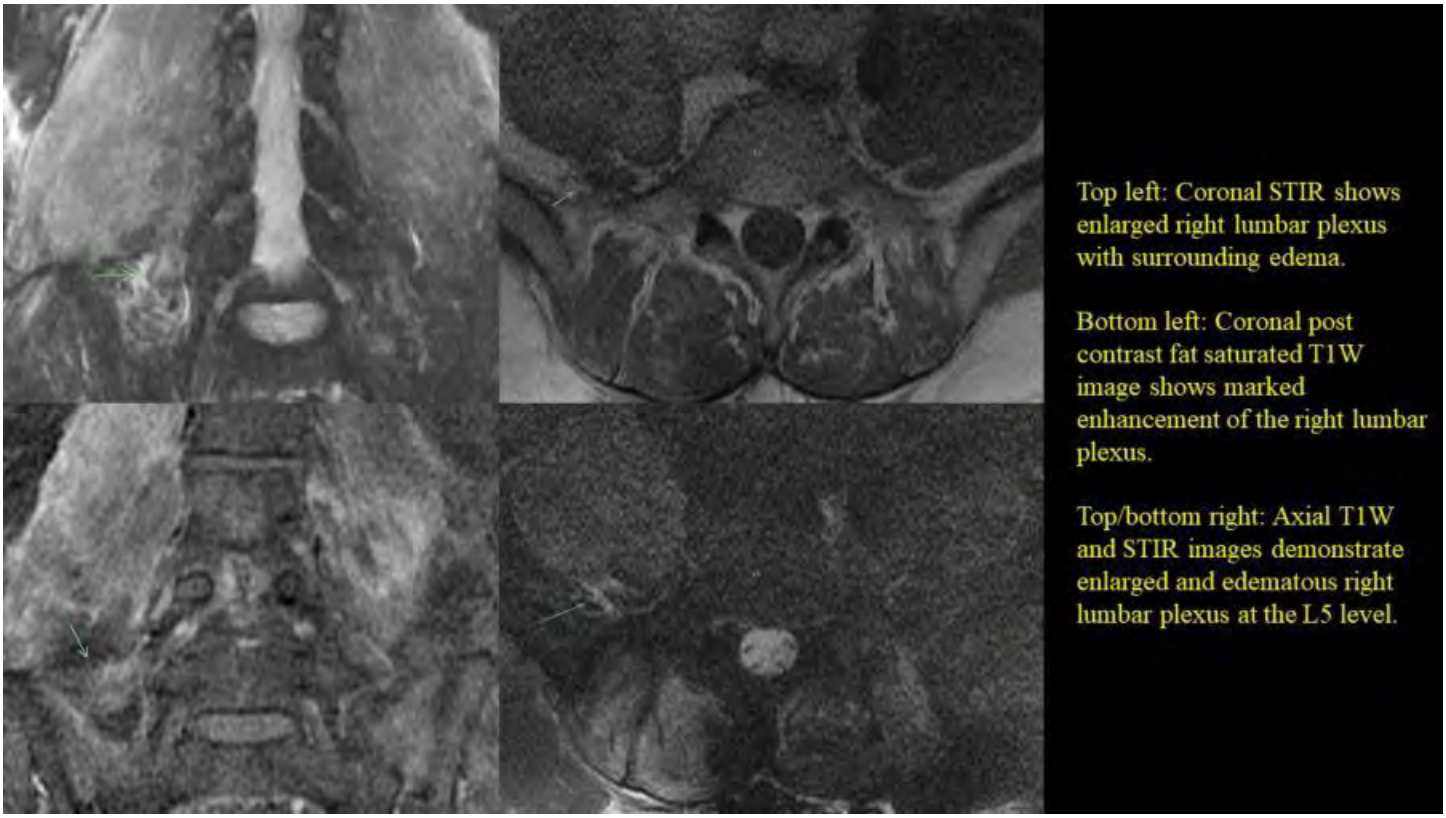

(Filename: TCT_1355_LSplexus.jpg)

1365

Collision Tumor: Meningioma with Intra-tumoral Breast Cancer Metastases

T Abdulsalam[1], A Paydar[2], O Raslan[3], M Bobinski[3], L Hacein-Bey[4], K Oguz[3], A Ozturk[1]

[1]UC Davis Medical Center, Sacramento, CA, [2]University of Califronia-Davis, Sacramento, CA, [3]UC Davis, Sacramento, CA, [4]University of California Davis, Sacramento, CA

Clinical History

A 60-year-old female presented following a fall. Workup revealed a solitary right frontal extra-axial mass, multiple calvarial, and skeletal lesions, and lower extremity pathologic fractures. Medical history was significant for remote breast cancer treated with chemo-radiotherapy 20 years prior.The solitary intracranial lesion was surgically resected and intra-operative frozen section was compatible with meningioma. Final pathological diagnosis reported a meningioma (WHO grade 1) with discrete intratumoral metastatic deposits consistent with breast cancer.

Imaging Findings

Magnetic Resonance Imaging of the brain demonstrated a large right frontal extra-axial mass with heterogenous enhancement, small internal cystic components (Figure 1A,B,C) and surrounding edema. Elevated cerebral blood flow was present within the mass on ASL perfusion images (Figure 1D). Multiple areas of abnormal marrow signal with focal expansion and contrast enhancement were present, concerning for metastatic lesions within the skull base, face and calvarium, the largest within the left frontal bone (Figure 1, star).

Discussion

A collision tumor is a neoplastic lesion that consists of two or more distinct cell populations that maintains distinct borders. They can be composed of two benign tumors, one benign the other malignant, or two malignant tumors. Intracranially meningioma is the most common hosting tumor. Breast and lung cancers are the most common to results in tumor-tumor metastases [1]. Although the underlying mechanism is unknown, the observation that intratumoral metastases are more common within meningiomas, that are characterized by relative increased vascularity, slow growth and low metabolic activity, suggests that those may provide a favorable environment for intra-tumoral metastases [2]. The most common type of intracranial collision tumor is composed of a benign meningioma and a malignant glioma. Meningiomas, especially meningothelial and fibrous meningiomas, can affect the genesis and growth of adjacent gliomas [3].

Teaching Point

Neuroradiologists should be aware of the possibility of primary intracranial collision tumors in patients with meningiomas, particularly when unusual imaging features are present in a patient with known metastases or a prior history of cancer, such as unusually prominent perilesional edema. More precise tumor characterization with imaging may become possible in the future with advanced imaging techniques.

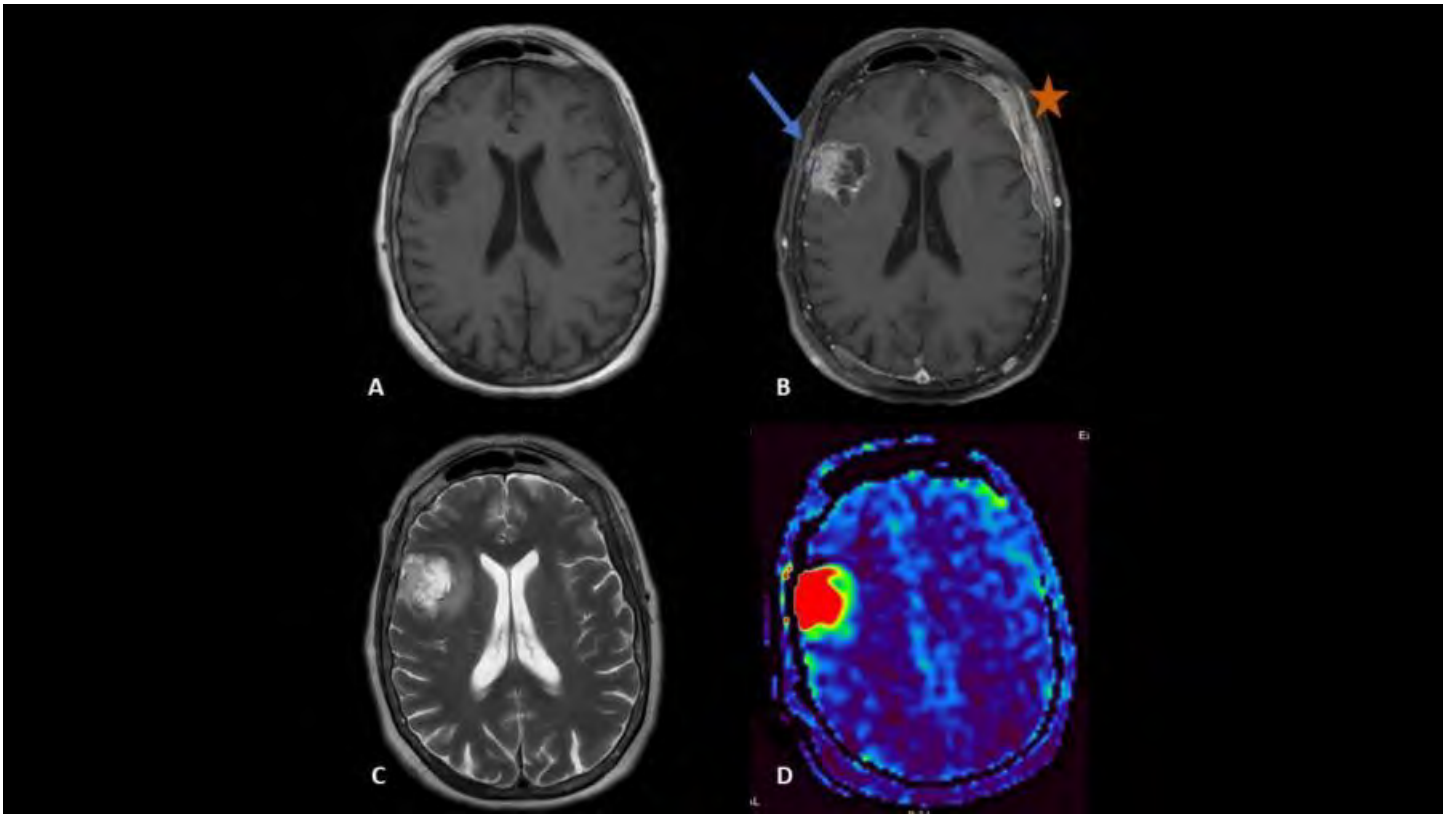

(Filename: TCT_1365_COLISIONTUMOR.jpg)

269

Contrast-Induced Encephalopathy Mimicking Stroke After Cardiac Catheterization: A Rare Case Report

H Uppal[1], M Quinlan[2], J Quinlan[2]
[1]Albany Medical College, Albany, NY, [2]Albany Medical College, Albany , NY

Clinical History

An 84-year-old Caucasian female with a history of hypertension and chronic kidney disease presented to the emergency room with an episode of hypertensive crisis, left upper extremity numbness, and diarrhea. Her troponin was 4.7 ng/ml, and electrocardiogram showed T-wave inversion in leads I and aVL. She also had new onset heart failure with reduced ejection fraction, and transesophageal echocardiogram demonstrated a hypokinetic apex. Patient was diagnosed with NSTEMI. Patient underwent successful cardiac catheterization with stent placement. She tolerated the procedure well. A few hours after the procedure, patient developed new onset left upper extremity (LUE) weakness and was transferred to an academic tertiary medical center's intensive care unit (ICU) for a higher level of care. On examination, patient was comatose with a Glasgow Coma Scale score of 7. She was localizing to pain with her right upper extremity, had a flaccid LUE, and had flexion withdrawal to pain in her bilateral extremities with no cranial nerve palsies. An emergent non-contrast computer tomography (CT) was obtained. While in the ICU, patient exhibited 0/5 strength in her LUE and 2/5 strength in her left lower extremity (LLE). Two days post-event, her strength improved to 3/5 in the LUE and LLE. Patient returned to baseline four days post-event with supportive care and daily physical and occupational therapy. She was discharged from the hospital to subacute rehabilitation two weeks post-event.

Imaging Findings

Non-contrast CT of the brain showed right hemispheric sulcal effacement secondary to edema and subtle subarachnoid hyperdensity due to contrast leakage (Figure 1). Iodine-suppressed CT imaging showed a lack of persistence of the right subarachnoid hyperdensity, indicating the presence of contrast staining (Figure 2).

Discussion

Patient's left hemiparesis resolved four days post-event, which appears to be prolonged compared to other case reports. A plausible explanation for our patient's prolonged recovery time is that she has chronic kidney disease. Patient's renal dysfunction could have prolonged recovery time as the iodinated contrast is primarily renally excreted.

Teaching Point

Dual-energy CT should be used to diagnose CIE; it can distinguish between contrast and hemorrhage as the cause of the hyperdensity in the subarachnoid space. Magnetic Resonance Angiography and Magnetic Resonance Venography of the head provides a suitable alternative to CT angiography as part of the stroke workup in a patient with suspected CIE.

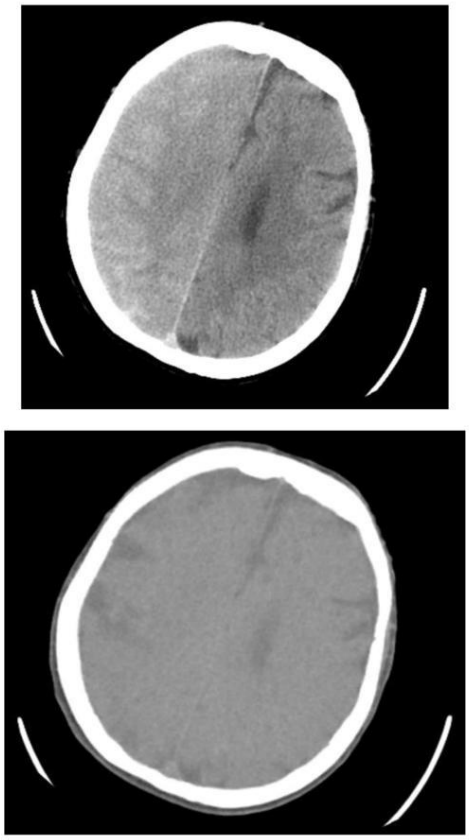

(Filename: TCT_269_0001.jpg)

1442

Disseminated Pilocytic Astrocytoma: Case Series

R Singh[1], A Ahmed[1], A Agarwal[1], S Sandhu[1], V Gupta[2], P Vibhute[1]

[1]Mayo Clinic, Jacksonville, FL, [2]Mayo Clinic Florida, Jacksonville, FL

Clinical History

This case series describes 23 biopsy confirmed Pilocytic Astrocytoma (PA) patients with radiologic evidence of Disseminated Pilocytic Astrocytoma (DPA). 13 (57%) were men and the median age at which their primary PA was detected was 18 years (Interquartile range (IQR): 5.5–28.5). Patient presentation varied based on the location of their tumor, with all but 2 exhibiting symptoms. At the time of detection of their primary tumor, 10 (44%) patients exhibited radiological evidence of spread. The remaining 13 (57%) patients had a median time to metastasis of 31 months (IQR: 6-76). 10 (44%) patients had a history of subtotal resections of their primary. After the detection of dissemination 15 (65%) patients underwent chemotherapy. The median duration of follow-up after the detection of metastasis was 48 months (IQR: 22-117.5). Dissemination was progressive in 15 (65%) patients, and 16 (70%) patients are presently alive.

Imaging Findings

Primary tumors were found in the hypothalamus 7 (30%), the posterior fossa 6 (26%), the spine 4 (17%), the cerebral 3 (13%), the midbrain/pineal region 2 (9%), and the thalamus 1 (4%). 18 patients had preoperative MRI images of their primary tumor at the time of detection of spread. Of these patients, 15 (83%) had primary tumors located near CSF, 9 (50%) exhibited a nodulocystic appearance, 5 (28%) a nodular/solid appearance, and 4 (22%) a cystic appearance. The median size of primary tumors at the time of detection was 33 mm (IQR 22.9-46.7). All 23 patients showed leptomeningeal spread, whereas 9 (39%) showed both subependymal and leptomeningeal spread. The most common pattern of spread was diffuse leptomeningeal dissemination to both the brain and spinal cord that was present in 15 (65%) patients.

Discussion

Due to the rarity of DPA, little is known about optimal screening and management techniques.[1][2] Our cases are consistent with the findings of other authors who have suggested that risk factors for DPA include subtotal resection of the primary tumor, the primary tumor being located near CSF, and a primary tumor located in the hypothalamus.[2][3] Further research is needed to determine if patients with these features could benefit from increased screening using contrast-enhanced MRI.

Teaching Point

DPA most often presents with diffuse involvement of both the brain and spine. A primary PA that was subtotally resected, located near CSF or in the hypothalamus may be more likely to undergo leptomeningeal dissemination.

Pt.	Age/Sex	Presenting Features	Location of Primary	Imaging Features (Primary)	Tumor Size (mm)	Treatment for Primary	Time to Metastasis (mths)	Location of Metastasis	Imaging Features (Secondary)	Treatment of Metastasis	F/U After Spread (mths) / Dead or Alive
1	30/M	Altered Mental Status	Hypothalamus	Mixed	18.1	STR	0	Diffuse Brain and Spine	Leptomeningeal	-	8 / Alive
2	35/M	Seizure	Posterior fossa	Solid	20.9	-	0	Diffuse Brain and Spine	Leptomeningeal	Trametinib	48 / Alive
3	3/F	Torticollis, Photophobia	Posterior fossa	Solid	32.3	STR, carboplatin, vincristine, STR, STR	31	Diffuse Brain and Spine	Leptomeningeal	Temozolomide, Vinblastine, Irinotecan, Bevacizumab	174 / Alive
4	26/F	Back Pain	Spine	Solid	50.2	STR	0	Spine	Leptomeningeal	STR, RT 5400 cGy,	66 / Alive
5	21/F	Amenorrhea, Galactorrhea	Hypothalamus	Mixed	29	RT 4500 cGy	0	Diffuse Brain and Spine	Leptomeningeal	STR, 4500 cGy, Temezolomide, Carboplatin, Avastin	195 / Alive
6	18/M	Optic Nerve Edema	Hypothalamus	Mixed	45.8	RT 5400 cGy	0	Diffuse Brain and Spine	Leptomeningeal	RT 5400 cGy	15 / Alive
7	18/M	Hypogonadism	Hypothalamus	Cystic	31	-	3	Diffuse Brain and Spine	Leptomeningeal Subependymal	RT 5040 cGy	37 / Alive
8	3/M	Difficulty Walking	Midbrain/Pineal	Mixed	18.4	-	6	Diffuse Brain and Spine	Leptomeningeal Subependymal	Vincritine/Carboplatin x2	27 / Alive
9	11/M	Seizure	Cerebral	Mixed	33.8	GTR	0	Midbrain, Tentorium	Leptomeningeal	-	120 / Alive
10	3/M	Asymptomatic	Posterior fossa	Mixed	16.2	GTR	6	Cerebellum, 4th Ventricle	Leptomeningeal	-	0 / Unknown
11	10/M	Headache	Cerebral	N/A	N/A	STR, GTR	19	Diffuse Brain and Spine	Leptomeningeal	Vincritine/Carboplatin x 7 cycles, RT 4500 cGy	153 / Alive
12	14/F	Asymptomatic	Midbrain/Pineal	Cystic	42.3	STR x3	61	Diffuse Brain	Leptomeningeal	Vincritine/Carboplatin	115 / Alive
13	3/F	Headache	Hypothalamus	Mixed	N/A	STR, Vinctistine, Etoposide, Cyclophosphamide, STR	5	Diffuse Brain and Spine	Leptomeningeal	5400 cGy to brain, 3600 cGy (spine), Etoposide, Cyclophosmpamide, Cytarabine, Temozolomide, Tamoxifen, A9952, Bevacizumab, Iriotecan, Vinblastine, Trametinib	267 / Dead
14	27/M	Headache	Posterior fossa	Mixed	47	STR x2, 5100 cGy x2	6	Diffuse Brain	Leptomeningeal Subependymal	Bevacizumab, Temozolomide, Lomustine,	47 / Dead
15	1/M	Abnormal Weight Gain	Hypothalamus	Cystic	29.2	-	0	Diffuse Brain and Spine	Leptomeningeal	Vincristine, Carboplatic, Vinblastine, Mirdametinib	36 / Alive
16	8/F	Headache	Posterior fossa	N/A	N/A	STR	195	Diffuse Brain and Spine	Leptomeningeal Subependymal	STR	77 / Alive
17	20/F	Lower Extremity Numbness	Spine	Mixed	105.6	STR	0	Diffuse Brain and Spine	Leptomeningeal	STR, 5900 cGy, Temezolomide	73 / Alive
18	31/F	Lower Extremity Numbness	Spine	Solid	18.8	STR, 2700 cGy, STR x 2, Temozolomide, Bevacizumab, 40 cGy, Lomustine, Palbociclib	90	Diffuse Brain and Spine	Leptomeningeal	3960 cGy to Spine, Palbociclib	12 / Dead
19	3/M	Seizure	Hypothalamus	N/A	N/A	STR x2, Cisplatin, Vincristine, STR	131	Diffuse Brain and Spine	Leptomeningeal Subependymal	1800 cGy to brain, 3600 cGy to brain, 3600 cGy brain, 480 cGy boost to spine, Tioguanine, Procarbazine, Lomustine, Vincristine	292 / Alive
20	41/F	Headache	Cerebral	N/A	N/A	STR, GTR	76	Diffuse Brain	Leptomeningeal Subependymal	STR, 5940 cgy, temozolomide, cisretinoic acid	86 / Dead
21	48/F	Difficulty Walking	Spine	Solid	106.8	STR, 5040 cGy, Temozolomide, Lomustine, ONC201, Bevacizumab	70	Diffuse Brain and Spine	Leptomeningeal Subependymal	-	0 / Dead
22	16/M	Difficulty Walking	Thalamus	Mixed	51	STRx3	0	Diffuse Brain	Leptomeningeal Subependymal	Bevacizumab, Irinotecan, Carboplatin, RT 5940 cGy, Temozolomide	40 / Dead
23	39/M	Headache	Posterior fossa	Mixed	38.38	STR	0	Diffuse Brain	Leptomeningeal Subependymal	5040 cGy, Bevacizumab	17 / Alive

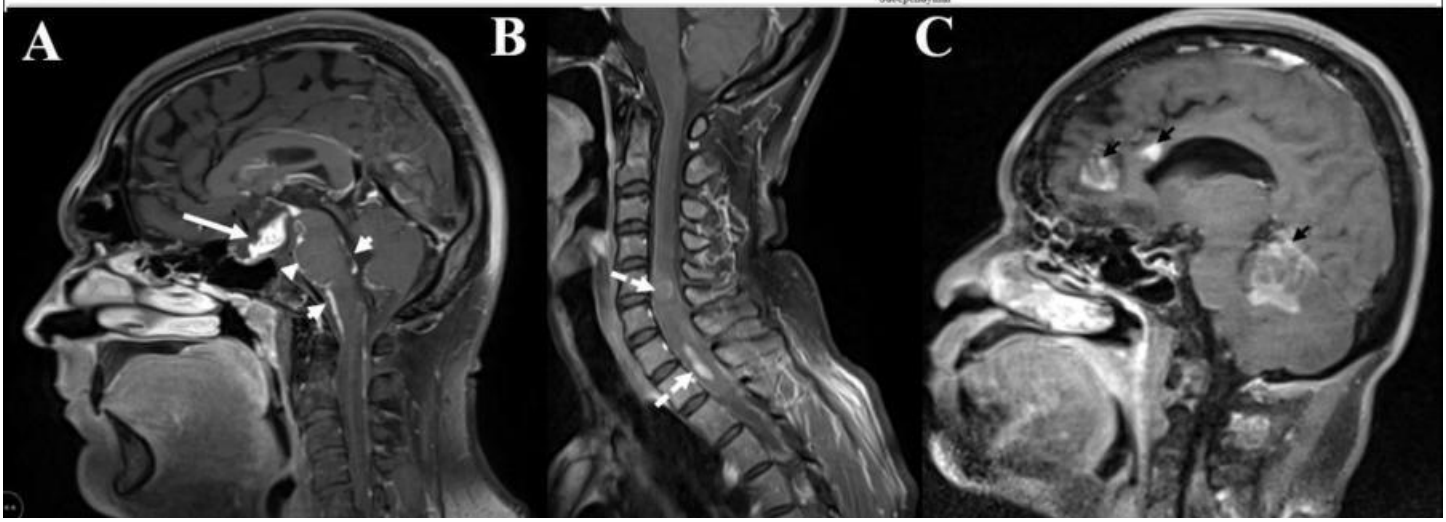

(Filename: TCT_1442_DPA_ASNR_Rb300.JPG)

685

Distal radial artery (snuffbox) access for carotid artery stenting using "Highway" Simmons 2 guiding catheter.

S Tadisetty[1], S Kokkula[2], A Guntamukkala[3], K Sajja[4]

[1]University of Kentucky, Lexington, KY, [2]Guntur medical college, Guntur, Andhra Pradesh, [3]Life hospital, Guntur, Andhra Pradesh, [4]Life hospital, Guntur, Guntur, CO

Clinical History

A 55-year-old male with a past medical history of diabetes mellitus, hypertension, and hyperlipidemia, came to the emergency department with transient right hemiparesis. On imaging, he was found to have a left ICA stenosis. The patient was anesthetized under local anesthesia. The distal radial artery (snuffbox) was used to access the ICA using 6F highway guiding Simmons 2 guide wire (DCGI approved and indigenously developed in India by GRK medical devices, Hyderabad), and a PRECISE PRO stent was deployed.

Imaging Findings

The stenting was successful; reperfusion was achieved in the left ICA with no post-procedure complications and reduced hospital stay than other conventional access.

Discussion

DRA access in the anatomical snuff box has similar safety and efficacy profile to the conventional transradial approach (3) with lower radial artery occlusions (2). The current literature also suggests that DRA has some additional advantages, including decreased time to hemostasis, decreased risk of hand ischemia, and excellent patient and operator comfort (2). When there is an acute angle between the

right common carotid artery and the right subclavian artery or between the innominate artery and the left common carotid artery, placing a 6 F straight guide sheath can be challenging (1). Using Simmons 2 guide catheters can overcome this barrier (1), but presently, there are significant limitations in the available technology due to a lack of devices specifically designed for this approach. Usage of indigenously developed highway Simmons 2 guide wire may exceed this limitation, especially in India.

Teaching Point

Usage of indigenously developed "Highway" Simmons 2 guide wire which is deployed using the DIstal radial access is advantageous and apt for a low economic setting.

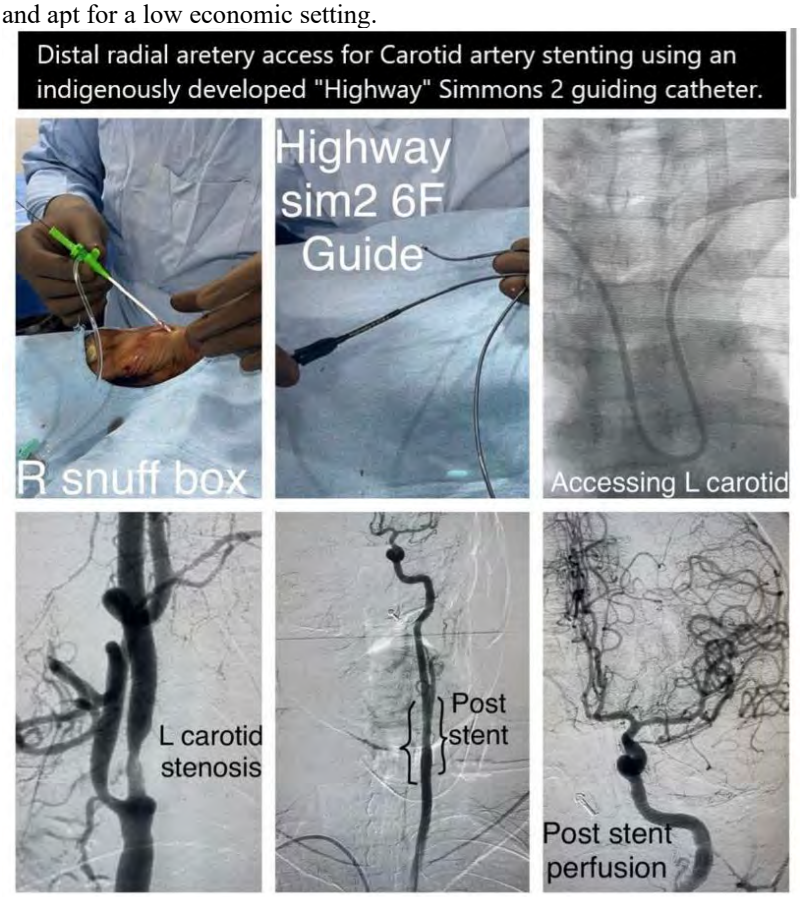

(Filename: TCT_685_DRA.jpg)

285

Don't Push Me Around: Parapharyngeal Pleomorphic Liposarcoma with Myxoid Features

R Rigsby[1], A Bhatt[1]

[1]Mayo Clinic, Jacksonville, FL

Clinical History

A 66-year-old female presented to her primary physician for routine care. Review of systems was positive for left facial swelling. Around the same time, the patient underwent an MRI of the cervical spine for chronic neck pain, which revealed a partially visualized left neck mass, prompting additional imaging. Biopsy revealed malignancy, and surgical pathology was consistent with grade 2 pleomorphic liposarcoma with myxoid features.

Imaging Findings

On presurgical MRI (Fig. 1), there is a large lobulated mass with internal septations centered in the left parapharyngeal space that is T1 hypointense, strongly T2 hyperintense, and homogeneously enhancing. There is lack of fat along the anteromedial margin of the mass, implying that it is arising from the parapharyngeal space itself, as opposed to arising from the parotid space and displacing parapharyngeal fat. There is a thin curvilinear intrinsically T1 hyperintense focus extending into the tumor from the anteromedial margin, representing fat within a septum.

Discussion

The parapharyngeal space is located at the center of the pharyngeal, carotid, parotid, and masticator spaces and contains fat, minor salivary gland rests, vessels, lymph nodes, and small branches of the trigeminal nerve. The most common pathology of the parapharyngeal space is direct spread of tumor or infection. The most common primary pathology is benign salivary tumors and benign nerve sheath tumors, such as pleomorphic adenomas and schwannomas. Salivary gland malignancies, lipomas, and soft tissue sarcomas are rare [1,2]. There are 13 cases of parapharyngeal liposarcoma reported in the literature, including well differentiated, dedifferentiated, myxoid, and pleomorphic subtypes [3]. The imaging features of these subtypes are thoroughly described in the musculoskeletal literature [4]. Pleomorphic liposarcoma has nonspecific imaging features, usually presenting as a rapidly growing

large well circumscribed mass, sometimes with infiltrative margins. Myxoid features, intratumoral hemorrhage, and necrosis are common. Macroscopic fat on MRI is present in 75% of cases but usually limited to small foci.
Teaching Point
It is important to recognize when a lesion arises from the parapharyngeal space as this determines the differential diagnoses and thereby dictates clinical decision making. On MRI, intratumoral fat can usually be identified in liposarcoma, even if it is just a small nodule or along a septum, which is the key to the correct diagnosis.

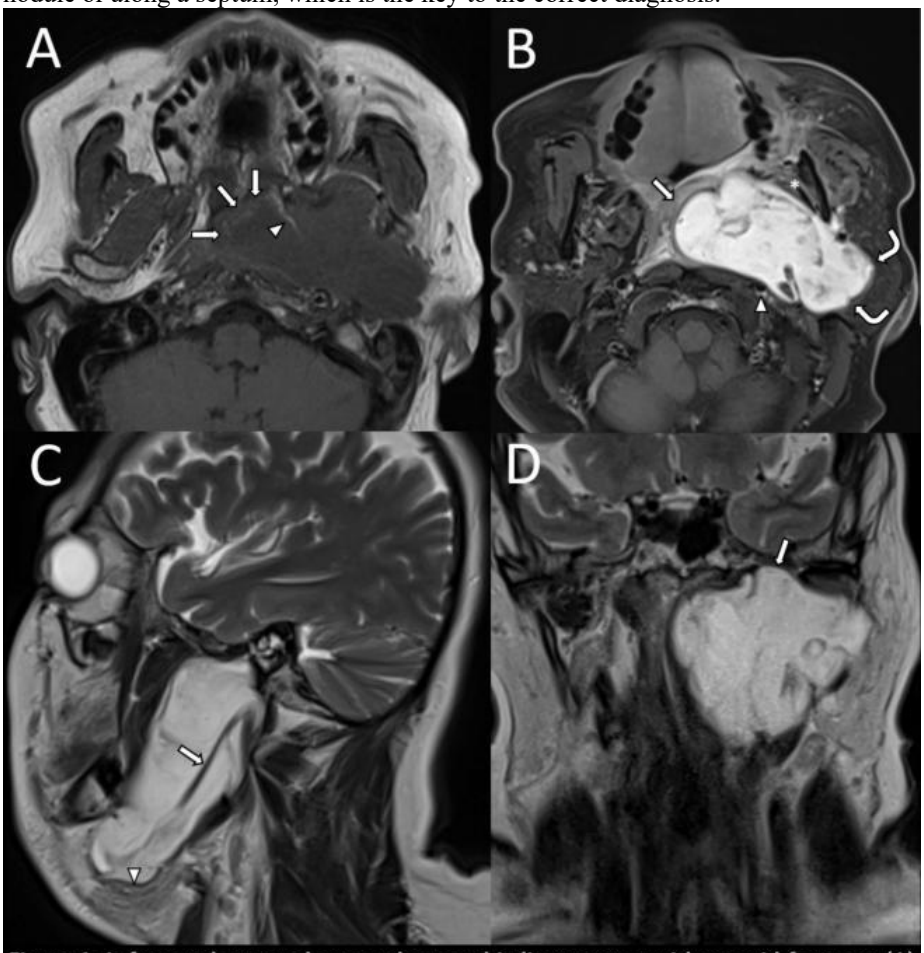

Figure 1: Left parapharyngeal space pleomorphic liposarcoma with myxoid features. (A) Axial T1-weighted non-contrast image at the level of the hard palate shows a large mass centered in the left parapharyngeal space. Note the relative lack of fat along the anteromedial border of the mass (arrows), implying that the mass is arising from the parapharyngeal space, not the parotid space. Notably, a small amount of fat along an intratumoral septum is present (arrowhead). (B) Axial T1-weighted fat-suppressed post-contrast image just inferior to (A) shows mass lobulations with diffuse enhancement and anteromedial displacement of the pharyngeal space (arrow), anterior displacement of the masticator space (asterisk), slight posterior displacement of the internal carotid artery (arrowhead), and abutment of the deep parotid gland (curved arrows), which was invaded on surgical pathology. (C) Sagittal T2-weighted image along the long axis of the mass demonstrates high signal of the mass with encasement of the stylohyoid ligament (arrow) and abutment of the left submandibular gland (arrowhead), which was not invaded on surgical pathology. (D) Coronal T1-weighted post-contrast image shows superior extension of the mass to the skull base at the level of the foramen ovale (arrow).

(Filename: TCT_285_Fig1.jpg)

346
Ecchordosis Physaliphora: A Case Report and Discussion
R Shinar[1], E Kuoy[1], E CHU[2], C Li[1], M Khan[1]
[1]University of California, Irvine, Orange, CA, [2]UNIVERSITY OF CALIFORNIA, IRVINE, ORANGE, CA

Clinical History
58-year-old female with tinnitus. IAC MR showed incidental prepontine lesion for which additional imaging was performed.
Imaging Findings
MR and CT showing a 16 mm prepontine cistern cystic lesion with peripheral DWI restriction and an osseous stalk.
Discussion
Ecchordosis physaliphora (EP) was first described in 1856 by pathologist von Luschka as ectopic notochord tissue near the posterior clivus. EP is typically incidental, asymptomatic, found in 2% of autopsies and less than 2% of MRs. It is a benign intradural congenital hamartomatous entity usually located along the dorsal clivus/prepontine cistern. The notochord is a mesodermal structure

along the ventral CNS forming during embryonic week 3, ultimately replaced by vertebrae, with the nucleus pulposus its physiologic remnant. EP is derived from ectopic notochord remnants and can be located anywhere along its axis. Classic EPs are well-defined cystic/peripherally sclerotic with a bony or soft tissue stalk and clival scalloping. MR is the preferred modality, typically T2 bright/T1 dark with variable DWI restriction, and dark relative to clival marrow. CT has lower sensitivity due to posterior fossa artifact and similarity to CSF. The main differential is chordoma, though there is controversy as to whether EP and intradural chordoma are separate entities. Wolfe advocates the term intradural chordoma for all intradural notochordal remnants. Rodriguez recommends use of EP for all these lesions until proven to be chordoma. At present, EP and chordoma remain separately classified. Unlike EP, chordomas typically enhance, tend to occur in older patients and are often symptomatic. Additional considerations include arachnoid cyst, dermoid/epidermoid cyst, metastases/myeloma, lymphoma, and other fibro-osseous lesions. Unlike classic EP, dermoid/epidermoids typically occur in the cerebellopontine angle and lack a stalk. Arachnoid cysts can occur anywhere intracranially, but retroclival location is uncommon. Moreover, they follow CSF on all sequences. EPs do not appear to grow, typically requiring no treatment. Symptomatic EP is uncommon; however, can occur related to mass effect. Intralesional hemorrhage has also been reported.
Teaching Point
EP is a benign congenital notochord remnant usually located along the dorsal clivus/prepontine cistern, typically incidentally discovered, asymptomatic, requiring no treatment. The main differential is intradural chordoma, though there is controversy as to whether they are separate entities.

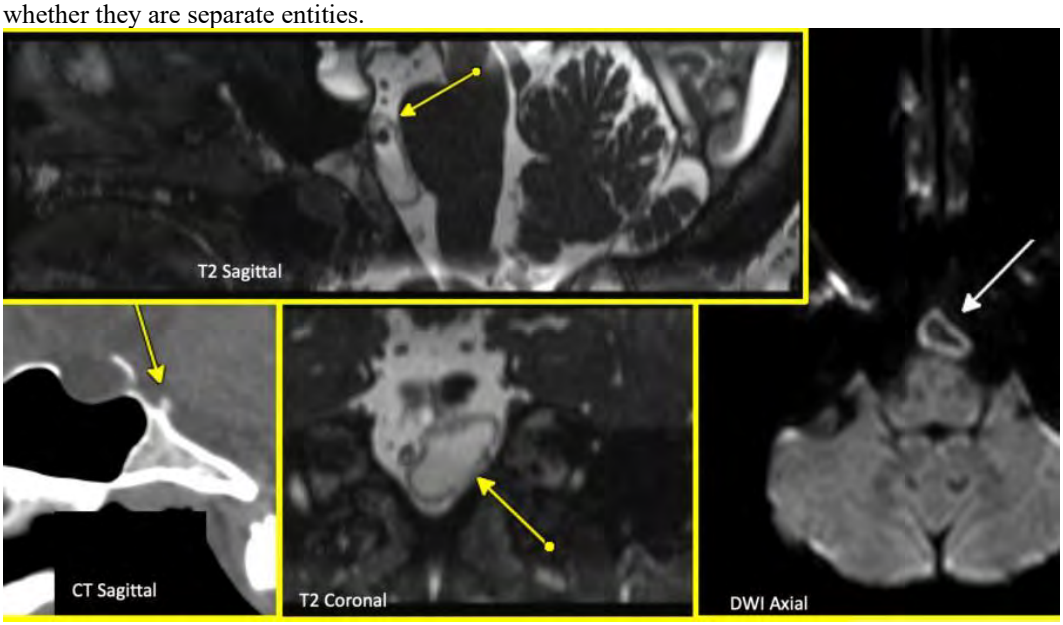

(Filename: TCT_346_EPimagescopy.jpg)

240
Ethylmalonic Encephalopathy, a Rare Primary Mitochondrial Metabolism Disorder
M Bergquist[1]
[1]*University of Wisconsin Hospitals and Clinics, Verona, WI*

Clinical History
A 6 year old with history of ethylmalonic encephalopathy secondary to an ETHE1 gene mutation status post deceased donor, orthotopic liver transplant five years prior presents with worsening flaccidity, cognitive decline, and respiratory failure ultimately requiring tracheostomy and ventilator dependence.
Imaging Findings
On MR, this patient had confluent, symmetric areas of increased signal on T2 FLAIR, diffusion restriction on DWI , and T1 hypointensity involving the periventricular and subcortical white matter in the bilateral cerebral hemispheres & cerebellum, entire corpus callosum, bilateral red nuclei, and basal ganglia, specifically the anterior commissure, caudate, and putamen. Single voxel MR spectroscopy (MRS) at intermediate TE of 144 ms in the centrum semiovale demonstrated a lactate peak, significantly elevated NAA, and elevated choline to creatine peaks.
Discussion
Ethylmalonic encephalopathy (EE) is a rare, autosomal recessive in-born error of mitochondrial metabolism. The ETHE1 gene mutation that causes this clinical phenotype is responsible for metabolizing hydrogen sulfide (H2S) and its failure results in elevated H2S inhibiting cytochrome c oxidase (COX) causing elevated lactate levels and mitochondrial dysfunction. The imaging appearance of ethylmalonic encephalopathy has significant overlap with other primary mitochondrial encephalopathies, such as Leigh syndrome and Kearns-Sayre syndrome, with symmetric signal abnormality in the deep grey matter, corpus callosum, and periventricular/juxtacortical deep white matter. The MRS findings in this patient were also typical of other primary mitochondrial disorders with failure of oxidative metabolism evidenced by the lactate peak and elevated choline relative to creatinine & elevated NAA suggesting myelinolysis and resultant cell membrane turnover. The clinical course of these patients is severe, progressive

neurological decline and treatment is typically focused on supportive measures, but liver transplantation has emerged as a viable therapeutic option to improve neurological outcomes in the short term.

Teaching Point

Although an infrequently encountered in-born error of primary mitochondrial metabolism, ethylmalonic encephalopathy MR and MRS spectroscopy imaging findings have significant overlap with other primary mitochondrial disorders.

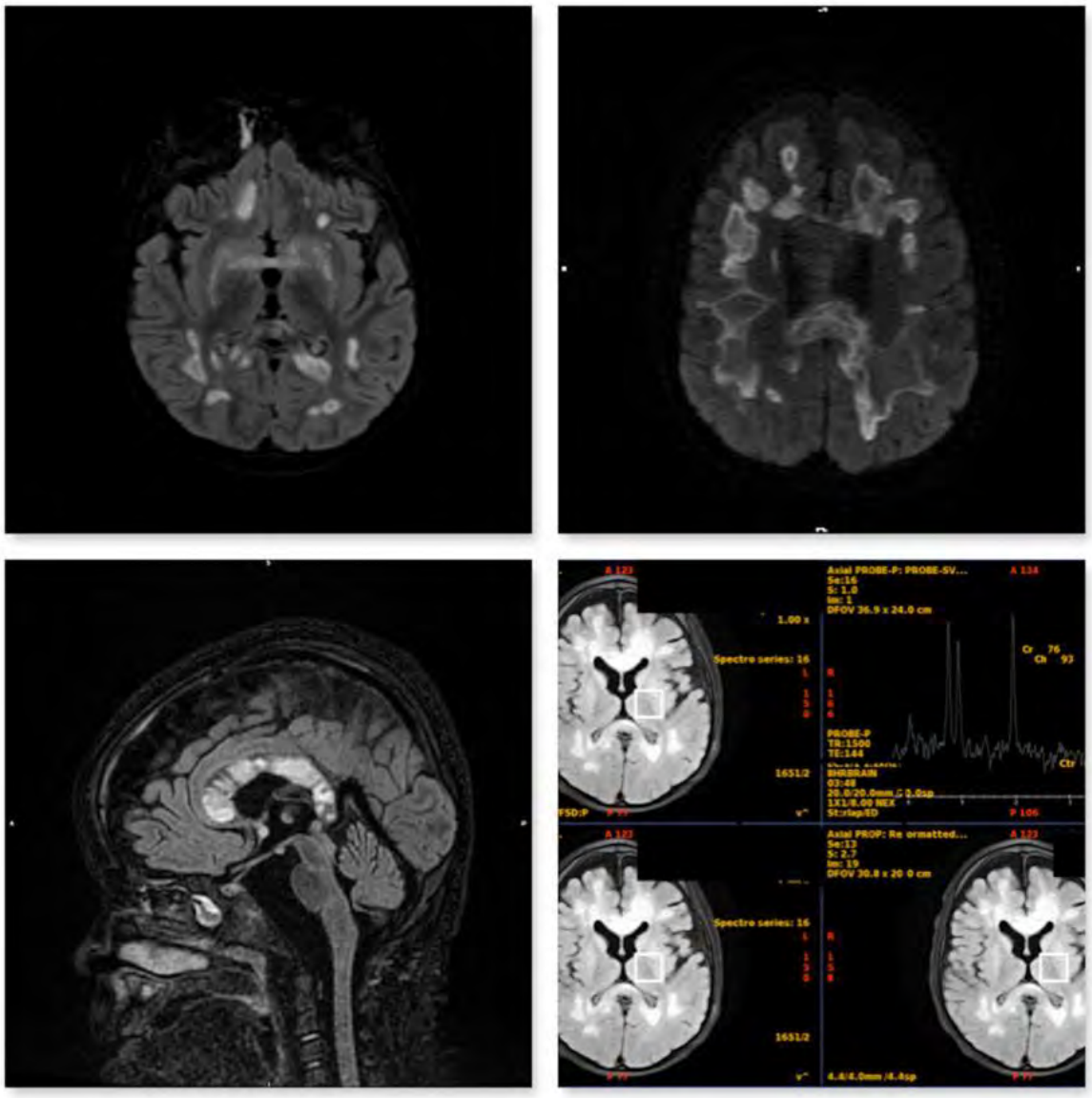

(Filename: TCT_240_Figures.jpg)

1060

Extensive Paravertebral Myonecrosis After Radiation Therapy and Gemcitabine Administration

M Moler[1], N Nagornaya[2]

[1]University of Miami/Jackson Health, Miami, FL, [2]Jackson Memorial Hospital/University of Miami, Miami, FL

Clinical History

A 76-year-old male with high grade pleomorphic leiomyosarcoma of the right thigh and extensive metastatic disease throughout the lumbar spine treated with radiation therapy and gemcitabine chemotherapy. He complained of intense bilateral hip and lumbosacral area pain radiating to both legs prompting imaging.

Imaging Findings

Widespread metastatic lesions preset throughout the lumbar spine within the vertebral bodies and posterior elements. Extensive areas of T2 hyperintense signal and irregular areas of non-enhancement involving the bilateral psoas muscles, the paravertebral muscles, and gluteus muscles.

Discussion

Radiation associated myonecrosis is a known complication of therapy, which results from direct and indirect effects of radiation. The inflammatory state from radiation therapy leads to fibrosis, arterial vasoconstriction, hypoxia, and death of surrounding tissue.

Gemcitabine is a known radiosensitizer, most likely by preferentially redistributing cells into S-phase and lowering the threshold for radiation induced apoptosis.
Teaching Point
Myonecrosis refers to infarction of muscle which is typically followed by tissue liquefaction. We present a rare case of extensive radiation myonecrosis of the paravertebral muscles associated with prior radiation treatment and gemcitabine administration. It is important for the radiologist to be familiar with the imaging appearance of this rare complication and be able to differentiate it from malignancy to help provide optimal patient care and management.

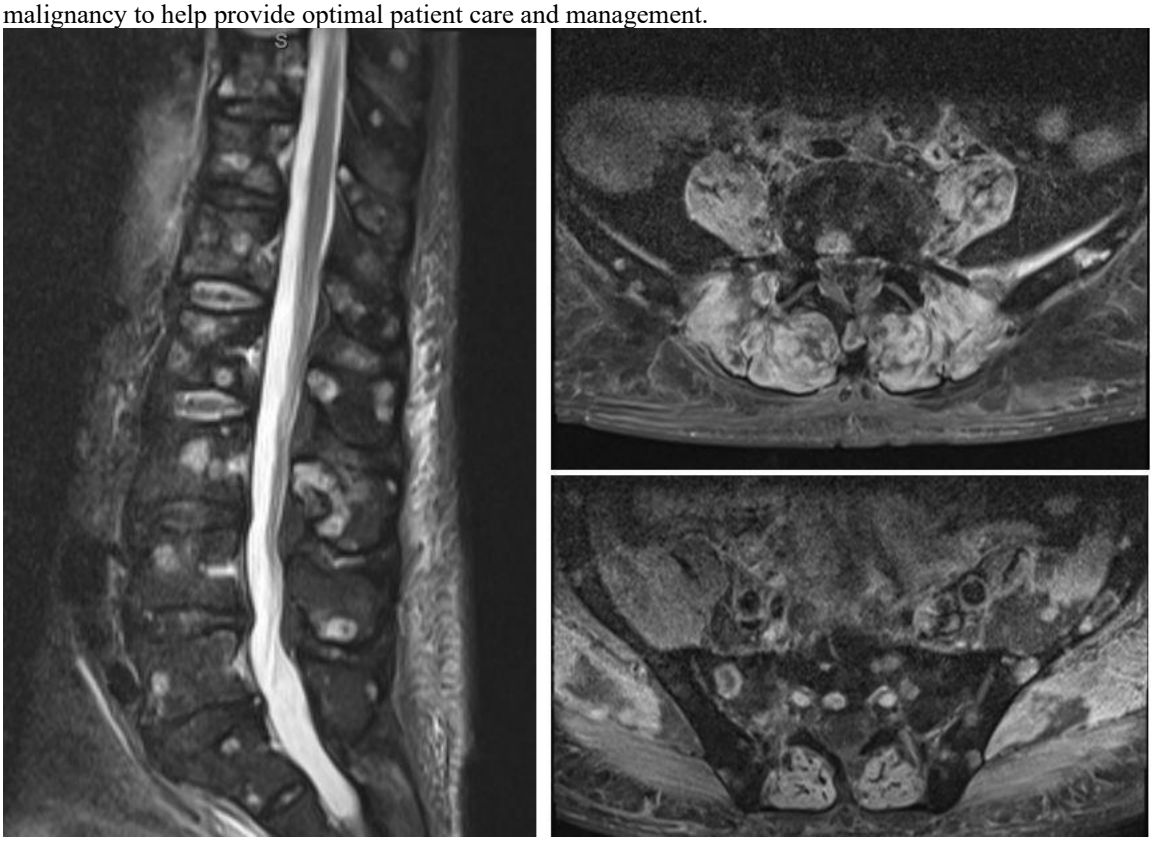

(Filename: TCT_1060_mynecrosis.JPG)

988

FMRI-Localized Motor Cortex Stimulation for Intractable Trigeminal Neuralgia: A Case Series

D Sloane[1], Z Khokhar[2], D Anderson[3], A Mallik[3]
[1]Loyola University Medical Center, Maywood, IL, [2]Loyola University, Maywood, IL, [3]Loyola University Medical Center - Strich School of Medicine, Maywood, IL

Clinical History
We present a case series of patients treated at Loyola University Medical Center for medically intractable trigeminal neuralgia (TN) to demonstrate the efficacy of functional magnetic resonance imaging (fMRI) in motor cortex stimulation (MCS). Patient 1 was a 54-year-old male who presented with axe-like pain in his forehead, with constant pain that started above the right eyebrow and extended down his face close to his jawline due to postherpetic TN. Patient 2 was a 62-year-old female who presented with daily upper and lower jaw pain with "zaps" up her right mouth and lateral nose caused by TN secondary to multiple sclerosis (MS).
Imaging Findings
Patients underwent fMRI to map the facial areas of the precentral gyrus. Activation maps were superimposed over anatomic images and provided to neurosurgery to guide subdural anchoring of electrodes and configuration of parameters to achieve maximal analgesia (Figure 1A-C). A proposed mechanism for MCS is presented in Figure 1D.
Discussion
This expands upon a previous case series at the same institution by Esfahani et al, in which 3 patients presented with postherpetic TN, trigeminal deafferentation pain, and trigeminal neuropathic pain (1). Analgesia gradually increased over the course of MCS in each of the patients in the previous case series, as well as in Patient 1. Persistence in analgesia in these patients may be due to alterations in stimulation settings when analgesia decreased. It may also be due to the use of fMRI localization. Patient 2 had persistent recurrent intractable facial pain despite frequent reprogramming, which is consistent with other case series discussing surgical treatment of TN secondary to MS (2-4).
Teaching Point
Motor cortex stimulation for medically intractable TN is an uncommon procedure and not widely discussed in the literature. A simple task-based fMRI motor paradigm increases surgeon confidence for MCS lead placement, resulting in a promising, often effective, treatment for patients with severe intractable pain failing to respond to other therapies.

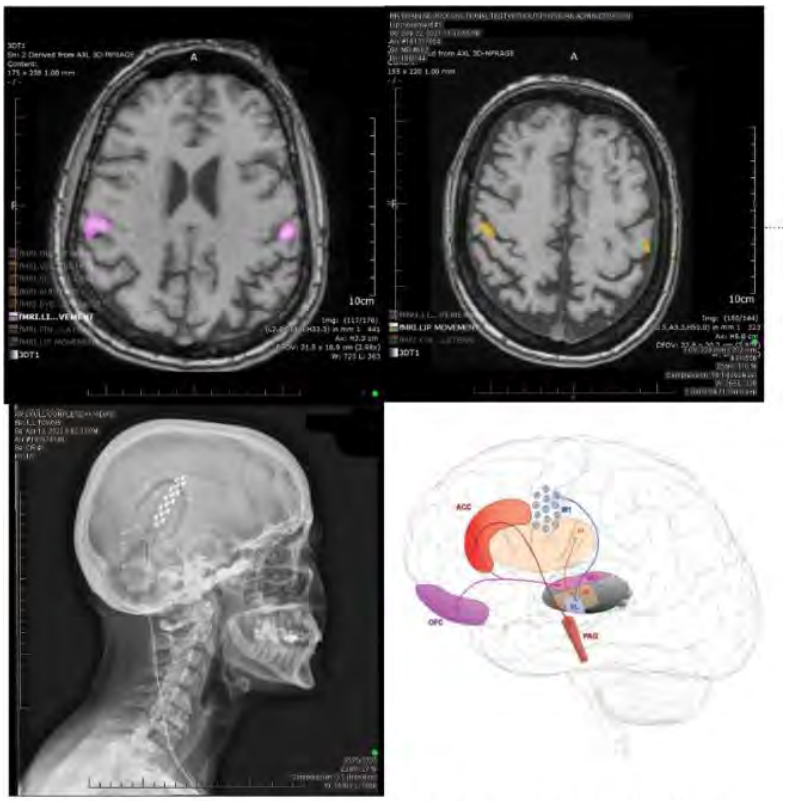

Figure: A Patient 1 Task based lip motor fMRI. B. Patient 2 lip motor fMRI C. Lateral radiograph demonstrates motor cortex stimulation electrode grid placement. D. Proposed substrate of MCS analgesia. Motor cortex stimulation (M1) inputs travel along afferents to the ventrolateral thalamus (VL). Nearby thalamic relays (ventromedial [VM] and mediodorsal [MD]) convey the signal to the OFC, ACC, and posterior insula (pI), each activated during MCS and associated with pain processing. The ACC in turn projects to the PAG, a region associated with analgesia. Modifed from Esfahani....Anderson et al. with permission.

(Filename: TCT_988_mcs_fig1.jpg)

545

Foreign-Body Granuloma after Trigeminal Microvascular Decompression

K Mani[1]

[1]*University Radiology, East Brunswick, NJ*

Clinical History

78 year-old woman with a history of right trigeminal neuralgia status post microvascular decompression in 2010, with new vestibular symptoms including dizziness, imbalance, vertigo and nausea.

Imaging Findings

CT temporal bone was performed demonstrating platelike mineralization within the right cerebellopontine (CP) angle extending across the porus acusticus (A and B, arrows). Post surgical changes after right retrosigmoid craniotomy can also be seen (arrowhead, A). Coronal image from an MRI IAC demonstrating platelike low signal in the CP angle cistern corresponding to the mineralization on CT (C, arrow). Axial image demonstrates thickening and lateral displacement of the cisternal 5th cranial nerve in the lateral prepontine cistern (D, arrow).

Discussion

Trigeminal neuralgia is a neuropathic pain condition in which people classically experience intermittent, electric-shock-like facial pain brought on by minor mechanical stimulation of the face. The most common etiology is vascular compression of the cisternal trigeminal nerve, often by the superior cerebellar artery (SCA), though the anterior inferior cerebellar artery (AICA), venous structures, and rarely aberrant posterior inferior cerebellar artery (PICA) and persistent trigeminal artery have also been implicated. Other etiologies include demyelinating diseases, CP angle tumors, and surgical injuries. First-line therapy is medical management usually with anticonvulsants, and microvascular decompression is an option in refractory cases. Foreign body (teflon, lintene) granulomatous reactions are a rare but known complication of trigeminal microvascular decompression. Patients often present with recurrent trigeminal neuralgia, but other cranial neuropathies, including sensorineural hearing loss, have also been described. MR imaging in cases of foreign body granuloma demonstrates a nodular or platelike, low signal structure in the lateral prepontine and/or

CP angle cistern adherent to, and often distorting, the cisternal trigeminal nerve. Contrast enhancement can be variably present, mimicking a tumor. By CT, foreign body granulomas typically appear as partially mineralized lesions.
Teaching Point
It is useful for Neuroradiologists to be aware of foreign body granulomas after trigeminal microvascular decompression, as they may be the first to suggest this entity given characteristic imaging appearance in the context of post surgical changes. This is particularly true in cases where the symptomatology may be atypical, as in our case.

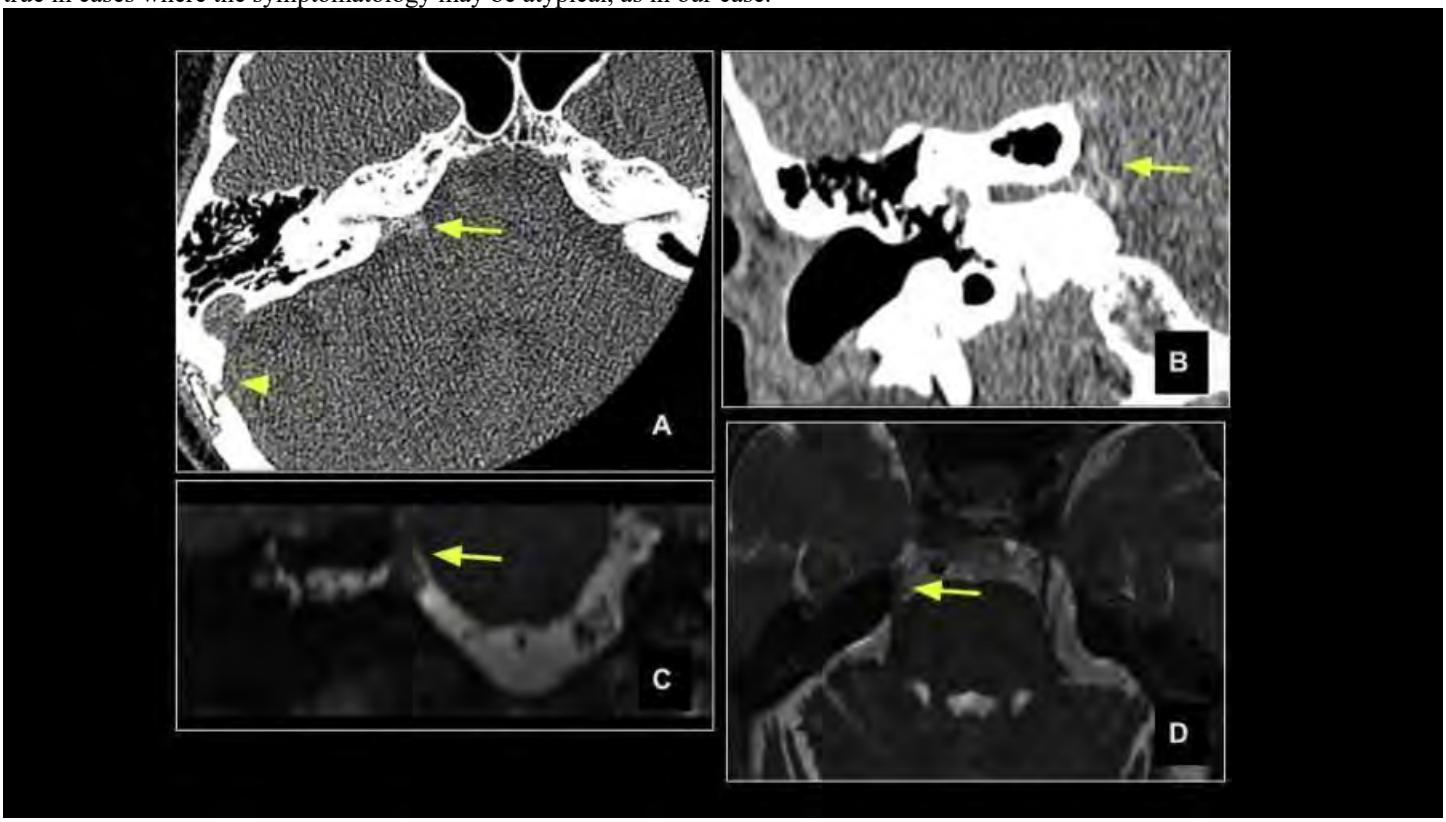

(Filename: TCT_545_TeflonGranuloma1.jpg)

1277
Fracture Erasure from Discitis Osteomyelitis after Traumatic Endplate Fracture: A Potentially Underrecognized Complication of Trauma in High-risk Patients
N Seto[1], A Frazzitta[2], A Bhandari[2], S Rogers[2]
[1]NYIT College of Osteopathic Medicine, Chandler, AZ, [2]University of Arizona, Tucson, AZ

Clinical History
We present a case of a 31 y/o male with history of IVDU, latent syphilis, and untreated HCV who presented after motor vehicle roll over. An acute L2 compression fracture was found on CT, as well as extremity, pelvic, sacral, and sternal fractures. He was afebrile with leukocytosis, thrombocytosis, and anemia and received 2 blood transfusions. Blood cultures remained negative. CT obtained 2 weeks later showed similar appearance of the L2 compression fracture. The patient underwent several orthopedic surgeries including femoral intramedullary nail and was discharged. 3 months later, he returned after ground level fall on L hip with complaints of low back pain and persistent R lower extremity weakness. He was afebrile and on PE showed R hip radiculopathy. Imaging was consistent with spondylodiscitis. CT-guided biopsy with cultures of disc aspiration were positive for MSSA, though blood cultures remained negative. He was subsequently treated with 6-week course of IV cefazolin with resolution of radiculopathy symptoms. Later on, hematology workup for thrombocytosis demonstrated abnormal SPEP, possible MGUS, reactive thrombocytosis, and ACD.
Imaging Findings
Select CT L-spine images obtained at initial presentation show L2 superior endplate compression fracture, similar on 2-week CT follow-up imaging. 3-month follow-up CT shows osseous erasure of the fracture with erosion and progressive vertebral body height loss, concerning for discitis osteomyelitis. MRI L-spine w/wo contrast images subsequently obtained confirm L1-L2 discitis osteomyelitis and demonstrate bilateral psoas abscesses.
Discussion
The development of discitis osteomyelitis after vertebral fracture is rare, only reported 21 times in the literature. The most common mechanism appears to be hematogenous seeding at the fracture site in individuals with predisposing conditions [1,2]. Only a minority of reported cases occurred after direct penetration and inoculation (e.g. ballistic or stab injury) [3]. Trauma may be under appreciated as a cause of spinal infection because the endplate fracture gets "erased" by the infection and may never be discovered. For those individuals with high-risk comorbidities, it may be prudent to provide closer clinical follow-up after vertebral fracture to allow for earlier diagnosis of subsequent discitis osteomyelitis and prevent associated complications.

Teaching Point
Patients with predisposing comorbidities may be at increased risk for discitis osteomyelitis after spinal trauma, and this may be underrecognized.

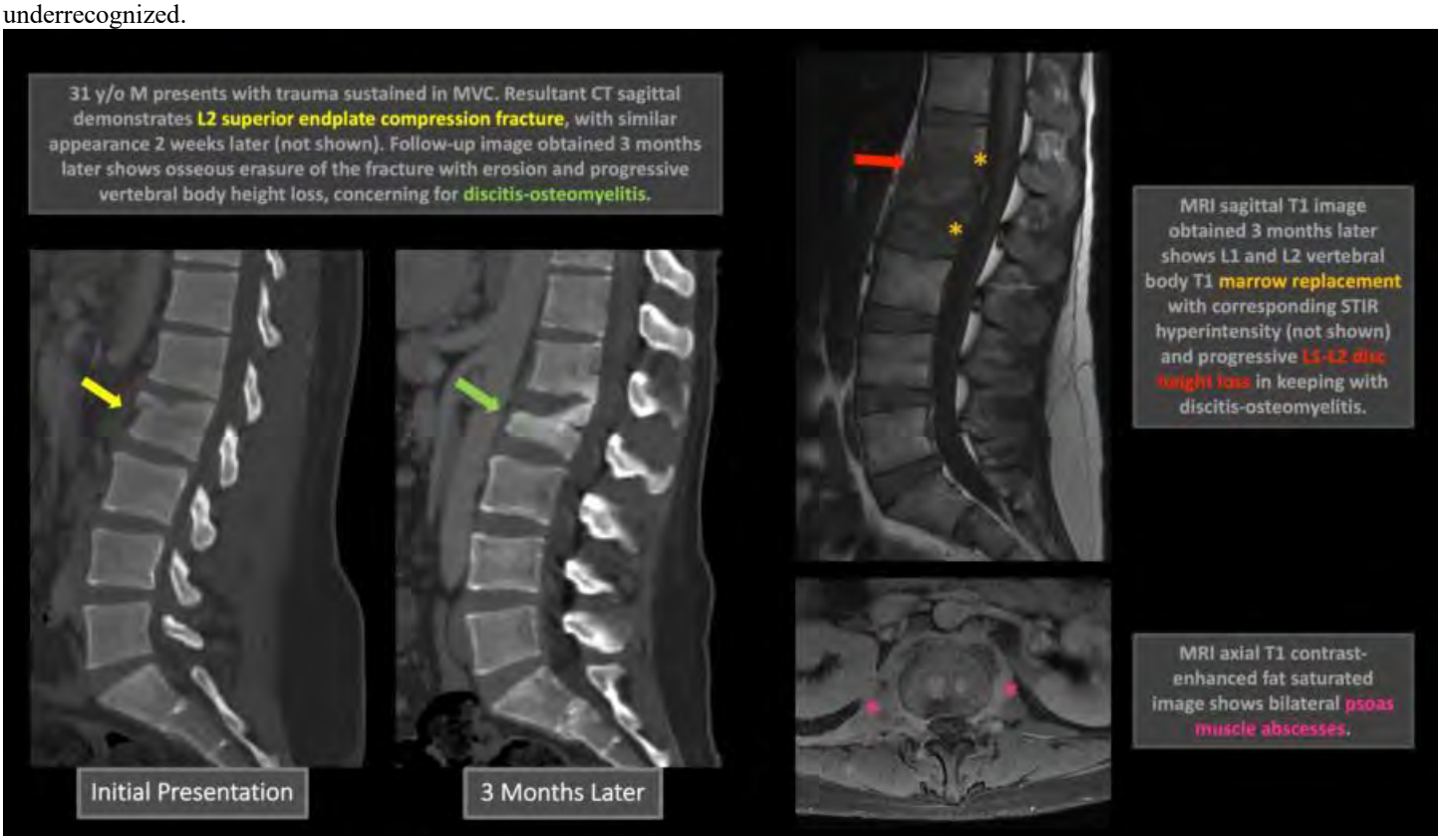

(Filename: TCT_1277_DiscitisFigure3.jpg)

585
Granulocytic sarcoma (Chloroma) presenting as subcutaneous masses of the face
W McLean[1], C Soto[2], R Gilbow[1], C Stevens[1], O Arevalo[1]
[1]LSU Health Shreveport, Shreveport, LA, [2]National University of Colombia, Shreveport, LA

Clinical History
57-year-old Caucasian Female presented with initial left eye and maxillary swelling that transitioned to bilateral swelling, and elevated WBC of 65K, recent 30-pound weight loss, and night sweats. Further work up demonstrated a Chronic Myelogenous Leukemia (CML).
Imaging Findings
Multiple confluent areas of T1 hypointensity and superimposed masslike enhancement and restricted diffusion are seen in the bilateral pre maxillary fat and periorbital subcutaneous soft tissues.
Discussion
Granulocytic Sarcoma or Myeloid Sarcoma can also be known as Chloroma is an extra-medullary manifestation commonly associated with AML or other myeloproliferative disorders. Differential diagnosis for facial swelling can be vast and includes some more common causes such as cardiovascular, respiratory, or infectious causes, as in this case the initial leading diagnosis was a facial abscess. Characteristic MR findings show either diffuse bone marrow infiltration or soft-tissue mass, with our findings having diffuse mass-like enhancement and restricted diffusion seen. Bilateral facial chloromas are rare findings, and in the setting of the laboratory findings shifted the differential from an infectious source to malignant cause. This case shows a rare case of diffuse bilateral periorbital and premaxillary extramedullary manifestations of myelogenous leukemia combined with clinical features helped to guide to diagnosis and management of the leukemia in this patient.
Teaching Point
Granulocytic Sarcoma (Chloroma) is a tumor-like collection of immature myeloid precursor cells, either in a patient previously known to have Acute Myeloid Leukemia (AML), as part of a blast transformation in a patient with Chronic Myeloid Leukemia (CML), or associated with other chronic myeloproliferative disorders.

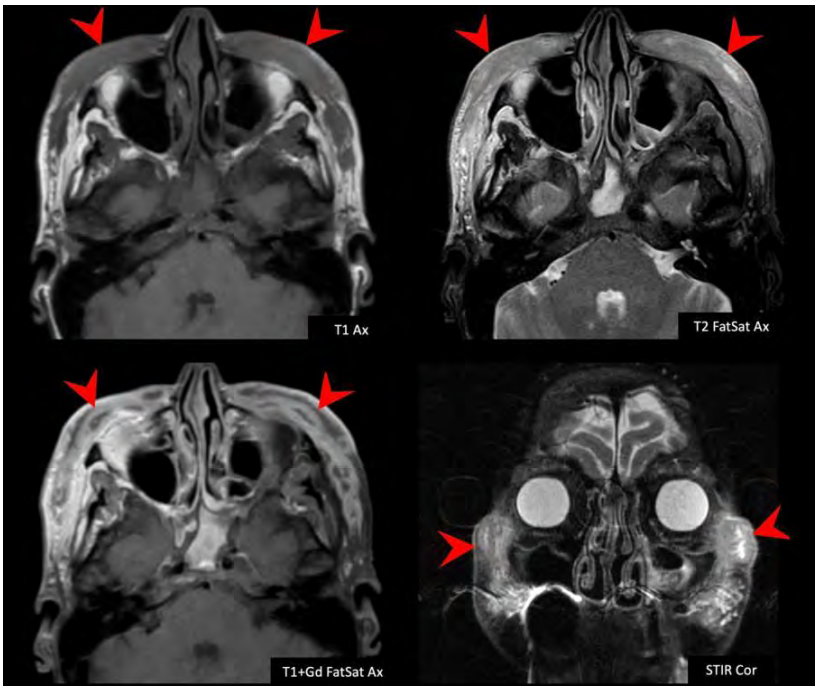

(Filename: TCT_585_Chloroma.jpg)

634

Having Fun with Foramina without Getting Lost. Aberrant Internal Carotid Artery: A Case-Based Pictorial Approach

I Yardimcioglu[1], A Saeed Bamashmos[2], G Cheraya[3], A Neupane[3]

[1]Yale New Haven Health - Bridgeport Hospital, Bridgeport, CT, [2]Yale New Haven Health Bridgeport Hospital, Bridgeport, CT, [3]Bridgeport Hospital, Bridgeport, CT

Clinical History

Case 1: 18 yo F with no PMHx presents with right-sided tinnitus. Case 2: 74 yo F with PMHx of paroxysmal atrial fibrillation comes in for stroke alert. Case 3: 40 yo F with PMHx of HTN presents with left ear fullness.

Imaging Findings

Case 1: Soft tissue mass on the right cochlear promontorium which elongates on reformatted images, consistent with aberrant ICA. Case 2: Right MCA M1 occlusion. Incidental bilateral aberrant ICA. Case 3: Left aberrant ICA extending through the middle ear. Enlarged left ascending pharyngeal artery. Asymmetrically enlarged left foramen of Vesalius which contains a left maxillary artery branch, consistent with an additional collateral supply to the cavernous left ICA. ACoA fenestration is noted incidentally.

Discussion

Aberrant ICA is a congenital vascular abnormality that occurs due to lack of normal development of the cervical ICA. Alternative blood flow theory emphasizes the aplasia of cervical ICA and the persistence of ascending pharyngeal arterial system which supplies blood flow into the horizontal portion of petrous ICA. The patients are usually asymptomatic. Imaging is essential prior to performing any invasive procedure. Temporal bone CT is often reliable and effective to reach an accurate diagnosis which reveals tubular structure running through the middle ear, absent carotid plate, and expanded inferior tympanic canal. Evaluation of the reformatted images is the key to differentiate it from glomus tumor by revealing the tubular configuration of the vessel. Additional findings include persistent stapedial artery, or persistent internal maxillary artery branches. CTA is not required for diagnosis; however, it provides greater vascular anatomic details and should be obtained if bone CT is equivocal. Contrast enhanced images demonstrate the aberrant ICA entering the skull base posterolaterally with focal narrowing of the transverse petrous ICA. Correctly identifying the aberrant ICA is important to avoid any potential consequences of invasive procedures. No surgical treatment is recommended.

Teaching Point

* Describe the clinical presentation. * Overview of ICA anatomy and embryology and key imaging features of aberrant ICA types. * Identify anatomical landmarks in reaching the diagnosis of aberrant ICA with focused highlight on related skull base foramina. * Distinguish aberrant ICA from the other common differential diagnoses to avoid iatrogenic catastrophic complications. * Summarize the role of different modalities in order to make a definite diagnosis.

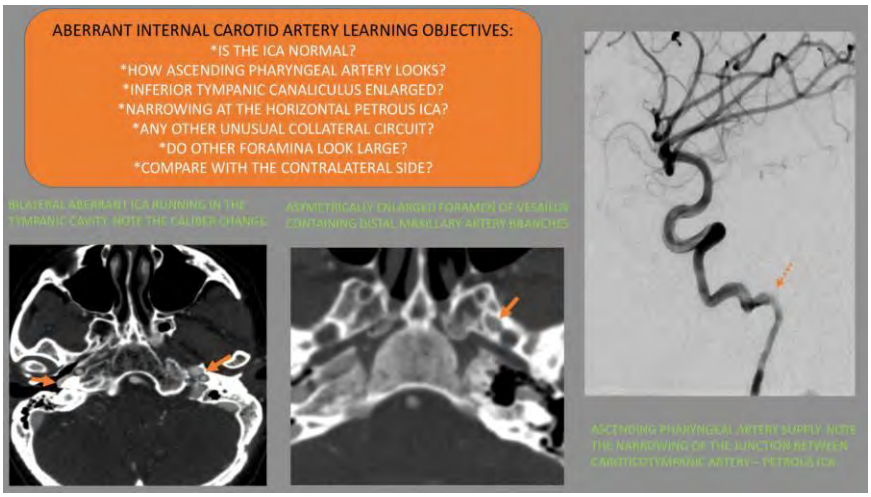

(Filename: TCT_634_ABERRANT-ICA-SINGLE.jpg)

170

Hippocampal Herniation in Over Shunting

G Wong[1], L Heier[2]
[1]University of South Florida Morsani, Tampa, FL, [2]Weill Cornell Medicine, New York, NY

Clinical History

Twenty years after a shunt placement, a 21-year-old male with a history of a Dandy-Walker malformation with hydrocephalus presented with a few months of intermittent memory and cognitive decline but not the typical postural headache seen in over shunting. Shortly after birth, he was treated with a nonprogrammable cystoperitoneal shunt due to hydrocephalus. Besides the memory and cognitive loss, there were no other neurological abnormalities.

Imaging Findings

MRI of the brain revealed marked bilateral central/uncal herniation with compression of the midbrain. Continued inferior displacement of the medial temporal lobes led to the bilateral hippocampi herniating through the tentorial apex resulting in a vertical orientation in lieu of their normal horizontal position and marked impingement.

Discussion

Over drainage from shunting is a common complication seen in the treatment of hydrocephalus that can manifest the multiple side effects of intracranial hypotension including central herniation, extra-axial hemorrhage, dorsal midbrain syndrome, and myelopathy. The condition classically presents with postural headache, which is associated with nausea, emesis, and irritability that is exacerbated in the upright position while alleviated in the supine position. The pathophysiology theorized is that the shunt removes excessive CSF creating a negative pressure gradient in the posterior fossa, leading to central and descending transtentorial herniation. This can cause varying clinical manifestations depending on the severity of herniation and compression of local structures, ranging from headaches and nerve palsies to hemiparesis and coma.

Teaching Point

Over shunting inducing hippocampal herniation has been documented in only a few case reports without featuring cognitive decline. Our patient did not present with symptoms characteristically seen as a result of chronic over drainage, but with memory difficulties that likely were attributable to the herniation and compression of the hippocampi. Shunt series did not demonstrate any evidence of malfunction. The shunt was revised with incorporation of a programmable valve and simultaneous intracranial pressure monitoring. Follow up CT 4 months later revealed a mild decrease in the bilateral uncal herniation with clinical improvement in memory.

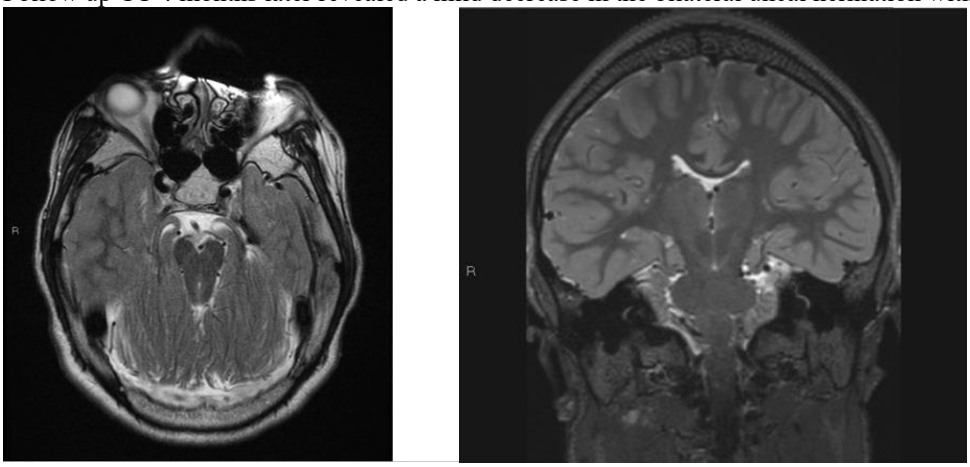
(Filename: TCT_170_Picture1.jpg)

546

HIV associated CD8+ T-lymphocyte Encephalitis

T Pomeranz[1], L Robinson[1], K Salzman[1], A Osborn[2]
[1]University of Utah, Salt Lake City, UT, [2]Univ. Utah Med. Ctr., Salt Lake City, UT

Clinical History

42 year HIV+ man on antiretroviral therapy (ART) for 9 years, with fluctuating confusion for 1 year and acute worsening of neurocoginitive symptoms/encephalopathy following a brief interruption of ART.

Imaging Findings

A: Axial FLAIR MR at presentation shows volume loss and progressive confluent white matter hyperintensity with new involvement of the subcortical u-fibers. B: Axial T1 post-contrast at presentation shows new perivascular enhancement with enlarged and enhancing medullary veins. C: H&E stain shows perivascular lymphoplasmacytic infiltrates. D: Lymphoplasmacytic perivascular infiltrates are composed of predominantly CD8 cells, as seen on CD8 stain.

Discussion

HIV associated CD8+ T-lymphocyte encephalitis is a severe inflammatory brain disorder characterized by perivascular and parenchymal lymphoplasmacytic infiltration, with predominance of CD8+ T-lymphocytes. It typically occurs in patients who are well controlled on ART and presents with acute/subacute cerebral deterioration. While the pathogenesis is unknown, IRIS, intercurrent infection, interruption of ART, and CSF HIV viral escape have all been proposed as triggers. Imaging findings are characterized by progressive non-enhancing white matter leukoencephalopathy, and linear perivascular enhancement. CNS lymphoma and vasculitis are the main differential considerations, and definitive diagnosis is made by brain biopsy or autopsy.

Teaching Point

Radiologists should recognize the distinct imaging characteristics of HIV associated CD8+ T-Lymphocyte Encephalitis, a progressive but treatable entity which responds well to prompt corticosteroid therapy +/- exchange of HAART. Untreated disease results in significant morbidity and mortality, progressing to coma and eventual death.

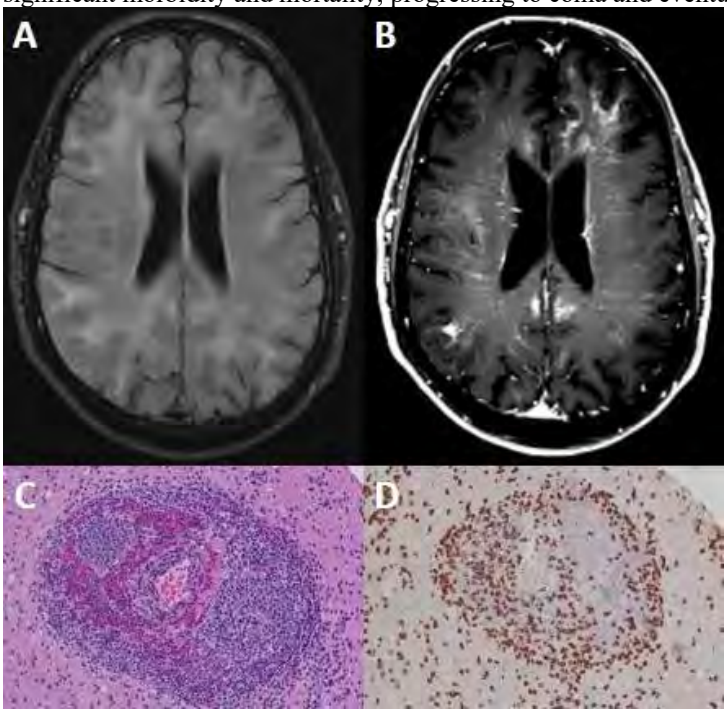

(Filename: TCT_546_HIVencephalitis.jpg)

455

How to Protocol Brain Imaging : For Beginners and Clinicians

G Harshe[1], D Patkar[1], M Verma[1], K Mundada[2], A Narang[1], G Ahuja[1]
[1]Nanavati max super speciality hospital, Mumbai, Maharashtra, [2]H.B.T. Medical college and Dr.R.N. Cooper Hospital, Mumbai, Maharashtra

Clinical History

The excerpta has 7 cases, each with a different presentation, signifying the importance of the protocol that we describe. The aim is to introduce and revisit disease specific simple protocols in brain imaging. Case 1: 71 year old female presented to emergency with acute right sided weakness. Case 2: 44 year old female presented with an episode of epilepsy (clinical opinion), with unknown previous history. Case 3: An 81 year old man presented with acute onset right sided weakness. Case 4: 40 yr old middle-age female presented with occipital headache for the past 7 days. Case 5: A 30 year old female with history of migraine presented with complaints of acute

onset headache. Case 6: 45-year old female presented with left side weakness. Case 7: COVID 19 positive patient, detected with Guillain Barre syndrome.

Imaging Findings

Case 1:Intra-arterial thrombus site was perceived on non-contrast MR angiography. Case 2: MRI brain was performed which revealed a large area of blooming on SWAN images with fluid debri level within the left temporal lobe. However, MRI contrast TRICKS with postcontrast T1 sequence was performed after assessing the patient. Case 3: multiple tuberculomas and associated tubercular meningitis. Case 4: 'Droopy Penis' sign along the posterior third of corpus callosum. Case 5: FIESTA revealed vertical tortuosity and perioptic halo as well as empty sella with stenosis at the lateral segments of transverse sinuses. Case 6: DW/ ADC, FLAIR, SWAN: no significant findings. MRA: Cut off of entire right MCA. According to institute protocol ASL performed. Case 7: In the localiser and c spine screening images, a predominantly T2 hyperintense mucosal thickening, fluid and soft tissue were identified in the right maxillary sinus. Following which protocol was changed.

Discussion

Following a certain protocol, in which each sequence is arranged one after the other to narrow down to one differential and rule out others, is usually important in most of the conditions. However, consciously assessing the medical condition and interacting with the treating physician or point of contact doctor is also an important skill especially in changing the protocol dynamic for eg : In stroke patients which have worsening condition or increasing agitation, MR angio can be performed early, after DW and ADC, as the sequence requires the patient to be stable.

Teaching Point

Teaching points have been described after each case, as we highlight how onsite radiologists can help in changing protocols after assessing doctors.

Basic brain	DW, ADC, SWAN, T2 and T1W and FLAIR	**Basic brain**	DW, ADC, SWAN, T2 and T1W and FLAIR
Stroke	DW ADC FLAIR SWAN Coronal diffusion – in case of brain stem infarct and doubtful cases If positive for infarct then -MR angiography(MRA) ASL / Contrast perfusion	Stroke	DW ADC FLAIR SWAN Coronal diffusion – in case of brain stem infarct and doubtful cases If positive for infarct then -MR angiography(MRA) ASL / Contrast perfusion
Intracranial bleed	SWI, DWI, ADC, T1W, FLAIR coronal (DW will have its inbuilt T2 sequence -If time permits you can do T2 weighted)	Intracranial bleed	SWI, DWI, ADC, T1W, FLAIR coronal (DW will have its inbuilt T2 sequence -If time permits you can do T2 weighted)
Hemorrhagic infarct	Additional MR venography(MRV)	Hemorrhagic infarct	Additional MR venography(MRV)
Vascular malformations including arteriovenous malformation, dural arteriovenous fistulas	Normal brain with additional Time -resolved imaging of contrast kinetics (TRICKS) which acquires dynamic images in arterial, capillary and venous phases, Postcontrast T1 weighted 3D sequence	Vascular malformations including arteriovenous malformation, dural arteriovenous fistulas	Normal brain with additional Time -resolved imaging of contrast kinetics (TRICKS) which acquires dynamic images in arterial, capillary and venous phases, Postcontrast T1 weighted 3D sequence
Known case of carcinoma in any part of the body	Basic brain sequences + Postcontrast T1W 3D sequence	Known case of carcinoma in any part of the body	Basic brain sequences + Postcontrast T1W 3D sequence
Epilepsy	Child: DW, ADC, SWAN, Coronal Cube FLAIR Coronal Inversion Recovery (IR) 2mm. T1 weighted BRAVO / SPGR, Arterial Spin Labelling(ASL)(to look for ictal or postictal changes) Adult: DW, ADC, SWAN, Coronal Cube FLAIR, T1 BRAVO / SPGR seq, ASL (recent episode of epilepsy)	Epilepsy	Child: DW, ADC, SWAN, Coronal Cube FLAIR Coronal Inversion Recovery (IR) 2mm. T1 weighted BRAVO / SPGR, Arterial Spin Labelling(ASL)(to look for ictal or postictal changes) Adult: DW, ADC, SWAN, Coronal Cube FLAIR, T1 BRAVO / SPGR seq, ASL (recent episode of epilepsy)

(Filename: TCT_455_FinalImage300.jpg)

1104

Idiopathic Acquired Nasal Cavity Encephalocele: Presentation & Management

A Bhatt[1], B Kelley[2], R Fouche[3], S Montoya[4]

[1]Vidant Medical Center, Cary, NC, [2]Eastern Carolina University, Brody School of Medicine, Greenville, NC, [3]ECUHMC, Wilson, NC, [4]Eastern Radiologists, Inc, Greenville, NC

Clinical History

A 46-year-old woman presented with altered mental status, several days of progressive headache and neck pain, and a long history of cough and nasal congestion unresponsive to over-the-counter treatment. CT head demonstrated right-sided sinusitis with possible right nasal cavity polyp, while lumbar puncture yielded cloudy, milk-like fluid, raising concern for meningitis secondary to obstructive nasal process. Targeted CT and MRI revealed a polypoid mass originating intracranially and extending into the nasal cavity with associated infectious/inflammatory changes, while bedside nasal endoscopy after right nasal cavity decongestion revealed a flesh-colored lesion extending medial to the middle meatus, suspected to be a tumor with skull base erosion or an encephalocele extending into the nasal cavity. After resolution of meningitis, an extradural craniofacial approach was used to resect the anterior skull base lesion.

Imaging Findings

Head and maxillofacial CT demonstrate bilateral paranasal sinus mild chronic inflammatory changes, and a 2.0 x 3.0 x 3.3 cm (RL x AP x CC) mildly heterogeneous expansile polypoid mass with possible mild central enhancement and bone defect (B in Figure 1g) at the adjacent right fovea ethmoidalis. MRI (Figure 1c, d, f, and g) confirmed moderate right frontoethmoid encephalocele and meningeal enhancement consistent with meningitis and superimposed congestion/reactive change.

Discussion

Nasal encephalocele is a rare condition in the adult population. The differential diagnosis for nasal obstruction includes schneiderian papilloma, antrochoanal polyp, angiofibroma, and, especially when the patient also presents with meningitis, encephalocele, squamous cell carcinoma, esthesioneuroblastoma, nasal lymphoma and rhabdomyosarcoma. Intranasal neoplastic processes may present very similarly to nasal encephalocele on clinical examination, nasal endoscopy, and even CT— the diagnosis was only confirmed by MRI. Although not present in this case, MRI may also identify associated CNS pathology including abscess, meningeal enhancement, neoplasm, Dandy-walker malformation, porencephaly, and encephalitis.

Teaching Point

Symptoms and clinical features of intranasal meningoencephalocele may mimic those of a nasal polyp. It is important to determine the type of basal meningoencephalocele present to plan surgical intervention. CT may help delineate the encephalocele sac and the precise position and extent of the cranial bone defect, while 3D CT is particularly useful in planning operative strategy.

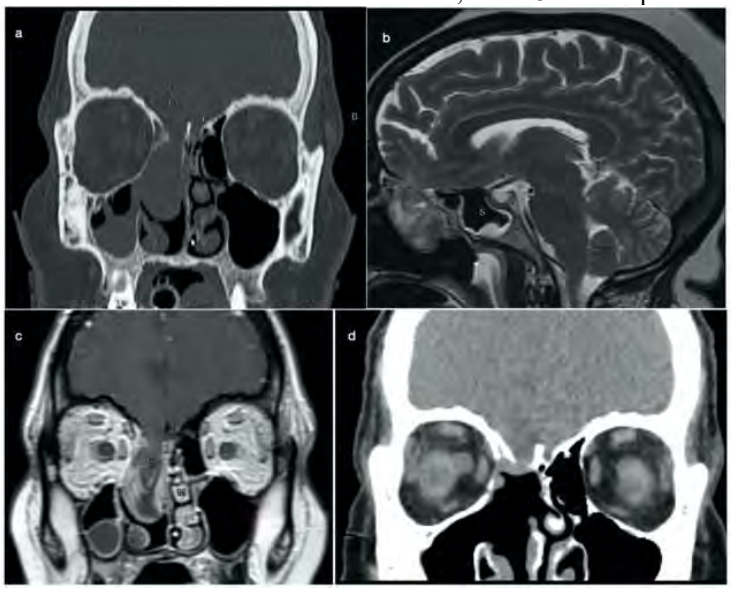

Figure 1: CT bone (*a*) demonstrating an erosion of the skull base, specifically the region of the cribriform plate along the floor of the anterior cranial fossa, as well as a severely downsloping olfactory plate (**C**) and a Type 3 olfactory fossa by the Keros classification: both congenital variants that may predispose to bony defects. T2 weighted MRI (*b*) demonstrates herniation of brain tissue though a defect in the floor of the anterior cranial fossa into the nasal cavity. T1 weighted MRI post-contrast (*c*) demonstrate the encephalocele with surrounding enhancing dura and mucosa; f also showing the encephalocele obstructing the middle meatus. Postoperative CT bone and sinus (*d*) shows the intruding tissue resected and reduced, supported by a Durepair inlay.

F = fovea ethmoidalis; **G** = gyrus rectus ± olfactory bulb; **C** = (line) usual course from the lateral lamella superior to the olfactory fossa to the cribriform plate to the cristae gallae overlaying CT to emphasize the anatomical variation predisposing to this condition; **M** = middle meatus (obliterated on other side); **S** = sphenoidal sinus; **B** = bony defect along medial portion of right-side cribriform plate

(Filename: TCT_1104_Encephalocelecase001.jpg)

968

Imaging Findings of Microcystic Meningiomas

J Cline[1], P Rajagopalan[2], T Wang[3], J Acharya[4]

[1]University of Southern California, Los Angeles, CA, [2]USC, Los Angeles, CA, [3]University of Southern California Keck School of Medicine, South Pasadena, CA, [4]Cedars Sinai Medical Center, Los Angeles, CA

Clinical History

A 56-year-old female presents with progressive headache without additional symptoms. No focal neurologic deficit on physical exam.

Imaging Findings

CT Head revealed a hypodense extra-axial mass without calcification (Figure 1). Subsequent MRI revealed a T1-weighted (T1W)

hypointense and T2-weighted (T2W) hyperintense dural-based mass (Figure 2). It demonstrated facilitated diffusion, peripheral and inhomogeneous internal contrast enhancement, and a prominent alanine peak on MR Spectroscopy (Figure 3).

Discussion

Findings of an extra-axial, well-circumscribed, dural-based mass with alanine peak on MR Spectroscopy suggest a meningioma. The combination of T2W hyperintensity and facilitated diffusion point toward microcystic meningioma. This lesion did not demonstrate the most classic pattern of peritumoral edema and homogenous contrast enhancement, but the peripheral and inhomogeneous internal contrast enhancement seen here has been described.

Teaching Point

• Microcystic meningiomas represent roughly 1.6% of intracranial meningiomas with similar clinical and epidemiological findings compared to classic meningiomas. • Microcysts represent prominence of the extracellular spaces within the meningioma accounting for the T2W hyperintensity on MRI. • Characteristic imaging findings include an extra-axial, dural-based T1W hypointense and T2W hyperintense mass with variable degree of homogenous enhancement and high incidence of peritumoral edema. Less commonly, heterogeneous enhancement may be secondary to interdigitation of enhancing tumor between microcysts. • Decreased apparent diffusion coefficients (ADC) have been shown to suggest higher grade tumor (Figure 4). • On MR Spectroscopy, creatine, choline, and alanine peaks suggest meningioma, but not a particular subtype. • Microcystic meningiomas are WHO Grade I tumors managed by resection. These are important to differentiate from WHO Grade II and III masses, which often require systemic and/or radiation therapy. • Differential diagnosis: WHO Grade I, II, or III meningioma, metastatic disease, solitary fibrous tumor of the dura, neurosarcoidosis, lymphoma with some additional lesions included depending on the location (Cerebellopontine angle mass)

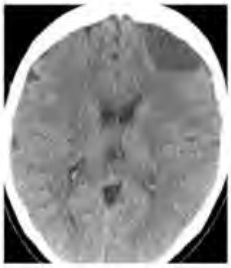

Figure 1. CT Head demonstrates hypodense mass convex to the brain parenchyma displacing white and grey matter.

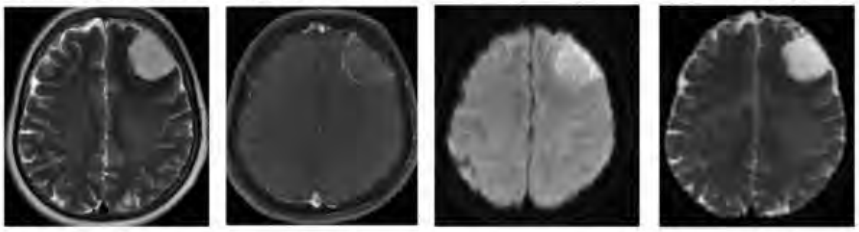

Figure 2. MRI Brain demonstrates T2W hyperintensity (first image), hyperintensity on both DWI and ADC likely due to T2 shine-through phenomenon, and mild heterogeneous contrast enhancement.

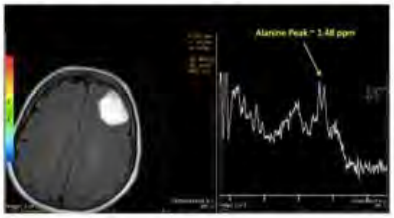

Figure 3. MR Spectroscopy with alanine peak at 1.48 ppm suggesting the mass represents a meningioma.

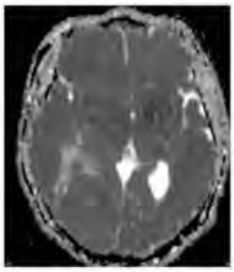

Figure 4. Diffusion Weighted Imaging can help to suggest higher grade tumor—demonstrating low ADC values in this WHO Grade II tumor (pathology diagnosis of Atypical Meningioma) with mass effect on the right occipital lobe.

(Filename: TCT_968_microcysticmeningiomafinalfigure.jpg)

964

Imaging Findings of Opiate Inhalation Toxicity

J Cline[1], S Ceglar[2], P Rajagopalan[3]

[1]University of Southern California, Los Angeles, CA, [2]Harbor-UCLA, Rolling Hills Estates, CA, [3]USC, Los Angeles, CA

Clinical History

A 42-year-old female with history of multiple substance use was found down and responded to Narcan. Patient had improved ventilatory function but was persistently altered. On arrival, the patient had alternating lateral gaze deviation and intermittent decerebrate posturing and was subsequently intubated for airway protection.

Imaging Findings

CT Head revealed large acute bilateral cerebellar hemisphere hypodensities in superior cerebellar artery distribution with findings concerning for cerebral edema (Figure 1). No large vessel occlusion was noted on CT Angiography. MRI Brain demonstrated non-enhancing T2W/FLAIR hyperintensity and diffusion restriction in the bilateral centrum semiovale, internal capsule, hippocampi, cerebellar hemispheres, and splenium of corpus callosum (Figure 2). Patient subsequently developed diffuse cerebral edema with cerebellar tonsillar herniation and resultant obstructive hydrocephalus.

Discussion

This case reflects the classic findings of heroin/opiate vapor inhalation injury: symmetric white matter lesions involving the cerebellum and posterior limb of the internal capsule with relative sparing of the anterior limb of the internal capsule. Corticospinal tracts were involved with sparing of the subcortical white matter.

Teaching Point

• Thought to be caused by impurity released during the process of heating the aluminum foil underneath the drug, classically associated with heroin • Clinical presentation has 3 stages: cerebellar signs and motor restlessness followed by pyramidal and pseudobulbar signs, and finally spasms, hypotonic paresis, and death • Characteristic imaging findings include symmetric white matter T2W FLAIR hyperintense lesions involving the cerebellum and posterior limb of the internal capsule • Relative sparing of the anterior limb of the internal capsule and subcortical white matter help to distinguish this toxicity from toluene toxicity and posterior reversible encephalopathy syndrome (PRES)

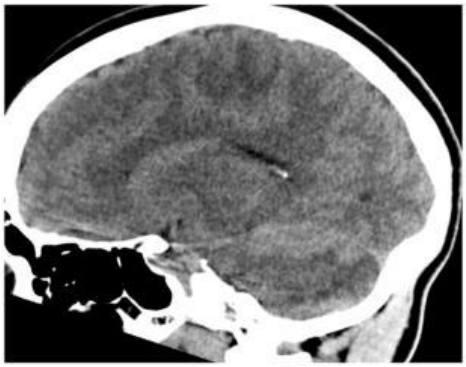

Figure 1. CT Head demonstrates accentuated grey-white differentiation in the cerebellum reflecting edema in the cerebellar white matter.

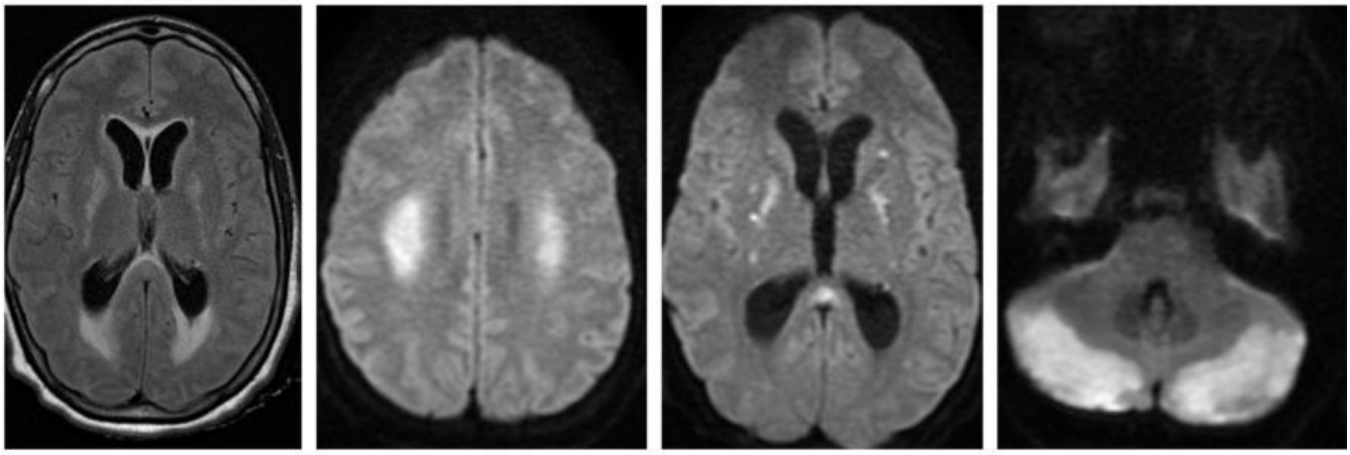

Figure 2. T2W FLAIR sequence (first image) demonstrates hyperintensity in the internal capsule with ventriculomegaly and juxtaventricular edema suggestive of transependymal flow of CSF. Diffusion restriction seen in the bilateral centrum semiovale, internal capsule and cerebellar hemispheres on DWI (subsequent images).

(Filename: TCT_964_toxicinhalationfigurefinal.jpg)

298

Indirect Carotid Cavernous Fistula presenting as Unilateral Opthalmoplegia

Z Izhar[1], J Shields[1]
[1]*University at Buffalo, Buffalo, NY*

Clinical History

70-year-old female with recently treated bacterial conjunctivitis presents with right opthalmoplegia.

Imaging Findings

Axial CT of the orbit at presentation demonstrates right sided proptosis, preseptal edema, inflammatory infiltration of the retrobulbar fat (rectangle). Additional axial CT image of the orbit at presentation demonstrates asymmetric enlargement of the right superior ophthalmic vein (arrow) and inflammatory infiltration of the retrobulbar fat. Axial CTA of the head at baseline demonstrates abnormal asymmetric opacification (arrow) of the right superior ophthalmic vein during arterial phase demonstrated by opacification of the basilar artery and cavernous portions of the ICA (rectangle). Contrast enhanced coronal reconstruction of the head and face demonstrates abnormal asymmetric opacification and prominence of the right superior ophthalmic vein (arrow) during arterial phase (circle). Additionally present is asymmetric enlargement of right sided extra-ocular muscles. Cerebral angiography confirms presence of an indirect carotid cavernous fistula (arrow) with shunting and early venous drainage to the right superior ophthalmic vein. Cerebral angiography demonstrates successful coil and onyx embolization (arrow) of the carotid-cavernous fistula with obliteration of early venous drainage in the ophthalmic vein.

Discussion

In our patient, baseline non-contrast CT of the orbit demonstrated unilateral propotosis, right sided preseptal edema and gross asymmetric enlargement of the right superior ophthalmic vein. A CCF or cavernous sinus thrombosis was suspected based on presenting image findings. Subsequent CTA imaging of the head demonstrated abnormal early arterial opacification of the superior ophthalmic vein. In conjunction with preseptal and post-septal inflammatory changes, a carotid cavernous fistula was now the leading diagnosis. Upon angiography, a dilated right ophthalmic vein with early venous drainage of the cavernous sinus into the ophthalmic vein was observed confirming the presence of an indirect carotid cavernous fistula.

Teaching Point

CCF symptoms vary based on etiology, size & location. CTA and catheter-based DSA are diagnostic tests of choice. Orbital proptosis, retrobulbar fat stranding, enlargement of extraocular muscles, venous engorgement and enhancement of an enlarged superior ophthalmic vein are typical findings. DSA confirms diagnosis when enlarged draining veins with retrograde flow from cavernous sinus most commonly into the ophthalmic vein are appreciated.

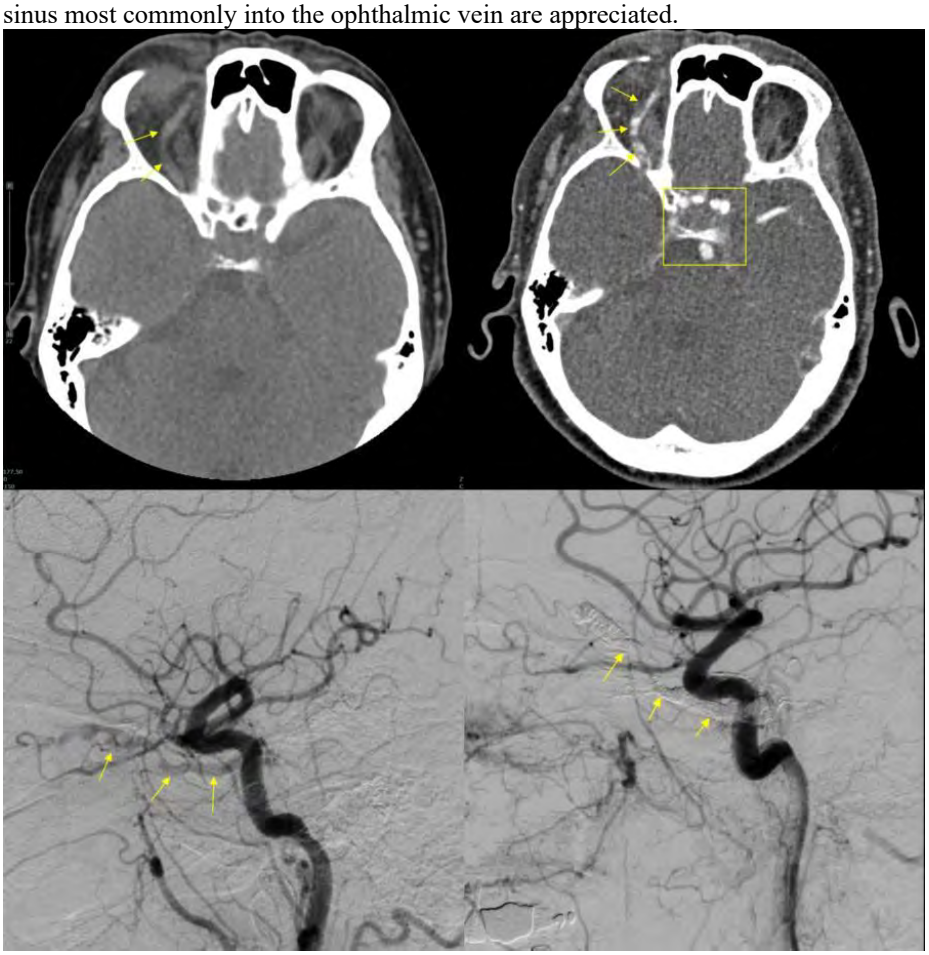

(Filename: TCT_298_CCF.jpg)

819

Infratentorial Progressive Multifocal Leukoencephalopathy Masquerading as an Infiltrative Glioma

P Rock[1], S Fung[1]
[1]Houston Methodist Hospital, Houston, TX

Clinical History

A 68-year-old man, with a history of pancytopenia, hypertension, hyperlipidemia, and remote heavy-alcohol use, presented with right lower extremity weakness, ataxia and dysarthria, worsening over the course of two days. He was undergoing treatment for iron deficiency anemia.

Imaging Findings

MR imaging of the brain was performed and revealed an abnormal infiltrating lesion centred in the right cerebellum with extension into the left cerebellum, vermis , pons, and midbrain. The lesion was hyperintense on T2 FLAIR sequences and showed scattered punctate areas of enhancement on T1 post contrast images. There was diffusely increased DWI signal of the right middle cerebellar peduncle and right cerebellar hemisphere corresponding to variably increased ADC from T2 shine through.

Discussion

The patient was admitted and a lumbar puncture was suggestive of demyelinating disease. A CT was performed and showed an area of wall thickening in the sigmoid colon, which was biopsied and shown to be invasive adenocarcinoma. The brain lesion was followed with serial MRIs over the course of the next week, over which time it extended into the left cerebellum and further into the pons. The patient underwent a right cerebellar biopsy. Immunohistochemical stains were performed and were reactive for both P53 and the BK virus. A bone marrow biopsy was performed and showed normal marrow and peripheral pancytopenia, thought secondary to chronic fecal occult blood loss. HIV antibody tests were nonreactive. The patient was started on pembrolizumab. He presented to the ER one month later with a colonic obstruction and underwent an uncomplicated colectomy. He continued pembrolizumab with six-month follow-up MR brain imaging showing good response.

Teaching Point

Progressive multifocal encephalopathy can present with a variety of imaging findings and in a variety of clinical contexts. Although most cases occur in immunocompromised patients and patients with HIV, PML can occur without any documented immunodeficiency. PML arises secondary to JC virus, or rarely BK virus, reactivation. PD-1 blockade with pembrolizumab has been shown to lower viral load and lead to clinical improvement in patients with PML. Demyelination in the setting of PML is most often observed supratentorially, less commonly infratentorially, and rarely in the brain stem. These lesions are often asymmetric. The differential includes: glioma, encephalitis, vasculitis, lymphoma, demyelinating disease, and paraneoplastic syndrome.

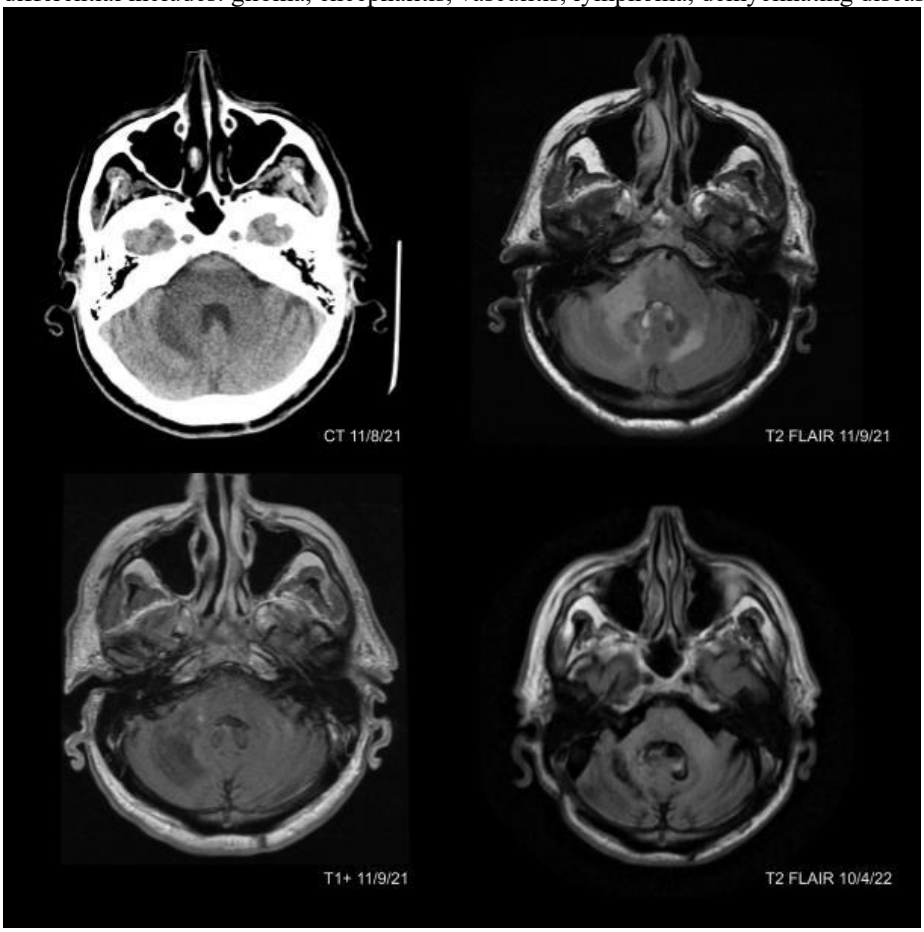

(Filename: TCT_819_asnr.jpg)

1090

Intracranial Germinoma Presenting With Bilateral Orbital Involvement: A Diagnostic Enigma

Y Sanchez-Padilla[1], S Stone[1], R WOLF[1], S MOHAN[1]
[1]Hospital of the University of Pennsylvania, Philadelphia, PA

Clinical History

32-year-old right-handed man with no significant past medical history, presented with sudden onset blurred vision in the left eye in the setting of COVID-19 infection. The patient noticed vision gap in right eye, described as a "black circle missing in the peripheral vision". Patient was evaluated by ophthalmology who noted papilledema on physical examination. Additional workup with lumbar puncture revealed: Cerebrospinal Fluid (CSF) pleiocytosis, lymphocytic predominance, positive oligoclonal bands, no clonal population and a negative cytology.

Imaging Findings

MRI of the brain and orbits was performed which demonstrated patchy enhancement of the bilateral (R>L) perioptic nerve sheaths (white arrows in A) with asymmetric enhancement along the right more than left posterior globes/sclera (black arrows in A) and right optic nerve head. B. Post-contrast Magnetization-Prepared Rapid Gradient Echo (MPRAGE) sequence at the level of the fourth ventricle demonstrated punctate enhancement along the anterior margin of the fourth ventricle (black arrow), as well as enhancement along the posterior fourth ventricle (white arrow). C. Post-Contrast MPRAGE demonstrates enhancement predominantly located around the anterior horn of right lateral ventricle, anterior septum pellucidum (arrow in C), right fornix, and right caudothalamic groove. D. Sections showed Sall4(+), OCT4(+), Ckit (+, membranous), HCG(-), AFP(-), and CD30(-) large neoplastic cells with clear cytoplasm and high nuclear to cytoplasmic ratio admixed with numerous lymphocytes.

Discussion

Patient underwent right frontal stereotactic brain biopsy and final pathology was consistent with germinoma. Primary intracranial germinomas are rare tumors that represent less than 5% of all intracranial neoplasms. Most intracranial germinomas arise from midline, with the sella/suprasellar and pineal regions being the most common locations. However, Germinomas can sometimes arise off midline, including the basal ganglia, thalamus, the ventricular system, and even the cerebral lobes, but orbital involvement is extremely rare. Prognosis is generally favorable, with some series reporting up to 90% overall survival at 10 years.

Teaching Point

Intracranial germinomas are rare tumors with predilection for specific anatomic locations within the brain. When occurring in atypical locations, the diagnosis can be extremely challenging. A combination of robust clinical, imaging, and pathologic data is critical for timely diagnosis and management of this neoplasm.

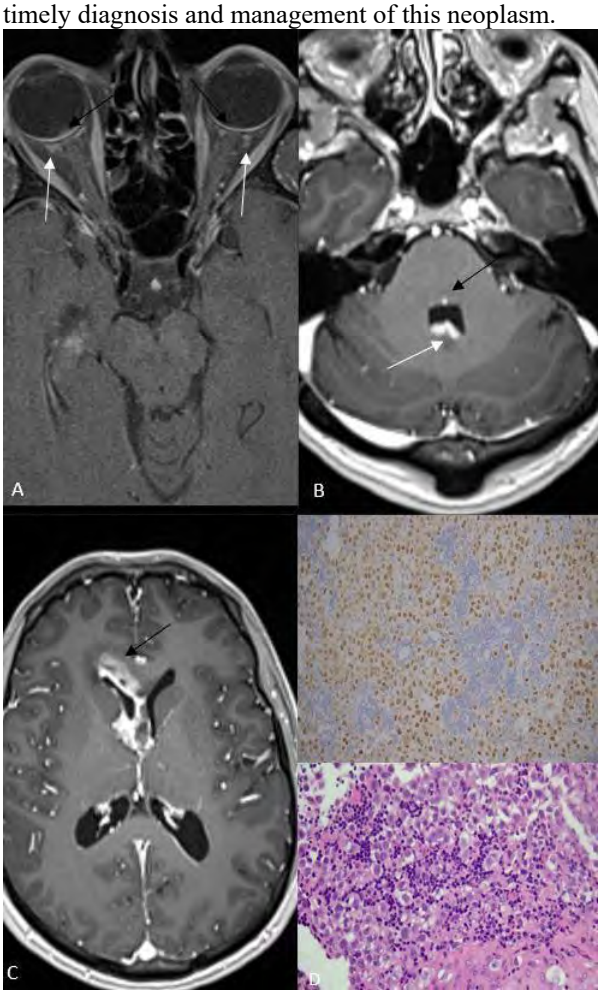

(Filename: TCT_1090_Germinomawithpath.JPG)

1219

Iron Infusion Confusion

K Riley[1], D Murphy[2], K Salzman[3]

[1]Indiana University School of Medicine, Indianapolis, IN, [2]University of Utah School of Medicine, South Salt Lake, UT, [3]University of Utah, Salt Lake City, UT

Clinical History

Patient 1: A 44-year female patient with a history of multiple sclerosis presented for a routine follow up brain MRI. One day prior to her appointment she had received an intravenous (IV) iron infusion for anemia. Patient 2: A 19-year-old female presented for brain MRI for dizziness and right sided hearing loss after an IV iron infusion the same day.

Imaging Findings

Brain MRI demonstrated marked susceptibility artifact involving the subarachnoid spaces and vasculature on susceptibility weighted (SWI) (A). Additionally, there was also pronounced intravascular T1 shortening on pre-contrast T1 sequences (B). A follow up MRI several months later demonstrated normalization of these findings (C).

Discussion

This case demonstrates the dramatic imaging findings seen in the setting of recent intravenous iron administration. Intravenous iron therapy results in extensive susceptibility artifact on SWI imaging and is a result of the T2* effects associated with intravenous iron administration and lack of a 180-degree refocusing pulse to compensate for these effects. This can also result in intravascular T1 shortening on 3D T1 inversion recovery gradient echo sequences such as MPRAGE and diminished enhancement on spin echo T1 weighted post gadolinium imaging. It is important to recognize the striking appearance associated with intravenous iron administration on brain MRI, particularly on susceptibility weighted sequences, to avoid confusion with an underlying pathologic process. In addition, recent IV iron administration may potentially mask the enhancement of pathologic brain lesions.

Teaching Point

Recent intravenous iron administration results in extensive artifact on brain MRI, particularly on susceptibility weighted sequences. It may also mask enhancement on T1 spin echo sequences following gadolinium administration. Knowledge of this phenomenon is important so as to not mistake these findings for underlying pathology.

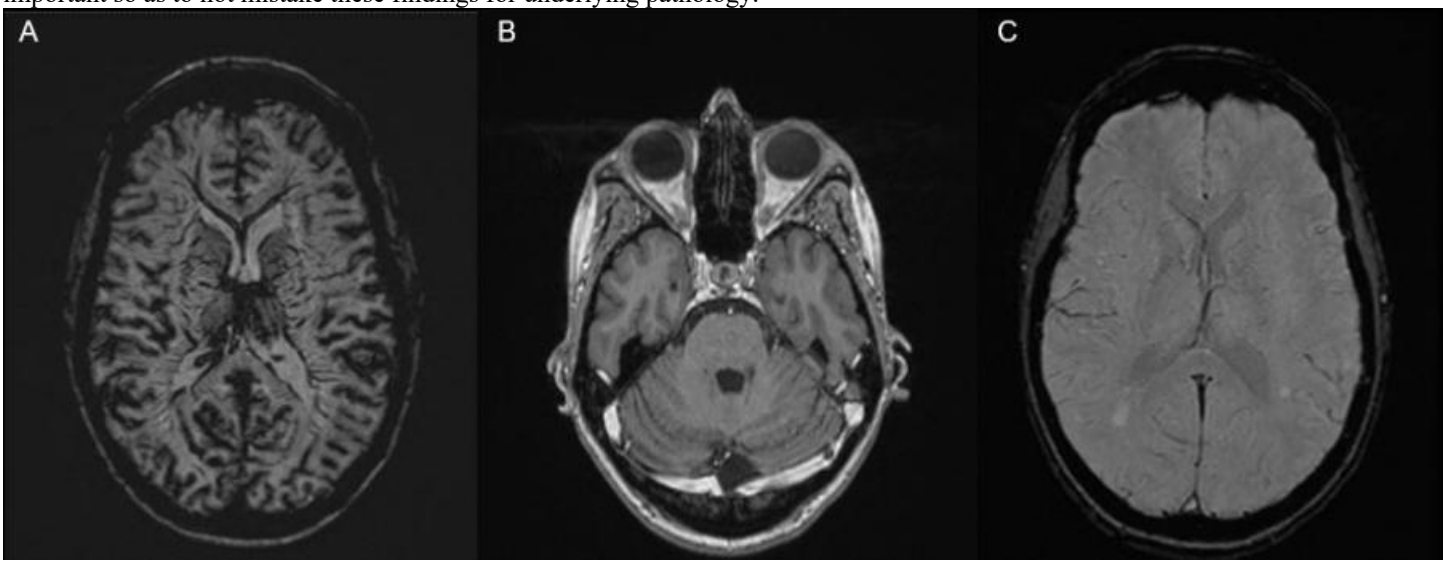

(Filename: TCT_1219_IronInfusionAbstractFigure.JPG)

899

Juvenile Xanthogranuloma: a Congenital Tumor in an Unusual Location

J Ormsby[1], H Vines[1], E Funsten[1]

[1]University of New Mexico, Albuquerque, NM

Clinical History

A young mother presented for a routine prenatal ultrasound. On the examination the baby was found to have severe third and lateral ventricular enlargement. This prompted the ordering of a fetal MRI of the brain for further evaluation. The MRI showed a questionable mass within the posterior fossa. At time of birth the newborn then received an MRI with and without contrast for further evaluation of the suspected mass. After confirmation of mass the patient was taken to the operating room for a suboccipital craniotomy for partial resection of tumor with pathology diagnosing it as a juvenile xanthogranuloma.

Imaging Findings

Fetal MRI shows a subtle mass within the posterior fossa with both cystic and solid portions. There is also obstructive hydrocephalus of the third and lateral ventricles secondary to the mass. Postnatal MRI better depicts the mass with diffuse enhancement of the solid portions along with slight decreased ADC compared to the adjacent brain parenchyma.

Discussion
Juvenile Xanthogranuloma is a rare tumor found in early childhood, with about 20% being present at the time of birth. This is most commonly seen within the skin, though has been reported in locations throughout the body including in the spine and head and neck region. while this has a high predilection for being within the dura it can also be found in the parenchyma such as our case where the tumor was within the cerebellum. Imaging features are nearly identical as descried in several papers with diffuse homogenous enhancement, decreased signal on T2-weighted imaging, and mild reduced diffusion compared to the brain parenchyma. The tumor is a non-Langerhans cell histiocytosis and diagnosis is confirmed on histology. The tumor is benign, however given location it can still present serious health issues.
Teaching Point
While this is a very rare tumor, the imaging characteristics of diffuse homogenous enhancement and mild reduced diffusion can help one feel more confident on diagnosing it as a juvenile xanthogranuloma. The decreased signal on T2-weighted imaging may also help to diagnosis this on fetal MRI.

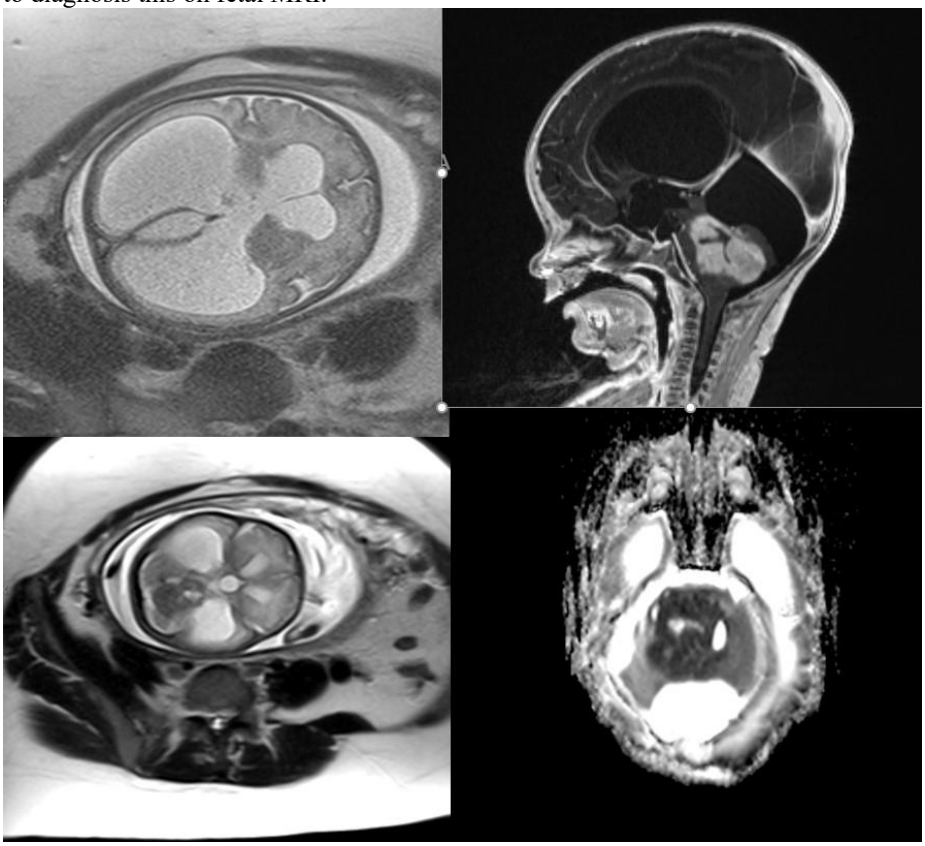

(Filename: TCT_899_JXGFinal.jpg)

708

Listeria Rhombencephalomyelitis Mimicking Neuromyelitis Optica: An Important Differential Diagnosis

J Yousef[1], A Weyer[2]
[1]UPMC, Pittsburgh, PA, [2]University of Pittsburgh, Pittsburgh, PA

Clinical History
A 79-year-old male presented with 3 weeks of left upper extremity weakness which progressed to involve the left lower extremity and then the right lower extremity. CSF analysis revealed neutrophilic pleocytosis and elevated protein but negative immunologic and infectious markers. Blood culture revealed Listeria monocytogenes. Despite appropriate antibiotic management, the patient's symptoms did not improve.
Imaging Findings
Spine MRI demonstrated long segment expansile T2 hyperintensity in the cervical and thoracic cord with peripheral enhancement. Brain MRI demonstrated abnormal enhancement, restricted diffusion, and T2 hyperintensity in the right cerebral peduncle, internal capsule, and corona radiata. The extent of these findings progressed over 2 weeks.
Discussion
The MRI findings of long segment T2 hyperintensity and rim enhancement in the cord concurrent with brainstem signal abnormalities are classically observed in neuromyelitis optica as well as MOG antibody-associated disease and autoimmune inflammatory demyelinating disease. However, these features are nonspecific, and neoplasm and infection are additional differential considerations. Listeria is an infection which classically manifests with rhombencephalitis, but the cord is rarely affected. Additionally, CSF analysis in neurolisteriosis may be nonspecific, which can delay diagnosis if this pathogen is not considered. Neurolisteriosis may progress

rapidly and mortality is high, so inclusion of this particular infection in the imaging differential diagnosis can improve the patient's clinical outcome.

Teaching Point

Concurrent signal abnormalities involving long segments of the spinal cord and brainstem are frequently observed with neuromyelitis optica. However, these features are nonspecific, and the differential diagnosis should include the rare but treatable infection Listeria.

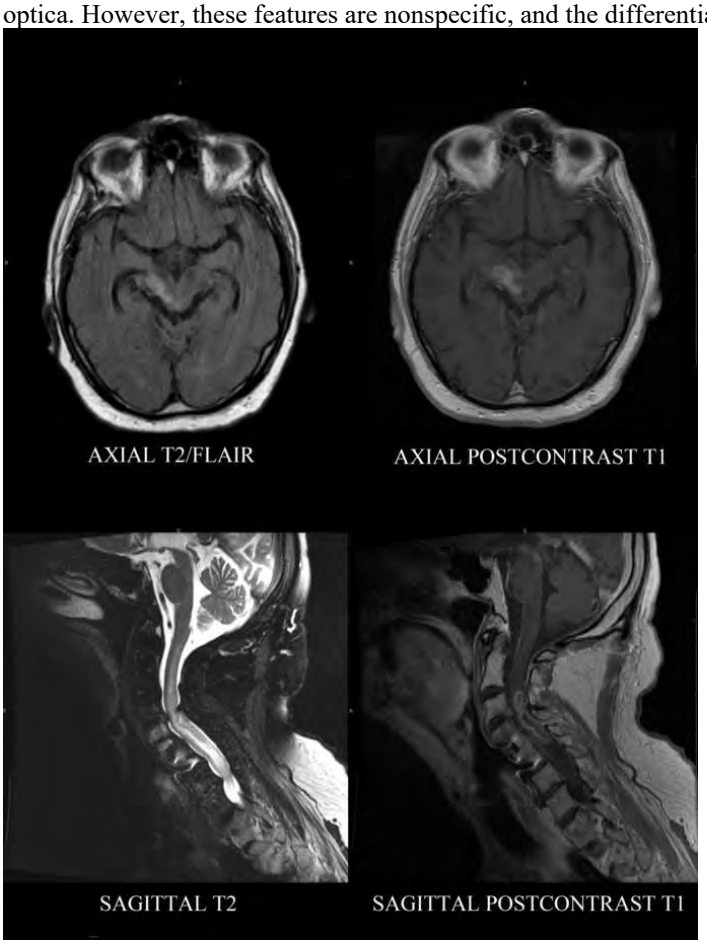

(Filename: TCT_708_LISTERIA1.jpg)

1296

Longitudinal Neurovascular and Vessel Wall Imaging Features in Patients with ACTA2 Mutations

R Brotman[1], N Yahyavi-Firouz-Abadi[2], D Paul[3], P RAGHAVAN[4], B Wasserman[5]

[1]University of Maryland, Baltimore, MD, [2]N/A, N/A, [3]University of Maryland Medical Center, Baltimore, MD, [4]UNIVERSITY OF MARYLAND SCHOOL OF MEDICINE, ELLICOTT CITY, MD, [5]University of Maryland School of Medicine, Baltimore, MD

Clinical History

We report longitudinal neurovascular findings and vessel wall imaging features in two patients with ACTA2 mutation undergoing serial imaging over a three year period. Patient 1, a 19-year-old female with a family history of ACTA2 mutation in mother (aortic dissection) and a sibling (intracranial stenosis status post bypass). Patient 2 is an asymptomatic 19-year-old male who presented with intermittent headaches for 2-3 years and carotid artery stenosis concerning for possible moyamoya disease.

Imaging Findings

Patient 1. Initial MRA showed classic broomstick appearance of the intracranial vessels with a patent intracranial ICA. She has moderate long-segment fusiform dilation of the right cavernous internal carotid artery (ICA) (Fig A) and severe focal stenosis of the communicating segment of the left ICA. Subsequent MRA (Fig B) and catheter angiography show progressive stenosis of the bilateral distal ICAs. Post-contrast black-blood images revealed probable mild abnormal vessel wall enhancement in the region of focal stenosis; however, interpretation is limited due to suboptimal acquisition parameters. Patient 2. Initial MRA (Fig C) showed bilateral supraclinoid ICA narrowing with associated focal eccentric wall thickening and enhancement (Fig D). Findings remained stable over three years of follow-up imaging.

Discussion

To our knowledge, this is the first report of longitudinal vessel wall imaging features in ACTA2 arteriopathy using black-blood MRI. In Patient 2, persistent focal vessel wall enhancement of the supraclinoid carotid in the region of stenosis was noted. Similar findings are suspected in Patient 1. While the precise cause of this vessel wall enhancement is unknown, it may be due to neovascularization (similar to intracranial FMD or moyamoya spectrum abnormality) or fibrosis as reported histopathologic features include thickening of the intima and massive intimal smooth muscle cell proliferation with increases in medial collagen and smooth muscle cells.

Teaching Point
- ACTA2 mutations demonstrate variable penetrance with heterogenous phenotype spectra and clinical/radiological courses. - ACTA2 arteriopathy can be a progressive disease with longitudinal studies showing worsening supraclinoid large vessel stenosis over time without development of basal collaterals. - Vessel wall imaging of at least one patient with ACTA2 arteriopathy demonstrated persistent vessel wall enhancement, despite stability of disease.

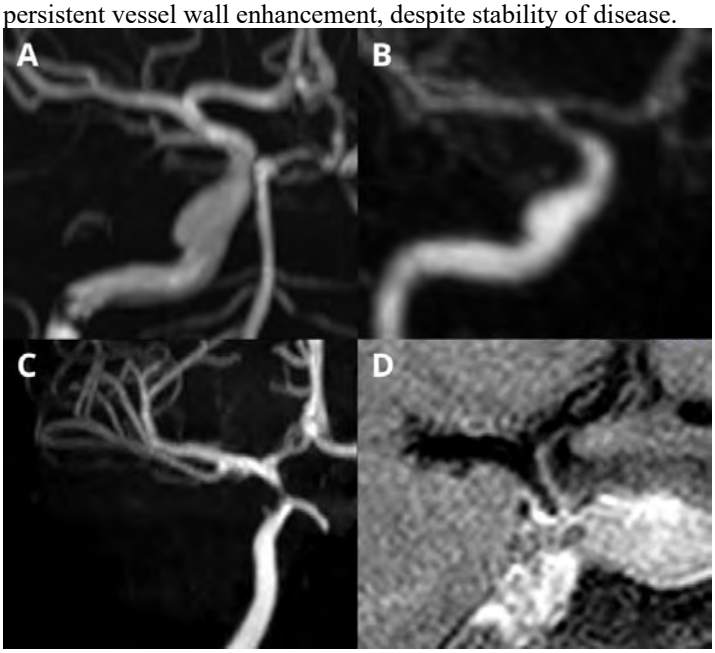

(Filename: TCT_1296_Myproject.jpg)

873

MRI Characteristics of a Tongue Hematoma and Lingual Artery Pseudoaneurysm Developed Following Outpatient Tooth Extraction

F Ahmed[1], M Koneru[2], R Garg[3], H Shaikh[3]
[1]Rowan School of Osteopathic Medicine, Voorhees, NJ, [2]Cooper Medical School of Rowan University, Camden, NJ, [3]Cooper University Health Care, Camden, NJ

Clinical History
A 61 year old female with history of atrial fibrillation on anticoagulation and hypertension underwent a tooth extraction. One week post-procedure, she presented with progressively worsening left-sided tongue pain and swelling. Oral Maxillofacial team initially discussed a needle biopsy of the tongue lesion given concerns for infection or tumor on magnetic resonance imaging (MRI). In contrast, the neuroradiologist on service identified it as a hematoma with lingual artery pseudoaneurysm. Immediate concern was blood in the oral cavity potentially causing fatal airway obstruction, prompting urgent endovascular intervention. The patient underwent successful liquid embolization with an uncomplicated postoperative course.
Imaging Findings
Axial computed tomography (CT) with contrast of neck showed a vascular-appearing, heterogenous 2.5cm lesion on left, ventral surface of the tongue (Fig 1). T1-weighted flair (Fig 2A) and T2-weighted (Fig 2B) axial MRI with contrast further characterized it as a vascular lesion with nodular enhancement, consistent with central pseudoaneurysm with surrounding hematoma. Onyx 18 (Medtronic, Minneapolis, MN) liquid embolization agent was injected into the left lingual artery, and repeat angiography over several months demonstrated pseudoaneurysm occlusion (Fig 3A-D).
Discussion
Pseudoaneurysms are rare lesions between vessel wall layers (1). They occur following trauma, such as after surgical procedures as seen in this case (2). MRI of these lesions may be misread as other similarly-appearing pathology by non-radiology teams, and understanding pseudoaneurysm imaging characteristics is essential for prompt identification and prevention of fatal rupture from surgical instrumentation. Prior treatment approaches included plugs, coils, and surgical repair (1-2). This case used a novel liquid embolic agent.
Teaching Point
MRI characteristics of head and neck hematomas and pseudoaneurysms are important to understand for identification and prevention of unnecessary and potentially lethal surgical instrumentation.

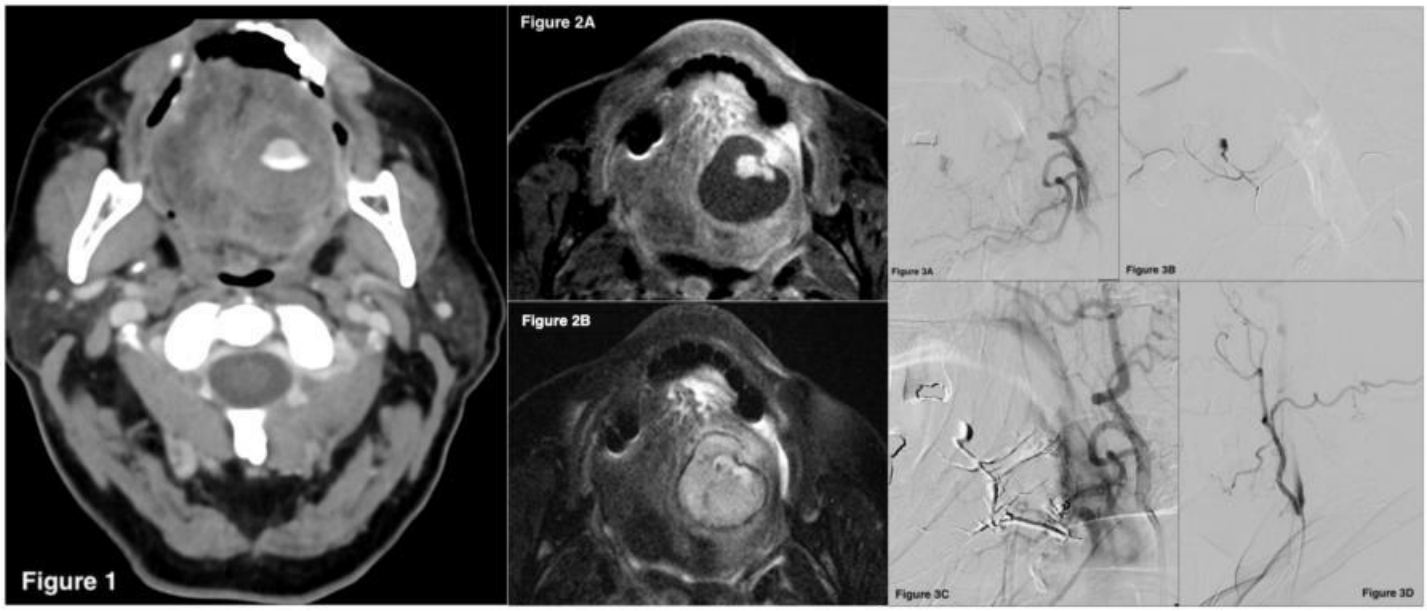

(Filename: TCT_873_ASNR_PSAImage.jpg)

842

Multiple Patients with Clinical Manifestations of Degenerative Cervical Myelopathy due to Cervical Malalignment.

A Kamali[1], A Ngo[2], L Nunez[3], R Patel[4], A Kamali[1]

[1]University of Texas Health Science Center Houston, Houston, TX, [2]McGovern Medical School, , Houston, TX, [3]University of Texas Health Science Center at Houston, Houston, TX, [4]Texas Children's Hospital, Houston, TX, Houston, TX

Clinical History

Cervical myelopathy is a known complication of degenerative changes of the cervical spine. Limited observations have been made to the effects of loss of cervical lordosis in causing degenerative myelopathy in relatively young patients. The goal of this case presentation is to raise awareness about this finding and pave the way for future studies to explore the relationship between loss of cervical lordosis and the clinical manifestations. This case review focuses on the clinical manifestations of multiple patients with MRI findings of ventral cord remodeling due to degenerative cervical spinal malalignment, which to the best of our knowledge, has had limited exploration.

Imaging Findings

Reversal of the normal cervical vertebral body lordosis is seen in all cases of this report. This finding resulted in remodeling of the ventral aspect of the cord at the levels with even small endplates spurring, disc bulge or disc protrusion. T2 hyperintensity of the cord is seen at the levels of endplate degenerative changes.

Discussion

The symptoms of degenerative changes within the cervical spine are well known, including numbness/tingling, pain/stiffness within the neck and arms, muscle weakness, gait issues, hyperreflexia, and decreased fine motor skills. Many of these clinical symptoms are seen with the patients presented in this report, who all had findings of ventral spinal cord remodeling due to cervical spondylosis. The reversal of the cervical vertebral body alignment invoked physical compression of the spinal cord even by mild cervical endplate degenerative changes and resulted in degenerative myelopathy. The proposed pathobiological mechanism that leads to the symptoms are physical compression, possibly micro ischemic changes that lead to axonal degeneration, changes in myelin and eventually cord atrophy and apoptosis.

Teaching Point

- Importance of the normal cervical vertebral body lordosis - In reversal of the normal cervical lordosis, even mild endplate degenerative changes will be problematic. - Change in alignment exposes the cord to these degenerative changes specially in repetitive flexions of the neck.

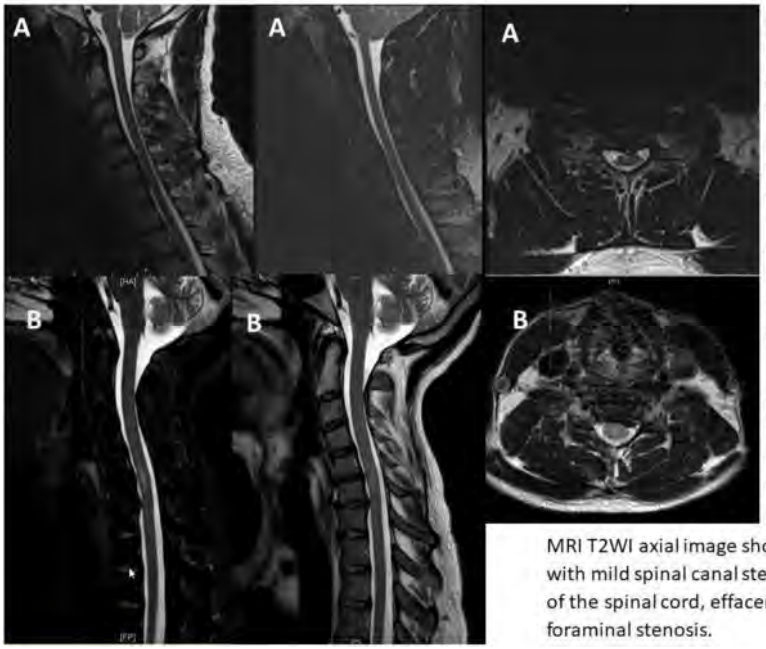

Patient A: Sagittal MRI T2WI and STIR images show reversal of the normal cervical vertebral body alignment with the apex at C5-C6 and C6-C7.
Axial image at C6-C7, shows endplate spurring and disc bulge with superimposed central/left paracentral focal disc extrusion result in moderate spinal canal narrowing and indentation of the ventral aspect of the cord. Mild T2 hyperintensity of the ventral aspect of the cord at the level of C5-C6 and C6-C7.

Patient B: Sagittal MRI STIR and T2WI images show reversal of normal cervical vertebral body alignment with T2 hyperintense signal abnormality of the cord at C5-C6 and C6-C7.

MRI T2WI axial image shows small left lateral recess disc extrusion with mild spinal canal stenosis, mass effect on the ventral aspect of the spinal cord, effacement of CSF, and mild left neural foraminal stenosis.

(Filename: TCT_842_Degenerativemyelopathy.jpg)

306

Neuromyelitis Optica Mimicking Cervical Cord Neoplasm

M Dopp[1], Q Mao[2], M Montesinos[1], S Harder[3]
[1]Loma Linda University, Loma Linda, CA, [2]Wayne State University, Detroit, MI, [3]Loma Linda University, Loma Linda , CA

Clinical History
17 year old female presented with acute onset left sided: numbness, tingling, and mildly decreased strength; for 4 days. Routine laboratory workup and LP were unrevealing.
Imaging Findings
MRI of the cervical spine demonstrated heterogeneous T2 hyperintensity with expansion and cavitation as well as patchy enhancement. While spinal cord neoplasm was initially considered from an imaging perspective, a history of area postrema syndrome (intractable hiccups with nausea and vomiting) was revealed. Retrospective review of MRI Brain imaging from 6 months prior showed subtle area postrema T2 lengthening and contrast enhancement. Given the clinical features and the imaging findings, there was a high suspicion of neuromyelitis optica spectrum disorder (NMOSD), confirmed by aquaporin 4 antibody (AQP4-Ab) positivity.
Discussion
Cord expansion, heterogeneous signal and enhancement is often seen with primary spinal cord neoplasm, such astrocytoma, ependymoma or ganglioglioma. However, the clinical and imaging findings of area postrema syndrome lead to a diagnosis of NMOSD. NMOSD is an autoimmune, inflammatory, and demyelinating disease of the CNS which is associated with disease-specific AQP4-Ab. This is a rare disease with prevalence rate of 0.3–4.4 per 100,000. The average age of presentation of 40-45 years old. There is a high prevalence rate in females, (F/M ratio: 9.1-3.1:1). It is traditionally characterized by optic neuritis and longitudinally extensive transverse myelitis. Patients can present with varied neurological findings such as blindness, weakness, numbness, and area postrema syndrome. In the acute phase, treatment is intravenous steroids, followed by immunosuppressive therapy with azathioprine or rituximab. Prognosis is variable depending on the spectrum of disease, with a small portion of patients demonstrating full recovery. Often the course is relapsing/remitting with persistent neurological deficits. Patients with multiple sclerosis may present with similar symptoms, however periventricular white matter involvement and short segment cervical cord involvement would be expected. Patients with MOGAD would also present with similar symptoms, however they would have positive MOG instead of AQP4 antibodies.
Teaching Point
The presence of a cavitary spinal cord lesion in the setting of area postrema syndrome suggests the diagnosis of NMOSD rather than neoplasm.

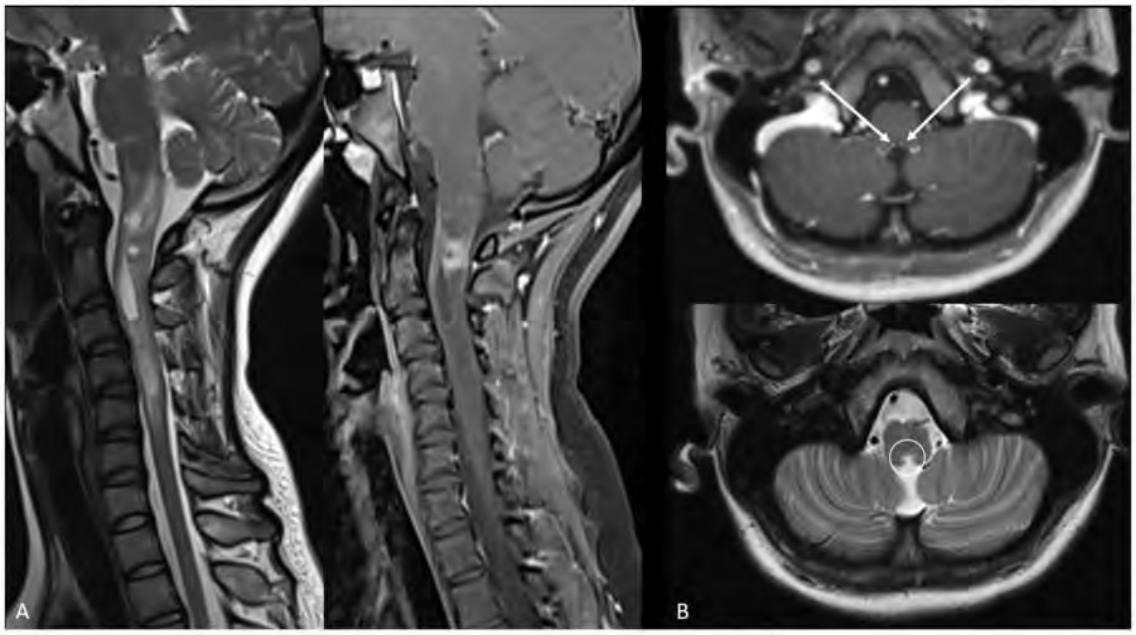

Figure 1: (A) Sagittal T2 and sagittal post-contrast T1 weighted images demonstrate a heterogeneous, long-segment, expansile, cavitary lesion extending from the brainstem to the C5-6 level with patchy regions of enhancement. (B) Axial T1 post-contrast and axial T2 weighted images from more remote imaging reveal tiny foci of enhancement (arrows) and regional T2 hyperintensity (circle) in the area postrema.

(Filename: TCT_306_NMOSD_v1.jpg)

436

Neuroradiological Manifestations of Gorlin Syndrome: A Case Review Series

C Johnson[1], J Nickerson[2]

[1]Oregon Health & Science University, Portland, OR, [2]Oregon Health Sciences University, Portland, OR

Clinical History

8-year-old female presented with jaw numbness, tenderness and enlargement over 1-2 months, patient was also noted to have obvious facial asymmetry and a bossed forehead. Patient was found to have multiple odontogenic keratocysts. Two months later when seen by a dermatologist, patient was noted to have several small moles that were biopsy proven to be basal cell carcinomas (BCCs). The patient underwent surgical resection of the keratocysts and several BCCs. Ten years later, the patient presented to the ED with stroke like symptoms and an emergent CTA head and neck was found to be negative, however there was progression of dural calcifications (see image) and post-surgical changes of odontogenic keratocyst resection (not pictured).

Imaging Findings

Multiple large keratogenic odontogenic cysts Prominent dural calcifications Ventriculomegaly Corpus callosal dysgenesis Alveolar ridge cyst with unerupted tooth Frontal bossing/macrocephaly

Discussion

Gorlin-Goltz syndrome or Basal Cell Nevus Syndrome is an autosomal dominant tumor syndrome characterized by multiple basal cell epitheliomas, odontogenic keratocytes, palmoplantar pits, dural calcifications and medulloblastoma. Approximately 1/3 of cases are new mutations, however. It is characterized by mutations of the PTCH1 gene approximately 60% of the time other cases involve SUFU mutations. Typically, patients present by 5 – 10 years old with jaw pain +/- deformity, though the presenting symptom may be a desmoplastic medulloblastoma causing obstructive or neurological symptoms in a toddler. In the 3rd decade, patients typically have multiple nevoid basal cell carcinomas with a typical onset in the late teenage years. A definitive diagnosis of Gorlin syndrome should be made by a multidisciplinary team imaging and genetic testing. The gold standard for imaging diagnosis is bone algorithm CT. Early identification of findings, diagnosis, treatment and regular follow up decreases complications.

Teaching Point

Diagnosis of Gorlin can be made with 2 major or 1 major and 2 minor criteria, which can be solely craniofacial. In a young patient with a preponderance of dural/tentorial calcifications, look for mandibular/maxillary cysts to potentially suggest a diagnosis of Gorlin or recommend genetic testing for PTCH1, if there is no known prior diagnosis. In a male toddler patient with neurological symptoms, presenting with a medulloblastoma, check for dural calcifications, check for frontal bossing, hypertelorism and the mandible/maxilla for cysts.

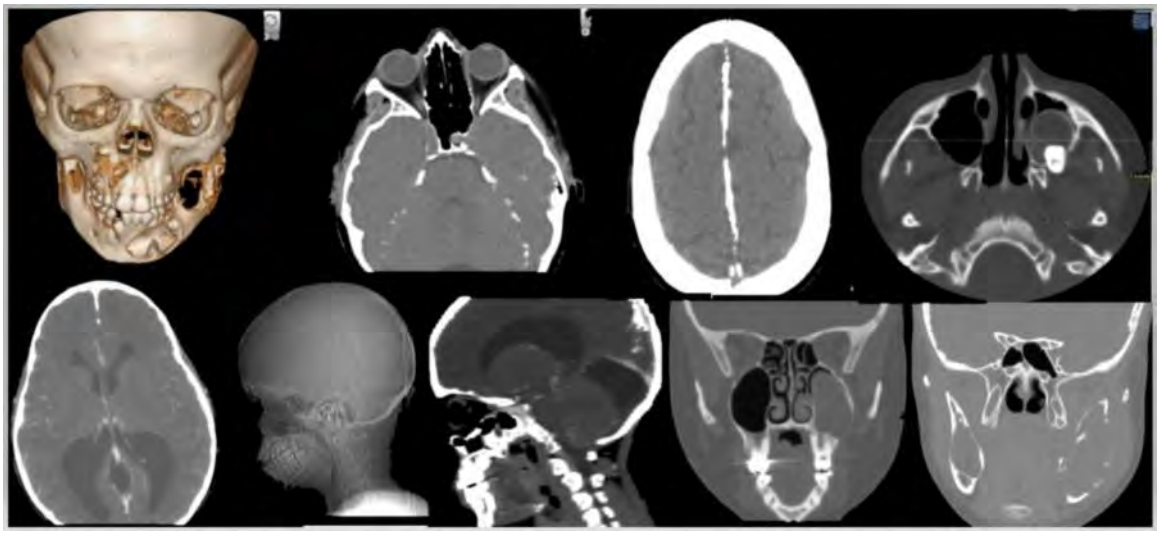
(Filename: TCT_436_images.jpg)

1469

Non-enhancing Meningioma: Is it possible?

W McLean[1], O Arevalo[1], T Block[1], L De Alba[1]
[1]*LSU Health Shreveport, Shreveport, LA*

Clinical History

55 year old caucasian female who presents with past medical history of hypertension, anxiety, ulcerative colitis, and hyperlipidemia. She presents with complaints of facial paresthesias, bilateral, and shoulder paresthesias. Patient has had additional complaints of ataxia and gait imbalance for the past month with headache, nausea and vomiting.

Imaging Findings

Nonspecific T1 hypointense, T2 hyperintense, non-restricting, faint to non-enhancing, extra-axial, dural based mass measuring 5 x 4 x 3 cm (AP, TV, CC). Associated thickened enhancing tentorium was seen adjacent to this lesion, resembling a dural tail.

Discussion

Meningiomas are the most common neoplasm of the dura mater, which are composed of meningothelial cells and range from WHO Grade 1 to Grade 3 neoplasms. Meningiomas typically present as lobular masses with broad-based dural attachment with isointensity to slight hyperintensity on T2 imaging, isointensity to hypointensity on T1 imaging, with prominent enhancement after contrast administration (1). Our patient presented with paresthesias and ataxia, and was subsequently found to have a left posterior fossa, extraaxial, dural based, minimally to non-enhancing mass, that was initially thought to represent an arachnoid cyst due to the atypical features on imaging. A study in the literature found that non-enhancing lesions of the cerebellopontine angle and petroclival regions could represent meningiomas but found only 14 reported cases of non-enhancing meningiomas, making this a rare finding (3).

Teaching Point

Meningiomas are a common tumor that classically presents with prominent enhancement after contrast administration but can also present as a faint to non-enhancing mass. An extremely rare presentation. Therefore, such faint to non-enhancing lesions such be included in the differential diagnosis for dural based posterior fossa masses.

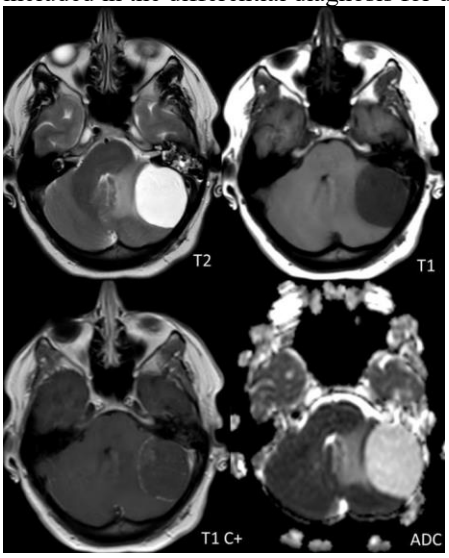

(Filename: TCT_1469_2023EXCERPTACASE.jpg)

954

Not Another Puff of Smoke: Neurovascular and Parenchymal Findings of ACTA2 Mutation

L Guzhva[1], S Moum[2]

[1]Northwestern University McGaw Medical Center, Chicago, IL, [2]Ann & Robert H. Lurie Children's Hospital of Chicago, Chicago, IL

Clinical History

This is an adolescent who initially developed respiratory distress during the first year of life, with cardiac evaluation identifying persistent patent ductus arteriosus. Follow-up imaging was significant for a dilated aortic root and ascending aorta. Genetic evaluation identified an ACTA2 mutation. The patient's current neurological exam is negative except for chronically dilated pupils and mild developmental delay. Prophylactic aspirin was prescribed.

Imaging Findings

Noncontrast MR angiogram of the brain exhibits dilatation of the petrous and cavernous segments of the internal carotid arteries (ICAs), with abrupt narrowing in the supraclinoid segments and tapering at the carotid termini. The anterior and middle cerebral arteries are diminutive, demonstrating a "broomstick" appearance (Fig1A). Noncontrast MR brain imaging shows extensive confluent T2/FLAIR hyperintensity in the periventricular white matter of both cerebral hemispheres (Fig1B). The anterior corpus callosum is truncated. The fornix is thickened with a horizontal orientation (Fig1C). Dynamic susceptibility contrast MR perfusion imaging demonstrates abnormal perfusion in the cerebral white matter with prolonged mean transit time (MTT) (Fig1D). Associated matched areas of decreased rCBV and rCBF were seen (not shown), corresponding to extensive white matter gliosis.

Discussion

ACTA2 is expressed in vascular smooth muscle, and mutations cause a nonatherosclerotic arteriopathy with large artery ectasia and small artery occlusion(1). Cerebrovascular findings include proximal ICA dilatation with more distal narrowing or occlusion. There is abnormal straightening of the intracranial arteries arising from the circle of Willis, with a characteristic "broomstick" appearance(1). Abnormal cerebral perfusion predisposes to stroke and white matter gliosis(1), as shown with the presented imaging. Parenchymal findings include anterior callosal hypoplasia and forniceal thickening(1). Extracranial manifestations include patent ductus arteriosus and aortic aneurysm(2). The clinical course of ACTA2 mutations is poorly understood; however, the prognosis is poor. Medical management is preferred over surgical intervention due to poor reported revascularization outcomes(3).

Teaching Point

We report the case of an adolescent with ACTA2 mutation, a rare mutation of vascular smooth muscle causing a distinct pattern of neurovascular abnormalities with recognizable brain parenchymal findings. Long-term clinical and imaging outcomes are poorly understood.

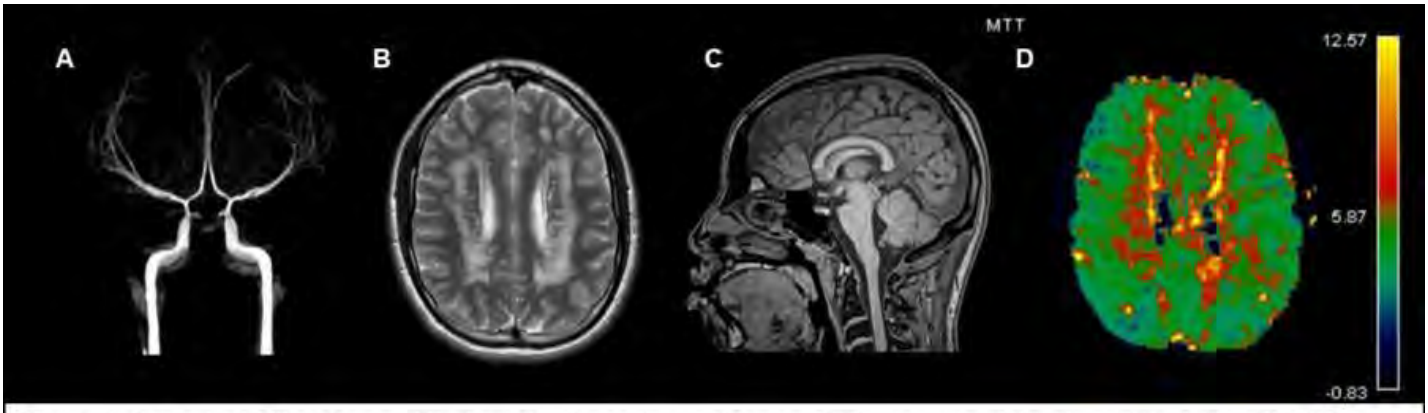

Figure 1. A. Noncontrast MR angiogram of the brain showing an abnormal "broomstick" appearance of the intracranial arteries with relative ectasia of the more proximal intracranial ICAs. **B.** Noncontrast axial T2 brain image exhibiting extensive gliosis of the periventricular white matter. **C.** Noncontrast sagittal T1 MR brain image demonstrating an abnormal truncated appearance of the corpus callosum, with forniceal thickening. **D.** Mean Transit Time (MTT) map from dynamic susceptibility contrast MR perfusion imaging showing prolonged transit time in the cerebral white matter related to the underlying arteriopathy.

(Filename: TCT_954_ACTA2images.jpg)

1114

Novel Presentation of a Myxoid Glioneuronal Tumor

R Camara[1], A Mlikotic[2], S Ceglar[3], S FARZIN[4]

[1]Harbor UCLA, Torrance, CA, [2]HARBOR UCLA, Los Angeles, CA, [3]Harbor-UCLA, Rolling Hills Estates, CA, [4]HARBOR UCLA MEDICAL CENTER, TORRANCE, CA

Clinical History

A 19-year-old woman presented with five months of progressive dizziness. She reported syncopal episodes associated with nausea, occurring while recumbent or while walking.

Imaging Findings

CT head shows a smooth oval low-density mass in the right temporal lobe measuring approximately 4.3 x 5.5 x 3.5 cm with resultant

mild mass-effect. MR imaging shows a temporal lobe 3.9 x 4.3 x 5.5 cm well-circumscribed heterogeneously T2 hyperintense, T1 hypointense, partially cystic, heterogeneously enhancing mass. T2 hyperintensity surrounds the mass, possibly reflecting cerebrospinal fluid (CSF) of the right lateral ventricle. A small amount of surrounding T2 FLAIR hyperintensity suggests vasogenic edema. There is no susceptibility to suggest hemorrhage or diffusion restriction (susceptibility and DWI sequences not shown). The mass is either within the temporal horn of the right lateral ventricle or medially displaces the temporal horn of the right lateral ventricle.
Discussion
Pathology confirmed a myxoid glioneuronal tumor; however, prior to surgery the differential included an intraventricular mass (possibly choroid plexus papilloma/carcinoma, ependymoma, or intraventricular meningioma) or a pilocytic astrocytoma. Myxoid glioneuronal tumor is a newly recognized, rare, WHO grade 1 entity that typically involves the septum pellucidum, corpus callosum, subcallosal area, periventricular white matter and septal nuclei. Known cases, as in this case, typically demonstrate T1 hypointensity, T2 hyperintensity and bright peripheral rims on FLAIR, similar to dysembryoplastic neuroepithelial tumor (DNET). This case departs form the usual imaging presentation in that there is heterogeneous enhancement, and the size of the lesion is much larger than reported in recent literature.
Teaching Point
Recognition of these additional imaging findings of rare myxoid glioneuronal tumors should help broaden the differential considerations of ventricular neoplasms.

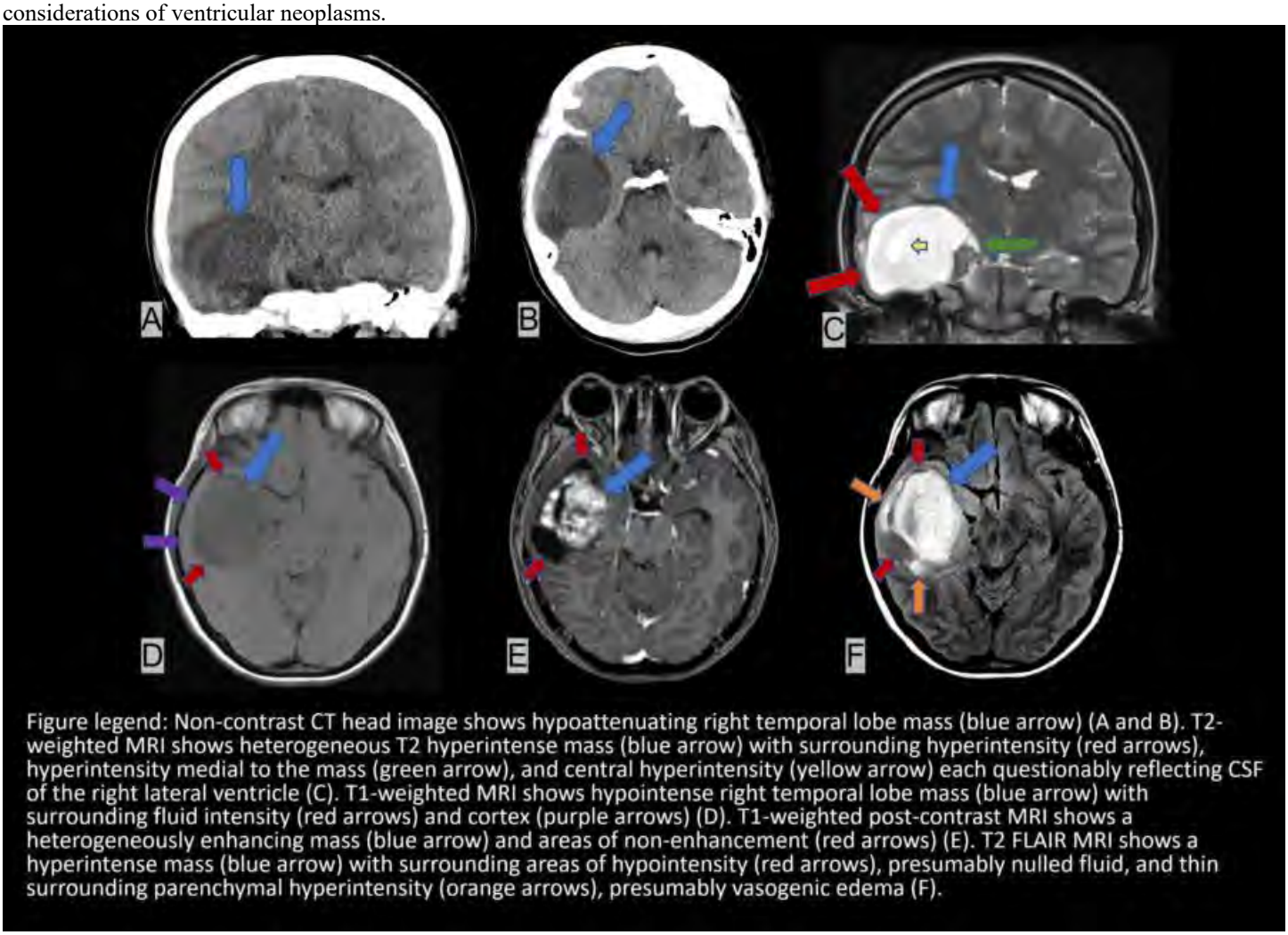

Figure legend: Non-contrast CT head image shows hypoattenuating right temporal lobe mass (blue arrow) (A and B). T2-weighted MRI shows heterogeneous T2 hyperintense mass (blue arrow) with surrounding hyperintensity (red arrows), hyperintensity medial to the mass (green arrow), and central hyperintensity (yellow arrow) each questionably reflecting CSF of the right lateral ventricle (C). T1-weighted MRI shows hypointense right temporal lobe mass (blue arrow) with surrounding fluid intensity (red arrows) and cortex (purple arrows) (D). T1-weighted post-contrast MRI shows a heterogeneously enhancing mass (blue arrow) and areas of non-enhancement (red arrows) (E). T2 FLAIR MRI shows a hyperintense mass (blue arrow) with surrounding areas of hypointensity (red arrows), presumably nulled fluid, and thin surrounding parenchymal hyperintensity (orange arrows), presumably vasogenic edema (F).
(Filename: TCT_1114_Images.JPG)

279
One Side is Not Like the Other: A Case of Congenital Hemifacial Hypertrophy
J Gao[1], K Dahlstrom[2]
[1]University of Kansas Medical Center, KANSAS CITY, KS, [2]University of Utah, Salt Lake City, UT

Clinical History
10-year-old female presents with concern for left facial mass. Notes a "fullness" of her left facial structures since birth. This was reportedly previously biopsied as a "lipoma" and subsequently treated with liposuction. Patient reports discomfort due to the excess tissue, and frequent inadvertent biting of her left cheek. Patient denies any pain, vision or breathing difficulty.
Imaging Findings
CT neck axial (1) and coronal (2) reformat images demonstrating asymmetric lipomatous enlargement/replacement of the left facial

structures including the parotid gland (arrows), masticator musculature and subcutaneous tissue. CT neck axial image (bone window) demonstrating asymmetric enlargement of the left zygomatic bone (arrow) and hyperexpansion of the left maxillary sinus. MRI Neck axial T1 (4) and post contrast fat saturation (5) images demonstrating asymmetric lipomatous enlargement/replacement of the left facial structures including the parotid gland, masticator musculature (arrow) and subcutaneous tissue. No appreciable abnormal enhancement in the left facial structures.

Discussion

Hemifacial hypertrophy, also known as hemifacial hyperplasia, is a rare development abnormality involving asymmetric growth of the facial soft tissue and osseous structures, more commonly in females (ratio 3:2). Often present at birth, with progression throughout childhood and adolescence. Pathogenesis is uncertain, multiple theories related to abnormal neural fold development and neural crest cell hyperplasia. Radiologic findings include unilateral enlargement of hard and soft facial tissues bounded anteriorly by the frontal bone, inferiorly by the inferior aspect of the mandible, medially by the midline, and laterally by the ear. Hemifacial lipomatosisis the dominant feature. Orbital structures are uninvolved. Partial hemifacial hypertrophy- not all hemifacial structures enlarged. Diagnosis of exclusion with several differential diagnoses: Proteus syndrome, Beckwith-Wiedemann syndrome, Neurofibromatosis 1, Klippell-Trenaunay syndrome. Case: Patient referred by maxillofacial surgery, plan for flap debulking, parotidectomy, and cervicofacial flap reconstruction.

Teaching Point

N/A, combined with 'Discussion" category.

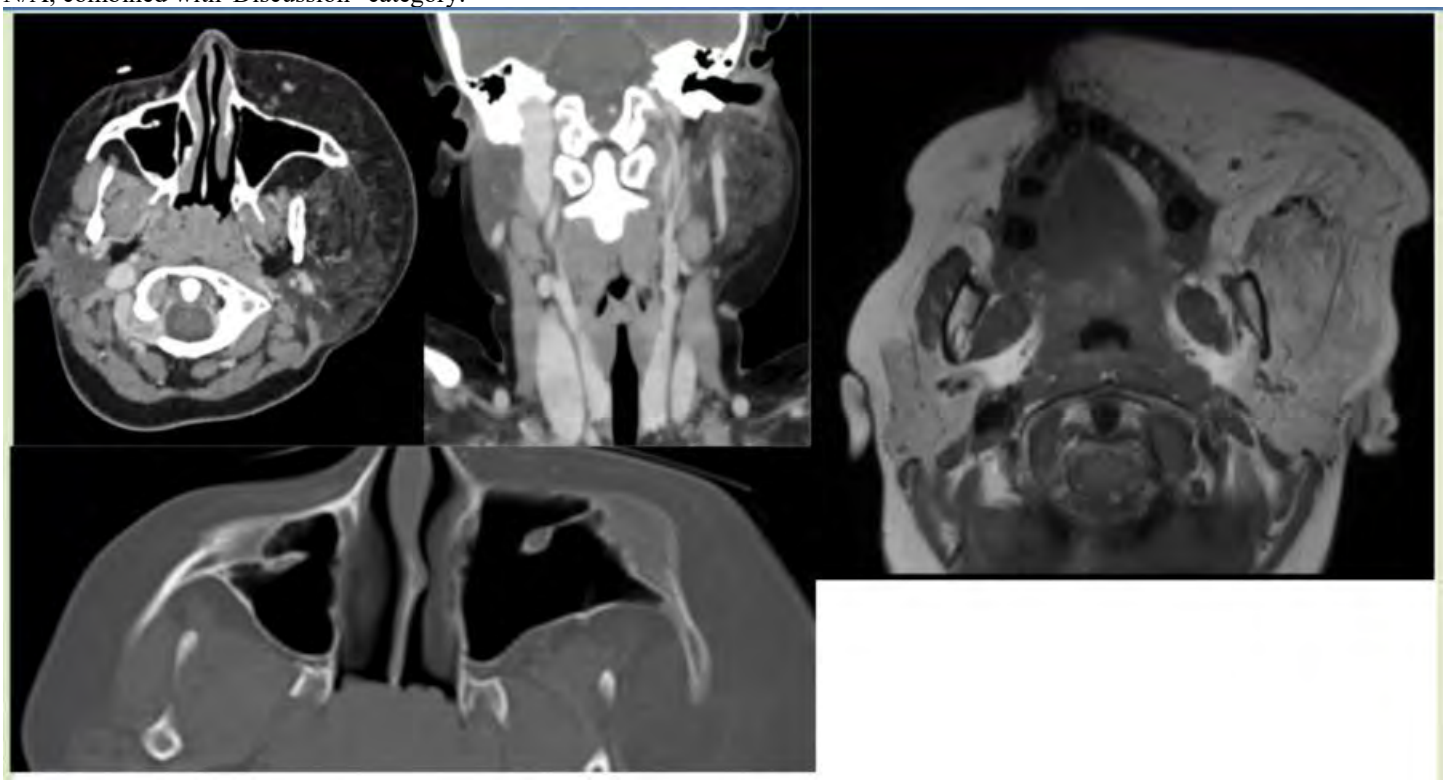

(Filename: TCT_279_hemifacialhypertrophy.jpg)

1387

Pediatric Idiopathic Intervertebral Disc Calcification: A Case Series

R Okpara[1], A Pham[2], R Jacob[3]

[1]Texas Tech University Health Sciences Center School of Medicine, Sugar Land, TX, [2]Texas Tech University Health Sciences Center School of Medicine, Houston, TX, [3]University Medical Center, Lubbock, TX

Clinical History

The first patient was a four-year-old boy who presented with a 3-day history of progressive back pain and abnormal movements, including neck stiffness, shoulder shrugging, and tongue rolling. Neurological examination revealed mild right arm weakness with normal deep tendon reflexes. Additional physical exam findings included postural kyphosis. X-rays of the cervical spine were unremarkable. However, MRI and CT revealed a small posterior disc bulge with associated disc extrusion at the C4-C5 level abutting the ventral aspect of the thecal sac. This radiological finding revealed a diagnosis of PIIVDC. The patient was treated conservatively with a C-collar and followed up for pain assessment. The second patient was an eight-year-old boy who presented with a 1-week history of progressive left-sided neck stiffness and pain along with restricted movement when rotating his head to the left. Physical examination revealed head tilt and right-sided head pain upon touch. Neurological exam was unremarkable. X-rays of the cervical spine reported abnormal findings of disc space calcification. Due to concern of PIIVDC, a CT of the cervical spine was performed, confirming calcification of the intervertebral disc space at C2-C3 and C3-C4 levels with no extension into the spinal canal. Imaging findings are consistent with PIIVDC. The patient was treated with supportive care.

Imaging Findings
Noncontrast CT of the cervical spine demonstrates a calcific density in the intervertebral disc space at C4-C5 level with associated calcified disc extrusion. This abuts the ventral aspect of the thecal sac.
Discussion
Pediatric idiopathic intervertebral disc calcification (PIIVDC) is a rare and poorly understood disease characterized by calcification of an intervertebral disc, which can progress to symptomatic inflammation, causing worsening progressive neck and spinal pain. Typical clinical presentations include neck pain, fever, neck stiffness, and torticollis. Potential neurologic deficits can occur due to significant ossification of the posterior longitudinal ligament or disc herniation, leading to spinal cord compression.
Teaching Point
PIIVDC is considered a self-limiting manifestation, typically resolving spontaneously. Treatment of this condition is managed with conservative treatment, including analgesics, anti-inflammatory drugs, and cervical collars. Because PIIVDC is a poorly understood and rare disease, the long-term effects of this manifestation are unknown and warrant more awareness in the pediatric population.

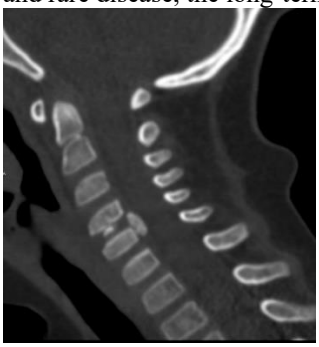

(Filename: TCT_1387_PIIVDC.jpg)

781

Pituicytoma in a Young Female – A Case Report and Review of the Literature

V Tiwari[1], S Szczesniak[1], H Marin[1], B Griffith[1], J Corrigan[1]
[1]Henry Ford Health, Detroit, MI

Clinical History
A 22-year-old female presents with a history of panic attacks and hyperprolactinemia on laboratory evaluation.
Imaging Findings
MRI evaluation demonstrates an elongated, T1 isointense (A) and slightly T2 hyperintense (C) sellar mass replacing the pituitary gland and stalk. This lesion demonstrates mildly heterogeneous enhancement (B) and no diffusion restriction (D).
Discussion
Pituicytomas are extremely rare, slow-growing and benign tumors of pituitary glial cells (pituicytes) that arise in the sellar/suprasellar region. Due to their slow-growing nature, patients typically present with progressive and chronic symptoms. The imaging features of pituicytomas overlap with other more common pituitary lesions, but certain findings should raise the possibility of this lesion in the appropriate clinical setting. Treatment is resection of the lesion, though this is often difficult and subtotal due to the highly vascular nature of the lesion. The diagnosis is made by histopathology.
Teaching Point
Though imaging features can overlap with other lesions, the possibility of a pituicytoma should be raised for patients who present with chronic and progressive symptoms, in the presence of an enhancing and slow-growing lesion within the suprasellar/sellar region which lacks cystic changes and calcification.

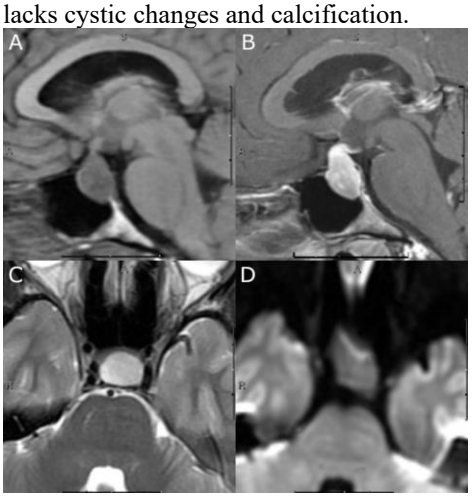

(Filename: TCT_781_Figure.jpg)

789

Plasmacytoma of the Cricoid and Thyroid Cartilage: A Rare Location of an Uncommon Tumor

S Szczesniak[1], K Eteer[1], V Tiwari[1], J Corrigan[1], B Griffith[1], H Marin[1], D Noujaim[1]
[1]*Henry Ford Health, Detroit, MI*

Clinical History

Case 1: 50-year-old female presents to our facility with enlarging left-sided neck mass. After imaging and endoscopy (E), the patient underwent ultrasound-guided biopsy of the cricoid mass (D). She was diagnosed with plasmacytoma with plasma cell dyscrasia that improved with chemotherapy. Case 2: 85-year-old male presents to outside facility for a fall with imaging notable for incidental cervical spine and right thyroid cartilage masses. At our facility, CT-guided biopsy of the thyroid cartilage lesion and transoral biopsy of the C2 lesion were obtained (F, G), in addition to endoscopy (H). Patient was diagnosed with plasmacytoma without plasma cell dyscrasia.

Imaging Findings

Case 1: CT neck images (A, B) demonstrate expansile and lytic lesions within the cricoid and left thyroid cartilage without FDG uptake on PET-CT (C). Case 2: On outside imaging, lytic and expansile lesions are seen in the right thyroid cartilage on T1-weight MRI (A) and CT (B) and of the C2 vertebral body on CT (C) with uptake seen on respective PET-CT images (C, E) obtained at our facility.

Discussion

Plasmacytoma is a discrete solitary mass of monoclonal neoplastic plasma cells that may arise from medullary or extramedullary sites. Extramedullary plasmacytoma (EMP) is more commonly found in the head and neck; however, EMP of the larynx is extremely rare. EMP accounts for less than 4% of plasma cell tumors. Head and neck imaging is important in identifying and diagnosing lesions via CT and/or MRI, as well as for image-guided biopsy. Patients can then be treated with a combination of radiation and chemotherapy. Our two cases illustrate this uncommon pathology located in the cricoid and thyroid cartilage, respectively, with Case 2 also demonstrating a solitary skeletal involvement of the C2 vertebral body.

Teaching Point

Extramedullary plasmacytoma (EMP) is a rare form of plasmacytoma that is found in the head and neck. While classic imaging characteristics have not been well-defined given the rarity of EMP, it is an important consideration for radiologists when providing differential diagnoses of head and neck lesions.

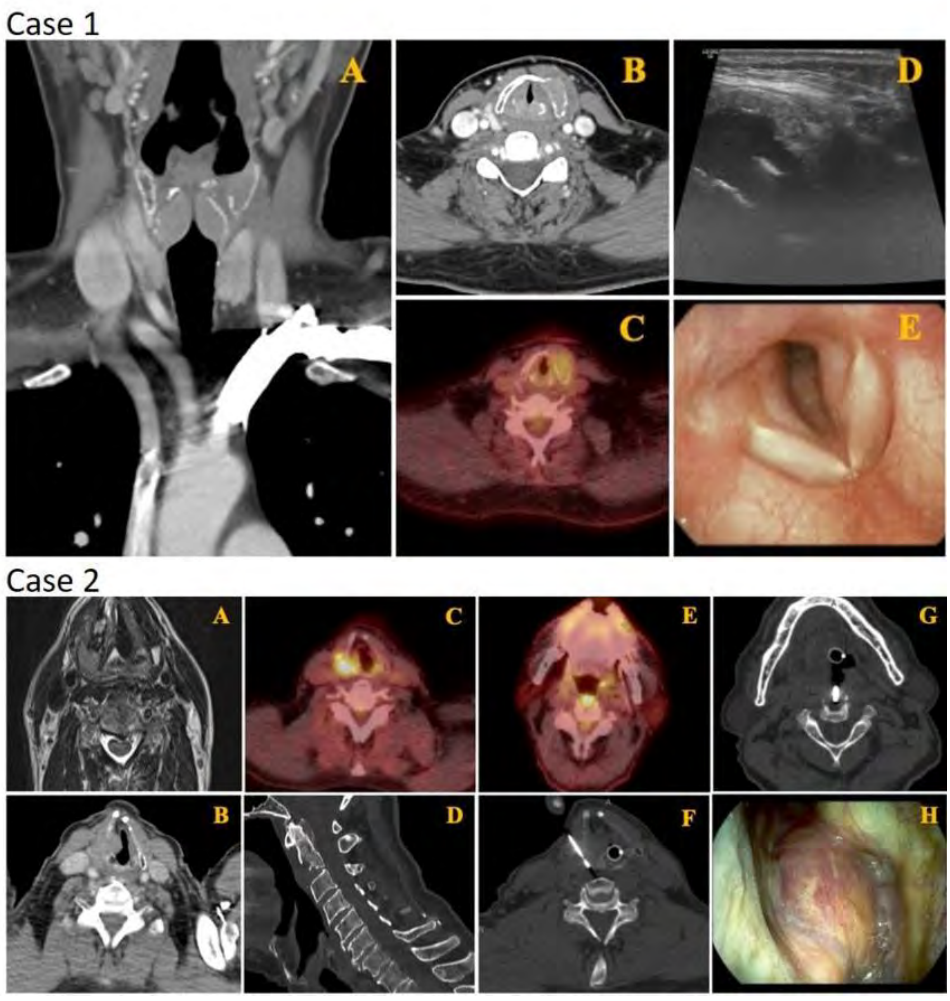

(Filename: TCT_789_FIg.jpg)

500

PLNTY More to Learn: Polymorphous low-grade neuroepithelial tumor of the young

J Martin[1], M Shiroishi[1], R Assadsangabi[1], A Lerner[1]
[1]*USC Keck School of Medicine, Los Angeles, CA*

Clinical History

We present two cases of pathologically confirmed polymorphous low-grade neuroepithelial tumor of the young (PLNTY) with preoperative imaging. Case 1: 19 year old female presenting with epilepsy. Case 2: 25 year old female presenting with right facial paresthesias and headaches. No history of seizures. In both cases presented, pathology was consistent with PLNTY, with oligoid features, strong positivity to CD34, distinct methylation, and BRAF V600E mutations. Both patients did well postoperatively following resection without evidence of recurrence after 2 year follow up. Seizures completely resolved in Case 1.

Imaging Findings

Case 1: A coarsely calcified 1.0 cm right temporal lesion was found demonstrating heterogeneous hypointense signal on T2-weighted images with associated susceptibility artifact, and minimal peripheral contrast enhancement. Case 2: A 1.6 cm left temporal/occipital lesion, hyperintense on T2-weighted images, was seen with remodeling of adjacent cortex.

Discussion

PLNTY are rare, recently described low-grade brain tumors which occur in pediatric and young adults and can be associated with epilepsy. Prognosis is good after surgical resection similar to WHO grade I tumors. On imaging, PLNTY are typically localized in the temporal lobe, with subcortical location and characteristic central calcification. They are typically well circumscribed and may have solid and peripheral cystic components. There is overlap in clinical and imaging features with low-grade glioma or other mixed neuronal-glial tumors. Further research is needed to better characterize these lesions.

Teaching Point

PLNTY are rare, recently described low-grade brain tumors which occur in pediatric and young adults. On imaging, PLNTY are typically localized in the temporal lobe, well-circumscribed, with subcortical location and characteristic central calcification. There is overlap in clinical and imaging features with low-grade glioma or other mixed neuronal-glial tumors.

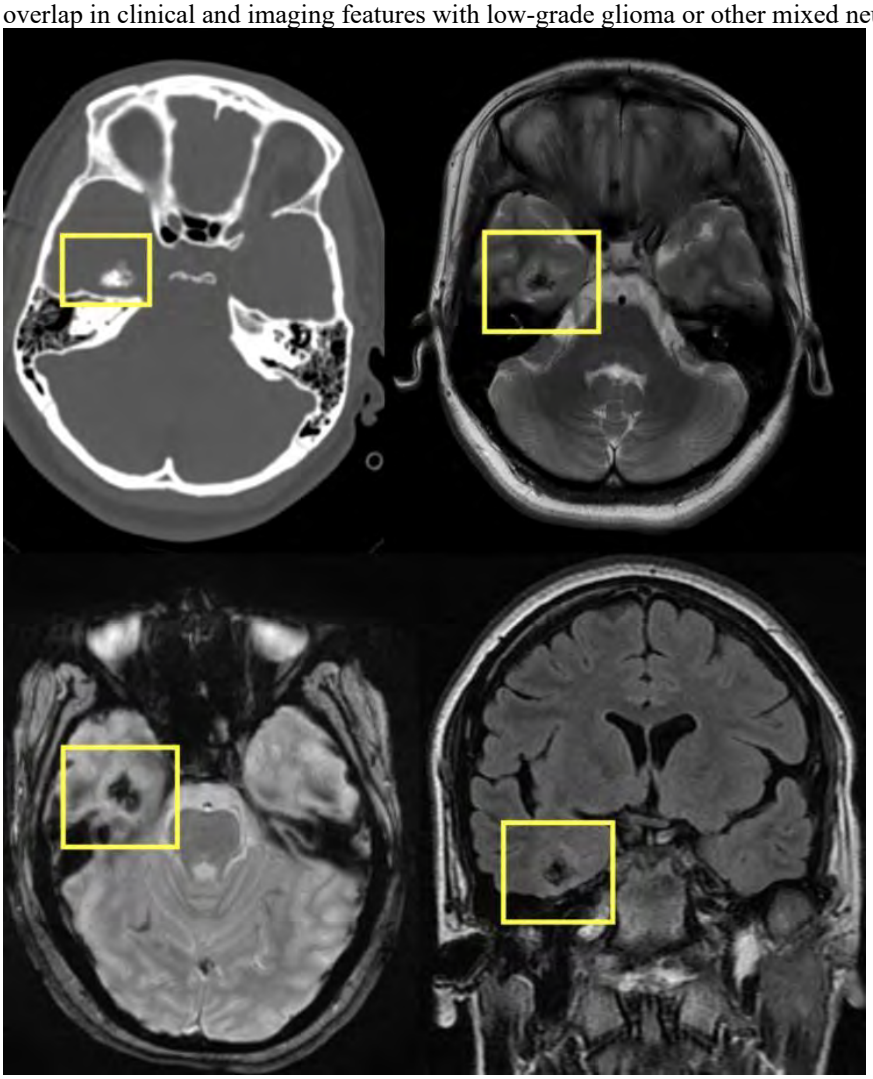

(Filename: TCT_500_ASNRPLNTYGraphicFile.jpg)

702Primary Meningeal Melanoma

R Alkhaibari[1], O Alaslani[2], M Aljehani[1], G Waggas[1], K Kurdi[1]
[1]King Faisal Specialist Hospital & Research Center - Jeddah, Jeddah, Jeddah, [2]the ottawa hospital, ottawa, ontario

Clinical History

14 years old male patient previously medically free presented to Emergency Department complaining of sudden repeated attacks of vomiting after minor head trauma. On physical exam patient was alert and conscious with GCS of 15 and no neurological deficit.

Imaging Findings

(A) axial T1-weighted image showing large left frontotemporal cystic lesion with mural nodule that show area of hyperintensity, representing hemorrhagic component/melanin. (B) axial T2-weighted fat-saturated image showing intra-nodular small cyst with layering blood products. (C) axial contrast enhanced T1-weighted fat-saturated image showing enhancement of the mural nodule with partial rim enhancement of the cyst and no leptomeningeal enhancement. (D) axial contrast enhanced T1-weighted image 3-months post-surgical resection, showing nodular dural and leptomeningeal enhancement at the surgical site.

Discussion

Melanocytic tumors of the central nervous system (CNS) is usually metastatic with the primary form being rare (1). It can be focal, presenting as dural based mass which is more common in adults, or diffuse, presenting as leptomeningeal melanomas which is more common in children as part of neurocutanous melanosis (1). Neuro-radiological differentiation between primary and metastatic intracranial melanoma is difficult. However, Haywards et al. established the following criteria for diagnosing primary CNS melanoma: No melanoma outside the CNS, involvement of the leptomeninges, intra-medullary spinal lesions, hydrocephalus, tumor in the pituitary or pineal gland and presence of single intra-cerebral lesion (1). The usual imaging appearance of intracranial meningeal melanomas is solid masses (2). In our case, the lesion presented as a large cyst with a mural nodule, which is a very rare appearance with handful of cases described in literature, mimicking the appearance of pleomorphic xanthoastrocytoma and ganglioglioma (2). Postoperative histopathological examination in this case revealed malignant neoplasm with melanocytic differentiation. Thereafter, full clinical examination was carried out and extra-cranial melanoma was excluded. The patient had further disease progression 3 months following the diagnosis and did not survive.

Teaching Point

Although most intracranial melanomas are solid masses, lesions with large cystic component and mural nodule has been described. Our case contributes to current few data in the literature and may guide future efforts to understand the significance and effect on prognosis of such appearance.

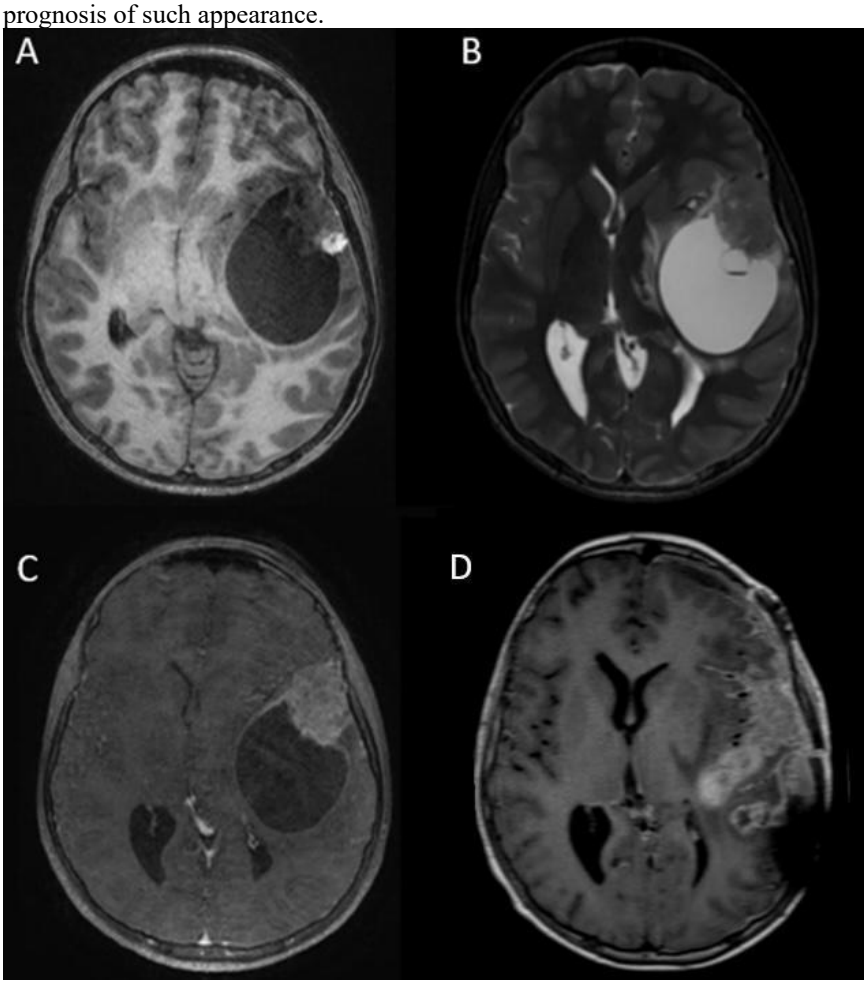

(Filename: TCT_702_Melanoma.jpg)

1385

Radiation Induced Malignant Transformation of Vestibular Schwannoma

A Goncalves Filho[1], A Reda[2], P Puac Polanco[3], S Chakraborty[4], E Portela de Oliveira[5]

[1]University of Ottawa, Ottawa, Ontario, [2]university of Ottawa, ottawa, Ontario / canada, [3]McMaster University, Hamilton, ON, [4]The Ottawa Hospital, U. of Ottawa, Ottawa, ON, [5]The Ottawa Hospital, Ottawa, Ontario

Clinical History

A 58-year-old woman with a right vestibular schwannoma was treated with stereotactic radiosurgery (SRS) in 2014. Surveillance MRI showed stable residual tumor size with increasing vasogenic edema and a new area of enhancement in the adjacent brainstem. She underwent surgery in December 2020, and the pathology was consistent with a malignant peripheral nerve sheath tumor. She completed adjuvant radiation in 2021. Post-radiation MRI demonstrated increase in size of the residual lesion, likely representing treatment-related changes or disease progression. She is being treated medically and there are no plans for new surgery.

Imaging Findings

Right cerebellopontine angle (CPA) enhancing lesion extending into the porus acusticus and mass effect over the brachium pontis was consistent with a vestibular schwannoma. Post SRS surveillance MRI in 2020 demonstrated new vasogenic edema of the brainstem and focal enhancement involving the lateral pons, inseparable from the tumor. Findings are suspicious for malignant transformation with brainstem invasion. Subsequent MRI showed progression of heterogeneous enhancement and edema in the brainstem, likely due to radiation changes or residual/recurrence.

Discussion

Vestibular schwannomas are adults' most common CPA masses, representing nearly 80% of CPA tumors. Treatment strategies can be divided into conservative, irradiation, microsurgery, and a combination of these methods. Radiosurgery is best indicated for tumors under 3 cm. The aim of radiosurgery is to prevent tumor growth, as treatment does not confer a radiographic cure. However, the long-term effects of stereotactic radiosurgery are not fully understood. Malignant nerve-sheath tumors rarely arise from the eighth cranial nerve, and malignant transformation of benign vestibular schwannoma is rare in patients without underlying neurofibromatosis. Therefore, this new treatment modality should be used with caution, especially in young individuals, and patients should be informed of the possible risk of malignant transformation as a rare but potentially severe complication.

Teaching Point

Radiation-induced malignancy is rare but given the increasing use of stereotactic surgery, it is essential to understand the imaging features of this unfavorable treatment complication. Serial MRI surveillance following treated schwannomas is essential to understanding disease progression and response to treatment.

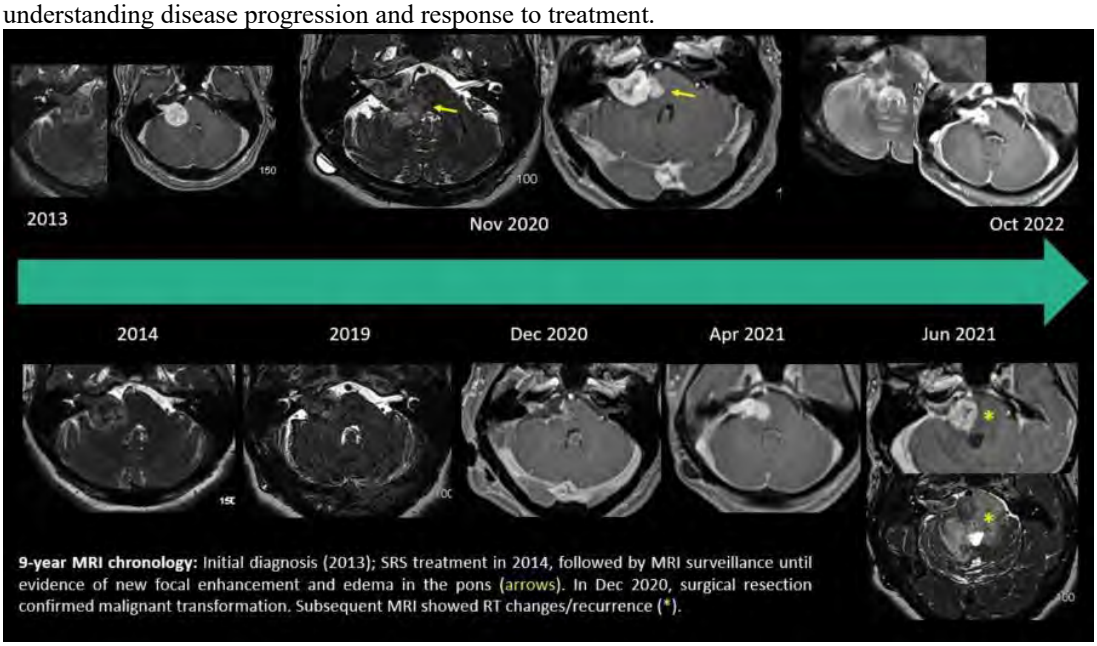

(Filename: TCT_1385_Slide1.jpg)

625

Radiculopathy in a Young Athlete with Spondylolysis without Spondylolisthesis

G Vilanilam[1], S Vattoth[1]

[1]University of Arkansas for Medical Sciences, Little Rock, AR

Clinical History

A 19-year-old male athlete presented to the sports medicine clinic with two weeks of low back pain with radiation to the left lower extremity. The patient reported no definite history of preceding trauma. Physical examination was significant for limited range of motion of the lower back and left lower extremity.

Imaging Findings
An MRI of the lumbar spine without intravenous contrast obtained showed a right-sided L5 pars interarticularis defect with increased signal in the right-sided L5 posterior elements extending to the pedicle on T2-weighted images (T2WI) and Short Tau Inversion Recovery (STIR) sequences. Evaluation of the left side did not demonstrate a pars interarticularis defect. However, on the left side there was more T2 and STIR signal in the posterior elements surrounding the pars and extending into the pedicle and left side of the vertebral body. This edema (denoted by increased T2 and STIR signal) extends superiorly into the left L4-L5 neural foramen and inferiorly into the left L5-S1 neural foramen, with fat stranding surrounding the exiting left L4 and left L5 nerve roots.
Discussion
Spondylolysis is a bony defect in the vertebral pars interarticularis, prevalent in up to 63% of patients engaging in certain sporting activities. While the etiology is not clearly known, chronic microtrauma and congenital predisposition are the leading hypotheses. Patients with this condition (most commonly adolescent males) present with a hyperlordotic posture and low back pain. Radiating pain to the lower extremities (radiculopathy) is rare in the absence of concurrent vertebral slippage (spondylolisthesis) wherein nerve root compression occurs due to a narrowed neural foramen associated with spondylolisthesis. Modic-like MRI signal in pedicles adjacent to pars defects have been previously reported, however to our knowledge, only one study (Sairyo K et al.) has reported extraosseus edema causing radiculopathy in spondylolysis in the absence of spondylolisthesis. It is postulated that this exhuberant edema (as in our case) at and adjacent to the site of the fracture demonstrated by increased T2/STIR marrow signal and fat stranding can irritate the exiting nerve roots leading to radiculopathy. Treatment is usually conservative as with our patient, with improvement of clinical symptoms in one month and radiological abnormalities in 3-6 months.
Teaching Point
Extraosseus edema in the vicinity of a pars interarticularis fracture or stress response can cause radiculopathy in the absence of spondylolisthesis.

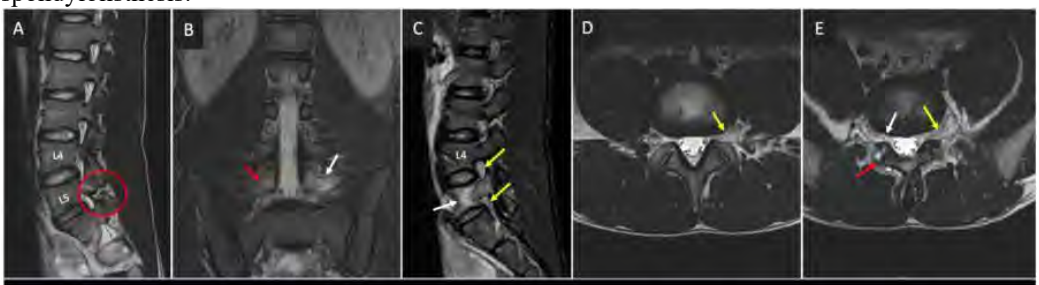

Multiplanar STIR sequences of the non-contrast MRI lumbar spine demonstrates a right-sided L5 pars interarticularis defect (A, red circle; E, red arrow) with mildly increased signal in the right-sided L5 posterior elements extending to the pedicle (B, red arrow). Note that there is no evidence of spondylolisthesis.

Coronal (B) and Sagittal (C) STIR sequences demonstrate increased signal in the posterior elements surrounding the left L5 pars, extending into the pedicle and left side of the vertebral body (B, C, white arrows). This increased signal extends superiorly into the left L4-L5 neural foramen (C, D, yellow arrows) and inferiorly into the left L5-S1 neural foramen (C,E, yellow arrows) with fat stranding surrounding the exiting left L4 and L5 nerve roots.

Increased signal is also seen extending into the right L5-S1 neural foramen (E, white arrow).

(Filename: TCT_625_Excerpta.jpg)

1481

Rare Cause of Traumatic Brown Sequard Syndrome

R Reid[1], P Rajagopalan[2], R Assadsangabi[1], D Phung[3], J Go[4]
[1]University of Southern California, Los Angeles, CA, [2]USC, Los Angeles, CA, [3]Keck School of Medicine of USC, Los Angeles, CA, [4]Keck Medicine of USC, Los Angeles, CA

Clinical History
A 30 y/o male was brought to the ER with multiple stab wounds to the face, neck, and back. At the time of presentation, the patient did not have motor strength of the right upper and lower extremity and markedly diminished sensation on the contralateral side to pinprick. The patient had full strength and sensation of the left upper and lower extremity.
Imaging Findings
CT Head demonstrated trace pneumocephalus and associated communicated fracture of the left frontal bone due to knife wound without subarachnoid hemorrhage. CT angiogram of the head and neck was performed demonstrating no evidence of fracture or vascular injury of the cervical spine, though laceration was identified in the right posterolateral upper neck. Further neurological examination demonstrated decreased pain and temperature sensation of the left aspect of body, suggestive of a Brown-Sequard syndrome (BSS). MRI of the cervical spine demonstrated knife injury with penetrating trauma with fluid and blood along the tract in the right posterolateral upper neck, partial thickness tear of the interspinous ligament and focal injury of the ligamentum flavum extending to the central canal with right hemi transection of the cervical cord due to a knife wound entering the central canal.
Discussion
In the US, 12,000 cases of SCI occur in the US with BSS accounting for 1-4%. Spinal cord injury is rare and account for 1.5% of

cases. This excerpta will discuss the incidence, pathophysiology, and presentation of BSS in the setting of spinal cord transection, and the findings of BSS and BSS plus syndrome. This excerpta will also discuss the incidence of penetrating knife wound injury to the spine.

Teaching Point

In the setting of penetrating trauma to the head and neck, a negative CT angiogram in the initial assessment for fracture or vascular injury does not preclude a neurological injury. The initial assessment of a Brown Sequard syndrome in the setting of a negative CTA should warrant an immediate in-depth imaging analysis of the cervical cord with emergency MRI.

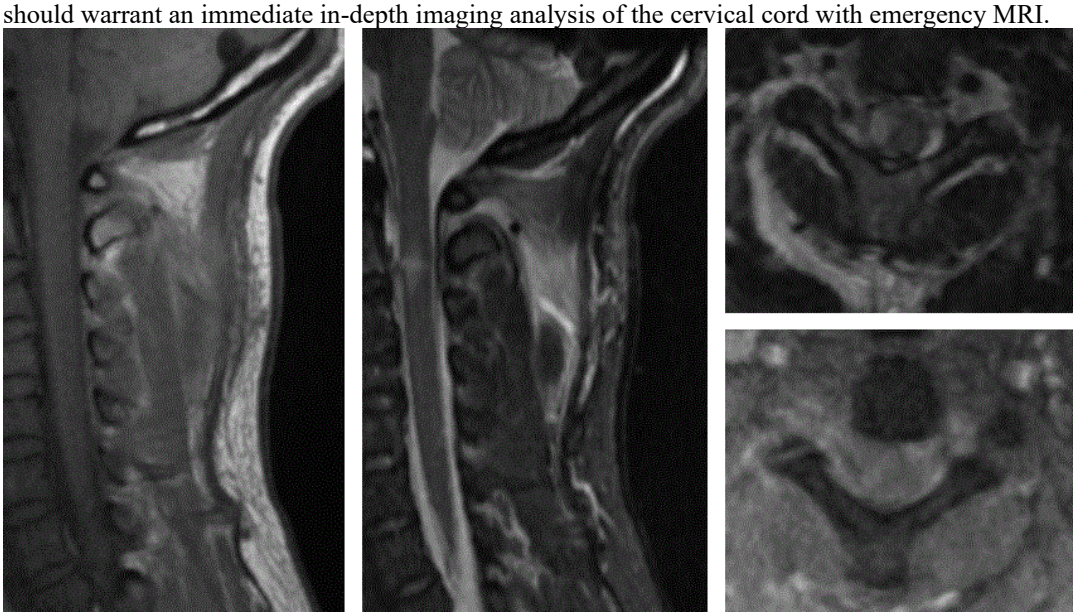

(Filename: TCT_1481_composite.GIF)

916

Reversible Parkinsonism due to Dural Arterio-venous Fistula

G Chaudhari[1], V Gorolay[2], C GLASTONBURY[3], R MATTAY[4], M Amans[5], A Rauschecker[6]

[1]University of California, San Francisco, San Francisco, CA, [2]University of California San Francisco, San Francisco, CA, [3]UCSF, SAN FRANCISCO, CA, [4]HOSPITAL OF THE UNIVERSITY OF PENNSYLVANIA, PHILADELPHIA, PA, [5]Ucsf, San Francisco, CA, [6]UCSF Radiology, Mill Valley, CA

Clinical History

A 60 year old male presented to his primary care provider with five months of progressive gait disturbance, memory loss, confusion, headaches and recurrent falls concerning for new onset Parkinson's disease. Past medical history was remarkable for hypertension, prior venous thrombo-embolism, and cerebral venous sinus thrombosis. Physical examination revealed delayed recall, cog-wheel rigidity, dysdiadochokinesia and festinating gait.

Imaging Findings

MRI brain was ordered to rule out structural abnormalities and revealed extensive tortuous flow voids, with engorged vascular structures exerting mass effect on the midbrain with associated vasogenic edema. Time-of-flight MR angiography confirmed arterialized flow in the dural venous sinuses consistent with dural AV fistulae - with left occipital artery feeding fistulae at the transverse sinus and superior sagittal sinus. Digital subtraction angiography was performed demonstrating two separate superior sagittal sinus dural AV fistulae, a left transverse sinus parallel channel dural AV fistula, and a right parietal "variant" dural AV fistula. All of these dural AV fistulae were deemed very high risk with extensive venous reflux into dilated cortical veins. There was associated significant delay in cerebral parenchymal venous drainage. Angio-embolization of all four dural AV fistulae were performed in two separate procedures. Post-procedural clinical follow-up demonstrated reversal of Parkinsonism, and a 1-month follow-up angiogram redemonstrated no residual AV shunting.

Discussion

This case shows the rare diagnosis of dural AV fistulae causing reversible Parkinsonism and adds to the literature of 27 previously reported cases [1]. DAVF complicates up to 2.4% of cerebral venous sinus thrombosis cases, with the most common locations of shunting occurring at the transverse and sigmoid sinuses (16/27, 59%), the superior sagittal sinus (3/27, 11%), and the straight sinus (3/27, 11%) [2]. Hypothesized pathophysiologies include hypoxia-induced angiogenesis and venous hypertension causing reopening of preexisting arteriovenous channels [3, 4].

Teaching Point

Imaging can play an important role in the evaluation of patients presenting with Parkinsonian symptoms, including patients who are refractory to medical therapy. MRI permits exclusion of alternate neurodegenerative disorders or unexpected pathology . Though rare, dural AV fistula is a recognized cause of Parkinsonism for which symptoms and signs may resolve following angio-embolization of dural AVF.

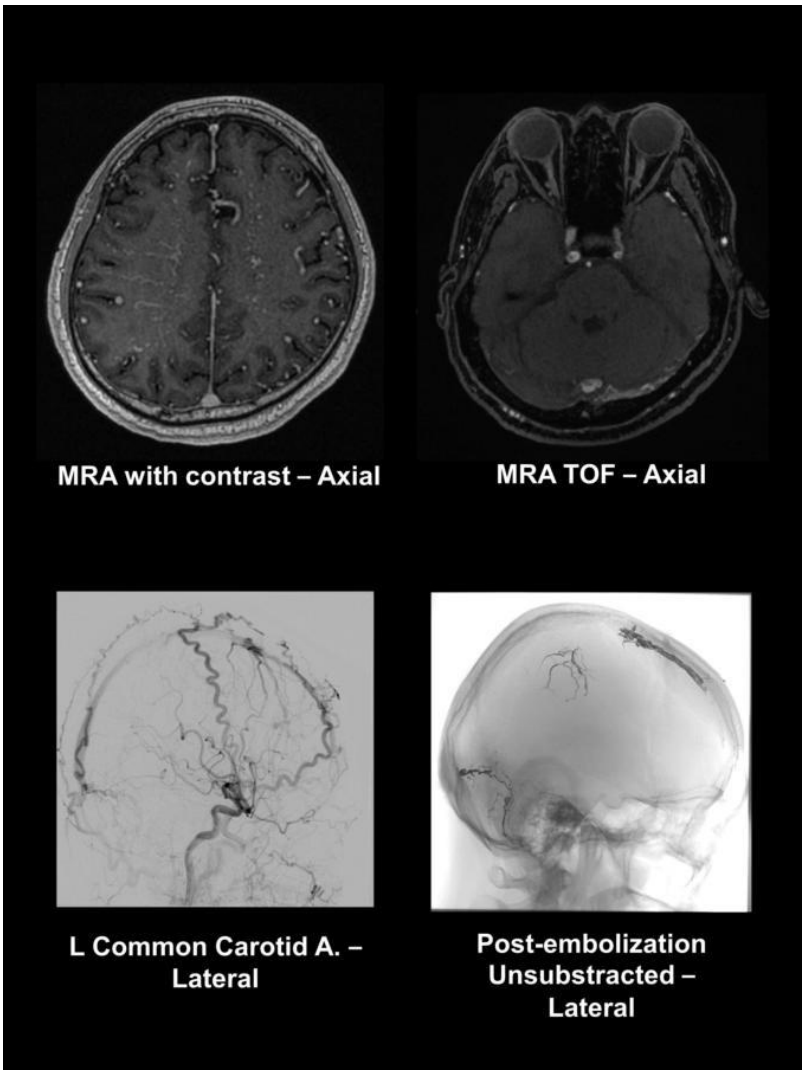

(Filename: TCT_916_ASNR2023ExcerptaIamge.jpg)

312

Satisfaction of Search Errors in a Toddler with Abusive Head Trauma

E Fourgas[1], Z Gardner[2]
[1]Geisinger Health System, Wilkes Barre, PA, [2]Geisinger Health System, Danville, PA

Clinical History

An unresponsive 2 year-old boy was brought to the ER by his father after a seizure. The child's mother reported lethargy and vomiting for the past two weeks. Vital signs were within normal limits. Physical exam revealed multiple bruises in the back and lower extremities. Ophthalmology exams showed bilateral retinal hemorrhages and papilledema. Laboratory findings were normal. The child was placed under the care of the child and youth services.

Imaging Findings

Noncontrast CT of the head showed bilateral supratentorial subdural hematomas of different attenuation and hematohygromas in the posterior fossa. A hypodense infarct in the right cerebellar hemisphere was also noted. CTA of neck showed a right cervical vertebral artery dissection as well as avulsion fractures of C2 spinous process and C7 lamina which were missed in the initial CT of the cervical spine. MR of the brain and cervical spine confirmed the CT findings and also revealed bilateral optic nerve head protrusion. MR of the lumbar spine showed subdural hematomas effacing the caudal equina. The bone survey revealed diastasis of the sagittal and coronal sutures.

Discussion

Abusive head trauma is the preferred term for describing inflicted injuries to the central nervous system of infants and young children. It is the leading cause of fatal head injuries in children under 2 years of age. The diagnosis is made by a multidisciplinary team based on history, physical exam, imaging and laboratory findings. Mixed attenuation subdural hematomas are more common in abusive head trauma than in the accidental setting. However the exact estimation of their age on CT should be avoided. The diastatic sutures seen in the bone survey was missed in the initial CT head study and in retrospect could be appreciated in the 3D reconstructed images. These reconstructions are helpful in detecting calvarial injuries and should be performed in every pediatric patient with head trauma. The tiny avulsion injuries missed in the initial CT of the cervical spine can be a harbinger of significant trauma as confirmed by the MR

study. Due to a high incidence of spine injuries in abusive head trauma patients, obtaining an MRI of the entire spine should be considered in all such cases, regardless of whether a CT is initially performed.
Teaching Point
The radiologist should be familiar with the multitude of imaging abnormalities in abusive head trauma in order to prevent satisfaction of search errors.

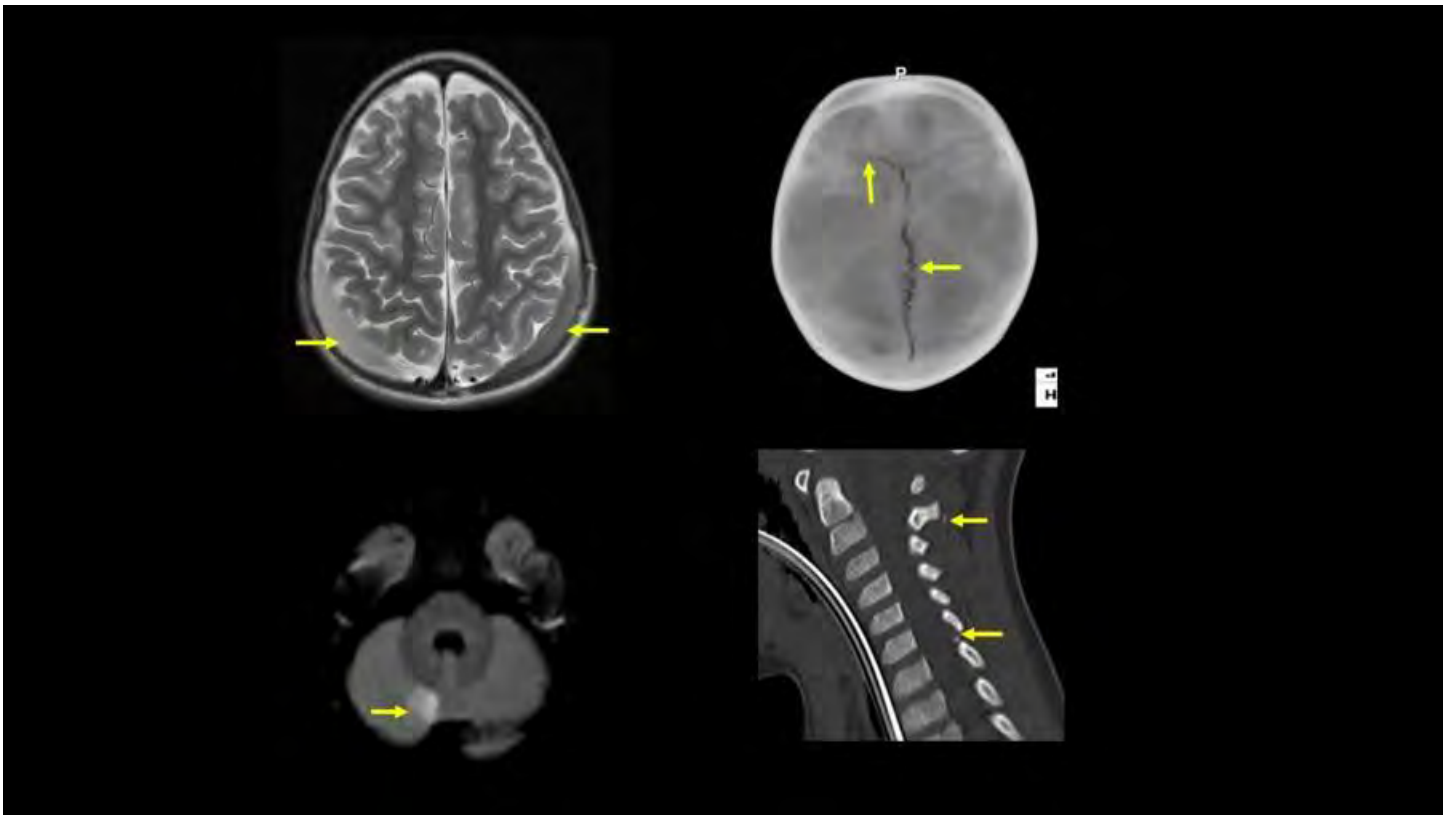

(Filename: TCT_312_AHT1.jpg)

1020
Shield-Shaped Spinous Processes Resulting in Difficult Epidural Access for Spinal Cord Stimulator Trial
P Vazirnia[1], R Moheimani[2], K Bruno[3], J Chen[4]
[1]The Medical College of Wisconsin, Milwaukee, WI, [2]Coast Spine & Sports Medicine, Santa Ana, CA, [3]UC San Diego Health System, La Jolla, CA, [4]San Diego VA Medical Center/UC San Diego Health System, La Jolla, CA

Clinical History
A 67 year-old male with prior L3-5 laminectomy for stenosis and refractory pain, presented for evaluation for Nevro© Spinal Cord Stimulator (SCS) Trial and potential implant. Pain was refractory to physical therapy, acupuncture and pain procedures including spinal muscle trigger point injections, caudal epidural steroid injection, and lumbar epidural steroid injections as well as Baclofen and pregabalin. During the SCS trial epidural space access with an interlaminar approach at T12-L1 was unsuccessful. Unusually superficial ossific-feeling resistance was encountered, but no bone was visible on fluoroscopy. Re-attempt one level higher was unsuccessful. Pre-procedure imaging was re-reviewed showing enlarged shield-shaped spinous processes at essentially all lumbar and thoracic levels obstructing typical epidural access trajectories, leading to a difficult access. Eventually epidural access was obtained at L1-L2 and the leads were guided per normal protocol resulting in patient-reported 60 to 70% percent pain relief one week following the procedure.
Imaging Findings
Figure 1: Coronal surface-shaded rendering from CT shows "shield-shaped" spinous process tips that would block normal needle trajectories. Figure 2: Axial CT image shows the shield-shaped nature of the spinous process. Figure 3: Fluoroscopic image shows the successful more oblique approach of the needle.
Discussion
Limited literature describes "shield" shaped spinous processes. There are reports of similar phenomena in the literature, most notably Baastrup's Disease, which has enlargement, apposition, and sclerotic changes of interspinous surfaces [1]. Classically the approximation of adjacent spinous processes apposition is described as a "kissing" spine [2]. Additional reports describe spinous processes not in contact with each other, but rather the passing of the caudal portion of the upper spinous processes beyond the cranial portion of the next lower level ("passing spine") [3]. These conditions are commonly underrecognized, highlighting the importance of careful pre-procedural evaluation for difficult and uncommon anatomic variants.
Teaching Point
"Shield" shaped spinous processes may require alternative epidural access trajectory. This finding should be recognized by

proceduralists and pre-procedure diagnosticians for procedural planning to prevent difficult and increased procedural time when epidural access is necessary.

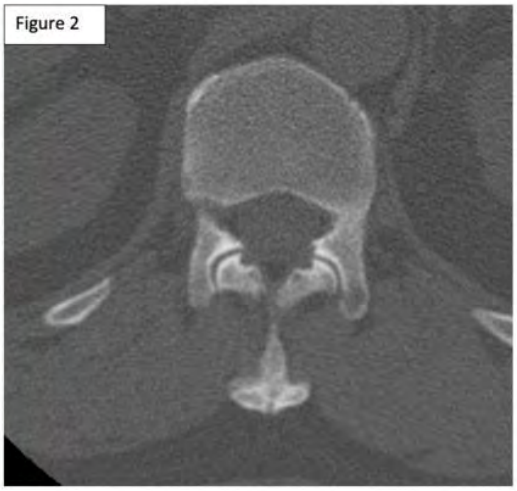

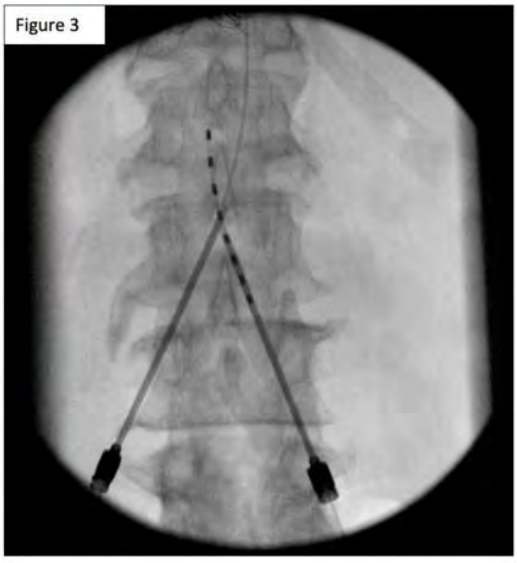

(Filename: TCT_1020_UpdatedASNRGraphics.jpg)

892

Sinonasal Alveolar Rhabdomyosarcoma in an Adult Patient: A Rare Tumor with Unfavorable Prognosis

M Brun-Vergara[1], E Portela de Oliveira[2], V Tsehmaister-Abitbul[3]
[1]THE OTTAWA HOSPITAL, OTTAWA, ONTARIO, [2]The Ottawa Hospital, Ottawa, Ontario, [3]University of Ottawa, Ottawa, Ontario

Clinical History

A 19-year-old male presented with a 3-week history of new painful cystic-like appearance lesion on the forehead, steadily increasing in size over the past few davs. Symptoms became more significant and persistent 1 week prior, with increasing pain, bifrontal pressure/headache, fever, right eye pain and pain with eye movements. Patient referred associated intermittent epistaxis that he has noted over the last year, but began occurring daily since 3 months ago. His past medical history is otherwise unremarkable. On clinical and physical examination, the patient had proptosis and lateral displacement of the right eye. Soft and boggy central forehead, nontender to palpation, and right-sided V1 parietal temporal numbness and superior forehead numbness was also noted. Anterior rhinoscopy demonstrated crusted blood present to the right nare obstructing the view inside the nasal cavity. Nasopharyngoscopy was also performed which showed pink fleshy mass to the anterior nasal cavity and obstructing further view to the right nare with edematous and swollen septum seen to the left nare.

Imaging Findings

A CT scan of the paranasal sinuses and head was performed at admission, which revealed a large, heterogeneously enhancing sinonasal mass with associated bony destructive changes with bilateral orbital extension, more on the right side resulting in right-sided proptosis. There was also intracranial extension of the mass causing focal mass effect on the anterior frontal lobes. Contrast-enhanced MRI confirmed an infiltrative and avidly enhancing sinonasal mass, mildly hyperintense on T2-WI, with restricted diffusion, extending into the bilateral orbits and intracranially. 18FDG-PET found hypermetabolic cervical lymph-node. Further evaluation was negative.

Discussion
Given the findings, an aggressive neoplastic process was suspected. Biopsy was performed, revealing a Rhabdomyosarcoma, alveolar type. Immunohistochemistry showed cells strongly positive to Desmin, Myogenin, and MyoD1. Strong evidence for a PAX3 and FOXO1 fusion was also detected. Tumor was considered inoperable patient was initiated on VAC chemotherapy and Radiotherapy.
Teaching Point
RMS is a rare H&N tumor in adultswith poor prognosis. One of the most common sarcomas in newborns and childhood, (peak 2-6 years) RMS is classified as parameningeal, orbital and non-parameningeal non-orbital. Parameningeal (including PNS), carry the worst prognosis. Sinus involvement presents as early epistaxis. Diagnosis is based on immunohistochemical analysis.

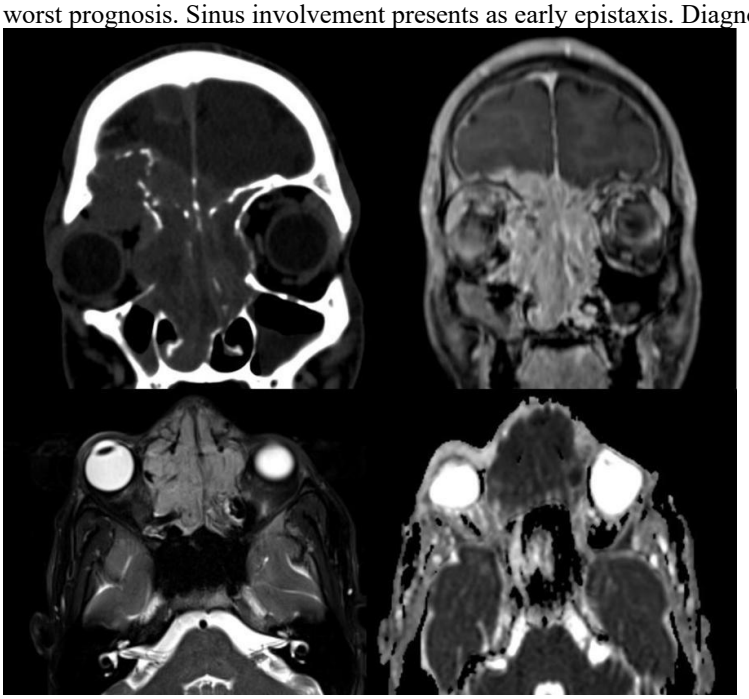

(Filename: TCT_892_Imagenes.jpg)

646

Sinonasal Leiomyosarcoma in a Patient with History of Retinoblastoma

G Biddle[1], T Abdulsalam[1], O Raslan[2], L Hacein-Bey[3], A Ozturk[1], K Oguz[2], M Bobinski[2]
[1]UC Davis Medical Center, Sacramento, CA, [2]UC Davis, Sacramento, CA, [3]University of California Davis, Sacramento, CA

Clinical History
A 49-year-old male with history of left eye enucleation and radiotherapy as a child for retinoblastoma (RB) presented to the emergency department with a nasal mass. Physical exam demonstrated a dilated and fixed right eye not reactive to light as well as a left eye orbital prosthesis. Biopsy performed by Otolaryngology revealed leiomyosarcoma. Tumor was determined to be currently unresectable, and patient was started on chemotherapy and radiation.
Imaging Findings
Magnetic Resonance Imaging (MRI) demonstrated avidly but heterogeneously enhancing mass filling the ethmoid labyrinth and extending into the nasal cavity and through the left choana into the nasopharynx and, to a lesser degree, oropharynx (Figure 1). The tumor extended into both sphenoid sinuses eroding the posterior walls and invading the clivus, sella and suprasellar cistern. There was also invasion of the extraconal orbits bilaterally, right greater than left. There was no brain invasion or abnormal enhancement of the brain or dura.
Discussion
Leiomyosarcomas are uncommon malignant mesenchymal tumors that are most often found in the GI tract, uterus, and retroperitoneum with 3% occurring in head and neck area. Most of the previously reported cases of head and neck leiomyosarcoma have occurred in the paranasal sinuses or nasal cavity. Sinonasal leiomyosarcoma can be seen in patients with a history of retinoblastoma, irradiation, and chemotherapy, sometimes decades after treatment. These tumors demonstrate local aggressive behavior and local recurrence. Surgery with or without radiation offers the best treatment for oncologically resectable tumors. Unresecatble tumors are generally treated with neoadjuvant chemotherapy and radiation though with largely ineffective results. The minimum overall 5-year survival rate was 20%- and 10-year minimum overall survival rate of 6%.
Teaching Point
While exceedingly rare, it is important to include leiomyosarcoma in the differential diagnosis in a patient with history of DNA mutation disorders such as retinoblastoma and prior radiation. Accurate description of tumor extent and invasion is paramount to guiding appropriate management.

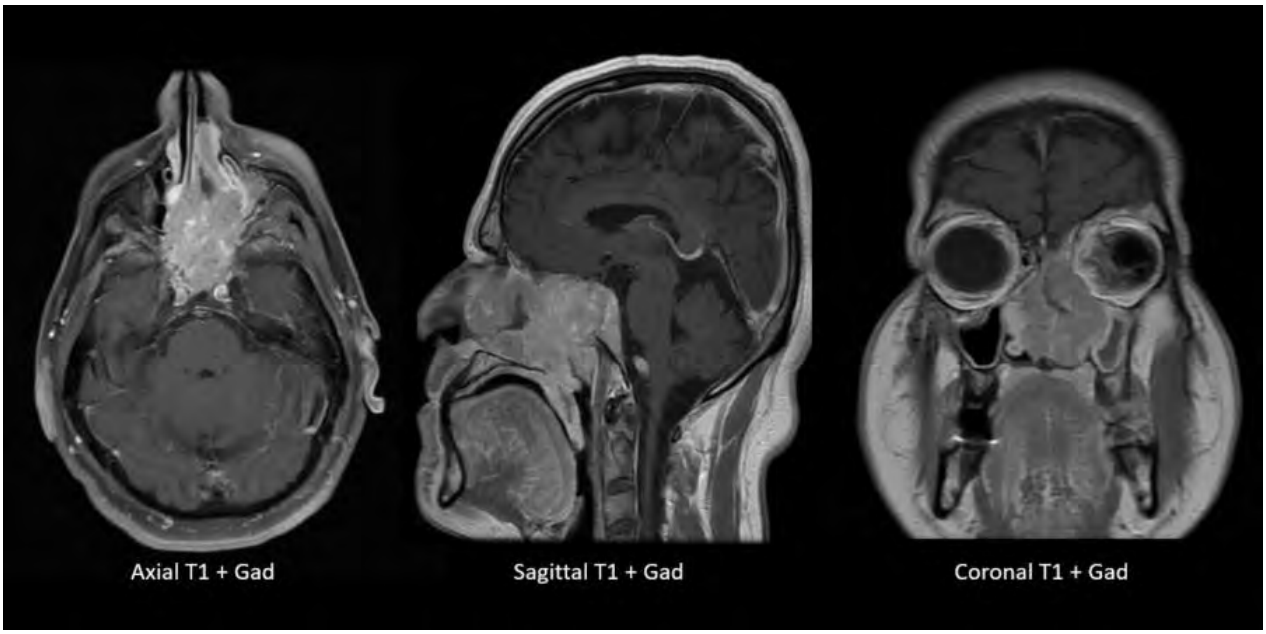

(Filename: TCT_646_leio.gif)

387

Sinus Pericranii

A Shariat[1], M Soleman[2], L Feng[1]

[1]Kaiser Permanente Los Angeles Medical Center, Los Angeles, CA, [2]Kaiser Permanente Los Angeles Medical Center, Pasadena, CA

Clinical History

7 month-old male autistic patient with frequent uncontrollable crying episodes presented with a soft 2x2cm lesion in the left parietal region that would bulge when he would cry. A head CT showed a 1.9x1.6 cm left parietal scalp lesion with erosive changes to the calvarium. A subsequent brain MRI showed hyperintense T2 signal with internal flow voids. A repeat CT venogram at 18 months old showed an increase in size to 4.7x1.7 cm with calcifications, progressive erosion, and venous communication with the superior sagittal sinus. At 21 months, angiogram was requested. Successful angiogram was performed and percutaneous embolization of the extracranial portion was carried out at 21 months using n-Butyl Cyanoacrylate liquid embolic. The bulge recurred two months after embolization during a fit of crying. Repeat angiogram at 33 months with successful occlusion of the intracranial portion of the sinus pericranii with intravascular embolic, and occlusion of the extracranial portion with thrombin.

Imaging Findings

1: CTV showing an enhancing soft tissue lesion causing bony remodeling 2: Catheter angiogram pre-treatment showing central venous sinus communication 3: Catheter angiogram post initial treatment showing extracranial embolic cast with small intracranial nub 4: Catheter angiogram post repeat treatment showing extracranial and intracranial embolic casts, with no central venous drainage

Discussion

Sinus pericranii (SP) is a rare venous anomaly characterized by an abnormal communication between intracranial dural sinuses and extracranial veins. It is associated with blue rubber bleb nevus syndrome, a rare and sporadic syndrome, that results in multifocal venous anomalies. The differential diagnosis would include cystic hygroma or meningocele. Although SP is considered a low flow vascular malformation, it can be more prominent when the patient is in the supine position or during Valsalva maneuvers. In the case presented, frequent and prolonged crying was believed to transduce pressure to the venous system and dislodge the first n-BCA cast, resulting in recurrence.

Teaching Point

This case highlights successful management of recurrent sinus pericranii. Initial treatment failure was likely due to incomplete occlusion of the dural vein. Repeat embolization was carried out from a combined percutaneous and transvenous approach, followed by surgical exclusion to prevent recurrence.

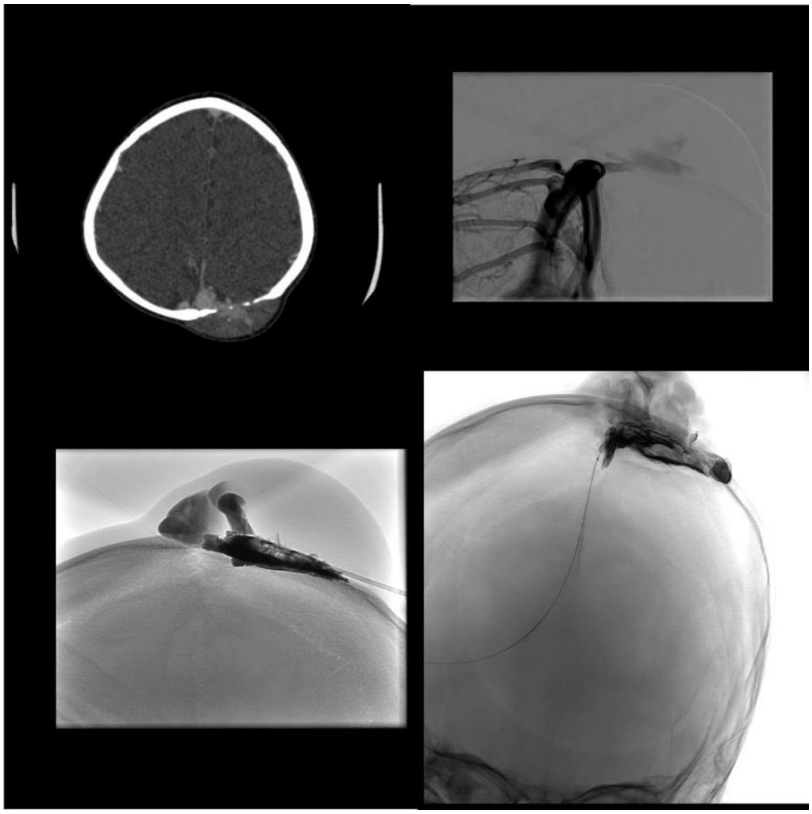
(Filename: TCT_387_Sinus_Pericranii_Images.jpg)

582

Soft tissue desmoid-type fibromatosis manifesting as a cervical mass

C Soto[1], W McLean[2], C Stevens[2], O Arevalo[2]
[1]National University of Colombia, Shreveport, LA, [2]LSU Health Shreveport, Shreveport, LA

Clinical History

48-year-old African American female patient with no significant past medical history, complaining of a slowly enlarging right-sided neck mass associated with pain radiating in the distribution of sternocleidomastoid muscle for the past three months. She endorses right-sided numbness of the anterior neck/shoulder region but denies speech changes, difficulty swallowing, or weight loss.

Imaging Findings

An ill-defined and homogeneously enhancing soft tissue mass is identified centered at the right anterolateral paraspinal soft tissues at the level of C4-C5, measuring approximately 44 x 23 x 36 mm. The mass demonstrates an intermediate-low signal on T1w and T2w images. Of note, the mass invades the superior and anterior aspect of the right anterior scalene muscle, contacts the right transverse process of C4, and abuts the right C3-C4 neural foramen. There is no extension into the cervical spinal canal or abnormal bone marrow signal intensity of the adjacent vertebrae.

Discussion

Desmoid fibromatosis (DF) is a rare, locally aggressive connective tissue tumor developing in musculoaponeurotic tissues. DF has an incidence of approximately 2 – 4 cases per million population per year, and accounts for 0.03% of all neoplasms (1). The clinical presentation in DF is highly variable and may be influenced by the tumor location and derives primarily from mass effect and direct infiltration of the neighboring anatomical structures (2)(4). MR characteristics of DF depend upon the histological components of the tumor. Fibrotic and collagenous portions of DF typically demonstrate low signal intensity on T2 weighted sequences and mild to moderate enhancement; in contrast, prominent cellular stroma and myxoid matrix in DF manifest as heterogeneous T2 hyperintense areas and demonstrate moderate to intense enhancement following intravenous contrast administration. The presence of linear, non-enhancing, T1- and T2-hypointense bands seen within the tumor (band sign, yellow arrowhead on the images) is reported to a characteristic MR finding as the fascial tail sign, which refers to the presence of a linear infiltrative border extending from the tumor along the fascial plane (3).

Teaching Point

Desmoid fibromatosis is a benign but locally agressive tumor that shows a low signal intensity on T1 and T2, and may also show homogeneous, inhomogeneous, or no significant enhancement.

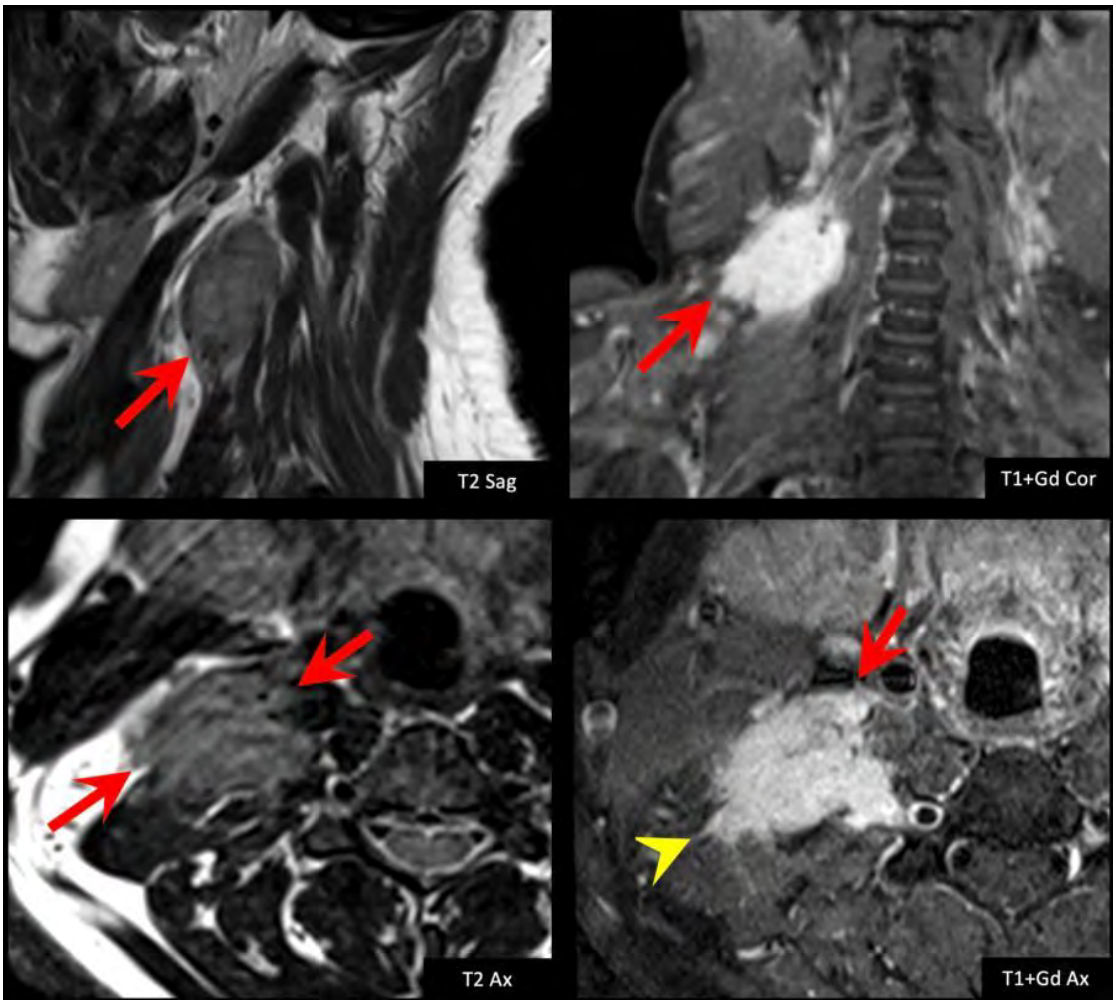

(Filename: TCT_582_Desmoid-typefibromatosis.jpg)

486

Steroid-Responsive Encephalopathy Associated with Autoimmune Thyroiditis (SREAT): Imaging Findings of a Rare Entity

A Alqabbani[1], S Chakraborty[2], R Aviv[3]

[1]University of Ottawa, Ottawa, Ontario, [2]The Ottawa Hospital, U. of Ottawa, Ottawa, ON, [3]The Ottawa Hospital, Ottawa, Ontario

Clinical History

Middle-aged male presented with new onset dysarthria, ataxia and aphasia. The patient later developed a seizure episode. The patient was noted to have a neck swelling on exam. Further workup revealed elevated CRP (30 mg/L), TSH (11.2 mIU/L) and Anti-TPO antibodies (>20,000 kIU/L). CSF analysis showed elevated protein. Paraneoplastic and neuronal antibodies were negative. The patient's condition improved after starting levothyroxine and prednisone.

Imaging Findings

CT Head: Normal. (Could not be included. Only one graphic file with a maximum of four (4) images is permitted) CTA: No vessel occlusion. The thyroid was noted to be diffusely enlarged and hypoattenuating. (Could not be included. Only one graphic file with a maximum of four (4) images is permitted) MR: Cortical/Subcortical subtle FLAIR hyperintense signal with associated enhancement on the postcontrast images. These findings were completely resolved on the 6-month follow-up MRI.

Discussion

Steroid-responsive encephalopathy with autoimmune thyroiditis (SREAT), first described by Brain et al, is neurologic complication of autoimmune thyroid disease. It is clinically characterized by encephalopathy (100%), seizures (66%), myoclonus (38%), neuropsychiatric symptoms (36%), and stroke-like symptoms (27%) (1). Improvement in response to treatment with glucocorticoids is characteristic. Although elevated thyroid antibodies were thought to play a role in the pathogenesis of the disease, the relationship between thyroid disease, antibody titers and the clinical manifestations remains unclear (2). MR Imaging often reveals no abnormalities. However, when present, cortical and subcortical increased signal intensity on T2/FLAIR and meningeal enhancement are frequently seen (3,4). These may or may not resolve with treatment (5).

Teaching Point

Cortical and subcortical T2/FLAIR increased signal and meningeal enhancement in patients with autoimmune thyroiditis raise the suspicion for SREAT in the right clinical context.

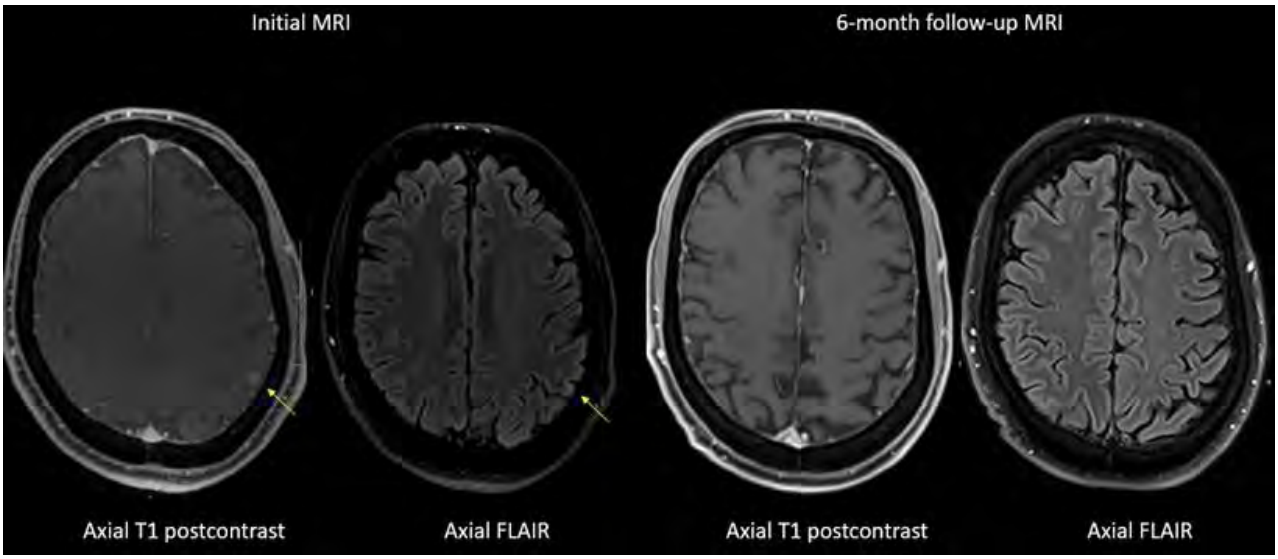

(Filename: TCT_486_STERAT.jpg)

1520

Suspected Propofol Infusion Syndrome: A Cause of Toxic-Metabolic Encephalopathy.

J Kim[1]

[1]*Keck School of Medicine of USC, LOS ANGELES, CA*

Clinical History

68 year old female status-post elective instrumented posterior spinal fusion for lumbar spondylosis reported to be "not waking up post-operatively". In the PACU, the anesthesiologist found the patient to be decreased in responsiveness after surgery. Naloxone was administered for suspected opioid overdose with little change in the patient's mental status. After a second dose was administered, the patient had a reported seizure episode and was promptly given IV Ativan and intubated. Immediate STAT CT head showed no definite abnormalities. STAT MRI brain was then obtained which showed symmetric signal abnormalities of the bilateral basal ganglia, suggestive of a toxic/metabolic encephalopathy. Patient remained encephalopathic for 2 days post-operatively until sedation was changed from propofol to ketamine + precedex. Following change from propofol, the patient slowly improved in mental status to return close to baseline by day 8.

Imaging Findings

Diffuse Sulcal FLAIR non-suppression was present. Symmetric T2/FLAIR hyperintense signal was present throughout the bilateral basal ganglia, greatest involving the putamen. Small foci of restricted diffusion were present in the bilateral basal ganglia.

Discussion

Toxic metabolic encephalopathy remains a very non-specific entity with a wide array of potential causes. We present a case of suspected Propofol Infusion Syndrome following routine outpatient surgery.

Teaching Point

Propofol Infusion Syndrome is a rare, but often overlooked cause of toxic-metabolic encephalopathy, particularly in the hospitalized patient. Propofol Infusion Syndrome should be considered as a potential cause of reversible encephalopathy.

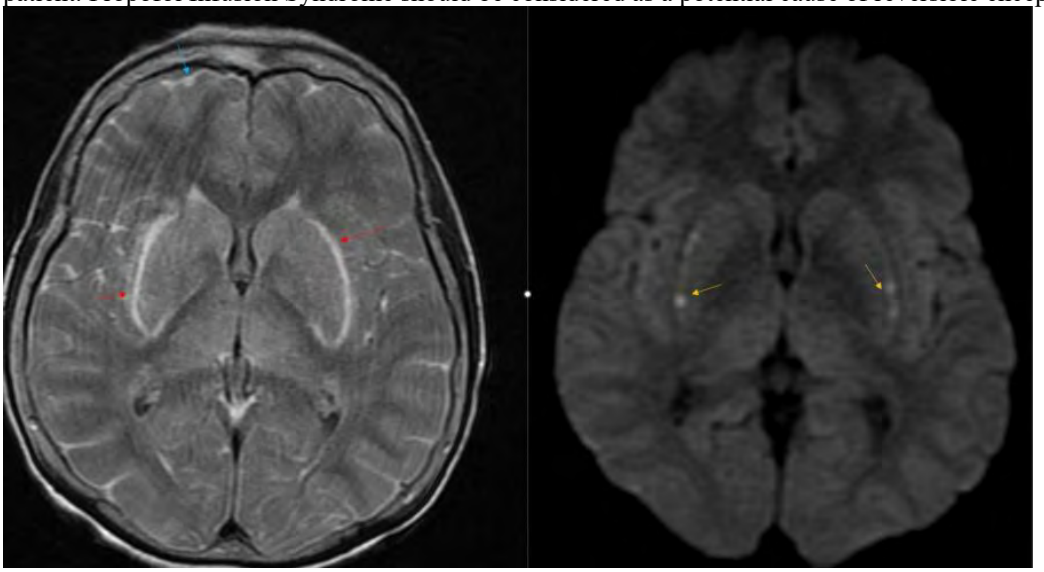
(Filename: TCT_1520_propofolinfusion.jpg)

1383

Syphilitic Gumma Masquerading as Nasopharyngeal Mass

A Joshi[1], T Combs[1], A Ali[2]

[1]University of Kansas School of Medicine - Wichita, Wichita, KS, [2]University of San Diego, La Jolla, CA

Clinical History

Syphilis is a sexually transmitted infection caused by the spirochete, Treponema pallidum. While the infection can have several clinical manifestations, the most common radiologic manifestation is neurosyphilis. The presentation of this disease and radiographic signs vary and depend on the temporal stage of the disease along with the region of the nervous system that has been affected. Asymptomatic neurosyphilis occurs weeks to months after the infection and there are typically no radiographic features signifying its presence. When imaging manifestations of neurosyphilis are present, they are best detected through CT and MR imaging. In the early stages of this disease, CT imaging typically does not display abnormalities although post-contrast imaging can show linear enhancement of the meninges.3 On the other hand, meningovascular syphilis occurs months to years after infection and its radiographic features include leptomeningeal enhancement and the presence of syphilitic gummas.1 Osseous involvement is exceedingly rare, occurring 0.15-0.23% percent of the time. Here we present a case of a 60-year-old caucasian male presenting with sinonasal pain radiating to the right ear and symptoms of right sided nasal obstruction.

Imaging Findings

MRI: Peripherally enhancing, centrally necrotic centered in the right fossa of Rosenmuller with invasion of the right aspect of the clivus and right petrous apex with obstruction of right eustachian tube. PET: FDG avid mass in right fossa of Rosenmuller extending into right foramen lacerum Biopsy: Nasal pharyngeal mucosa with chronic inflammation, ulceration, and spirochete bacteria consistent with syphilis. No evidence of malignancy.

Discussion

Studies have demonstrated the associations between syphilis infection and current smoking status as well as higher rates of confection with syphilis among patients presenting with a chief complaint of HPV infection. Therefore, while osseous involvement of the skull base is exceedingly rare in tertiary syphilis, early identification of at risk patients can lead to improved diagnostic accuracy and better patient care.

Teaching Point

In patients presenting with a nasopharyngeal mass, evaluation of risk factors for syphilitic infection can potentially avoid unnecessary workup and/or treatment for presumed malignancy.

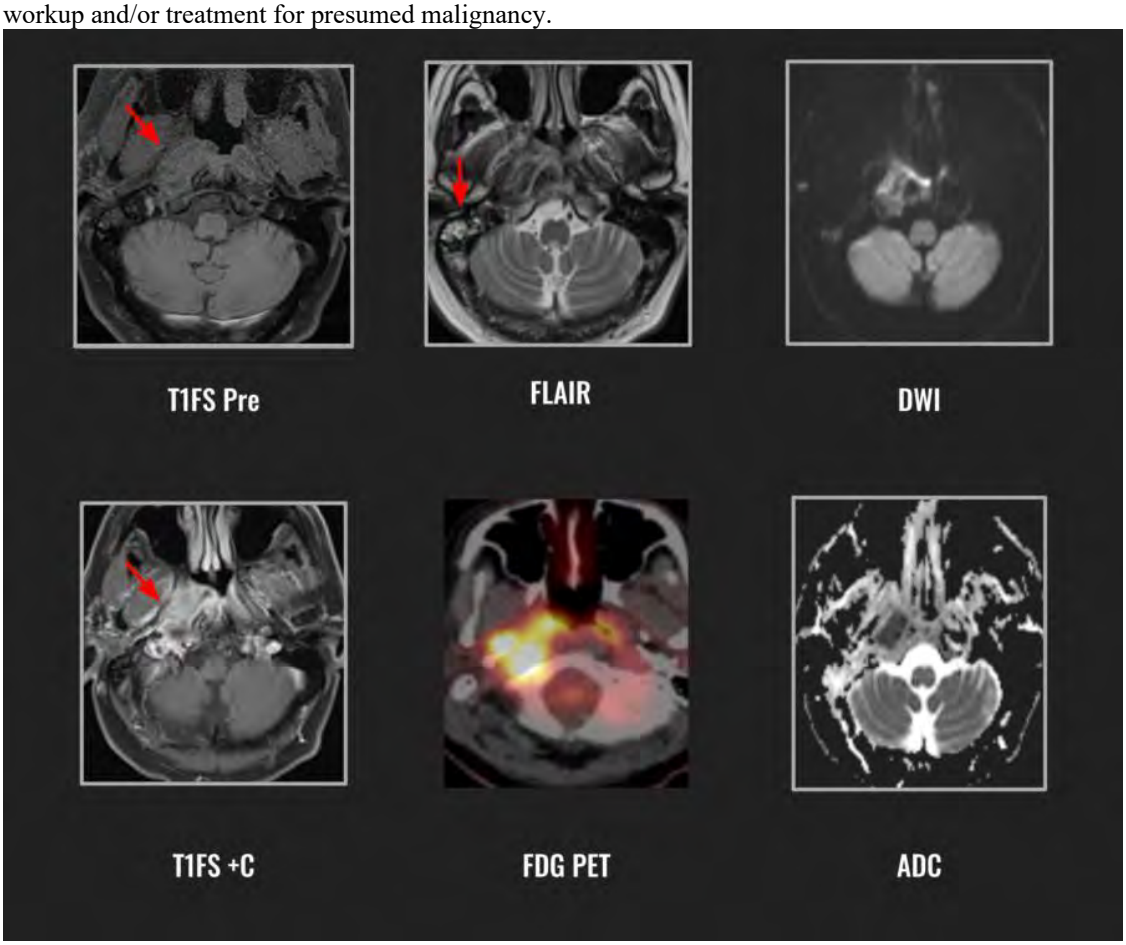

(Filename: TCT_1383_SyphilisNPMass.jpg)

257

Terson Syndrome: Intraocular Hemorrhage in the Setting of Increased Intracranial Pressure

T Henrie[1], C Carr[1]
[1]Mayo Clinic, Rochester, MN

Clinical History

We present the case of a 25-year-old man who was found down unresponsive and intoxicated. Initial non-contrast head CT showed intracranial hemorrhage, evidence of increased intracranial pressure (ICP), and right vitreous hemorrhage (figure 1). Follow up CT 5 hours later showed increased bilateral vitreous hemorrhage and swelling of the optic nerve sheaths (figure 2). Given refractory elevated ICP, a decompressive hemicraniectomy and evacuation of subdural hematoma (SDH) was performed. The patient improved, but had significant visual deficits in both eyes, greater on the right. Given the degree of vitreous hemorrhage and extremely poor visual prognosis on the right, right vitrectomy was not felt to be indicated. He underwent left vitrectomy with improved visual acuity.

Imaging Findings

Figure 1: Large scalp hematoma, acute bilateral SDH, diffuse SAH, and right vitreous hemorrhage. Diffuse sulcal effacement, effacement of the basilar cisterns, tonsillar herniation, and mild swelling of the optic nerve sheaths. Figure 2: Increased right greater than left vitreous hemorrhage. Dilated optic nerve sheaths.

Discussion

Vitreous hemorrhage in the setting of SAH is known as Terson Syndrome (TS). Modern definitions include any intraocular hemorrhage in the setting of SAH, traumatic brain injury, or intracranial hemorrhage. A proposed etiology of TS is that an abrupt increase in ICP results in increased cerebrospinal fluid in the optic nerve sheath, with resultant compression of the central retinal vein and venous outflow obstruction. The smaller retinal veins then rupture into the vitreous body.

Teaching Point

The incidence of TS is higher in patients with low Glasgow Coma Scale scores and is associated with up to 90% mortality. Visual complications include retinal detachment and vision loss. Spontaneous resolution of vitreous hemorrhage is possible, but many patients require vitrectomy to prevent visual deficits. CT findings of elevated ICP include effacement of the ventricles and basilar cisterns, herniation, and loss of grey-white matter differentiation. The optic nerve sheaths may be dilated. An optic nerve sheath diameter ≥ 6 mm measured 3 mm from the globe has been shown to correlate with an elevated ICP ≥ 20 mmHg. Although there may be distracting findings on the initial head CT, particular attention should be paid to the orbits in the setting of increased ICP. Radiologists can suggest TS early, aiding in recognition and treatment of vitreous hemorrhage to prevent vision loss.

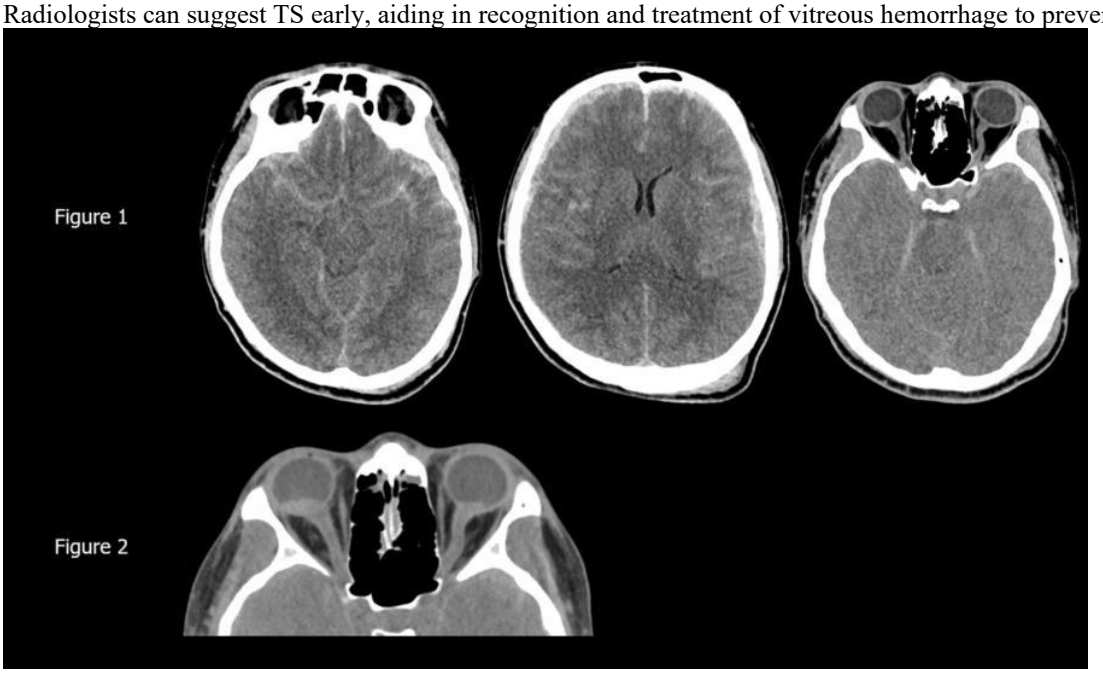

(Filename: TCT_257_Figure1-2.jpg)

1035

The Many Faces of Primary CNS Lymphoma

E Vilarello[1], Y Hussain[2], B Cohen[3], R Patel[3]
[1]Morristown Medical Center, Morristown, NJ, [2]Atlantic Health System, East Hanover, NJ, [3]Overlook Medical Center, Summit, NJ

Clinical History

Primary CNS lymphomas (PCNSL) are relatively uncommon tumors, accounting for 2.5% of all brain tumors. There is no co-existing systemic disease at the time of diagnosis, distinguishing it from CNS involvement from systemic lymphoma (secondary CNS lymphoma). In this exhibit, we present several cases of PCNSL which either occur in an unusual patient population, occur in an atypical location, or demonstrate abnormal imaging characteristics. We will review the typical features of PCNSL, including patient

demographics, location, presenting signs/symptoms, imaging features, pathology, and prognostic factors. We will also review characteristics of PCNSL described in literature that may mimic more aggressive lesions, such as those seen in immunocompromised patients.

Imaging Findings

We present several atypical imaging presentations of CNS lymphoma, such as infiltrative FLAIR pattern without corresponding diffusion restriction, lesions without associated enhancement, and cases presenting with hemorrhage. We also report a case that required several biopsies and several imaging modalities, including FDG-PET, to ascertain a definitive diagnosis, given concurrent use of steroid administration.

Discussion

PCNSL characteristically presents as a supratentorial lesion, commonly periventricular, with signs and symptoms related to size, location, and any associated mass effect. The classic imaging appearance of PCNSL is a circumscribed mass with restricted diffusion and enhancement. However, lymphoma should be considered in differential despite the lack of classic appearance. Infiltrative pattern in the periventricular white pattern with or without diffusion abnormality and use of advanced imaging should all be taken in the account. Lastly, administration of glucocorticoids may lead to a transient but profoundly altered appearance of a lesion with decreased size and surrounding edema and inconclusive histopathologic evaluation.

Teaching Point

Primary CNS Lymphoma can present with varying imaging patterns and therefore, atypical features should not exclude the possibility of PCNSL. Additionally, a more aggressive lesion may be masked if glucocorticoids were administered prior to imaging.

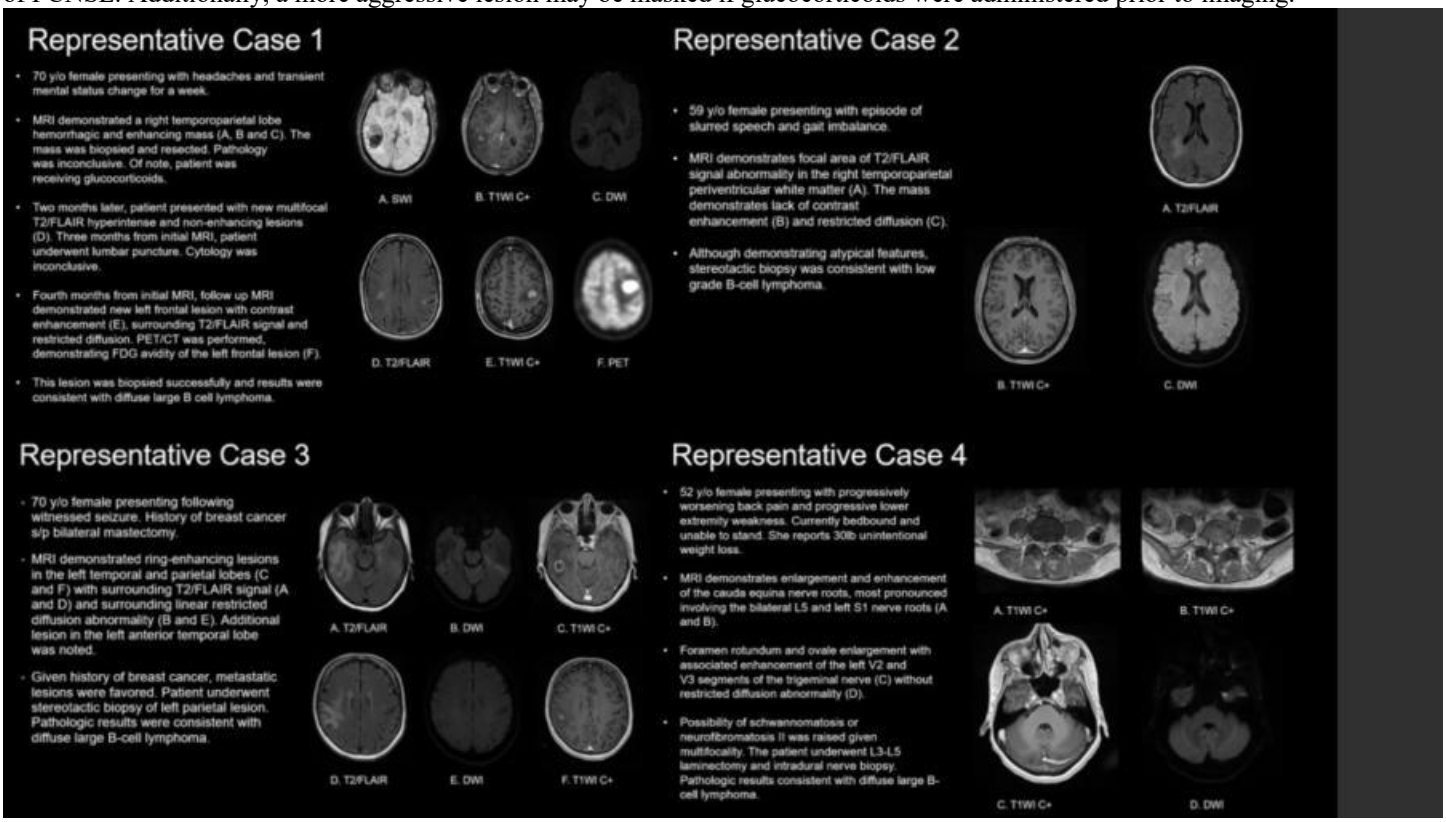

(Filename: TCT_1035_ASNR_Slides_Lymphoma.jpg)

437

The Mind Reflects the Face

H Reis[1], C McKinney[1], S Harder[2]

[1]Loma Linda University, Loma Linda, CA, [2]Loma Linda University, Loma LInda, CA

Clinical History

The study analyzed 12 patients diagnosed with Parry-Romberg syndrome (PRS) with an age range from 11-59 years (average 26.6 years, median 22.5 years). 9 patients were female and 3 were male. Patients were often diagnosed in the 1st or 2nd decade of life, presenting with hemifacial atrophy although one of our patients was an older adult who presented with recurrent focal neurologic symptoms. Other common presentations included monocular vision change, headache, seizure, stroke, paresthesia, pain, and weakness.

Imaging Findings

Common imaging features in our cohort included unilateral loss of subcutaneous fat with thinning of the ipsilateral calvarium and regional facial bones, atrophy of facial muscles and salivary glands, and associated enophthalmos. Intracranial features included ipsilateral cerebral calcifications, T2 hyperintensity and sulcal effacement. Advanced imaging in some patients demonstrated

decreased regional CBV and CBF and prolonged TTP in the areas of parenchymal abnormality with reduced metabolites noted on MR spectroscopy.

Discussion

Parry-Romberg syndrome is a rare, acquired disorder characterized by slowly progressive atrophy of the skin and soft tissues of half of the face (hemifacial atrophy) (1). Imaging findings have been broad and varied throughout multiple case studies and series. CT findings include atrophy on one side of the face or scalp, calcification in subcortical areas, and adjacent white matter decreased densities in the cingulate gyrus, corpus callosum, and in the frontoparietal parenchyma (2,3). Increased (T2/FLAIR) signal of white matter within the ipsilateral, and less commonly, contralateral brain parenchyma has been reported on MRI. In addition, ipsilateral, and less often, contralateral leptomeningeal enhancement as well as microhemorrhages have been identified on MRI (3,4,5,6,7). In certain case series, MRI abnormalities have been found on the ipsilateral side of migraine symptoms (4).

Teaching Point

Parry-Romberg syndrome demonstrates unique findings on imaging. Although not always present, intracranial findings can be prominent and a search for overlying cutaneous, osseous and muscular changes can be helpful in making the diagnosis from an imaging perspective. We add to the literature some features seen on advanced imaging (PWI and MRS) in this patient population.

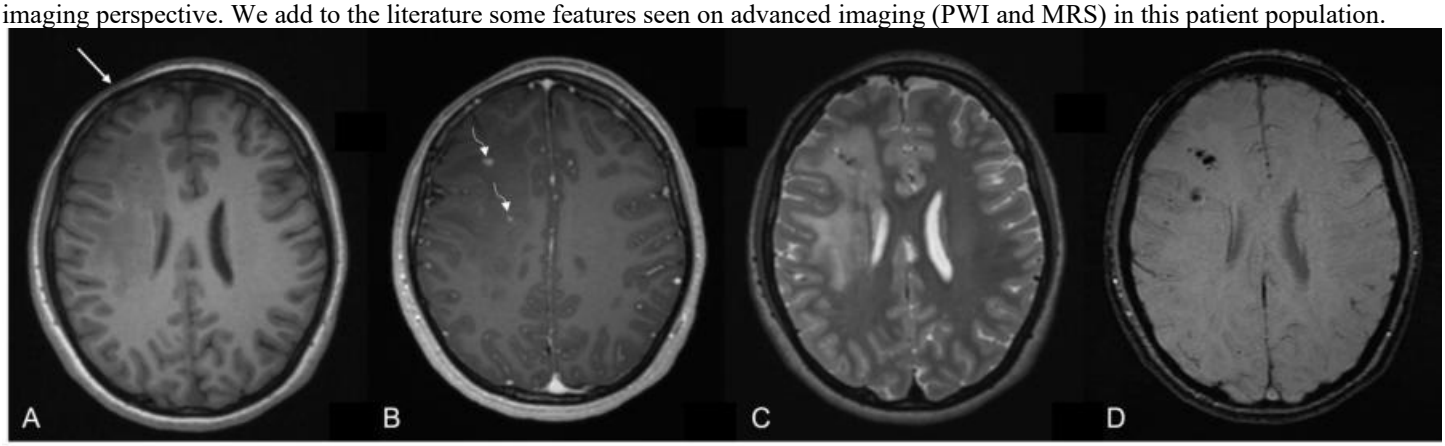

Figure 1: Axial T1 weighted image (A) demonstrates thinning of the right frontal scalp and subtle thinning of the underlying frontal bone (arrow). Axial post-contrast T1 weighted images (B) show foci of parenchymal enhancement (curved arrow). Axial T2 weighted images (C) show surrounding T2 hyperintensity within the surrounding white matter and axial susceptibility weighted images (D) demonstrate several foci of susceptibility hypointensity.

(Filename: TCT_437_PRS.jpg)

1257

The straw that broke the spinal cord: Use of diffusion-weighted imaging in spinal cord infarct

I Boykov[1], S Montoya[2]

[1]East Carolina University, Greenville, NC, [2]Eastern Radiologists, Inc, Greenville, NC

Clinical History

A 47-year-old man with a past medical history of hypertension, hyperlipidemia, smoking, and alcohol use presented to the emergency department with sudden onset acute quadriplegia. The morning prior to the visit, he noticed right-hand weakness that progressed to the left arm; shortly after, he was unable to walk, which prompted an urgent visit.

Imaging Findings

T2 sagittal imaging of the cervical spine shows spinal cord abnormality at C4-5 and corresponding degenerative changes (Fig. 1), although the degree of spondylosis appears inconsistent with the severity and acuity of clinical findings. Previous CT angiography (not included) showed patency of the right vertebral artery, but fat-suppressed T1 axial imaging (Fig. 2) shows an attenuated right vertebral artery flow void with circumferential hyperintesity suggestive of vascular injury. Sagittal DWI of the cervical spine shows concomitant restricted diffusivity at C4-5 (Fig. 3), indicative of infarction; additionally, axial DWI of the cerebellum shows concurrent infarction within the right PICA territory (Fig. 4).

Discussion

Most spinal cord infarcts are complications of aortic surgeries or due to aortic pathologies, although up to 50% have unknown etiology. Here we present an unusual case of acute SCI in an unclear clinical picture and confounding imaging findings, united by right vertebral artery injury leading to both spinal cord and right PICA territorial infarction. DWI and fat-suppressed T1-weighted imaging of the spine are not used routinely, however this case illustrates how both sequences can provide vital information for accurate diagnosis.

Teaching Point

Cervical spinal cord infarction secondary to spontaneous vertebral artery injury is a rare entity, but should be considered in a patient with acute paraplegia and vascular comorbitdities. DWI and fat-suppressed T1-weighted imaging are not standard sequences for a typical spinal MRI, but if added to the protocol in the appropriate clinical scenario may prove to be useful.

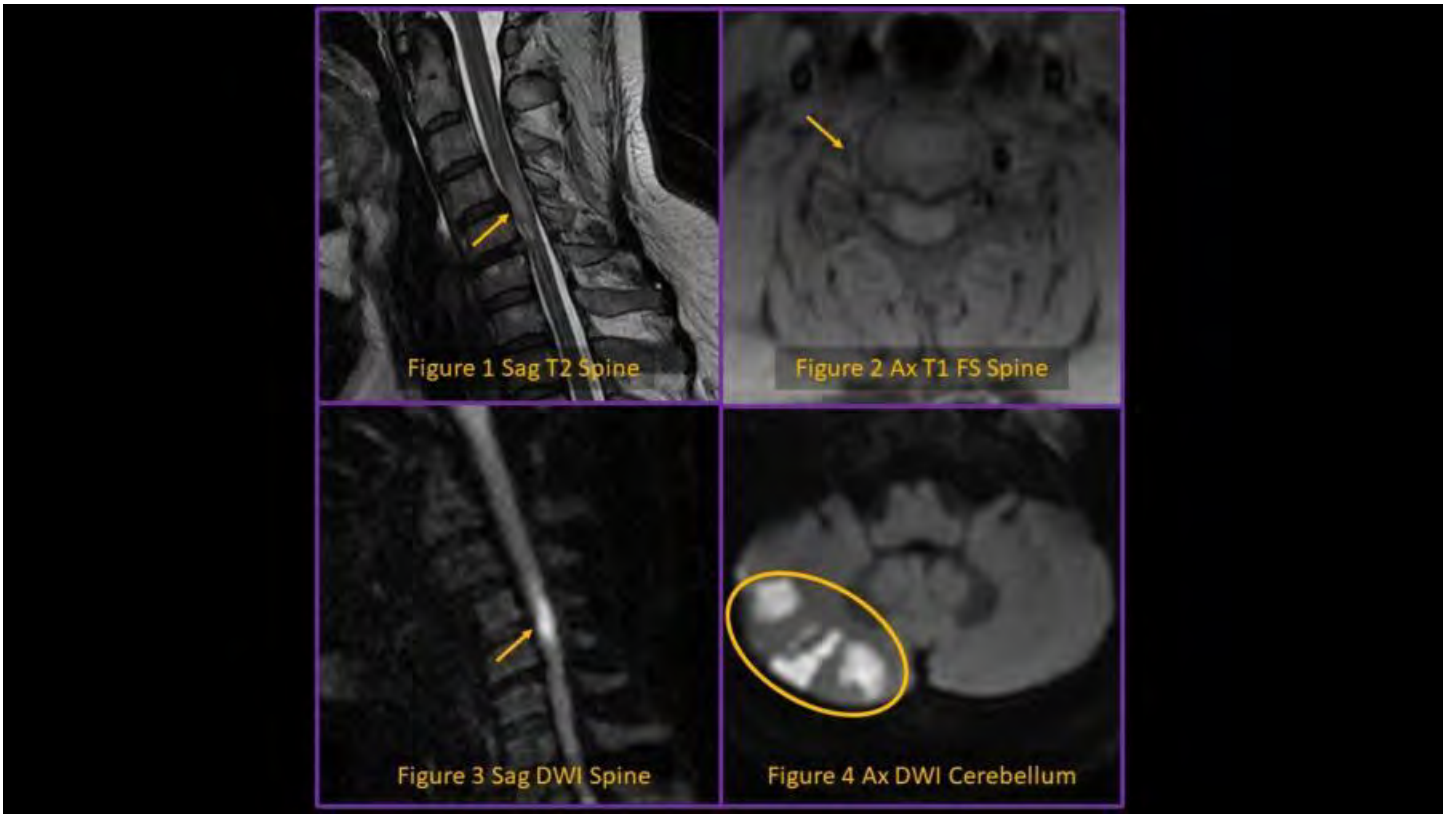

(Filename: TCT_1257_ASNR_Abstract_images.jpg)

770

The Value of High Spatial Resolution, Highly T2-Weighted Imaging in the Evaluation of Patients with Normal Pressure Hydrocephalus: a Case Series

Y Nikanpour[1], B Elder[1], j Graff-Radford[2], D Jones[3], H Botha[1], J Cutsforth-Gregory[1], J Huston[1], P COGSWELL[1]
[1]Mayo Clinic, Rochester, MN, [2]Mayo clinic, Rochester, MN, [3]Mayo Clinic, Rochseter, MN

Clinical History

We retrospectively studied 82 patients with suspected normal pressure hydrocephalus (NPH) who underwent 3T Siemens MRI between June 2020 and September 2022. Sequences included sagittal CISS and axial cine phase contrast of the cerebral aqueduct. The CISS sequence is a high spatial resolution, highly T2-weighted sequence, which was performed to evaluate patency of the cerebral aqueduct. Of these 82 patients, 9 (11%) had imaging features of congenital hydrocephalus, and three of these nine had an aqueductal web. Case 1: A 75-year-old man with progressive difficulties in walking, cognitive impairment, and urinary incontinence. Case 2: A 69-year-old man with longstanding seronegative rheumatoid arthritis and new unsteady gait, numbness in lower extremities, and cognitive decline. Case 3: A 74-year-old man with stable ventriculomegaly identified since age 37 and six months of progressive forgetfulness.

Imaging Findings

All three cases had marked lateral and third ventriculomegaly, a web within the cerebral aqueduct, and a normal caliber fourth ventricle. The cine phase contrast flow study performed at the cerebral aqueduct, superior to the web, showed no detectable flow at a venc of 10 cm/s. In contrast to patients with idiopathic NPH (iNPH) and features of disproportionately enlarged subarachnoid space hydrocephalus (DESH) [1], these patients had diffusely narrowed cerebral sulci and no features of extraventricular hydrocephalus.

Discussion

A subset of patients with NPH that remained asymptomatic until advanced age may have congenital hydrocephalus. Patients with congenital hydrocephalus may be differentiated from patients with iNPH by imaging features of lateral and third ventriculomegaly and diffusely narrowed cerebral sulci, with or without stenosis or web of the cerebral aqueduct. High spatial resolution highly T2-weighted imaging (CISS, FIESTA) is a key part of MRI examination of NPH to assess the patency of the cerebral aqueduct and potentially guide patient management. Specifically, patients with an obstructing web may be treated by endoscopic third ventriculostomy rather than shunt placement [3, 4].

Teaching Point

Improved visualization of the patency of the cerebral aqueduct and the presence of an obstructing web afforded by high-resolution T2-weighted imaging translates into better diagnostic performance of MRI in the detection of features of congenital hydrocephalus.

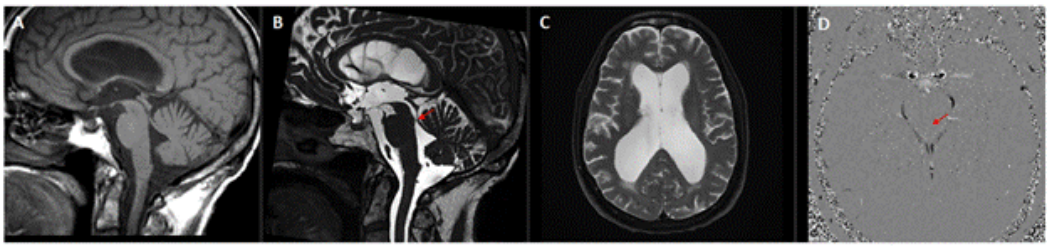

Case 2. 69-year-old male with congenital hydrocephalus. (A) Sagittal T1 from outside institution exam performed 5 months prior to exam at our institution shows lateral and third ventriculomegaly. (B) Sagittal CISS demonstrates a thin web at the inferior aqueduct (red arrow), not visible on the standard clinical sagittal T1-weighted imaging. (C) Ax T2 FSE demonstrates marked lateral ventriculomegaly, relatively diffusely narrow cerebral sulci, and mild periventricular T2 hyperintense signal. (D) No detectable flow in the aqueduct on the cine phase contrast exam with venc = 10cm/s (red arrow).

(Filename: TCT_770_Picture1.gif)

764

This Is Not The Neoplasm You Are Looking For: Two Cases Highlighting The Development of Chronic Encapsulated Intracerebral Hematoma (CEIH)

E Chen[1], E Dedekam[2]

[1]Madigan Army Medical Center, Joint Base Lewis-McChord, WA, [2]Madigan Army Medical Center, OLYMPIA, WA

Clinical History

Patient 1: 19-year-old male with no past medical history presented with the worst headache of his life and was found to have a right basal ganglia hemorrhage that was medically managed. Follow up imaging showed development and enlargement of an intraparenchymal cystic lesion causing mass effect that coincided with the patient experiencing worsening somnolence. He underwent emergent surgery with the operative report describing the cystic lesion as containing old hematoma with an adjacent mass consistent with an arteriovenous malformation (AVM). Patient 2: 93-year-old female with past medical history of stereotactic radiosurgery in 2009 for AVM in the right temporal lobe presented for near syncope without focal neurologic deficit. Patient had been receiving regular imaging to follow up post-radiation changes in the right temporal lobe as well as monitor an enlarging cystic lesion in the right temporal lobe. The patient elected for medical management of her symptoms and entered hospice care one month after presentation.

Imaging Findings

Patient 1 (A&B): Enlarging well-circumscribed right basal ganglia cystic lesion in the area of prior hemorrhage causing midline shift.
Patient 2 (C&D): Enlarging well-circumscribed cystic lesion in area of a previously treated right temporal lobe AVM.

Discussion

CEIH is a rare cause for an enlarging cystic brain lesion that was first described in 1981 with several dozen cases described in systematic reviews. This lesion presents with a progressive neurologic symptoms depending on location and is characterized by hematoma with a surrounding fibrous capsule on histology. There is an association with vascular lesions, such as patient 1's occult AVM, and history of stereotactic radiosurgery like patient 2. CT and MRI findings include a well-circumscribed intraparenchymal lesion with possible mass effect, adjacent edema, and T2 hypointense rim. Vascular imaging may not show an underlying malformation. Surgery is recommended with craniotomy or endoscopic aspiration due to risk of worsening mass effect symptoms.

Teaching Point

In a patient presenting with intracerebral hemorrhage, the etiology can often be occult on initial imaging. The presence of an expanding intraparenchymal cystic lesion on follow-up imaging may be interpreted as a potential neoplasm, but other etiologies such as CEIH should be considered. While CEIH are more likely seen in association with AVMs that have been treated with stereotactic radiosurgery, they can also be seen with untreated occult AVMs.

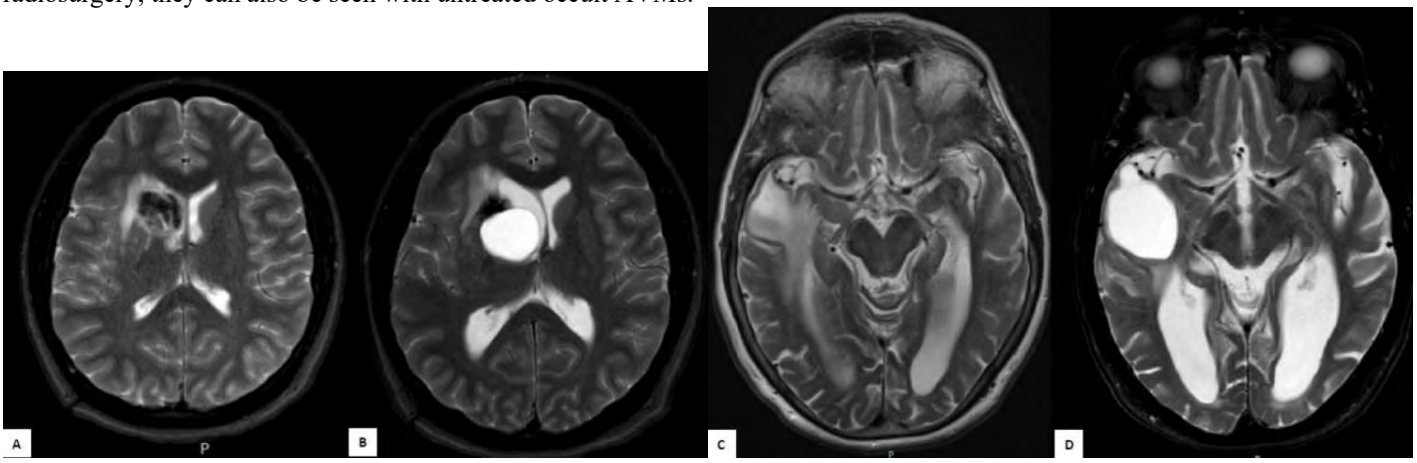

(Filename: TCT_764_Capture2b.jpg)

552

Torcular Pseudomass in Neonates and Infants: A Diagnostic Challenge

A Mao[1], E Yekeler[1], T Massini[1], I TUNA[1]
[1]*University of Florida Shands Hospital, Gainesville, FL*

Clinical History

Patient 1, a 6-day-old newborn male, former 41 weeks gestational age, was referred to MRI for evaluation of hypoxic ischemic encephalopathy and dural sinus thrombosis. Patient 2, a 3-month-old male who was born at 39 weeks gestational age via uncomplicated vaginal delivery presents with atypical head shape and bony prominence at the posterior head. There was no history of inciting trauma. Physical exam revealed no signs of increased intracranial pressure, but demonstrated prominent inion (external occipital protuberance) on palpation. Patient was referred to MRI for further evaluation after CT imaging was performed for suspected craniosynostosis.

Imaging Findings

For Patient 1, Figure A (T2 axial) and Figure B (DWI axial) show T2 hyperintense mass-like lesion adjacent to the sinus confluence without diffusion restriction (arrows). For Patient 2, Figure C (reformatted sagittal CT) and Figure D (T1 post-contrast sagittal) at 6 months of age demonstrate a mass-like lesion under the inner table at the level of the occipital protuberance and its relationship to the torcular Herophili and dural layers (arrows). An underlying anomaly in the adjacent parenchyma or venous structures was not depicted in either patient.

Discussion

Torcula/torcular Herophili or sinus confluence, is a region in the posterior fossa where the superior sagittal sinus, straight sinus, and transverse sinus connect the dural venous sinuses. In neonates and infants, there may be redundant soft tissue in the torcula, which has been described as "torcular pseudomass" and likely represents a benign developmental variant. Imaging characteristics includes T1 isointensity/hypointensity and T2 hyperintensity on MRI with variable contrast enhancement without considerable mass effect on the adjacent sinuses. Differential diagnoses include arachnoid, dermoid, or epidermoid cysts. Risk-benefit does not favor interventional procedure and follow-up imaging could be considered if there are clinical changes.

Teaching Point

"Torcular pseudomass" is an incidental finding in neonates and infants and presents a diagnostic challenge as to whether or not to pursue further imaging workup due to its unfamiliarity. It likely represents a benign neonatal developmental variation reflecting redundant soft tissue in the torcula.

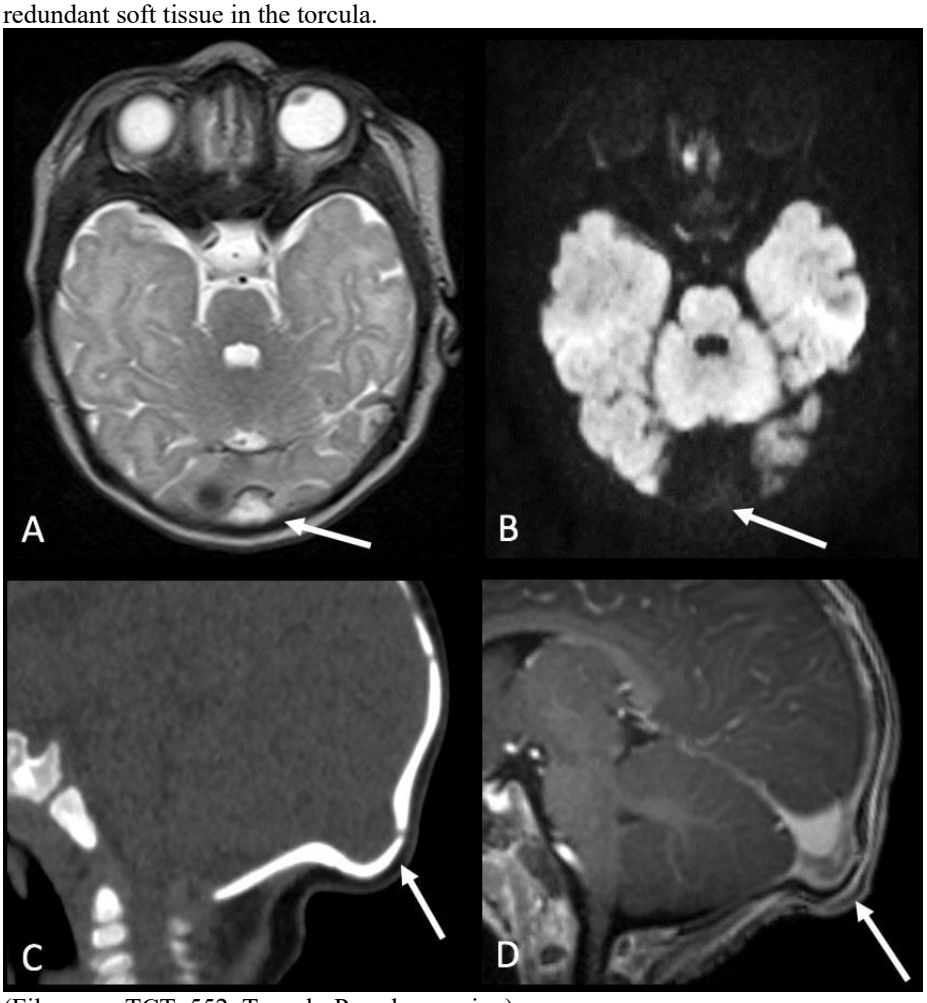

(Filename: TCT_552_TorcularPseudomass.jpg)

151

Torcular Pseudomass Mimicking an Occipital Meningocele

M Baggett[1], J Chang[2], A Ozturk[3]

[1]University of California, Davis, Sacramento, CA, [2]UCSD, San Diego, CA, [3]UC Davis Medical Center, Sacramento, CA, Folsom, CA

Clinical History

39-year-old G1P0 female presents for routine second trimester fetal ultrasound (US). On US study, the posterior skull is not well visualized, raising concern for an occipital meningocele. Patient is referred for amniocentesis and fetal Magnetic Resonance Imaging (MRI). Amniotic fluid AFP is within normal limits.

Imaging Findings

Fetal MRI reveals a small extra-axial T2 hyperintense structure adjacent to the Torcula Herophili with an intact outer table of the occipital calvarium (images). No spinal meningocele is present.

Discussion

The findings are most consistent with a torcular pseudomass, a benign proliferation of soft tissue adjacent and posterior to the torcula Herophili. The differential diagnosis includes an arachnoid cyst, a prominent arachnoid granulation, but much less likely an occipital meningocele, given the intact outer table of the calvarium. Follow-up post-natal MRI is recommended for definitive diagnosis, as a pseudomass will not suppress on T2 FLAIR sequences, whereas the CSF within an arachnoid cyst/granulation or meningocele will suppress. Torcular pseudomass may exhibit postcontrast enhancement, however this should not be confused for a malignant process. The case discussion will include a brief discussion of imaging characteristics of torcular pseudomass, with examples of the differential diagnoses including arachnoid cysts/granulations and meningocele/encephalocele, on both ultrasound and MRI.

Teaching Point

The case discussion will include a brief discussion of imaging characteristics of torcular pseudomass, with examples of the differential diagnoses including arachnoid cysts/granulations and meningocele/encephalocele, on both ultrasound and MRI.

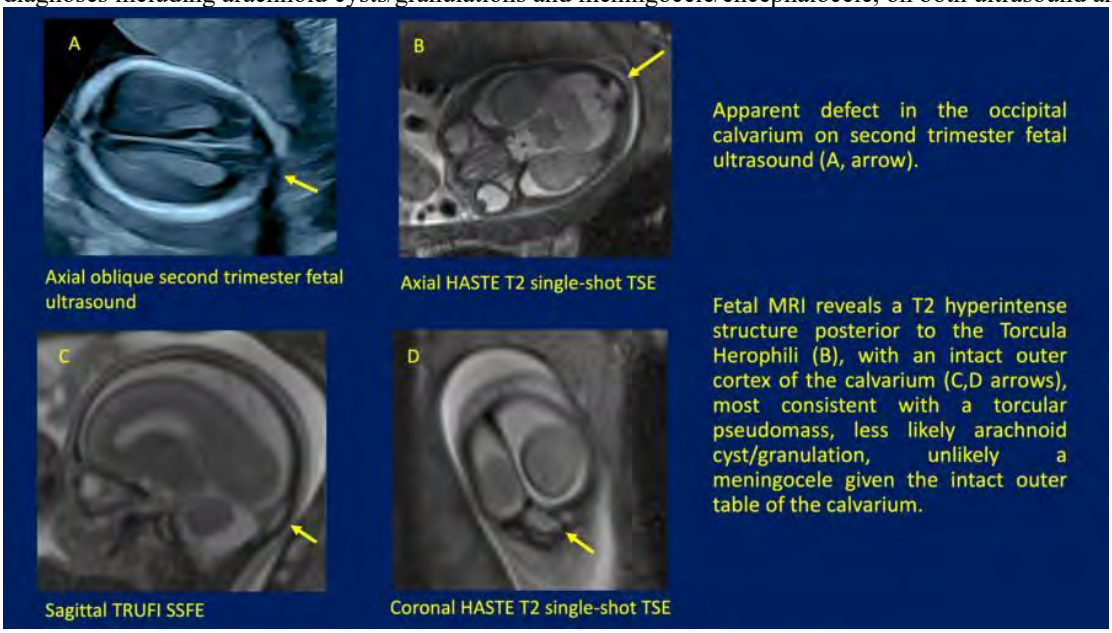

(Filename: TCT_151_ASNR2023TorcularPseudomassabstractimageBAGGETT.jpg)

1266

Transient Plexopathy Following Endovascular Embolisation of Cervical Paraspinal Epidural AV Shunts

G PADMASRI[1], K Kulanthaivelu[1], D Sharma[1]

[1]National Instituite of Mental Health and Neurosciences, Bangalore, Karnataka

Clinical History

This case series describes the transient post procedure complications of embolization in two patients with cervical paraspinal epidural shunts done in a single centre over a period of one year. Uniqueness of this case series lies in its rarity and limited literature regarding this benign complication. Two male patients, 26 year old and 47 year old, presented with unilateral radicular pain along neck, shoulder and arm since 2 years, followed by progressive weakness of ipsilateral upper limb. Imaging workup revealed paravertebral AVM with enlarged epidural venous plexus at C3 to C6 level with cord compression – right side for one patient and left side for other patient. Arterial feeders in both cases noted from ipsilateral vertebral artery, thyro-cervical and costo-cervical feeders. Post transarterial liquid embolisation via the ascending cervical artery, complete occlusion of the shunt was observed. Post extubation, there was deterioration of power in the ipsilateral upper limb in both the patients. MRI cervical spine showed acute thickening & hyperintensity involving C4 through C6 nerve roots of the ipsilateral brachial plexus without any cord signal changes. Patients were started on steroids and improvement in the upper limb power noted, following which the patients were discharged in stable condition.

Imaging Findings
Described in clinical history section
Discussion
Cervical paraspinal epidural AVFs are rare spinal vascular malformations. In our series, both the patients had similar presenting history, arterial feeders and developed symptoms secondary to nerve root and cord compression by engorged epidural venous plexus. Following complete successful embolization, transient worsening of weakness of the ipsilateral upper limb noted secondary to hyperintensities along the brachial plexus. We propose a theory that transient increase in venous pressure immediately post embolization has led to transient venous hypertension and ipsilateral plexopathy. However, larger data is required to validate the hypothesis.
Teaching Point
Transient increase in venous pressure immediately post embolization in cervical paraspinal epidural AV shunts may lead to plexopathy and weakness which can potentially be improved by steroid administration.

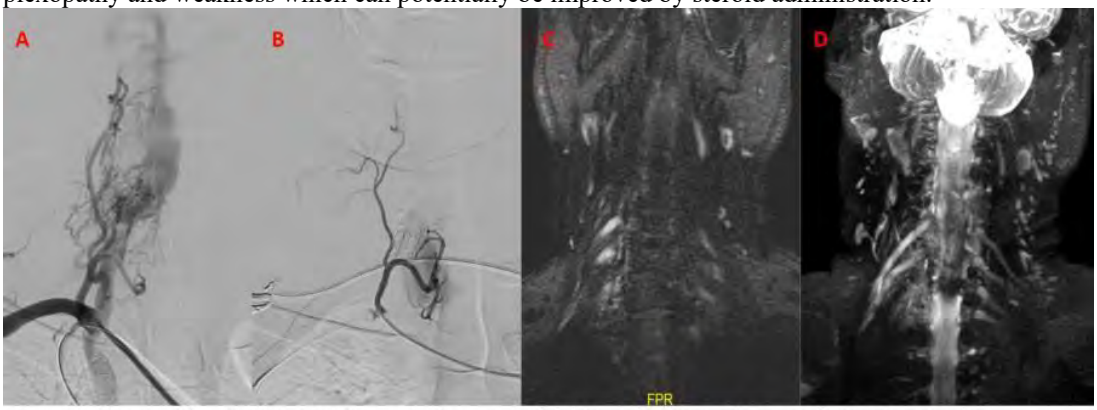

Figure ; 47 year old male with A) right cervical paraspinal Epidural AV shunt. B) Post embolization showing complete obliteration of the shunt. C) and D) shows transient thickening of C4-C6 nerve roots post embolisation
(Filename: TCT_1266_abstract.JPG)

742
Traumatic Herniation of Bowel into the Spinal Canal
A Vij[1], K Oguz[1], J Huynh[1], O Raslan[1], L Hacein-Bey[1], M Bobinski[1], A Ozturk[1]
[1]*University of California Davis, Sacramento, CA*

Clinical History
We report a rare case of post traumatic entrapment of bowel in the spinal canal in a two-year-old female after a rollover motor vehicle accident. On arrival, the patient's physical exam was notable for inability to move her bilateral lower extremities, sensory deficits in the bilateral lower extremities, and loss of rectal tone. The patient underwent numerous interventions with the pediatric neurosurgery and general surgery teams to stabilize her condition and is paraplegic due to the consequences of her injury.
Imaging Findings
Computerized tomography of the abdomen and pelvis demonstrated devascularization of the left kidney and a small bowel loop that appeared to be herniated posteriorly into the lumbar spinal canal after a 180-degree twist of the bowel in the region of the retroperitoneum. There was also complex a fracture of the L2 inferior endplate and the posterior elements including the pars interarticularis bilaterally and the spinous process. Subsequently Magnetic Resonance Imaging (MRI) of the lumbar spine was performed which demonstrated the aforementioned fractures with posterior retropulsion of the L2 vertebral body, ventral epidural hematoma (Figure, star), hematomyelia, cord edema, entrapment of a small bowel loop within the epidural space at L2 (Figure, arrows) with dilation of both ends of the bowel loop contributing spinal canal narrowing.
Discussion
Traumatic herniation of bowel into the spinal canal is an extremely rare entity. A review of the literature revealed few case reports documenting similar phenomena. Jing et. al reported traumatic incarceration of jejunum in a patient with L4 vertebral body fracture after being pinned between two railroad tracks. Silver et. al reported a case of a three-week-old female with entrapment of jejunum after sustaining a fracture dislocation of L2 where abdominal radiographs demonstrated a distal obstructive pattern with subsequent CT at a tertiary care center showing air within the spinal canal. Air within the spinal canal with associated spinal fracture is a key imaging finding, which may indicate hollow viscus injury. Each of these cases highlights the importance of awareness of this diagnosis in trauma patients, as most of these cases were discovered at abdominal exploration.
Teaching Point
Herniation of small bowel into the spinal canal is a potential complication of trauma. Radiologists should be aware of this entity as they play a key role in the recognition of this entity and help to guide accurate diagnosis and management.

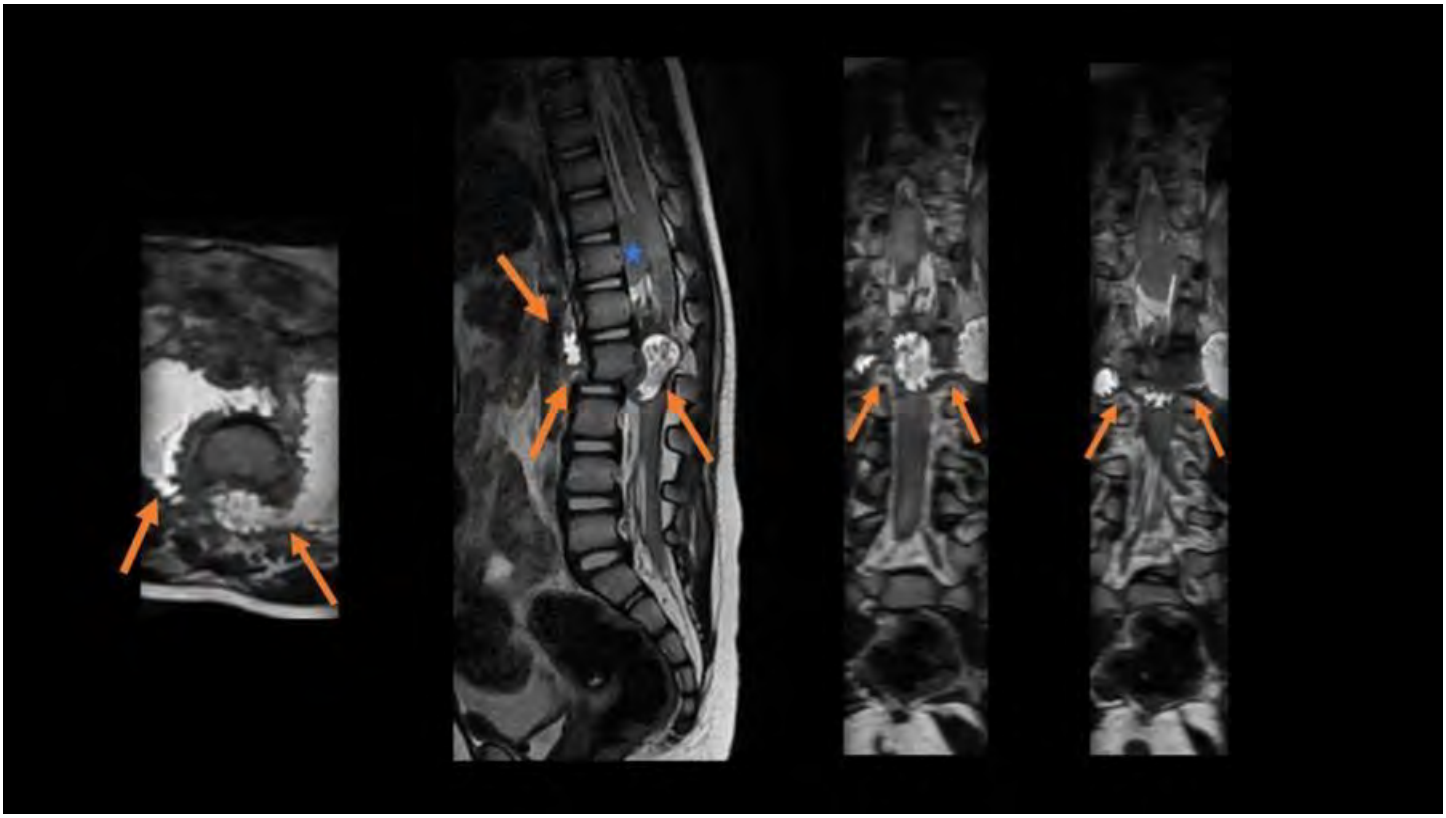

(Filename: TCT_742_entrappedbowel.jpg)

1373

Traumatic Intravestibular Displacement of Stapes Footplate

A Gonzalez[1], D Aasen[2], C Grindle[3], R Hynecek[1]

[1]Hartford Hospital, Hartford, CT, [2]University of Connecticut Health, Farmington, CT, [3]Connecticut Children's Medical Center, Hartford, CT

Clinical History

The patient is a 12-year-old female with a history of premature birth, language developmental delay, patent ductus arteriosus who presented to the emergency department for severe vertigo, nausea, and vomiting after a non-specific otologic injury from a rat-tail comb. She was discharged with supportive medications, but returned to clinic with persistent symptoms, with exam findings including small posterior-superior tympanic membrane perforation, wobbly gate, slouching posture, normal head impulse test, and no nystagmus. An audiogram showed right moderate to moderately-severe conductive hearing loss across all frequencies with normal range contralateral hearing. A subsequent CT of the internal auditory canals was ordered.

Imaging Findings

Noncontrast temporal bone CT images demonstrated mild nonspecific thickening of the right tympanic membrane. There was an abnormal orientation of the otherwise normal right ossicular structures with medial displacement of the incudostapedial joint and an intravestibular hyperdensity (red arrow) representing the dislocated stapes footplate visible on axial (left) and coronal (right) images. The remainder of the otic capsule and labyrinthine anatomy was unremarkable.

Discussion

Although rare, stapediovestibular luxations and dislocations are most often caused by penetrating trauma to the external auditory canal. Patients present with nonspecific vestibular symptoms such as nausea, vertigo, and tinnitus and conductive, sensorineural, or mixed hearing loss1. Treatment varies from conservative management2 to surgery3 with varying levels of hearing recovery. Some patients require to be fitted with hearing aids as a supportive treatment. The patient improved with supportive care and the tympanic membrane perforation spontaneously healed. Based on this patient's clinical improvement, it was elected to forego corrective surgery in favor of conservative management. She is being fitted for a hearing aid to overcome her conductive hearing loss.

Teaching Point

The mechanism of traumatic injury plays a role in determining the direction of stapediovestibular luxations and dislocations. While the stapes can shift throughout the middle ear space, it is not limited to the middle ear space alone. Although rare, with the right mechanism of trauma the stapes can displace into the vestibule. As a result, the vestibule should be closely evaluated when the patient is experiencing vestibular symptoms and an abnormal appearance of the ossicular structures is identified.

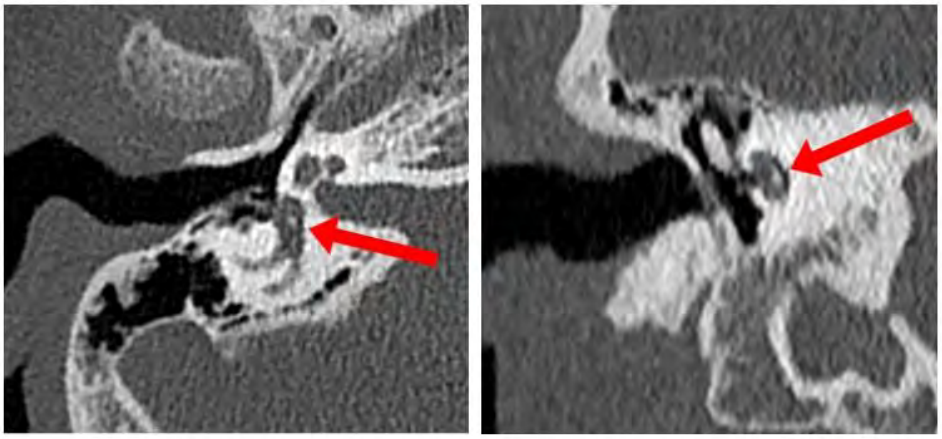

(Filename: TCT_1373_imageforASNR.jpg)

1272

Treatment of a meningioma from middle meningeal artery embolization for a subdural hematoma

T Chaudhry[1], S Ansari[2]

[1]Northwestern University Feinberg School of Medicine, Westmont, IL, [2]Northwestern University, CHICAGO, IL

Clinical History

A 95 year-old female with history of atrial fibrillation (on Xarelto) and hypertension presented with an acute on chronic subdural hematoma after a fall. She was scheduled for a right middle meningeal artery embolization to provide a minimally invasive option for the treating mass effect and decrease risk of rebleeding. An ipsilateral high frontoparietal convexity meningioma was incidentally noted.

Imaging Findings

Serial coronal head CTs at the level of the foramen of Monroe demonstrate a)a right frontoparietal convexity acute on chronic subdural hematoma (white arrow) and a high right frontoparietal meningioma measuring 2.5 x 2.1 x 2.4 cm (transverse by anterioposterior by craniocaudal) (blue arrow). b) Four months follow-up after MMA embolization demonstrates resolution of the right subdural hematoma and marked decrease in size of the meningioma, measuring 1.3 x 1.3 x 0.8 cm. c) Follow-up head CT 18 months after MMA embolization demonstrates persistent resolution of the right subdural hematoma and continued decrease in size of the meningioma, now measuring 1.1 x 1.1 x 0.6 cm.

Discussion

Middle meningeal artery embolization is a new and rising treatment for subacute and chronic subdural hematomas. This is due to in part by the microvasculature of the dura becoming fragile and hypertrophied due to trauma or underlying insult resulting in hyperpermeability and inflammation. The subsequent membrane that develops is highly vascular and prone to bleeding. Majority of dural convexity arterial supply arises from the middle meningeal artery (MMA), over 65%. Although there are multiple meningeal arteries that supply the dura, the MMA often vascularizes the membrane prone to bleeding. Neuroendovascular surgical radiology has evolved to incorporate MMA embolization as a minimally invasive treatment for subacute subdural hematoma. However, it is still being investigated as a treatment for tumors. Meningiomas arise from the dura with majority of its blood flow from the MMA and other meningeal arteries which accounts for its highly vascular appearance. It makes sense then that embolizing the MMA could serve as a minimally invasive treatment for intracranial meningiomas. This is a case demonstrating incidental simultaneous embolization with near complete resolution of the meningioma as a potential treatment outcome to explore.

Teaching Point

MMA anatomy and blood supply Physiology of subdural hematoma and membrane formation Meningioma treatment and blood supply Meningioma imaging appearances.

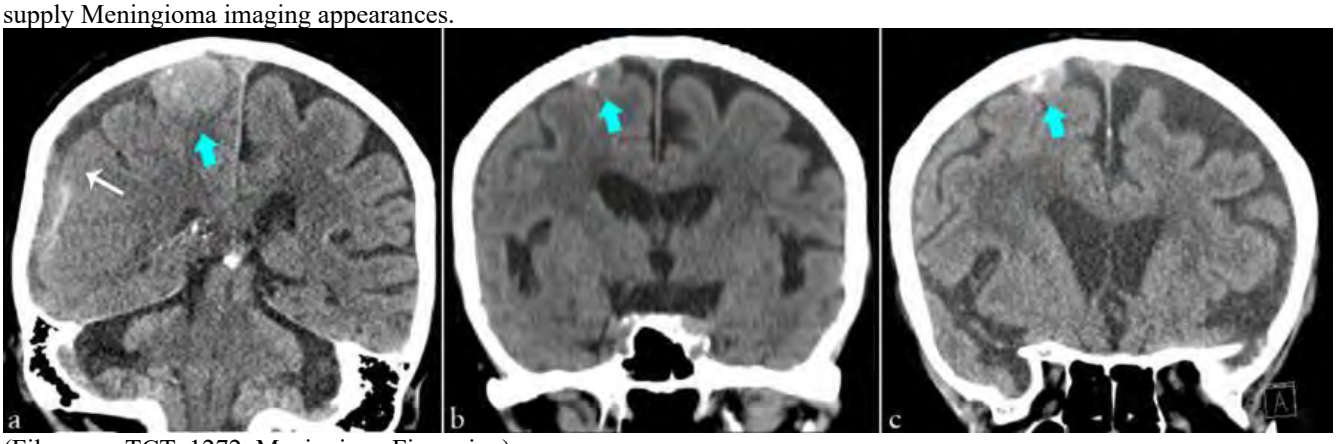

(Filename: TCT_1272_MeningiomaFigure.jpg)

1006

Trichotillomania and a Case of Cranial Osteomyelitis: Getting to the Root of the Problem

C Castro[1], V Jewells[1], S Hung[1]
[1]*Department of Radiology, University of North Carolina at Chapel Hill, Chapel Hill, NC*

Clinical History

62-year-old female with past medical history of trichotillomania, hypertension, hyperlipidemia, and diabetes mellitus type II presents with large calvarium vertex defect with exposed dura and bone and blood oozing.

Imaging Findings

1) Approximately 6.6 cm roughly circular vertex wound overlying the medial parietal bones with an underlying 3.9 x 3.5 cm osseous defect of both medial parietal bones that extends to the level of the inner table of the skull and abuts the superior sagittal sinus. 2) 4mm outpouching along the superior aspect of the sagittal sinus overlying the central portion of calvarium vertex osseous defect. 3) No evidence of venous sinus thrombosis.

Discussion

Cranial osteomyelitis requires a prolonged course of intravenous antibiotics and, usually, surgical intervention. The correct imaging protocol and prompt interpretation of the involved structures to obtain a radiographic answer is of the utmost importance. In this case, from external visualization the patient had a large calvarium vertex defect with exposed dura and hemorrhage. The primary clinical concern was for osteomyelitis and thrombosis of the superior sagittal sinus. Therefore, a CT venogram was obtained. The patient was found to have a pseudoaneurysm of the superior sagittal sinus without extravasation. Even without definite radiographic evidence of osteomyelitis on initial CT, the patient is presumed to have or be at high-risk for osteomyelitis due to exposed bone.

Teaching Point

Trichotillomania, a chronic psychiatric illness defined by repeated trauma to follicles of hair, is not historically thought of as a risk factor for cranial osteomyelitis. Trauma to underlying structures and osteomyelitis are potential sequela as demonstrated here. Areas of concern in this case include the bony calvarium, the brain itself, and the superior sagittal sinus with potential thrombosis or pseudoaneurysm.

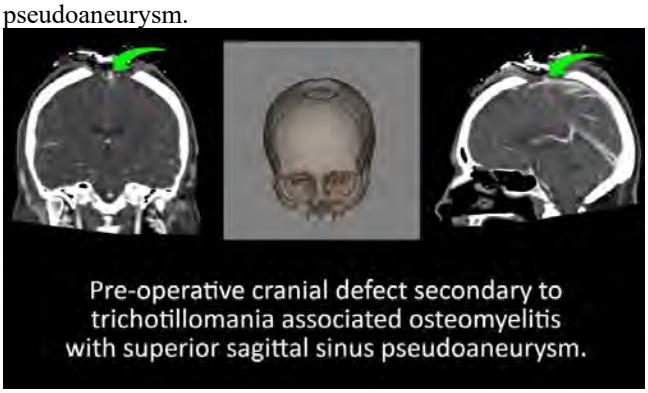

(Filename: TCT_1006_excerpta.jpg)

906

Variant Course of the Subarcuate Vein and Canal: An Underrecognized Entity

M Muzaffar[1], A Mehta[2], A PYRROS[3]
[1]*Dupage Medical Group, Oak Brook, IL,* [2]*Duly Health and Care, Lisle, IL,* [3]*Duly Health and Care, HINSDALE, IL*

Clinical History

This a case series of five patients who presented for temporal bone CT for a variety of symptoms from hearing loss to vertigo. A unilateral enlarged subarcuate (SA) canal was identified in three patients and bilateral enlarged SA canals were identified in the other two patients on CT. No concomitant abnormalities were identified in the otic capsule or middle ear cavity. These enlarged channels prompted additional workup with contrast-enhanced MRI in three patients, confirming the presence of dilated aberrant veins in the petrous apex.

Imaging Findings

Temporal bone CT revealed an enlarged channel contiguous with the SA canal in all patients. In two patients, the SA vein then descended between the crura of the lateral semicircular canal (LSC) and joined a widened tympanic segment of the facial nerve canal (FNC). In another patient, bilateral enlarged SA veins assumed a similar course in the otic capsule and then descended posterior to the sinus tympani. In yet another patient, the SA vein emanated from an enlarged SA canal and emptied into a slightly widened vestibular aqueduct. In the last patient, the dilated SA canal gave rise to two branching channels, an anterior vein following the tympanic segment of the FNC, and a posterior vein descending into the mastoid segment of the FNC.

Discussion

While the normal course of the SA canal is well documented in the literature, there have been only a few case reports describing an atypical course in adults. These isolated reports have identified this structure only on CT and ascribed it to an artery. However, in our series, three patients had MRI correlation depicting a venous drainage pattern, confirming the SA vein rather than the accompanying

artery as the culprit vessel. Furthermore, prior reports describe a vessel descending between the crura of the LSC; while this course was the most encountered in this series, it is only one of several paths that an aberrant SA vein can assume.
Teaching Point
An enlarged SA canal is uncommon, but the radiologist should be familiar with this entity to avoid misinterpretation. The enlarged SA vein commonly descends lateral to the vestibule and should not be mistaken for demineralization from otospongiosis. The SA vein tends to be associated with the facial nerve, and widening of the FNC should not be misconstrued for a schwannoma or persistent stapedial artery. The SA vein can drain into the vestibular aqueduct, mimicking an enlarged aqueduct. Tracing the venous channel back to the SA canal avoids misdiagnosis.

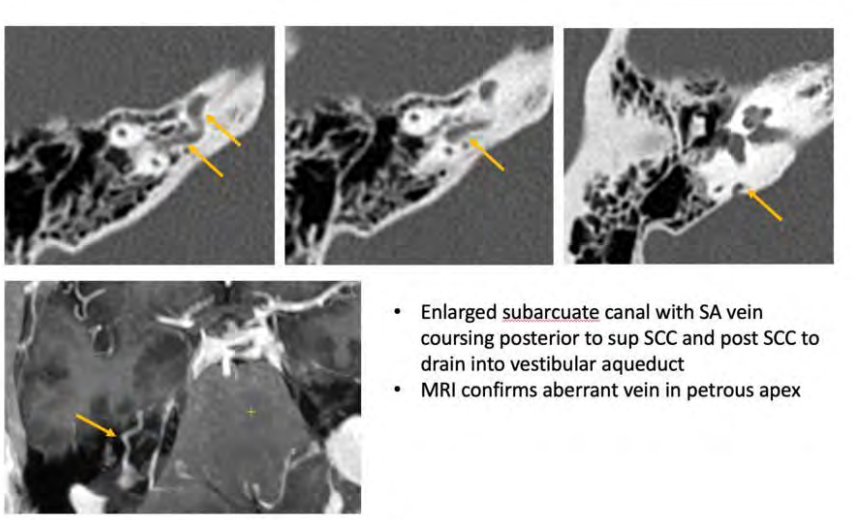

(Filename: TCT_906_Subarcutecanalexample1.jpg)

650
What Can Neuroradiologists Do to Protect Eloquent Areas? Initial Experiences with Establishing Clinical Functional Magnetic Resonance Imaging and Diffusion Tensor Imaging at a Tertiary Care Hospital
B Forgo[1], K Åberg[1], P Thunberg[1], A Buki[2], M Wegener[1], J Ulin[1], M Olivecrona[3]
[1]Department of Radiology and Medical Physics, Faculty of Medicine and Health, Örebro University, Örebro, Sweden, [2]Department of Neurosurgery, Faculty of Medicine and Health, Örebro University, Örebro, Sweden, [3]Orebro University, Orebro, Narke

Clinical History
Preserving patients' quality of life while removing brain tumors as radically as possible is the ultimate goal of modern neurosurgical oncology [1]. Functional magnetic resonance imaging (fMRI) and diffusion tensor imaging (DTI) are tools that help achieve this oncofunctional balance [2]. Nevertheless, getting started with fMRI/DTI in clinical practice remains a challenge for radiology departments with no prior experience. The aim of this case series is to demonstrate how establishing presurgical fMRI/DTI at a center with no prior routine in functional brain imaging may impact clinical decisions and patient outcomes. We present the first cases who underwent presurgical mapping at our tertiary care center. Clinical fMRI/DTI protocols were set up according to the American Society of Functional Neuroradiology guidelines [3]. fMRI with language and motor mapping and DTI with corticospinal tract (CST) and arcuate fasciculus (AF) tractography was performed in five patients with left frontal and temporal masses. Two patients were subjected to reoperation for recurrent glioblastoma multiforme and three patients had a newly discovered lesion of suspected neoplastic origin.
Imaging Findings
In patient 1, the primary motor area of the right hand was displaced and infiltrated by the tumor. Patient 2 with a left frontal lesion demonstrated robust, consistent language premotor activity adjacent to the mass. In patient 3, the primary motor cortex of the right foot and the CST was identified in close proximity to the lesion. Putative Wernicke's area and AF fibers were closely abutting left temporal lobe lesions in patients 4 and 5.
Discussion
Using presurgical fMRI/DTI likely impacted patient outcomes and the choice of intraoperative mapping. Intraoperative stimulation of the right hand primary motor area was used in patient 1, showing excellent agreement with presurgical fMRI. The lesion was partially resected, preserving the motor area of the right hand. For patient 2, awake surgery was offered due to the robust language premotor activity adjacent to the tumor. No intraoperative mapping was used in patients 3, 4 and 5. Patient 1, 3 and 4 had no new neurological deficits at 6-months follow-up. Patient 5 had a slight worsening of word finding difficulties but overall good language function.
Teaching Point
Establishing clinical fMRI/DTI in centers without prior experience in the field is achievable and encouraged. Our initial experiences confirm that these techniques affect clinical decisions and patient outcome.

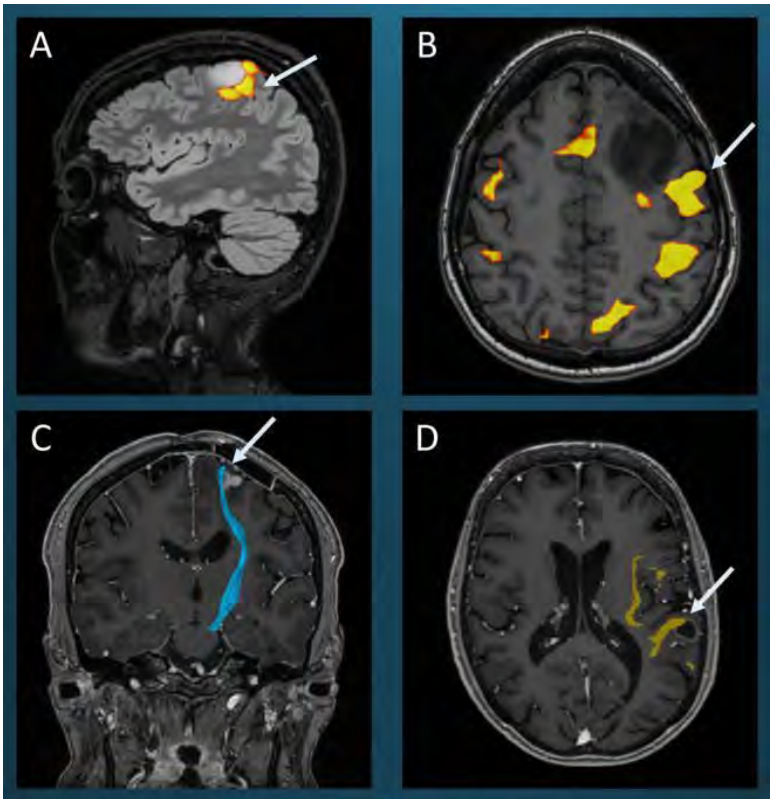

Functional magnetic resonance image (fMRI) and diffusion tensor imaging (DTI) tractography images illustrating our first experiences with presurgical mapping. Patient 1 (A): fMRI activity map of the finger tapping paradigm showing a left frontal mass in close proximity to the primary motor cortex of the right hand (arrow). Patient 2 (B): fMRI activity map indicating robust premotor activity (arrow) adjacent to the lesion's posterolateral margin. Patient 3 (C): Tractography showing the corticospinal tract of the left cerebral hemisphere closely abutting along the lesion's medial border (arrow). Patient 4 (D): Tractography visualising left arcuate fasciculus fibers closely abutting along the anterior margin of the mass (arrow).

(Filename: TCT_650_ASNR2023_abstract_image_Forgo_et_al.jpg)

558

What is the Matter with the White Matter? A Selection of Adult and Pediatric Leukodystrophy Cases.

S Ebden[1], H Jaber[2], M Wheeler[3], L Ashleigh[4], S Musale[5], S Owen[6]

[1]Univeristy Hospital of Wales, Cardiff, Cardiff, [2]Princess of Wales hospital, Bridgend, United Kingdom, [3]University Hospital of Wales, Cardiff, Wales, [4]Royal Glamorgan Hospital, Pontyclun, Wales, [5]Aneurin bevan University health board, Cwmbran, Wales, [6]Cardiff and Vale, Cardiff, Wales

Clinical History

Patients presented from 13 months to 35 years old. The paediatric cases had developmental regression, one had consanguineous parents. The adult patients had more varied presentations. These included Addisons disease with subsequent lower limb spasms and another with longstanding upper limb tremor and cognitive impairment.

Imaging Findings

Bilateral symmetrical confluent white matter T2 hyperintensity on MRI with different patterns of anatomical involvement. One of the paediatric cases showed restricted diffusion, enhancement and a lactate peak on spectroscopy. A tigroid appearance of the white matter abnormality was evident on another infantile case.

Discussion

Although more common in children, leukodystrophy can present late and there are some that only have adult forms. X-linked adrenoleukodystrophy is one of the more common entities that has an adult form. The case we present had the classic posterior predominance with involvement of the splenium of corpus callosum. This case was unusual due to presenting with Addisons disease, which usually does not have a symptomatic leukodystrophy. Krabbe disease mostly commonly presents in infancy but there is a slowly progressive late onset form. This can have a tigroid appearance of white matter involvement with u-fibre sparing early on, as demonstrated in the infantile case we present. In cases where the presentation and imaging appearances do not suggest a particular leukodystrophy, gene panel results clinch the diagnosis. A rare compound heterozygous mutation in the AARS2 was found in one of our adult cases with frontal predominant changes. This mutation is autosomal recessive and part of a syndromic picture associated with ovarian failure. If a lactate peak is identified on spectroscopy, a mitochondria disorder is suspected, as in our case of a cavitating leukodystrophy (LYRM7 mutation).

Teaching Point

Leukodystrophies do not just affect children, suggest late onset forms in adult patients with a symmetrical white matter abnormality. Some have a typical imaging phenotype, for example X-linked adrenoleukodystrophy. Post contrast imaging and spectroscopy can be helpful in suspected cases of leukodystrophy. A lactate peak points to a mitochondrial disorder.

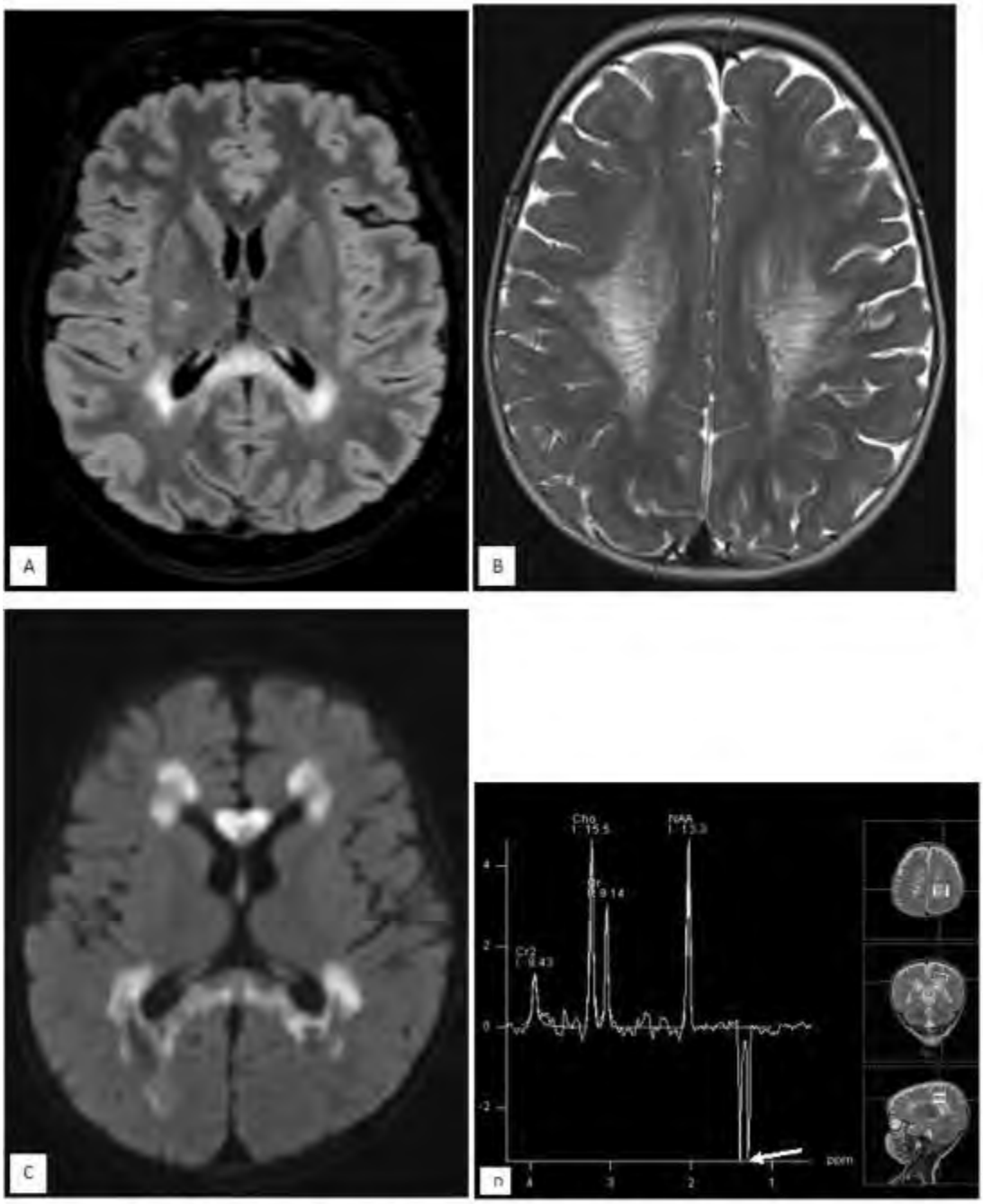

A Adult onset x linked adrenoleukodystrophy. Axial T2W FLAIR showing hyperintensity in the splenium of corpus callosum.

B Krabbe disease. Axial T2W demonstrating a tigroid appearance of the affected white matter.

C and D Cavitating mitochondrial leukodystrophy with LYRM7 mutation. Diffusion weight imaging (C) shows marked hyperintensity of the white matter abnormality which was shown to be restricted diffusion when compared to the apparent diffusion coefficient (ADC) map. Magnetic resonance spectroscopy (MRS) TE 135 (D) showing a lactate peak at 1.3ppm (arrow).

(Filename: TCT_558_ANSR2023LEUKODYSTROPHYIMAGES.jpg)

1166

"Jazz up your MRI report on MCDs-' Guide to Pattern Recognition and Phenotype-Genotype Correlates in Children with Malformations of Cortical Development

K Al-Dasuqi[1], V Rameh[1], F Dehghani Firouzabadi[2], S Prabhu[3]
[1]Boston Children's Hospital, Boston, MA, [2]Deprtment of Radiology, Children's Hospital, Harvard Medical School, Boston, MA, [3]Boston Children's Hospital, Boston, MA

Summary and Objectives
In this presentation, we will use a case-based approach to illustrate various malformations of cortical development (MCDs) and provide useful imaging tips and phenotype-genotype correlation that can help enhance the MRI report in patients with MCDs.
Purpose
1. List optimal protocols & timing of MRIs in children presenting with clinical symptoms suggestive of malformations of cortical development (MCDs) and use of standardized terminology to describe MCDs. 2. Illustrate the appearance of more commonly encountered malformations of cortical development with phenotype-genotype correlation. 3. Provide a readily accessible table correlating pathogenic variants with the imaging phenotype of MCDs for use in MRI reports.
Materials and Methods
We retrospectively reviewed clinical records & imaging data of pediatric patients ((0-18 years) presented at multidisciplinary (epilepsy and neurometabolic & brain malformation) conferences over a 10-year period, supplemented by a database search of radiology reports at a large tertiary care children's hospital to identify patients with malformations of cortical development. We correlated the imaging appearances with genetics, surgical pathology, & other relevant lab data in cases where this was available. Based on this data, we use a case-based approach to illustrate the more common patterns seen on MRI in children presenting with clinical symptoms & signs referrable to MCDs. We provide a ready reckoner table correlating the imaging patterns with most likely pathogenic genetic variants in each group.
Results and Conclusions
Imaging features & genetic correlates of MCDs are illustrated including ASPM in microcephaly with simplified gyri & WDR62 in microlissencephaly, LIS1, TUBA1A, DYNCH1, DCX, ARX & RELN in lissencephalies, DCX, CEP85L in band heterotopias, FLNA, ARFGEF1 in periventricular heterotopias, FKRP. POMT1, PMOT2, POMGnT1 & ADGRG1 in cobblestone malformations, various genes including PIK3CA, PIK3R2 & AKT3 genes in polymicrogyria, genes associated with tubulinopathies, mTOR pathway genes (TSC1, TSC2, NPRL2, NPRL3, DEPDC5 in cortical dysplasias, & SLC35A2 in MOGHE. Conclusion: Standardized MRI interpretation in children with MCDs & including genetic correlates helps clinicians optimize clinical care. Having a regularly updated "ready-reckoner" guide with characteristic phenotype-genotype correlates will help radiologists keep up with the constant developments in this field.

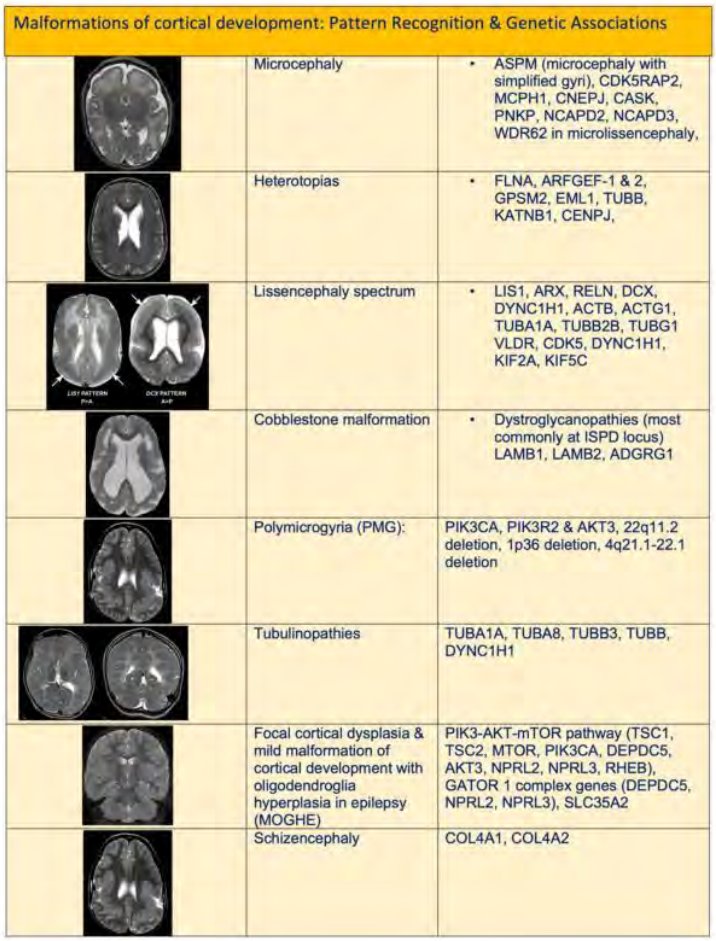

(Filename: TCT_1166_MCDsandGeneticsASNR2022.jpg)

987

7T T1-MPRAGE generated angiography (MPRAGE-MRA) for evaluation of intracranial vasculature in the setting of headache.

A Swenson[1], S Alabsi[2], M White[1], W Elvendahl[1], Z Cayci[1], C OZUTEMIZ[3]
[1]University of Minnesota, Minneapolis, MN, [2]University of Minnesota, MinnEapolis, MN, [3]UNIVERSITY OF MINNESOTA, MINNEAPOLIS, MN

Summary and Objectives

The prevalence of active headache disorder among adults worldwide is estimated to be approximately 46%(1). The etiology of headache is vast, including but not limited to tension-type headache, migraine, intracranial hemorrhage, malignancy, reversible cerebral vasoconstriction syndrome, arteriovenous malformations (AVMs) and aneurysms(2). Imaging is often negative in the setting of migraine or chronic tension type headache. Magnetic resonance imaging (MRI) is used to aid diagnosis and exclude other pathologies. Evaluation of the intracranial vasculature with magnetic resonance angiography (MRA) is often included to exclude underlying vascular etiologies such as aneurysms or AVMs. Time-of-flight (TOF) MRA takes about 8-10 minutes with 3T and 1.5T MRI, respectively. In our institution, TOF-MRA with 7T MRI takes about 15-19 minutes. Another pulse sequence with diagnostic utility within intracranial vasculature is T1-magnetization-prepared rapid gradient-echo imaging (MPRAGE). 7T T1-MPRAGE is superior to 1.5T and 7T TOF-MRA in numerous metrics for the visualization of AVMs(3). It also showed superiority in detection and assessment of unruptured intracranial aneurysms compared to 1.5T and 7T TOF-MRA(4). MRA images can be reconstructed from 7T T1-MPRAGE, creating MPRAGE-MRA(5). We generate MPRAGE-MRA from our standard 3D non-enhanced and enhanced T1-MPRAGE sequence in patients scanned with Siemens 7T Magnetom Terra machine with a total scan time of 30 minutes. We predict these images are comparable to TOF-MRAs obtained with 1.5T or 3T. MPRAGE-MRA images would decrease image acquisition time and may show subtle vascular pathologies not appreciated with routine brain MRI techniques. We predict reduced acquisition time will increase patient satisfaction and provide financial benefit. Educational objectives: 1. Discuss physical principles of sequences such as TOF-MRA and 3D T1-MPRAGE 2. Provide examples of 3D T1 MPRAGE-MRA 3. Compare institutional sequence parameters of routine brain MRI/MRA obtained with 1.5T and 3T to 7T.

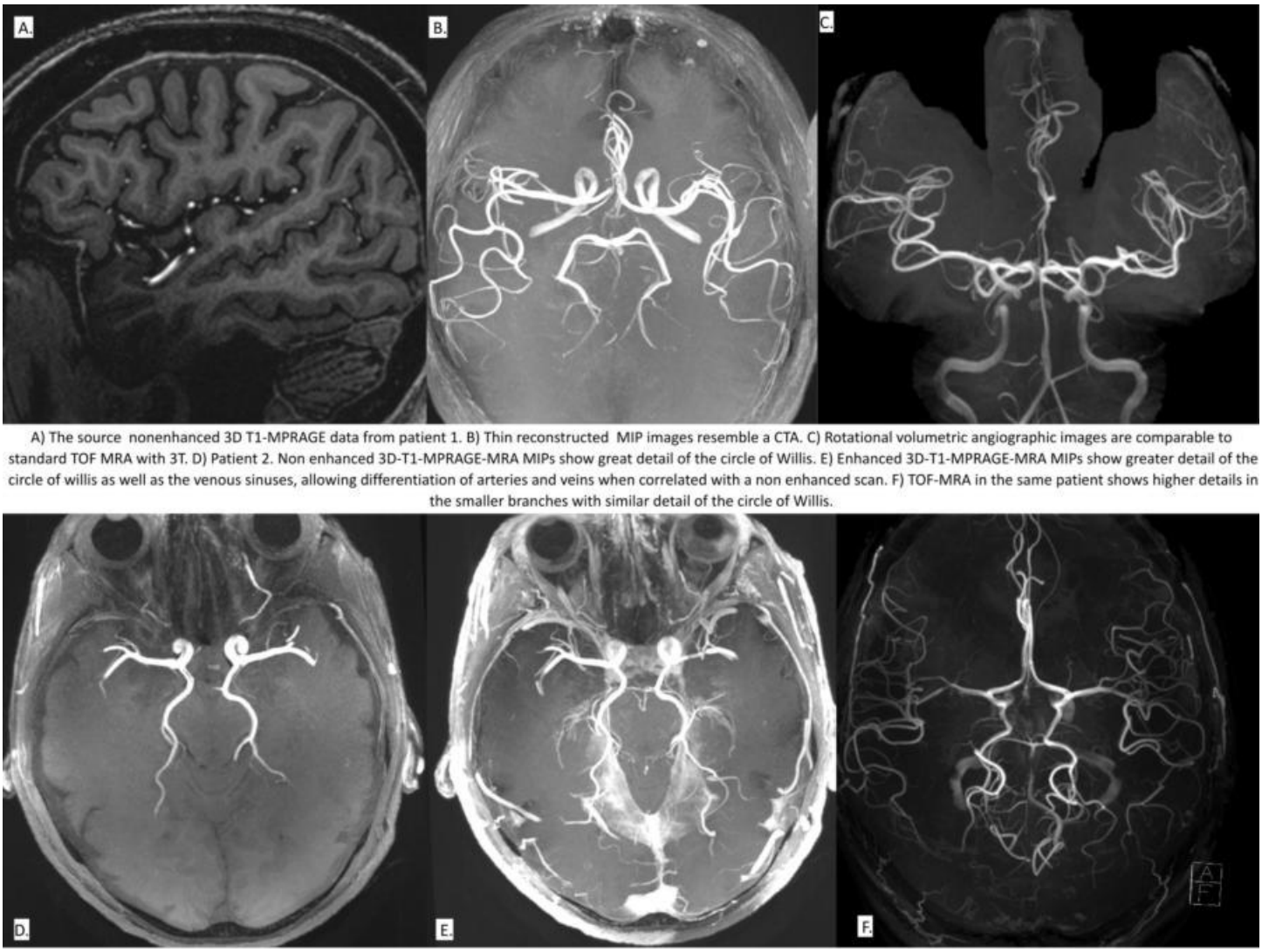

A) The source nonenhanced 3D T1-MPRAGE data from patient 1. B) Thin reconstructed MIP images resemble a CTA. C) Rotational volumetric angiographic images are comparable to standard TOF MRA with 3T. D) Patient 2. Non enhanced 3D-T1-MPRAGE-MRA MIPs show great detail of the circle of Willis. E) Enhanced 3D-T1-MPRAGE-MRA MIPs show greater detail of the circle of willis as well as the venous sinuses, allowing differentiation of arteries and veins when correlated with a non enhanced scan. F) TOF-MRA in the same patient shows higher details in the smaller branches with similar detail of the circle of Willis.

(Filename: TCT_987_7TPosterpptx.jpg)

554

A Case of Tolosa Hunt Syndrome Related to COVID-19 Infection with a Literature Discussion and Pictorial Review of the Differential for Skull Base Lesions

T Wang[1], L Spear[1], C Cankurtaran[1]
[1]*University of Southern California Keck School of Medicine, Los Angeles, CA*

Summary and Objectives
Tolosa Hunt syndrome (THS) is a rare idiopathic inflammatory disease primarily affecting the cavernous sinus with imaging features mimicking conventional skull base pathology. Given its rarity and overlapping imaging characteristics THS is ultimately a challenging diagnosis of exclusion, predicated on symptomatic improvement following steroid treatment. The hyperinflammatory state seen in COVID 19 infection, as evidenced by cytokine storm and multi-system inflammatory syndrome, has implications in inducing or exacerbating underlying inflammatory conditions. Here we present a case of Tolosa Hunt Syndrome likely related to COVID-19 infection and a literature review of similar cases. As THS remains a difficult diagnosis of exclusion we conduct a pictorial review for the differential of skull base lesions. Outline: • Tolosa Hunt Syndrome Background o Typical clinical presentation and imaging findings of THS • Case Presentation of THS related to COVID-19 Infection and Literature Review o Clinical and imaging findings (including CT and MR) of a suspected cause of THS related to COVID-19 infection o Current literature review regarding cases of THS related to COVID-19 infection • Pictorial Review of the Differential for Skull Base Lesions When Considering THS o Neoplastic etiologies including meningiomas o Non-Tumor pathologies including sarcoidosis and tuberculosis After viewing this exhibit the participant will be able to: 1. Consider Tolosa Hunt Syndrome in their differential for skull base lesions in patients presenting with COVID-19 infection 2. Understand current literature suggesting a relationship between Tolosa Hunt Syndrome and COVID-19 infection 3. Understand the differential of neoplastic and non-neoplastic lesions of the skull base when considering Tolosa Hunt Syndrome.
Purpose
1. Present a case of Tolosa Hunt Syndrome related to COVID-19 infection. 2. Review recent literature regarding the association

between Tolosa Hunt Syndrome and COVID-19 infection 3. Pictorial review of a differential of skull base lesions when considering Tolosa Hunt Syndrome

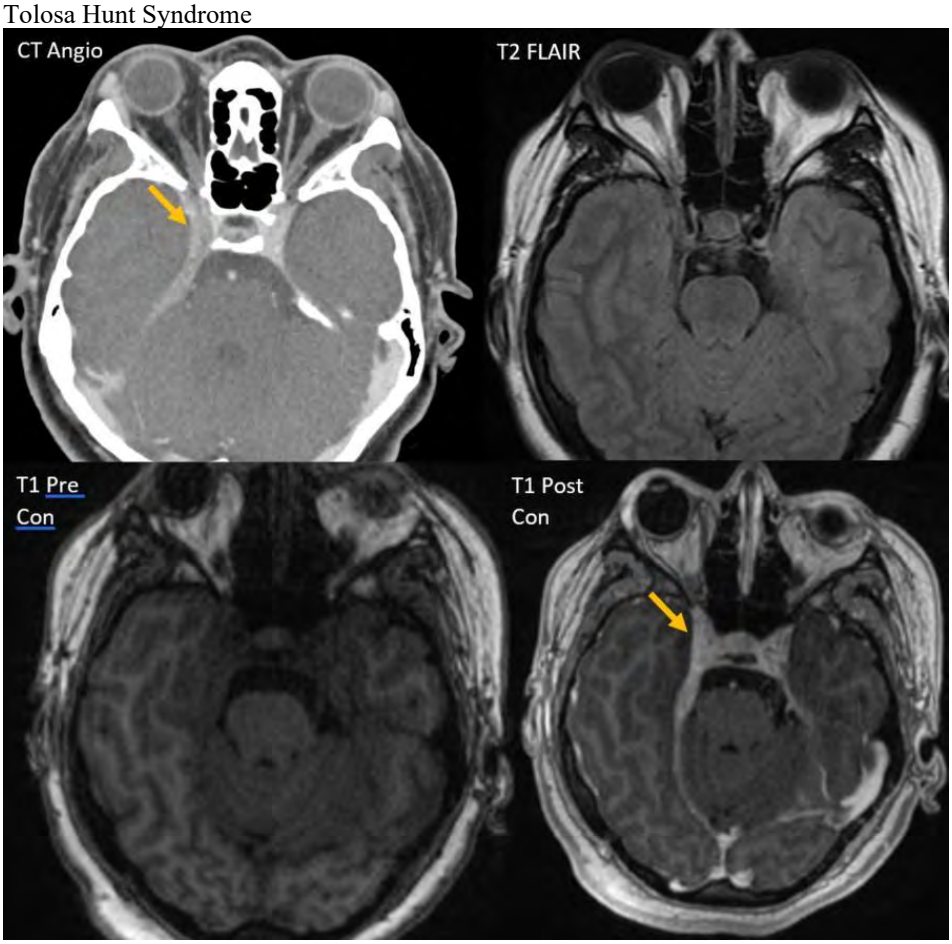

(Filename: TCT_554_THS.JPG)

826

A Concise Review of Neuro-imaging Patterns of Pediatric Myelin Oligodendrocyte Glycoprotein Antibody Associated Disorders.

I Atre[1], S Narayanan[2], K Thakkar[1]

[1]Children's Hospital of Pittsburgh of UPMC, Pittsburgh, PA, [2]UPMC Children's Hospital of Pittsburgh, Pittsburgh, PA

Summary and Objectives

Objectives: 1. To highlight the spectrum of imaging patterns of MOGAD 2. To delineate the imaging features that overlap with and separate this entity from other acquired demyelinating disorders such as NMOSD and MS Summary: Brain: Imaging patterns seen in pediatric MOGAD, include a) Acute Disseminated Encephalomyelitis (ADEM)- supratentorial subcortical and deep white matter as well as the deep grey matter (thalamus and pons) involvement seen. Lesions are characteristically fluffy, poorly demarcated, large (>2 cm in size) and T2- hyperintense. b) Meningitis c) Cortical encephalitis, Isolated T2 hyperintense cortical lesions visible on fluid-attenuated inversion recovery sequences with seizures referred to as FLAMES and d) Leukodystrophy like pattern. Spine: Pattern of spine involvement is Longitudinally extensive transverse myelitis (LETM) with predilection for the conus medullaris. Imaging findings include centrally located T2 hyperintense lesions with preferential involvement of grey matter (H sign) and involvement of more than 50% of the axial section of the cord. Contrast enhancement and cavitation favors NMOSD over MOGAD, while meningeal enhancement favors MOGAD. Short segment, less than 50% of involvement with peripheral dorsal lesions favor diagnosis of MS on MR. Optic nerves: Up to half of the patients with MOGAD present with bilateral optic neuritis. Long segment retrobulbar involvement with sparing of optic chiasm and tracts is a characteristic feature of MOGAD whereas chiasmal and bilateral optic tract involvement is seen in NMOSD.

Purpose

Pediatric Myelin Oligodendrocyte Glycoprotein Antibody Associated Disorders (MOGAD) represent a group of CNS inflammatory demyelinating disease in children caused by presence of IgG antibodies to the Myelin Oligodendrocyte Glycoprotein. Apart from MOGAD, the diverse spectrum of relapsing demyelinating syndromes includes Neuromyelitis Optica Spectrum Disorder (NMOSD), Multiple Sclerosis (MS) and other unclassified monophasic and relapsing demyelinating disorders. Imaging features on MR can help identify pediatric MOGAD and differentiate it from other demyelinating diseases in many cases.

Materials and Methods

Retrospective review of proven cases of MOGAD from MARS imaging database.

Results and Conclusions
Pediatric MOGAD is an evolving field with multiple neuroimaging patterns now known to be associated with MOGAD. Appropriate diagnosis will help with management and can help differentiate MOG ab associated disorders from other pediatric demyelinating disorders.

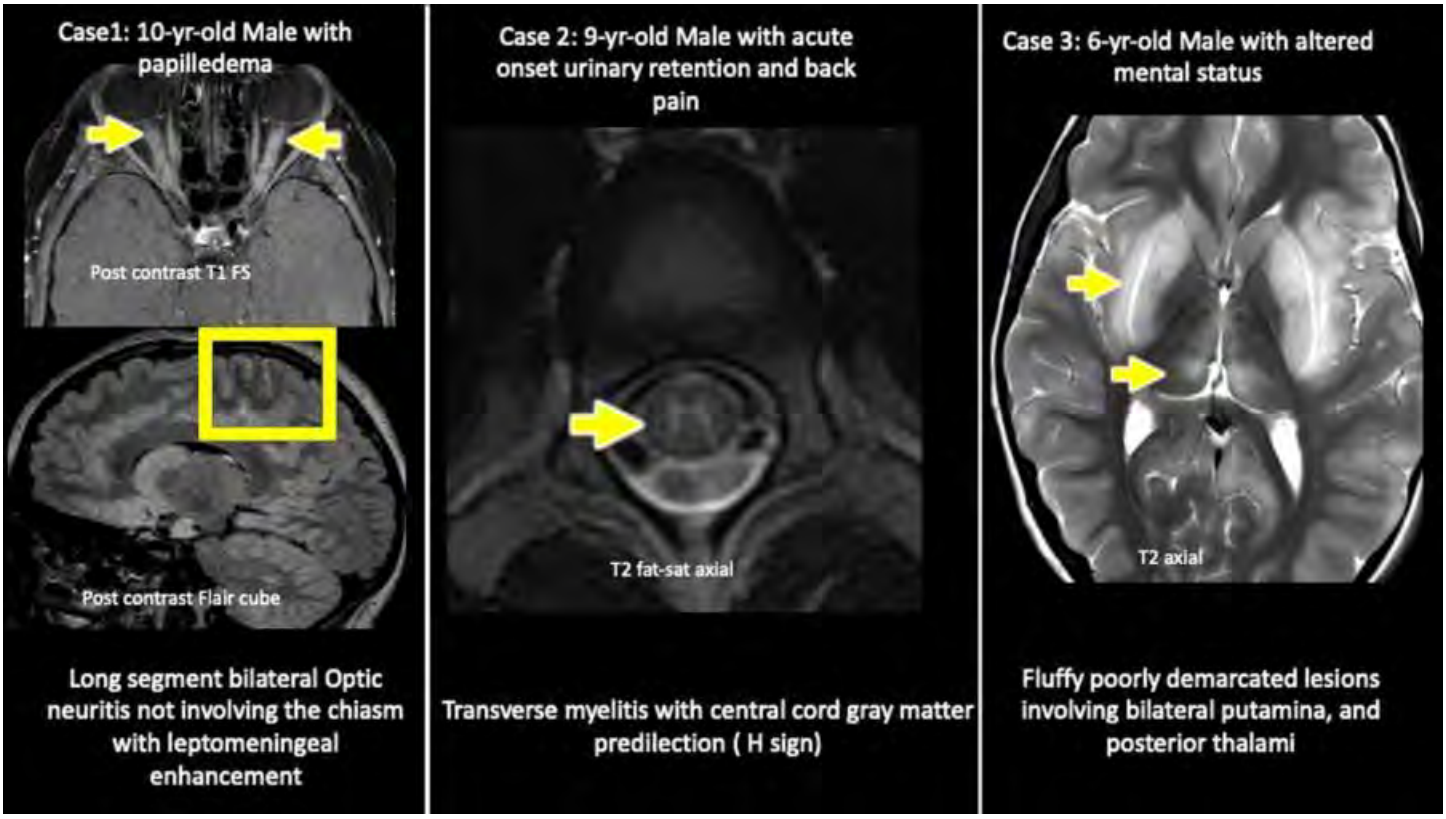

(Filename: TCT_826_MOGAD.jpg)

850

A Guide to Approach Atypical Neuroimaging Findings

M BHALLA[1], R Samant[2], S Khanpara[3], R Patel[4]
[1]UT Houston, Houston, TX, [2]UT Health, McGovern School of Medicine, Texas Medical Center, Houston, TX, [3]University of Texas MD Anderson Cancer Center, Houston, TX, [4]Texas Children's Hospital, Houston, TX

Summary and Objectives
General Radiologist and Neuroradiology trainee's often encounter atypical findings in Neuroimaging cases, that sometimes often go unnoticed. These could be incidental or sometimes component of a condition that is being evaluated. The significance of these findings is not always specifically related to presenting symptomatology but potentially contributing to assessment of an underlying condition, thereby improving diagnostic yield of the exam besides appropriate patient care. The exhibit summarizes the significance of these findings, the suggested next step in imaging and the relevant information to be provided to clinicians.
Purpose
The goal of this exhibit is to review some of the incidental imaging findings in Neuroimaging exams and discuss their possible etiologies and significance. Relevant information that clinicians would want to know, and additional suggestions or recommendations a radiologist can provide, will be discussed.
Materials and Methods
A punctate focus (1-3 mm) of DWI restricted diffusion in hippocampus on MRI brain that can suggest Transient Global Amnesia (TGA). Enlarged bilateral Meckel's cave could represent Idiopathic intracranial hypertension. Superior margin of pituitary is typically flat or concave upwards in elderly age group, and a convex superior contour is atypical. A venous pouch in a case of Arteriovenous Malformation (AVM) is a higher risk for rupture. Diffusely T1-weighted hypointense marrow MR signal beyond certain age represents abnormality that could be indicative of red marrow conversion. A good reference for signal intensity is intervening disc signal. Attenuated transverse venous sinus flow void on MRI axial 2D FLAIR image is a common artifact that can be differentiated from occlusive sinus on correlation with DWI, Susceptibility-weighted imaging and T1-weighted images. Non suppression of CSF sulcal FLAIR signal on MRI warrants correlation with other sequences and history. Treatment related Neuroimaging features such as hypophysitis with immunomodulation treatment, pseudo-response and pseudo-progression, and post-laser ablation parenchymal changes will be discussed.
Results and Conclusions
A review of unusual and atypical imaging findings that might be encountered in Neuroradiology exams could have significant clinical

implications in patient care by suggesting diagnoses and altering management. The exhibit compiles such findings and reviews the relevant information, serving as a resource while interpreting Neuroimaging exams.

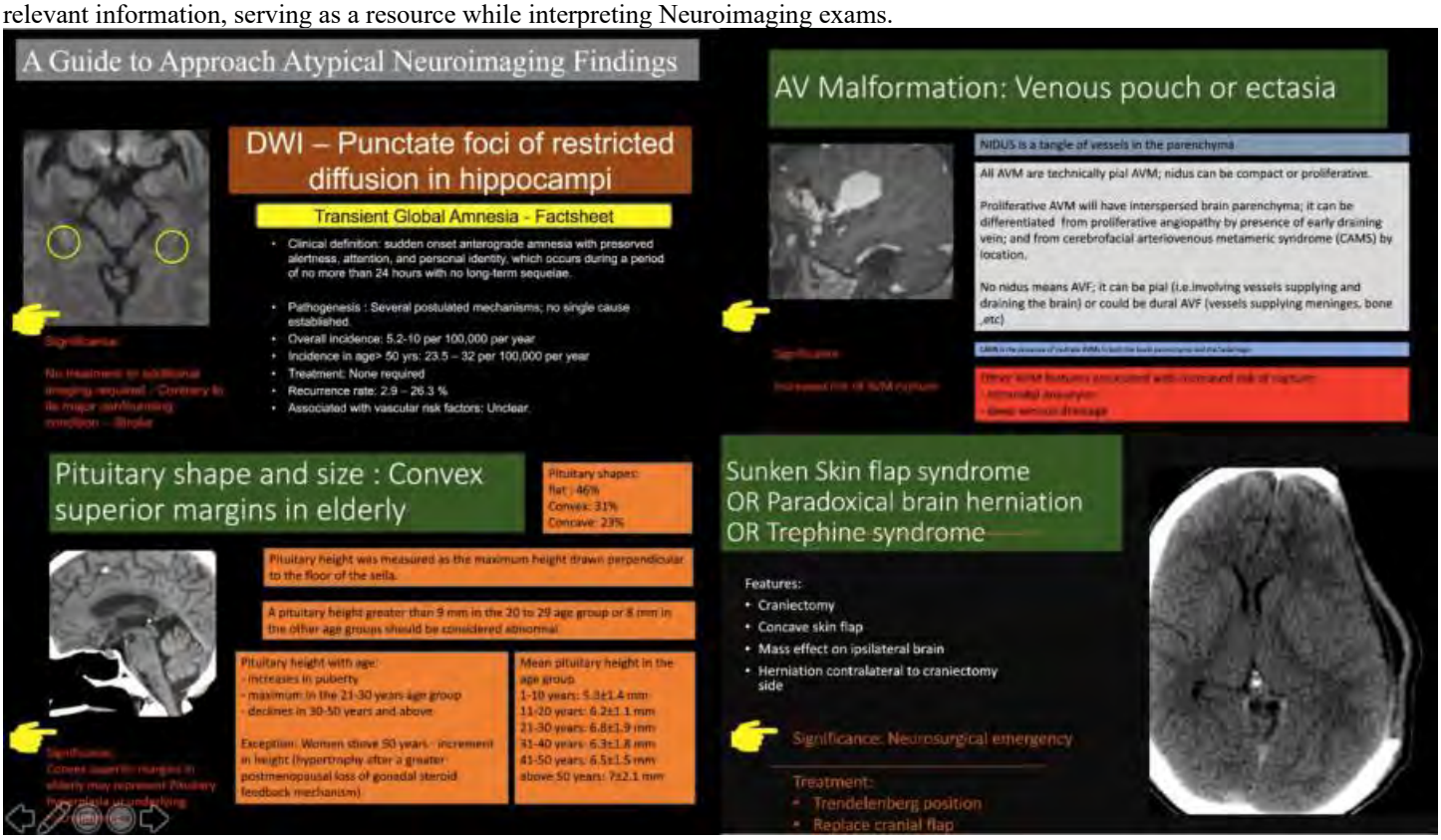

(Filename: TCT_850_ASNR23.jpg)

830

A Pictorial Review and Discussion of the Applications of CT Perfusion in Cerebral Vasospasm and Delayed Cerebral Ischemia Secondary to Aneurysmal Subarachnoid Hemorrhage

T Wang[1], A Lerner[1], R Assadsangabi[1]
[1]*USC Keck School of Medicine, Los Angeles, CA*

Summary and Objectives
Cerebral vasospasm (CVS) and delayed cerebral ischemia (DCI) are the leading complications of patients with aneurysmal subarachnoid hemorrhage (aSAH) resulting in increased morbidity and mortality. Although timely diagnosis of these complications is critical in initiating treatment and likely preventing sequela including cerebral infarction, permanent neurological deficits, and death, clinical evaluation is frequently challenging due to a multitude of factors including low GCS scores/sedation. Current imaging such as CT, CT angiogram, and transcranial doppler are also limited as they primarily rely on vascular diameter or velocity measurements. As a result, they do not provide a comprehensive assessment of DCI which has a multifactorial pathophysiology. Since cerebral hypoperfusion is the key pathophysiologic mechanism to CVS/DCI, CT Perfusion (CTP) has increasingly been seen to provide more accurate data for evaluation of these complications. Here we present a review of current imaging of aSAH, CVS, and DCI with a focus on the emergence of CTP in the evaluation of these complications. Content Organization • aSAH Background and Complications Including CVS and DCI o Clinical evaluation including challenges of diagnosis o Pictorial review of current imaging evaluation of aSAH and complications o Limitations of CVS and DCI diagnosis with current imaging techniques • Application of CTP to aSAH, CVS, and DCI o Pictorial review of CTP findings in aSAH and associated complications o Review of current literature on the role of CTP in evaluation of aSAH • Future directions of research in CTP for the evaluation of aSAH and associated complications After viewing this exhibit the participant will: 1. Understand the current role of the different imaging modalities in evaluating aSAH, CVS, and DCI 2. Understand the current research behind applying CTP to aSAH, CVS, and DCI 3. Appreciate the methods under investigation of CTP in aSAH and associated complications
Purpose
1. Pictorial review of existing imagining modalities in the evaluation of aSAH, CVS, and DCI 2. Review of existing literature demonstrating the utility of CTP aSAH 3. Present the role of CTP in the evaluation of aSAH and its complications under investigation

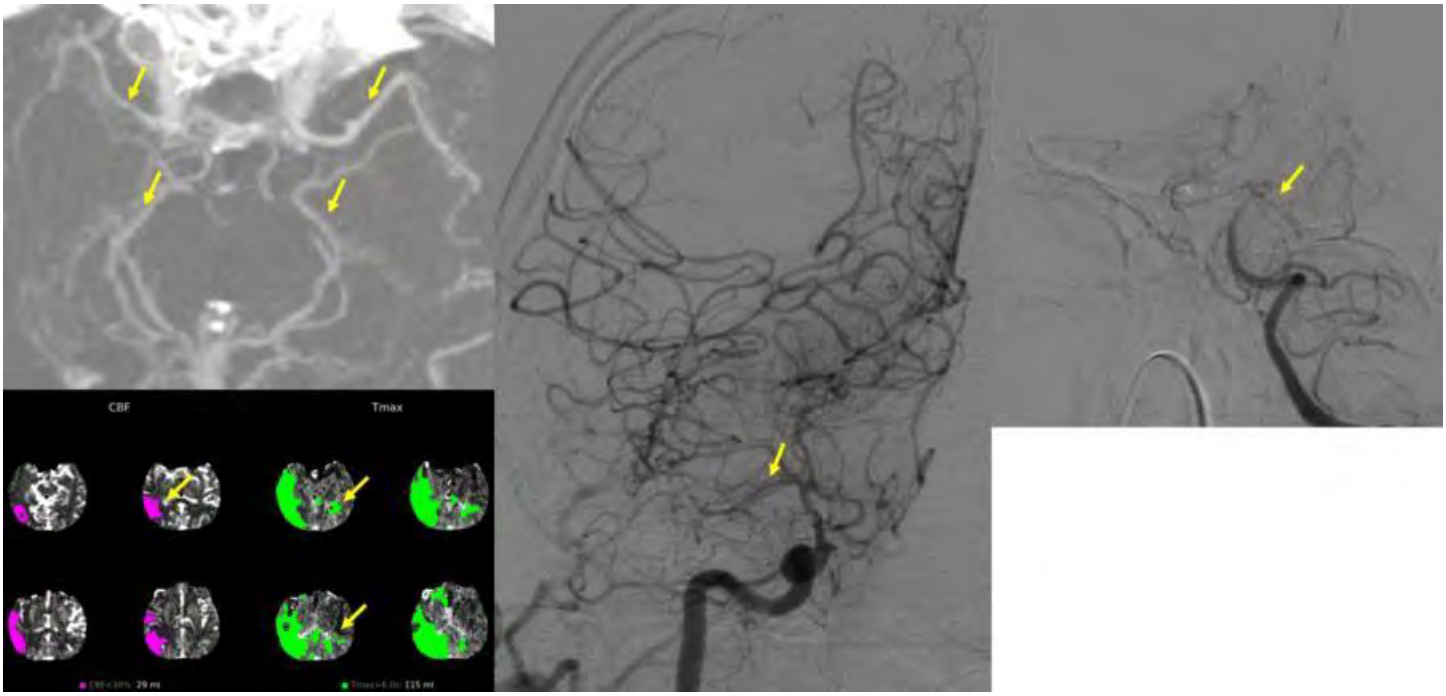

(Filename: TCT_830_SubarachnoidHemorrhage.JPG)

1089

A Pictorial Review of Craniocerebral Gunshot Injuries

S Ameli[1], J Palakunnel[2], R Mcallister[2], M Mian[2], S Vattoth[3], M Kumar[4], R Ramakrishnaiah[5], S Viswamitra[6], R Van Hemert[4], S Patro[2]

[1]UAMS, Little rock, AR, [2]University of Arkansas for Medical Sciences, Little Rock, AR, [3]University of Arkansas for Medical Sciences, LITTLE ROCK, AR, [4]UAMS, Little Rock, AR, [5]Univ of Arkansas for Medical Sciences, Little Rock, AR, [6]University of Arkansas for Medical Sciences, Bengaluru, Karnataka

Summary and Objectives

Summary: The firearm related deaths have been on the rise since 1950s in the United States. Cranial gunshot wounds are the most lethal form of firearm injuries and accounts for 12% of all traumatic brain injuries. The overall survival rate of cranial gunshot wounds is between 7% to 15%[1]. Most deaths happen either at the site of injury or within the first few hours[2]. Additionally, survivors can undergo long term rehabilitation and further suffer from long term complications. Radiologists, with accurate and timely recognition of initial intracranial manifestations can assist the care team in planning the best treatment options for the patients in the emergent setting. Also, help with identifying the possible delayed complications. Objectives: Discussing most common radiographic manifestations of craniocerebral gunshot injuries. Discussing associated intracranial vascular injuries. Recognizing important prognostic and therapeutic imaging criteria. Identifying secondary vascular and non-vascular complications.

Purpose

To highlight some of the salient imaging features of craniocerebral gunshot injuries on unenhanced head CT and CT angiogram. Different patterns of gunshot injuries, identifying the bullet trajectory, evaluating the extension of brain injury, and recognizing the intracranial hemorrhages will be discussed. We will review common associated intracranial vascular injuries as well as delayed vascular and non-vascular complications including infection, infarction, hydrocephalus, aneurysm, pseudoaneurysm and arteriovenous fistula. Additionally, we will review the important prognostic and therapeutic considerations.

Materials and Methods

Institutional data from 2017-2022 was utilized for imaging manifestations of patients who presented to emergency department of our facility following a cranial gunshot injury.

Results and Conclusions

Results: We will use actual cases of patients seen at the emergency department of our institution. Conclusion: Radiologists can contribute substantially to the evaluation and treatment of the patients with craniocerebral gunshot injuries. Our educational exhibit will familiarize the audience with most common radiographic appearances of firearm related craniocerebral injuries, related vascular injuries and possible secondary complications.

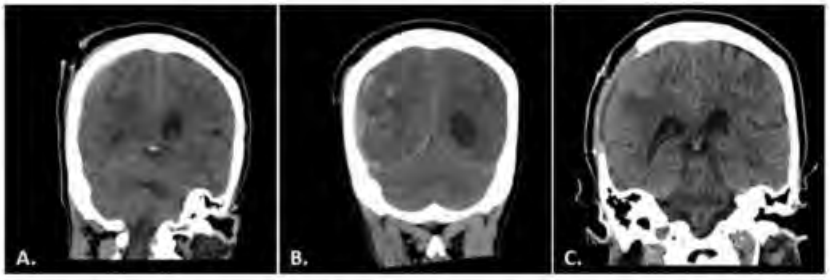

Figure 1: (A) Initial noncontrast coronal head CT in a patient with nonpenetrating cranial gunshot wound shows laceration injury of the scalp and a small subdural hematoma in the right frontoparietal convexity. (B) Follow-up imaging demonstrates progression of subdural hematoma as well as subarachnoid hemorrhage and cerebral hematoma. (C) Post craniectomy and evacuation of the hematoma coronal head CT shows improvement of cerebral edema and hematoma.

Figure 2: (A) Radiograph of a patient with perforating cranial gunshot injury. Entry wound was identified at thehard palate while the exit wound was through frontal bone (B) 3D reconstruction of the same patient's head CT scan shows comminuted fracture of the frontal bone at the exit wound with extension of fractures to bilateral orbital roof.

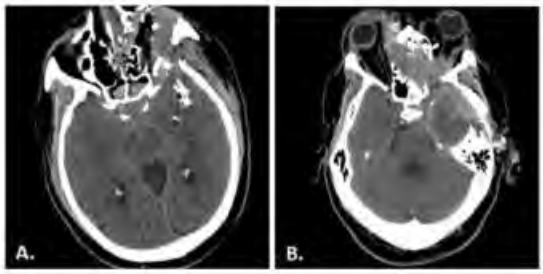

Figure 3: (A) axial head CT shows penetrating gun shot injury involving the left orbit and middle cranial fossa with multiple bullet and bony fragments. No exit wound vs. (B) axial head CT

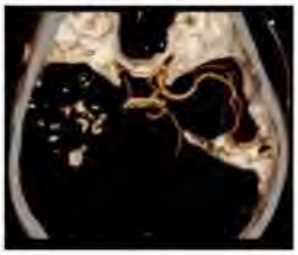

Figure 4: 3D reconstruction of CTA head reveals complete transection of the right cavernous internal carotid artery and occlusion of the right middle cerebral artery with multiple bony and bullet fragments in the

(Filename: TCT_1089_Gunshotimages.jpg)

717

A Primer on Primary Sinonasal Tumor Classification, Staging and Routes of Tumor Spread

A Moeller[1], G AVEY[1], A Kuner[1], I Koszewski[1], T Kennedy[1]
[1]*University of Wisconsin, Madison, WI*

Summary and Objectives

The educational objectives of our exhibit are to describe the classification of primary sinonasal tumors, showcase specific cases to highlight imaging findings, staging features, routes of spread, and review important updates from the 2022 5th edition of the World Health Organization (WHO) Classification of Head and Neck Tumors. Primary sinonasal tumors can be grouped by cellular origin. This includes epithelial tumors (papilloma, squamous cell carcinoma [SCC], and NUT carcinoma), adenocarcinomas, neuroendocrine tumors (olfactory neuroblastoma and sinonasal undifferentiated carcinoma [SNUC]), and mesenchymal tumors (angiofibroma, sinonasal glomangiopericytoma, and biphenotypic sinonasal sarcoma). This exhibit will include examples of these entities. Squamous cell carcinoma (SCC) is the most common sinonasal tumor, comprising 80% of cases. These typically occur in 6th-7th decade males, with a 2:1 male to female ratio and nearly 95% of cases occurring in patients over age 40. Occupation exposures to nickel, chromium, and isopropyl alcohol increase the risk of sinonasal SCC. These tumors typically originate in the maxillary antrum and will appear as a large mass with bone destruction on CT. On MRI, the tumor will demonstrate T2 intermediate signal and variable post-contrast enhancement. Sinonasal SCCs will spread through direct extension, lymphatics, or perineural invasion. When staging a maxillary SCC, T1 tumors are confined to the mucosa. T2 tumors may invade the hard palate or middle nasal meatus. T3 tumors will show invasion of the posterior wall maxillary sinus, subcutaneous tissues, floor or medial wall of the orbit, pterygoid fossa, or ethmoid sinuses. T4 tumors are subdivided into T4a and T4b and have even more advanced local invasion. Finally, we will highlight updates from the 5th edition of the WHO Classification of Head and Neck Tumors. Two new entities are introduced including SWI/SNF complex-deficient sinonasal carcinoma and HPV-related multiphenotypic sinonasal carcinoma (HMSC). SWI/SNF complex-deficient sinonasal carcinoma was previously classified under SNUC, but immunohistochemistal advances have defined this highly aggressive neoplasm. HMSC is a re-defined neoplasm that appears restricted to the sinonasal area. It demonstrates pathologic features of both a salivary-type and squamous cell carcinoma. Despite appearing aggressive on pathology, this tumor typically has a favorable prognosis.

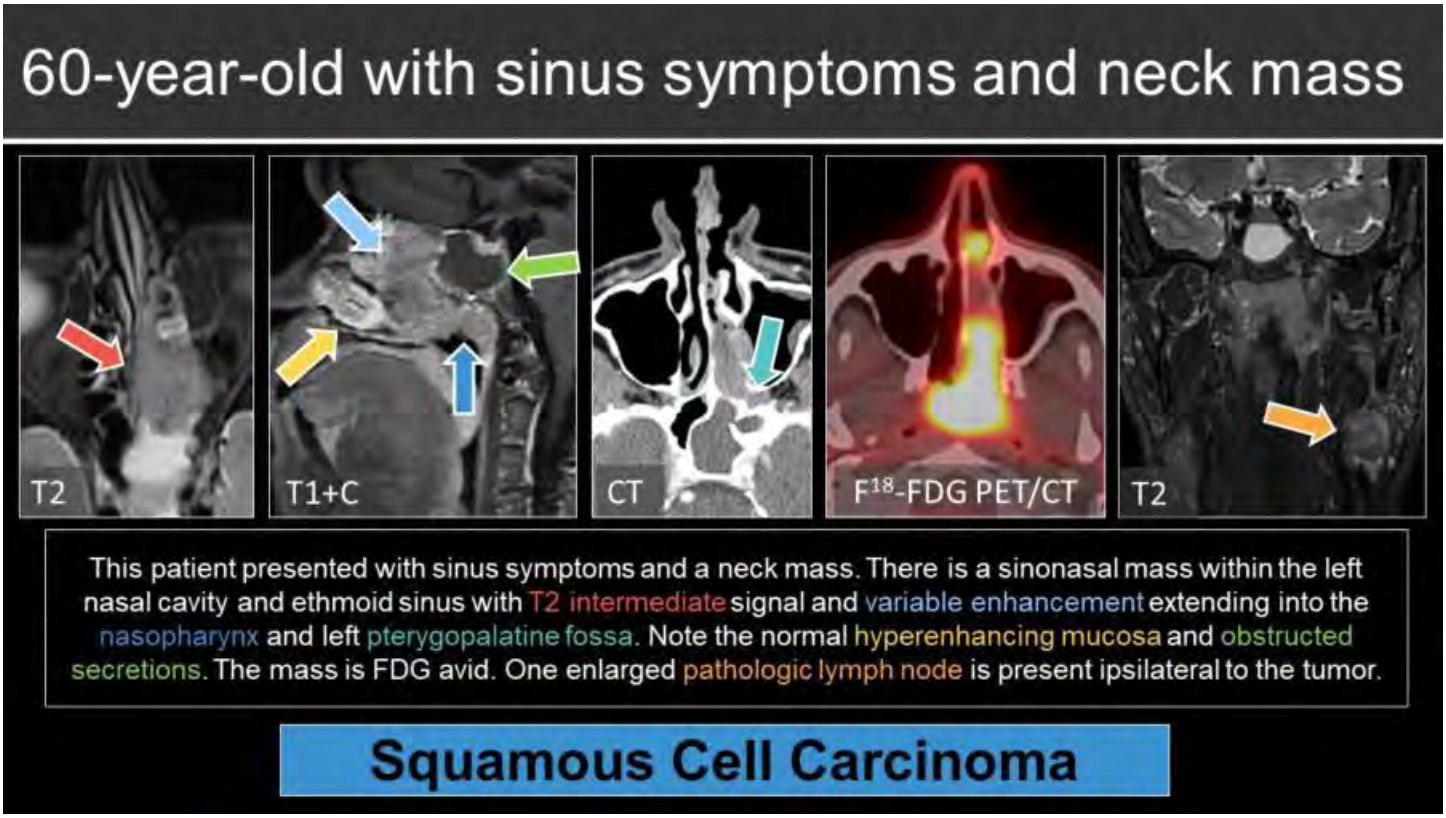

(Filename: TCT_717_ASNRImage.jpg)

924

A Primer on the Updated WHO Classification of Glioneuronal and Neuronal Tumors in the Pediatric/Young Adult Population.

A Dutta[1], A Moats[2], F Goncalves[2], A Vossough[2], C O'Connor[3]

[1]Cooperman Barnabas Medical Center, Livingston, NJ, [2]Children's Hospital of Philadelphia, Philadelphia, PA, [3]SUNY Downstate, Brooklyn, NY

Summary and Objectives

Glioneuronal and neuronal tumors (GNTs) represent a diverse group of rare tumors commonly featuring neuronal differentiation. GNTs primarily affect infants, children, and young adults and are strongly associated with seizures. Surgery is the cornerstone of seizure treatment. GNT classification is constantly evolving, and several newly recognized types have been added to 2021 WHO Classification of Tumors of the CNS. Overall, data regarding presurgical diagnosis of GNTs remains scant.

Purpose

This primer aims to assist in recognizing critical clinical and neuroimaging features to narrow the presurgical differential diagnosis and introduce the changes made in the updated WHO classification.

Materials and Methods

A retrospective analysis was done based on pathology-proven cases of GNTs. Electronic medical records, CT (when available), and MRI imaging features were reviewed. Dozens of pathology-proven cases of GNTs with addition of the new categories were obtained, including gangliogliomas, gangliocytomas, desmoplastic infantile ganglioglioma/desmoplastic infantile astrocytoma, dysembryoplastic neuroepithelial tumor, diffuse glioneuronal tumor with oligodendroglioma-like features and nuclear clusters, papillary glioneuronal tumor, rosette-forming glioneuronal tumor, myxoid glioneuronal tumor, diffuse leptomeningeal glioneuronal tumor, multinodular and vacuolating neuronal tumor, dysplastic cerebellar gangliocytoma, central neurocytoma, extraventricular neurocytoma, and cerebellar liponeurocytoma.

Results and Conclusions

Differential diagnoses will be discussed based on presenting age and neurological signs. In addition, several neuroimaging features will be discussed, such as location: supratentorial (lobar, septum pellucidum and intra-/periventricular), infratentorial (cerebellum, brainstem, vermis, and intra-/periventricular), spinal, and disseminated disease. Additional findings such as tumoral characteristics (solid, cystic, necrotic, or a mixture thereof), enhancement (absent, solid, ring enhancement, or patchy) and other features such as bubbly appearance, edema, infiltration, septations, and bone remodeling will also be discussed. Susceptibility weighted imaging (hemorrhage or calcification) and diffusion weighted imaging (normal, restricted, or facilitated) findings will be also reviewed. With the new WHO classification, reviewing these key findings for each GNT will help neuroradiologists in recognizing these rare tumors.

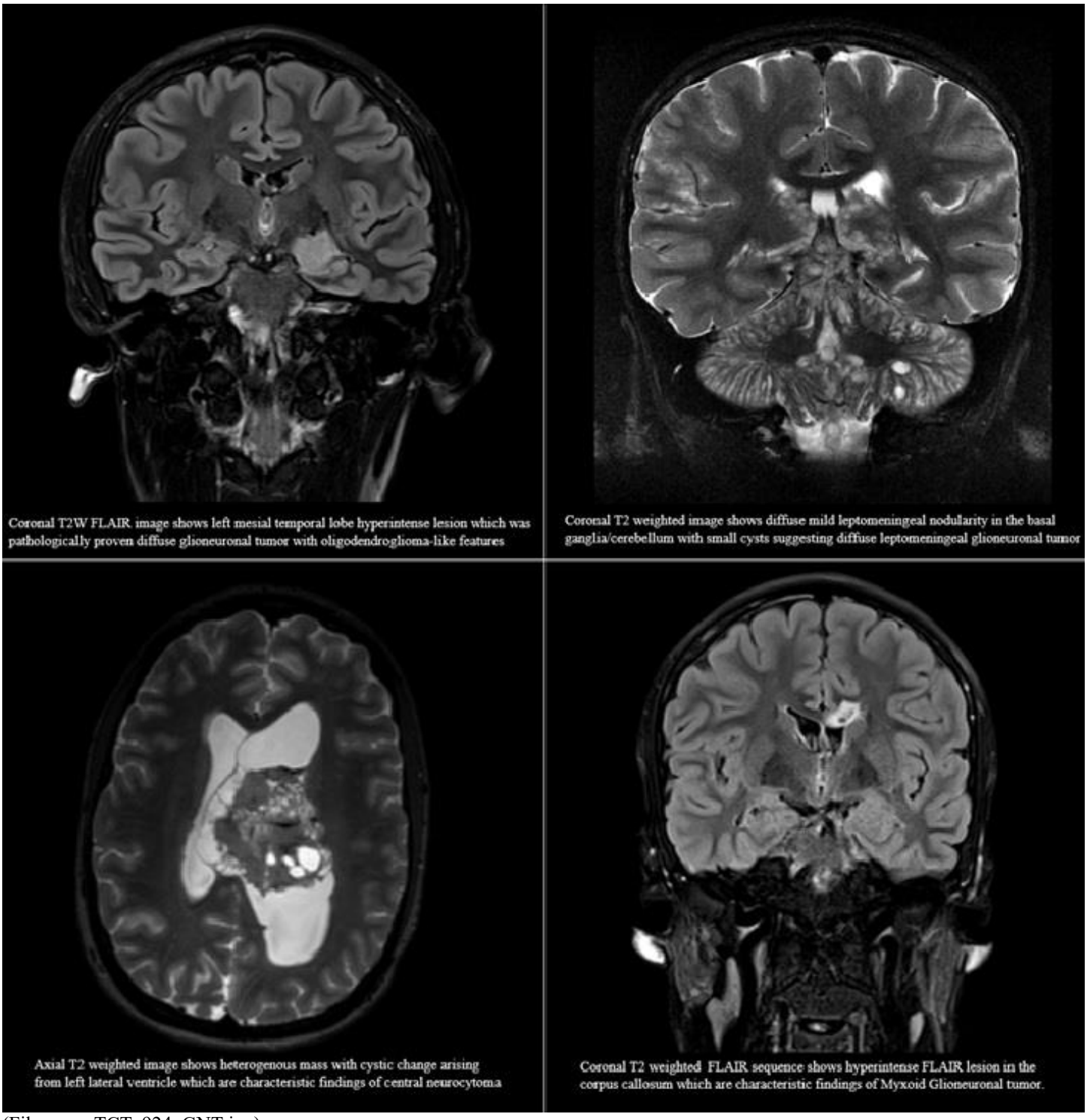

(Filename: TCT_924_GNT.jpg)

244

A Review of Carotid Cavernous Sinus Fistulae Findings and Diagnosis

C Zoppo[1], T Taros[2], A Puri[3], J Singh[1], A Kuhn[4]

[1]University of Massachusetts Medical School, Worcester, MA, [2]University of Massachusetts Chan Medical School, Worcester, MA, [3]Currently at Univ. of Massachusetts Medical Center., Worcester, MA, [4]UMass Medical Center, Worcester, MA

Summary and Objectives

Carotid-Cavernous Fistulae are an abnormal connection between the carotid artery and the cavernous sinus. They form through a variety of mechanisms, though trauma is the most common. They can be classified by Barrow type depending on the specific branches of the carotid artery that are involved. Though there are several classic findings on non-invasive imaging, catheter angiography remains the gold diagnostic standard. Treatment requires occlusion of the fistula, which was traditionally done through a surgical approach. Today, there are several endovascular options including balloon occlusion and stents. - Define what constitutes a carotid-

cavernous fistula. - Understand the types of CCF and Barrow classification system. - Review common etiologies. - Understand the radiographic evaluation of these lesions including common imaging findings. - Discuss treatment strategies.
Purpose
Carotid cavernous fistulae (CCF) are abnormal malformations of the cerebral vasculature resulting in communication between branches of the carotid artery and cavernous sinus (CS). There are two types of CCF. Direct lesions are usually caused by trauma and account for approximately 75% of all CCF.1 Indirect CCF are thought to form via primary thrombosis of CS venous outflow channels and resultant vascular alterations to provide collateral flow.2 Many indirect CCF are linked to hypertension, atherosclerosis, fibromuscular dysplasia, or Ehlers-Danlos.3
Results and Conclusions
CCF can be classified by Barrow type based on the carotid branches involved. Type A represents a direct connection between ICA and CS. Type B fistulae involve internal carotid artery (ICA) meningeal branches. Type C lesions involve branches of the external carotid artery (ECA). Type D lesions include the meningeal branches of both the ICA and ECA.4 The gold standard imaging modality for evaluation of CCF is digital subtraction angiogram, however CT angiogram and MRI studies both provide value.3 On CT angiography, major findings suggestive of CCF include engorged ophthalmic vein, engorged cavernous sinus, similar enhancement of the CS and ICA, and greater enhancement of the CS than the transverse sinus.5 Treatment is based on occlusion of the fistula without interrupting normal flow in the carotid artery. This can be accomplished surgically, though endovascular treatment is the preferred modality in the modern era. Many strategies for endovascular therapy exist and include balloon occlusion, embolization or covered graft stent placement.

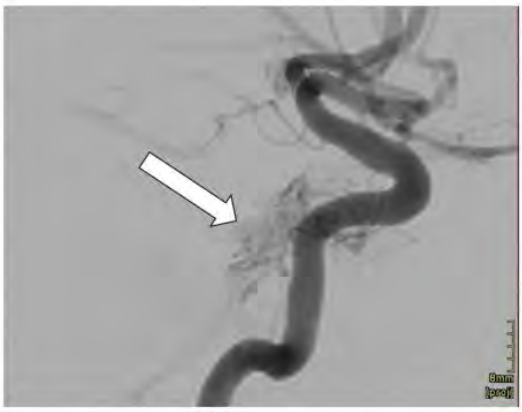

Figure 1: Digital subtraction angiography shows extravasation of contrast from internal carotid artery into the cavernous sinus (white arrow), signifying a Barlow type A fistula.

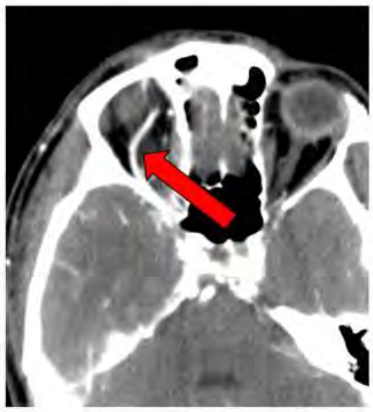

Figure 2: CTA of the head shows a unilaterally engorged right ophthalmic vein (red arrow) in a patient with carotid-cavernous fistula.

(Filename: TCT_244_CCFforASNRImage.jpg)

431
Abnormal Non-Neoplastic Spinal Cord Signal Abnormality - Beyond Multiple Sclerosis
M Minor[1], R Thakkar[2]
[1]Medstar Georgetown University Hospital, Washington, DC, [2]Medstar Georgetown University Hospital, Washington, DC, DC

Summary and Objectives
After viewing this exhibit, the individual should have a better appreciation for the differential for abnormal non-neoplastic spinal cord signal abnormalities. It is important for the interpreting radiologist to remember that multiple sclerosis is not the only entity that can cause short segment T2 hyperintense spinal cord lesions.
Purpose
Acute noncompressive short segment T2 hyperintense intramedullary spinal cord signal abnormalities are most commonly attributed to multiple sclerosis. However, as viral epidemics become more prevalent, acute disseminated encephalomyelitis or parainfectious acute transverse myelitis should be included in the differential for short segment spinal cord signal abnormalities. The purpose of this educational exhibit is to provide several cases of both short segment spinal cord signal abnormality and long segment abnormalities as comparisons to broaden the viewers differential when presented with abnormal non-neoplastic spinal cord signal abnormality.
Materials and Methods
The radiology database using departmental search engine was queried for T2 hyperintense spinal cord lesions from 2012-2022.
Results and Conclusions
This exhibit will review the possible etiologies of short and long segment acute non-neoplastic T2 hyperintense lesions in the spinal cord beyond multiple sclerosis. Multiple examples will be provided of viral, inflammatory, metabolic, autoimmune, and vascular etiologies for non-neoplastic spinal cord lesions. Within the exhibit, viral etiologies will be highlighted as they become more important on a global scale with acute cases of monkeypox and varicella zoster encephalomyelitis. Additionally, the cases will demonstrate the utility of DWI and MRA TWIST is narrowing down the differential.

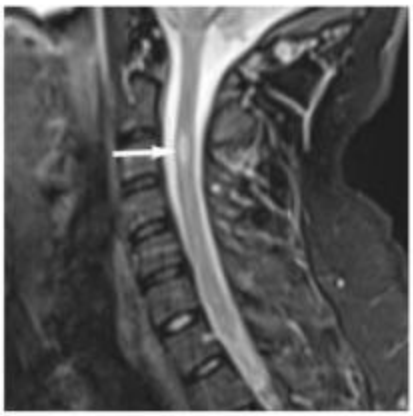

Figure 1

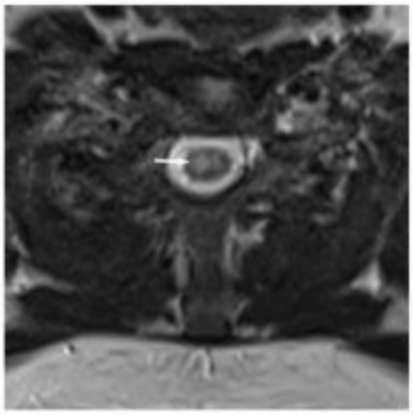

Figure 2

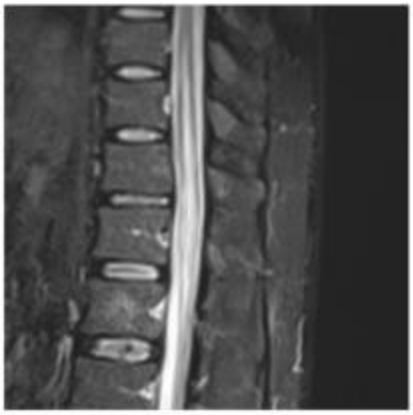

Figure 3

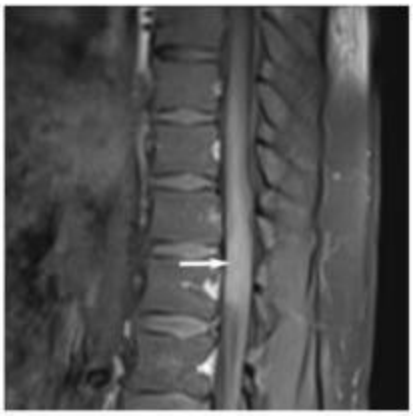

Figure 4

Monkeypox Case:

Initial MRI of spine demonstrate focal short segment hyperintense cord signal at the level of C3 (white arrow) on STIR sagittal (figure 1) and T2 axial (figure 2) sequences. Follow up MRI spine demonstrate diffuse long segment hyperintense signal involving lower thoracic cord and conus (Figure 3) with abnormal enhancement (figure 4).

(Filename: TCT_431_Slide1.jpg)

1308

Ace of Skull Base: A Primer of ASL in Skull Base Mass Lesions

G Mendez[1], N Fischbein[2]

[1]Stanford University, Palo Alto, CA, [2]Stanford University, Stanford, CA

Summary and Objectives

We illustrate the clinical utility of arterial spin labeling (ASL) perfusion imaging in assessing and characterizing masses of the skull base. ASL can help increase specificity in differential diagnoses of masses and can also help identify potential pitfalls, notably vascular lesions such as aneurysms and dural arteriovenous fistulae (dAVFs). ASL can help distinguish disease recurrence from treatment-related change, and it is useful in assessing treatment response of lesions that are treated with radiation therapy.

Materials and Methods

Review of skull base conference cases for skull base lesions imaged with ASL perfusion techniques was performed. Lesions were assessed with routine MR imaging sequences as well as ASL perfusion, and ASL characteristics (hypo-, iso- or hyperperfusing compared to brain tissue) were ascribed to each lesion. Final diagnosis was obtained with tissue sampling (primary diagnosis) or repeat biopsy or imaging follow up (post-treatment lesions).

Results and Conclusions

Results: 83 cases from the skull base conference archives were reviewed and categorized by skull base region (anterior, central, lateral) and pathology-proven diagnosis. Diagnoses included the following lesions: meningioma, metastasis, paraganglioma, schwannoma, lymphoma, esthesioneuroblastoma, chondrosarcoma and chordoma. Confounding lesions included giant aneurysms and dural arteriovenous fistulae. 56 patients had follow-up imaging after surgery, endovascular intervention and/or radiation therapy.

Conclusion: We demonstrate the diagnostic power of ASL perfusion in augmenting the accuracy of differential diagnoses in skull base masses. Recognizing the ASL perfusion characteristics of specific tumors is a helpful addition to any neuroradiologist's armamentarium when evaluating lesions of the skull base. Assistance in avoiding pitfalls is also useful as demands on radiologists continue to grow, and there is limited time available to spend assessing a given imaging study.

Patient with left sided pulsatile tinnitus.

Figure 1:

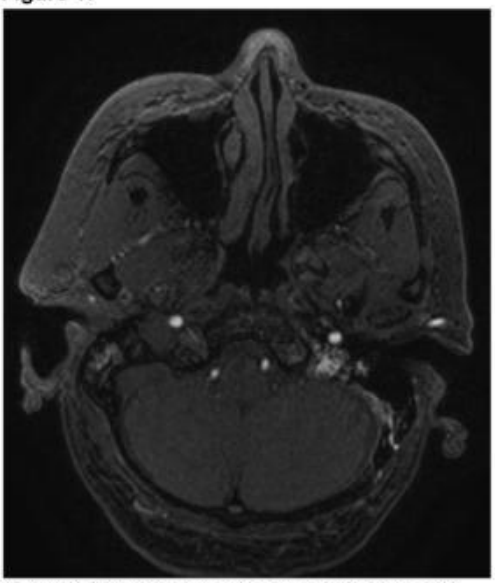

A: MRA images demonstrate asymmetric reticulated abnormal flow related enhancement at the left jugular bulb and sigmoid sinus.

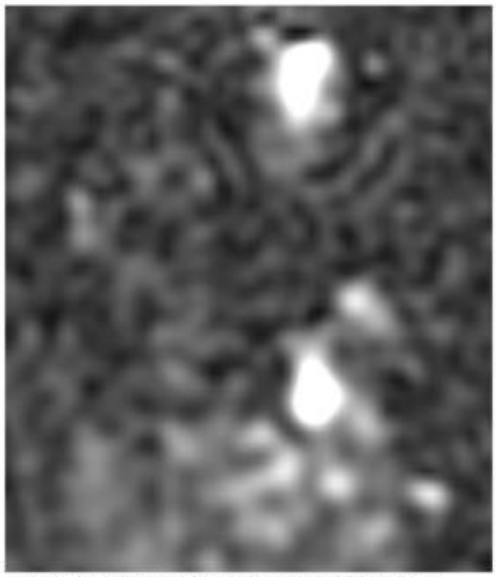

B: ASL images with corresponding hyperintensity consistent with a shunting lesion, likely a dural arteriovenous fistula (dAVF).

History of multiple meningiomas with more subtle left sphenoid wing lesion best seen on ASL perfusion sequences, in the absence of gadolinium contrast-enhanced images.

Figure 2:

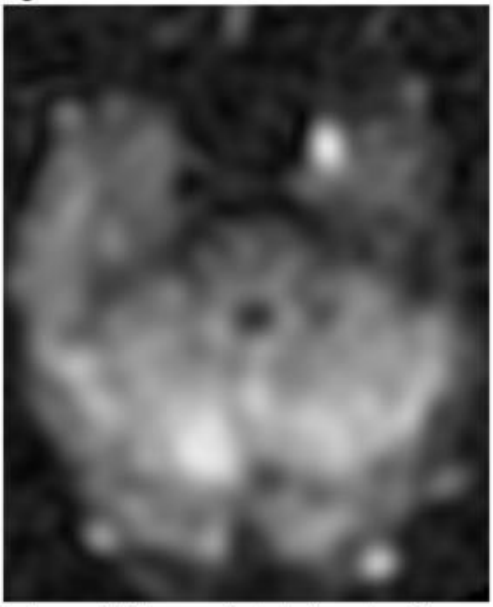

A: Focus of ASL hyperperfusion in the region of the left sphenoid wing and corresponding to a subtle meningioma, less clearly delineated on structural sequences.

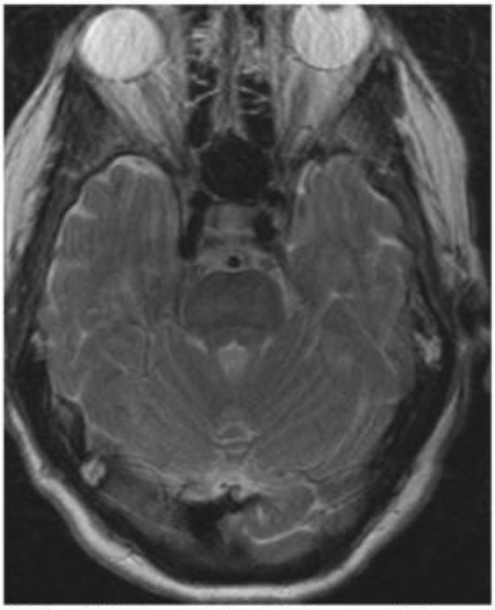

B: T2 weighted images demonstrating a small T2 intermediate extra-axial mass at the left middle cranial fossa and corresponding to the ASL bright focus.

(Filename: TCT_1308_Gustavo-ASNR2023Images-85x11_updated.jpg)

1350

Acing the Basics: Why Understanding the Fundamentals is Everything in Pediatric Giant Intracranial Aneurysms?

C Parra-Farinas[1], S Hiremath[1], A Alfalahi[1], V Pai[1], P Muthusami[1]

[1]The Hospital for Sick Children (SickKids), University of Toronto, Toronto, Ontario

Summary and Objectives

BACKGROUND Neurovascular disorders are an important cause of brain injury in the pediatric population leading to substantial mortality and morbidity. Giant intracranial aneurysms (GIA) represent an extremely complicated subset of aneurysm pathology and remain among the most difficult lesions to manage. Full awareness of GIA imaging features leads to a crucial change in the disease course. OBJECTIVE To offer a comprehensive and illustrative review of the 1. Clinical presentation; 2. Pathophysiological mechanism: A. Etiology: Congenital, idiopathic, infectious, flow-related, traumatic; B. Growth; C. Rupture; D. Type: Saccular, dissecting. 3. Imaging characteristics: Ultrasound (US); computed tomography (CT); magnetic resonance imaging (MRI); digital subtraction angiography (DSA); and 4. Treatment: A. Conservative; B. Endovascular; C. Surgical, of both arterial and venous GIA in childhood. DISCUSSION Aneurysms exceeding 25 mm in their maximal diameter are classified as GIA. Patients present as slow-growing space occupying masses rather than with subarachnoid hemorrhage. GIA have a broad pathophysiological mechanism as well as associations and links with a variety of systemic and intracranial disorders. There are multiple theorized pathways that result in either internal elastic lamina de novo defect or dynamic evolution from smaller lesions with intermittent breakdown of the aneurysmal wall. Growth is promoted by the presence of intraluminal thrombus associated with persistent intramural hemorrhage and neovascularization. Compared to non-giant aneurysms there is an increased incidence in the posterior circulation. There are unique imaging features. US shows a large mass. CT may demonstrate a peripheral calcified rim. MRI shows non-enhancement inside the thrombus and an onion skin appearance in case of thrombosis of the aneurysm. DSA is the gold standard for anatomical characterization and treatment planning. Management decision must incorporate an understanding of how treatment strategies may affect the normal development of the central nervous system. The best treatment option is a multimodal approach to provide a curative result with favorable outcomes. CONCLUSION Understanding of the pediatric GIA pathophysiological mechanism in combination with recognition of the imaging patterns will lead to accurate and prompt diagnosis and subsequently correct treatment.

(Filename: TCT_1350_CPF_ASNR2023.jpg)

891

Advanced Magnetic Resonance Imaging Techniques in the Evaluation of Parkinson's Disease and Atypical Parkinsonian Disorders

A Tejani[1], K Raj[2], B Shah[3], R Dewey[2], J Maldjian[4], F Yu[5]

[1]UT Southwestern Medical Center, Frisco, TX, [2]UT Southwestern Medical Center, Dallas, TX, [3]UT Southwestern, Irving, TX, [4]University of Texas Southwestern Medical Center, Dallas, TX, [5]UT Southwestern, Dallas, TX

Summary and Objectives

Educational Objectives: 1. Provide an overview of advanced MR imaging techniques in the evaluation of Parkinson's disease (PD) and atypical Parkinsonian disorders (APDs), focusing on MRI physics, clinical protocol, and interpretation. 2. Review pertinent anatomy of the basal ganglia and brainstem as they pertain to the pathophysiology of PD and APDs. 3. Review manifestations of PD and APDs using advanced MR techniques, noting correlation with key anatomical structures. 4. Highlight future applications of novel imaging techniques for disease monitoring and treatment planning. Presentation Summary: • Introduction o Conventional MR protocol in evaluation of PD and APDs o Discuss potential role of novel techniques as an unmet need in diagnosis, monitoring, and treatment • Review of MRI physics concepts and clinical protocol for advanced techniques o Three-dimensional fluid-attenuated inversion recovery o Neuromelanin-sensitive imaging o Iron-sensitive imaging ♣ Quantitative susceptibility mapping o Diffusion imaging ♣ Diffusion tensor imaging ♣ Multi-shell diffusion techniques • Neurite orientation dispersion and density imaging (NODDI) • Diffusion kurtosis-based methods including white mater tract integrity (WMTI) o Fast gray matter acquisition T1 inversion recovery • Case-guided review of pathological findings in: o PD o APDs (progressive supranuclear palsy, multiple system atrophy) • Role of advanced imaging techniques in guiding surgical intervention, disease monitoring, and diagnosis.

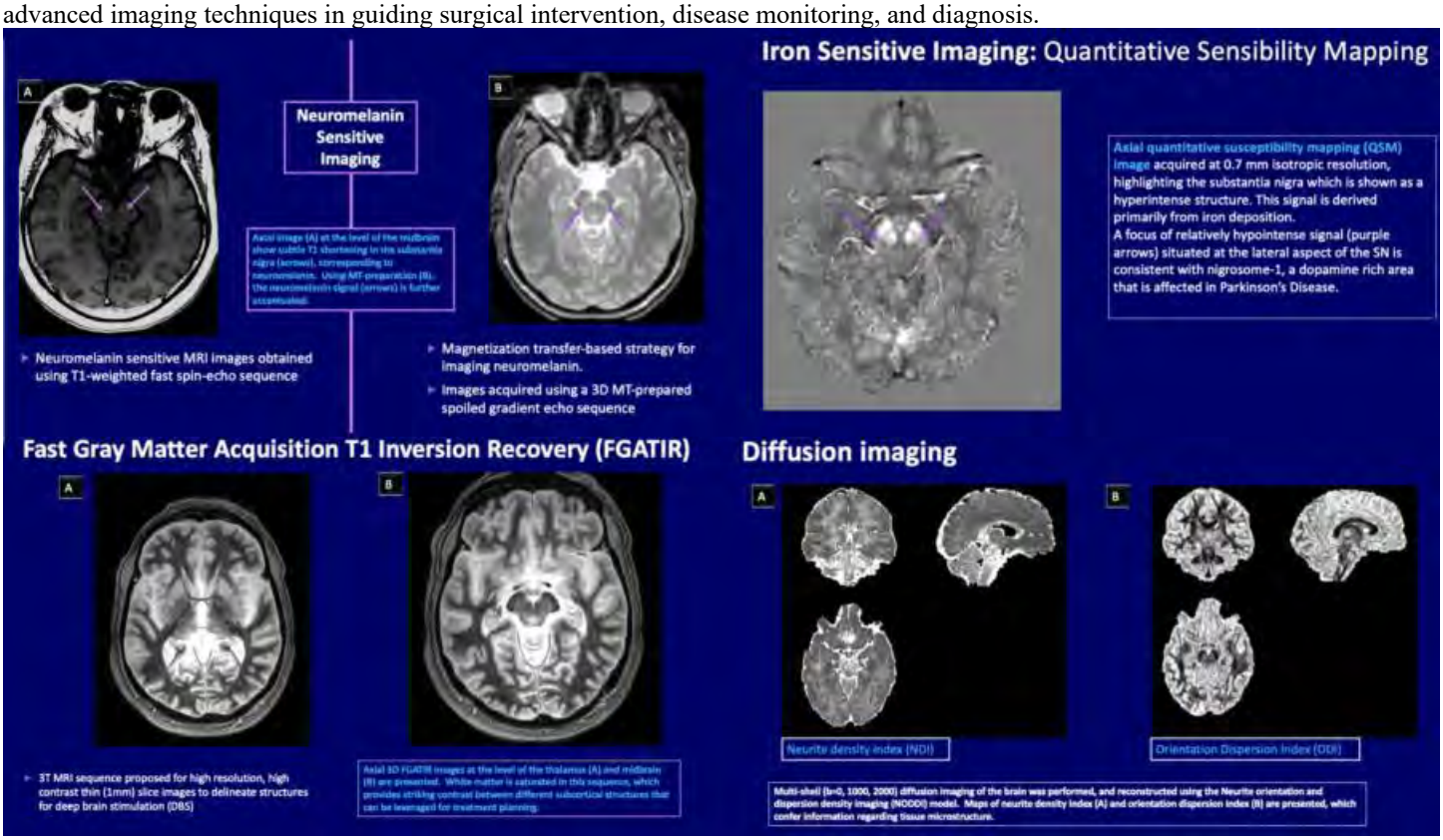

(Filename: TCT_891_Tejani_MD_fyu.jpg)

275

Amyloid-Related Imaging Abnormalities (ARIA): A Primer for Clinical Practice

F Mashriqi[1], K Al Tawil[1], M Roytman[2], P Schulz[3], G Zaharchuk[4], T Benzinger[5], A FRANCESCHI[1]

[1]Northwell Health, New York, NY, [2]Weill Cornell Medicine, New York, NY, [3]McGovern Medical School at The University of Texas Health Science Center at Houston, Houston, TX, [4]Stanford University, Stanford, CA, [5]Washington University in St.louis, Saint Louis, MO

Summary and Objectives

Amyloid-Related Imaging Abnormalities (ARIA) are a collective group of adverse pathologies that occur in patients undergoing anti-Amyloid β (Aβ) therapy for the treatment of Alzheimer's Disease (AD). Numerous therapies are being developed and tested in clinical trials to combat the accumulation of Aβ plaques in the central nervous system. The most common therapy includes monoclonal antibodies (mAb) directed at specific Aβ moieties. Numerous mAb have been developed and tested with varying clinical efficacies and rates of adverse ARIA. ARIA-H is defined as superficial siderosis or microhemorrhages (Figure 1A). ARIA-E is defined as vasogenic edema or sulcal effusions (Figure 1B). This educational exhibit aims to introduce ARIA by discussing its pathophysiology,

epidemiology, and symptomatology. This is followed by a discussion of imaging features including review of clinical cases, and lastly treatment options and prognosis.
Results and Conclusions
As the prevalence of mAb therapy for the treatment of AD increases, so does the likelihood of encountering ARIA in the reading room. In fact, routine ARIA monitoring is likely to be implemented clinically. It therefore becomes imperative for the radiology trainee and neuroradiologist to recognize the diagnostic clues of ARIA and properly convey the relevant information to the consulting clinician.

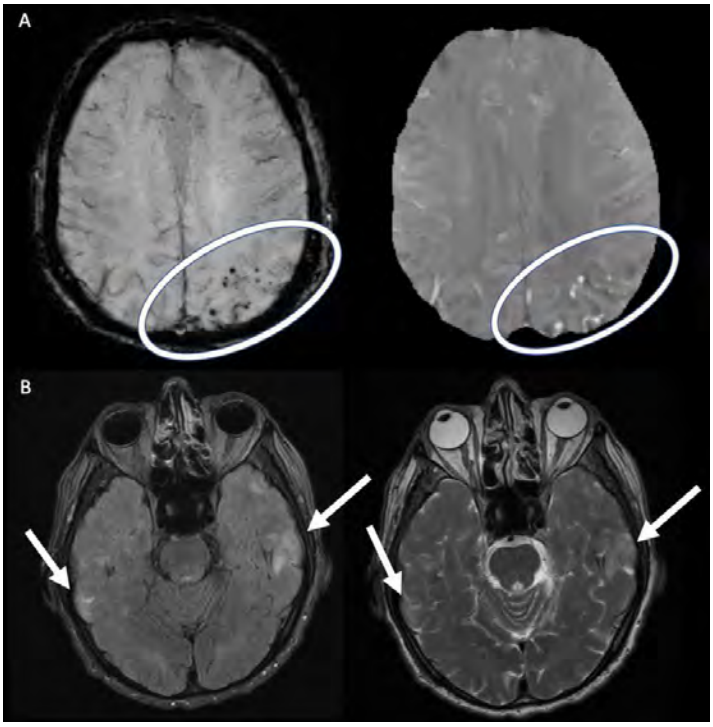

(Filename: TCT_275_ASNRARIAIMAGE.jpg)

1378
Amyotrophic Lateral Sclerosis: Multimodal Imaging and Differential Diagnosis
S Mishra[1], M Kurokawa[1], A Capizzano[1], R Kurokawa[1], S Naganawa[1], J Kim[1], T Moritani[1]
[1]University of Michigan, Ann Arbor, MI

Summary and Objectives
Amyotrophic lateral sclerosis (ALS) is a fatal, progressive disease, characterized by both upper (UMN) and lower (LMN) motor neuron involvement. TDP-43 and iron accumulation play a crucial role in the pathophysiology. Recent development of genetics, molecular biology, and advanced imaging of ALS has been remarkable. ALS can be familial, 10-15% of cases or sporadic. About 70% of familial cases have mutations within known genes, of which more than 40 have been identified with the most common being SOD1, FUS, C9orf72, TARDBP. The purpose of this exhibit is to demonstrate multimodal imaging findings including advanced imaging of ALS and the differential diagnosis. Classic MR imaging features of ALS includes T2/FLAIR signal abnormality of the corticospinal tract (CST) (Figure) including the posterior limb of the internal capsule (A), cerebral peduncle (B), medullary pyramids (C), although the sensitivity and specificity of conventional MRI for diagnosis have been reported at 48% and 76%, respectively. Diffusion tensor imaging (DTI) in sporadic ALS patients demonstrated correlation between clinical scores and CST fractional anisotropy. Iron accumulation in the primary motor cortex as evidenced by T2* hypointensity and reduced signal in susceptibility weighted imaging (SWI) has been demonstrated and correlated with the severity of UMN signs (Figure, panel D). Quantitative susceptibility mapping (QSM) measures have been observed in the motor cortex and CST regions and may demonstrate greater diagnostic accuracy. On MR spectroscopy, the ratio of Glu to NAA or GABA is increased in patients with ALS. Positron emission tomography (PET) is useful to analyzing CNS changes in ALS and the differential diagnosis. Cervical cord imaging demonstrated higher T2* signal within the lateral CST. UMN-predominant presentations can be mimic to primary lateral sclerosis, hereditary spastic paraplegias or primary progress multiple sclerosis. ALS-like syndrome (Pseudo ALS sign) can also be seen in CNS lymphoma, progressive multifocal leukoencephalopathy and POLG-related disorder. For LMN-predominant presentations, common mimickers include chronic inflammatory demyelinating polyneuropathy, Hirayama's disease, multisegmental amyotrophy, subacute combined degeneration, inclusion body myositis, myasthenia gravis, multifocal motor neuropathy, and spinobulbar muscular atrophy. For both UMN and LMN presentation, cervical stenosis and hyperparathyroidism should be excluded.

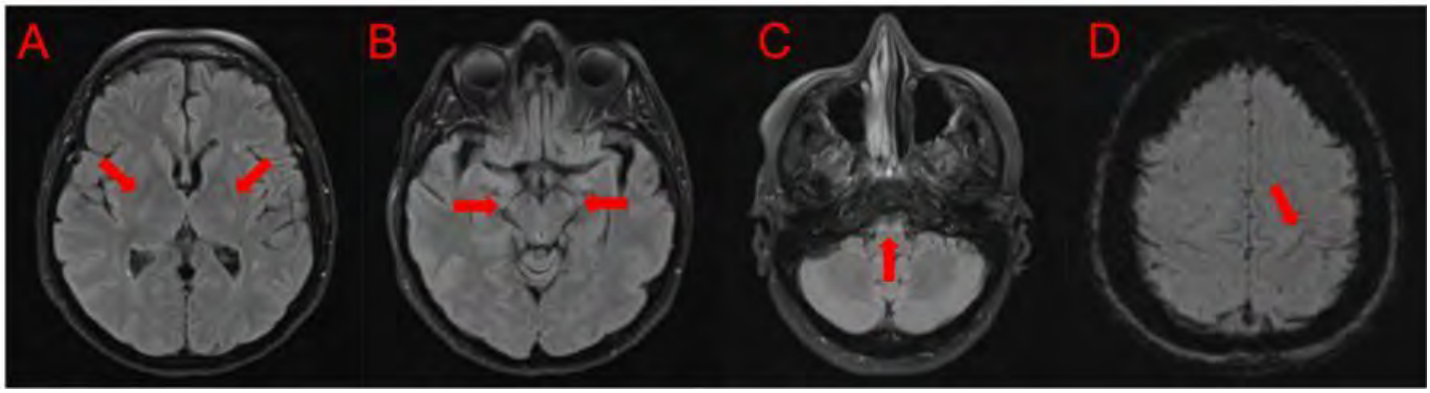

(Filename: TCT_1378_Figure.jpg)

599

An Insidious Complication of Spontaneous Spinal CSF Leak: Superficial Siderosis

A Krysiewicz-Bell[1], A Tsiouris[2], A Kim[3]

[1]Harvard College, Cambridge, MA, [2]New York-Presbyterian Hospital/Weill Cornell Medicine, New York, NY, [3]NewYork-Presbyterian Hospital/Weill Cornell Medicine, New York, NY

Summary and Objectives

Summary: Spontaneous spinal CSF leaks are an important etiology of superficial siderosis (SS) of the CNS, which can result in significant long-term morbidity for a patient with spontaneous intracranial hypotension even after successful treatment of the CSF leak. Spontaneous CSF leaks are categorized by causative mechanisms, which include dural tears, meningeal diverticula, and CSF-venous fistulas. SS can occur with all three types of CSF leaks with varying frequency, but SS secondary to ventral dural tears is by far most common and detected in 10% of patients with ventral CSF leaks. Case reports implicate bleeding from vertebral venous plexi as a cause for SS secondary to ventral dural tears, which may explain why ventral CSF leaks more commonly cause SS compared to other types of leaks. Our case series demonstrates that infratentorial SS appears to be most common with spontaneous spinal CSF leaks, occasionally with associated cortical SS. The clinical symptoms of our patients are in line with those of classical infratentorial SS, including hearing and vestibular impairment, gait ataxia, myelopathy, and cognitive dysfunction. Educational Objectives: 1. Pictorial review of the wide spectrum of SS of CNS secondary to spontaneous spinal CSF leaks 2. Cases demonstrate preferential involvement of the cerebellum (infratentorial SS) 3. Cases correlate with a spectrum of clinical symptoms, mostly in line with those of classical infratentorial SS 4. Pictorial and educational review of the different types of spontaneous spinal CSF leaks

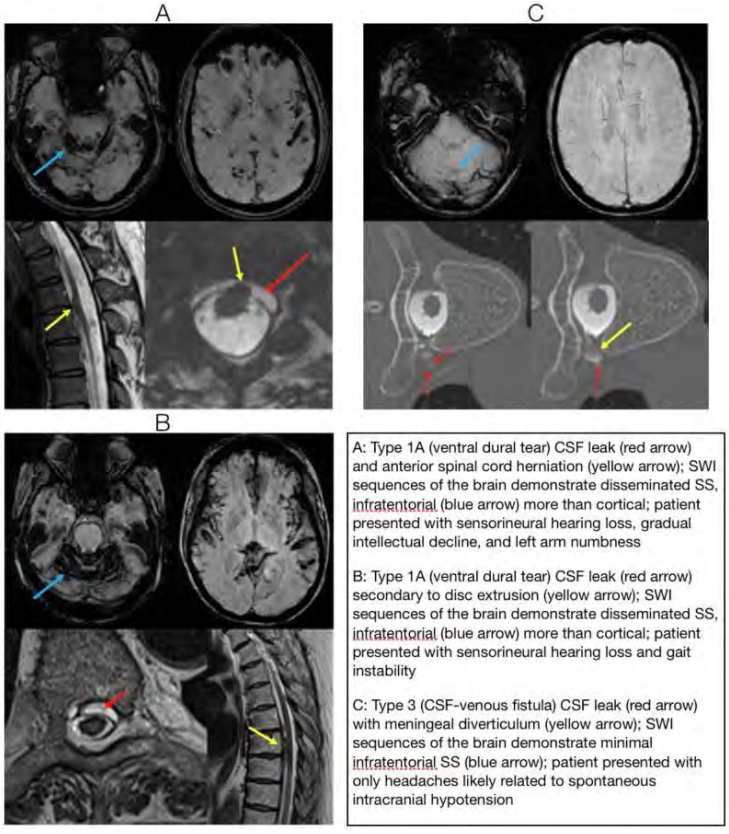

(Filename: TCT_599_ImageFinal.jpg)

1204

An Update on the CNS Manifestations of NF2: Imaging Findings, Clinical and Histological Features, and Assessment of Treatment Effects

Y Ota[1], E Liao[1], G Shah[2], A Srinivasan[1]
[1]University of Michigan, Ann Arbor, MI, [2]Univ. Michigan Health System, Ann Arbor, MI

Summary and Objectives
Neurofibromatosis type II (NF2) is a tumor predisposition syndrome characterized by the development of distinctive nervous system lesions. NF2 is commonly associated with bilateral vestibular schwannomas, trigeminal schwannomas, meningiomas, and spinal cord tumors including astrocytomas and ependymomas. This exhibition reviews imaging features, clinical and pathological characteristics, and treatment effect assessment in NF2-related CNS tumors, with emphasis on DWI, DSC-MRI, and DCE-MRI.
Purpose
1. Present common imaging findings, clinical features, and pathological characteristics of each tumor 2. Present advanced imaging evaluation for each tumor using DWI, DSC-MRI, and DCE-MRI 3. Present other familial schwannomatosis and meningiomatosis such as SMARCB1 and LZTR1, and demonstrate how to differentiate them from NF2.
Materials and Methods
Common imaging features and clinical/pathological characteristics 1. Vestibular schwannoma 2. Trigeminal schwannoma 3. Meningioma 4. Spinal Ependymoma 5. Spinal astrocytoma Advanced imaging evaluation of each tumor by DWI, DSC-MRI, and DCE-MRI Other familial schwannomatosis and meningiomatosis
Results and Conclusions
1. NF2 is associated with CNS tumors such as schwannomas, meningiomas, spinal ependymoma, and other tumors, and common imaging features and clinical/pathological characteristics are reviewed. 2. Advanced imaging can enable further evaluations such as gene mutation and treatment response assessment. 3. Other familial meningomatosis and schwannomatosis such as SMARCB1 and LZTR1 can mimic NF2.

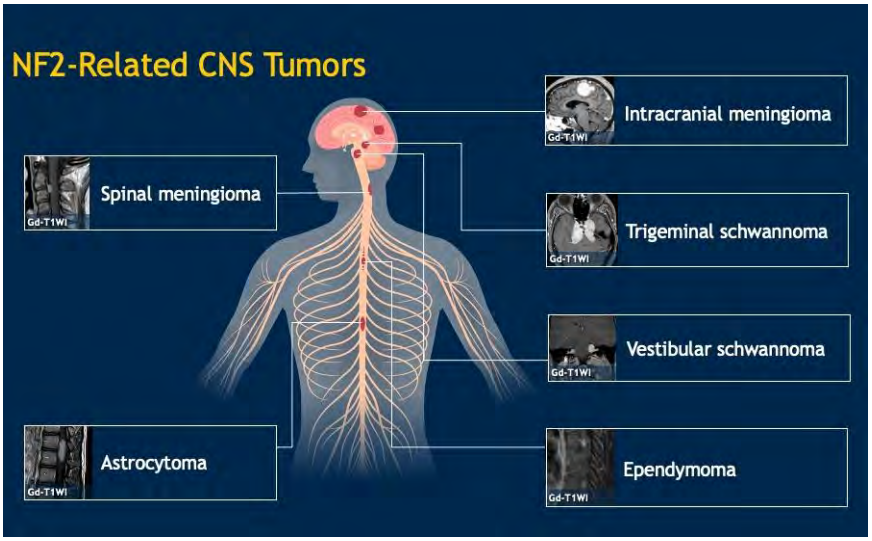

(Filename: TCT_1204_NF2slide2.jpg)

481

Application of Interactive 3D Visualization in Epilepsy Surgery for Periventricular Heterotopia

F Khan[1], C Curtis[2], K Sarkar[3], J Rini[3]
[1]The International Center for Epilepsy at Ochsner, Ochsner Neuroscience Institute, Ochsner Health, New Orleans, LA, [2]Medical 3D Lab, Ochsner Health, New Orleans, LA, [3]Ochsner Neuroscience Institute, Ochsner Health, New Orleans, LA

Purpose
With advances in computer technology, we see a rapid growth in the applications of 3-dimensional (3D) computer models in medical and surgical care, clinical research, and education. Furthermore, adding interactive features to the 3D models provides users an enhanced understanding of complex structures and their spatial features and relationships that can guide surgical decisions. We propose that this technology can be useful during the evaluation and surgical planning of patients with periventricular heterotopia (PH).
Materials and Methods
We describe two patients with medically refractory epilepsy related to extensive PH who previously underwent extensive phase 1 workup and were selected for phase II intracranial monitoring with stereo electroencephalography (SEEG). A 26-year-old male had extensive heterotopic clustering bilaterally along the inferior aspect of the lateral ventricles from the temporal horn through the occipital horn (patient A). A 48-year-old female had heterotopia along the inferolateral aspect of the right lateral ventricle from the temporal horn through the occipital horn, as well as along the left lateral ventricle anterior to the temporal horn and posterior to the

occipital horn (patient B). Planning was based on a hypothesis that focused on potential regions of seizure onset within PH. The hypothesis was formulated upon review of a personalized 3D models of the patients' brain, ventricles, and heterotopia made from their respective MRIs and viewed on an internally developed 3D visualization application. This information guided robotic placements of SEEG electrodes. The intracranial SEEG data was analyzed and correlated with additional 3D models of brain with electrodes. The data supported a shared decision making with the patient guiding the surgical intervention.
Results and Conclusions
In epilepsy surgery, the objective is to use the minimum number of intracranial electrodes to safely and sufficiently sample regions of interest to formulate a precise surgical plan. The 3D models allow easy differentiation of abnormal heterotopia from normal brain structures that helps in pinpointing targets of interest. The interactive features assist in identifying feasible trajectories within the brain to obtain the highest yield of intracranial data, and during planning for stereotactic ablation procedures and placement of neurostimulator leads. The interactive 3D model can be correlated with SEEG data obtained during interpretation.

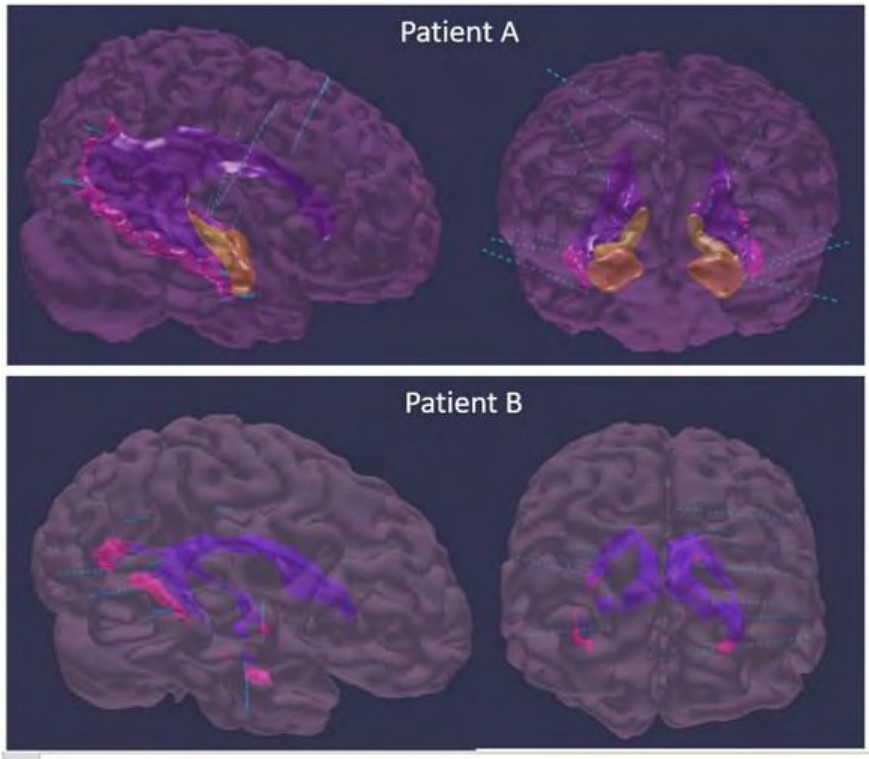

(Filename: TCT_481_Picture2.jpg)

547

Assessment of Traumatic Brain Injury with Diffusion Tensor Imaging - An Educational Approach

O Ferreira Dalla Pria[1], V Dayaram[2], M RAMIREZ GUZMAN[2], A CUETO RAMIREZ[2], P Mehta[2], R Thakur[2], L Chopra[2]
[1]University of Iowa, Iowa City, IA, [2]AD Healthcare System, Houston, TX

Summary and Objectives
OBJECTIVES: An introduction to Diffusion Tensor Imaging (DTI) and its importance for evaluating white matter integrity. Review relevant neuroanatomy and illustrate main DTI/tractography findings in patients with traumatic brain injury (TBI). This is an image-based approach with educational points: a.What radiologists need to know; b. Review the basics of DTI and tractography in TBI; c.Take-home messages. SUMMARY: History of DTI as a raising technique to evaluate white matter integrity. How to interpret fractional anisotropy (FA), apparent diffusion coefficient (ADC) and tractography. Assessment of white matter injury in TBI by comparing conventional MR sequences with DTI/tractography. Assessment of white matter injury demonstrated by DTI/Tractography when structural MRI is normal and correlating these findings with clinical history. LIMITATIONS AND CONFOUNDERS: Challenges on an innovative technique to evaluate white matter in TBI. Confounders on evaluating FA/ADC values. Availability of DTI analysis software is limited to a few centers.
Purpose
Conduct a review of concepts in DTI and their applicability in TBI. Review the main theoretical points on DTI, FA, ADC, and tractography. Discuss clinical practice and challenges of using DTI to evaluate white matter injury in patients with brain trauma and correlate with symptoms.
Materials and Methods
The same physician did all post-processing and FA/ADC charts from August 2021 to the present which includes over 400 patients. All patients with TBI attended one of our services for acute trauma or due to neurological complaints after brain trauma.
Results and Conclusions
Evaluation of TBI is difficult since structural MRI does not show evident positive findings in some cases, even with presenting

symptoms like focal weakness, behavior changes, dizziness, etc. These symptoms are due to white matter injury that may not be seen on structural MRI. DTI with FA and ADC analysis is a reliable method to assess white matter tract integrity. As this is a challenging technique that requires expert anatomic knowledge, radiologists must be aware of these additional tools to help evaluate white matter integrity in TBI.

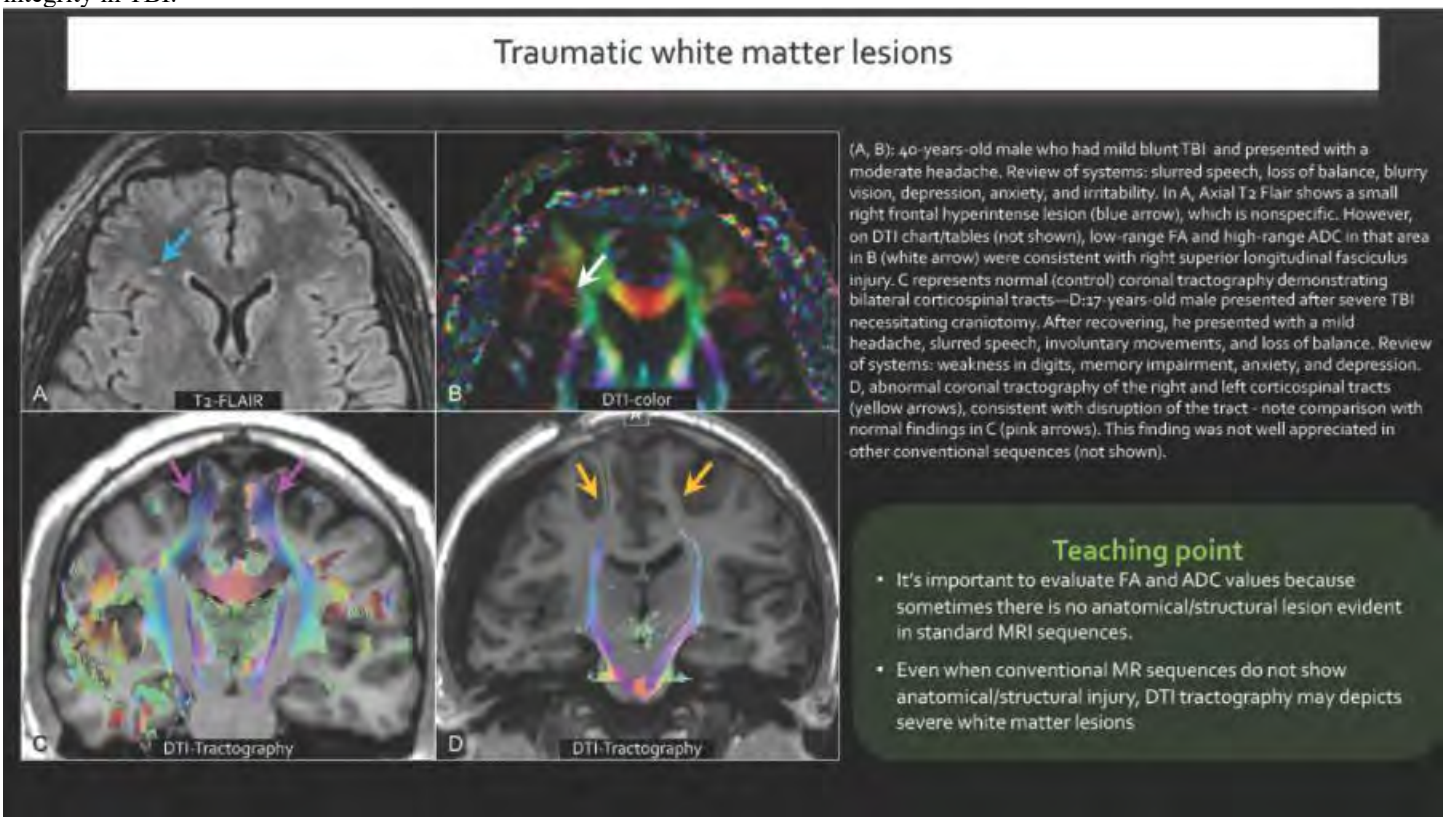

(Filename: TCT_547_Traumaticwhitematterlesions1024_1.jpg)

603

Atypical Etiologies of Stroke in the Young: A Radiologic Exhibit

C Zoppo[1], J Hanna[2], T Taros[3], J Singh[1], A Puri[4], A Kuhn[5]

[1]University of Massachusetts Medical School, Worcester, MA, [2]UMass Chan Medical School, Worcester, MA, [3]University of Massachusetts Chan Medical School, Worcester, MA, [4]Currently at Univ. of Massachusetts Medical Center., Worcester, MA, [5]UMass Medical Center, Worcester, MA

Summary and Objectives

• Identify etiologies of stroke in young patients • Review and discuss underlying pathologies • Utilize various modalities to demonstrate key cross-sectional and angiographic imaging findings in specific stroke etiologies

Purpose

Stroke is uncommon in young patients (age 18-50) compared to older adults, but etiologies of stroke in the young are more expansive. There are specific atypical etiologies to consider when evaluating these patients.

Results and Conclusions

Moyamoya disease accounts for less than 1% of strokes in this population but is more prevalent in those of Asian heritage.1 Skullbase artery stenosis may lead to generation of lenticulostriate collaterals, producing a characteristic "puff of smoke" – "Moyamoya" in Japanese - on angiograms. Carotid artery dissection is the leading identifiable cause of stroke in patients under age 40.2 Interestingly, there is increased incidence during autumn due to seasonal changes in blood pressure, and in areas of poor air quality.2 Meanwhile, paradoxical embolism migrating through a patent foramen ovale is the most common cause of cryptogenic stroke in young patients without cerebrovascular risk factors.3 Cerebral involvement of vasculitis is rare, but in cases such as Takayasu Arteritis, thrombosis with stenosis of proximal aortic arch great vessels may extend into the proximal carotid arteries and precipitate large vessel occlusion. Cocaine use is highly prevalent worldwide, with consequences of use including intraparenchymal hemorrhage. The appearance of these hemorrhages on imaging has been described as similar to hemorrhages seen in chronically hypertensive older adult patients.4 Infectious etiologies of stroke include mycotic cerebral aneurysm, which is the result of direct infection of the blood vessel wall. COVID-19 may induce cytokine storm, causing a hypercoagulable state. HIV vasculopathy typically presents in young patients with congenital HIV/AIDS.5 Syphilis and Mucormycosis have been associated with endothelial invasion and cerebral vessel damage. Chagas Disease can cause a dilated cardiomyopathy, a risk factor for cardioembolic stroke.

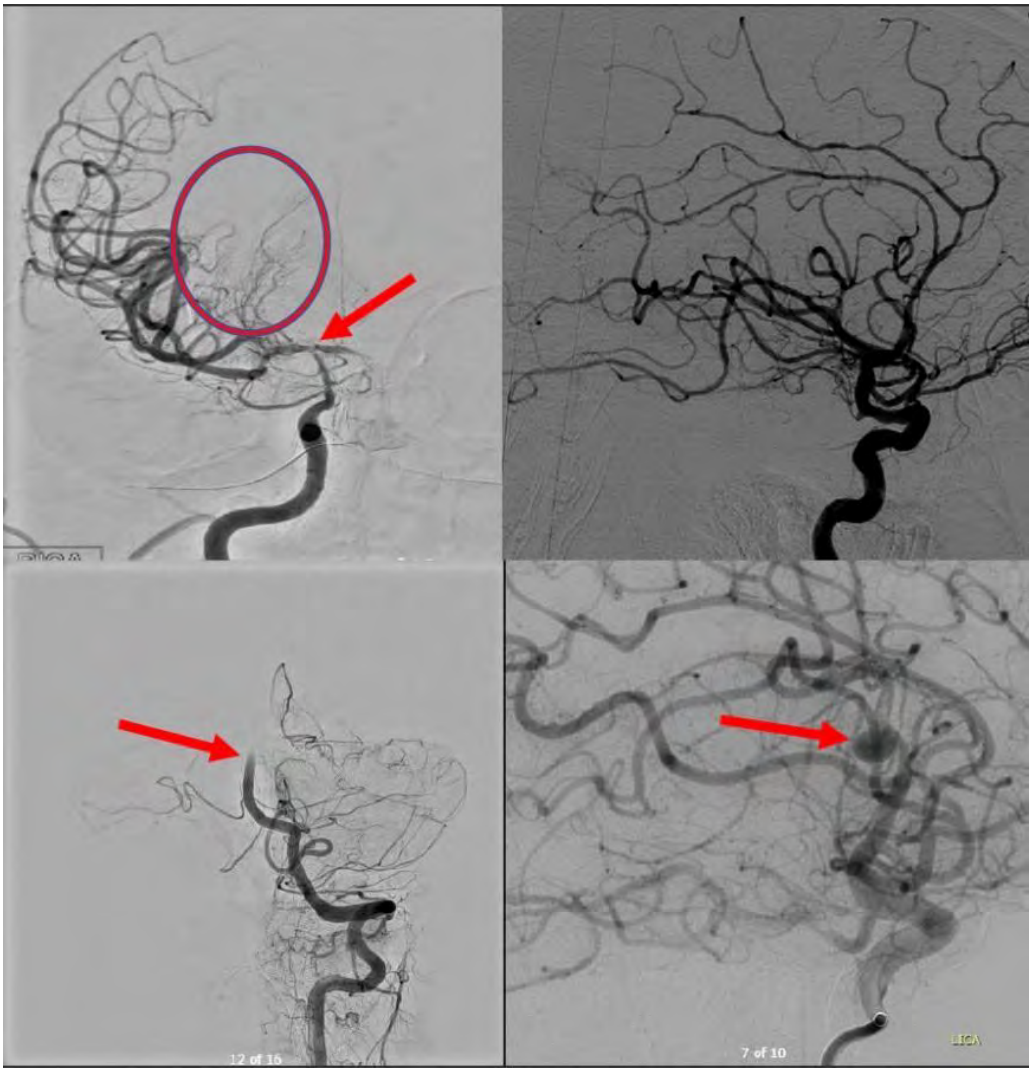

(Filename: TCT_603_YoungStrokeImagesCropped.jpg)

1151

Ballad of blood and brains: A review of cerebral microbleed imaging patterns

S Sun[1], P Wang[1], K Wei[1], E CHU[1], J Soun[1], E Kuoy[1]
[1]*University of California Irvine, Orange, CA*

Summary and Objectives
The detection of cerebral microbleeds (CMB) has dramatically increased due to widespread use of sequences such as gradient-recalled echo (GRE) and susceptibility-weighted imaging (SWI). Although CMBs were initially associated with intracranial hemorrhage, they are now linked with many disease processes and also found in the healthy elderly population. The main microangiopathies of CMBs, namely hypertensive vasculopathy and cerebral amyloid angiopathy, have a classic spatial distribution of deep basal ganglia and infratentorial for the former and a lobar predominance for the latter. There are also alternative causes including traumatic brain injury, post-radiation changes, critical medical conditions such as endocarditis, extracorporeal membrane oxygenation or sepsis, and micro-metastases of hemorrhagic tumors. More uncommon etiologies include familial cerebral cavernous malformations, cerebral vasculitis, post-cardiac valve replacement, sickle cell disease, and end stage renal disease (ESRD). Previously thought to be more an incidental finding, CMBs have now been shown to predict future risk of intracerebral hemorrhage and ischemic stroke. There is also an association between CMBs and cognitive decline and dementia. Certain populations, including patients with ESRD and atrial fibrillation, have a high prevalence of CMBs associated with adverse outcomes. As the clinical significance of CMBs grows, the imaging interpretation of this entity will become paramount.
Purpose
The purpose is to present a case-based review of the common and uncommon etiologies of cerebral microbleeds (CMB), highlight distinct imaging patterns, and discuss the growing clinical significance and prognostic implications of CMBs.

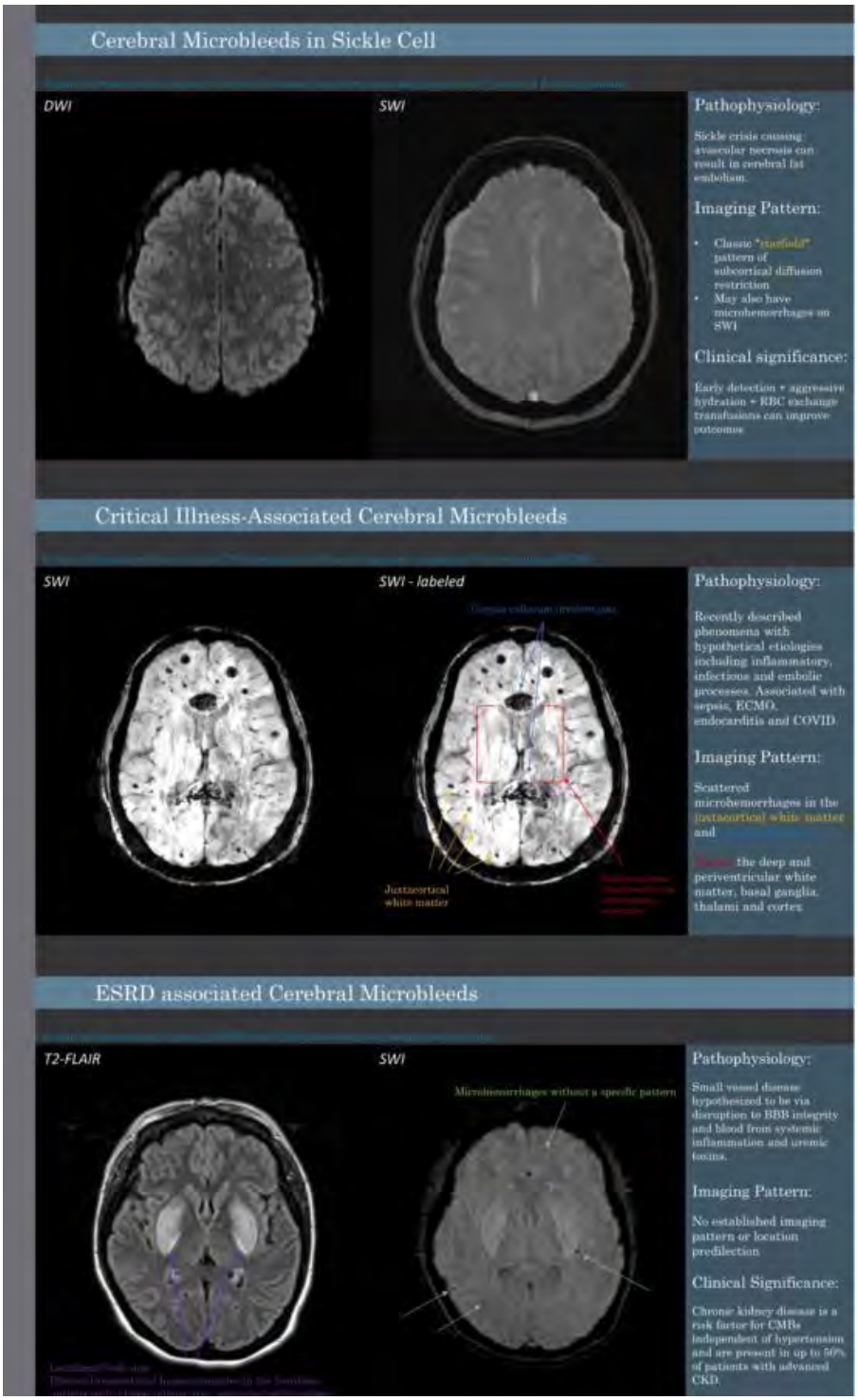

(Filename: TCT_1151_CerebralMicrobleeds-ASNR2023AbstractFigure.jpg)

718

Bevacizumab in Recurrent Glioma: A Review of Concepts and Neuroimaging Findings

J Brunelli[1], C Leite[2], I Alves[3], H Lee[3], O Feher[3], C Amancio[3]

[1]Hospital Sírio-Libanês, São Paulo, AK, [2]University of São Paulo, Sao Paulo, São Paulo, [3]Hospital Sírio-Libanês, São Paulo, São Paulo

Summary and Objectives

Glioblastoma (GBM) is the deadliest primary brain tumor. Despite the multiple advances in diagnostic and treatment, the prognosis remains somber. In 2009, the FDA approved the use of bevacizumab (Avastin) for the treatment of recurrent GBM. Bevacizumab is a recombinant humanized monoclonal immunoglobulin G 1 antibody that prevents the proliferation of endothelial cells and formation of new blood vessels. The evaluation of GBM to treatment response is a clinical dilemma, especially with the use of antiangiogenic

therapy such as bevacizumab. Imaging may play a critical role in the management of the patient with glioma, but in the context of antiangiogenic therapy the analyses is even more challenging. The objectives of this exhibit are: review of Bevacizumab therapy and the mechanisms of action; review and application of the Response Assessment in Neuro-Oncology (RANO) criteria; and review the literature in a case-based approach.

Purpose

- Review of Bevacizumab (BEV) therapy - Show the timeline evolution of GBM treatment with focus on RANO criteria, and the application of it on MRI - Review of the literature with teaching points in a case-based approach of high grade glioma: effects of BEV; restriction diffusion induced by BEV: viable tumor vs coagulative necrosis; possible imaging biomarkers of response to BEV therapy (CBV, Ktrans and ADC values); radiological progression patterns after BEV failure (classification) and patterns of perffusion imaging - Limitations and future perspectives in MRI Assessment of BEV therapy

Materials and Methods

Review the literature of glioblastoma treatment with focus on antiangiogenic therapy with Bevacizumab (BEV) and RANO criteria. After a retrospective analysis of the medical records and MRI of our digital archive we illustrated a case-based approach focusing on high grade glioma.

Results and Conclusions

Developing better imaging tools to evaluate the therapeutic effect of different interventions in real time will have a direct impact on the process of developing new and more effective treatments. RANO-HGG criteria are the standard for assessment of treatment response; nonetheless, it is still considered a work in progress while some advanced MRI techniques become more widely available, standardized, and reproducible. Despite no single biomarker with sufficient sensitivity and specificity has been generally recognized for anti-angiogenic therapy of glioma, we need to know what already exists and is possible to do and say about those patients examinations.

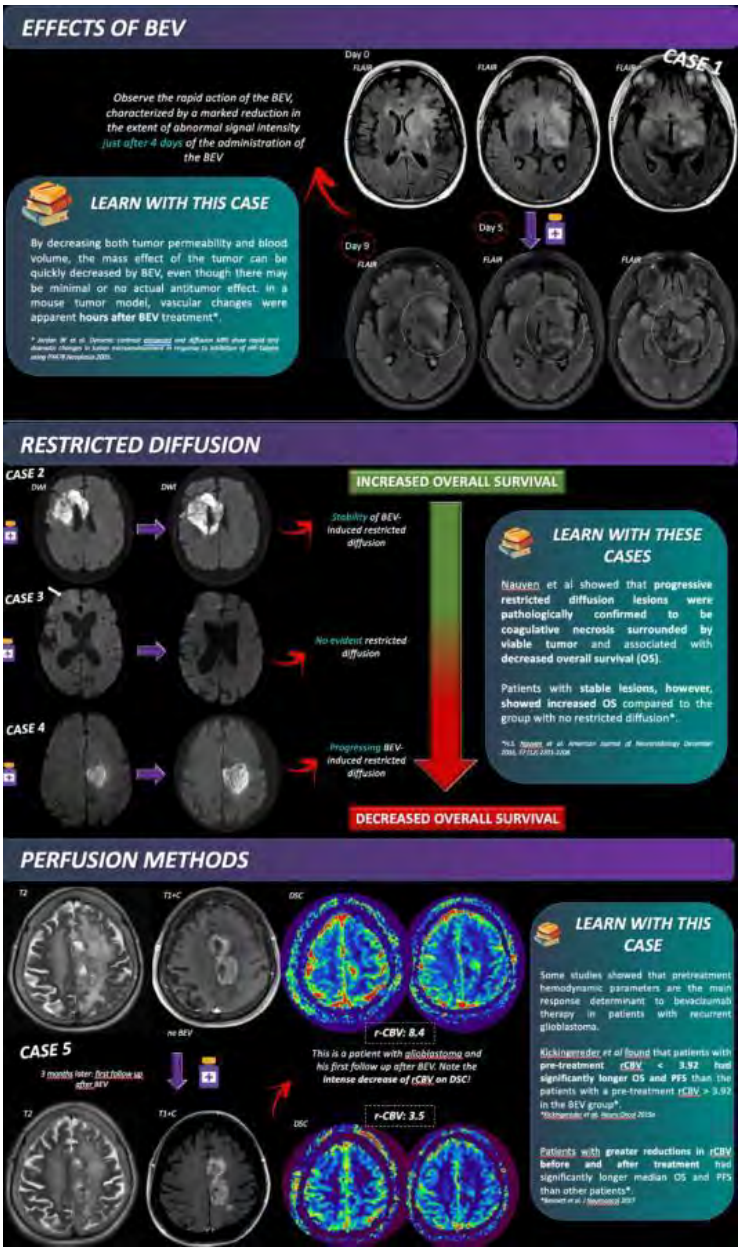

(Filename: TCT_718_asnr_bev.jpg)

673

Blunt Cerebrovascular Injury and pitfalls: a pictorial essay

B Mazini[1], V Dunet[2], S Schmidt Kobbe[3]

[1]Chuv, LAUSANNE, Vaud, [2]Lausanne University Hospital, Lausanne, Vaud, [3]CHUV, Lausanne, Switzerland

Summary and Objectives

BCVI is a serious spectrum of pathologies encountered in patients who suffer from high-energy blunt force trauma or direct cervical and/or craniofacial injury. The diagnosis of BCVI can be challenging, also because the damage of the vessel wall may not always be associated with cervical fractures and vice versa. Cervical CT angiography has widely been accepted as the emergency technique of choice in these severely injured patients. However, in challenging cases, CT may yield equivocal results so that MRI is a useful noninvasive adjunct, namely thanks to 3D fat-saturated T1-weighted MR sequences centered on the supra-aortic vessels.

Purpose

To give an overview of the different lesion types encountered in blunt cerebrovascular injury (BCVI) To enable radiologists to become familiar with the CT and MR features of BCVI and to describe potential pitfalls

Materials and Methods

We created a database of patients who visited our emergency department and underwent a cervical imaging (cervical CT angiography, cervical angio-MRI or both) between 2001 and 2020, collecting almost 100 cases of cervical injury in the setting of high energy trauma. We used this database to create a pictorial essay. Considering the educational aim of this poster, we also included examples of mimics and pitfalls, in order to provide a comprehensive overview.

Results and Conclusions

The radiologist plays a key role in the diagnosis and management of BCVI. Indeed, both therapy and prognosis are based on the Biffl grade, a scale based on imaging findings. According to our database, the most encountered lesion is arterial dissection. Interestingly, between patients who suffered from this lesion, about a half did not have an associated bone cervical fracture.

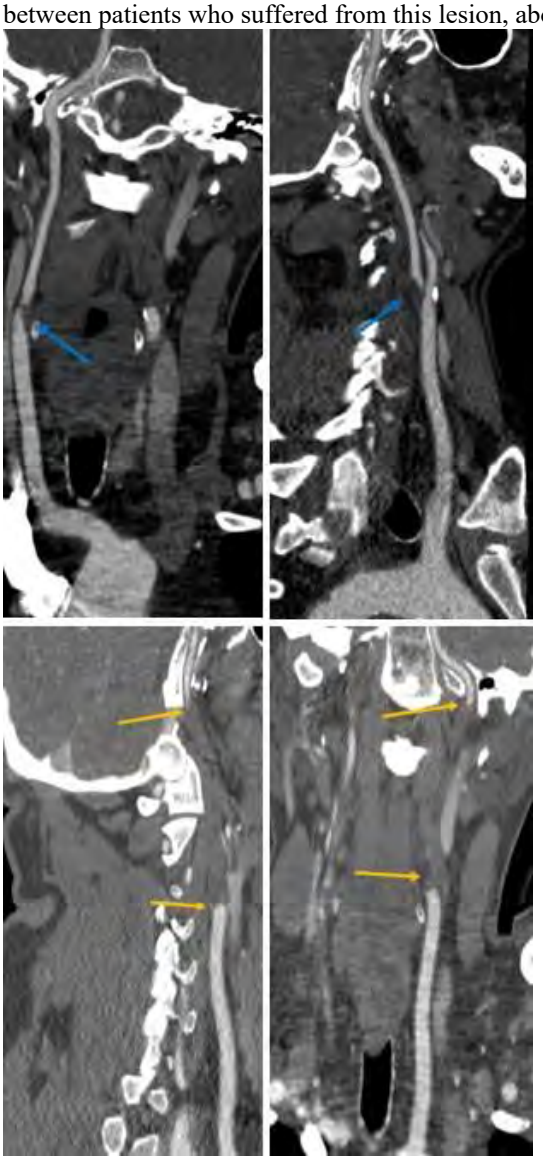

(Filename: TCT_673_5555.jpg)

506

Castleman Disease of the Neck: Imaging Considerations in its Immunotypes, Imaging Differentials and Mimics

M Tan[1]
[1]*Singapore General Hospital, Singapore*

Summary and Objectives
This Educational Exhibit presents an: 1) Overview of Castleman Disease 2) Imaging findings of Castleman Disease (in the neck) 3) The Clinical Immunotype Classification of Castleman Disease 4) The Histological Classification of Castleman Disease 5) The Role of the radiologist in the treatment of Castleman Disease with regard to: a) In iMCD i.e. HHV-8 negative Multicentric Disease i) Investigating the Extent of Disease ii) Assessing for imaging evidence of POEMS syndrome b) In HHV-8 negative Unicentric Disease i) Excluding other sites of Disease ii) Assessing for resectability c) in HHV-8 positive Multicentric Disease i) Investigating the Extent of Disease ii) Assessing for imaging evidence of Kaposi Sarcoma 6) Other Educational Objectives covered include: a) Differentials of High Attenuation Cervical Adenopathy and their imaging features i) i.e. Castleman, Sarcoidosis, Metastasis, TB, Kimura, Kikuchi b) A mimic of Castleman Disease and its differentiating features i) an Epidermal Cyst References: 1) Fajgenbaum DC et al. Unicentric , multicentric Castleman Disease. UpToDate. Referenced 8 Mar 2022 2) Talat N et al. Surgery in Castleman's disease: a systematic review of 404 published cases. Ann Surg. 2012 Apr;255(4):677-84. 3) Tanrıvermiş Sayıt, Aslı et al. Carcinoma ex pleomorphic adenoma of the infratemporal fossa: a case report with magnetic resonance imaging findings. Oral Radiology 33 (2016): 157-160. 4) Fernandes, Teresa & Lobo, J & Castro, Richard & Oliveira, M & Som, P. (2013). Anatomy and pathology of the masticator space. Insights into imaging. 4. 10.1007/s13244-013-0266-4. 5) Jiang XH, Song HM, Liu QY, Cao Y, Li GH, Zhang WD. Castleman disease of the neck: CT and MR imaging findings. Eur J Radiol. 2014;83(11):2041-2050. doi:10.1016/j.ejrad.2014.08.013
Purpose
To provide an overview of a Castleman disease and its imaging appearance (with focus on the neck). To outline the role of the radiologist in the treatment of Castleman Disease with regard to its Clinical Immunotype. To provide Differentials of High Attenuation Cervical Adenopathy and their imaging features, as well as a mimic of Castleman Disease and its appearance.
Materials and Methods
Case and literature review
Results and Conclusions
The presentation provides an overview of Castleman disease, the role of the radiologist in the treatment of Castleman Disease with regard to its Clinical Immunotype, differentials and a mimic of high attenuation cervical adenopathy

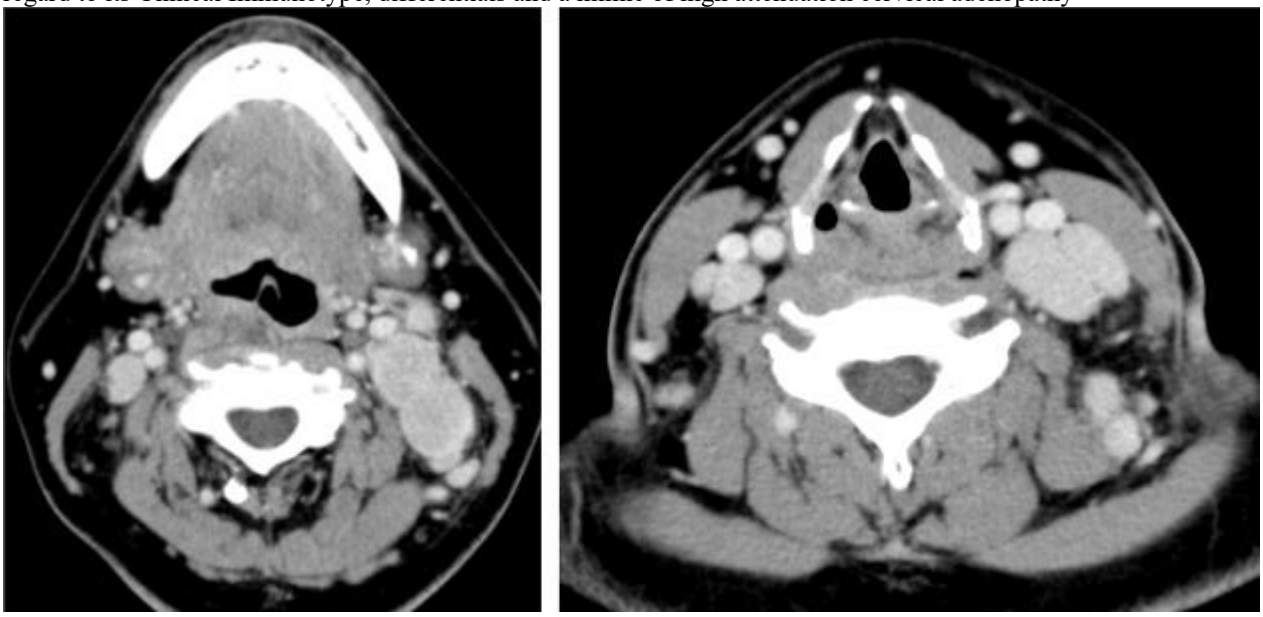

(Filename: TCT_506_CastlemanDisease.jpg)

349

Central Nervous System Imaging Findings in Patients with Solid Organ Transplants

M Bourne[1], Z Angel[1], R Thakkar[1], E Lee[1]
[1]*MedStar Georgetown University Hospital, Washington, DC*

Summary and Objectives
Transplant patients take lifelong immunosuppressants to prevent organ rejection. They suffer a multitude of complications related to being in an immunosuppressed state and from the immunosuppressant drugs themselves. In this report, we provide a pictorial essay on the various CNS disorders in transplant patients, including opportunistic infections, immune reconstitution inflammatory syndrome

(IRIS), posterior reversible encephalopathy syndrome (PRES), Tacrolimus-associated neurotoxicity, posttransplant lymphoproliferative disorder (PTLD), and CNS malignancies.
Purpose
Central nervous system disorders in transplant patients are rare but serious. We aim to discuss the imaging findings in transplant-related CNS disorders through a case review. Our educational purpose is to share experiences in our hospital regarding the CNS complications and present plausible causes for encephalopathy in transplant patients. Given that transplant patients are immunocompromised, they are susceptible to a certain subset of diseases as detailed in our exhibit. They also suffer from multiple drug related complications.
Materials and Methods
We compiled cases of transplant-related CNS complications from our institution.
Results and Conclusions
We include cases varying from opportunistic infections, immune reconstitution inflammatory syndrome (IRIS), posterior reversible encephalopathy syndrome (PRES), Tacrolimus-associated neurotoxicity, posttransplant lymphoproliferative disorder (PTLD), and CNS malignancies. For each case, we will provide a brief clinical history and images depicting the various conditions.

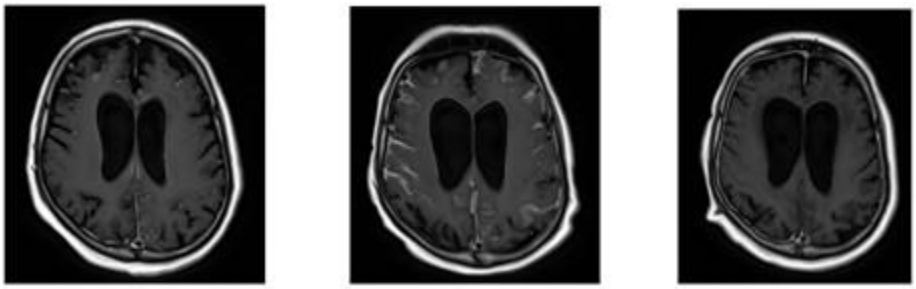

67-year-old post orthotopic liver transplant on tacrolimus presented with altered mental status. A). Initial T1 post contrast brain imaging shows leptomeningeal enhancement and ventriculomegaly. CSF diagnosis of cryptococcal meningoencephalitis was made and antifungal started and discontinuation of tacrolimus.
B). Three weeks post treatment there was worsening of the neurological status. Repeat T1 post contrast MR brain shows increased extensive leptomeningeal enhancement. Given CSF was negative of cryptococcal antigen, diagnosis of immune reconstitution inflammatory syndrome was made. Tacrolimus was restarted.
C). 3 months later, neurological improvement. Repeat T1 post contrast brain shows much reduced leptomeningeal enhancement.

(Filename: TCT_349_ASNR2023exampleIRIS.jpg)

707
Cerebral Fat Embolism in Sickle Cell Disease: MR imaging Patterns
E Al Ajmi[1], S Raniga[1], S Al-Kindi[1]
[1]*Sultan Qaboos University, Muscat, Oman*

Summary and Objectives
Cerebral fat embolism (CFE) in patients with sickle cell disease (SCD) is an under-recognized entity with significant morbidity. In SCD, vaso-occlusive crises cause bone marrow necrosis and result in the migration of marrow fat into circulation, as seen in acute chest syndrome. Multi-organ involvement results from more severe bone marrow necrosis, with CFE being a known uncommon manifestation. Magnetic resonance imaging (MRI) of the brain is crucial in identifying CFE and supporting the clinical findings in patients with SCD. The imaging findings of CFE in SCD patients are comparable to those of patients with CFE from other etiologies, with trauma accounting for the vast majority. We present here the different imaging patterns of CFE in patients with SCD.
Purpose
1. To present the MR imaging patterns of CFE in SCD patients. 2. To highlight the variation in the imaging findings based on the time of imaging from the onset.
Results and Conclusions
The five main MR imaging patterns of CFE in SCD are similar to those described by Kuo et al. The most commonly described pattern in the acute phase is a starfield appearance manifested by scattered foci of diffusion restriction in the deep gray matter and white matter (Figure 1A). The second pattern is observed in the subacute phase with bilateral symmetric confluent diffusion restriction in the white matter (Figure 1B). The signal changes are best characterized in this pattern on diffusion-weighted images and ADC maps, as the white matter can appear faintly hyperintense or normal on T2-weighted images. On the other hand, the other pattern in the subacute phase shows white matter hyperintensities that don't restrict but might enhance. The fourth described imaging feature is petechial hemorrhage, which is seen mainly in the cerebral and cerebellar white matter and the corpus callosum (Figure 1C). This

pattern can be present in the acute, subacute, or chronic phases. Some of the foci of susceptibility effects might resolve on follow-up in patients with SCD, which can be attributed to micro-thrombi that have dissolved. The last pattern seen in the chronic phase is brain atrophy, with possible residual signal changes due to the injury in the earlier phases (Figure 1D). Conclusion CFE is a serious manifestation of fat embolism syndrome in SCD and should be suspected in patients with severe vaso-occlusive crises and neurological manifestations. Recognizing the brain's MR imaging patterns is crucial for early diagnosis and management.

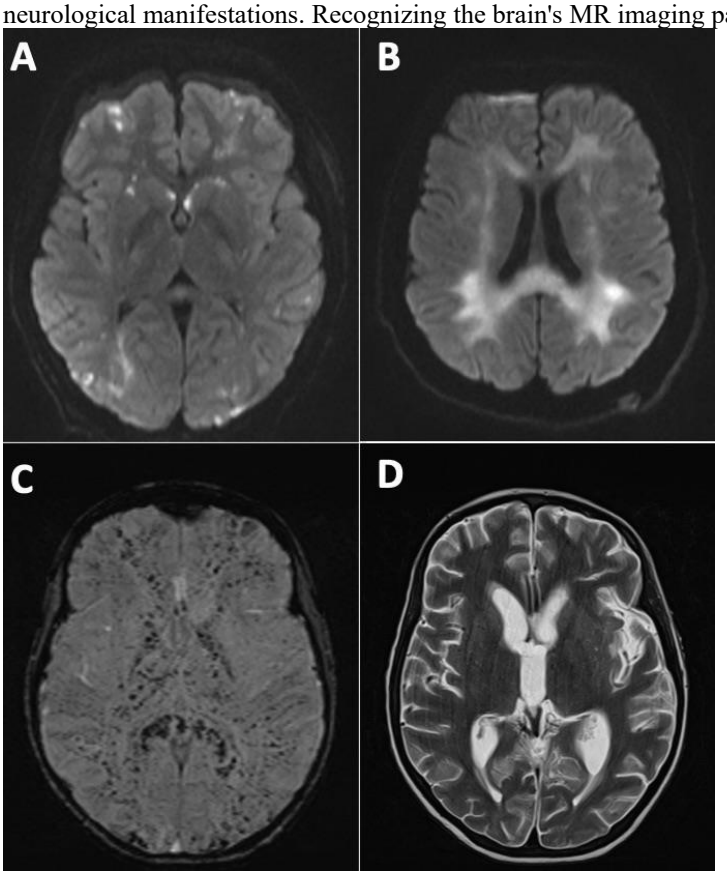

(Filename: TCT_707_Figure1.jpg)

1124

Characterization of the Glioma Immune Microenvironment Using Radiomics

N Khalili[1], A Fathi Kazerooni[2], A Familiar[2], A Nabavizadeh[3]

[1]Children's Hospital of Philadelphia, philadelphia, PA, [2]Children's Hospital of Philadelphia, Philadelphia, PA, [3]University of Pennsylvania, Wynnewood, PA

Summary and Objectives

1. Pathophysiology, prognosis, and current treatments for glioma. 2. Basic principles of radiomics and its role in understanding tumor immune biology. 3. Correlation between radiomic features and immune biomarkers and clinical outcomes in glioma. 4. Current challenges and future directions for the application of radiomics in the immune characterization of glioma.

Purpose

Although complete resection is the mainstay of therapy for gliomas, this is not feasible for all tumors; thus, immunotherapy approaches are being increasingly applied. The tumor immune microenvironment (TIME) is a powerful tool for predicting tumor behavior and determining response to immunotherapy. Radiomics has the potential to unravel the underlying immunobiological processes within the TIME based on global tumor characteristics. Here, we aim to elaborate the latest progress towards radiomic-based immune profiling of gliomas based on a review of current literature.

Materials and Methods

We searched Scopus, Medline (PubMed), Web of Science, Embase (Elsevier), and Google Scholar using the following keywords: "radiomic", "radiomics", "'imaging", "immune profile", "immune", "immunologic", "glioma", "glioblastoma" and "brain tumor".

Results and Conclusions

Several studies have shown that volumetric (i.e., edema-to total tumor volume) and non-volumetric imaging features (i.e., texture features) are associated with immune processes such as regulation of T-cell activation, T-cell proliferation, cytokine production and NFkB signaling pathway in samples with glioma. Also, temporal changes in minimum Apparent Diffusion Coefficient (rADCmin) could predict response to immunotherapeutic strategies such as dendritic cell vaccines. Taken together, radiomics seems to be a promising non-invasive tool for unraveling underlying immunological pathways involved in the development and/or progression of glioma. For future progress of this field, challenges such as standard immune profiling, unifying imaging techniques and increasing data transparency should be addressed.

398

Cinematic Rendering of Lobar-Specific Atrophy Patterns in Different Clinical-Radiologic Dementia Syndromes

M Young[1], T Shepherd[1], D Swahn[2]
[1]NYU School of Medicine, New York, NY, [2]NYU Langone Health, New York, NY

Summary and Objectives
Visualization of brain surface anatomy helps with surgical planning and can illustrate lobar-specific gyral changes in dementia. Multiplanar MRI can help us infer cortical surface anatomy but requires substantial experience with cross-sectional imaging and cortical anatomy. Perceiving surface anatomy is difficult for many non-expert clinical consumers of MR images, including referrers and trainees. We combined recent technical improvements in digital removal of the skull with Cinematic Rendering (CR) to generate 3D models of the brain in patients with cognitive impairment. These images help reveal classic lobar atrophy patterns for common dementia syndromes.
Purpose
We created a workflow for high-quality 3D CR of brains from clinical MRI studies in patients with cognitive impairment. We compare and contrast 3D renderings of the most common neurodegenerative diseases to improve recognition of the most common associated lobar-specific atrophy patterns.
Materials and Methods
3D images were generated using a standard 1-mm isotropic T1-weighted MR sequence. Data were postprocessed with Siemens Syngo.via software with automated skull stripping and global illumination with CR. Rotational ranges and multiplanar clip planes were sent to PACS. These images are available to view without any additional effort by the interpreting radiologist. Classic clinical-radiologic dementia syndromes with concordant clinical history and PET-MRI imaging results will be presented.
Results and Conclusions
Currently radiologists must learn to infer atrophy patterns with 2D images, but this can be challenging. CR makes this problem much easier and may improve teaching and clinical reporting of typical lobar-specific patterns of atrophy in different dementia syndromes. A limitation is that CR obscures deep and basal structures that can also be affected (e.g. insula in fronto-temporal degeneration), but these can be revealed with dedicated clip plane images. CR of brains also has clear utility for teaching cerebral sulcal anatomy to trainees and represents a low-cost, efficient means for presenting multiple individual variations. Atrophy may be easier to detect with CR for other chronic disorders like multiple sclerosis where the neurodegenerative component is sometimes underemphasized in radiology reports. CR of the brain surfaces may also have additional clinical uses, such as surgical planning or detection of pediatric brain malformations.

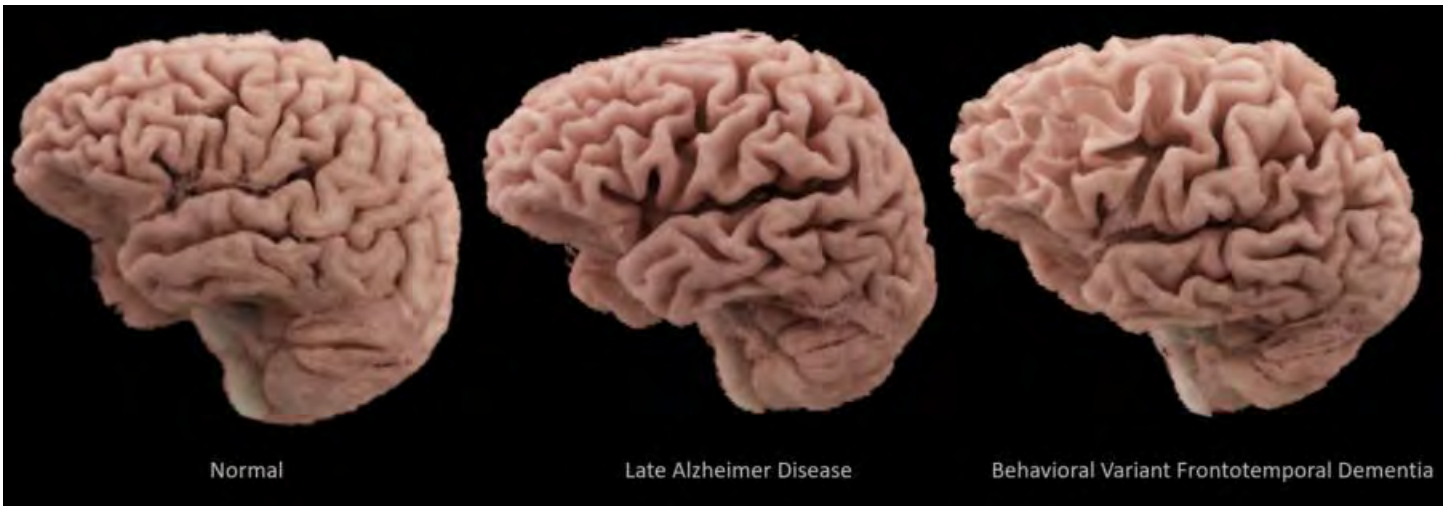

(Filename: TCT_398_figure1-version2300.jpg)

510

Classification and Molecular Subgroups of Meningiomas in the Era of Tumor Genomics and Whole Exome Sequencing

R McLean[1], J Moliterno[2], M Aboian[3]
[1]Yale School of Medicine, Hamden, CT, [2]Yale School of Medicine, New Haven, CT, [3]Yale University, Woodbridge, CT

Summary and Objectives
1. Provide background information on The World Health Organization (WHO) grading scale for meningiomas. 2. Highlight the current molecular landscape of meningiomas, their anatomic location, and the clusters of distinct genetic mutations. 3. Discuss the utility of tumor genomics integration in evaluation of meningiomas in clinical practice.
Purpose
Meningiomas, though largely benign, are the most common tumors of the central nervous system. Historically, these tumors have been categorized using WHO model, determined by histomorphologic features. While the WHO grading scale has been used extensively in clinical practice, it has been shown to have inadequate or inconsistent predictability of clinical parameters that influence outcomes, such as mitotic activity in addition to timing and likelihood of recurrence in the postoperative period. On the other hand, imaging

features of meningiomas do not reliably predict the WHO grade, therefore requiring invasive pathologic sampling for determination of whether the meningioma will display aggressive traits. To address this, advances in tumor genomics have detailed a molecular landscape of meningiomas that allows further subdivision of tumors into clusters with distinct features. This educational exhibit outlines these clusters and how tumor genomics is utilized clinically to predict prognostic factors and provide an avenue for guided therapies.

Materials and Methods

A literature review of research evaluating molecular subgroups of meningiomas was performed. The findings of these studies were then contrasted with current WHO classification, with an emphasis on current clinical utility and limitations. Additionally, key points of genomic data implementation into routine practice was addressed with consideration of the use of individualized therapies.

Results and Conclusions

This educational exhibit summarizes the WHO grading and molecular subgroups for meningiomas. The parameters, clinical relevance, and limitations of were discussed with emphasis on clinical utility and future directions in routine practice. We address current challenges of whole exome sequencing and why the need for further investigation into tumor genomics is warranted. In conclusion, combined evaluation of tumor genomics, location, clinical behavior including long-term recurrence patterns, and imaging characteristics can act as a useful adjunct to WHO classification in guiding meningioma characterization and treatment and may influence future WHO classification criteria.

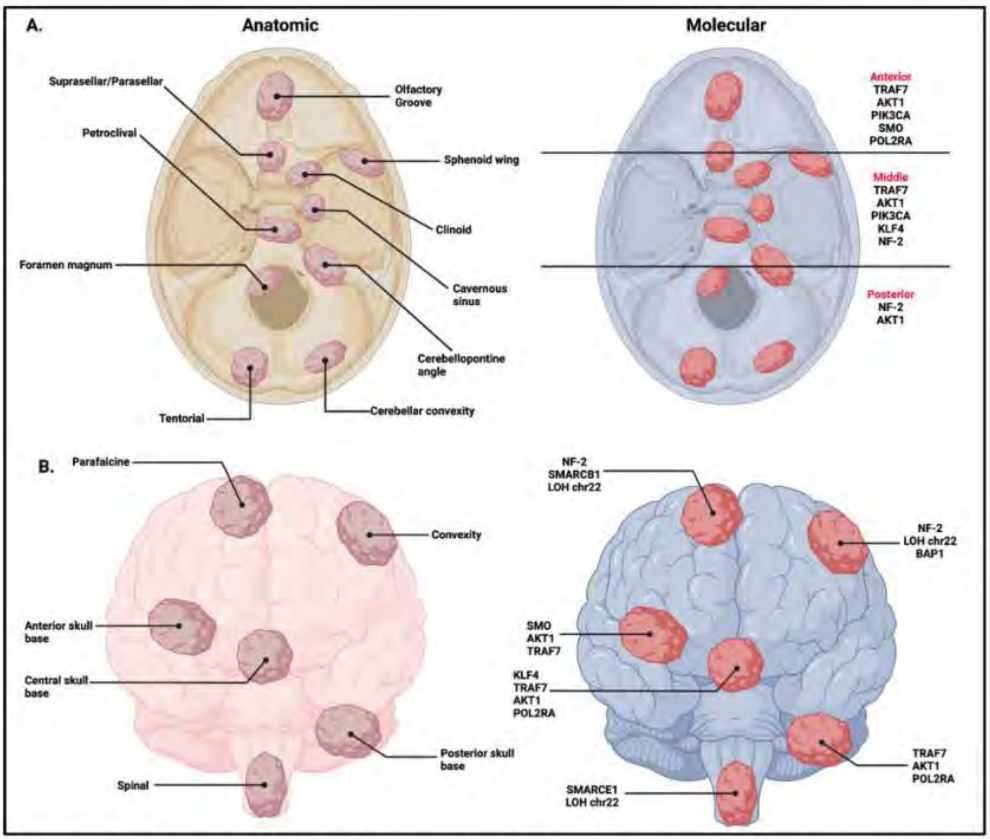

Figure 1: Visual representation of meningioma anatomical locations (left) versus molecular subgroup (right), categorized by intracranial region (anterior, middle, posterior). (A) shows a sagittal view of meningioma tumor locations and reported molecular subgroups for the respective region. "Anterior" includes the anterior fossa, anterior skull base, and parasellar regions; "middle" includes the middle cranial fossa, central skull base, and sphenoid wing; "posterior" includes the posterior fossa. (B) shows a coronal view of meningioma tumor locations and molecular subgroups for each corresponding anatomical location.

(Filename: TCT_510_2023ASNREducationExhibitFigure.jpg)

1453

CNS Manifestations of Multisystem Disorders in Children: A Pictorial Review

P Kennedy[1], S Cohen[1], E Weidman[1]
[1]*Weill Cornell Medicine, New York, NY*

Summary and Objectives

Children with disorders affecting multiple organ systems may present with neurologic symptoms. It is important for radiologists to be aware of these disorders and their CNS imaging manifestations in order to formulate a differential diagnosis and recommend

appropriate follow-up care. We will use a case-based approach to review a range of multisystem disorders and their CNS manifestations and highlight the importance of considering the whole patient when evaluating pediatric neuroimaging.
Materials and Methods
Review CNS manifestations including CNS and limited body and musculoskeletal imaging of multisystem disorders in children at our institution, highlighting examples from each category including: ● Neoplasm (neuroblastoma, LCH) ● Hematologic disorders (sickle cell, thalassemia) ● Immune-mediated (HLH, SARS-CoV-2 MIS-C) ● Metabolic (mucopolysaccharidoses, hypoglycemia) ● Phakomatoses (NF1, Gorlin syndrome, tuberous sclerosis) ● Other heritable disorders (congenital muscular dystrophies, skeletal dysplasias including collagenopathies)
Results and Conclusions
While not meant to be a comprehensive review, we will highlight CNS imaging manifestations of multiple common and several interesting uncommon multisystem disorders in children, emphasizing the importance of reviewing clinical information and all available imaging when formulating a differential diagnosis.

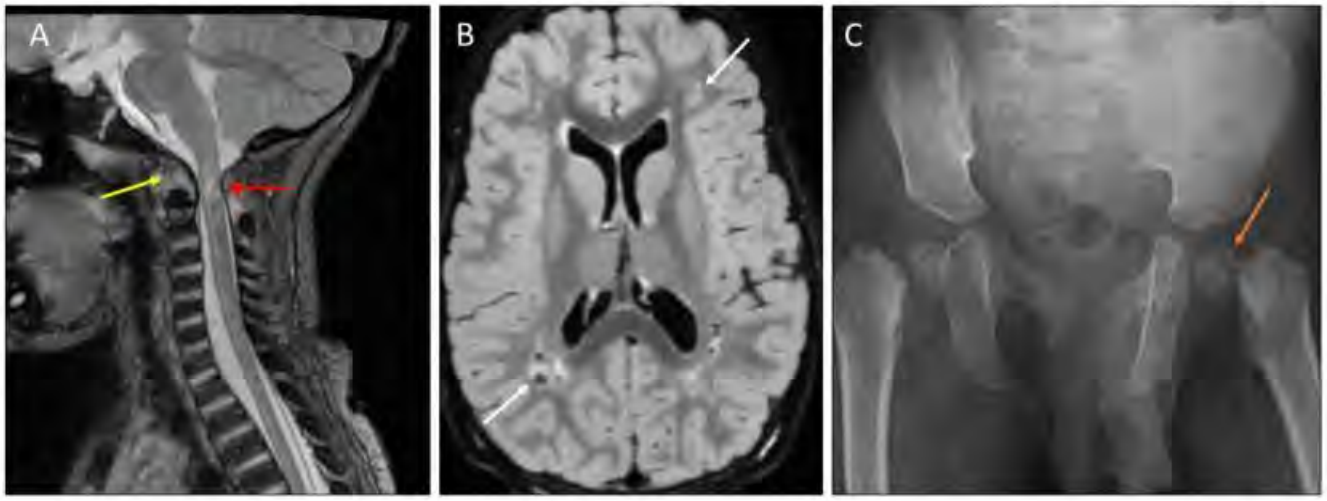

3 year old male found down at home with paraplegia. (A) Sagittal T2 GRE demonstrates irregular morphology of the dens with lobular soft tissue at the tip of the odontoid (yellow arrow) and associated narrowing of the cervical canal. Hemorrhagic cord contusion (red arrow). (B) Brain MRI with dilated perivascular spaces and patchy supratentorial T2 hyperintensity (white arrows). (C) AP radiograph of the pelvis reveals small irregular femoral head epiphyses with stippled appearance (orange arrow) and developmental coxa vara. Constellation of findings raised concern for heritable skeletal dysplasia with associated odontoid dysplasia and atlantoaxial instability; mucopolysaccharidosis was a consideration. Genetic analysis revealed type II collagen - COL2A1-disorder. Family referred to genetic counseling for siblings as this heritable disorder confers increased risk of injury with low impact trauma.

(Filename: TCT_1453_CNSManifestationsofMultisystemDisordersinChildren.jpg)

1302
Common and Uncommon Stroke Syndromes: Clinical information that can aid Radiologist.
R Samant[1], J McCarty[2]
[1]UT Health, McGovern School of Medicine, Texas Medical Center, Houston, TX, [2]UTHealth Houston, Houston, TX

Summary and Objectives
Stroke syndrome is a set of symptoms and signs that help identify the part of brain injured. Stroke physicians utilize the knowledge of these syndromes to confirm small infarcts on imaging. A basic understanding of these syndromes will help Radiologist improve their accuracy in localizing infarcts.
Purpose
The purpose of this exhibit is to review common and uncommon stroke syndromes and provide imaging examples of strokes that correlate with these clinical syndromes.
Materials and Methods
Our single institute electronic medical record was reviewed to identify patients presenting with stroke syndromes. Imaging exams on these patients were reviewed and cases with good clinico-imaging correlation were collected to present this educational exhibit.
Results and Conclusions
The following stroke syndromes and their imaging findings will be presented in this exhibit: Middle cerebral artery: 1. Complete 2. Superior division (Broca's Aphasia) 3. Gerstmann syndrome 4. Ataxia hemiparesis Posterior Cerebral Artery: 1. Balint syndrome 2. Anton Syndrome 3. Weber Syndrome 4. Claude Syndrome 5. Benedikt Syndrome 4. Thalamic pain syndrome (Dejerine-Roussy Syndrome) AICA: 1. Lateral pontine syndrome (Marie-Foix) PICA: 1. Lateral medullary syndrome (Wallenberg) Basilar Artery: 1. Locked-in syndrome 2. Marie-Foix 3. Ventral Pontine (Raymond) 4. Ventral Pontine (Millard-Gubler) 5. Inferior Medial Pontine (Foville syndrome) 6. Ataxia hemiparesis 7. Cortical blindness (Anton syndrome) 8. Medial Medullary (Dejerine Syndrome)

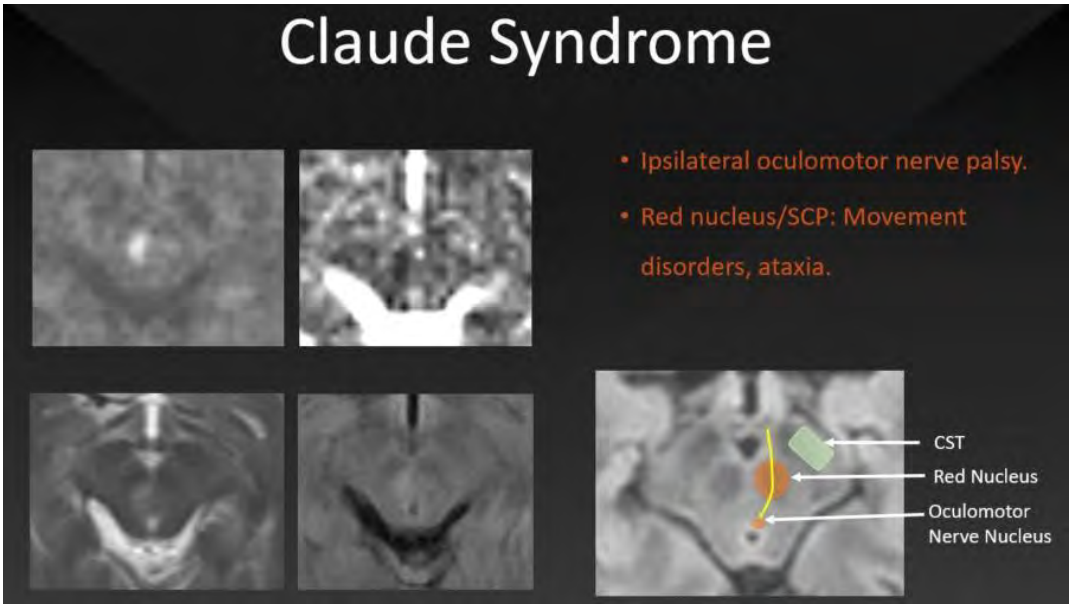

(Filename: TCT_1302_ASNR2023_StrokeSyndromes.JPG)

1447

Common Pitfalls in Seizure Imaging: A Practical Approach

R Joshi[1], J Sharma[2], A Abbas[3], A Krishnan[4]

[1]Beaumont Hospital - Royal Oak, Royal Oak, MI, [2]Oakland University William Beaumont School of Medicine, Detroit, MI, [3]Beaumont Hospital, Royal Oak, Royal Oak, MI, [4]Beaumont Health-Royal Oak, Royal Oak, MI

Summary and Objectives

Summary of Presentation: Seizures can be debilitating for both patients and their families and often are very clinically challenging to address with approximately 1 in 5 patients being classified as drug resistant. Moreover, recurrent seizures in children can profoundly impact their development and affect quality of life for patients, their families and society. Neuroimaging can be critical in anatomic localization – eventually leading to surgical resection or localized treatment that can allow for an improved quality of life for patients with drug-resistant epilepsy. Epilepsy imaging is a particularly challenging area of neuroradiology with a high degree of dependence on radiologist expertise as well as technical factors such as magnet strength, and protocol. As a result, subtle abnormalities may be missed, and lead to a "negative brain MRI", which in turn can delay or prevent appropriate management. Close attention to commonly missed areas, and recognition of the unique imaging patterns is important to improve detection rate, and prevent misclassification of findings. List of Educational Objectives: - Overview of the role of the neuroradiologist in anatomic localization of seizures in drug-resistant epilepsy and the downstream positive implications of accurate detection. - Discussion of commonly missed or mislabeled findings involved with seizures, with practical tips that may improve detection rates and patient outcomes particularly for radiologists who are less experienced in epilepsy imaging. - Case-based review of common misses and mimics including focal cortical dysplasia, temporal pole dysplasia, band heterotopia, temporal lobe encephaloceles, among others. - Outline role of appropriate MRI protocols to improve anatomic localization and brief discussion of the importance of correlation with semiology of seizures, EEG and MEG results to improve detection of abnormalities.

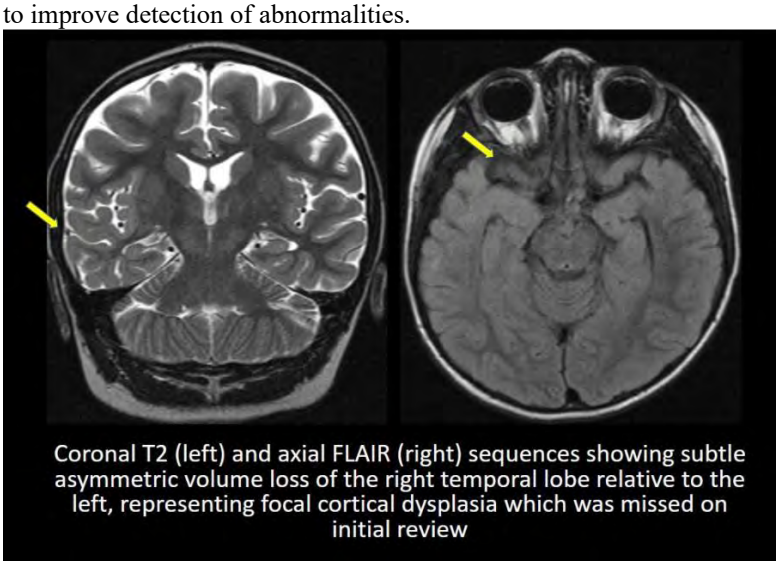

(Filename: TCT_1447_FCD.jpg)

1100

Comprehensive review of the anatomy and pathology of the skull base.

M Sarpi[1], S Mukherji[2], B Nóbrega[3], M Cintra[1], M Garcia[1], M Decnop[1], S Souza[4]

[1]DASA, São Paulo, São Paulo, [2]ProScan Imagng, Carmel, IN, [3]Hospital São Camilo, São Paulo, SP, [4]InRad, Sao Paulo, AK

Summary and Objectives

Abnormalities of the skull base are frequently encountered in clinical practice as either incidental findings or obvious pathology. The anatomy of the skull base is complex and the differential diagnoses can be challenging. The objectives of this educational exhibit will be 1. Review the anatomy of the skull base with schematic illustrations, 2. Demonstrate a variety of congenital, neoplastic, inflammatory and infectious lesions that involve the anterior, central, lateral and posterior skull base, in pediatric and adult patients, 3. Help identify clinically occult "don't touch" lesions of the skull base.

Purpose

To review the imaging features of common and uncommon skull base lesions that may be encountered in clinical practice and its clinical repercussion in correlation to anatomy.

Materials and Methods

The images were obtained of our digital archives. We will review the normal anatomy and the imaging findings of a variety of developmental, neoplastic and inflammatory/infectious lesions involving the anterior, central, lateral and posterior skull base, in pediatric and adult patients. We will discuss important clinically occult anatomic spread patterns that will help determine clinical management.

Results and Conclusions

It is important for neuroradiologists to be familiar with the complex anatomy and wide-range of pathology that can involve the pediatric and adult skull base. This educational exhibit will review the skull base anatomy and illustrate a variety of congenital, neoplastic, inflammatory and infectious lesions that involve the anterior, central, lateral and posterior skull base, in pediatric and adult patients. An understanding of the various pathologies arising in this challenging anatomical site will improve patient outcome and management.

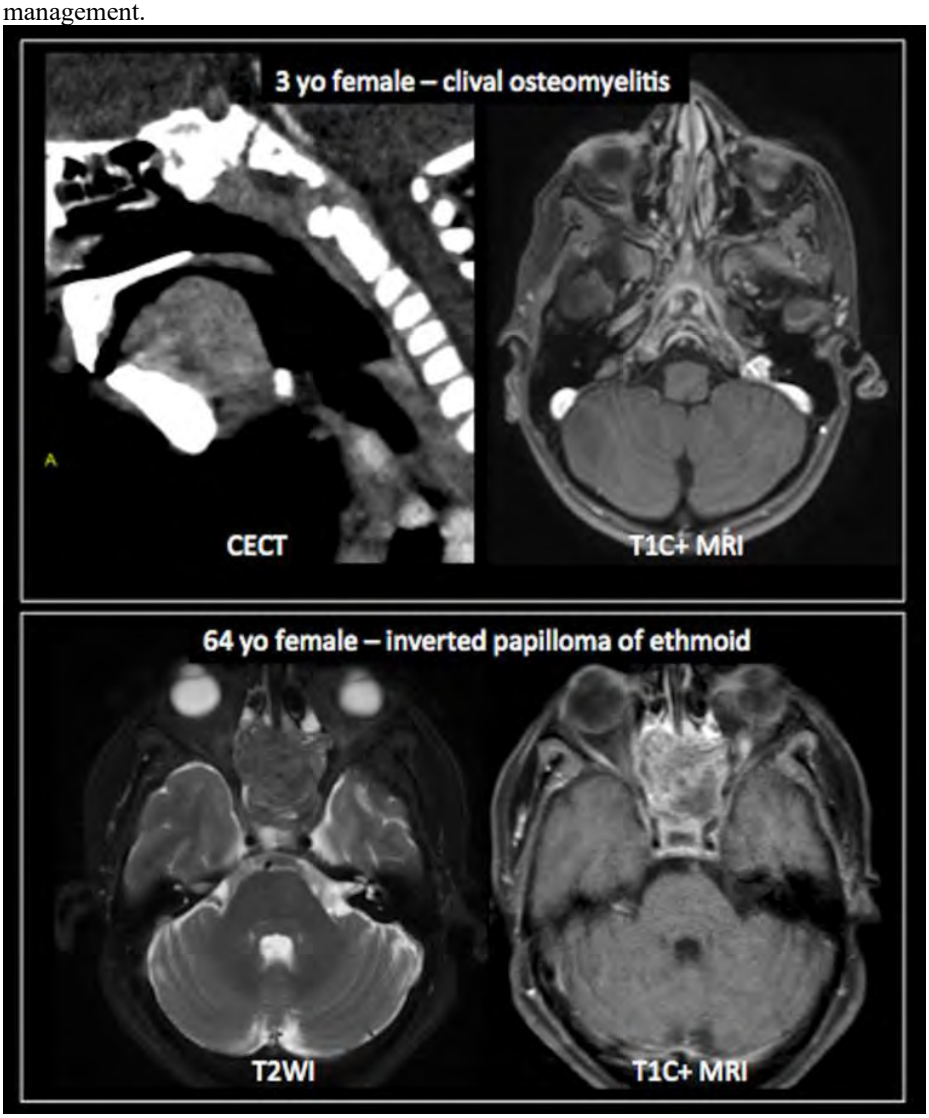

(Filename: TCT_1100_skullbase.jpg)

699

Congenital and Acquired Anomalies of the Globe for the Neuroradiologist

C Paton[1], T Marini[2], Y Zhao[2], A Portanova[2], S ELLIKA[2]

[1]University of Rochester School of Medicine, Rochester, NY, [2]University of Rochester Medical Center, Rochester, NY

Summary and Objectives

Summary: The development of the orbit requires a precise execution of multiple embryologic processes involving gene expression and complex hormonal signaling. Problems occurring at any point in development can lead to congenital anomalies. As the orbit is composed of multiple different tissue types, these anomalies are highly diverse. The eye can be imaged with ultrasound (US), computed tomography (CT), and magnetic resonance imaging (MRI).

Purpose

Purpose and Educational Objectives: This exhibit seeks to review the imaging findings in various congenital and developmental eye abnormalities. The ocular anomalies will be listed by size of the globe, position of the globes, congenital retinopathies, optic nerve and disc anomalies, and ocular manifestations of phakomatosis.

Materials and Methods

Key Points: Eye anomalies can be categorized by morphology, position, tissue of origin, and syndromic association. Topics covered include: -Morphologic variants: Anophthalmia, Microphthalmia, Coloboma, Congenital Cystic Eye, Staphyloma, Macrophthalmia, and Buphthalmos. -Positional variants: Hypo and Hypertelorism, Proptosis, Exorbitism, Enophthalmos, and Exophthalmos. -Retinopathies: Persistent Fetal Vasculature, Exudative Retinitis/Coats Disease, Retrolental Fibrodysplasia, and Toxocariasis. -Optic Disc Abnormalities: Optic fissure closure defects, Morning Glory Disc Anomaly, Peripapillary staphyloma, and Cavitary malformations. -Phakomatoses: Neurofibromatosis Type 1, Tuberous Sclerosis Complex, Sturge-Weber Syndrome, and Von Hippel-Lindau Syndrome.

Results and Conclusions

Conclusions: Ocular anomalies are highly diverse due to the multiple constituent tissue types. By organizing the most frequent of these anomalies into a schema for assessment with imaging examples for each, we will enable neuroradiologists to increase their confidence in assessing ocular lesions.

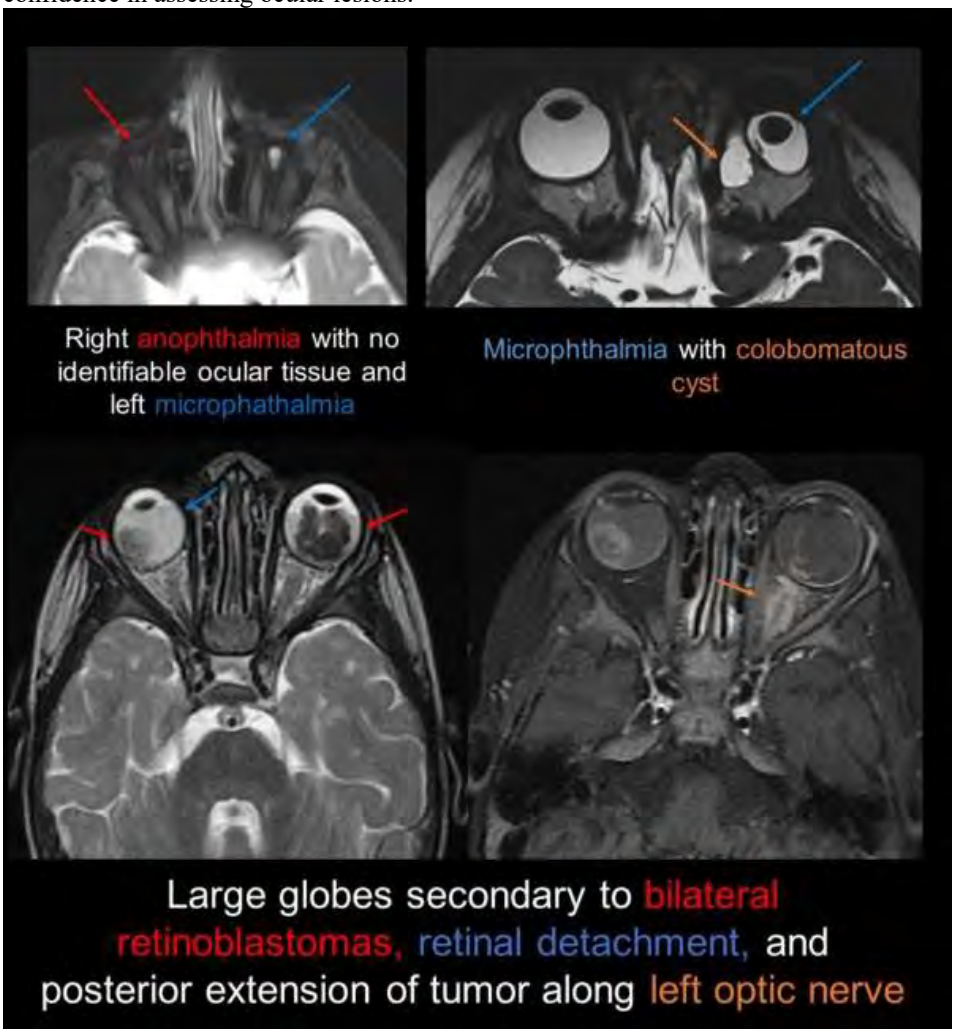

(Filename: TCT_699_ASNROrbitalAnomalies.jpg)

309

Congenital and Acquired Pathologies of the Pediatric Brainstem – An Imaging Travelogue.

S Hiremath[1], C Parra-Farinas[2], P Krishnan[3], S Laughlin[1], M Shroff[4], B Ertl-Wagner[5]

[1]The Hospital for Sick Children, Toronto, Ontario, [2]The Hospital for Sick Children (SickKids), University of Toronto, Toronto, Ontario, [3]The Hospital for Sick Children, University of Toronto, Toronto, ONTARIO, [4]Hospital for Sick Children University of Toronto, Toronto, Ontario, [5]The Hospital for Sick Children, University of Toronto, Toronto, Ontario

Summary and Objectives

• Review the cross-sectional imaging anatomy and typical congenital anomalies of the brainstem • Illustrate typical imaging findings in metabolic and infectious disorders involving the brainstem • Demonstrate imaging findings in demyelinating disorders, as well as low- and high-grade tumors of the brainstem

Purpose

The anatomical assessment of the brainstem forms the basis to understanding congenital and acquired pathologies. Imaging appearances of different brainstem lesions will be described in a case-based format, illustrating the salient features. Structural MR imaging, along with advanced sequences such as diffusion tensor imaging, play an essential role in the assessment of congenital anomalies affecting the brainstem with or without the cerebellar involvement. Metabolic disorders may be classified based on the associated involvement of the long tracts including the medial lemniscus, corticospinal and central tegmental tracts, deep cerebral nuclei and cortex, as well the spinal cord. This educational exhibit will also highlight brainstem infections, classifying them by etiology and by the usually affected brainstem regions. Demyelinating disorders will be illustrated, including Myelin Oligodendrocyte Glycoprotein (MOG) antibody-associated disease, Neuro-Myelitis Optica Spectrum Disorder, and Multiple Sclerosis. Typical imaging appearances of low- and high-grade tumors arising from the brainstem will also be discussed with a special focus on molecular subtypes of brainstem tumors that affect prognosis and outcome.

Materials and Methods

Sagittal post contrast T1 (A) shows an expansile brainstem mass in a 2 day old with congenital pontine glioma. Sagittal T2 (B) shows dorsal tegmental bulge with brainstem and superior vermian volume loss, in a known pontine tegmental cap dysplasia. Axial T2 (C) shows an expansile heterogenous pontine lesion, in a child with RANBP2 positive ANEC. Axial T2 (D) shows an expansile left posterior midbrain lesion, in a child with orogenital ulcers, suggesting Behcet's disease.

Results and Conclusions

The pediatric brainstem may be affected by a variety of congenital and acquired disorders and diagnostic decision-making may be challenging. It is important to be aware of the typical location and imaging appearance of the various disorders affecting the brainstem to arrive at a concise differential diagnosis.

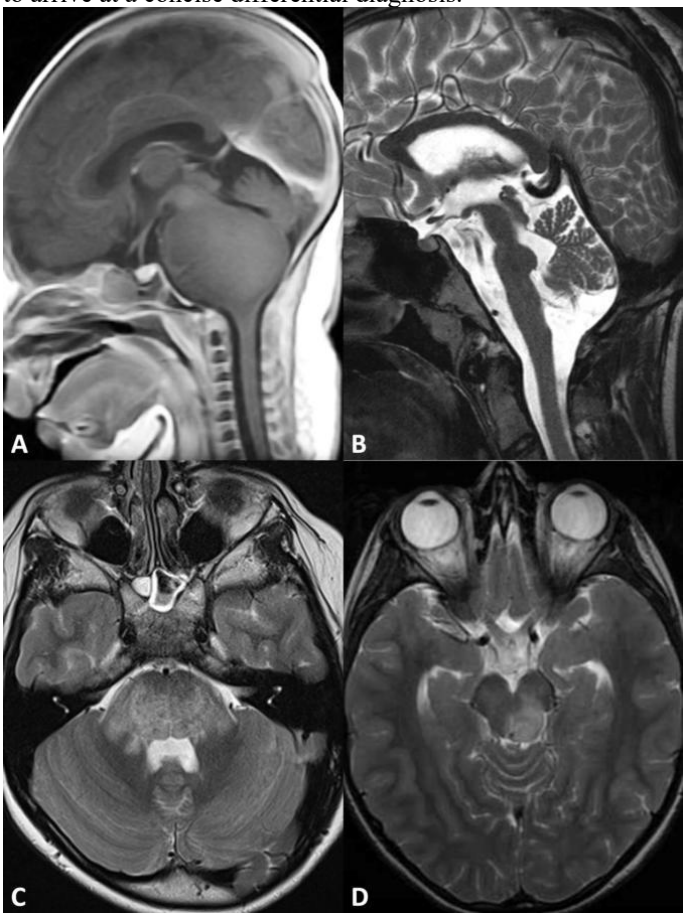

(Filename: TCT_309_Brainstem.jpg)

1075

Congenital spine pathology: A Pictorial review.

K Parashar[1], V Jewells[2], C Guimaraes[1]

[1]University of North Carolina, Chapel Hill, NC, [2]UNC Chapel Hill, Chapel Hill, NC

Summary and Objectives

Spinal Development begins early in embryonic life. The majority of congenital spinal malformations can be traced to errors in either primary or secondary neurulation. The cases that we have collected include: 1. Anomalies of Formation and Segmentation: Persistent sagittal clefts between vertebrae ("butterfly vertebrae") hemivertebrae, and mutli-level incomplete segmentation blocks. Klippel-Feil anomaly is an example of this type of anomaly. 2. Neural Tube Defects: Open and closed dysraphism. Diastematomyelia. Currarino triad. Intraspinal developmental masses/lesions. 3. Congenital Cranio-cervical Junction Anomalies: Basilar Impression can be related to multiple etiologies including OI, achondroplasia and can also be secondary to rickets, mucopolysaccharidosis, or rarely skull base infection. Chari Malformations; 1, 1.5 and 2 will be discusses along with their associated brain abnormalities. Atlanto-occipital assimilation can result in spinal cord/ medullary compression. CSF flow studies are sometimes utilized with this anomalies.

Purpose

Congenital spine pathology comprises a wide variety of developmental defects involving the vertebral elements, soft tissues, cord or the canal/dura. Given the associated morbidity and mortality, early and timely assessment and diagnosis is critical. Thus, it is extremely important for practicing radiologists and trainees to be familiar with imaging manifestations to assist the clinician.

Materials and Methods

After review of teaching files collected over two decades, CT, MRI and US cases were collected for this educational exhibit to present imaging features of a wide variety of uncommon and rare congenital spinal pathologies including anomalies of formation and segmentation, neural tube defects, and congenital cranio-cervical junctional anomalies and variants. We will review the normal embryogenesis of the spine and discuss terminal ventricle.

Results and Conclusions

Congenital spine malformations represent a broad spectrum of lesions that need timely and accurate identification leading to appropriate surgical care.

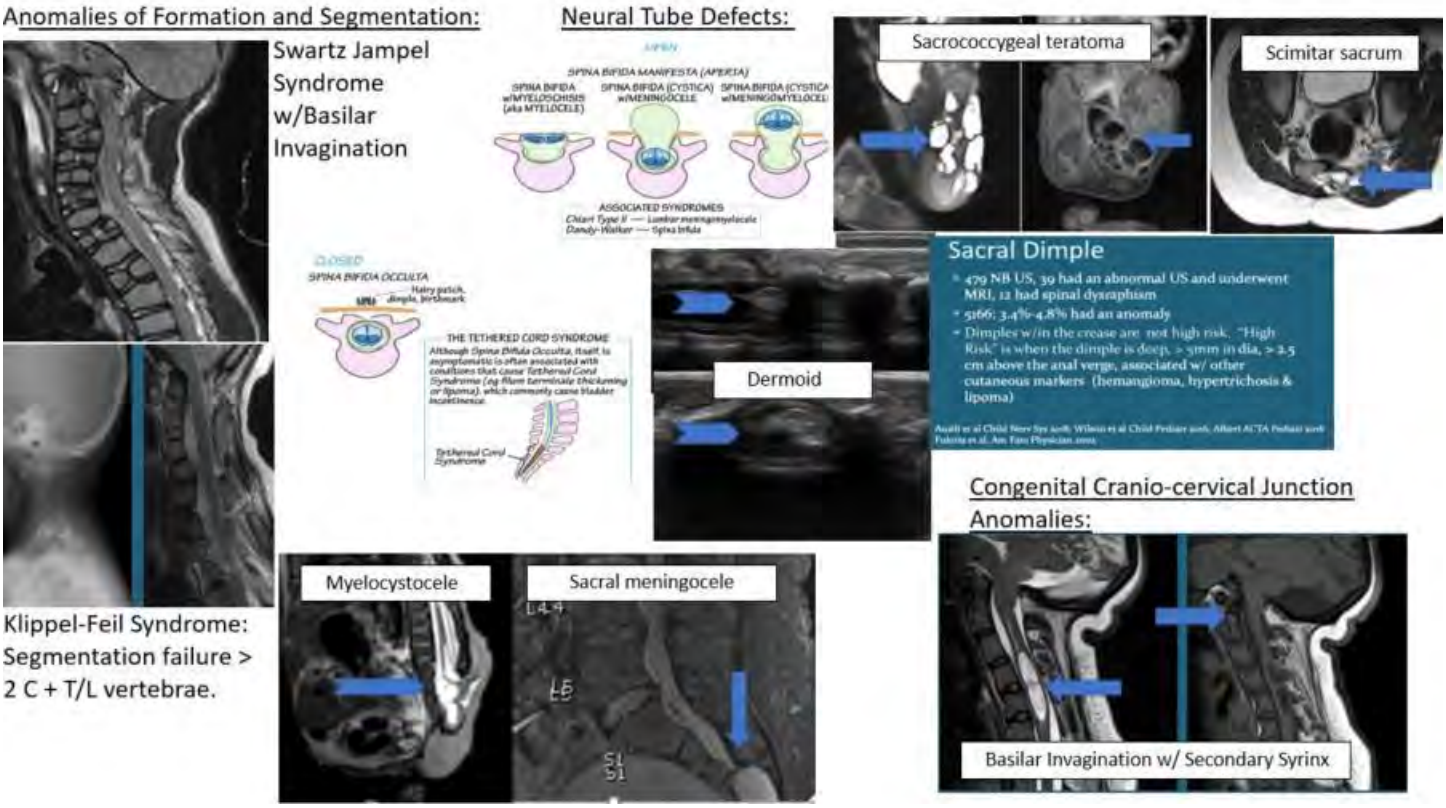

(Filename: TCT_1075_Slide1.jpg)

511

Correlation of Visual Field Defects and Lesions in Different Portions of the Visual Pathway.

M Marsiglia[1]

[1]Massachusets General Hospital, Boston, MA

Summary and Objectives

The visual pathway represents a complex anatomical structure that transmits the visual information received by the photoreceptors in the retina to the visual cortex in the occipital lobes. Lesions in different locations will result in different visual field defects, depending

on the anatomical structures that are damaged. The objectives of this presentation are to review the anatomy of the visual pathway, to correlate the location of lesions along the visual pathway with resulting visual field defects and to illustrate ophthalmological and neurological lesions with imaging examples
Purpose
To familiarize the audience with lesions in the visual pathway and the corresponding visual field defects
Materials and Methods
Literature review and collection of cases seen in the author's practice, including ophthalmological and neurological lesions that resulted in different types of visual field defects. Chart review including examples of perimetry to practically illustrate visual field defects
Results and Conclusions
Intraocularly, lesions involving the retinal pigment epithelium, different layers of the retina and portions of the optic nerve head can result in a variety of visual field defects. Some examples include retinitis pigmentosa, with predominantly peripheral visual field defect; advanced dry age-related macular degeneration resulting in a central scotoma; Nasal hypoplasia of the optic disc with partial optic nerve head defect, resulting in temporal visual field defect. Regarding retrobulbar lesions, involvement of all fibers of one optic nerve cause blindness of the ipsilateral eye. Lesions at the level of the optic chiasm will cause bitemporal defects. Lesions compressing the lateral edge of the optic chiasm cause a nasal hemianopsia of the ipsilateral eye. Lesions of the optic tract extending to the lateral geniculate and primary lesions of the lateral geniculate nucleus cause a contralateral homonymous hemianopsia. Lesions of the geniculocalcarine tract or visual cortex cause a contralateral homonymous hemianopsia. In conclusion, being familiar with the anatomy of the visual pathways and understanding the visual field defect associated with lesions in different locations can aid in improving search patterns when interpreting studies for patients with specific visual field defects as well as when interpreting advance imaging techniques such as functional MRI in lesions along the optic pathway

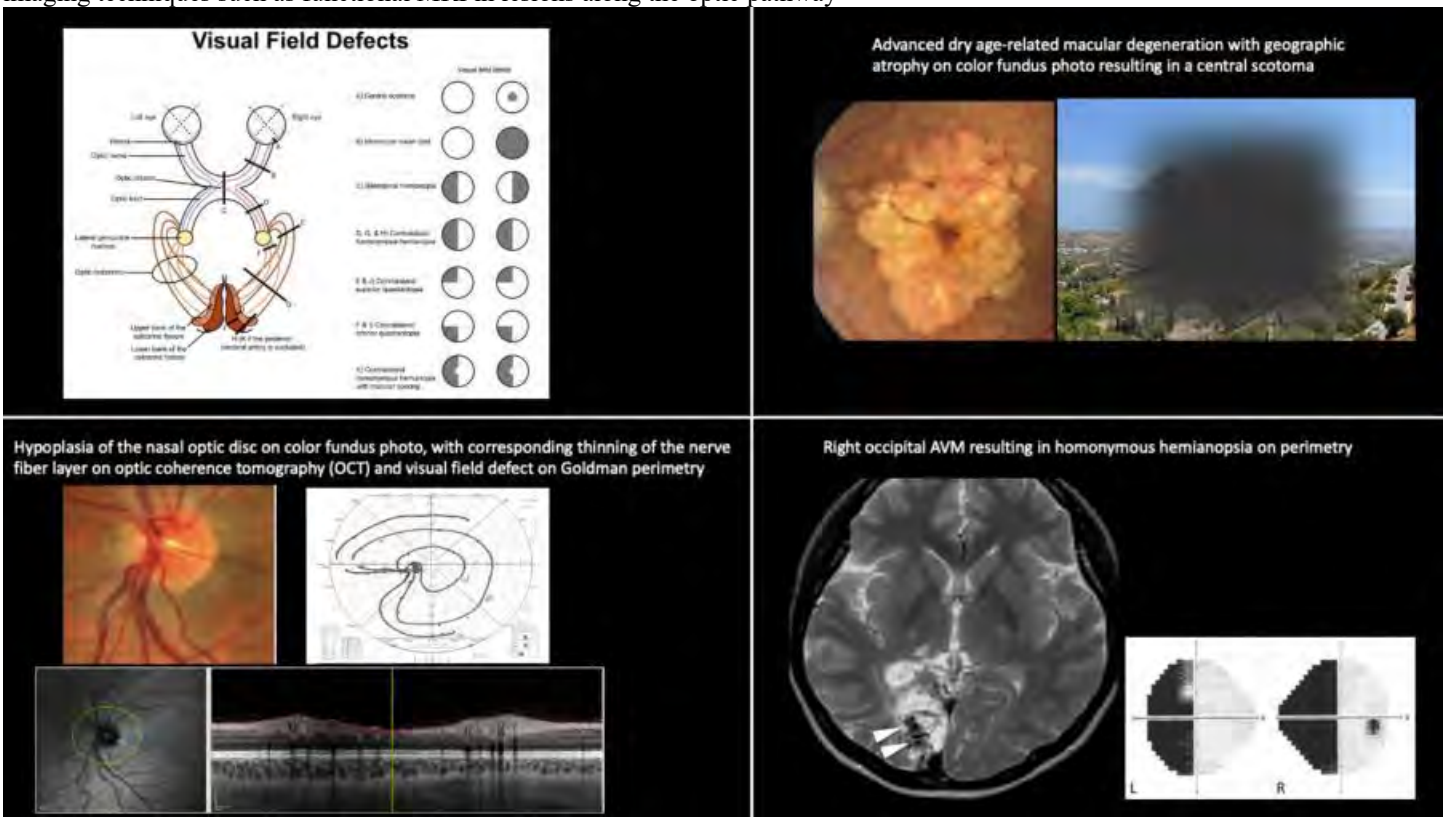

(Filename: TCT_511_Visualfielddefects.jpg)

572
Cranial and Spinal Cerebrospinal Fluid Leaks: A Pictorial Review of Common and Atypical Presentations
C Zuchowski[1], X Li[2]
[1]Emory University School of Medicine, Atlanta, GA, [2]Emory University Hospital, Atlanta, GA

Summary and Objectives
-Review common and atypical clinical presentations of cranial and spinal CSF leaks. -Recommended imaging techniques for appropriate work-up of a suspected CSF leak. -Pictorial review of common findings seen in cranial and spinal CSF leaks. -Brief discussion of treatment options.
Purpose
Cerebrospinal (CSF) leak is an uncommon condition that can have a wide range of presentations and underlying etiologies. As a result, the diagnosis of CSF leak can be challenging. Clinical presentations in the cranial settings often include CSF rhinorrhea or otorrhea and sometimes meningitis. Presentations in the spinal settings include symptoms of intracranial hypotension, such as postural

headaches, nausea, vomiting, and tinnitus. Accurate diagnosis of CSF rhinorrhea and otorrhea and precise localization of the CSF leak helps in surgical planning and enhances chances of successful dural repair. Similarly, spinal CSF leak localization is important, as localized treatment can result in long-term resolution. This educational exhibit describes a pictorial review of common and atypical clinical presentations of cranial and spinal CSF leaks with associated imaging findings on different modalities. Additionally, a brief discussion of treatment options will be provided.

Materials and Methods

A HIPAA compliant retrospective review of cranial and spinal CSF leak cases at our institution will be conducted to gather illustrative cases.

Results and Conclusions

Magnetic resonance imaging (MRI) plays an important role in the diagnosis of both spinal and cranial CSF leaks. As spinal CSF leaks often result in intracranial hypotension, typical findings can be seen, including diffuse pachymeningeal enhancement, sagging of the brain, pituitary enlargement, and subdural fluid collections. For cranial CSF leaks, close attention should be turned to the skull base to evaluate for any possible source of intracranial CSF leak. These findings include skull base osseous defects with associated CSF signal intensity and contrast pooling in the anterior nasal cavity or middle ear cavity. Findings of intracranial hypotension should raise suspicion for a spinal CSF leak, which is commonly seen in the thoracic region. Techniques for detecting spinal CSF leaks include radioisotype cisternography, CT myelography, or spinal MRI, evaluating for extradural collection and/or extravasated contrast. These techniques can be used independently or in conjunction with one another, as a targeted CT myelography can be performed in a specific region detected on spinal MRI.

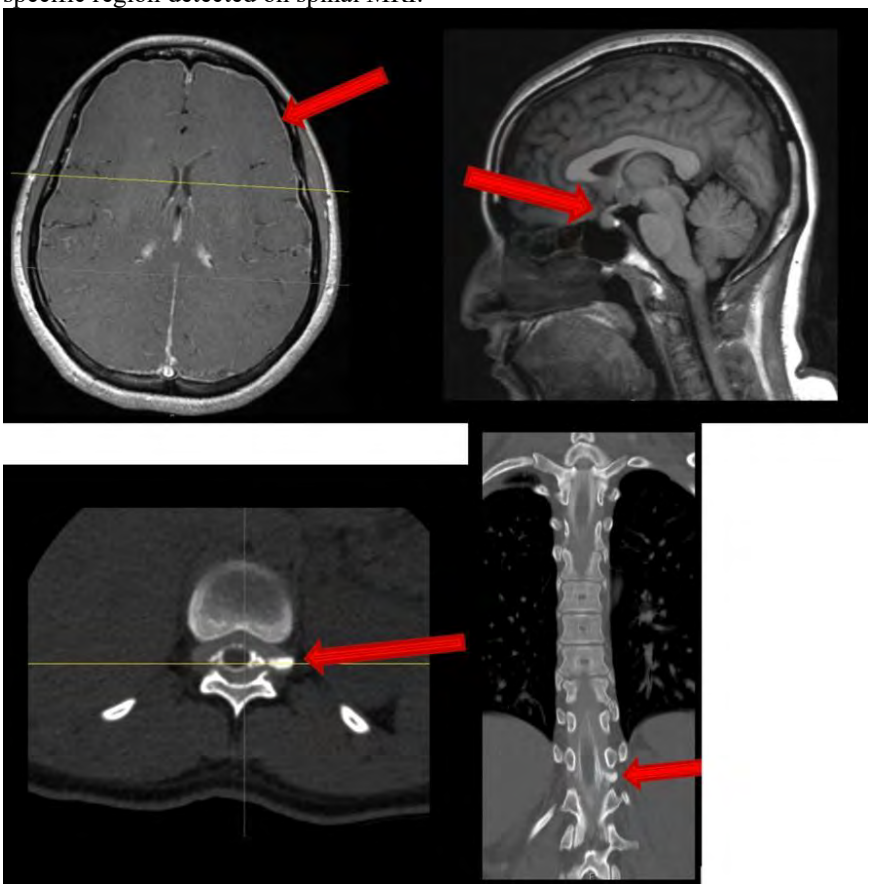

(Filename: TCT_572_ASNR.jpg)

329

Cranial Cerebrospinal Fluid Leaks

M Spano[1], G Salama[1], J Park[1]
[1]*Weill Cornell, New York, NY*

Purpose

To review cranial cerebrospinal fluid (CSF) leaks.

Results and Conclusions

Cranial CSF leaks occur from traumatic, post-surgical, or spontaneous etiologies. Signs and symptoms of leaks vary and include rhinorrhea, otorrhea, hearing loss, aural fullness, pulsatile tinnitus, vertigo, cranial nerve dysfunction or meningismus. The typical orthostatic headache of spinal CSF leaks is often not present. In adults, craniofacial trauma causes ~85% of CSF leaks. Leaks often occur soon after trauma, with 50% occurring within 2 days. Leaks in the post-surgical setting are most commonly from functional endoscopic sinus surgery (FESS) or skull base surgery. Spontaneous cranial CSF leaks are often secondary to idiopathic intracranial hypertension (IIH), neoplasms, and congenital skull defects. The goal of imaging a suspected leak is to determine the defect location,

etiology and assist pre-operative planning. High resolution CT provides a detailed view of the skull base, paranasal sinuses, or temporal bone anatomy. An osseous defect with adjacent air-fluid level or opacification of the adjacent sinus is suspicious for CSF leak. MRI with skull base or internal auditory canal protocol with high resolution 3D-gradient echo sequence with IV gadolinium allows for imaging of a CSF tract extending from the subarachnoid space to the sinonasal or temporal compartments. It also allows for the evaluation of associated meningoceles. CT and MRI cisternograms, defined by the injection of intrathecal contrast via lumbar puncture, can be used if prior imaging is insufficient. In a CT cisternogram, after contrast injection, maneuvers are performed to exacerbate a leak. A positive test shows contrast opacification within the associated compartment. MR cisternogram with high resolution T1 fat suppressed imaging is performed 30-60 minutes after intrathecal gadolinium administration, which is not FDA approved. Radionuclide cisternography with Tc-99m DTPA or indium 111 DTPA can be performed for leaks occult on other imaging. Accumulation of radiotracer within nasal pledgets confirms the presence of CSF leak, but does not allow for localization. Traumatic CSF leaks can be treated either conservatively or operatively depending on the mechanism of injury, location, and degree of leakage. Postsurgical leaks can be treated with compression wrapping, lumbar drain, or surgical repair if needed. Spontaneous CSF leaks are generally repaired surgically, either with endonasal endoscopic techniques or mastoidectomy.

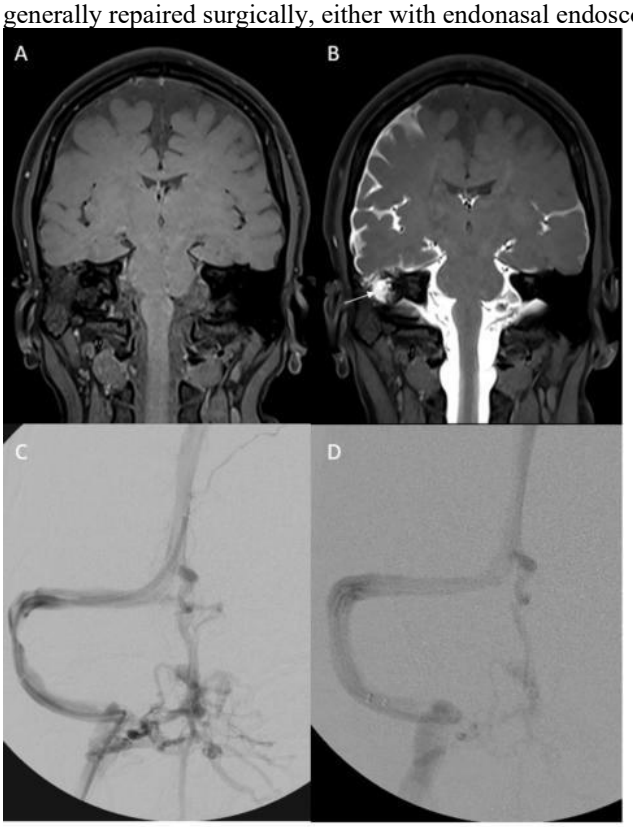

33 year old female with history of multiple sclerosis presented with intermittent clear rhinorrhea, right aural fullness and right hearing loss. (A) Coronal T1 without contrast shows right middle ear effusion. (B) Coronal T1 after intrathecal administration of contrast with extrathecal contrast extravasation in the right middle ear cavity. Cisternogram also notable for intracranial hypertension with opening pressure of 34 cm H20. (C) Superior sagittal sinus venogram with moderate to severe stenosis involving the right transverse/sigmoid junction. (D) Interval placement of 2 overlapping stents measuring 7 x 40 mm and 8 x 40 mm extending from the proximal transverse sinus through the distal sigmoid sinus with significant improvement of stenosis.

(Filename: TCT_329_CSFleaksfigureV11.jpg)

453

Craniosynostosis: A Pictorial Review

M Greenhill[1], A Frazzitta[1], S Rogers[1], T Chandra[2], U Udayasankar[1]

[1]University of Arizona, Tucson, AZ, [2]Nemours Children's Health, Orlando, FL

Summary and Objectives

The craniosynostoses are a mixed group of disorders affecting the pediatric skull resulting from the early fusion of one or more cranial sutures. This exhibit overviews these diseases and the imaging workup including screening radiograph, 3-D CT, 3D printing for preoperative surgical planning, and MRI including the promising technique of black bone MRI for radiation reduction. Educational

Goals/Teaching Points: Review relevant anatomy, underlying pathogenesis, and treatment of craniosynostosis. Overview of the classification of craniosynostoses. Review the imaging appearance of craniosynostosis and associated abnormalities. Review Black Bone MRI and 3D printing.

Purpose

To familiarize the radiologist with nonsyndromic craniosynostosis, syndromic craniosynostosis/associated abnormalities, secondary craniosynostosis, and mimics of craniosynostosis including deformational plagiocephaly via pictorial review.

Results and Conclusions

The craniosynostoses are a diverse group of pediatric skull abnormalities that leads to protean clinical presentations. It is important that the radiologist is aware of this condition to provide a succinct and accurate diagnosis for the patient and their family.

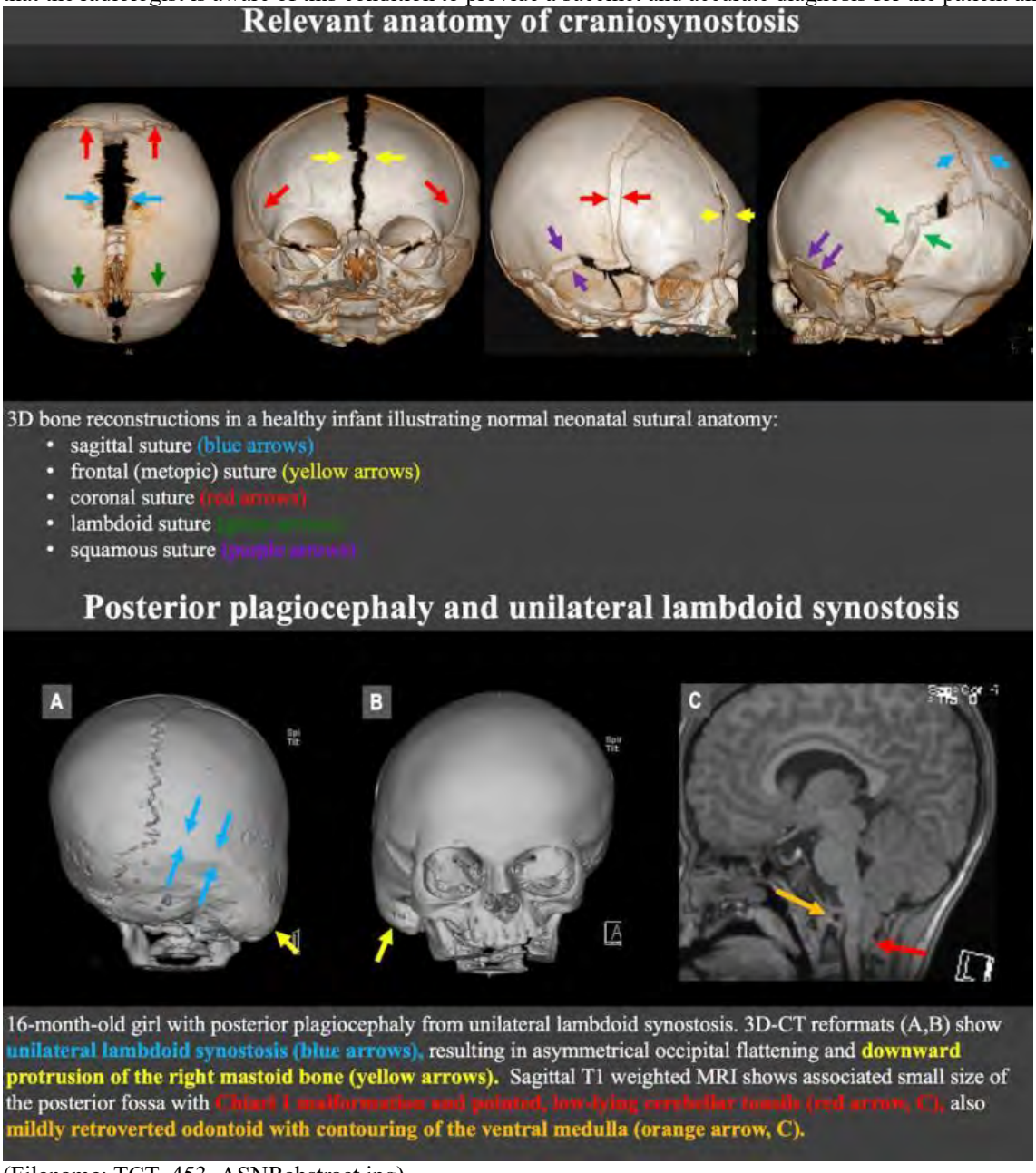

(Filename: TCT_453_ASNRabstract.jpg)

878

Creating a "Deliberate Practice" Approach to Radiology Education for Stroke and Intracranial Hemorrhage Image Interpretation

L Penn[1], B Johnson[1], T Kennedy[2]

[1]University of Wisconsin School of Medicine and Public Health, Madison, WI, [2]The University of Wisconsin, Middleton, WI

Summary and Objectives

An essential component of acute stroke management and evaluation of patients suspected of intracranial hemorrhage is the accurate diagnosis of a head CT examination by the on-call radiologist. Many residents start taking independent overnight call in their second year of training and most residents will have completed 2 rotations in Neuroradiology before independent call. One of the biggest

challenges in radiology education, however, is that residents learn as they work with inherent heterogeneity in the types of clinical cases to which they are exposed in daily routine practice. Residents may not see all types of acute pathology while working during the day and, as a result, may be ill prepared to recognize life-threatening conditions when taking independent call. A growing field of research has been the accuracy of acute radiology diagnoses and the effects of incorporating new methods of instruction for more precise image analysis during the training of radiology residents. In his broader studies of expertise, Anders Ericsson suggests that including "deliberate practice" in radiology residency, implemented by providing learners with a large volume of annotated digital cases that encompass the variability of pathology presentations, will create more effective memory systems for recognizing patterns and better train expert radiologists who consistently provide accurate diagnoses.[1] However, no such comprehensive database currently exists for stroke code or intracranial hemorrhage head CT scans, despite the vast prevalence of strokes and intracranial hemorrhage in the United States. Assessing a head CT for stroke and recognizing ICH on a head CT draw on different, but complementary skills. The purpose of this exhibit is to review concepts in adult learning practice. We will develop a framework for implementing adult learning theory into radiology instruction and a how-to-guide to create a validated training set of cases to help facilitation the instruction of stroke and hemorrhage detection on CT imaging for radiology residents.
Purpose
The purpose of this exhibit is to review concepts in adult learning practice. We will develop a framework for implementing adult learning theory into radiology instruction. We will then develop a how-to-guide to create a validated training set of cases to help facilitation the instruction of stroke and hemorrhage detection on CT imaging for radiology residents.

1077
CSF circulation and glymphatic system of the spinal cord: pathophysiology and related diseases
T Moritani[1], S Naganawa[1]
[1]*University of Michigan, Ann Arbor, MI*

Summary and Objectives
Summary: CSF circulation and glymphatic–lymphatic fluid transport system play a critical role in fluid homeostasis in the spine associated with the CSF flow. We demonstrate many variable diseases related to CSF circulation and glymphatic system. The glymphatic system, a network of perivascular spaces promoting fluid exchange between CSF and interstitial space, can be utilized for drug delivery from the CSF to the brain and spinal cord. Intrathecal drug administration is an effective strategy to bypass the BBB via direct delivery to the CNS, especially in antibody or oligonucleotide-based therapeutics. Table of Contents CSF circulation in the spine Glymphatic–lymphatic fluid transport system of the spinal cord Spinal cord diseases related to CSF production, absorption, and loss (leakage) -CSF leakage and CSF venous fistulas -Hypersecretion of CSF after subarachnoid hemorrhage Spinal cord diseases related to CSF flow abnormality -Chiari malformation -Spinal canal stenosis -Amyotrophic lateral sclerosis (ALS) -Spinal web, spinal cord herniation Spinal cord diseases related to glymphatic system -Iatrogenic intrathecal Gd administration -Spinal neurosarcoidosis -Neuromyelitis optica -Presyrinx state Drug delivery and glymphatic system -Spinal muscular atrophy (Nusinersen) -ALS (Tofersen) and other neurodegenerative diseases -Intrathecal chemotherapy/rituximab Educational Objectives: 1. Gain a deeper understanding of the glymphatic–lymphatic fluid transport system with recently updated concepts 2. Review CSF circulation in the spinal cord 3. Explore spinal cord diseases related to CSF circulation and glymphatic system in the spinal cord 4. Drug delivery related to CSF circulation and glymphatic system in the spinal cord

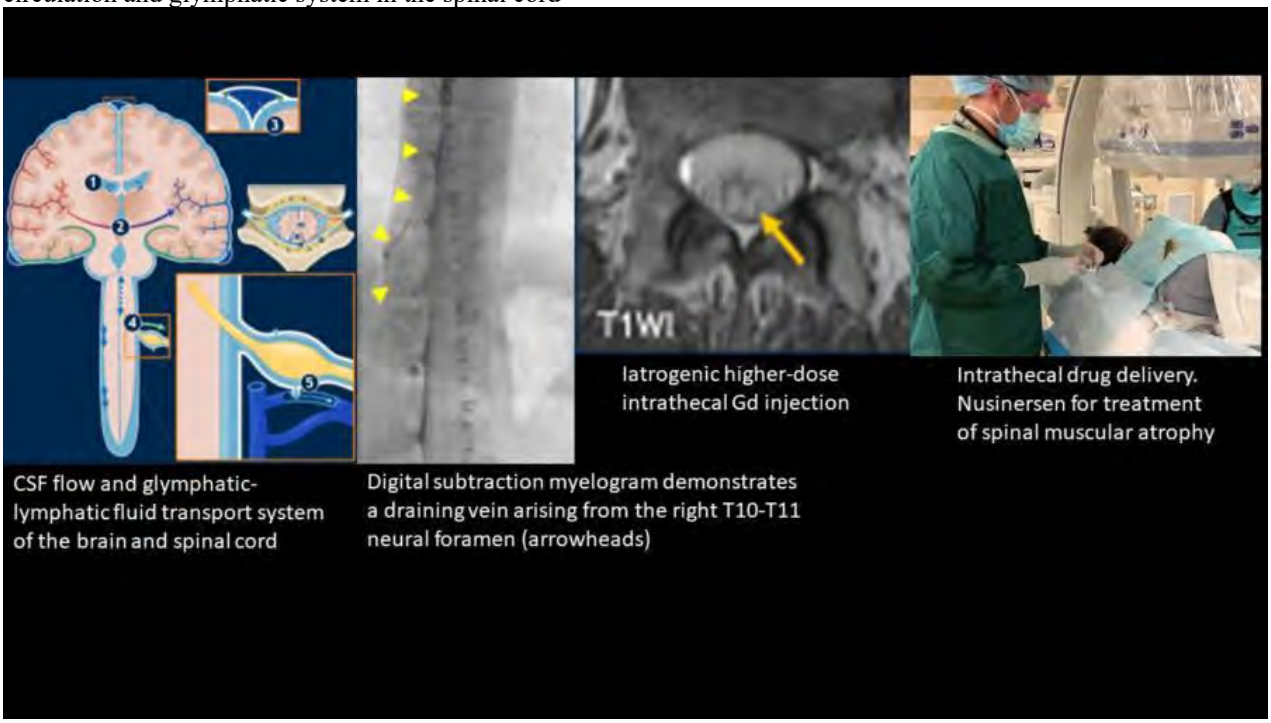

(Filename: TCT_1077_ASNR20234imagesPresentation1.jpg)

972

CTA and MRA Appearance of Cerebral Aneurysm Recurrence after Surgical or Endovascular treatment: Patterns and Blindspots

J Le[1], S Mirbagheri[1], D Johnson[1], S Raymond[1]
[1]The University of Vermont Medical Center, Burlington, VT

Summary and Objectives
Summary Cerebral aneurysms are treated with a variety of modern microsurgical and endovascular techniques depending on aneurysm location, morphology, and local expertise. Despite technically satisfactory results, aneurysms reoccur at 0.5-20% depending on the method of treatment (Crobeddu et al., 2013). Most recurrences happen in the first 6 months after treatment, but there is a tail of recurrence over the lifetime of the patient. Digital subtraction angiography remains the gold standard for evaluation of aneurysms 6-12 months after treatment, but noninvasive imaging including MRA is increasingly becoming the modality of choice for long term imaging follow up (Soize et al., 2016). Several mechanisms explain aneurysm recurrence including incomplete treatment, new inflammation at the diseased vessel, and interactions between the device and the aneurysm sac. Recurrence follows specific patterns depending on the treatment technique. For example, recurrence after clipping may occur at the tip of the clip or at the aneurysm neck due to clip slippage. Coils may compact, with growth at the neck, or unfurl into adjacent clot in large and giant aneurysms, with growth at the periphery. Intrasaccular flow diverters undergo shape modification (compression) and resultant uncovering at the neck of the aneurysm. In this exhibit, we describe patterns of recurrence specific for commonly employed techniques including microsurgical clipping, coiling, endoluminal flow diversion, and intrasaccular flow diversion/disruption. We provide examples of these recurrences on both CTA and MRA and review the relative merits of each modality for follow up. Educational Objectives - Review common microsurgical and endovascular embolization devices and appearance on CTA and MRA. - Recognize patterns of aneurysm recurrence for each device on CTA and MRA. - Discuss factors that impact aneurysm recurrence including patient demographics, aneurysm size and morphology, and device-dependent parameters. - Discuss device artifacts for each modality and the impact on detecting recurrence. - Discuss the most appropriate follow up modalities for each device.

1208

CTA Head and Neck: Imaging Pearls to Decrease Misses and Misinterpretations

R Samant[1], M BHALLA[2], R Patel[3]
[1]UT Health, McGovern School of Medicine, Texas Medical Center, Houston, TX, [2]UT Houston, Houston, TX, [3]Texas Children's Hospital, Houston, TX

Summary and Objectives
A recent study in AJR by Andrew ElHabr et al. reported that growth of head and neck CTA far outpaces the growth of other modalities among neuroimaging utilization [1]. The utilization rates per 1000 ED visits increased by 1100% for CTA-head and 1300% for CTA-Neck between 2007 to 2017. A study from 2011 in AJNR by K Lian et al. has reported that significant discrepancies that would have influenced follow-up or management occur with a low but not insignificant rate on CTA's of the head and neck[2]. This makes it important to have targeted learning strategies to avoid these misses. Learning from our common misses and knowing our blind spots will be helpful in interpreting these studies with higher confidence and accuracy.
Purpose
1. Present misses and misinterpretations on CTA Head and Neck that were identified and discussed in peer learning meetings. 2. Discuss imaging pearls which would help interpret these studies rapidly with higher confidence and decrease misses and misinterpretations.
Materials and Methods
Our peer learning database was investigated and CTA misses, misinterpretations and great call cases discussed over 4 years were identified. Below are some of the cases that will be presented. 1. Missed Intracranial aneurysms: Common blind spots and tips to improve detection. 2. Distal Medium Vessel Occlusions (DMVO's): Significance and tips to avoid misses. 3. Tapering Stenosis: How to differentiate between true dissection, ICA terminus occlusion and thrombotic blub occlusion. 4. Dissecting intracranial pseudoaneurysm: Significance and tips to diagnose with confidence. 5. Carotid Web: Commonly missed and diagnosed as cryptogenic stroke in young. 6. Traumatic pseudoaneurysm in the neck. 7. Focal intraluminal clot along the wall. 8. Fibromuscular dysplasia 9. Non traumatic pseudoaneurysm in the neck due to tumor invasion. 10. Nonvascular misses such as soft tissue tumors, leptomeningeal disease, traumatic laryngeal injury, cervical spine and cranio-cervical junction injury and cord compression.
Results and Conclusions
This exhibit presents misses, misinterpretations and great call's on CTAs of the head and neck discussed in peer learning sessions over the last 4 years. Pointers to avoid the misses and misinterpretations are discussed. Learning from our misses and knowing our blind spots will help interpret these studies with higher degree of confidence and accuracy.

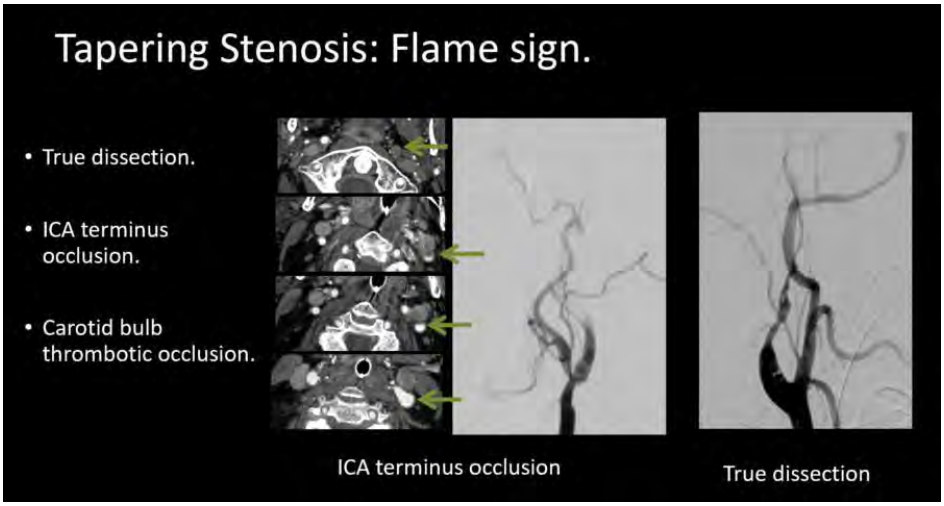

(Filename: TCT_1208_ASNR2023_CTAmissesandmisinterpretations.jpg)

1267

Diagnostic Accuracy and Reliability of Magnetic Resonance Imaging for Detection Of Posterior Ligamentous Complex Injuries Of Spine; A Systematic Review

D Shakoor[1], A Malhotra[2]

[1]Yale University, New Haven, CT, [2]Yale University School of Medicine, New Canaan, CT

Summary and Objectives

In this study, we intend to assess the diagnostic performance of MRI for detection of PLC injuries and evaluate the reliability of this technique between different readers.

Purpose

Spine trauma is very common with thoracolumbar spine fracture accounting for 75% of all spine injuries. Fracture morphology, mechanical and neurological stability are primary determinants of treatment decision making for spine fractures. Although some fractures are clearly unstable, others have more equivocal findings, emphasizing the role of ligamentous structures in assessing spinal stability. Posterior ligamentous complex (PLC) is considered a vital component of spinal stability, and its integrity and status may alone be the determining factor for surgical treatment.

Materials and Methods

An electronic literature search of MEDLINE, EMBASE and Central Cochrane were performed by 2 independent reviewers to identify studies which reported performance of MRI for detection of PLC injuries or reported the inter-reader reliability of readers with different levels of training in detection of PLC injuries using MRI. Studies were included which used operative findings as the reference standard. Methodological quality was performed using Mixed Methods Appraisal Tool, version 2018.

Results and Conclusions

2024 title and abstracts from inception to October 2022 were reviewed. 58 studies were reviewed at the level of full text review. Finally, 11 studies were included in the systematic review (Table 1). Eight studies reported the diagnostic accuracy of MRI for detection of different ligaments of PLC, with interspinous ligament being the most reported. The diagnostic accuracy of studies varied significantly with sensitivity ranging between 50%-100% and specificity ranging between 37.5%-100% (Table 2). Five studies reported the inter-reader reliability of different readers, with the highest reliability of 0.91and two studies reported correlation of MRI findings with the operative findings (Table 3). Conclusion: Current data on the accuracy of MRI for detection of PLC injuries is scarce and inconsistent. Additionally, the reliability of MRI is fewer which raises concern. Further robust studies are warranted to determine the accuracy of MRI for detection of PLC injuries and investigate its impact in clinical decision making as well as surgical treatment for spinal fractures.

Table 1. Included studies in the systematic review

N	Author	Country	Journal	Publication date	Institution	Study Design	N/ Female	Patient Enrollment: Age Mean/Median ± SD (Range)	Cervical spine	Thoracic spine	Lumbar spine
1	Crosby C	USA	The Spine Journal	[illegible]	Department of Orthopaedic Surgery, Vanderbilt University Medical Center	Prospective	[illegible]	N/A	[illegible]	[illegible]	[illegible]
2	Dai LY	China	The Journal Of Trauma Injury, Infection, and Critical Care	[illegible]	Department of Orthopedic Surgery, Xinhua Hospital	Prospective	[illegible]	[illegible]	[illegible]	[illegible]	[illegible]
3	Haba H	Japan	J Neurosurg	[illegible]	Departments of Orthopaedic Surgery and Radiology	Retrospective	[illegible]	[illegible]	[illegible]	[illegible]	[illegible]
4	[illegible]	India	Journal of Clinical and Diagnostic Research	[illegible]	Department of Radiology, [illegible] University	Prospective	[illegible]	[illegible]	[illegible]	[illegible]	[illegible]
5	Khurana B	USA	The spine Journal	[illegible]	Department of Radiology, Brigham and Women's Hospital	Retrospective	[illegible]	[illegible]	[illegible]	N/A	N/A
6	Lee HM	Korea	Spine	[illegible]	Department of Orthopaedic Surgery, Yonsei University College of Medicine	Prospective	[illegible]	[illegible]	[illegible]	[illegible]	[illegible]
7	[illegible]	India	Asian Spine Journal	[illegible]	Department of Orthopaedics, Government Medical College	Prospective	[illegible]	[illegible]	[illegible]	[illegible]	[illegible]
8	Rhin J	USA	J Neurosurg Spine	[illegible]	Department of Orthopaedic Surgery, The Rothman Institute, and Departments of Radiology and Neurosurgery, Thomas Jefferson University Hospital	Prospective	[illegible]	[illegible]	N/A	N/A	N/A
9	Vaccaro AR	USA	Spine	[illegible]	The Rothman Institute, Thomas Jefferson University Hospital	Prospective	[illegible]	[illegible]	N/A	N/A	N/A
10	[illegible]	Korea	Korean Journal of Radiology	[illegible]	Department of Radiology, Seoul National University Bundang Hospital	Retrospective	[illegible]	N/A	[illegible]	[illegible]	[illegible]
11	Zhuge W	USA	J Spinal Disord Tech	[illegible]	Department of Orthopedic Surgery, Baylor College of Medicine	Both	[illegible]	[illegible]	[illegible]	[illegible]	[illegible]

Study	Readers	Sensitivity	Specificity	Accuracy	PPV	NPV
Supraspinous Ligament						
Crosby et al	Orthopaedic surgeons and radiologist	[illegible]	[illegible]	[illegible]	N/A	N/A
Haba et al	Radiologist	[illegible]	[illegible]	[illegible]	N/A	N/A
Lee et al	MSK radiologist	[illegible]	[illegible]	[illegible]	[illegible]	[illegible]
Mehta et al	Radiologist	[illegible]	[illegible]	N/A	[illegible]	[illegible]
Rhin et al	Orthopaedic surgeons and radiologist	[illegible]	[illegible]	N/A	[illegible]	[illegible]
Vaccaro et al	Orthopaedic surgeons and radiologist	[illegible]	[illegible]	N/A	[illegible]	[illegible]
Interspinous Ligament						
Crosby et al	Orthopaedic surgeons and radiologist	[illegible]	[illegible]	[illegible]	N/A	N/A
Haba et al	Radiologist	[illegible]	[illegible]	[illegible]	N/A	N/A
Harris et al	Radiologist	[illegible]	[illegible]	75	N/A	N/A
Lee et al	MSK radiologist	100	[illegible]	[illegible]	[illegible]	[illegible]
Mehta et al	Radiologist	[illegible]	[illegible]	N/A	[illegible]	[illegible]
Rhin et al	Orthopaedic surgeons and radiologist	[illegible]	[illegible]	N/A	[illegible]	[illegible]
Vaccaro et al	Orthopaedic surgeons and radiologist	[illegible]	[illegible]	N/A	[illegible]	[illegible]
Zhuge et al	Neuroradiologist	100	[illegible]	[illegible]	[illegible]	100
Ligamentum Flavum						
Crosby et al	Orthopaedic surgeons and radiologist	[illegible]	[illegible]	[illegible]	N/A	N/A
Harris et al	Radiologist	[illegible]	100	[illegible]		
Lee et al	Radiologist	[illegible]	[illegible]	[illegible]	[illegible]	[illegible]
Mehta et al	Radiologist	[illegible]	[illegible]	N/A	[illegible]	[illegible]
Rhin et al	Orthopaedic surgeons and radiologist	[illegible]	[illegible]	N/A	[illegible]	[illegible]
Vaccaro et al	Orthopaedic surgeons and radiologist	[illegible]	[illegible]	N/A	[illegible]	[illegible]
Zhuge et al	Neuroradiologist	[illegible]	[illegible]	[illegible]	[illegible]	[illegible]

Table 2. Diagnostic accuracy of MRI for detection of Posterior Ligamentous Complex Injuries of the Spine.

Kappa Values for Inter-reader Agreement						
Study	Readers	Supraspinatus	Interspinous Ligament	Posterior Longitudinal Ligament	Ligamentum Flavum	Posterior Ligamentous Complex
Dai et al	3 neuroradiologists	0.63	0.63	0.56	N/A	N/A
Haba et al	3 radiologists	0.69	0.91	N/A	N/A	N/A
Khurana et al	MSK radiologist and spine surgeon	N/A	N/A	N/A	N/A	0.91
Mehta et al	Radiologists	0.52	0.64	N/A	0.22	N/A
Young et al	6 radiologists	N/A	N/A	N/A	N/A	0.44
Spearman Correlation between Radiology Report and Operative Findings						
Rhin et al	Radiologist	0.56	0.58	N/A	0.48	N/A
Vaccaro et al	Radiologist	0.5	0.53	N/A	0.55	N/A

Table 3. Inter-reader reliability of MRI for detection of Posterior Ligamentous Complex Injuries of the Spine.

(Filename: TCT_1267_NewMicrosoftPowerPointPresentation.jpg)

478

Differential Diagnoses within the Skull Base: A Guide for Navigating the Complex Pathology

C Tournade[1], T Moritani[1]
[1]University of Michigan, Ann Arbor, MI

Summary and Objectives
Recognize the differential considerations for complex skull base pathology. Learn how to differentiate between neoplastic and non-neoplastic disease within the skull base. Understand how to utilize different imaging techniques to narrow a differential and arrive at a diagnosis. Identify imaging features specific for certain disease processes.

Purpose

A vast number of different pathologies can affect the skull base given the various structures and tissue types that reside within this region such as vessels, nerves, and lymphoid tissue among others. Examples of disease which can affect the skull base include metastases; lymphoproliferative and hematopoietic disease; primary neoplasms such as chordoma and chondrosarcoma; local extension of neoplastic processes such as nasopharyngeal carcinoma, squamous cell carcinoma, or basal cell carcinoma; benign neoplasms such as schwannomas, meningiomas, and pituitary disease; inflammatory processes such as inflammatory pseudotumor; and infection such as bacterial or fungal osteomyelitis. Given this, there can be overlap in the imaging features of disease processes which can create diagnostic dilemmas and difficulty in diagnosis. Through this demonstration, we will walk through the numerous pathologies and highlight unique characteristics and patterns of disease processes affecting the skull base utilizing different imaging modalities and techniques with the goal of improving understanding of pathology that can occur in this region and improve accuracy in diagnosis.

Materials and Methods

Representative cases and images were retrieved from the University of Michigan imaging archives to illustrate imaging findings and pathologic slides of various neoplastic and non-neoplastic skull base diseases utilizing multiple different imaging modalities.

Results and Conclusions

Pathology within the skull base can be complex and difficult to diagnose. Given the various neoplastic and non-neoplastic etiologies of disease, there can be significant overlap in the imaging findings which can create diagnostic dilemmas. Through the use of multiple different imaging modalities and techniques, differential diagnoses can be narrowed in order to assist in guiding management. Knowledge of the different imaging characteristics of various pathologies and how to utilize certain imaging modalities and techniques is critical in providing accurate differentials to more quickly reach a diagnosis and improve patient management.

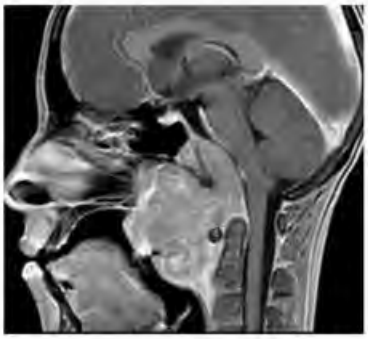

Figure 1. Sagittal post-contrast T1W imaging shows an aggressive enhancing mass involving the clivus and invading contiguous structures within the skull base. This was proven to be a chordoma.

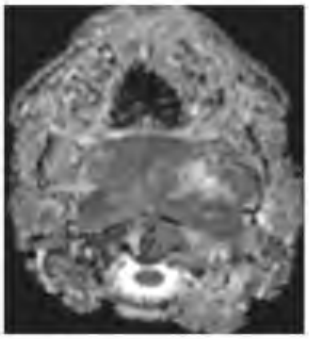

Figure 2. ADC imaging of the same mass shows a reduced average diffusion coefficient (0.77×10^{-3} mm^2/s). Diffusion weighted imaging can be useful in differentiating chordomas and chondrosarcomas as hypercellular chordomas will have lower ADC values.

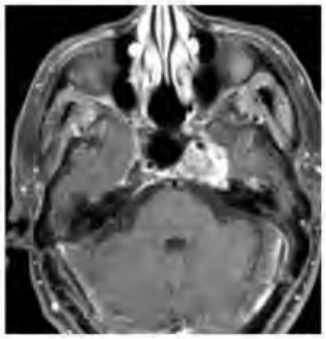

Figure 3. Axial post-contrast T1W imaging shows a heterogeneously enhancing mass centered at the left petro-occipital synchondrosis and petrous apex. This was proven to be a chondrosarcoma.

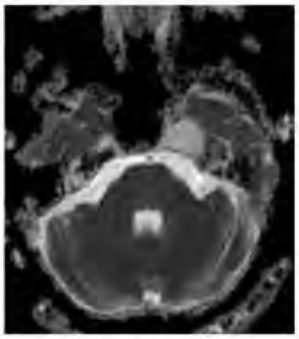

Figure 4. ADC imaging shows an elevated average diffusion coefficient (2.02×10^{-3} mm^2/s). This is related to the lesion's internal extracellular matrix rather than cellularity, in contrast to a chordoma.

(Filename: TCT_478_Slide1.JPG)

570

Do You Hear That Whooshing? - An Interactive Angiographic Evaluation of Pulsatile Tinnitus Etiologies

Z Wilseck[1], L Lin[1], S Panicker[2], J Gemmete[1], N Chaudhary[1]

[1]University of Michigan - Michigan Medicine, Ann Arbor, MI, [2]University of Michigan Medical School, Ann Arbor, MI

Summary and Objectives

Tinnitus is a common clinical problem and can be classified as pulsatile or continuous. Pulsatile tinnitus (PT) is typically related to an underlying vascular etiology and is a common indication for performing radiological imaging of the intracranial vasculature as well as the temporal bone and inner ear structures. A thorough understanding of the etiologies of pulsatile tinnitus by the neuroradiologist is important for accurate diagnosis. This interactive 3D exhibit of various causes of PT utilizes multi-modality neurological imaging in the form of CTA, MRA, MRI, and digital subtraction angiography (DSA). Educational objectives: 1. Review the common and uncommon causes of pulsatile tinnitus. 2. Discuss the clinical and imaging work-up of pulsatile tinnitus. 3. Presentation of an interactive, 3D models created utilizing multi-modality neurologic imaging. 4. Brief review of the utilization of interactive models for patient and referring provider education.

Purpose

The purpose of this exhibit is to present various causes of PT. Cases will be presented with intuitive, interactive 3D models. These models will concatenate structures that are typically visualized on different modalities to illustrate anatomic relationships. For example, vessels (best visualized on angiography) can be seen in relationship with cranial nerves (best visualized on MRI).

Materials and Methods

Cases will be presented in a multi-modality fashion. QR codes will be presented to allow viewers access to interactive 3D models of neurovascular pathology. Cases presented will include: 1. Vascular malformations and fistulae 2. Paraganglioma 3. Idiopathic intracranial hypertension and venous stenosis 4. Venous anatomic variations 5. Endolymphatic sac tumor

Results and Conclusions

43-year-old male with left-sided pulsatile tinnitus. Initial MRA (A) reveals flow-related enhancement of the jugular bulb (→) suspicious for a dural arteriovenous fistula. Lateral external carotid angiogram in the arterial phase (B) confirms early contrast filling of the jugular bulb (↠) and the vertebral venous plexus (➤), with the mastoid branches of the occipital artery being the main arterial supply (⇨). 3D model (C) illustrates the relationship between the arterial feeders (3, 7), fistula (1), and venous drainage (2, 4). Scan QR code to visualize interactive model and labels.

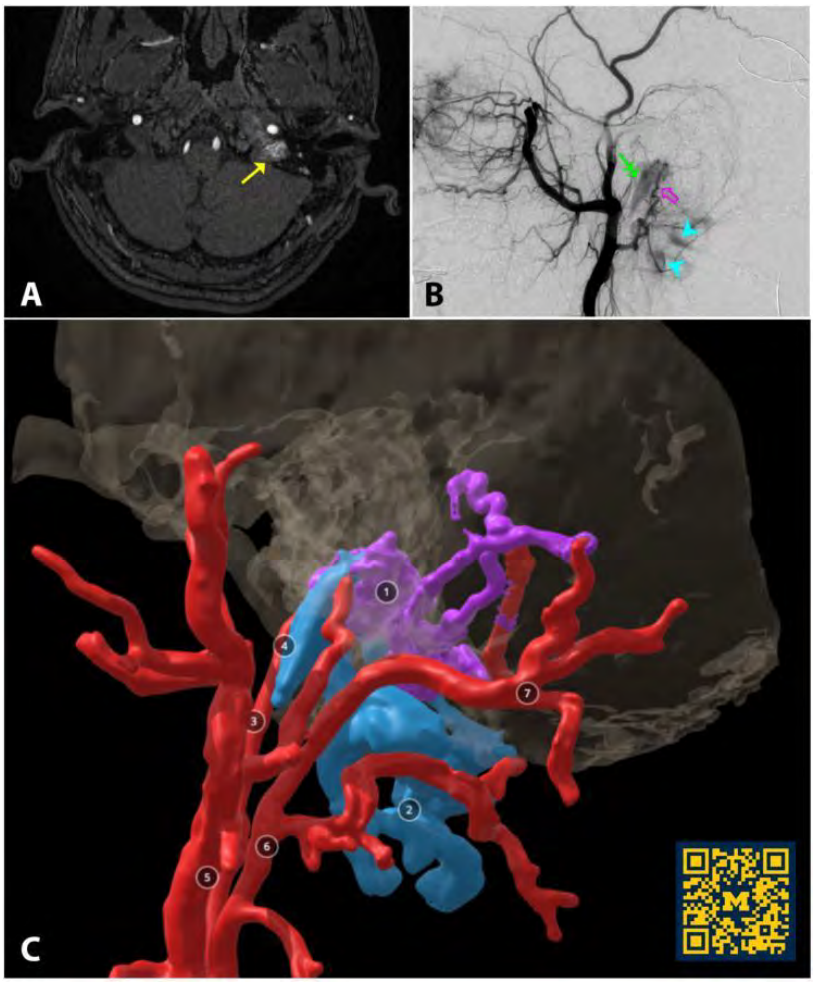

(Filename: TCT_570_figure1.jpg)

1482

Don’t Let the Brain Bugs Bite: A Case-Based Review of Intracranial Infections

K Wei[1], P Wang[1], S Sun[1], E CHU[1], J Soun[1], E KUOY[1]
[1]*University of California, Irvine Medical Center, Orange, CA*

Summary and Objectives
There are a wide variety of infectious diseases which can affect the central nervous system including a broad array of bacterial, viral, fungal and parasitic etiologies. Infectious agents can be introduced to the central nervous system through a variety of different routes of transmission, most commonly through hematogenous spread (ie from bacteremia), direct introduction (ie through iatrogenic or traumatic mechanisms), and direct spread (ie from local infection such as acute sinusitis). Imaging is essential in the diagnosis of intracranial infections, however imaging findings as well as clinical presentation frequently overlap and may also mimic neoplastic or vascular disease. In the majority of cases of intracranial infection, there is disruption of the blood-brain barrier resulting in associated abnormal enhancement and vasogenic edema. Restricted diffusion is also another common feature and may be seen in certain infections. Localization of the lesion, including which space the disease process involves (ie whether the lesion is epidural, subdural, subarachnoid, intraventricular, or intraparenchymal) can help to narrow the differential diagnosis. Furthermore, a thorough understanding of the patient's clinical history such as immunocompetency status and travel history can help differentiate between infectious etiologies when imaging features are equivocal. We aim to provide a case-based review of multiple different bacterial, viral, fungal and parasitic pathogens and discuss their characteristic neuroimaging features, disease progression, common imaging mimics/pitfalls, and associated distinguishing clinical features. Some cases that will be highlighted include tuberculosis, Balamuthia mandrillaris, neurocysticercosis, neuroschistosomiasis, HIV encephalopathy, HIV with associated PML, herpes encephalitis, cryptococcosis, cerebral mucormycosis, and Creutzfeldt-Jakob disease (CJD).

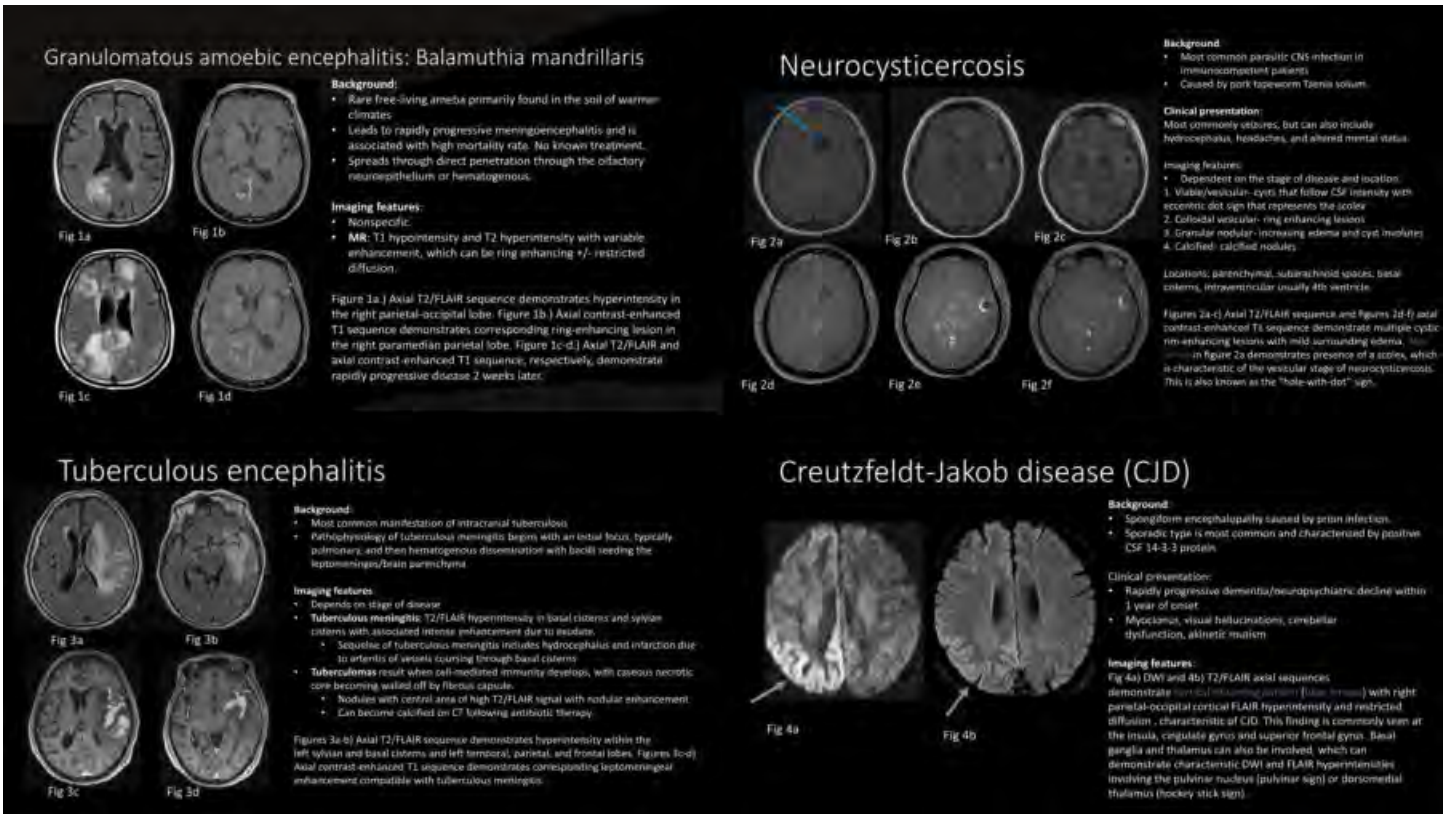

(Filename: TCT_1482_DontLettheBrainBugsBiteACase-BasedReviewofIntracranialInfections.jpg)

822

Dual Energy CT in Acute Neurological Conditions

S Mohn[1], Q Sahi[1], S MATHUR[2], D Lyndon[1], N Murray[3]

[1]University of British Columbia, Vancouver, British Columbia, [2]UNIVERSITY OF TORONTO, TORONTO, ON, [3]University of British Columbia, VANCOUVER, BC

Summary and Objectives

Summary: DECT is an evolving tool with many useful applications in the setting of acute neurological conditions because of its increased ability over single energy computer tomography (SECT) in performing molecular composition analysis. While magnetic resonance imaging (MRI) is the gold standard for most diagnostic neuroimaging, DECT offers faster acquisition times than MRI along with increased tissue characterization than SECT, making it an ideal imaging modality for acute neurological conditions. Some important applications of DECT include detection and characterization of intracranial bleed, calcifications and contrast staining, spinal canal hematoma, spinal fractures, and intracranial and spinal infections. Educational Objectives: 1. Understand the basic principles of CT and DECT acquisition and material characterization using DECT. 2. Highlight the added value of using DECT in the setting of acute neurological conditions in detecting pathologies not seen by SECT, increasing diagnostic confidence, and improving patient's prognostication. 3. Review current applications of DECT in acute neurological conditions such as detecting brain edema, intracranial and spinal hematomas, bone marrow edema, and intracranial and spinal infections.

Purpose

To review the principles of dual energy computed tomography (DECT) and current clinical applications in detection of acute neurological conditions.

Results and Conclusions

Many clinical applications of DECT in acute neurological conditions exist and offer benefit over SECT because of its molecular composition analysis, and over MRI because of its greater speed of image acquisition.

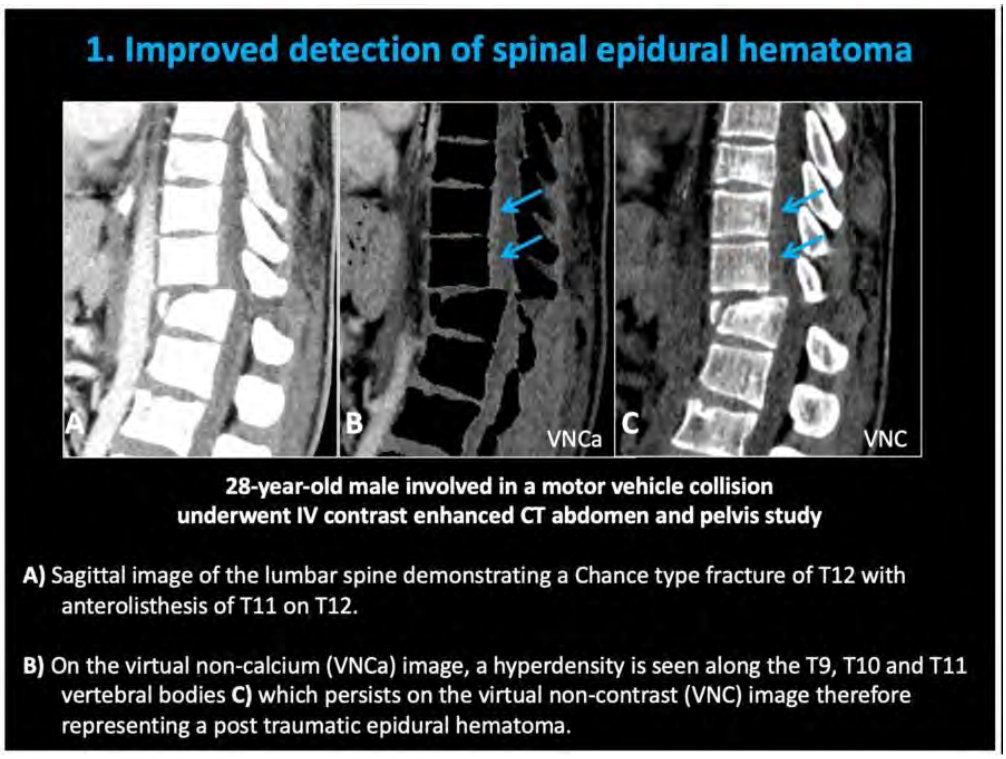

(Filename: TCT_822_AbstractFigure.jpg)

573

Emerging Neuroimaging Applications of Magnetic Resonance Elastography

S Mishra[1]
[1]*University of Michigan, Ann Arbor, MI*

Summary and Objectives

Objectives: 1. Understand magnetic resonance elastography (MRE) as an imaging technique, including required components of the pulse sequence, hardware and post-processing reconstruction 2. Get an overview of the published literature on applications of MRE in brain tumors, multiple sclerosis (MS), aging and Alzheimer disease (AD), and as a potential functional neuroimaging technique.

Summary: MRE is a technique for noninvasively measuring a tissue's shear stiffness via imaging an externally induced propagating mechanical wave. Pulse sequences include motion encoding gradients which are synchronized to the frequency of the mechanical wave. The phase data is unwrapped allowing for measurement of displacement with respect to wave phase (A). Solving the 3D Helmholtz wave-equation allows for solving for the isotropic wavelength (B). Current elastography techniques measure the complex shear modulus, depicted as G*. Frequently reported quantities in the literature report shear wave speed or wavelength, the magnitude of the complex shear modulus, or simply the real part of the complex shear modulus. MRE applications have been explored in brain tumors, multiple sclerosis (MS), and Alzheimer disease and aging. MRE-based stiffness correlated better with surgeons' qualitative assessment of meningioma stiffness when compared to T1-/T2-weighted characteristics1. In glioma patients, shear stiffness decreased with increasing tumor grade and correlated with IDH2 mutation status with wild-type being softer than IDH2-mutant2. Patients with relapsing-remitting MS had lower global shear modulus in comparison to controls, but stiffness measurements of MS lesions is similar to that of unaffected white matter. MRE in healthy subjects found that stiffness in various brain regions goes down with age and AD patients had softer brains compared with age-matched controls. The first demonstration that changes in stiffness could be neuronally mediated was done using electrical hind-limb stimulation in anesthetized mice3 which showed activation of pain centers including the primary and secondary somatosensory cortices. At 20-second timescales in humans, the visual cortex became stiffer with visual stimulation4. However, faster times of 2-seconds, preliminary data shows decreased stiffness in the motor cortex with a motor task with functional maps showing high spatial correlation to fMRI5, suggesting MRE may differentiate different functional mechanisms at different timescales.

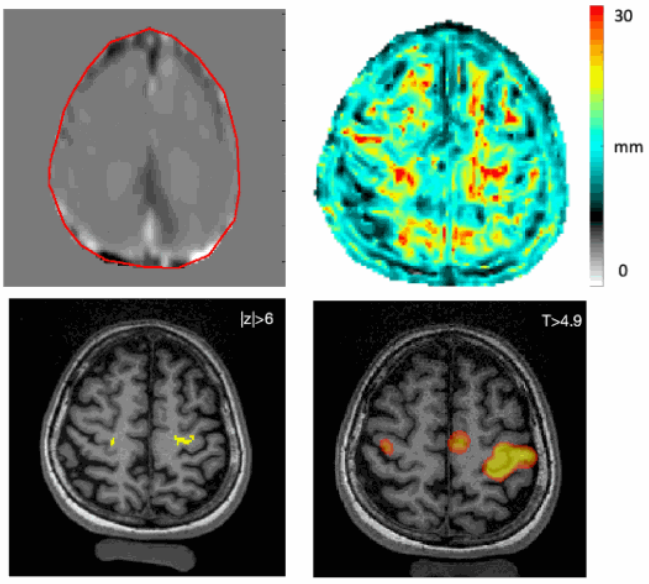

Magnetic Resonance Elastography in the Brain: A) Wave image showing displacement as a function of wave phase. B)Reconstructed wavelength image of the brain. C) Functional MRE activation map showing voxels |z| > 6 during right-hand finger-tapping task with 2-second switching time D) BOLD fMRI activation map using right-hand finger-tapping with 20-second switching.

(Filename: TCT_573_MRE_abstract_figure.gif)

644

Endonasal Endoscopic Indications to Skull Base and Orbit: a Cased-Based Review.

a costacurta[1], M Tepedino[2], R Neves[3]

[1]Clínica Felippe Mattoso, Rio de Janeiro, Brazil, [2]Policlínica de Botafogo, Rio de Janeiro, RJ, [3]Policlínica Botafogo, Rio de Janeiro , Rio de Janeiro

Summary and Objectives

Great improvements in instrumentation and surgeon skills in the last decade has opened a whole new spectrum of indications to endoscopic endonasal surgery, from treatment of benign conditions to the management of malignant tumors. This progress enabled access to anterior and central skull base, and also to the orbit, with less facial deformity and scars, less morbidity and shorter hospitalisation.

Purpose

Endoscopic endonasal surgery is gaining wide acceptance in the management of a number of conditions as a valuable tool, specially for oncologic patients who often need a more tailored or targeted approach. Radiologists should be aware of these new procedures in order to contribute to the multidisciplinary team and correctly read these exams. The aim of this review is to show some examples of the current use of this technique pointing out the post-operative findings.

Materials and Methods

Interesting cases illustrating different endoscopic approaches for a series of pathologies, along with the radiological pre and post operative findings will be displayed such as: Dacryocystorhinostomy Orbital decompression Orbital tumor surgery Drainage of infratemporal fossa and retropharynx abscess Nasopharynx/ base of skull biopsy and surgery CSF leak repair

Results and Conclusions

Endoscopic endonasal surgery for skull base and orbit pathologies, albeit restricted to larger centers, is no longer a promising tool but already an important part of the armamentarium in the diagnosis and treatment of skull base and orbit pathologies. Radiologists needs to be acquainted with the surgical accesses and expected findings after such procedures to better understand it's limitations, search for treatment failure and related complications.

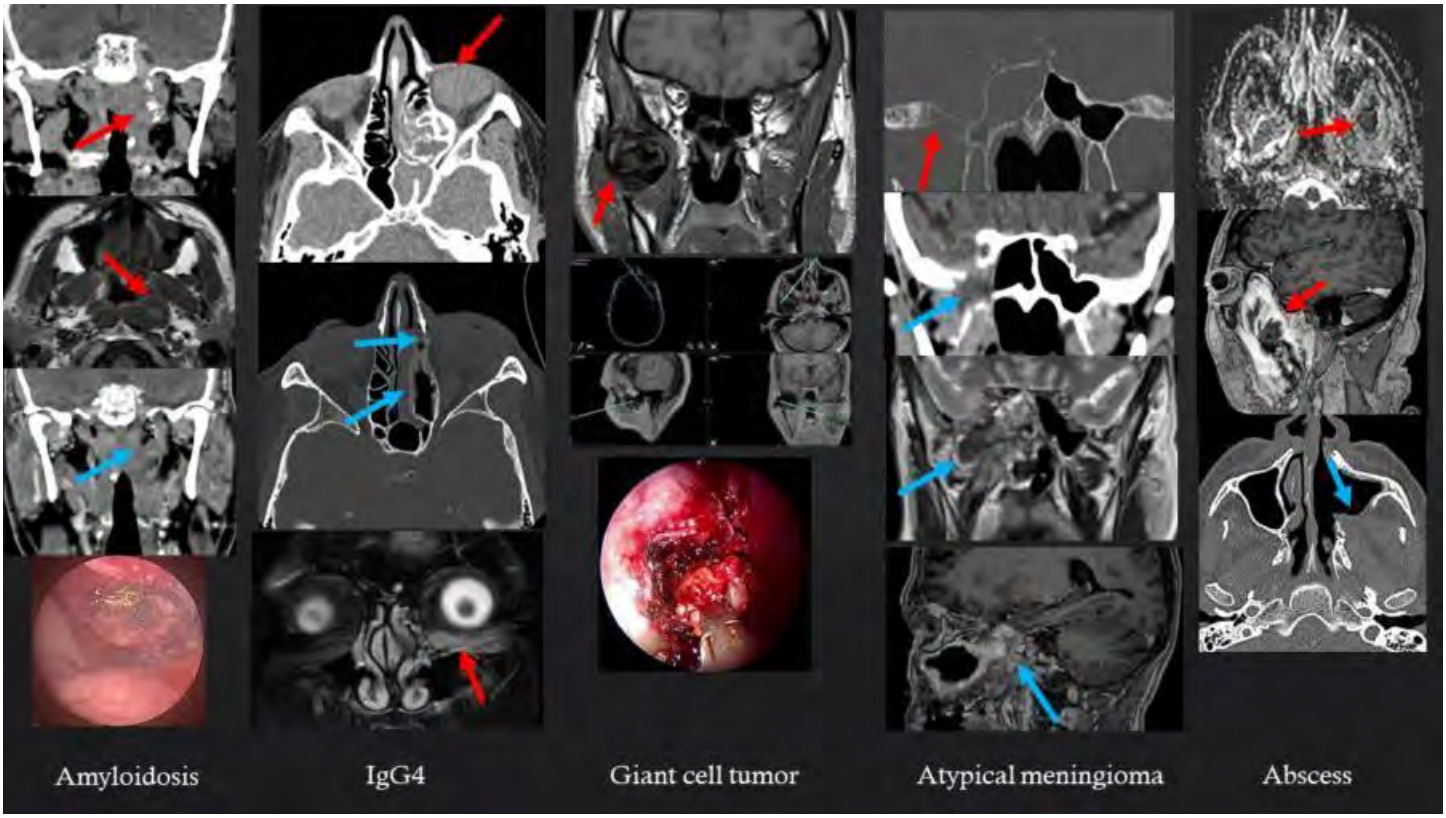

(Filename: TCT_644_abstractendoscopia.jpg)

1363

Enhancing Trigeminal Nerve: Where to look and What to look for

A Rodriguez[1], L Nunez[1], D Timaran[2], R Samant[3], R Riascos[1]

[1]The University of Texas Health Science Center at Houston, Houston, TX, [2]University of Texas Health Science Center Houston, Houston, TX, [3]UT Health, McGovern School of Medicine, Texas Medical Center, Houston, TX

Summary and Objectives

The trigeminal nerve is the largest of all cranial nerves and is composed of sensory and motor roots that innervate muscles of the face and mastication. The trigeminal nerve is formed by a brainstem, cisternal, and Meckel's cave-cavernous sinus segments, with three extracranial divisions: ophthalmic (V1), maxillary (V2), and mandibular (V3). Dysfunction of the trigeminal nerve is frequent and can present with a wide variety of clinical signs and findings. Imaging is considered essential to assess this nerve. Numerous implicated conditions may manifest with enhancement and usually share similar findings between this variety of entities. As there is a broad differential diagnosis, including demyelinating disease, infection, tumors, post-radiation, and inflammatory conditions, MRI represents the imaging modality of choice in detecting, evaluating, and characterizing these lesions. In this review, we will focus on nerve imaging and related findings that may help orientate the diagnosis. Educational Objectives • To describe the key imaging features that may facilitate the diagnosis of trigeminal nerve enhancement pathologies.

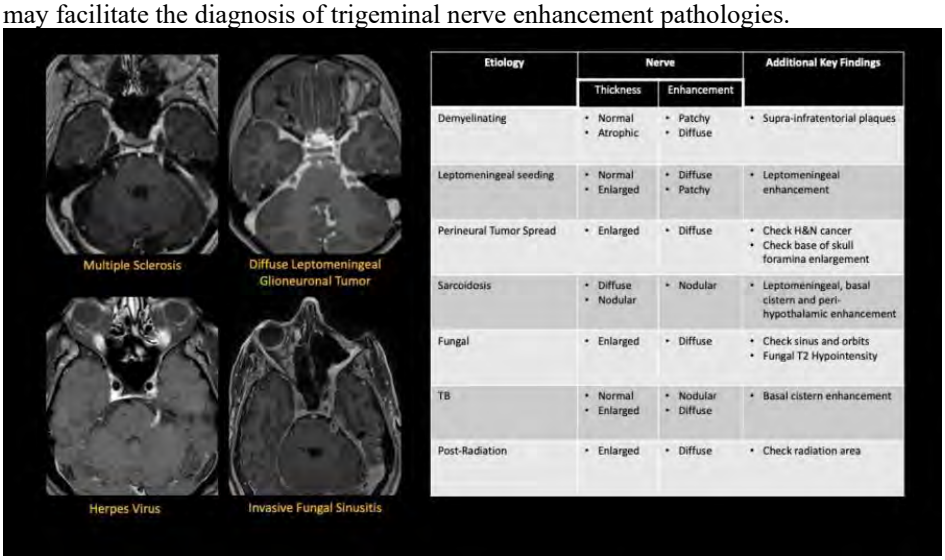

Etiology	Nerve		Additional Key Findings
	Thickness	Enhancement	
Demyelinating	• Normal • Atrophic	• Patchy • Diffuse	• Supra-infratentorial plaques
Leptomeningeal seeding	• Normal • Enlarged	• Diffuse • Patchy	• Leptomeningeal enhancement
Perineural Tumor Spread	• Enlarged	• Diffuse	• Check H&N cancer • Check base of skull foramina enlargement
Sarcoidosis	• Diffuse • Nodular	• Nodular	• Leptomeningeal, basal cistern and peri-hypothalamic enhancement
Fungal	• Enlarged	• Diffuse	• Check sinus and orbits • Fungal T2 Hypointensity
TB	• Normal • Enlarged	• Nodular • Diffuse	• Basal cistern enhancement
Post-Radiation	• Enlarged	• Diffuse	• Check radiation area

(Filename: TCT_1363_TNenhancement.jpg)

141

Etiologies of Pulsatile Tinnitus: What the Radiologist Needs to Look For

S Scheller[1], M Kontzialis[1]
[1]Northwestern University, Chicago, IL

Summary and Objectives
Pulsatile tinnitus is a common clinical complaint for which imaging studies are frequently ordered. An identifiable cause for pulsatile tinnitus can be discovered in over 70% of patients with a thorough clinical, physical, and imaging evaluation. However, the potential etiologies for pulsatile tinnitus are numerous and the imaging findings can be subtle. The purpose of this educational exhibit is to highlight the vascular, non-vascular, and tumor-related etiologies for pulsatile tinnitus and the imaging features of each, so that the radiologist can be confident and thorough in their search for an underlying cause of pulsatile tinnitus, which can have significant impact on management and prognosis. By the completion of this education exhibit, the radiologist will be able to: 1. Describe the difference between continuous and pulsatile tinnitus 2. Understand the benefits of CT versus MRI in evaluation of tinnitus, and be able to recommend an adequate imaging study when given a patient's clinical history 3. List the vascular causes of pulsatile tinnitus 4. Understand the developmental mechanisms and imaging features of an aberrant internal carotid artery and persistent stapedial artery 5. Recognize the imaging features of venous abnormalities including dehiscent jugular bulb, high-riding jugular bulb, jugular diverticulum, sigmoid sinus diverticulum, sigmoid sinus dehiscence, dural venous sinus stenosis, and dilated emissary veins 6. Recognize the imaging features of arteriovenous malformations, dural arteriovenous fistulas, fibromuscular dysplasia, and arterial dissection 7. Understand the potential endovascular and surgical treatment options for vascular-related causes of pulsatile tinnitus 8. Recognize the imaging features of tumor-related etiologies including glomus tympanicum and glomus jugulotympanicum paragangliomas, hypervascular metastases, meningiomas, and hemangiomas 9. Recognize the imaging features of non-vascular etiologies of pulsatile tinnitus including otosclerosis and superior semicircular canal dehiscence

1249

Extradural and Intradural Extramedullary Spinal Lesions: a Pictorial Essay

M Akuri[1], M Akuri[2], H SILVA[3]
[1]UNIFESP, Sao Paulo, Sao Paulo, [2]FAMEMA, Marília, São Paulo, [3]FAMEMA, Marília, Brazil

Summary and Objectives
Summary: Spine lesions can be didactically divided into extradural, intradural extramedullary and intradural intramedullary lesions. According to the space that the tumor occupies, some possibilities of differential diagnoses will be considered. Intramedullary intradural injuries will not be addressed in this exhibit. The two most common tumors of the extramedullary intradural space are meningiomas and schwannomas. Other pathologies that may occur include lipoma, myxopapillary ependymoma and metastasis. The imaging features can help in differentiating these lesions. Extradural compartment lesions include primary bone tumors extending into the extradural space, and other lesions such as schwannoma and metastasis. Non-tumor lesions such as infection and arachnoid web can be also finding and cannot be forgotten among the differential diagnoses. Educational Objectives The purpose of this exhibit is to: 1. Discuss and review the different tumors and lesions that can affect the spine, with emphasis on tumors that affect the intradural extramedullary compartment and extradural compartments. 2. Show didactic cases and illustrate the imaging findings of these different diseases such as meningioma, neural sheath tumors, myxopapillary ependymoma, metastasis, and others. 3. Review and discuss non-tumor differential diagnoses such as infection and arachnoid web.
Purpose
Review extradural and intradural extramedullary spinal lesions
Results and Conclusions
There are several differential diagnoses for spinal lesions. The most common intradural extramedullary tumors are meningioma and schwannoma. Other tumors that should be remembered include metastases and myxopapillary ependymoma. Differential diagnoses such as malformation and infection should be remembered. Imaging findings as well as clinical features aid in the diagnosis.

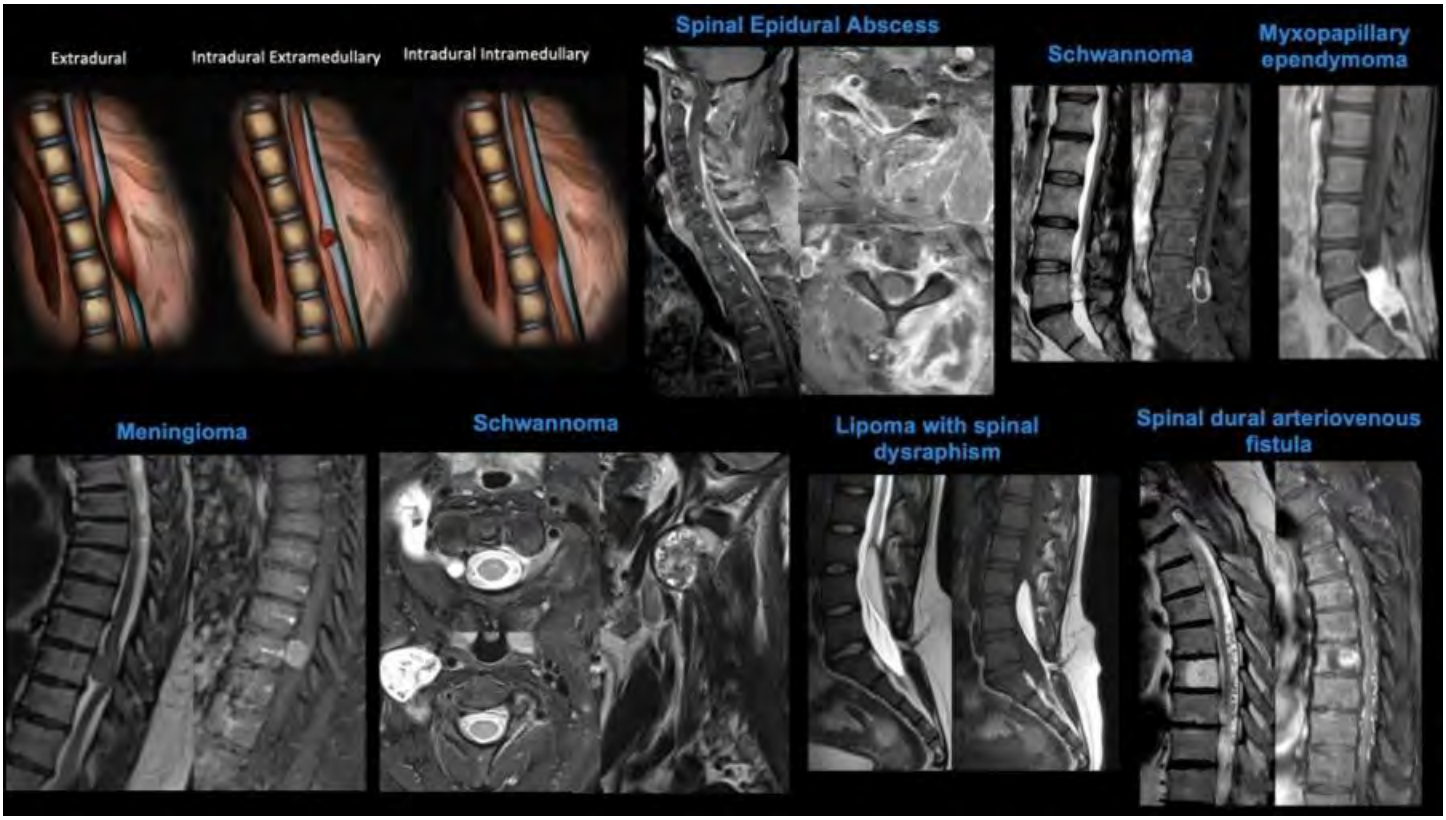

(Filename: TCT_1249_ASNRimages.jpg)

1380

Eye as a Window to the Soul aka Orbital Anomalies with Underlying Central Nervous System Pathologies

K Hendzel[1], J Gadde[2], N Saran[1], M Mocan[1], B Ozgen Mocan[1]

[1]University of Illinois at Chicago, Chicago, IL, [2]Lurie Children's Hospital of Chicago, Chicago, IL

Summary and Objectives

The embryonic development of the eye is a complex, integrated process and any error in this process can lead to a large spectrum of developmental anomalies. The eye forms as an outgrowth from the anterolateral portion of the embryonic neural tube and although the ocular malformations can occur in isolation, they are frequently accompanied by brain malformations or can be a part of multisystem anomaly.

Purpose

This exhibit will review the classic developmental orbital pathologies that can have associated intracranial anomalies. Additionally, orbital findings of most common congenital central nervous system (CNS) disorders will be discussed.

Materials and Methods

The imaging findings of congenital optic nerve and ocular lesions (including optic nerve hypoplasia, microphthalmia, coloboma, morning glory anomaly) with associated brain anomalies will be reviewed will illustrating cases. The typical orbital anomalies in well-known syndromes (such as PHACES) and developmental CNS disorders (such as neurocutaneous syndromes) will also be discussed with case examples.

Results and Conclusions

This exhibit will review the associated orbital and intracranial imaging findings of developmental anomalies. The orbital component of the anomaly might be the tip of an iceberg, warning for crucial intracranial conditions that can affect the management. Similarly, the orbital components of the more complex CNS syndrome might be more subtle and overlooked if unknown but they may still result in lifelong visual handicap, functional difficulties or cosmetic problems.

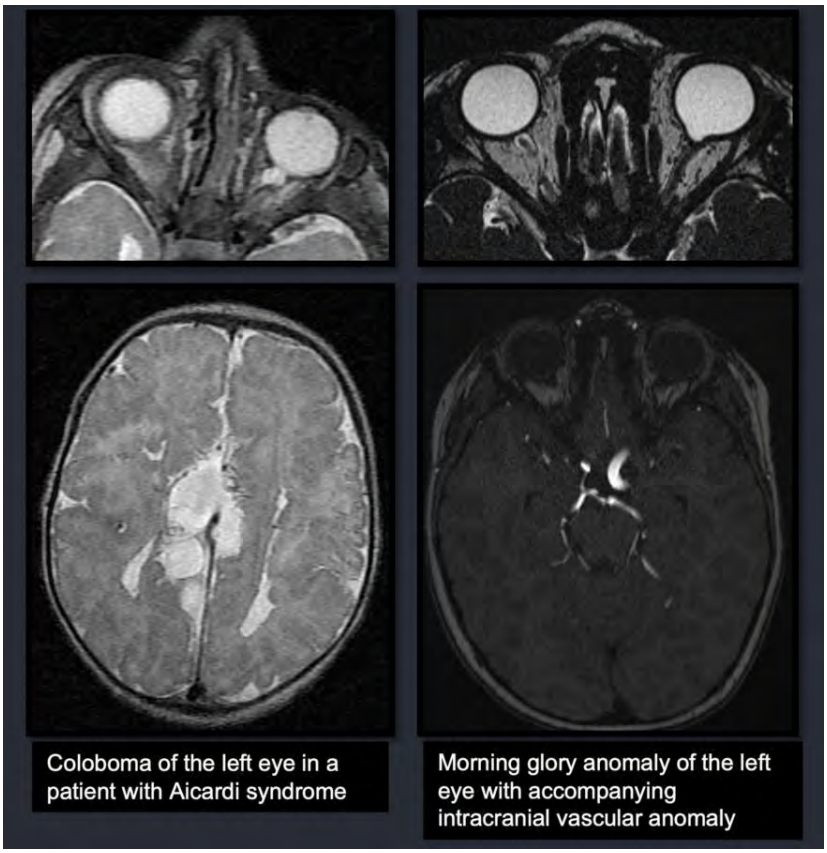

(Filename: TCT_1380_Figure.jpg)

701

Fibromuscular Dysplasia: Considerations for the Neuroradiologist

C Paton[1], T Marini[2], S ELLIKA[3]

[1]University of Rochester, Rochester, NY, [2]University of Rochester, East Syracuse, NY, [3]UNIVERSITY OF ROCHESTER MEDICAL CENTER, ROCHESTER, NY

Summary and Objectives

Fibromuscular dysplasia (FMD) is a vascular disease of small and medium-sized arteries, most frequently the extracranial carotid vessels but also the renal or vertebral arteries. FMD presents with unique imaging manifestations, which are important to recognize early to prevent the dangerous outcomes of transient ischemic attack, stroke, and carotid or vertebral artery dissection.

Purpose

This exhibit seeks to review Fibromuscular Dysplasia pathology, signs and symptoms, and negative outcomes. Our goal is to familiarize Neuroradiologists with the imaging modalities available for evaluating FMD, the various imaging manifestations of different variants of FMD, and contrast these with the imaging characteristics of alternate differential diagnoses. Additionally, the exhibit will emphasize the harmful outcomes that can be prevented with early recognition.

Materials and Methods

Vascular anatomy of the head and neck, pathophysiology of FMD, imaging techniques and specific findings will be enumerated. The most common manifestation of FMD is the canonical "string of beads" pattern of luminal irregularity (Type 1 FMD). Less common presentations of FMD include: long segment tubular stenosis (Type 2 FMD), and eccentric outpouching due to periadventitial fibroplasia (Type 3 FMD). Differential diagnoses, which are important to distinguish from FMD include: other vasculopathies, arterial "standing waves," and atherosclerotic disease.

Results and Conclusions

Fibromuscular Dysplasia of the head and neck frequently exhibits a characteristic "beads on a string" appearance. But variations in presentation do occur and are important for neuroradiologists to identify. Increased knowledge of the distinct presentations of FMD will assist in the recognition of this condition in all forms, preventing the subsequent development of ischemic stroke, subarachnoid hemorrhage, arterial dissection, and aneurysm.

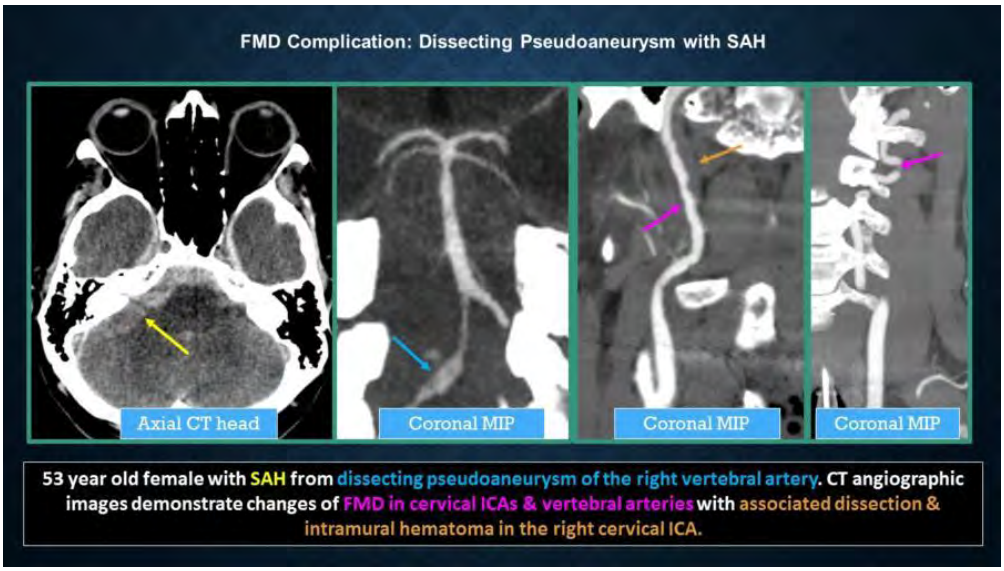

(Filename: TCT_701_FMDImage.jpg)

1332

Gallium-68 DOTATATE PET/CT evaluation of Head and Neck Paragangliomas: Spectrum of Case based Multi-modality Pictorial Review

P Suthar[1], S Virmani[1]
[1]*Rush University Medical Center, Chicago, IL*

Summary and Objectives
Paragangliomas may carry underlying hereditary pathogenic variants that are associated with increased risk for multifocal and metastatic disease, indicating the need for genetic testing in all patients with paragangliomas. Paraganglioma are best assessed by Gallium-68 DOTATATE PET/CT imaging. Recent availability of this positron emitting radio labeled somatostatin analogue has a huge impact in the diagnosis, staging and surveillance of patients with head and neck paragangliomas.
Purpose
The purpose of this case based pictorial exhibit is to highlight: • Imaging spectrum of various findings including normal physiological distribution/variation, benign, incidental and pathologic abnormalities. • Multimodality comparison and its superiority over conventional CT/MR and octreotide imaging when available. • Gallium-68 DOTATATE PET CT impact over patient management in head and neck paraganglioma.
Materials and Methods
We present a case based multimodality pictorial review (Gallium-68 DOTATATE PET/CT, CT, MR, Indium-111 pentetreotide, Iodine-131 or 123 MIBG, 18F-FDG PET/CT scans) highlighting the spectrum of different 10 interesting cases of head and neck paraganglioma including carotid body, jugulotympanic, glomus jugulare, glomus vagale, etc.
Results and Conclusions
Gallium-68 DOTATATE PET/CT is the new Gold standard for neuroendocrine tumor diagnosis and has a huge impact in the patient's management. The presented PET/CT based pictorial review with multimodality correlation raises awareness and strengthens the judgment of the reading physician for extra gastro-entero-pancreatic neuroendocrine tumors.

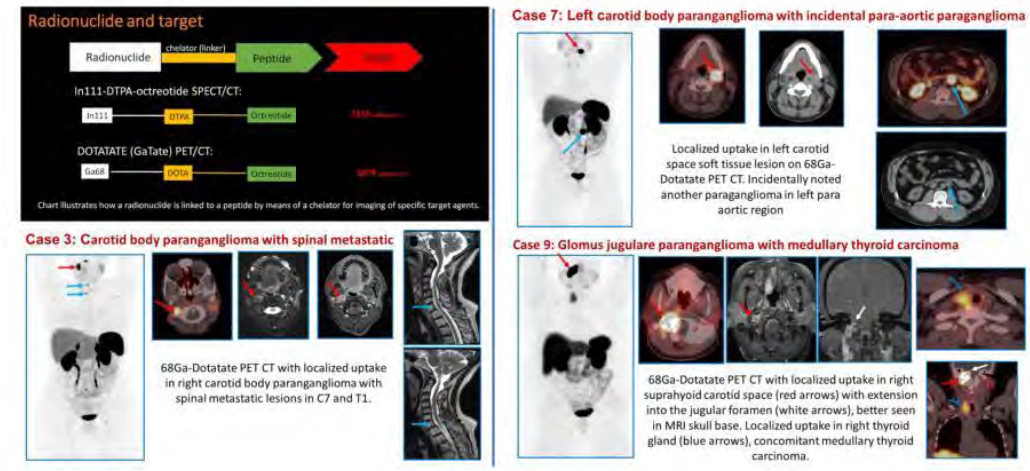

(Filename: TCT_1332_Slide1.JPG)

825

Glaucoma-related Findings in Neuroimaging

J Kim[1]

[1]University of Kentucky, Lexington, KY

Summary and Objectives

Glaucoma, a leading cause of blindness worldwide, is caused by various eye conditions resulting in damage to retinal cells and the optic nerve. Although glaucoma is generally diagnosed clinically and treated medically and/or surgically without neuroimaging such as CT and MRI, patients may have findings on neuroimaging which may be potentially unfamiliar or confusing. One of the more frequently encountered findings are tube shunt devices, of which there are a variety with different appearances. Because these may be radiopaque and are implanted into the orbit, their presence may cause MRI safety concerns. Also on imaging, a "giant reservoir," which signifies dysfunction of the tube shunt device, initially may be confused for a cystic lesion. Alterations in the appearance of the optic nerve, lateral geniculate nucleus, and visual cortex as sequela of glaucoma have been reported in literature. In pediatric patients with congenital glaucoma, an abnormal optic globe and neuroimaging abnormalities related to the underlying congenital syndrome may be seen. Familiarity with glaucoma and glaucoma-related neuroimaging findings, although often incidental, remains important as some findings may become pitfalls and recognition potentially may facilitate patient care. Educational Objectives: To become familiar with implants seen in radiologic imaging of patients with glaucoma. To learn about the imaging appearance of complications and sequela of glaucoma.

Purpose

To discuss and show glaucoma-related findings seen in neuroimaging so that radiologists and clinicians may gain basic working knowledge of the condition and the appearance of postsurgical and other related findings of this eye disease.

Materials and Methods

Computed tomography (CT) and magnetic resonance imaging (MRI) examples will be shown to illustrate the educational exhibit's content.

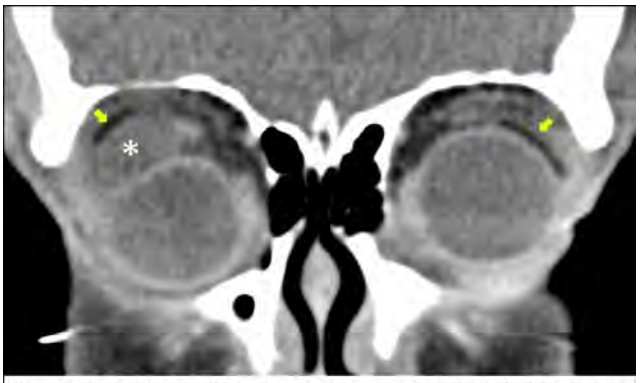

A noncontrast CT scan of the orbits was obtained to evaluate for hypoglobus (inferior displacement of optic globe). This coronal reformatted image shows an approximately 2 cm fluid density focus (asterisk) along the superior aspect of the globe. Lymphangioma and cystic lesions may be of consideration. There are, however, two hypodense bands (yellow arrows), one in each orbit, which are parts of implanted glaucoma shunt reservoirs. The device on the right is abnormally distended with fluid, compatible with a "giant reservoir."

(Filename: TCT_825_ASNR2023abstractglauc.jpg)

1021

Guess WHO? A Pictorial Review of New Brain Parenchymal Tumor Types Introduced in the 5th Edition of the WHO Classification of CNS Tumors.

D Alzate[1], L Gagnon[2], V Goodwill[3], Y Guo[4]

[1]UC San Diego, La Jolla, CA, [2]Department of Radiology, UC San Diego, La Jolla, CA, [3]UCSD, La jolla, CA, [4]UC San Diego, San Diego, CA

Summary and Objectives

Recent advances in molecular testing have led to improved understanding of the behavior of CNS tumors, leading to refinements in their classification, development of more targeted therapy, and better prognostication. We review the new tumor types introduced in the 2021, 5th edition of the WHO classification of CNS tumors, with a focus on brain parenchymal tumors. Awareness of these new entities and their underlying molecular basis of disease will help guide the neuroradiologist with image interpretation within the new classification framework.

Purpose

Identification of CNS tumors is paramount to treatment planning and prognostication. The 5th edition of the WHO classification of tumors of the central nervous system (CNS), published in 2021, built upon the revised 4th edition from 2016 by further delineating the molecular characteristics of CNS tumors. As a result, previously defined tumor types have had revisions, and new tumor types have

been introduced. Awareness of the typical appearance of new tumor types as defined by the 5th edition and the impact of molecular testing on the identification of these tumors will help formulate a working differential diagnosis.

Materials and Methods

We describe our approach to assessing brain parenchymal tumors on imaging. Subsequently, we present the clinical, imaging, histologic, and molecular features of biopsy proven CNS tumors.

Results and Conclusions

Our exhibit features molecularly proven CNS tumors involving the brain parenchyma, with a focus on new entities introduced in the 5th edition within the families of pediatric-type low-grade and high-grade gliomas, circumscribed astrocytic gliomas, and glioneuronal and neuronal tumors.

Axial T2 image of a *high-grade astrocytoma with piloid features (HGAP)* within the cerebellum, the most common location for this tumor type.

Axial 3D T1 image of a *rosette-forming glioneuronal tumor (RGNT)* demonstrating the typical midline posterior fossa distribution.

Axial T2 image of a *multinodular and vacuolating neuronal tumor (MNVT)* featuring the conglomerate and individualized cystic appearance that is typical for this tumor type.

Axial postcontrast T1 image of a *diffuse pediatric-type high-grade glioma, H3-wildtype, IDH-wildtype, subtype RTK1* manifesting as a large, aggressive cyst with a mural nodule in the supratentorial brain.

(Filename: TCT_1021_ASNREducationalExhibitCombinedImages.jpg)

848

Head and Neck, What the Heck? On-Call Prep

L Varanitskaya[1], M Ismoilov[2], N Bondarenko[3], E Grik[4], A Heidenreich[5]

[1]MetroHealth, Cleveland, OH, [2]University of Pennsylvania, Philadelphia, PA, [3]Samara State Medical University, Washington, DC, [4]Lincoln Medical Center, New York, NY, [5]MetroHealth Cleveland, Cleveland, OH

Summary and Objectives

- Presentation of different nontraumatic conditions commonly encountered on call in other imaging modalities. – Review appropriate imaging modalities and protocol to examine these patients according to age, clinical presentation, and risk of development of further complications. – Present in a friendly format to residents and general radiologists with acute head and neck pathologies.

Purpose

In this exhibit, we would like to review nontraumatic head and neck emergencies in an accessible way for residents and general radiologists based on clinical cases. The cases are presented with clinical history and appropriate imaging modalities to understand the diagnosis better.

Materials and Methods

Misdiagnosis or inaccurate diagnosis of these conditions can result in significant morbidity or fatalities, therefore, radiologists should be aware of these diseases and thoroughly investigate each patient for any relevant imaging abnormalities. The complications of inaccurate diagnosis may include airway obstructions; vascular complications (thrombosis, pseudoaneurysm formation, and hemorrhage); spread of the disease to neighboring regions (mediastinum, spine, or intracranial compartments). We are illustrating these conditions with a collection of 25 relevant cases.

Results and Conclusions

Patients with nontraumatic emergency conditions of the head and neck region may present to the emergency department with different symptoms of infectious and inflammatory diseases. Infections of the neck region are the most common than other diseases in this region. Usually, infections in the head and neck region are treated by primary care providers without any complications. However, older patients, patients with diabetes, and immunocompromised individuals have an increased risk of developing complications.

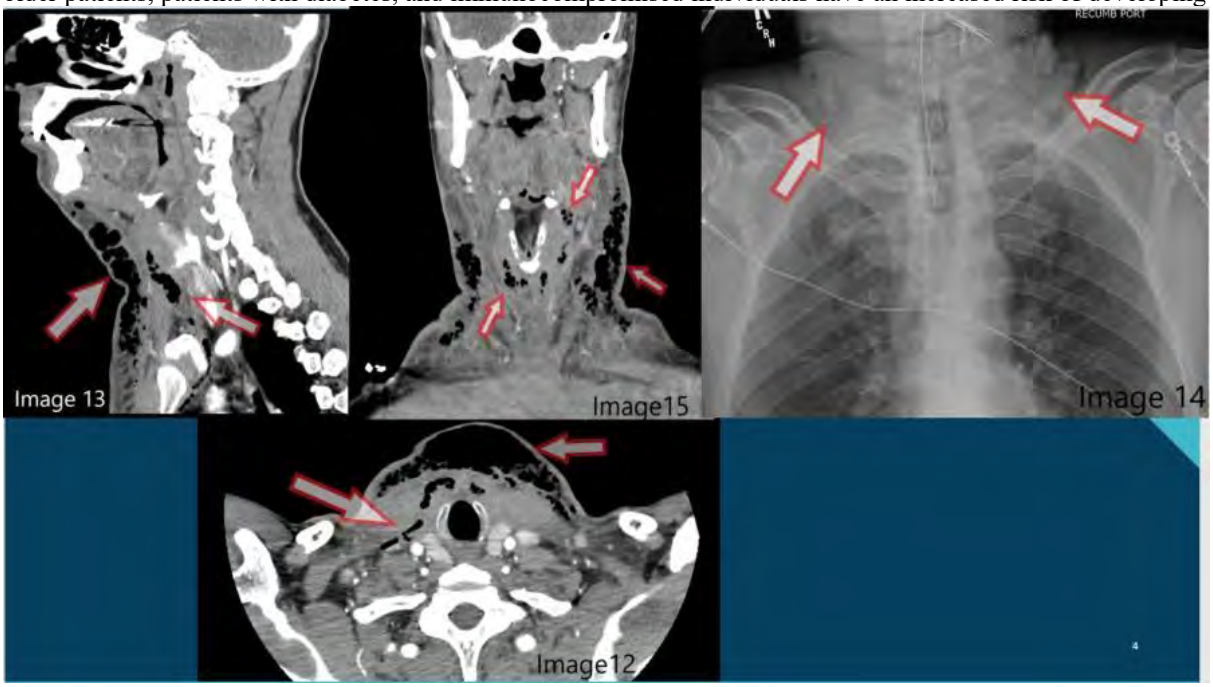

(Filename: TCT_848_pic4.jpg)

794

Imaging Approach to Characteristic Pattern of Leptomeningeal Enhancement on Contrast-Enhanced Fluid-Attenuated Inversion Recovery MR imaging: Looking beyond Infectious Meningitis

E LEE[1]

[1]Dongguk University Ilsan Hospital, Goyang-si, Gyeonggi-do

Summary and Objectives

To understand different mechanisms of both contrast-enhanced T1 weighted imaging (CE-T1WI) and contrast-enhanced fluid-attenuated inversion recovery MR imaging (CE-FLAIR). To describe the characteristic pattern of leptomeningeal enhancement on CE-FLAIR To help narrow the differential diagnosis of leptomeningeal enhancement on CE-FLAIR To evaluate the clinical and prognostic value of leptomeningeal enhancement in each disease.

Purpose
To describe the characteristic pattern of leptomeningeal enhancement on CE-FLAIR To help narrow the differential diagnosis of leptomeningeal enhancement on CE-FLAIR To evaluate the clinical and prognostic value of leptomeningeal enhancement in each disease.
Materials and Methods
1. Fundamental pathophysiologic mechanism of gadolinium enhancement on CE-FLAIR 2. Review of the characteristic pattern of leptomeningeal enhancement (morphology, extension, laterality, and location) 3. Review of various pathologic conditions according to the characteristics of leptomeningeal enhancement (1) meningitis - infection: pyogenic meningitis, viral meningitis, tuberculous meningitis - autoimmune - neurosarcoidosis presenting as leptomeningitis - leptomeningeal inflammation in rheumatoid arthritis (2) Neoplastic spread into the subarachnoid space (primary and metastatic tumors) (3) Hyperglycemia-induced seizures (4) Multiple sclerosis (5) Sturge-Weber Syndrome (6) Blood-brain barrier breakdown in reversible cerebral vasoconstriction syndrome (7) Cerebral amyloid angiopathy related Inflammation with meningeal involvement (8) Post-operative changes (9) Hyperintense acute reperfusion marker (HARM) - HARM sign after acute ischemic stroke - HARM after carotid stent insertion (10) Retention of gadolinium in cerebrospinal fluid (11) Others
Results and Conclusions
CE-FLAIR might offer information not available on CE-T1WI when detecting meningeal disease. Many clinical studies have shown that CE-FLAIR offers more information than CE-T1WI alone. Various diseases can show leptomeningeal enhancement on CE-FLAIR, but differential diagnosis of patients with leptomeningeal enhancement may not be easy. Although the pattern of leptomeningeal enhancement on CE-FLAIR is not indicative of a specific pathology, a detailed study of its characteristics together with underlying clinical data may provide useful information for the differential diagnosis of patients with leptomeningeal enhancement. CE-FLAIR can improve specificity and overall accuracy in delineating and diagnosing various leptomeningeal diseases.

728
Imaging Features and Management of Spontaneous Spinal CSF Leaks
T KALELIOGLU[1], D Joyner[2]
[1]UVA, C/ville, VA, [2]University of Virginia, Charlottesville, VA

Summary and Objectives
Spontaneous intracranial hypotension is a debilitating medical condition caused by loss of CSF, which can occur due to either cranial or spinal sites of leakage. The clinical presentation is often highly suggestive, typically with a positional headache which improves by lying down and worsens with standing. While cranial CSF leaks are often clinically evident due to rhinorrhea or otorrhea, spinal leaks can be more difficult to diagnose. Imaging modalities to localize the site of CSF leaks include radionuclide cisternography, digital subtraction myelography, CT myelography, and spine MRI. Brain MRI should be performed to document findings of intracranial hypotension. Treatment options include conservative management, empiric/nontargeted epidural blood patch, targeted epidural blood patch, sealant injection, or surgical repair. Objectives: Understanding key imaging features of spinal CSF leaks on different imaging modalities. Discussing localization and treatment options.
Purpose
We emphasize the importance of understanding the imaging features of spontaneous intracranial hypertension in patients with spinal CSF leaks as well as minimally invasive treatment options with illustrated diagrams.
Materials and Methods
Cases of intracranial hypotension secondary to CSF leaks have been retrospectively reviewed in PACS from our institution. Didactic cases were selected to illustrate key imaging features. Medical illustrations were created by one of the authors using Procreate digital illustration app.
Results and Conclusions
Familiarity with the spectrum of presentations and causes of SIH is critical to accurate and timely diagnosis and management. Challenges exist in both diagnosis and treatment, and require understanding of the underlying pathogenesis of the condition in order to appropriately select testing and treatment.

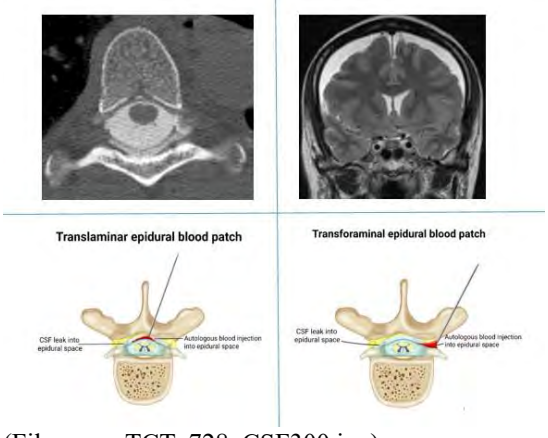

(Filename: TCT_728_CSF300.jpg)

1328

Imaging in Tremor: Spectrum of Case based Multi-modality Pictorial Review

P Suthar[1], J Singh[1]

[1]*Rush University Medical Center, Chicago, IL*

Summary and Objectives

Tremor is an involuntary, rhythmic muscle contraction leading to shaking movements in one or more parts of the body. Clinically tremor classified into two categories, resting tremor and action tremor. Structure and functional neuroimaging techniques valuably diagnose the different etiology of tremor. This educational exhibit demonstrates multimodality neuro and nuclear medicine imaging for the evaluation of tremor etiologies.

Purpose

• Purpose of this educational exhibit is to learn I123 DAT scan protocol, technique, imaging findings and associated false positive and false negative findings in various tremors. • Multimodality comparison and its correlation with conventional CT/MR imaging when available. • To learn post treatment (MRI guided focused ultrasound (MRgFUS)/ DBS) imaging evaluation in tremor.

Materials and Methods

We present a case based multimodality structural and functional neuro-imaging pictorial review (I123 DAT scan, MRI, CT, conventional radiography etc) highlighting the spectrum of different interesting cases of tremor etiologies.

Results and Conclusions

After reviewing this educational exhibit radiologist learn structural and functional neuro-imaging findings in tremor.

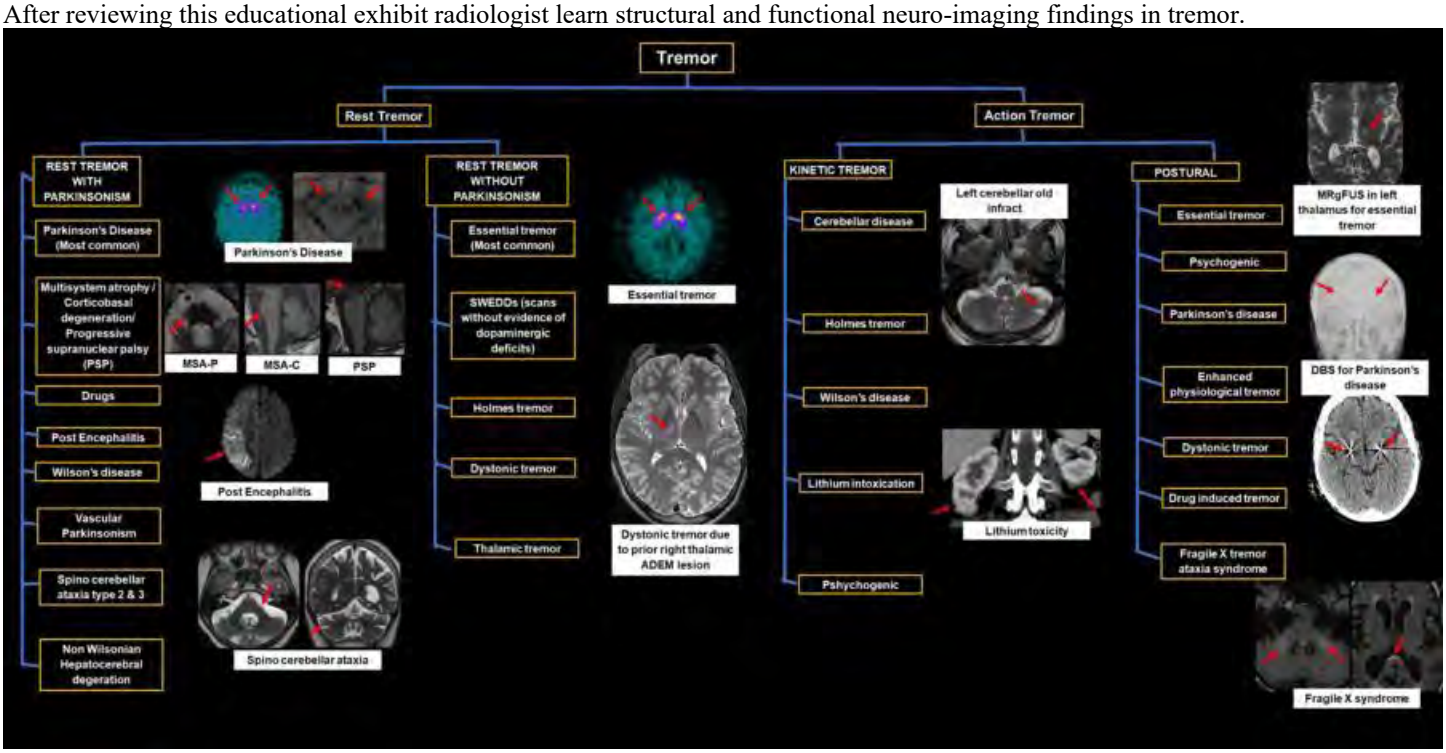

(Filename: TCT_1328_Slide1.JPG)

509

Imaging of Head and Neck Complications of Systemic Lupus Erythematosus

R Alowaisheq[1], S Aldeheshi[1], M Nicolas-Jilwan[2]

[1]*King Faisal Specialist Hospital and Research Centre, Riyadh, Saudi Arabia* , [2]*King Faisal Specialist Hospital and Research Centre, Riyadh, Saudi Arabia*

Summary and Objectives

The head and neck complications of systemic lupus erythematosus are underrecognized and insufficiently discussed in the medical literature. The educational objectives of the presentation are: 1. To present the full spectrum of head and neck manifestations of the disease. 2. To emphasize their imaging features and a systematic approach in reviewing head and neck studies of these patients.

Purpose

The head and neck complications of systemic lupus erythematosus are underrecognized and insufficiently discussed in the medical literature. We present an overview of these with an emphasis on their imaging features and a systematic approach to review head and neck studies of these patients.

Materials and Methods

We selected head and neck CT and MRI studies of adult patients with systemic lupus erythematosus, aged 19 to 48 years. These illustrate the full spectrum of lupus panniculitis of the face, orbits, neck and parotid glands. Also included is a 19 year-old female who

presented with necrotic cervical adenitis and panniculitis. Lymph node biopsy revealed a lymphohistiocytic infiltrate without malignancy or infection. FDG PET showed no uptake. Findings improved on followup. The overall features were supportive of a histiocytic necrotizing lymphadenitis. Additionally, we present the CT and MRI studies of systemic lupus erythematosus patients with subglottic stenosis, salivary gland atrophy and nasopharyngeal lymphoma complicating the disease course.
Results and Conclusions
The medical literature pertaining to the head and neck complications of systemic lupus erythematosus is very scarce. Awareness of the full spectrum of these manifestations of the disease and a systematic review of the head and neck studies of these patients are crucial for an accurate diagnosis.

503

Imaging of intracranial neoplasms. How to read like a pro!

U Chaudhry[1], U Shafique[2]
[1]University of Texas Medical Branch, Galveston, TX, [2]Indiana University School of medicine, Carmel, IN

Summary and Objectives
This educational exhibit aims to provide an easy and up to date approach to intracranial neoplasms. We discuss the three main settings in which a radiologist may encounter these entities. Starting from pre-operative (first time you 'see' the tumor), immediate post-operative and surveillance setting. Individual needs for the read and challenges are addressed with emphasis on a simple checklist.
Purpose
Adult intracranial tumor imaging is a vast topic. With updates in World Health Organization tumor classification in the CNS (2021), as well as new treatment options and trials (such as convection enhanced delivery) it is imperative that the neuroradiologist be aware of these changes and what the referring clinician and patient require. This presentation aims to elevate the day to day reading that the radiologist produces to a level that adds maximum value and efficiency.
Materials and Methods
A background on current classification system is given as a primer with radiology relevant implications. Next important things to know or ask in history of the patient before interpretation are discussed. For example, cell markers, operative reports and treatment options are discussed. Their individual implications are also briefly discussed in each setting. Also briefly reviewed are supplementary imaging such as perfusion, spectroscopy, functional imaging, tractography and PET imaging.
Results and Conclusions
Pre-operative imaging: When a tumor is encountered for the first time. Is it a tumor? Differentials to consider. What important things to include such as location, adjacent structures, and margins? Immediate Post-op period: Importance of imaging within 24-48 hours. Special considerations, such as detecting any infarcts close to the resection bed. These can enhance later and mimic a recurrence. Surveillance: Response Assessment in Neuro-Oncology is reviewed. Challenges and options for assessing recurrence and post treatment changes. New treatment modalities such as convection trials and radiotherapy are discussed.

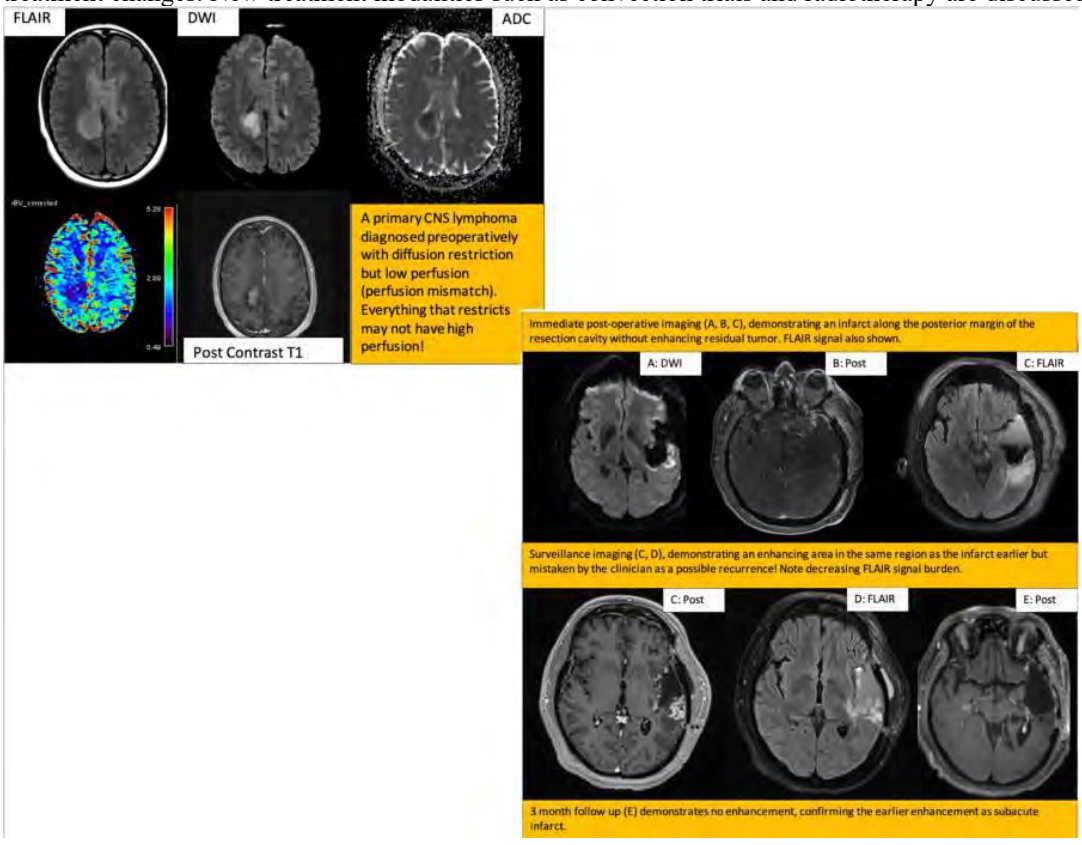

(Filename: TCT_503_ASNRTUMOR.jpg)

973

Imaging of Minimally Invasive Surgical Techniques in Epilepsy – What is the Radiologist's Role and How Can We Add Value

R Gray[1], J Allen[1], L Bonilha[1], D Drane[1], R Hu[1]
[1]*Emory University School of Medicine, Atlanta, GA*

Summary and Objectives

Introduce minimally invasive surgical techniques involved in the evaluation and treatment of refractory epilepsy and review the benefits these techniques have over traditional resective epilepsy surgery Review the role of imaging in the work up and pre-operative planning for minimally invasive epilepsy surgery, including conventional and advanced magnetic resonance (MR) imaging techniques, optimized protocol development, and important findings to tell your surgeon Discuss the role and importance of post-operative imaging of minimally invasive epilepsy surgery, including the expected post-operative appearance for each technique, potential complications, and additional imaging pitfalls

Purpose

Introduction - Epilepsy – epidemiology, common etiologies - Role of imaging in diagnosis - Treatment options: Traditional resective surgery vs alternative minimally invasive techniques Alternative minimally invasive techniques - Nonresective surgical techniques – radiofrequency ablation, MR imaging-guided laser interstitial thermal therapy (LITT) - Neuromodulation – deep brain stimulation (DBS), vagal nerve stimulation (VNS), responsive neurostimulation (RNS) - How does the surgeon decide which technique is best for their patients? Pre-operative work up and the role for imaging - Importance of a multidisciplinary team and discussion in dedicated epilepsy conferences - Non-radiologic diagnostic tools – phase 1 monitoring (scalp EEG and video monitoring), neuropsychological testing --- Possible phase 2 monitoring (stereotactic EEG) - Role of imaging – MR imaging (structural and functional), F18-FDG PET Pre-operative imaging techniques, protocols, and findings - Conventional MR techniques – optimized seizure-specific imaging protocols --- Additional protocols / sequences specific to the planned surgical technique - Advanced MR techniques – role for task-based fMRI and DTI - Important findings to tell your surgeons Post-operative imaging findings - Expected post-operative imaging appearance and findings - Post-operative complications – general and technique-specific - Imaging pitfalls – normal findings that may look abnormal Conclusion

Materials and Methods

N/A

Results and Conclusions

N/A

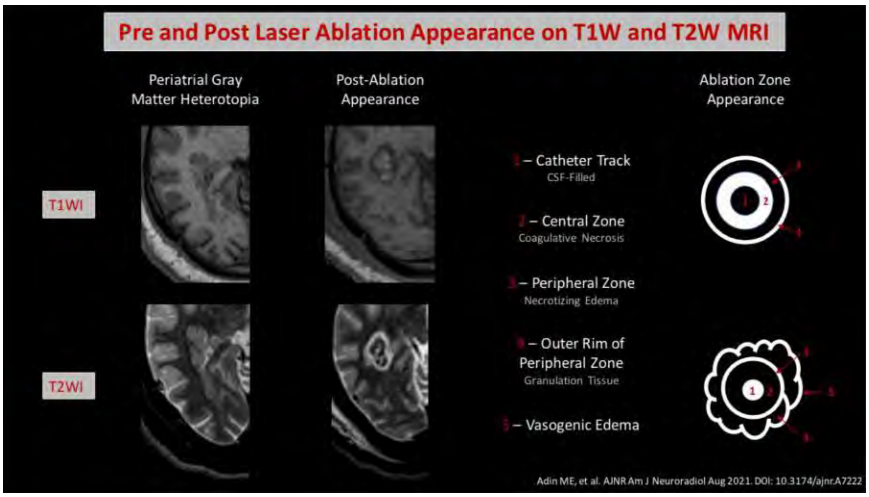

(Filename: TCT_973_ASNR2023AbstractFigure.jpg)

1410

Imaging of Sialolithiasis and Sialadenitis

T Do[1], A Wang[1], A Yu[1], J Gupta[1], N Gupta[1]
[1]*Tulane University School of Medicine, New Orleans, LA*

Summary and Objectives

Sialolithiasis is the presence of stones in the salivary gland ductal system and results from the precipitation of calcium salts on a nidus of epithelial cells, bacteria, or mucus. Sialadenitis is a bacterial infection of the ductal system of the salivary gland, which may be due to acute inflammatory causes or chronic secondary to sialolithiasis. Unilateral gland swelling is present in sialadenitis with pain exacerbated with ingestion of food. Common associations with sialolithiasis include decreased salivary flow, history of tobacco smoking, reduced fluid intake, and diminished saliva secondary to medication. Diagnostic imaging and image-guided interventions serve a critical role in diagnosis, treatment, and surveillance of sialolithiasis. Sialolithiasis and sialadenitis treatment include both conservative and surgical management. In this presentation, we describe three patients with sialolithiasis of which two patients developed sialadenitis. Characteristic findings of sialolithiasis using ultrasound, computed tomography (CT), and magnetic resonance

imaging (MRI) will be delineated and discussed. Additionally, we will review the current epidemiology, comorbidities, pathophysiology, and complications of sialolithiasis and sialadenitis. Educational Objectives - Describe epidemiology, associations, and complications of sialolithiasis and sialadenitis - Discuss the mechanisms for pathophysiology of sialolithiasis and sialadenitis - Recognize the key clinical features and diagnostic criteria for sialolithiasis and sialadenitis - Define characteristic imaging findings of sialolithiasis and sialadenitis - Discuss the role of imaging in guiding treatment and surgical planning

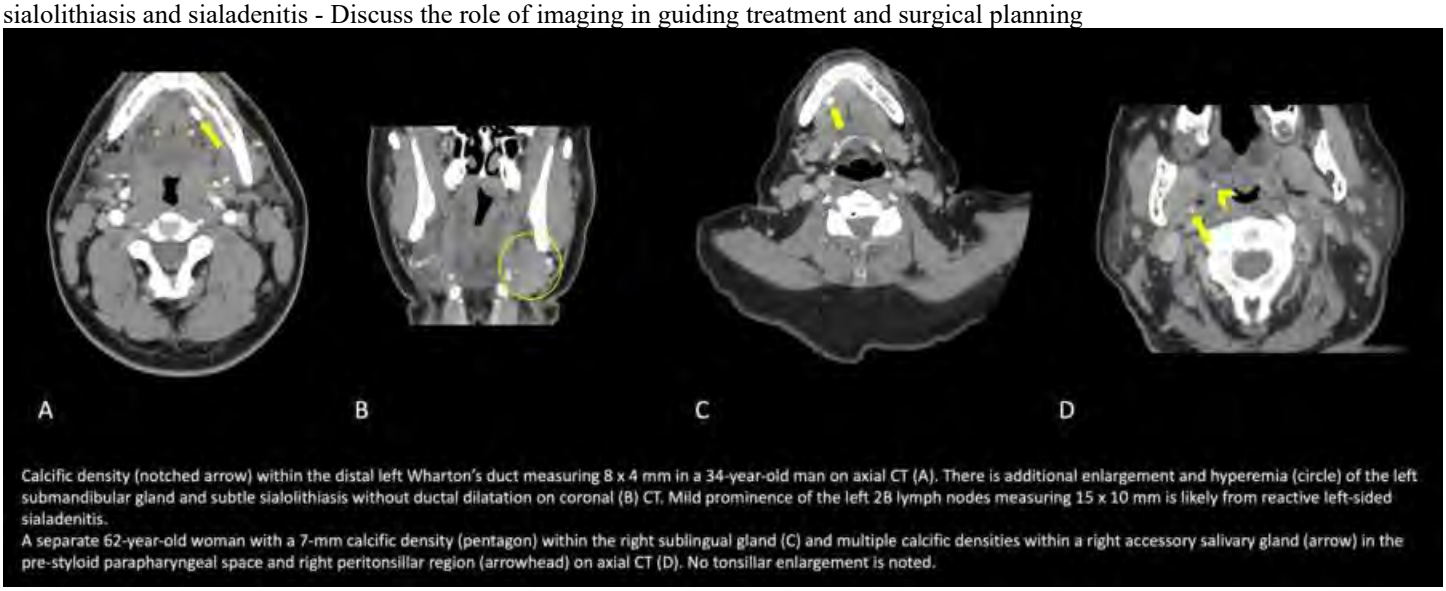

Calcific density (notched arrow) within the distal left Wharton's duct measuring 8 x 4 mm in a 34-year-old man on axial CT (A). There is additional enlargement and hyperemia (circle) of the left submandibular gland and subtle sialolithiasis without ductal dilatation on coronal (B) CT. Mild prominence of the left 2B lymph nodes measuring 15 x 10 mm is likely from reactive left-sided sialadenitis.
A separate 62-year-old woman with a 7-mm calcific density (pentagon) within the right sublingual gland (C) and multiple calcific densities within a right accessory salivary gland (arrow) in the pre-styloid parapharyngeal space and right peritonsillar region (arrowhead) on axial CT (D). No tonsillar enlargement is noted.

(Filename: TCT_1410_ASNRGraphic.jpg)

1446
Imaging of the Craniocervical Junction Anatomy and Traumatic injuries
A Zeinoddini[1], D Yousem[2]
[1]UTMB-Galveston, Galveston, TX, [2]Johns Hopkins Medical Institution, Evergreen, CO

Summary and Objectives
• To describe the relevant craniocervical osseo-ligamentous anatomy • To describe classification of post traumatic craniocervical injuries • To identify the common post traumatic craniocervical injuries • To discuss potentials pitfalls of post traumatic craniocervical injuries
Purpose
Craniocervical junction traumatic injury is a challenging topic for radiologic residents. Here, we provided a practical educational source for traumatic injury of the Craniocervical junction.
Materials and Methods
Please refer to the uploaded image. We will describe the osseoligamentous anatomy of the craniocervical junction and then we will categorize the traumatic injuries into craniocervical dislocation, ligamentous injuries , bony injuries and their pitfalls.
Results and Conclusions
Atlanto-occipital Joint Dissociation Classification: The Traynelis classification system: based on the displacement of the occipital condyle relative to the C1 (Atlas). The AO Spine classification of upper cervical injuries: is part of type C fractures (any injury with displacement in CCJ). How to Diagnose AOD on CT? Measurements: Basion-dens interval (BDI) >10 mm in adults: highly suggestive of dissociation Power's Ratio >1 Condyle-C1 Interval (CC1I) <2.5 mm Lateral Mass Interval (C1-C2) Basion-dens interval (BDI) >10 mm in adults: highly suggestive of dissociation Which ligaments will be injured in AOD? The tectorial membrane and alar ligaments are the main stabilizers of the atlanto-occipital joint, given the low inherent atlanto-occipital osseous stability. Examples of ligamentous injuries will be provided. Occipital condyle fractures: C1 fracture: Jefferson fracture: C2 Fracture: Odontoid fractures: Hangman fracture Atlantoaxial distraction and atlantodental instability Pitfalls of craniocervical junction injuries:

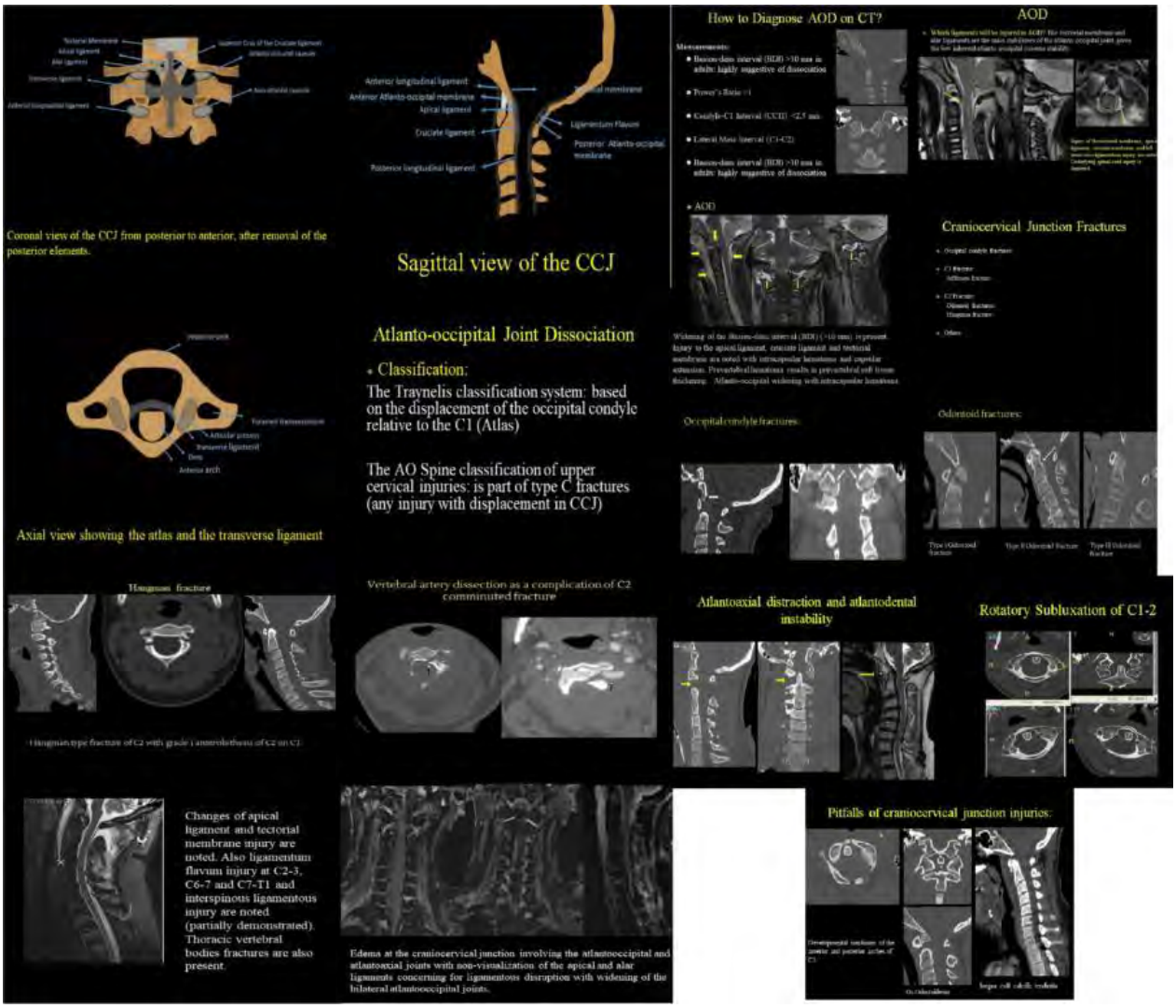

(Filename: TCT_1446_Fig1-4.jpg)

456

Imaging of the Pediatric Cranial Sutures in Abusive Head Trauma

S Kriss[1], A Sarma[2], S PRUTHI[2]

[1]Vanderbilt University School of Medicine, Nashville, TN, [2]Monroe Carell Jr Children's Hospital at Vanderbilt, Nashville, TN

Summary and Objectives

Skull fractures are seen in one third of abused children under age 2 and in 41% of abusive fatalities. Nuanced understanding of skull fracture characteristics is essential to differentiating abusive from accidental head trauma—both false positive and negative diagnoses may lead to devastating outcomes. Recent advances indicate that certain fracture patterns with respect to the patent cranial sutures are more highly associated with abusive head trauma (AHT), a helpful adjunct in AHT workup. In this educational exhibit we: 1. Review skull fracture findings in AHT (diastasis, depression, comminution, greater than 3 terminal ends, and bilateral/multiple fractures) including differentiation of normal skull variants from fractures. Examples include accessory sutures, particularly near the lambdoid sutures that lead to diagnostic dilemmas with posterior head trauma, common in AHT. 2. Explore AHT-associated fractures with the cranial sutures such as skull fracture widening or crossing sutures. We also discuss a more specific skull fracture finding associated with AHT: skull fracture that contacts 2 or more cranial sutures. A variety of interactive imaging cases will be shown to test the reader on which skull fractures are concerning for abuse. 3. Recommend possible AHT imaging protocol changes. Given the variable and often multiple skull fractures with high-energy AHT mechanisms, 3D-CT is an important tool for adequately imaging and confirming abusive fracture association with the cranial sutures. Robust literature supports the assertion that 3D-CT obviates the need for concurrent skull radiographs. However, skull radiographs are often still obtained as a component of radiographic skeletal surveys for suspected abuse. Like other authors, we recommend changing standard skeletal survey protocols to eliminate skull radiographs IF head CT (particularly 3D-CT) has been obtained. 4. Discuss ultrashort TE/zero TE MRI as an emerging modality for head trauma with image quality similar to 3D-CT. Decreasing acquisition times (currently ~5 min) may bring this technique into common clinical usage. Educational Objectives: Discuss characteristic abusive skull fracture findings with attention to the pediatric cranial sutures: fractures crossing, widening, or contacting two or more cranial sutures are more highly associated with AHT. Summarize data supporting the recommendation to eliminate concurrent skull radiographs IF helical head CT (3D-CT) is obtained.

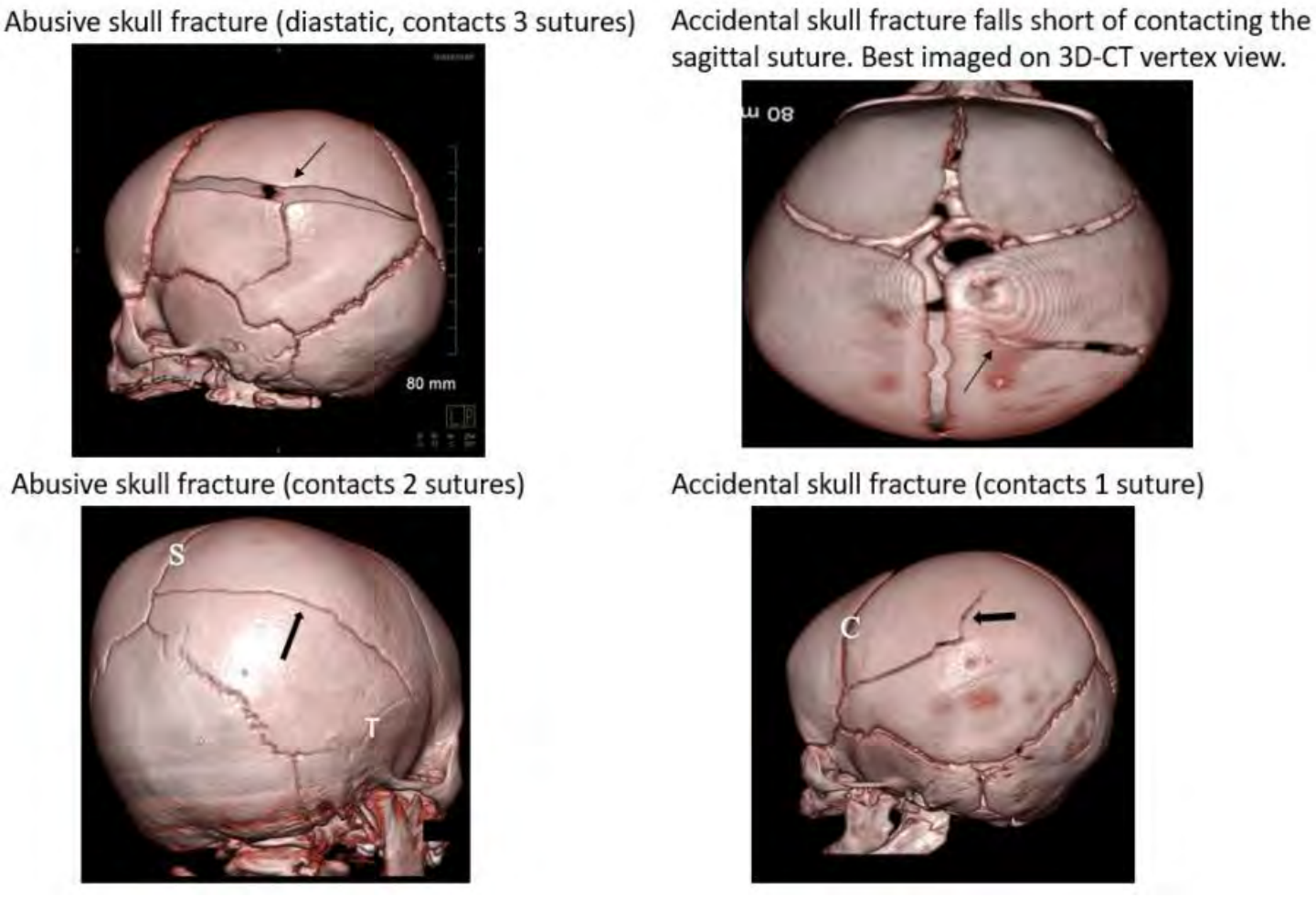

(Filename: TCT_456_KrissASNR2023AbstractImage.jpg)

1180

Imaging Pearls and Pitfalls of Brachial Plexus Pathologies: MR imaging features of traumatic and inflammatory plexopathy

J Lee[1], C Liang[1], A Lerner[1], V Patel[2], P Kim[1], R Assadsangabi[1]

[1]Keck Medicine of USC, Los Angeles, CA, [2]Mayo Clinic, Jacksonville, FL

Summary and Objectives

MRI is the imaging modality of choice for understanding the anatomy and pathology of the brachial plexus (BP), but remains challenging to interpret. The objective of this exhibit is to provide a brief clinical guide to approach the following cases: 1) Normal imaging of the brachial plexus 2) Traumatic neuroma 3) Pseudomeningocele

Purpose

Damage to the BP can result in serious neurological sequelae and compromise of the upper extremity. MRI can help distinguish between pre- and post-ganglionic injury which is critical for effective management. [1] However, interpretation of BP imaging remains challenging because of complex anatomy, shared features with other diseases, and the low frequency of cases. Reviews of normal and abnormal BP imaging often lack practical, stepwise guidance for interpretation. [2,3] The purpose of this educational exhibit is to provide an effective approach toward imaging diagnosis of complex BP pathologies on MR, highlight imaging pearls and pitfalls, and provide clinical and pathological correlates for salient image findings.

Materials and Methods

We queried our institutional database for patients with BP pathologies on 3 T MRI in a systematic approach based on several findings: 1) Predominant local thickening 2) Location in the upper plexus 3) Arm edema and sensory symptoms in patients

Results and Conclusions

We present 3 illustrative cases of BP imaging through this exhibit, including 1 case of normal anatomy and 2 cases of trauma and inflammation as shown in Figures 1 - 4. BP injury can be devastating, and classification of these injuries remains challenging for radiologists due to the complex anatomy and clinical correlations. After reviewing this exhibit, we expect viewers will have a stronger understanding of traumatic and inflammatory plexopathies and will refer to this guide as an additional resource when reviewing BP pathology.

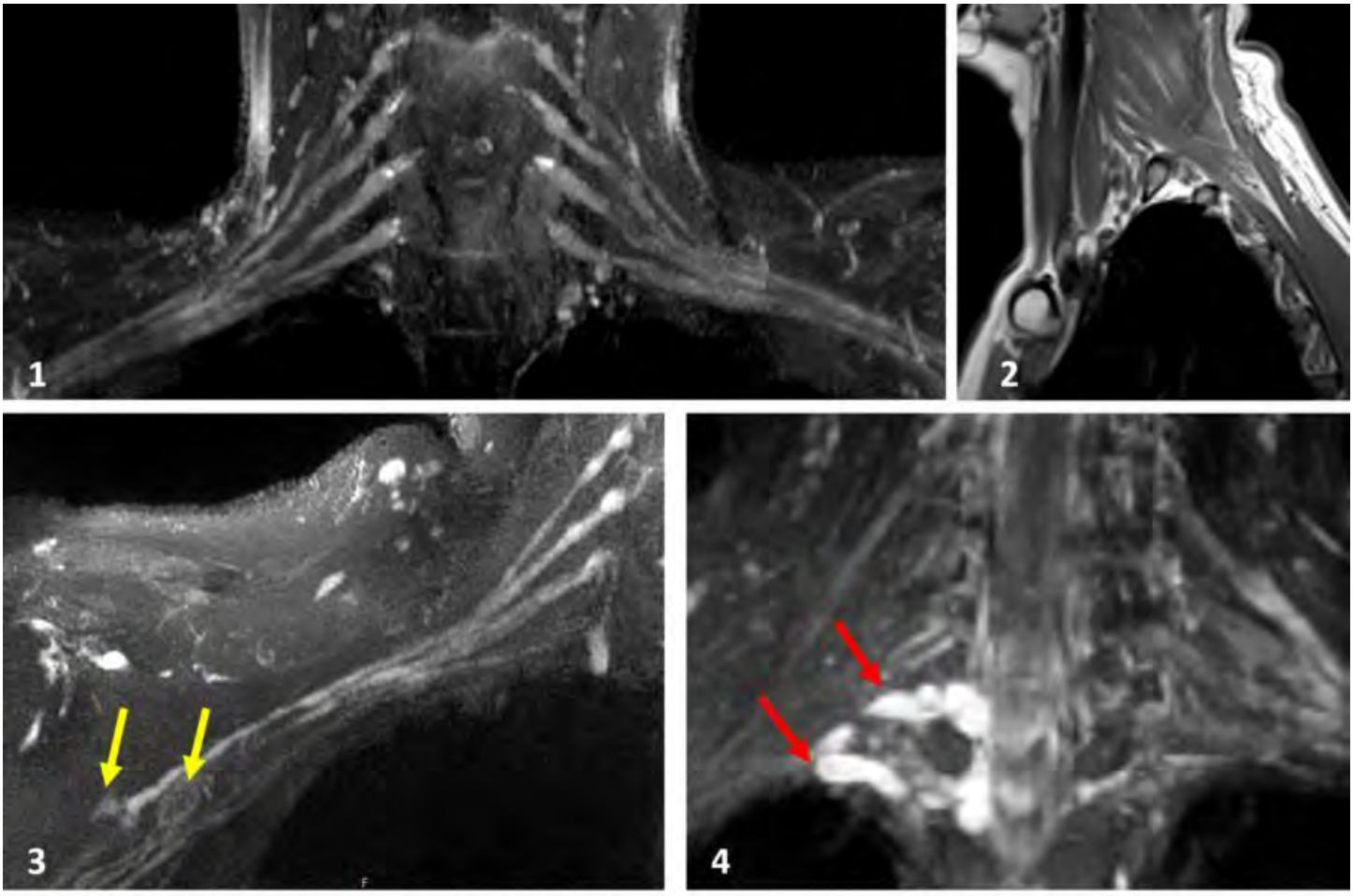

Figure 1: Normal coronal imaging anatomy of the brachial plexus
Figure 2: Normal sagittal imaging anatomy of the brachial plexus
Figure 3: Traumatic neuromas involving the lateral and posterior cords of the right brachial plexus, consistent with axonotmesis
Figure 4: Pseudomeningoceles of C8 and T1 nerve roots through trunk

(Filename: TCT_1180_Figures-01.jpg)

1103

Imaging Spectrum of Paragangliomas of the Head and Neck

R Suazo Aguero[1], N Madan[1]
[1]*Tufts Medical Center, Boston, MA*

Summary and Objectives
Paragangliomas are neuroendocrine tumors that originate from the paraganglia of the autonomic nervous system, with the majority arising in the head and neck. The most common locations in the head and neck are the carotid body, jugular foramen, middle ear and along the course of the vagal nerve. Their characteristic feature is over expression of somatostatin receptors. While most of the cases are sporadic, there is a strong hereditary predisposition and genetic testing is currently recommended among patients and relatives. The classic manifestation is a non-tender enlarging neck mass, pulsatile and associated with bruit, sometimes pulsatile tinnitus and in the case of vagal nerve involvement, hoarseness. At the end of this review, you will be able to: 1. Understand the utility of multimodality imaging for paragangliomas. 2. Differentiate a benign paraganglioma from a potentially more aggressive tumor. 3. Identify treatment strategies for paragangliomas, including directed peptide therapy. 4. Strategize the best imaging approach for patient's with a genetic predisposition, with concern for multifocal or metastatic disease.
Purpose
To learn the common anatomic locations of paragangliomas in the head and neck and understand imaging hallmarks on cross-sectional imaging including, CT, MR, MRA and nuclear medicine studies. To acknowledge theranostics as an additional treatment option.
Results and Conclusions
Paragangliomas in the head and neck commonly occur within the carotid space, jugular foramen, middle ear and along the course of the vagal nerve. These are hypervascular tumors which demonstrate avid enhancement on post contrast imaging modalities and each type has their own characteristic imaging findings. Understanding imaging hallmarks and anatomic involvement impact subsequent management decisions for the patient. While CT and MR techniques provide excellent anatomic characterization, nuclear medicine

studies are preferred when there is concern for multifocal or metastatic disease. Therapeutic nuclear medicine is increasingly becoming a treatment option to consider, in addition to surgery and radiation.

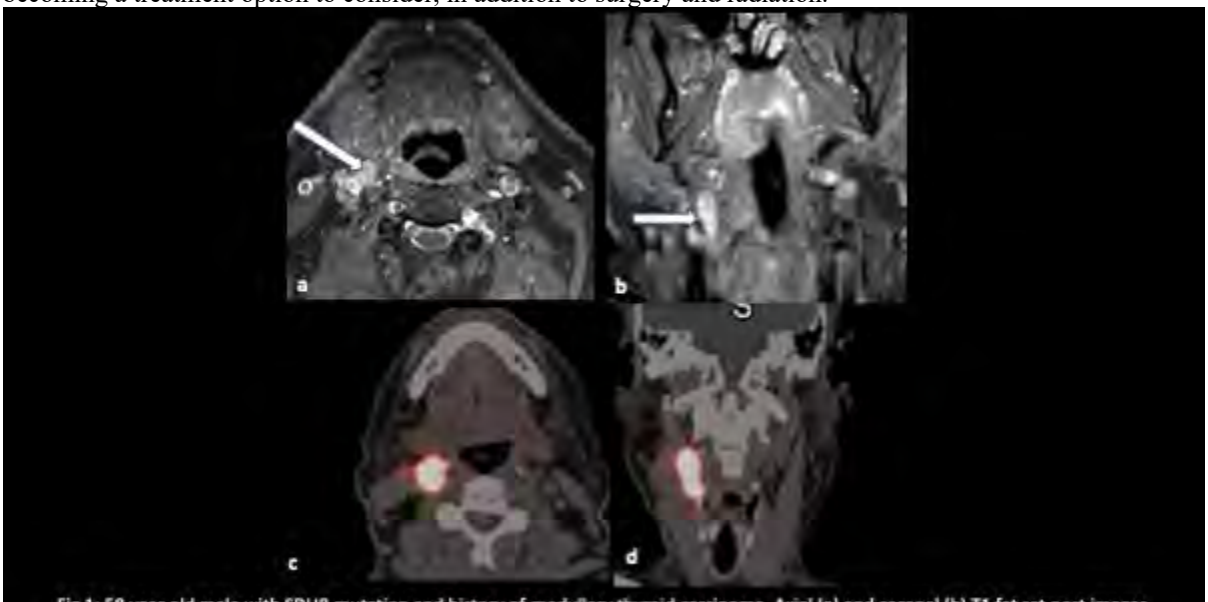

Fig 1: 58 year old male with SDHB mutation and history of medullary thyroid carcinoma. Axial (a) and coronal (b) T1 fat sat post images demonstratre a well defined avidly enhancing mass in the carotid space (arrow). Axial (c) and coronal (d) fused Ga 68 DOTATE PET/CT images show an increased radiotracer uptake in the right carotid space. Pathology revealed Carotid body Paraganglioma.

(Filename: TCT_1103_paraganglioma.jpg)

948

Imaging Spectrum Of Pediatric Diffuse High-Grade Gliomas In Correlation With Molecular Diagnosis

A Jaju[1], S Budhiraja[2], N Wadhwani[3], M RYAN[4]

[1]Ann and Robert H Lurie Children's Hospital of Chicago, Chicago, IL, [2]Northwestern University Feinberg School of Medicine, Chicago, IL, [3]Lurie Children's Hospital, Chicago, IL, [4]ANN & ROBERT H. LURIE CHILDREN'S HOSPITAL OF CHICAGO, CHICAGO, IL

Summary and Objectives

One of the major changes incorporated in the 2021 WHO classification of CNS tumors is the separation of diffuse gliomas into 'adult type' and 'pediatric type', acknowledging the biological and prognostic differences between the two. The pediatric diffuse high-grade gliomas differ from adult gliomas by the absence of IDH mutations and high frequency of histone H3 mutations. The 'pediatric type' diffuse high-grade gliomas have been subclassified into four types, which are described below. The purpose of this educational exhibit is to illustrate the typical and atypical imaging appearances of these different subtypes, in correlation with the specific molecular diagnoses. A discussion of imaging findings that are relevant to the treatment and prognosis of these tumors will be included. A brief overview of emerging diagnostic and therapeutic approaches will also be provided. Diffuse midline glioma, H3K27-altered: The typical presentation is an expansile, T2 hyperintense mass involving the ventral pons, although rarely they can be centered in the dorsal pons. Approximately 20% of these tumors arise in the thalamus (unilateral thalamic or bithalamic), and rarely they can arise in this spinal cord. Diffuse hemispheric glioma, H3 G34-mutant: These present as large hemispheric masses with a variable degree of cyst formation, hemorrhage, and calcifications, with surrounding vasogenic edema. Diffusion restriction and post-contrast enhancement are common. Diffuse pediatric-type high-grade glioma, H3-wildtype and IDH-wildtype: Both IDH and histone mutations are absent, however can demonstrate a variety of other different genotypes. Although more commonly supratentorial, these can be seen in infratentorial and midline locations. Infant-type hemispheric glioma: These are tumors of early childhood that exhibit high-grade astrocytic histologic features with alterations in ALK/ROS1/NTRK/MET. Typically present as a large, heterogeneous appearing tumor with intratumoral hemorrhage. Astrocytoma, IDH-mutant: Included under 'adult-type' diffuse glioma, although rarely seen in children (6%). Image Caption: Six different imaging examples of pediatric-type diffuse high-grade glioma: (a) 'typical' ventral pontine H3K27-altered, (b) 'atypical' dorsal pontine H3K27-altered, (c) bithalamic H3K27-altered, (d) spinal cord H3K27-altered, (e) hemispheric H3 G34R mutant, (f) 'adult-type' IDH-mutant, (g) and (i) diffuse, infiltrating H3-wildtype and IDH-wildtype

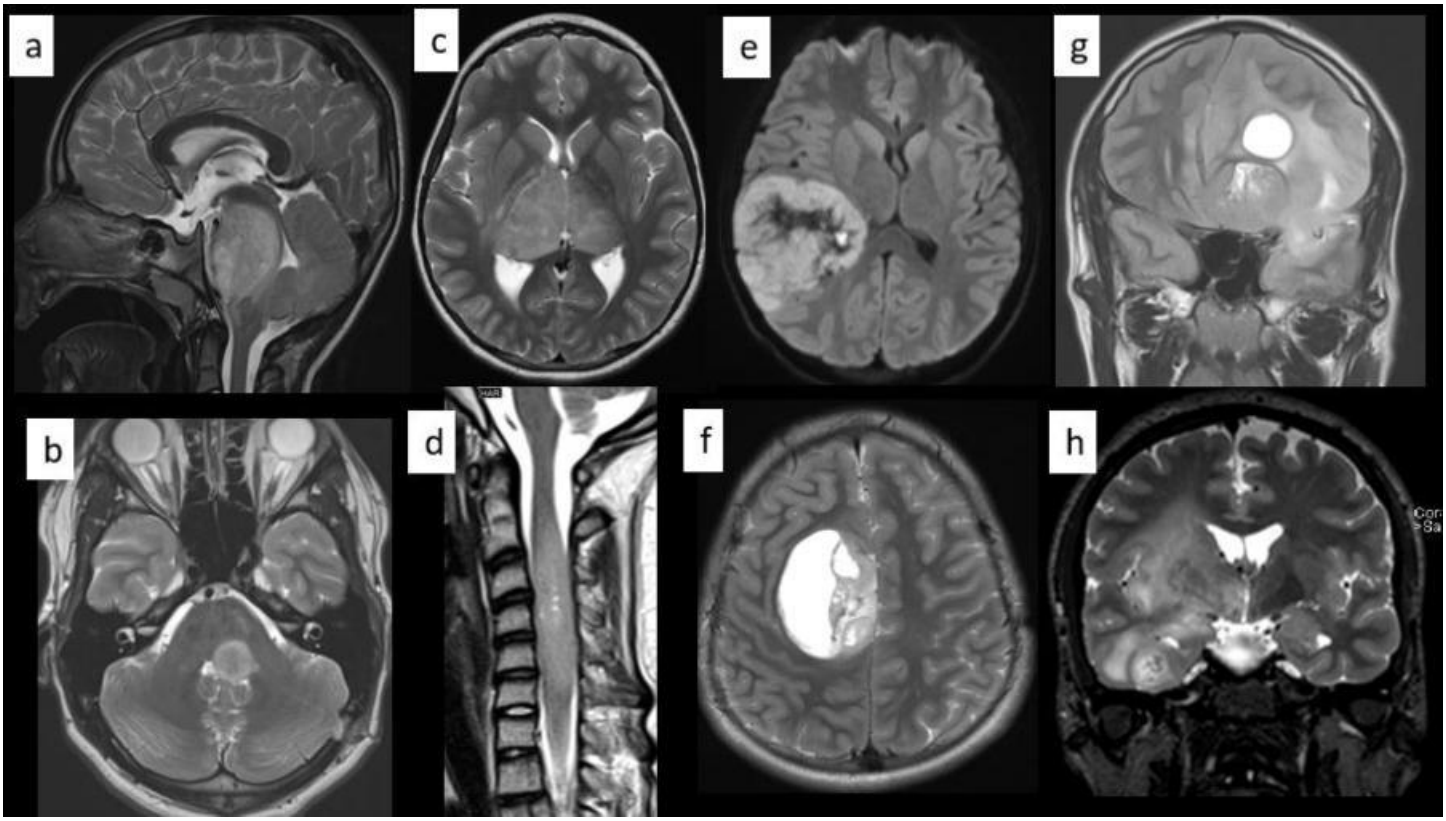

(Filename: TCT_948_collage.JPG)

682

Improving Patient MRI Access: a Few Tips and Tricks from a Neuroimaging Perspective

C Pritchard[1], C Horsley[1], H Sotoudeh[1], K Porter[1], A Singhal[1]
[1]University of Alabama at Birmingham, Birmingham, AL

Summary and Objectives

As imaging volumes continue to increase, it is increasingly important to use MRI scanner time, a limited resource, judiciously. This is especially important in neuroimaging, which accounts for a large proportion of MRI volume. Decreasing scan time improves patient access to MRI, increases tolerability, and decreases motion. In recent years, our department has taken steps to improve access to MRI, specifically with regard to neuroimaging, as we will discuss here. Optimizing MRI protocol selection increases efficiency (1). We codified our protocols to be indication-based, e.g., for dementia, stroke, epilepsy, and combined indications, amongst others. This reduces protocol selection time and improves throughput. Another approach to be discussed is abbreviated protocols designed to answer a clinical question, with extraneous sequences removed, e.g., for pituitary and internal auditory canal. We have abbreviated total spine protocols based on clinical concern, e.g., for metastases or cord compression. Chang et al. found that an abbreviated total spine protocol using only sagittal STIR and axial T2 sequences was noninferior to standard MRI in detecting spinal cord and cauda equina compression with significantly reduced scan time (2). We will discuss vendor specific technologies which can obtain multiple sequences/orientations within one acquisition, including Siemens GoBrain and GE MAGiC. Other technologies include compressed sensing (can reduce acquisition times by 50%) and simultaneous rather than sequential image acquisition. All vendors have options to reduce the audible noise of scans, which can improve the patient experience and decrease motion, minimizing repeated sequences. Recently, vendor neutral software is using deep learning to improve image quality, allowing for reduced scan time, e.g., Subtle (3). In a nutshell, optimizing MRI scanner time utilization efficiency requires a collaborative, interdisciplinary team effort and benefits patient access.

200

In Tune with an ARIA: A Radiologist's Guide to Complications of Amyloid Immunotherapy

C Wheeler[1], R Shahidi[2], M Alizadeh[3], P Shobeiri[4], M Natelson Love[5], H Sotoudeh[1]
[1]UAB Heersink School of Medicine, Department of Radiology, Birmingham, AL, [2]School of Medicine, Bushehr University of Medical Sciences, Bushehr, Iran, [3]Iran University of Medical Sciences, Tehran, Iran, [4]School of Medicine, Tehran University of Medical Sciences, Tehran, Iran, [5]UAB Heersink School of Medicine, Department of Neurology, Birmingham, AL

Summary and Objectives

This exhibit will cover: 1. Future burden of Alzheimer's on healthcare and radiology 2. Established pathophysiology of Alzheimer's disease 3. Hypothesized mechanism of investigational amyloid-modifying drugs and risk factors for ARIA 4. Radiologist's role in identification of ARIA 5. Diagnostic criteria for ARIA-E and ARIA-H subtypes with severity grading scale 6. Teaching cases

(Clinicoradiological case series with interactive questions for knowledge application) 7. Practical tips for optimizing workup, surveillance, and communicating findings Teaching Points: 1. Review the mechanism of new investigational therapies for Alzheimer's disease, specifically monoclonal antibodies designed to reduce cerebral amyloid-beta burden. 2. Become familiar with the nomenclature of ongoing clinical trials, which reveal that these disease-modifying agents can cause reactive changes detectable on neuroimaging, known as amyloid-related imaging abnormalities (ARIA). 3. Appreciate the radiologist's role in ARIA and the need for close collaboration with treating physicians, who can provide a relevant history key to making the diagnosis. 4. Develop an awareness of specific criteria to reference in the literature when identifying subtypes of ARIA and grading severity. 5. Learn to recognize findings in context and alert the neurologist to potential complications, even in asymptomatic cases. Appreciate that ARIA-type changes can mimic other pathologies. 6. Develop an understanding of appropriate MR imaging to optimize evaluation and follow-up, including T2-weighted FLAIR sequence for ARIA-E and T2*-weighted GRE/SWI for ARIA-H.
Purpose
With the advent of Alzheimer's immunotherapy and recent FDA approval of Aducanumab, radiologists will increasingly encounter ARIA in the clinical workplace. Accelerated greenlighting of these drug agents underscores the urgency for both neuroimagers and general practice radiologists to familiarize themselves with treatment complications. Moreover, it will be incumbent upon the radiologist to adequately protocol these studies for evaluation and recommend appropriate follow-up.
Materials and Methods
A pictorial review of the imaging spectrum of ARIA will be presented.
Results and Conclusions
A select number of high-yield cases will be presented to demonstrate the spectrum of ARIA and progression/resolution over time. By honing the radiologist's clinical acumen and diagnostic checklist, this exhibit can improve accurate interpretation and quality of patient care by minimizing errors of perception.

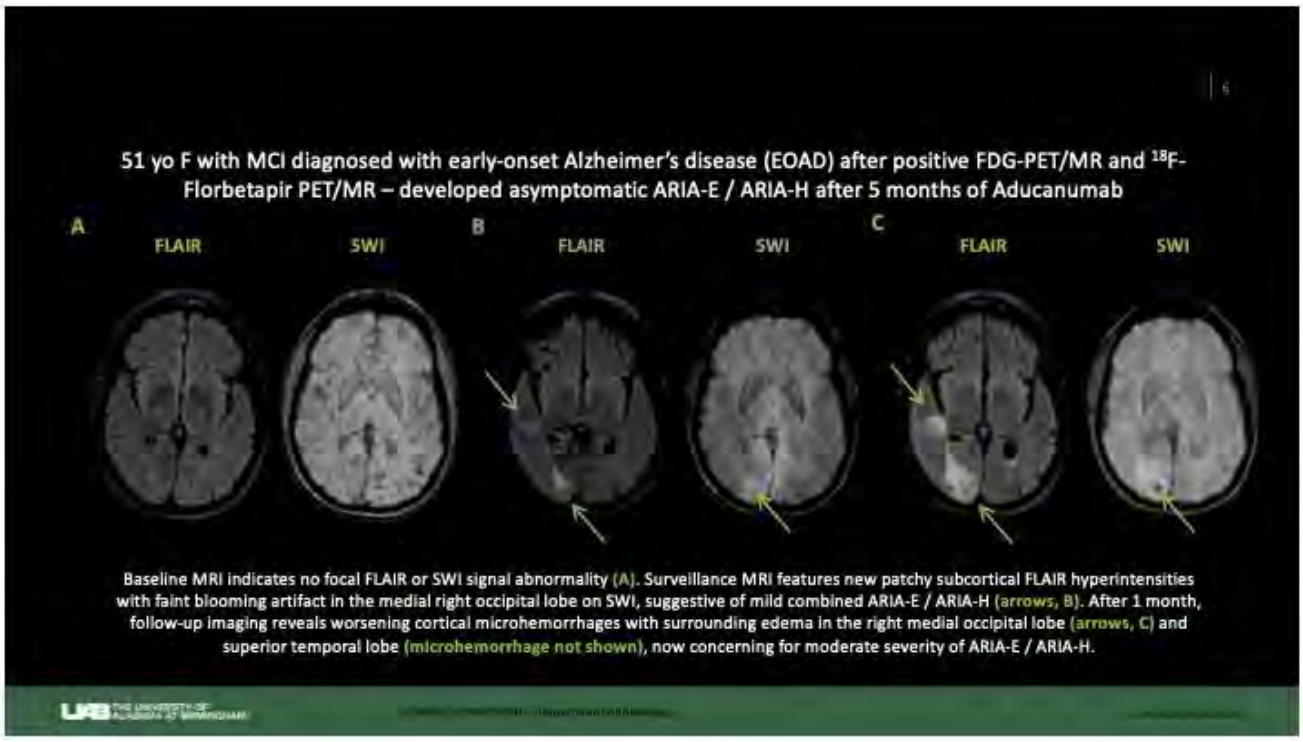

(Filename: TCT_200_ASNR22ARIAFigure.jpg)

1138
Incidentally Detected Thyroid Nodules on CT - The Thyroid Incidentalomas
B Rathore[1], J Joyce[2]
[1]University of Cincinnati Medical Centre, Cincinnati, OH, [2]UC Health, Cincinnati, OH

Summary and Objectives
· Case wise demonstration of spectrum of thyroid incidentalomas on CT Neck with subsequent diagnosis. · Each case will be discussed with relevant key radiological and clinical findings. · Discussion of pertinent radiologic findings that should serve as 'Danger signs'
Purpose
· Demonstration of spectrum of incidental thyroid nodules detected on CT Neck. · To explain the radiographic findings in thyroid nodules which merit further evaluation.

Materials and Methods
Retrospective evaluation of CT Neck contrast and non-contrast studies will be performed for Thyroid Nodules. The final diagnosis of thyroid nodules with thyroid ultrasound images and pertinent clinical findings will be discussed.
Results and Conclusions
After reviewing this educational exhibit, the viewer will be able to better appreciate the clinical significance of incidentally detected thyroid nodules. They will also have an improved understanding of pertinent radiologic findings to guide further management where appropriate.

(Filename: TCT_1138_Screenshot2022-11-15203810.jpg)

726
Inflammatory Arthritis of the Spine
T KALELIOGLU[1], D Joyner[2]
[1]UVA, C/ville, VA, [2]University of Virginia, Charlottesville, VA

Summary and Objectives
Spondyloarthropathy is an umbrella term for a group of chronic inflammatory rheumatic diseases that predominantly affect the spine including ankylosing spondylitis, reactive arthritis, psoriatic arthritis and enteropathic arthritis. Differentiation of axial spondyloarthropathy from other conditions including spondylosis, DISH, and infectious spondylodiscitis is vital for correct patient management. MR imaging is especially sensitive for detection of early or active inflammatory involvement, while radiographs and CT are often better able to demonstrate bone proliferation and ankylosis. Objectives: - Review spine anatomy - Understand key imaging features of inflammatory spondyloarthropathy and its complications such as fracture, pseudarthrosis and arachnoiditis. - Review imaging features of other conditions that are sometimes confused with spondyloarthropathy to prevent misdiagnosis.

Purpose
We emphasize the importance of understanding normal spine anatomy and key imaging features of inflammatory spondyloarthropathy and its complications with illustrated diagrams.
Materials and Methods
Multiple cases from our institution have been retrospectively reviewed in PACS. Didactic cases were selected to illustrate imaging features of a variety of disorders. Medical illustrations were created by one of the authors using Procreate digital illustration app.
Results and Conclusions
We review normal spine anatomy and key imaging features of inflammatory spondyloarthropathy, its complications, and mimics with illustrated diagrams.

(Filename: TCT_726_spine300.jpg)

189
Intracranial Dural Arterio-Venous Fistula: A Pictorial Review of Imaging Findings.
P Nguyen[1], J Gajera[2], H Bell[3], J Rajah[1], T Jo[1], P Phadke[1], R McConnell[1]
[1]Nepean Hospital, Kingswood, NSW, [2]Royal North Shore Hospital, St Leonards, NSW, [3]Royal Hobart Hospital, Hobart, TAS

Summary and Objectives
Educational Objectives: 1. Illustrate the radiographic features in the classification of intracranial dAVFs 2. Describe the imaging findings in the multimodal evaluation of intracranial dAVFs
Purpose
Dural arteriovenous fistulas (dAVFs) represent 10-15% of intracranial vascular malformations and are typically encountered in middle-aged adults. Anatomically they are described as an abnormal connection between a dural artery and a dural venous sinus or cortical vein. The clinical presentation may be benign or aggressive and, in a few patients, dAVFs follow a progressive clinical course despite intervention. Structural imaging modalities such as CT angiography (CTA) and MR angiography (MRA) have a role in screening and risk stratification based on lesion grading, location, and pattern of drainage as specified in the Borden and Cognard criteria, respectively(1). Non-invasive imaging is accurate in diagnosing parenchymal abnormalities, haemorrhage, vascular dysfunction and retrograde leptomeningeal venous drainage reflux, the latter considered a prognostic hallmark(2,3). We provide a pictorial review of the multimodal imaging of intracranial dAVFs and tips for specific diagnosis.
Materials and Methods
A literature search using Medline, Embase and Cochrane databases was performed. Images obtained from our institution were utilised for illustration of the radiographic findings.

Results and Conclusions
Digital subtraction angiography is considered the most accurate method for the complete characterisation and classification of dAVFs. Quantitative assessments such as direction of flow or number of anastomoses are often assessed with 3D time-resolved and time-of-flight MRA. CTA in dAVFs may demonstrate cerebral oedema secondary to venous congestion or intracranial haemorrhage. Typical MR findings with non-haemorrhagic manifestations may include: cerebral sinus venous thrombosis; parenchymal oedema; engorged intradural vessels; dilated venous pouches; flow-voids on T2-weighted imaging; prominent cortical veins on susceptibility-weighted imaging; and asymmetrical contrast opacification of the jugular veins. Presence of intraparenchymal haemorrhage, subarachnoid haemorrhage or ischaemic stroke predicts aggressive manifestation. dAVFs represent a potential treatable entity which may pose a risk for severe disability if unrecognised.Clinicians should be aware of the imaging features and risk stratification of dAVFs to facilitate early multidisciplinary team discussion and consideration of management.

336

Intraventricular lesions: review of cerebrospinal fluid circuit and differential diagnosis

J Brunelli[1], S Alves[2], I Alves[2], C Amancio[2], C Barbosa[2], C Leite[3]
[1]Hospital Sírio-Libanês, São Paulo, AK, [2]Hospital Sírio-Libanês, São Paulo, São Paulo, [3]University of São Paulo, Sao Paulo, São Paulo

Summary and Objectives
Through this pictorial essay will be made a review based on cases and original drawings about the cerebrospinal fluid (CSF) circuit, and intraventricular lesions that can interrupt this flow. Intraventricular pathologies will be addressed by typical imaging patterns (such as diffusion restriction, cysts, solids with or without enhancement) and an algorithm to narrow differential diagnoses. Table of Contents / Outline: ANATOMICAL CONCEPTS • Ventricular system and MRI anatomy CEREBROSPINAL FLUID DYNAMICS • Classical CSF Flow • The new CDF Dynamics INTRAVENTRICULAR LESIONS • Didactic algorithm of imaging differential diagnosis • Imaging aspects of intraventricular pathologies INTERACTIVE CASE-BASED DIDACTICS • Sample cases to illustrate and solidify the concepts
Purpose
The purpose of this exhibition is to: - Review the anatomy of the Ventricular System; - Describe how is the cerebrospinal fluid circulation according to the classic and the new theories; - Recognize the main etiologies of intraventricular lesions, according to their main MR imaging findings; - Organize the radiologic reasoning with an algorithm.
Materials and Methods
After a retrospective analysis of the medical records and MRI of our digital archive we illustrated a pictorial essay on the radiological findings of the mains etiologies of intraventricular lesions. We selected the images from well-documented cases with established diagnosis.
Results and Conclusions
The "cerebrospinal fluid (CSF) circulation theory" of CSF flowing unidirectionally and circulating through the ventricles and subarachnoid space has been widely recognized. Today, a shared consensus regarding CSF motion is being formed, as follows: CSF motion is not a circulatory flow, but a combination of various directions of flow in the ventricles and subarachnoid space. Intraventricular lesions of the central nervous system (CNS) can present a diagnostic challenge due to a range of differential diagnoses and radiological appearances. The imaging findings, in combination with location and patient's age, can help limit the differentials. The discovery of an intraventricular mass poses the challenge of correctly deriving a focused differential diagnosis. Patient age, lesion location and imaging findings together can assist to narrow the differential diagnosis of intraventricular lesions in an otherwise heterogeneous group of conditions.

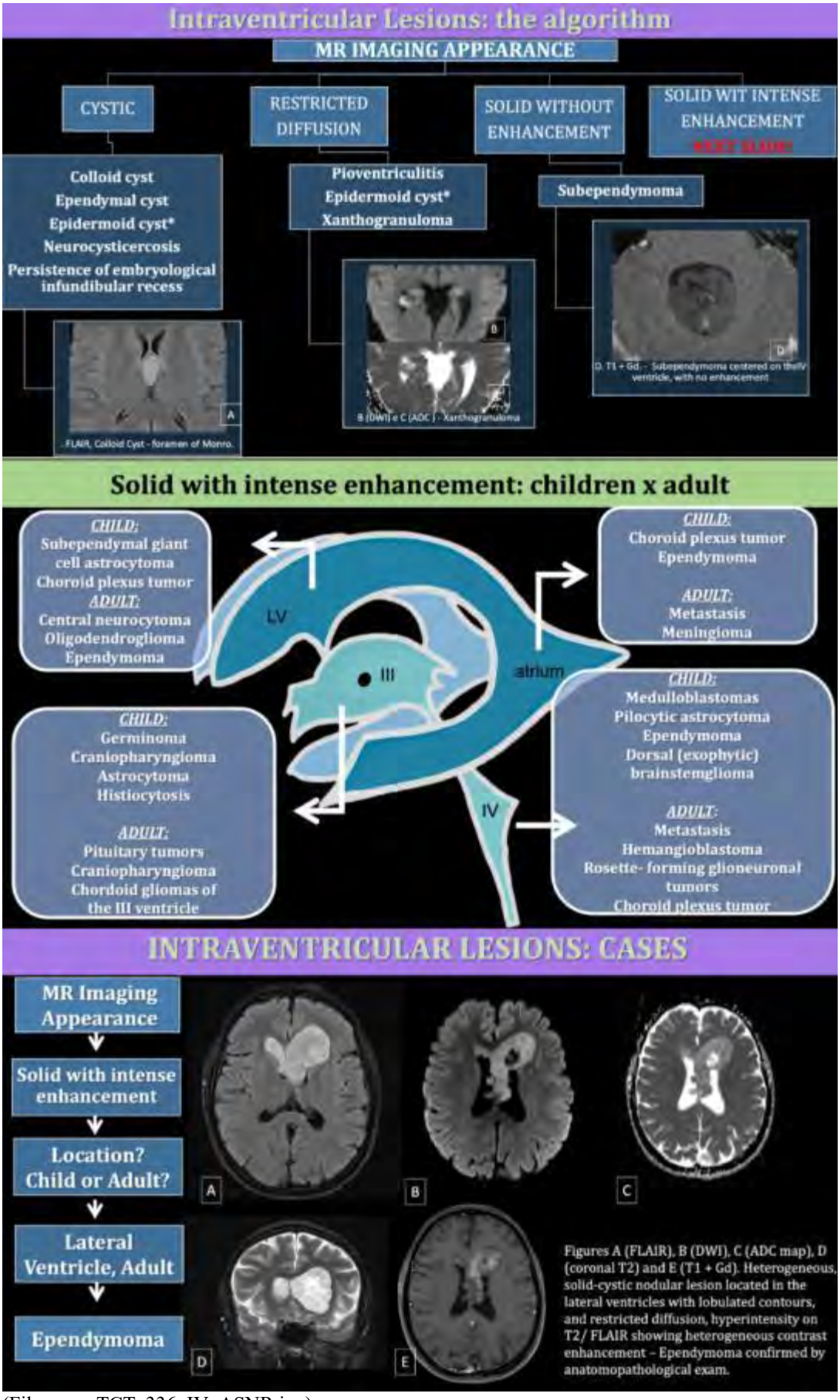

(Filename: TCT_336_IV_ASNR.jpg)

1029

Labyrinthitis ossificans: different pathways, similar outcome

E Bonfante-Mejia[1], L Nunez[2], A Rodriguez[2]
[1]UTHealth, Houston, TX, [2]The University of Texas Health Science Center at Houston, Houston, TX

Summary and Objectives
Labyrinthitis is an inflammatory disorder of the inner ear that most commonly results from an infectious process. Additional causes include inflammatory conditions, temporal bone trauma, hemorrhage, and tumors. Acute labyrinthitis is usually self-limited, resulting in complete resolution of symptoms and imaging findings. Progression of this condition may lead to labyrinthitis ossificans, which consists of pathological ossification of the peri lymphatic spaces. The scala tympani of the basal turn of the cochlea is the most frequently involved site. This process disrupts the transmission of sensory information from the ear to the brain, leading to irreversible sensorineural hearing loss, vertigo, vomiting, and visual disturbances. Cochlear implantation may effectively restore hearing function in patients with sensorineural hearing loss. CT and MRI play complementary roles in the assessment of acute and chronic labyrinthitis. We analyze a series of cases of labyrinthitis ossificans with emphasis on the imaging features that guide the differential diagnosis. Educational objectives: - To illustrate different causes of labyrinthitis ossificans using a case-based format. - To describe the imaging features that help with the differential diagnosis.

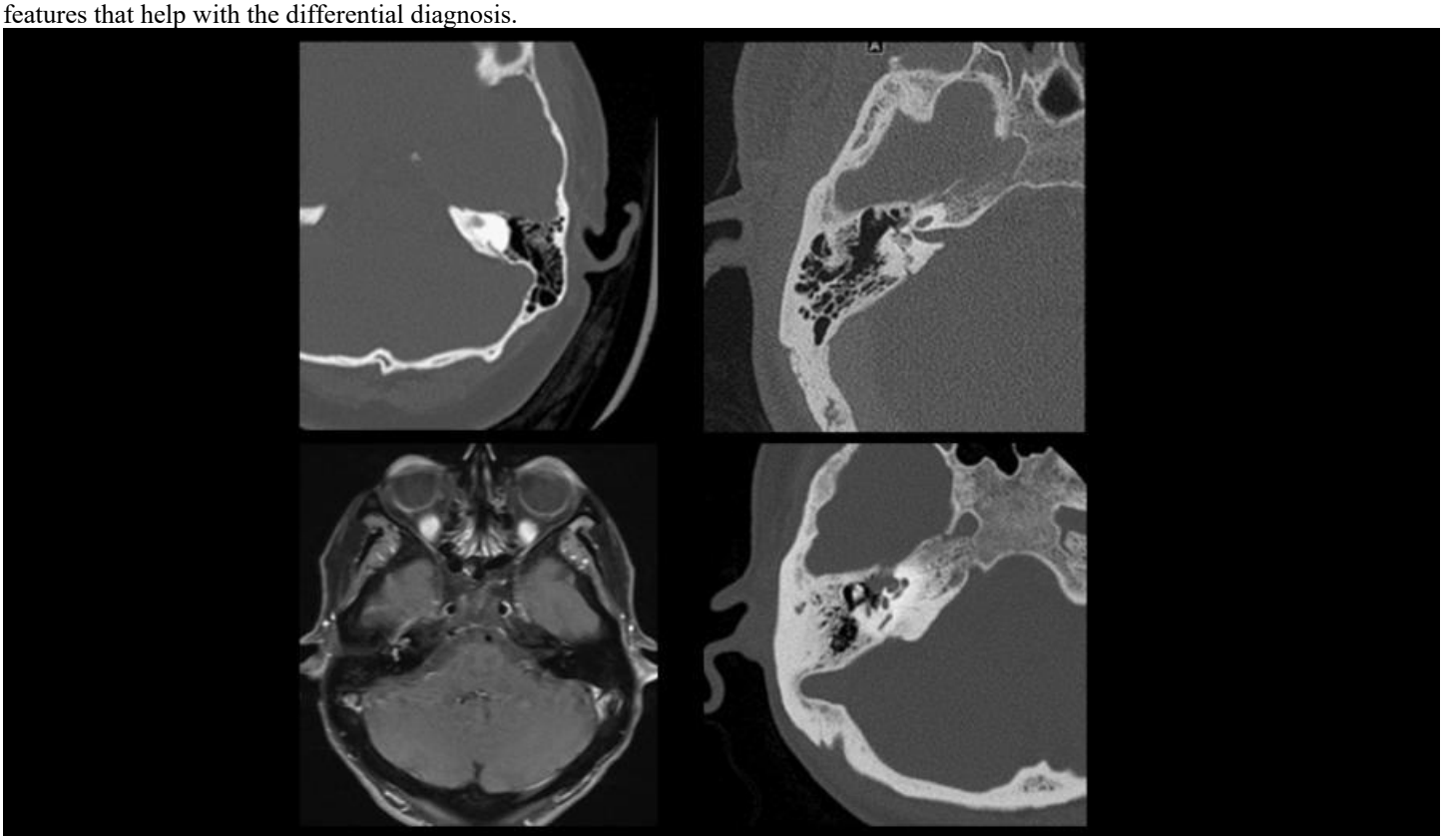

(Filename: TCT_1029_Labrynthitisossificansimage.jpg)

1066

Let's Evacuate Before We Herniate: Radiologic Determinants of Emergent Operative Management and a Review of Neurosurgical Clinical Practice Guidelines in TBI

M McCartney[1], C Kendall[1], K Soderlund[1], V Makler[1], C Carroll[1]
[1]Naval Medical Center Portsmouth, Portsmouth, VA

Summary and Objectives
Distill the broad array of grading schemes surrounding traumatic brain injury into a succinct, organized, and actionable guide to the interpreting neuroradiologist to effectively communicate imaging features that are crucial to the neurosurgeon in determining the need for operative management.
Purpose
Traumatic brain injury is a dynamic process in which the mechanism and location of injury can drastically alter the pathophysiology and management. The complex array of imaging presentations including injuries from blunt or penetrating trauma, intraaxial and extraaxial manifestations, and the timeline of primary and secondary effects have prevented a single grading schema from being universally accurate or adopted. While TBI is initially triaged with the Glasgow Coma Scale, imaging has substantially decreased TBI-associated mortality. CT and MR allow for early detection of emergent findings that may be initially clinically occult, guiding treatment and redirecting the course from further injury. An understanding of the various existing classification schemas with their

nuanced strengths and weaknesses can equip the radiologist with the tools to classify the injury and to expeditiously communicate key features which may require neurosurgical intervention in a timely manner.
Materials and Methods
We will discuss the various injury types and associated findings that require emergent operative management. We will principally refer to both radiologic criteria and various neurosurgical clinical practice guidelines. We will demonstrate key features of epidural, subdural, intraventricular, subarachnoid and parenchymal injuries. Imaging patterns will include various hemorrhagic lesions with significant hematoma thickness, large hematoma volume, herniation patterns, compression of basilar cisterns, and findings consistent with active bleeding. We will also demonstrate evolution of imaging findings to include increasing contusions, varying extent of mass effect, as well as herniation. We will provide MR correlates to CT findings. Finally, we will demonstrate pitfalls in diagnosing emergent findings, and discuss intraoperative correlate findings. We will conclude by synthesizing key metrics for operative management and proposing a search pattern for patients with brain injury.
Results and Conclusions
After participating in this educational exhibit, radiologists will be up to date in the current trends in diagnosing severe brain injury and conveying key features in an efficient manner to guide neurosurgical management.

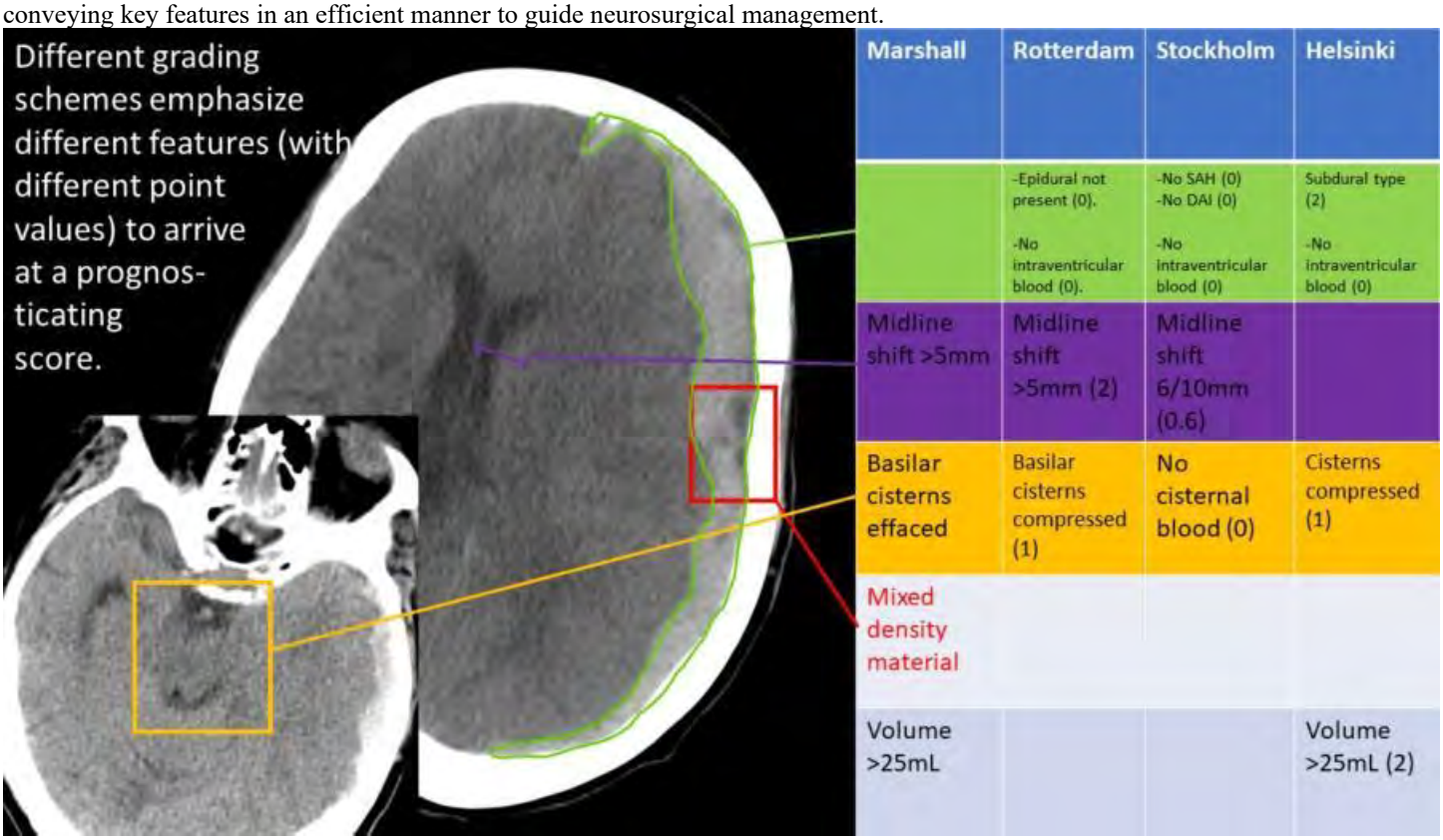

(Filename: TCT_1066_sampleimage1.jpg)

774
Let's Get Hyphae: A Review of the Subtypes of Invasive Fungal Rhinosinusitis
S Girn[1], E Kuoy[2], E Shin[1], E Kuan[3]
[1]UC Irvine Medical Center, Orange, CA, [2]University of California, Irvine, Irvine, CA, [3]University of California Irvine, Orange, CA

Summary and Objectives
Background information: The two major subtypes of invasive fungal rhinosinusitis (IFS) include acute invasive fungal rhinosinusitis (AIFS) and chronic invasive fungal rhinosinusitis (CIFS). AIFS is a rapidly progressive infectious process characterized by tissue and vascular invasion with associated high mortality. Broadly, it is a disease process that primarily afflicts the immunocompromised. More specifically Zygomycetes species such as Mucor, Rhizopus, Rhizomucor, and Absidia spp. affect diabetic patients and Aspergillus species affect severely neutropenic patients. Concern for AIFS should be highest when an immunocompromised patient presents with symptoms such as vision change, diplopia, proptosis, or cranial neuropathy. In comparison, CIFS has a prolonged course usually longer than 12 weeks which may not necessarily afflict immunocompromised patients. Educational Objectives: -Learn the epidemiology of IFS -Understand imaging findings suggestive of IFS on CT and MR -Be able to list the risk factors most associated with IFS by subtype -Be able to explain similarities and differences between subtypes of IFS -Be able to explain similarities and differences between the common differential considerations and mimics for IFS such as chronic sinusitis, sinonasal carcinoma, and sinonasal lymphoma -Be aware of common treatment strategies for IFS and possible post-treatment imaging findings
Purpose
The incidence of IFS has been increasing in recent decades. Radiologists should be aware of clinical scenarios and imaging features suggestive IFS. AIFS is a fulminant process where early detection and treatment can improve outcome. This educational exhibit will

review the presentation, epidemiology, subtypes, imaging findings, risk factors/associations, differential considerations, and treatments/complications of IFS.
Materials and Methods
A review of the literature on IFS will be performed. Case examples will be obtained from our institutional database to create this educational exhibit in a case-based review format. Examples will include classic rhinosinusitis features, aggressive orbital and intracranial extension, fulminant retrograde perineural spread, and cases that largely spare the sinoasal cavities.
Results and Conclusions
Table of Contents: I. Subtypes II. Epidemiology III. Typical imaging findings (see below for example) IV. Associations/Risk Factors/Presentation V. Differential considerations VI. Treatment strategies with posttreatment imaging findings VII. Complications

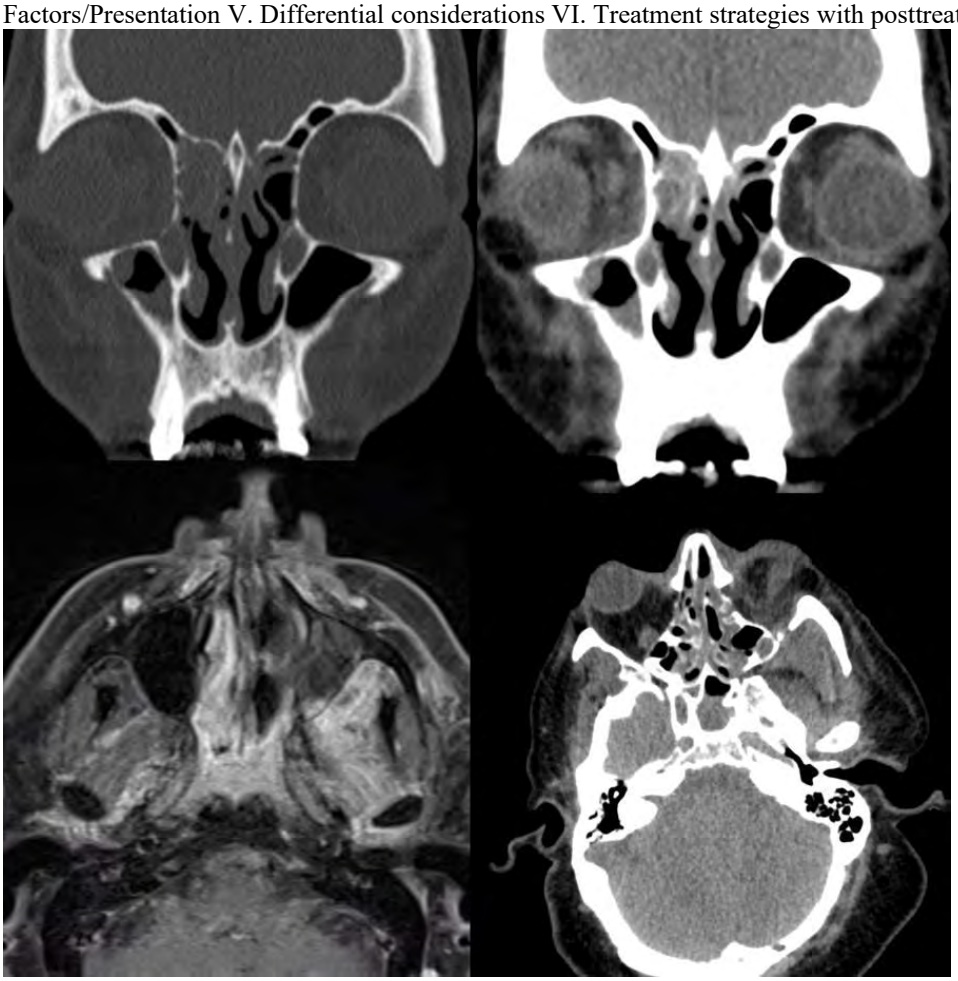
(Filename: TCT_774_sampleimage.jpg)

1491
Limbic Predominant Age-Related TDP-43 Encephalopathy: A Newly Recognized Entity with Hippocampal Atrophy
C Christensen[1], Y Anzai[1]
[1]*University of Utah, Salt Lake City, UT*

Summary and Objectives
Limbic-predominant age-related TDP-43 encephalopathy (LATE) is a recently recognized amnestic neurodegenerative disorder that can mimic and co-exist with other disorders, including Alzheimer's dementia (AD). LATE has distinct pathological, epidemiological, and radiologic imaging manifestations that distinguish it from other neurodegenerative disorders, including AD. LATE commonly affects individuals in extreme old age (i.e., >80 years old) and demonstrates a unique pattern of volume loss, often in concert with hippocampal sclerosis. It is critical that radiologists understand the features that distinguish LATE from other disorders to ensure that patients are accurately diagnosed and receive appropriate management.
Purpose
Our primary objectives are as follows: 1. Explore the imaging and clinical manifestations of LATE. 2. Distinguish LATE from other neurodegenerative disorders including AD.
Materials and Methods
The authors identified 417 consecutive subjects who underwent both brain MRI exams with brain volumetry using NeuroQuant and brain FDG-PET/CT from 2019-2021. Among these, 18 subjects 75 years or older demonstrated hippocampal volume corresponding to the 10th normative percentile or less compared to age-matched controls. After excluding one subject with severe traumatic brain

injury, the FDG-PET imaging for the remaining 17 subjects was then evaluated to correlate patterns of metabolic brain activity with the patterns of volume loss characteristic of various neurodegenerative disorders.
Results and Conclusions
Among the 17 subjects with hippocampal volume corresponding to the 10th percentile or less, five subjects demonstrated some distinguishing features of LATE, six subjects exhibited patterns of volume loss consistent with AD and LATE, three had dominant features of AD, and three had features of both frontotemporal lobar degeneration and AD. Structures more severely affected in patients with both AD and LATE included the parietal lobes. Although LATE features may predominate, particularly in individuals >80 years old, LATE often co-exists with other neurodegenerative disorders. It is essential that radiologists recognize that in addition to AD, hippocampal atrophy in elderly patients with cognitive can be seen with a variety of pathologies, including LATE. Continued efforts to recognize and differentiate these disorders will help to ensure patients undergo appropriate therapeutic intervention.

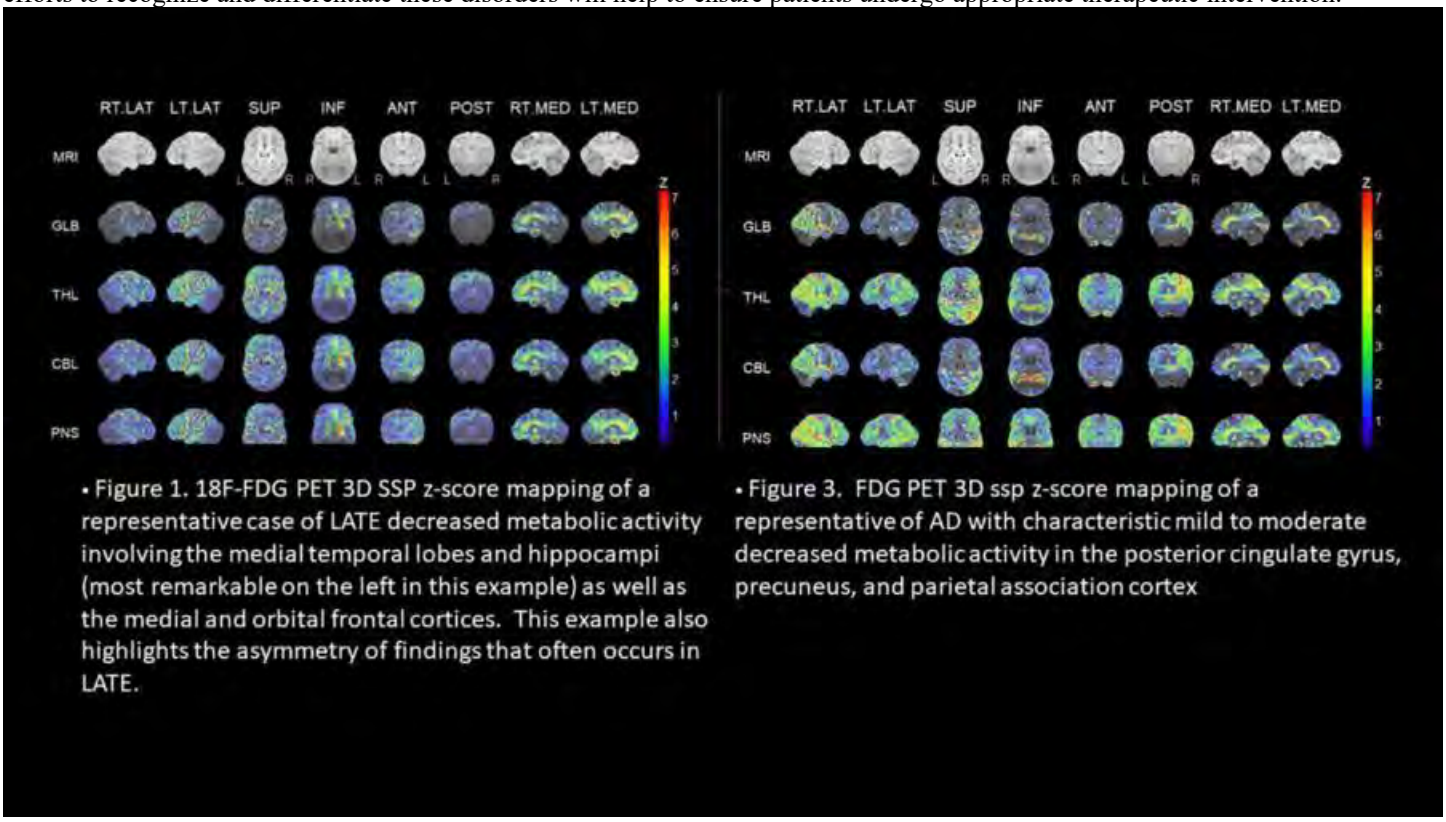

(Filename: TCT_1491_LATEAbstractImages.jpg)

743

Literature Review and Current Guidelines of MRI Safety in Neurostimulators

V Pai[1], S Hiremath[2], A Boutet[3], W Lam[4], R Chan[5], P Jabehdar Maralani[1]
[1]University of Toronto, Toronto, Ontario, [2]The Hospital for Sick Children, Toronto, Ontario, [3]Toronto Western Hospital, Toronto, Ontario, [4]Sunnybrook Research Institute, Toronto, Ontario, [5]Sunnybrook Research Institute, Toronto, ON

Summary and Objectives
1. To review the concepts of static magnetic fields, gradient fields and RF pulse in the context of MRI safety 2. To review concepts of Specific Absorption Rate (SAR) and B1+rms 3. To review the MRI safety concerns of commonly used neurostimulators
Purpose
To provide an up-to-date resource of the current practices related to MR imaging of patients with neurostimulators. This would be useful for radiologists and technologists to adequately triage and safely scan patients with these devices/implants.
Materials and Methods
Neurostimulators are typically composed of electrodes, implanted to achieve necessary neuromodulation, connected to pulse generator (or audio processor for cochlear implants). When placed in a magnetic field, safety concerns include heating, current induction, device movement or alterations of function. A detailed review of literature on the MRI safety concerns and published practice recommendations in the context of the following neurostimulators will be discussed: 1. Deep Brain Stimulator 2. Spinal Cord Stimulator 3. Cochlear Implant 4. Vagal Stimulator 5. Sacral Nerve Stimulator
Results and Conclusions
Historically, MRI in patients with neuroaugmentative devices/implants was considered an absolute contraindication. With the advent of newer technology and ongoing research, MRI can now be performed in patients with such devices/implants, contingent to specifications. Adequate knowledge of potential interactions of these devices/implants or their components or fragments in a magnetic field is vital to ensure patient safety and to obtain images of diagnostic quality.

DEEP BRAIN STIMULATOR

Author	Year	Patients	DBS Brand; IPG brand	B0	Design	DBS activity	SAR/B1+rms	Results
Tagliati	2009	3304	Not specified (N/S)	1.0 T / 1.5 T	Clinical evaluation DBS assessment post MRI.	N/S	N/S	No adverse effect (AE), 1 IPG malfunction
Sammartino	2017	10	Medtronic 3387; Activa PC	3.0 T GE	Clinical evaluation DBS assessment post MRI.	OFF	SAR <2.3 W/kg	No AE
Hancu	2019	13	Medtronic 3387, 3389; Activa PC	1.5T / 3.0T	Clinical evaluation DBS assessment post MRI.	ON	SAR <0.3 W/kg, B1+rms < 1.32 uT	No AE
Boutet	2019	41	Medtronic 3387; Activa PC	3.0T	Clinical evaluation DBS assessment post MRI.	ON	SAR <0.3 W/kg, B1+rms <1.8 uT	No AE
Boutet	2019	102	Medtronic 3387, 3389; Activa PC/RC/S	1.5T / 3.0T	Clinical evaluation DBS assessment post MRI.	ON	SAR <1.09 W/kg, B1+rms < 1.4 uT	No AE

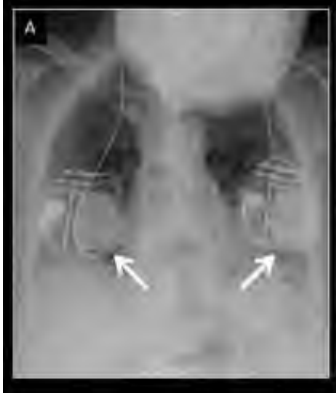

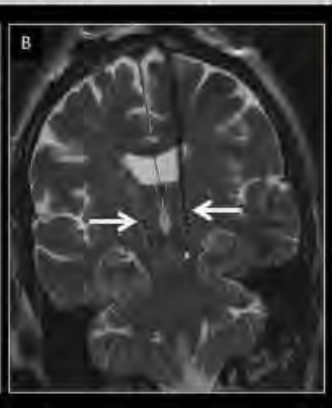

DEEP BRAIN STIMULATION (DBS). Chest radiograph (A) shows two implantable pulse generators (IPG; arrows), for bilateral DBS electrodes. Coronal T2W image (B) shows bilateral DBS electrodes (arrows), terminating in the subthalamic nuclei.

Major Concerns

IPG: Movement and / or Dysfunction.

DBS electrodes:

- Radiofrequency related induction of currents (antenna effect); induced currents dissipate as heat; brain damage > 45°C (113°F).
- Gradient switching may induce low kilohertz currents. This could lead to neuronal firing causing patient discomfort; rarely seizures.

Recommendations

- Confirm device brand, model. If outside specific instructions - assess risk-benefit; Use sequences with low SAR.
- DBS is usually turned off; assess clinical status with DBS OFF.
- Patient monitoring at all times. Re-program to initial settings after the MRI.

(Filename: TCT_743_DBS_ASNR.JPG)

297

Making the Diagnosis with ASL Perfusion Imaging

A Robinson[1], D Bolar[2], P Manning[3], N Farid[4]

[1]University of California San Diego, San Diego, CA, [2]UC San Diego Health, La Jolla, CA, [3]University of California, San Diego, La Jolla, CA, [4]UC San Diego, San Diego, CA

Summary and Objectives

1. To review arterial spin labeling (ASL) and its advantages and disadvantages compared to other MRI perfusion techniques. 2. To highlight the clinical applications of ASL perfusion in neuroimaging, with an emphasis on cases in which ASL is essential to or confirmatory in making a particular diagnosis. 3. To discuss cases in which ASL outperforms other MR perfusion techniques.

Results and Conclusions

Unlike other MR perfusion techniques, arterial spin labeling (ASL) allows for the measurement of cerebral blood flow without an exogenous contrast agent. This educational exhibit seeks to highlight the clinical applications of ASL perfusion in neuroimaging, with an emphasis on cases in which ASL is essential to or confirmatory in making a particular diagnosis. The role of ASL perfusion in neuro-oncology will be discussed, including tumor detection and assessment of treatment response. This exhibit will review cases in which ASL outperforms dynamic susceptibility contrast (DSC) perfusion in neuro-oncology imaging, including differentiating tumor progression from pseudoprogression involving malignancies near the skull base. The role of ASL perfusion in assessment of head and neck cancer will also be discussed, especially with respect to osseous and soft tissue metastases. Applications of ASL perfusion in neurovascular imaging will also be reviewed, including imaging of arteriovenous malformations and dural arteriovenous fistulas, cerebrovascular stenoses, carotid-cavernous fistulas, and reversible cerebral vasoconstriction syndrome. Other cases discussed will include the role of ASL in the diagnosis of intracranial infection, seizure, hemiplegic migraine, hypoxic-ischemic brain injury, and posterior reversible encephalopathy syndrome.

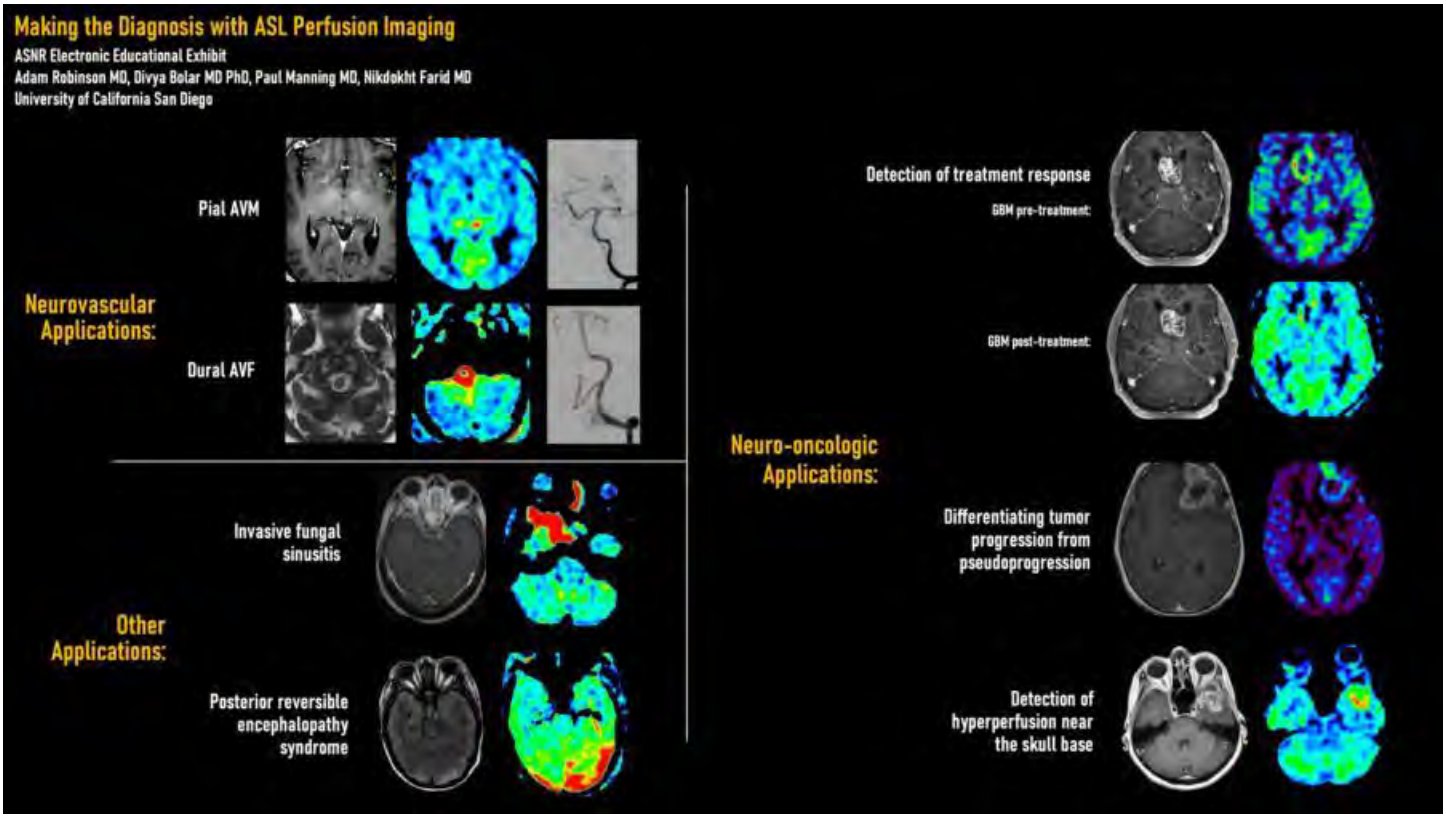

(Filename: TCT_297_ASNR2023submission.jpg)

961

Mastoid Emissary Vein Embolization to Treat Pulsatile Tinnitus

B Ryu[1], J Moirano[1], E Cyphers[2], T White[3], A Patsalides[3]

[1]Donald and Barbara Zucker School of Medicine at Hofstra/Northwell, Hempstead, NY, [2]Philadelphia College of Osteopathic Medicine, Philadelphia, PA, [3]Northwell Health, Manhasset, NY

Summary and Objectives

Pulsatile tinnitus (PT) is an abnormal auditory perception that is rhythmic and synchronous with the patient's heartbeat. The root cause of PT can stem from the venous or arterial side of the cerebrovascular system. The most common etiologies of PT include structural and/or flow abnormalities of the intracranial and extracranial venous territory such as the transverse sinus and emissary veins [1]. Advances in neuroimaging and neuro-endovascular procedures allow identification of the specific cause of PT and successful treatment with endovascular intervention [2]. The following are the educational objectives for the exhibit: (1) To understand the anatomy of the intracranial and extracranial cerebral venous sinus system. (2) To distinguish the various emissary vein anomalies and variants causing PT. (3) To review the radiographic workup and findings to identify a venous cause of PT. (4) To examine the emissary vein embolization technique to treat PT.

Purpose

The purpose of the educational exhibit is to review the cerebral venous sinus system clinically relevant to PT, including various emissary vein anomalies and variants. The workup and management of PT with an emissary vein etiology will be reviewed.

Materials and Methods

A comprehensive literature review of mastoid emissary vein as the etiology of pulsatile tinnitus was conducted. Three case reports and one case series (six patients) were published in the literature [2,3,4,5].

Results and Conclusions

Emissary vein as the etiology of PT is rare; however, the possibility of emissary vein as the cause of PT should be considered if the symptom weakens or disappears when certain areas are compressed. Temporal bone CT, cranial MRV, and cerebral venous angiography can be used for diagnosis. Successful treatment outcomes can be achieved through emissary vein embolization.

521

Metallic foreign bodies and MRI clearance. The current state of affairs.

U Chaudhry[1], S Hamid[2], U Shafique[3]

[1]UTMB, Galveston, TX, [2]UTMB, league City, TX, [3]Indiana University School of medicine, Carmel, IN

Summary and Objectives

This educational exhibit reviews the current literature and studies on metallic foreign bodies and MRI safety. Understand background and various school of thought on this topic. Logical approach to handling these daily questions in a more standardized way.

Purpose
MRI guidelines for these scenarios are often not completely clear with many facilities having similar guidelines, with some room left to radiologist discretion. This leads to a considerable difference between radiologists and programs once a metallic foreign body has been encountered. This is further aggravated by many of these scenarios being in the after hour settings, where residents or fellows are involved. This creates trepidation on part of the MRI technologist and frustration on part of clinicians and patients. Our aim is to make the reader aware of the current landscape and hopefully come up with a uniform approach that junior radiologist and trainees can easily reproduce.
Materials and Methods
History of foreign bodies and various standards for MRI are discussed. Incidence of adverse effects are mentioned. Types of metallic foreign bodies with emphasis to ballistic shrapnel are discussed. ACR MRI safety guidelines and MRIsafety.org are reviewed which are vague or in the case of the later overly stringent considering recent research.
Results and Conclusions
Algorithm and various gray areas are discussed. Also mentioned are some medico legal aspects including patient counseling, documentation, and consent. In conclusion this exhibit serves as good resource for current landscape of safety in metallic foreign bodies that can hopefully lead to a more uniform and clearer understanding of this topic.

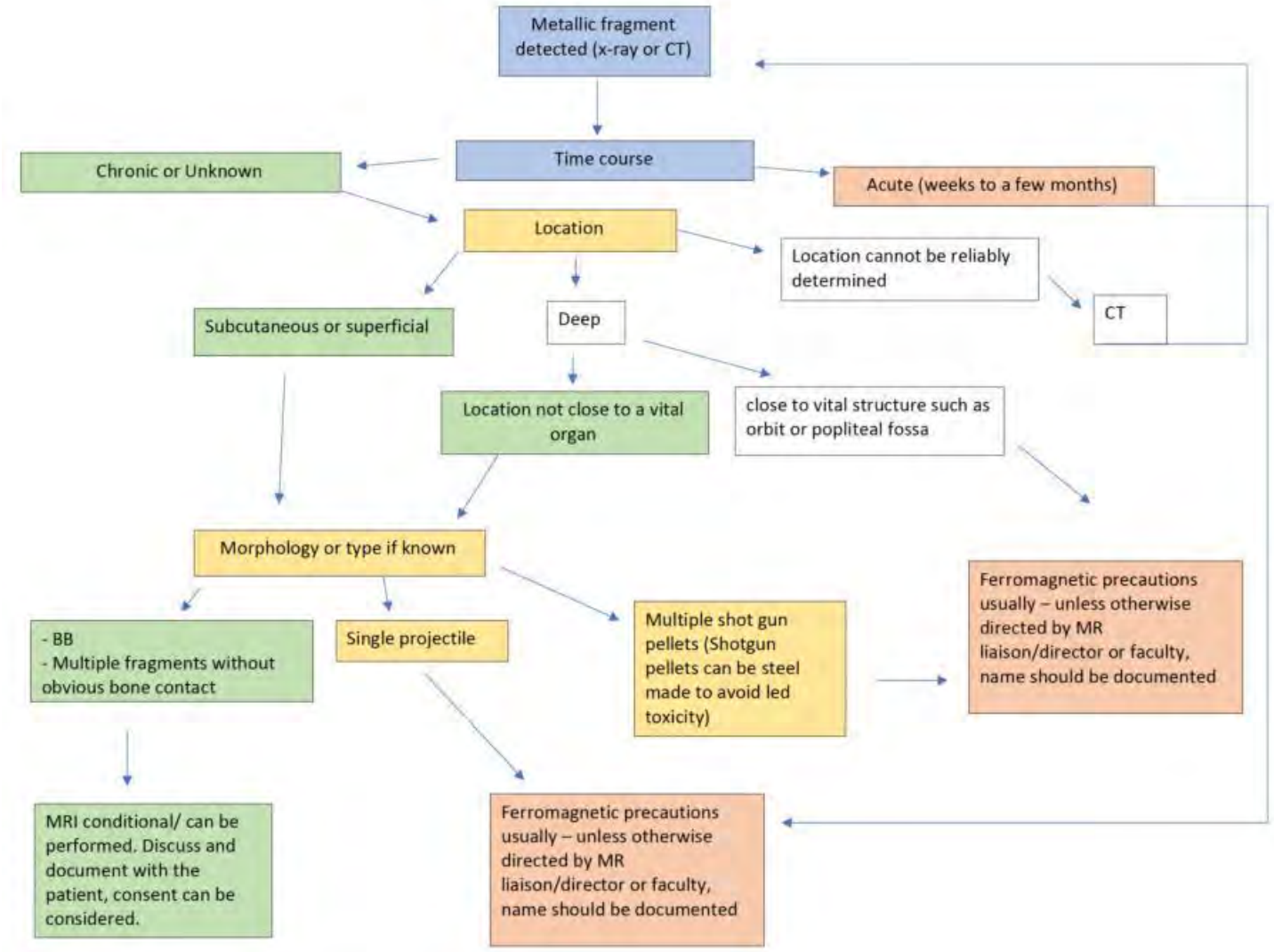

(Filename: TCT_521_ScreenShot2022-11-02at83602PM.jpg)

679

Midline and Paramidline Tumors of the Brain; A Case-Based Cruise Through the Neuro-Oncology Realm, With Insights from the Updated 2021 WHO CNS Tumor Classification.

A Hanafy[1], C Hart[1], B Tantiwongkosi[1], A Singh[1], P Kesava[1], A Gregorat[1], J Lally[1]
[1]*University of Texas Health San Antonio, San Antonio, TX*

Summary and Objectives
The discussion of brain tumors has been an evolving topic since the 2016 WHO update to CNS tumor classification, with several smaller updates on the subsequent cIMPACTs that finally came together to make the most recent 2021 WHO update. Imaging remains

pivotal in identifying location and extent of these tumors as well as surgical planning and follow up. While overall staging of brain tumors has shifted away from histologic and radiologic assessment to genetic and molecular analysis, due to their close correlation with prognosis; a unique feature to CNS tumors. The educational objectives of this exhibit are: - Identify several midline and para-midline tumors of the brain - Describe their imaging features - Build a simplified scheme of the genetic and molecular profile of these tumors - Integrate given data to form a tumor class with predictable treatment response, in light of 2016 WHO classification and 2021 updates.

Purpose

This exhibit aims at reviewing imaging features of several brain tumors, with focus on tumors frequently occurring at the midline/ para-midline. It also aims at familiarizing the practicing radiologist with the 2021 WHO updates to the CNS tumor classification and its original 2016 version, with emphasis on the clinical application.

Materials and Methods

Several brain tumors from our institutional registry presented in a case-based approach, with corresponding genetic data and treatment approach.

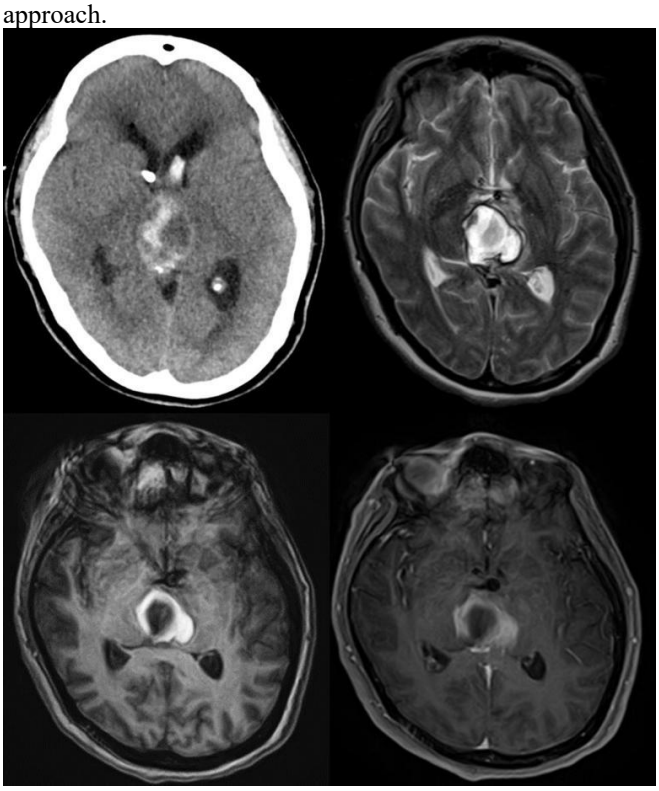

(Filename: TCT_679_figureforabstract.jpg)

377

MOGAD Disease? Learning About an Emergent Demyelinating Disease

S Aristizabal[1], S Marquez zuchini[1], S Bermúdez[2], A Guarnizo[3]

[1]Fundación Santa Fe de Bogotá, Bogotá, Cundinamarca, [2]Fundación Santa Fe de Bogotá, Bogotá, DC, [3]Fundación Santa Fe de Bogotá, Bogotá, Colombia

Summary and Objectives

TEACHING POINTS After reading this educational exhibit participants will be able to: ■ Describe common clinical scenarios associated with Myelin Oligodendrocyte Glycoprotein Antibody-Associated Disease (MOGAD Disease) ■ Recognize the typical imaging findings of MOGAD disease ■ Discuss the imaging and clinical approach in the diagnosis of MOGAD disease and its differentials diagnoses

Purpose

1. To review the clinical aspects and epidemiology of myelin oligodendrocyte glycoprotein antibody disease (MOGAD) 2. To describe the imaging findings of myelin oligodendrocyte glycoprotein antibody disease (MOGAD) and the differential diagnosis.

Materials and Methods

We will illustrate this educational exhibit with proven cases of MOGAD disease. Description of the imaging features will be performed.

Results and Conclusions

Imaging Findings: Optic neuritis in MOGAD disease was found in 1 case involving a long segment of the bilateral optic nerves sparing the chiasm and retrochiasmatic pathways. Cord lesions involving the gray and white matter and covering more than 50% of the axial surface were found. Conus involvement, an imaging finding highly specific for the diagnosis was seen in 2 cases. "H shaped" hyperintensity was seen on axial images in 2 cases, this finding is associated with MOG antibody positivity seen in about 28% of the

cases. Conclusion: Imaging findings in MOG antibody disease including bilateral extensive optic neuritis and longitudinally extensive transverse myelitis with conus involvement are key to differentiate this pathology from other demyelinating diseases such as multiple sclerosis and neuromyelitis optica spectrum disease. Clinical history, imaging findings and cerebrospinal fluid analysis are essential in the diagnosis of this pathology.

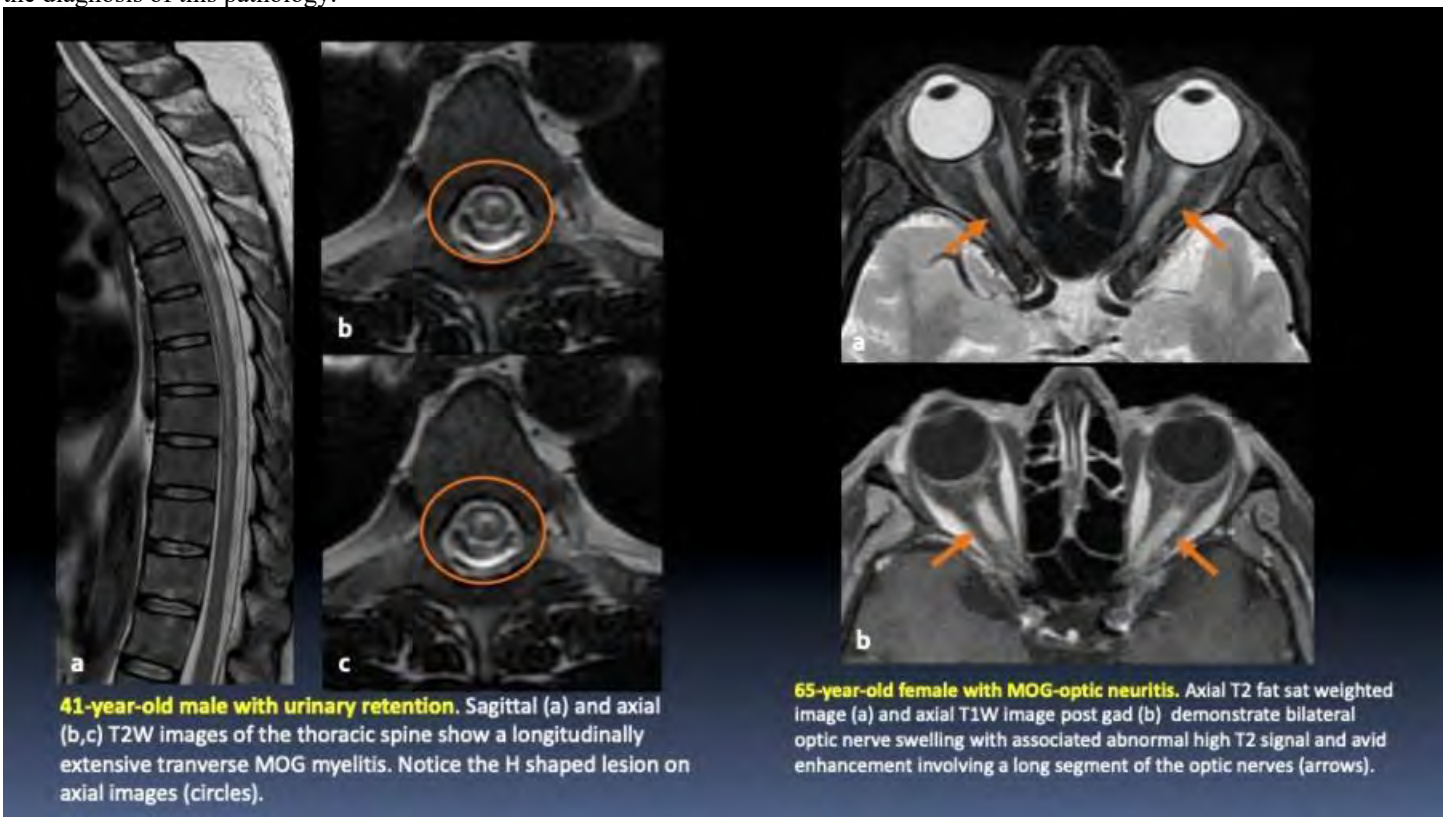

(Filename: TCT_377_Mogaddiseasecopy.jpg)

920

MR Bone Imaging of the Brain Region: Fundamentals and Clinical Applications

M Gomyo[1], K Tsuchiya[2], K Yokoyama[1]

[1]Department of Radiology, Faculty of Medicine, Kyorin University, Mitaka-shi, Tokyo, Japan, [2]Department of Radiology, JR Tokyo General Hospital, Shibuya-ku, Tokyo, Japan

Summary and Objectives

MR bone imaging, which is a novel imaging technique with short echo times has been developed and has become possible to visualize structures such as cortical and spongy bones as well as calcification, which have been difficult to visualize by conventional MR imaging techniques because of low proton density and very short T2- and T2* tissue. This exhibit illustrates the principles and imaging methods of MR bone imaging and shows clinical applications to depict several head diseases.

Purpose

The purposes of this educational exhibit are the followings; 1. To learn the basic principle of MR bone imaging, 2. To know the clinical applications to head lesions of MR bone imaging, 3. To introduce the MR vessel wall bone imaging as an advanced application, 4. To know the pitfalls of MR bone imaging.

Materials and Methods

This educational exhibit presents the basic principle and various scanning methods of MR bone imaging and shows the clinical applications to the structures and brain lesions using MR bone imaging. They include physiological calcifications, bone fracture, sellar or parasellar lesions, skull tumors, reactive bone sclerosis/erosion, bone deformity by tumors, and tumor calcification. Furthermore, we introduce MR vessel wall bone imaging as an advanced application of MR bone imaging. We will also present actual clinical cases of pitfalls in MR bone imaging.

Results and Conclusions

Adding MR bone imaging to routine MR examinations enables the evaluation of bones, bone lesions, and intratumoral calcifications. Furthermore, by combining the use of MR vessel wall bone imaging with conventional vessel wall imaging, it is possible to evaluate the characteristics of plaques that contain calcification.

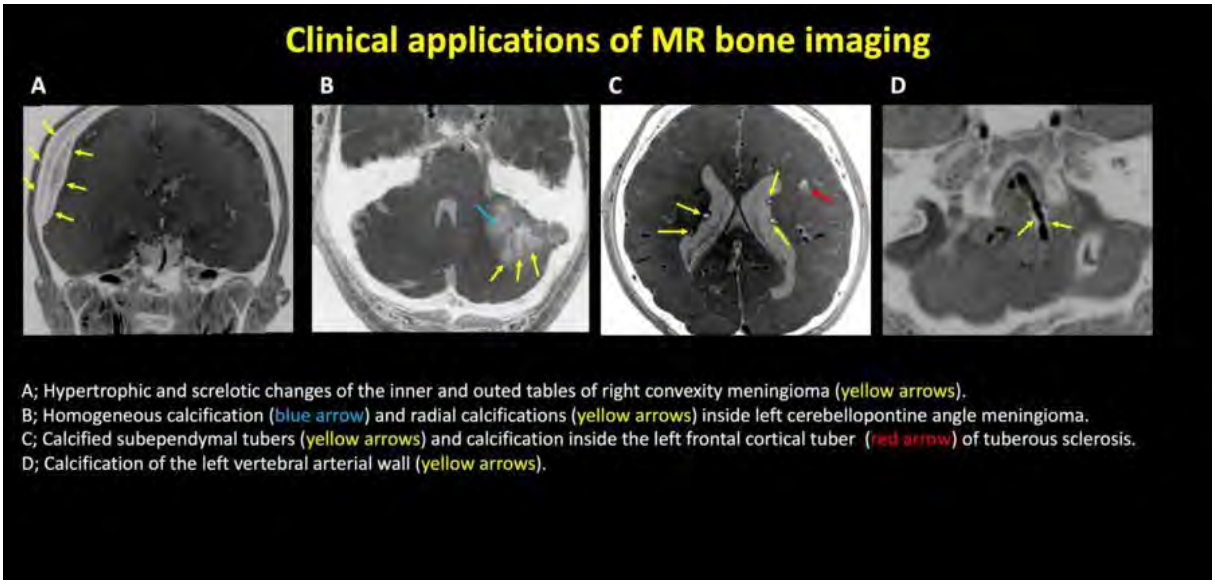

(Filename: TCT_920_ASNR2023figure.jpg)

836

MRI Thermal Injury: A Discussion of Common and Uncommon Causes

J Reagan[1], W Dennis[1], M Antonucci[1]
[1]*Medical University of South Carolina, Charleston, SC*

Purpose

Magnetic resonance imaging is an essential tool in modern medicine. While relatively safe, and while avoiding radiation associated with CT, the MR environment presents a unique set of risks. A recent 10-year review of the FDA Manufacturer and User Facility Device Experience (MAUDE) database revealed thermal injuries as the most commonly reported adverse event in MRI, comprising 59% of entries. The goal of this presentation is to review common causes of MR-induced burns and their associated methods of prevention. We will also discuss more atypical scenarios with the aim of facilitating an understanding of the multifactorial etiology of thermal injury and techniques to mitigate their clinical impact.

Materials and Methods

Our exhibit will include: 1) An introductory section reviewing the incidence and more common known causes of MRI thermal injury. 2) A list of established interventions utilized to minimize this risk through addressing the specific cause. 3) Examples of safety events that occurred despite the implementation of protective mechanisms.

Results and Conclusions

During MRI, different mechanisms can produce burns including direct contact between the patient and the bore, coil, or other hardware, which can induce significant heating. These events can be avoided by careful placement of insulated padding, continual monitoring during image acquisition, and informing patients to remain still and to report unusual sensations during scanning. However, thermal injuries can also result in the absence of direct patient-hardware contact. Specifically, changing magnetic fields used to generate signal may induce a current in conductive material in or on a patient. This unpredictable process can result in burns from unexpected sources including clothing impregnated with metal. We also have also observed more unique scenarios of facial burns from pooling tears near the edge of a radiofrequency coil in a patient with a lesion obstructing the nasolacrimal duct (Fig1a), which resolved two days later (Fig1b). Summary/Conclusion: Despite the frequency of its reporting to the FDA, thermal injury during MRI remains under recognized and underreported. A thorough understanding of both the common and uncommon causes of MRI thermal injury can help avoid patient harm through prevention of these causative mechanisms. With appropriate preventative measures and awareness of atypical etiologies, the incidence of thermal injury can be greatly reduced and improve the safety of performing a MRI study.

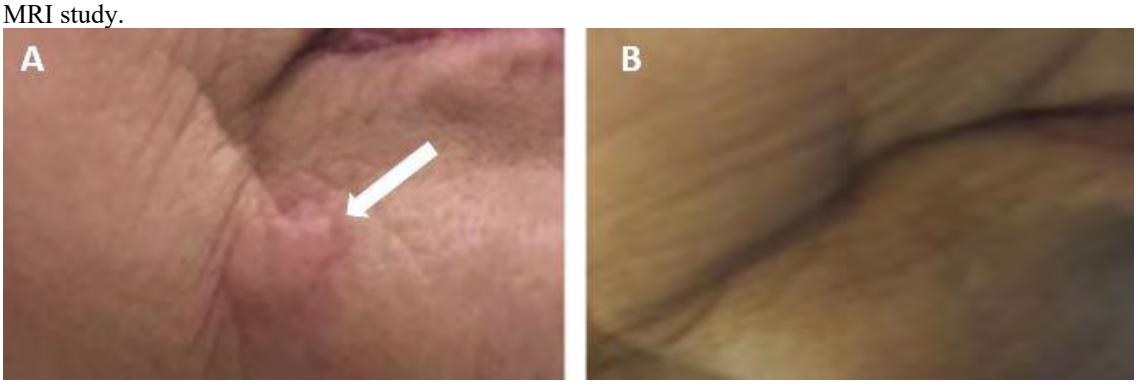

(Filename: TCT_836_ASNR.JPG)

1377

MS Imaging at 7 tesla: Does 7T MRI Teach Us Something New in MS Imaging?

N Fullerton[1], G Keith[2], T Hopkins[3], R Woodward[3], S Martin[4], G Chavada[4], N MacDougall[4], P Shah[4], C O'Leary[4], D Porter[5], K Muir[6]

[1]Institute of Neurosciences, Glasgow, United Kingdom, [2]University of Glasgow, Glasgow, United Kingdom, [3]Queen Elizabeth University Hospital, Glasgow, Scotland, [4]Institute of Neurological Sciences, Queen Elizabeth University Hospital, Glasgow, Scotland, [5]University of Glasgow, Glasgow, Scotland, [6]University of Glasgow, Glasgow, na

Summary and Objectives

Summary: 7T MRI offers unique benefits compared to lower field strengths because of increased spatial resolution and contrast, increased spectral dispersion, and increased susceptibility-related dephasing1. Some of these greatly benefit Multiple Sclerosis (MS) imaging at 7T2-4. MS plaques have unique imaging features, however it can be a challenging differentiating MS plaques from other pathologies. We will show 7T examples to highlight characteristics of MS imaging, clinical context, diagnostic dilemmas and advantages of ultra-high field imaging. Educational objectives: - Understand advantages of 7T compared to 3T MRI, and underlying physics principles - Understand MS imaging and recognise characteristic and diagnostic findings - Understand the clinical context and relevance of imaging - Show areas in MS imaging where 7T is superior to conventional MRI, including cortical lesions

Purpose

Revised MS diagnostic criteria (McDonald Criteria, MAGNIMS Consensus Guidelines, CMSC Consortium) give imaging a pivotal role in the diagnosis of MS. Ever advancing highly efficacious MS treatments depend on accurate diagnosis of new lesions; treatment complications such as progressive multifocal leukoencephalopathy (PML) rely on early diagnosis. Improvement and advances in imaging, such as those 7T MRI can offer, facilitate faster diagnosis and better understanding of MS, treatment effects and sequelae. We aim to advance understanding of the benefits of 7T MRI in general, and in MS imaging in particular; re-emphasize imaging appearances of MS and their importance in a clinical context; and highlight particular areas of strength for 7T in MS.

Materials and Methods

We present an early clinical experience with 7T MRI imaging at our institution. Patients were scanned under research ethics approval as part of a 3T/7T comparison study. We present a variety of 7T images in MS, some with comparison to lower field strength clinical MRIs, to highlight MS imaging, clinical correlation and benefits of imaging at 7T.

Results and Conclusions

7T MRI shows cortical lesions not clearly seen at 3T, of relevance for cognitive functioning of patients. 7T depicts central venules and iron-laden plaques much better than conventional imaging, which may aid diagnosis. Spectroscopy at 7T due to its high spectral resolution facilitates interrogation of lesions such as tumefactive plaques and PML, aiding in conjunction with improved resolution of structural imaging differential diagnosis.

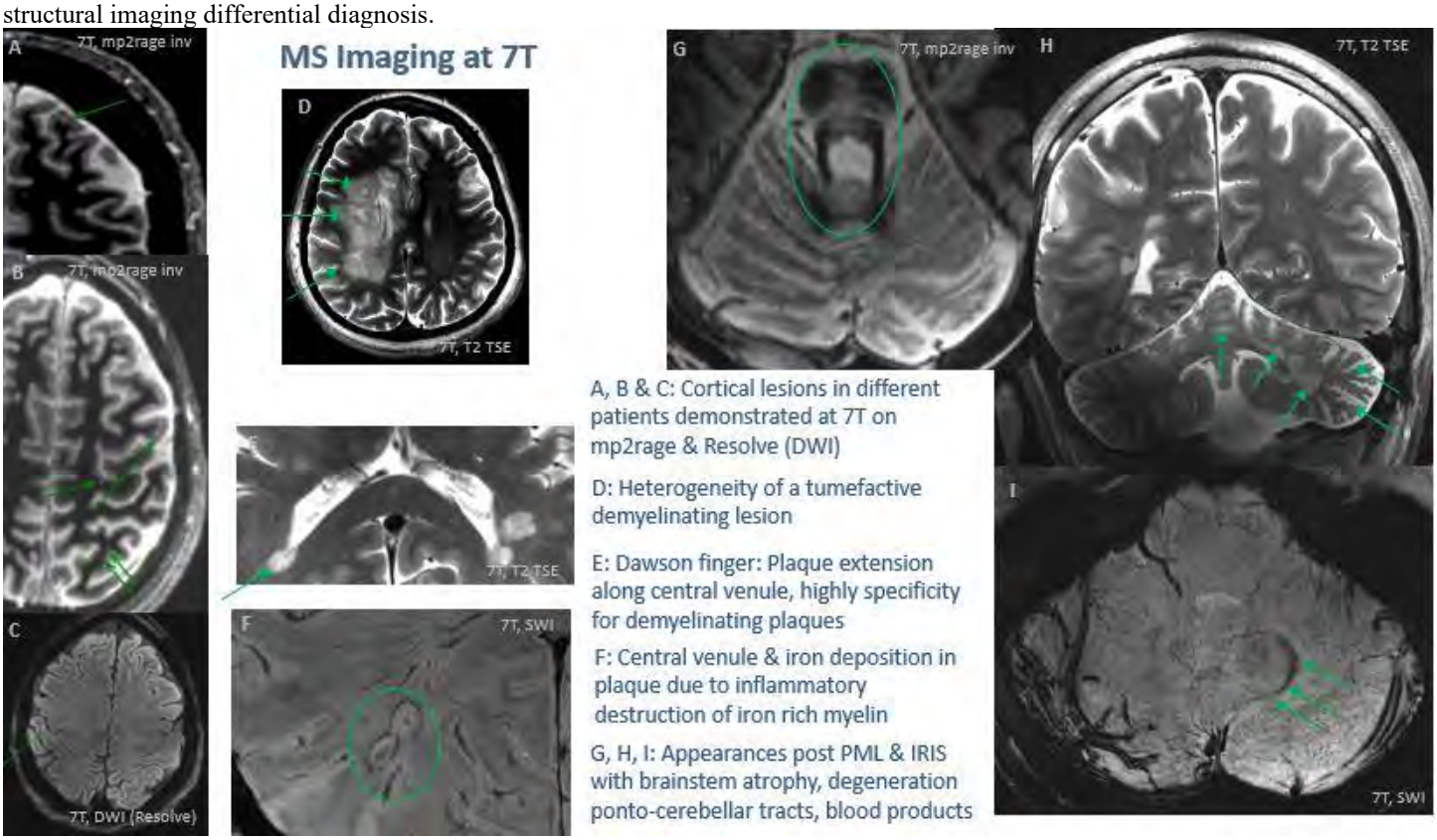

(Filename: TCT_1377_ASNR_7TMS.jpg)

1320

Multimodality imaging for the diagnosis of laryngeal cancer: Dual energy CT, MRI and histopathological correlation.

A Miranda Merchak[1], A Schilling[2]
[1]Hospital Barros Luco, Santiago, chile, [2]Universidad Mayor, Santiago, chile

Summary and Objectives
To perform a case review of laryngeal cancer staging with DUAL energy CT and its correlation with MRI and histopathology.
Purpose
To compare advantages and disadvantages of Dual energy CT vs MRI in the diagnosis of laryngeal cancer.
Materials and Methods
We performed a case review series for all patients undergoing laryngeal cancer staging at the Hospital Barros Luco Trudeau in Santiago of Chile, from November 2021 to September 2022. Definitive diagnosis was made with histopathological confirmation.
Results and Conclusions
MRI is the best radiological method in the context of laryngeal cancer, with good discrimination of soft tissue alterations and intracranial involvement. Dual energy CT was the best choice for characterizing cartilage involvement. Definitive diagnosis requires histopathological confirmation. Late diagnosis and treatment leads to increased mortality and risk of complications.

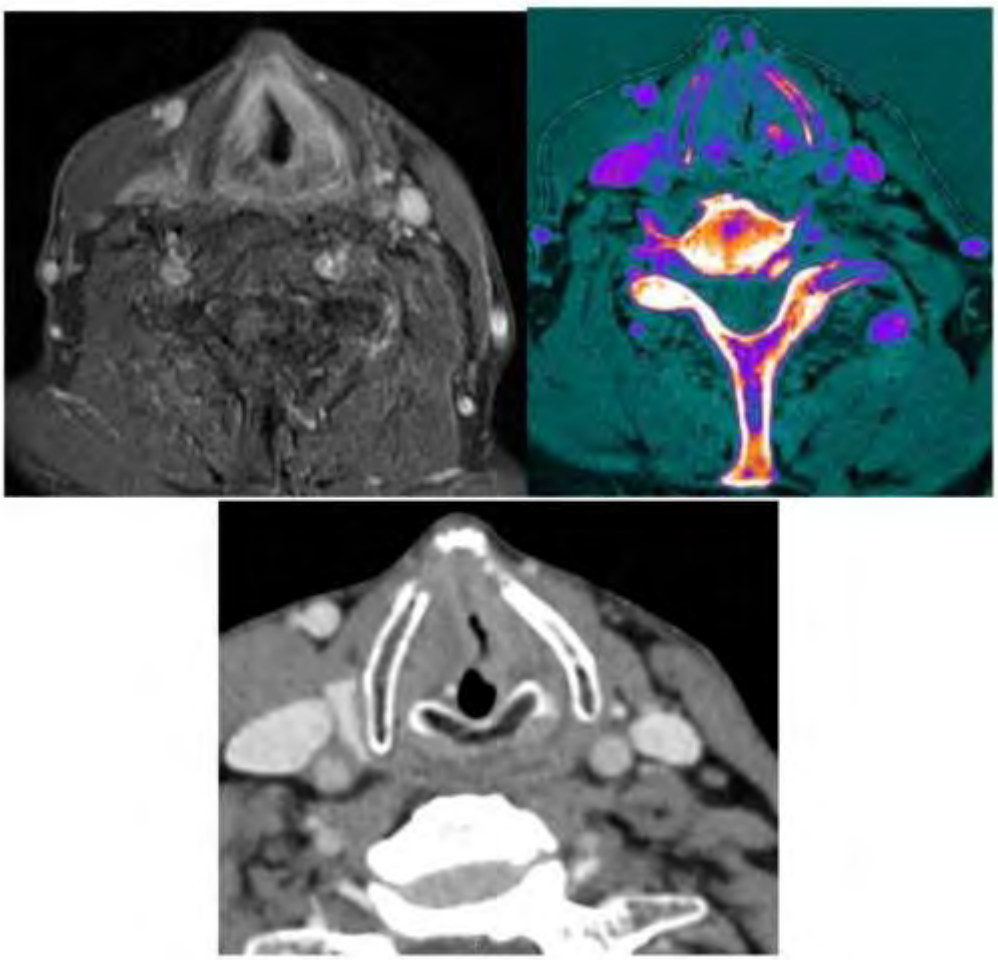

(Filename: TCT_1320_DualCTvsMRI.jpg)

788

Neuroimaging of Dementia: Review of Characteristic Imaging Findings on Structural Brain MRI

K Peng[1], A Ajam[2], A Kalnin[2], A Ramamurthy[2], S Bouchachi[2], X Nguyen[2]
[1]Ohio State University, Columbus, OH, [2]Ohio State University Wexner Medical Center, Columbus, OH

Summary and Objectives
SUMMARY: Dementia is a growing health issue with a high prevalence among elderly individuals. Because a heterogeneous group of underlying disease processes may present clinically as dementia, structural brain magnetic resonance imaging is commonly performed for workup of patients presenting with new cognitive impairment to aid in differentiation and diagnosis of various neurodegenerative diseases and dementia pathologies. Disease entities discussed in this pictorial review include Alzheimer disease, dementia with Lewy bodies, vascular dementia, frontotemporal lobar degeneration, Parkinson disease, and atypical parkinsonian syndromes such as multiple system atrophy, progressive supranuclear palsy, and corticobasal degeneration. Alzheimer disease is by far the most common

neurodegenerative disease and characteristically demonstrates structural neuroimaging findings of medial temporal atrophy and parietotemporal cortical atrophy. Frontotemporal dementia manifests as predominantly frontal and temporal lobe atrophy, with relative sparing of the parietal lobes and hippocampi compared to Alzheimer disease. Vascular dementia can demonstrate heterogeneous patterns of large-vessel strokes or small-vessel disease, often with lacunar infarcts in the basal ganglia, thalamus and periventricular white matter. Other causes of dementia include atypical parkinsonian syndromes, which sometimes can be identified by characteristic neuroimaging findings. Notable structural MRI findings in multiple system atrophy include volume loss and signal abnormalities of the putamina or of the pons and cerebellum, depending on the subtype. Structural MRI in progressive supranuclear palsy typically shows disproportionate midbrain atrophy, leading to characteristic signs such as the "hummingbird sign" on sagittal images or the "morning glory sign" and "Mickey Mouse sign" on axial images. Appropriate detection and recognition of characteristic structural brain MRI features may facilitate diagnostic decision-making in dementia workup. EDUCATIONAL OBJECTIVES: • Provide a practical image-rich guide to improve neuroimaging interpretation skills involved in care of dementia patients • Review and summarize typical neuroradiology findings and helpful differentiating neuroimaging features of common dementia disorders on structural brain MRI

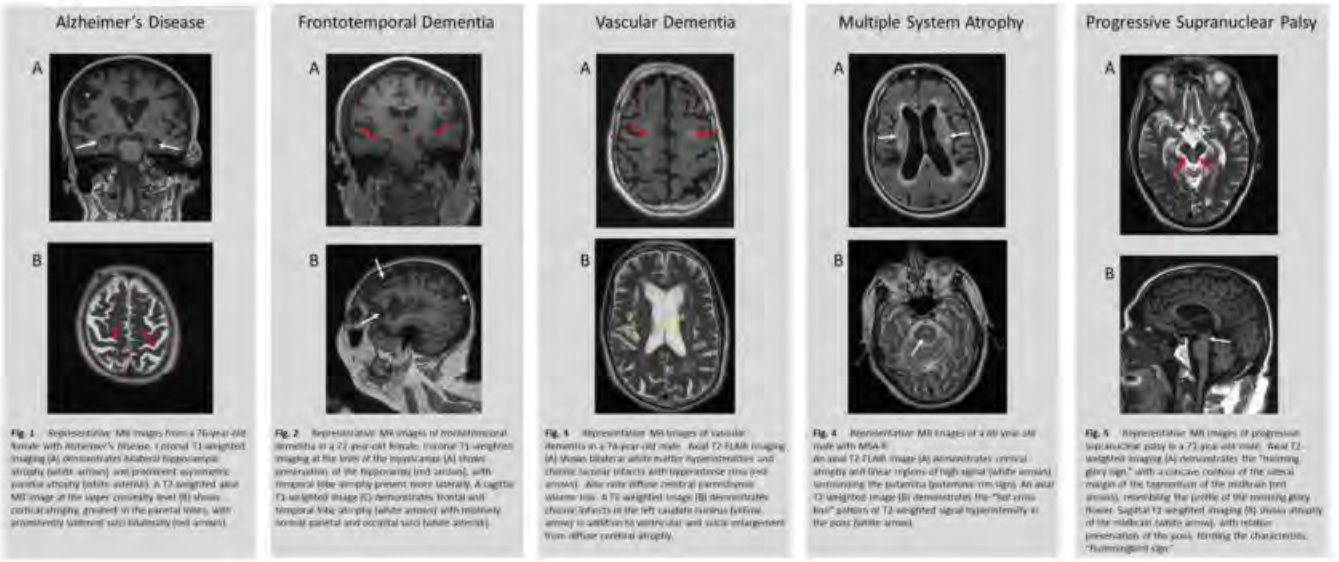

(Filename: TCT_788_ASNRsubmissionfigure.jpg)

1376

Neuroimaging of Infectious, Inflammatory and Autoimmune Diseases of the Brain.

G Romero Sanchez[1], A Sosa[2], K Ramirez Garcia[3], M Gonzalez Putoy[4], A Pérez-Lara[5], J Ortiz Jimenez[6]

[1]Instituto Nacional de Ciencias Médicas y Nutrición Salvado Zubirán, Mexico City, Mexico, [2]Instituto Nacional de Ciencias Medicas y Nutricion Salvador Zubiran, Ciudad de Mexico, Not Applicable, [3]instituto tecnologico de monterrey de estudios superiores, mexico city, mexico, [4]Instituto Nacional de Ciencias Médicas y Nutrición Salvador Zubiran, Ciudad de México, Mexico, [5]Hospital Regional Universitario de Málaga, Málaga, Malaga, [6]Queen's University, Kingston, Ontario

Summary and Objectives

Learning objectives: 1. Explain through case presentation how to use imaging to distinguish between infectious, inflammatory and autoimmune diseases. 2. Review key imaging findings, epidemiology and clinical features to narrow the differential diagnosis in this pathologies. 3. Introduce diagnostic algorithms for meningeal and focal enhancing lesions. 5. Review the use of Vessel Wall Imaging in this pathologies.

Purpose

After reviewing this exhibit, the reader should be able to. Understand the utility of CT, MRI and PET-CT in these group of infectious, inflammatory and autoimmune pathologies of the adult brain Learn in which pathologies it is useful the Multimodal MR Imaging (Diffusion, Perfusion, MRI-VWI and Spectroscopy) Establish adequate differential diagnosis with the imaging findings and clinical history

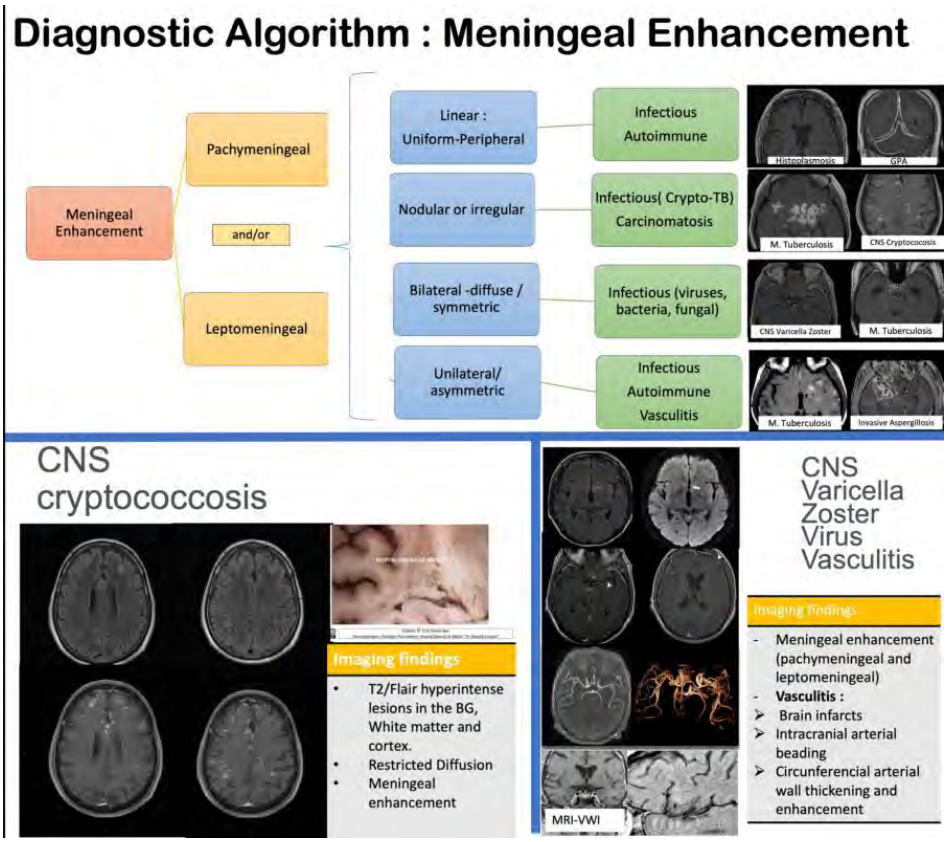

(Filename: TCT_1376_ASNR-2023.jpg)

1191

Neuromyelitis Optica Spectrum Disorder: A Review of Imaging Findings

S Haq[1], R Pandit[2]

[1]Santa Clara Valley Medical Center, San Jose, CA, [2]Santa Clara Valley Medical Center, Santa Clara, CA

Summary and Objectives

Neuromyelitis optica spectrum disorder (NMOSD) is a demyelinating disorder with a diverse set of manifestations in the central nervous system. Classically characterized by the combination of optic neuritis, myelitis, and positive autoantibodies to aquaporin-4, the disorder is now understood to have a variety of additional findings in the central nervous system, and differs from the more commonly diagnosed and more widely recognized multiple sclerosis in a number of key features. This presentation will: 1. Identify imaging characteristics of NMOSD 2. Review MRI cases 3. Discuss differential diagnosis, particularly with regards to multiple sclerosis 4. Review treatment options, including new and emerging therapies

Purpose

To describe the distinct imaging features of NMOSD with an aim to differentiating the condition from multiple sclerosis.

Materials and Methods

This exhibit presents a set of cases collected from our institution from patients with confirmed diagnoses of NMOSD. Included are MRI findings of the brain, orbits, and cervical spine.

Results and Conclusions

Demyelinating disorders can present a challenge to the diagnostic radiologist due to their overlapping imaging features. However, by recognizing the characteristic imaging findings of NMOSD, radiologists can help facilitate timely diagnosis and improve patient outcomes, particularly given the advent of new tailored therapies for NMOSD.

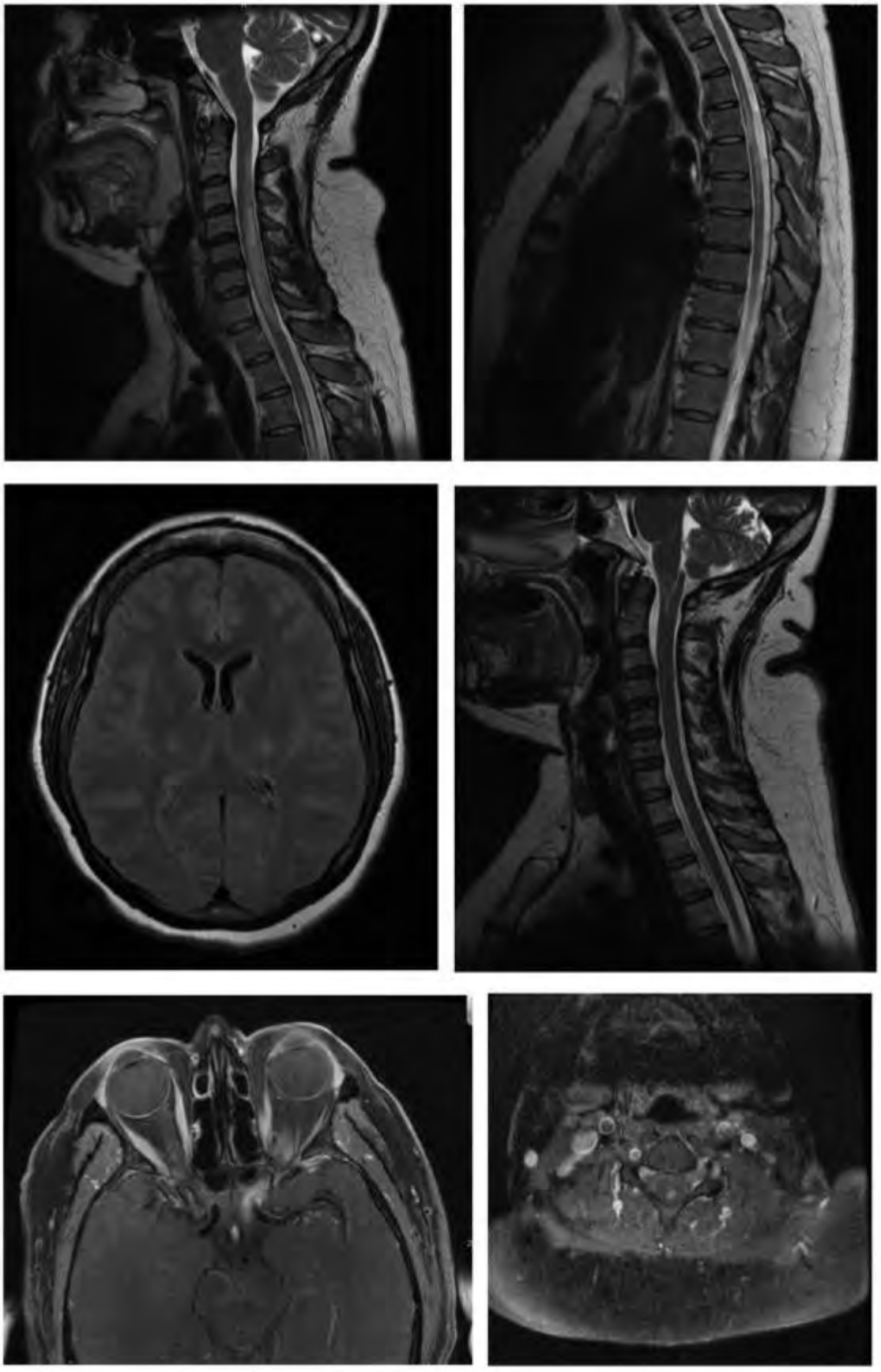

(Filename: TCT_1191_Keyimages.jpg)

1398

Neuroradiology is Fun! - Gamification as an Educational Tool to Enhance Resident Engagement

A Landman[1], R Aromiskis[2], A Sarkar[3], S Lev[4]

[1]NYITCOM, Glen Head, NY, [2]New York Institute of Technology College of Osteopathic Medicine, Rockville Centre, NY, [3]NUMC, East meadow, NY, [4]Nassau University Medical Center, East Meadow, NY

Summary and Objectives

To show how gamification of Neuroradiology education can be used as an additional teaching resource to engage students and facilitate small group discussions. To emphasize how flipping the educational paradigm can reinforce learning and expand the students' creative thought processes.

Purpose

1. To gamify the teaching of neuroradiology by creating an interactive group learning experience for both radiology residents and faculty preceptor. 2. To provide an adjunct to traditional case-based teaching. Rather than confronting an unknown image, the student must draw cards from specific category decks, such as Location, Morphology, Radiological Characteristics, Clinical History and Etiology. The trainee must progressively hone his or her differential diagnosis based on the hand he or she receives.

Materials and Methods

The Neuroradiologist faculty facilitator will divide the classroom into teams. The game can be played as a variant of traditional rummy and use either real cards or an electronic format. The teams must choose a card from each of the categorized decks, which can be modified by the facilitator. Each card will demonstrate a pictograph corresponding to a featured element within the category. While playing a hand, teams have the option of either constructing a differential diagnosis or exchanging a card for another one in the deck. At each point, group discussion is encouraged to develop and understand the decision process of the team. This continues until the facilitator calls the round to a close and awards a point to the team with the most cogent and accurate diagnosis. The facilitator can choose to pair images from his or her teaching file to complement and reinforce the conversation. Radiology educators can create their own game versions to highlight specific aspects of their curriculum.

Results and Conclusions

Gamification of learning has been demonstrated to have positive effects in the healthcare field. In our highly adaptable game, a neuroradiologist facilitator encourages the students to partake in small group discussions and aptly discern differential diagnoses. Both the visual and cognitive aspects of radiology are emphasized. The student must employ deductive reasoning to arrive at a logical conclusion, one that can be supported by the cards in hand. The facilitator has acquired a fun and useful means to further assess the residents' knowledge base, while reinforcing didactic lectures and traditional learning techniques.

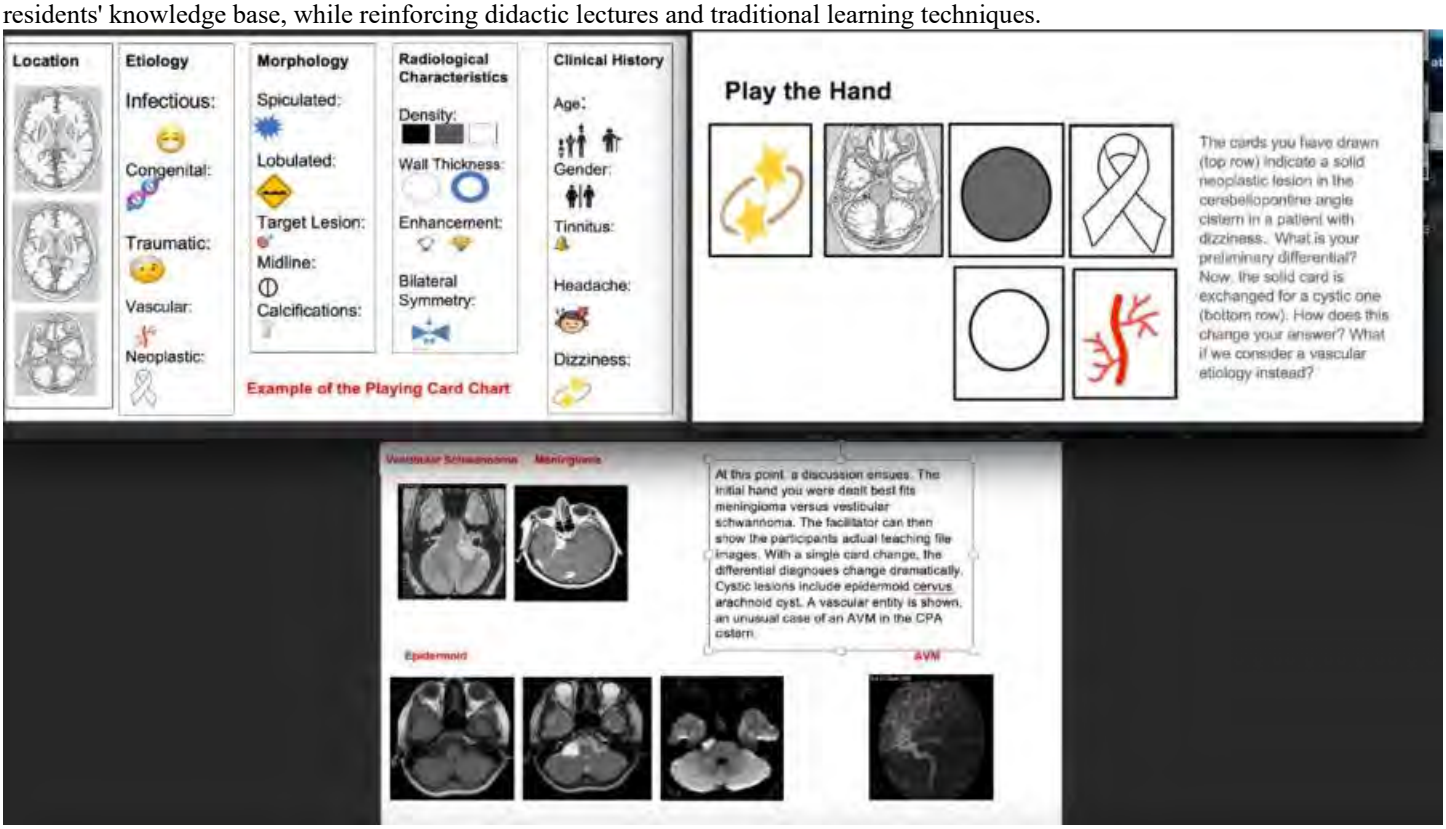

(Filename: TCT_1398_NeuroCardGame_page-0001.jpg)

875

New Frontiers for Domain-inspired Radiomics and Radiogenomics: Increasing role of molecular diagnostics in CNS tumors classification and grading following WHO CNS5 updates

G Singh[1], A Singh[2], P Prasanna[3], A Lignelli[1]

[1]Columbia University Irving Medical Center, New York, NY, [2]Atal Bihar Vajpayee Institute of Medical Sciences, Ghaziabad, Uttar Pradesh, [3]Stony Brook University,, Stony Brook, NY

Summary and Objectives

1. Review key 2021 WHO CNS5 updates 2. Radiomics and Radiogenomics workflow 3. Role of radiomics/radiogenomics in precision medicine- 'Use case scenarios' 4. Limitations and future directions

Purpose

The fifth edition of the WHO Classification of Tumors of Central Nervous System (CNS) was published in 2021. It incorporated the work of the Consortium to Inform Molecular and Practical Approaches to CNS Tumor Taxonomy (c-IMPACT) and built on top of the 2016 updated fourth edition to advance the role of molecular diagnostics in CNS tumor classification and grading. In this educational exhibit, we will describe the radiomics/radiogenomics workflow and its applications and its increasing importance in the setting of WHO CNS5 updates.

Materials and Methods

Discussion: Traditionally, CNS tumor grading has been reliant only on histological features. c-IMPACT updates highlighted the role of molecular markers in providing critical prognostic information. This led to inclusion of molecular parameters in tumor grading in the 2021 WHO fifth edition. For ex, CDKN2A/B homozygous deletion in IDH-mutant astrocytomas upgrades the tumor to grade 4, irrespective of histopathology features. Similarly, TERT promoter mutation, EGFR amplification, and +7/−10 copy number changes in IDH-wildtype diffuse astrocytomas upgrade the tumor to molecular glioblastoma, even in cases that otherwise appear histologically lower grade. Tumor grading is now no longer restricted to being a histological grade only. This provides a new frontier to already ongoing drive for developing in-vivo imaging markers for molecular characterization. There are many defined radiomics techniques in the literature that provide information regarding tumors' molecular characterization and genotypic alterations such as detecting IDH mutation, 1p/19q codeletion, EGFR amplification status etc. The role of in-vivo markers has become even more impactful with WHO CNS5 updates; therefore, understanding the radiomics workflow and its various current applications is vital for current training and practicing neuroradiologists. We will showcase examples of multiple radiomics/radiogenomics and deep learning applications along with major 2021 CNS5 updates to illustrate its clinical significance.

Results and Conclusions

In WHO CNS5 update, more emphasis has been given to molecular/genetic alterations, which in some cases, triumph over histopathological findings. This further increases the importance of finding in-vivo marker equivalents of underlying molecular/genetic alterations.

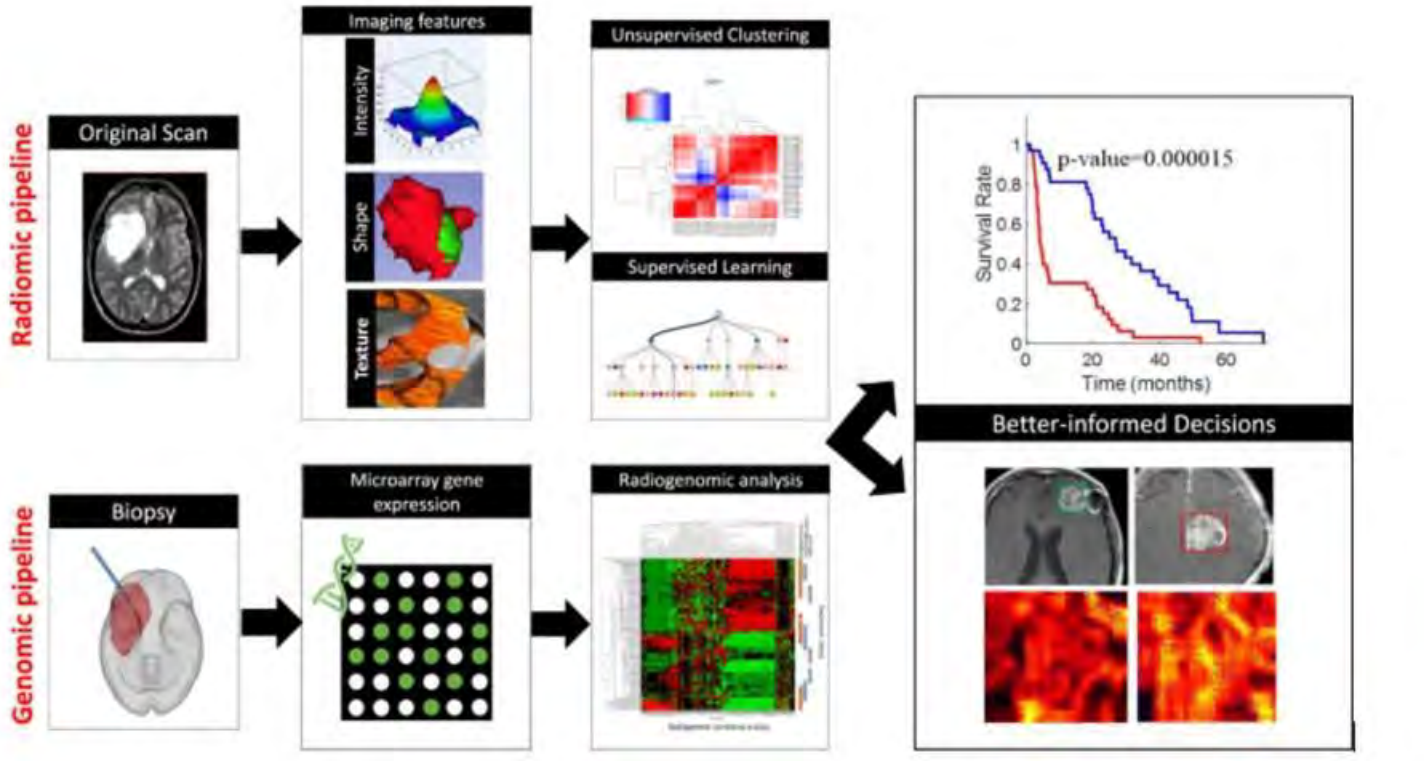

Fig. 1: Radiomics and Radiogenomics workflow.

(Filename: TCT_875_Figure1.jpg)

1088

Newly Discovered Limbic Pathways and Associated Newly Added Limbic Circuits

A Kamali[1], A Kamali[1], L Nunez[2], A Rodriguez[3], R Patel[4]

[1]University of Texas Health Science Center Houston, Houston, TX, [2]University of Texas Health Science Center at Houston, Houston, TX, [3]The University of Texas Health Science Center at Houston, Houston, TX, [4]Texas Children's Hospital, Houston, TX, Houston, TX

Summary and Objectives

The dorsal thalamo-hypothalamic tract, amygdalo-thalamic tract and prefronto-caudo-thalamic tract are some of the newly introduced limbic pathways creating the thalamo-hypothalamic, amygdalo-thalamic and caudo-thalamic connectivity. The purpose of this study is to illustrate these pathways using high angular and high spatial diffusion weighted imaging technique.

Purpose

The limbic system is involved in emotions, memory formation and storage. The Papez circuit is a circuit believed to control memory and emotion, composed of the cingulate cortex, entorhinal cortex, parahippocampal gyrus, hippocampus, hypothalamus and thalamus. Multiple new pathways including the dorsal thalamo-hypothalamic tract, amygdalo-thalamic tract, prefronto-caudo-thalamic tract have been recently described. The new pathways create multiple additional limbic circuits to the original Papez circuit. The purpose of this study is to delineate and distinguish these pathways and associated limbic circuits.

Materials and Methods

Fifteen healthy adults (age range 24-37 years) were studied. Conventional and DT-MRI Acquisition: Data were acquired using a Philips 3.0 T Intera system using a SENSE receive head coil. Diffusion-weighted image (DWI) data were acquired axially using single-shot multi-slice 2-D spin-echo diffusion with the balanced Icosa21 tensor encoding scheme. The b-factor = 500 sec mm-2, TR/TE = 14460/60 msec, FOV = 256 mm x 256 mm and slice thickness / gap/ #slices = 1 mm / 0 mm / 120. The EPI phase encoding used a SENSE k-space under sampling factor of two, with an effective k-space matrix of 112x112 and an image matrix after zero-filling of 256x256. Fiber Tracking: We used the FACT algorithm (DTIStudio) to reconstruct limbic structure fiber tracts with a fractional anisotropy (FA) threshold of 0.22 and angle threshold of 60 degrees.

Results and Conclusions

The dorsal thalamo-hypothalamic (DTH), amygdalo-thalamic tract (ATT) and prefronto-caudo-thalamic tract (PFCT) are traced in all subjects. Unlike the PFCT which is a large pathway connecting the dorsal thalamus to the caudate and prefrontal cortex, the DTH and ATT are much smaller tracts creating the thalamo-hypothalamic and amygdalo-thalamic connectivity. Using a high angular and high spatial resolution diffusion weighted tractography technique, we were able to show trajectories of these important thalamo-hypothalamic, amygdalo-thalamic and caudo-thalamic connectivity in the human brain. These pathways add multiple new circuits to the limbic system as illustrated in the figure 1.

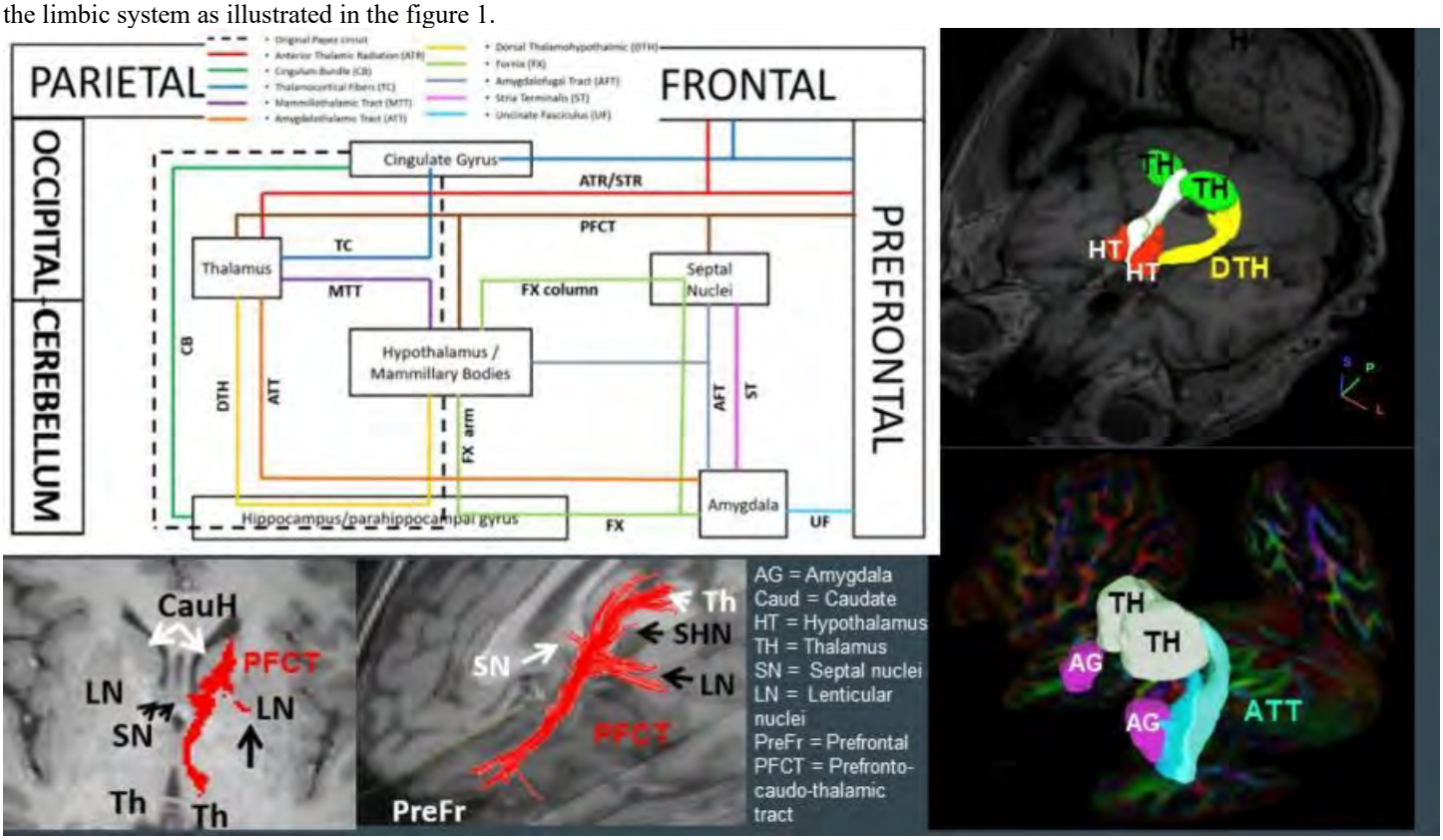

(Filename: TCT_1088_Limbictracts.jpg)

683

Non-Primary Neoplasms of the Sinonasal Cavity

S Aktan[1], G AVEY[1], I Koszewski[1], A Kuner[1], T Kennedy[1]
[1]University of Wisconsin, Madison, WI

Summary and Objectives

Summary: Non-primary neoplasms of the sinonasal cavity are rare and present clinically like primary neoplasms of this region. However, patients with metastatic neoplasms of the sinonasal cavity often have a worse prognosis than those with primary neoplasms, and may require different treatment. Therefore, it is important for radiologists to raise the possibility of these lesions in their report, particularly if the patient has a history of malignancy. In this educational exhibit, we present multiple cases of non-primary tumors of the sinonasal cavity including lymphoproliferative and non-lymphoproliferative entities. Plasmacytoma, lymphoma, metastatic renal cell cancer, metastatic papillary thyroid cancer, melanoma, and a rare case of pituitary adenoma of the nasal cavity due to a seeded surgical tract will be among the cases presented. This exhibit will highlight any unique imaging features that may help to distinguish primary from non-primary tumors of the sinonasal cavity supplemented by a literature review. The exhibit is designed to aid radiologists of all training levels and aims to raise radiologists' awareness of these rare lesions. Educational Objectives: 1. Demonstrate non-primary neoplasms of the sinonasal cavity, a rare but important addition to the differential diagnosis of masses in this location. 2. List the most common malignancies that metastasize to the sinonasal cavity. 3. Compare and contrast imaging features of primary and non-primary tumors of the sinonasal cavity.

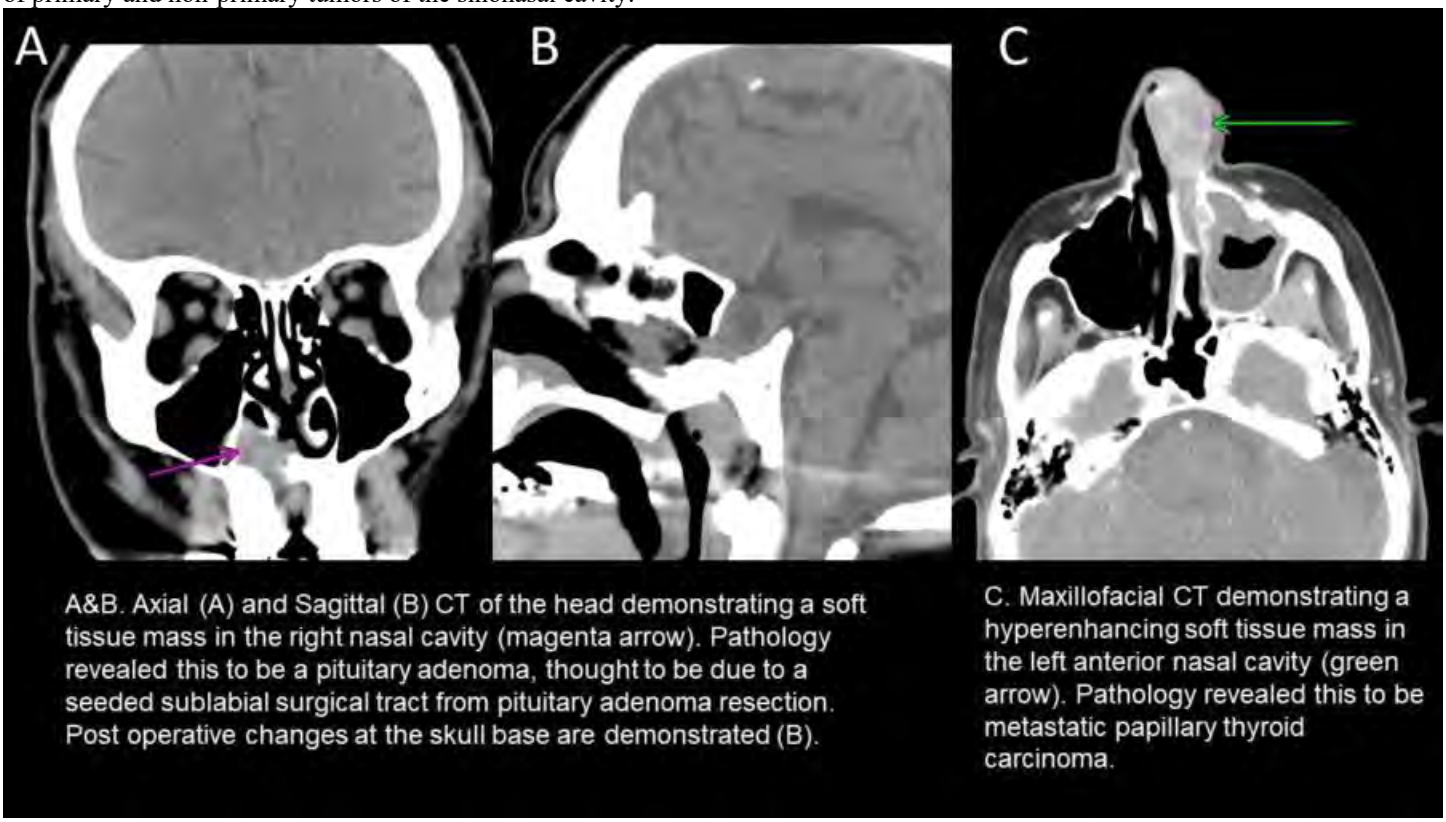

(Filename: TCT_683_asnr3sinonasalimages300.jpg)

1188

Novel imaging features in Central Nervous System Rosai-Dorfman Disease

A Saravanan[1], J Saini[2], K Kulanthaivelu[3]
[1]National Institute of Mental Health and Neurosciences, Bengaluru, Karnataka, [2]NATIONAL INSTITUTE OF MENTAL HEALTH & NEURO SCIENCES, BANGALORE, India, [3]National Instituite of Mental Health and Neurosciences, Bangalore, Karnataka

Summary and Objectives

Rosai-Dorfman disease (RDD), or sinus histiocytosis with massive lymphadenopathy, is a rare, benign, non-Langerhans cell histiocytic lymphoproliferative disease of uncertain etiology. The objective of this study is to describe the imaging features of central nervous system RDD, with a particular focus on the SWI characteristics of the lesions and provide a novel insight on the pathology of the disease.

Purpose

To present imaging observations of histologically confirmed cases of CNS-RDD and identify the imaging characteristics that may aid in accurate preoperative diagnosis.

Materials and Methods

Retrospective analysis of histopathologically proven cases of CNS-RDD was undertaken. Clinicodemographic profiles, multimodality MRI (T1W/T2W/DWI/SWI/Perfusion & Contrast imaging) findings, and histopathological characteristics were recorded.

Results and Conclusions

14 cases were included in the final analysis (mean age = 32 years; M: F =11:3). The location of the lesions were - purely intracranial in 12 cases, purely intraspinal in 1 case and multicentric lesions with intracranial and intraspinal involvement in 1 case. In our study, CNS-RDD lesions presented as extra-axial, well-circumscribed, dural-based masses, isodense or hyperdense on CT, isointense on T1-weighted imaging and iso- tohypointense on T2-weighted imaging. No calcification was found in any of the cases on CT. All cases showed enhancement post contrast that varied in the homogeneity. Remarkably, ten cases (72%) showed strong hypointensity on T2-weighted images. A "lace-like" morphology on susceptibility weighted imaging was observed in 12 (86%) cases. We defined "lace-like" morphology on SWI as the presence of grouped low-signal contiguous, serpiginous tubular-like structures (seen as dots or lines depending on the orientation in reference to the axial plane) that appear like small vessels but present a disorganized distribution, none of which is more than 2mm in maximum dimension, none of which appears as discrete/discontinuous focus. The "lace-like" morphology of blooming is most likely ascribed to the free-radical or mineral deposition (manganese and non-heme iron) seen with chronic inflammation; it is usually not caused by calcification, which is never seen in dural cases of Rosai-Dorfman disease. Hence, the definition of "lace-like" morphology is based on its radiologic appearance, although the nature of such finding may need further confirmation in pathology studies.

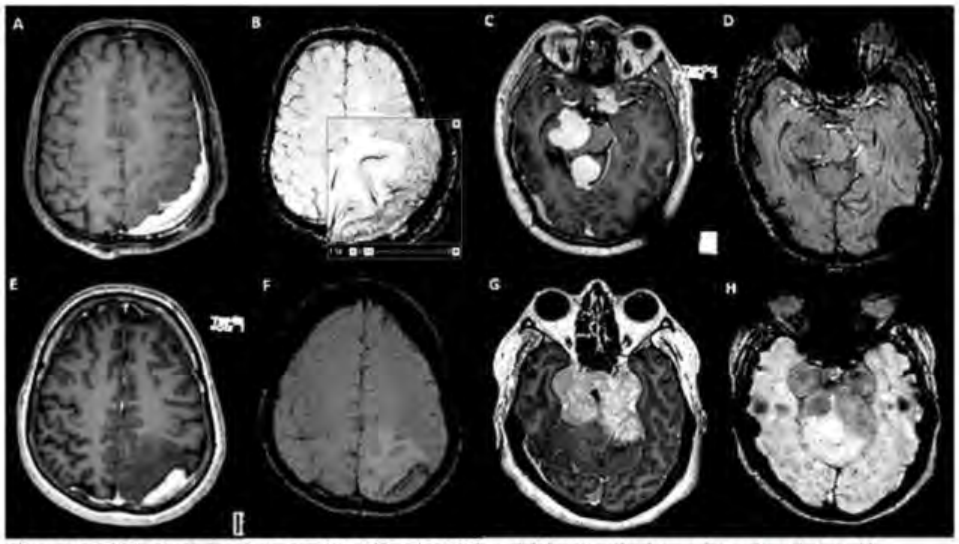

Figure 2: CNS-RDD: SWI findings in 4 cases. Post Gd imaging (A) shows left fronto-parietal convexity enplaque lesion with magnified SWI image (B) showing "lacy" or "reticular" morphology of blooming. Post Gd imaging shows right petroclival-tentorial- left clinoidal dural-based enhancing lesions (C), left parietal convexity enplaque lesion (E) and bilateral cavernous sinus-Meckel's cave lesions (G) - all lesions show similar "lacy" morphology of blooming on SWI (D, F & H).

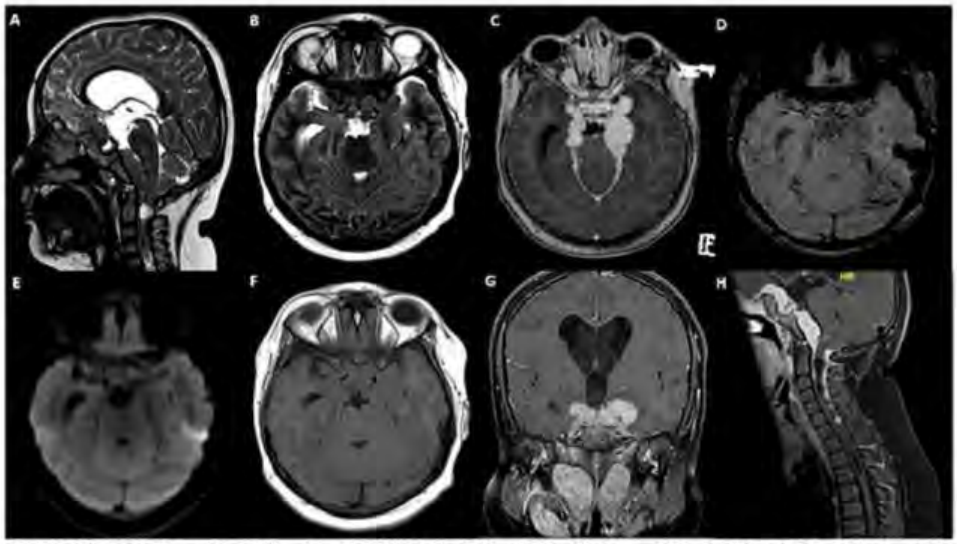

Figure 1: CNS-RDD with multicentric involvement - T2WI Sagittal (A) and Axial (B) show multiple dural based T2 hypointense nodular lesions involving the clivus, dorsum sella, pituitary fossa, planum sphenoidale, cavernous sinuses, tentorial leaflets with extension anteriorly along optic canals. Post Gd images (C) show homogenous enhancement of the lesions. On SWI (D) "lacy" morphology of blooming is noted within the lesions. No diffusion restriction (E) is seen and the lesions are T1 isointense (F). Note the additional bilateral cervical lymphadenopathy and adenoid enlargement (G). Also notice is made of involvement of the cervical canal and posterior cervical dura leading to foramen magnum compromise with altered CSF dynamics and resultant long segment syrinx formation (H).

(Filename: TCT_1188_RDDfinall.jpg)

889

Nuclear Medicine 101 for the Neuroradiologist

A Tejani[1], K Raj[2], F Yu[3], W Moore[4], O Oz[5], A Agarwal[6]

[1]UT Southwestern Medical Center, Frisco, TX, [2]UT Southwestern Medical Center, Dallas, TX, [3]UT Southwestern, Dallas, TX, [4]University Of Texas Southwestern Medical Center, Dallas, TX, [5]University of Texas Southwestern, Dallas, TX, [6]Mayo Clinic, Jacksonville, FL

Summary and Objectives

Educational Objectives: 1. Review common molecular imaging techniques used in the evaluation of neurologic pathology. 2. Discuss applications of nuclear medicine for the evaluation of neurologic disease. 3. Understand advances in precision medicine, such as theranostics, for the diagnosis and treatment of neurological conditions. Presentation Summary: 1. Introduction 2. Nuclear medicine techniques for neurologic pathology a. Workflow diagram integrating nuclear medicine and diagnostic modalities b. Brief review of the physics underlying nuclear medicine techniques 3. Case-guided review of applications of nuclear medicine for imaging of intracranial and head/neck pathology a. Discussion of radiotracers, modalities, protocols, and benefits versus pitfalls of molecular imaging techniques to evaluate the following categories of neuropathology i. Demyelinating disease A. Quantifying disease burden B. Monitoring treatment response ii. Neurodegenerative disease (i.e., Alzheimer's disease, Parkinsonian syndromes) iii. Neuro-oncology (i.e., glioblastoma, somatostatin receptor positive tumors, metastases, lymphoma) iv. Epilepsy v. Vascular abnormalities (i.e., Moya Moya, brain death) vi. CSF flow (i.e., shunt evaluation) vii. Head and neck oncology (i.e., squamous cell carcinoma, neuroendocrine tumors, metastases) A. Initial diagnosis and staging B. Precision medicine approach for treatment selection C. Monitoring treatment response and recurrence D. Planning intervention (i.e., resection, lymph node dissection) viii. Parathyroid and thyroid pathology 4. Emerging technology and modalities a. PET/MRI b. Precision medicine applications for personalized radiotracer and therapy selection i. Theranostics c. Proteomic and genomic applications 5. Summary/conclusion

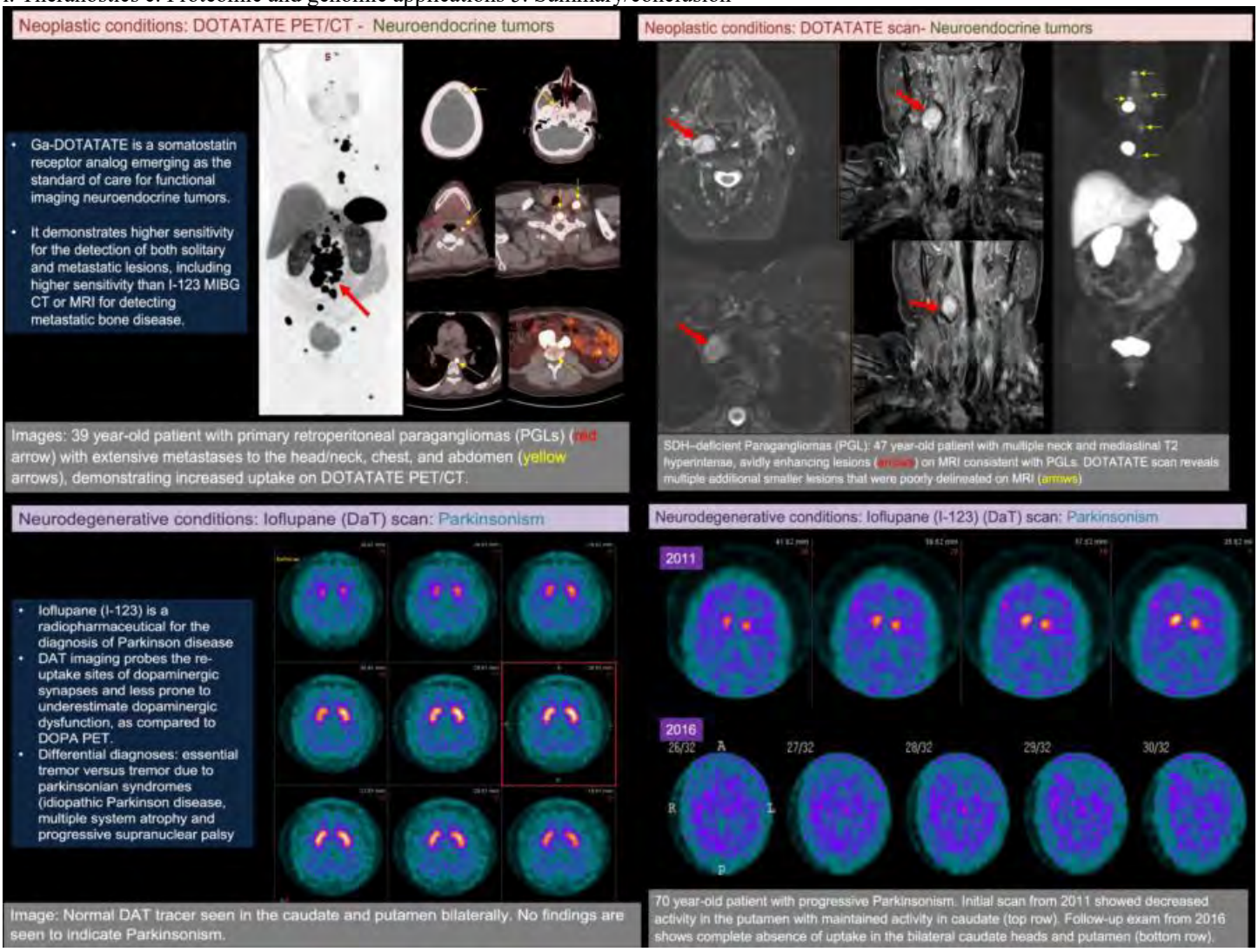

(Filename: TCT_889_Tejani_NucMedSlides.jpg)

833

Offerings From the Dead: Interesting Postmortem CT Neuroradiology Cases.

M Thomas[1], R Parks[2], C Yim[1], D Davila[1], O Ukpo[3]

[1]Olive View-UCLA Medical Center, Sylmar, CA, [2]Los Angeles County Medical Examiner-Coroner, LOS ANGELES, CA, [3]Los Angeles County, Department of Medical Examiner-Coroner, Los Angeles, CA

Summary and Objectives

Postmortem Imaging or Virtual autopsy is an exciting yet challenging field in utilizing radiological imaging to assist the forensic pathologist or medical examiner-coroner. The imaging interpretation is performed by either the forensic pathologist or radiologist. In some centers, radiologists with specialty training, such as neuroradiologists, are requested to assist the medical examiner in interpretation. It is important that the neuroradiologist be aware of the normal postmortem imaging appearance of the deceased as well as the benefits and limitations of postmortem imaging. They should be able to identify pathology seen on postmortem imaging which may assist in the interpretation of cause of death. This presentation will focus on the neuroradiological imaging findings of pathology in decedents on postmortem CT as well as mimickers of disease pathology on postmortem CT. Objectives: Identify and learn about the normal postmortem neuroradiological CT imaging appearance of the decedents. Review normal postmortem appearance that may mimic pathology Review in a case presentation format, the postmortem CT findings of a variety of neurological causes of death. Review the benefits and limitations of postmortem CT.

Purpose

As postmortem imaging in forensic radiology is expanding, in some centers radiologists are assisting with the interpretation of the imaging studies. The purpose of this exhibit is to review the appearance of expected postmortem changes on CT of the normal neuroanatomy, review the benefits and limitations of postmortem CT in neuroradiology with case-based examples of pathology.

Materials and Methods

The decedents were scanned on a Phillips Brilliance 16 slice CT scanner (Philips Medical Systems, Madison, WI) and images were obtained from head to lower extremities without contrast. The postmortem CT images were evaluated by 2 board certified radiologist with subspecialty certification in neuroradiology and over 15 years of radiology experience and over 5 years of experience in postmortem imaging. The CT images were reviewed using a viewing console (Nil Read, Hyland Software, Ontario, Canada). The image interpretation is reviewed with the medical examiner.

Results and Conclusions

Postmortem CT is a useful tool for the forensic pathologist and medical examiner-coroner. The neuroradiologist may provide insight and assistance on the imaging findings but should be aware of the normal postmortem CT findings, be able to identify pathology and identify common mimickers of disease.

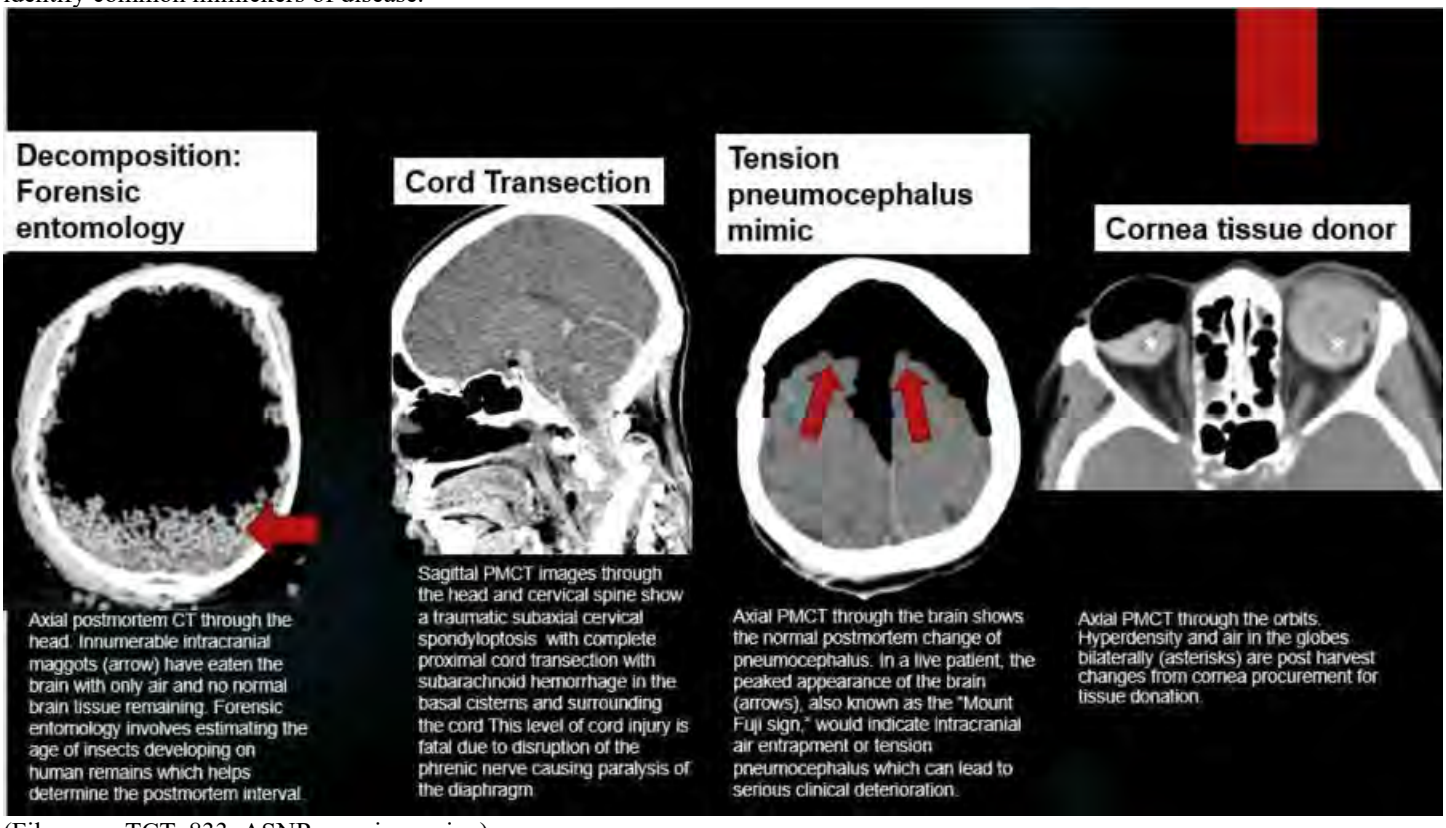

(Filename: TCT_833_ASNRneuroimage.jpg)

1494

Orbital Foreign Bodies: What We Can See...

A McCalla[1], D Theotoka[2], M Maeng[2], M Johnson[3]

[1]Central Michigan University, College of Medicine, Mt. Pleasant, MI, [2]Yale School of Medicine, New Haven, CT, [3]Yale University, New Haven, CT

Summary and Objectives

Blunt and penetrating trauma to the orbit is a common cause of emergency ophthalmologic evaluation, imaging and treatment. These patients will often present with pain, discomfort, bleeding or visual loss. Frequently physical evaluation for extent of injury is challenging. Emergency imaging is leveraged to diagnose extent and pattern of orbital injury. Precise anatomic delineation of the imaging pattern of orbital injury includes careful scrutiny for orbital foreign bodies. Orbital foreign bodies may lead to globe rupture, vision loss, infection and retinal toxicity. Imaging plays a critical role in injury assessment and development of effective treatment plan. Educational Objectives: • Overview the anatomy of the orbit in the setting of trauma • Discuss the predominant forms of foreign bodies to the orbit • Discuss how to distinguish between different forms of foreign bodies to the orbit via imaging • Review the risks of intraorbital foreign bodies including globe rupture, infection and visual loss • Discuss the different treatment plans for foreign bodies to the orbit

Purpose

The purpose of this educational exhibit is to review the clinical and radiologic anatomy of blunt and penetrating orbital injuries with a focus on identification of orbital foreign bodies which may determine the need for surgical treatment. The foreign body composition may include wood, glass, metal, and bone fragments among other more unusual materials.

Materials and Methods

Retrospective clinical and teaching cases are utilized to demonstrate anatomic patterns of injury as well as subtle and unmistakable orbital foreign bodies. Characterization of the type of foreign body through the use of clinical images, plain films, CT and MRI is demonstrated through real world examples. Imaging features to differentiate various materials will be highlighted.

Results and Conclusions

Multiple case examples of blunt and penetrating orbital trauma are presented each containing a foreign body. Wood, glass, metal, including BBs and bullets and unusual penetrating objects such as pens and pencils, fishhooks and lawn darts, have been reported. While some inert materials may be safely left in place without consequence, others may present an ongoing risk of infection or toxicity to orbital structures. Meticulous imaging can assist the ophthalmologist in the assessment of the extent of orbital injury and to determine optimal management for preservation of function.

974

Orbital Imaging: An overview of the anatomy, approach, imaging techniques and pathology

V Feeney[1], R Sinha[2]

[1]Northern Care Alliance, Manchester, Greater Manchester, [2]Royal Preston Hospital, BURNLEY, Lancashire

Summary and Objectives

The bony orbits contain vital structures for visual perception. Orbital anatomy is complicated and we provide a basic understanding of the anatomical compartmental principles required in order to approach orbital pathology. The compartmental location can determine a lesion's origins and differential diagnosis. Computed tomography (CT) imaging is most useful in the acute setting for identifying orbital pathology; typically required in emergent situations. Magnetic resonance (MR) imaging has acute and non-acute roles but ultimately provides vastly greater orbital detail and is the factotum in imaging orbital pathology. We describe the optimum imaging protocols and their rationale. We provide the natural history when appropriate, clinical presenting features, key imaging characteristics with separate key teaching points outlined, differential diagnosis and treatment options, when applicable, of more than twenty orbital pathologies pertaining to vascular, inflammatory, endocrinological, neoplastic, osseous, iatrogenic and congenital origins. Pathologies covered include capillary haemangioma, orbital varix, AVM, carotid-cavernous fistula, orbital cellulitis, optic neuritis, neuromyelitis optica, perineuritis, orbital pseudotumour, thyroid orbitopathy, optic nerve sheath meningioma, optic nerve glioma, choroidal melanoma, ocular haemangioblastoma, ocular metastasis, sphenoid wing meningioma, sphenoid wing dysplasia, fibrous dysplasia, ocular prothesis, exenteration, post-cataract surgery, optic nerve drusen, coloboma and staphyloma. The imaging findings of each orbital pathology outlined are unique and we describe how they are differentiated. This is achieved predominately through MR imaging that provides lesion-specific and characteristic imaging findings. Ultimately the role of this pictorial review is to educate radiologists and aligned specialists on common and obscure orbital pathologies. Providing an inaccurate differential diagnosis can lead to catastrophic consequences for patients who may establish permanent visual loss. Educational objectives: - Provide a concise overview of orbital anatomy - Describe an anatomical compartmental approach to orbital lesions - Provide optimum imaging protocols for CT and MR modalities and their rationale. - Provide characteristic imaging findings of more than twenty orbital pathologies pertaining to vascular, inflammatory, endocrinological, neoplastic, osseous, iatrogenic and congenital

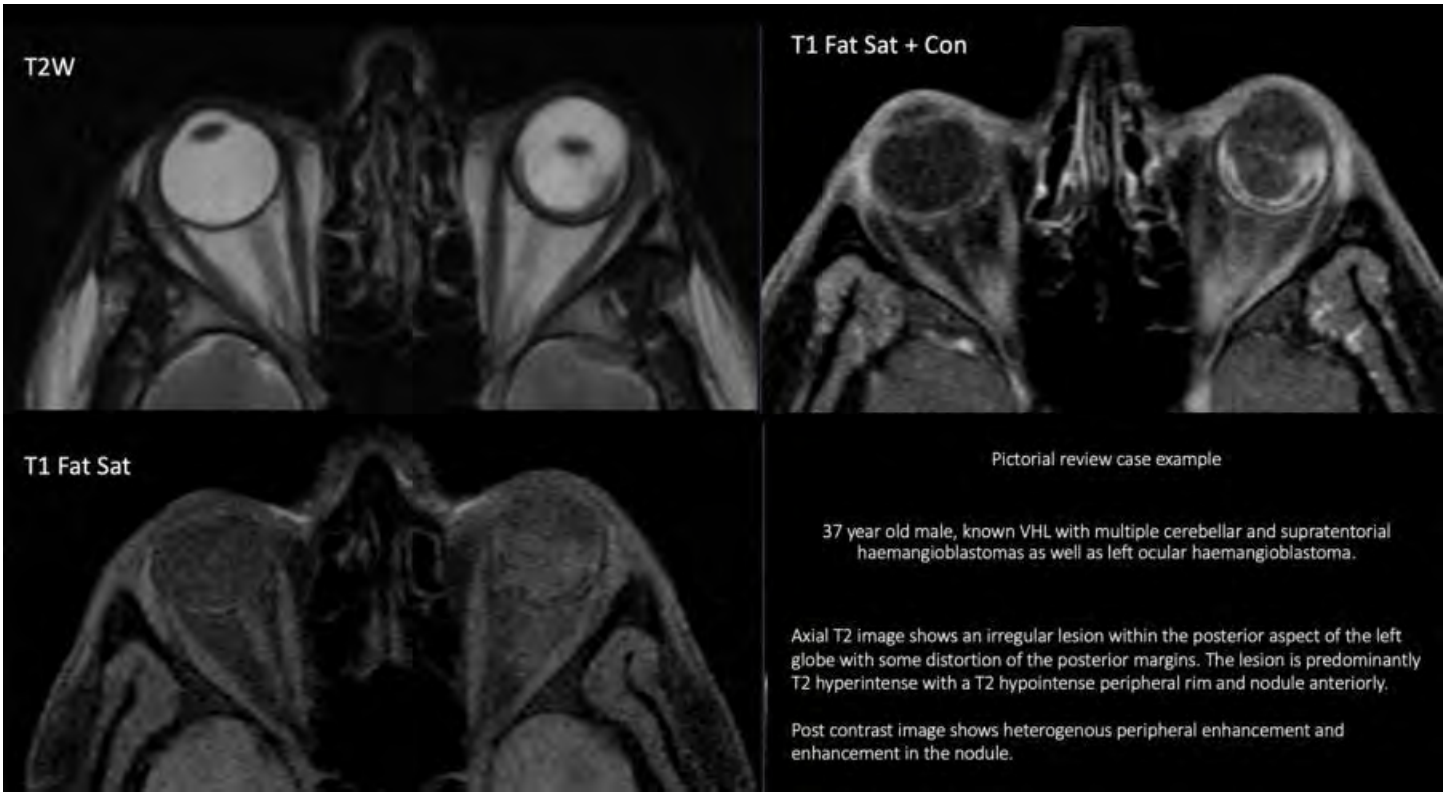

(Filename: TCT_974_OcularHaemangioblastomaAbstractImage14112022.jpg)

653

Orbital Neoplasms and Pseudotumors: An Eye-catching Review

C Burgos-Sanchez[1], E Dedekam[1], J Costello[1]
[1]Madigan Army Medical Center, Joint Base Lewis-McChord, WA

Summary and Objectives
This educational exhibit highlights the role of the radiologist in diagnosing orbital masses. Interactive images will be used to delineate pertinent anatomy and to lay the framework for evaluating the orbits. Salient CT and MRI characteristics will provide an approach to narrowing the differential for these lesions. In the exhibit, multiple unique orbital cases will be used to highlight our approach. Our stated aims are to: -Provide a brief overview of orbital anatomy -Present a systematic approach to analyzing orbital masses -Review and narrow the differential for orbital masses through multiple interactive cases
Purpose
Orbital masses are uncommonly encountered in daily radiology practice and can be difficult to characterize. Although challenging, with careful cross-sectional imaging evaluation, the radiologist can provide diagnostic considerations beyond the scope of the fundoscopic exam. We highlight a structured imaging approach to orbital masses and ultimately aid the clinician in obtaining an accurate diagnosis.
Materials and Methods
Relevant orbital anatomy, including intraconal and extraconal components, and skull base foramina will be reviewed through medical illustrations, and annotated CT and MR images. Three components will then be used to interpret orbital lesions. (1) Critical clinical history including features such as rapid or gradual onset, painful or painless, and history of malignancy. (2) Evaluation of the mass margin (circumscribed or infiltrative) and MRI signal characteristics. (3) Localizing a lesion to a specific anatomic structure in the orbits. Classic and unusual orbital cases will be discussed, including vascular masses, optic nerve lesions, nerve sheath tumors, inflammatory lesions, metastases, and lymphoma. Figure: (A) CT images show a circumscribed mass in the left orbit, favored to represent a cavernous venous malformation (CVV). Clinical history included painful proptosis and history of breast cancer. (B) Low T2 signal within the mass suggested a hypercellular process and (C) enhancement characteristics are atypical for CVV. The final pathology for this mass was a breast cancer metastasis, which could be suggested preoperatively, using a structured imaging approach. This and many more difficult orbital masses will be discussed in detail in this educational exhibit.
Results and Conclusions
Understanding orbital anatomy and narrowing the differential allows the radiologist to provide a useful adjunct to the clinical ophthalmologic evaluation and ultimately guides management.

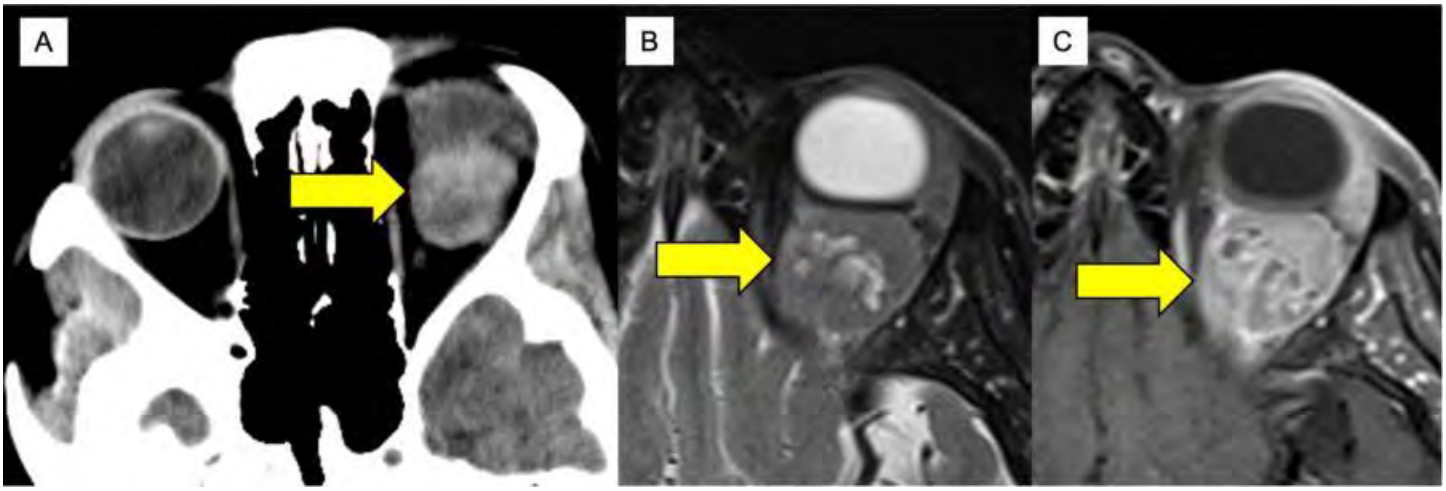

(Filename: TCT_653_Figure1.jpg)

1080

Orbital pain: Imaging Features and Clinical Manifestations

E Zamora[1], C Zamora[2]

[1]Thomas Jefferson University, Philadelphia, PA, [2]UNC Department of Radiology, Chapel Hill, NC

Summary and Objectives

Orbital pain (OP) is a physiologic response to averse stimuli affecting orbital or periorbital tissues, and it is a common cause of urgent care referrals. Pain is mainly transmitted through the V1 branch of CN V, although intra-orbital connections with other branches have been demonstrated (CNs III, IV, and VI) with a potential role in pain transmission. Ophthalmic examination is necessary for management guidance and selection of appropriate imaging studies, which are not typically indicated in minor and self-limited conditions (e.g., corneal abrasions, foreign bodies). However, around 35% of patients presenting to the ED with OP are true emergencies with sight threatening potential, often requiring diagnostic imaging evaluation. Emergent CT of the orbits is indicated in trauma (noncontrast) as well as in nontraumatic emergent conditions. The latter typically present with abnormal ophthalmological findings that may suggest an underlying etiology and guide selection of appropriate diagnostic studies. Contrast-enhanced CT is usually indicated in infection, while CT angiography is appropriate for suspected cavernous sinus thrombosis, arteriovenous fistulas, or aneurysms, particularly in the setting of ophthalmoplegia. MRI is better able to characterize the extent of disease as it provides greater contrast resolution in addition to advanced sequences such as perfusion and diffusion. It is useful to differentiate various conditions that may result in orbital pain, including multiple sclerosis and neoplasia. MRI is mainstay for the evaluation of other causes of optic neuropathy and is the modality of choice for inflammatory conditions (e.g., Tolosa-Hunt, IgG4-related disease). This case-based exhibit will review the role of imaging as well as the disease manifestations of orbital pain in different clinical settings. Pathologies will be categorized based on acuity and will include traumatic, infectious, inflammatory/granulomatous, neuropathic, and neoplastic etiologies. Educational objective: Present an overview of pathological entities leading to orbital pain with emphasis on their clinical presentation and imaging features.

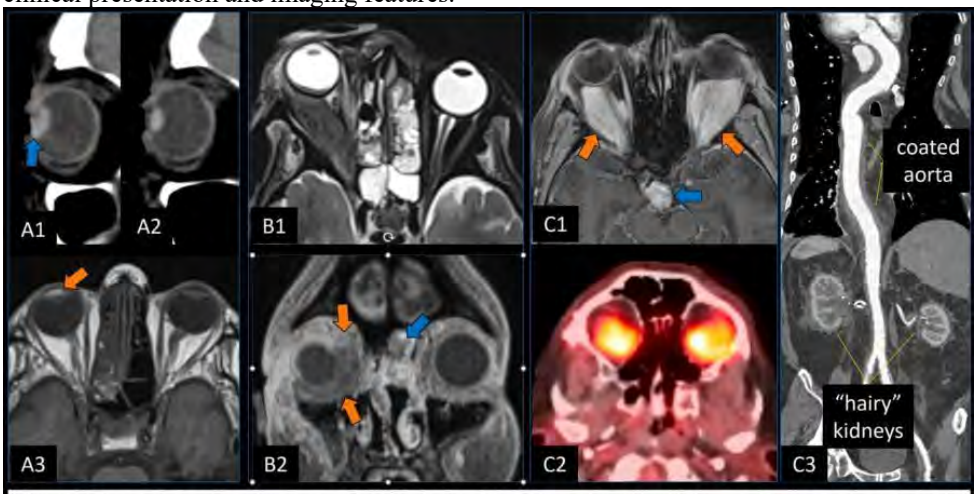

Figure. Different patients with various causes of orbital pain. **Panel A:** CT in a patient with orbital trauma demonstrates hyperdensity in the anterior chamber consistent with hyphema (**A1**, blue arrow), also seen as T1 hyperintensity on MRI (**A3**, orange arrow). Compare with normal contralateral globe (**A2**). **Panel B:** Axial T2 (**B1**) and coronal CET1 (**B2**) in acute invasive fungal infection show extensive inflammatory change in the right orbit with sites of nonenhancement (orange arrows) along with areas of nonenhancing mucosa ("black turbinate" sign, blue arrow). **Panel C:** CET1 shows sellar (blue arrow) and orbital (orange arrows) masses in a patient with Erdheim-Chester disease. Note avid FDG uptake (**C2**) as well as typical periaortic and perirenal infiltration on CT (**C3**).

(Filename: TCT_1080_Figure.jpg)

1505

Oropharyngeal Squamous Cell Carcinoma Treatment Options based on Stage and Key Radiologic Features: A Primer for Radiologists and Trainees

M Pasyk[1], M Nance[1], S Tedla[1], J Remick[1], M Patel[1], K BAUGNON[1], A Aiken[1]
[1]*Emory University, Atlanta, GA*

Summary and Objectives
Oropharyngeal squamous cell carcinoma (OPSCC) staging, prognosis and management is continually evolving. In the most recent edition of the American Joint Committee on Cancer (AJCC8) two distinct TNM classifications were devised for HPV-positive and HPV-negative OPSCC to better reflect patient prognosis. Prognosis for HPV-positive OPSCC is known to have significantly improved outcomes with a higher proportion of patients eligible for de-escalated management following transoral robotic surgery (TORS) when compared to its smoking-related HPV-negative OPSCC counterpart. De-escalated management reduces the morbidity associated with adjuvant chemoradiation therapy (CRT) while providing a similar outcome compared to standard treatment doses. Therefore, an important treatment decision is whether a patient is a candidate for TORS or requires standard CRT - a decision which requires accurate staging and identification of key radiologic characteristics of OPSCC. Despite the importance of imaging in the management of OPSCC, the complexity of the new OPSCC staging system and how it relates to guiding treatment has become a source of confusion for radiologists and trainees. Here, we present a road-map of the key radiologic features (figure 1) integrated into the current TNM staging for management decisions in OPSCC. We provide a simplified paradigm for radiologists based on our institutional algorithm derived from the current literature[1]. This paradigm focuses on two key decision points: 1) is the patient a candidate for TORS and 2) is the patient a candidate for de-escalation of CRT? We summarize key imaging features which generally favor TORS over standard CRT treatment including T1 or T2 stage, exophytic primary, < 4 metastatic regional lymph nodes, and unilateral nodal disease without ENE. Additionally, we present features disfavoring TORS including T3 and T4 stage, soft palate location, endophytic primary, close proximity of the primary to the hyoid bone or lingual surface of the epiglottis, >4 metastatic regional lymph nodes, bilateral nodal disease and ENE. In summary, as treatment and staging paradigms for OPSCC continue to evolve, it is important that radiologist have a framework of the key imaging features which impact management. With improved awareness and knowledge of OPSCC specific staging algorithms, it is hoped that an increasing proportion of OPSCC patients become candidates for TORS with CRT de-escalation.

Figure 1.

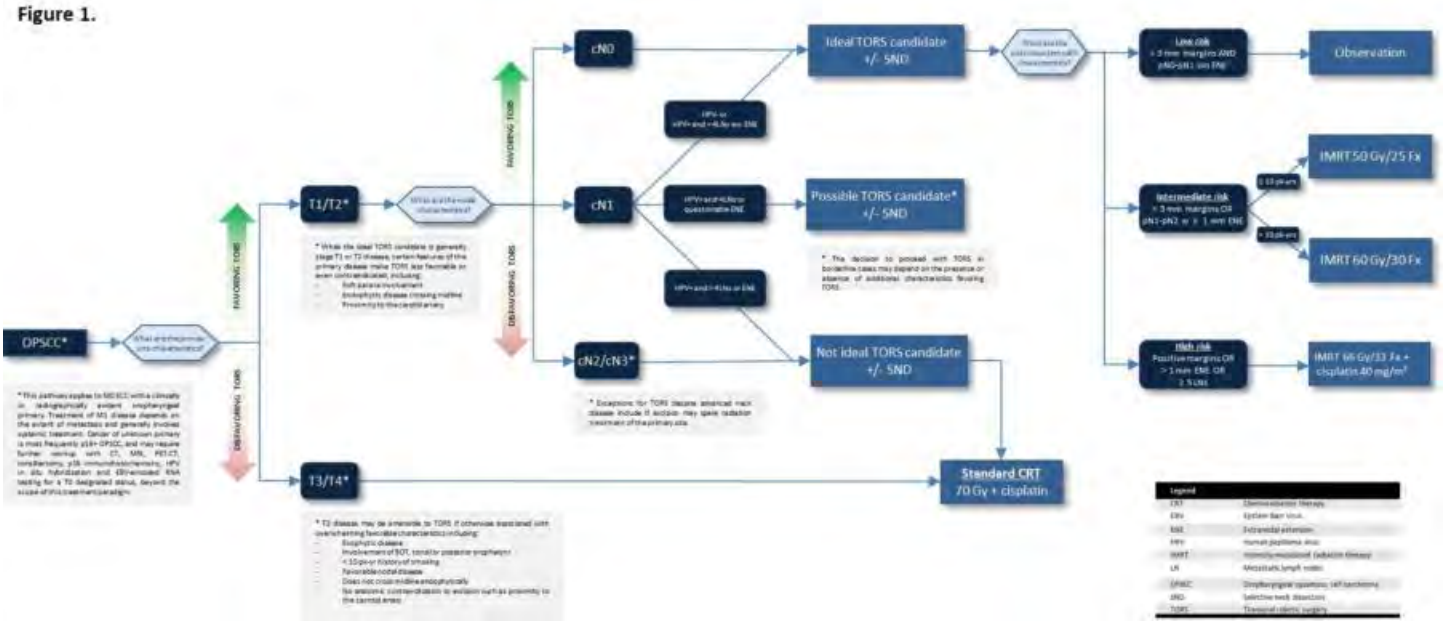

(Filename: TCT_1505_treatmentOPSCCpathway.jpg)

852

Other (Non-Medulloblastoma) Embryonal Tumors of the Central Nervous System: a Review Based on the 5th Edition of the World Health Organization (WHO 2021) Central Nervous System Classification

R Fernandes[1], G Bandeira[2], C Cavalcante[1], F Souza[1], M Yamanari[1], G Teixeira[1], Y Casal[3], L Lucato[4], A Mamere[1]
[1]*Barretos Cancer Hospital, Barretos, SP,* [2]*Faculadde de Medicina da Universisdae de São Paulo, Sao Paulo, Sao Paulo,* [3]*Faculdade de Medicina da Universidade de São Paulo, São Paulo, SP,* [4]*Instituto de Radiologia, Hospital das Clínicas da Faculdade de Medicina da Universidade de São Paulo, São Paulo, São Paulo*

Summary and Objectives
The embryonal tumors (ET) of the central nervous system (CNS) are a collection of mainly, but not exclusive, pediatric solid lesions thought to originate from aberrant development with relatively low mutational burden in comparison to adult neoplasms. Recent

incorporation of molecular phenotypes of CNS tumors brought major changes to ET classification, laying emphasis on its heterogeneous biology. The 5th Edition of the World Health Organization (WHO) classification of CNS tumors has divided the ET into medulloblastomas (MB) and other embryonal tumors (OET), the latter being the most common in infants younger than 1 year old and represented by the preexisting atypical teratoid/rhabdoid tumor (AT/RT) and embryonal tumor with multilayered rosettes (ETMR), and the new aditions known as FOXR2-activated CNS neuroblastoma, cribriform neuroepithelial tumor (CRINET) and CNS tumor with BCOR internal tandem duplication. The diagnostic approach for other embryonal tumors following the new WHO classification (2021) includes the analysis of biallelic inactivation of the SMARCB1 gene in AT/RT, C19MC alteration or DICER1 mutation in ETMR. As for the new types of genetically-defined other ET of the CNS there should be the analysis of FOXR2 activation in CNS neuroblastoma and heterozygous internal tandem duplication (ITD) in BCOR exon 15 in CNS tumor with BCOR ITD. There is a significant overlap in the imaging findings of these uncommon neoplasms, therefore the patient's age plays an important role regarding its diagnosis. MRI is the preferential imaging modality and the Diffusion Weighted Image (DWI) sequence is key to demonstrate its typical restricted diffusion, since ET are known to be high cellular lesions with a high nucleus-cytoplasm ratio. As in MB, other ET are not bound to enhance after contrast media injection.
Purpose
To show and discuss the imaging findings of patients diagnosed with the following ET types: atypical teratoid/rhabdoid tumor, embryonal tumor with multilayered rosettes, FOXR2-activated CNS neuroblastoma, CNS tumor with BCOR internal tandem duplication, CNS neuroblastoma, SOE. Teaching Points: To review what the neuroradiologist needs to know about the oncogenesis of other embryonal tumors. To review the main changes regarding the other embryonal tumors based on the 5th WHO classification of CNS tumors. To illustrate imaging findings related to other embryonal tumors.

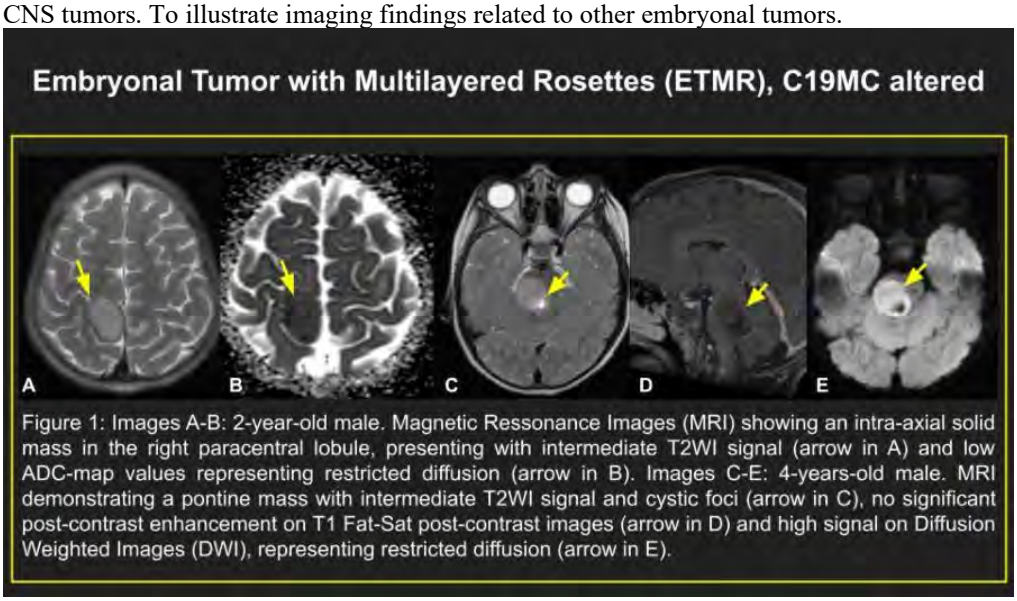

Figure 1: Images A-B: 2-year-old male. Magnetic Ressonance Images (MRI) showing an intra-axial solid mass in the right paracentral lobule, presenting with intermediate T2WI signal (arrow in A) and low ADC-map values representing restricted diffusion (arrow in B). Images C-E: 4-years-old male. MRI demonstrating a pontine mass with intermediate T2WI signal and cystic foci (arrow in C), no significant post-contrast enhancement on T1 Fat-Sat post-contrast images (arrow in D) and high signal on Diffusion Weighted Images (DWI), representing restricted diffusion (arrow in E).
(Filename: TCT_852_ASNR23.jpg)

1339

Parathyroid adenomas: Utility of Tc-99m Sestamibi Parathyroid scan and its Multi-modality Correlation. A case based multi-modality pictorial review of interesting cases

P Suthar[1], S Virmani[1]
[1]*Rush University Medical Center, Chicago, IL*

Summary and Objectives
Parathyroid adenomas are one of the most common benign tumors of parathyroid gland often presenting as primary hyperparathyroidism with elevated serum calcium and parathyroid hormone level (PTH). Parathyroid adenoma can be perithyroidal or ectopic in location. Tc-99m sestamibi scan with SPECT/CT gives better localization of adenoma even in ectopic location.
Purpose
• Purpose of this educational exhibit is to learn Tc-99m sestamibi scan protocol, technique, imaging findings and associated false positive and false negative findings. • To learn benign, incidental and pathologic abnormalities seen on Tc-99m sestamibi scintigraphy. • Multimodality comparison and its correlation with conventional CT/MR imaging when available.
Materials and Methods
We present a case based multimodality pictorial review (Tc-99m sestamibi parathyroid scintigraphy, 4DCT, and MR) highlighting the spectrum of different interesting cases of parathyroid adenoma including ectopic location as well as post operative implants in forearm.
Results and Conclusions
Parathyroid Scintigraphy is helpful in localizing the parathyroid adenoma and is nearly essential in patients with negative ultrasound, recurrent hypercalcemia in patients with prior parathyroidectomy, indeterminate ultrasound findings and in patients with suspected parathyroid adenomas with thyroid nodules. After reviewing this educational exhibit, the interpreting radiologist would learn Tc-99m

sestamibi scan protocol, technique, imaging findings, its multi-modality correlation and associated false positive and false negative findings.

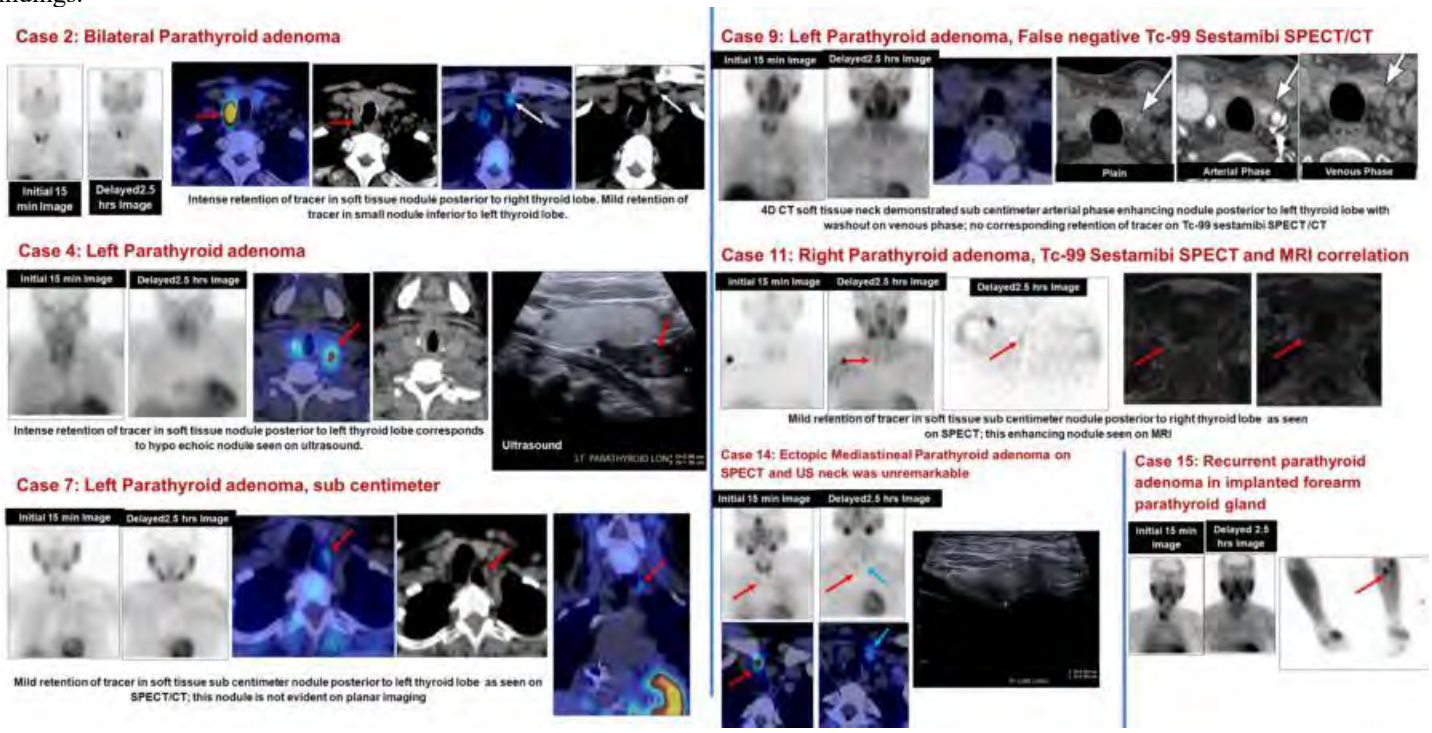

(Filename: TCT_1339_Slide1.JPG)

1419

Parotid tumors revisited, A new perspective for an old topic

A Moawad[1], M Alnoury[2], O Teytelboym[3], A Honarmand[4]

[1]Mercy Catholic Medical Center, Darby, PA, [2]University of Pennsylvania, Philadelphia, PA, [3]Mercy Fitzgerald Hospital, Darby, PA, [4]Massachusetts General Hospital, Harvard Medical School, Boston, MA

Summary and Objectives

• Brief review of anatomy of the parotid gland and parotid space relevant to imaging diagnosis and treatment options • Case based imaging review of common and uncommon but clinically important parotid gland tumors (including pleomorphic adenoma, Warthin tumor, lipoma, benign lymphoepithelial lesions, mucoepidermoid carcinoma, adenoid cystic carcinoma, etc.) and tips for most accurate differential diagnosis • Brief review of most common parotid tumors (and mimickers) in the pediatric population including benign epithelial and mesenchymal tumors as well as most common malignant tumors in the pediatric population • Discussing the role of the neuroradiologist in using different imaging techniques in treatment planning • Reviewing NCCN/ASCO guidelines for management and what neuroradiologists need to know

Purpose

• Anatomy o Practical guide in understanding basic parotid gland anatomy and appearance in MRI, CT and US modalities o Anatomic review of lymph nodal levels relevant to parotid gland tumors • Diagnosis o Basic imaging characteristic of different parotid tumors/lesions with emphasis on MRI features including signal characteristics, morphology, associated enhancement, surrounding structure findings etc. o How to interpret DWI/ADC map to optimize differential diagnosis o Potential role of MR spectroscopy in differentiation of parotid lesions and when it is useful o TNM staging of major salivary gland tumors (including parotid gland tumors) o The importance of perineural spread and how to diagnose it o Ultimately, crucial imaging finding checklist to include in the report and what the clinician needs to know • Management and Treatment Planning o Role of radiology in management and treatment planning of the major salivary gland tumors according to NCCN and ASCO guidelines o Tissue biopsy and indication of fine needle aspiration vs. core biopsy • Surgical strategies in treatment of parotid gland lesions: o Brief review of different surgical approach including partial, superficial, total parotidectomy • Common post-treatment findings of parotid tumors including post-radiation changes • Best strategies for most-treatment imaging follow-up including time intervals

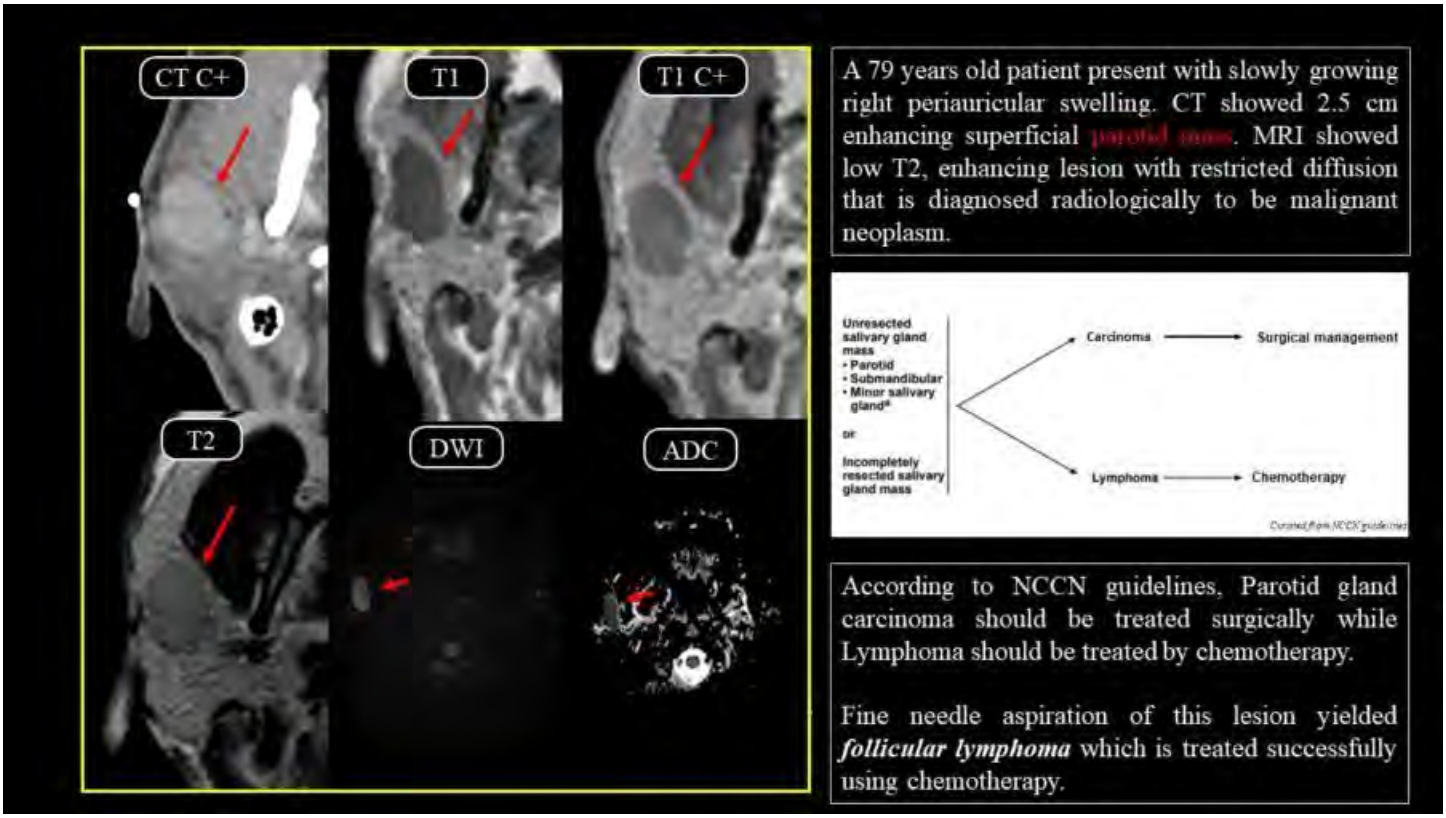

(Filename: TCT_1419_ASNR23-parotid.jpg)

199
Peculiar Parathyroid
J Bykowski[1], I Ailes[2], M Bouvet[3], K Brumund[4]
[1]UC San Diego, San Diego, CA, [2]Sidney Kimmel Medical College, Philadelphia, PA, [3]University of California San Diego, La Jolla, CA, [4]UCSD Health System, La Jolla, CA

Summary and Objectives
While a solitary parathyroid adenoma remains the most common finding during imaging of hyperparathryoidism, Neuroradiologists need to maintain a targeted search pattern across ectopic locations, recognize atypical adenoma appearance and be familiar with causes for multi-gland involvement and other pathology that involves the parathyroid gland. After reviewing this exhibit, participants will be able to: -recognize variant locations and appearance of parathyroid adenoma; -refine differential diagnosis for multi-gland parathyroid involvement; -recommend complimentary imaging studies (US, multiphase CT, Tc 99m Sestamibi/SPECT, Fluorocholine PET/MRI) as appropriate for complicated cases. Overview of Cases: -Ectopic parathyroid adenoma -Intrathyroidal parathyroid adenoma -Parathyroid cyst -Lithium-related parathyroid hyperplasia -MEN-1 related multiple parathyroid adenoma -Parathyromatosis -Reimplant parathyroid adenoma -Parathyroid carcinoma

Peculiar Parathyroid

ASNR 2023: Transforming the Future of Neuroradiology

Teaching Points

After reviewing this exhibit, participants will be able to:

- recognize variant locations and appearance of parathyroid adenoma
- refine differential diagnosis for multi-gland parathyroid involvement
- recommend complimentary imaging studies (US, multiphase CT, Tc 99m Sestamibi/SPECT, Fluorocholine PET/MRI) as appropriate for complicated cases.

Overview of Cases

- Ectopic parathyroid adenoma
- Intrathyroidal parathyroid adenoma
- Parathyroid cyst
- Lithium-related parathyroid hyperplasia
- MEN-1 related multiple parathyroid adenoma
- Parathyromatosis
- Implant parathyroid adenoma
- Parathyroid carcinoma

Implant Parathyroid Adenoma

- Parathyroid transplantation may be performed if the vascular supply cannot be maintained during thyroid surgery.
- Gland is often minced into pieces and implanted into the sternocleidomastoid muscle.
- May also be implanted into the brachioradialis, outside the field of view of routine imaging for hyperparathyroidism.

Patient with prior thyroidectomy and radioactive iodine therapy for thyroid cancer presented with hypercalcemia consistent with primary hyperparathyroidism.

The arterial phase neck CT with contrast shows the avid enhancement of the previously implanted parathyroid gland superficial and deep to the right sternocleidomastoid muscle (A, arrows), with rapid contrast washout on venous phase (B, arrows).

Final pathologic diagnosis was multinodular hypercellular parathyroid tissue.

(Filename: TCT_199_ASNRParathyroidBykowski.jpg)

1041

Pediatric CNS tumors: What's new in fifth edition of WHO classification?

A Alfalahi[1], S Hiremath[2], C Parra-Farinas[3], C Hawkins[2], U Tabori[4], V Ramaswamy[2], S Laughlin[2], B Ertl-Wagner[5]

[1]University of Toronto, Department of Medical Imaging-Diagnostic Neuroradiology, Toronto, Canada, [2]The Hospital for Sick Children, Toronto, Ontario, [3]The Hospital for Sick Children (SickKids), University of Toronto, Toronto, Ontario, [4]the hospital for Sick children, toronto, Ontario, [5]The Hospital for Sick Children, University of Toronto, Toronto, Ontario

Summary and Objectives

• Describe the updates in the 5th WHO classification of CNS tumours pertaining to the pediatric population. • Illustrate the radiological findings of newly classified pediatric CNS tumor types. • Highlight the salient genetic and molecular markers necessary to arrive at the diagnosis. • Emphasize the importance of molecular and genetic markers in diagnosis, management and outcome.

Purpose

The recent 5th edition of the WHO classification of CNS tumors focuses on categorizing paediatric and adult type tumor designations based on underlying differences in molecular alteration despite similar histopathological findings. It is important to recognize the new classified tumor types due to inherent differences in tumoral biological behaviour, response to chemoradiotherapy and prognosis. We will illustrate the salient imaging findings in the recent additions to the categories of gliomas, glioneuronal and neuronal tumors, CNS embryonal tumors and tumors of the sellar region. We will also briefly describe the molecular markers necessary for diagnosis and the impact on the therapeutic approach and outcome.

Materials and Methods

Figure legends: A: Diffuse astrocytoma – MYB altered. T1WI post contrast demonstrates periphery and nodular areas of enhancement. B: Supratentorial ependymoma – YAP1 fusion positive. Coronal T2WI demonstrates large lobulated intra-axial space occupying lesion in the right cerebral hemisphere with multiple T2WI hyperintense rounded components C: Posterior fossa ependymoma – Group PFA. T1WI post contrast demonstrates a heterogenous expansile 4th ventricle lesion. D: CNS Neuroblastoma – FOXR2 activated. T1WI post contrast demonstrates intrinsically T1WI hyperintense fluid-fluid levels with peripheral irregular enhancement.

Results and Conclusions

WHO CNS tumor classification is constantly updating with new additions based on evolving evidence on new type and subtypes that found to have a distinct clinical course and treatment response. As a neuroradiologist, its crucial to be aware of the new classification of CNS tumors and associated molecular alterations to effectively interpret radiological findings and facilitate appropriate management. Further research of these tumors would highlight a characteristic imaging findings and aid in early diagnosis.

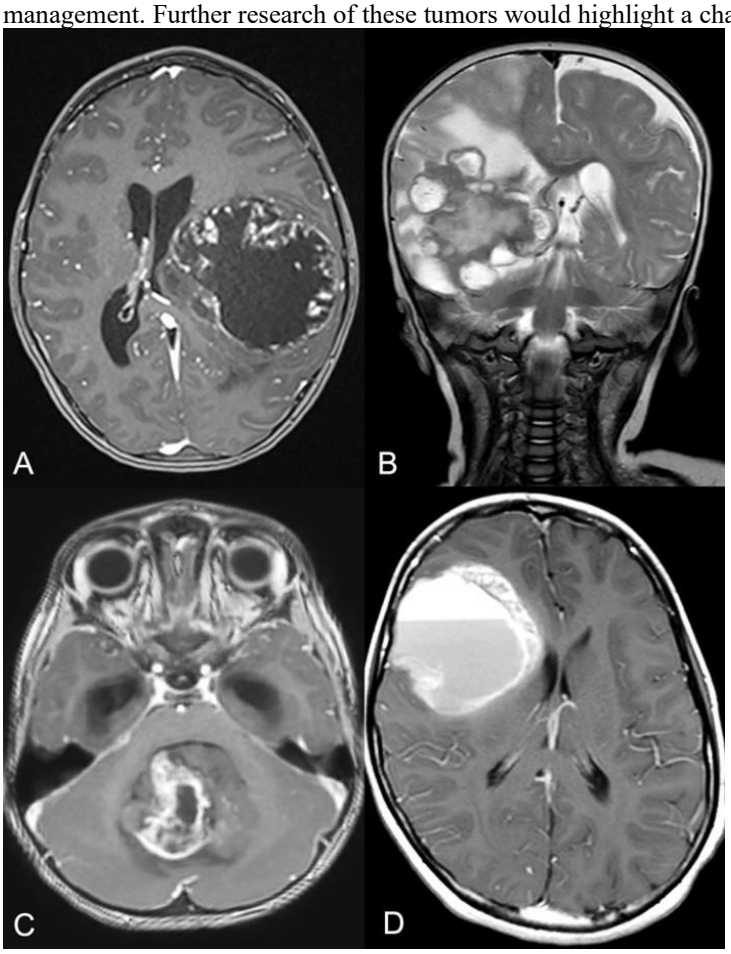

(Filename: TCT_1041_Pedstumors.jpg)

800

Pediatric Hypomyelinating Disorders: Identification, Classification, and Diagnostic challenges

N Gupta[1], A Pauranik[2], H Rajani[2], E Miller[3]
[1]CHEO Univ of Ottawa, Ottawa, Ontario, [2]BC Children's, Vancouver, BC, [3]CHEO, Ottawa, Ontario

Summary and Objectives
1. To discuss the role of imaging and advanced imaging protocol in the diagnosis and differentiation of hypomyelinating disorders in children. 2. To describe the CNS and extra-CNS imaging findings of pediatric hypomyelinating disorders. 3. To review the current literature on pediatric hypomyelinating disorder focusing on the classification and diagnostic challenges.
Purpose
The purpose of this exhibit is to outline hypomyelinating disorders in children with a broad review of the literature. We will describe the distinctive CNS and extra-CNS imaging findings associated with each entity to facilitate the precise diagnosis. We will also focus on the role of combined clinical and radiological approaches in arriving at the final diagnosis along with a dedicated genetic workup.
Materials and Methods
1. Comprehensive discussion of the various disease entity resulting in hypomyelinating disorders in children. 2. Identify and familiarize with the salient imaging features of pediatric hypomyelinating disorder to reach the final diagnosis and differentiate them from demyelination and delayed myelination. 3. A systematic clinico-radiological approach that could help in guiding the appropriate treatment and genetic evaluation.
Results and Conclusions
A pediatric hypomyelination is a diverse group of disorder resulting in the undermyelination of the neurons due to defective myelin formation and deposition. Genetic disorders are the most predominant group contributing to the hypomyelinating disorder in children that presents early in life and are a risk for future pregnancies. The role of imaging is to identify the vital imaging findings to establish the diagnosis of hypomyelination and differentiate it from demyelination and delayed myelination which may create a diagnostic dilemma. Imaging will also help to recognize the associated extra-CNS imaging findings that could guide the diagnosis and pertinent differentials prompting the dedicated genetic workup.

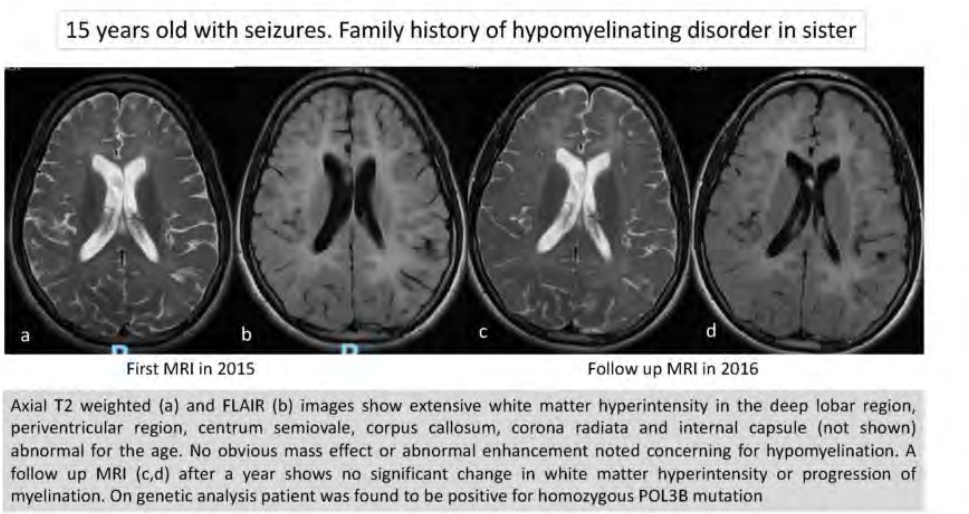

(Filename: TCT_800_ASNR2023Image.jpg)

308

Pediatric Neuroinflammatory Diseases and Mimics: A Systematic Imaging Approach.

S Hiremath[1], M Soldatelli[2], G Longoni[1], E Yeh[3], H Branson[4], B Ertl-Wagner[5]
[1]The Hospital for Sick Children, Toronto, Ontario, [2]The Hospital for Sick Children (Sickkids), Toronto, Ontario, [3]University of Toronto, Toronto, Ontario, [4]Sickkids, Toronto, Ontario, [5]The Hospital for Sick Children, University of Toronto, Toronto, Ontario

Summary and Objectives
This educational exhibit aims to: • Review the basic concepts of neuroinflammatory diseases in childhood • Describe the imaging manifestations of Myelin Oligodendrocyte Glycoprotein antibody-associated disease (MOGAD) in different age groups • Illustrate both common and uncommon findings in Neuromyelitis Optica Spectrum Disorder (NMOSD) and Multiple Sclerosis • Illustrate mimics of these entities based on imaging phenotypes encompassing pathologies that target the optic nerves, deep grey nuclei, white matter, and the spinal cord.
Purpose
Neuroinflammatory diseases in childhood may affect the brain parenchyma, optic nerves, and spinal cord. The typical neuroinflammatory diseases include entities such as myelin oligodendrocyte glycoprotein antibody-associated disease (MOGAD), AQP4-associated neuromyelitis optica spectrum disorder (NMOSD), and Multiple Sclerosis (MS). This educational exhibit will focus on recently described imaging phenotypes of MOGAD including acute disseminated encephalomyelitis (ADEM) like phenotypes,

encephalitis-like phenotypes, leukodystrophy-like phenotypes with emphasis on varied manifestations in different age groups. We will illustrate the typical imaging manifestations in NMOSD and MS in childhood involving the brain and the spinal cord including imaging features of tumefactive lesions. We will also depict pathologies that mimic these lesions divided by anatomic regions including brain, optic nerves and spinal cord.

Materials and Methods

Figure legends: Figure 1 – Axial FLAIR (A) shows multiple bilateral hemispherical white matter lesions, in a 6-year-old male with ADEM like phenotype of MOG positive disease. Axial FLAIR (B) shows right medial temporal cortical thickening and hyperintensity, in a 9-year-old girl with encephalitis-like phenotype with recurrent MOG positive disease. Axial FLAIR (C) shows multiple scattered discrete and confluent supratentorial white matter hyperintensities in a child with oligoclonal band positivity and Multiple Sclerosis. Axial T2 (D) shows a heterogeneous non-enhancing brainstem signal abnormality, in a 4-year-old girl with AQP4 associated astrocytopathy.

Results and Conclusions

Pediatric neuroinflammatory diseases are commonly encountered in children. Knowledge of the typical imaging appearances and their mimics is essential for radiologists and neurologists to aid in early diagnosis, guide further laboratory work up and to initiate appropriate early treatment where possible.

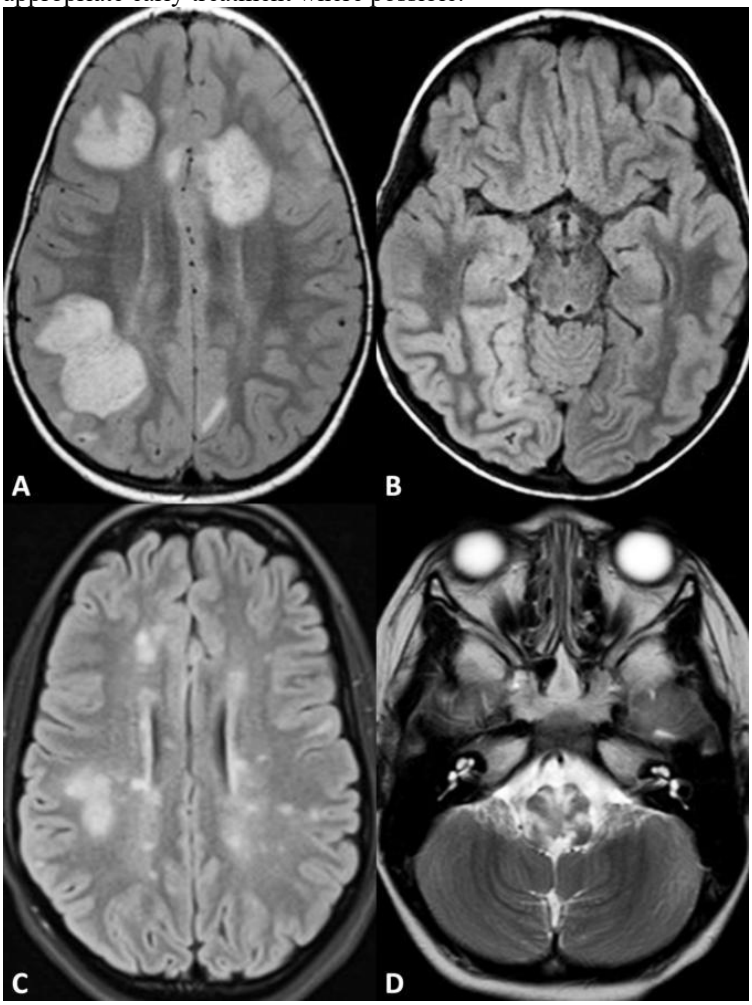

(Filename: TCT_308_Pediatricneuroinflammatorydisease.jpg)

1407

Petrous Apical Lesions: Imaging Findings

P Rao[1], R Ismail[1], C Paton[2], A Rahman, MD; DO[1]

[1]University of Rochester Medical Center, Rochester, NY, [2]University of Rochester, Rochester, NY

Summary and Objectives

1. To review the anatomy of the petrous apex and its relationships with adjacent structures. 2. To identify the characteristic imaging characteristics of a variety of pathologic process affecting the petrous apex. 3. To improve understanding of petrous apex lesions amongst neuroradiologists.

Purpose

The petrous apex is a pyramidal shaped structure that forms the most medial portion of the temporal bone. It forms a unique bridge between the suprahyoid neck inferiorly and the intracranial compartment superiorly. The apex normally composed of bone marrow and dense bone, and is variably pneumatized with aerated connections to the middle ear or it may contain predominantly marrow fat.

The petrous apex is adjacent to several important structures such as Dorello's canal, Meckel's cave, and the petrous portion of the internal carotid artery (ICA). A wide variety of pathologic processes can occur in the petrous apex, including lesions of bone, pneumatized air cells, petrous ICA, inferior extension of intracranial processes, and superior extension of suprahyoid neck processes. Clinical presentations of petrous apex lesions depend on involvement of adjacent structures, and thus cannot accurately be diagnosed based on clinical findings. In this educational exhibit, we present a collection of cases demonstrating the characteristic CT and MRI appearances of various petrous apex lesions. Representative topics covered include anatomic variants such as asymmetric fatty marrow and cephaloceles, infectious/inflammatory lesions such as trapped effusion, cholesterol granuloma, cholesteatoma, and apical petrositis, and tumors such as chondrosarcoma, chordoma, and metastases.
Materials and Methods
In this educational exhibit, various petrous apex abnormalities and lesions will be presented with their relevant CT and MRI images. A brief discussion of clinical presentation and lesion management will be covered
Results and Conclusions
As petrous apex lesions cannot be reliably diagnosed based on clinical findings, imaging plays a vital role in the evaluation this diverse group of pathologic processes. In this education exhibit, we present an overview of the anatomy of the petrous apex and a collection of cases covering the classic imaging appearances of the most common petrous apex abnormalities. This review will provide a foundation for the reader to use imaging to diagnose common petrous apex lesions.

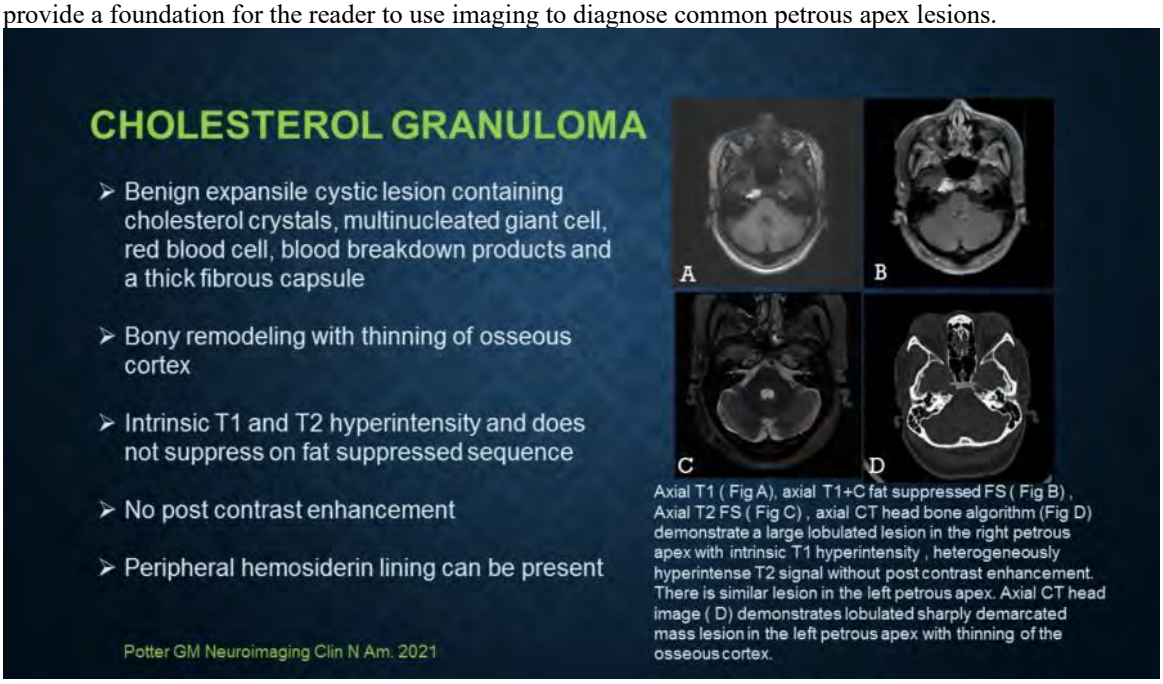

(Filename: TCT_1407_PetrousapexlesionASNR1imge.jpg)

311
Photon-Counting CT Scanners: Imaging Principles and Applications
W Dennis[1], J Reagan[1]
[1]*Medical University of South Carolina, Charleston, SC*

Summary and Objectives
This educational presentation will review the basic physics principles of how photon-counting CT detector arrays (PCDs) function, describe how they differ from the more conventional energy-integrating detectors (EIDs), and use this foundation to explain both the benefits and novel applications of this technology compared to its predecessor. In particular, three data manipulation concepts unique to photon-counting detectors will be reviewed - energy weighting, monoenergetic image creation, and material decomposition. Relevant literature examples of each will be presented with a focus on conceptual understanding. Next, attention will be turned to a discussion of how photon-counting detector arrays compare and contrast with regard to various metrics of image quality (eg. spatial resolution, contrast resolution, signal to noise ratio, artifact reduction) and patient safety (eg. radiation dosage). By the end of the presentation the attendee will: 1) Understand the basic physics principles of photon counting detectors; 2) be able to describe how PCDs differ from EIDs; 3) understand the concepts of energy weighting, monoenergetic virtual image formation, and material decomposition as features of photon-counting detectors; 4) and, lastly, compare and contrast PCDs with EIDs as they relate to spatial resolution, contrast resolution, contrast to noise ratio, radiation dosage, and artifact.
Purpose
This presentation will create a tailored and practical description of photon-counting detectors in language that is both accessible and relevant to the practicing radiologist. The most essential underlying physics principles will be highlighted in a way that accentuates important concepts while avoiding delving into minutiae that are of less consequence to the physician. The attendee will leave with a more intuitive understanding of why this next generation technology will improve the practice of medical imaging.

112

Pictorial Review of Extracranial Head and Neck Schwannomas

T KALELIOGLU[1], D Joyner[2]
[1]UVA, C/ville, VA, [2]University of Virginia, Charlottesville, VA

Summary and Objectives
Schwannomas are benign, encapsulated peripheral nerve sheath tumors. Neck schwannomas can arise from any nerves in the neck, including the hypoglossal nerve, vagus nerve and cervical sympathetic chain. Differential considerations are dependent on the space in which a mass occurs and can include paragangliomas, salivary gland neoplasms, and abnormal lymph nodes. In this presentation we will focus on neck spatial anatomy in detail with demonstrative illustrations, imaging features of schwannomas and anatomical landmarks to illustrate multiple locations of schwannomas in the supra- and infrahyoid neck. Objectives are: - Understanding general imaging features of schwannomas. - Reviewing common and uncommon locations of schwannomas in the neck. - Understanding key anatomical features useful to differentiate schwannomas from their mimics using illustrations.
Purpose
We emphasize the importance of sectional imaging (CT and MRI) and key features to differentiate extracranial head and neck schwannomas from their mimics using clinical images and illustrated diagrams.
Materials and Methods
Extracranial head and neck schwannomas from our institution have been retrospectively reviewed in PACS. Didactic cross sectional cases were selected to illustrate a variety of schwannoma locations. Medical illustrations were created by one of the authors using Procreate digital illustration app.
Results and Conclusions
Schwannomas may arise from many extracranial nerve segment of the head and neck. Understanding neck anatomy and key imaging features of schwannomas as well as anatomic landmarks help radiologists make an accurate diagnosis.

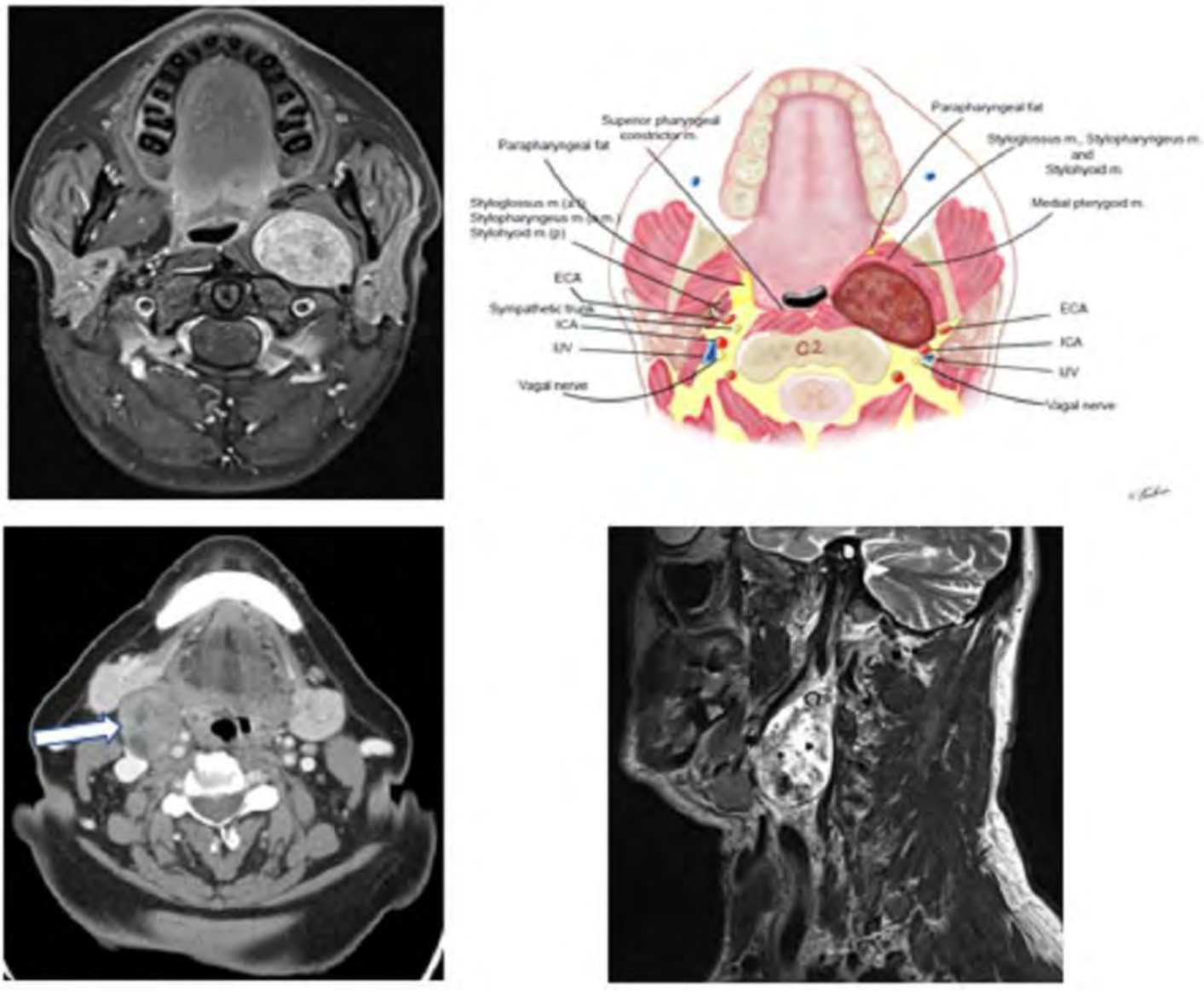

(Filename: TCT_112_Annotation2022-09-16193240300.jpg)

1078

Pictorial Review of Peripheral Trigeminal Nerve Pathologies with emphasis on MR Neurography

B Rathore[1], G Udstuen[1]
[1]*University of Cincinnati Medical Centre, Cincinnati, OH*

Summary and Objectives
Anatomy of Trigeminal Nerve and its branches will be demonstrated using graphical representations and MR Neurography images. Detailed description of peripheral trigeminal nerve branches on MR neurography with helpful pointers for their identification Pathologies will be discussed with relevant key radiological and clinical findings
Purpose
To review MR neurography anatomy of peripheral trigeminal nerve branches. Pictorial demonstration of radiological findings of peripheral trigeminal nerve pathologies. To explain the pertinent radiological positives and negatives in order to guide management.
Materials and Methods
Retrospective evaluation of MRI studies for trigeminal nerve pathologies, particularly MR Neurography, and correlation with the subsequent clinical diagnosis. CUBE STIR, T2 STIR, T2 IDEAL, FIESTA and 3D Merge constitute the major MR Neurography sequences.
Results and Conclusions
After reviewing this education exhibit, the viewer will: Develop a detailed understanding of the anatomy of peripheral trigeminal nerve branches in MR Neurography. Better appreciate the clinical and radiological correlation in Trigeminal pathologies. Understand the pertinent radiologic findings to guide management.

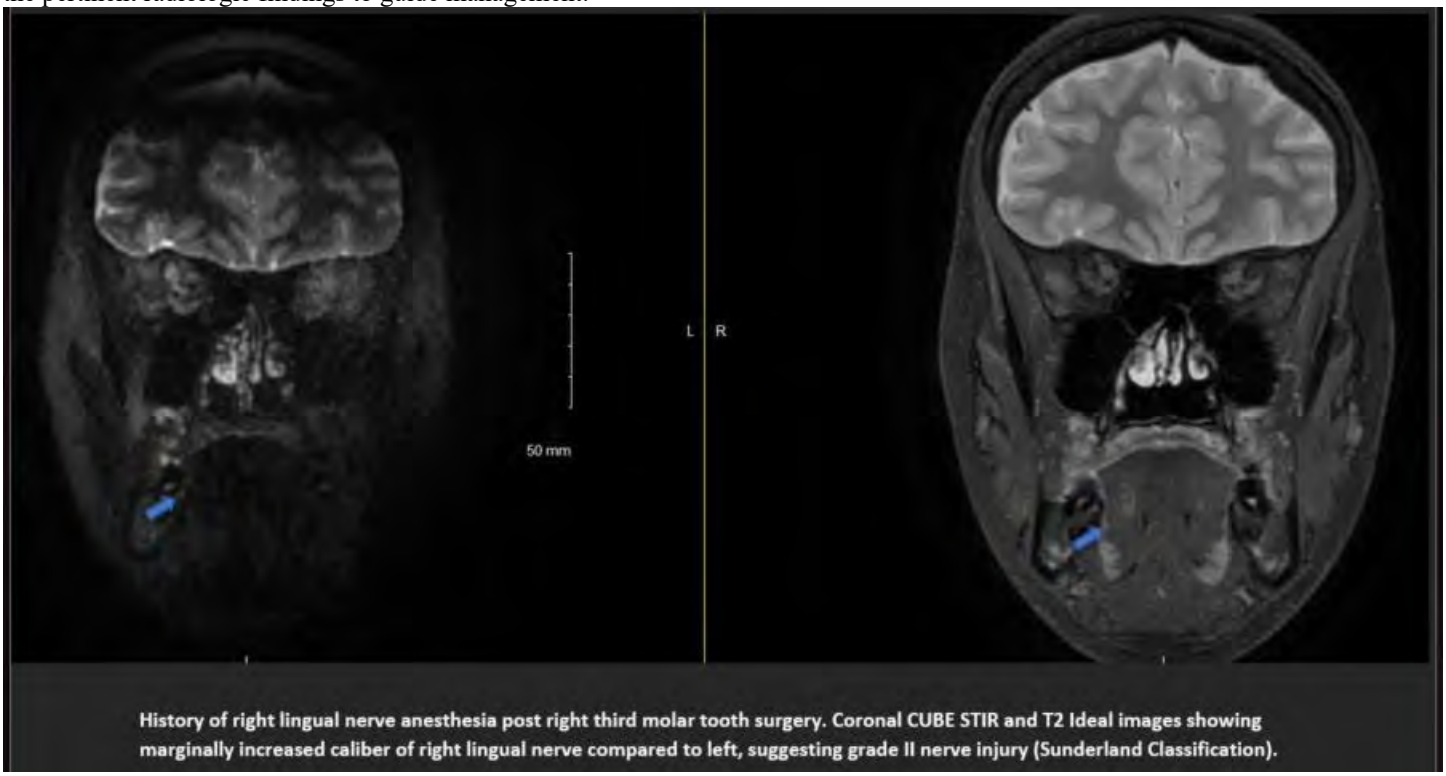

History of right lingual nerve anesthesia post right third molar tooth surgery. Coronal CUBE STIR and T2 Ideal images showing marginally increased caliber of right lingual nerve compared to left, suggesting grade II nerve injury (Sunderland Classification).

(Filename: TCT_1078_mrneurography.jpg)

581

Pictorial Review of Usual and Unusual Presentations of Parotid Neoplasms and Inflammatory Mimics

M Muzaffar[1]
[1]*Dupage Medical Group, Oak Brook, IL*

Summary and Objectives
There is considerable overlap in the imaging features of neoplastic and non-neoplastic processes involving the parotid glands, and biopsy is frequently required for definitive evaluation. This educational exhibit is divided into three sections: benign parotid neoplasms, malignant parotid neoplasms, and inflammatory mimics. Each section provides a multitude of examples of both the classic and less familiar presentations of parotid pathology with the aim to educate the viewer as to what common elements may be present to assist the neuroradiologist in narrowing the differential and deriving a more accurate diagnosis on both CT and MRI. Key anatomic landmarks relevant for tumor localization and surgical planning will be highlighted. In addition, the advantages and disadvantages of ultrasound, CT, and MRI with respect to the salivary gland evaluation will be briefly reviewed, and strategies to improve image quality, particularly with attention to MR sequences, will be elucidated.

Purpose
The purpose of this exhibit is to familiarize viewers with the spectrum of neoplasia and neoplastic mimics encountered in the parotid glands in the adult population.
Materials and Methods
Imaging of the following entities will be included in this exhibit. Benign parotid neoplasms: typical and atypical examples of pleomorphic adenoma, pleomorphic adenoma with seeding, Warthin's tumor, oncocytoma, and lipoma. Malignant parotid neoplasms: mucoepidermoid carcinoma, adenoid cystic carcinoma, acinic cell carcinoma, carcinosarcoma, carcinoma ex pleomorphic, lymphoma. Inflammatory mimics: acute bacterial parotitis, viral parotitis, subacute parotitis, parotid abscess, sialocele, Sjogren's syndrome, IgG4-related sialadenitis, HIV-related lymphoepithelial cysts, accessory parotid tissue, first branchial cleft cyst.
Results and Conclusions
While tissue sampling is frequently required for definitive evaluation, this pictorial review illustrates certain imaging patterns which when recognized will boost the confidence of the interpreting radiologist and guide subsequent imaging or treatment.

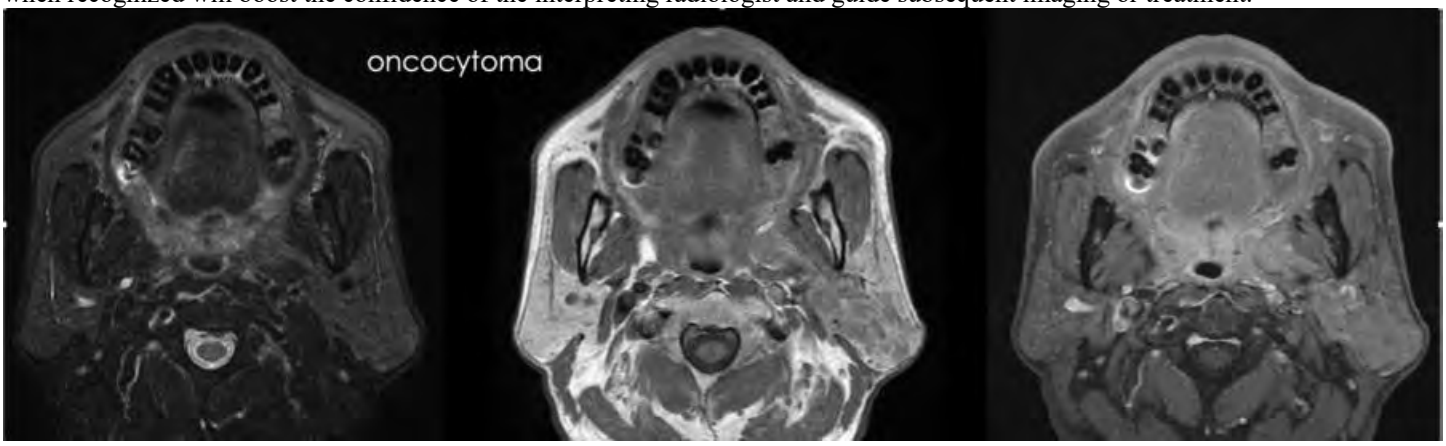

(Filename: TCT_581_Parotidreview--example1.jpg)

786
Pituitary/Sellar Pathology – A Review of the Differential and Imaging Findings
V Tiwari[1], S Szczesniak[1], H Marin[1], B Griffith[1], J Corrigan[1]
[1]*Henry Ford Health, Detroit, MI*

Summary and Objectives
- Review the normal anatomy of sellar/parasellar structures - Review the typical imaging appearance of both common and less frequent sellar pathologies, including key differentiating features - Review typical clinical presentations, diagnoses, and treatments for various sellar pathologies and what role imaging plays in the clinical decision-making process for each
Purpose
The purpose of this exhibit is to familiarize the audience with sellar/parasellar anatomy, as well as the typical clinical presentations, diagnoses, imaging findings and treatments for various sellar pathologies.
Materials and Methods
The educational objectives are accomplished through the use of illustrative cases with a relevant and concise discussion of the literature for each case.
Results and Conclusions
Sellar lesions can vary broadly and include pathology that is vascular (Fig 1), neoplastic (Fig 2), congenital (Fig 3), and infectious/inflammatory (Fig 4). Lesions can range from common causes such as pituitary adenomas, which account for 10-15% of all intracranial tumors, to pituicytomas, of which fewer than 200 cases have been reported. As such, treatment for the various lesions can involve drastically different approaches, which is why imaging characterization is vital and plays a key role in clinical decision-making. Specifically, MRI evaluation is often utilized, though CT also plays a role in the evaluation of adjacent osseous structures. In this exhibit, clinical cases will be utilized to illustrate common imaging findings for a variety of sellar lesions falling into the above categories.

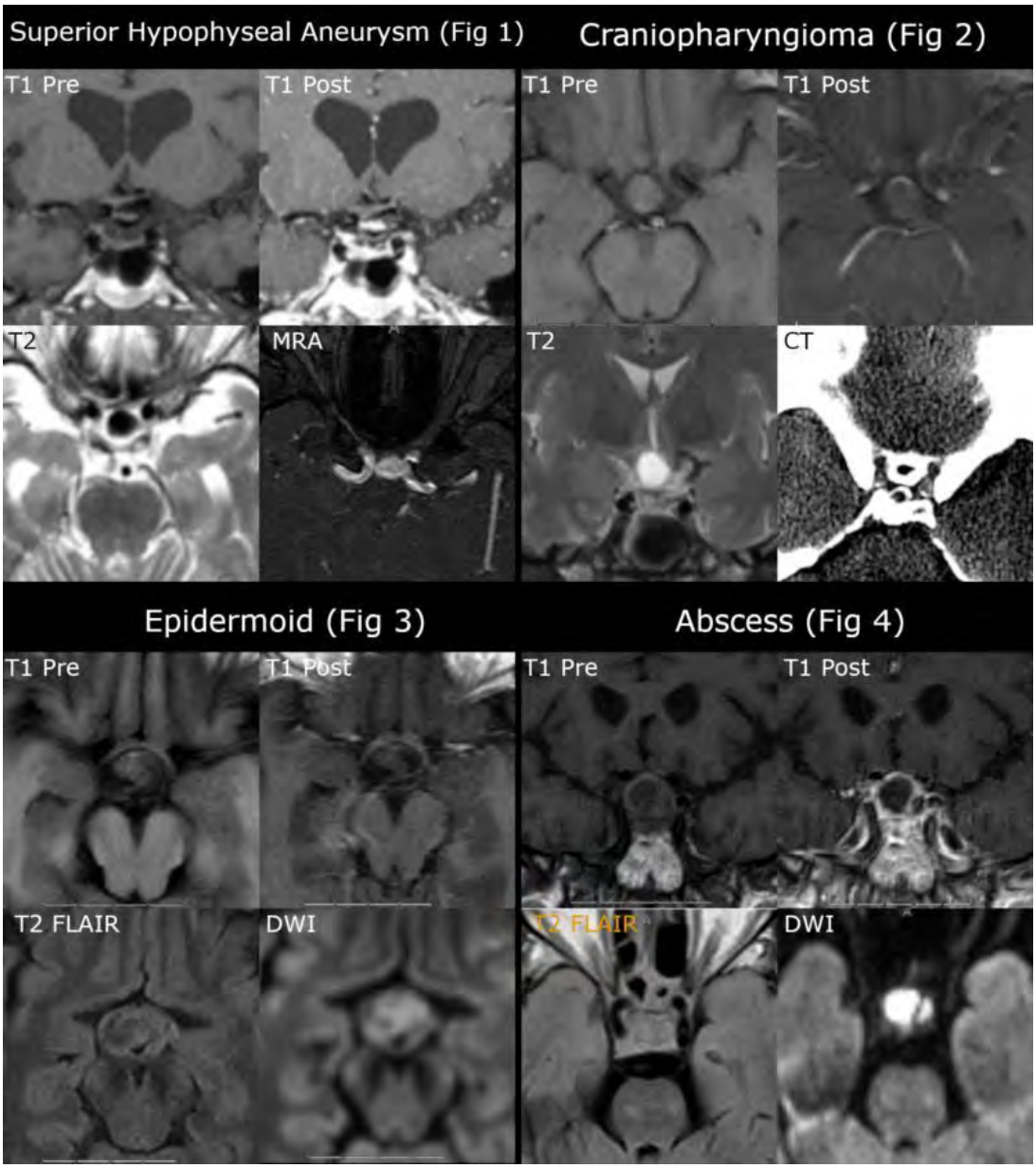

(Filename: TCT_786_Figure.jpg)

215

Posterior Fossa Ischemic Cerebrovascular Syndromes: Correlating Imaging Features with Location Dependent Symptoms

M Gad[1], T Garg[2], R Wang[3], V Yedavalli[4]

[1]Diagnostic Radiology Department, Faculty of Medicine, Mansoura University, Mansoura, Egypt, [2]Johns Hopkins University School of Medicine, Baltimore, MD, [3]Johns Hopkins School of Medicine, Baltimore, MD, [4]Johns Hopkins School of Medicine/Johns Hopkins Hospital, Baltimore, MD

Summary and Objectives

Educational Objectives: 1. Review the vascular supply of the posterior fossa and etiology of ischemia. 2. Identify important functional brainstem neuroanatomy. 3. List common patterns of posterior fossa ischemic insults. 4. Recognize location dependent symptoms of posterior fossa infarcts and correlate them with imaging findings.

Purpose

The primary goal of this exhibit is to improve image interpretation, optimize efficient diagnosis and promote precise clinical and radiological correlation in regard to posterior fossa infarcts with different clinical scenarios.

Materials and Methods

In this exhibit, the following points will be discussed and illustrated with diagrams and real cases. A. Anatomy of the vertebro-basilar system and its topographic vascular supply. B. Common anatomical variants of the posterior circulation. C. Etiology of posterior circulation ischemia. D. Diagnostic imaging approach for localization of clinical brainstem cerebrovascular syndromes which will include: - Identification of cross sectional anatomy of complex brainstem tracts and cranial nerve nuclei. - Correlation of the clinical

presentation of classic posterior fossa cerebrovascular syndromes with involved anatomical structures and their key imaging features. E. Patterns of cerebellar infarcts. F. Differential diagnosis of posterior fossa infarcts.
Results and Conclusions
Results: N/A Conclusion: Posterior fossa infarcts can present with some characteristic imaging findings and a wide clinical spectrum. Hence, proper recognition of brainstem functional neuroanatomy is essential for understanding such clinical syndromes to enable radiologists to identify even subtle imaging findings.

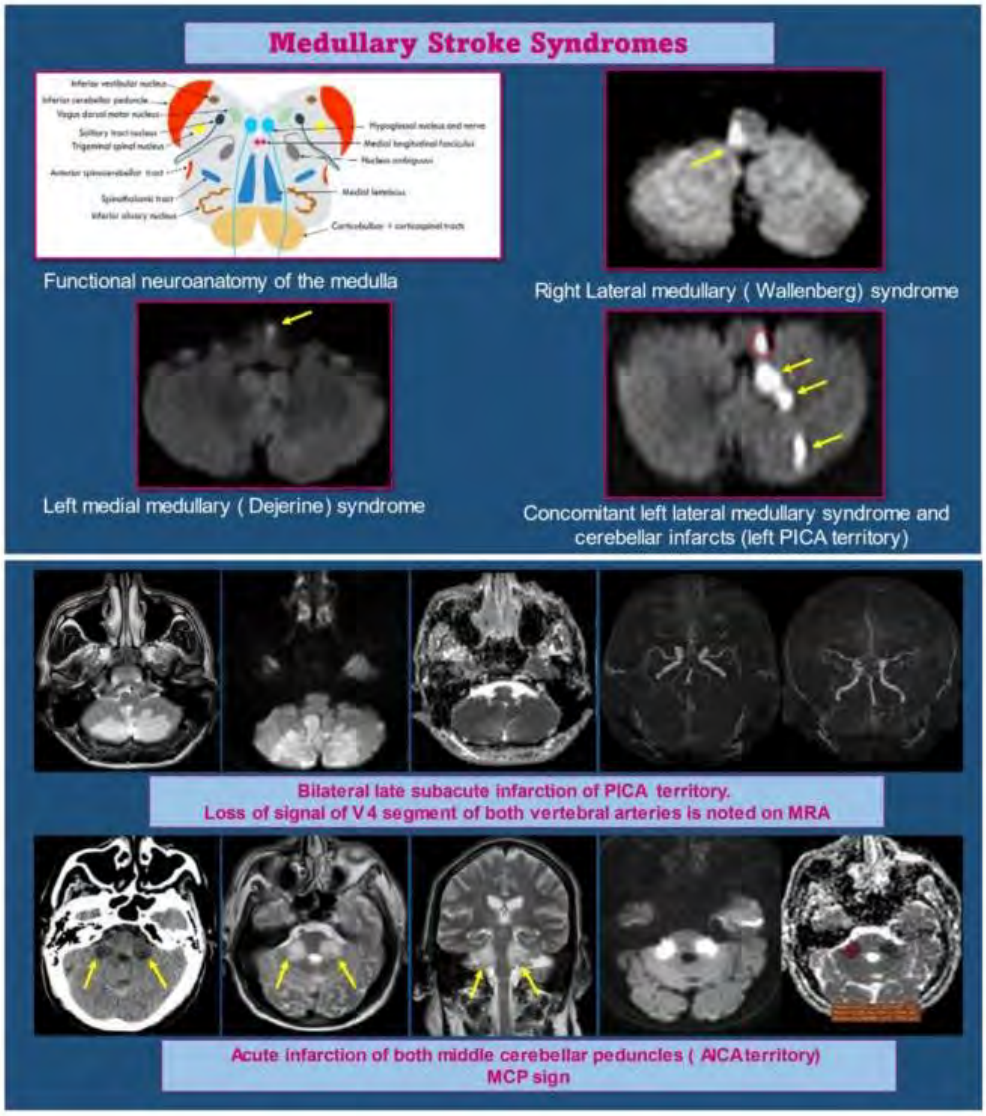

(Filename: TCT_215_ASNR-abstarct1.jpg)

710

Prevalence of Sphenoid Wing Defects/Temporal Encephaloceles in Patients with Spontaneous Otorrhea

V Singh[1], D Ledet[1], J Chetta[2], M Yazdani[1]
[1]Medical University of South Carolina, Charleston, SC, [2]Medical University of South Carolina, Charleson, SC

Summary and Objectives
Sphenoid wing bony defects and temporal encephaloceles can be seen in the setting of spontaneous otorrhea and CSF leak. This study will examine the degree of correlation based on chart review of 89 patients who underwent lateral skull base spontaneous CSF leak.
Purpose
To report the prevalence of sphenoid wing bony defects/temporal encephaloceles in a large group of patients who presented with spontaneous otorrhea and surgically confirmed CSF leak.
Materials and Methods
A retrospective chart review of patients who underwent lateral skull base spontaneous CSF leak repair from January 1st, 2011, to December 31st, 2020 was performed. Collected data included patient demographics, physical exam, imaging findings, and operative details. Imaging features from high resolution temporal bone CT were reviewed independently by a neuroradiologist. The total number and location of temporal bone defects (tegmen tympany or tegmen mastoideum) for each patient was recorded. Additionally,

the presence or absence of empty sella, sphenoid wing bony defects, anterior temporal encephalocele (if high resolution T2 weighted MRI of the temporal lobes was available), and superior semicircular canal dehiscence was recorded.
Results and Conclusions
A total of 89 patients were included, of which 86 underwent unilateral and 3 underwent bilateral skull base repair. The overall mean age was 59.6±12.9, mean BMI was 34.9±8.3, and female sex preponderance was 64.1% (n=51). CT temporal bone images were available on 83 patients with 29 patients also having temporal MRIs. 59/83 patients had an empty sell configuration. 35/83 patients had bony defects of the sphenoid wings (24 bilateral, 5 right, and 6 left). Among the patients with bony defects of the sphenoid wing, 13 had MRIs, 12 of which confirming the presence of anterior temporal encephaloceles. 20/83 patients also had superior semicircular canal dehiscence. The presence of sphenoid wing bony defects (most of which likely correspond to anterior temporal encephaloceles) is common in patient with spontaneous lateral skull base/temporal CSF leaks. Interestingly enough, none of these patients suffered from epilepsy (given association of anterior temporal encephaloceles with seizures).

530

Primary Angiitis of the Central Nervous System (PACNS): Radiological Features and Differential Diagnosis.

A Rovira[1], C Auger[1], M Mossa-Basha[2], S Sceppacuercia[1], J Tortajada Bustelo[1], S Sarria[1], E Rodríguez[1], S Siurana[1], M Castillo[2]
[1]Hospital Universitari Vall d'Hebron, Barcelona, Spain, [2]University of North Carolina School of Medicine, Chapel Hill, NC

Summary and Objectives
To illustrate and describe the radiological appearance and differential diagnosis of primary angiitis of the central nervous system (PACNS), and imaging's role in diagnosis.
Purpose
To provide a detailed review of the literature on this topic To review the different radiological features of PACNS To know the most frequent mimickers of PACNS
Materials and Methods
This educational exhibit discusses the various neuroradiological manifestations of PACNS, with institutional case examples.
Results and Conclusions
PACNS is a rare inflammatory vasculopathy (affecting the medium and small vessels) in brain and spinal cord that is frequently difficult to diagnose. The neurological manifestations vary, but they typically include chronic headache, encephalopathy, focal weakness, or stroke. Brain biopsy is the gold standard and only definitive test for PACNS, but has limited sensitivity, is invasive, and is associated with high rates of morbidity. Lumbar puncture is also performed, but has limited specificity for diagnosis. Catheter angiography is the imaging reference standard and is frequently employed, even though it has limited sensitivity and specificity. Neuroimaging is critical in the diagnosis of PACNS. PACNS may present with diffuse or multi-focal white matter abnormalities, hemorrhagic stroke, single or multi-territorial ischemic infarcts, micro-hemorrhages and pseudotumoral lesions. Vessel wall MRI increases diagnostic accuracy by showing concentric mural thickening and contrast enhancement in brain arteries affected by vasculitis. Reversible cerebral vasoconstriction syndromes, atherosclerosis, Moyamoya disease, CLIPPERS, primary CNS diffuse lymphoma, and secondary cerebral vasculitis are the most common differential diagnoses. PACNS is a rare vasculopathy that is difficult to diagnose through conventional approaches. Although histopathological confirmation is required for a definitive diagnosis, neuroimaging plays an important role in establishing this diagnosis.

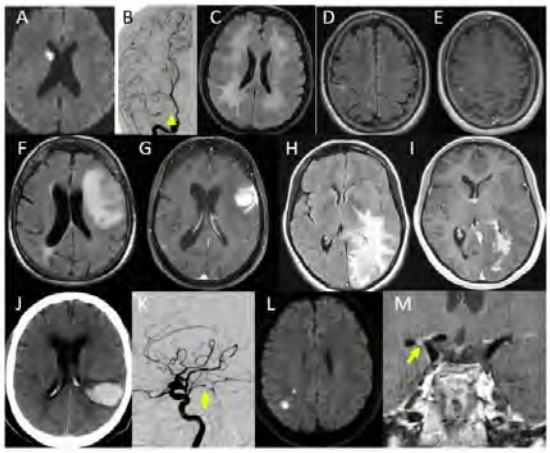

Figure: The different radiological features of PACNS. A-B: Acute lacunar infarct associated with focal stenosis of M1 (arrow). C: Diffuse pattern, mimicking leukodystrophy. D-E: Multinodular pattern with contrast enhancement mainly involving the cortical grey matter. F-G: Pseudotumoral pattern with leptomeningeal enhancement. H-I: Pseudotumoral pattern with heterogeneous enhancement. J-K: Lobar hemorrhage with focal stenosis of posterior cerebral artery (arrow). L-M: Small acute infarcts with concentric enhancement of the internal carotid artery (arrow).

(Filename: TCT_530_figure.jpg)

424

Quantitative MRA: Applications in Cerebrovascular Neuroradiology

Z Nigogosyan[1], S Amin-Hanjani[2], Z Zhang[1], A Chatterjee[3]

[1]Mallinckrodt Institute of Radiology, St. Louis, MO, [2]University Hospitals Cleveland Medical Center, Cleveland, OH, [3]Washington University School of Medicine, St. Louis, MO

Summary and Objectives

Quantitative magnetic resonance angiography (Q-MRA) is a method of quantifying blood velocity in cerebral blood vessels. This educational exhibit explores the potential applications of Q-MRA. Many modalities and techniques have been used to evaluate extra- and intra-cranial blood flow patterns, however, the physical and physiological limitations are still existing. Ultrasound is limited by its inter-operator variability and limited penetration of the cerebral circulation. Time-resolved MRA techniques do not have the spatial or time resolution to quantify blood flow. The current gold standard of digital subtraction angiography provides flow information through temporal resolution but is limited by its qualitative interpretation. Q-MRA provides unique and quantitative vessel flow that independently complements structural anatomic information obtained by more traditional MR and X-ray based modalities. Currently, Q-MRA is typically performed as a two-step process. First, a time of flight (TOF) or contrast enhanced MRA is performed for vessel scout. Next, a 2D through-plane phase contrast MRI is performed to quantify volumetric flow velocity, waveforms and flow direction of the target vessels of interest. The additional value of Q-MRA has been investigated in a variety of cerebrovascular pathologies. In the category of stenosis, it has been used to evaluate extracranial carotid stenosis and analysis of flow related changes after treatment and the functional stenosis of stents. Q-MRA can provide pre-procedural information regarding vessel collateralization. For cerebral aneurysms, Q-MRA flow dynamics, wall shear stress and waveform analysis may better predict the risk of rupture than current diagnostic approaches that measure shape, location, size, and interval growth. 4D flow MRI or 4D Phase Contrast MRI, as an extension of 2D phase contrast MRI, is time-resolved, 3D volume data acquisition with blood flow encoding applied in all three spatial directions. The 4D flow data can be used to generate a non-contrast 3D PC-MRA dataset which overcomes the need for a scout MRA and the a priori selection of a set acquisition imaging plane that is required with current 2D Q-MRA techniques. The recent development of rapid data acquisition techniques, such as compressed sensing, also enables 4D flow MRI to measure the complex blood flow patterns with high spatial and temporal resolution.

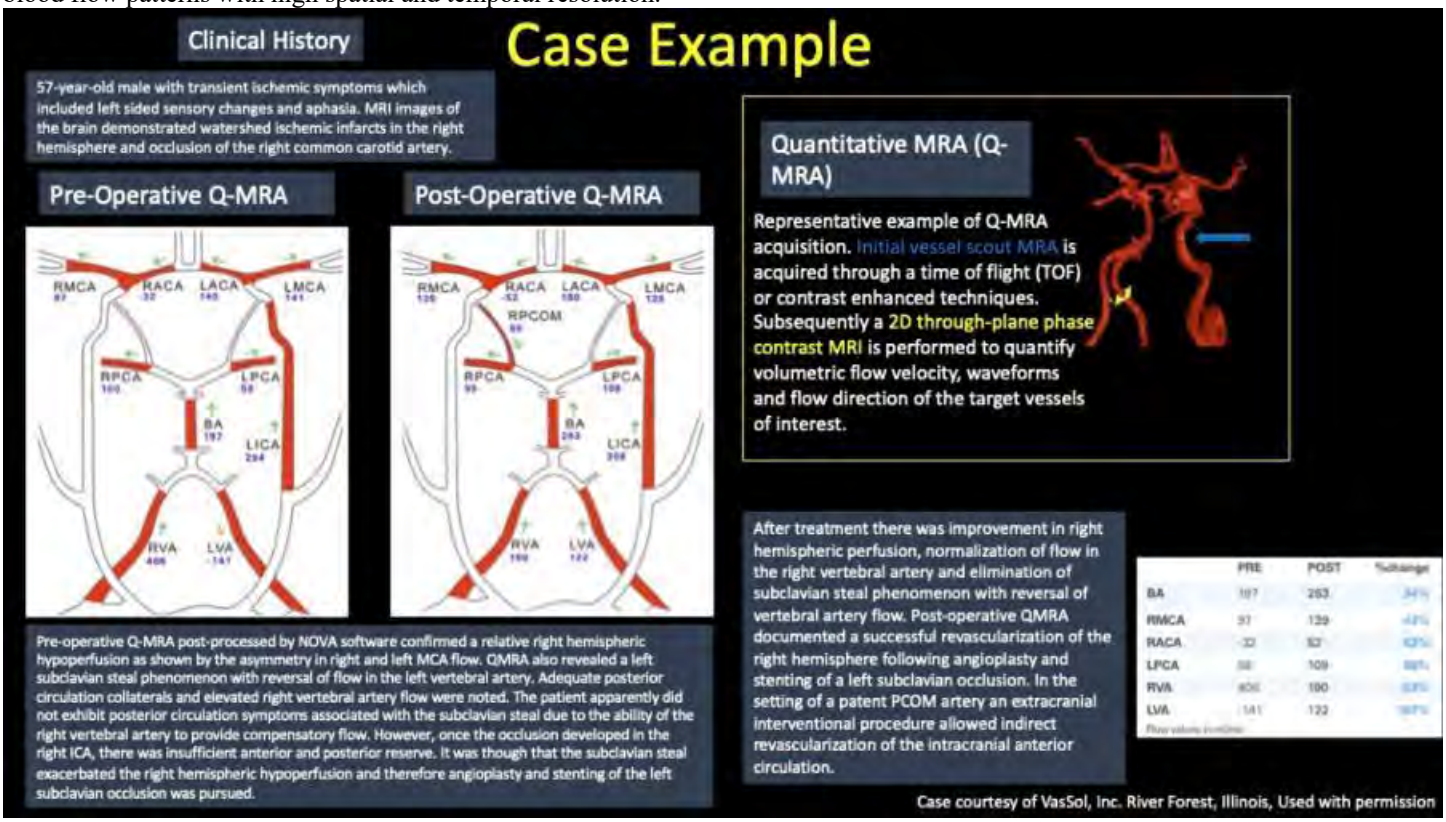

(Filename: TCT_424_ASNRAbstractPDF.jpg)

1222

Radiological Findings post Endovascular Neuro-interventions: What a radiologist needs to know

A Alfalahi[1], C Parra-Farinas[2], T Marotta[3]

[1]University of Toronto, Toronto, Ontario, [2]The Hospital for Sick Children (SickKids), University of Toronto, Toronto, Ontario, [3]St. Michael's Hospital, University of Toronto, Toronto, Ontario

Summary and Objectives

In this pictorial review, we demonstrate various radiological findings that had been related to endovascular neuro-interventions for both diagnostic and therapeutic procedures. We also propose a scheme of recommended imaging modality selection depending on the indication.

Purpose

Almost all patients who have had any type of neuro-intervention will require regular medical imaging follow-up or may require a neuroradiological study for any other clinical indication. As the field of endovascular neuro-intervention is constantly incorporating new devices and techniques, the long-term outcome of various treatments is the primary concern for the majority of currently ongoing studies in the literature; however, there have been scattered reports regarding anticipated asymptomatic transient radiological abnormalities or symptomatic complications whether endovascular device or procedure related that most diagnostic radiologists may be unaware of. Furthermore, imaging techniques will differ depending on the indication of the cross-sectional study, emphasizing the added value of using a specific imaging technique such as dual-energy CT scan, CT perfusion and contrast enhanced MRA.

Materials and Methods

Number: Total of 16 radiological findings (18 cases). Clinical cases: Ruptured and unruptured intracranial aneurysms, cervical ICA stenosis, post endovascular intervention arterial dissection, endovascular thrombectomy in acute stroke and arteriovenous malformation. Modalities: CT, cerebral CTA, MRI and contrast enhanced MRA, cerebral catheter angiogram, Dual energy CT with metal reduction algorithm. Dual energy CT for iodine and virtual non contrast mapping and CT perfusion.

Results and Conclusions

Figure A: Outcome: divided into 3 categories: 1. Vessel related, 2. Device related and 3. Parenchymal related. Figure B: Recommendations: imaging modality and or technique of choice to address specific clinical question. Figure C: Vessel wall imaging with Contrast enhanced T1 and blood signal suppression demonstrates a circumferential and smooth vessel wall enhancement after recent endovascular treatment of acute right MCA occlusion (white arrow) that is an expected finding and should not be mistaken for an underlying vasculopathy. Figure D: Dual energy CT with metal reduction algorithm demonstrate a type of device related post endovascular aneurysm treatment complication where a flow diverter proximal tip (arrow head) had displaced into right A1 aneurysm (white arrow).

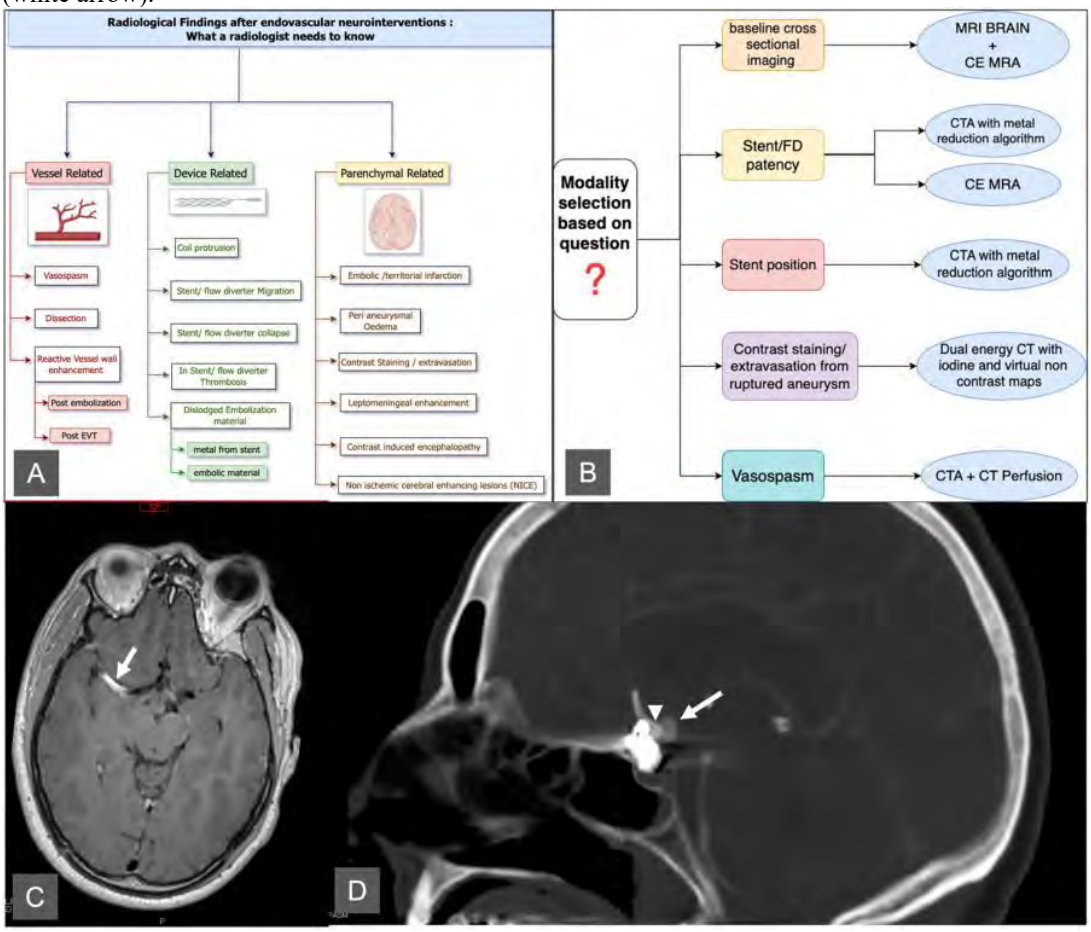

(Filename: TCT_1222_INRfiguresdpiadjusted.jpg)

488

Radiotherapy and the brain: the challenge of imaging follow up of treated brain metastasis

A Ayres[1], S Ferraciolli[2], L Lucato[3], R Moreno[4], A Chen[5], E Weltman[6], H Alves[7], G Bandeira[8], J de Oliveira[9]

[1]ICESP- FMUSP, São Paulo, Sao Paulo, [2]InRad - HC- FMUSP, Sao Paulo, -- SELECT --, [3]Instituto de Radiologia, Hospital das Clínicas da Faculdade de Medicina da Universidade de São Paulo, São Paulo, São Paulo, [4]Instituto do Câncer do Estado de São Paulo- SP, Sao Paulo, Brazil, [5]Icesp/ FMUSP, Sao Paulo, Sao Paulo, [6]FMUSP, Sao Paulo, Sao Paulo, [7]ICESP- FMUSP, Sao paulo, Sao Paulo, [8]Faculadde de Medicina da Universisdae de São Paulo, Sao Paulo, Sao Paulo, [9]Inrad - HC/FMUSP, Sao Paulo, Sao Paulo

Summary and Objectives

Brain metastases occur in up to 30% of oncologic patients. Whole-brain radiotherapy (WBRT) plays an important role in the treatment of cancer patients. Stereotaxic radiosurgery (SRS) with or without WBRT improves local control of treated lesions. SRS without WBRT is an acceptable standard in patients with limited number of brain metastases, potentially reducing neurocognitive decline. The median survival of patients with brain metastases treated with SRS is 8-10 months. Within this period, studies have shown SRS to achieve a radiographic lesion control rate of 90%, defined as lesions with stable or decreasing size. However, transient increase in lesion size during follow up after SRS is not unsual, raising the question of tumor recurrence versus treatment related changes. Therefore we reviewed the evolution of selected cases treated for brain metastases, highlighting the main challenges of imaging follow-up and the tools available to manage them.

Purpose

To illustrate follow-up imaging findings of brain metastases treated with various strategies of RT, including WBRT, SRS, and SRS and immunotherapy.

Materials and Methods

We reviewed illustrative cases of post RT brain metastasis and the main imaging features of the follow-up over time. The findings of conventional and advanced (DSC, DCE and spectroscopy) MR sequences were evaluated during the treatment follow-up and correlated with patient outcome and anatomopathological reports. Based on these cases, the literature was reviewed, highlighting the clinical application of published knowledge, the tools that help distinguish tumor recurrence and treatment-related changes and the limitations of the methods.

Results and Conclusions

Imaging evaluation of patients with brain metastases treated with RT can be challenging, as up to 30% may show an increase of the treated lesion during follow-up, and can occur as early as 6 weeks after the end of SRS, decreasing later or remainning stable. The improvement of available therapies resulted in longer survival of oncologic patients, which made possible to document later growth (over 1 year) of SRS-treated lesions. Thus, monitoring these cases only with conventional MRI sequences, using size as the main parameter to distinguish between radiotherapy-related changes and tumor recurrence could be insufficient. The combination of conventional and advanced MR sequences and, when available, PET MET, increases the diagnostic sensitivity and specificity.

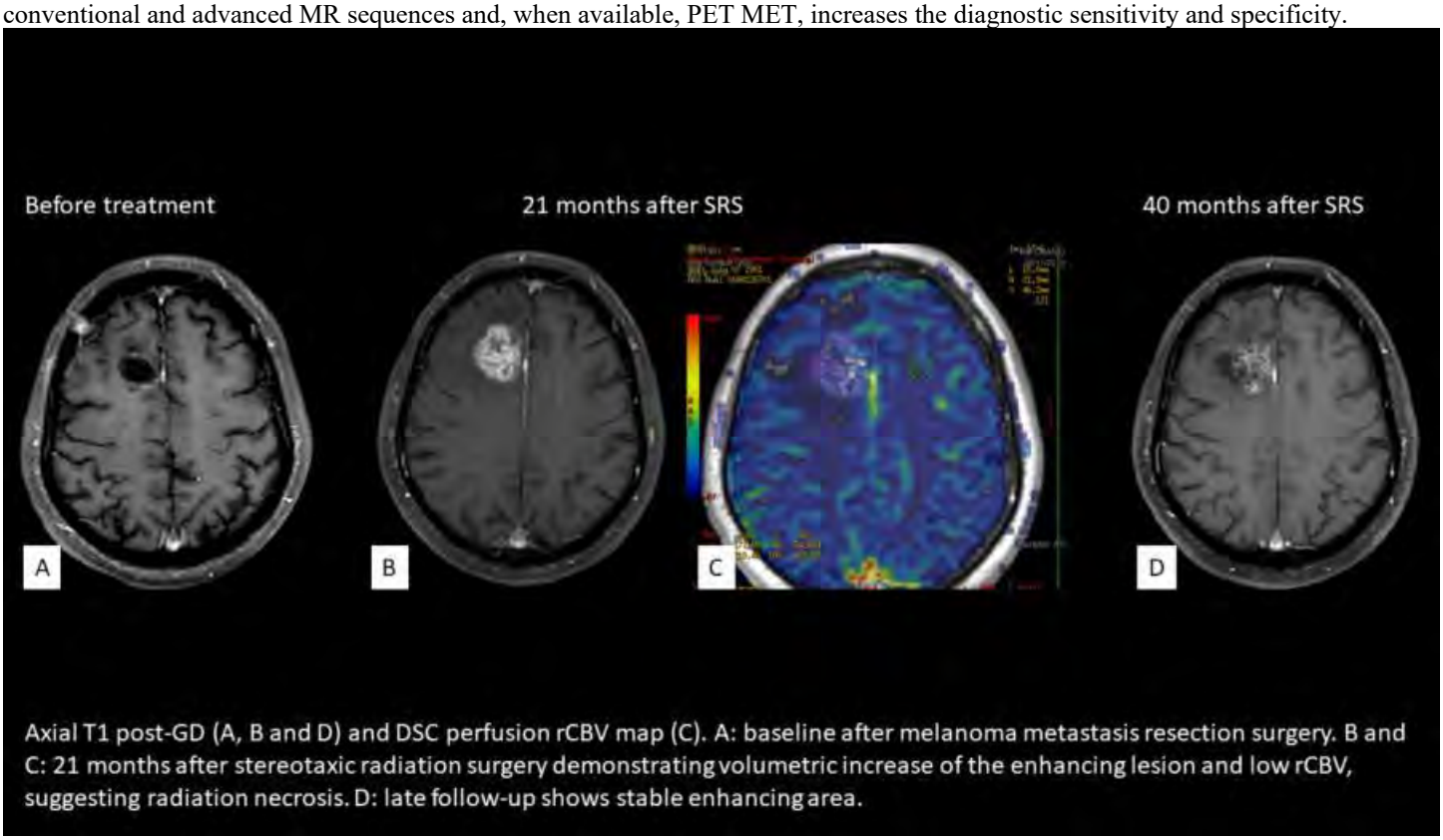

Axial T1 post-GD (A, B and D) and DSC perfusion rCBV map (C). A: baseline after melanoma metastasis resection surgery. B and C: 21 months after stereotaxic radiation surgery demonstrating volumetric increase of the enhancing lesion and low rCBV, suggesting radiation necrosis. D: late follow-up shows stable enhancing area.

(Filename: TCT_488_Slide1.JPG)

1149

Real World Value of Diffusion Weighted Imaging of the Spine

M Ling[1], A Lerner[2], N Sheikh-Bahaei[3], P Rajagopalan[4], P Kim[1], R Assadsangabi[1]

[1]University of Southern California, Los Angeles, CA, [2]USC Keck School of Medicine, Los Angeles, CA, [3]University of Southern California, Irvine, CA, [4]USC, Los Angeles, CA

Summary and Objectives

Diffusion-weighted imaging (DWI) characterizes the tissue-specific random Brownian motion of water molecules. This principle can be utilized to increase sensitivity and specificity to and further characterize various pathologies compared to conventional MR imaging alone. While DWI has been established as a critical tool in evaluation of brain pathology, its usefulness in evaluation of important spinal pathology remains controversial and less recognized. An area where DWI has great potential is for evaluation of marrow disease, such as neoplasm or infection. Here we will outline the clinical applications of DWI in detection and characterization of a variety of osseous and intraspinal canal pathologies. Educational Objectives: -To depict the uses of DWI in addition to conventional MRI in osseous spinal pathologies. -To depict the uses of DWI in intraspinal canal (extra and intradural) pathologies. Content Organization: We will briefly review diffusion-weighted imaging, including techniques, limitations of DWI in the spine, and diffusion tensor imaging (DTI). The majority of the presentation will then focus on a pictorial review of the clinical applications of DWI in the spine. First, we will discuss the use DWI in osseous spinal pathology such as differentiating infection versus degenerative disc disease using the claw sign. We will also discuss how DWI can add information to conventional MRI in assessing vertebral and paraspinal neoplasm and particularly in evaluation of treatment response. Next we will turn our attention to intraspinal canal pathology, including the following: spinal cord neoplasm, spinal cord infarct, demyelinating diseases, and spinal cord injury. We will also briefly discuss how DTI can be used to differentiate ependymoma from astrocytoma, to increase sensitivity for detection of demyelinating lesions, and to better characterize the true extent of spinal cord injuries. Figure 1: 50-year-old male with chronic back pain. MRI of the thoracic spine demonstrates a lobulated septated posterior epidural cystic lesion at T3-T5 which is hyperintense on T2 STIR (a), T1 hypointense (b), demonstrates minimal peripheral enhancement on T1 post-contrast images (c), and demonstrates increased signal on DWI (d). The diffusion restriction characterizes the lesion as an epidermoid cyst.

Purpose

To depict the uses of DWI in conjunction with conventional MR imaging in detection and characterization of a variety of osseous and intraspinal canal pathologies.

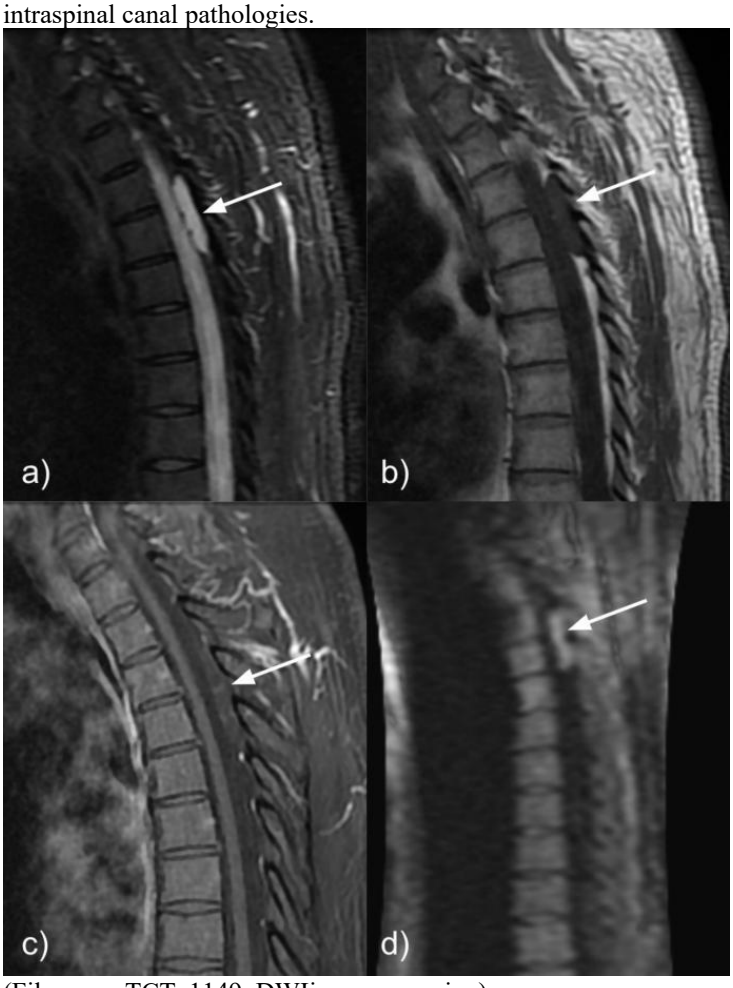

(Filename: TCT_1149_DWIimages-new.jpg)

888

Reporting Aortic and Great Vessel Dissection: What Do Neuroradiologists Need to Know?

A Tejani[1], A Bhatt[2], P Mani[2], N Raiker[2], W Abdellatif[2], A Hussien[3]

[1]UT Southwestern Medical Center, Frisco, TX, [2]UT Southwestern Medical Center, Dallas, TX, [3]UT Southwestern, Garland, TX

Summary and Objectives

Context: Cases of aortic dissection with acute neurological symptoms are time-sensitive with regards to clinical action aimed at preventing complications from delayed care. Reporting pertinent findings on neuroimaging studies, such as CT or MR angiography, to guide non-radiology clinicians is crucial in this context. However, scarcity of head and neck imaging cases with acute aortic pathology can predispose to a lack of familiarity for neuroradiologists, leading to potential delays in care. Educational Objectives: 1. Review pertinent anatomy of the aorta and vascular structures of the neck. 2. Understand optimal imaging technique for high-resolution and high-contrast resolution of the aorta and great vessels. 3. Review imaging manifestations of acute and chronic aortic and great vessel dissection. 4. Detail pertinent findings to include in reporting of aortic and great vessel dissection from non-radiology clinician perspectives. 5. Discuss appropriate terminology for describing acute and chronic aortic and great vessel dissection. Presentation Summary: 1. Introduction 2. Review of imaging technique a. Conventional CT and MR angiography protocol in evaluation of vascular pathology b. Comparison of CT angiography, MR angiography, and digital subtraction angiography 3. Anatomy of the aorta and great vessels 4. Common neurological symptoms in aortic dissection that require head and neck vascular imaging 5. Review of imaging manifestations and guidance for reporting findings a. Classification system and clinical implications b. Imaging findings on CT and/or MR angiography head and neck c. Identifying true versus false lumen d. Information to report from cardiology and surgery perspective e. Potential complications concurrently visualized on imaging f. Imaging mimics (fibromuscular dysplasia, ulcerated plaque) 6. Summary of suggested reporting guidelines and non-radiologist clinical perspective

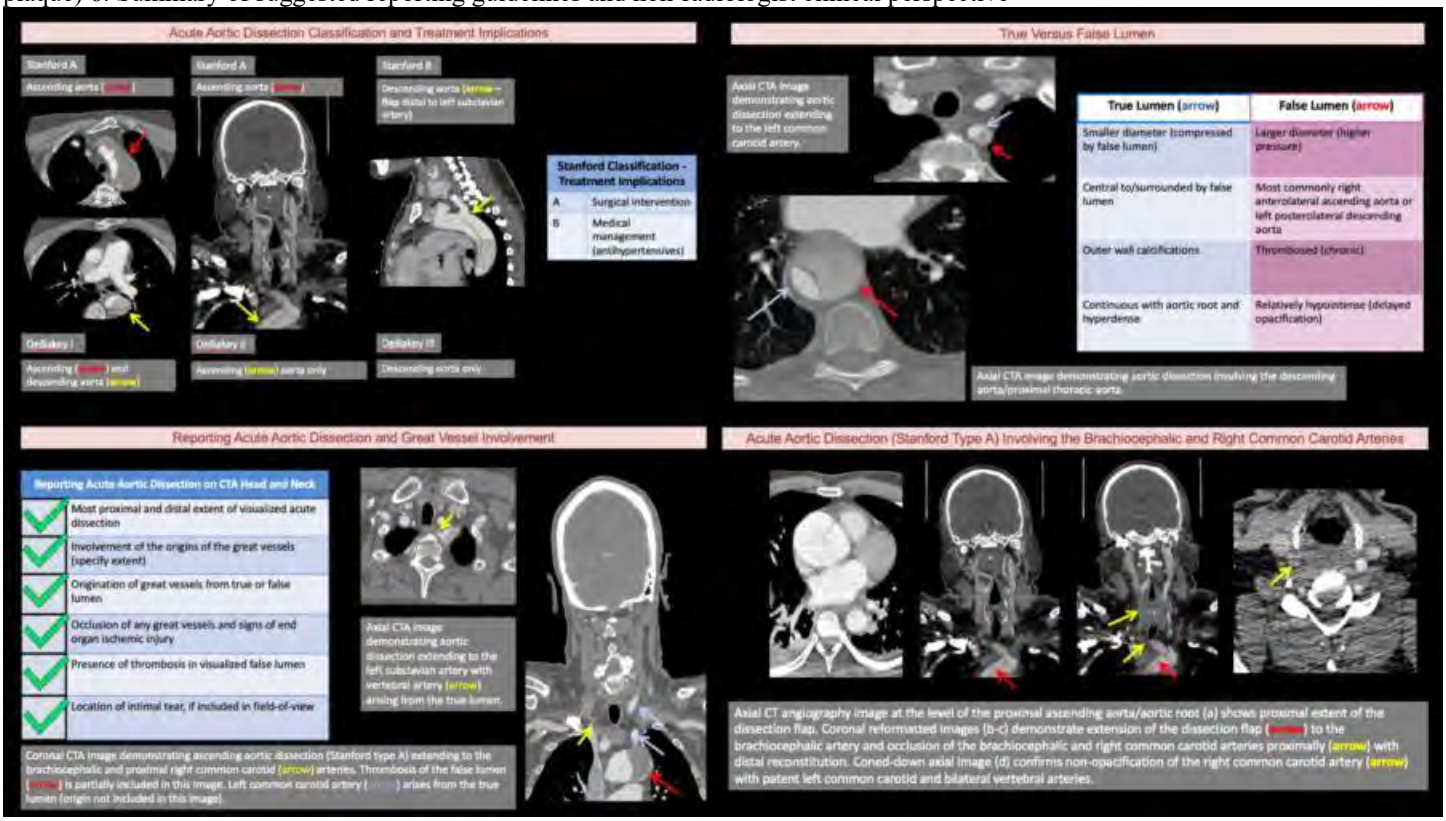

(Filename: TCT_888_Tejani_CTA.jpg)

705

Response Assessment in Brain Tumors: Successes and Challenges

D Ramakrishnan[1], M von Reppert[2], M Krycia[3], M Sala[1], I Ikuta[4], F Memon[5], B Weinberg[6], M Aboian[7]

[1]Yale School of Medicine, New Haven, CT, [2]Brain Tumor Research Group, Yale School of Medicine, New Haven, CT, [3]Yale New Haven Hospital, New Haven, CT, [4]Mayo Clinic Arizona, Phoenix, AZ, [5]Yale University, New Haven, CT, [6]Emory University, Atlanta, GA, [7]Yale University, Woodbridge, CT

Summary and Objectives

Response assessment in neuro-oncology is complicated by the heterogenous appearance of brain tumors after treatment that is difficult to quantify and characterize. This in combination with heterogeneity of brain tumor subtypes, difficulty of correlating radiographic to clinical response, and the evolving nature of brain tumor classification makes definition of treatment response variable and difficult to standardize. Many frameworks have been proposed over the years to address these challenges, but there is no golden standard for response assessment. EDUCATIONAL OBJECTIVES: • Describe the evolution of the RANO criteria from the MacDonald criteria •

Describe the challenges in applying the RANO criteria • Describe the development of the BT-RADS reporting system • Propose the future of advanced imaging in treatment response assessment

Purpose

To discuss the development of response criteria in neuro-oncology, to address the challenges in applying existing criteria across brain tumor subtypes, to discuss the development of a standardized BT-RADS reporting system, and to explore the potential role of advanced imaging techniques in contributing to response assessment

Materials and Methods

Literature review of the MacDonald and RANO criteria and their application to various tumor subtypes (e.g. high-grade glioma, low-grade glioma, medulloblastoma), challenges in applying RANO criteria to pediatric low-grade gliomas, development of the BT-RADS system, and the role of advanced imaging techniques (e.g. DTI, perfusion imaging, amino acid PET, and MR spectroscopy) in response assessment

Results and Conclusions

We describe the development of response assessment methods in neuro-oncology. First, we describe how the RANO criteria addresses gaps in the MacDonald criteria by including assessment of non-enhancing tumor on T2/FLAIR and therapy-related phenomena, such as pseudo-progression. We discuss the limitations of the RANO criteria, focusing on the challenges of applying it to pediatric low-grade gliomas. Response assessment of pediatric low-grade gliomas is challenging due to their heterogenous quality, variable enhancement, and cystic components. We discuss how the RAPNO criteria address the limitations of the RANO criteria. We also discuss the development of BT-RADS criteria, which integrate radiographic and clinical information to assign tumor response categories (coded from 0-4) that are tied to specific management recommendations. Finally, we explore advanced imaging techniques in neuro-oncology.

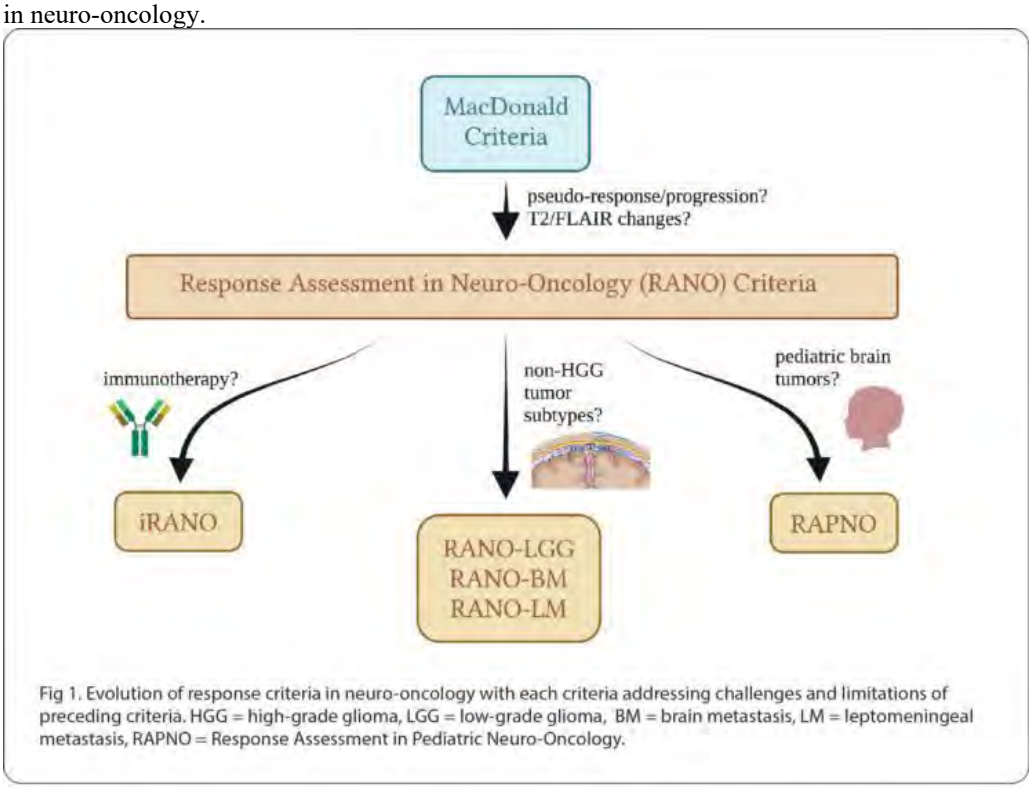

Fig 1. Evolution of response criteria in neuro-oncology with each criteria addressing challenges and limitations of preceding criteria. HGG = high-grade glioma, LGG = low-grade glioma, BM = brain metastasis, LM = leptomeningeal metastasis, RAPNO = Response Assessment in Pediatric Neuro-Oncology.

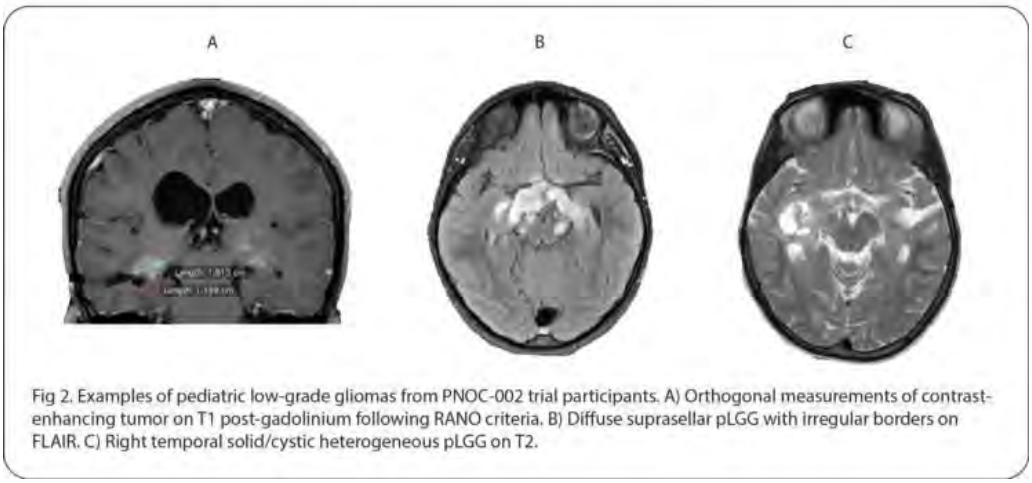

Fig 2. Examples of pediatric low-grade gliomas from PNOC-002 trial participants. A) Orthogonal measurements of contrast-enhancing tumor on T1 post-gadolinium following RANO criteria. B) Diffuse suprasellar pLGG with irregular borders on FLAIR. C) Right temporal solid/cystic heterogeneous pLGG on T2.

(Filename: TCT_705_Response_figs.jpg)

649

Restricting Your Differential - Utilizing Diffusion Weighted Imaging for Orbital Pathology.

K Hendzel[1], A Tran[1], P Setabutr[1], B Ozgen Mocan[1]
[1]University of Illinois at Chicago, Chicago, IL

Summary and Objectives
The orbit is a relatively small and complex space hosting a diverse range of pathology with overlapping imaging features. Timely and accurate imaging diagnosis is crucial given the devastating complications of orbital disease. This exhibit will review the utility of diffusion weighted imaging (DWI) and how it can help differentiate various congenital, inflammatory, infectious, and neoplastic processes by reviewing well-established DWI techniques and characteristics with case examples. Additionally, the limitations of DWI within the orbit will be discussed.
Purpose
To show the utility of diffusion weighted imaging (DWI) in differentiating various orbital pathologies.
Materials and Methods
The different techniques of DWI will be reviewed. Case examples will show the diffusion changes of various orbital pathologies including developmental lesions, subperiosteal and intraorbital abscesses, inflammatory and granulomatous conditions, benign and malignant tumors. Well established ADC threshold values documented in the literature will be reviewed. Additionally, the limitations of this technique will also be reviewed with case examples.
Results and Conclusions
Accurate imaging diagnosis of orbital pathology is important for proper patient management . DWI is a useful tool for radiologists and can help narrow the differential diagnosis.

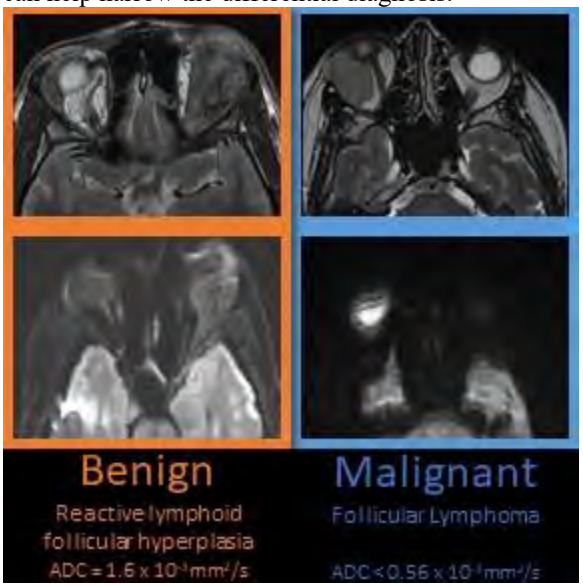

(Filename: TCT_649_abstractphoto.jpg)

1262

Role of MRI in management of prolactinoma; what radiologists need to know?

A Moawad[1], A Honarmand[2], O Teytelboym[3]
[1]Mercy Catholic Medical Center, Darby, PA, [2]Massachusetts General Hospital, Harvard Medical School, Boston, MA, [3]Mercy Fitzgerald Hospital, Darby, PA

Summary and Objectives
• Reviewing the imaging appearance of prolactinomas • Discussing the role of radiology in treatment of prolactinomas • Highlighting special clinical situations of prolactinomas and our role in management of these situations • Case based review of radiology role in monitoring patients with prolactinoma • Reviewing post-operative and post-radiation imaging of prolactinoma.
Purpose
• Introduction and definition of prolactinoma o Definition of prolactinoma o Histopathological content of prolactinoma o MRI appearance of prolacting secreting microadenoma and macradenoma • Role of imaging in initiation of therapy: o Role of MRI in treatment decisions o MRI prior to dopamine agonist withdrawal • Role of MRI in monitoring therapy o MRI monitoring dopamine agonist therapy o MRI monitoring in patients on estrogen therapy o MRI monitoring after surgery o MRI monitoring after radiation • Role of MRI in special situations o MRI in postmenopausal women o MRI monitoring during pregnancy and lactation o Resistant Prolactinomas • What should be included in the report o Size and extension of the adenoma o Ratio of cystic component of the adenoma o Ratio of hemorrhagic component of the adenoma o ADC value of the adenoma.

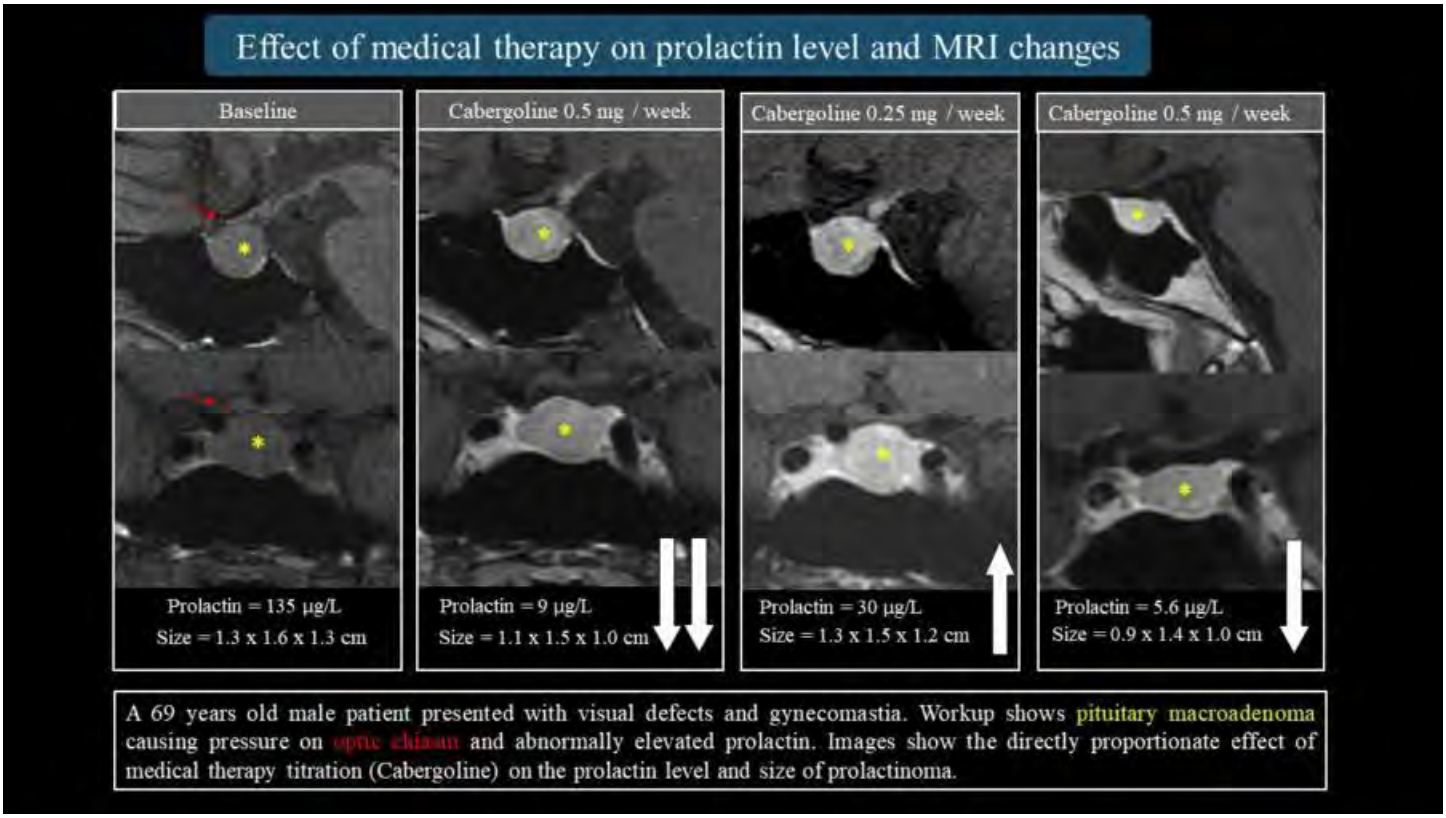

(Filename: TCT_1262_ASNR23-prolactinoma.jpg)

1255
Seal the drip: A Multimodality Approach for CSF Leakage Diagnosis and Management
M Soliman[1], A Megahed[2], R Abdalla[3], S Ansari[4]
[1]Saint Vincent's Medical Center, Fairfield, CT, [2]Yale New Haven Health, Bridgeport Hospital, Bridgeport, CT, [3]Northwestern University, Chicago, IL, [4]Northwestern University, CHICAGO, IL

Summary and Objectives
• Describe the anatomy and physiology of CSF flow. • Outline the various etiologies of CSF leak as a cause of intracranial hypotension. • Describe the common imaging modalities used to diagnose CSF leak • Elaborate Imaging findings and pitfalls associated with CSF leak. • Discuss the role of IR (Interventional Radiology) in the management of CSF leak.
Purpose
To provide a comprehensive overview of CSF leakage and an algorithm for diagnosis and management.
Materials and Methods
1. Introduction: a. Anatomy of Dural spaces. b. Physiology of normal CSF circulation. 2. Etiological classification of intracranial hypotension: a. Congenital b. Acquired i. Traumatic ii. Iatrogenic c. Spontaneous 3. Clinical presentation and diagnostic workup. 4. Imaging features of intracranial hypotension 5. Imaging findings of CSF leak: a. Conventional Myelography (standard and lateral decubitus) i. Technique ii. Image interpretation b. CT and MRI Cysternography c. CT Myelogram (static and dynamic) d. MRI Myelogram (CSF leak protocol) 6. Algorithmic imaging approach for the diagnosis of CSF leak 7. Differential diagnoses, concurrent diagnoses, and imaging pitfalls 8. Therapeutic interventions a. Epidural blood patch (directed and multilevel) b. Epidural Fibrin patch injection c. Epidural glue injection d. Transvenous embolization for CSF venous fistulas 9. Follow-up imaging. 10. Conclusion and take-home message
Results and Conclusions
CSF leak presents with symptoms that can be debilitating to patients. Different imaging modalities and interventions are available to thoroughly evaluate and treat the leak and provide life-changing symptomatic relief.

1135
Seize the Day: Image-Guided Interventions in Epilepsy
S Majumdar[1], N Salamon[1]
[1]University of California Los Angeles, Los Angeles, CA

Summary and Objectives
1) Detailed summary of various etiologies of medication-resistant focal epilepsy, the relevant imaging findings, and the established percutaneous MR-guided laser or radiofrequency interventions for each disease entity, including: a. Cortical Tubers in Tuberous Sclerosis b. Hypothalamic Hamartoma c. Periventricular nodular heterotopia d. Hippocampal/Mesial Temporal Lobe Sclerosis 2)

Additional discussion of generalized epilepsy syndromes responsive to percutaneous corpus callosotomy, including Lennox-Gastaut Syndrome 3) Brief discussion on investigative noninvasive interventions in epilepsy using MR-guided focused ultrasound (MRgFUS) ablation OBJECTIVES: Provide practicing neuroradiologists and trainees with: 1) Knowledge about etiologies of medication-refractory epilepsy, the relevant imaging findings, and any described anatomic networks implicated in the generation of epileptogenic discharges 2) Comprehensive review of established image-guided interventions for each disease entity, with a focus on outcomes after percutaneous MR-guided laser or radiofrequency ablation
Purpose
Please see Objectives section above.
Materials and Methods
A comprehensive literature review using peer-reviewed medical and scientific journals was performed, focused on types of established interventions in various etiologies of medication-refractory epilepsy
Results and Conclusions
Medication-refractory epilepsy can be extremely debilitating for patients. Radiologists play a significant role in recognizing epileptogenic foci on imaging and guiding treatment in these syndromes. Familiarity with various types of epilepsy syndromes and knowledge of available image-guided interventions is therefore critical. Image-guided percutaneous laser thermal ablation and radiofrequency ablation have been studied in a number of different epilepsy syndromes with good outcomes. These types of interventions are minimally invasive, offering clear advantages and improved safety profiles compared to open resective surgery. Noninvasive thermal ablation with focused ultrasound is also in early stages of investigation for its role in epilepsy treatment. Given that both percutaneous and noninvasive procedures alike are typically MR-guided, they are often performed by proceduralists in conjunction with diagnostic imagers, generating new opportunities for radiologists to broaden their practices and improve the standard of care in epilepsy therapy.

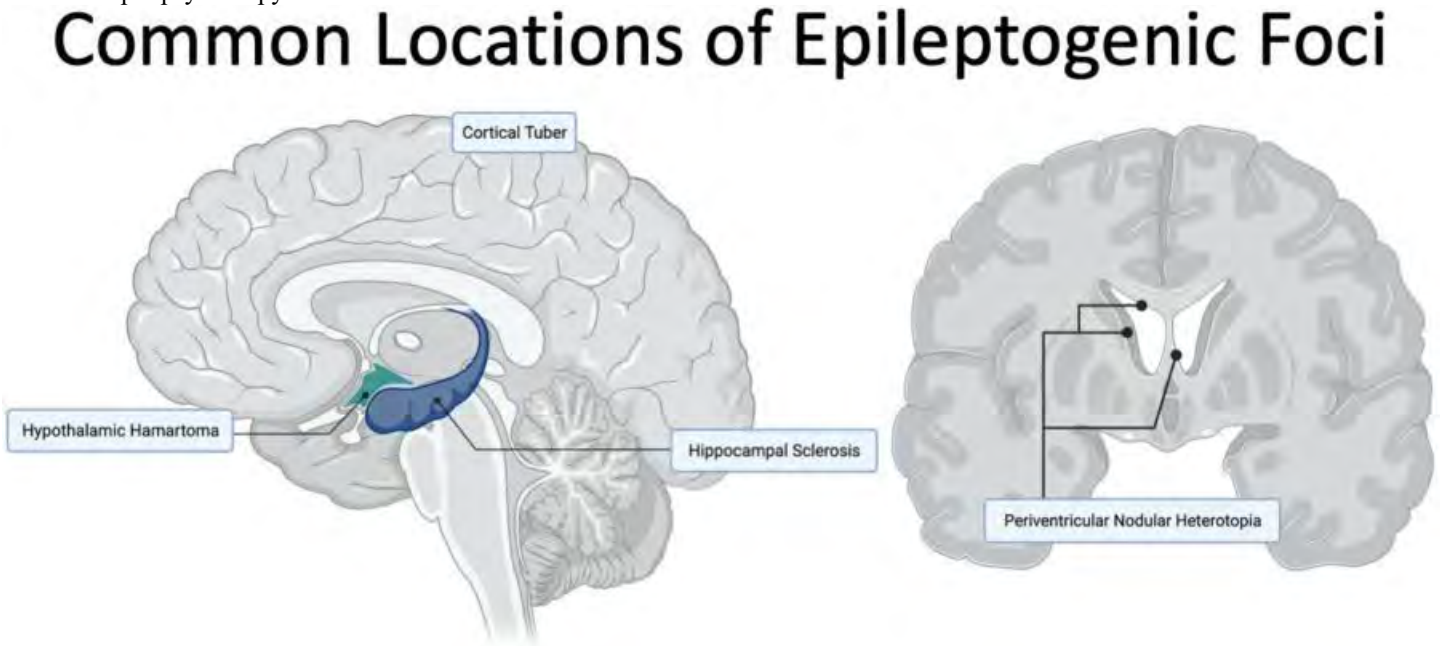

(Filename: TCT_1135_CommonEpileptogenicFoci.jpg)

943
Shining Crystals in the Spine: Spinal Involvement in Gout.
A Saeed Bamashmos[1]
[1]*Yale New Haven Health, Bridgeport Hospital, Bridgeport, CT*

Summary and Objectives
Summary: In this presentation we present several cases of spine involvement in patients with gout, their clinical presentation, epidemiology, imaging features and complications of advanced disease. Learning objectives: - Elucidate gout pathophysiology with detailed focus on gout arthroplasty. - Describe the most common spinal segments involvement and epidemiology of gout of the spine. - Depict the imaging features of gout involvement of the spine. - Discuss the potential complications of gout arthropathy of the spine.
Purpose
Background: Gout is the most common crystal arthropathy that presents with frequent episodes of arthritis resulting in chronic arthropathy, tophi formation, uric acid renal stones, and chronic nephropathy. Gout presents with severe pain and inflammation at the first metatarsophalangeal joint. However, other joint involvement is sometimes seen with polyarticular gout flares. Rarely, gouty arthritis may involve the spine which can be asymptomatic or cause back pain and radiculopathy. The exact prevalence of spine involvement in gout is not well reported in the literature, but is favored to be more common than expected. In this presentation, we present imaging features of spine involvement in patients with gout.

Materials and Methods
Content: - Overview of gout. - Epidemiology of gout of the spine. - Imaging features of spine gout. - Complications of gout involvement of the spine.
Results and Conclusions
Conclusion: Spinal involvement in gout is uncommon yet it has unique imaging features. The accurate detection in addition to the early management of spinal gout may have a profound impact on the prognosis of the patients and their lifestyle. Being familiar with theses radiological findings is the crucial for timely diagnosis and prevention of complications.

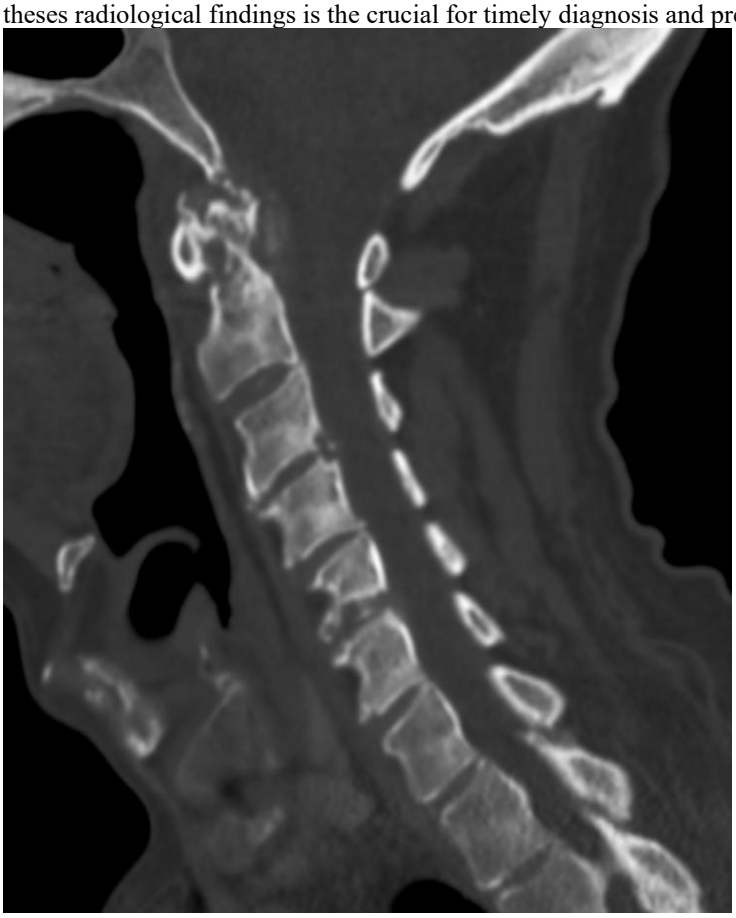

(Filename: TCT_943_NEW1.jpg)

1471

Simulation in Radiology Education using a Virtual World (Metaverse), a Gather implementation of a supplemental education platform for Skull base and Cranial Nerves.

B Currier[1], M Hadi[1]
[1]*University of Louisville, Louisville, KY*

Summary and Objectives
Many methods of delivering education beyond the traditional didactic format have been proposed. The objective of this presentation is to describe our methodology, implementation and outcomes of creating a virtual space for radiology learning in a metaverse with both asynchronous and synchronous learning components, where the learner enters a virtual world and navigates the spaces within this virtual world interacting with various forms of educational content, and also interacts with other learners or teachers within this space via real-time video-conferencing.
Purpose
The project is implemented using the Gather platform, which has widely been used for large scale virtual conferences during the Covid-19 pandemic, but not as widely used in the our educational realm. The purpose is to gain insight into new methods of learning that can be spread across the breath of radiologic disciplines as a resident progresses through their training. Teachings will not be limited to only a didactic setting, with the opportunity for residents/fellows to contribute their own methods/content on an approved basis. Quizzes, games, to virtually navigating anatomy with point/click descriptions is the focus for a comprehensive experience.
Materials and Methods
Upon entering the space, the student navigates an avatar through a gross-anatomic depiction of the skull base, and as they identify and enter various foramina on the gross specimen, and as they do so, additional virtual spaces open up specific to those foramina and their contents and pathology as well as radiologic anatomy with case examples, and when the student is finished with one of these spaces, they are returned to the gross-anatomic depiction of the skull base precisely at the foramina that they just explored, so they can navigate another portion of skull base. The visuospatial nature of both the content and interaction complements , mirrors and

reinforces the complex anatomy involved. Additionally, there are small group discussion areas where a virtual classroom, complete with interactive whiteboards, can be run by the faculty member to supplement the asynchronous portion of the education.
Results and Conclusions
Supplementing traditional radiology didactics with a simulation learning platform using a virtual world allows a variety of educational content, allowing participation with other learners and teachers, maintaining student interest and attention in a game like environment complementing the visuospatial nature of the underlying content .

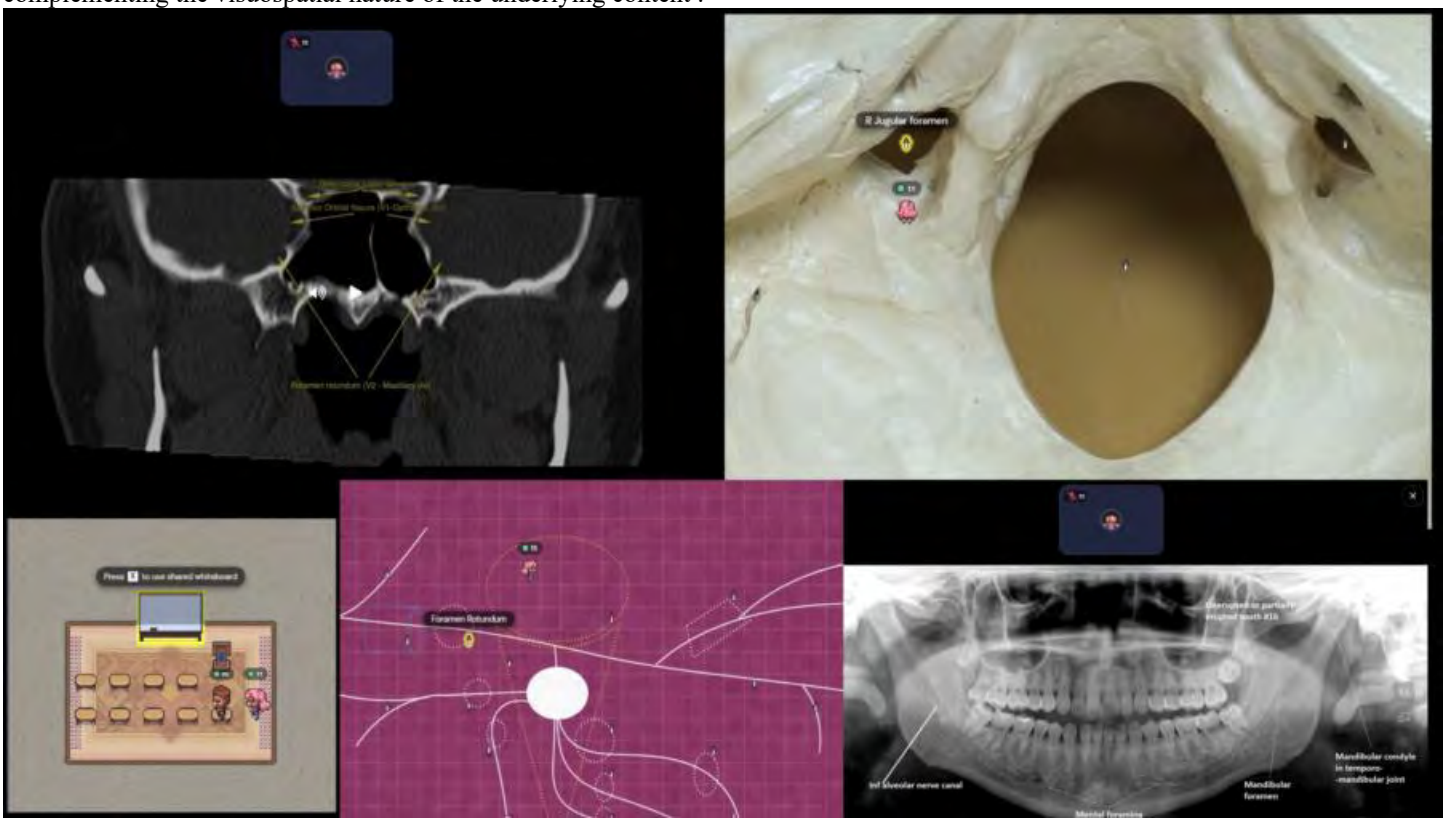

(Filename: TCT_1471_SimulationplatformScreenshots.jpg)

1057
Smoking Guns in the Head and Neck: Clues to Diagnosis
B Damadian[1], J Steinklein[1], D Shatzkes[1]
[1]*Lenox Hill Hospital, New York, NY*

Summary and Objectives
Head and neck (H&N) radiology is a complex subspecialty which requires a deep understanding of intricate anatomy and a plethora of pathologies. While systematic image analysis is always required to generate a differential diagnosis, there are a few diagnoses in the H&N that can be identified with a high level of certainty by the presence of a so-called "smoking gun": an irrefutable imaging finding that pinpoints a specific diagnosis. Our objective is to provide a pictorial review of "smoking gun" diagnoses in the H&N highlighting common clinical presentations and the often-subtle characteristic imaging findings.
Purpose
To provide a case-based review of H&N imaging diagnoses that have pathognomonic imaging findings, the so-called "smoking guns", which lead to correct diagnosis.
Materials and Methods
Utilizing a standardized graphic format, the reader is directed towards the imaging findings to search for in a variety of clinical settings (Figure 1). Clinical and imaging features of the individual entities are then reviewed. Some of the entities and "smoking guns" discussed are odontogenic infections (periapical lucency), obstructive sialadenitis (distal ductal calculi), longus colli calcific tendinitis (prevertebral calcification), Rathke cleft cyst (waxy nodule) and invasive fungal sinusitis (periantral fat infiltration).
Results and Conclusions
Knowledge of often subtle "smoking gun" imaging findings can aid the radiologist in providing a quick and accurate diagnosis of a variety of entities in the H&N.

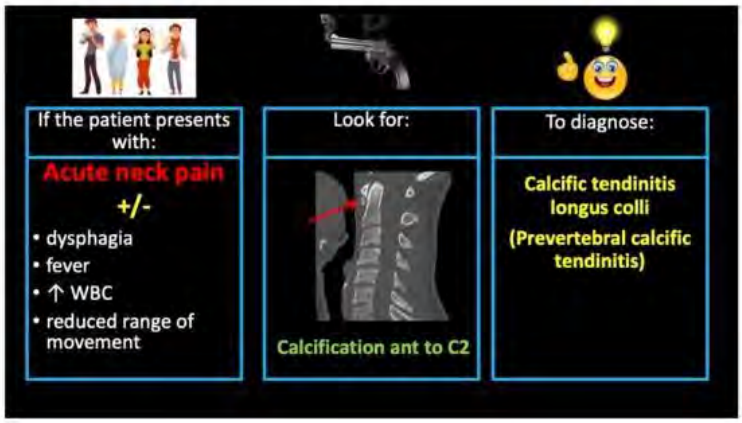

1

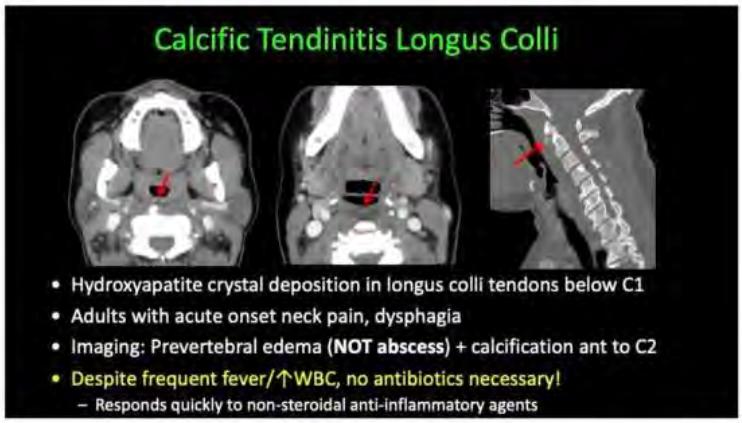

(Filename: TCT_1057_SmokingGunASNR_Fig1.jpg)

1498

Something Smells Fishy: A Pictorial Review of Olfactory Groove Lesions

J Sharma[1], A Abbas[1], R Joshi[1], A Krishnan[1]
[1]*William Beaumont University Hospital, Royal Oak, MI*

Summary and Objectives

Summary of Presentation: The olfactory grooves or fossae are depressions within the ethmoid bone that contain the olfactory bulbs and tracts. Lesions in this region are uncommonly encountered and patients can often have nonspecific or delayed presentation of symptoms. Once identified, it is often difficult to distinguish different lesions of the olfactory groove from one another. This pictorial review aims to identify the more common olfactory groove pathologies as well as to discuss key imaging and clinical features which can be utilized to make the correct diagnosis and guide clinical treatment. List of Educational Objectives: - Overview of the relevant anatomy of the olfactory groove/fossae including the skull base particularly the cribriform plate, and its contents. Brief review of embryology of the olfactory apparatus. - Discussion of select lesions of the olfactory groove and adjoining region and their relevant imaging features including: congenital lesions (such as Kallman syndrome), olfactory hypoplasia, olfactory groove meningioma, esthesioneuroblastoma and malignancies of the head and neck, unusual tumors such as olfactory groove schwannoma, traumatic abnormalities, and infectious/inflammatory etiologies, which can disrupt olfaction. - Case-based review of olfactory groove lesions encountered at our institution. - Outline role of appropriate skull base CT and MRI protocols to improve anatomic localization and lesion characterization through technical parameters.

Purpose

This pictorial review aims to identify the more common olfactory groove pathologies as well as to discuss key imaging and clinical features which can be utilized to make the correct diagnosis and guide clinical treatment.

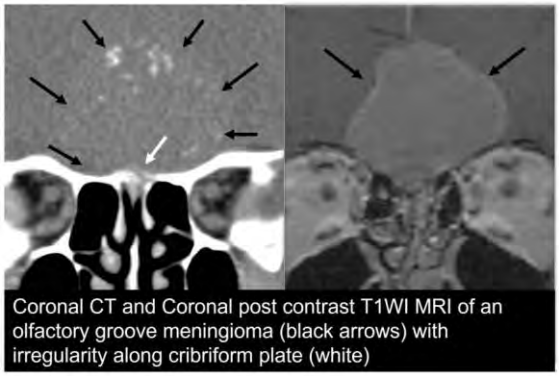

(Filename: TCT_1498_Olfactorygroovecase.jpg)

259

Spectrum of Osseous Lesions in Pediatric Orbit

A Metry[1], S Narayanan[1]
[1]*UPMC Children's Hospital of Pittsburgh, Pittsburgh, PA*

Summary and Objectives
Summary Spectrum of osseous lesions within the pediatric orbit can be categorized into primary bony lesions and secondary changes from intraorbital process. Causes can be broadly classified into Congenital/developmental, neoplastic (benign and malignant), infectious/inflammatory, vascular, traumatic and idiopathic. CT and MRI play a critical role in evaluating different lesions and identifying characteristic features for each. Educational Objectives: • Recognize different lesions affecting bony orbit in the pediatric population • Review CT/MRI imaging findings in each entity
Materials and Methods
• Recognize primary and secondary osseous orbital lesions • Review differential diagnosis • Identify key features for osseous evaluation
Results and Conclusions
Spectrum of osseous lesions within the pediatric orbit can be categorized into primary bony lesions and secondary changes from intraorbital process. Causes can be broadly classified into Congenital/developmental, neoplastic (benign and malignant), infectious/inflammatory, vascular, traumatic and idiopathic. Congenital /Developmental lesions include dermoid and epidermoid cysts, cephalocele. Infectious/Inflammatory causes include subperiosteal abscess and reactive changes from recurrent inflammation such as in idiopathic orbital inflammation. Neoplastic: Primary malignant bone tumors such as osteosarcomas, metastasis from neuroblastoma, leukemia like granulocytic sarcoma with myelogenous leukemia. The bony orbit can be Infiltrated and remodeled with orbital-periorbital plexiform neurofibroma and orbital rhabdomyosarcoma as well. Langerhans Cell Histiocytosis and Infantile myofibroma will be discussed Vascular: Bone infarct in the setting of sickle cell disease and subperiosteal hematoma. Traumatic: Different patterns for orbital fractures will be discussed Idiopathic: Fibrous dysplasia CT and MRI play a critical role in evaluating different lesions and identifying characteristic features for each.

Figure 1: Langerhans cell histiocytosis (A) Coronal CT image (bone window) shows osseous lytic mass arising from the superolateral orbital roof (red arrow) with intraorbital and intracranial extension. (B) Post-contrast coronal T1 weighted MR images shows avidly homogenously enhancing mass in the superolateral orbit (yellow arrow) with intracranial epidural extension and intraorbital extraconal extension.

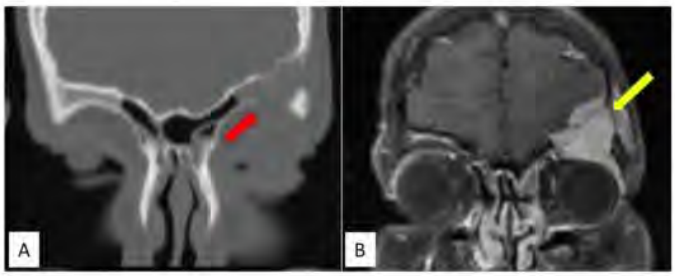

Figure 2: Neuroblastoma Metastasis (A) Coronal CT image (soft tissue window) shows a well-defined hyperdense homogenous masses involving both the orbital roof medially (blue arrows). (D) Coronal CT image (bone window) shows underlying characteristic 'spiculated' periosteal reaction seen with neuroblastoma metastasis involving the left orbital roof (green arrow)

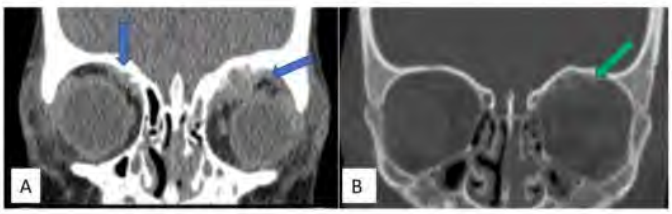

(Filename: TCT_259_AnnotatedimagesASNR2023-1.jpg)

1101

Standing at the Crossroad: A Roadmap for Navigating the Pterygopalatine Fossa

S Ameli[1], J Palakunnel[2], S Patro[2], S Vattoth[3]

[1]UAMS, Little rock, AR, [2]University of Arkansas for Medical Sciences, Little Rock, AR, [3]University of Arkansas for Medical Sciences, LITTLE ROCK, AR

Summary and Objectives

Summary: Pterygopalatine fossa is a small but complex space in the deep face. The PPF is shaped as an inverted pyramid which is bounded by maxilla, palatine, and sphenoid bones[1]. Multiple important structures lie within the PPF, such as pterygopalatine ganglion, maxillary division of trigeminal and Vidian nerve and distal branches of maxillary artery[2]. PPF's multiple communications with the deep cervical spaces predispose this junction as a potential route for loco-regional spread of infections and tumors. While high resolution computed tomography is the modality of choice for evaluating the bony anatomy of PPF, MR imaging is excellent for evaluating the PPF pathologies[3]. Precontrast axial SE T1W, axial FSE T2W and coronal SE T1W images followed by gadolinium-enhanced, fat-saturated axial and coronal SE T1W images are most routinely used sequences for PPF evaluation[4]. Objectives: -Familiarizing the audience with normal anatomy of pterygopalatine fossa. -Discussing different inflammatory and neoplastic pathologies involving the PPF.

Purpose

To familiarize the audience with normal anatomy of the pterygopalatine fossa. Most important pterygopalatine contents and most pertinent communications like inferior orbital fissure leading to infraorbital canal anterosuperiorly, foramen rotundum leading to cavernous sinus/middle cranial fossa posterosuperolaterally, Vidian canal and the inconsistent palatovaginal and vomerovaginal canals posteroinferiorly, sphenopalatine foramen leading to nasal cavity medially, pterygomaxillary fissure leading to masticator space laterally and greater palatine canal leading to greater and lesser palatine canals inferiorly will be reviewed. Other important adjacent skull base foramina like foramen ovale and spinosum will also be discussed. The key CT and MR imaging findings in pterygopalatine pathology will be discussed. We will discuss several inflammatory and neoplastic conditions involving the PPF. The direct invasion of these pathologies versus perineural spread will be discuss separately. At the end we will review some of the most common pitfalls in evaluating the PPF.

Results and Conclusions

Results: N/A Conclusion: Pterygopalatine fossa is a small junction which serves as a potential pathway for the spread of tumor or infection from head and neck to the skull base. Being familiar with normal anatomy of pterygopalatine fossa and its variant pathologies on CT or MR imaging can have a major role in formulating the diagnostic and therapeutic plans.

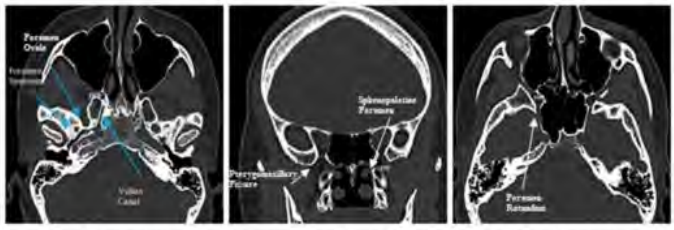

Normal Anatomy of Pterygopalatine fossa in 33-year-old female presented for acute sinusitis evaluation.

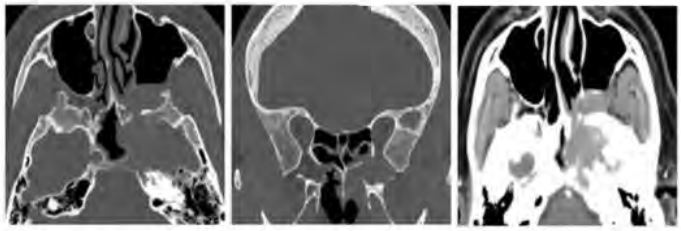

46-year-old male presents with reduced sensation in left upper and lower extremities. Incidentally noted large aggressive soft tissue lesion with bony erosive changes centered at left Pterygopalatine fossa also involving left clivus, sphenoid bone and nasopharynx concerning for malignancy.

(Filename: TCT_1101_PPF.jpg)

1367

Structural and Functional Neuroimaging in the evaluation of seizures and epilepsy: Spectrum of Case based Multi-modality Pictorial Review

P Suthar[1], S Virmani[1]

[1]Rush University Medical Center, Chicago, IL

Summary and Objectives

Epilepsy is a condition characterized by the recurrent unprovoked seizures. The diagnosis of the epileptic focus is not straightforward. A detailed history along with structural and functional neuroimaging plays prime important role in localization of epileptic focus, and

surgical planning for the potential candidates. The purpose of this educational exhibit outlining various structural and functional neuroimaging modalities for localization of epileptic focus, and surgical planning.

Purpose

• To learn 99mTc-hexamethylpropyleneamine-oxime (HMPAO) or 99mTc-ethyl cysteinate dimer (ECD) SPECT scan protocol, technique, imaging findings and associated false positive and false negative findings. • To learn functional imaging of brain (fMRI) and interventional WADA technique for surgical planning of epilepsy. • Multimodality comparison and its correlation with conventional CT, MR, PET/CT imaging when available.

Materials and Methods

We present a case-based multimodality pictorial review highlighting different spectrum of interesting cases of presurgical epilepsy evaluation including 99mTc HMPAO or 99mTc ECD SPECT, CT, MRI, fMRI, FDG PET/CT and interventional WADA imaging. Its post-surgical imaging correlation whenever available.

Results and Conclusions

The above case based pictorial review aims to increase the confidence of the interpreting radiologist and thus help in better patient management. Important to correlate the clinical symptoms, biochemical workup with various available functional and structural neuroimaging modalities.

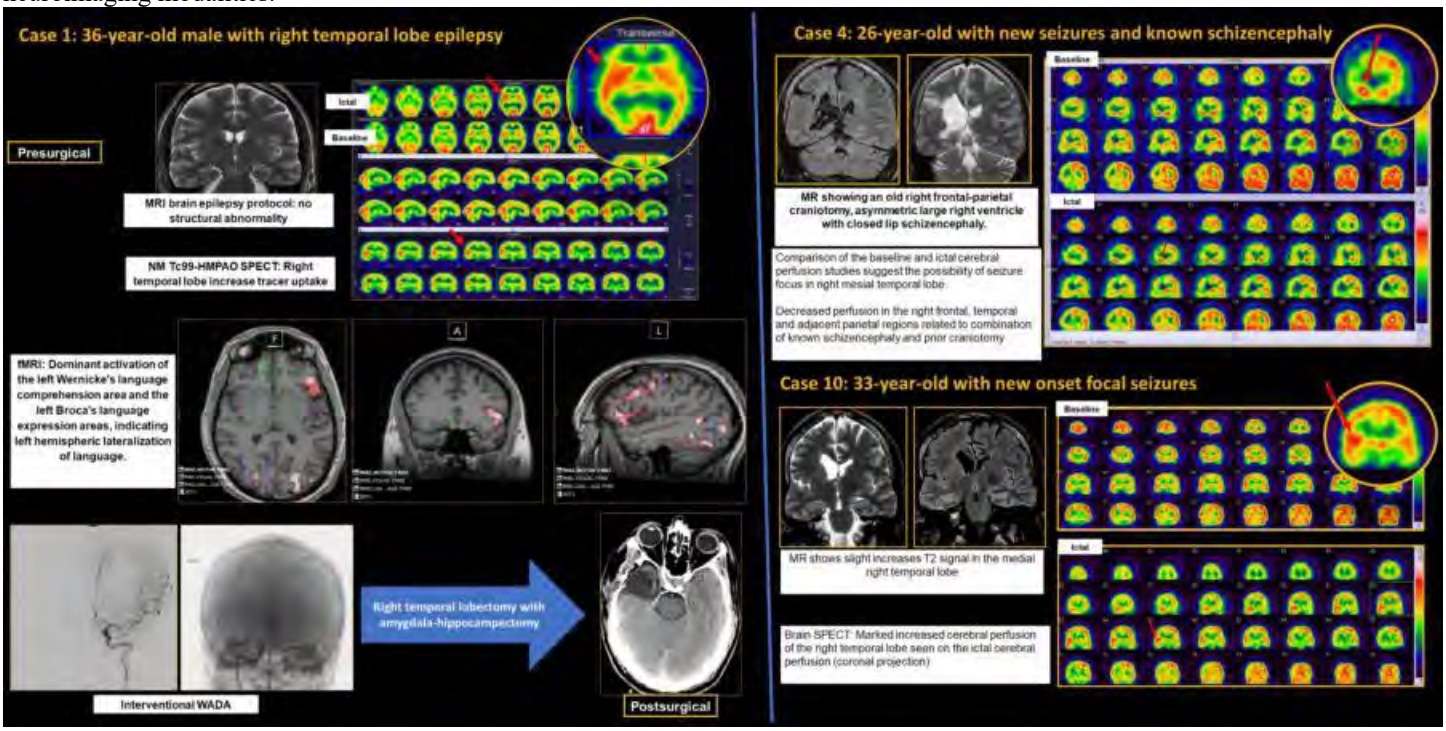

(Filename: TCT_1367_Slide1.JPG)

1233

Structural Brain Imaging in Normal Aging and Dementia

L Portella[1], D Santos[1], I Alves[2], F ASSUNÇÃO[3], L Martins[4], V Marussi[5], B Inada[5], L Amaral[6], C Campos[5], R Carmo[7], S Omar[8]

[1]BP - Hospital Beneficência Portuguesa de São Paulo, São Paulo, São Paulo, [2]Hospital Sírio-Libanês, São Paulo, São Paulo, [3]Hospital Beneficencia Portuguesa de São Paulo, São Paulo, Sao Paulo, [4]Beneficiência Portuguesa de São Paulo, São Paulo, -- SELECT --, [5]BP - A Beneficência Portuguesa de São Paulo, São Paulo, SP, [6]Hospital Beneficência Portuguesa de São Paulo, São Paulo, São Paulo, [7]BP - A Beneficência Portuguesa de São Paulo, São Paulo, São Paulo, [8]Beneficência Portuguesa de São Paulo, São Paulo, São Paulo

Summary and Objectives

Aging is associated with many changes in the cerebral parenchyma, which have been better characterized in the past decades with the use and development of brain imaging modalities, particularly MRI. Neurodegenerative diseases are an increasingly common social and economic burden whose diagnosis relies heavily on clinical findings, which can be difficult to detect or nonspecific, hence the need of complimentary diagnostic methods. Traditionally, the role of structural neuroimaging in dementia has been to exclude other possible causes and support the clinical diagnosis, supported by molecular and functional imaging, whose findings have been classically earlier and more reliable. However, advances of anatomical imaging and its increase in daily clinical practice as the main complimentary tool make so that practicing radiologists should be familiar with its main uses and common findings, and how to differentiate them from normal age-related changes. In this regard, the purpose of this exhibit is to: define structural imaging of the brain and its use in neurodegenerative diseases and dementia; review the findings associated with normal aging in contrast to pathological processes; present a series of cases in which structural imaging was helpful to determine the final diagnosis of a demential syndrome, and discuss the limitations of structural imaging and present how functional studies can aid in the differential diagnosis.

Purpose
• Define structural imaging of the brain and its use in neurodegenerative diseases and dementia; • Review the findings associated with normal aging in contrast to pathological processes; • Present a series of cases in which structural imaging was helpful to determine the final diagnosis of a demential syndrome; • Discuss the limitations of structural imaging and present how functional studies can aid in the differential diagnosis, highlighting them as complimentary methods.
Materials and Methods
We present a pictorial essay based on cases and original drawings the main findings associated with aging, the most prevalent neurodegenerative disorders and the main uses of structural imaging in their diagnosis.
Results and Conclusions
Structural imaging has gained importance in the diagnosis of neurodegenerative and demential syndromes in the past decades, including new modalities and AI-based tools. It is important that radiologists are familiar with the main findings of the most prevalent neurodegenerative diseases and is able to distinguish them from normal findings related to aging.

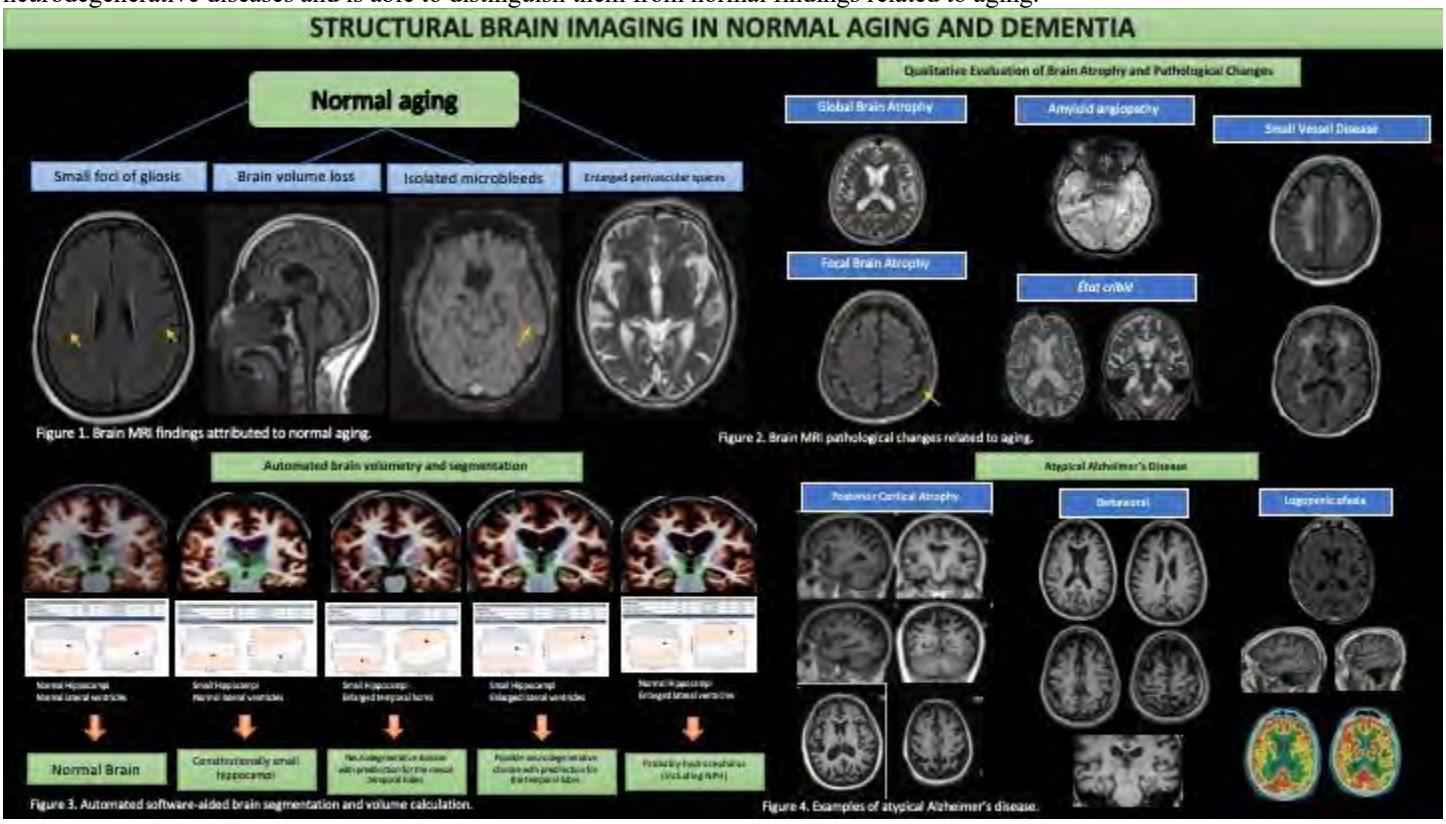

(Filename: TCT_1233_ASNR-StructuralImaginginDementia.jpg)

808

Surgical materials and medical devices in head and neck - have you seen this?

M Sarpi[1], I Padilha[2], S Souza[3], M Garcia[1], S Mukherji[4], N da Silva Junior[1], L Palhiari Duarte[1]
[1]DASA, São Paulo, São Paulo, [2]Centre Hospitalier de l'Université de Montréal, Montreal, Quebec, [3]InRad, Sao Paulo, AK, [4]ProScan Imagng, Carmel, IN

Summary and Objectives
The intent of this educational exhibit is to review the imaging features of various surgical implants that may be encountered in clinical practice. The exhibit will review both the expected appearance and complications. The objectives of this exhibit are to 1. Educate the radiologist with their expected appearance, 2. Ensure these devices are not confused with foreign bodies and 3. Help identify various complications that may be only identified on imaging and be clinically occult.
Purpose
To review the imaging features of various surgical implants that may be encountered in clinical practice.
Materials and Methods
The images were obtained through a retrospective review of our digital archives. The devices and implants involve multiple areas of the head and neck, which may be encountered in the orbit, globe, maxillofacial, temporomandibular joint, orthodontic and soft tissues. We will discuss their indications, normal appearance and potential complications.
Results and Conclusions
It is important for radiologists to be familiar with the appearance of various implantable devices and implants in head and neck imaging. This educational exhibit will educate the radiologist with their expected appearance, ensure these devices are not confused with foreign bodies and help the radiologist identify various complications which may be only identified on imaging and be clinically occult which can improve patient outcome.

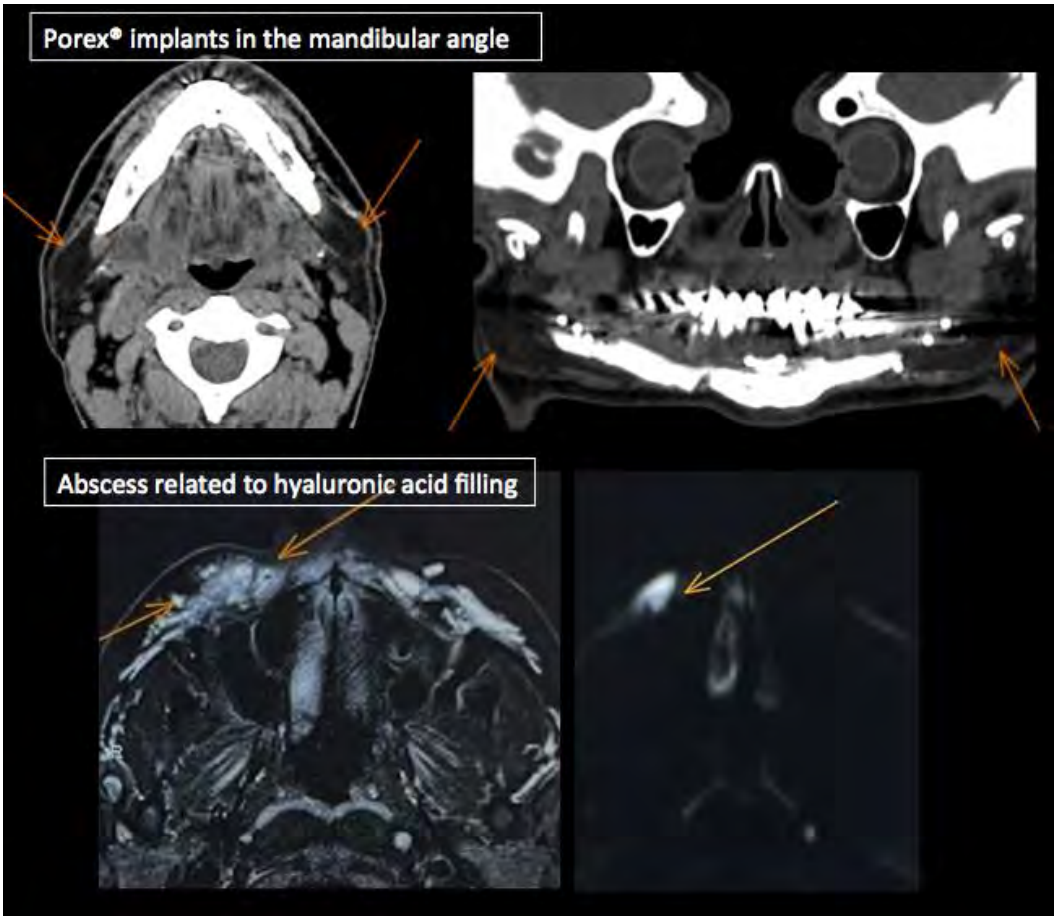

(Filename: TCT_808_devices.jpg)

1159

Susceptability weighted imaging findings for various intracranial conditions: "Smoking gun" in tricky case

J LEE[1]
[1]*SOONCHUNGHYANG UNIV HOSPITAL, BUCHUN, Gyeonggi-do*

Summary and Objectives
SWI is a high resolution 3D gradient echo MR imaging that is sensitive to substances that induce local magnetic fields inhomogeneity, such as blood products. Resulted from these characteristics, additional SWI-specific findings may appear in various intracranial pathologies. If you are familiar with these findings, you can receive decisive help in diagnosing a tricky case.
Purpose
Understand SWI specific findings in various intracranial pathologies and use them for correct diagnosis.
Materials and Methods
1. Vascular disease 1) Developmental venous anomaly with venous congestion : Caput medusa 2) Venous sinus and cortical venous thrombosis : venous thrombus 3) Venous infarction resulted from pial AVF : hemorrhagic lesions in vasogenic edema without venous thrombus 4) Vertebral artery dissection : intramural hematoma 5) Cerebral amyloid angiopathy related inflammation : superficial cortical siderosis and lobar microbleeds 2. Trauma 1) Diffuse axonal injury 2) Fat embolism syndrome : innumerable microbleeds on follow up SWI (about 3 weeks) 3. Inflammatory & infections 1) Multiple sclerosis : central vein sign on CE-SWI 2) Brain abscess : Dual rim sign 3) Septic emboli : innumerable microbleeds 4. Neurodegenerative 1) Evaluation for Parkinsonism a: Multiple systemic atrophy, P type : putaminal hypointensity b: Primary vs secondary Parkinsonism (HR-SWI) : Nigrosome 1 imaging 2) Amyotrophic lateral sclerosis : Motor band sign 5. Miscellaneous 1) Chronic encapsulated hematoma : dark SI rim (ref.1) 2) Thrombotic microangiopathy : cortically distributed microbleeds 3) Pulmonary embolism : prominent cerebral veins (ref.2) 4) Critical illness associated microbleeds 5) Remote cerebellar hemorrhage : cerebellar zebra sign 6) Radiation induced microbleeds
Results and Conclusions
Even for lesions that show non-specific findings in conventional images, SWI-specific findings can help in discrimination, so becoming familiar with the SWI findings of various intracranial pathologies can be helpful for neuroimage interpretation.

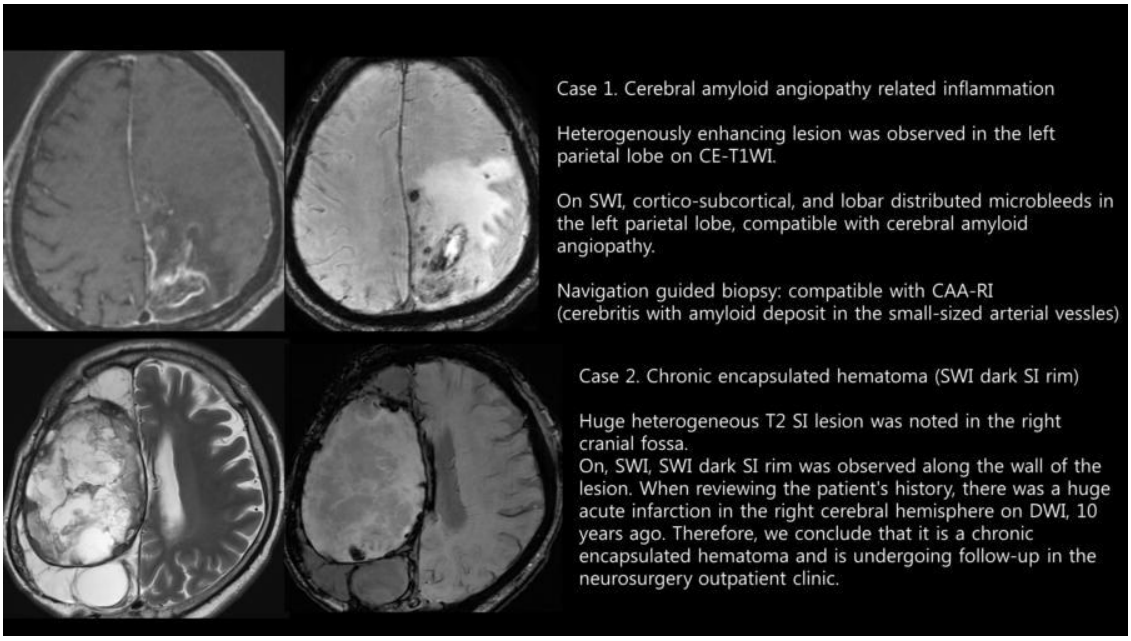

(Filename: TCT_1159_asnr2022.jpg)

137

Tangled? Unraveling The Neuroimaging of Alzheimer's Disease

P Brahmbhatt[1], G Virador[1], T Kumar[1], A Sharma[1], V Gupta[2]
[1]Mayo Clinic, Jacksonville, FL, [2]Mayo Clinic Florida, Jacksonville, FL

Summary and Objectives
We aim to present the current, state-of-the-art MR and molecular imaging of AD, focusing on amyloid as well as emerging tau imaging. Our case-based review will demonstrate the clinical utility of Amyloid PET and Tau PET in helping diagnose AD as well as ensuring proper management.
Purpose
To educate the viewer on the utility and temporal relationship of MR and Amyloid PET imaging in AD as well as introducing newer Tau imaging as a viable, more specific, biomarker.
Materials and Methods
We conducted an extensive literature review on neurodegenerative disorder imaging and decided to focus on Alzheimer's Disease (AD). Under IRB approval, we took cases from our own institution to demonstrate the different biomarkers and imaging characteristics seen in AD and their clinical utility.
Results and Conclusions
N/A: This is an educational exhibit with no results/conclusion. Our educational abstract is attached below. Alzheimer's disease (AD) is the leading cause of progressive memory loss and cognitive dysfunction in the elderly, however, dominant inheritance of AD can lead to patient presentation at a younger age. It is caused by progressive accumulation of amyloid and subsequently hyperphosphorylated tau protein resulting in neuritic plaques and neurofibrillary tangles, leading to neurodegeneration and cognitive decline (1). Current diagnosis is based on the history and neuropsychological testing, with imaging evidence of atrophy playing a supportive role. Extensive amyloid deposits are visible well before the symptom onset of AD and can help in differentiating the disease in early stages of mild cognitive impairment from other causes of neurodegeneration (2). While MR is the initial imaging evaluation, positron emission tomography (PET) with tracers targeting beta amyloid plaque burden (florbetapir) certainly improve diagnostic confidence. Amyloid PET scans have been shown to alter management in 60% of patients (3). Additionally, deposition of tau correlates well with neurodegeneration and cognitive deficits in AD, with tau binding being a more specific disease-defining biomarker (4). Therefore, Tau PET may have a higher prognostic value for predicting cognitive change when compared to amyloid PET and T1-weighted MRI (5).
We aim to present the current, state-of-the-art MR and molecular imaging of AD, focusing on amyloid as well as emerging tau imaging. Our case-based review will demonstrate the clinical utility of Amyloid PET and Tau PET in helping diagnose AD as well as ensuring proper management.

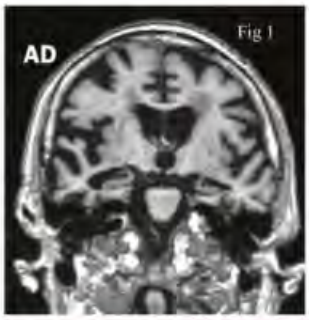

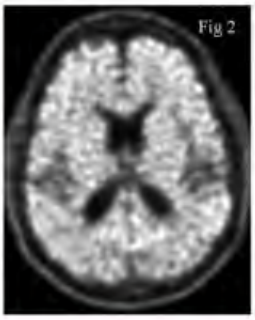

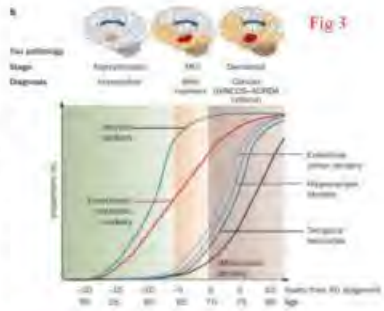

Table 2. Changes in Management Composite — Fig 4

	Mild Cognitive Impairment (n = 6905)		Dementia (n = 4504)	
	No.	% (95% CI)	No.	% (95% CI)
Primary Outcome				
Overall change	4159	60.2 (59.1-61.4)[a]	2859	63.5 (62.1-64.9)[a]
Changes by Component[b]				
Alzheimer disease drugs	3014	43.6 (42.5-44.8)	2022	44.9 (43.4-46.3)
Non-Alzheimer disease drugs[c]	1582	22.9 (21.9-23.9)	1144	25.4 (24.1-26.7)
Counseling	1681	24.3 (23.3-25.4)	934	20.7 (19.6-21.9)

[a] $P < .001$ for testing the primary hypothesis (≥30% overall change in management in the MCI and dementia cohorts).
[b] Post hoc analysis.
[c] Include drugs that affect cognition, mood, or behavior and drugs used to treat other neurologic conditions or address dementia risk factors.

Fig 1: MR imaging features of AD, particularly extensive bilateral hippocampal and entorhinal atrophy
Fig 2: Amyloid PET with complete loss of grey-white matter differentiation suggesting high beta plaque burden
Fig 3: Temporal relationship in Alzheimer's Disease and various available markers
Fig 4: Illustration of the number of times amyloid PET changed patient management

(Filename: TCT_137_FinalImagesForAmyloidAbstract.jpg)

1047

Temporal lobe tumors: Radiological approach

A Santos[1], D Santos[1], L Martins[1], R Carmo[1], C Campos[1], B Inada[1], V Marussi[1], S Omar[1], F ASSUNÇÃO[1], I Alves[2], L Amaral[1]
[1]BP – A Beneficência Portuguesa de São Paulo, São Paulo, SP, [2]Hospital Sírio-Libanês, São Paulo, SP

Summary and Objectives
Temporal lobe disorders are associated with several conditions, including seizures, dementia and memory impairment, followed by a spectrum of behavioral disorders. It is noteworthy that about 10% of temporal lobe epilepsies are caused by focal temporal lobe lesions. In this sense, most primary CNS tumors can potentially occur in the temporal lobe, but entities with a predilection for being diagnosed in this location include: ganglioglioma (40%), DNET (20%), diffuse low-grade astrocytoma (20%) and others (20%). Some of these lesions may present specific imaging characteristics, which allow narrowing the differential diagnosis. Didactically, these lesions can be grouped based on imaging features into solid-cystic, bullous, or solid. In this context, this work has as main objectives: 1. Review the anatomy of the temporal lobe 2. Group the main primary CNS tumors that affect the temporal lobe according to imaging characteristics 3. Synthesize the main imaging features of each tumor that help in the differential diagnosis on flashcards for quick reference.
Purpose
The purpose of this study is to: 1. Review the anatomy of the temporal lobe 2. Group the main primary CNS tumors that affect the temporal lobe according to imaging characteristics 3. Synthesize the main imaging features of each tumor that help in the differential diagnosis on flashcards for quick reference.
Materials and Methods
We will illustrate in a pictorial essay based on cases and original drawings, anatomy of the temporal lobe and the primary central nervous system tumors that involves this lobe highlighting the specifics clinical and imaging aspects of each tumor.
Results and Conclusions
Besides any primary CNS tumor can arise from temporal lobe, this location has specific clinical symptoms, and some tumors has a particular predilection for the temporal lobe. The radiologist has a special rule to recognize and narrow the differential diagnosis that will guide the treatment or follow up on each case.

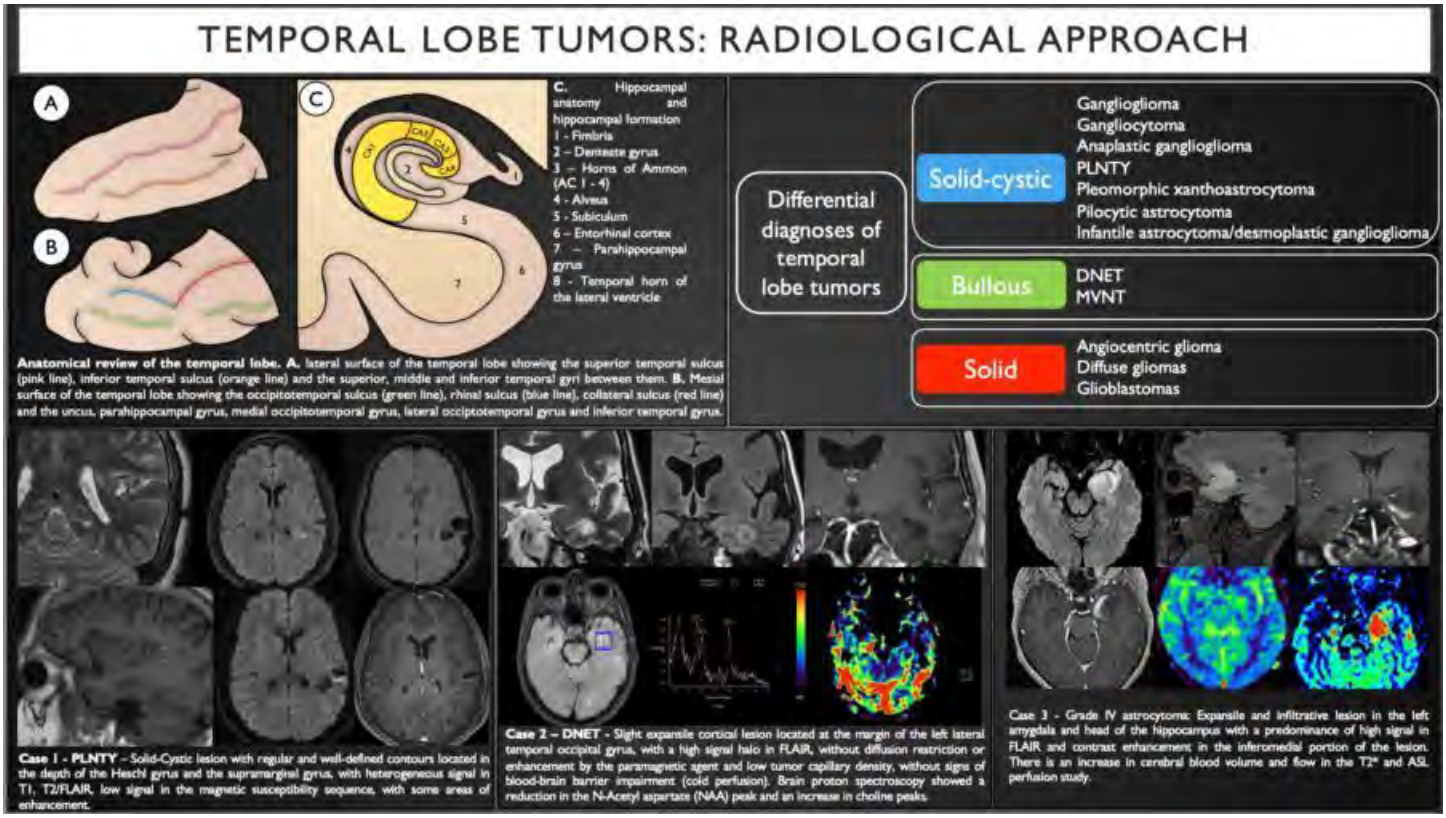

(Filename: TCT_1047_Temporal-Lobe-Tumors-Radiologic-Approach.jpg)

400

Temporomandibular joint Imaging: Checklist and simplified approach to interpretation

U Chaudhry[1], A Aein[2], U Shafique[3], A Morshid[1], K Kabeel[1], Z Akhtar[2]

[1]UTMB, Galveston, TX, [2]University of Texas Medical Branch at Galveston, Galveston, TX, [3]University of Indiana, Indianapolis, IN 46202, IN

Summary and Objectives

To review the imaging anatomy of Temporomandibular Joint (TMJ) with brief background on embryology of the joint. To illustrate spectrum of common pathologies involving TMJ and their typical imaging findings. To develop a standard MRI and CT protocol and checklist.

Purpose

Temporomandibular joint pathology has wide spectrum and is frequently encountered in clinical practice. For example some studies quote temporomandibular disorders in 10-15 percent of adults. The American Academy of Orofacial Pain classifies these disorders as articular (degenerative, disc derangement, infection etc) and masticatory muscle disorders. Interpretation of this joint can be daunting for junior radiologist and residents. However, if a simple approach with clear examples is present, this can be completed quickly and accurately.

Materials and Methods

The modality of choice to visualize the TMJ soft tissue and articular structures is MRI. The standard MR protocol may contain more sequences, however many times excessive sequences are utilized adding to image fatigue and adding to anxiety by the relatively inexperienced radiologist. The essential sequences are as follows: - Localizer (T1 Axial, Sag and Cor) - Axial T2 TSE Axial: from the corpus callosum to the angle of jaw (Slice thickness 5 mm) - Sagittal Oblique SE PD right side and left side in close-mouth position (Slice thickness 3 mm) - Sagittal Short Tau Inversion Recovery (STIR) right side and left side in close-mouth position (Slice thickness 3 mm) - Sagittal Oblique SE PD right side and left side in open-mouth position (Slice thickness 3 mm) Additionally, wedges can be utilized for open mouth sequences based on clinical scenario. CT imaging is the most useful modality in evaluation of osseous abnormalities such as joint space narrowing, condylar flattening, chondrocalcinosis, erosions, deposition disease, subchondral cyst and sclerosis, and cortical breakdown. CT is also useful to check for large joint effusion, and synovial involvement (contrast enhancement). Knowing normal anatomy in setting of emergency room scans for trauma or infection is also useful.

Results and Conclusions

Checklist is attached (Table 1). It is the hope of the authors that after a practically relevant discussion on anatomy, pathology and a pragmatic approach to joint, the reader will become much more confident in tackling this region of Neuroradiology.

Checklist and simplified approach to MRI of TMJ

Structure	Checklist of MRI findings
Disc	Morphology (biconcave)
	Normal disc position changes in the close- and open-mouth positions
	Subluxation/Displacement/Dislocation
	Reduction following opening mouth
	Normal Signal intensity (T2 hypointensity of anterior band and intermediate zone and slightly hyperintensity of posterior band)
Degenerative changes	Condylar flattening
	Joint space narrowing
	Marginal osteophytosis
	Subchondral cyst formation
	Subchondral sclerosis
Internal derangement of the TMJ	*Definition:* Abnormal relationship of the disc to the condyle
	Disc displacement, deformity and perforation
	+/- Joint effusion (hyperintense in PD/T2)
	+/- Rupture of retrodiscal layers or T2 signal changes in layers
	+/- Thickening of a lateral pterygoid attachment
	Osseous changes and progressive osseous deformity
Bone marrow	Edema (hyperintense in STIR)
Lateral pterygoid muscle	Thickening of an LMP attachment

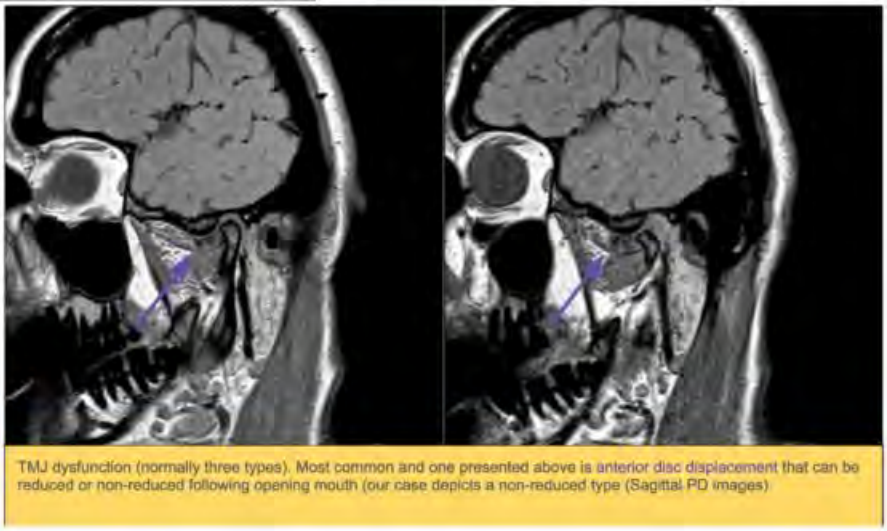

(Filename: TCT_400_ScreenShot2022-10-30at72850PM.jpg)

1369

The 3 Easy Steps Approach to Susceptibility Phase Maps: A Painless and Accurate Way To Differentiate Calcifications From Hemorrhages.

F Feltrin[1], H Elbelasi[2], A Hussien[3]

[1]UTSouthwestern Texas University, Dallas, TX, [2]University of Texas Southwestern, Dallas, TX, [3]UT Southwestern, Garland, TX

Summary and Objectives

Summary: The use of susceptibility imaging phase map for differentiation or paramagnetic substances (such as blood products) and diamagnetic substances (such as calcifications) is an extremely useful toll in MRI. However, the interpretation is not straightforward. Different scanners with different imaging parameters may result in opposite signal intensity for the same lesion if subjected to examination in left or right-handed scanners (1). In addition, susceptibility image is prone to aliasing which results in artifacts inside the lesions. All that contributes to low adherence to this technique in most imaging centers. However, the interpretation of this imaging modality may be very easy. The first step is the use of the midsize veins which are in an orthogonal direction to B0 to establish the behavior of any paramagnetic substance. The second step is to evaluate the lesion in comparison to the veins identified in step one. If the lesions are not punctate, but complex, a third step is required: evaluation of the lesion in the coronal plane and observe the magnetic dipole created by the susceptibility in the external limits of the lesion. With these 3 simple steps it is possible to classify nearly any lesion, regardless of the direction of B0 and complexity of the lesion. In this presentation we will exhibit this approach step by step, demonstrate examples an add additional test slides with explanations for further comprehension. Educational Objectives: - Explain in an easy approach the diamagnetic and paramagnetic effects over B0. - Explain the use of certain veins as ground truth for the diamagnetic and paramagnetic behavior. - Demonstrate the effective use of coronal reformat to observe the magnetic dipole and avoid confusions related to the aliasing inside the lesions. - Test the learned topics with additional challenge slides.

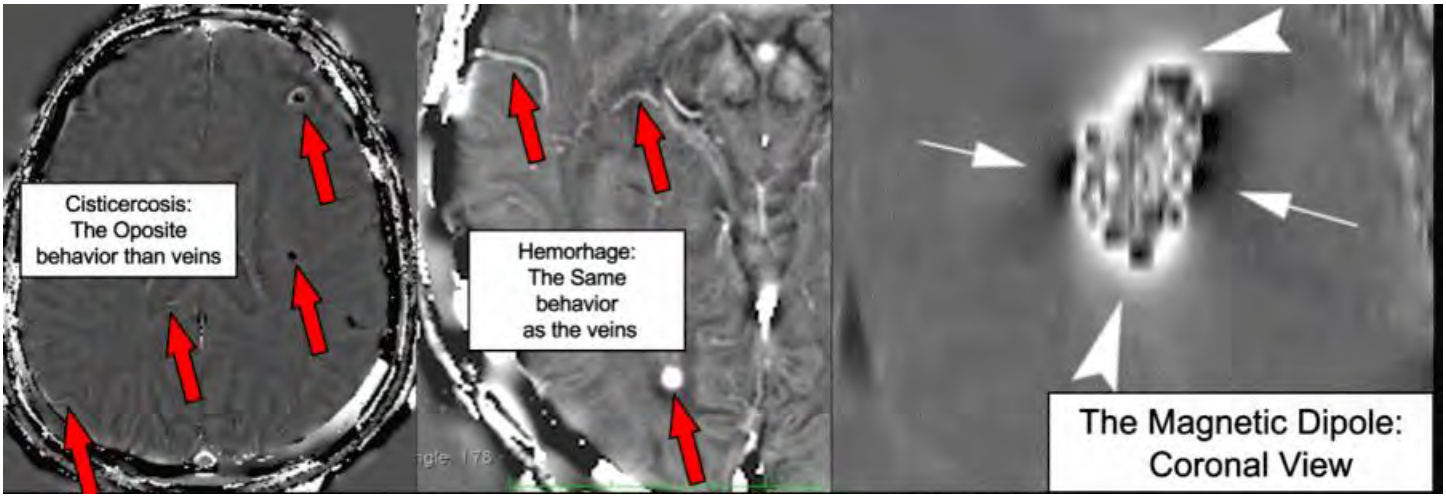

(Filename: TCT_1369_SWI.GIF)

855

The Inner Ear: An Anatomy, Physiology, and Pathology Primer

E Zamora[1], C Zamora[2]

[1]Thomas Jefferson University, Philadelphia, PA, [2]UNC Department of Radiology, Chapel Hill, NC

Summary and Objectives

Summary: The inner ear is a complex anatomical region of the temporal bone that contains structures of high functional relevance. Disorders of the inner ear are common and can manifest as hearing loss, vertigo, or tinnitus. The inner ear is the target of different surgical procedures, including cochlear implantation, repair of semicircular canal dehiscence, and labyrinthectomy. Anatomically, the inner ear is composed of the membranous and bony labyrinths which form the cochlea and vestibular apparatus. During embryonic life, the membranous labyrinth is encased in mesenchyme which progressively differentiates into cartilage and latter ossifies to become the bony labyrinth or otic capsule. The bony cochlea contains perilymph within the scala tympani and scala vestibuli which surround the membranous labyrinth, communicating with CSF through the cochlear aqueduct. On the other hand, the membranous labyrinth is filled with endolymph which does not communicate with the perilymph or CSF. The scala tympani and scala vestibuli communicate with each other at the apex of the cochlea through a small opening called the helicotrema (Figure). The endolymph-filled membranous labyrinth is separated from the perilymph-containing scala tympani by the vestibular (Reissner's) membrane and from the scala vestibuli by the osseous spiral lamina and basilar membrane. Sound waves transmitted through the stapes and oval window propagate through the perilymph of the scala vestibuli and back into the scala tympani to be released at the round window. Pressure waves coursing through the perilymph result in differential motion of the tectorial and basilar membranes, stimulating hair cells within the organ of Corti (membranous labyrinth) and ultimately the cochlear nerve resulting in the generation of sound. In addition to anatomy and physiology, this exhibit will cover pathologies that affect the inner ear, including congenital anomalies (e.g., aplasias, incomplete partitions), syndromic entities (e.g., branchio-oto-renal spectrum disorders), neoplastic (e.g., labyrinthine schwannoma, endolymphatic sac tumors), and various etiologies (membranous, ossifying, and hemorrhagic labyrinthitis; otospongiosis; 3rd window phenomena). Educational objectives: Illustrate the anatomy of the inner ear with relevant imaging correlates on CT and MRI. Understand basic physiology of the inner ear. Review different pathologic entities that affect the inner ear.

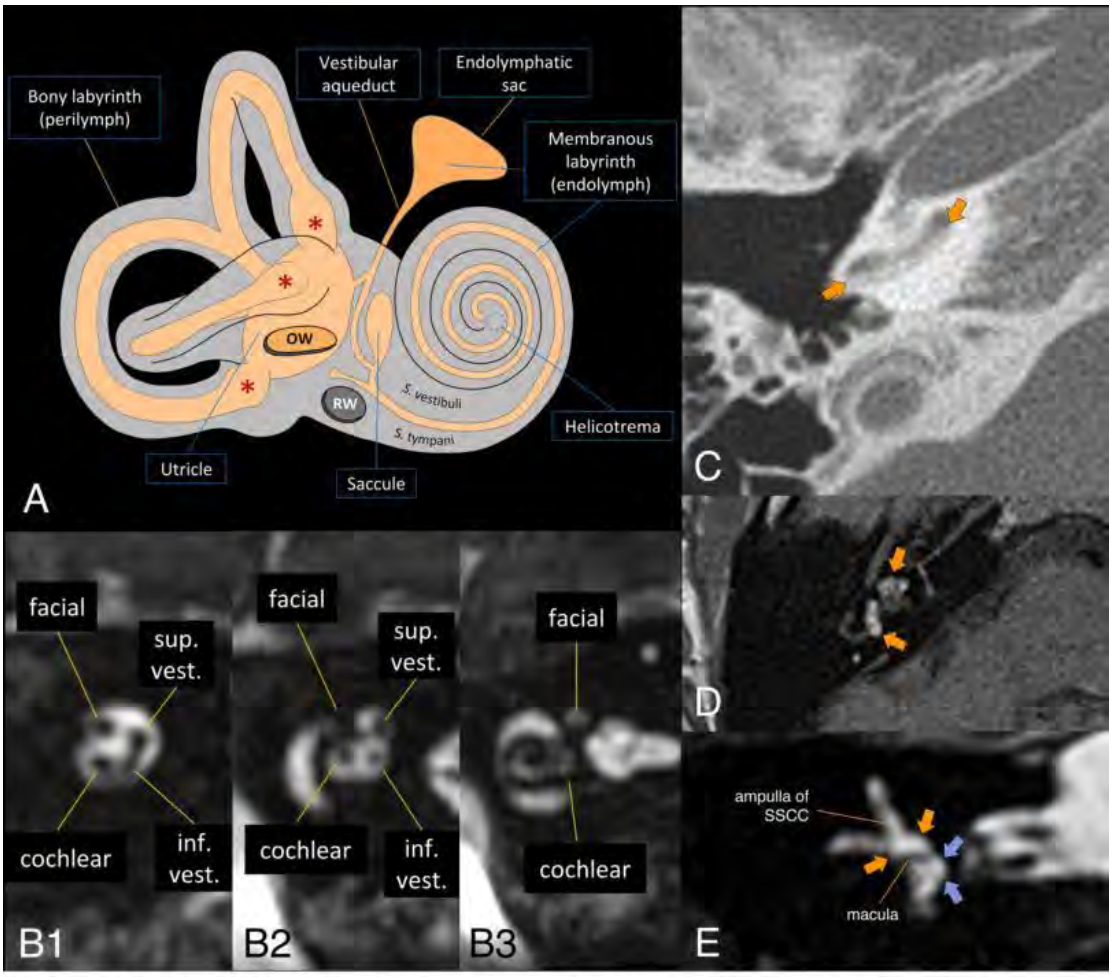

A. Anatomic illustration of the inner ear shows different components of the bony and membranous labyrinths. The ampullae (*) of the semicircular canals can be seen connecting with the utricle which is housed in the vestibule. Small ducts from the utricle and saccule converge to form the vestibular aqueduct. **OW**: oval window; **RW**: round window. **B1**-**B3**. Consecutive cross sections showing the different nerves coursing through the internal auditory canal to reach the cochlea, vestibular apparatus, and facial canal. **C**. Axial CT in a patient with labyrinthitis ossificans shows ossification of the basal and middle turns of the cochlea primarily affecting the scala tympani (arrows). **D**. Axial noncontrast T1 shows hyperintensity in the inner ear consistent with hemorrhagic labyrinthitis (arrows). **E**. Coronal CISS sequence shows the utricle (orange arrows) and smaller saccule (purple arrows). Note the macula along the inferior margin of the utricle.

(Filename: TCT_855_imagefilejpegcomp.jpg)

1397

This or That: Differentiating Orbital Masses and Mass-Like Lesions with Imaging and Histology

C Paton[1], R Ismail[2], P Rao[2], A Rahman, MD; DO[2]

[1]University of Rochester, Rochester, NY, [2]University of Rochester Medical Center, Rochester, NY

Summary and Objectives

To review the anatomy of the orbit, intraorbital compartments and its contents. To identify unique imaging characteristics of each lesion and their differentiating imaging and histologic features. To improve understanding of orbital pathologies amongst radiologists.

Purpose

Orbital lesions are classified on the basis of location, imaging characteristics and histological features. The orbit is divided into multiple compartments including ocular compartment, muscle cone, intraconal and extraconal spaces. Besides the optic globe, optic nerve, and extraocular muscle, the orbit contains a glandular structure which is the lacrimal gland and a lacrimal sac. Orbital lesions can originate in one compartment and potentially extend into other compartments. The clinical presentation of these lesions can vary depending on the intraorbital structures involved. Imaging characteristics can depict the tissue composition, however histological features play an important role in making the final diagnosis. Two histologically different lesions can have similar imaging characteristics. For example, cavernous hemangiomas (CH) and orbital lymphomas (OL) are both enhancing lesions. However, CH have gradual progressive enhancement with delayed washout versus OL which have diffuse homogenous enhancement with T2 hypointensity and diffusion restriction. Osseous involvement is rare in cases of orbital lymphoma. In this educational exhibit, we present a collection of cases demonstrating the wide variety of orbital lesions including some rare unique cases. These cases are

grouped by point of origin or compartmental location and then further subdivided by oncologic tissue types. We will focus on identifying imaging characteristics of each lesion, their specific differentiating imaging findings and histologic features.
Materials and Methods
In this educational exhibit, a diverse series of orbital lesions will be displayed with their characteristic CT and MRI findings. A short discussion of each case's pathology and the scientific etiology will also be provided.
Results and Conclusions
With this educational exhibit, we will review the anatomy of the orbit and work through a series of cases displaying the most common presentations of orbital pathology on imaging with associated clinical presentations.

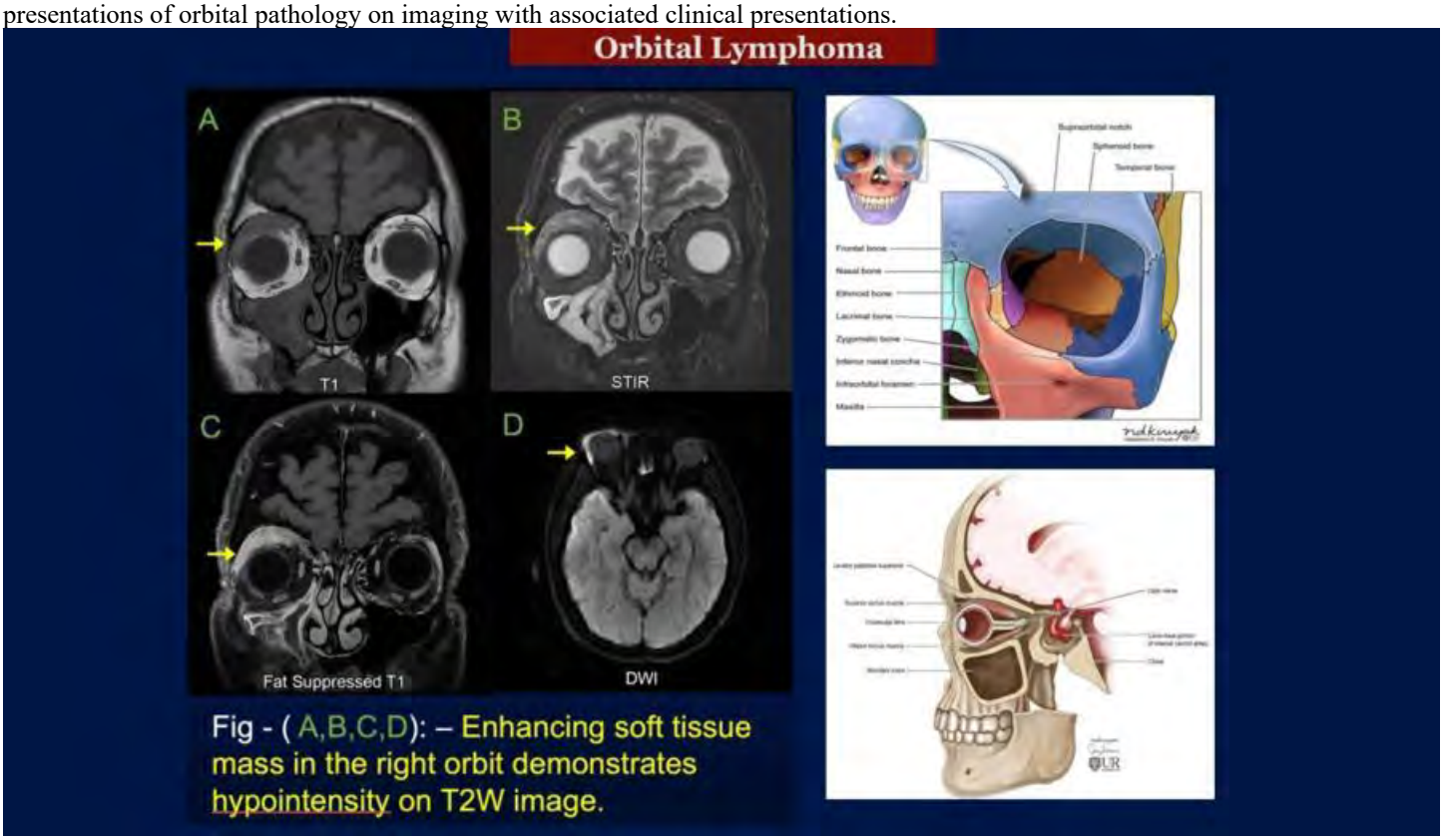

(Filename: TCT_1397_OrbitalLesionspic.jpg)

1391
Tumors of the Salivary Glands: Imaging and Histological Findings
C Paton[1], P Rao[2], R Ismail[2], A Rahman, MD; DO[2]
[1]University of Rochester, Rochester, NY, [2]University of Rochester Medical Center, Rochester, NY

Summary and Objectives
1. To review the anatomy of the salivary glands. 2. To distinguish benign from malignant salivary gland tumor types. 3. To develop a classification system for tumors by gland and histology. 4. To understand the incidence of common and rare pathologies. 5. To understand the critical pathology of each tumor type. 6. To gain familiarity with recognizing salivary gland tumors on MRI imaging.
Purpose
Tumors of the salivary glands are highly diverse. The occurrence of tumors descends anatomically, with 70% of tumors occurring in the parotid gland, 22% in the minor salivary glands, and 8% in the submandibular glands. They tend to follow a pattern of malignancy from superior to inferior, with most of the parotid gland tumors being benign, about half of the submandibular glands being malignant, and the majority of the sublingual and accessory glands being malignant. We present a case collection of four original salivary gland tumors. We start by reviewing the anatomy of the salivary glands and the head and neck regions at risk of tumor spread. We review the blood circulation and lymphatic drainage of the areas. We then present a table organizing the types of salivary gland tumors into benign and malignant subtypes. We proceed to further categorize these tumors by gland: parotid, submandibular, sublingual, or accessory glands. We then walk through each of the four cases: the imaging, and the pathology of the tumor and the sequelae to consider and recognize, with special emphasis on the lymphatic drainage of the head and the risk of metastasis and life-threatening abscess.
Materials and Methods
Specifically, we will present a parotid gland Schwannoma, a benign mixed tumor (Pleomorphic Adenoma), a parotid gland HIV Cystic Lesion, and a submandibular Psilocyte. We will thoroughly review each case by radiography and pathology and encourage familiarity with recognition of these unique tumors of the head and neck.
Results and Conclusions
Tumors within the salivary glands are highly diverse with important risks for malignancy and treatment requiring prompt proper

diagnosis. Differentiating between the different tumor types presenting in each of the three glands requires precise interpretation of medical imaging and collaboration with pathology. With this educational exhibit, we will review the anatomy of the salivary glands and work through a series of cases displaying the most common presentations for these tumor types on imaging. We will also provide a useful overview of the pathology associated with these tumors.

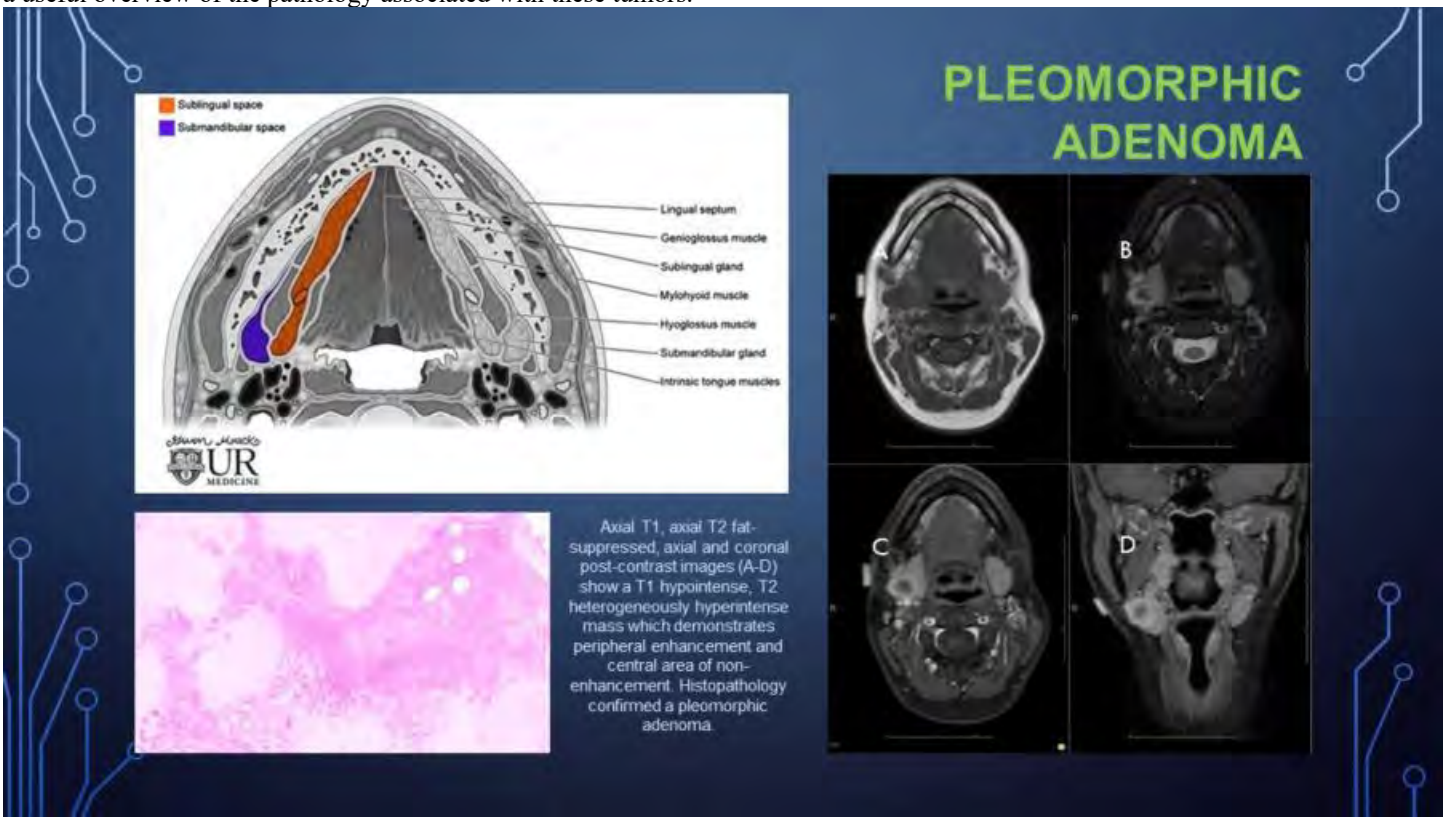

(Filename: TCT_1391_SalivaryGlandTumorsCP.jpg)

1408
Tumors of the Ventricular System
R Ismail[1], P Rao[1], C Paton[2], A Rahman, MD; DO[1]
[1]University of Rochester Medical Center, Rochester, NY, [2]University of Rochester, Rochester, NY

Summary and Objectives
1. Review the structural anatomy of the ventricles and adjacent structures. 2. Categorize and characterize tumors occurring in the ventricular system in children and adults, by incidence. 3. Familiarize neuroradiologists with the most frequent presentations of ventricular tumors on MRI imaging. 4. Present a categorization schema for differentiating tumors by location and appearance.
Purpose
Intraventricular masses may have a large differential. While their contrast with the CSF may enable detection on imaging more quickly, further identification of the specific tumor type can be difficult. Intraventricular neoplasms are uncommon in adults but are more frequent in children, with different etiologies and presentations between these populations. Ependymomas comprise nearly one third of all pediatric brain tumors in children younger than 3 years. They more commonly arise in the 4th ventricle in pediatric patients but are frequently outside the ventricles and supratentorial in adults. Conversely, choroid plexus papillomas present more frequently in the lateral ventricles of children but in the 4th ventricle in adults. In this educational exhibit, we present a collection of cases demonstrating the characteristic CT and MRI appearances of ventricular tumors. These selected cases are a representative subset of tumors which appear the most frequently in adults and children.
Materials and Methods
In this educational exhibit, a diverse series of ventricular tumors will be shown with their characteristic CT and MRI findings. A short discussion of each case's clinical presentation and subsequent management will also be provided.
Results and Conclusions
Tumors within the ventricular system often present with the canonical symptoms of increased intracranial pressure: headache, nausea and emesis, papilledema. Differentiating between the common causes of this presentation necessitates more than the clinical findings; often these cases require precise interpretation of medical imaging. With this educational exhibit, we will review the anatomy of the ventricles and work through a series of cases displaying the most common presentations for these ventricular tumors on imaging with associated clinical presentations. We will also provide a useful categorization of these tumor types to aid in future recognition.

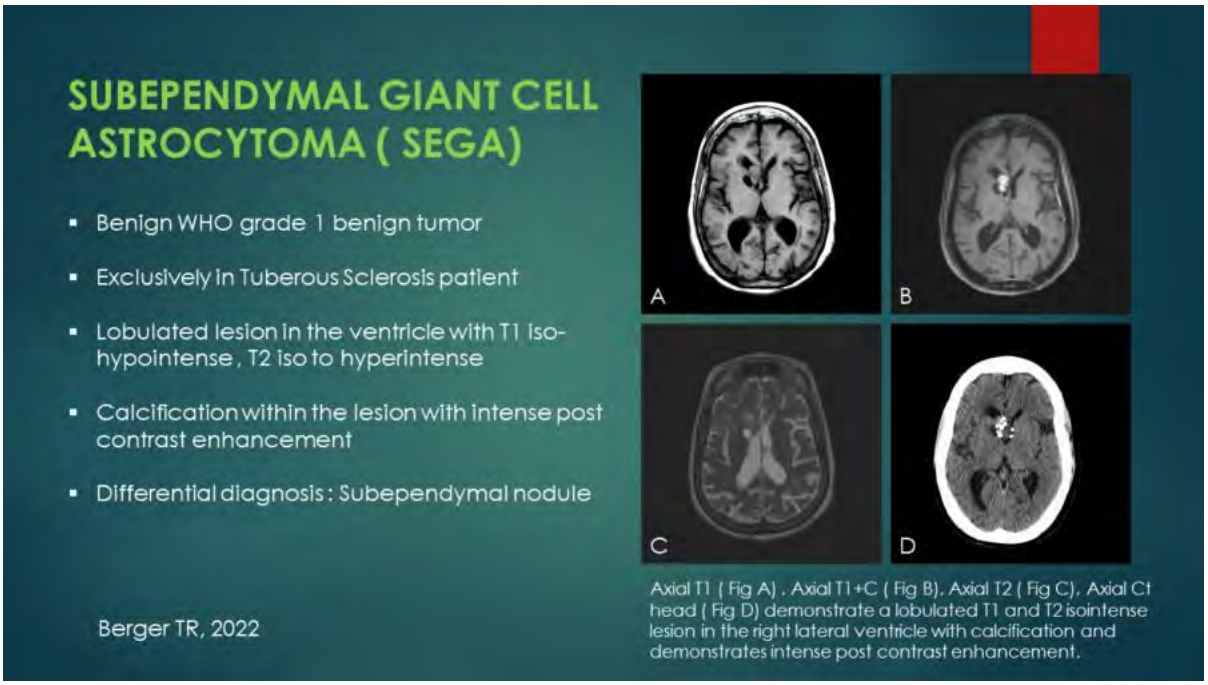

(Filename: TCT_1408_OrbitallesionsASNR1slide.jpg)

1094

Uncommon infectious and inflammatory disorders of the larynx & hypopharynx

M Sarpi[1], M Garcia[1], S Souza[2], R Reali[1], C Coelho Neto[1], A Araujo[1], S Mukherji[3]
[1]DASA, São Paulo, São Paulo, [2]InRad, Sao Paulo, AK, [3]ProScan Imagng, Carmel, IN

Summary and Objectives
Larynx and pharynx inflammatory and infectious diseases are relatively uncommon and clinically difficult to diagnose. The objectives of this exhibit are to 1. Demonstrate imaging findings of these uncommon disorders, 2. Discuss clinical aspects that are important to the differential diagnosis and 3. Explore characteristic radiological findings that help the neuroradiologists make the correct diagnosis.
Purpose
The purpose of this educational exhibit is to review the imaging features of uncommon infectious and inflammatory disorders of the larynx and pharynx and focus on the characteristic radiological findings that help the neuroradiologists make the correct diagnosis
Materials and Methods
The images were obtained through a retrospective review of our digital archives. We will demonstrate typical findings of a variety of unusual disorders including relapsing polychondritis, abscesses, necrotizing fasciitis and chondronecrosis, amyloidosis, sarcoidosis, granulomatosis with polyangiitis, tuberculosis, leishmaniasis and paracoccidioidomicosis with special focus on the characteristics imaging findings.
Results and Conclusions
It is important for radiologists to have an understanding of the various inflammatory and infectious diseases that may be encountered in larynx and pharynx imaging evaluation. Some of them may mimic laryngeal malignancies and being familiar with their imaging aspects will contribute to improve accuracy in the management of patients.

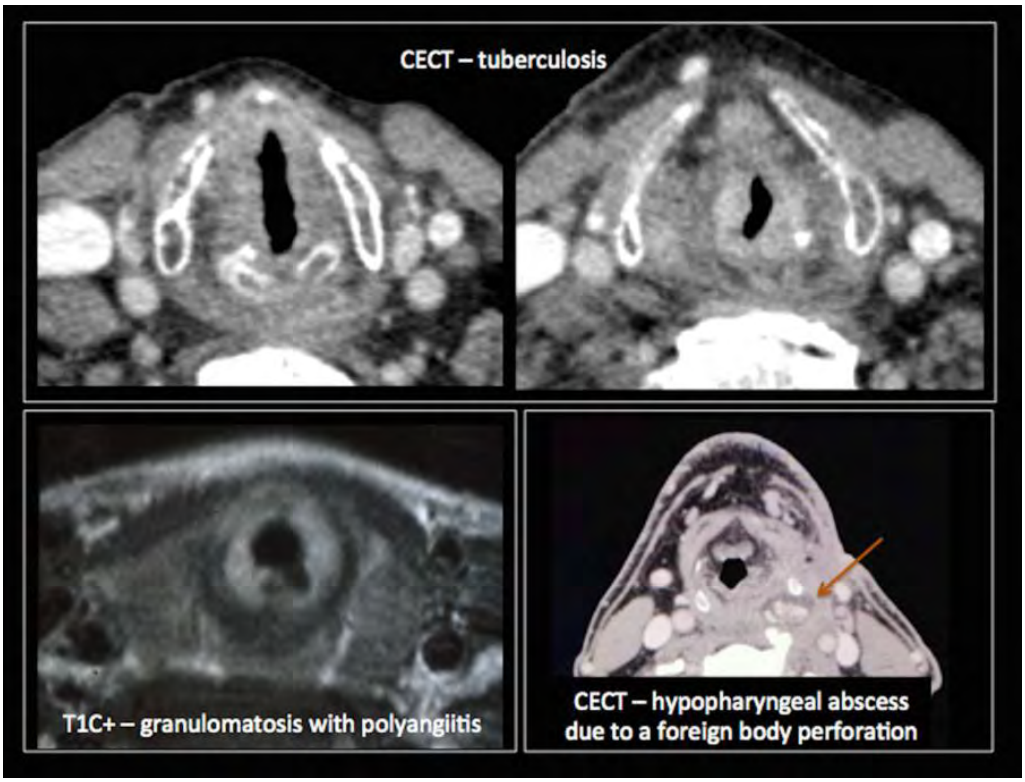

(Filename: TCT_1094_larynx.jpg)

305

Unexpected Findings on Diffusion Weighted Imaging of the Brain

S Elias[1], H Bueno[2], E Nimchinsky[1], J Valles Feliciano[3]
[1]Rutgers University, Newark, NJ, [2]Rutgers New Jersey Medical School, Newark, NJ, [3]Rutgers Radiology NJMS, Newark, NJ

Summary and Objectives
Many non-radiologists understand that diffusion weighted imaging (DWI) is essential for the detection of intraparenchymal pathology such as acute infarction. As neuroradiologists, however, we should be well aware of the strengths and limitations of DWI in detecting extraparenchymal and even extracranial pathologies. For example, small pus layering in the ventricles in ventriculitis can be easily recognized on DWI and may be the only indication of otherwise occult infection. Looking beyond the brain, structures at or below the skull base are characterized by complex anatomy and evaluation may be limited by the presence of artifacts. However, DWI's inherent high signal to noise ratio may highlight abnormalities including vascular pathology such as dural venous sinus thrombosis or arterial dissection. Calvarial lesions are readily detected against the normal low signal of mature bone. Moreover, DWI is useful for the detection of often unexpected extracranial pathology more inferiorly in the head and neck, including infection and tumor. Diligent review of the extracranial soft tissues and vessels may allow for the detection of many important and unexpected pathologies, and guide further imaging.
Purpose
The purpose of this educational exhibit is to review the utility of DWI in evaluating extraparenchymal and extracranial pathology.
Materials and Methods
Each case presented was collected from our home institution. A brief clinical history is provided for every case and DWI imaging is reviewed. Imaging correlates from different modalities such as computed tomography angiography or digital subtraction angiogram are also presented where appropriate. Lastly, key teaching points discussing imaging pearls, strengths, and/or limitations are presented.
Results and Conclusions
Careful review of the extraparenchymal and extracranial anatomy on DWI may help the neuroradiologist detect otherwise subtle pathology

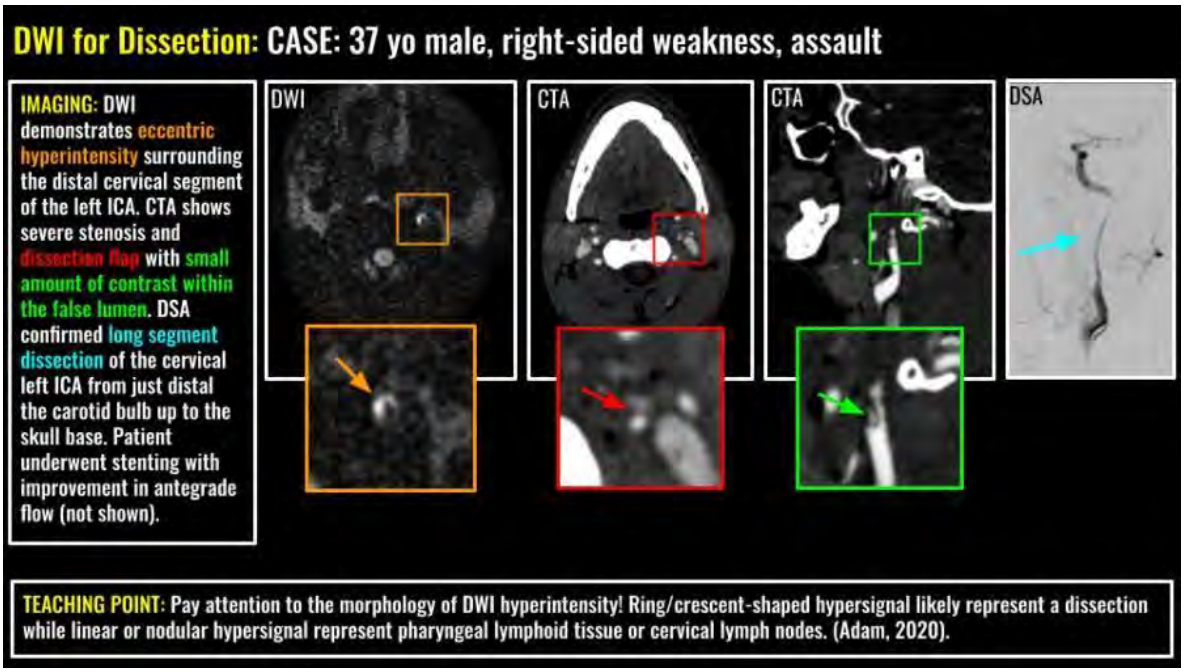

(Filename: TCT_305_DWIPathology2.jpg)

326

Unilateral or Asymmetric Basal Ganglia and Thalamus Lesions

S Alves[1], J Brunelli[1], C Barbosa[1], G Chaves[1], I Alves[1], P Kraichete[1], J Takahashi[2], H Lee[1], C Leite[3], C Amancio[4]
[1]Hospital Sírio-Libanês, São Paulo, São Paulo, [2]HCFMUSP, São Paulo, SP, [3]University of São Paulo, Sao Paulo, São Paulo, [4]Hospital Sírio Libanês, São Paulo, Brazil

Summary and Objectives
Introduction; Anatomy of centrencephalic structures; Differential diagnosis flowchart; Case presentation; Conclusion Review basal ganglia and thalamus anatomy Recognize the wide range of ethiologies that may present as unilateral or asymmetrical abnormalities and features that differentiate them
Purpose
Bilateral and symmetrical centrencephalic abnormalities are well described and established in the literature, common related to toxic-metabolic diseases. However, there is a lack of a systematic approach for evaluating unilateral or asymmetrical lesions in the same topography. The present exhibit intends to offer a flowchart for those etiologies, with a pure didactic division, as many of the mentioned conditions have timed-phase presentations and may fit in two or more categories.
Materials and Methods
We have assembled cases from our service database in which imaging portrayed unilateral or asymmetrical basal ganglia and/or thalami abnormalities. A literature review was made, although it lacks similar approach of this content. We sorted ethiologies by volume alteration of compromised structures and imaging characteristics, offering a pure didactic division.
Results and Conclusions
Our educational exhibit was able propose a didactic flowchart for the wide range of differential diagnosis of unilateral or asymmetric basal ganglia/thalamus abnormalities. As it comprises many kinds of ethiologies, we hope to facilitate radiologists' reasoning when in face of any of these.

- Bilateral and symmetrical centrencephalic abnormalities are well described and established in the literature, common related to toxic-metabolic diseases.
- However, there is a lack of a systematic approach for evaluating unilateral or asymmetrical lesions in the same topography
- The present exhibit intends to offer a flowchart for those etiologies, with a pure didactic division, as many of the mentioned conditions have timed-phase presentations and may fit in two or more categories

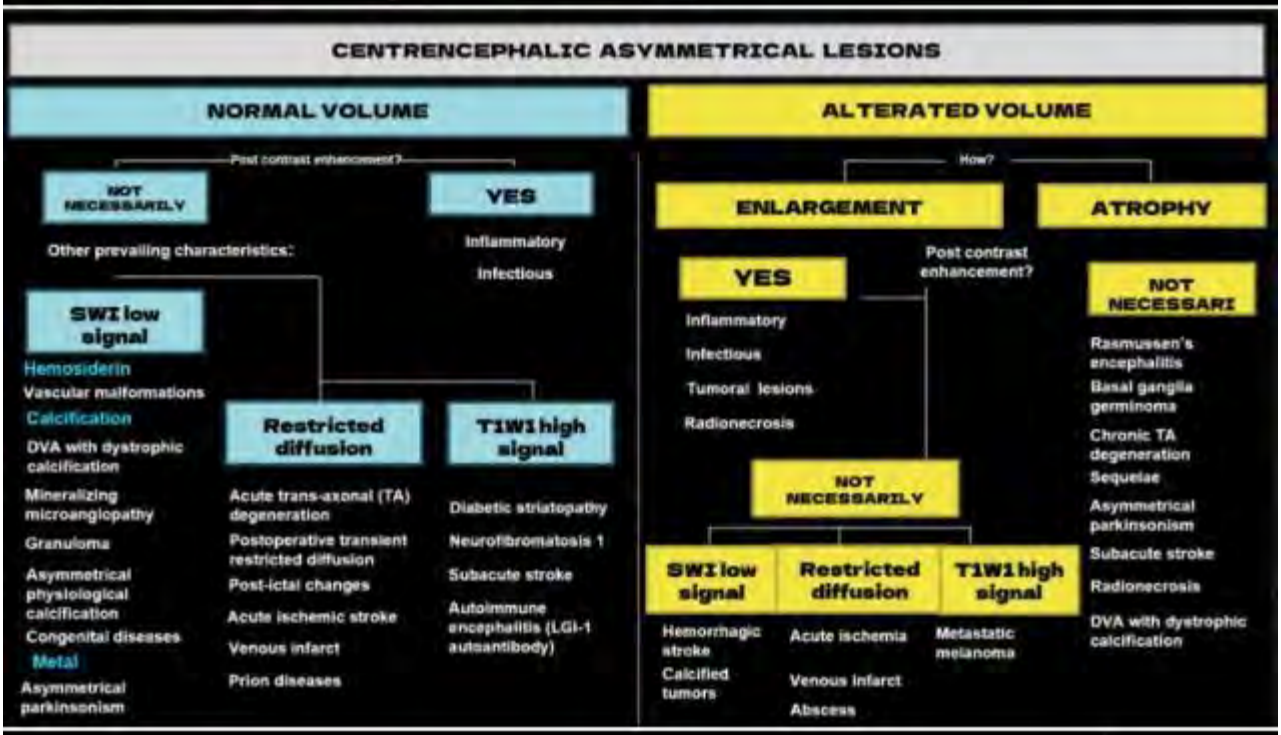

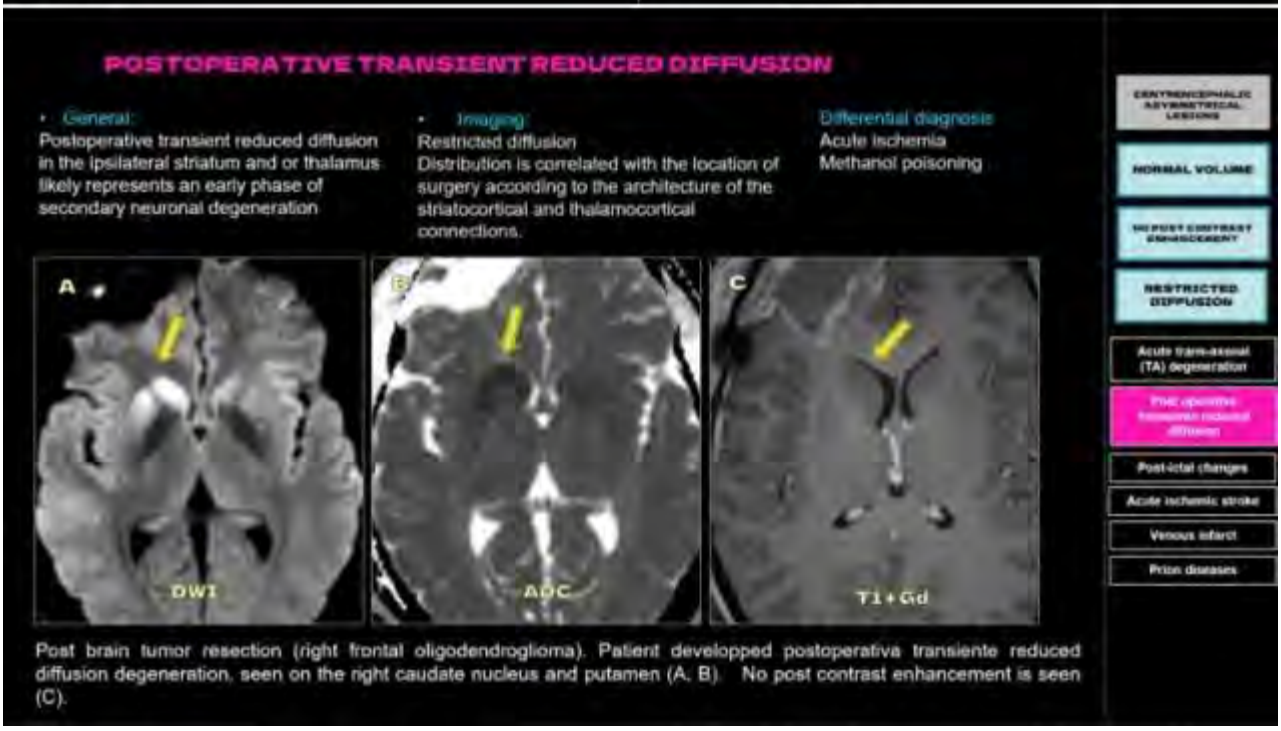

(Filename: TCT_326_panoramic5.jpg)

1121

Unmasking the Sixth Nerve Palsy: a Pictorial Review

V Munera[1], F Calle[2], D Herrera[3], S Osorio[4]

[1]Universidad Pontificia Bolivariana, Medellin, Antioquia, [2]Universidad Militar Nueva Granada, Bogotá, Cundinamarca, [3]Cedimed, Medellin, Antioquia, [4]Clinica Las Amércias, Medellin, Antioquia

Summary and Objectives

Summary -Anatomy of the VI cranial nerve Origin, Dorello canal, Cavernous sinus, Superior orbital fissure, Lateral rectus muscle -Clinical manifestations cranial nerve VI Palsy - Manifestations that help locating the lesion Imaging the cranial nerve VI -Indications -MRI Technique: bSSFP, contrast administration. Sixth Cranial Nerve Pathology by anatomical portion: -Pons medial longitudinal fasciculus Syndrome, Duane, Möbius, Demyelinating. -Subarachnoid space Aneurysm, altered intracranial pressure, Meningeal infiltration: Metastatic disease, Sarcoidosis. -Petrous apex and skull base Tumors: Chordoma, meningioma, metastasis.Infection/Inflammatory: Gradenigo, Trauma. -Cavernous sinus Cavernous sinus thrombosis, fistula, Tumor: Pituitary Adenoma, Vascular -Orbital Tumor: Schwannoma, Trauma. Educational Objectives: -MRI is fundamental for visualizing the abducens nerve (cranial nerve VI) and the structures that make up its expected course -Clinical examination and location of cranial nerve VI lesions narrows the differential diagnosis -Balanced steady-state free precession sequences (bSSFP) improve image resolution and are crucial to evaluate cranial nerve VI -The pathologies that affect the cranial nerve VI are divided in five anatomical portions: Pons, subarachnoid space, petrous apex/skull base, cavernous sinus and orbit -Spectrum of abducens pathologies: review of differential diagnosis

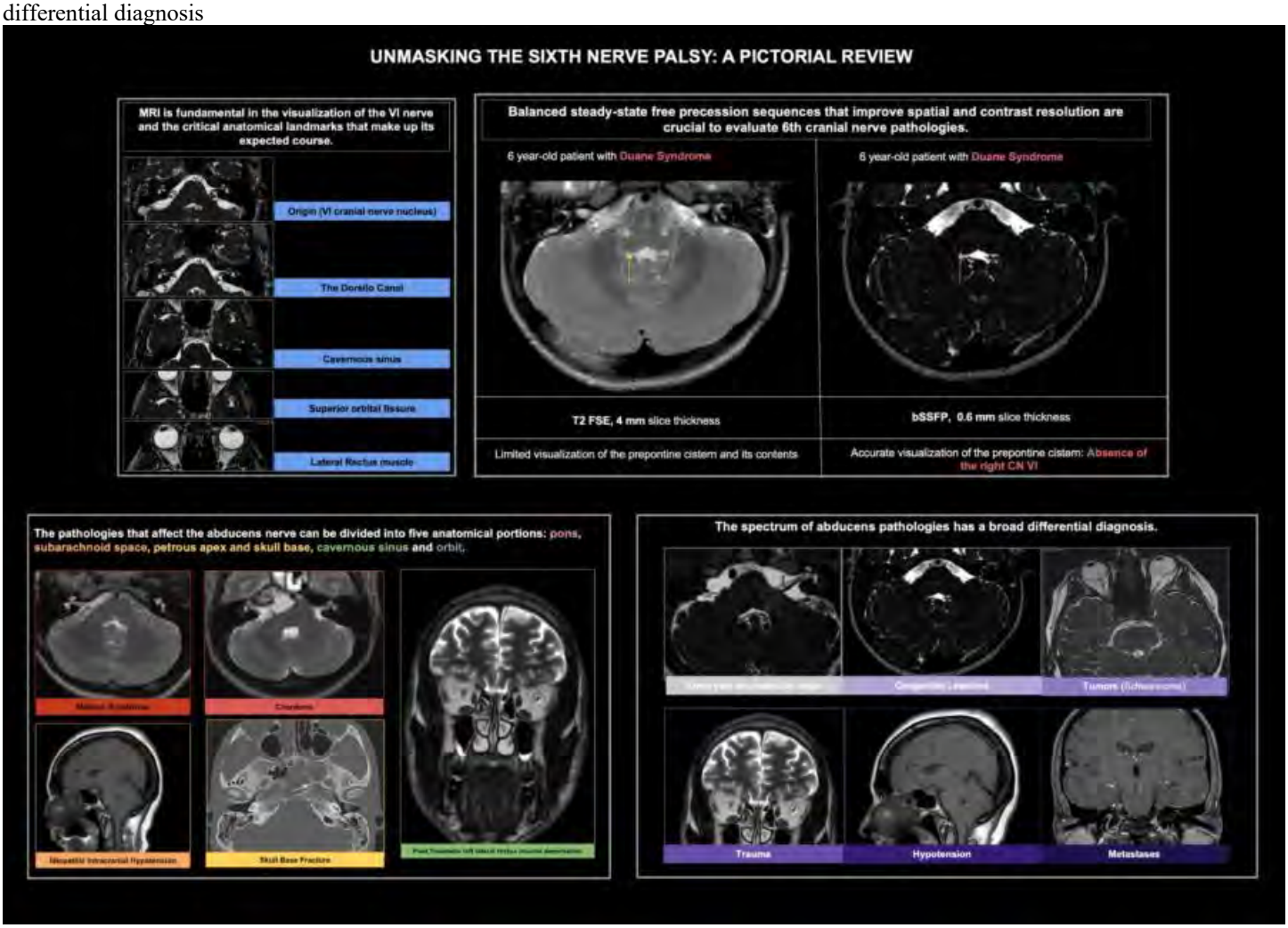

(Filename: TCT_1121_Unmaskingthesixthnervepalsy.jpg)

290

Unsuspected Diagnosis of Congenital or Perinatal Neurological Disorders in Adult Patients

Z Angel[1], R Thakkar[2], E MakariouMAKARIOU[1], E Lee[1]

[1]MedStar Georgetown University Hospital, Washington, DC, [2]Medstar Georgetown University Hospital, Washington, DC

Summary and Objectives

Congenital neurological disorders and perinatal neurological disorders are well described in the pediatric population. Pediatric patients, however, do not remain as children, and may present to the unsuspecting adult radiologist for common adult diseases. In this

educational exhibit, we review cases of common congenital and perinatal disorders in the adult population, as a reminder that pediatric conditions can persist into adulthood.

Purpose

Patients with congenital neurological disorders or perinatal neurological disorders do grow up and can present with common adult diseases such as stroke or altered mental status. Unsuspecting adult radiologists who are unfamiliar with pediatric diseases may not recognize the underlying congenital conditions or find it a challenge. We aim to present representative cases of congenital and perinatal disorders seen in adult patients and describe their typical imaging characteristics, so that trainees, general radiologists, and neuroradiologists who specialize in adult patients may become familiar with or be reminded of these findings, and provide a more accurate, comprehensive differential diagnosis.

Materials and Methods

We compiled cases of adult neuroimaging studies showing underlying congenital or perinatal neurologic disorders from our institution.

Results and Conclusions

We present various congenital and perinatal neurological disorders in adult patients, including sequelae of perinatal hypoxic ischemic changes, sequalae of perinatal hydrocephalus, focal cortical dysplasia, schizencephaly, Sturge-Weber syndrome, tuberous sclerosis, septo-optic dysplasia, rhomboencephalosynapsis, pericallosal lipoma, pontocerebellar hypoplasia, congenital aqueductal stenosis, and Moya Moya disease. We illustrate a case of septo-optic dysplasia as an example.

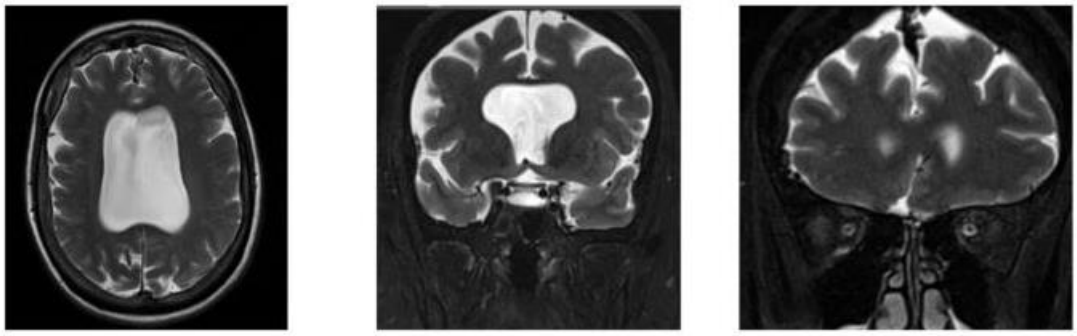

60 year old female presented for stroke with history of blindness. The finding of ventriculomegaly can be mistaken for hydrocephalus. This appearance, however, represents congenital absence of septum pellucidum, which is seen in septo-optic dysplasia. Additional findings of small optic chiasm / atrophic optic nerves are also features of septo-optic dysplasia.

(Filename: TCT_290_imagesadultpresentationofpediatricconditions.jpg)

115

Unusual and Strange Presentations of Pituitary Adenomas

S Siala[1], C Zamora[1], M Castillo[1]

[1]*UNC Department of Radiology, Chapel Hill, NC*

Summary and Objectives

Summary: Pituitary adenomas are benign epithelial tumors accounting for 10-15% of intracranial neoplasms [1]. Although most have characteristic MRI features, they can present with atypical findings making a definite diagnosis difficult. Invasive pituitary adenomas are relatively rare, with varying reported frequencies in the literature [2]. Extrasellar extension varies from cavernous sinus invasion and displacement/encasement of the optic chiasm to extensive skull base invasion and extension through the foramina. This highly invasive pattern mimics skull base malignancies and confounds diagnosis. Conversely, ectopic pituitary adenomas are located outside the sella without obvious continuity with the gland. A widely accepted hypothesis suggests that formation of ectopic pituitary adenomas is related to the embryological development of the anterior pituitary [3]. Such tumors are thought to arise from pituitary cells along the embryonic migratory path of Rathke's pouch, which normally ascends from the pharyngeal roof during embryogenesis [4]. Remnants of Rathke's pouch can reside along its course from the pharynx to the sella and explain ectopic adenomas in the nasopharynx, sphenoid sinus, clivus and sometimes suprasellar cistern [4,5]. In patients with pituitary apoplexy, adenomas present acutely with hemorrhage, sometimes extensive. Additionally, pituitary adenomas may undergo cystic degeneration following medical therapy. In this exhibit we aim to illustrate unusual imaging presentations of pituitary adenomas that may be a function of their extent, morphology, local invasiveness, unusual ectopic location, or other associated imaging findings. Educational objectives: Illustrate various atypical and potentially confounding appearances of pituitary adenomas and provide clues that may aid in their diagnosis.

Understand the potential locations of ectopic pituitary adenomas as a function of the embryological development of the pituitary gland.

(Filename: TCT_115_ImageFile.jpg)

612

Using Diffusion Tensor Imaging and Fiber Tractography as Biomarkers for Spinal Cord Injury in the Pediatric Population

N Joshi[1], S Shahrampour[1], M Alizadeh[1], D Middleton[1], S Faro[1], F Mohamed[1], K Talekar[1]
[1]Thomas Jefferson University, Philadelphia, PA

Summary and Objectives
Pediatric SCI can result in permanent neurological damage and efforts to curtail the extent of injury have been futile. There is a scarcity of literature in terms of how the inherent microstructure of the whole spinal cord (SC) changes after injury. The main objectives of this exhibit are 1) to define DTI parameters, 2) describe image acquisition techniques specifically in the pediatric population, 3) delineate white matter (WM) tracts automatically as well as using fiber tractography to generate whole spinal cord tracts and 4) to use DTI metrics and their correlation with injury severity in the clinical setting.
Purpose
The purpose is to provide a review of how to use diffusion tensor imaging (DTI) and tractography, which are noninvasive tools to assess tissue microstructure, as biomarkers for spinal cord injury (SCI) in the pediatric population. This will help researchers build foundational knowledge to further explore this field.
Materials and Methods
We start by defining quantitative DTI parameters such as fractional anisotropy (FA), radial diffusivity (RD), mean diffusivity (MD), and axial diffusivity (AD) and how they provide insight into the microstructure of SC WM tracts within the lesion and distant perilesional areas. DTI not only highlights the extent of primary injuries but also the late consequences of secondary axonal injury, including Wallerian degeneration. Special attention is given to technical aspects such as image acquisition and automated atlas-based extraction of white matter tracts. We also discuss the advantages and pitfalls of using DTI for pediatric SCI. The immediate usefulness of DTI metrics is assessing the severity of injury SCI in conjunction with the International Standards for Neurological Classification of Spinal Cord Injury (ISNCSCI) examination as well as the American Spinal Injury Association impairment Scale (AIS).
Results and Conclusions
DTI is a powerful tool that provides insight into the structural changes in SCI apart from what may be seen on conventional MRI sequences. This enhances our understanding of the underlying plastic changes in vivo after injury within sensory and motor tracts and changes the way we approach new treatments. Using DTI as a biomarker may help enhance patient care as part of multimodal diagnostic and treatment planning.

806

Vascular Complications of Head and Neck Infections

C Christensen[1], M Alexander[1], J McNally[1]
[1]*University of Utah, Salt Lake City, UT*

Summary and Objectives
Infectious processes involving the head and neck are common and can result in a variety of complications. In particular, vascular complications associated with sinonasal infections can result in devastating and potentially lethal consequences. Therefore, it is critical that radiologists look for and recognize the imaging manifestations of vascular complications related to head and neck infections given that these are often subtle and precede clinical symptoms or stroke. It is also imperative that radiologists are aware of the most effective imaging methods for the diagnosis of vascular complications. Early recognition can result in timely intervention, prevent disease progression, and avoid other associated comorbidities. The process of determining the type as well as the timing of appropriate intervention can be complex. These decisions require a solid understanding of the possible risks and benefits associated with neurointerventional treatment options.
Purpose
The primary purposes of this exhibit are the following: 1. Review the imaging techniques best suited for vascular evaluation in the setting of head and neck infectious processes. 2. Explore the imaging manifestations of vascular complications related to these infections. 3. Discuss potential neurointerventional treatment options for vascular complications and inherent benefits and risks.
Materials and Methods
Selected cases from our institution were reviewed and representative images provided to illustrate: 1. The imaging techniques that can be used for the diagnosis of vascular complications. 2. The imaging manifestations associated with vascular complications related to head and neck infections including sinonasal disease. 3. The benefits and risks of various neurointerventional techniques employed to treat vascular complications of head and neck infections.
Results and Conclusions
Vascular complications associated with head and neck infections have potential devastating consequences, and imaging findings can be subtle. Increased awareness of the imaging techniques, imaging manifestations, and neurointerventional methods related to vascular complications of head and neck infections can result in earlier detection and allow more effective intervention.

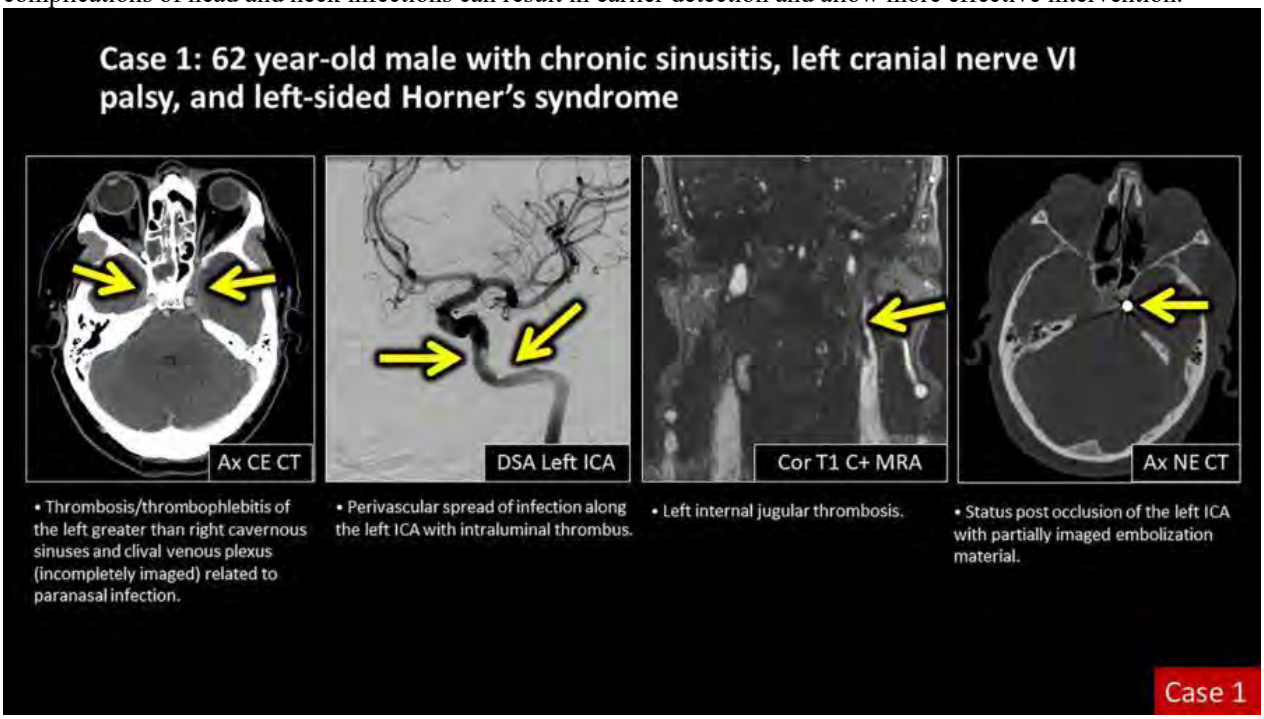

(Filename: TCT_806_VascularComplicationImages.jpg)

1457

Vasculitis of the Central Nervous System: The role of neuroimaging.

C Garcia Moreno[1]
[1]*Vancouver General Hospital / University British Columbia, Vancouver, British Columbia*

Summary and Objectives
Objectives: Review the classification of the vasculitis according to the size of the involved arteries. Describe the vascular imaging findings of vasculitis involving the central nervous system. Discuss the nonvascular imaging findings of vasculitis involving the central nervous system.

Purpose
To review of the imaging findings of central nervous system vasculitis.
Materials and Methods
It is important to distinguish the difference between vasculopathies and vasculitis. Vasculopathies include all vessel diseases, the noninflammatory and inflammatory. Vasculitis refers to the inflammatory vasculopathies and are the center of this exhibit. It is also important to keep in mind that most of the times the noninflammatory vasculopathies will be associated inflammation that leads to flares or progression of this diseases. According to the 2012 Revised International Chapel Hill Consensus Conference on the Nomenclature of Systemic Vasculitides, these can be divided according to the size of the affected vessel or as primary and secondary. There are vascular and nonvascular findings that can be seen on each of these categories, many of which overlap. For this reason, it is crucial to have knowledge about the clinical and laboratory findings to be able to reach this challenging diagnosis.
Results and Conclusions
The main imaging tools in the diagnosis of central nervous system vasculitis are Magnetic Resonance and Computed Tomography, leaving digital subtraction imaging only for the small vessel disease vasculitis. Ultrasound also has specific and limited role in this diagnosis. Imaging alone is not sufficient to make the diagnosis of vasculitis. The clinical and laboratory findings are equally important, making it fundamental for radiologist to have a knowledge of these features.

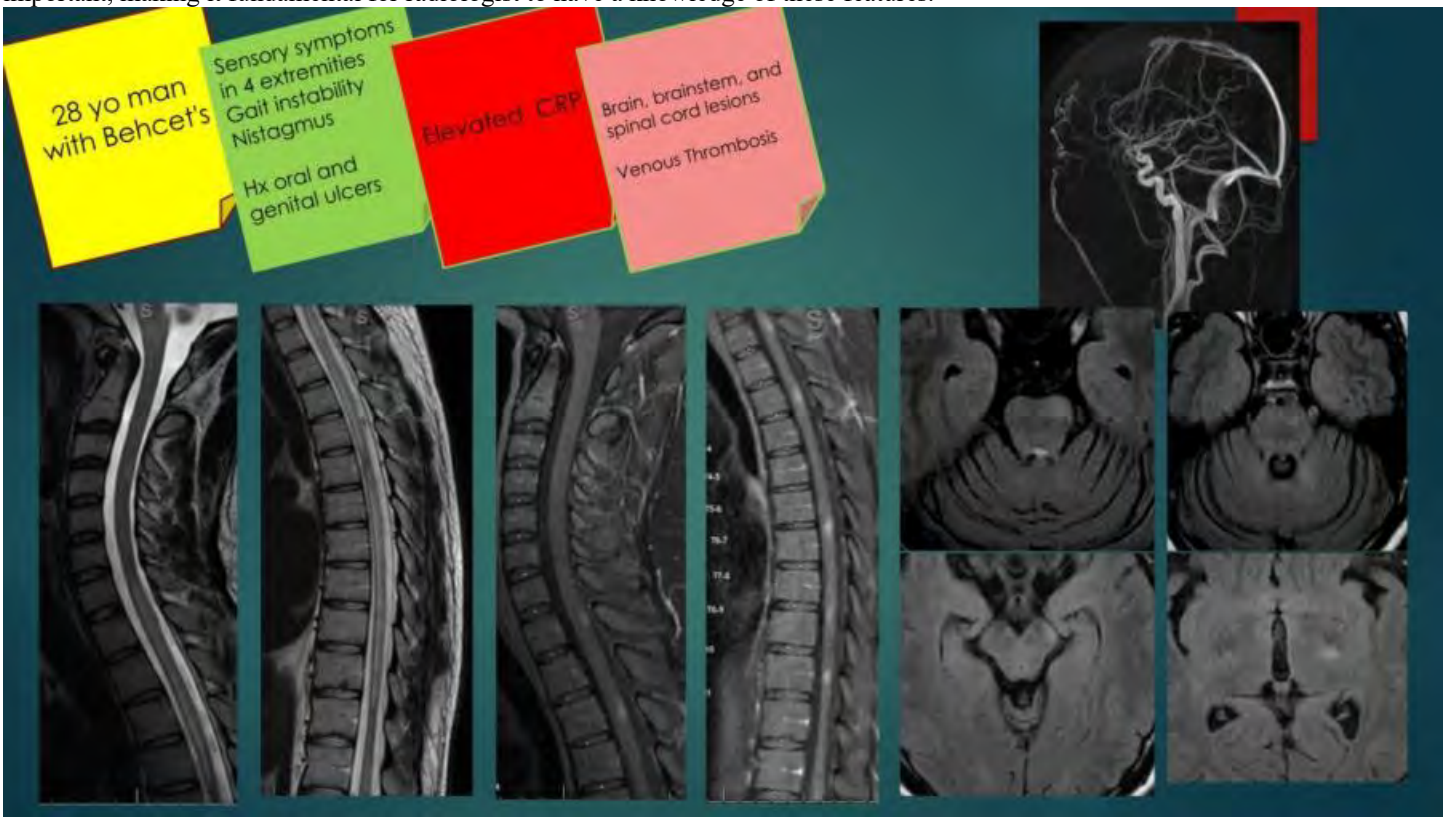

(Filename: TCT_1457_BehcetsCNSVasculitispptx2.jpg)

1525
Vertebral Body T1 Hypointense Marrow Signal. How to Solve a Frequent Diagnostic Dilemma?
A Honarmand[1]
[1]*Massachusetts General Hospital, Harvard Medical School, Boston, MA*

Summary and Objectives
Focal T1 hypointense signal within the spinal bone marrow is not an uncommon finding in routine neuroradiology practices. It can be a diagnostic puzzle as multiple benign and malignant lesions can overlap in demonstrating T1 hypointensity and therefore put the neuroradiologist and clinician in a dilemma for clinical decision making especially in certain groups of patients (1). A common approach to these lesions is offering more imaging examinations including different modalities depending on clinical setting and/or post-contrast T1-weighted images which does not necessarily lead to definitive characterization and appropriate follow-up or treatment planning.
Purpose
The purpose of the current educational exhibit is to provide case-based imaging review of variety of malignant and not-malignant entities demonstrating T1 hypointense signal with providing problem solving tips.
Materials and Methods
The educational contents of this review include: • Case-based review of non-malignant etiologies such as atypical hemangioma, infection, degenerative processes, trauma, metabolic related etiologies as well as malignant etiologies such as metastatic lesions, multiple myeloma, leukemia etc. • Useful imaging tips to differentiate benign versus malignant etiologies of T1 marrow hypointense

signal including location (vertebral body, endplate or posterior element involvement), morphology (ill-defined, well defined, geographic), distribution (diffuse, focal, multifocal), pattern of enhancement, and correlate helpful findings on other sequences or modalities. • Role of patient demographics, clinical history and associated medical conditions • Most appropriate and efficient additional imaging strategies and follow up

Results and Conclusions

Establishing appropriate knowledge and radiological skills to interpret and manage vertebral body T1 hypointense marrow signal are crucial for efficient clinical decision making and minimizing futile additional imaging follow up.

(Filename: TCT_1525_ASNR2.jpg)

574

Warning - May Cause Pain and Vision Loss! A Pictorial Review of Orbital Infections.

D Pinto[1], J Telleria-Cano[1], R Wang[1], G Saigal[1]

[1]Jackson Memorial Hospital/University of Miami, Miami, FL

Summary and Objectives

Orbital infections account for more than half of all primary orbital disease processes. These infections can affect any age group and may have severe, even life threatening, consequences if not properly diagnosed and promptly treated. Management is dependent on location and extent of infection and whether or not secondary complications have developed. Given the limitations of clinical history and physical examination upon patient presentation, imaging, most commonly cross-sectional, plays a key role in accurate diagnosis. Exposure to the distinct imaging findings of these entities will ensure the radiologist can make an appropriate diagnosis and ensure the patient receives proper care. In this exhibit, we will review relevant normal orbital anatomy on computed tomography (CT) and magnetic resonance (MR) imaging, the spectrum of orbital infections based on location with key distinguishing imaging features, potential complications, risk factors for infection as well as mimics of infection. Structure of the presentation: *List of educational objectives *Normal orbital anatomy on CT and MRI *Epidemiology *Represented cases from the database of two health systems include: 1. Evaluation and imaging findings based on location - Infection of the eyelid: Pre-septal cellulitis, Infection of the Meibomian gland. - Infection of the intra-conal and extra-conal space: Orbital cellulitis (bacterial, fungal and viral) - Infection of the globe: Endophthalmitis, Panophthalmitis - Lacrimal gland: Dacryoadenitis 2. Complications - Orbital abscess - Subperiosteal abscess - Ischemic optic neuropathy - Intracranial spread of infection including meningitis and abscess - Superior ophthalmic vein thrombosis - Cavernous sinus thrombosis 3. Risk Factors - Sinusitis - Foreign body - Trauma 4. Mimics of infection - Orbital Pseudotumor - Tumor (lymphoma) - Thyroid associated orbitopathy Educational Objectives: 1. Identify normal orbital anatomy on CT and MRI. 2. Describe CT and MR imaging findings of orbital infections based on location. 3. Recognize and differentiate mimics for orbital infections.

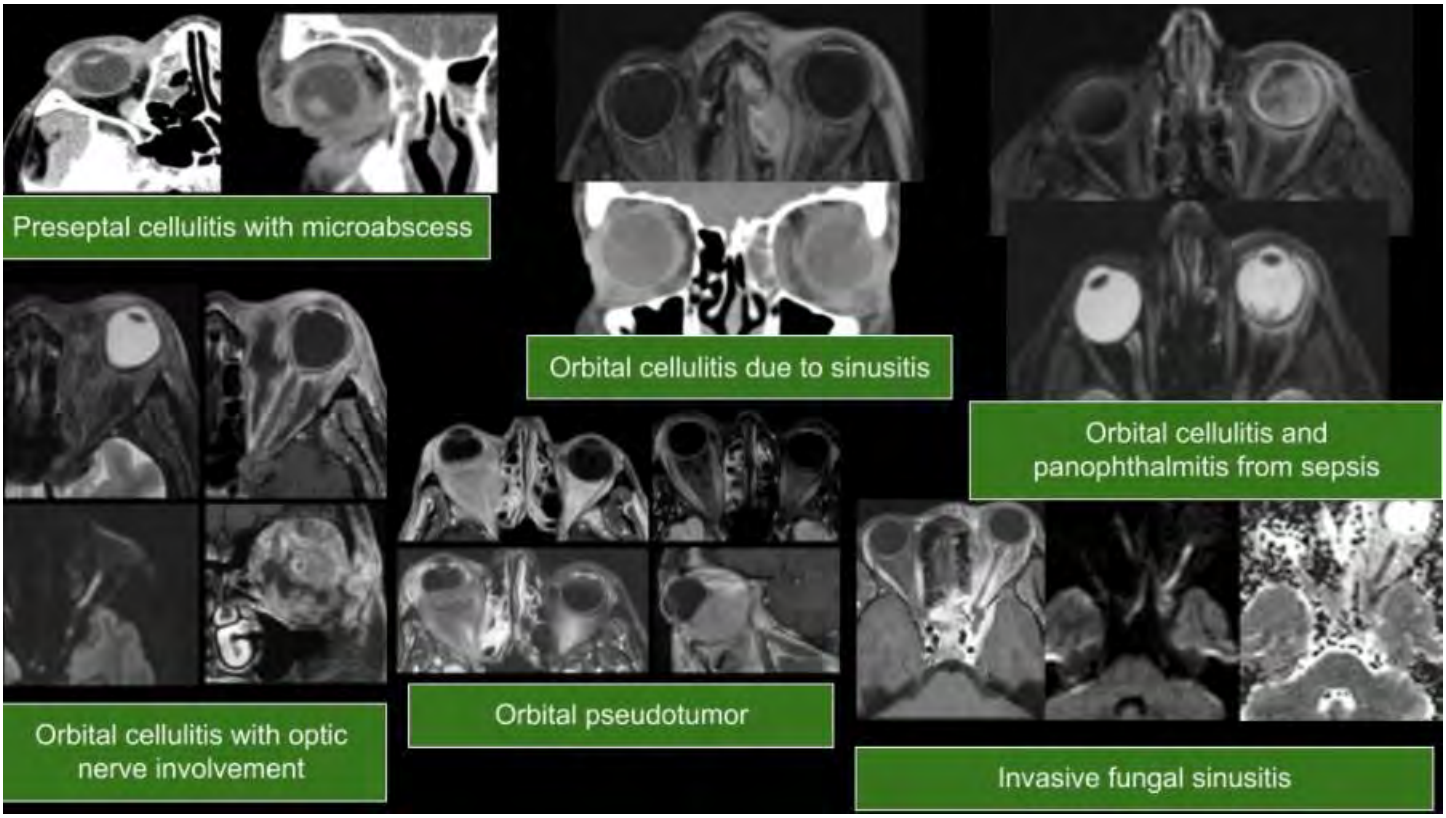

(Filename: TCT_574_Untitledpresentation.jpg)

780

Watch the Flow!: an Overview of Orbital Vascular Anomalies

N Matari[1], A Coombs[1], A Kassotis[1], M Kazim[1], A Lignelli[1]
[1]*Columbia University Irving Medical Center, New York, NY*

Summary and Objectives
Orbital vascular anomalies have typical appearances on imaging and correct diagnosis of these lesions predicates management and intervention decisions. This presentation will highlight differences and similarities among imaging findings of different orbital vascular anomalies, with emphasis on intra-lesional flow characteristics, to facilitate diagnosis. Cases presented will be correlated intraoperative and pathology findings.
Purpose
Orbital vascular anomalies are a group of discrete congenital vascular malformations with differential imaging appearances and flow characteristics. Management decisions are predicated upon correct diagnosis of these lesions on imaging. This presentation seeks to provide an overview of similarities and differences among these lesions, with specific emphasis on intra-lesional flow characteristics, to better delineate and facilitate diagnosis of these lesions for the radiologist. Orbital cavernous venous malformation, lymphangioma, venous varix, arteriovenous malformation, and arteriovenous fistula from adult populations will be reviewed utilizing CT/CTA and MRI/ MRA . Clinical scenarios will be highlighted and, when appropriate, pathology reviewed. This presentation will conclude with a brief juxtaposition of presented cases to leave viewers with a potent impression of similarities and differences among the different types of orbital vascular anomalies. Educational Objectives: • Recognize and differentiate vascular orbital anomalies on CT/MRI. • Understand how different intra-lesional flow characteristics of each lesion predicates appearance on contrast enhanced imaging and management and intervention decisions. • Cases will be correlated with pathology and intraoperative findings.
Materials and Methods
This presentation seeks to provide learners with an overview of known orbital vascular anomalies. Labeled CT and MRI images of orbital cavernous venous malformation, lymphangioma, venous varix, arteriovenous malformation, and arteriovenous fistula will be presented alongside commentary regarding their underlying pathophysiology and flow dynamics to enable learners to not only understand the differential appearances of the lesions, but also to understand how the differences in their underlying pathophysiology predicates their appearance on imaging. This exhibit will enable learners to better recognize and understand the etiology of orbital vascular anomalies.

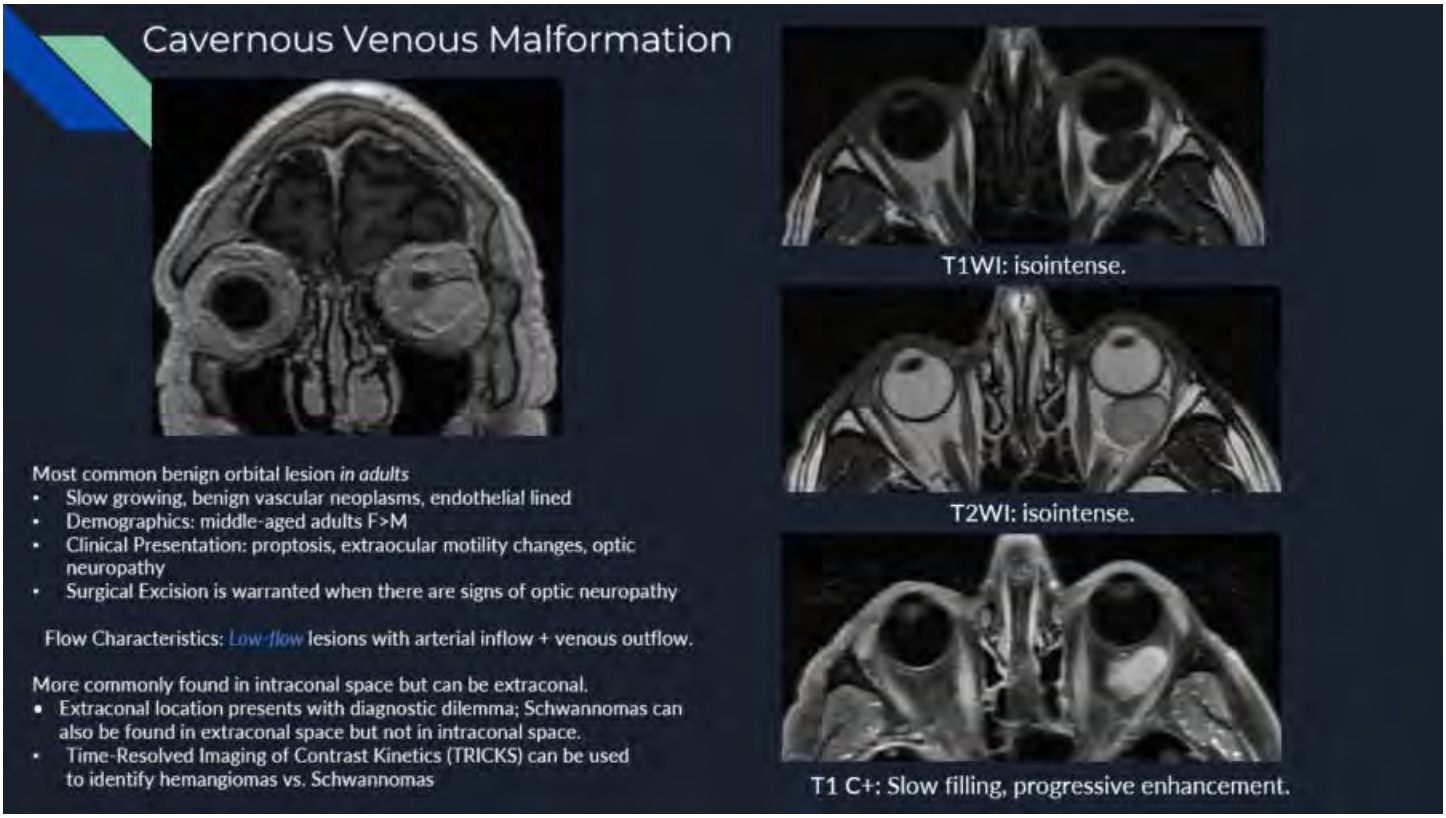

(Filename: TCT_780_VascularAnomaliesSlide.jpg)

1190

What is this bump in my face? CT and MRI review of pediatric sinonasal masses.

G Shadmani[1], A Vossough[2], H Dahmoush[3]

[1]Mallinckrodt Institute of Radiology, Saint louis, MO, [2]CHOP-UPENN, Philadelphia, PA, [3]Stanford University, Stanford, CA

Summary and Objectives

Pediatric sinonasal tumors are uncommon and can be benign or malignant in nature. These tumors have distinct epidemiologic, clinicopathologic, and prognostic differences compared with adult sinonasal tumors. The early symptoms of sinonasal tumors are similar to rhinosinusitis with runny nose, lacrimation and epistaxis and therefore the diagnosis is often delayed because of these non-specific symptoms. Most cases are diagnosed at an advanced disease stage. While in adult population, malignant tumors arising from epithelial cell origin including squamous cell carcinoma, minor salivary gland tumor, and adenocarcinoma are common entities, in children, on the other hand, mesenchymal tumors(sarcoma) arising from the supporting tissue and lymphomas are more common. Familiarity of radiologists with these uncommon tumors in pediatric age group increases the index of suspicion that is critical for a timely diagnosis and treatment. The aim of this article is to describe the characteristic findings of the tumors and tumor mimics arising from paranasal sinuses, many of which are unique to the pediatric populations.

Purpose

Our aim is to provide a practical diagnostic approach based on the unique and common radiological findings of pediatric sinonasal tumors. We devided pediatric sinonasal tumors into four groups. These include: 1. Benign neoplasms (Juvenile Nasopharyngeal Angiofibroma, Olfactory neuroblastoma, Desmoplastic Fibroma, Melanotic Neuroectodermal Tumor of Infancy); 2. Primary malignant tumors (Rhabdomyosarcoma, Ewing Sarcoma, Osteosarcoma); 3. Metastatic malignant neoplasms (Metastatic neuroblastoma, Leukemia, Lymphoma); 4. Tumor mimics (Lobular Capillary Hemangioma, Nasal Glioma, Giant Cell Granuloma). Each entities' unique imaging and clinical features will be discussed.

Materials and Methods

All examples in our case collection had pathologically or clinically proven diagnoses and were selected from the Electronic Medical Record of three referral children hospital centers.

Results and Conclusions

Sinonasal tumors are uncommon in children. We hope our imaging review and description of salient radiologic features will help radiologists expand their basic understanding and awareness of the discussed disease entities.

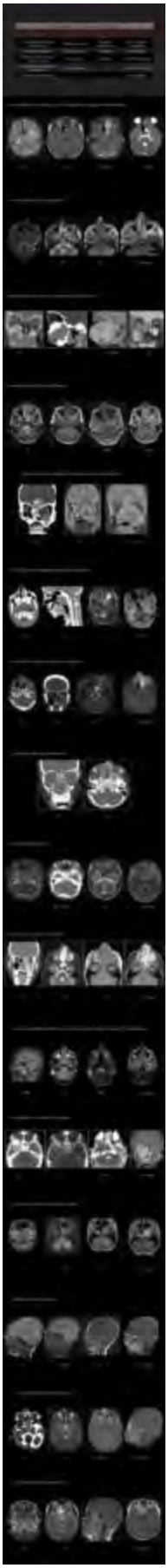

(Filename: TCT_1190_merge_from_ofoct.jpg)

783

When It's Not "Just a Nosebleed" -- Diagnosis and Management of Epistaxis Emergencies

S Szczesniak[1], V Tiwari[1], J Corrigan[1], B Griffith[1], H Marin[1]
[1]*Henry Ford Health, Detroit, MI*

Summary and Objectives
Otolaryngological emergencies, particularly epistaxis, can be catastrophic. In those cases, a quick diagnosis and prompt treatment can be lifesaving. While most epistaxis episodes arise from the anterior nasal cavity and are treated with conservative management, about 5% of epistaxis arise from the posterior nasal cavity and often require further evaluation and treatment. Angiography is essential in the management of posterior nasal cavity epistaxis emergencies to detect an uncommon underlying vascular abnormality and/or potentially dangerous anatomical variants, including external and internal carotid artery anastomoses. Angiography is often followed by endovascular treatment, usually with embolization. Upon completion of this educational exhibit, the learner will become familiar with the various imaging features of the etiologies of epistaxis, including the relevant vascular head and neck anatomy and treatment strategies.
Purpose
The purpose of the exhibit is to provide a pictorial review of the imaging features of various etiologies of epistaxis, in addition to illustrating the relevant vascular head and neck anatomy and case-based treatment strategies.
Materials and Methods
• Review the various etiologies of epistaxis, including spontaneous (Fig. 1), post-nasal/endoscopic surgery (Fig. 2), and sinus pathology (Fig. 3). • Review the common imaging features of the etiologies of epistaxis on CT, CTA, and DSA images. • Review the vascular anatomy of the nose and paranasal sinuses. • Review case-based treatment strategies with each case of epistaxis presented.
Results and Conclusions
Epistaxis can be an otolaryngological emergency. The approach to the patient with an epistaxis emergency is done in close collaboration with the otolaryngological surgeon and, after base life support, airway security, and hemodynamic resuscitation, in addition to endoscopic diagnosis and treatment, neuroimaging diagnosis and endovascular treatment is usually the main clinical strategy. By understanding the relevant head and neck anatomy in the setting of various etiologies of epistaxis emergencies, radiologists are best able to tailor treatment strategies that may influence overall patient prognosis.

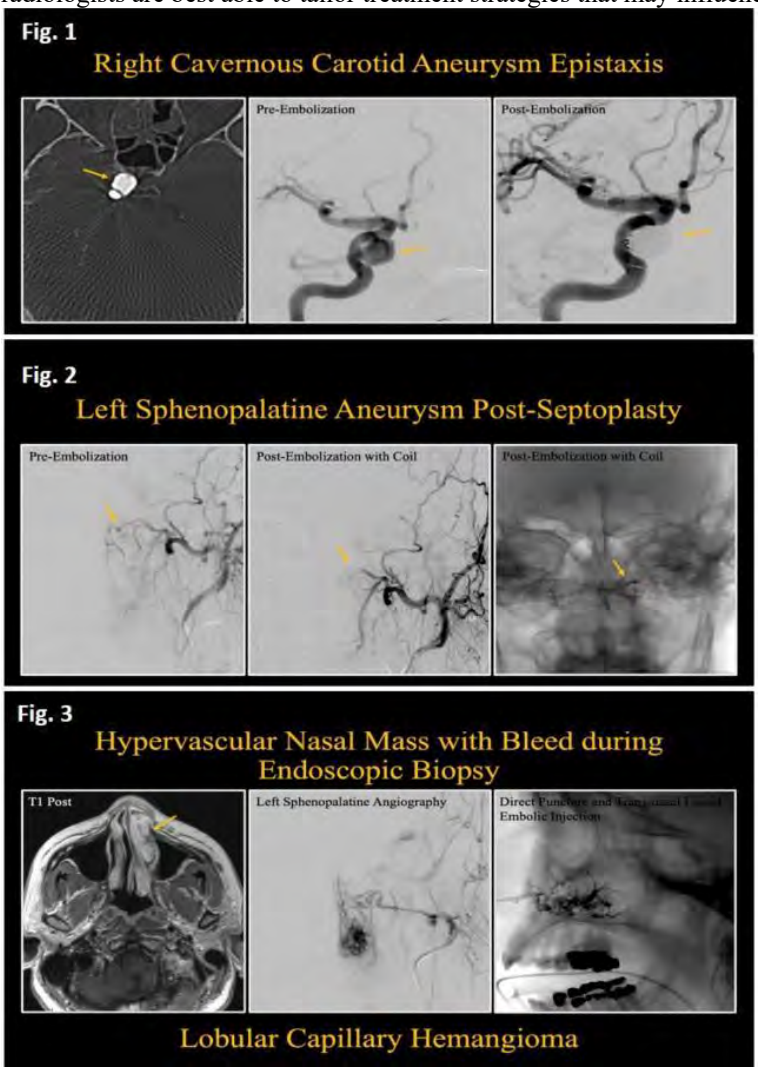

(Filename: TCT_783_Figure.jpg)

636

Which Is The Abnormal Side? A Diagnostic Approach of Cerebral Asymmetry

S Siala[1], C Guimaraes[2]
[1]UNC Hospital, Carrboro, NC, [2]University of North Carolina, Chapel Hill, NC

Summary and Objectives
Summary: Cerebral hemispheric asymmetry is a known physiological entity that has been studied from both functional and anatomical perspectives and has been recognized as a normal variant by anatomists, anthropologists, neurologists and radiologists. Beyond this physiologic entity, abnormal cerebral asymmetry encompasses a wide spectrum of etiologies. Knowing the clinical presentation is of great importance when assessing neuroimaging studies. This pattern can be the result of a heterogeneous spectrum of neurological diseases. The affected brain hemisphere is most commonly the smaller side, resulting in volume loss/hemiatrophy, or less commonly the bigger side, in cases of hemimegalencephaly or unilateral cerebral edema. Cerebral asymmetry etiologies are classically grouped into two broad categories: congenital and acquired. The congenital group arises from genetic mutations or in-utero insults which may result in either lack of cerebral development or overgrowth in cases of hemimegalencephaly. The acquired causes are often a consequence of postnatal insult, most commonly vascular. Various diseases processes can lead to abnormal asymmetry of one cerebral hemisphere, with very different pathophysiological mechanisms. These conditions include, but are not limited to, vascular insult (ischemic or hemorrhagic), Rasmussen encephalitis, Sturge Weber syndrome, Dyke-Davidoff-Masson syndrome, hemiconvulsion-hemiplegia-epilepsy (HHE) syndrome, hemimegalencephaly and asymmetric hemispheric involvement of malformations of cortical development. Many of the above-mentioned diseases can show overlapping neuroimaging findings. However, some key typical imaging findings can be recognized and may narrow down the differential diagnosis, especially when considering crucial clinical findings. Educational objectives: Illustrate etiologies of cerebral asymmetry (case-based approach). Describe distinguishing imaging patterns leading to specific etiologic diagnosis.

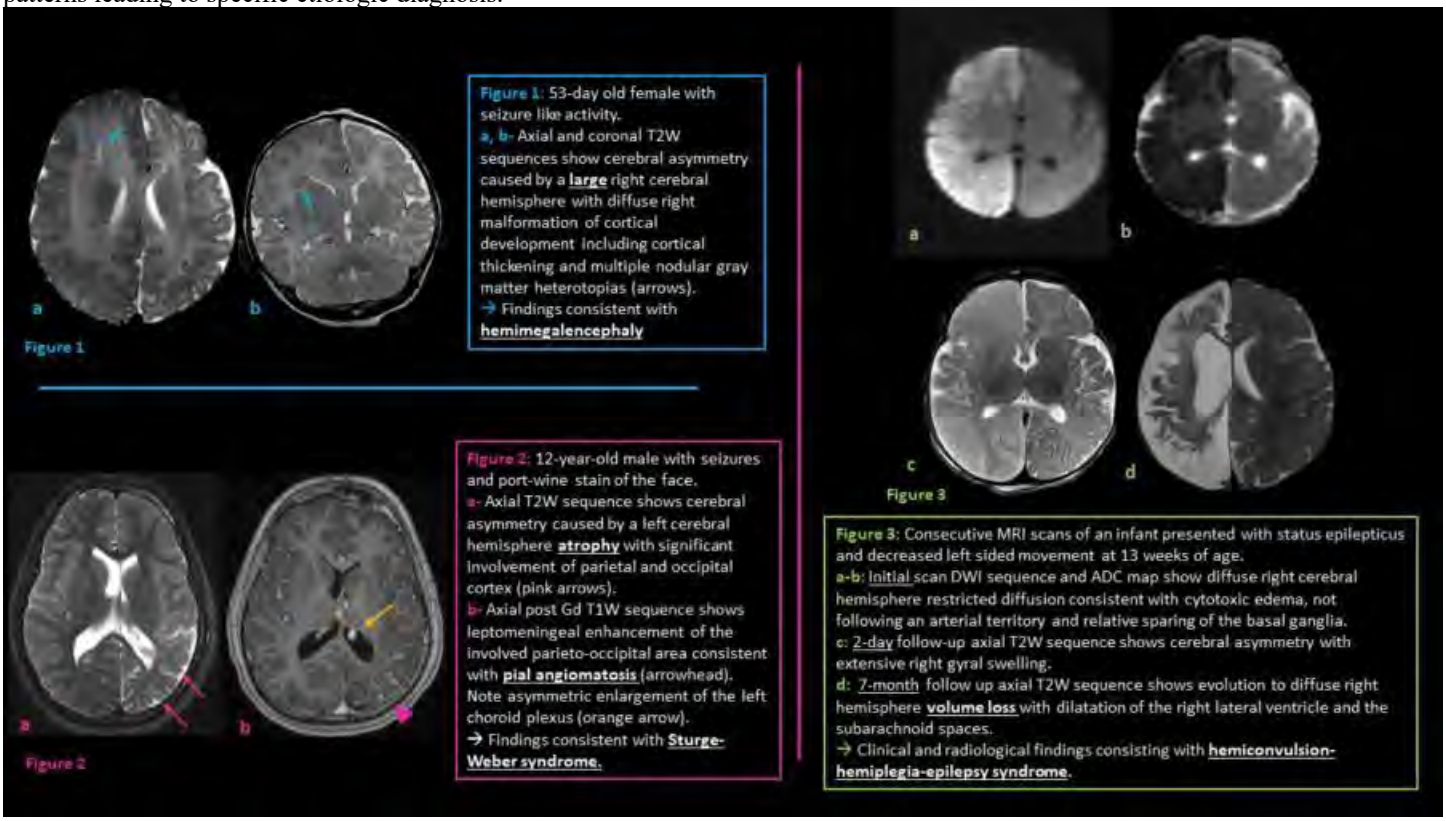

(Filename: TCT_636_Cerebralasymmetryimagefile.jpg)

442

Why Are You Making That Face? An Interactive Midface Fracture Learning Module

D Paul[1], E Smith[1]
[1]University of Maryland Medical Center, Baltimore, MD

Summary and Objectives
Educational Objectives 1) Improve understanding of midface fractures amongst radiology trainees via an image-rich document and a series of interactive, annotated real world cases. 2) Identify the subunits that comprise the classically described Le Fort fractures. 3) Apply the Zingg and Markowitz-Manson classifications for ZMC and NOE fractures, in order to improve multidisciplinary communication. Summary Midface fractures are often considered a challenging topic amongst radiology trainees. Although many excellent text-based, image-rich resources are available to improve understanding of midface fractures, it can be difficult to apply

those concepts at the workstation, particularly when evaluating a time-sensitive CT scan of a trauma patient. Further, articles and textbooks often provide a great amount of detail. While these details are important to understand and provide context for these injuries and their treatment, they can also be overwhelming for trainees looking for an introduction to midface fracture patterns. To address these challenges, we have developed a module consisting of two components. First, we have created an image-rich, cloud-based document utilizing Google Docs (Google, Mountain View, CA, docs.google.com) that summarizes salient points from several resources regarding midface anatomy and fracture evaluation. Second, we have compiled a series of annotated cases in Pacsbin (Orion Medical Technologies, Baltimore, MD, pacsbin.com), a cloud-based DICOM viewer, that allows for application of concepts presented in the aforementioned document. All cases include axial, coronal, and sagittal images, as well as 3D reconstructed images. Additionally, all cases are fully scrollable with windowing/leveling capabilities, similar to working on a PACS workstation. Annotations can be toggled on and off, so trainees may test their understanding of fracture patterns against the final diagnosis made by an attending radiologist. Please find a sample case here: https://www.pacsbin.com/c/byL1oxDFn_ Compared to static images seen in articles and textbooks, an interactive module provides trainees with the opportunity to evaluate complex cases as they would at the workstation. This provides trainees the time to digest concepts and apply them, prior to evaluating a trauma case in real time. An additional benefit to our cloud-based approach is that additional annotated cases may be added as they are encountered in real time.

Figure 1: A portion from the cloud-based document summarizing the findings and classification of ZMC fractures with an associated image from "Multidetector CT of Midfacial Fractures: Classification Systems, Principles of Reduction, and Common Complications" published in Radiographics in 2018 by Dreizin D, et al.

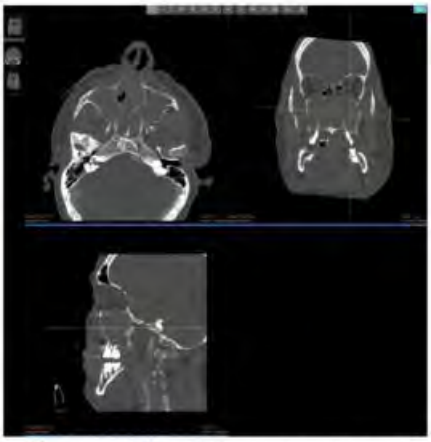

Figure 2: Pacsbin, a web based DICOM viewer, allows trainees to evaluate cases as if they were at a PACS workstation. Cases are fully scrollable, can be windowed/leveled, and include multiple planes.

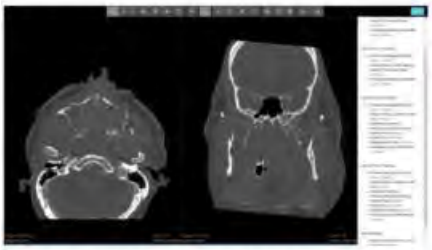

Figure 3: Annotations highlight the important findings in each fracture pattern present, often on multiple planes.

Figure 4: Annotations are also provided for 3D reconstructed images to help trainees better conceptualize the fracture patterns.

(Filename: TCT_442_AbstractFigures.jpg)

1518

Why Eye See Double: One and a Half Syndrome Explained.

A Silberzweig[1], J Junn[1], M Konner[2], A Khorsandi[3]

[1]Mount Sinai Hospital Icahn School of Medicine, NYC, NY, [2]Mt. Sinai West, New York, NY, [3]New York Eye and Ear Infirmary of Mount Sinai, New York, NY

Summary and Objectives

Case-based pictorial and educational review of presentations of 'One and a half syndrome' which will aid in efficient diagnosis, interpretation, and clinical management.

Purpose

One and a half syndrome is characterized by ipsilateral conjugate horizontal gaze palsy in one direction and ipsilateral internuclear ophthalmoplegia. The diagnosis of one and half syndrome relies on distinctive clinical presentation, neuroanatomy, and imaging features. Common etiologies include ischemic events, demyelinating diseases, arteriovenous malformations, and brainstem malignancies. Rapid diagnosis is crucial to optimal management and atypical presentations may confound or delay diagnosis.

Materials and Methods

Our presentation obtains clinical data from the electronic medical record including initial presenting signs and symptoms, suspected alternate diagnoses, clinical confounders, as well as clinical course and interventions. Illustrative imaging include CT and MRI modalities.

Results and Conclusions

Our review highlights varying etiologies of One and a half syndrome including malignancy, stroke, and autoimmune disorders. Associated ophthalmologic abnormalities are linked to imaging findings. Our goal is to emphasize the classical imaging and ophthalmologic physical exam findings of one and a half syndrome in order to swiftly diagnose and avoid delays in time sensitive intervention and adverse patient outcomes. Focus will be placed on the critical role Radiologists have in recognizing and assisting clinicians towards an accurate diagnosis.

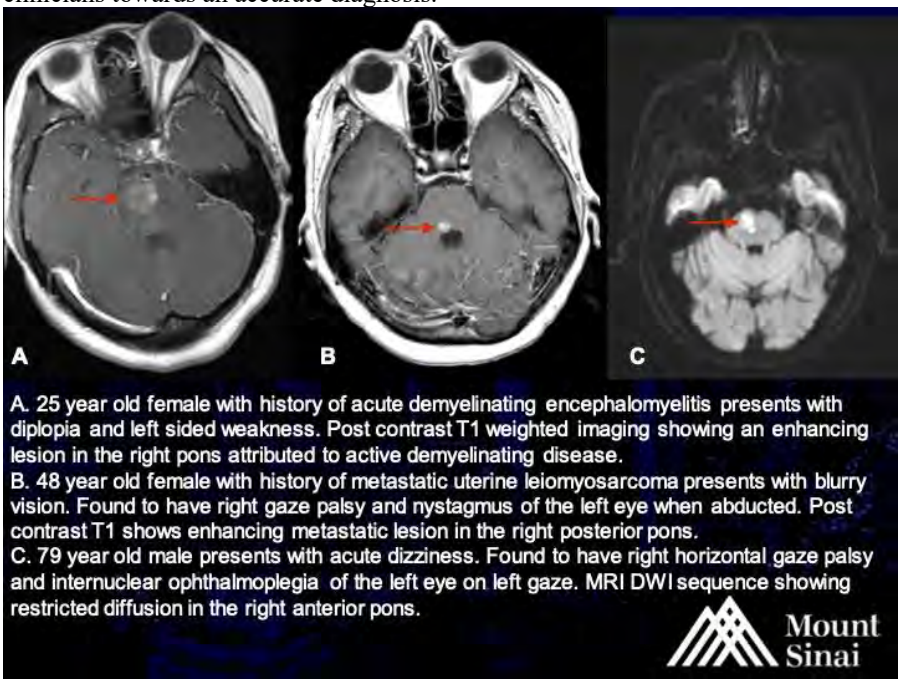

(Filename: TCT_1518_15syndrome.jpg)

477

Why the Headache and Confusion? MR Imaging, Dynamic CT and Fluoroscopic Imaging, and Treatment of Spontaneous Intracranial Hypotension - A Structured Approach.

C Tournade[1], Z Wilseck[2], T Moritani[1], J Kim[1]

[1]University of Michigan, Ann Arbor, MI, [2]UNIVERSITY OF MICHIGAN HEALTH SYSTEMS, CANTON, MI

Summary and Objectives

Identify intracranial and spinal imaging findings of spontaneous intracranial hypotension. Recognize the algorithmic approach for diagnosing spontaneous intracranial hypotension. Understand the different methods and indications for dynamic and conventional CT myelogram and lateral decubitus digital subtraction myelography. Recognize the various types of CSF leaks. Understand the treatment options of spontaneous intracranial hypotension.

Purpose

Spontaneous intracranial hypotension is caused by CSF leakage through the dural membrane. This can contribute to debilitating

symptoms for patients, most characteristically presenting as a positional headache. Utilizing a systematic approach for the diagnosis and management of these patients is important in order to more quickly diagnose and localize these dural leaks to further patient management. It is important to be aware of the intracranial and spinal imaging findings associated with intracranial hypotension and their significance. Additionally, knowing the indications and procedural options used to identify and localize CSF leaks is important for the neuroradiologist. Diagnostic myelographic work-up depends on whether an extradural fluid collection is or is not identified which informs when to order a dynamic or conventional CT myelogram and ultimately when to perform lateral decubitus digital subtraction myelography. Through this presentation, we will present a structured approach for the diagnosis and management of spontaneous intracranial hypotension. Relevant imaging findings, the indications for the various diagnostic procedures, how they are performed, and the findings to evaluate for will be presented. Improved awareness and knowledge of the diagnosis and management of CSF leaks will assist with improving patient care.
Materials and Methods
Representative cases and images were retrieved from the University of Michigan imaging archives to illustrate findings of spontaneous intracranial hypotension, methods of diagnosis, and treatment.
Results and Conclusions
Spontaneous intracranial hypotension can be a cause of debilitating symptoms. It is important to be aware of the imaging findings, methods of identification, and management of the causal CSF leak. Knowledge of the structured algorithmic approach for diagnosis and management of spontaneous intracranial hypotension, and increased awareness of how different procedures are performed and their indications, will assist in expediting patient care and allow for faster treatment and relief of patients' symptoms.


Figure 1. Axial T2W imaging shows a large ventral T2 hyperintense epidural collection.

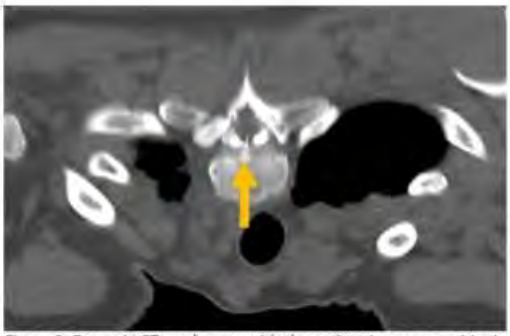
Figure 2. Dynamic CT myelogram with the patient in prone positioning shows focal extravasation of contrast into the epidural collection at T1-T2, identifying the level of the leak.


Figure 3. Right lateral decubitus digital subtraction myelography shows layering contrast with opacification of a cranially extending vessel, diagnostic of a CSF-venous fistula.

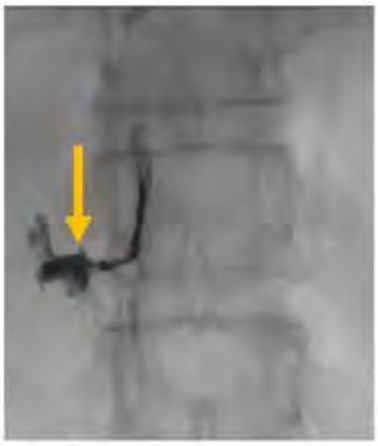
Figure 4. Digital subtraction angiography in a different patient shows post-treatment onyx embolization of a CSF-venous fistula.

(Filename: TCT_477_Slide1.JPG)

1229

'Touch me not!': An Overview Of Must-Know Eloquent Cortical Areasessential For Optimal Neurosurgical Planning.

A Vijan[1], A Sahu[2]
[1]Tata Memorial Hospital, MUMBAI, MAHARASHTRA, [2]Tata Memorial Hospital, Mumbai, MAHARASHTRA

Summary and Objectives
Eloquent brain regions control identifiable neurological functions and lead to neuro-deficit if injured/involved during resection. fMRI is a pre-operative tool utilised to assess for relation between operative site and areas of cortical eloquence. Accurate anatomic knowledge is crucial to appropriately elicit and interpret BOLD signal activations during task-based studies. We discuss the primary motor cortex (hand, foot, lips/orofacial) along with supplementary motor area with case-based examples.
Purpose
To review functional neuroanatomy and currently accepted functional rolesof important eloquent motor and language control areas of the cerebral cortex, with emphasis on neurosurgical relevance.
Materials and Methods
We present with the help of illustrations and fMRI cases the functional anatomy of various eloquent cortical areas governing motor and language control. Their variants and laterality along with presently postulated functions are also reviewed. With the advent of

newer functional brain mapping techniques such as tractography, our understanding of neural substrates of language has grown from a localizationist approach to a hodological or connectome-based idea, comprising the Dorsal and Ventral streams. We briefly review this novel neuroscientific concept, focusing on anticipated functional neuroanatomy of the nodal 'hubs' in these connectome based pathways. The most important of these include the ventral pre-motor cortex (vPMC) which shows maximum correspondence with intra-operative anarthria, the Broca's, and the Wernicke's areas among others.
Results and Conclusions
In-depth and updated functional neuroanatomic knowledge of important eloquent areas is essential to discern the precise inter-relationships between lesions and major areas of cortical eloquence. This in turn contributes to good surgical planning and positive postoperative outcomes.

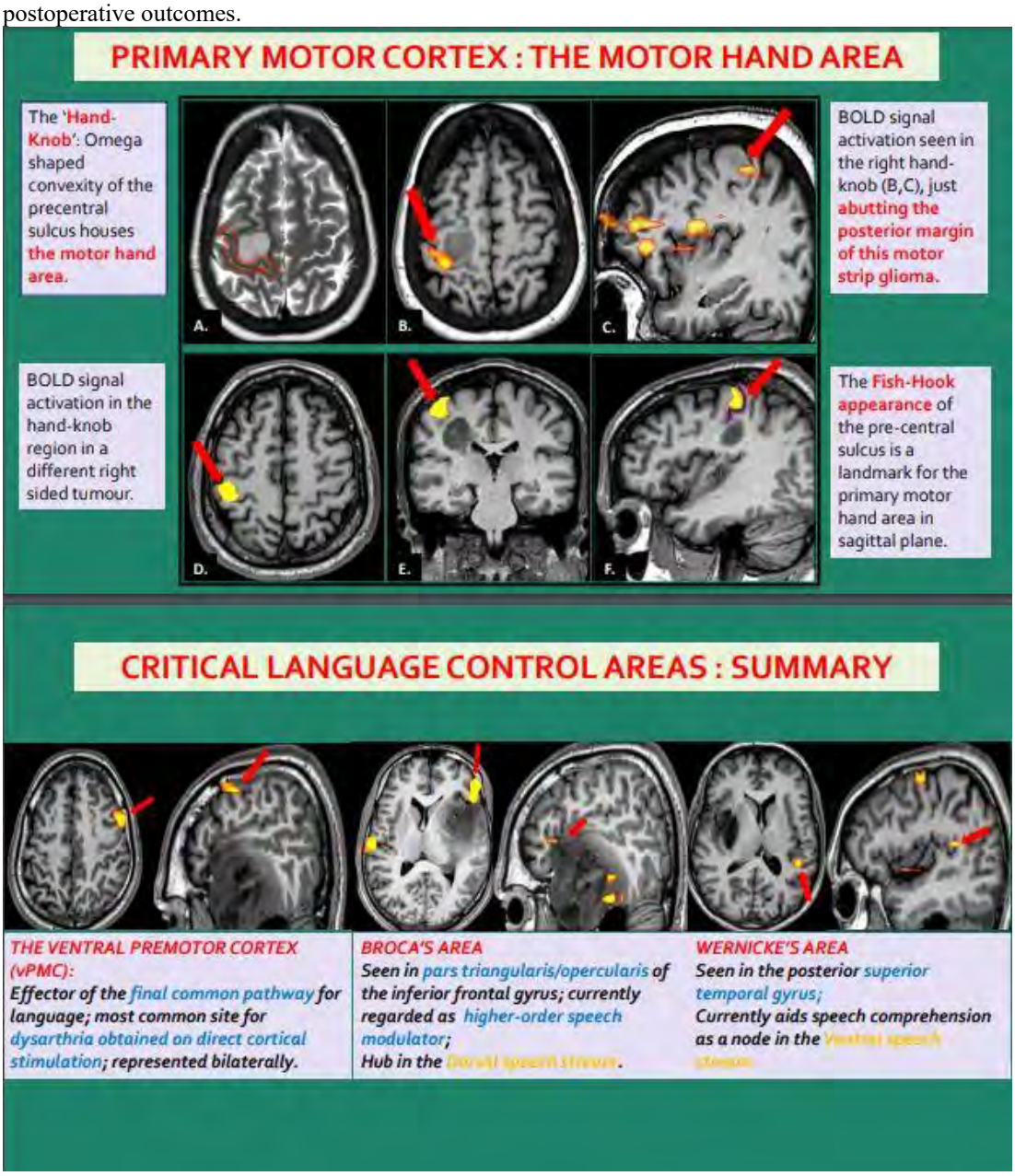

(Filename: TCT_1229_TOUCH.JPG)

785
"How much worse can it get?" -- Diagnosis and Management of Nontraumatic Head and Neck Otolaryngological Vascular Emergencies
S Szczesniak[1], V Tiwari[1], J Corrigan[1], B Griffith[1], H Marin[1]
[1]*Henry Ford Health, Detroit, MI*

Summary and Objectives
Head and neck otolaryngological vascular emergencies are often life-threatening situations that require escalation from conservative management to angiographic intervention. The most common etiology of head and neck hemorrhage is head and neck cancer due to a variety of causes, including spontaneous tumor hemorrhage, recurrent cancer, carotid blow-out, vascular erosion from tumor invasion, infection, radiation necrosis, and anastomotic dehiscence. Upon completion of this educational exhibit, the learner will become

familiar with the various imaging features of the etiologies of head and neck vascular emergencies, including the relevant vascular head and neck anatomy and treatment strategies.

Purpose

The purpose of this exhibit is to provide a pictorial review of the imaging features of various etiologies of head and neck vascular emergencies, in addition to illustrating relevant vascular head and neck anatomy and case-based treatment strategies.

Materials and Methods

• Review the various etiologies of head and neck vascular emergencies, including head and neck cancer and post-surgical complications (Figs. 1-3). • Review the common imaging features of the etiologies of head and neck vascular emergencies on CT, CTA, DSA, and MR images. • Review the relevant vascular head and neck anatomy and case-based treatment strategies with each case of head and neck vascular emergency discussed.

Results and Conclusions

Head and neck hemorrhage is an otolaryngological emergency. The approach to the patient with a head and neck hemorrhage is done in close collaboration with the otolaryngological surgeon. After basic life support, airway security, and hemodynamic resuscitation, in addition to endoscopic diagnosis and treatment, neuroimaging diagnosis and endovascular treatment is usually the main clinical strategy. By understanding the relevant head and neck anatomy in the setting of various etiologies of head and neck hemorrhages, radiologists are best able to tailor treatment strategies that may influence overall patient prognosis.

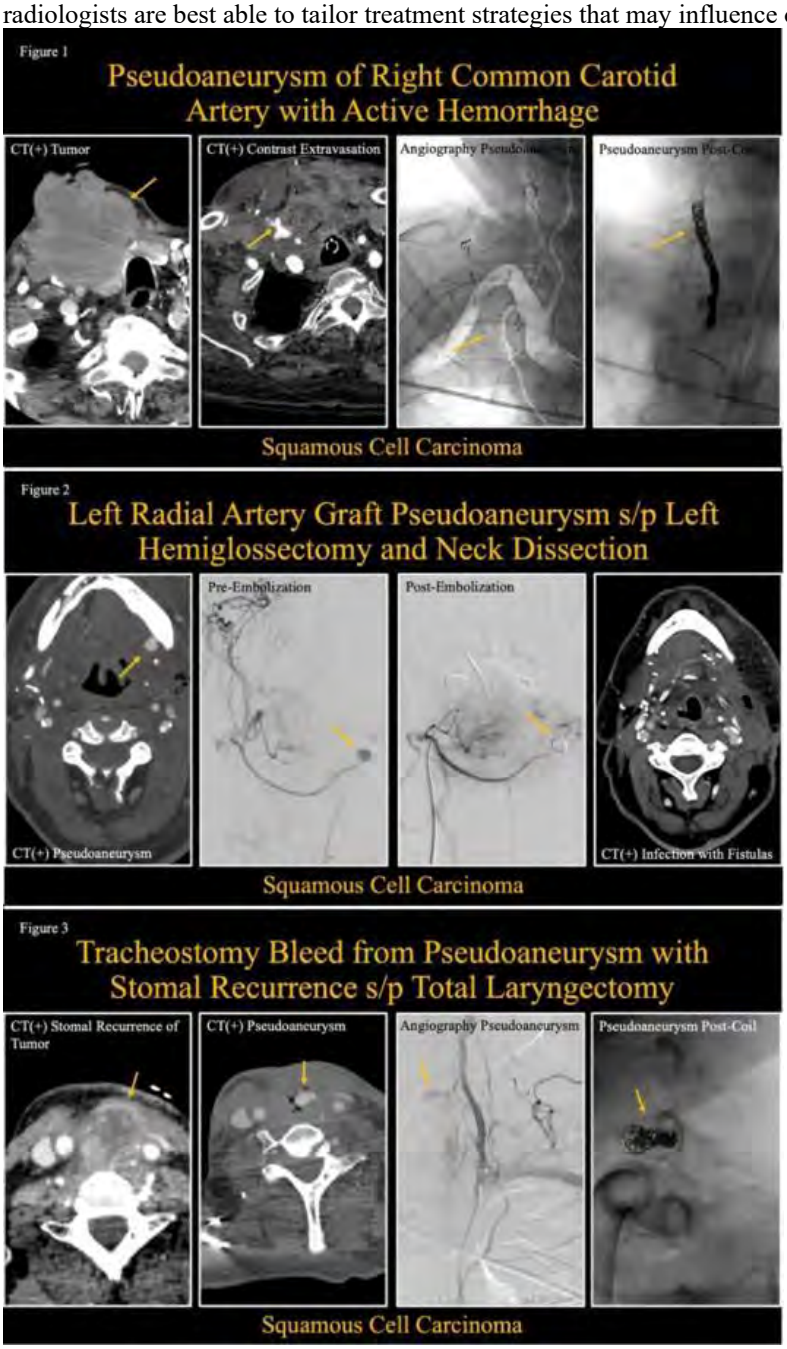

(Filename: TCT_785_Figure.jpg)